

Materials Science of Membranes for Gas and Vapor Separation

Materials Science of Membranes for Gas and Vapor Separation

Edited by

Yuri Yampolskii

*A. V. Topchiev Institute of Petrochemical Synthesis, Russian Academy of
Sciences, Moscow, The Russian Federation*

Ingo Pinnau

Membrane Technology and Research Inc., Menlo Park, California, USA

Benny Freeman

The University of Texas at Austin, Austin, Texas, USA



John Wiley & Sons, Ltd

Copyright © 2006 John Wiley & Sons Ltd, The Atrium, Southern Gate, Chichester,
West Sussex PO19 8SQ, England

Telephone (+44) 1243 779777

Email (for orders and customer service enquiries): cs-books@wiley.co.uk
Visit our Home Page on www.wileyeurope.com or www.wiley.com

All Rights Reserved. No part of this publication may be reproduced, stored in a retrieval system or transmitted in any form or by any means, electronic, mechanical, photocopying, recording, scanning or otherwise, except under the terms of the Copyright, Designs and Patents Act 1988 or under the terms of a licence issued by the Copyright Licensing Agency Ltd, 90 Tottenham Court Road, London W1T 4LP, UK, without the permission in writing of the Publisher. Requests to the Publisher should be addressed to the Permissions Department, John Wiley & Sons Ltd, The Atrium, Southern Gate, Chichester, West Sussex PO19 8SQ, England, or emailed to permreq@wiley.co.uk, or faxed to (+44) 1243 770620.

Designations used by companies to distinguish their products are often claimed as trademarks. All brand names and product names used in this book are trade names, service marks, trademarks or registered trademarks of their respective owners. The Publisher is not associated with any product or vendor mentioned in this book.

This publication is designed to provide accurate and authoritative information in regard to the subject matter covered. It is sold on the understanding that the Publisher is not engaged in rendering professional services. If professional advice or other expert assistance is required, the services of a competent professional should be sought.

Other Wiley Editorial Offices

John Wiley & Sons Inc., 111 River Street, Hoboken, NJ 07030, USA

Jossey-Bass, 989 Market Street, San Francisco, CA 94103-1741, USA

Wiley-VCH Verlag GmbH, Boschstr. 12, D-69469 Weinheim, Germany

John Wiley & Sons Australia Ltd, 42 McDougall Street, Milton, Queensland 4064, Australia

John Wiley & Sons (Asia) Pte Ltd, 2 Clementi Loop #02-01, Jin Xing Distripark, Singapore 129809

John Wiley & Sons Canada Ltd, 22 Worcester Road, Etobicoke, Ontario, Canada M9W 1L1

Wiley also publishes its books in a variety of electronic formats. Some content that appears in print may not be available in electronic books.

Library of Congress Cataloging-in-Publication Data

Materials science of membranes for gas and vapor separation/[edited by]

Yuri Yampolski, Ingo Pinnau, Benny Freeman.

p. cm.

Includes bibliographical references and index.

ISBN-13: 978-0-470-85345-0 (acid-free paper)

ISBN-10: 0-470-85345-X (acid-free paper)

1. Membrane separation. 2. Gas separation membranes. 3. Pervaporation.

4. Polymers—Transport properties. I. Yampol'skii, Yu. P. (Yuri P.) II.

Pinnau, I. (Ingo) III. Freeman, B. D. (Benny D.)

TP248.25.M46M38 2006

660'.2842—dc22

2005034536

British Library Cataloguing in Publication Data

A catalogue record for this book is available from the British Library

ISBN-10 0-470-85345-X

ISBN-13 978-0-470-85345-0

Typeset in 9/11 pt Times by Thomson Press (India) Limited, New Delhi, India

Printed and bound in Great Britain by Antony Rowe, Chippenham, Wiltshire

This book is printed on acid-free paper responsibly manufactured from sustainable forestry in which at least two trees are planted for each one used for paper production.

Contents

Contributors	xiii
Preface	xvii
1 Transport of Gases and Vapors in Glassy and Rubbery Polymers	1
<i>Scott Matteucci, Yuri Yampolskii, Benny D. Freeman and Ingo Pinnau</i>	
1.1 Background and Phenomenology	1
1.2 Effects of Gas and Polymer Properties on Transport Coefficients	7
1.2.1 <i>Effect of Gas Properties on Solubility and Diffusivity</i>	7
1.2.2 <i>Effect of Polymer Properties on Transport Parameters</i>	14
1.3 Effect of Pressure on Transport Parameters	18
1.3.1 <i>Sorption</i>	18
1.3.2 <i>Diffusion</i>	22
1.3.3 <i>Permeability</i>	22
1.3.4 <i>Selectivity</i>	22
1.4 Effect of Temperature on Transport Parameters	30
1.5 Structure/Property Relations	31
1.5.1 <i>Connector Groups</i>	35
1.5.2 <i>CF₃ and Other Fluorinated Moieties as Side-chains</i>	36
1.5.3 <i>Polar and Hydrogen Bonding Side-chains</i>	36
1.5.4 <i>Para versus Meta Linkages</i>	37
1.5.5 <i>Cis/Trans Configuration</i>	37
1.6 Conclusions	38
References	40
2 Principles of Molecular Simulation of Gas Transport in Polymers	49
<i>Doros N. Theodorou</i>	
2.1 Introduction	49
2.2 Generating Model Configurations for Amorphous Polymers	50
2.2.1 <i>Models and Force Fields</i>	50
2.2.2 <i>Molecular Mechanics</i>	52
2.2.3 <i>Molecular Dynamics</i>	52
2.2.4 <i>Monte Carlo</i>	53
2.2.5 <i>Coarse-graining Strategies</i>	54
2.2.6 <i>Generating Glasses from Melts</i>	55
2.3 Validating Model Amorphous Polymer Configurations	57
2.3.1 <i>Thermodynamic Properties</i>	57
2.3.2 <i>Molecular Packing</i>	58
2.3.3 <i>Segmental Dynamics</i>	59
2.3.4 <i>Accessible Volume and its Distribution</i>	61

2.4	Prediction of Sorption Equilibria	64
2.4.1	<i>Sorption Thermodynamics</i>	64
2.4.2	<i>Calculations of Low-pressure Sorption Thermodynamics</i>	67
2.4.3	<i>Calculations of High-pressure Sorption Thermodynamics</i>	68
2.4.4	<i>Ways to Overcome the Insertion Problem</i>	70
2.5	Prediction of Diffusivity	72
2.5.1	<i>Statistical Mechanics of Diffusion</i>	72
2.5.2	<i>Self-diffusivities from Equilibrium Molecular Dynamics</i>	73
2.5.3	<i>Diffusivities from Nonequilibrium Molecular Dynamics</i>	74
2.5.4	<i>Diffusion in Low-temperature Polymer Matrices as a Sequence of Infrequent Penetrant Jumps</i>	75
2.5.5	<i>Gusev–Suter TST Method for Polymer Matrices Undergoing Isotropic ‘Elastic’ Motion</i>	77
2.5.6	<i>Multidimensional TST Approach to Gas Diffusion in Glassy Polymers</i>	80
2.5.7	<i>Anomalous Diffusion: Its Origins and Implications</i>	86
2.6	Conclusions and Outlook	87
	Acknowledgements	89
	References	89
3	Molecular Simulation of Gas and Vapor Transport in Highly Permeable Polymers	95
	<i>Joel R. Fried</i>	
3.1	Fundamentals of Membrane Transport	95
3.1.1	<i>Solubility</i>	95
3.1.2	<i>Diffusivity</i>	96
3.1.3	<i>Permeability</i>	97
3.1.4	<i>Free Volume</i>	99
3.1.5	<i>d-Spacing</i>	101
3.1.6	<i>Transport in Semicrystalline Polymers</i>	101
3.2	Computational Methods	101
3.2.1	<i>Solubility</i>	102
3.2.2	<i>Diffusivity</i>	102
3.2.3	<i>Free Volume</i>	104
3.2.4	<i>d-Spacing</i>	105
3.2.5	<i>Pair Correlation Functions</i>	105
3.2.6	<i>Molecular Mobility</i>	105
3.2.7	<i>Guidelines for Molecular Simulations</i>	105
3.3	Polymer Studies	106
3.3.1	<i>Polyetherimide</i>	107
3.3.2	<i>Polysulfones</i>	107
3.3.3	<i>Polycarbonates</i>	108
3.3.4	<i>Poly(2,6-dimethyl-1,4-phenylene oxide)</i>	109
3.3.5	<i>Polyimides</i>	110
3.3.6	<i>Polyphosphazenes</i>	114
3.3.7	<i>Main-chain Silicon-containing Polymers</i>	116
3.3.8	<i>Poly[1-(trimethylsilyl)-1-propyne]</i>	120
3.3.9	<i>Amorphous Teflon</i>	124
3.4	Conclusions	126
	Appendices: Primary Force Fields Used in the Simulation of Transport in Polymeric Systems	126
	<i>Appendix 1: DREIDING</i>	126

<i>Appendix 2: GROMOS</i>	126
<i>Appendix 3: COMPASS</i>	127
References	127
4 Predicting Gas Solubility in Membranes through Non-Equilibrium Thermodynamics for Glassy Polymers	137
<i>Ferruccio Doghieri, Massimiliano Quinzi, David G. Rethwisch and Giulio C. Sarti</i>	
4.1 Introduction	137
4.2 Background	138
4.2.1 Pseudo-solubility Calculation	140
4.2.2 Lattice Fluid Model (Sanchez and Lacombe)	141
4.2.3 Tangent-Hard-sphere-Chain Equation of State	142
4.2.4 Retrieving Parameters and Building Pseudo-Equilibrium Solubility Models	143
4.3 Solubility Calculation and Comparison with Experimental Data	144
4.3.1 Prediction of the Low-pressure Gas Solubility in Glassy Polymers	144
4.3.2 Prediction of the Low-pressure Solubility Coefficient of Gases in Glassy Polymers	148
4.3.3 Correlation of Low-pressure Solubility Coefficients in Glassy Polymers	151
4.3.4 Correlation of High-pressure Gas Solubility in Glassy Polymers	153
4.4 Discussion and Conclusions	155
Acknowledgements	157
References	157
5 The Solution–Diffusion Model: A Unified Approach to Membrane Permeation	159
<i>Johannes G. (Hans) Wijmans and Richard W. Baker</i>	
5.1 Introduction	159
5.2 The Solution–Diffusion Model	159
5.3 One-component Transport in Hyperfiltration (Reverse Osmosis), Gas Separation and Pervaporation Membranes	163
5.3.1 Hyperfiltration (Reverse Osmosis)	163
5.3.2 Gas Separation	166
5.3.3 Pervaporation	167
5.4 A Unified View	170
5.5 Multi-component Transport in Hyperfiltration (Reverse Osmosis), Gas Separation and Pervaporation Membranes	173
5.5.1 Hyperfiltration (Reverse Osmosis)	173
5.5.2 Gas Separation	178
5.5.3 Pervaporation	182
5.6 Conclusions and Future Directions	187
References	188
6 Positron Annihilation Lifetime Spectroscopy and Other Methods for Free Volume Evaluation in Polymers	191
<i>Yuri Yampolskii and Victor Shantarovich</i>	
6.1 Introduction	191
6.2 Free Volume: Definitions and Effects on the Transport Parameters	192
6.3 Positron Annihilation Lifetime Spectroscopy	193
6.4 ¹²⁹ Xe NMR Study	200
6.5 Inverse Gas Chromatography	201
6.6 Other Probe Methods	205

6.6.1	<i>Photochromic Probes</i>	205
6.6.2	<i>Electrochromic Probes</i>	205
6.7	Conclusions	206
	<i>Appendix: List of Polymers</i>	206
	References	207
7	Prediction of Gas Permeation Parameters of Polymers	211
	<i>Alexander Alentiev and Yuri Yampolskii</i>	
7.1	Introduction	211
7.2	Group Contribution Methods	215
7.3	Graph Theoretical Approach	222
7.4	Artificial Neural Networks	223
7.5	Computer Simulations	224
7.6	Conclusions	226
	References	227
8	Synthesis and Permeation Properties of Substituted Polyacetylenes for Gas Separation and Pervaporation	231
	<i>Toshio Masuda and Kazukiyo Nagai</i>	
8.1	Introduction	231
8.2	Polymer Synthesis	233
8.2.1	<i>General Features of the Polymerization</i>	233
8.2.2	<i>Poly[1-(trimethylsilyl)-1-propyne] and its Analogues</i>	234
8.2.3	<i>Polydiarylacetylenes and their Derivatives</i>	236
8.2.4	<i>Ring-substituted Polyphenylacetylenes</i>	238
8.3	Gas and Vapor Separation	239
8.3.1	<i>Gas/Gas Separation</i>	239
8.3.2	<i>Vapor/Gas Separation</i>	241
8.3.3	<i>Vapor/Vapor Separation</i>	243
8.4	Pervaporation	244
8.4.1	<i>Alcohol/Water Separation</i>	244
8.4.2	<i>Organic Liquid/Water Separation</i>	245
8.4.3	<i>Organic Liquid/Organic Liquid Separation</i>	246
8.5	Concluding Remarks	246
	References	247
9	Gas and Vapor Transport Properties of Perfluoropolymers	251
	<i>Tim C. Merkel, Ingo Pinnau, Rajeev Prabhakar and Benny D. Freeman</i>	
9.1	Introduction	251
9.2	Amorphous Perfluoropolymers as Membrane Materials	252
9.3	The Nature of Fluorocarbon/Hydrocarbon Interactions	260
9.3.1	<i>Differences in Ionization Potentials between Fluorocarbons and Hydrocarbons</i>	261
9.3.2	<i>Non-central Force Fields</i>	263
9.4	Conclusions	266
	References	267
10	Structure and Transport Properties of Polyimides as Materials for Gas and Vapor Membrane Separation	271
	<i>Kazuhiro Tanaka and Ken-Ichi Okamoto</i>	
10.1	Introduction	271

10.2	Fundamentals	273
10.2.1	<i>Packing Density of Polyimides</i>	273
10.2.2	<i>Transport Properties</i>	274
10.2.3	<i>Diffusion and Solubility Coefficients of Gases</i>	275
10.3	Effect of Morphology	276
10.4	Factors Controlling Transport Properties	277
10.4.1	<i>Factors Controlling Diffusion Coefficient</i>	277
10.4.2	<i>Factors Controlling Solubility Coefficient</i>	280
10.5	Structure–Property Relationship	281
10.5.1	<i>Effect of Structures of Acid Dianhydrides</i>	281
10.5.2	<i>Effect of Structures of Diamines</i>	282
10.5.3	<i>Separation Performance for Particular Systems</i>	283
10.5.4	<i>A Group Contribution Method for Polyimides</i>	285
10.5.5	<i>Enhancement of Solubility Selectivity for CO₂/N₂ Separation</i>	285
10.5.6	<i>Enhancement of Diffusivity Selectivity for H₂/CH₄ Separation</i>	287
10.5.7	<i>Water Vapor Permeation</i>	287
10.6	Conclusions	288
	References	288
11	The Impact of Physical Aging of Amorphous Glassy Polymers on Gas Separation Membranes	293
	<i>Peter H. Pfromm</i>	
11.1	Introduction	293
11.2	Scope	294
11.3	Observations on Integral–Asymmetric Membranes	294
11.4	Physical Aging of Glassy Polymers	295
11.4.1	<i>The Experimental Challenge Posed by Glassy Polymers</i>	295
11.4.2	<i>The Glassy State in Amorphous Polymers</i>	295
11.4.3	<i>Aging Mechanisms and Models</i>	296
11.5	The Thickness-dependence of Aging in Glassy Polymers	297
11.5.1	<i>Influence of the Thickness on T_g, Density, and Free Volume</i>	297
11.5.2	<i>A Phenomenological Model for Thickness-Dependent Aging</i>	298
11.5.3	<i>Influence of the Thickness on Time-dependent Properties of Thin Polymer Films far below the T_g</i>	298
11.5.4	<i>Special Case: Aging of Poly(trimethylsilyl propyne)</i>	302
11.6	Implications of Thickness-dependent Aging for Practical Membrane Gas Separations	304
11.7	Concluding Remarks	304
	References	304
12	Zeolite Membranes for Gas and Liquid Separations	307
	<i>George R. Gavallas</i>	
12.1	Introduction	307
12.2	Membrane Preparation	309
12.2.1	<i>General Issues</i>	309
12.2.2	<i>MFI Membrane Preparation</i>	310
12.2.3	<i>Zeolite A Membrane Preparation</i>	315
12.2.4	<i>Zeolite Y Membrane Preparation</i>	316
12.3	Characterization	316
12.3.1	<i>General on Techniques and Results</i>	316
12.3.2	<i>Membrane Defects</i>	320

12.4 Permeation Measurements	321
12.4.1 Measurement Techniques	321
12.4.2 Survey of Permeation Results	323
12.5 Theory and Modeling of Transport in Zeolite Membranes	331
12.6 Concluding Remarks	332
Acknowledgements	333
References	333
13 Gas and Vapor Separation Membranes Based on Carbon Membranes	337
Hidetoshi Kita	
13.1 Introduction	337
13.2 Preparation and Characterization of Carbon Membranes	338
13.2.1 Self-supported Carbon Membranes	338
13.2.2 Supported Carbon Membranes	345
13.3 Gas Transport and Separation	349
13.4 Vapor Permeation and Pervaporation	351
13.5 Conclusions	352
References	353
14 Polymer Membranes for Separation of Organic Liquid Mixtures	355
Tadashi Uragami	
14.1 Introduction	355
14.2 Structural Design of Polymer Membranes	355
14.2.1 Chemical Design of Membrane Materials	355
14.2.2 Physical Construction of Polymer Membranes	356
14.3 Separation Mechanism	356
14.3.1 Pervaporation	356
14.3.2 Evapomeation	358
14.3.3 Temperature-difference Controlled Evapomeation	359
14.4 Separation of Organic Liquid Mixtures	359
14.4.1 Alcohol/Water Separation	359
14.4.2 Hydrocarbon/Water Separation	362
14.4.3 Organic/Organic Separation	364
14.4.4 Benzene/Cyclohexane Separation	365
14.5 Conclusions	368
References	369
15 Zeolite Membranes for Pervaporation and Vapor Permeation	373
Hidetoshi Kita	
15.1 Introduction	373
15.2 Zeolite Membranes for Water/Organic Liquid Separation	374
15.2.1 Hydrophilic Membranes	374
15.2.2 Organophilic Membranes	379
15.3 Zeolite Membranes for Organic/Organic Separation	381
15.3.1 Alcohol/Ether Separation	381
15.3.2 Aromatic/Non-Aromatic Separation	383
15.3.3 Xylene Isomer Separation	384
15.4 Integrated Systems Involving Pervaporation or Vapor Permeation by Zeolite Membranes	385
15.5 Manufacture of Zeolite Membranes for Pervaporation and Vapor Separation	386

15.6 Conclusions	387
References	388
16 Solid-State Facilitated Transport Membranes for Separation of Olefins/Paraffins and Oxygen/Nitrogen	391
<i>Yong Soo Kang, Jong Hak Kim, Jongok Won and Hoon Sik Kim</i>	
16.1 Introduction	391
16.2 Carrier Properties and Transport Mechanism	392
16.2.1 Carrier Properties	392
16.2.2 Transport Mechanism	398
16.3 Mathematical Models	400
16.3.1 Dual-sorption Model	400
16.3.2 Effective Diffusion Coefficient Model	401
16.3.3 Limited Mobility of Chained Carriers Model	401
16.3.4 Concentration Fluctuation Model	402
16.3.5 Hopping Model versus Concentration Fluctuation Model	403
16.4 Separation Performance of Olefins and Oxygen	403
16.4.1 Olefins/Paraffins Separation	404
16.4.2 Oxygen/Nitrogen Separation	405
16.5 Membrane Stability	405
16.6 Conclusions	407
References	408
17 Review of Facilitated Transport Membranes	411
<i>Richard D. Noble and Carl A. Koval</i>	
17.1 Introduction	411
17.2 Experimental Methods	412
17.3 Modeling	413
17.4 Membrane Configurations	416
17.5 Hybrid Processes	418
17.6 Additional Driving Forces	418
17.7 Methods for Implementation of Active Transport	419
17.8 Novel Liquid Phases – Ionic Liquids	421
17.9 Novel Liquid Phases – Electrohydrodynamic Fluids	422
17.10 Incorporation of the Complexing Agent into the Membrane	423
17.11 Unsaturated Hydrocarbons	423
17.11.1 Scope of Research	423
17.11.2 Mechanistic Studies	424
17.11.3 Membrane Morphology	424
17.11.4 Olefin–Ag(<i>t</i>) Complexation	424
17.11.5 Effect of Water on Performance	425
17.11.6 Other Complexing Agents	426
17.12 Gas Separations	426
17.12.1 Oxygen/Nitrogen Separations	426
17.12.2 Carbon Dioxide Separations	427
17.13 Organic Substances	427
17.14 Biological Complexing Agents	428
17.15 Concluding Remarks	428
References	428
Index	437

Contributors

Alex Alentiev

A. V. Topchiev Institute of Petrochemical Synthesis, Russian Academy of Sciences, 29 Leninsky Prospekt, Moscow 117912, The Russian Federation

Richard W. Baker

Membrane Technology and Research, Inc., 1360 Willow Road, Suite 103, Menlo Park, CA 94025, USA

Ferruccia Doghieri

Dipartimento di Ingegneria Chimica, Mineraria e delle Tecnologie Ambientali Università di Bologna, Viale Risorgimento 2, 40136 Bologna, Italy

Benny D. Freeman

Department of Chemical Engineering, Center for Energy and Environmental Resources, Building 133, The University of Texas at Austin, 10100 Burnet Road, Austin, TX 78758, USA

Joel R. Fried

Center for Computer-Aided Molecular Design and the Polymer Research Center, Department of Chemical and Materials Engineering, University of Cincinnati, Cincinnati, OH 45221-0012, USA

George R. Gavalas

Division of Chemistry and Chemical Engineering, California Institute of Technology, Pasadena, CA 91125, USA

Yong Soo Kang

Center for Facilitated Transport Membranes, Korea Institute of Science and Technology, PO Box 13, Cheongryang, Seoul 130-650, Korea

Hoon Sim Kim

Center for Facilitated Transport Membranes, Korea Institute of Science and Technology, PO Box 13, Cheongryang, Seoul 130-650, Korea

Jong Hak Kim

Center for Facilitated Transport Membranes, Korea Institute of Science and Technology, PO Box 13, Cheongryang, Seoul 130-650, Korea

Hidetoshi Kita

Department of Advanced Materials Science and Engineering, Faculty of Engineering, Yamaguchi University, 2-16-1 Tokiwadai, Ube, Yamaguchi 755-8611, Japan

Carl A. Koval

Department of Chemical and Biological Engineering, University of Colorado at Boulder, Boulder, CO 80309-0215, USA

Toshio Masuda

Department of Polymer Chemistry, Graduate School of Engineering, Kyoto University, Kyoto 606-8501, Japan

Scott Matteucci

Department of Chemical Engineering, Center for Energy and Environmental Resources, Building 133, The University of Texas at Austin, 10100 Burnet Road, Austin, TX 78758, USA

Tim C. Merkel

Membrane Technology and Research, Inc., 1360 Willow Road, Suite 103, Menlo Park, CA 94025, USA

Kazukiyo Nagai

Department of Industrial Chemistry, Meiji University, Higashi-mita, Tama-ku, Kawasaki 214-8571, Japan

Richard D. Noble

Department of Chemical and Biological Engineering, University of Colorado at Boulder, Boulder, CO 80309-0424, USA

Ken-Ichi Okamoto

Department of Advanced Materials Science and Engineering, Faculty of Engineering, Yamaguchi University, 2-16-1 Tokiwadai, Ube, Yamaguchi 755-8611, Japan

Peter H. Pfromm

Department of Chemical Engineering, 105 Durland Hall, Kansas State University, Manhattan, KS 66506, USA

Ingo Pinnau

Membrane Technology and Research, Inc., 1360 Willow Road, Suite 103, Menlo Park, CA 94025, USA

Rajeev Prabhakar

Department of Chemical Engineering, Center for Energy and Environmental Resources, Building 133, The University of Texas at Austin, 10100 Burnet Road, Austin, TX 78758, USA

Massimiliano Quinzi

Dipartimento di Ingegneria Chimica, Mineraria e delle Tecnologie Ambientali Università di Bologna, Viale Risorgimento 2, 40136 Bologna, Italy

David G. Rethwisch

Department of Chemical and Biochemical Engineering, University of Iowa, 4139 Seamans Center, Iowa City, IA 52242-1527, USA

Giulio C. Sarti

Dipartimento di Ingegneria Chimica, Mineraria e delle Tecnologie Ambientali Università di Bologna, Viale Risorgimento 2, 40136 Bologna, Italy

Victor P. Shantarovich

A. V. Topchiev Institute of Petrochemical Synthesis, Russian Academy of Sciences, 29 Leninsky Prospekt, Moscow 117912, The Russian Federation

Kazuhiro Tanaka

Department of Advanced Materials Science and Engineering, Faculty of Engineering, Yamaguchi University, 2-16-1 Tokiwadai, Ube, Yamaguchi 755-8611, Japan

Doros N. Theodorou

School of Chemical Engineering, Department of Materials Science and Engineering, National Technical University of Athens, 9 Heron Polytechniou Street, Zografou Campus, 157 80 Athens, Greece

Tadashi Uragami

Unit of Chemistry, Faculty of Engineering, Kansai University, 3-3-35, Yamate-cho, Suita, Osaka 564-8680, Japan

Johan (Hans) G. Wijmans

Membrane Technology and Research, Inc., 1360 Willow Road, Suite 103, Menlo Park, CA 94025, USA

Jongok Won

Department of Applied Chemistry, Sejong University, Gunja, Gwangjin-ku, Seoul 143-747, Korea

Yuri Yampolskii

A. V. Topchiev Institute of Petrochemical Synthesis, Russian Academy of Sciences, 29 Leninsky Prospekt, Moscow 117912, The Russian Federation

Preface

Membrane-based gas- and vapor separation has emerged into an important unit operation in the chemical industry during the past thirty years. The efficiency of this technology strongly depends on the selection of membrane materials, their physico-chemical properties, and the mechanism through which permeation occurs. The optimum choice of materials for ultrathin, dense gas separation membranes is much more demanding than that of other membrane processes, such as ultrafiltration or microfiltration, where pore size and pore size distribution are the key factors.

The first achievements in practical implementation of membrane-based gas separation processes occurred between 1970 and 1980 and were based on a more or less random choice of well-known polymeric materials, such as polysulfone (Prism Separators of Monsanto, USA) and polyvinyltrimethylsilane in the former USSR. However, these early developments had a powerful impact on the fundamental studies of transport properties of polymers for a wide variety of chemical structures. Today, information on gas permeation properties is available for more than 1000 glassy and rubbery polymers. Permeation data have been collected for many structurally-related polymers, and, hence, qualitative and, to some extent, the quantitative effects of chemical structures of polymers on their gas and vapor permeation properties can be analyzed and predicted as a guideline for developing more advanced membrane materials. In addition, the apparent natural limits of permeability and selectivity of polymers for gas separation applications are well known. One of the very few books dealing solely with polymer membranes for gas and vapor separation was published more than ten years ago [1]. The significant technological and scientific changes that have occurred during the intervening decade has made us consider an entirely different layout for this book, rather than simply updating the chapters in the earlier version.

The goal of this book is to provide a state-of-the-art review, including fundamental as well as practical aspects of membrane-based gas and vapor separations. We hope that the book will serve as a reference for the professional academic and industrial scientist, while also providing enough basic material to introduce students to the subject. It is also our hope that the contents will provide guidance for future research, development and applications in this emerging field.

The introductory chapter is intended to provide background information necessary for all subsequent chapters – a brief historical survey and a detailed discussion of the fundamentals of the solution–diffusion mechanism, definitions of the permeation, diffusion and sorption parameters and units, and a short discussion of the influence of gas and polymer properties, as well as the operating conditions on the observed transport parameters.

During the last decade, much progress has been made in developing physically meaningful computer simulation methods to more accurately predict the permeation, diffusion and sorption mechanisms in membranes. This subject is treated in two chapters written by acknowledged experts in this field. Chapter 2, by D. N. Theodorou, is focused on the methodology – basic principles, applicability and limitations of different modeling approaches, and the ways they can validate, complement and predict experimental results. On the other hand, Chapter 3 by J. R. Fried, summarizes and discusses specific results of molecular computer modeling for glassy and rubbery polymers.

Sorption of gases and vapors in polymers is an integral part of the solution/diffusion process by which permeation occurs through dense polymer membranes. Chapter 4, written by F. Doghieri *et al.*, describes a modern sorption model in glassy polymers. Models, such as Non-Equilibrium

Thermodynamics (NET) and Statistical-Associating-Fluid Theory (SAFT), are based on reliable equations-of-state of polymers (a core subject of materials science) and will probably eventually replace the conventional Dual Mode Sorption (DMS) model. An important achievement of these more advanced models is their ability to predict sorption isotherms based on thermodynamic properties, a quality the DMS model does not provide.

Of great fundamental importance is the chapter written by J. G. Wijmans and R. W. Baker (Chapter 5). Its core subject is the solution–diffusion model for non-porous membranes as applied to various membrane processes, including reverse osmosis, which, strictly speaking, is beyond the scope of this present book. Although the solution–diffusion model was proposed about 150 years ago, this chapter shows that its actual application to real systems, especially multi-component ones with deviations from ideality, is not simple. The approach of the authors applies basic equations for different processes, such as gas separation, pervaporation and reverse osmosis.

Today, the free-volume model is the main concept to describe diffusion in polymers (as well as other phenomena such as micro-viscosity, sorption and mechanical properties). Nowadays, it can be computed by molecular simulations, as described in Chapters 2 and 3; however, there are several experimental methods that allow quantitative determination of the free volume, and this is the subject of Chapter 6. The most developed and established approach for determination of free-volume hole size and size distribution is positron annihilation lifetime spectroscopy, which is the main focus of this chapter. However, other, less popular methods for the investigation of free volume in polymers are also considered (^{129}Xe NMR and inverse gas chromatography). An important point is that different methods give relatively similar estimates of micro-cavity size in different polymers.

A wealth of information collected during the last two decades on the gas permeation properties of polymers having different chemical structures have prompted several research groups to develop methods for prediction of the transport properties of polymers. Such predictions are the subject of Chapter 7. After a critical survey of several methods based on the van Krevelen group-contribution concept, the authors describe their version of such an approach, based mainly on the available database on gas separation parameters of glassy polymers. Apparently, the accuracy of the predictions that can be achieved today approaches the level that is determined by sample–sample variations in the non-equilibrium state of membrane materials and by experimental errors in the permeability coefficients. Hence, the predicted values can be regarded as a guide for preliminary quantitative assessment of polymers when looking for future, more advanced membrane materials.

The following three chapters are devoted to interesting new groups of polymers as potential membrane materials. Chapter 8, by K. Nagai and T. Masuda, discusses polyacetylenes, which include some of the most permeable polymers known. The most permeable polymer, poly(1-trimethylsilyl-1-propyne) (PTMSP) was synthesized more than 20 years ago at Kyoto University in Japan. The unique and unusual properties of this polymer have induced very systematic studies of other, related substituted polyacetylenes. This chapter summarizes synthetic procedures and membrane permeation properties of this class of membrane materials. Equally interesting is another group of glassy membrane materials – amorphous perfluorinated polymers, the subject of Chapter 9 by T.C. Merkel *et al.* Some of these polymers also reveal a very high permeability (e.g. amorphous ‘Teflon’ AF 2400); however, other properties, such as extremely high chemical stability in contact with aggressive media, low tendency to fouling and swelling, and the ease of forming ultrathin composite membranes, make them a very attractive group of materials. Perfluorinated polymers demonstrate a low solubility of hydrocarbon vapors. This has very important implications for some large-scale membrane separation applications in the natural gas and petrochemical industry. Furthermore, perfluoropolymers are characterized by a permeability–selectivity combination better than those of common, hydrocarbon-based polymers for a variety of gases. In some cases, they even exceed the upper bound lines in the Robeson diagrams developed for conventional hydrocarbon-based glassy and rubbery polymers.

Rigid, glassy polyimides are an extremely important class of membrane materials for gas-separation applications. The diversity of polyimides tested for their gas-permeation properties is far greater than that of any other chemical class of polymer. Some important contributions in this field were made by Japanese researchers. Hence, the corresponding Chapter 10 is presented by K. Tanaka and K. Okamoto.

The text is focused on the structure–transport properties of polyimides for gas separation and, to some extent, vapor permeation. The objects of the discussion are mainly based on a wide variety of polyimides prepared in the laboratory of the authors. A major conclusion made by these authors is that polyimides exceed the upper bound lines of other polymers for a wide variety of important applications, such as CO_2/CH_4 and H_2/CH_4 separation.

All amorphous, glassy polymers undergo physical aging. This phenomenon results from their non-equilibrium state which leads to an increase in polymer density and loss in free volume. As a consequence, upon physical aging, the permeability decreases. If the more permeable feed gas is the smaller component, physical aging leads to an increase in selectivity due to compaction of the polymer, which increases its size-sieving properties. On the other hand, if the more permeable gas or vapor is the larger component, physical aging results in a decrease in selectivity. The aging behavior of membrane materials enjoys much fundamental attention in the literature, and P. Pfromm summarizes observations made in his own and other peoples studies in Chapter 11. The emphasis of this chapter is focused on the behavior of ultra-thin films versus thicker polymer films. The results of the discussed behavior are very important for the practical implementation of glassy polymer membranes in any process involving the solution–diffusion process.

Today, polymeric membranes are challenged by the superior gas permeation properties and thermal stability of inorganic membranes. Only the poor mechanical properties and currently high cost of inorganic membranes prevent them from seriously penetrating the membrane-based gas separation market. Furthermore, inorganic membranes can possibly be used successfully, not only in gas separation and vapor permeation, but also in pervaporation applications. Hence, the following four chapters are devoted to gas separation and pervaporation using inorganic membranes. G. Gavalas (Chapter 12) describes, in detail, the methods for preparation of zeolite membranes. Various procedures for membrane synthesis are described, and much attention is devoted to the methods of membrane characterization. The examples given for zeolite membranes are (i) separation of light gases, (ii) gaseous hydrocarbons, (iii) permeation of heavier C_5 – C_8 hydrocarbon vapors, and (iv) a short section on pervaporation of alcohol–water mixtures. Pervaporation through zeolite membranes is discussed in more detail by H. Kita in Chapter 13, where separate sections deal with hydrophilic, organophilic and organic/organic pervaporation membranes. In Chapter 14, T. Uragami provides a summary of the state-of-the-art of polymeric membranes for the separation of azeotropes, such as ethanol/water and isopropanol/water separation.

A very interesting type of inorganic material is based on carbon membranes. Chapter 15, by H. Kita, starts with a description of the methods used for preparation of carbon flat- and hollow-fiber membranes and considerations for the choice of polymer precursors subjected to pyrolysis. Various separations, applying carbon membranes, prepared by different techniques clearly indicate that the performance of some of these membranes can be far superior than any other membrane type; however, the high current cost and their brittleness, that is, poor mechanical integrity, prevent their current large-scale application.

Facilitated transport is a membrane process that uses specific chemical interactions with selective components in a feed mixture to provide very high selectivities, neither achievable with polymeric membranes nor inorganic zeolite or carbon membranes. Facilitated transport membranes are the equivalent of chemical absorption versus physical absorption processes.

Accordingly, two chapters are devoted to facilitated transport. Y. S. Kang *et al.* (Chapter 16) discuss solid-state systems containing fixed carriers for the selective separation of olefin/paraffin mixtures and air separation using oxygen-selective carriers. Solid-state facilitated transport membranes do not suffer from some of the shortcomings of facilitated transport in liquid-filled containing carrier membranes. However, as pointed out by the authors, a pending question for practical applications of this membrane type is the stability of the metal ion carriers, which often fail to show long-term stability due to chemical poisoning by other feed stream components (poisoning of membranes for olefin/paraffin separation by H_2 , H_2S and acetylene) or their limited feed pressure applicability (air separation or CO_2 applications). On a similar subject, R. D. Noble and C. A. Koval present a review on various aspects of liquid-state facilitated transport membranes of different types for various separations. An important

conclusion of the authors is that recently a major research thrust has been on new materials, structures, carriers and methods for incorporating carriers into a membrane matrix.

In our opinion, further progress in membrane science will benefit from a close collaboration between synthetic chemists (to prepare novel polymeric and inorganic membrane materials), physical chemists (to explore what the materials science limitations are) and engineers (who know what is required to make a membrane process technically and economically viable). As in many other scientific areas, membrane science is not just based on a single discipline but involves co-operation between scientists with different backgrounds. The limiting size of this book prevented us from including other, also relevant subjects of interest. Further industrial contributions are needed to provide a guideline for future materials science aspects. A recent comprehensive review provides some detailed information on this subject [2].

The editors are very thankful to all contributors and the reviewers for each chapter of this book. It is not an easy task to summarize the state-of-the-art in any field of science. We believe that the contributors of this book are world-class experts in their specific fields. Furthermore, we would like to express our sincere thanks to the publishers of this book, John Wiley and Sons, Ltd, Chichester, UK for their support and guidance. Finally, our support staff, Ms Sande Storey and Mr Gary Eberle, are also gratefully acknowledged for their contributions.

References

- [1] D. R. Paul and Yu. P. Yampolskii (Eds), *Polymeric Gas Separation Membranes*, CRC Press, Boca Raton, FL, USA (1994).
- [2] R. W. Baker, 'Future Direction of Membrane Gas Separation Technology', *Industrial and Engineering Chemistry Research*, **41**, (2002), 1393.

Transport of Gases and Vapors in Glassy and Rubbery Polymers

Scott Matteucci, Yuri Yampolskii, Benny D. Freeman and Ingo Pinnau

1.1 Background and Phenomenology

Transport in non-porous polymeric membranes is based on the so-called ‘solution–diffusion’ concept [1,2]. This model, formulated in the 19th century, is grounded in the works of J. K. Mitchell [3], T. Graham [4] and S. von Wroblewski [5], who demonstrated that the presence of microscopic open pores or capillaries was not a prerequisite for mass transfer through polymeric films (or septa as they were referred to), such as natural rubber. First, Graham in 1829 [4], and then Mitchell in 1831 [3], noted that gases were capable of permeating through non-porous rubber films and that this process was related to gas dissolution and diffusion in the polymeric materials. The currently accepted interpretation of such experiments was given several decades later by Graham [4] (this and other articles from the early history of membrane science have been reproduced, in part, in a special issue of the *Journal of Membrane Science*) [6]. Because he did not find a monotonic correlation between the rates of transport and the known gas phase diffusion coefficients of the penetrant molecules, Graham concluded that the process of permeation comprised two stages: sorption of gas by the rubber ‘that must depend upon a kind of chemical affinity’ and diffusion of the sorbed gas molecules [4]. The sorbed gas, as he wrote, ‘comes to evaporate . . . and reappears as gas on the other side of the membrane. Such evaporation is the same into vacuum and into another gas, being equally gas-diffusion in both circumstances’ [4].

Empirical observations of the pressure and thickness dependence of the steady-state gas permeation rate or flux, N , led von Wroblewski [5] to propose the following relation:

$$N = P(\Delta p/l) \quad (1.1)$$

where Δp is the pressure difference across the membrane, and l is its thickness. The proportional coefficient in this equation, P , was defined as the permeability coefficient. While permeability defines gas transport as an intrinsic physical property for a given polymer/gas pair, this expression does not reveal the molecular basis of permeation.

A more fundamental basis for permeation may be derived by considering a plane polymer film of thickness l separating two regions filled with a single gas, as shown in Figure 1.1. The gas pressure on the upstream (or high-pressure) side of the film is p_2 , while the gas pressure on the downstream (or low-pressure) side is p_1 . At steady-state, the gas flux at any point inside the polymer is given by Fick’s first law [7]:

$$N = \left(\frac{-D_{\text{loc}}}{1-w} \right) \left(\frac{dC}{dx} \right) \quad (1.2)$$

where N is the gas flux relative to fixed coordinates, C is the gas concentration, x is the distance across the film, w is the mass fraction of gas in the polymer, and D_{loc} is the binary mutual diffusion

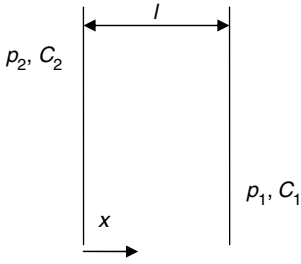


Figure 1.1 Representation of gas or vapor transport through a non-porous polymeric membrane; p_2 is presumed to be greater than p_1

coefficient of the gas in the polymer. Integration across the film (from $x = 0$ to $x = l$) yields:

$$N = \frac{1}{l} \int_{C_1}^{C_2} \frac{D_{loc}}{1-w} dC \quad (1.3)$$

where C_1 and C_2 are the gas concentrations in the polymer at the downstream and upstream faces of the membrane, respectively, which are in equilibrium with the external pressures p_1 and p_2 , respectively. This relationship can be written as follows:

$$N = \frac{C_2 - C_1}{l} D \quad (1.4)$$

where D , the average effective diffusion coefficient, is defined as:

$$D = \frac{1}{C_2 - C_1} \int_{C_1}^{C_2} \frac{D_{loc}}{1-w} dC \quad (1.5)$$

With this definition, the permeability of a gas in a polymer can be expressed as:

$$P = \frac{Nl}{p_2 - p_1} = \left(\frac{C_2 - C_1}{p_2 - p_1} \right) D \quad (1.6)$$

Equation (1.6) is derived for ‘pure-gas’ permeation. To extend the definition to mixtures, the total pressures p_2 and p_1 should be replaced with the corresponding partial pressures of the component of interest on the upstream and downstream sides of the membrane, respectively. To account for the effects of gas-phase non-idealities on the driving force for permeation, the pressures (or partial pressures, in the case of mixtures) are

typically replaced by fugacities (e.g. with high-pressure CO₂ feed streams) [8].

When the upstream pressure and concentration (p_2 and C_2 , respectively) are much greater than their downstream analogs, this result simplifies as follows:

$$P = \frac{C_2 D}{p_2} \quad (1.7)$$

The equilibrium solubility coefficient of a gas in a polymer is the ratio of the concentration of gas dissolved in the polymer at equilibrium to the pressure of gas (or partial pressure in the case of mixtures) in the contiguous gas phase [7]:

$$S = C/p \quad (1.8)$$

When this result is applied to Equation (1.7), one obtains:

$$P = DS \quad (1.9)$$

where the solubility coefficient, S , is evaluated at the upstream face of the membrane (i.e. $S = C_2/p_2$). From this result, P depends upon two factors: (1) a thermodynamic term, S , characterizing the number of gas molecules sorbed into and onto the polymer and (2) a kinetic or mobility term, D , characterizing the mobility of gas molecules as they diffuse through the polymer. In other words, permeability, which is the pressure- and thickness-normalized gas flux through the polymer film (cf. Equation (1.1)), depends upon the product of the number of gas molecules that dissolve in the polymer and their rate of migration through the polymer matrix. Equation (1.9) emphasizes that high permeability coefficients can result from large D values, large S values, or both. For example, some so-called ‘fast’ (i.e. high-permeability) gases display (i) large diffusion coefficients (e.g. He or H₂), (ii) high solubility coefficients (e.g. CO₂) or (iii) both (e.g. H₂O).

Many different experimental strategies are used to determine the P , D , and S values in polymers, and these methods have been thoroughly reviewed [9,10]. A common technique involves measuring permeability in a steady-state gas permeation experiment and D in the transient regime that precedes the attainment of steady-state in a permeation experiment, which is the so-called time-lag method [11]. S is then estimated (using the solution–diffusion model) as the ratio of P divided by D . A more accurate procedure relies

on independent determinations of P in steady-state permeation experiments and S in equilibrium-sorption measurements [12–14]. In this case, D is estimated, using the solution–diffusion model (i.e. Equation (1.9)), as the ratio of P divided by S . The third possible alternative – direct measurement of S and D in kinetic sorption experiments and estimating P as the product of S and D – is not used very often [14]. In any event, it is extremely rare to independently determine S , D , and P for mass transport in polymers, underscoring the popularity of the solution–diffusion mode. A more thorough review and in-depth discussion of this model is presented in the chapter by Wijmans and Baker. This topic has also been the subject of several articles [2,15].

In the SI system, permeability coefficients are expressed in the following units:

$$P = \text{mol} \cdot (\text{m}^2 \text{ s Pa}) \quad (1.10)$$

However, a more widely used and accepted unit for P is:

$$1 \text{ barrer} = 10^{-10} \text{ cm}^3(\text{STP})\text{cm}/(\text{cm}^2 \text{ s cmHg})$$

Permeability coefficients of common gases in polymers span a range of more than seven orders of magnitude, from 10^{-3} to 10^4 barrer or more.

Commercial gas separation membranes differ significantly in their morphology from that of the thick, isotropic dense polymer films considered above. A typical integral-asymmetric or thin-film composite membrane has a thin selective layer (often in the range of 200 Å to 1 μm) supported by a microporous layer [16,17]. Ideally, the microporous layer provides mechanical support for the thin selective layer, which is the dominant mass-transfer resistance of the entire structure. Often, the thickness of the selective layer is difficult or impossible to measure because, in commercial gas separation membranes based on glassy polymers, there is often very little chemical contrast between the selective layer and the support layer. Furthermore, the selective layer is often estimated to be of the order of 50 to 100 nm in thickness (and, in some cases, perhaps less), making it difficult to image. In such cases, pressure-normalized steady-state flux, or permeance (Q or P/l), is used to characterize the gas transport rate through such separating membranes. The accepted units for Q are: $\text{mol}/(\text{m}^2 \text{ s Pa})$ (SI), $\text{m}^3(\text{STP})/(\text{m}^2 \text{ h atm})$ or

$\text{cm}^3(\text{STP})/(\text{cm}^2 \text{ s} (\text{cm Hg}))$. Permeance is also expressed in Gas Permeation Units (GPU), where $1 \text{ GPU} = 10^{-6} \text{ cm}^3(\text{STP})/(\text{cm}^2 \text{ s} (\text{cm Hg}))$. A permeance of 1 GPU corresponds to a membrane exhibiting an intrinsic permeability of 1 barrer and having a selective layer thickness of 1 μm.

Another key characteristic of gas separation membranes is their selectivity. The ideal selectivity is defined as follows [7]:

$$\alpha_{AB} = P_A/P_B \quad (1.11)$$

where P_A and P_B are the permeability coefficients of gases A and B, respectively. Commonly, the more permeable gas is taken as A, so that $\alpha_{A/B} > 1$. Bearing in mind Equation (1.9), the ideal selectivity can be partitioned into diffusivity and solubility selectivity as follows:

$$\alpha_{AB} = (D_A/D_B)(S_A/S_B) = \alpha_{AB}^D \alpha_{AB}^S \quad (1.12)$$

where S_i and D_i are the solubility and diffusion coefficients of species i , respectively. The independent analysis of α_{AB}^D and α_{AB}^S is very helpful in rationalizing gas separation properties in polymers. The ideal separation factor can also be determined from pure-gas permeance values as follows:

$$\alpha_{AB} = \frac{Q_A}{Q_B} \quad (1.13)$$

The magnitudes of α_{AB} depend sensitively on the gas pair under consideration. For example, for air separation, the values of $\alpha_{\text{O}_2/\text{N}_2}$ vary from approximately 2 to 15 in polymers [18]. In contrast, $\alpha_{\text{H}_2/\text{CH}_4}$ values range from 5 to 1000 or more [18].

When gas mixtures permeate across a membrane, the presence of one gas can, in some circumstances, influence the transport of other gases in the membrane; this phenomenon will be discussed in more detail towards the end of this chapter. In such systems, the ideal selectivity, determined from pure-gas measurements, can be a rather crude (i.e. inaccurate) measure of the ‘actual’ selectivity, or separation factor, of a membrane.

The separation factor, α_{AB}^* , determined from the ability of a membrane to separate a binary feed gas mixture, is defined as follows [7]:

$$\alpha_{AB}^* = (y_A/y_B)/(x_A/x_B) \quad (1.14)$$

where y_A and y_B are the mole fractions of the components produced in the permeate, and x_A and x_B are their corresponding mole fractions in the feed. The connection between α_{AB}^* and α_{AB} is provided by the following relationships, which give the mole fractions of each component produced at steady-state on the permeate (i.e. downstream) side of a membrane when the upstream side is fed with a binary mixture of gases A and B:

$$y_A = \frac{N_A}{N_A + N_B} \quad (1.15)$$

$$y_B = \frac{N_B}{N_A + N_B} \quad (1.16)$$

where N_i is the steady-state flux of component i through the membrane. Combining these expressions with the equation defining the separation factor yields:

$$\alpha_{AB}^* = \frac{N_A/N_B}{x_A/x_B} \quad (1.17)$$

The fluxes in the above expression may be related to the permeability by Equation (1.1):

$$\alpha_{AB}^* = \left(\frac{P_A}{P_B} \right) \left(\frac{p_2 x_A - p_1 y_A}{x_A} \right) \left(\frac{x_B}{p_2 x_B - p_1 y_B} \right) \quad (1.18)$$

This result may be further simplified as follows:

$$\alpha_{AB}^* = \alpha_{AB} \frac{p_2 - p_1 \left(\frac{y_A}{x_A} \right)}{p_2 - p_1 \left(\frac{y_B}{x_B} \right)} \quad (1.19)$$

Thus, the separation factor of a membrane depends not only on the properties of the gas-polymer system but also on process parameters such as upstream and downstream pressure, and composition [19]. When the upstream pressure is much greater than the downstream pressure, so that $p_2 \gg p_1 y_A/x_A$ and $p_2 \gg p_1 y_B/x_B$, this equation reduces to:

$$\alpha_{AB}^* = \alpha_{AB} \quad (1.20)$$

indicating that, under appropriate simplifying assumptions, the ideal selectivity is equal to the actual separation factor. In the remainder of this chapter, ideal selectivity is discussed primarily as a yardstick for characterizing mem-

brane separation performance, since this parameter does not depend explicitly on engineering factors such as upstream/downstream pressure ratio, etc. However, ideal selectivity values determined based on pure-gas permeation properties do not necessarily capture the effects of one component in a gas mixture on the permeation properties of another component and, in some cases, (discussed later in this chapter) these effects are important.

Despite decades of systematic efforts, it has proven elusive to synthesize polymers that combine the highly desirable properties of high permeability and high selectivity. Among size-selective polymers (i.e. those that are more permeable to smaller gas molecules (e.g. H_2) than to larger gas molecules (e.g. CH_4)), there is a trade-off between permeability and selectivity, as shown in Figures 1.2(a)–1.2(c). Polymers that are more permeable tend to be less selective and vice versa. This behavior was cataloged systematically by Robeson [18], who observed empirically the existence of so-called ‘upper bound lines’, which define the practical upper limit of the ‘clouds’ of permeation data points (c.f. Figure 1.2). The upper bound lines can be predicted from rather straightforward theoretical considerations based on either free-volume or transition-state models [20,21]. For example, beginning from Equation (1.9), using concepts from Section 1.4 of this chapter on activated state diffusion and a widely used correlation of activation energy of diffusion with the square of the penetrant kinetic diameter, one can derive a relation of the following form [21]:

$$\alpha_{A/B} = \frac{\beta_{A/B}}{P_A^{\lambda_{A/B}}} \quad (1.21)$$

where P_A is the permeability of the more permeable gas (which, by convention, is always plotted on the abscissa of permeability/selectivity maps such as those presented in Figure 1.2), $\alpha_{A/B}$ is the selectivity of the more permeable (A) to the less permeable (B) gas and $\beta_{A/B}$ and $\lambda_{A/B}$ are model parameters. Most of the gas permeation data used to construct such diagrams are based on pure-gas permeation data, and so they are subject to the same cautions mentioned earlier regarding their utility in practical separations. Additionally, the data used to prepare the upper bound diagrams were in the range of ambient temperature. The slope of the upper bound lines, $\lambda_{A/B}$, can be

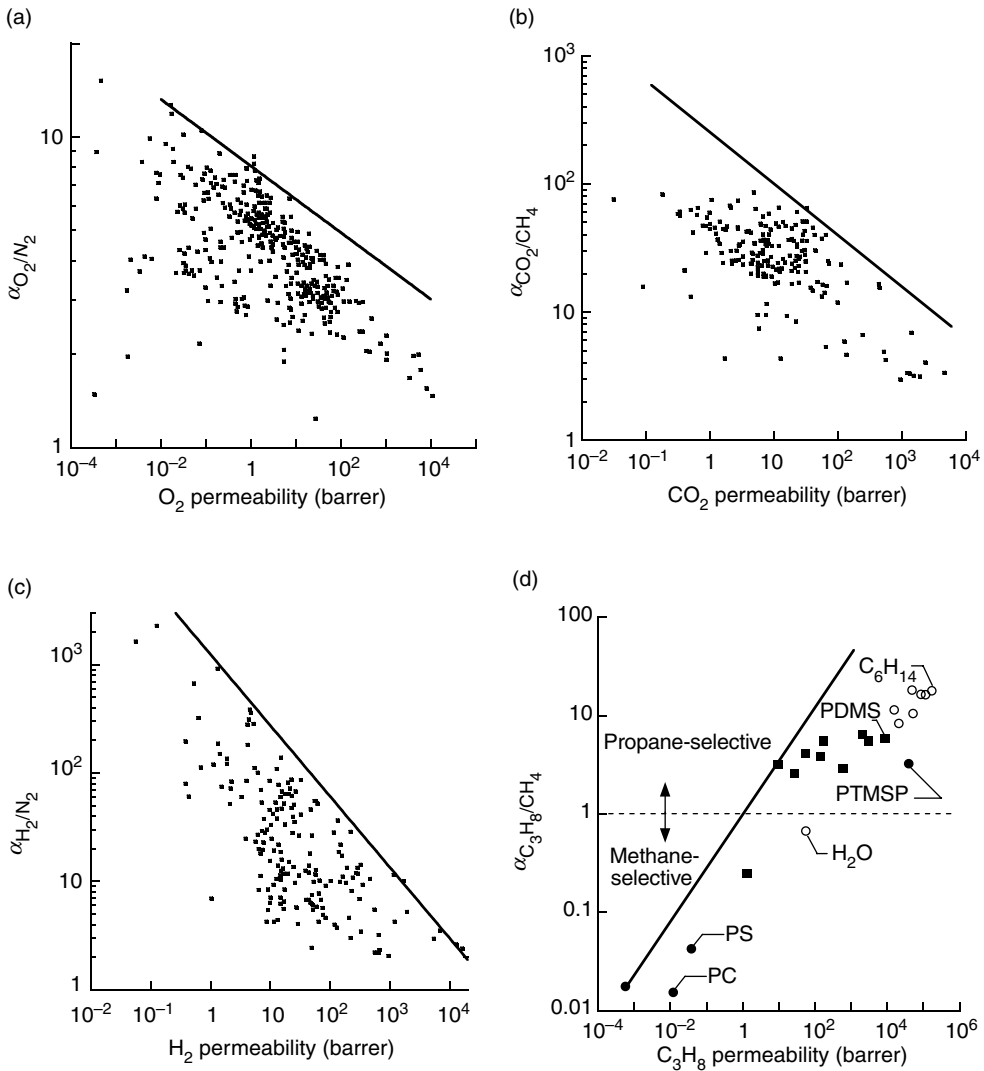


Figure 1.2 Permeability/selectivity trade-off maps for: (a) O_2/N_2 ; (b) CO_2/CH_4 ; (c) H_2/N_2 ; (d) C_3H_8/CH_4 [28]. For O_2/N_2 , CO_2/CH_4 and H_2/N_2 , the upper bound line was estimated by using the model given in Freeman [21], while for C_3H_8/CH_4 , the upper bound line was drawn by eye. (a–c) Reprinted from *Journal of Membrane Science*, **62**, I. M. Robeson. ‘Correlation of separation factor versus permeability for polymeric membranes’, 165–185, Copyright (1991), with permission from Elsevier. (d) Reprinted from *Trends in Polymer Science*, **5**, B. D. Freeman and I. Pinnau, ‘Separation of gases using solubility-selective polymers’, 167–173, Copyright (1997), with permission from Elsevier

calculated to remarkable precision from the kinetic diameters of the gas molecules [21]:

$$\lambda_{A/B} = \left(\frac{d_B}{d_A}\right)^2 - 1 \quad (1.22)$$

where d_B and d_A are the kinetic diameters of the larger and smaller gas molecules, respectively.

A list of kinetic diameters of various gases is available in the literature and in Table 1.1 [22]. This result emphasizes the close connection between gas molecule size and permeation and separation properties in strongly size-sieving polymers. The position of the upper bound line, $\beta_{A/B}$, depends on gas molecule size as well

Table 1.1 Gas and vapor properties often used in correlating sorption and transport properties

Gas	Critical temperature, T_C (K) ^a	Lennard–Jones well depth, ε/k (K) [31,48]	Critical volume, V_C (cm ³ /mol) ^a	Kinetic diameter, d_k (Å) [22]	Lennard–Jones diameter, d_{LJ} (Å) [48]	Chung diameter, d_C (Å) ^b [48]
He	5.2	10.2	57.5	2.6	2.551	3.123
H ₂	33.2	59.7	64.9	2.89	2.827	3.251
O ₂	154.6	106.7	73.5	3.46	3.467	3.389
N ₂	126.2	71.4	89.3	3.64	3.798	3.616
CO	134.5	91.7	90.1	3.76	3.69	3.627
CO ₂	304.2	195.2	91.9	3.3	3.941	3.651
CH ₄	190.6	148.6	98.6	3.8	3.758	3.737
C ₂ H ₆	305.3	215.7	147	—	4.443	4.27
C ₂ H ₄	282.5	224.7	131.1	3.9	4.163	4.11
C ₃ H ₈	369.9	237.1	200	4.3	5.118	4.731
C ₃ H ₆	365.2	298.9	184.6	4.5	4.678	4.606
<i>n</i> -C ₄ H ₁₀	425	531.4	255	4.3	4.971 [47]	5.13
<i>i</i> -C ₄ H ₁₀	407.7	330.1	259	5	5.278	5.157
H ₂ O	647	809.1	55.9	2.65	2.641	3.093
H ₂ S	373.3	301.1	87.7	3.6	3.623	3.594

^awww.NIST.gov.^bChung correlation [48], where $d_C = 0.809 V_C^{1/3}$.

as solubility:

$$\beta_{A/B} = \frac{S_A^{1+\lambda_{A/B}}}{S_B} \exp \left\{ -\lambda_{A/B} \left[b - f \left(\frac{1-a}{RT} \right) \right] \right\} \quad (1.23)$$

where S_A and S_B are the solubility coefficients of the more permeable and less permeable gases, respectively. The parameters a and b are from a so-called linear free energy model, and their values are fixed for glassy polymers ($a = 0.64$, $b = 11.5$) [21]. The only adjustable constant is f , which characterizes the product of the energy barriers to open a gap to allow a penetrant to diffuse and the equilibrium interchain spacing. When f is set to 12 600 cal/mol, one achieves the best-fit to the upper bound data available in the literature [21].

From a qualitative viewpoint, the existence of permeability/selectivity trade-off relations is most easily understood from a free-volume viewpoint. The most typical way to significantly enhance the permeability of glassy polymers, such as those commonly considered as gas separation polymers, is to change the chemical structure by introducing packing-disrupting units into the polymer backbone, thereby increasing the free volume [23]. Increasing the free volume usually strongly increases the diffusion coefficients [23,24] and reduces the diffusivity selectivity,

accordingly. The increase in diffusion coefficients increases permeability while the reduction in diffusivity selectivity reduces the overall permeability selectivity.

In some applications, such as the removal of higher hydrocarbons from natural gas and the removal of volatile organic compounds from air gases, it is economically desirable to use membranes that are more permeable to the larger species in the gas mixture [25–27]. Such performance can only be achieved by harnessing the much higher solubility of the larger component and selecting materials with very weak size-sieving properties, so that the diffusion selectivity, which will always favor the smaller molecule, is not so strong that the polymer is selective for the smaller molecule [28]. The permeability/selectivity map for such separations looks quite different than for the strongly size-sieving separations presented in Figures 1.2(a)–1.2(c). An example of such a reverse-selective separation, C₃H₈/CH₄, is presented in Figure 1.2(d). In this case, propane is much more soluble than methane, and so solubility selectivity favors propane [28]. However, propane is larger than methane, and so diffusion selectivity favors methane. In strongly size-sieving polymers (e.g. aromatic polyimides, aromatic polyamides, polysulfones, etc.), the diffusion selectivity is so high that it overwhelms the solubility selectivity,

and, therefore, these materials are methane-selective ($\alpha_{\text{C}_3\text{H}_8/\text{CH}_4} < 1$). However, many rubbery and certain ultrahigh-free-volume glassy polymers have very weak size-sieving ability, and so solubility selectivity dominates, and these materials are propane-selective ($\alpha_{\text{C}_3\text{H}_8/\text{CH}_4} > 1$). In any event, as materials become more permeable to propane, their propane/methane selectivity increases. In these cases, permeability and selectivity increase together, rather than opposing one another. Qualitatively, propane permeability is higher in materials (such as very flexible rubbery polymers (e.g. polydimethylsiloxane) or ultra-high-free-volume polymers (e.g. poly(1-trimethylsilyl-1-propyne)) having a very high propane diffusion coefficient. Such materials tend to be weakly size-sieving, and so the diffusivity selectivity, which would always favor methane, the smaller molecule, would be weaker than the solubility selectivity in favor of propane [28]. Thus, as one systematically explores a series of materials of higher and higher propane permeability (due to higher and higher gas diffusion coefficients), one could generally expect to observe higher and higher propane/methane selectivity (as $D_{\text{C}_3\text{H}_8}/D_{\text{CH}_4}$ becomes closer to 1 in materials with higher diffusion coefficients and, in turn, weaker size-sieving ability).

1.2 Effects of Gas and Polymer Properties on Transport Coefficients

As indicated earlier, permeability is an intrinsic property of a gas–polymer system. Gases are much simpler materials than polymers, and so correlations are available to relate diffusion and solubility coefficients (and, hence, permeability values) of different gases in a given polymer. The situation with polymers is more complex. Nevertheless, some properties of polymers also correlate with the D , S and P values for a given gas, which has given rise to group contribution models aimed at predicting the permeability of polymers to gases [29–31]. However, universal correlations are typically worse than those valid for limited sets of polymers, such as, for example, rubbers and glasses, certain chemically similar classes of polymers, etc.; this limitation on such approaches reflects our lack of complete understanding of the detailed relation between polymer structure and gas transport properties. The sections below outline the most common approaches

used to correlate gas and vapor sorption and transport properties in polymers.

1.2.1 Effect of Gas Properties on Solubility and Diffusivity

The diffusion coefficients of gas molecules characterize their dynamics or mobility in a polymer, and diffusion coefficients generally increase as gas molecule size decreases. As shown in Figure 1.3, for both rigid, glassy polymers and flexible, rubbery polymers, the square of a characteristic dimension of a penetrant molecule, d^2 , is most often used as a scaling parameter for the logarithm of D [32–39]. This dependence arises from models such as the one developed by Meares, which supposes that the activation energy of diffusion is proportional to the effective cross-sectional area of the gas molecules [40]. More rarely, diffusion coefficients have been correlated with d or d^3 [41]. Linear correlations of the logarithm of D with d^2 are especially good for roughly spherical molecules, such as inert gases.

Different scales can be used for estimating the effective penetrant diameter, d , important for gas diffusion in polymers. There is no obvious single choice for effective molecular diameter that is both easily traceable to fundamental molecular properties and provides a scale for molecular size so that diffusion coefficients reliably decrease as molecular size increases. One might argue that such a universal scale cannot exist when, for example, polar or quadrupolar gases (e.g. CO_2 , H_2S , H_2O , etc.) diffuse in polymer matrices that either promote aggregation of penetrants (e.g. H_2O in hydrophobic polymers) [42–44] or provide sites for strong and favorable interactions with the gases, such as CO_2 diffusion in amine-containing polymers [45]. However, in many cases, such strong interaction effects are not present, and diffusion coefficients of gases should decrease systematically with an appropriate and increasing measure of penetrant size.

The most widely used scales of penetrant size for gas diffusion are the so-called kinetic diameter, d_k , and the Lennard–Jones collision diameter, d_{LJ} , determined from gas viscosity or second virial coefficient data [22,46]. Widely quoted values of kinetic diameter are from the book by Breck, and these values are recorded for a number of gases in Table 1.1 [22,47]. Lennard–Jones collision diameter values are

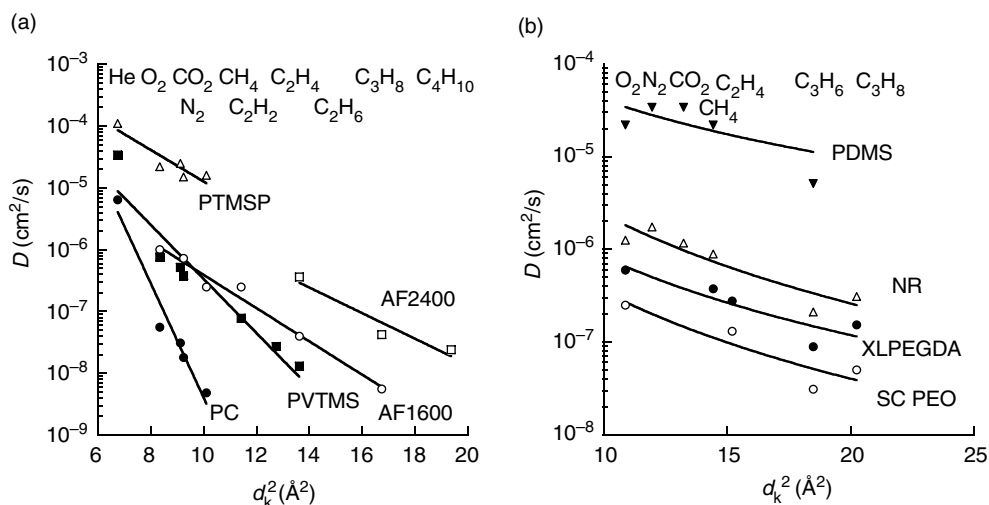


Figure 1.3 Dependence of diffusion coefficients on penetrant kinetic diameter in (a) glassy polymers at 23°C , including poly(1-trimethylsilyl-1-propyne) (PTMSP), polyvinyltrimethylsilane (PVTMS), polycarbonate (PC), perfluorocarbon copolymers of 2,2-bis(trifluoromethyl)-4,5-difluoro-1,3-dioxole (BDD) and tetrafluoroethylene (TFE) containing 65 mol% BDD (AF1600) and 87 mol% BDD (AF2400) [39], and (b) rubbery polymers including cross-linked poly(ethylene glycol diacrylate) (XLPEGDA) at 35°C [101], semicrystalline poly(ethylene oxide) (SC PEO) at 35°C [32], natural rubber (NR) at 25°C [33] and polydimethylsiloxane (PDMS) at 35°C [34]. (a) Reprinted with permission from V. P. Shantarovich *et al.*, *Macromolecules*, **33**, 7453–7466 (2000). Copyright (2000) American Chemical Society. (b) (i) Reprinted from *Journal of Membrane Science*, **239**, H. Lin and B. D. Freeman, ‘Gas solubility, diffusivity and permeability in poly(ethylene oxide)’, 105–117, Copyright (2004), with permission from Elsevier; (ii) From ‘Flow of gases through polyethylene’, A. S. Michaels and H. J. Bixler, *J. Polym. Sci.*, **50**, 412–439, Copyright © 1961, John Wiley & Sons, Inc. Reprinted with permission of John Wiley & Sons, Inc.; (iii) From ‘Gas sorption, diffusion and permeation in polydimethylsiloxane’, T. C. Merkel, V. Bondar, K. Nagai, B. D. Freeman and I. Pinnau, *J. Polym. Sci. Part B: Polym. Phys. Ed.*, **38**, 415–434, Copyright © 2000, John Wiley & Sons, Inc. Reprinted with permission of John Wiley & Sons, Inc.; (iv) Reprinted with permission from H. Lin and B. D. Freeman, *Macromolecules*, **38**, 8394–8407 (2005). Copyright (2005) American Chemical Society

also used frequently in the literature, and so they are also reported in Table 1.1 for comparison [48]. As explained below, these two scales are quite closely related. An additional penetrant size scale is also reported in Table 1.1; this is based on a correlation due to Chung *et al.*, which relates Lennard–Jones collision diameter to penetrant critical volume [48–50].

Because there appears to be some confusion in the literature regarding these penetrant size scales, a short discussion of their molecular basis is provided. The collision diameter is the intermolecular separation between two molecules of the same gas when the potential energy of interaction (calculated from the Lennard–Jones potential energy model) is equal to zero [51]. Many of the values referred to as kinetic diameter, d_k , in Breck [22] are, in fact, Lennard–Jones collision diameters reported in Hirschfelder, Curtiss

and Bird (HCB) [51]. In fact, all of the values reported as kinetic diameters in Breck that are from HCB (Ar, O_2 , N_2 , Kr, Xe, CH_4 , CF_4 and SF_6) are Lennard–Jones collision diameters that were originally determined using second virial coefficient data (i.e. *not* gas viscosity data). The kinetic diameters reported in Breck for H_2O and NH_3 (i.e. polar gases) are the collision diameters from the Stockmeyer potential model for polar substances, which is the distance of separation between two identical molecules at which the potential energy of interaction would be zero in the absence of dipole forces; these parameters were determined by fitting second virial coefficient data to the Stockmeyer potential [52]. The value reported as the kinetic diameter by Breck for CO_2 , 3.3 \AA , is significantly lower than the Lennard–Jones collision diameter considered by Breck (4.05 \AA); Breck rationalizes the lower

value based on the observation that KA zeolite (KA zeolites contain $\text{AlO}_4/\text{SiO}_4$ at a 1:1 ratio and potassium cations) [22] adsorbs CO_2 but not N_2 , which has a kinetic diameter of 3.64 Å. Breck argues that, for CO_2 to adsorb into this zeolite, it must have a kinetic diameter smaller than that of N_2 . He also asserts that adsorption phenomena suggest that the critical molecular dimension characterizing whether or not a molecule will adsorb into a zeolite is the so-called minimum equilibrium separation, r_{\min} , (i.e. the separation distance corresponding to the maximum attractive energy from the Lennard–Jones potential). He uses a value of 3.7 Å for the minimum equilibrium separation for CO_2 and the known relation between r_{\min} and d_k ($r_{\min} = 2^{1/6}d_k$) to calculate an effective kinetic diameter for CO_2 of 3.3 Å, which is a value widely quoted when CO_2 diffusion properties in polymers are discussed. This strategy was used in several cases by Breck to estimate effective kinetic diameters for gas molecules, including most of the hydrocarbons considered by Breck.

Several shortcomings of the above procedure are evident. First, when the effective gas molecular size is estimated from Lennard–Jones parameters, there is no systematic accounting for the influence of molecular shape anisotropy on effective molecular size since such effects are not included in the Lennard–Jones model. This issue may have stimulated Breck to propose the alternative procedure described above for CO_2 . Secondly, the Lennard–Jones parameters determined from gas viscosity (i.e. transport) data and from second virial coefficient (i.e. thermodynamic) data for the same gas often show significant differences [53]. In a related issue, often several sets of fairly different Lennard–Jones parameters can be found that offer an essentially equivalent fit to the underlying experimental data [48]. Both of these effects frustrate the identification of a unique effective molecular diameter based on such data.

These shortcomings have led to a number of alternative proposals of effective molecular size appropriate for correlating diffusion coefficients [54,55]. For example, a special scale convenient for prediction of gas diffusivity in polymers was suggested [37,38]. However, the gas diameters from this scale do not give good predictions of upper bound relations when they are used in models to predict such phenomena [21]. For a homo-

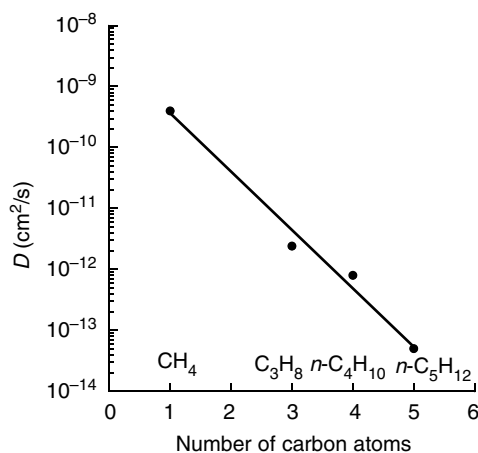


Figure 1.4 Infinite-dilution, estimated amorphous-phase diffusion coefficients of linear alkane hydrocarbons in poly(ethylene terephthalate) at 25 °C [14,58]. (i) Reprinted with permission from S. N. Dhoot *et al.*, *Industrial and Engineering Research*, **43**, 2966–2976 (2004). Copyright (2004) American Chemical Society; (ii) From ‘Sorption and transport of linear alkane hydrocarbons in biaxially oriented poly(ethylene terephthalate)’, S. N. Dhoot, B. D. Freeman, M. Stewart and A. J. Hill, *J. Polym. Sci. Part B: Polym. Phys. Ed.*, **43**, 1160–1172, Copyright © 2005, John Wiley & Sons, Inc. Reprinted with permission of John Wiley & Sons, Inc.

logous series of penetrants (e.g. n -alkanes), it is convenient and simple to use a single parameter, such as the number of carbon atoms in the molecule, because this provides a convenient (albeit empirical) and simple way to prepare correlations for D and, in many cases, P , with gas size [56–58], as shown in Figure 1.4. For the light gases (i.e. H_2 , He, N_2 , O_2 , CH_4 and CO_2), kinetic diameter gives the most faithful scaling of diffusion coefficients with penetrant size [22]. However, for larger gas molecules, kinetic diameter breaks down as a useful scaling parameter for penetrant size. For example, as shown in Table 1.1, the kinetic diameters of propane and n -butane are equal (4.3 Å). This result is consistent with the methodology used by Breck to estimate these kinetic diameters; as indicated above, the calculation was based on the minimum molecular width, which is the same for propane and n -butane [22]. However, diffusion coefficients of n -butane are always lower than those of propane in any polymer, which indicates that both molecular length and width influence diffusion coefficients;

the longer *n*-butane diffuses slower than the shorter propane. As another example, the kinetic diameter of propylene (4.5 Å) is larger than that of propane (4.3 Å), even though propylene diffusion coefficients are always higher than those of propane [59]. Additionally, only a limited set of kinetic diameter (d_k) values have been proposed [22], and so kinetic diameter values are not available for all penetrants of interest.

If many penetrants of varying size and shape are considered, estimates of size such as the van der Waals volume or critical volume are often more convenient scaling parameters since these values are available for practically any gas or vapor of interest [48]. The resulting empirical correlations often roughly obey a relation of the following form [60]:

$$D = \frac{\tau}{V_C^\eta} \quad (1.24)$$

where τ and η are polymer-dependent parameters, and V_C is the penetrant critical volume. Correlations such as this are only valid in the limit of low penetrant concentrations, when D is independent of penetrant concentration. Additionally, parameters such as critical volume do not carry any special shape-dependent information useful for correlating diffusion coefficients, and therefore such parameters should be used with care. Extrapolation beyond the range of penetrants studied, particularly to those of molecular shape markedly different from those used to establish the parameters of the correlation (e.g. branched versus unbranched penetrants), is not recommended and can lead to significant variance from the correlation [14]. Molecular diameters based on the Chung *et al.* model correlating collision diameter with critical volume are also provided in Table 1.1 in case a linear penetrant dimension is preferred over a volumetric measurement; since d_C and V_C are directly related. As indicated in the footnote of Table 1.1, there is no obvious advantage to using one or the other.

For many polymers, gas solubility coefficients over short ranges of penetrant critical temperature are well described by a linear relationship between the logarithm of S and some convenient measure of solute condensability, such as critical temperature, T_c , normal boiling point, T_b [61] or Lennard–Jones energy parameter, ϵ/k [31]. Two of these parameters, T_c and ϵ/k , are presented in Table 1.1 for common gases and vapors. An

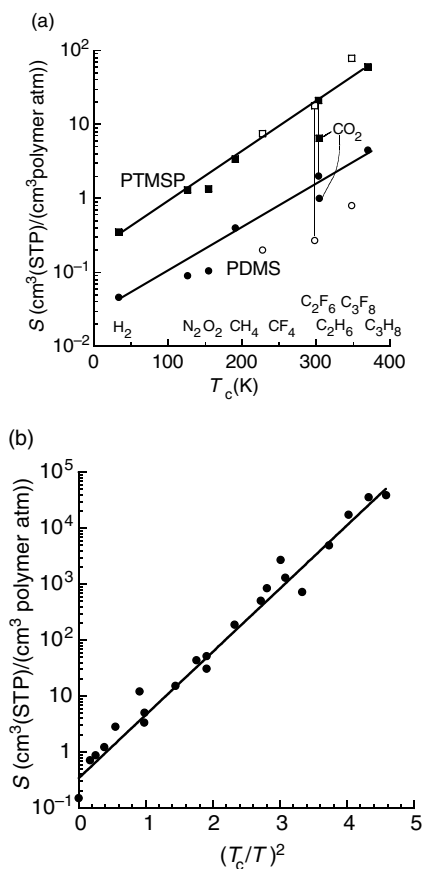


Figure 1.5 Correlation of low-pressure-limit solubility coefficients with solute critical temperature in (a) PTMSP and PDMS, and (b) AF2400 [12,88]. (a) From ‘Sorption and transport of hydrocarbon and perfluorocarbon gases in poly(1-trimethylsilyl-1-propyne)’, T. C. Merkel, V. Bondar, K. Nagai and B. D. Freeman, *J. Polym. Sci. Part B: Polym. Phys. Ed.*, **37**, 273–296, Copyright © 1999, John Wiley & Sons, Inc. Reprinted with permission of John Wiley & Sons, Inc. (b) (i) Reprinted with permission from V. Bondar *et al.*, *Macromolecules*, **32**, 6163–6171 (1999). Copyright (1999) American Chemical Society; (ii) Reprinted with permission from T. C. Merkel *et al.*, *Macromolecules*, **32**, 8427–8440 (1999). Copyright (1999) American Chemical Society

example of such a correlation is presented in Figure 1.5(a) for a rubbery polymer, polydimethylsiloxane (PDMS), and for a glassy polymer, poly(1-trimethylsilyl-1-propyne) (PTMSP). In the rubbery polymer, solubility of the light

gases and hydrocarbons (closed symbols) follows solubility is singular a rather linear progression with increasing critical temperature. The fluorocarbon gases (open symbols) fall considerably below this line due to the unfavorable interactions between fluorocarbon gases and hydrocarbon-based polymers such as PDMS; this effect is discussed in more detail in the chapter by Merkel *et al.* in this book. This result demonstrates the applicability of such correlations and an example of their failure, when specific interactions between the polymer and penetrant become significant. In the high-free-volume glassy polymer, PTMSP, the unfavorable interactions between this hydrocarbon-based polymer and perfluorinated penetrants are less obvious than in the lower-free-volume rubber, PDMS; this lack of sensitivity to mismatches in polymer/penetrant interaction energies has been ascribed to the strong driving force, in the glassy polymer, to fill the unoccupied non-equilibrium excess free volume of the polymer with penetrant molecules [62]. At conditions far from infinite dilution, when the so-called Langmuir excess free volume sites of the glassy polymer are predominantly filled, PTMSP exhibits higher solubility for hydrocarbon penetrants than for fluorocarbons, more consistent with the behavior shown by PDMS [62].

The fundamental basis for gas solubility to scale with penetrant condensability follows from simple, classical solution thermodynamics [8,63]. The enthalpy of sorption, ΔH_s , in the van't Hoff equation for gas dissolution is [8]:

$$S = S_0 e^{-\Delta H_s/RT} \quad (1.25)$$

Historically, for both gas solubility in liquids [48] and polymers [8], the enthalpy of sorption can be thought of in terms of two contributions:

$$\Delta H_s = \Delta H_c + \Delta H_m \quad (1.26)$$

where ΔH_c is the enthalpy of condensation of the pure gaseous penetrant to the liquid phase or, for penetrants which are above their critical temperature at the measurement conditions, to a condensed density consistent with that of the polymer, and ΔH_m is the partial molar enthalpy of mixing the condensed (or compressed) penetrant with the polymer segments. The enthalpy of condensation of the penetrant is related to its enthalpy of vaporization: $\Delta H_V = -\Delta H_C$.

Table 1.2 Slope, a_c , of the linear relationship between $\ln S$ and T_c for gas solubility in organic liquids at 20 °C [66]. Reprinted with permission from R. Prabbakar *et al.*, *Macromolecules*, **38**, 1899–1910 (2005). Copyright (2005) American Chemical Society

Solvent	$a_c \times 10^3 (\text{K}^{-1})$
Methyl alcohol	14
Ethyl alcohol	15
Amyl alcohol	16
Ethyl ether	14
Acetone	17
Methyl acetate	16
Ethyl acetate	15
Benzene	18
Toluene	14
Xylene	13
Cyclohexane	16
Cyclohexanol	13
Tetrachloromethane	15
Chloroform	19
Chlorobenzene	19

Experimentally, there are strong correlations between ΔH_V and any of several convenient scales of gas condensability [64]:

$$\Delta H_V/R = a_b T_b = a_c T_c = a_e (\varepsilon/k) \quad (1.27)$$

where a_b , a_c and a_e are all adjustable constants. If $|\Delta H_m| \ll |\Delta H_c|$, which is often the case for many gases [64,65], then:

$$\begin{aligned} \ln S &= \ln S_0 + a_b T_b = \ln S_0 + a_c T_c \\ &= \ln S_0 + a_e (\varepsilon/k) \end{aligned} \quad (1.28)$$

For most polymers and penetrants the values of a_c are quite similar. That is, a_c is a near-universal parameter. Similar behavior is observed for gas dissolution in liquids. To illustrate this point, Table 1.2 presents a_c values for many gases in a number of organic liquids; the solubility data used to determine these values of a_c range over three orders of magnitude, depending on the gas [66,67].

Gas solubility in polymers obeys similar trends to those observed in liquids. That is, a_c is approximately independent of polymer chemical structure, as shown in Table 1.3 [67–72]. In fact, a comparison of the values in Tables 1.2 and 1.3 indicate that the values of a_c are very similar for gases dissolving in liquids and in

Table 1.3 Slope, a_c , of the linear relationship between $\ln S$ and T_c for gas solubility in polymers. Reprinted from *Polymer*, **42**, G. E. Serad, B. D. Freeman, M. E. Stewart and A. J. Hill, 'Gas and vapor sorption and diffusion in poly(ethylene terephthalate)', 6929–6943, Copyright (2001), with permission from Elsevier

Classification	Medium	$a_c \times 10^3 (\text{K}^{-1})$
Rubbers	Natural rubber [70]	18 ^a
	Amorphous polyethylene [70]	16 ^a
	Polybutadiene – hydrogenated [70]	17 ^a
	Polydimethylsiloxane [68]	17 ^b
	Polysulfone [72]	17 ^c
Glassy polymers	Poly(phenylene oxide) [69]	16 ^d
	Poly(ethylene terephthalate) [71]	19 ^e

^a25 °C and 1 atm.

^b35 °C

^c35 °C and 10 atm for all gases, except *n*-C₄H₁₀, which is at infinite dilution.

^d35 °C and infinite dilution.

^e24–45 °C and infinite dilution.

polymers, which underscores the similarity of gas dissolution in liquids and polymers. Exceptions to the general rule that a_c is independent of polymer structure occur in fluorocarbon/hydrocarbon mixtures [67]. Complications may arise for glassy polymers and for solutes (in both rubbery and glassy polymers) with large values of ΔH_m . In glassy polymers, partial molar enthalpies of sorption are often negative and can differ significantly from zero [12]. Moreover, ΔH_m values in glassy polymers are typically concentration-dependent, particularly for strongly sorbing components. In both glassy and rubbery polymers, for more condensable (i.e. heavier) solutes, such as higher hydrocarbons and organic vapors, $|\Delta H_c| > |\Delta H_m|$, and ΔH_c is directly proportional to T_c^2 [73]. For such cases, correlations of the following type have been proposed [12,74]:

$$\ln S = M + NT_c^2 \quad (1.29)$$

$$\ln S = M' + N'(T_c/T)^2 \quad (1.30)$$

An example of such a correlation is shown in Figure 1.5(b). However, for studies involving only light gases, the correlations given by Equations (1.28) (i.e. solubility scaling with T_c) are obeyed with sufficient accuracy to be used for correlating solubility.

If van der Waals forces dominate gas–polymer interactions during dissolution, then solubility coefficients have also been linked to appropriately defined surface areas of molecules. Good correlations between $\ln S$, van der Waals surface areas, as estimated using (UNIFAC), and solvent accessible surface areas have been demonstrated for numerous polymers (both rubbery and glassy) [75]. In contrast to Equation (1.8), these correlations are linear for a wide range of solutes.

In a series of penetrants, as the size of the diffusing molecules increases, the D values decrease. On the other hand, for many penetrants, T_c increases (roughly) as penetrant size increases, and so S often increases as the penetrant size increases. The resulting permeability coefficients reflect these often competing trends in D and S with increasing penetrant size. Water is a notable exception to these trends. It has a very high T_c value (647.3 K [48]) and a small kinetic diameter value, 2.65 Å [22], making it often the most permeable gas in a polymer.

As illustrated in Figure 1.3, the slopes of the dependence of D on d^2 , or the size-sieving ability of the polymer, can be quite different for polymers in the rubbery and glassy states. All other factors being equal, for polymers above their glass transition temperatures (T_g), D is often less sensitive to penetrant size than in traditional, stiff-chain, low-free-volume glassy polymers because polymers with higher molecular chain mobility (i.e. lower T_g) tend to provide larger and more frequent availability of free volume elements of sufficient size to accommodate diffusion steps of both large and small penetrant molecules, which is the basis of their weaker size-sieving ability (i.e. D depends weakly on penetrant size). Low-free-volume, rigid, glassy polymers have very restricted chain motion, which provides small free-volume elements, suitable for diffusion steps of small gases, much more often than free-volume elements large enough to allow diffusion of larger gas molecules; the large disparity in the availability of free-volume elements suitable for small and large penetrants leads to strong size-sieving ability (i.e. a strong dependence of D on penetrant size). However, in addition to the influence of molecular mobility on diffusion coefficients and size-selectivity, there is a substantial

influence of free volume on both D and diffusivity selectivity. As discussed in Chapter 11, diffusivity selectivity increases as the size of free-volume elements in the polymer decreases. These two effects (chain mobility, as characterized by T_g , and free volume) can oppose one another so

that, for example, materials with higher T_g values, high diffusion coefficients and stronger size-sieving ability can be prepared [76].

If one uses a single scaling parameter for correlations involving D , S and P (e.g. V_c , the gas critical volume) (cf. Figure 1.6), then for

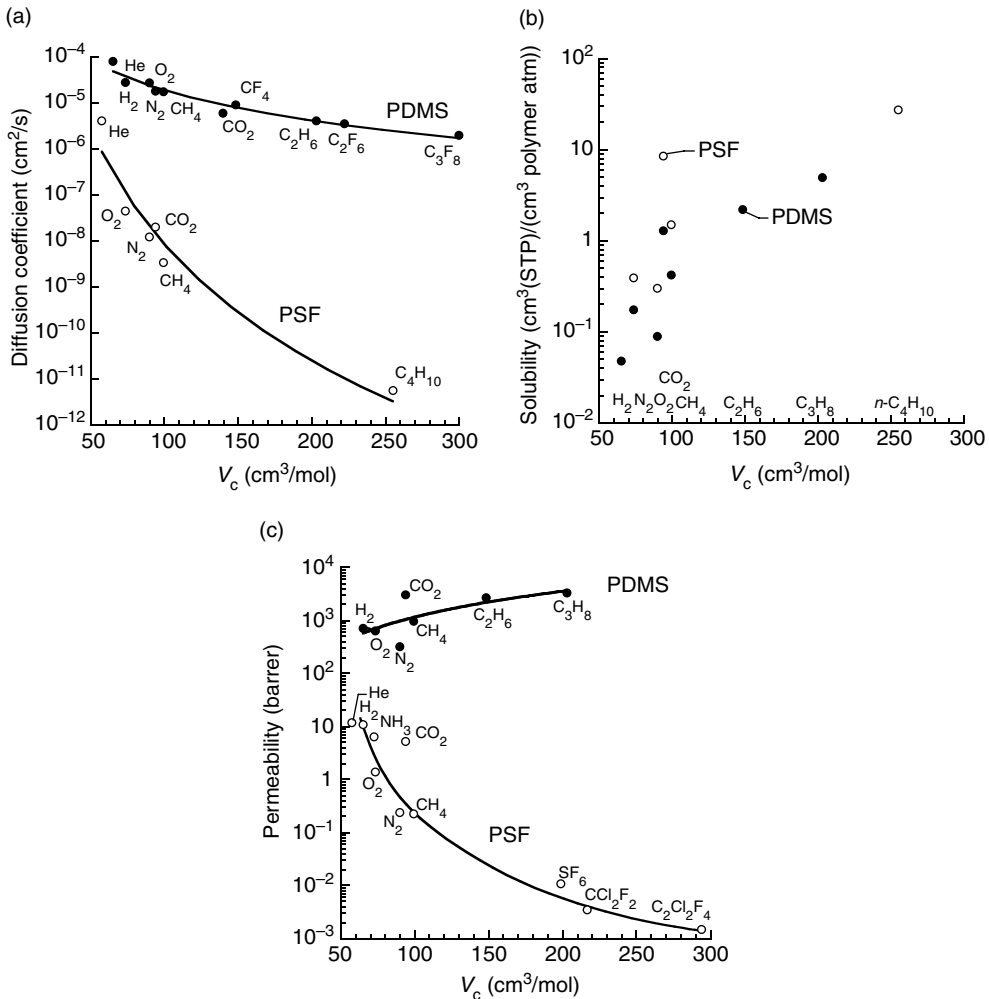


Figure 1.6 Correlations of (a) diffusion, (b) solubility and (c) permeability values with penetrant critical volume in polysulfone (PSF) and PDMS [34,45]. Solubility and permeability experiments were conducted at an upstream pressure between 3 and 20 atm for all penetrants, except for n -butane which was conducted at an upstream pressure of less than 1 atm. The downstream pressure was ‘at vacuum’ and atmospheric pressure for PSF and PDMS, respectively. Diffusion coefficients were calculated from the permeability and solubility data, while PSF and PDMS data were collected at 23 and 35 °C, respectively. (a–c) (i) From ‘Gas sorption, diffusion and permeation in polydimethylsiloxane’, T. C. Merkel, V. Bondar, K. Nagai, B. D. Freeman and I. Pinnau, *J. Polym. Sci. Part B: Polym. Phys. Ed.*, **38**, 415–434, Copyright © 2000, John Wiley & Sons, Inc. Reprinted with permission of John Wiley & Sons, Inc.; (ii) Reprinted with permission from K. Ghosal *et al.*, *Macromolecules*, **29**, 4360–4369 (1996). Copyright (1996) American Chemical Society

low-free-volume conventional glassy polymers, such as polysulfone, similar dependences of D and P on V_c are observed. As illustrated by this example, solubility is not correlated nearly as well with V_c as with T_c . Therefore, in membranes based on conventional, low-free-volume glassy polymeric materials (e.g. polysulfone), the smaller, faster diffusing components of the feed mixture is always enriched in the permeate. In contrast, in some flexible, high-free-volume rubbers, such as PDMS, the dependence of P on V_c is similar to the effect of S on V_c (cf. Figure 1.6). In such a membrane, permeate streams are enriched in the heavier (i.e. larger, more soluble) components in the feed stream. Although not all rubbery polymers exhibit such ‘reverse-selective’ properties, PDMS has high permeability and organic-vapor/gas selectivity, and is used commercially as a membrane for separations requiring this capability [28].

A notable exception from the regularity described above is PTMSP and the related highly permeable, substituted acetylene polymers discussed in detail in Chapter 9. These rigid, glassy polymers are characterized by very high levels of free volume, which contribute to extremely high diffusion coefficients and very weak size-sieving ability. Hence, in these polymers, larger, more soluble penetrants are more permeable than smaller, less soluble penetrants. Membranes based on such materials could be used for enrichment of the heavier components of gas streams, (e.g. removal of higher hydrocarbons from natural gas), if other requirements are fulfilled, such as long-term stability of permeability and chemical stability in the feed streams to be separated [77,78].

1.2.2 Effect of Polymer Properties on Transport Parameters

1.2.2.1 Glass Transition Temperature

The effects of the T_g on permeability and diffusivity are especially evident for rubbers or semicrystalline polyolefins when the T_g is below room temperature. In elastomers, polymer segmental mobility creates the transient free-volume elements that allow gas and vapor diffusion through the polymer to occur. Free volume in such media, like in liquids, undergoes rapid fluctuations, and so the difference between the

measurement temperature, T_m , and T_g has a strong effect on free volume and serves as a crude indicator of segmental mobility at T_m . Indeed, good correlations of D and P with T_g have been demonstrated by several authors [36,79,80], while the S values are essentially independent of T_g . Example of such correlations for D and P are shown in Figure 1.7.

While there is a general trend evident in these figures, there is also quite a bit of scatter, suggesting that factors other than T_g contribute in an important way to diffusivity and permeability. Side-chain mobility can also affect the T_g values and, in turn, the transport parameters [81,82]. In glassy polymers, increasing T_g in a group of structurally related glassy polymers (e.g. by adding substituents to the aromatic rings of low-free-volume, aromatic polysulfones) often results in increases in P and D [76]. As such, attempts to find general correlation between glass transition temperature in glassy polymers and permeation properties failed (e.g. see Hirayama *et al.* [83]). For example, high- T_g polymers can display very large (e.g. PTMSP [84]) and rather small (e.g. Kapton polyimide [85]) diffusivity and permeability values. However, this phenomenon can be explained by the complex nature of factors that influence gas diffusion and permeability. Diffusion coefficients are exquisitely sensitive to free volume in a polymer. However, free volume is only one of several factors that affect T_g , which depends on both intermolecular interactions (which may be sensitive to free volume) and intramolecular interactions (which may depend more on the energy barriers to rotation about backbone covalent bonds than on free volume). Hence, correlations of gas diffusivity or permeability with T_g often do not characterize the free volume or its distribution adequately as they relate to diffusion properties. Consequently, free volume is usually viewed as more relevant than T_g for correlating transport properties in polymers.

In addition to the rather large-scale segmental mobility that is important in T_g -type motions of polymer chains, smaller-scale main- or side-chain motions that determine sub- T_g behavior also influence gas permeation in polymers. In fact, low-temperature transitions (e.g. T_γ) in substituted polysulfones correlate well with gas permeability coefficients. However, this correlation derives from intramolecular packing or free-volume effects that change both T_γ and P in

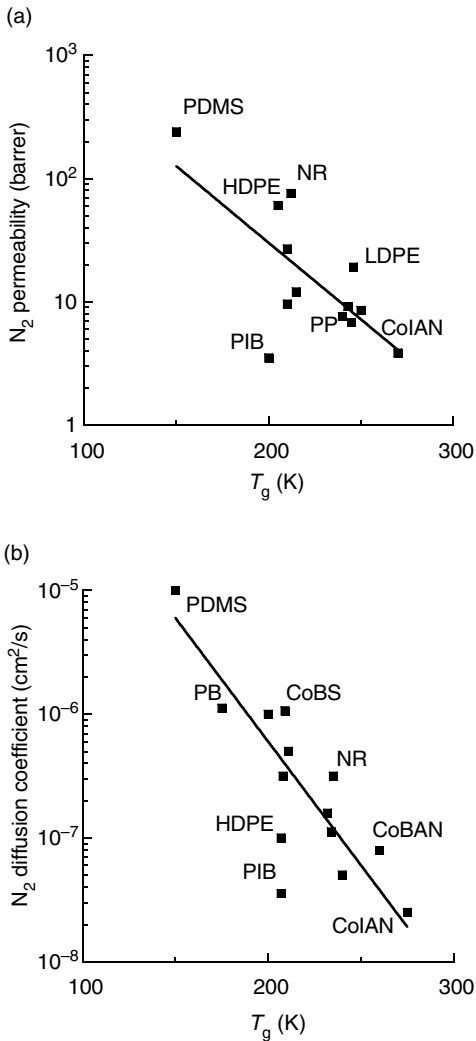


Figure 1.7 (a) Permeability and (b) diffusion coefficients for nitrogen in rubbers with different glass transition temperatures: polydimethylsiloxane (PDMS), high-density polyethylene (HDPE), low-density polyethylene (LDPE), natural rubber (NR), polyisobutylene (PIB), polypropylene (PP), polybutadiene (PB), poly(butadiene-*co*-styrene) (CoBS), poly(isoprene-*co*-acrylonitrile) (CoIAN), poly(butadiene-*co*-acrylonitrile) (CoBAN), methyl rubber (MR) and polychloroprene (PCP). Experiments were conducted at room temperature and in a pressure range where P and D are independent of pressure [79]. (a, b) Reproduced by permission of 'Nauka' RAN, Moscow from Y. P. Yampolskii, S. G. Durgaryan and N. S. Nametkin, 'Translational and rotational mobility of low molecular mass compounds in polymers with different glass transition temperatures', *Vysokomolekuliarnye Soedineniia*, **24**, 536–541 (1982)

similar ways [76], suggesting a subtle interplay between local polymer chain mobility, chain packing and gas transport properties.

1.2.2.2 Molecular Mass

The molecular mass of polymers typically does not significantly influence the gas permeation parameters. That is, chain end-groups rarely exert a significant influence on the transport properties. At low molecular weights, where one might anticipate the strongest effects of molecular weight, it is often difficult to prepare mechanically stable, free-standing films; at molecular weights high enough to prepare films which can undergo permeation testing, the effect of molecular weight on the transport properties is usually small. In this regard, the literature reports fairly weak effects of polymer molecular mass on P and D values (e.g. see [86–88]). Toi and Paul reported some variation in the solubility coefficient of CO_2 in polystyrene samples with molecular masses in the range of 3600 to 850 000 [89]. However, these effects can be partly ascribed to a concomitant increase in T_g from 345 to 374 K. The situation is different in cross-linked rubbery polymers; in these materials, chain end-groups can be introduced via pendant side-chains, while mechanical properties can be controlled somewhat independently by varying the cross-linking density. Thus, it is possible to prepare mechanically robust materials with high concentrations of chain-ends. Lin *et al.* have observed strong effects of chain-end concentration on transport properties in such systems [90], where increasing chain end $-OCH_3$ concentration in poly(ethylene glycol) network polymers from essentially 0 wt% of total sample mass to 6.7 wt% increases the CO_2 diffusivity fivefold [90].

Permeability is sensitive to various parameters that characterize chain packing, such as polymer density [91] or mean interchain distance (d -spacing deduced from wide-angle X-ray diffraction (WAXD) studies) [83,92]. However, the most relevant measure of chain packing efficiency is *free volume*. According to free-volume theory [5]:

$$D = A_0 \exp\left(-\frac{\gamma V^*}{V_f}\right) \quad (1.31)$$

where A is a prefactor, V_f is the average free volume in the system, γ is a parameter of order unity introduced to prevent double counting of free-volume elements in the theory leading to this equation, and V^* characterizes the size of diffusing molecules; to be coherent with the correlations described earlier and with emerging experimental data related to this issue, γV^* is often found to be proportional to d^2 .

Chapters 3, 4 and 7 in this volume discuss at length many of the definitions and methods for determining free volume in polymers. The simplest and most popular way employs the definition suggested by Bondi [93]. According to this method, the specific free volume in a polymer, V_f (cm^3/g), is the difference between the specific volume of a polymer, $V_{sp} = 1/\rho$, where ρ (g/cm^3) is the polymer density, and its occupied volume, V_{oc} . Bondi proposed calculating V_{oc} as $1.3 V_w$, where V_w is the sum of the increments of van der Waals volumes (values tabulated in van Krevelen [31]). Hence:

$$V_f = V_{sp} - 1.3 V_w \quad (1.32)$$

In most cases, a dimensionless, reduced value of the free volume, called the fractional free volume ($\text{FFV} = V_f/V_{sp}$), gives better correlations than V_f with transport properties within a family of polymers. Thus, it is most common to replace V_f in Equation (1.31) with FFV:

$$D = A e^{-B/\text{FFV}} \quad (1.33)$$

where A and B are empirical constants which vary from gas to gas and from one polymer to another. Based on the arguments given above for γV^* , B should be expected to scale with some measure of penetrant size. Strictly speaking, this equation applies only to the gas self-diffusion coefficient [94,95]. However, from a practical viewpoint, since the concentration of gas in the polymer is typically less than 10 vol%, the correction factor between the self-diffusion coefficient and the mutual-diffusion coefficient is typically small. As a result, in the gas transport field, the key result from free volume theory (Equation (1.33)) is usually applied directly to mutual-diffusion coefficients, and we adopt that approach here.

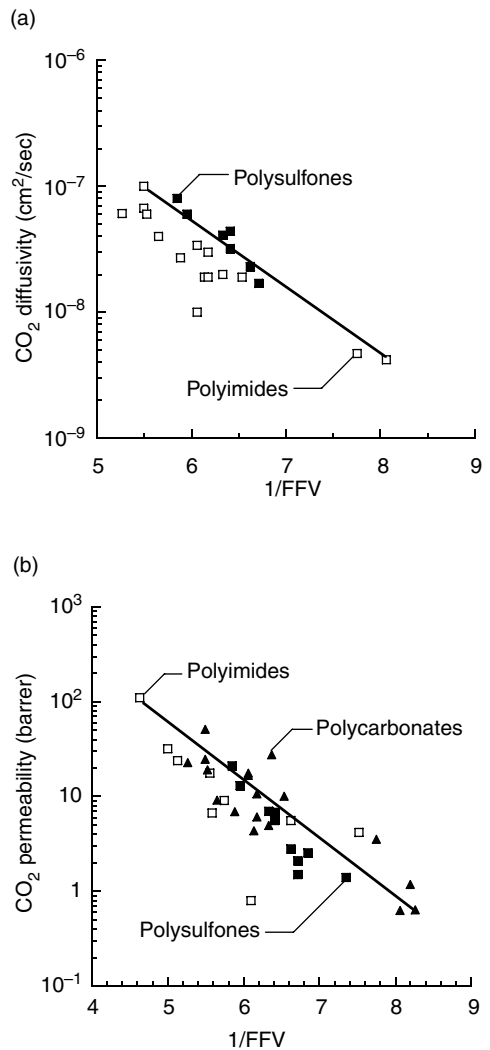


Figure 1.8 Correlations of (a) CO_2 diffusion and (b) CO_2 permeability coefficients with fractional free volume in glassy aromatic polysulfones, polyimides and polycarbonates. The experiments were conducted at 35°C , a feed pressure of 10 atm while the permeate pressure was ‘at vacuum’ [76]

Figure 1.8 presents an example of such a correlation of mutual diffusion coefficients with fractional free volume. Gas solubility coefficients in polymers vary over a much narrower range than diffusivity, and the effect of free volume on solubility is generally much weaker than on diffusivity. Therefore, gas permeability coefficients are

often directly correlated with fractional free volume [54]:

$$P = A_P e^{-B/FFV} \quad (1.34)$$

where, to be consistent with Equation (1.9), $A_P = SA$. A correlation of this type is presented for CO_2 in Figure 1.8(b).

For reasons discussed in Chapter 7, the Bondi method gives rather rough estimates of the influence of free volume upon gas diffusion and permeation properties in polymers. Good correlations for P and D are usually obtained for structurally related polymers (e.g. Figures 1.8(a) and 1.8(b)), whereas attempts to draw predictable correlations for extensive sets of polymers from very different families of polymers show more scatter (cf. Figure 1.9) [96–100]. It has been suggested that systematic errors in the van der Waals increments might lead to such discrepancies among widely varying families of polymers. One method for checking the validity of Equations (1.28) and (1.29) might be to examine the dependence of P and D on FFV for gases with different molecular dimensions. In rubbery polymers, recent results by Lin and Freeman have shown remark-

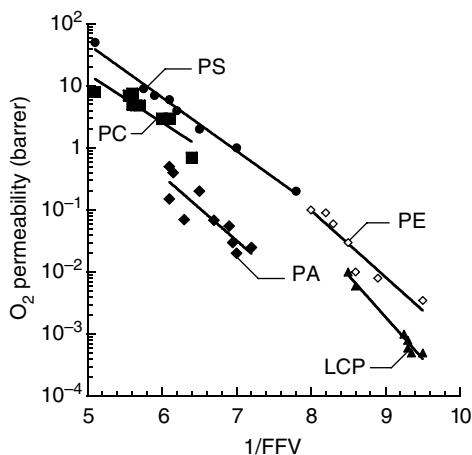


Figure 1.9 O_2 permeability for glassy polystyrenes (PS) at 35 °C [96], polycarbonates (PC) at 35 °C [97,170], polyamides (PA) at 25 °C [54], polyesters (PE) at 30 °C [98] and liquid crystalline polyesters (LCP) at 35 °C [99,100]

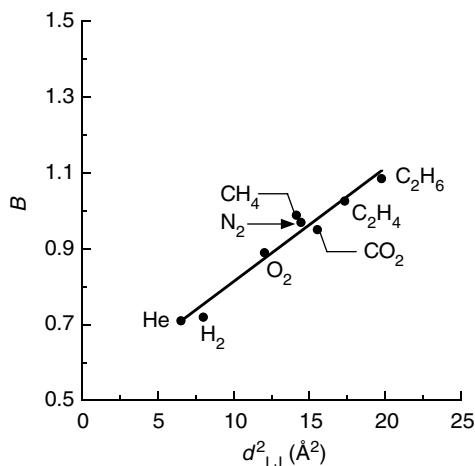


Figure 1.10 The dependence of B on penetrant Lennard–Jones diameter squared in cross-linked poly(ethylene glycol diacrylate), the equation for the best-fit line is $B = 0.51 + 0.030 d_{LJ}^2$ when the units of d_{LJ} are Å [101]. Reprinted with permission from H. Lin and B. D. Freeman, *Macromolecules*, **38**, 8394–8407 (2005). Copyright (2005) American Chemical Society

ably strong correlations between B and penetrant size for a series of rubbery polymers. An example of such a correlation is presented in Figure 1.10 [101].

However, in glassy polymers, only approximate correlations between diffusivity and permeability with free volume have been observed when Bondi's method is used to estimate FFV [102,103]. Better correlations can be obtained after accounting for interchain interactions (cohesive energy density) or via direct determination of free volume in polymers using, for example, positron annihilation lifetime spectroscopy [103,104]. Gas diffusion in polymers should be hampered by strong interchain interactions, and so cohesive energy density ($\text{CED} = E_{\text{coh}}/V_{\text{sp}}$) [31] can be included in correlations such as those described earlier to improve the correlation [103]. A simple equation:

$$\log P = A' - B'(\text{CED}/\text{FFV}) \quad (1.35)$$

has been proposed to account for interchain interactions in gas-transport-impacting glassy polymers [105].

1.3 Effect of Pressure on Transport Parameters

1.3.1 Sorption

Figure 1.11 shows schematically the basic isotherm shapes that are often observed. The simplest behavior is presented in Figure 1.11(a), which shows the sorption isotherm of O₂ in rubbery polydimethylsiloxane (PDMS). These linear isotherms obey Henry's law, and are characterized in terms of a Henry's law parameter, k_D , which is defined as follows:

$$C = k_D p \quad (1.36)$$

Such isotherms are observed for light gas (e.g. He, H₂, N₂, O₂, CH₄) sorption in rubbery polymers at essentially all pressures of practical interest.

For more condensable gases (e.g. CO₂, higher hydrocarbons and vapors), at sufficiently high pressure (typically pressures that are significant relative to the vapor pressure for penetrants below their critical temperature), strong deviation from Henry's law and, consequently, non-linear sorption isotherms are observed. A sorption isotherm which is convex to the pressure axis is characteristic of vapor dissolution in polymers above their glass transition temperatures and is historically described by using the Flory–Huggins equation [8]:

$$\ln a = \ln(p/p_s) = \ln \phi_v + (1 - \phi_v) + \chi(1 - \phi_v)^2 \quad (1.37)$$

where a is penetrant activity in the gas phase contiguous to the polymers, p and p_s are the pressure and saturation vapor pressures of the gas, respectively, ϕ_v is the volume fraction of penetrant dissolved in the polymer, and χ is the so-called Flory–Huggins interaction parameter. The first equality in Equation (1.37) ($a = p/p_s$) presumes that the gas phase is ideal, which can be relaxed by using an appropriate equation of state if the gas phase is non-ideal. When $\chi > 2$, polymer–gas interactions are small, and if $\chi \leq 0.5$ interactions are so strong that non-cross-linked polymer can dissolve in the penetrant. Figure 1.11(b) pro-

vides an example (acetone sorption in PDMS) where the Flory–Huggins model has been used to describe the experimental data [106]. Although the polymer presented in Figure 1.11(b) (PDMS) is cross-linked, the cross-linking has not been accounted for in the sorption data analysis. For cases of typical interest in gas and vapor separations, cross-linked polymers such as PDMS often do not sorb sufficient amounts of penetrants for the elastic constraints imposed by the cross-linked network to have a significant influence on the penetrant chemical potential. That is, the terms in, for example, the Flory–Rehner model [107,108] which would account for the effect of cross-linking on the gas sorption level in a polymer, are typically negligible. Another typical case where isotherms are convex to the pressure or activity axis is realized in sorption of water or lower alcohols into hydrophobic polymers [42,43,109,110]. These isotherms are evidence of solute cluster formation, which becomes progressively more important at higher activity. One drawback of the Flory–Huggins model is that, to successfully describe the experimental data, χ often must be treated as an empirical parameter that depends on temperature and penetrant concentration. Recently, more effort has focused on using more modern equations of state, such as the Sanchez–LaCombe equation, to model sorption in rubbery polymers in an attempt to improve the ability to model sorption properties without relying on *ad hoc* empirical additions to the Flory–Huggins model [111].

Sorption isotherms which are concave to the pressure axis are typical for glassy polymers. An example is presented in Figure 1.11(c). The three-parameter dual-mode sorption isotherm model has been widely used to describe gas sorption in this case [112]:

$$C = k_D p + C'_H \frac{bp}{1 + bp} \quad (1.38)$$

where k_D is the Henry's law parameter characterizing sorption into the densified equilibrium matrix of the glassy polymer, C'_H is the Langmuir sorption capacity, which characterizes sorption into the non-equilibrium excess volume associated with the glassy state, and b is the Langmuir affinity parameter. In this model, two “popula-

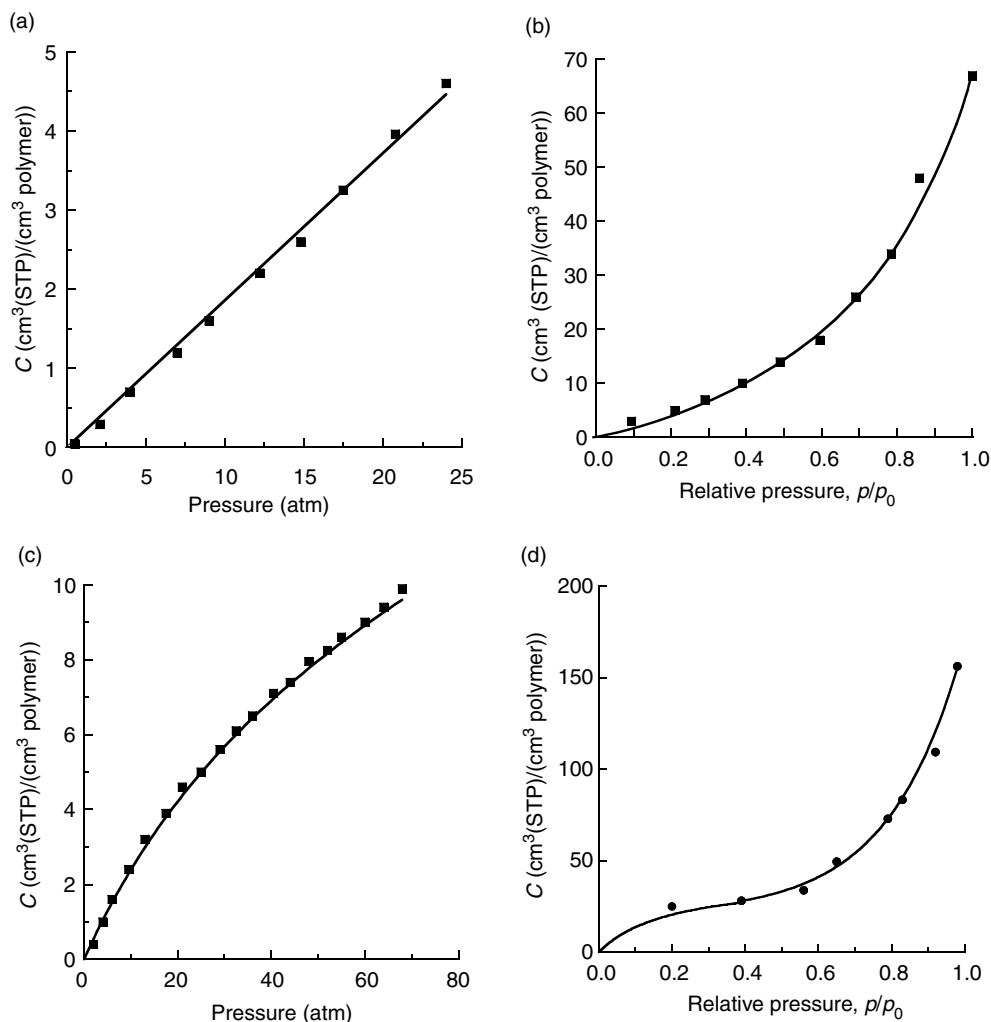


Figure 1.11 Typical gas sorption isotherms: (a) Henry's law (O_2 in PDMS at 35°C [34]); (b) Flory-Huggins (FH) (acetone in PDMS at 28°C [106]), where p_0 is the acetone vapor pressure, which is 258 mmHg at 28°C ; (c) dual-mode sorption (DMS) (Argon in PSF at 25°C [120]); (d) DMS + FH (vinyl chloride monomer (VCM) in poly(vinyl chloride) (PVC) at 30°C [121] (p_0 is the VCM vapor pressure, which is 2980 mmHg at 30°C). (a) From 'Gas sorption, diffusion and permeation in polydimethylsiloxane', T. C. Merkel, V. Bondar, K. Nagai, B. D. Freeman and I. Pinnau, *J. Polym. Sci. Part B: Polym. Phys. Ed.*, **38**, 415–434, Copyright © 2000, John Wiley & Sons, Inc. Reprinted with permission of John Wiley & Sons, Inc. (b) From 'Pure and mixed gas acetone/nitrogen permeation properties of polydimethylsiloxane', A. Singh, B. D. Freeman and I. Pinnau, *J. Polym. Sci. Part B: Polym. Phys. Ed.*, **36**, 289–301, Copyright © 1998, John Wiley & Sons, Inc. Reprinted with permission of John Wiley & Sons, Inc. (c) From 'On pressure dependence of the parameters of the dual-mode sorption model', V. Bondar, Y. Kamiya and Y. P. Yampolskii, *J. Polym. Sci. Part B: Polym. Phys. Ed.*, **34**, 369–378, Copyright © 1996, John Wiley & Sons, Inc. Reprinted with permission of John Wiley & Sons, Inc. (d) Reproduced by permission of Wiley-VCH from 'The solubility of vinyl chloride in poly(vinyl chloride)', A. R. Berens, *Angew. Makromol. Chemie*, **47**, 97–110 (1975)

tions" of sorbed species, in local chemical equilibrium with one another, are envisioned – those in long-lived, non-equilibrium free-volume ele-

ments and those dissolved in more densely packed regions within polymers. In the low-pressure limit, as $p \rightarrow 0$, one obtains the infinite

dilution gas solubility coefficient:

$$S = k_D + C'_H b \quad (1.39)$$

which determines the initial slope of the isotherm. At higher pressure, the slope is determined by the Henry's law solubility coefficient, k_D , and the transition between these two sections of the isotherm occurs at $p = 1/b$. At low to moderate pressures, gas sorption in glassy polymers is often dominated by the Langmuir term in Equation (1.38) (i.e. $C'_H b \gg k_D$) [113], especially in polymers with high T_g . The k_D and b parameters are treated as equilibrium constants whose temperature-dependence is given by van't Hoff relationships with negative enthalpies of sorption ΔH_s , (usually, ΔH_s that corresponds to the temperature-dependence of b is more exothermic than that of k_D) [8,62,88]. Both k_D and b values are often correlated with penetrant condensability. For example, k_D and b are presented as a function of gas critical temperatures in Figure 1.12 in a manner consistent with the correlation of total solubility with T_c , as shown in Figure 1.5 [114].

The Langmuir sorption capacity parameter, C'_H , is interpreted as a measure of non-equilibrium or unrelaxed volume in polymers. For CO_2 sorption, this parameter, as determined from analysis of experimental sorption isotherms, is often consistent with the value estimated as follows:

$$C'_H = 22414 \frac{V_g - V_r}{V_g} \quad (1.40)$$

where V_g is the total specific volume of the polymer, V_r is the total specific volume of the equilibrium liquid or rubbery polymer if vitrification is precluded, and ρ^* is the hypothetical density of liquid-like solutes sorbed in Langmuir sites [7,115,116]. The non-equilibrium excess volume providing the locus of the Langmuir sorption derives from the excess volume inherently present in glassy polymers at temperatures below T_g . Figure 1.13 presents the effect of temperature on the density of Ultem[®] 1000 polyetherimide. As the polymer is cooled from above to below the T_g , there is an abrupt change in the slope of the specific volume versus temperature plot, marking the onset of severe kinetic constraints in the polymer's ability to reorga-

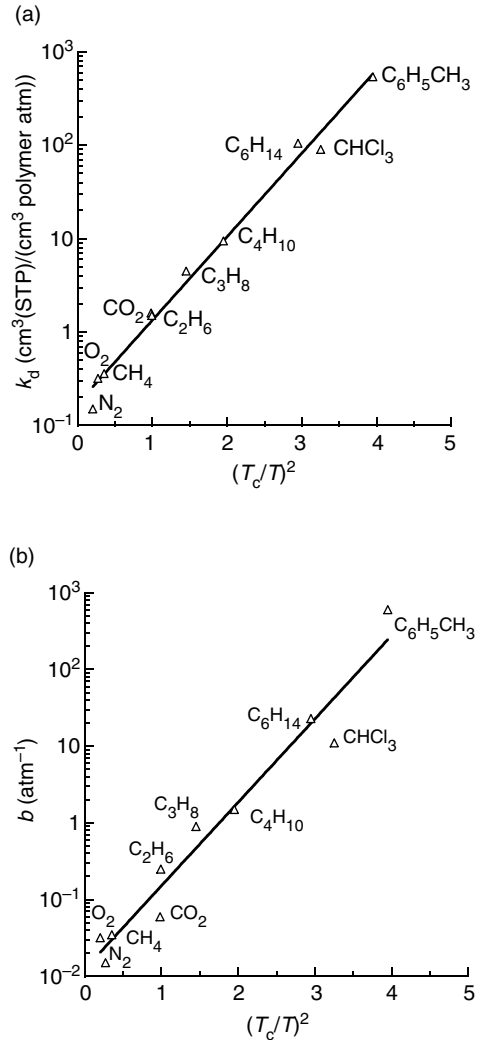


Figure 1.12 Correlation of (a) k_D and (b) b with squared reduced critical temperature in amorphous Teflon AF2400 [114]

nize itself to attain its equilibrium specific volume, V_r . The material is kinetically trapped in a higher-volume state, V_g . The difference between the observed specific volume and the equilibrium specific volume, $V_g - V_r$, is believed to be the locus of the non-equilibrium excess sorption characterized by the Langmuir capacity parameter, C'_H . According to this interpretation, C'_H should depend upon temperature. It should decrease as temperature increases and vanish when the experimental temperature T

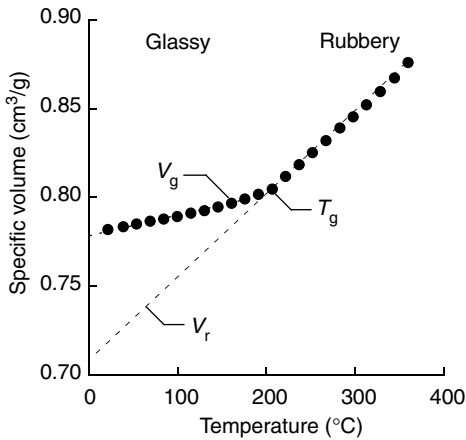


Figure 1.13 Effect of temperature on specific volume in the rubbery and glassy states of Ultem[®] 1000 polyetherimide at 0 MPa; the data have been extrapolated to 0 MPa from higher pressures [175]. Copyright © 1995 from Standard Pressure, Volume, Temperature Data by P. Zoller and D. J. Walsh. Reproduced by permission of Routledge/Taylor & Francis Group, LLC

becomes equal to T_g . Therefore, when considering the sorption properties of a single gas in many different polymers, C'_H should increase as T_g increases. Such behavior is well documented [76,112,115]. Figure 1.14 provides an illustration of this principle. If one considers a variety of gases in a single polymer, for gases below their critical temperature, T_c , the observed C'_H values roughly decrease with increasing molecular size (cf. Figure 1.15) [12,62,114,117]. That is, larger gas molecules sample progressively smaller fractions of available unrelaxed (free) volume in glassy polymers during sorption.

In spite of the intuitive consistency of the dual-mode sorption model, it must be considered an empirical, phenomenological model that fits the experimentally measured isotherms but lacks a molecular foundation. That is, it cannot be used to predict sorption isotherms in the absence of experimental data, and its parameters, including the equilibrium parameters k_D and b , are observed to depend on sample processing history [118,119]. The parameters also depend on the range of pressure explored in sorption measurements, especially when working at higher pressures [120]. Recent efforts have focused on

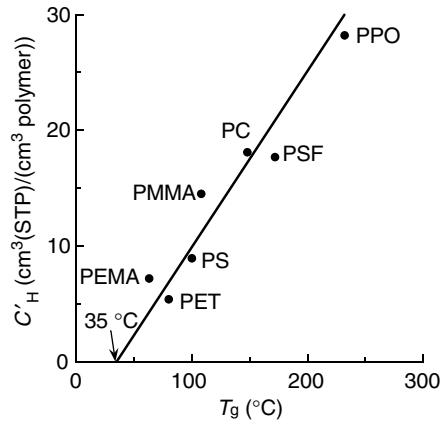


Figure 1.14 Variation of C'_H for carbon dioxide with polymer glass transition temperature. The sorption data used to evaluate C'_H were measured at 35 °C, and the polymers are poly(2,6-dimethyl-1,4-phenylene oxide) (PPO), polysulfone (PSF), polycarbonate (PC), poly(methyl methacrylate) (PMMA), polystyrene (PS), poly(ethyl methacrylate) (PEMA) and poly(ethylene terephthalate) (PET) [69]. From 'Gas sorption and transport in poly(phenylene oxide) and comparisons with other glassy polymers', K. Toi, G. Morel and D. R. Paul, *J. Appl. Polym. Sci.*, **27**, 2997–3005, Copyright © 1982, John Wiley & Sons, Inc. Reprinted with permission of John Wiley & Sons, Inc.

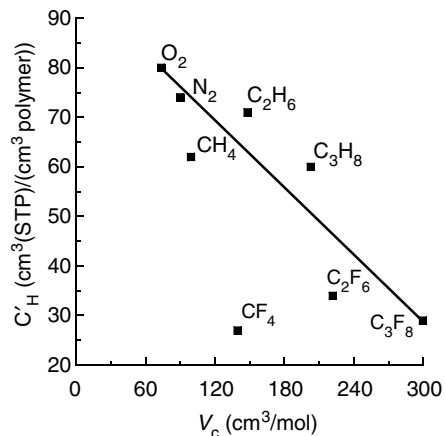


Figure 1.15 The effects of gas molecular size on C'_H in PTMSP at 35 °C [62]. From 'Sorption and transport of hydrocarbon and perfluorocarbon gases in poly(1-trimethylsilyl-1-propyne)', T. C. Merkel, V. Bondar, K. Nagai and B. D. Freeman, *J. Polym. Sci. Part B: Polym. Phys. Ed.*, **37**, 273–296, Copyright © 1999, John Wiley & Sons, Inc. Reprinted with permission of John Wiley & Sons, Inc.

developing sorption models based on applying statistical mechanics concepts to develop equations-of-state for non-equilibrium systems such as glassy polymers. These equations-of-state can then form the foundations of new sorption models that have more predictive ability than the dual-mode model. A review of this approach is presented in Chapter 5.

Sigmoidal-shaped sorption isotherms, such as the one presented in Figure 1.11(d) are often observed in glassy polymers when the solute concentration becomes high enough that Henry's law is no longer adequate for modeling sorption in the equilibrium structure of the polymer. In these cases, the isotherm is often modeled by using a combination of the Langmuir contribution of the dual-mode model and the Flory–Huggins model to replace the Henry's law component of the dual-mode model. Often, in the region where the isotherm becomes convex to the abscissa, the polymer is believed to contain sufficient amounts of penetrant to become plasticized and to have the T_g of the gas–polymer system reduced towards the experimental temperature [121]. It is easiest to observe such isotherms for highly sorbing gases (e.g. CO₂ and organic vapors) and polymers having relatively low glass transition temperatures.

1.3.2 Diffusion

Figure 1.16 presents various examples of the observed dependence of diffusivity on concentration. For low-sorbing permanent gases in polymers, the diffusion coefficients are usually independent of gas concentration in the polymer, as illustrated in Figure 1.16(a) [122]. Plasticization due to sorption of high concentrations of penetrants, such as organic vapors, often result in linear (cf. Figure 1.16(b)) or even exponential increases in D [123–126]. One of the principle explanations of this behavior is that penetrant molecules contribute free volume to a polymer/penetrant mixture when they sorb into it, and the increase in free volume due to penetrant sorption increases the polymer chain mobility and penetrant diffusion coefficients. Clustering is accompanied by an effective increase in the mean size of the diffusing species and is manifested by a decrease in D with increasing concentration (cf. Figure 1.16(c)) [127]. The dependence of D on concentration allows one to distinguish

between the two possible mechanisms of sorption isotherms which are convex to the pressure axis: Flory–Huggins behavior is usually accompanied by increases in D , whereas clustering phenomena lead to reduced diffusion coefficients at higher vapor activity and solute concentration. Finally, Figure 1.16(d) is characteristic of diffusion coefficients for many penetrants at relatively low concentrations in glassy polymers, and the line through the data in Figure 1.16(d) represent fits of the transport model based on dual-mode concepts [128].

1.3.3 Permeability

The forms of $S(p)$ and $D(p)$ determine the pressure and concentration behavior of permeability, as shown in Figure 1.17. The permeability of low-sorbing penetrants exhibit little or no change in permeability with increasing pressure, as shown in Figure 1.17(a). However, some penetrants sorb into polymers to such a degree that they plasticize the polymer. Plasticization effectively increases the chain spacing in the polymer and increases the chain mobility so that the diffusion and permeation coefficients increase with increasing penetrant pressure, as shown in Figure 1.17(b). Another situation resulting in permeability increases with increasing upstream pressure can be found in rubbery polymers, such as PDMS; diffusion coefficients of organic vapors can remain approximately constant (or even decrease slightly) up to even high penetrant concentrations, but if solubility follows the Flory–Huggins model and increases at high penetrant activity, then permeability can also increase strongly with increasing penetrant pressure [106]. In glassy polymers, the dual-mode sorption and mobility model predicts a decrease in permeability with increasing pressure, as exemplified by CO₂ in polycarbonate in Figure 1.17(c) [129]. This trend has been confirmed by many other studies [112]. However, plasticization can occur at higher penetrant concentrations, which often leads to an increase in permeability values at higher pressures, as shown in Figure 1.17(d) [124].

1.3.4 Selectivity

Most of the permeation data reported in the literature were measured by using one gas at a

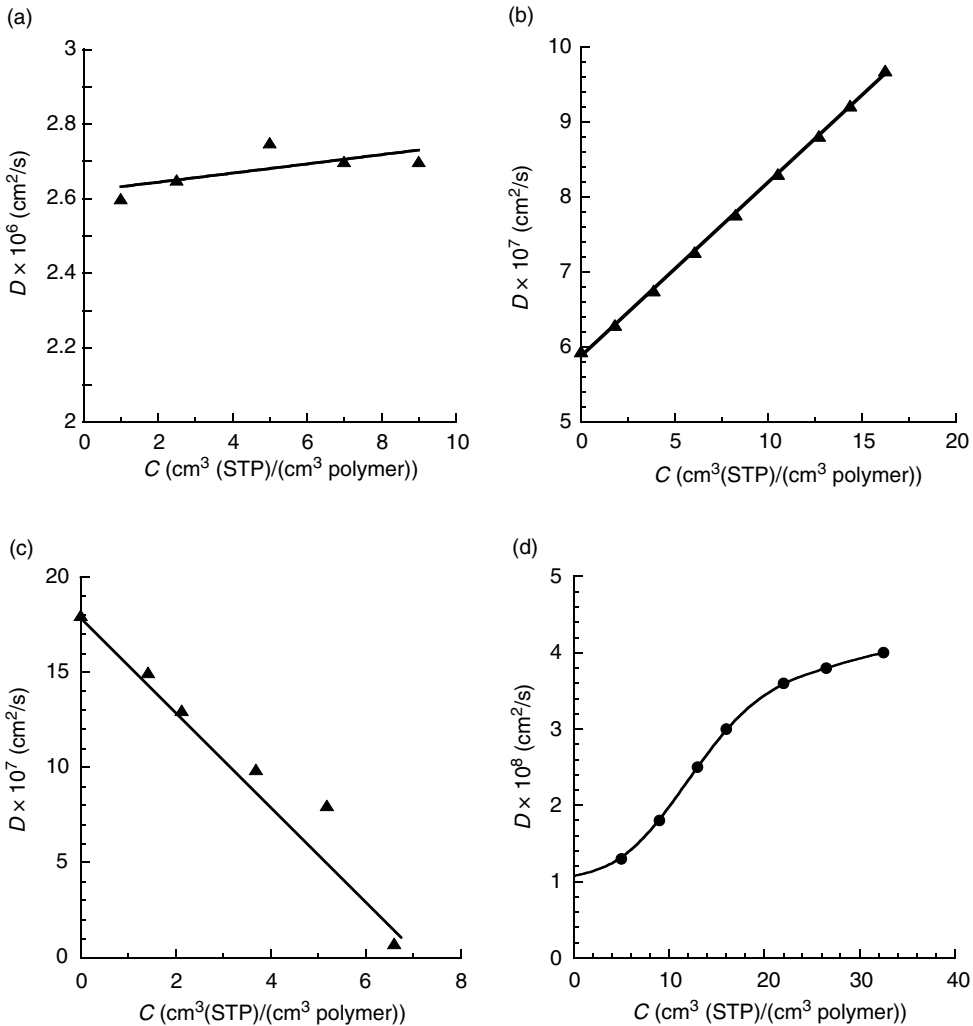


Figure 1.16 Concentration-dependence of diffusion coefficients: (a) low-sorbing gases (O_2 in Teflon AF1600 [122] at 35°C); (b) plasticization in rubbery polymers (CO_2 in cross-linked poly(ethylene glycol diacrylate) [126] at 35°C); (c) cluster formation (water in ethylcellulose at 25°C) [127]; (d) dual-mode behavior in a glassy polymer (CO_2 in polycarbonate at 35°C [128]). (a) Reprinted with permission from A. Y. Alentiev *et al.*, *Macromolecules*, **35**, 9513–9522 (2002). Copyright (2002) American Chemical Society. (b) Reprinted in part with permission from H. Lin and B. D. Freeman, *Macromolecules*, **38**, 8394–8407 (2005). Copyright (2005) American Chemical Society. (c) Reproduced by permission of Wiley-VCH from ‘Temperature effects during the sorption and desorption of water vapor in high polymers. I. Fibers, with particular reference to polymers’, A. A. Armstrong and V. T. Stannett, *Angew. Makromol. Chemie*, **90**, 145–160 (1966). (d) From ‘Carbon dioxide sorption and transport in polycarbonates’, *J. Polym. Sci. Part B: Polym. Phys. Ed.*, **14**, 687–702, Copyright © 1976, John Wiley & Sons, Inc. Reprinted with permission of John Wiley & Sons, Inc.

time (i.e. single gas or pure gas measurements). However a key commercial application is the separation of gas mixtures, and so it is of significant interest to understand the transport proper-

ties of mixtures of gases in polymers and to understand how they are similar to and different from the pure-gas transport properties. Examples of the most common types of behavior are

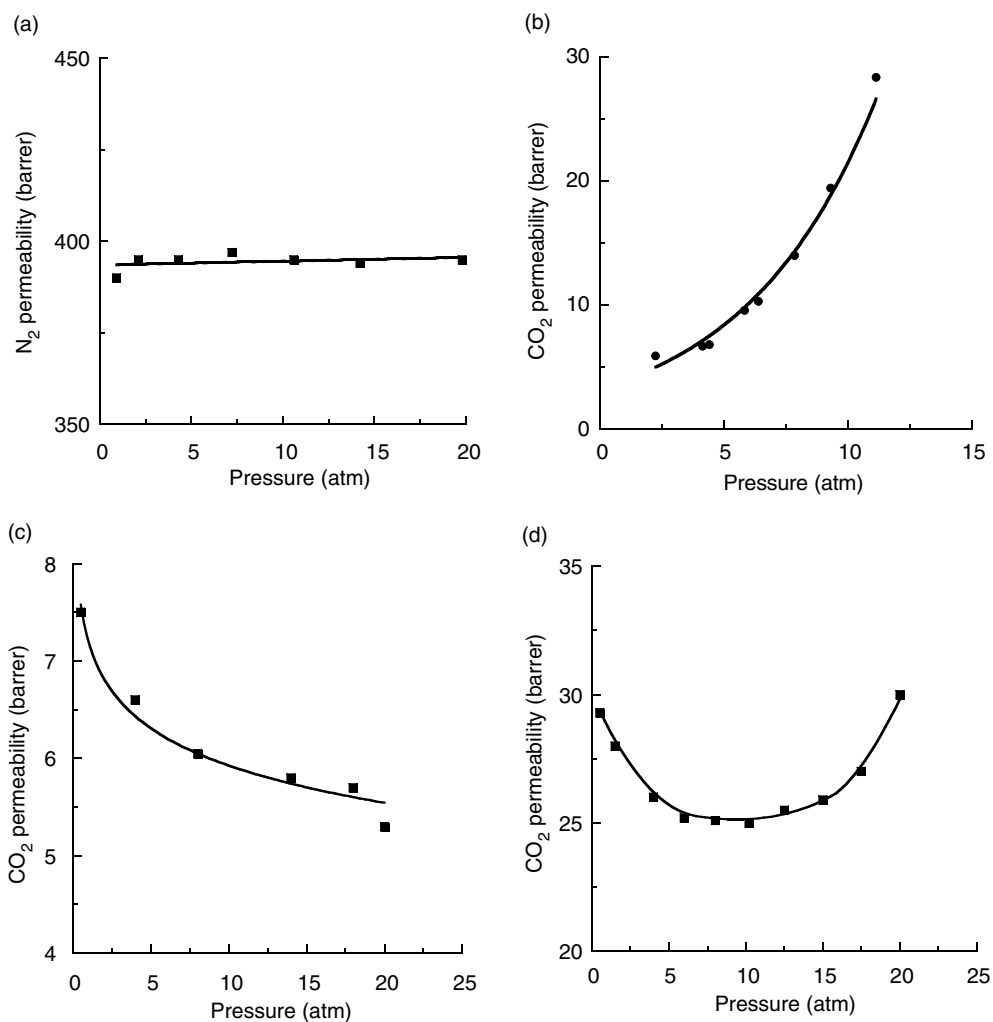


Figure 1.17 Influence of upstream pressure on permeability coefficients: (a) low-sorbing gases (N_2 in PDMS at 35 °C [34]); (b) plasticization of a rubbery polymer (cross-linked poly(ethylene glycol diacrylate) at -20 °C [138]); (c) dual-mode behavior in a glassy polymer (CO_2 in Lexan polycarbonate [129]); (d) dual-mode behavior at low pressure (<10 atm) and plasticization at higher pressure (CO_2 in polytetrabromophenolphthalein at 35 °C [124]). (a) From ‘Gas sorption, diffusion and permeation in polydimethylsiloxane’, T. C. Merkel, V. Bondar, K. Nagai, B. D. Freeman and I. Pinnau, *J. Polym. Sci. Part B: Polym. Phys. Ed.*, **38**, 415–434, Copyright © 2000, John Wiley & Sons, Inc. Reprinted with permission of John Wiley & Sons, Inc. (b) Reprinted with permission from H. Lin, E. van Wagner, B. D. Freeman, L. G. Toy and P. Ragubir, ‘New membrane materials for CO_2/H_2 separation and a model for pure and mixed gas permeability’, *Science*, **311**, 639–642 (2006). Copyright (2006) AAAS. (c) From ‘Carbon dioxide sorption and transport in polycarbonates’, *J. Polym. Sci. Part B: Polym. Phys. Ed.*, **14**, 687–702, Copyright © 1976, John Wiley & Sons, Inc. Reprinted with permission of John Wiley & Sons, Inc. (d) Reprinted in part from R. T. Chem and C. N. Provan, *Macromolecules*, **24**, 2203–2207 (1991). Copyright (1991) American Chemical Society

provided. Mixed-gas selectivity is discussed first, and then examples of mixed-gas permeability are presented.

Often, mixed-gas and pure-gas selectivity values are different. However, there are some examples where this is not the case. For exam-

ple, the mixed- and pure-gas selectivities for rubbery polymers can be equivalent or nearly so. Figure 1.18(a) presents such a case; it involves acetone and nitrogen copermeation in PDMS [106]. In this case, acetone and nitrogen essentially copermeate through PDMS as if they were each the only penetrant in the polymer. That is, the presence of acetone in the polymer does not influence the transport of nitrogen, and vice versa. This pattern of behavior might be classified as ideal, since it implies that one can predict mixture permeation properties based only on pure-gas permeation data. A similar behavior is expected for light gas mixture copermeation through glassy and rubbery polymers (e.g. O₂/N₂ or H₂/N₂ mixture separation by membranes).

A counter-example to the behavior in Figure 1.18(a) is presented in Figure 1.18(b) [130]. In rubbery poly(ethylene glycol diacrylate) (and in many strongly size-sieving glassy polymers as well), the sorption of a more condensable component (CO₂ in this case) apparently decreases the T_g of the polymer [21,131], thereby increasing the free volume available to both CO₂ and CH₄. The most important effect of the increase in free volume is believed to be an increase in gas diffusivity and, in turn, permeability, as expected when based on Equations (1.33) and (1.34). Thus, pure gas CO₂ permeability increases significantly with increasing CO₂ feed pressure; methane (which exhibits much lower sorption than CO₂) has a minimal effect on free volume, and so its permeability is approximately independent of methane feed pressure. As a result, the selectivity estimated based on pure-gas permeability coefficients increases with increasing CO₂ pressure. However, when CO₂ and CH₄ permeabilities are measured in mixture permeation experiments, the selectivity actually decreases with increasing CO₂ partial pressure. This effect may be rationalized by considering the effect of increasing free volume (due to increased CO₂ sorption at higher CO₂ partial pressure) on the diffusivity selectivity:

$$\frac{D_{\text{CO}_2}}{D_{\text{CH}_4}} = \frac{A_{\text{CO}_2}}{A_{\text{CH}_4}} \exp\left(\frac{B_{\text{CH}_4} - B_{\text{CO}_2}}{\text{FFV}}\right) \quad (1.41)$$

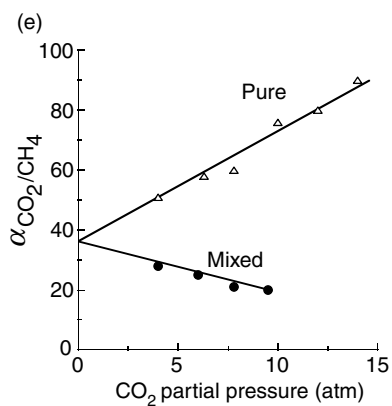
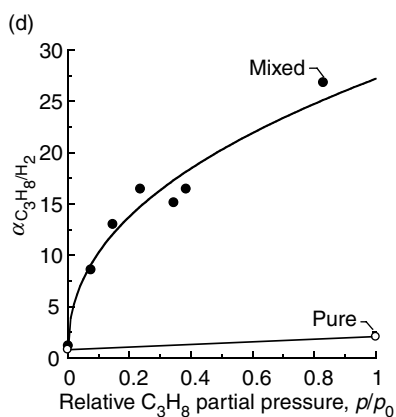
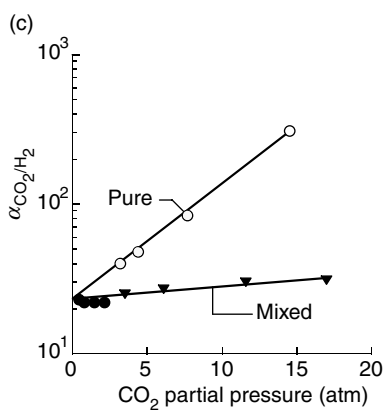
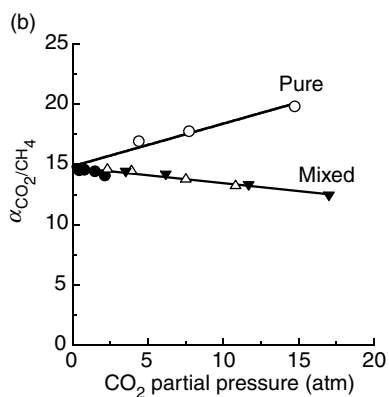
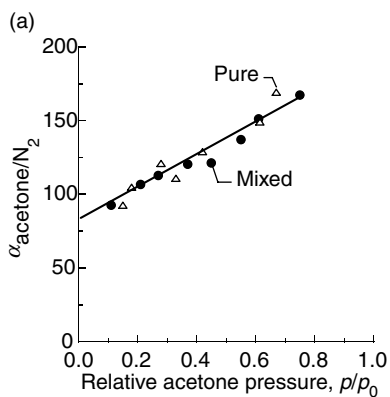
The value of B_{CH_4} is greater than that of B_{CO_2} (cf. Figure 1.10), and so as fractional free volume

increases, the diffusivity selectivity (i.e. $D_{\text{CO}_2}/D_{\text{CH}_4}$) decreases, and so overall mixture selectivity decreases. That is, increasing free volume reduces the size-sieving ability of the polymer. In other words, as CO₂ partial pressure in the CO₂/CH₄ mixture increases, the diffusivity of CH₄ increases more than that of CO₂, which reduces diffusivity selectivity and overall selectivity.

However, reduced size-sieving ability as a result of plasticization by a strongly sorbing component is not necessarily always detrimental to membrane separation performance. Using the same cross-linked rubbery polymer just discussed, separation experiments were performed by using CO₂/H₂ mixtures rather than CO₂/CH₄ mixtures [130]. The results are presented in Figure 1.18(c). The polymer is 'reverse-selective' for this separation. That is, it is more permeable to the larger component (CO₂) than to the smaller component (H₂). Presumably, the solubility selectivity strongly favors CO₂ (the more condensable molecule), and is apparently large enough to more offset than the diffusion selectivity, which would presumably favor H₂, since it is the smaller molecule. As CO₂ partial pressure in the feed gas increases, the CO₂ concentration in the polymer increases, T_g apparently decreases, and FFV apparently increases. As discussed earlier pure gas selectivity increases with increasing CO₂ pressure because CO₂ permeability increases strongly with increasing CO₂ feed pressure (cf. Figure 1.17(b)), and H₂ permeability is essentially independent of H₂ feed pressure. In the mixture, H₂ permeability also increases with increasing CO₂ partial pressure in the feed gas, and so mixture selectivity is lower than pure-gas selectivity. However, CO₂/H₂ mixed-gas selectivity actually increases (from 15 to 18) as CO₂ partial pressure in the feed increases. This observation can be rationalized by considering the effect of free volume on diffusivity selectivity for this 'reverse-selective' case:

$$\frac{D_{\text{CO}_2}}{D_{\text{H}_2}} = \frac{A_{\text{CO}_2}}{A_{\text{H}_2}} \exp\left(\frac{B_{\text{H}_2} - B_{\text{CO}_2}}{\text{FFV}}\right) \quad (1.42)$$

As shown in Figure 1.10, B_{CO_2} is greater than B_{H_2} . Therefore, as FFV increases due to increasing CO₂ sorption at higher CO₂ partial pressures,

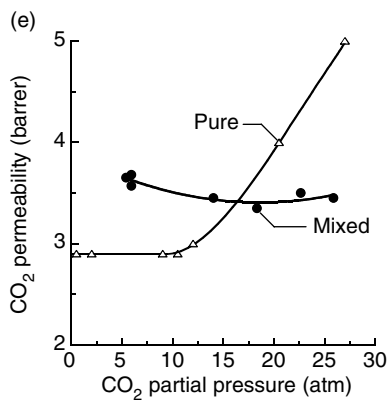
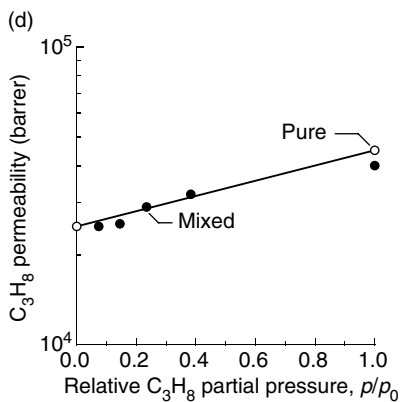
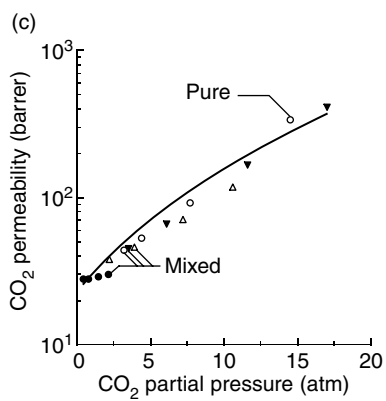
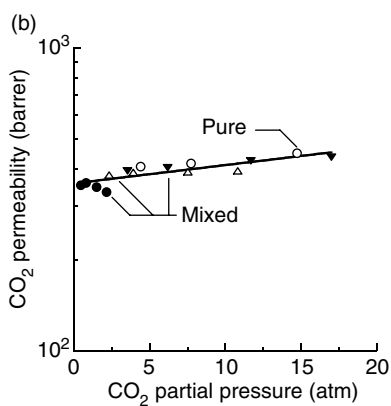
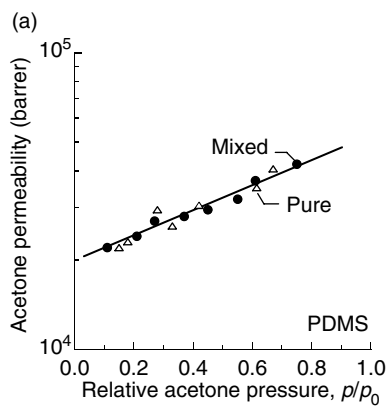


$D_{\text{CO}_2}/D_{\text{H}_2}$ (which is presumably less than 1 since H_2 is smaller than CO_2) comes closer to 1, which improves overall mixture selectivity. So, in such ‘reverse-selective cases’ plasticization, which weakens the polymer’s size-sieving ability, can be harnessed to simultaneously improve both permeability and selectivity [28]. It should be noted that, because hydrogen sorbs to very low levels, it is very difficult or impossible to measure its solubility in many polymers. Furthermore, there are no mixed-gas sorption data available for mixtures such as CO_2 and H_2 , and so the above analysis should be considered as a hypothesis. It is conceivable, although perhaps less likely, that the observed increase in CO_2/H_2 mixed-gas selectivity with increasing CO_2 partial pressure could be due to changes in mixed-gas solubility selectivity. Increases in mixed-gas selectivity with increasing partial pressures of strongly sorbing components (i.e. higher hydrocarbons) in the feed stream have also been reported for PDMS [132].

As shown in Figure 1.18(d), the mixed-gas selectivity in ‘solubility-selective’ (i.e. ‘reverse-selective’) glassy polymers such as PTMSP can

reach high values due to the preferential sorption of the more condensable penetrant in the free volume of the polymer, which blocks the transport of the less condensable penetrant [78]. In this case, selectivity increases strongly with increasing partial pressure of the more condensable component in the feed gas stream, similar to the case just discussed. However, the mechanism for the observed increase in selectivity could be quite different from that in the rubbery polymers (i.e. Figure 1.18(c)), since materials such as PTMSP have large amounts of non-equilibrium excess free volume while rubbers, as equilibrium materials, do not have, and this excess free volume is believed to be the locus of most of the transport in such materials. To date, there are no mixture-sorption studies in such materials which would allow one to understand if the change in selectivity is due to changes in solubility selectivity or changes in diffusivity selectivity [62,133]. Because the transport properties of organic vapor/light gas mixtures in PTMSP often resembles that of selective surface flow in microporous materials such as microporous carbon [134], there are some interpretations of

Figure 1.18 Comparison of pure- and mixed-gas selectivities for: (a) acetone/ N_2 in PDMS at 28 °C, with feed-gas mixture total pressures ranging from 10 to 12 atm and a permeate pressure at atmospheric [106]; (b) CO_2/CH_4 in cross-linked poly(ethylene glycol diacrylate) (XLPEO) at 35 °C feed-gas mixtures of 10:90 (●), 50:50 (▲), and 80:20 (▼) (mol:mol) $\text{CO}_2:\text{CH}_4$ in XLPEO with feed-gas mixture total pressures ranging from 0 to 17 atm and a permeate pressure at atmospheric [130]; (c) CO_2/H_2 in cross-linked XLPEO at –20 °C feed-gas mixtures of 10:90 (●), 50:50 (▲), and 80:20 (▼) (mol:mol) $\text{CO}_2:\text{H}_2$ in XLPEO with feed-gas mixture total pressures ranging from 0 to 17 atm and a permeate pressure at atmospheric [138]; (d) $\text{C}_3\text{H}_8/\text{H}_2$ in PTMSP at 25 °C feed-gas mixture total pressure of 13.7 atm and a permeate pressure at atmospheric [78]; (e) CO_2/CH_4 in cellulose acetate, with feed-gas mixture total pressures ranging from 15 to 47 atm and a permeate pressure at atmospheric [136]. In these examples, acetone, CO_2 , and C_3H_8 exhibit significant changes in pure-gas permeability with increasing values of their partial pressure in the feed gas. In contrast, the other components (H_2 , N_2 and CH_4) exhibit little or no change in permeability with feed pressure over the ranges of pressure considered in these examples. Therefore, the pure-gas selectivity values were calculated as the pure-gas permeability of the ‘more-pressure-dependant component’ at a feed pressure equal to the partial pressure of that component indicated on the abscissa, divided by the average permeability of the ‘less-pressure-sensitive component’ (i.e. N_2 , CH_4 , and H_2). (a) From ‘Pure and mixed gas acetone/nitrogen permeation properties of polydimethylsiloxane’, A. Singh, B. D. Freeman and I. Pinnau, *J. Polym. Sci. Part B: Polym. Phys. Ed.*, **36**, 289–301, Copyright © 1998, John Wiley & Sons, Inc. Reprinted with permission of John Wiley & Sons, Inc. (b) Reproduced by permission of Wiley-VCH from ‘High performance polymer membranes for natural-gas sweetening’, H. Lin, E. van Wagner, B. D. Freeman and I. Roman, *Adv. Mater.*, **18**, 39–44 (2006). (c) Reprinted with permission from H. Lin, E. van Wagner, B. D. Freeman, L. G. Toy and P. Ragubir, New membrane materials for CO_2/H_2 separation and a model for pure and mixed gas permeability, *Science*, **311**, 639–642 (2006). Copyright (2006) AAAS. (d) From ‘Hydrocarbon/hydrogen mixed gas permeation in poly(1-trimethylsilyl-1-propyne) (PTMSP), poly(1-phenyl-1-propyne) (PPP) and PTMSP/PPP blends’, I. Pinnau, C. G. Casillas, A. Morisato and B. D. Freeman, *J. Polym. Sci. Part B: Polym. Phys. Ed.*, **34**, 2613–2621, Copyright © 1996, John Wiley & Sons, Inc. Reprinted with permission of John Wiley & Sons, Inc. (e) From ‘Effect of gas composition and pressure on permeation through cellulose acetate membranes’, S. Y. Lee, B. S. Minhas and M. D. Donohue, *AIChE Symposium Series No. 261*, Vol. 84, K. Sirkar and D. Lloyd (Eds), pp. 93–101 (1988). Reproduced with permission. Copyright © 1988 AIChE



PTMSP transport properties based qualitatively at least, on this concept [133,135].

Conventional, size-sieving glassy polymers generally have a much lower mixed-gas selectivity than pure-gas selectivity due to plasticization, as shown in Figure 1.18(e) for CO₂/CH₄ permeation in cellulose acetate [136]. Other examples of this behavior are available in the literature [123,137]. In such cases, the presence of the more condensable component (CO₂ in this case) is assumed to plasticize the polymer matrix and decrease the diffusivity selectivity, which decreases the permeability selectivity, as explained in detail for the data presented in Figure 1.18(b). However, there are no mixed-gas diffusion and sorption data available to confirm this hypothesis.

Figure 1.19 presents the pure- and mixed-gas permeabilities for the more permeable penetrants in Figures 1.18(a)–1.18(c). For the rubbery polymers (Figures 1.19(a)–1.19(c)), the permeability of the more permeable component increases with increasing partial pressure of this component in the feed. However, the reasons for this behavior are somewhat different. In the case of PDMS, the increase in acetone permeability with increasing acetone feed pressure is due solely to the increase in acetone solubility with increasing acetone feed pressure; acetone diffu-

sivity actually decreases slightly with increasing acetone feed pressure [106]. However, for poly(ethylene glycol diacrylate), the increase in CO₂ permeability (cf. Figures 1.19(b) and 1.19(c)) is due mainly to an increase in CO₂ diffusion coefficient as the CO₂ content in the polymer increases [130,138]. In this sense, the presence of the more soluble (and more permeable) component in poly(ethylene glycol diacrylate) appears to have more influence on the polymer properties (e.g. T_g) than in the case of PDMS and, consequently, the permeation properties of the less soluble species (H₂ and CH₄) are strongly affected by the presence of CO₂ in poly(ethylene glycol diacrylate), whereas nitrogen permeability is essentially unaffected by the presence of even rather high levels of acetone in PDMS. The fundamental basis for this difference in behavior in these rubbery polymers remains an open question. Figure 1.19(d) shows that the permeability of propane in PTMSP is hardly influenced by propane feed pressure, and so the strong increase in propane/hydrogen selectivity shown in Figure 1.19(d) is due essentially entirely to the decrease in H₂ permeability with increasing C₃H₈ partial pressure in the feed. The final case, CO₂ in cellulose acetate, is interesting because, as CO₂ partial pressure in the feed gas mixture increases, CO₂ permeability in the mixture is

Figure 1.19 Comparison of pure- and mixed-gas permeabilities for: (a) acetone in acetone/N₂ mixtures in PDMS at 28 °C, with feed-gas mixtures total pressures ranging from 10 to 12 atm and a permeate pressure at atmospheric [106]; (b) CO₂ in CO₂/CH₄ mixtures in poly(ethylene glycol diacrylate) (XLPEO) at 35 °C feed-gas mixtures of 10:90 (●), 50:50 (Δ), and 80:20 (▼) (mol:mol) CO₂:CH₄ with feed-gas mixtures total pressures ranging from 0 to 17 atm and a permeate pressure at atmospheric [130]; (c) CO₂ in CO₂/H₂ mixtures in XLPEO at –20 °C feed-gas mixtures of 10:90 (●), 50:50 (Δ) and 80:20 (▼) (mol:mol) CO₂:H₂ with feed-gas mixture total pressures ranging from 0 to 17 atm and a permeate pressure at atmospheric [138]; (d) C₃H₈ in C₃H₈/H₂ mixtures in PTMSP at 25 °C feed-gas pressure of 13.7 atm absolute pressure and a permeate pressure at atmospheric [78]; (e) CO₂ in CO₂/CH₄ in cellulose acetate at 35 °C, with feed-gas mixture total pressures ranging from 0 to 30 atm and a permeate pressure at atmospheric. The mixed gas composition was 46.1 mol% CO₂ [139]. (a) From ‘Pure and mixed gas acetone/nitrogen permeation properties of polydimethylsiloxane’, A. Singh, B. D. Freeman and I. Pinnau, *J. Polym. Sci. Part B: Polym. Phys. Ed.*, **36**, 289–301, Copyright © 1998, John Wiley & Sons, Inc. Reprinted with permission of John Wiley & Sons, Inc. (b) Reproduced by permission of Wiley-VCH from ‘High performance polymer membranes for natural-gas sweetening’, H. Lin, E. van Wagner, B. D. Freeman and I. Roman, *Adv. Mater.*, **18**, 39–44 (2006). (c) Reprinted with permission from H. Lin, E. van Wagner, B. D. Freeman, L. G. Toy and P. Ragubir, ‘New membrane materials for CO₂/H₂ separation and a model for pure and mixed gas permeability’, *Science*, **311**, 639–642 (2006). Copyright (2006) AAAS. (d) From ‘Hydrocarbon/hydrogen mixed gas permeation in poly(1-trimethylsilyl-1-propyne) (PTMSP), poly(1-phenyl-1-propyne) (PPP) and PTMSP/PPP blends’, I. Pinnau, C. G. Casillas, A. Morisato and B. D. Freeman, *J. Polym. Sci. Part B: Polym. Phys. Ed.*, **34**, 2613–2621, Copyright © 1996, John Wiley & Sons, Inc. Reprinted with permission of John Wiley & Sons, Inc. (e) From ‘Permeability of dense (homogeneous) cellulose acetate membranes to methane, carbon dioxide and their mixtures at elevated pressures’, A. Y. Houde, B. Krishnakumar, S. G. Charati and S. A. Stern, *J. Appl. Polym. Sci.*, **62**, 2181–2192, Copyright © 1996, John Wiley & Sons, Inc. Reprinted with permission of John Wiley & Sons, Inc.

hardly affected, even though selectivity (cf. Figure 1.19(e)) is strongly affected [139]. Additionally, cellulose acetate, which is a glassy polymer, is known to be sensitive to its prior history of exposure to strongly sorbing gases such as CO₂. This sensitivity to history may explain, in part, why the pre- and mixed-gas data do not exhibit the same CO₂ permeability at very low CO₂ partial pressure. Such mixed-gas data are not widely available, and so it is not known to what extent the examples presented here are relevant to other gas mixtures and other polymers. This area could be a very fruitful one for future experimental and modeling studies.

1.4 Effect of Temperature on Transport Parameters

The temperature-dependence of the transport parameters is typically described by Arrhenius–van’t Hoff equations [7]:

$$D = D_0 e^{-E_D/RT} \quad (1.43)$$

$$P = P_0 e^{-E_P/RT} \quad (1.44)$$

and Equation (1.25) for solubility. In the equations above, E_D and E_P are the activation energies of diffusion and permeation, respectively. From Equation (1.25), ΔH_s is the enthalpy of sorption, and $E_P = E_D + \Delta H_s$; E_D is always positive, whereas the sign of E_P depends on the relative magnitudes of E_D and ΔH_s . For strongly size-sieving gas separation polymers, such as those used for air separation and H₂ removal from mixtures with hydrocarbons, $E_D > |\Delta H_s|$, and so the resulting values of E_P are positive and permeability increases as temperature increases. However, E_P can be negative in vapor separation applications, such as the removal of volatile organic compounds from air or other light gases using membrane materials such as PDMS [140] and PTMSP, where ΔH_s values exhibit large absolute values or in polymers with very low energy barriers for diffusion (i.e. small E_D values). While E_P and E_D values are typically independent of temperature for transport in glassy polymers, these activation energies can be temperature-dependent in rubbery polymers [36]. A marked break in the Arrhenius behavior is observed in most cases when the measurement temperature passes through T_g [141].

The parameters of the Arrhenius equations (1.43) and (1.44) are strongly interrelated due to the so-called compensation effect – larger preexponential factors correspond to higher activation energies and vice versa [61,142]. For rubbers, van Amerongen observed the following correlation [143]:

$$\ln D_0 = a(E_D/R) - b \quad (1.45)$$

where a and b are constants. For a variety of gases and rubbery polymers, a recent study by Prabhakar *et al.* has shown an apparent universal value of a of 0.002 K⁻¹ [144], which was very close to the value proposed by van Amerongen (0.0023 K⁻¹) more than 50 years ago [143]; van Amerongen proposed a universal value of 9.7 for b (when D_0 has units of cm²/s) [143]. However, Prabhakar *et al.* found that the best single value for b , describing a wide range of data in rubbery polymers, was 8.3 [144]. The agreement between the experimental data and the linear free energy relation for a variety of polymers was more successful if b was allowed to vary from 7.6 to 10.6, depending on the penetrant and the polymer [145]. While there may not be a single, universal value of b , it appears that b values in this narrow range describe the linear free energy relationship for many rubbery polymers and gases. A similar relation has also been observed in glassy polymers [146]. Such equations enable activation energies to be estimated when the D or P values are known at a single temperature; hence, the values of D and P at different temperatures can be estimated from an observation at a single temperature.

As shown in Figure 1.19, E_D is a strong function of the molecular size of the penetrants. A simple interpretation of this phenomenon was given by Meares [40]:

$$E_D = 0.25 N_0 \pi d^2 \lambda \text{CED} \quad (1.46)$$

where N_0 is the Avogadro constant, d is the kinetic cross-sectional area of a diffusant, CED is the polymer cohesive energy density, and λ is the diffusion jump length, which is usually treated as an adjustable parameter. This equation rationalizes the dependence of E_D on d^2 (Figure 1.20), which then leads to the decrease in gas diffusivity with increasing size (Figure 1.3). However, Equation

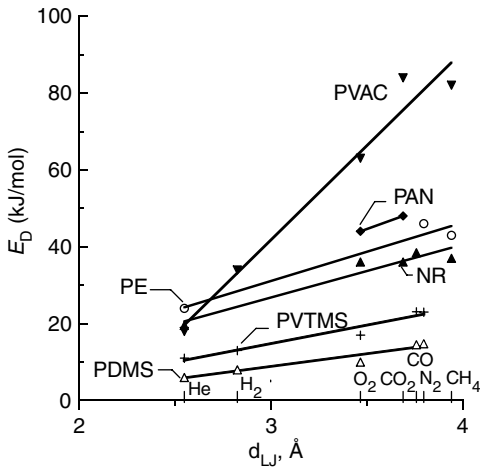


Figure 1.20 Effect of penetrant size on activation energy of diffusion in poly(vinyl acetate) (PVAC) (\blacktriangledown), polyacrylonitrile (PAN) (\blacklozenge), polyethylene (PE) (\circ), natural rubber (NR) (\blacktriangle), PVTMS ($+$) and PDMS (\blacktriangle) [103]

(1.46) is not predictive, because the λ values are not known a priori. Analysis of the Meares equation (Equation (1.46)), in conjunction with data from positron annihilation lifetime spectroscopy on the size and concentration of free-volume elements in polymers indicates that the diffusion jump length λ is close to the average distance between adjacent free-volume elements in glassy polymers [105].

Traditionally, the temperature-dependence of D and activation energy, E_D , are interpreted based on transition-state theory [147]. However, activation energies E_D and E_P also correlate with free volume. Polymers with large free volume usually exhibit fairly low activation energies and vice versa [146]. Thus, these two theoretical approaches (free volume and activated-state theory) must be very strongly related because each can provide a rational explanation of much of the available experimental data. Recently, Lin and Freeman have pursued this line of reasoning and have developed the following relation between the activation energy of diffusion and fractional free volume [101]:

$$E_D = \frac{A + b - \left(\frac{B}{FFV}\right)}{\left(\frac{a}{R} - \frac{1}{RT}\right)} \quad (1.47)$$

where A and B are from the free-volume model of diffusion (Equation (1.33)), and a and b are constants from the linear free-energy relation (i.e. Equation (1.45)). It is rather straightforward to build an appropriate concentration-dependence into FFV (and, by extension, into E_D) by allowing FFV to depend on the difference between the experiment temperature and the T_g , and allowing T_g to vary with penetrant concentration using, for example, Chow's model [131], which can be implemented with no adjustable parameters. Because FFV depends on temperature and penetrant concentration, this approach allows E_D to depend in a systematic and consistent fashion on these variables as well. Furthermore, for the series of cross-linked rubbers that Lin *et al.* considered, the following relation was observed for B [101]:

$$B = B_1 + B_2 d_{LJ}^2 \quad (1.48)$$

where B_1 and B_2 are adjustable constants, and d_{LJ} is the Lennard-Jones diameter of the penetrants. This result is consistent with the Meares model scaling of E_D with the square of the penetrant diameter. While the model of Lin *et al.* has not been tested on a wide variety of polymers, it provides a reasonable first step towards integrating the free volume and activated state approaches to describe small molecule transport in polymers. It also provides an indication that these two theoretical viewpoints (i.e. activated state and free volume) are quite probably two equivalent ways of interpreting gas and vapor diffusion in polymers.

1.5 Structure/Property Relations

All physico-chemical properties of polymers depend upon the chemical structure of the polymer repeat units. It is possible to consider directly the chemical structure effects of linear polymers on their transport properties. The manifestation of these effects is different for polymers above and below their glass transitions.

As has been mentioned, permeability and diffusion coefficients in rubbers are strongly influenced by their glass transition temperatures, and T_g values are sensitive to the main- and side-chain structure of elastomers. Table 1.4 illustrates the effect of side-chains on T_g and permeability

Table 1.4 Permeability of siloxane polymers, $[\text{Si}(\text{CH}_3) - \text{O}]_n$, at 35 °C. From 'Structure-permeability relationship in silicone polymers', S. A. Stern, V. M. Shah and B. J. Hardy, *J. Polym. Sci. Part B. Polym. Phys. Ed.*, **25**, 1263–1298, Copyright © 1987, John Wiley & Sons, Inc. Reprinted with permission of John Wiley & Sons, Inc.

R	T_g (K)	P (barrer) [148]		
		O ₂	CH ₄	C ₃ H ₈
CH ₃	150	930	1350	18 000
<i>n</i> -C ₃ H ₇	153	380	570	9 000
<i>n</i> -C ₈ H ₁₇	181	190	310	5 600
C ₆ H ₅	245	32	36	480

of polysiloxanes. As the silicon atom substituents become larger, glass transition temperature increases, and permeability coefficients decrease [148]. It is also interesting to follow the changes of the properties when the structure of the main-chain is changed in a systematic manner. As shown in Table 1.5, chain flexibility is reduced

when the oxygen atom in siloxane is replaced by a methylene group, as is indicated by the increase in T_g and reduction in permeability. Further decreases in permeability by virtue of reduced main-chain flexibility can be observed for polyisobutylene, where the silicon atom is replaced by carbon.

The repeat unit chemical structure also influences gas permeability in glassy polymers. Abundant data on this subject can be found in numerous reviews [23,64,83,84,149–151]. For example, striking effects are produced by introducing bulky $\text{Si}(\text{CH}_3)_3$ groups into various main-chains. Thus, in vinylic polymers, replacement of small polar CN groups in polyacrylonitrile by this group to form poly(vinyltrimethyl silane) results in an increase in oxygen permeability from 0.0005 to 44 Barrer [37,38,152], a change of nearly five orders of magnitude. The effect on permeability of introducing trimethylsilyl (TMS) groups into various polymers is illustrated in Table 1.6 [153–156]. Permeability increases in all cases upon introduction of $\text{Si}(\text{CH}_3)_3$ groups

Table 1.5 Glass transition temperatures and permeabilities of a systematic series of elastomers

Polymer	Structure	T_g (K)	P (barrer) ^a		
			He	CH ₄	CO ₂
Polydimethylsiloxane [148]	$\left[\begin{array}{c} \text{CH}_3 \\ \\ \text{---Si---O---} \\ \\ \text{CH}_3 \end{array} \right]_n$	150	560	1350	4500
Polydimethylsilylmethylene [148]	$\left[\begin{array}{c} \text{CH}_3 \\ \\ \text{---Si---CH}_2\text{---} \\ \\ \text{CH}_3 \end{array} \right]_n$	185	98	130	550
Polyisobutylene [36]	$\left[\begin{array}{c} \text{CH}_3 \\ \\ \text{---C---CH}_2\text{---} \\ \\ \text{CH}_3 \end{array} \right]_n$	199	8.4	—	5.2

^aPermeability data for polydimethylsiloxane and polydimethylsilylmethylene are at 35 °C, a feed pressure of 9 atm, and atmospheric permeate pressure; permeability data for polyisobutylene are at 25 °C and a pressure range in which the permeability is constant.

Table 1.6 The effect of introduction of trimethylsilyl (i.e. Si(CH₃)₃ (TMS)) groups into polymers on the gas transport properties [153–156]

Polymer	Modified polymer	Polymer P_{O_2} (barrer) ^a	Polymer α_{O_2/N_2}	Modified polymer P_{O_2} (barrer) ^a	Modified polymer α_{O_2/N_2}
		2.9	3.0	44	4.3
		1.2	5.5	14	3.3
		2.8	1.7	30	3.8
		2.8	1.7	95	3.8

^aPermeability measurements were performed at 22 °C and at low pressure.

and often without changing selectivity. Extensive studies of glassy polymers indicate that TMS groups lead to increases in both diffusion and solubility coefficients due to an enhancement in polymer free volume [153].

In glassy polymers, increasing the size of side-groups often, but not always, increases free volume and gas permeability. Detailed studies of polyacetylenes of varying structures [84] showed that: (i) certain sizes and shapes of side-groups most efficiently disrupt chain packing (thereby increasing gas permeability) and (ii) symmetry of side-groups contributes to greater gas permeability (cf. Table 1.7). More detailed considerations of these issues and the structure-dependence of transport properties of polyacetylenes are found in Chapter 9.

In densely packed materials, like aromatic polycarbonates, substitution of hydrogen atoms on aromatic rings by methyl groups or other

large substituents can disrupt chain packing, which leads to marked increases in gas permeability, as shown by the experimental data in Table 1.8 [157]. The methyl substitution reduced both chain motion and packing as indicated by the T_g and FFV changes [157]. Substitution of halogens (i.e. Cl, Br) introduces additional polar groups into the polymer, which caused T_g and T_f to increase significantly, indicating reductions in chain mobility. The halogen substitution also reduced FFV. The more efficient chain packing and loss of chain mobility in the halogen tetrasubstituted polycarbonates lowered CO₂ and CH₄ permeability. These systematic studies of gas transport properties in polycarbonates were driven, in part, by the commercial use of substituted polycarbonates as gas separation membrane materials by the Dow Chemical Company and later by Generon, which was ‘spun off’ from Dow’s gas separation membrane effort.

Table 1.7 Effect of substituent size and symmetry on permeability and selectivity in substituted acetylene polymers [-CMe=CR-]_n [84]. Reprinted from *Progress in Polymer Science*, **26**, K. Nagai, T. Masuda, T. Nakagawa, B. D. Freeman and I. Pinnau, 'Poly[1-(trimethylsilyl)-1-propyne] and related polymers: synthesis, properties and functions', 721–798, Copyright (2001), with permission from Elsevier

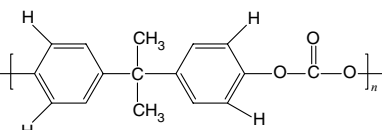
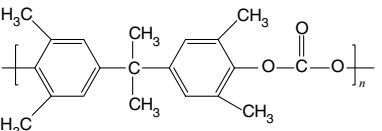
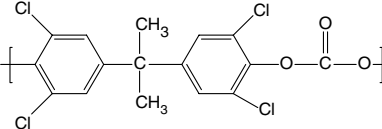
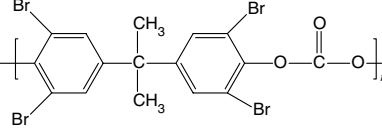
R	P_{O_2} (barrer) ^a	$\alpha_{\text{O}_2/\text{N}_2}$
SiMe ₃	6000	1.8
GeMe ₃	1800	1.5
SiMe ₂ Et	970	2.0
SiEt ₃	860	2.0
SiMe ₂ Pr	100	2.8
SiMe ₂ CH ₂ SiMe ₃	75	3.6

^aPermeability data are reported at 25 °C.

Because polysulfone has been used for quite some time by Air Products (through their Permea division) as a commercial gas separation mem-

brane material, there have been many studies of its permeation properties [158–160] and attempts to modify it chemically to improve its gas transport properties [161–163]. Table 1.9 presents data for polysulfone and a few variants that have similar modifications as those presented in Table 1.8 for the polycarbonates. In this regard, tetramethyl substitution of polysulfone, to produce TMPSPF, has a similar effect on the gas transport properties of polysulfone and polycarbonate; CO₂ permeability increases strongly and CO₂/CH₄ selectivity remains essentially constant relative to values for the unsubstituted polymer [161]. The tetramethyl substituted material has significantly higher T_g and higher free volume. That is, placing the four methyl substituents symmetrically on the aromatic rings stiffens the chain backbone and increases the free volume of the polymer. Higher free volume leads to higher permeability, and the stiffer chain backbone

Table 1.8 Physical, thermal and transport properties of substituted polycarbonates [76,157]. From 'Gas sorption and transport in substituted polycarbonates', N. Muruganandam, W. J. Koros and D. R. Paul, *J. Polym. Sci. Part B: Polym. Phys. Ed.*, **25**, 1999–2026, Copyright © 1987, John Wiley & Sons, Inc. Reprinted with permission of John Wiley & Sons, Inc.

Polymer	FFV ^a	T_g (°C)	T_γ (°C)	P_{CO_2} (barrer) ^b	$\alpha_{\text{CO}_2/\text{CH}_4}$
	0.164	150	-100	6.0	23.3
	0.180	193	50	17.6	22.0
	0.179	230	112	6.7	29.7
	0.133	263	120	4.2	33.6

^aDensity measurements were conducted at 30 °C [76].

^bPermeability measurements were conducted at 35 °C, 20 atm feed pressure and a permeate pressure 'at vacuum'.

Table 1.9 Physical, thermal and transport properties of substituted polysulfones [161]. Reprinted from *Polymer*, **32**, J. S. McHattie, W. J. Koros and D. R. Paul, 'Gas transport properties of polysulfones. 1. Role of symmetry of methyl group placement on bisphenol', 840–850, Copyright (1991), with permission from Elsevier

Polymer	FFV	T_g (°C)	P_{CO_2} (barrer) ^a	α_{CO_2/CH_4}
	0.156	186	5.6	22
	0.149	180	2.1	30
	0.171	242	21	22

^aPermeability measurements were conducted at 35 °C, 10 atm feed pressure and a permeate pressure 'at vacuum'.

mitigates losses in selectivity that would typically accompany an increase in free volume. In contrast, dimethyl substitution (DMPSF) significantly lowers CO_2 permeability and increases CO_2/CH_4 selectivity relative to that of either polysulfone or TMAPSF [161]. FFV in DMPSF is lower than that in polysulfone. This reduction in free volume has been ascribed to more efficient chain packing in the dimethyl substituent than in the unsubstituted analog. Based on dynamic mechanical thermal analysis studies, local segmental mobility in dimethyl-substituted PSF is markedly more constrained than in PSF, and this decrease in local segmental mobility is probably linked to the decrease in free volume and the observed changes in properties. The dimethyl substitution of the aromatic rings may strongly decrease the ability of the phenyl rings to undergo segmental rotation, resulting in a greater tendency for the polymer chains to pack efficiently [161,164].

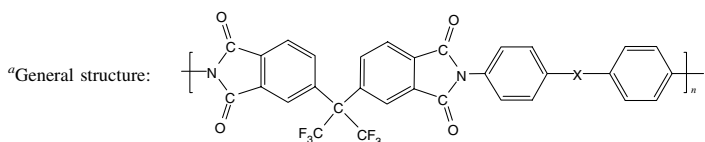
As the preceding text suggests, many chemical structural variations have been pursued in an attempt to produce polymers with better gas separation properties. A few of the more widely studied effects are mentioned in the text that follows, and illustrative examples of the effect of these variables on transport properties are provided.

1.5.1 Connector Groups

Gas transport properties are influenced by the polymer connector groups due to the effect of these groups on chain mobility and chain packing. T_g and FFV are macroscopic characteristics of polymer chain mobility and packing. Linkages that have low energy barriers for intersegmental bond rotations, such as $-O-$ and $-CH_2-$, typically facilitate torsional movement within the polymer backbone, which reduces the chain stiffness, and, in turn, the polymer T_g [165]. By increasing the torsional movement of polymer segments, and thus reducing T_g , penetrant diffusion coefficients often increase. However, bulky groups that stiffen the chain backbone and increase T_g , which tends to decrease diffusion coefficients, can also introduce additional free volume into the polymer matrix, which tends to increase diffusion coefficients. So, it is not unusual that the introduction of non-polar, large groups increases both T_g and gas diffusion coefficients simultaneously. This situation is illustrated in the family of polyimides shown in Table 1.10 [165,166]. Both T_g and FFV increase as more and more bulky connector groups are introduced into the polymers [165]. The diffusion coefficient and permeability increase as T_g increases due to the enhancement in FFV.

Table 1.10 The effect of connector group type on physical properties and gas transport characteristics in a systematic series of aromatic polyimides^{a,b} [165,166]. Reprinted from *Journal of Membrane Science*, **50**, M. R. Coleman and W. J. Koros, 'Isomeric polyimides based on fluorinated dianhydrides and diamines for gas separation applications', 285–297, Copyright (1990), with permission from Elsevier

×	T_g (°C)	FFV	P_{CO_2} (barrer)	α_{CO_2/CH_4}	$D_{CO_2} \times 10^8$ (cm ² /s)	S_{CO_2} (cm ³ (STP)/ cm ³ atm)
—O—	304	0.164	23	60.5	3.6	4.89
$\begin{array}{c} \text{H} \\ \\ \text{---C---} \\ \\ \text{H} \end{array}$	304	0.160	19.3	44.9	3.7	3.96
$\begin{array}{c} \text{CH}_3 \\ \\ \text{---C---} \\ \\ \text{CH}_3 \end{array}$	310	0.168	30	42.9	5.4	4.24
$\begin{array}{c} \text{CF}_3 \\ \\ \text{---C---} \\ \\ \text{CF}_3 \end{array}$	320	0.190	63.9	39.9	10	4.72



^bExperiments were conducted at 35 °C and a feed pressure of 10 atm.

1.5.2 CF_3 and Other Fluorinated Moieties as Side-chains

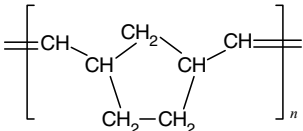
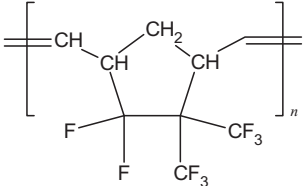
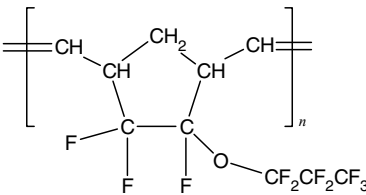
Generally, $-C(CF_3)_2$ groups have been added to aromatic polymers, such as polyimides and polycarbonates, to disrupt chain packing (i.e. increase free volume). However, $-C(CF_3)_2$ moieties also affect chain packing and overall gas transport differently when added as a side-chain [167]. As shown in Table 1.11, in polynorbornenes containing fluorinated side-chains, the permeability enhancement is mainly due to increases in solubility and, depending on the side-chain, on changes in diffusion coefficients to a lesser extent. The change in solubility has been attributed to the change in T_g with fluorinated side-groups, which results in an increase in Langmuir sorption in the fluorinated materials relative to the unfluorinated base polymer. The increase in diffusion coefficients was attributed to the increase in

FFV, as corroborated by positron annihilation lifetime spectroscopy [167].

1.5.3 Polar and Hydrogen Bonding Side-chains

The degree of polarity and hydrogen bonding in side-chains or vinyl groups can cause a significant increase in interactions between polymer chains. This increased interchain interaction raises T_g and density in such polymers, as shown in Table 1.12 [168–170]. These effects can also contribute to significant levels of crystallinity in such materials, and crystallinity can strongly reduce gas permeability. The strength of the polarity or hydrogen bonding strongly influences the gas permeability; decreases in chain mobility are observed when polarity and hydrogen bonding increase. For example, polar polyacrylonitrile is over six orders of magnitude less permeable to CO_2 than 1,2-polybutadiene. Dry poly(vinyl alco-

Table 1.11 Effect of fluorinated side-chains on transport properties of polynorbornenes^a [167]. Reprinted with permission from Y. P. Yampolskii *et al.*, *Macromolecules*, **27**, 2872–2878 (1994). Copyright (1994) American Chemical Society

Structure	T_g (°C)	FFV	P_{CO_2} (barrer)	α_{CO_2/CH_4}	$D_{CO_2} \times 10^7$ (cm ² /s)	$S_{CO_2} \times 10^2$ cm ³ (STP)/(cm ³ atm)
 <p>Polynorbornene</p>	31	0.156	15.4	6.3	1.6	0.96
 <p>Poly(5,5-difluoro-6,6-bis (trifluoromethyl)norbornene)</p>	169	0.165	200	15.4	0.84	24
 <p>Poly(5,5,6-trifluoro-6- neptafluoropropoxynorbornene)</p>	77	0.187	200	11	4.0	5.0

^aPermeability and diffusivity experiments were conducted at 22 °C, the feed pressure was held steady in a range from 0.01 to 0.65 atm, and the downstream pressure ranged from 0 to 0.01 atm; sorption experiments were conducted at 25 °C.

hol) is three orders of magnitude less permeable to CO₂ than polar poly(vinyl chloride), which shows that hydrogen bonding between polymer chains severely inhibits gas permeation.

1.5.4 Para versus Meta Linkages

In polymers with aromatic backbones, such as polysulfones, changing the aromatic structure from *para* to *meta* reduces the T_g and FFV, as indicated in Table 1.13 [158,159]. *Meta*-connected materials pack more efficiently than analogous *para*-configured polymers [158]. Moreover, chain mobility is impeded in the *meta*-configuration since any significant motion of these segments require multisegment co-operation, whereas *para*-connected phenyl rings require much less co-operative motion for rotation. Both of these effects contribute to reducing the FFV of *meta*-connected polysulfones relative to

that of their *para*-connected analogs. The *meta*-configuration has consistently lower permeability, solubility and diffusivity than the equivalent *para*-connected polymer due to lower FFV and T_g in the *meta*-connected material. The influence of *para/meta* connections on gas transport properties in polysulfones is consistent with similar data for other families of glassy polymers, such as polyesters and polyimides [76]. This effect has recently been the focus of molecular modeling studies which confirm these experimental observations [171].

1.5.5 Cis/Trans Configuration

The packing efficiency of polymers with unsaturated backbones depends on the amount of *cis* and *trans* configurations of the double bond. For poly(*tert*-butylacetylene), the packing efficiency increased as the *cis* content increased [172].

Table 1.12 Effect of vinyl polar groups on physical properties and gas transport. Reprinted from *Journal of Membrane Science*, 2, S. M. Allen, M. Fujii, V. T. Stannett, H. B. Hopfenberg and J. L. Williams, 'The barrier properties of polyacrylonitrile', 153–163, Copyright (1977), with permission from Elsevier

Polymer	Structure	T_g (°C) [161]	Density (g/cm ³) [161]	P_{CO_2} (barrer) ^a
Polyethylene (PE)	$\left[-CH_2-CH_2- \right]_n$	-44	1.008	35.2 [162]
Poly(1,2-butadiene) (PB)	$\left[-\overset{\text{CHCH}_2}{\underset{ }{\text{CH}}}-CH_2- \right]_n$	-50	0.950	138 [162]
Poly(vinyl chloride) (PVC)	$\left[-\overset{\text{Cl}}{\underset{ }{\text{CH}}}-CH_2- \right]_n$	81	1.450	0.029 [162]
Polyacrylonitrile (PAN)	$\left[-\overset{\text{CN}}{\underset{ }{\text{CH}}}-CH_2- \right]_n$	125	1.125	0.000 28 [152]
Poly(vinyl alcohol) (PVOH)	$\left[-\overset{\text{OH}}{\underset{ }{\text{CH}}}-CH_2- \right]_n$	85	1.291	0.000 02 [163]

^aData reported at 30 °C for PE, PB and PVC, at 25 °C for PAN and at 23 °C for PVOH.

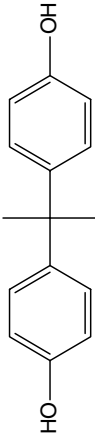
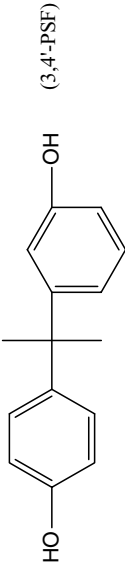
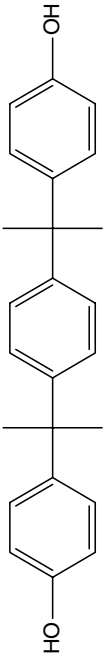
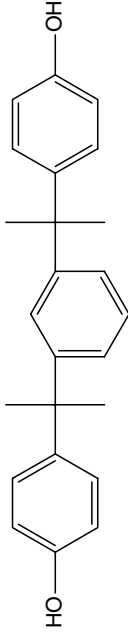
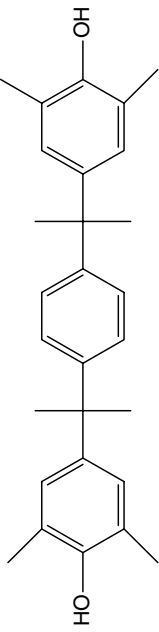
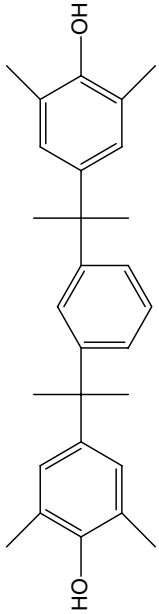
As the *cis* content increased, the gas diffusion coefficients increased initially and reached a maximum at a *cis* content of 50.2 %, as shown in Figure 1.21(a). At higher *cis* content, diffusivity decreased monotonically. Gas solubility also decreased at higher *cis* content in this polymer. The reduction in gas sorption was linked to a decrease in Langmuir sorption sites (cf. Figure 1.21(b)), which is consistent with a loss in excess free volume at higher *cis* contents (cf. Equation (1.38)). The reduction in diffusivity was also consistent with the increased chain packing efficiency at higher *cis* contents. It was speculated that chains with very high levels of *cis* or *trans* linkages formed rather regular helical structures that might pack very efficiently in the solid state, which would lead to reductions in FFV and, in turn, solubility and diffusivity. Polymers with intermediate concentrations of *cis* or *trans* linkages were thought to yield more disordered polymer structures, which packed less efficiently in the solid-state, which would lead to higher FFV, solubility and diffusivity. Similar

gas transport behavior has been observed in other unsaturated polymers such as poly(trimethylsilyl norbornene) [173] and poly(methacrylate azobenzene) [174].

1.6 Conclusions

Gas and vapor transport is described by the 'solution-diffusion' concept, where permeability is the product of solubility and diffusivity. Both the solubility and diffusion coefficients are polymer- and penetrant-dependent. Although polymer structure and properties influence gas and vapor transport, there are very few parameters that apply universally. One of the few parameters that does correlate well with changes in gas transport in polymers is the fractional free volume (FFV). The latter is an indication of the open volume between polymer chains through which penetrant molecules can pass. Changes in polymer structure do not consistently affect gas transport behavior. However, altering polymer structure within closely related polymer families

Table 1.13 Effect of *meta/para* configuration in aromatic polysulfones on transport properties^a [159]. Reprinted with permission from C. L. Aitken *et al.*, *Macromolecules*, **25**, 3424–3434 (1992). Copyright (1992) American Chemical Society

Bisphenol monomer	T_g (°C)	FFV	ρ (g/cm ³)	P_{CO_2} (barrer)	α_{CO_2/CH_4}	$D_{CO_2} \times 10^8$ (cm ² /s)	S_{CO_2} (STP) (cm ³ atm)
 (PSF)	186	0.156	1.24	5.6	22	2.0	2.1
 (3,4'-PSF)	156	0.149	1.25	1.5	29	0.9	1.3
 (PSF-P)	191	0.156	1.191	6.8	20	3.2	2.1
 (PSF-M)	140	0.151	1.201	2.8	25	2.7	1.1
 (TMPSF-P)	214	0.168	1.127	13	22	5.0	2.0
 (TMPSF-M)	175	0.158	1.141	7.0	25	4.5	1.6

^aPermeability and solubility measurements were conducted at 35 °C, 10 atm feed pressure and a permeate pressure 'at vacuum'.

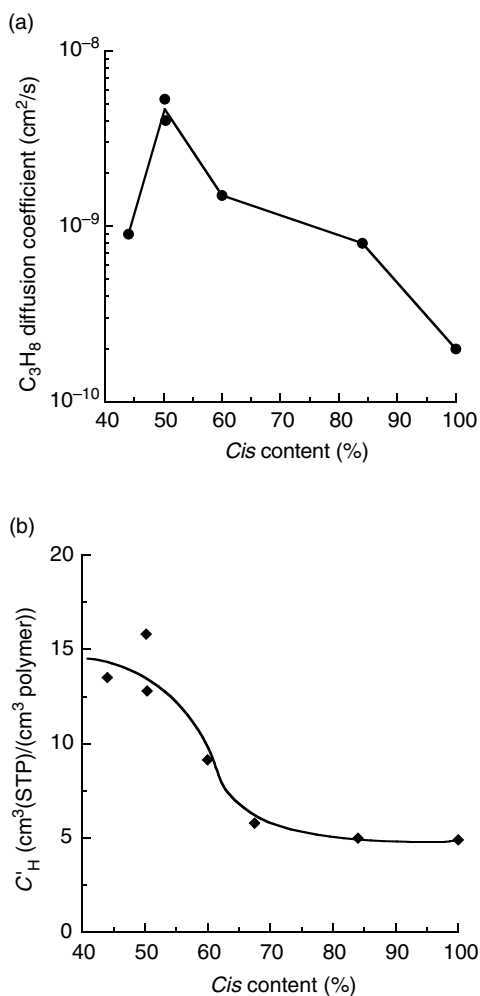


Figure 1.21 Relationship between *cis* isomer content in poly(*tert*-butylacetylene) and (a) infinite diffusion coefficient at 35 °C and (b) Langmuir capacities at 35 °C [172]. (a, b) From ‘The influence of chain configuration and, in turn, chain packing on the sorption and transport properties of poly(*tert* butyl acetylene)’, A. Morisato, N. R. Miranda, B. D. Freeman and H. B. Hopfenberg, *J. Appl. Polym. Sci.*, **49**, 2065–2074, Copyright © 1993, John Wiley & Sons, Inc. Reprinted with permission of John Wiley & Sons, Inc.

does have the ability to significantly influence solubility and diffusivity via changes in T_g and FFV. Structural changes which increase the efficiency of polymer chain packing cause FFV to decrease and also decrease the permeability. Diffusion coefficients decrease with increasing

penetrant size. Solubility is related to the condensability of the penetrant and generally increases with increasing T_c of the penetrant.

Pressure and temperature strongly influence gas and vapor transport in polymers. Increasing the pressure increases the solubility according to Henry’s law in rubbery polymers, and dual-mode sorption in glassy polymers. Increasing temperature generally has the opposite effect. Diffusivity for non-interacting, low-sorbing gases is largely independent of pressure; however, diffusivity for highly sorbing gases is strongly dependent on pressure (i.e. plasticization).

Finally, mixed-gas permeation properties do not necessarily correlate with those obtained in pure-gas measurements. In ideal, non-interactive cases, such as oxygen/nitrogen or hydrogen/methane separation, pure-gas permeability and selectivity are essentially identical to mixed-gas permeability and selectivity. However, separations involving condensable, highly sorbing feed components, such as carbon dioxide or organic vapors, can suffer from plasticization or competitive sorption, each of which often lowers selectivity. In addition, non-idealities, which can generally be neglected in pure-gas measurements, even at high pressure, require the use of fugacity for accurate analysis in mixed-gas systems. Other systems, such as reverse-selective vapor separations, actually exhibit better mixed-gas separation properties than pure-gas separation properties, and so plasticization and enhanced solubility selectivity effects can also act to improve separation performance in these cases.

References

- [1] D. R. Paul, ‘The solution-diffusion model for swollen membranes’, *Separation and Purification Methods*, **5** (1976), 33–50.
- [2] J. G. Wijmans and R. W. Baker, ‘The solution-diffusion model: a review’, *Journal of Membrane Science*, **107** (1995), 1–21.
- [3] J. K. Mitchell, ‘On the penetrativeness of fluids’, *Journal of Membrane Science*, **100** (1995), 11–16.
- [4] T. Graham, ‘On the absorption and dialytic separation of gases by colloid septa. Action of a septum of caoutchouc’, *Philosophical Magazine*, **32** (1866), 401–420.
- [5] S. von Wroblewski, ‘Ueber die natur der absorption der gase durch flussigkeiten unter hohen drucken’, *Ann Physik u Chem*, **8** (1879), 29–52.

- [6] K. W. Boeddeker, 'Commentary Tracing Membrane Science', *Journal of Membrane Science*, Special Issue: The Early History of Membrane Science, **100** (1995), 1–68.
- [7] K. Ghosal and B. D. Freeman, 'Gas separation using polymer membranes: An overview', *Polymers for Advanced Technology*, **5** (1994), 673–697.
- [8] J. H. Petropoulos, 'Mechanisms and theories for sorption and diffusion of gases in polymers', in D. R. Paul and Y. P. Yampolskii (Eds), *Polymeric Gas Separation Membranes*, CRC Press, Boca Raton, FL, USA (1994), pp. 17–82.
- [9] R. M. Felder and G. S. Huward, *Permeation, Diffusion and Sorption of Gases and Vapors*, Methods of Experimental Physics, Vol. 16C, Academic Press, New York, NY, USA (1980), pp. 315–377.
- [10] H. Lin and B. D. Freeman, *Permeation and Diffusion*, Springer-Handbook of Materials Measurement Methods, Vol. 16C, Springer-Verlag, Berlin, Germany (2005).
- [11] W. J. Koros and C. M. Zimmerman, 'Transport and Barrier Properties', in R. F. J. Brady (Ed.), *Comprehensive Desk Reference of Polymer Characterization and Analysis*, Oxford University Press, Washington, DC, USA (2003), pp. 680–699.
- [12] V. Bondar, B. D. Freeman and Y. P. Yampolskii, 'Sorption of gases and vapors in an amorphous glassy perfluorodioxide copolymer', *Macromolecules*, **32** (1999), 6163–6171.
- [13] V. I. Bondar, B. D. Freeman and I. Pinnau, 'Gas sorption and characterization of poly(ether-*b*-amide) segmented block copolymers', *Journal of Polymer Science, Part B: Polymer Physics*, **37** (1999), 2463–2475.
- [14] S. N. Dhoot, B. D. Freeman and M. Stewart, 'Sorption and transport of linear esters and branched alkanes in biaxially oriented poly(ethylene terephthalate)', *Industrial and Engineering Chemistry Research*, **43** (2004), 2966–2976.
- [15] V. T. Stannett, W. J. Koros, D. R. Paul and H. K. Lonsdale, 'Recent advances in membrane science and technology', *Advances in Polymer Science*, **32** (1979), 69–121.
- [16] I. Pinnau and B. D. Freeman, *Membrane Formation and Modification Overview*, in I. Pinnau and B. D. Freeman (Eds.) American Chemical Society Symposium Series 744, American Chemical Society, Washington, D.C. (2000), pp. 1–22.
- [17] W. J. Koros and I. Pinnau, 'Membrane formation for gas separation processes', in D. R. Paul and Y. P. Yampolskii (Eds), *Polymeric Gas Separation Membranes*, CRC Press, Boca Raton, FL, USA (1994), pp. 209–272.
- [18] L. M. Robeson, 'Correlation of separation factor versus permeability for polymeric membranes', *Journal of Membrane Science*, **62** (1991), 165–185.
- [19] D. T. Coker, B. D. Freeman and G. K. Fleming, 'Modeling multicomponent gas separation using hollow-fiber membrane contactors', *AIChE Journal*, **44** (1998), 1289–1302.
- [20] A. Y. Alentiev and Y. P. Yampolskii, 'Free volume model and tradeoff relations of gas permeability and selectivity in glassy polymers', *Journal of Membrane Science*, **165** (2000), 201–216.
- [21] B. D. Freeman, 'Basis of permeability/selectivity tradeoff relations in polymeric gas separation membranes', *Macromolecules*, **32** (1999), 375–380.
- [22] D. W. Breck, *Zeolite Molecular Sieves: Structure, Chemistry and Use*, John Wiley & Sons, Inc. New York, NY, USA (1974), pp. 593–724.
- [23] S. A. Stern, 'Polymers for gas separations: The next decade', *Journal of Membrane Science*, **94** (1994), 1–65.
- [24] M. Cohen and T. Turnbull, 'Molecular transport in liquids and glasses', *Journal of Chemical Physics*, **31** (1959), 1164–1169.
- [25] R. W. Baker, 'Future directions of membrane gas separation technology', *Industrial and Engineering Chemistry Research*, **41** (2002), 1393–1411.
- [26] R. W. Baker, J. G. Wijmans and J. H. Kaschemekat, 'The design of membrane vapor–gas separation systems', *Journal of Membrane Science*, **151** (1998), 55–62.
- [27] X. Wang, R. Daniels and R. W. Baker, 'Recovery of VOCs from high-volume, low-VOC-concentration air systems', *AIChE Journal*, **47** (2001), 1094–1100.
- [28] B. D. Freeman and I. Pinnau, 'Separation of gases using solubility-selective polymers', *Trends in Polymer Science*, **5** (1997), 167–173.
- [29] D. V. Laciak, L. M. Robeson and C. D. Smith, 'Group contribution modeling of gas transport in polymeric membranes', in B. D. Freeman and I. Pinnau (Eds), *Polymer Membranes for Gas and Vapor Separations*, ACS Symposium Series 733, American Chemical Society, Washington, DC, USA (1999), pp. 151–177.
- [30] J. Y. Park and D. R. Paul, 'Correlation and prediction of gas permeability in glassy polymer membrane materials via modified free volume based group contribution method', *Journal of Membrane Science*, **125** (1997), 23–39.
- [31] D. W. van Krevelen, *Properties of Polymers*, 3rd Edn., Elsevier, Amsterdam, The Netherlands (1990).
- [32] H. Lin and B. D. Freeman, 'Gas solubility, diffusivity and permeability in poly(ethylene oxide)', *Journal of Membrane Science*, **239** (2004), 105–117.
- [33] A. S. Michaels and H. J. Bixler, 'Flow of gases through polyethylene', *Journal of Polymer Science*, **50** (1961), 412–439.

- [34] T. C. Merkel, V. Bondar, K. Nagai, B. D. Freeman and I. Pinnau, 'Gas sorption, diffusion, and permeation in poly(dimethylsiloxane)', *Journal of Polymer Science, Part B: Polymer Physics*, **38** (2000), 415–434.
- [35] A. S. Michaels, W. R. Vieth and J. A. Barrie, 'Diffusion of gases in polyethylene terephthalate', *Journal of Applied Physics*, **34** (1963), 13–21.
- [36] G. J. van Amerongen, 'Diffusion in Elastomers', *Rubber Chemistry and Technology*, **37** (1964), 1065–1153.
- [37] V. V. Teplyakov and S. G. Durgaryan, 'Correlation analysis of permeation parameters for polymers', *Vysokomolekuliarnye Soedineniia (Polymer Science, Series A)*, **26** (1984), 1498–1505.
- [38] V. V. Teplyakov and P. Meares, 'Correlation aspects of the selective gas permeabilities of polymeric materials and membranes', *Gas Separation and Purification*, **4** (1990), 66–73.
- [39] V. P. Shantarovich, I. B. Kevdina, Y. P. Yampolskii and A. Y. Alentiev, 'Positron annihilation lifetimes of high and low free volume glassy polymers: effects of free volume sizes on the permeability and permselectivity', *Macromolecules*, **33** (2000), 7453–7466.
- [40] P. Meares, 'The diffusion of gases through polyvinyl acetate', *Journal of the American Chemical Society*, **76** (1954), 3415–3422.
- [41] G. S. Park, *Transport Principles-Solution, Diffusion and Permeation in Polymer Membranes*, NATO ASI Series, Series C, 181 Kluwer Academic Publishers, Dordrecht, The Netherlands (1986), pp. 57–107.
- [42] P. E. J. Rouse, 'Diffusion of vapors in films', *Journal of the American Chemical Society*, **69** (1947), 1068–1073.
- [43] J. D. Wellons and V. T. Stannett, 'Permeation, sorption, and diffusion of water in ethyl cellulose', *Journal of Polymer Science*, **4** (1966), 593–602.
- [44] K. A. Schult and D. R. Paul, 'Water sorption and transport in a series of polysulfones', *Journal of Polymer Science, Part B: Polymer Physics*, **34** (1996), 2805–2817.
- [45] K. Ghosal, R. T. Chern and B. D. Freeman, 'Effect of basic substituents on gas sorption and permeation in polysulfone', *Macromolecules*, **29** (1996), 4360–4369.
- [46] E. L. Spotz, 'The equation of state of gases at low and moderate densities', in J. O. Hirschfelder, C. F. Curtiss and R. B. Bird (Eds), *Molecular Theory of Gases and Liquids*, Structure of Matter Series, John Wiley & Sons, Inc., New York, USA (1954), pp. 131–230.
- [47] T. Titani, 'Viscosity of vapors of organic compounds. II', *Bulletin of the Chemical Society of Japan*, **5** (1930), 98–108.
- [48] B. E. Poling, J. M. Prausnitz and J. P. O'Connell, *The Properties of Gases and Liquids*, 5th Edn, McGraw-Hill, New York, NY, USA (2000).
- [49] T. H. Chung, M. Ajlan, L. L. Lee and K. E. Starling, 'Generalized multiparameter correlation for nonpolar and polar fluid transport properties', *Industrial and Engineering Chemistry Research*, **27** (1988), 671–679.
- [50] T. H. Chung, L. L. Lee and K. E. Starling, 'Application of kinetic gas theories and multiparameter correlation for prediction of dilute gas viscosity and thermal conductivity', *Industrial and Engineering Chemistry Research*, **23** (1984), 8–13.
- [51] E. L. Spotz, 'Transport phenomena of dilute gases', in J. O. Hirschfelder, C. F. Curtiss and R. B. Bird (Eds), *Molecular Theory of Gases and Liquids*, Structure of Matter Series, John Wiley & Sons, Inc., New York, NY, USA (1954), pp. 131–230.
- [52] J. S. Rowlinson, 'The second virial coefficients of polar gases', *Transactions of the Faraday Society*, **45** (1949), 974–984.
- [53] L. S. Tee, S. Gotoh and W. E. Stewart, 'Molecular parameters for normal fluids. The Lennard-Jones 12-6 potential', *Industrial and Engineering Chemistry Research*, **5** (1966), 346–363.
- [54] W. M. Lee, 'Selection of barrier materials from molecular structure', *Polymer Engineering and Science*, **20** (1980), 65–69.
- [55] A. Reynier, P. Dole, S. Humbel and A. Feigenbaum, 'Diffusion coefficients of additives in polymers. I. Correlation with geometric parameters', *Journal of Applied Polymer Science*, **82** (2001), 2422–2433.
- [56] H. Fujita, A. Kishimoto and K. Matsumo, 'Concentration and temperature dependence of diffusion coefficients', *Transactions of the Faraday Society*, **56** (1960), 424–437.
- [57] Y. P. Yampolskii, S. G. Durgaryan and N. S. Nametkin, 'Permeability, diffusivity, and solubility of *n*-alkenes in polymers', *Vysokomolekuliarnye Soedineniia (Polymer Science, Series B)*, **21** (1979), 616–621.
- [58] S. N. Dhoot, B. D. Freeman, M. Stewart and A. J. Hill, 'Sorption and transport of linear alkane hydrocarbons in biaxially oriented poly(ethylene terephthalate)', *Journal of Polymer Science, Part B: Polymer Physics*, **39** (2001), 1160–1172.
- [59] K. Tanaka, A. Taguchi, J. Hao, H. Kita and K. Okamoto, 'Permeation and separation properties of polyimide membranes to olefins and paraffins', *Journal of Membrane Science*, **121** (1996), 197–207.

- [60] B. D. Freeman and I. Pinnau, 'Polymeric materials for gas separations', in B. D. Freeman and I. Pinnau (Eds), *Polymer Membranes for Gas and Vapor Separations*, ACS Symposium Series 733, American Chemical Society, Washington, DC, USA (1999), pp. 1–27.
- [61] R. M. Barrer and G. Skirrow, 'Transport and equilibrium phenomena in gas elastomer systems. Part II. Equilibrium phenomena', *Journal of Polymer Science*, **3** (1948), 564–575.
- [62] T. C. Merkel, V. Bondar, K. Nagai and B. D. Freeman, 'Sorption and transport of hydrocarbon and perfluorocarbon gases in poly(1-trimethylsilyl-1-propyne)', *Journal of Polymer Science, Part B: Polymer Physics*, **38** (1999), 273–296.
- [63] G. Gee, 'Some thermodynamic properties of high polymers and their molecular interpretation', *Quarterly Reviews of the Chemical Society*, **1** (1947), 265–298.
- [64] Y. P. Yampolskii and V. V. Volkov, 'Studies in gas permeability and membrane gas separation in the Soviet Union', *Journal of Membrane Science*, **64** (1991), 191–228.
- [65] W. J. Koros, D. R. Paul and G. S. Huvard, 'Energetics of gas sorption in glassy polymers', *Polymer*, **20** (1979), 956–960.
- [66] F. Korosy, 'Two rules concerning solubility of gases and crude data on solubility of krypton', *Transactions of the Faraday Society*, **33** (1937), 416–425.
- [67] R. Prabhakar, M. G. De Angelis, G. C. Sarti, B. D. Freeman and M. C. Coughlin, 'Gas and vapor sorption, permeation and diffusion in poly(tetrafluoroethylene-co-perfluoromethyl vinyl ether) Macromolecules', **38** (2005), 1899–1910.
- [68] Y. Kamiya, Y. Naito, K. Terada and K. Mizoguchi, 'Volumetric properties and interaction parameters of dissolved gases in poly(dimethylsiloxane) and polyethylene', *Macromolecules*, **33** (2000), 3111–3119.
- [69] K. Toi, G. Morel and D. R. Paul, 'Gas sorption and transport in poly(phenylene oxide) and comparisons with other glassy polymers', *Journal of Applied Polymer Science*, **27** (1982), 2997–3005.
- [70] A. S. Michaels and H. J. Bixler, 'Solubility of gases in polyethylene', *Journal of Polymer Science*, **50** (1961), 393–412.
- [71] G. E. Serad, B. D. Freeman, M. E. Stewart and A. J. Hill, 'Gas and vapor sorption and diffusion in poly(ethylene terephthalate)', *Polymer*, **42** (2001), 6929–6943.
- [72] K. Ghosal, R. T. Chern, B. D. Freeman and R. Savariar, 'The effect of aryl nitration on gas sorption and permeation in polysulfone', *Journal of Polymer Science, Part B: Polymer Physics*, **33** (1995), 657–666.
- [73] D. R. Stull, E. F. Westrum and G. C. Sinke, *The Chemical Thermodynamics of Organic Compounds*, John Wiley & Sons, Inc., New York, NY, USA (1969).
- [74] S. A. Stern, J. T. Mullhaupt and P. J. Garries, 'The effect of pressure on the permeation of gases and vapors through polyethylene. Usefulness of the corresponding states principle', *AIChE Journal*, Special Issue: The Early History of Membrane Science, **15** (1969), 64–73.
- [75] Y. P. Yampolskii, D. Wiley and C. Maher, 'Novel correlation for solubility of gases in polymers: effect of molecular surface area of gases', *Journal of Applied Polymer Science*, **76** (2000), 552–560.
- [76] M. R. Pixton and D. R. Paul, 'Relationships between structure and transport properties for polymers with aromatic backbones', in D. R. Paul and Y. P. Yampolskii (Eds), *Polymeric Gas Separation Membranes*, CRC Press, Boca Raton, FL, USA (1994), pp. 83–154.
- [77] T. C. Merkel, B. D. Freeman, R. J. Spontak, Z. He, I. Pinnau, P. Meakin and A. J. Hill, 'Ultrapermselective, reverse-selective nanocomposite membranes', *Science*, **296** (2002), 519–522.
- [78] I. Pinnau, C. G. Casillas, A. Morisato and B. D. Freeman, 'Hydrocarbon/hydrogen mixed gas permeation in poly(1-trimethylsilyl-1-propyne) (PTMSP), poly(1-phenyl-1-propyne) (PPP) and PTMSP/PPP blends', *Journal of Polymer Science, Part B: Polymer Physics*, **34** (1996), 2613–2621.
- [79] Y. P. Yampolskii, S. G. Durgaryan and N. S. Nametkin, 'Translational and rotational mobility of low molecular mass compounds in polymers with different glass transition temperatures', *Vysokomolekuliarnye Soedineniia*, **24** (1982), 536–541.
- [80] M. W. Fitch, W. J. Koros, R. L. Nolen and J. R. Carnes, 'Permeation of several gases through elastomers, with emphasis on the D₂/H₂ pair', *Journal of Applied Polymer Science*, **47** (1993), 1033–1046.
- [81] Y. Kawakami, H. Karasawa, T. Aoki, Y. Yamamura, H. Hisada and Y. Yamashita, 'Polymers with oligoorganosilicone side chains as materials for oxygen permeable membranes', *Polymer Journal*, **17** (1985), 1159–1172.
- [82] Y. Kawakami, H. Toda, M. Higashino and Y. Yamashita, 'Polynorbornenes with oligodimethylsiloxanyl substituents for selectively oxygen permeable membrane material', *Polymer Journal*, **20** (1988), 285–292.
- [83] Y. Hirayama, T. Yoshinaga, Y. Kusuki, K. Ninomiya, T. Sakakibara and T. Tamari, 'Relation of gas permeability with structure of aromatic

- polyimides I', *Journal of Membrane Science*, **111** (1996), 169–182.
- [84] K. Nagai, T. Masuda, T. Nakagawa, B. D. Freeman and I. Pinnau, 'Poly[1-(trimethylsilyl)-1-propyne] and related polymers: synthesis, properties and functions', *Progress in Polymer Science*, **26** (2001), 721–798.
- [85] R. T. Chern, W. J. Koros, E. S. Sanders and R. Yui, 'Second Component effects in sorption and permeation of gases in glassy polymers', *Journal of Membrane Science*, **15** (1983), 157–169.
- [86] A. R. Berens and H. B. Hopfenberg, 'Diffusion of organic vapors at low concentrations in glassy PVC, polystyrene and PMMA', *Journal of Membrane Science*, **10** (1982), 283–303.
- [87] R. T. Chern, W. J. Koros, H. B. Hopfenberg and V. T. Stannett, 'Material selection for membrane-based gas separations', in D. R. Lloyd (Ed.), *Material Science of Synthetic Membranes*, ACS Symposium Series 269, American Chemical Society, Washington, DC, USA (1985), pp. 25–46.
- [88] T. C. Merkel, V. Bondar, K. Nagai, B. D. Freeman and Y. P. Yampolskii, 'Gas sorption, diffusion and permeation in poly(2,2-bis(trifluoromethyl)-4,5-difluoro-1,3-dioxole-co-tetrafluoroethylene)', *Macromolecules*, **32** (1999), 8427–8440.
- [89] K. Toi and D. R. Paul, 'Effect of polystyrene molecular weight on the carbon dioxide sorption isotherm', *Macromolecules*, **15** (1982), 1104–1107.
- [90] H. Lin, B. D. Freeman, L. G. Toy, V. Bondar, R. P. Gupta, S. J. Pas and A. J. Hill, 'Reverse-selective polymeric membranes for hydrogen purification', *Polymer Preprints (American Chemical Society Division of Polymer Chemistry)*, **45** (1) (2004), 23–24.
- [91] L. A. Pilato, L. M. Litz, B. Haritay, A. G. Farnham, J. H. Kawakami, P. E. Fritze and J. E. McGrath, 'Polymers for permselective membrane gas separations', *Polymer Preprints (American Chemical Society Division of Polymer Chemistry)*, **161** (1) (1975), 41–46.
- [92] S. G. Charati, A. Y. Houde and S. S. Kulkarni, 'Transport of gases in aromatic polyesters: correlation with WAXD studies', *Journal of Polymer Science, Part B: Polymer Physics*, **29** (1991), 921–931.
- [93] A. Bondi, *Physical Properties of Molecular Crystals, Liquids and Gases*, John Wiley & Sons, Inc., New York, NY, USA (1968).
- [94] J. S. Vrentas and C. M. Vrentas, 'Predictive methods for self-diffusion and mutual diffusion coefficients in polymer-solvent systems', *European Polymer Journal*, **34** (1998), 797–803.
- [95] J. L. Duda, Y. C. Ni and J. S. Vrentas, 'An equation relating self-diffusion and mutual diffusion coefficients in polymer-solvent systems', *Macromolecules*, **12** (1979), 459–462.
- [96] A. Puleo, N. Muruganandam and D. R. Paul, 'Gas sorption and transport in substituted polystyrenes', *Journal of Polymer Science, Part B: Polymer Physics*, **27** (1989), 2385–2406.
- [97] D. H. Weinkauff and D. R. Paul, 'Gas transport properties of thermotropic liquid-crystalline copolyesters. II. The effects of copolymer composition', *Journal of Polymer Science, Part B: Polymer Physics*, **30** (1992), 837–849.
- [98] R. R. Light and R. W. Seymour, 'Effect of sub- T_g relaxations on the gas transport properties of polyesters', *Polymer Engineering and Science*, **22** (1982), 857–864.
- [99] D. H. Weinkauff and D. R. Paul, 'Gas transport properties of thermotropic liquid-crystalline copolyesters. I. The effects of orientation and annealing', *Journal of Polymer Science, Part B: Polymer Physics*, **30** (1992), 813–835.
- [100] D. H. Weinkauff and D. R. Paul, 'Gas transport properties of liquid crystalline poly(ethylene terephthalate-co-p-oxybenzoate)', *Journal of Polymer Science, Part B: Polymer Physics*, **29** (1991), 329–340.
- [101] H. Lin and B. D. Freeman, 'Gas permeation and diffusion in crosslinked poly(ethylene glycol diacrylate)', *Macromolecules*, **38** (2005), 8394–8407.
- [102] J. S. McHattie, W. J. Koros and D. R. Paul, 'Gas transport properties in polysulfones. 3. Comparison of tetramethyl-substituted bisphenols', *Polymer*, **33** (1992), 1701–1711.
- [103] A. Thran, G. Kroll and F. Faupel, 'Correlation between fractional free volume and diffusivity of gas molecules in glassy polymers', *Journal of Polymer Science, Part B: Polymer Physics*, **37** (1999), 3344–3358.
- [104] C. Nagel, K. Guenther-Schade, D. Frisch, T. Strunskus and F. Faupel, 'Free volume and transport properties in highly selective polymer membranes', *Macromolecules*, **35** (2002), 2071–2077.
- [105] A. Y. Alentiev and Y. P. Yampolskii, 'Meares equation and the role of cohesion energy density in diffusion in polymers', *Journal of Membrane Science*, **206** (2002), 291–306.
- [106] A. Singh, B. D. Freeman and I. Pinnau, 'Pure and mixed gas acetone/nitrogen permeation properties of polydimethylsiloxane', *Journal of Polymer Science, Part B: Polymer Physics*, **32** (1998), 289–301.
- [107] P. J. Flory and J. J. Rehner, 'Statistical mechanics of cross-linked polymer networks II. Swelling', *The Journal of Chemical Physics*, **11** (1943), 521–526.
- [108] G. K. Fleming and W. J. Koros, 'Dilation of polymers by sorption of carbon dioxide at elevated pressures. 1. Silicone rubber and

- unconditioned polycarbonate', *Macromolecules*, **19** (1986), 2285–2291.
- [109] Y. Yang, Y. Huang, D. Wang, H. Liu and C. Hu, 'Sorption and diffusion of ethanol vapor in polybutadiene/acrylonitrile, polybutadiene/styrene and polybutadiene based polyurethanes', *European Polymer Journal*, **40** (2004), 855–863.
- [110] J. A. Barrie, 'Water in polymers', in J. Crank and G. S. Park (Eds), *Diffusion in Polymers*, Academic Press, New York, NY, USA (1968), pp. 259–314.
- [111] M. G. De Angelis, T. C. Merkel, V. Bondar, B. D. Freeman, F. Doghieri and G. C. Sarti, 'Hydrocarbon and fluorocarbon solubility and dilation in poly(dimethylsiloxane): Comparison of experimental data with predictions of the Sanchez–Lacombe equation of state', *Journal of Polymer Science, Part B: Polymer Physics*, **37** (1999), 3011–3026.
- [112] D. R. Paul, 'Gas sorption and transport in glassy polymers', *Berichte der Bunsen-Gesellschaft*, **83** (1979), 294–302.
- [113] R. Patterson and Y. P. Yampolskii, 'Solubility of gases in glassy polymers', *Journal of Physical Chemistry Reference Data*, **28** (1999), 1255–1450.
- [114] A. Tokarev, K. Friess, J. Machkova, M. Sipek and Y. P. Yampolskii, 'Sorption and diffusion of organic vapors in amorphous Teflon AF2400', *Journal of Polymer Science, Part B: Polymer Physics*, (2000), Vol. 44(5), (2006) 832–844.
- [115] W. J. Koros and R. T. Chern, 'Separation of gaseous mixtures using polymer membranes', in R. W. Rousseau (Ed.), *Handbook of Separation Progress Technology*, John Wiley & Sons, Inc., New York, NY, USA (1987), pp. 862–953.
- [116] W. J. Koros and D. R. Paul, 'Carbon dioxide sorption in poly(ethylene terephthalate) above and below the glass transition', *Journal of Polymer Science, Part B: Polymer Physics*, **16** (1978), 1947–1963.
- [117] V. V. Volkov, A. K. Bokarev, S. G. Durgaryan and N. S. Nametkin, 'Sorption of low-molecular-weight compounds in glassy PVTMS in vicinity and below the critical temperature of the solute', *Doklady Akademii Nauk SSSR*, **282** (1985), 641–644.
- [118] S. M. Jordan and W. J. Koros, 'Characterization of CO₂-induced conditioning of substituted polycarbonates using various "exchange" penetrants', *Journal of Membrane Science*, **51** (1990), 233–247.
- [119] S. M. Jordan, M. A. Henson and W. J. Koros, 'The effects of carbon dioxide conditioning on the permeation behavior of hollow fiber asymmetric membranes', *Journal of Membrane Science*, **54** (1990), 103–118.
- [120] V. Bondar, Y. Kamiya and Y. P. Yampolskii, 'On pressure dependence of the parameters of the dual-mode sorption model', *Journal of Polymer Science, Part B: Polymer Physics*, **34** (1996), 369–378.
- [121] A. R. Berens, 'The solubility of vinyl chloride in poly(vinyl chloride)', *Die Angewandte Makromolekulare Chemie*, **47** (1975), 97–110.
- [122] A. Y. Alentiev, V. P. Shantarovich, T. C. Merkel, V. Bondar, B. D. Freeman and Y. P. Yampolskii, 'Gas and vapor sorption, permeation, and diffusion in glassy amorphous Teflon AF1600', *Macromolecules*, **35** (2002), 9513–9522.
- [123] C. Staudt-Bickel and W. J. Koros, 'Improvement of CO₂/CH₄ separation characteristics of polyimides by chemical crosslinking', *Journal of Membrane Science*, **155** (1999), 145–154.
- [124] R. T. Chern and C. N. Provan, 'Gas-induced plasticization and the permselectivity of poly(tetrabromophenolphthalein) to a mixture of carbon dioxide and methane', *Macromolecules*, **24** (1991), 2203–2207.
- [125] S. Zhou and S. A. Stern, 'The effect of plasticization on the transport of gases in and through glassy polymers', *Journal of Polymer Science, Part B: Polymer Physics*, **27** (2003), 205–222.
- [126] H. Lin and B. D. Freeman, 'Gas and vapor solubility in crosslinked poly(ethylene glycol diacrylate)', *Macromolecules*, **38** (2005), 8394–8407.
- [127] A. A. Armstrong and V. T. Stannett, 'Temperature effects during the sorption and desorption of water vapor in high polymers. I. Fibers, with particular reference to wool', *Makromolekulare Chemie*, **90** (1966), 145–160.
- [128] W. J. Koros, D. R. Paul and A. A. Rocha, 'Carbon dioxide sorption and transport in polycarbonate', *Journal of Polymer Science, Part B: Polymer Physics*, **14** (1976), 687–702.
- [129] V. T. Stannett, 'The transport of gases in synthetic polymer membranes – a historic perspective', *Journal of Membrane Science*, **3** (1978), 97–115.
- [130] H. Lin, E. van Wagner, B. D. Freeman and I. Roman, 'High performance polymer membranes for natural gas sweetening', *Advanced Materials*, **18** (2006), 39–44.
- [131] T. S. Chow, 'Molecular interpretation of glass transition temperature of polymer-diluent systems', *Macromolecules*, **13** (1980), 362–364.
- [132] I. Pinnau and Z. He, 'Pure- and mixed-gas permeation properties of polydimethylsiloxane for hydrocarbon/methane and hydrocarbon/hydrogen

- separation', *Journal of Membrane Science*, **244** (2004), 227–233.
- [133] I. Pinnau and L. G. Toy, 'Transport of organic vapors through poly(1-trimethylsilyl-1-propyne)', *Journal of Membrane Science*, **116** (1996), 199–209.
- [134] R. Ash, R. M. Barrer and P. Sharma, 'Sorption and flow of carbon dioxide and some hydrocarbons in a microporous carbon membrane', *Journal of Membrane Science*, **1** (1976), 17–32.
- [135] R. Srinivasan, S. R. Auvil and P. M. Burban, 'Elucidating the mechanism(s) of gas transport in poly[1-(trimethylsilyl)-1-propyne] (PTMSP) membranes', *Journal of Membrane Science*, **86** (1994), 67–86.
- [136] S. Y. Lee, B. S. Minhas and M. D. Donohue, 'Effect of gas composition and pressure on permeation through cellulose acetate membranes', *AIChE Symposium Series*, **84** (1988), 93–101.
- [137] L. S. White, T. A. Blinka, H. A. Kloczewski and I.-F. Wang, 'Properties of a polyimide gas separation membrane in natural gas streams', *Journal of Membrane Science*, **103** (1995), 73–82.
- [138] H. Lin, E. van Wagner, B. D. Freeman, L. G. Toy and P. Ragubuir, 'New membrane materials for CO₂/H₂ separation and a model for pure and mixed gas permeability', *Science*, **311** (2006), 639–642.
- [139] A. Y. Houde, B. Krishnakumar, S. G. Charati and S. A. Stern, 'Permeability of dense (homogeneous) cellulose acetate membranes to methane, carbon dioxide, and their mixtures at elevated pressures', *Journal of Applied Polymer Science*, **62** (1996), 2181–2192.
- [140] S. V. Dixon-Garrett, K. Nagai and B. D. Freeman, 'Ethylbenzene solubility, diffusivity and permeability in poly(dimethylsiloxane)', *Journal of Polymer Science, Part B: Polymer Physics*, **38** (2000), 1461–1473.
- [141] H. Yasuda and T. Hirotsu, 'The effect of glass transition on gas permeability', *Journal of Applied Polymer Science*, **21** (1977), 105–112.
- [142] R. M. Barrer, 'Permeability in relation to viscosity and structure of rubber', *Transactions of the Faraday Society*, **38** (1942), 322–331.
- [143] G. J. van Amerongen, 'The permeability of different rubbers to gases and its relation to diffusivity and solubility', *Journal of Applied Physics*, **17** (1946), 972–985.
- [144] R. Prabhakar, B. D. Freeman and I. Roman, 'Gas and vapor sorption and permeation in poly(2, 2, 4-trifluoro-5-trifluoromethoxy-1, 3-dioxole-co-tetrafluoroethylene)', *Macromolecules*, **37** (2004), 7688–7697.
- [145] R. Prabhakar, R. Raharjo, L. G. Toy, H. Lin and B. D. Freeman, 'Self-consistent model of concentration and temperature dependence of permeability in rubbery polymers', *Industrial and Engineering Chemistry Research*, **44** (2005), 1547–1556.
- [146] Y. P. Yampolskii, S. Shishatskii, A. Y. Alentiev and K. Loza, 'Correlations with and predictions of activation energies of gas permeation and diffusion in glassy polymers', *Journal of Membrane Science*, **148** (1998), 59–69.
- [147] S. Glasstone, K. J. Laidler and H. Eyring, *The Theory of Rate Processes*, McGraw-Hill, New York, NY, USA (1941).
- [148] S. A. Stern, V. M. Shah and B. J. Hardy, 'Structure-permeability relationship in silicone polymers', *Journal of Polymer Science, Part B: Polymer Physics*, **25** (1987), 1263–1298.
- [149] W. J. Koros and G. K. Fleming, 'Membrane-based gas separation', *Journal of Membrane Science*, **83** (1993), 1–80.
- [150] Y. P. Yampolskii and N. A. Plate, 'Is it possible to predict transport properties of polymers proceeding from chemical structure of the chains?', *Polymer Science*, **36** (1994), 1599–1609.
- [151] H. Ohya, V. V. Kudryavtsev and S. I. Semenova, *Polyimide Membranes – Applications, Fabrications and Properties*, Gordon & Breach, Tokyo, Japan (1996).
- [152] S. M. Allen, M. Fujii, V. T. Stannett, H. B. Hopfenberg and J. L. Williams, 'The barrier properties of polyacrylonitrile', *Journal of Membrane Science*, **2** (1977), 153–163.
- [153] N. A. Plate and Y. P. Yampolskii, 'Relationship between structure and transport properties for high free volume polymeric materials', in D. R. Paul and Y. P. Yampolskii (Eds), *Polymeric Gas Separation Membranes*, CRC Press, Boca Raton, FL, USA (1994), pp. 155–207.
- [154] V. S. Khotimskii, V. G. Filippova, I. S. Bryantseva, V. I. Bondar, V. P. Shantarovich and Y. P. Yampolskii, 'Synthesis, transport and sorption properties and free volume of polystyrene derivatives containing Si and F', *Journal of Applied Polymer Science*, **78** (2000), 1612–1620.
- [155] E. S. Finkel'shtein, M. L. Gringolts, N. V. Ushakov, V. G. Lakhtin, S. A. Soloviev and Y. P. Yampolskii, 'Synthesis and gas permeation properties of new ROMP polymers from silyl substituted norbornadienes and norbornenes', *Polymer*, **44** (2003), 2843–2851.
- [156] E. S. Finkel'shtein, K. L. Makovetskii, Y. P. Yampolskii, E. Portnykh, I. Ostrovskaya and N. Kaliuzhnyi, 'Ring-opening polymerization of norbornenes with organosilicon substituents. Gas permeability of polymers obtained', *Makromolekulare Chemie*, **192** (1991), 1–9.
- [157] N. Muruganandam, W. J. Koros and D. R. Paul, 'Gas sorption and transport in substituted polycarbonates', *Journal of Polymer Science, Part B: Polymer Physics*, **25** (1987), 1999–2026.

- [158] C. L. Aitken, W. J. Koros and D. R. Paul, 'Gas transport properties of bisphenol polysulfones', *Macromolecules*, **25** (1992), 3651–3658.
- [159] C. L. Aitken, W. J. Koros and D. R. Paul, 'Effect of structural symmetry on gas transport properties of polysulfones', *Macromolecules*, **25** (1992), 3424–3434.
- [160] W. J. Koros and G. K. Fleming, 'Membrane-based gas separation', *Journal of Membrane Science*, **83** (1993), 1–80.
- [161] J. S. McHattie, W. J. Koros, D. R. Paul, 'Gas transport properties of polysulfones. I. Role of symmetry of methyl group placement on bisphenol', *Polymer*, **32** (1991), 840–850.
- [162] M. R. Pixton and D. R. Paul, 'Gas transport of polyarylates part II: Tetrabromination of the bisphenol', *Journal of Polymer Science, Part B: Polymer Physics*, **33** (1995), 1353–1364.
- [163] M. Aguilar-Vega and D. R. Paul, 'Gas transport properties of polycarbonates and polysulfones with aromatic substitutions on the bisphenol connector group', *Journal of Polymer Science, Part B: Polymer Physics*, **31** (1993), 1599–1610.
- [164] K. Ghosal, R. T. Chern, B. D. Freeman, W. H. Daly and I. I. Negulescu, 'Effect of basic substituents on gas sorption and permeation in polysulfone', *Macromolecules*, **29** (1996), 4360–4369.
- [165] M. R. Coleman and W. J. Koros, 'Isomeric polyimides based on fluorinated dianhydrides and diamines for gas separation applications', *Journal of Membrane Science*, **50** (1990), 285–297.
- [166] T. H. Kim, W. J. Koros, G. R. Husk and K. C. O'Brien, 'Relationship between gas separation properties and chemical structure in a series of aromatic polyimides', *Journal of Membrane Science*, **37** (1988), 45–62.
- [167] Y. P. Yampolskii, N. B. Bespalova, E. S. Finkel'shtein, V. Bondar and A. V. Popov, 'Synthesis, gas permeability, and gas sorption properties of fluorine-containing norbornene polymers', *Macromolecules*, **27** (1994), 2872–2878.
- [168] R. J. Andrews and E. A. Grulke, 'Glass transition temperatures of polymers, in J. Brandrup, E. H. Immergut, E. A. Grulke, A. Abe and D. R. Bloch (Eds), *Polymer Handbook*, 4th Edn, John Wiley & Sons, Inc., New York, NY, USA (1999), pp. VI 193–VI 278.
- [169] V. T. Stannett and M. Szwarc, 'The permeability of polymer films to gases – a simple relationship', *Journal of Polymer Science*, **16** (1955), 89–91.
- [170] M. Salame and S. Steingiser, 'Barrier polymers', *Polymer Plastics Technology and Engineering*, **8** (1977), 155–175.
- [171] X.-Y. Wang, P. J. in't Veld, Y. Lu, B. D. Freeman and I. C. Sanchez, 'A molecular simulation study of cavity size distributions and diffusion in *para* and *meta* isomers', *Polymer*, **46** (2005), 9155–9161.
- [172] A. Morisato, N. R. Mirando, B. D. Freeman and H. B. Hopfenberg, 'The influence of chain configuration and, in turn, chain packing on the sorption and transport properties of poly(*tert* butyl acetylene)', *Journal of Applied Polymer Science*, **49** (1993), 2065–2074.
- [173] Y. P. Yampolskii, E. S. Finkelshtein, K. L. Makovetskii, V. Bondar and V. P. Shantarovich, 'Effects of *cis-trans*-configurations of the main chains of poly(trimethylsilyl norbornene) on its transport and sorption properties as well as free volume', *Journal of Applied Polymer Science*, **62** (1996), 349–357.
- [174] K. Weh, M. Noack, R. Ruhmann, K. Hoffman, P. Toussaint and J. Caro, 'Modification of the transport properties of a polymethacrylate azobenzene membrane by photochemical switching', *Chemical Engineering Technology*, **21** (1998), 408–412.
- [175] P. Zoller and D. J. Walsh, *Standard Pressure–Volume–Temperature Data for Polymers*, Technomic, Lancaster, PA, USA (1995).

Principles of Molecular Simulation of Gas Transport in Polymers

Doros N. Theodorou

It will be perfectly clear that in my studies I was quite convinced of the real existence of molecules, that I never regarded them as a figment of my imagination, nor even as mere centres of force effects.

Johannes Diderik van der Waals, 1910

2.1 Introduction

Polymeric materials with controlled permeability properties are needed in packaging, industrial gas separations, water and air purification, biomedical engineering and energy storage, to name a few broad application areas. In all of these areas, product (as opposed to process) design is becoming increasingly important [1]. The successful design of products such as barrier films blocking the passage of atmospheric gases and water vapor, membrane modules for gas separation, pervaporation, ion exchange, diffusion dialysis, electrodialysis and reverse osmosis, controlled delivery devices, artificial organs and solid electrolytes, is principally a materials design problem. Maintaining competitiveness often requires developing a new chemical constitution or morphology for the material out of which the product is made that would result in more favorable sorption thermodynamics and/or transport rates in the application for which the product is developed, while at the same time affording the advantages of low cost, easy

processability, wear resistance and friendliness to the environment.

Successful materials design calls for a quantitative understanding of structure–property–processing–performance relations in materials. Developing precisely this understanding constitutes the main objective of materials modeling and simulation. Along with novel experimental techniques, which probe matter at increasingly finer scales, and new screening strategies, such as high-throughput experimentation, modeling has become an indispensable tool in the development of new materials and products.

Molecular simulations of materials have a history of less than 50 years. Thanks to continuous advances in computer hardware and algorithms, they are now capable of providing valuable insights into the microscopic mechanisms that shape material performance, and even quantitatively predicting properties for complex materials systems of immediate industrial interest. Today, the simulation of polymeric materials faces two serious challenges, both of which are the objects of intense research efforts. The first challenge is that force fields available for the atomistic simulation of real-life polymers are still of limited accuracy. This is especially true of polymers containing strongly polar, associating or inflexible moieties; such polymers are often used as barrier or separation materials. High-level *ab initio* quantum mechanical calculations on judiciously chosen (sets of) small-molar

mass analogues, fitting of the resulting energy hypersurfaces to computationally inexpensive force-field expressions, and refinement/validation of the force fields through comparison of simulation predictions against experiment are promising avenues for meeting this challenge. A second, and perhaps more serious challenge, is that the properties of real-life polymeric materials are governed by very broad spectra of length and time scales, ranging from 0.1 nm to mm and from 10 fs to years. These exceed by many orders of magnitude the longest time and length scales that can be simulated with conventional algorithms on currently available computers. For example, atomistic molecular dynamics (MD) simulations can track the temporal evolution of model systems of size on the order of 10 nm for times on the order of 10–100 ns. This challenge can be met through the development of multiscale, or hierarchical, modeling and simulation strategies based on systematic coarse-graining of the molecular representation. Such a strategy typically consists of several interconnected levels, with each level addressing phenomena over a specific window of length and time scales, receiving input from finer-grained levels and providing input to coarser-grained ones [2].

This chapter provides an overview of molecular simulation methods for the prediction of sorption thermodynamics and transport rates of gases and solvents in rubbery and glassy polymers. Emphasis is laid on the methods, their basic principles, applicability and limitations, the information that can be obtained from them and the ways in which this information can complement, and be validated against, experiments and used for materials design. Detailed statistical mechanical derivations are kept at a minimum; the reader is referred to earlier reviews or to the original literature for these derivations. It is not attempted to review the entire existing literature on the prediction of permeability properties through computer simulation; it is hoped that this chapter will systematize ideas and thus help the reader keep track of this literature, which is already sizable and rapidly expanding.

This chapter is organized as follows. Section 2.2 provides a brief overview of methods for generating model configurations representative of

amorphous polymers. Ways to validate these configurations against experiment and to extract key structural, thermodynamic, and dynamical properties relevant to sorption and diffusion are discussed in Section 2.3. Section 2.4 is devoted to methods for the prediction of sorption equilibria through MD and Monte Carlo (MC) techniques. MD and hierarchical techniques involving analysis of infrequent events and kinetic MC for the prediction of diffusivities are developed in Section 2.5. A summary and concluding remarks are provided in Section 2.6.

2.2 Generating Model Configurations for Amorphous Polymers

2.2.1 Models and Force Fields

With polymer crystallites being practically impermeable by small-molar mass penetrants in an overwhelming majority of cases, simulation efforts have focused mainly on the permeability properties of amorphous polymers, both above and below the glass transition temperature, T_g . The reliable prediction of sorption equilibria and diffusion rates hinges upon the availability of a good computer model for the polymer matrix of interest. The computational generation of atomistic configurations that faithfully represent the actual polymer matrix is, in general, a challenging problem; we discuss it first, since it is a prerequisite for the success of any effort to predict permeability properties.

A force field provides a mathematical description of the potential energy $\mathcal{V}(\mathbf{r}_p)$ as a function of the atomistic configuration \mathbf{r}_p of the polymer. Here, \mathbf{r}_p can be envisioned as the set of Cartesian coordinates of all atoms or, more generally, interaction sites, constituting the polymer. A good force field must be able to reproduce structural, thermodynamic and dynamical properties of the polymer under conditions of thermodynamic equilibrium (see Section 2.3). Atomistic force fields that can do this reasonably well, and at the same time are reasonably portable between different chemical constitutions, are available today thanks to painstaking efforts in modeling synthetic and biological macromolecules. As an example, the COMPASS force field (Condensed-phase Optimized Molecular

Potentials for Atomistic Simulation Studies [3]) represents $\mathcal{V}(\mathbf{r}_p)$ as follows:

$$\begin{aligned}
\mathcal{V} = & \sum_b \left[k_2^b (b - b_0)^2 + k_3^b (b - b_0)^3 + k_4^b (b - b_0)^4 \right] \\
& + \sum_\theta \left[k_2^\theta (\theta - \theta_0)^2 + k_3^\theta (\theta - \theta_0)^3 + k_4^\theta (\theta - \theta_0)^4 \right] \\
& + \sum_\phi \left[k_1^\phi (1 - \cos\phi) + k_2^\phi (1 - \cos 2\phi) \right. \\
& \left. + k_3^\phi (1 - \cos 3\phi) \right] + \sum_\chi k_2^\chi \chi^2 \\
& + \sum_{b,b'} k^{bb'} (b - b_0)(b' - b'_0) \\
& + \sum_{b,\theta} k^{b\theta} (b - b_0)(\theta - \theta_0) \\
& + \sum_{b,\phi} (b - b_0) \left[k_1^{b\phi} \cos\phi + k_2^{b\phi} \cos 2\phi + k_3^{b\phi} \cos 3\phi \right] \\
& \times \sum_{\theta,\phi} (\theta - \theta_0) \left[k_1^{\theta\phi} \cos\phi + k_2^{\theta\phi} \cos 2\phi + k_3^{\theta\phi} \cos 3\phi \right] \\
& + \sum_{\theta,\theta'} k^{\theta\theta'} (\theta - \theta_0)(\theta' - \theta'_0) \\
& + \sum_{\theta,\theta',\phi} k^{\theta\theta'\phi} (\theta - \theta_0)(\theta' - \theta'_0) \cos\phi \\
& + \frac{1}{4\pi\epsilon_0} \sum_{i,j} \frac{q_i q_j}{r_{ij}} + \sum_{i,j} \epsilon_{ij} \left[2 \left(\frac{r_{ij}^0}{r_{ij}} \right)^9 - 3 \left(\frac{r_{ij}^0}{r_{ij}} \right)^6 \right]
\end{aligned} \tag{2.1}$$

The two last terms in Equation (2.1) are non-bonded interaction terms, depending on the distances r_{ij} between pairs of atoms that are separated by three or more bonds or belong to different molecules. The r_{ij}^{-9} and r_{ij}^{-6} contributions represent repulsive (excluded volume) and dispersion interactions. The Coulombic contributions, dependent on partial charges q_i on atoms, are an important component of interactions between polar groups. All terms in Equation (2.1) before the last two are valence terms. They depend on bond lengths (b), bond angles (θ), torsion angles (ϕ) or out-of-plane angles (χ) formed by pairs, triplets and quadruplets of atoms bonded together, respectively.

The cross-coupling terms (dependent on more than one b , θ , ϕ or χ) in Equation (2.1) are necessary for the accurate prediction of vibrational frequencies and variations in bonded geometry associated with conformational changes. If these are not of primary interest, simpler expressions can be invoked for \mathcal{V} , wherein the valence part

is represented as a sum of contributions from individual b , θ and ϕ [4,5]. Such simpler force fields may invoke a constant bond length approximation [6,7] or even constrain some bond angles involving lighter atoms (e.g. hydrogens) for computational efficiency [6,8]. Constraining all bond angles is usually not practiced when dynamical properties are of interest; it drastically affects the dynamics without offering significant computational advantage. In lieu of the 9–6 potential expression of Equation (2.1), the Lennard–Jones 12–6 potential is more popular in simpler force fields. The three-parameter Buckingham (exp-6) form has also been used. Parameters (ϵ, r^0) for pairs of unlike atoms are usually estimated from those for pairs of like atoms through a combining rule [3–7], with the Lorentz–Berthelot rule [9] being quite popular because of its simplicity, but not necessarily the most correct physically. Different nonbonded interaction potentials are often used for local interactions (between sites that are three or four bonds apart along the backbone) and non-local ones (between topologically more distant sites) [6–8], as this generally allows a more accurate representation of intramolecular energetics.

United atom (UA) models, wherein quasospherical multiatom groups (e.g. CH_2 , CH_3) are lumped into single interaction sites, have fewer degrees of freedom than fully atomistic models and are therefore less expensive computationally. UA models capable of capturing thermodynamic properties and phase equilibria of alkanes [10,11] and polyethylene [12] have been developed. Anisotropic UA models [13] have been advanced as a physically more meaningful improvement. There has been some concern over the ability of UA force fields to predict diffusivities in polymers. Accumulating experience indicates that it is indeed possible to devise UA and AUA potential representations that yield accurate predictions for both sorption thermodynamics and transport rates, provided the size of penetrant molecules is large in comparison with the mean size of clusters of accessible volume in the polymer (see Section 2.2). For small penetrants (e.g. hydrogen), full atomistic detail is necessary for an accurate prediction of diffusion, as it is important to allow the penetrant to explore all the crevices of accessible volume present in the polymer structure.

Three-dimensional periodic boundary conditions [9,14] are typically used in the simulation

of amorphous polymer matrices. Ideally, the edge length of the simulation box should be significantly larger than (a) the root-mean-square unperturbed radius of gyration of chains, $\langle R_g^2 \rangle^{1/2}$, in order to avoid interactions between different images of the same chain, which may distort long-range conformational statistics and (b) the mean distance between accessible volume clusters, in order to avoid artificial periodicities and percolation effects in the network of sorption sites ‘seen’ by the penetrant. Thin film geometries have been used in cases where interfaces are important, for example, for lipid bilayer membranes exposed to water on both sides [15] and synthetic pervaporation membranes exposed to organic liquid mixtures [16]. In these cases, the macromolecular phase is periodic in two coordinate directions, and periodicity in the third direction is established through the fluid phase. Studies of gas/zeolite/polymer composite interfaces have also been reported which employ strictly two-dimensional periodic boundary conditions, with the model system being bounded in the third direction by repulsive barrier potentials [16].

2.2.2 *Molecular Mechanics*

The easiest way to create atomistic configurations representative of an amorphous polymer glass is to generate local minima of $\mathcal{V}(\mathbf{r}_P)$ at prescribed density through energy minimization with respect to all molecular degrees of freedom [17]. An initial ‘guess’ configuration for the energy minimization can be obtained through bond-by-bond growth of chains in the simulation box. In this growth procedure, the torsional states of successive bonds can be chosen on the basis of a discrete rotational isomeric state model for the polymer [18] or on the basis of a continuous model for local interactions, with modifications to avoid nonlocal intramolecular and intermolecular excluded volume overlaps. This idea for generating initial guess configurations is based on Flory’s random coil hypothesis, which states that conformational statistics in the amorphous bulk are very similar to single-chain statistics under Θ conditions, i.e. dictated only by local intramolecular interactions. Going from the initial guess configuration to a local minimum of $\mathcal{V}(\mathbf{r}_P)$ is best accomplished in a stagewise fashion, wherein one first minimizes an approximation of $\mathcal{V}(\mathbf{r}_P)$ based on purely repulsive nonbonded

interactions and reduced atomic radii, then progressively increases the radii to actual size, and finally introduces the attractive parts of the non-bonded potentials [17]. Alternative schemes have been proposed, wherein one generates the initial guess configuration at reduced density and then undertakes a series of minimizations of the full $\mathcal{V}(\mathbf{r}_P)$ at progressively higher densities, until the desired density level is reached [16]. Still another, newly proposed, scheme involves starting with noninteracting unperturbed chains at the correct density, pre-packing them with a MC simulation designed to reduce local density fluctuations, and then gradually introducing excluded volume interactions [19].

An advantage of energy minimization, or ‘molecular mechanics’ (MM), approaches is their speed. A disadvantage is that they do not directly provide rigorous sampling of a statistical mechanical ensemble. In the procedure proposed in Theodorou and Suter [17], packing constraints near the end of the initial guess generation procedure may enhance sampling of less probable conformational states; although ‘look-ahead’ schemes have been invented to reduce this bias, it may not be effaced at the end of the energy minimization. Alternative techniques of starting with randomly placed unperturbed chains and then introducing excluded volume interactions may lead to distorted chain conformations on short length scales [19]. Nevertheless, MM configurations constitute good initial guesses for more rigorous simulation methods which do sample thermal fluctuations, i.e. MC and MD, and can fully equilibrate polymer models (see MC methods and coarse-graining strategies discussed below in Sections 2.2.4 and 2.2.5, respectively).

2.2.3 *Molecular Dynamics*

Molecular dynamics (MD) tracks the temporal evolution of a microscopic model system by integrating the equations of motion for all microscopic degrees of freedom. Numerical integration algorithms for initial value problems are used for this purpose, and their strengths and weaknesses have been discussed in simulation texts [9,20,21]. MD is readily applicable to a wide range of models, with and without constraints. It has been extended from the original microcanonical ensemble formulation to a variety of statistical mechanical ensembles. It is flexible and

valuable for extracting dynamical information. The Achilles' heel of MD is its high demand of computer time, as a result of which the longest times that can be simulated with MD fall short of the longest relaxation times of most real-life macromolecular systems by several orders of magnitude. This has two important consequences. (a) Equilibrating an atomistic model polymer system with MD alone is problematic; if one starts from an improbable configuration, the simulation will not have the time to depart significantly from that configuration and visit the regions of phase space that contribute most significantly to the properties. (b) Dynamical processes with characteristic times longer than approximately 10^{-7} s cannot be probed directly; the relevant correlation functions do not decay to zero within the simulation time and thus their long-time tails are inaccessible, unless some extrapolation is invoked based on their short-time behavior.

Recently, rigorous multiple time step algorithms have been invented, which can significantly augment the ratio of simulated time to CPU time. Such an algorithm is the reversible Reference System Propagator Algorithm (rRESPA) [22,23]. This algorithm invokes a Trotter factorization of the Liouville operator in the numerical integration of the equations of motion: fast-varying (e.g. bond stretching and bond angle bending) forces are updated with a short time step δt , while slowly varying forces (e.g. nonbonded interactions, which are typically expensive to calculate, are updated with a longer time step Δt . Using $\delta t = 1$ fs and $\Delta t = 5$ ps, one can simulate 300 ns of real time of a polyethylene melt on a modest workstation [24]. This is sufficient for the full relaxation of a system of C_{250} chains, but not of longer-chain systems.

Domain decomposition strategies can significantly augment the length scales addressed by MD simulations on parallel machines [25]. Today, Beowulf clusters with large numbers of inexpensive processors are gaining ground as computational tools in most molecular modeling laboratories. Software packages implementing parallel MD strategies in an efficient way are available, an example being the LAMMPS package [26].

2.2.4 Monte Carlo

The Monte Carlo technique (MC) is a stochastic simulation method designed to generate a long

sequence, or 'Markov chain' of configurations that asymptotically sample the probability density of an equilibrium ensemble of statistical mechanics [9,20]. For example, a MC simulation in the canonical (NVT) ensemble, carried out under the macroscopic constraints of a prescribed number of molecules N , total volume V and temperature T , samples configurations \mathbf{r}_P with probability proportional to $\exp[-\beta\mathcal{V}(\mathbf{r}_P)]$, with $\beta = 1/(k_B T)$, k_B being the Boltzmann constant and T the absolute temperature. Thermodynamic properties are computed as averages over all sampled configurations.

The efficiency of a MC algorithm depends on the elementary moves it employs to go from one configuration to the next in the sequence. An attempted move typically involves changing a small number of degrees of freedom; it is accepted or rejected according to selection criteria designed so that the sequence ultimately conforms to the probability distribution of interest. In addition to usual moves of molecule translation and rotation practiced for small-molecule fluids, special moves have been invented for polymers. The reptation (slithering snake) move for polymer chains involves deleting a terminal segment on one end of the chain and appending a terminal segment on the other end, with the newly created torsion angle being assigned a randomly chosen value [27].

In most MC algorithms the overall probability of transition from some state (configuration) m to some other state n , as dictated by both the attempt and the selection stages of the moves, equals the overall probability of transition from n to m ; this is the principle of detailed balance or 'microscopic reversibility'. The probability of *attempting* a move from state m to state n may or may not be equal to that of attempting the inverse move from state n to state m . These probabilities of attempt are typically unequal in 'bias' MC algorithms, which incorporate information about the system energetics in attempting moves. In bias MC, detailed balance is ensured by appropriate design of the selection criterion, which must remove the bias inherent in the attempt [9,20].

The last twelve years have witnessed a renaissance in the MC simulation of polymers, with the advancement of algorithms that afford vigorous sampling of configuration space and true equilibration of long-chain systems at all length scales. Configurational Bias MC (CBMC) [28,29]

excises a terminal section of a chain and then proceeds to re-grow it, bond-by-bond, in a manner that avoids excluded volume overlaps with surrounding chains. Concerted Rotation MC (CONROT) [30,31] brings about local conformational rearrangements involving the change of seven or eight consecutive torsion angles along a backbone. In End Bridging Monte Carlo (EBMC) [31–33], a chain end ‘attacks’ an interior segment of another chain, separating it into two pieces. One of the pieces is appended to the attacking chain, while the other remains as a separate chain. The EBMC move relies on a geometric construction which respects the atomistic bonded geometry of the chain. It is cast in a semi-grand ensemble formalism which allows full control of the chain length distribution at equilibrium. In Double Bridging (DB) Monte Carlo [31,34], two nearby segments belonging to two different chains attack each other, separating the chains into four pieces. The pieces are then reconnected in a different way, to create two new chains. In a system where all chains are of exactly the same length, the DB move can be designed to preserve monodispersity. Intramolecular versions of EBMC and DB moves can be implemented when the chain repeat unit possesses a center of symmetry. The moves have been extended to nonlinear architectures. They have also been combined with CBMC to enhance the acceptance rate [31].

Connectivity-altering moves (EBMC, DB and their extensions) provide vigorous sampling of the long-range conformational features of chains (end to end-distance, radius of gyration) and are thus extremely efficient in inducing equilibration in long-chain polymer systems. For example, a C₆₀₀₀ polyethylene melt can readily be equilibrated at all length scales [31]; to equilibrate this system with MD, one would need five orders of magnitude more CPU time than is currently available. One might argue that equilibrating the long-length-scale features of an amorphous polymeric system is not really necessary for capturing small molecule sorption and diffusion properties therein, since the latter properties depend on local packing. It has been shown, however, that insufficient equilibration at the length scale of entire chains may introduce serious bias in local, segment-level, packing characteristics. For these local characteristics to assume their equilibrium values, it does not suffice to simulate for a

time commensurate with local segmental relaxation times; rather, full equilibration at the chain level is required [19].

For polymers with complex chemical constitution (e.g. bulky side groups, stiff backbones consisting of anisotropic moieties, highly polar interactions), the potential energy hypersurfaces of atomistic models become extremely rugged. This causes the acceptance rates of the ‘bolder’ MC moves discussed above (CBMC, EBMC, DB and their modifications) to drop, especially at low temperatures. Under these conditions, resorting to a parallel tempering strategy is very useful. Parallel tempering [31,35] considers a large ensemble of independent identical systems, each being equilibrated at a different temperature. The partition function being sampled is the product of the individual partition functions at the different temperatures. In addition to ‘regular’ MC moves, discussed above, there are ‘swapping’ moves, which exchange configurations between two different systems/temperatures. In this way, the vigorous sampling of configurations which takes place at high temperatures is partly transferred to the lower temperatures as well. A prerequisite for the scheme to work is that the energy histograms of systems adjacent in the temperature ladder overlap sufficiently. Parallel tempering can be used in conjunction not only with MC, but also with MD simulations. It can be implemented very advantageously on a parallel cluster. A recent application of parallel tempering in conjunction with constant-pressure simulations employing the EBMC algorithm to equilibrate a united-atom model of *cis*-1,4-polyisoprene at various temperatures is described in Doxastakis *et al.* [35].

2.2.5 Coarse-graining Strategies

As already mentioned, the complex chemical constitution of many polymers used as membrane or barrier materials greatly reduces the efficiency of MC and MD schemes designed for their equilibration. A promising solution to this problem can be based on the development of coarse-grained models for the polymers of interest, i.e. models cast in terms of a much smaller number of degrees of freedom than the fully atomistic representation. To equilibrate an atomistic polymer model, one needs to carry out the following. (a) Derive an effective potential $\mathcal{V}^{\text{eff}}(\mathbf{x}_P)$ for the coarse-grained model, cast in terms of the

coarse-grained degrees of freedom \mathbf{x}_p , from the atomistic potential energy function $\mathcal{V}(\mathbf{r}_p)$; in general, \mathcal{V}^{eff} is temperature- and density-dependent. (b) Equilibrate at the coarse-grained level, i.e. generate a collection of coarse-grained configurations that constitute a good sample of the configuration space spanned by \mathbf{x}_p at the thermodynamic state of interest. (c) ‘Reverse-map’ the sampled coarse-grained configurations back to the atomistic level, i.e. generate one or more \mathbf{r}_p from each \mathbf{x}_p . The benefit from adopting such a multistep strategy is that, with appropriate design of the coarse-grained model, equilibration at all length scales can be achieved in step (b), which may be impossible when using a fully atomistic model. The task of equilibration becomes easier at the coarse-grained level because of the lower dimensionality of \mathbf{x}_p in comparison to \mathbf{r}_p and because $\mathcal{V}^{\text{eff}}(\mathbf{x}_p)$ is generally a much smoother function of its arguments than is $\mathcal{V}(\mathbf{r}_p)$. The new MC moves described in Section 2.4 can be used to great advantage at the coarse-grained level. Reverse mapping will necessarily involve a geometric fitting of \mathbf{r}_p to \mathbf{x}_p , followed by local equilibration at the atomistic level with MD or MC, in order to iron out improbable local configurations generated by the fitting. Step (a) is the most challenging in coarse-graining; it has been implemented with various degrees of empiricism.

The polymer simulation literature contains many examples of coarse-graining. UA models, although seldom derived from more detailed atomistic models, are coarse-grained models. The choice of the coarse-grained representation and the dimensionality of \mathbf{x}_p depends on the physical judgment of the simulator and on the properties he/she wishes to address. The coarse-grained model may be a lattice-based model, for example, the bond fluctuation model in the work of Binder, Suter and collaborators [36,37] or the second-nearest neighbor lattice model applied to a variety of polymers by Mattice and collaborators [38,39]. It may be continuous and very coarse, each interaction site representing 20 or more monomer units, as in the work of Padding and Briels [40] and of Mavrantzas *et al.* [41] on rheological properties, or even an entire polymer chain, as in the work of Murat and Kremer [42] on polymer blends and of Hansen and collaborators on polymer solutions [43]. These coarse-graining approaches have been reviewed [44].

From the point of view of generating amorphous polymer configurations for the prediction of permeation properties, the continuous-space coarse-graining strategy proposed by Kremer and collaborators [45,46] seems most appropriate. Here, chains are represented as sets of spherical coarse-grained interaction sites connected by effective bonds. In their example, each monomer unit in bisphenol A polycarbonate is represented in terms of two coarse-grained interaction sites. Effective bond stretching and bond angle bending potentials are obtained by inverting the probability densities of these coarse-grained variables obtained from sampling atomistically detailed chains. In connection with this type of coarse-grained model, Müller-Plathe and collaborators have proposed an iterative scheme for obtaining nonbonded effective interaction potentials from the pair distribution functions accumulated for coarse-grained sites in the course of atomistic simulations of oligomeric analogues [47]. They have applied this strategy to *trans*-1,4-polyisoprene (see Figure 2.1(a)).

An alternative coarse-graining strategy was proposed by Zacharopoulos *et al.* [48] for polymers consisting of bulky, inflexible groups, such as aromatic polyamides, polyimides, and poly-(amide imides) (see Figure 2.1(b)). Here, each chain is represented as a set of inflexible moieties connected through (virtual) bonds of fixed length. Bond angles are fixed, while torsional potentials are obtained by conformational analysis and MC sampling of single unperturbed chains. The coarse-grained moieties may be anisotropic (this is the case for the phenyl, phthalimide, amide and $\text{C}(\text{CF}_3)_2$ moieties in Figure 2.1(b)). An effective interaction potential for each pair of coarse-grained moieties is calculated atomistically and pretabulated as a function of six degrees of freedom specifying the relative configuration of the moieties.

2.2.6 Generating Glasses from Melts

In the above discussion (Sections 2.2.4 and 2.2.5), it was implicitly assumed that the polymeric material is in thermodynamic equilibrium. This is a good assumption for polymer melts and rubbery polymers (above the glass transition temperature T_g), whose longest relaxation times are usually shorter than the time scales involved in the application of interest. Many important membrane

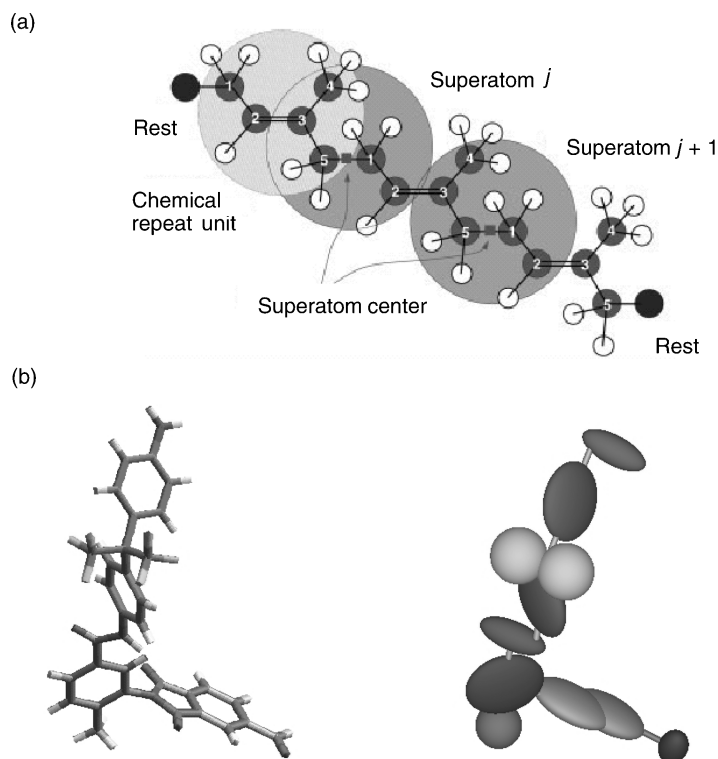


Figure 2.1 Illustration of coarse-grained models employed to enhance the equilibration of amorphous polymers. (a) Coarse-grained model of trans-1,4-polyisoprene proposed by Reith *et al.* [47]. There is one coarse-grained interaction site, or ‘superatom’, per repeat unit. Superatoms are centered at the centers of atomistic bonds connecting successive repeat units. Coarse-graining brings about a 13:1 reduction in the number of degrees of freedom. From D. Reith, M. Puetz and F. Müller-Plathe, *J. Comput. Chem.*, **24**, 1624–1636, Copyright 2003. © John Wiley & Sons, Inc. Reproduced with permission. (b) Coarse-grained model of poly(amide imide) membrane material proposed by Zacharopoulos *et al.* [48]. The repeat unit is shown on the left in an atomistic representation; it consists of H, C, O, N and F atoms shown in various shades of grey. It is represented at the coarse-grained level as a set of rigid phenyl, phthalimide, amide, $C(CF_3)_2$ and methyl moieties, shown on the right-hand side as three individual oblate ellipsoids, two merged oblate ellipsoids, three prolate ellipsoids, two touching spheres and an individual sphere, respectively. The coarse-grained model, which employs constant bond lengths and bond angles, has 7 degrees of freedom per repeat unit, in place of the 192 of the fully atomistic model, respectively

and barrier materials, however, are polymer glasses. Glasses are not in thermodynamic equilibrium; the characteristic times for their volume and enthalpy relaxations are extremely long and temperature-dependent (they are on the order of years at 20 °C below T_g) and their physical properties depend, to a certain extent, on the formation history (e.g. on the rate of cooling, \dot{T} , used to form them from the melt). How should one generate good atomistic models for polymer glasses?

It is frustrating for the polymer modeler that one cannot generate a computer glass whose for-

mation history is both well-defined and realistic. Two approaches have been practiced up until now, often in combination. One involves cooling melt configurations through T_g using MD [49]. This imitates common vitrification experiments in the laboratory. Computer time considerations, however, impose the use of cooling rates of $|\dot{T}| > 10^9 \text{ K s}^{-1}$, which are many orders of magnitude higher than those used in most applications; glasses formed by MD have a well-defined, but not realistic history. Another approach, already discussed in section 2.2.1, involves generating local minima of $\mathcal{V}(\mathbf{r}_p)$ at

prescribed density by MM [17]. This approach is based on the idea that the local configuration of a glass over ordinary time scales is trapped in the vicinity of a local minimum, or of a small set of local minima of $\mathcal{V}(\mathbf{r}_P)$. Multistage energy minimization procedures based on progressively increasing the atomic radii [17] yield model glasses with reasonable properties, which, however, do not correspond to a well-defined formation history. For polymers with complex chemical constitution, vitrification through either MD or MM becomes problematic. Complex, heuristic multistage schemes involving MD cooling, heating and compression [16] have been proposed for the generation of molecular packings at glassy densities.

Generating good model glassy configurations remains a frontier problem in molecular simulations. Based on experience, one can make the following recommendations. (a) Use fully equilibrated and validated melt configurations, sampled at the lowest temperatures where equilibration is possible, as initial configurations. The MC equilibration and coarse-graining strategies discussed in Sections 2.2.4 and 2.2.5 are valuable in this respect. (b) Obtain glassy configurations from the melt configurations through isobaric cooling to the desired T , using MD at the lowest practical $|\dot{T}|$. If this tends to give structures trapped at too low densities, MD annealing under compression will help. (c) Make sure that the final glassy configurations are stable (i.e. show no signs of accelerated structural, volume and enthalpy relaxations) under long isothermal–isobaric MD at the conditions of interest. (d) Generate a large number of glassy configurations. The properties are likely to vary considerably between the frozen-in configurations, and having a representative sample to average over is essential.

2.3 Validating Model Amorphous Polymer Configurations

Before proceeding to use a simulated polymer for the purpose of predicting solubility and diffusivity properties, it is important to validate it against experiment, in order to make sure that the force field we have used is reasonable and the simulation method we have invoked is free of errors. Validation is best carried out over a variety of temperatures and pressures, where experimental data are available. If we are interested in a glassy

polymer, it is important to validate our model in the melt state as well, since validation is more conclusive under conditions of thermodynamic equilibrium and plasticization effects may lead us to the melt state anyway. A brief discussion of property predictions that can be validated follows, with examples from the recent literature.

2.3.1 Thermodynamic Properties

An ability to predict the equation-of-state behavior of the polymer under equilibrium conditions is a prerequisite for the reliable prediction of permeability properties. Early efforts to predict solubilities suffered from the use of inaccurate force fields, which were not validated against density measurements because equilibration methods were not advanced enough.

The mass density, ρ , as calculated from constant temperature and pressure simulations capable of fully equilibrating the polymer model, should be within 1% of experiment. Otherwise, refinement of the force field (especially of the nonbonded interactions) is recommended. Figure 2.2 shows a satisfactory prediction of volumetric behavior for molten polyethylene, afforded by a refined UA force field and the use of DBMC simulations [34]. The characteristic hyperbolic dependence of the specific volume $V = 1/\rho$ on molecular weight is captured very well, as are the thermal expansion coefficient and the isothermal compressibility (not shown).

Another thermodynamic property worth validating against experiment is the cohesive energy,

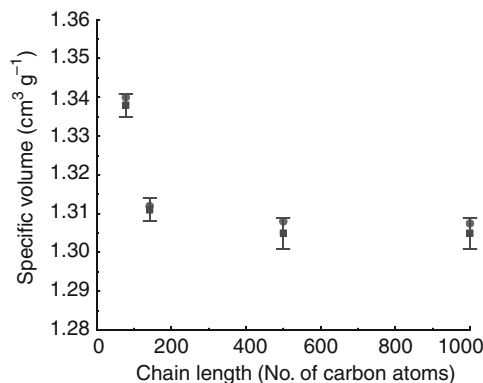


Figure 2.2 Experimental (circles) and simulated (squares) specific volumes for a series of monodisperse polyethylene melts at 450 K and 1 atm [34]

E_{coh} , or the solubility parameter $\delta = (E_{\text{coh}}/V)^{1/2}$. Here, E_{coh} is defined as the energy that keeps the chains together in the bulk polymer per unit mass of polymer, while δ is accessible experimentally through swelling of lightly cross-linked samples in different solvents [50]. E_{coh} can readily be calculated from the ensemble average of the difference in energy between the individual chains constituting a model configuration of the amorphous polymer and the model configuration itself [17].

2.3.2 Molecular Packing

A quantitative description of molecular packing in simulated polymers is given by the pair distribution functions, $g^{\alpha\beta}(r)$, for all pairs of sites (α, β) in the system. These can conveniently be partitioned into their inter- and intramolecular parts [51]. Experimentally, packing is probed from X-ray, neutron or electron diffraction measurements. The diffracted intensity at wavevector \mathbf{q} , $I(\mathbf{q})$, can readily be calculated though essentially a Fourier transformation of the quantities $g^{\alpha\beta}(r) - 1$. For an amorphous, unoriented material, $I(\mathbf{q})$ depends only on the modulus $|\mathbf{q}| = q$. Instead of $I(q)$, one may examine the static structure factor, $S(q)$; this equals $I(q)$ divided by what it would be in the hypothetical case where all scatterers present in the material formed a structureless ideal gas. Denoting by N_α the number of atoms of type α present in a volume V of the material and by $f^\alpha(q)$ their atomic structure factor, $S(q)$ is obtained as follows:

$$S(q) = 1 + \frac{\left\langle \frac{1}{V} \right\rangle}{\sum_{\alpha} \sum_{\beta} N_{\alpha} N_{\beta} f^{\alpha}(q) f^{\beta}(q) \int [g^{\alpha\beta}(r) - 1] e^{-i\mathbf{q}\cdot\mathbf{r}} d\mathbf{r}} \times \frac{\sum_{\alpha} N_{\alpha} [f^{\alpha}(q)]^2}{\sum_{\alpha} N_{\alpha} [f^{\alpha}(q)]^2} \quad (2.2)$$

Here and in the following, angular brackets denote ensemble averages.

Figure 2.3 [51] presents an example comparison of structure factors against X-ray diffraction data for isotactic and syndiotactic polypropylene melts at 450 K and 1 atm. The first diffraction peak at low q reflects intermolecular correlations in the bulk, while the rest are primarily intramo-

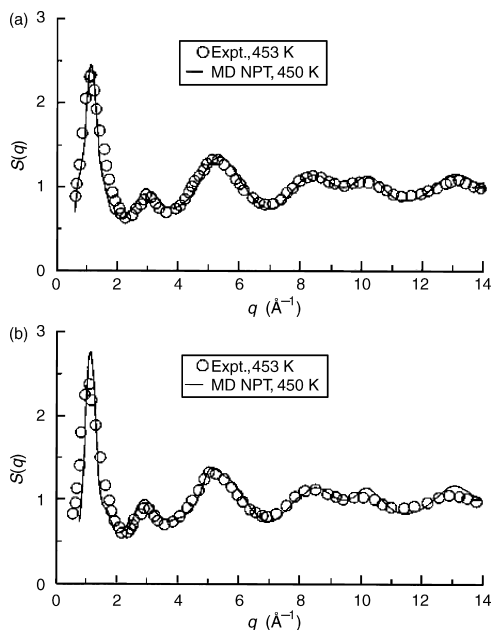


Figure 2.3 Experimental (points) and simulated (lines) X-ray structure factors from isotactic (a) and syndiotactic (b) polypropylene melts at 1 atm and 450 K [51]. Reprinted with permission from S. J. Antoniadis, C. T. Samara and D. N. Theodorou, *Macromolecules*, **32**, 8635–8644 (1999). Copyright (1999) American Chemical Society

lecular. The structure factors are very similar between the two different tacticities; the calculation predicts a somewhat sharper intermolecular peak for the syndiotactic polymer, whose chains are considerably stiffer. The mass density is also quite insensitive to tacticity, but the segmental dynamics are significantly faster in the isotactic melt, due to the different conformational free energy profile experienced by torsion angles in the two tacticities [51].

Neutron diffraction from isotopically substituted chains (e.g. deuterated chains dispersed at low concentration within a hydrogenous matrix of the same polymer [52]) is valuable as a means of measuring chain dimensions in the bulk. The single-chain structure factor can readily be computed from simulation by Fourier transformation of the intramolecular pair density functions, in a manner analogous to Equation (2.2) [53]. Related measures of conformational stiffness that are often compared between simulation and experiment include the characteristic ratio,

the persistence length and the Kuhn length [18,54]. These comparisons are a stringent test for the ability of the simulation to equilibrate the long-range conformational characteristics of chains [12,35,53].

2.3.3 Segmental Dynamics

The comparison of experimental data and simulation predictions for polymer dynamics has been very fertile in recent years. Experiments and molecular dynamics simulations can now access similar time scales; the former are valuable in validating the models used in the latter, while the latter are valuable in interpreting the former.

Molecular motion in amorphous polymers is characterized by very broad and strongly temperature-dependent spectra of characteristic times, which are dependent upon the length scale of examination. It is useful to distinguish between dynamics at the length scale of segments and dynamics at the level of entire chains. Chain dynamics govern chain self-diffusivity, melt viscosity and viscoelastic properties (e.g. stress relaxation modulus, storage and loss moduli) in the terminal region [55]. More relevant to small molecule diffusion in polymers are segmental dynamics, which are also intimately related to the glass transition and to mechanical toughness in the solid state.

How to analyze the results of MD simulations of bulk polymers and compare against experimental measurements of segmental dynamics has been reviewed [56]. Here, we will confine ourselves to a brief discussion and presentation of some examples.

NMR relaxation and solid-state NMR measurements probe the reorientational motion of specific bonds along the chains. In the case of a C–H bond vector, this can be quantified through the second-order orientational autocorrelation function:

$$P_2^{\text{CH}}(t) = \frac{1}{2} \left\{ 3 \left\langle \left[\frac{\mathbf{r}_{\text{CH}}(t) \cdot \mathbf{r}_{\text{CH}}(0)}{r_{\text{CH}}(t)r_{\text{CH}}(0)} \right]^2 \right\rangle - 1 \right\} \quad (2.3)$$

where $\mathbf{r}_{\text{CH}}(t)$ is the bond vector under examination at time t and $r_{\text{CH}}(t) = |\mathbf{r}_{\text{CH}}(t)|$ is its length;

$P_2^{\text{CH}}(t)$ decays from 1 at $t=0$ to 0 at long times. A correlation time for the reorientational motion is defined as follows:

$$\tau_c = \int_0^{\infty} P_2^{\text{CH}}(t) dt \quad (2.4)$$

In melts of flexible chains, $P_2^{\text{CH}}(t)$ exhibits a fast, practically exponential decay at short times (up to $t \approx 1$ ps), which is attributable to bond and bond angle vibrations and librations of torsion angles within the wells of conformational states, followed by a slower decay, which is shaped mainly by torsional transitions between energy wells. The latter decay is usually fitted by an empirical stretched exponential (Kohlrausch–Williams–Watts, or KWW) function with characteristic time τ_{KWW} and stretching exponent $\beta < 1$. The more cooperative the motion involved is, then the lower the value of β . Thus, $P_2^{\text{CH}}(t)$ is often fitted successfully by [57]:

$$P_2^{\text{CH}}(t) = \alpha \exp\left(-\frac{t}{\tau_0}\right) + (1 - \alpha) \exp\left[-\left(\frac{t}{\tau_{\text{KWW}}}\right)^\beta\right] \quad (2.5)$$

For the modified KWW expression of Equation (2.5), the correlation time τ_c defined by Equation (2.4) is expressed as follows (Γ here is the gamma function):

$$\tau_c = \alpha \tau_0 + (1 - \alpha) \frac{\Gamma(1/\beta)}{\beta} \tau_{\text{KWW}} \quad (2.6)$$

The characteristic time τ_{KWW} and the correlation time τ_c display strong, pronouncedly non-Arrhenius dependences on temperature, which are usually correlated with Williams–Landel–Ferry (WLF) or Vogel–Fulcher–Tammann (VFT) expressions [58].

An observable of ^{13}C NMR relaxation measurements is the spin-lattice relaxation time T_1 . This can be obtained from $P_2^{\text{CH}}(t)$ through the following:

$$\frac{1}{nT_1} = \frac{\hbar^2 \gamma_{\text{C}}^2 \gamma_{\text{H}}^2}{10r_{\text{CH}}^6} [J(\omega_{\text{H}} - \omega_{\text{C}}) + 3J(\omega_{\text{C}}) + 6J(\omega_{\text{H}} + \omega_{\text{C}})] \quad (2.7)$$

In Equation (2.7), n is the number of bonded hydrogens per carbon atom, $\hbar = h/(2\pi)$, with h being Planck's constant, and γ_C , ω_C and γ_H , ω_H are the gyromagnetic ratios and Larmor angular velocities of ^{13}C and ^1H nuclei, respectively ($\omega_H = (\gamma_H/\gamma_C) \omega_C \approx 3.977 \omega_C$). The spectral density function $J(\omega)$ is the Fourier transform of $P_2^{\text{CH}}(t)$:

$$J(\omega) = \frac{1}{2} \int_{-\infty}^{+\infty} P_2^{\text{CH}}(t) e^{-i\omega t} dt \quad (2.8)$$

Figure 2.4 displays the orientational correlation time τ_c for pendant bonds in a melt of atactic polypropylene as a function of time [6]. At low temperatures, $P_2^{\text{CH}}(t)$ does not decay to zero within the MD simulation time; τ_c was determined by fitting the long-time decay of $P_2^{\text{CH}}(t)$ with a KWW function and then using Equation (2.4). The temperature-dependence of the correlation time is seen to be strongly non-Arrhenius (nonlinear in the coordinates of Figure 2.4). One may attempt an estimation of T_g as the temperature at which τ_c becomes approximately 1 min. The resulting estimate is very close to the experimental glass transition temperature of atactic polypropylene, which is around 255 K.

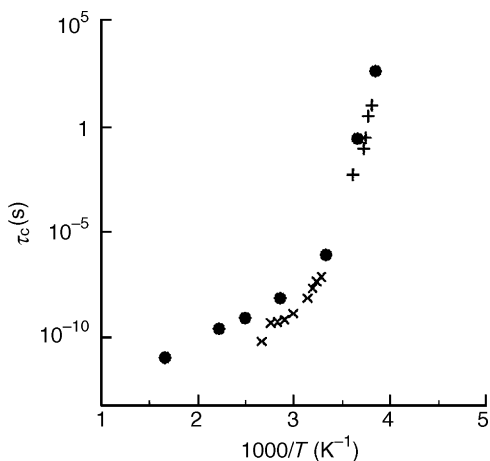


Figure 2.4 Correlation times τ_c for the reorientational motion of pendant bonds in atactic polypropylene, as determined from MD simulations at various temperatures (O), and as measured experimentally by NMR relaxation (x) and solid-state NMR (+) techniques [6]

The simulated correlation times are in reasonable, but not perfect agreement with NMR values. Deviations are attributable to the force field used in the simulation. Further MD [51] and NMR investigations of isotactic and syndiotactic polypropylene have been instrumental in clarifying the effect of tacticity on the dynamics of this polymer.

Figure 2.5 shows spin-lattice relaxation times for C–H bonds emanating from the sp^2 carbons of *cis*-1,4-polyisoprene, as determined from NMR relaxation experiments at different frequencies and from fully atomistic MD simulations [57]. Agreement is very satisfactory. The simulation gives somewhat smaller T_1 values (slower dynamics) than experiment.

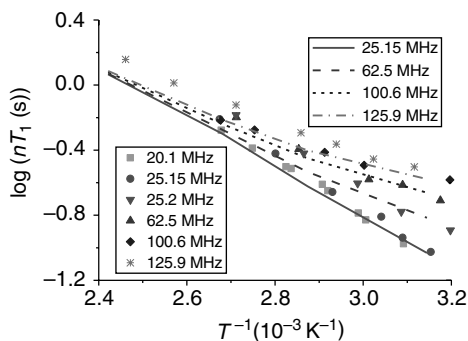


Figure 2.5 Spin lattice relaxation times T_1 for the $=\text{C}-\text{H}$ vector of *cis*-1,4-polyisoprene (PI) as measured experimentally and as predicted from MD simulation after fitting the data with a modified KWW model [57]. Points are data from the literature on various PI samples, while lines are predicted values from simulations at the same frequencies

A more complete characterization of segmental dynamics is provided by quasielastic neutron scattering (QENS), which can probe motion at different length scales through the dependence of its observables on the wavevector \mathbf{q} . Incoherent QENS is sensitive to the motion of individual hydrogens in a polymer sample, since ^1H has a much higher incoherent scattering cross-section to neutrons than other elements commonly encountered in polymer matrices.

A usual observable of incoherent QENS is essentially the spatial and temporal Fourier transform of the self-part of the van Hove correlation

function for hydrogen atoms, $G_s(\mathbf{r}, t)$. The latter is defined as follows:

$$G_s(\mathbf{r}, t) = \frac{1}{N} \left\langle \sum_{j=1}^N \delta[\mathbf{r} + \mathbf{r}_j(0) - \mathbf{r}_j(t)] \right\rangle \quad (2.9)$$

where N is the total number of scattering particles (hydrogen atoms) in the sample and $\mathbf{r}_j(t)$ denotes the position of particle j at time t . $G_s(\mathbf{r}, t)$ is essentially a probability density that a particle has moved by \mathbf{r} within time t .

The intermediate incoherent scattering function $I(\mathbf{q}, t)$ is the spatial Fourier transform of $G_s(\mathbf{r}, t)$:

$$\begin{aligned} I(\mathbf{q}, t) &= \int G_s(\mathbf{r}, t) e^{-i\mathbf{q} \cdot \mathbf{r}} d\mathbf{r} \\ &= \frac{1}{N} \sum_{j=1}^N \exp \langle -i\mathbf{q} \cdot [\mathbf{r}_j(t) - \mathbf{r}_j(0)] \rangle \quad (2.10) \end{aligned}$$

The time evolution of $I(\mathbf{q}, t)$ reveals how individual particles lose memory of their original position through motions occurring on a length scale $2\pi/|\mathbf{q}|$. A correlation time for this motion can be defined in a manner entirely analogous to equation (4) as follows:

$$\tau_c(\mathbf{q}) = \int_0^{\infty} I(\mathbf{q}, t) dt \quad (2.11)$$

Often, the time decay of $I(\mathbf{q}, t)$ can be fitted by a fast exponential decay at short times, reflecting vibrational and librational motion, plus a KWW function at longer times, reflecting more cooperative motion associated with conformational isomerization (see Equation (2.5)).

Incoherent QENS measures the incoherent dynamic structure factor $S(\mathbf{q}, \omega)$, which is the Fourier transform of $I(\mathbf{q}, t)$ with respect to time. In practice, $I(\mathbf{q}, t)$ has to be multiplied by an instrumental resolution function and then Fourier transformed to predict the observed $S(\mathbf{q}, \omega)$ [59].

Figure 2.6 displays correlation times of the intermediate scattering function (Equation (2.10)) for a melt of *cis*-1,4-polyisoprene, as extracted from QENS experiments and from MD simulation [57]. The agreement is good, but not perfect: Segmental dynamics is slower in the simulation, an observation already made in connection with the NMR observables of Figure 2.5. Note the

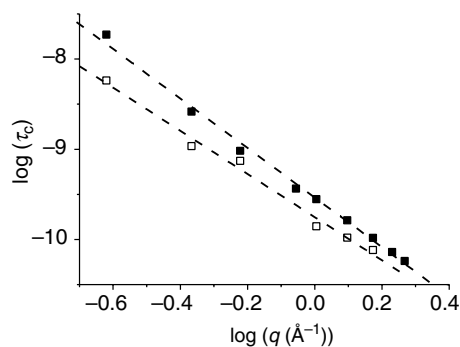


Figure 2.6 Correlation times, in seconds, from incoherent QENS experiments on *cis*-1,4-polyisoprene at 320 K and 1 atm (\square , - - -) and corresponding predictions from MD simulations at 318 K and 1 atm (\blacksquare , - - -) [57]. Reprinted with permission from M. Doxastakis, D. N. Theodorou, G. Fytas, F. Kremer, R. Faller, F. Müller-Plathe and N. Hadjichristidis, *Journal of Chemical Physics*, **119**, 6883 (2003). Copyright 2003, American Institute of Physics

q -dependence of the correlation times: the lower the value of q , then the longer the length scale of observation, and the longer the correlation time for segmental motion. This dependence has been described by the power law $\tau_c \sim q^{-2.8}$ in the experiment; MD simulation predictions are consistent with this dependence.

The observables of many other relaxation experiments can be computed from MD trajectories and used to validate the simulation from the point of view of its ability to predict segmental dynamics. An example is dielectric relaxation spectra, which can be predicted from the autocorrelation function of the polarization vector of the model system [57].

2.3.4 Accessible Volume and its Distribution

The magnitude, spatial distribution, connectivity and mobility of accessible volume within a polymer matrix are of paramount importance to sorption and diffusion phenomena, as the widespread use of free volume theories [60] attests. Atomistic simulations allow a detailed investigation of these geometric characteristics. The associated methodology has been reviewed [14], and so only a brief outline will be given here. To start the analysis, one assigns hard-sphere radii (usually taken equal to the van der Waals radii) r_i^0 to

each atom i in the polymer matrix and r_A^0 to each penetrant species A of interest.

The *unoccupied volume* is the volume of the three-dimensional domain consisting of points within a configuration which lie outside the van der Waals spheres of all polymer atoms. It can be calculated analytically [61] or by Monte Carlo integration. The fractional unoccupied volume (ratio of the unoccupied volume to the total polymer volume) is usually 0.30 to 0.35 for flexible amorphous polymers. Values up to 0.47 have been reported for stiff-chain, ultra-high-free-volume polymers, such as poly[1-(trimethyl silyl)-1-propyne] (PTMSP) [62].

The *accessible volume* for a given penetrant molecule is the volume of the domain composed of points that can be occupied by the center of mass of the penetrant without any overlap between the van der Waals spheres of the penetrant and those of the polymer atoms. For a spherical penetrant, accessible volume is most easily obtained by augmenting the radii of all polymer atoms by r_A^0 and calculating the unoccupied volume of the resulting medium [14,63]. This procedure has been extended to multisite, articulated molecules [64], where the analytical techniques allow a fast calculation of the small amount of accessible volume present for the center of mass. For a given matrix and a range of spherical probe molecules of progressively increasing r_A^0 , the accessible volume falls quasiexponentially with increasing r_A^0 [14,63].

For most polymer-penetrant pairs of practical interest, the accessible volume in any configuration is partitioned into disjoint *clusters*. The most rigorous way of identifying these clusters is to subject the set of atomic centers comprising the polymer matrix to Delaunay tessellation, and then apply a clustering algorithm on the resulting Delaunay tetrahedra [14,63,65]. Simpler ways of identifying accessible volume regions involve passing a fine cubic grid through the configuration and identifying accessible voxels in that grid [62,66]. The visualization of accessible volume clusters and the accumulation of their size distribution and shape characteristics provides valuable information on diffusion pathways for specific polymer-penetrant systems [62,63].

In recent years there has been growing interest in the experimental exploration of accessible volume in polymers with the technique of Positron

Annihilation Lifetime Spectroscopy (PALS). In PALS, spin-aligned positron-electron pairs are generated in the polymer. Each such pair, or quasi-atom, is termed an ortho-positronium (o-Ps) and lives for a few nanoseconds before the positron and electron annihilate each other. The lifetime of the 3S_1 state of o-Ps depends sensitively on the local electronic environment. The lower the electronic density around the o-Ps, then the longer its lifetime. Thus, the measured distribution (spectrum) of lifetimes, τ_3 , provides information on the free volume distribution in the polymer. Comparative studies of lifetimes and intensities from PALS have provided valuable qualitative or semiquantitative evidence on changes in the internal structure of polymeric and nanocomposite materials resulting from changes in chemical constitution, physical ageing or mechanical deformation [67].

Converting measured lifetimes τ_3 to volumes of accessible clusters for comparison with simulation results has presented some problems. Most work up to now has been based on the 'standard model' [68,69], which postulates [70] the following: (a) the o-Ps atom is a single point particle; (b) the 'holes' it encounters in the polymer are spheres of radius R_0 , which are bounded by hard walls; (c) the matrix electrons form a layer of homogeneous density ρ_0 and thickness $\Delta R = R_0 - R$ on the wall of the hole; (d) the temperature is low, so that o-Ps is in its ground state with respect to internal as well as translational degrees of freedom. These postulates constitute drastic simplifications. For example, past simulation work has shown that accessible volume clusters have irregular shapes and appreciable asphericity [63,70]. According to the standard model, the relation between lifetime τ_3 and hole size R or R_0 is as follows:

$$\frac{1}{\tau_3} = \pi r_c^2 c \rho_0 \left(\frac{\Delta R}{R + \Delta R} + \frac{1}{2\pi} \sin \frac{2\pi R}{R + \Delta R} \right) \quad (2.12)$$

where $r_c = 2.92 \times 10^{-15}$ m is the classical electron radius and c is the speed of light. In practice, $\pi r_c^2 c \rho_0$ is set equal to 2 ns^{-1} and ΔR is attributed the value of 0.1656 nm, based on fitting to experimental values from solid materials with precisely known hole sizes.

Using the standard model, Equation (2.12), a distribution of PALS lifetimes is transformed into a distribution of hole radii. Confronting these distributions with cluster size distributions from atomistic modeling has led to good qualitative agreement as far as comparisons between different polymers are concerned [62,71]. Quantitative agreement is not very satisfactory, however, as might be expected in view of the several assumptions involved in interpreting PALS data. In order to compute the volume ‘seen’ by o-Ps from the simulations, o-Ps is typically assigned an r_A^0 value of 1.1 to 1.3 Å, by analogy to a hydrogen atom [62,63,71]. Hofmann *et al.* [62] have suggested that large, nonconvex clusters of accessible volume are seen as several smaller clusters

of simpler shape by the o-Ps; the same investigators have proposed a method of geometric analysis for the identification of the simpler, smaller clusters (R_{\max} approach). Furthermore, they have introduced an empirical ‘surface correction’ to account for the size of the probe molecule. With this methodology, these workers have performed extensive comparisons of simulation predictions against PALS data for a number of stiff-chain membrane materials.

Figure 2.7 shows such a comparison for three of these materials [62]: poly[1-(trimethylsilyl)-1-propyne] (PTMSP), Teflon AF1600, a copolymer consisting of 65 mol% 2,2-bis(trifluoromethyl)-4,5-difluoro-1,3-dioxole (BDD) and 35 mol% tetrafluoroethylene (TFE), and Teflon AF2400, a

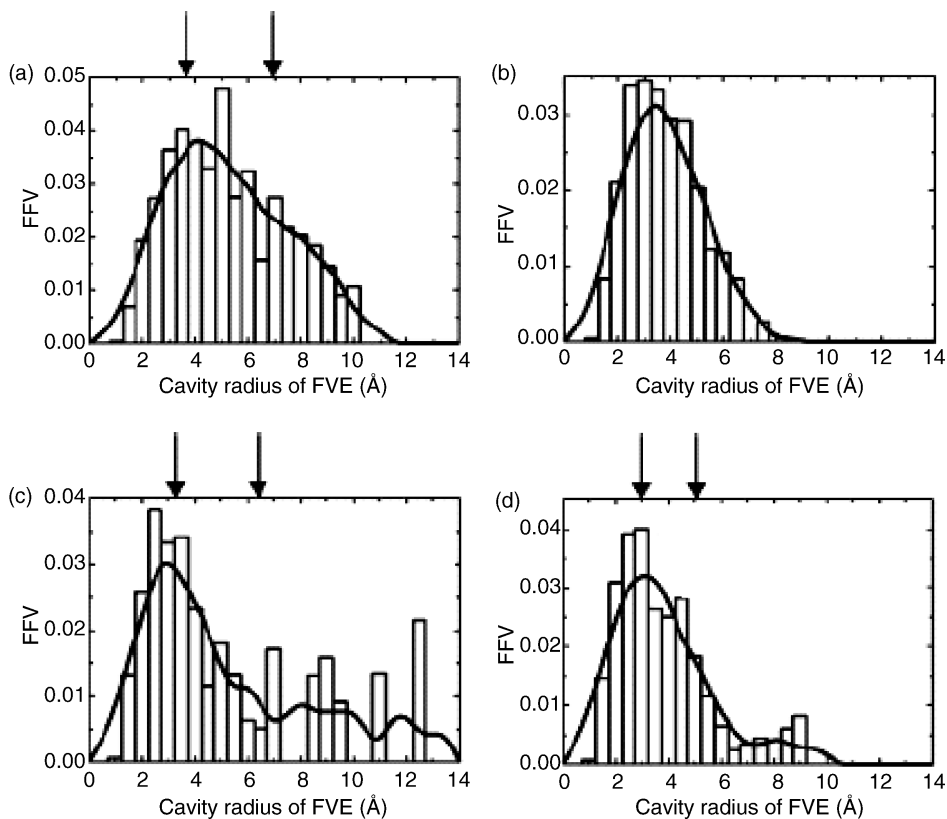


Figure 2.7 Distribution of radii of accessible volume clusters to o-Ps (‘free volume elements’ (FVEs)) in (a) PTMSP, (b) aged PTMSP of density 0.95 g cm⁻³, (c) Teflon AF2400 and (d) Teflon AF1600, as computed from atomistic modeling (R_{\max} approach [62], histograms and continuous curves (5 point smoothing)) and as determined experimentally (arrows). The chemical structures of the polymers are described in Hofmann *et al.* [62]. Reprinted with permission from D. Hofmann, M. Entrialgo-Castano, A. Lerbet, M. Heuchel and Y. Yampolskii, *Macromolecules*, **36**, 8528–8538 (2003). Copyright (2003) American Chemical Society

copolymer consisting of 87 mol% BDD and 35 mol% TFE. Also included is a simulation result for an aged PTMSP (PTMSP-095), generated at a mass density of 0.95 g cm^{-3} , which is significantly higher than the values ($0.7\text{--}0.8 \text{ g cm}^{-3}$) observed for the unaged polymer. Atomistic simulation results from the R_{max} approach with surface corrections are shown as histograms. The continuous curves are a smoothed rendition of the simulation results, while the arrows display average peak positions from the interpretation of PALS data with the standard model. Agreement is seen to be good. The data support the existence of a bimodal distribution of accessible volume clusters for ultrahigh-free-volume, high-permeability polymers, such as PTMSP and Teflon AF2400. One mode of the distribution, with a maximum at around $3\text{--}4 \text{ \AA}$, is comparable to the distributions encountered in dense glassy, low-permeability polymers. The other originates in large holes ($6\text{--}8 \text{ \AA}$ radius), which can be detected visually in the packing models. Ageing is seen to shift the distribution to smaller sizes and eliminate the bimodality.

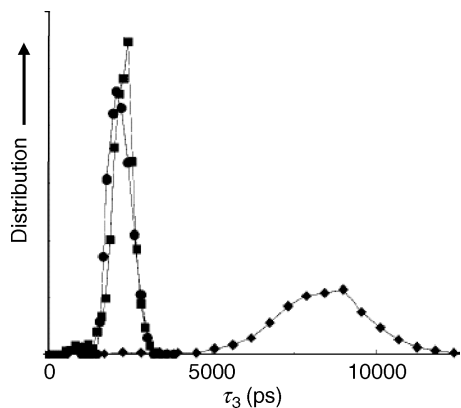


Figure 2.8 Experimental positronium lifetime spectrum in polystyrene at 300 K (●), along with two predictions based on atomistic simulations of the polymer, obtained through the quantum mechanical method of Schmitz and Müller-Plathe [70]. The first prediction (◆) is based on an original set of parameters for the electron density contributed by each carbon and hydrogen atom in the polymer. In the second prediction (■), the range of these electron densities has been increased by 40% for both atomic species. Reprinted with permission from Heiko Schmitz and Florian Müller-Plathe, *Journal of Chemical Physics*, **112**, 1040 (2000). Copyright 2000, American Institute of Physics

Schmitz and Müller-Plathe [70] have proposed a method for predicting the PALS spectrum by analyzing atomistic model polymer configurations. The positronium lifetime in the accessible volume sites is calculated at finite temperature with a path integral Monte Carlo method, using a realistic model for the potential energy felt by the positronium and for the electron density of the polymer. This model is free of the simplifying assumptions invoked by the standard model. There is some uncertainty in the parameters invoked, especially for the representation of the electron density of the polymer. Figure 2.8 shows an experimental positronium lifetime spectrum in polystyrene at 300 K (circles), along with two predictions: one based on original estimates of the electron density parameters (diamonds) and a second one obtained after adjustment of the parameters by 40% (squares). The second prediction is clearly in good agreement with the experimental spectrum.

2.4 Prediction of Sorption Equilibria

2.4.1 Sorption Thermodynamics

The physico-chemical properties that determine whether a polymer is appropriate as a membrane or barrier material are the solubility S and the diffusivity D for each of the components of a fluid mixture. The permeability, $\mathcal{P} = DS$, of a particular species must be as high as possible in membrane applications and as low as possible in barrier material applications. The permselectivity, $a_{A/B} = \mathcal{P}_A/\mathcal{P}_B$, for a binary mixture of components A and B must be significantly different from unity to facilitate their membrane separation. We now focus on how to predict solubilities and diffusivities in amorphous polymers, using atomistic models generated and validated as described in Sections 2.2 and 2.3. We will first turn to the prediction of solubilities, or, more generally, sorption equilibria.

Consider a mixture of c components indexed $1, 2, \dots, c$. In this formulation, component 1 will be the polymer, P, while components $2, 3, \dots$ will be the small-molecule species A, B, \dots , whose permeation properties are of interest. We consider sorption equilibria between a fluid phase, consisting mainly of components $2, \dots, c$, and a polymer phase containing all

components. The fugacity of component i is denoted by f_i . The number of molecules, mole fraction and molecular weight of component i in the polymer phase are denoted by N_i , x_i and M_i , respectively. We will use the symbol ρ_{molec} to denote the *molecular* density (total number of molecules of all species per unit volume) in the polymer phase and N_{Avo} to denote the Avogadro constant.

At a given temperature, a full description of the sorption thermodynamics is provided by the sorption isotherms. The sorption isotherm of i is a functional relationship between the molar ($\rho_{\text{molec}} x_i / N_{\text{Avo}}$) or mass ($\rho_{\text{molec}} x_i / (N_{\text{Avo}} M_i)$) density of i in the polymer phase and its fugacity f_i .

A statistical mechanical derivation of isotherms from molecular-level information can be performed in the framework of the constant-pressure Gibbs ensemble [72]. In this ensemble, the polymer and fluid phases are considered together at equilibrium; the temperature T , pressure P and total number of molecules of each component in both phases are fixed. If the polymer can be considered as completely involatile or insoluble, and therefore absent from the fluid phase, it is more convenient to consider the polymer phase alone in the $N_1 f_2 f_3 \dots f_c PT$ ensemble. In this ensemble, the total amount of polymer N_1 , the fugacities of all small-molecule species f_i ($2 \leq i \leq c$), the temperature T and the pressure P are fixed. Note that only c of the quantities $f_2, f_3, \dots, f_c, P, T$ are independent: If the fluid phase is pure, its fugacity can be obtained from P and T using an equation of state. Similarly, in a multicomponent fluid phase, f_2, f_3, \dots, f_c can be obtained from P, T and $(c - 2)$ mole fractions specifying the composition of the polymer-free fluid phase. A probability density for the $N_1 f_2 f_3 \dots f_c PT$ ensemble has been derived [14]. The mean numbers of molecules $\langle N_i \rangle_{N_1 f_2 \dots f_c PT}$ ($i = 2, \dots, c$) and the volume $\langle V \rangle_{N_1 f_2 \dots f_c PT}$ of the polymer phase, and hence the molar densities of the penetrant species and the swelling of the polymer as a result of sorption, are readily obtained as ensemble averages with respect to this probability density.

An alternative strategy for predicting isotherms is to consider the polymer phase under given temperature, pressure and composition (isothermal–isobaric or $N_1 N_2 N_3 \dots N_c PT$ ensemble) and estimate the fugacities f_i ($2 \leq i \leq c$) through the

excess chemical potentials, μ_i^{ex} :

$$\begin{aligned} \mu_i^{\text{ex}}(\rho_{\text{molec}}, x_2, x_3, \dots, x_c, T) \\ = \mu_i(\rho_{\text{molec}}, x_2, x_3, \dots, x_c, T) \\ - \mu_{i,\text{pure}}^{\text{ig}}(\rho_{\text{molec}} x_i, T) \quad (2 \leq i \leq c) \end{aligned} \quad (2.13)$$

The excess chemical potential of species i in the polymer phase is defined as the chemical potential minus the chemical potential that species i would have as a pure ideal gas at the same temperature and molecular density: μ_i^{ex} is related to the fugacity f_i through the relation:

$$\mu_i^{\text{ex}} = RT \ln \left(\frac{\beta f_i}{\rho_{\text{molec}} x_i} \right) \quad (2.14)$$

where $\beta = 1/(k_B T)$ and $k_B = R/N_{\text{Avo}}$ is the Boltzmann constant.

In the isothermal–isobaric ensemble, μ_i^{ex} can be obtained by the Widom test particle insertion method [9,14], from the intermolecular interaction energy ‘felt’ by a molecule of type i inserted randomly in the polymer phase:

$$\begin{aligned} \exp \left(-\frac{\mu_i^{\text{ex}}}{RT} \right) \\ = \frac{\int_0^\infty dV \exp(-\beta PV) \int \exp\{-\beta[V(\mathbf{r}) + \mathcal{V}_{\text{test}}(\mathbf{r}, \mathbf{r}_{\text{test}})]\} d\mathbf{r} d\mathbf{r}_{\text{test}}}{\int_0^\infty dV \exp(-\beta PV) \int \exp\{-\beta[V(\mathbf{r})]\} d\mathbf{r} \int \exp[-\beta \mathcal{V}_{\text{test}}^{\text{intra}}(\mathbf{r}_{\text{test}})] d\mathbf{r}_{\text{test}}} \\ \equiv \langle \exp\{-\beta[\mathcal{V}_{\text{test}}(\mathbf{r}, \mathbf{r}_{\text{test}}) - \mathcal{V}_{\text{test}}^{\text{intra}}(\mathbf{r}_{\text{test}})]\} \rangle_{\text{Widom}} \end{aligned} \quad (2.15)$$

In Equation (2.15), \mathbf{r} stands for a molecular configuration of the polymer phase (polymer plus penetrant molecules) under consideration, and $\mathcal{V}(\mathbf{r})$ is the total potential energy of this configuration. The symbol \mathbf{r}_{test} stands for the degrees of freedom of an additional molecule of type i which is inserted in the polymer phase.

$\mathcal{V}_{\text{test}}(\mathbf{r}, \mathbf{r}_{\text{test}})$ is the change in potential energy brought about by the insertion of the additional ‘test’ molecule of type i . The numerator of the right-hand side on the second line of Equation (2.15) is the isothermal–isobaric partition function of the considered polymer phase plus the ‘test’ molecule. The denominator can be viewed as an isothermal–isobaric partition function of a system consisting of the polymer phase plus the test molecule in a hypothetical ‘ghost’ or ideal gas state, wherein the test molecule is capable

of moving anywhere in the volume of the polymer phase, subject only to its intramolecular energy.

The third line of Equation (2.15) re-expresses $\exp[-\mu_i^{\text{ex}}/(RT)]$ as an ensemble average. The averaged quantity is the Boltzmann factor of the intermolecular energy of interaction felt by the test molecule inserted in the polymer phase due to its interactions with the polymer and the other penetrant molecules. The average is taken over all configurations of the polymer phase, weighted according to the probability density of the isothermal–isobaric ensemble, over all internal configurations of the test molecule, weighted according to the Boltzmann factor of its intramolecular energy, and over all positions of insertion of the test molecule within the current volume of the polymer phase. Although the position of insertion is chosen randomly within every configuration of the polymer phase, test molecule conformations conform to the distribution one would see in an ideal gas of component i . In the notation adopted in Equation (2.15), this is assumed to be part of the Widom averaging. Alternative expressions assuming random sampling of the internal configurations have been developed [7,73].

Following Petropoulos [74], we define the solubility S_i of component i ($2 \leq i \leq c$) in the polymer phase as the slope of the line connecting the origin to a point $(f_i, \rho_{\text{molec}}x_i/N_{\text{Avo}})$ on the isotherm. Thus, we can obtain the solubility of a gaseous penetrant in the commonly used units of $\text{cm}^3(\text{STP})/(\text{cm}^3 \text{ polymer atm})$ as:

$$S_i = \frac{22400 \text{ cm}^3(\text{STP})}{\text{mol}} \frac{\rho_{\text{molec}}x_i}{N_{\text{Avo}}f_i} \quad (2.16)$$

Combination of Equations (2.14) and (2.16) leads to the following:

$$S_i = \frac{22400 \text{ cm}^3(\text{STP})}{\text{mol}} \frac{1}{RT} \exp\left(-\frac{\mu_i^{\text{ex}}}{RT}\right) \quad (2.17)$$

From Equations (2.15) and (2.17) it is clear that the solubility, and therefore the sorption isotherm, can be computed by Widom insertion from simulations of the polymer phase at constant composition. As noted above, if one follows this route, one must make sure that the $(c-1)$ computed

fugacities are consistent with the total pressure P on the polymer phase.

In the limit of very low pressures, the sorption thermodynamics is described completely by the Henry's law constant, defined as:

$$H_i = \lim_{x_i \rightarrow 0} \frac{f_i}{x_i} \quad (2.18)$$

From Equations (2.14) and (2.18), the Henry's law constant can be expressed in terms of the excess chemical potential at infinite dilution, obtainable through Widom insertions of a molecule of component i in an i -free polymer phase:

$$H_i = \rho_{\text{molec}}k_{\text{B}}T \lim_{x_i \rightarrow 0} \left[\exp\left(\frac{\mu_i^{\text{ex}}}{RT}\right) \right] \quad (2.19)$$

More useful from the practical point of view is the Henry's law constant H'_i , based on weight fractions. This is defined as:

$$H'_i = \lim_{w_i \rightarrow 0} \frac{f_i}{w_i} \quad (2.20)$$

with w_i being the weight fraction of component i in the polymer phase. Combination with Equation (2.14) leads to:

$$H'_i = \frac{\rho RT}{M_i} \lim_{x_i \rightarrow 0} \left[\exp\left(\frac{\mu_i^{\text{ex}}}{RT}\right) \right] \quad (2.21)$$

where ρ is the mass density of the i -free polymer phase.

Swelling effects upon sorption can be explored in both the $N_1f_2f_3 \dots f_c PT$ and $N_1N_2N_3 \dots N_c PT$ statistical ensembles, where the total volume of the polymer phase can be readily tracked as an ensemble average.

The partial molar volume of penetrant i in the $N_1f_2f_3 \dots f_c PT$ ensemble is obtainable from the covariance of the instantaneous volume and the number of molecules of species i (here, angular brackets symbolize averages with respect to the probability density of the $N_1f_2f_3 \dots f_c PT$ ensemble):

$$\bar{V}_i = N_{\text{Avo}} \frac{\langle N_i V \rangle - \langle N_i \rangle \langle V \rangle}{\langle N_i^2 \rangle - \langle N_i \rangle^2} \quad (2.22)$$

In the $N_1N_2N_3\dots N_cPT$ ensemble, on the other hand, the partial molar volume is obtainable from the change in volume brought about by the addition of a molecule of species i . This, in turn, can be computed in the framework of Widom insertions as:

$$\bar{V}_i = N_{\text{Avo}} \left\{ \frac{\langle \text{Vexp}[-\beta(\mathcal{V}_{\text{test}} - \mathcal{V}_{\text{test}}^{\text{intra}})] \rangle_{\text{Widom}}}{\langle \text{exp}[-\beta(\mathcal{V}_{\text{test}} - \mathcal{V}_{\text{test}}^{\text{intra}})] \rangle_{\text{Widom}}} - \langle V \rangle \right\} \quad (2.23)$$

where $\langle V \rangle$ is the average volume in the $N_1N_2N_3\dots N_cPT$ ensemble, while Widom averages are taken in the sense of Equation (2.15).

Thermal effects upon sorption can be analyzed similarly. We define the differential heat of sorption for species i as the negative of the partial molar heat of mixing [14]:

$$Q_{s,i} = \bar{h}_i^{\text{fluid}} - \bar{h}_i \quad (2.24)$$

where \bar{h}_i^{fluid} and \bar{h}_i are the partial molar configurational enthalpies of i in the fluid and in the polymer phase, respectively. The quantity \bar{h}_i^{fluid} can be estimated from an equation of state for the fluid phase and from intramolecular energetics in the ideal gas phase [14].

In the $N_1f_2f_3\dots f_cPT$ ensemble, the partial molar enthalpy of i in the polymer phase can be obtained from the covariance between the number of molecules of species i and the instantaneous enthalpy $\mathcal{V} + PV$, where \mathcal{V} is the total potential energy of the polymer phase:

$$\bar{h}_i = N_{\text{Avo}} \frac{\langle N_i(\mathcal{V} + PV) \rangle - \langle N_i \rangle \langle \mathcal{V} + PV \rangle}{\langle N_i^2 \rangle - \langle N_i \rangle^2} \quad (2.25)$$

On the other hand, in the $N_1N_2N_3\dots N_cPT$ ensemble, \bar{h}_i is obtainable from Widom insertions as:

$$\bar{h}_i = N_{\text{Avo}} \left\{ \frac{\langle (\mathcal{V} + PV) \text{exp}[-\beta(\mathcal{V}_{\text{test}} - \mathcal{V}_{\text{test}}^{\text{intra}})] \rangle_{\text{Widom}}}{\langle \text{exp}[-\beta(\mathcal{V}_{\text{test}} - \mathcal{V}_{\text{test}}^{\text{intra}})] \rangle_{\text{Widom}}} - \langle \mathcal{V} + PV \rangle \right\} \quad (2.26)$$

2.4.2 Calculations of Low-pressure Sorption Thermodynamics

Widom insertions of penetrant molecules can be undertaken as a post-processing calculation in configurations accumulated in the course of a MD or MC simulation of a pure polymer. Via Equations (2.15), (2.19), (2.21), (2.23) and (2.26), these lead to the low-pressure sorption thermodynamics of each penetrant in the polymer. Early calculations of this type met with limited success, because the force fields used to describe the polymers were not sufficiently validated and equilibration of the polymer configurations was incomplete. The calculation of Henry's law constants is, in fact, a stringent test for the internal structure (distribution of accessible volume in the polymer) and the force field. As better simulations of polymer matrices became available, the quality of sorption equilibrium results increased.

Figure 2.9 displays the weight fraction-based Henry's law constant H' (Equations (2.20) and (2.21)) for C_1 – C_6 normal alkanes in polydimethylsilamethylene $[-\text{Si}(\text{CH}_3)_2-\text{CH}_2-]_n$, abbreviated as PDMSM, at 300 K and 0.1 MPa total pressure [7]. This silicon-containing polymer is promising as a membrane material for solubility-driven separations of heavy hydrocarbon components (C_4+) from the lighter components,

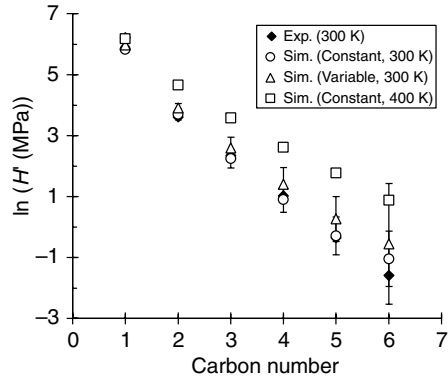


Figure 2.9 Weight fraction-based Henry's law constants of n -alkanes in PDMSM at 300 K and 0.1 MPa total pressure. Experimental data are shown as black diamonds, while simulation predictions using constant bond length and variable bond length models are shown as open circles and open triangles, respectively. The open squares depict simulation predictions from the constant bond length model at 400 K and 0.1 MPa

wherein the heavy components are separated as permeates and recovered from the main stream of lighter components. In comparison to polydimethylsiloxane materials typically used for such applications, it has the advantage of greater chemical stability towards sulfuric compounds (e.g. H_2S) found in natural gas.

A UA force field was developed for PDMSM based on quantum mechanical Density Functional Theory calculations [7] and validated against volumetric properties of the polymer and low-molecular-weight analogues. Alkane molecules were simulated using the TraPPE force field [10], which is known to reproduce phase equilibria of alkanes and their mixtures very well. The Henry's law constant predictions of Figure 2.9, obtained using configurationally biased Widom insertions [73] in the course of isothermal–isobaric MD simulations, are in very good agreement with experimental measurements. The base-case polymer model employed constant bond lengths. Making the bond lengths flexible, subject to a realistic stretching potential, increases the polymer density by 0.5% and reduces the predicted solubilities by an amount that is within the error bars of the calculation. Solubility is seen to increase significantly with increasing carbon number and to decrease with increasing temperature. Predicted (exothermic) heats of sorption of the alkanes at infinite dilution are also in excellent agreement with experiments [7].

2.4.3 Calculations of High-pressure Sorption Thermodynamics

As discussed in Section 2.4.1, calculations of sorption equilibria at high penetrant fugacities can be conducted in a variety of ensembles. Sorption isotherms for a penetrant (component 2) in a polymer (component 1) and associated swelling effects in rubbery polymers can be predicted conveniently through MC simulations in the N_1f_2PT ensemble. This type of simulations can be viewed as a hybrid between isothermal–isobaric and grand canonical ensemble MC, employing elementary moves of displacement, reorientation or conformational rearrangement of individual penetrant molecules, insertion and deletion of penetrant molecules, volume fluctuation and configurational rearrangement of the polymer phase (compare Section 2.2.3). The acceptance probabilities of these moves follow from the

probability density of the N_1f_2PT ensemble, developed in Theodorou [14].

Figure 2.10(a) displays a prediction for the sorption isotherm of normal pentane in molten polyethylene (PE) at 474 K, as calculated by Zervopoulou *et al.* [75]. Two UA models were used (TraPPE [10] and NERD [11]), which are known to give good predictions for the phase equilibria of small-molecular-weight alkanes and were shown to reproduce the volumetric properties of PE quite satisfactorily. Connectivity-altering EBMC moves were used to sample the polymer phase efficiently, while insertions of the alkane molecules were performed with a configurational bias scheme. The Henry's law line obtained from Widom insertions in a pure polymer phase is also shown in this figure; it is fully consistent with the high-pressure simulation results. The predicted isotherm is seen to be in excellent agreement with experimental data, and also with a calculation based on the Self-Associating Fluid Theory (SAFT) equation of state, which is known to give good results for this system. The isotherm has a characteristic convex, or 'Flory–Huggins' shape.

Figure 2.10(b) displays corresponding predictions of swelling of the molten PE phase upon sorption of *n*-pentane. The swelling is given as a fractional change in volume, referred to the volume of the pure polymer melt. Again, excellent agreement is seen between SAFT and the simulation results (especially those from the TraPPE model). Over a wide range of pressures, the mass density of the solvent-swollen PE phase remains practically independent of pressure [75]; this explains why a simple, incompressible theory of mixing, such as the Flory–Huggins, can capture the shape of the isotherm.

A second strategy for predicting isotherms is to simulate the polymer–penetrant system as a closed system at constant composition (e.g. in the N_1N_2PT ensemble) and obtain the corresponding penetrant fugacity through a method of estimating the excess chemical potential (compare Equations (2.13) and (2.14)). Such a strategy, based on MD simulations, has been used by van der Vegt to calculate sorption isotherms of CO_2 within a hypothetical glassy polymer of $T_g \approx 500\text{ K}$ [76]. The MD framework is convenient in this case, as it does not presuppose equilibration of the system; the polymer matrix can be trapped into a glassy state by high energy

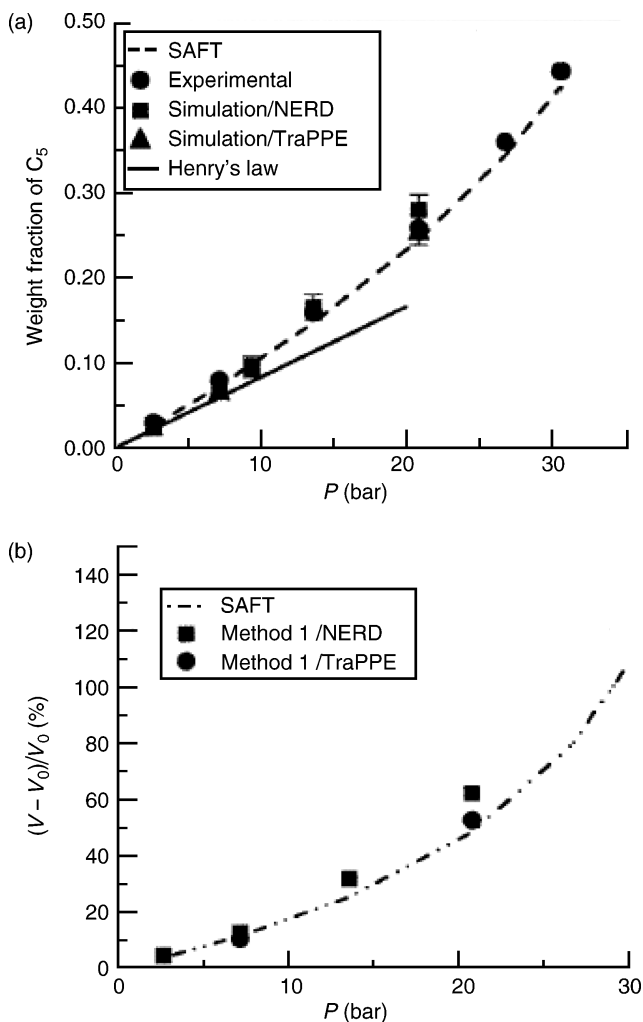


Figure 2.10 Sorption equilibria of normal pentane in molten polyethylene at 474 K, as predicted by N_1N_2PT ensemble simulations [75]: (a) sorption isotherm; (b) swelling effects upon sorption. Reprinted with permission from E. Zervopoulou, V. G. Mavrantzas and D. N. Theodorou, *Journal of Chemical Physics*, **115**, 1040 (2001). Copyright 2001, American Institute of Physics

barriers in configuration space, subject to the time scale limitations discussed in Section 2.2.5. Simulations were started at high penetrant concentrations, where the polymer was plasticized, and proceeded to lower and lower concentrations. At each loading, an iterative readjustment of the set pressure of the N_1N_2PT simulation was employed to make sure that P and f_2 were consistent with each other.

Figure 2.11(a) displays a desorption isotherm calculated by van der Vegt [76] at 350 K. Interest-

ingly, the predicted isotherm exhibits the ‘dual-mode’ shape characteristic of sorption in glassy polymers: It is concave at low pressures, with an inflection point at about 45 bar, beyond which a linear or ‘Flory–Huggins’ shape is observed. Figure 2.11(b) shows the accompanying volumetric behavior. The partial molar volume of the dissolved CO_2 is seen to change discontinuously from approximately $49 \text{ cm}^3 \text{ mol}^{-1}$ at high pressures (more than 80 CO_2 molecules dissolved, system in rubbery state) to approximately

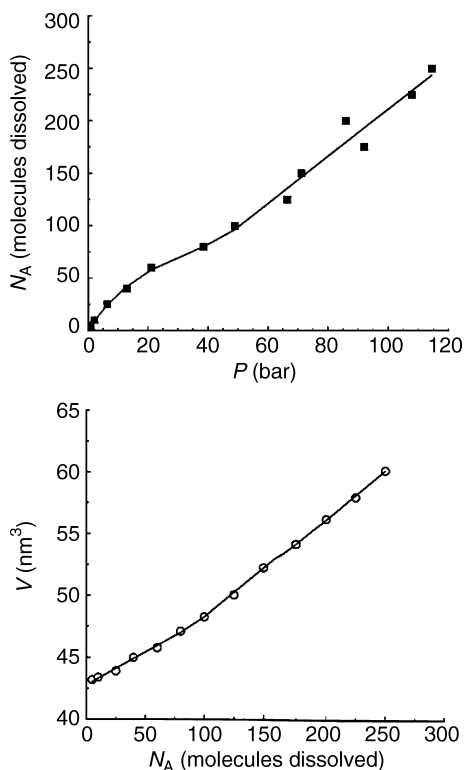


Figure 2.11 (a) Desorption isotherm of CO_2 in a polymer matrix of $T_g = 500$ K, as computed by MD simulations at 350 K. (b) Variation of the volume of the polymer phase with the number of penetrant molecules in the course of the desorption MD calculations [76]. Reproduced by permission of N. van der Vegt from ‘Molecular dynamics simulations of sorption and diffusion in rubbery and glassy polymers’, *Ph.D. Thesis*, University of Twente, Enschede, The Netherlands (1998)

$32 \text{ cm}^3 \text{ mol}^{-1}$ (less than 80 CO_2 molecules dissolved, system in glassy state). The computed intermediate incoherent scattering function $I(\mathbf{q}, t)$ similarly exhibits changes indicating transition from rubbery to glassy dynamics as the concentration of penetrant molecules decreases.

2.4.4 Ways to Overcome the Insertion Problem

When the size of penetrant molecules is large, clusters of accessible volume within the polymer that can accommodate the penetrant become scarce and very limited in extent. The probability of success of random insertion moves in $N_1 f_2 PT$

simulations becomes very small; similarly, estimates of f_2 through Widom insertion in $N_1 N_2 PT$ simulations become unreliable, as the overwhelming majority of insertions result in infinite energy of the test molecule. Solubility is strongly dependent on infrequent fluctuations of the polymer matrix resulting in the emergence of a hole big enough to accommodate the penetrant; such fluctuations may be poorly sampled in the course of an MD or MC simulation. The sampling is even poorer if favorable interaction requires specific orientations of the penetrant with respect to functional groups on the matrix, as happens, for example, with hydrogen bonding. As a result of all of these factors, traditional simulation techniques utilizing insertions of penetrant molecules become very inefficient for large or specifically interacting penetrants at low temperatures. We refer to this as the ‘insertion problem’ in simulations of sorption (more generally, of phase) equilibria.

Ways to overcome the insertion problem have been, and are actively being explored. We give a brief account of such methods here.

Configurationaly biased insertions, as already mentioned, are a great help for flexible molecules consisting of relatively small segments, such as the alkanes. They have been used very successfully to estimate solubilities of such molecules (see, for example, Raptis *et al.* [7] and Zervopoulou *et al.* [75]). They ultimately fail, however, for long molecules ($> \text{C}_{10}$ in molten polyethylene) at low temperatures (where the matrix density is high), or when bulky groups are present on the segments.

The strategy of *free energy perturbation* entails first calculating the solubility for an (often fictitious) penetrant of smaller size and simpler interactions with the matrix, for which the insertion problem is not severe. The system Hamiltonian is then progressively modified to the one of interest by introducing small stepwise changes in a coupling parameter modulating the penetrant potential energy. The solubility of the penetrant of interest is thus obtained by thermodynamic integration, through a series of simulations conducted at different values of the coupling parameter. The method, introduced by Swope and Andersen for small-molecule fluids [77] has been applied successfully to polymer systems. For example, Knopp *et al.* [78] have employed test particle insertions of Lennard–Jones particles

mimicking water molecules ('noble water') with thermodynamic integration to obtain chemical potentials of water in polyamides.

Expanded ensemble schemes also employ the idea of inserting or deleting molecules in a gradual manner. In an expanded ensemble simulation, configurations are sampled according to the partition function $\sum_{y=1}^M Q_y \exp(w_y)$, where y is a parameter in the Hamiltonian of the system, allowed to range over M discrete values or 'states', Q_y is a conventional (e.g. canonical) partition function evaluated at parameter value y , and w_y represent weighting factors modulating the probability of appearance of different y values. The scheme allows calculation of free energy differences between thermodynamic states corresponding to different y and can thus be thought of as an application of the free energy perturbation method 'on the fly', within a single simulation. It was originally proposed by Lyubartsev *et al.* [79] for the calculation of free energies of solvation in water at infinite dilution, with the parameter y corresponding to the strength of interaction between the solute and solvent molecules. It has been adapted within a configurational bias MC framework for the calculation of chemical potentials of polymers with y modulating the length of a 'tagged' chain, which is allowed to fluctuate in size [80]. More recently, it has been combined with parallel tempering in the so-called 'hyperparallel tempering' schemes [81].

In a related *extended ensemble MD method* designed by van der Vegt [76] and van der Vegt and Briels [82], the coupling parameter modulating penetrant-polymer interactions is treated as a fictitious dynamical variable. Fluctuations in the coupling parameter in the course of the simulation, which effectively change its size, allow it to escape from low-energy pockets, in which it would get trapped in a thermodynamic integration, and explore efficiently all of the volume accessible in the matrix.

A *scission-fusion MC method* has been presented by Zervopoulou *et al.* [75] for calculating sorption isotherms of oligomeric species within polydisperse polymer matrices. A requirement in the current implementation of the method is that the penetrant be of the same chemical constitution as the matrix, although chemical 'mutations' could be invoked to make it more general. Penetrant molecules are generated by internal trimer eliminations near the ends of

polymer chains (scissions) and destroyed by trimer bridgings to the ends of polymer chains (fusion). These connectivity-altering moves, carried out using the geometric bridging construction [31–34] are controlled by a modified fugacity of the penetrant, which is essentially a measure of the difference in chemical potential between a penetrant molecule and an equivalent amount of polymer. The composition of the system is predicted as a function of this relative fugacity, leading to the sorption isotherm. In this way, the need for inserting and deleting penetrant molecules is altogether obviated. Application of the method has given excellent predictions for the sorption isotherms of eicosane in PE at 474 K, which are very difficult to obtain by any other method.

Test particle deletion (the inverse Widom method) has been shown to be a viable technique for the calculation of chemical potentials by Boulougouris *et al.* [83]. To obtain correct chemical potentials by particle deletion, one has to take into account that deletion of a solute molecule from a solvent + solute system does not result in a typical configuration of the solvent, but rather in a configuration of the solvent with a hole in it; the bias associated with the presence of the hole must be taken into account. In the staged particle deletion method [83], one calculates the chemical potential through the free energy changes associated with (a) replacing the solute molecule in the solvent + solute system by a hard sphere, and (b) inserting a hard sphere in the solute-free solvent. The free energy of process (b) can be obtained efficiently through a fast analytic algorithm for the calculation of accessible volumes [61]. The diameter of the hard sphere must be chosen smaller than the distance of closest approach between solvent and solute, as obtained from the pair distribution function of the solvent + solute system. A direct particle deletion method, wherein the solute is first converted to a hard sphere and then to an ideal gas particle in each sampled configuration of the solvent + solute system, has also been developed. Moreover, particle deletion methods have been extended to deal with articulated (multisite) solute molecules [64]. Application of staged particle deletion for the calculation of Henry's law constants of methane in water afforded savings of a factor of 7 to 12 relative to Widom insertion. Staged particle deletion of multisite solutes has been used to

calculate Henry's law constants of benzene in polyethylene, with very promising results.

2.5 Prediction of Diffusivity

2.5.1 Statistical Mechanics of Diffusion

A formulation of the statistical mechanics of diffusion in a binary system consisting of polymer (component P) and penetrant (component A), based on linear response theory, has been presented in an earlier review [14]. Here we will summarize some key relations from this development.

We will use the symbol \mathbf{J}_i ($i = A, P$) to denote the macroscopic flux of component i , measured in moles per unit surface per unit time, in a coordinate frame which remains fixed with the center of mass of the system. At the microscopic level, we define the molecular flux \mathbf{j}_i of component i as the sum of the center-of-mass velocities of all molecules of that component:

$$\mathbf{j}_i = \sum_{\ell=1}^{N_i} \mathbf{v}_{\ell i} \quad (2.27)$$

The binary diffusivity or transport diffusivity D is defined through Fick's first law [84,85]:

$$M_A \mathbf{J}_A = -\rho D \nabla w_A = -\rho D \left(\frac{w_A w_P}{x_A x_P} \right) \nabla x_A \quad (2.28)$$

Through linear response theory, \mathbf{J}_A under nonequilibrium conditions (Equation (2.28)) is related to time integrals of the autocorrelation functions of the molecular fluxes \mathbf{j}_i under conditions of thermodynamic equilibrium. The binary diffusivity assumes the following expression in terms of the microscopic interdiffusion current, given by:

$$\mathbf{j}^c(t) = x_P \mathbf{j}_A(t) - x_A \mathbf{j}_P(t) \quad (2.29)$$

$$D = \frac{1}{x_A x_P} \left(\frac{\partial \ln f_A}{\partial \ln x_A} \right)_{T,P} \frac{1}{3(N_A + N_P)} \times \int_0^{\infty} \langle \mathbf{j}^c(0) \cdot \mathbf{j}^c(t) \rangle dt \quad (2.30)$$

Equation (2.30) is of the Green-Kubo form. An Einstein equation equivalent to Equation (2.30), but more convenient to use in simulations, is:

$$D = (N_A + N_P) x_A x_P \left(\frac{\partial \ln f_A}{\partial \ln x_A} \right)_{T,P} \lim_{t \rightarrow \infty} \frac{1}{6t} \times \left\langle \left\{ \left[\mathbf{r}_{\text{cm},A}(t) - \mathbf{r}_{\text{cm},P}(t) \right] - \left[\mathbf{r}_{\text{cm},A}(0) - \mathbf{r}_{\text{cm},P}(0) \right] \right\}^2 \right\rangle = N_A w_P \left(\frac{\partial \ln f_A}{\partial \ln w_A} \right)_{T,P} \lim_{t \rightarrow \infty} \frac{1}{6t} \times \left\langle \left\{ \left[\mathbf{r}_{\text{cm},A}(t) - \mathbf{r}_{\text{cm},P}(t) \right] - \left[\mathbf{r}_{\text{cm},A}(0) - \mathbf{r}_{\text{cm},P}(0) \right] \right\}^2 \right\rangle \quad (2.31)$$

with $\mathbf{r}_{\text{cm},i}(t)$ being the center of mass of all molecules of species i in the system at time t .

The self-diffusivity of species i provides a measure for the displacement of individual molecules of species i as a result of random thermal motion. In a system exhibiting diffusive behavior, the mean-square displacement of molecules grows linearly with time at long times. The self-diffusivity $D_{s,i}$ is extracted from the proportionality constant in this relationship:

$$D_{s,i} = \lim_{t \rightarrow \infty} \left\langle \frac{1}{6t} \left[\mathbf{r}_{\ell i}(t) - \mathbf{r}_{\ell i}(0) \right]^2 \right\rangle = \lim_{t \rightarrow \infty} \left\langle \frac{1}{6t} \frac{1}{N_i} \left\langle \sum_{\ell=1}^{N_i} \left[\mathbf{r}_{\ell i}(t) - \mathbf{r}_{\ell i}(0) \right]^2 \right\rangle \right\rangle \quad (2.32)$$

The expression on the second line of Equation (2.32), involving averaging over all molecules of species i , is most convenient for use in simulations, for it allows a larger sample size and therefore a smaller statistical uncertainty in estimating the self-diffusivity from equilibrium MD simulations. Such averaging over all molecules is not possible in the case of the binary diffusivity, Equation (2.31), which is by definition a collective property. This explains why the reliable estimation of D through equilibrium MD typically requires much longer runs than the estimation of $D_{s,i}$.

A Green–Kubo equation equivalent to Equation (2.32) for the self-diffusivity is:

$$D_{s,i} = \frac{1}{3} \int_0^{\infty} \langle \mathbf{v}_{\ell i}(t) \cdot \mathbf{v}_{\ell i}(0) \rangle dt$$

$$= \frac{1}{3N_i} \int_0^{\infty} \sum_{\ell=1}^{N_i} \langle \mathbf{v}_{\ell i}(t) \cdot \mathbf{v}_{\ell i}(0) \rangle dt \quad (2.33)$$

Relating D to $D_{s,i}$ is practically useful, given that the latter can be estimated much more readily from simulation.

By substituting the microscopic interdiffusion current from Equations (2.27) and (2.29) into Equation (2.30), one obtains the binary diffusivity in terms of a sum of integrals of velocity correlation functions of the penetrant and polymer molecules [14]. In the limit where A is infinitely dilute in P ($x_A, w_A \rightarrow 0$), the cross-correlation terms between the two species drop; also, the velocity correlation terms between different molecules of species A reduce to zero, as the A molecules are very far apart. Furthermore, the sorption isotherm is linear (well described by Henry’s law), making the thermodynamic derivative in Equation (2.30) equal to zero. In this limit, one rigorously obtains:

$$\lim_{w_A \rightarrow 0} D = \lim_{w_A \rightarrow 0} D_{s,A} \quad (2.34)$$

If one assumes that cross-correlations between velocities of different molecules of the same or different species are negligible even at finite concentrations, the above formulation leads to an approximate relation between binary and self-diffusivities [14]:

$$D \approx \left(\frac{\partial \ln f_A}{\partial \ln w_A} \right)_{T,P} D_{s,A} \quad (2.35)$$

The thermodynamic term in the rigorous Equations (2.30) and (2.31) and in the approximate Equation (2.35) can be obtained directly from sorption isotherms predicted by the methods discussed in Section 2.4. According to Equation (2.35), the self-diffusivity $D_{s,A}$ plays a dominant role in shaping the binary diffusivity. This perhaps justifies the emphasis that has been placed

on the prediction of $D_{s,A}$ in past simulation work, briefly discussed in the following.

2.5.2 Self-diffusivities from Equilibrium Molecular Dynamics

Equilibrium MD, already discussed in Section 2.2.3, is the most convenient method for predicting diffusivities in systems where $D_{s,A}$ exceeds $10^{-6} \text{ cm}^2 \text{ s}^{-1}$. The standard application of the method involves simulating an atomistic model consisting of polymer chains and a number of penetrant molecules for times on the order of several nanoseconds and extracting $D_{s,A}$ through Equation (2.33). Averaging over many penetrant molecules and also over many MD trajectories, initiated at different initial configurations, is essential in overcoming the difficulties associated with the sluggish dynamics of the matrix and accumulating good statistics.

Early equilibrium MD simulations, using simplified models, were valuable in elucidating the mechanism of elementary jumps through which diffusion of small molecules takes place, as well as the dependence of the diffusivity and activation energy for diffusion on penetrant size, unoccupied volume and its distribution, and torsional barriers within the polymer. This work has been reviewed [14,86]. More recent efforts, using more detailed atomistic models, have led to satisfactory predictions of self-diffusivities in a variety of polymer–penetrant systems above T_g over wide temperature and concentration ranges.

As an indication of the kind of agreement between equilibrium MD simulation and experiment that can be achieved nowadays, we present Figure 2.12. In this figure, MD predictions [87] and NMR pulsed field gradient spin echo measurements [88] of the self-diffusivities $D_{s,A}$ and $D_{s,P}$ in mixtures of normal dodecane (C_{12}) and normal hexacontane (C_{60}) are presented. Here, dodecane is taken as the ‘penetrant’ A and hexacontane as the ‘polymer’ P. The excellent quality of the experimental data allows a comparison over a wide range of compositions, quantified here through the weight fraction of dodecane, w_A , in the mixtures. Simulations were based on a united-atom force field, which was shown to yield excellent predictions for the self-diffusivities of pure alkanes and their temperature dependence [89]. Simulated and experimental self-diffusivities in the mixtures are seen to be in very good agreement. Also shown in

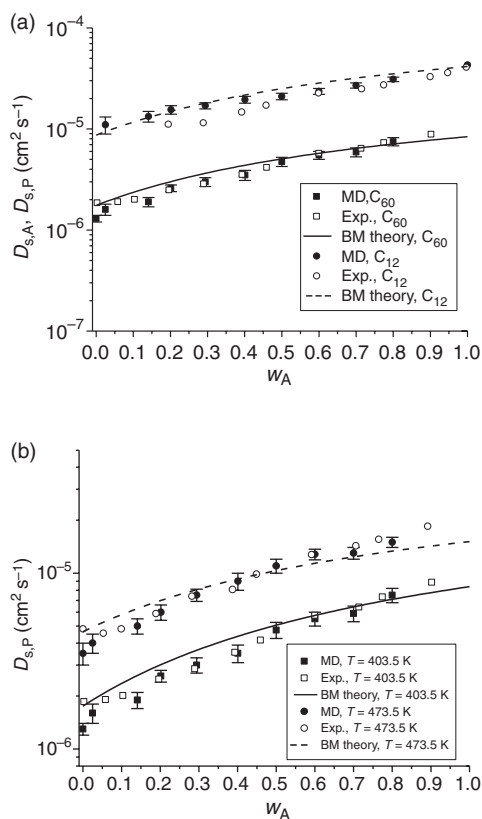


Figure 2.12 Self-diffusivities of *n*-dodecane ($D_{s,A}$) and *n*-hexacontane ($D_{s,P}$) in liquid mixtures of *n*-dodecane and *n*-hexacontane with various weight fractions of *n*-dodecane (w_A). Simulation predictions are shown as filled symbols with error bars, while experimental values from pulsed field gradient spin echo NMR measurements are shown as open symbols. Predictions of the von Meerwall *et al.* theory [90] are also shown as lines. (a) Variation of $D_{s,A}$ and $D_{s,P}$ with w_A at a temperature of 403.5 K. (b) Variation of $D_{s,P}$ with w_A at two different temperatures, 403.5 K and 473.5 K [87]. Reprinted with permission from V. A. Harmandaris, D. Angelopoulou, V. G. Mavrantzas and D. N. Theodorou, *Journal of Chemical Physics*, **116**, 7656 (2002). Copyright 2002, American Institute of Physics

Figure 2.12 are calculations based on the theory of von Meerwall *et al.* [90], which combines concepts from free volume theory and from the Rouse theory of unentangled chain dynamics. The theory is seen to capture the experimental self-diffusivities for both components over the entire concentration range rather well; agreement between simulation and experiment is clearly bet-

ter than between theory and experiment. Direct analysis of accessible volume around internal chain segments and around chain-ends in the simulations showed that the chain-end free volume parameter invoked by the von Meerwall *et al.* theory admits a concrete geometric interpretation.

Results from the same simulations have also been compared against predictions from the free volume theory of Vrentas and Duda [60], with parameters estimated through the scheme proposed by Vrentas and Vrentas [91]. Predictions of the Vrentas and Duda theory for the self-diffusivity of dodecane in the mixture were found to be in good agreement with the simulation results only for small and intermediate concentrations of dodecane ($w_A < 0.7$). In the dilute regime ($w_A > 0.7$), the free volume theory significantly underestimated the dodecane self-diffusivity. This is not unexpected, since one of the basic assumptions of the Vrentas–Duda theory is the presence of a significant number of polymer molecules in the mixture.

2.5.3 Diffusivities from Nonequilibrium Molecular Dynamics

Nonequilibrium molecular dynamics (NEMD) methods have found limited application in the study of diffusion phenomena in polymers. Typically, NEMD imposes uniform force fields on the molecules of the simulated system in a manner that keeps the center of mass of the system fixed. If the imposed forces are small enough for the system to remain in the linear response regime, the binary diffusivity can be obtained from the ratio of flux to driving force under steady-state conditions. Müller-Plathe *et al.* [92] employed NEMD to estimate the diffusivities of H₂, He and O₂ in polyisobutylene (PIB) but found no advantages over equilibrium MD methods: their nonequilibrium flux fluctuated widely and the linear response regime broke down at relatively small values of the imposed driving force.

An interesting NEMD method was proposed more recently by van der Vegt and coworkers for estimating the diffusivities of penetrants present at very low concentrations within liquid polymer matrices through measuring the friction coefficient characterizing penetrant–matrix interactions [76,93]. The method involves the isothermal simulation of two penetrant molecules connected by an artificial harmonic spring and immersed in the

polymer matrix. The spring is initially stretched, but is allowed to relax during the nonequilibrium simulation. Relaxation is tracked in a manner that allows identifying when the system is in the linear response regime (in this regime, the time decay of the penetrant separation averaged over many systems prepared with the same initial separation becomes exponential). The friction factor ζ describing interactions between the polymer and a penetrant molecule is computed from the exponential decay of the separation in the linear response regime. The method is based on invoking a Langevin stochastic differential equation to describe the evolution of the tethered penetrant–penetrant separation. Having obtained ζ , the diffusivity is estimated from the friction factor through the Einstein equation for Brownian motion:

$$D = \frac{k_B T}{\zeta} \quad (2.36)$$

2.5.4 Diffusion in Low-temperature Polymer Matrices as a Sequence of Infrequent Penetrant Jumps

As temperature is reduced towards and below T_g , penetrant diffusion in an amorphous polymer matrix becomes too slow to be predictable by MD simulations. Direct MD would require inordinately long simulation times for the prediction of diffusivity in low-temperature rubbery polymers and polymer glasses, which are most relevant from the point of view of membrane and barrier material applications. Fortunately, statistical mechanics-based techniques for the analysis and simulation of infrequent event processes come to the rescue.

Diffusion through a low-temperature amorphous polymer matrix is slow because the penetrant spends most of its time ‘trapped’ within clusters of accessible volume in the matrix and only infrequently jumps from cluster to cluster. A ‘brute-force’ MD simulation exhausts itself in tracking the relatively uninteresting ‘rattling’ motions of the penetrant within a cluster, but is much too short to accumulate sufficient statistics on the jumps that govern diffusion. It should be emphasized that this jump process is not confined to diffusion in polymers below T_g . As shown by MD work, it occurs in low-temperature melts and rubbery polymers as well, whenever the temperature is sufficiently low for the distribution of accessible volume clusters to remain relatively unchanged

over the time scale required for the penetrant to move by the mean distance between clusters.

The above observations on the mechanism of low-temperature diffusion of small molecules in low-temperature amorphous polymers suggest a description of diffusion as a sequence of successive, infrequent jump events, with the rate constant for each jump being estimatable from transition-state theory (TST). Each jump event is expected to involve a relatively small number of degrees of freedom in the configuration space of the polymer + penetrant system. In the following, we will concentrate on the problem of diffusivity prediction of a small molecule present at infinite dilution within a glassy polymer matrix (in this limit, the binary diffusivity and the self-diffusivity of the penetrant coincide, as discussed in Section 2.5.1). We will show how this problem can yield to a hierarchical modeling strategy, consisting of the following steps:

- (1) Identify the ‘states’ where the polymer + penetrant system spends most of its time and the ‘reaction paths’ along which transitions between neighboring states take place, through geometric/energetic analysis of a detailed molecular model of the system.
- (2) Calculate the rate constant k for each reaction path.
- (3) Model diffusion as a Poisson process consisting of elementary jumps between the sites determined in (1) with rate constants determined in (2), and estimate the diffusivity by tracking the mean-square penetrant displacement as a function of time, according to Equation (2.32).

We first discuss step (3) in the above hierarchy, whereby the mean-squared displacement of the penetrant can be determined once all states and interstate rate constants are known.

Assume that all states i in which the polymer + penetrant system spends most of its time have been determined and the ‘equilibrium’ (with respect to the distribution of the penetrant in the matrix) probabilities p_i^{eq} are known for each state. With each state i , we associate a position vector \mathbf{r}_i in three-dimensional space, which is representative of the position of the penetrant in state i .

The evolution of the polymer + penetrant system in time is viewed as a Poisson process [94], consisting of successive uncorrelated jumps between neighboring states. With each jump,

$i \rightarrow j$ is associated a first-order rate constant $k_{i \rightarrow j}$. Consider an (in general nonequilibrium) ensemble of polymer + penetrant systems which at time $t=0$ conform to a specified, but otherwise arbitrary distribution among states. As time elapses, this distribution evolves through transitions between states occurring in the individual systems of the ensemble. Let $p_i(t)$ be the probability of finding a system of the ensemble in state i at time t . The quantities $p_i(t)$ evolve according to the master equation:

$$\frac{dp_i}{dt} = - \sum_j k_{i \rightarrow j} p_i + \sum_i k_{j \rightarrow i} p_j \quad (2.37)$$

At very long times, the ensemble reaches its equilibrium distribution, wherein the probability of each state is p_i^{eq} . The equilibrium probabilities of each state obey the condition of microscopic reversibility (detailed balance):

$$k_{i \rightarrow j} p_i^{\text{eq}} = k_{j \rightarrow i} p_j^{\text{eq}} \equiv k_{ij} \quad (2.38)$$

In view of Equation (2.38) and the normalization condition $\sum_i p_i^{\text{eq}} = 1$, it is clear that in a system with a total of m states only $(m+2)(m-1)/2$ of the quantities $\{k_{i \rightarrow j}\}$, $\{p_i^{\text{eq}}\}$ are independent. (In practice, most of the independent constants $k_{i \rightarrow j}$ are zero, as they correspond to pairs of states that are not connected.) The average residence time in state i at equilibrium is as follows:

$$\tau_i = \frac{1}{\sum_j k_{i \rightarrow j}} \quad (2.39)$$

Combining Equations (2.37) and (2.38), we find that the reduced probabilities $\tilde{p}_i(t) \equiv p_i(t)/p_i^{\text{eq}}$ obey the evolution equations:

$$p_i^{\text{eq}} \frac{d\tilde{p}_i}{dt} = - \sum_j k_{ij} (\tilde{p}_i - \tilde{p}_j) \quad (2.40)$$

Equation (2.40) suggests a simple electrical analogue [14]: the network of states can be mapped onto a three-dimensional network with nodes at the representative points \mathbf{r}_i . With each node i is associated a capacitance p_i^{eq} and with each pair of connected nodes a resistance $1/k_{ij}$, with k_{ij} defined in Equation (2.38). The reduced probabi-

lity distribution $\{\tilde{p}_i(t)\}$ evolves exactly as the electrostatic potential in the electrical network.

The transient master equation (Equation (2.37)) can be solved numerically. A Kinetic Monte Carlo (KMC) method for doing so has been designed in the context of diffusion in zeolites [95]. This method directly simulates the continuous time – discrete space Markov process described by Equation (2.37) on an ensemble of model systems, as follows:

- (i) Consider a three-dimensional network with a large number m of sites placed at positions \mathbf{r}_i , $i=1, \dots, m$, with connectivity defined by the rate constants $k_{i \rightarrow j}$. The network provides a coarse-grained representation of the penetrant + polymer system. Its geometric and topological characteristics and the values of p_i^{eq} and $k_{i \rightarrow j}$ that characterize its nodes and bonds are derived from the atomistic analysis approaches described below in Sections 2.5.5 and 2.5.6.
- (ii) Distribute a large number $\mathcal{N}_E \gg m$ of random walkers on the sites of the network according to the equilibrium probability distribution $\{p_i^{\text{eq}}\}$. Multiple occupancy of sites is allowed in this deployment of the random walkers. The walkers will be allowed to hop between sites without interacting with each other, i.e. they behave as ghost particles towards each other. Each random walker summarily represents a system in the ensemble of polymer + penetrant systems whose temporal evolution we want to track with our KMC simulation. Let $\mathcal{N}_i(t)$ be the number of random walkers that find themselves in site i at time t .
- (iii) For each site i that is occupied at the current time t , calculate the expected fluxes $R_{i \rightarrow j}(t) = \mathcal{N}_i(t) k_{i \rightarrow j}$ to all sites j to which it is connected. In addition, compute the overall flux $R(t) = \sum_i \sum_j R_{i \rightarrow j}(t)$ and the probabilities $q_{i \rightarrow j}(t) = R_{i \rightarrow j}(t)/R(t)$.
- (iv) Generate a random number $\xi \in [0,1]$. Choose the time for occurrence of the next elementary jump event in the network as $\Delta t = -\ln(1 - \xi)/R(t)$. Choose the type of the next elementary jump event by picking one of the possible transitions $i \rightarrow j$ according to the probabilities $q_{i \rightarrow j}(t)$.
- (v) Of the $\mathcal{N}_i(t)$ walkers present in site i , pick one with probability $1/\mathcal{N}_i(t)$ and move it to site j .
- (vi) Advance the simulation time by Δt . Update the array, keeping track of the current positions of

all walkers to reflect the implemented hop.

Update the occupancy numbers $\mathcal{N}_i(t + \Delta t) = \mathcal{N}_i(t) - 1$ and $\mathcal{N}_j(t + \Delta t) = \mathcal{N}_j(t) + 1$.

- (vii) Return to step (iii) to implement the next jump event.

The outcome from performing this stochastic simulation over a large number of steps is a set of trajectories $\mathbf{r}_{kA}(t)$ for all \mathcal{N}_E random walkers. Additional sets of trajectories may be obtained by KMC simulation on independently generated networks of sites. The self-diffusivity D_{sA} is obtained from the mean-square displacement $\langle [\mathbf{r}_{kA}(t) - \mathbf{r}_{kA}(0)]^2 \rangle$ computed over all trajectories, through the Einstein equation (Equation (2.32)).

If the rate constants $k_{i \rightarrow j}$ are small, the time steps Δt taken by the simulation are long, and thus the simulation permits accessing times and displacements that may be by several orders of magnitude longer than those accessible through ‘brute-force’ atomistic MD. Thus, the long-time problem of MD is solved, perhaps at the expense of losing the short-time details of the polymer and penetrant motions.

2.5.5 Gusev–Suter TST Method for Polymer Matrices Undergoing Isotropic ‘Elastic’ Motion

Given an atomistic model for a low-temperature amorphous polymer phase, the simplest calculation one can perform to address the diffusion of a penetrant is to assume that the polymer matrix is rigid and map out the potential energy $\mathcal{V}^{\text{pen}}(\mathbf{r}_A)$ felt by the penetrant as a function of its configuration \mathbf{r}_A in the polymer matrix. \mathcal{V}^{pen} encompasses all penetrant–polymer interactions, as well as the intramolecular energy of the penetrant, if it can undergo changes in its internal configurations. It is entirely analogous to the quantity $\mathcal{V}_{\text{test}}$ considered in Section 2.4. On the potential energy hypersurface \mathcal{V}^{pen} , one can perform an exhaustive search for minima i and saddle points between the minima, define dividing surfaces between adjacent states i and j , and calculate all interstate rate constants $k_{i \rightarrow j}$. Such TST analyses of diffusion in a rigid matrix have been conducted in zeolites [95] with excellent results. In the case of a polymer, the static matrix assumption leads to underestimation of the diffusivity by many orders of magnitude [96] (diffusivities much lower than $10^{-12} \text{ cm}^2 \text{ s}^{-1}$ predicted for gases other than helium).

Clearly, the response of the polymer matrix to the presence of the penetrant must be incor-

porated in some way. Gusev and Suter [86,97] proposed a physically reasonable and computationally inexpensive approach for doing this. They assumed that, over the residence times of the polymer + penetrant system in a sorption ‘state’, the polymer atoms execute harmonic vibrations about their equilibrium positions in the penetrant-free matrix. These motions (small-amplitude vibrations of bond lengths and bond angles, librations of torsion angles) are termed ‘elastic motion’ and are distinguished from ‘structural relaxation’ involving, e.g., torsional transitions in the main chains or side-groups. In essence, the assumption of a double time scale separation is invoked: the characteristic time for elastic motions is much shorter than the time elapsing between penetrant jumps, and the latter is much shorter than the times governing matrix relaxation processes. The polymer contribution $\mathcal{V}_P(\mathbf{r}_P)$ to the potential energy is modeled by the simplified expression:

$$\mathcal{V}_P(\mathbf{r}_P) = \mathcal{V}_P(\mathbf{r}_{P,0}) + k_B T \sum_k \frac{(\mathbf{r}_{kP} - \mathbf{r}_{kP,0})^2}{2\langle \Delta^2 \rangle} \quad (2.41)$$

where k enumerates atoms in the polymer, \mathbf{r}_{kP} stands for the three-dimensional position vector of polymer atom k , \mathbf{r}_P is used to denote the coordinates of all polymer atoms collectively, and the subscript 0 denotes the minimum energy configuration used to represent the penetrant-free polymer matrix. In the work of Gusev and Suter, $\langle \Delta^2 \rangle$ is the variance in atomic position along each coordinate direction in the course of elastic motion. The quantity $k_B T / \langle \Delta^2 \rangle$ can be thought of as the force constant of a harmonic spring binding each polymer atom to its position in the minimum energy configuration. It should increase in proportion to the absolute temperature and can be made dependent on the atom type; a single value for all atom types has been used in most implementations to date. Note that, in this Debye-type approximation, atoms are assumed to move isotropically and independently of each other. A parameter related to $\langle \Delta^2 \rangle$, the Debye–Waller factor, is used in the analysis of X-ray diffraction patterns.

Let us consider a penetrant being represented by a single interaction site. In this case, \mathbf{r}_A is a three-dimensional vector. (Single-site, ‘united

atom' representations are typically used for small diatomic or polyatomic molecules, such as O₂, N₂, and CH₄ in the Gusev–Suter approach.) Under the assumption of Equation (2.41), the 'equilibrium' probability density of penetrant positions in the polymer matrix is governed by a three-dimensional free energy field, or potential of mean force, $A(\mathbf{r}_A)$, made up of additive contributions from all polymer atoms. This is because, as stated in Section 2.2.1, the penetrant–polymer potential energy \mathcal{V}^{pen} is modeled as a sum of central pairwise additive potential contributions depending on the distances between polymer atoms at \mathbf{r}_{kP} and the penetrant at \mathbf{r}_A . With the form of Equation (2.41) for \mathcal{V}_P , the equilibrium probability density of \mathbf{r}_A is then:

$$\begin{aligned} \rho^{\text{eq}}(\mathbf{r}_A) &= \frac{\int d\mathbf{r}_P \exp[-\beta\mathcal{V}(\mathbf{r}_P, \mathbf{r}_A)]}{\int d\mathbf{r}_A \int d\mathbf{r}_P \exp[-\beta\mathcal{V}(\mathbf{r}_P, \mathbf{r}_A)]} \\ &= \text{Const.} \prod_k \int d\mathbf{r}_{kP} \exp\left[-\frac{(\mathbf{r}_{kP} - \mathbf{r}_{kP,0})^2}{2\langle\Delta^2\rangle} - \beta\mathcal{V}_k^{\text{pen}}(\mathbf{r}_{kP} - \mathbf{r}_A)\right] \end{aligned} \quad (2.42)$$

Clearly, the integrations over the different \mathbf{r}_{kP} can be performed independently, leading to:

$$\begin{aligned} \rho^{\text{eq}}(\mathbf{r}_A) &= \text{Const.} \exp[-\beta A(\mathbf{r}_A)] \\ &= \text{Const.} \exp\left[-\beta \sum_k A_k(|\mathbf{r}_A - \mathbf{r}_{kP,0}|)\right] \end{aligned} \quad (2.43)$$

For a given $\langle\Delta^2\rangle$, the pair free energy functions A_k are precalculated from the pair potential functions $\mathcal{V}_k^{\text{pen}}$ by numerical integration for every atomic species in the polymer. The free energy function $A(\mathbf{r}_A)$ is thus readily obtainable, given a minimum energy configuration $\mathbf{r}_{P,0}$.

In the elastically moving matrix approach of Gusev and Suter, the transition-state analysis is conducted entirely on the three-dimensional free energy hypersurface $A(\mathbf{r}_A)$. The 'states' i are defined as three-dimensional domains around the local minima of $A(\mathbf{r}_A)$. An exhaustive determination of all these

minima is possible through construction of a fine cubic grid inside the atomistic configuration $\mathbf{r}_{P,0}$, exactly as has been done for the diffusion of spherical molecules in zeolites [95]. A steepest descent path in $A(\mathbf{r}_A)$ is initiated at the center of each voxel defined by the grid; the path terminates at a local minimum of $A(\mathbf{r}_A)$, assigning the voxel to that minimum. In this way, the entire polymer configuration is partitioned into three-dimensional states. In the actual calculations, an interval of 0.2 Å is typically used for constructing the grid. The actual number of states identified was quite large (around 50 for the largest penetrants in a model configuration of approximately 30 Å edge length).

Dividing surfaces are defined by the borders between voxels belonging to different states. The two-dimensional dividing surface S_{ij} between any two states i and j is thus represented as a collection of contiguous square facets, each oriented normal to one of the three coordinate axes.

The equilibrium probability of a state i is computed by straightforward numerical integration over the voxels of that state:

$$\begin{aligned} p_i^{\text{eq}} &= \int_{\text{state } i} d\mathbf{r}_A \rho^{\text{eq}}(\mathbf{r}_A) \\ &= \text{Const.} \int_{\text{state } i} d\mathbf{r}_A \exp[-\beta A(\mathbf{r}_A)] \end{aligned} \quad (2.44)$$

The constant in Equation (2.44) can be evaluated such that the sum of all p_i^{eq} in the primary amorphous cell equals 1.

The rate constant $k_{i \rightarrow j}^{\text{TST}}$ for transitions from state i to state j according to the Transition State Theory assumption (setting the dynamical correction factor, or transmission coefficient, to 1) is obtained from the ratio of the partition function of the system confined to the two-dimensional dividing surface S_{ij} to the partition function of the system in state i :

$$k_{i \rightarrow j}^{\text{TST}} = \frac{k_B T}{h} \frac{Q_{ij}}{Q_i} \quad (2.45)$$

with:

$$\begin{aligned} Q_i &= \left(\frac{2\pi m_A}{\beta h^2}\right)^{3/2} Z_i = \left(\frac{2\pi m_A}{\beta h^2}\right)^{3/2} \\ &\times \int_{\text{state } i} d\mathbf{r}_A \exp[-\beta A(\mathbf{r}_A)] \end{aligned} \quad (2.46)$$

and:

$$Q_{ij} = \left(\frac{2\pi m_A}{\beta h^2} \right) Z_{ij} = \left(\frac{2\pi m_A}{\beta h^2} \right) \times \int_{S_{ij}} d\mathbf{r}_A \exp[-\beta A(\mathbf{r}_A)] \quad (2.47)$$

where m_A is the mass of the penetrant molecule. The configurational integrals Z_i and Z_{ij} are three- and two-dimensional, respectively. In terms of these integrals,

$$k_{i \rightarrow j}^{\text{TST}} = \left(\frac{1}{2\pi\beta m_A} \right)^{1/2} \frac{Z_{ij}}{Z_i} \quad (2.48)$$

Z_i and Z_{ij} are computed readily from the pretabulated field $A(\mathbf{r}_A)$ by numerical or Monte Carlo integration. In the computation of Z_{ij} , Gusev and Suter used correction factors to account for the increase in surface area caused by the discrete (faceted) representation of the dividing surface [86].

In the Gusev–Suter approach, values of p_i^{eq} and $k_{i \rightarrow j}^{\text{TST}}$ determined through Equations (2.44) and (2.48) are used within a KMC procedure, as described in Section 2.5.4, to calculate the self-diffusivity $D_{s,A}$. Estimates of $D_{s,A}$ depend sensitively on the value of $\langle \Delta^2 \rangle$ used to describe ‘elastic’ fluctuations of the matrix. To avoid arbitrariness in the choice of this parameter, Gusev and Suter proposed a way of estimating it from short atomistic MD simulations of the pure polymer matrix. The $\langle \Delta^2 \rangle$ values obtained from such simulations were found to increase with time, following the approximate scaling $\log(\langle \Delta^2 \rangle^{1/2}) \propto \log t$. Gusev *et al.* [86] and Gusev and Suter [97] recommended using in the TST calculations that value of $\langle \Delta^2 \rangle$ which corresponds to the most probable residence time τ_i of the penetrant in a state. This introduces a self-consistent character in the calculation: a value for $\langle \Delta^2 \rangle$ is initially postulated and used to compute the rate constants $k_{i \rightarrow j}^{\text{TST}}$; the residence time distribution is extracted from the rate constants, and the time at which it goes through a maximum is identified; a new value of $\langle \Delta^2 \rangle$ is determined from this most probable τ_i , and the whole procedure is repeated. The self-consistent calculation is found to converge in a few iterations. In the case of He and H₂ in polyisobutylene, the most probable τ_i was approximately 0.15 ps and the corre-

sponding $\langle \Delta^2 \rangle^{1/2}$ was taken as 0.22 Å. In the case of O₂ and N₂ in the same polymer, the most probable τ_i was approximately 1 ps and $\langle \Delta^2 \rangle^{1/2}$ was 0.46 Å.

The Gusev–Suter elastically moving matrix approach is straightforward and computationally efficient. It has been applied to a variety of polymer + penetrant systems, including He, H₂, Ar, Kr, Xe, O₂ and N₂ in (glassy) polycarbonate, poly(vinyl chloride) (PVC), polyimides, (rubbery) polyisobutylene and even polydimethylsiloxane around room temperature, with considerable success [16,86,97]. Diffusivities obtained with reasonable values of $\langle \Delta^2 \rangle$ agree with experimental data. The self-consistent strategy of estimating $\langle \Delta^2 \rangle$ gives good results for $D_{s,A}$ in many cases, but is not always satisfactory [86].

As an example application of the Gusev–Suter method, we briefly discuss a recent study of O₂ diffusion in poly(ethylene terephthalate), (PET) and poly(ethylene isophthalate) (PEI) [98]. The objective of the study was to understand the molecular reasons for the superior barrier properties of PEI in comparison to PET. Use of these properties is made in packaging applications, where blends or copolymers of PET and PEI typically containing 2–5 % PEI units exhibit superior performance relative to pure PEI.

The generation of atomistic glassy amorphous model PEI and PET configurations based on the PCFF force field [99], a highly nontrivial task, proceeded through a multistage MD/MM scheme. Analysis of the simulation results showed that the two ‘poly-isomers’ are characterized by (practically) identical static properties: torsion angle distributions, total radial distribution functions and chain characteristic ratios were calculated to be similar between PET and PEI. However, a significant difference was detected in the segmental dynamics between the two polymers. This difference is related to phenyl-ring rearrangements: in PET, the phenyl ring was seen to undergo facile motions around the axis of rotation formed by the bonds connecting it to the rest of the chain, leading to fast decorrelation of the torsional angles about the latter bonds. Due to a cooperative effect, the faster local dynamics of the phenyl migrates throughout the PET repeat unit and is evidenced even in the glycol group. In PEI, on the other hand, where the phenyl ring possesses no natural in-plane axis of rotation as a result of its *para*-configuration, phenyl ring motions are

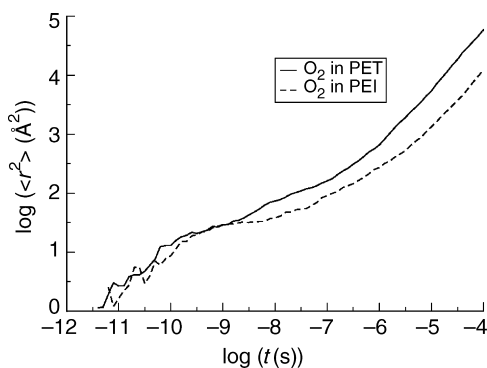


Figure 2.13 Mean-square displacement as a function of time for oxygen sorbed at infinite dilution within glassy poly(ethylene terephthalate) (PET) and poly(ethylene isophthalate) (PEI) at 300 K [98]. Each curve, displayed here in log–log coordinates, represents an average over 2000 uncorrelated kinetic Monte Carlo simulation trajectories in a single structure. Jump rate constants were calculated by the self-consistent Gusev–Suter method. The edge lengths of the primary simulation boxes were 26.74 and 26.60 Å for PET and PEI, respectively. Reprinted with permission from N. Ch. Karayiannis, V. G. Mavrantzas and D. N. Theodorou, *Macromolecules*, **37**, 2978–2995 (2004). Copyright (2004) American Chemical Society

more sluggish. The rate at which corresponding torsion angles decorrelate was calculated to be two to three times slower at 600 K. This difference in dynamics is less pronounced, but still observable, in the glassy state at room temperature.

Figure 2.13 displays mean-square displacement versus time curves of O_2 from KMC simulations using the self-consistent Gusev–Suter approach carried out in two individual configurations of PET and PEI. Attainment of a ‘Fickian’, or ‘Einstein’ diffusion regime is evident at long times, where the slope of $\log(\langle r^2 \rangle)$ with respect to $\log t$ equals unity. $D_{s,A}$ is extracted from that

Einstein regime. Results from averaging over 10 different configurations of each polymer are displayed in Table 2.1. All configurations were generated so as to match the experimental density practically exactly. The value of $\langle \Delta^2 \rangle^{1/2}$ in PET is seen to be higher than that in PEI, reflecting the difference in segmental dynamics discussed above. Primarily as a result of this difference, the diffusivity of oxygen in PET is predicted to be, by a factor of 1.8, higher than in PEI. This result is in favorable agreement with the ratio of around 2.5 reported experimentally. Predicted diffusivity values, shown in Table 2.1, are in what should be considered very good agreement with existing experimental values for this kind of calculation. One can conclude that the self-consistent Gusev–Suter approach can capture the difference in permeability behavior between the two isomeric polyesters. Furthermore, simulation provides a rather clear picture of the principal origin of this difference (more segmental motion in PET due to different connectivity of phenyl rings with the rest of the main chain).

2.5.6 Multidimensional TST Approach to Gas Diffusion in Glassy Polymers

As the penetrant size increases relative to the size of accessible volume cavities in a glassy polymer, the Gusev–Suter picture of penetrant hops in a matrix of atoms executing fast, uncorrelated harmonic vibrations around their static equilibrium positions in the penetrant-free state becomes less satisfactory. The polymer degrees of freedom have to change a lot to accommodate the sorbed penetrant. More importantly, infrequent, large-amplitude segmental motions of the polymer become significant in opening pathways among the chains that can enable the penetrant to hop

Table 2.1 Densities, ‘elastic’ Displacements of Matrix Atoms and O_2 Self-Diffusivity Values from Application of the Self-Consistent Gusev–Suter Approach to Amorphous Poly(ethylene Terephthalate) (PET) and Poly(ethylene Isophthalate) (PEI) at 300 K [98]. Experimental Densities and Diffusivities are also given. Experimental Values in Parentheses Come from Different Sources and Provide an Indication of Existing Uncertainties

Polyester	ρ (g cm ⁻³) ^a	ρ (g cm ⁻³) ^b	$\langle \Delta^2 \rangle^{1/2}$ (Å)	$D_{s,A}$ (10 ⁻⁹ cm ² s ⁻¹)	$D_{s,A}$ (10 ⁻⁹ cm ² s ⁻¹) ^b
PET	1.335	1.336 (1.333)	0.432 ± 0.008	9.6 ± 6.2	9.5 (6.5)
PEI	1.356	1.356 (1.346)	0.426 ± 0.005	5.4 ± 3.7	2.7

^aImposed in the simulations.

^bExperimental.

from cavity to cavity. The double time scale separation postulated by the Gusev–Suter approach breaks down, as ‘relaxational’ motions of the matrix are intimately involved in the infrequent events governing the translational progress of the penetrant, and dynamical characteristics of the polymer (e.g. atomic masses) start playing a role.

Even in such cases, of course, one can invoke the elastically fluctuating matrix picture with $\langle \Delta^2 \rangle^{1/2}$ treated as an adjustable parameter, but the predictive power of the approach is significantly diminished.

To resolve these problems, Greenfield and Theodorou [100–104] set out to develop a multi-dimensional TST approach, in which the polymer degrees of freedom are incorporated explicitly in the reaction coordinate of the infrequent events whereby diffusion takes place. Their approach is inspired by Vineyard’s [105] TST formulation of diffusion of interstitial atoms in crystalline solids. In the crystalline case, the identification of multi-dimensional reaction paths along which diffusive jumps are likely to occur is relatively straightforward, owing to the underlying symmetries. On the contrary, in the amorphous glassy polymer mapping out these paths poses serious conceptual and computational challenges.

Following Vineyard, we introduce mass-weighted Cartesian coordinates \mathbf{x}_A , \mathbf{x}_{kP} for the penetrant and for all polymer atoms:

$$\begin{aligned} \mathbf{x}_A &= m_A^{1/2} \mathbf{r}_A \\ \mathbf{x}_{kP} &= m_{kP}^{1/2} \mathbf{r}_{kP} \end{aligned} \quad (2.49)$$

We will use the symbol $\mathbf{x} = (\mathbf{x}_P, \mathbf{x}_A)$ to denote the mass-weighted coordinates of all atoms in the system. Clearly, the total potential energy \mathcal{V} can be expressed as a function of \mathbf{x} .

The polymer + penetrant system is envisioned as evolving through transitions $i \rightarrow j$ from the vicinity of one energy minimum \mathbf{x}_i in multidimensional configuration space to that of another minimum \mathbf{x}_j , along a reaction path (line in \mathbf{x} -space) which passes through a saddle point \mathbf{x}_{ij} of the function $\mathcal{V}(\mathbf{x})$. Let n be the number of elements in \mathbf{x} (dimensionality of configuration space of the polymer + penetrant system).

The dividing surface separating states i and j is a $(n - 1)$ -dimensional hypersurface with equa-

tion $C(\mathbf{x}) = 0$, that has the following properties [106]:

- (1) It passes through the saddle point \mathbf{x}_{ij} :

$$C(\mathbf{x}_{ij}) = 0 \quad (2.50)$$

- (2) At \mathbf{x}_{ij} , it is normal to the eigenvector \mathbf{n}_{ij} corresponding to the negative eigenvalue of the Hessian matrix \mathbf{H} of second derivatives of $\mathcal{V}(\mathbf{x})$:

$$\left. \frac{\nabla_{\mathbf{x}} C(\mathbf{x})}{|\nabla_{\mathbf{x}} C(\mathbf{x})|} \right|_{\mathbf{x}=\mathbf{x}_{ij}} = \mathbf{n}(\mathbf{x}_{ij}) = \mathbf{n}_{ij} \quad (2.51)$$

The vector \mathbf{n}_{ij} is tangential to the reaction path at \mathbf{x}_{ij} . Therefore, at \mathbf{x}_{ij} , the dividing surface and the reaction path are normal to each other.

- (3) At all points other than \mathbf{x}_{ij} , the dividing surface is tangent to the gradient vector of $\mathcal{V}(\mathbf{x})$:

$$\nabla_{\mathbf{x}} C(\mathbf{x}) \cdot \nabla_{\mathbf{x}} \mathcal{V} = 0, \quad \mathbf{x} \neq \mathbf{x}_{ij} \quad (2.52)$$

According to the TST approximation, whenever the system finds itself on the dividing surface with net momentum directed from state i to state j , a successful transition from i to j will occur. Under this assumption [106], the rate constant in a classical treatment can be expressed as follows:

$$\begin{aligned} k_{i \rightarrow j}^{\text{TST}} &= \int_{\text{state } i} d\mathbf{x} \int_{\mathbf{n}(\mathbf{x}) \cdot \mathbf{p} > 0} d\mathbf{p} |\mathbf{n}(\mathbf{x}) \cdot \mathbf{p}| \delta[C(\mathbf{x})] |\nabla_{\mathbf{x}} C(\mathbf{x})| \rho(\mathbf{x}, \mathbf{p}) \end{aligned} \quad (2.53)$$

where \mathbf{p} is the vector of mass-weighted momenta conjugate to \mathbf{x} , $\rho(\mathbf{x}, \mathbf{p})$ is the canonical ensemble probability density in phase space, and the Dirac delta function selects configurations on the dividing surface. Upon performing all momentum space integrations, one obtains:

$$k_{i \rightarrow j}^{\text{TST}} = \frac{1}{(2\beta\pi)^{1/2}} \frac{\int_{\text{state } i} d\mathbf{x} \delta[C(\mathbf{x})] |\nabla_{\mathbf{x}} C(\mathbf{x})| \exp[-\beta V(\mathbf{x})]}{\int_{\text{state } i} d\mathbf{x} \exp[-\beta \mathcal{V}(\mathbf{x})]} \quad (2.54)$$

For the highly constricted pathways that limit the overall rate of diffusion (see below), we expect the major contribution to the rate constant to come from the lowest energy region of the dividing surface, in the vicinity of \mathbf{x}_{ij} . This region will be well approximated by a hyperplane through \mathbf{x}_{ij} drawn normal to the direction \mathbf{n}_{ij} . In the following, we will be using this approximation; i.e. we will be representing the dividing surface by:

$$C(\mathbf{x}) \approx \mathbf{n}_{ij} \cdot (\mathbf{x} - \mathbf{x}_{ij}) = 0 \quad (2.55)$$

Equation (2.54) is still of the general form of Equation (2.45). Equation (2.48) of the Gusev–Suter method is a special case of Equation (2.54) with $A(\mathbf{r}_A)$ replacing $\mathcal{V}(\mathbf{x})$ (since integration over the polymer degrees of freedom has been performed within the fast elastic motion assumption), with the remaining $n = 3$ degrees of freedom being associated with the penetrant mass m_A .

Clearly, an exhaustive identification of all states and dividing surfaces in n -dimensional space, analogous to the one undertaken in the Gusev–Suter method for $n = 3$, is out of the question. The question then becomes, how does one identify the most relevant reaction paths in multidimensional configuration space that limit the rate of diffusion, and how does one implement Equations (2.45) or (2.54) to compute the corresponding transition rate constants?

For the identification of relevant states and dividing surfaces, Greenfield and Theodorou introduced a method based on geometric analysis of accessible volume within the penetrant-free minimum energy configuration representing the polymer matrix. Details of the method have appeared elsewhere [100–102,104,107]. The main objective of this geometric analysis is to identify initial guesses for the penetrant positions at the transition states of elementary jumps (i.e. for the projections of all relevant \mathbf{x}_{ij} s onto the three translational degrees of freedom of the penetrant center of mass). To this end, the accessible volume within the penetrant-free polymer configuration is analyzed (see Section 2.3.4) using a series of hard-sphere probes of progressively lower radii, ranging from the van der Waals radius of the penetrant r_A^0 down to the radius for which percolation of accessible volume through the periodic structure is observed. For large probe radii, small, disconnected accessible

volume clusters are identified. As the probe radius decreases, the clusters expand (not necessarily isotropically) and new clusters appear. Two different clusters may merge into a single cluster by coming together at a ‘neck’ of accessible volume. Greenfield and Theodorou’s geometric analysis identifies the positions of all of these ‘necks’ and uses them as initial guesses for the penetrant position at the saddle points of elementary jumps. At the same time, it records the connectivity of clusters originally identified at probe radius r_A^0 and of all the clusters that emerged in the course of geometric analysis with smaller probe radii.

Having determined a set of ‘necks’ through the computationally very efficient geometric analysis of accessible volume, one proceeds to convert them to actual saddle points of the potential energy $\mathcal{V}(\mathbf{x})$ in the multidimensional space of the polymer + penetrant system. Using a neck point as an initial guess for the penetrant position and keeping the polymer configuration fixed, a low-dimensional search is undertaken to determine the closest saddle point of \mathcal{V} in the subspace of penetrant degrees of freedom, \mathbf{r}_A . The set of system degrees of freedom considered flexible is then augmented to encompass generalized coordinates associated with polymer atoms within a sphere centered at the penetrant; a new saddle point of \mathcal{V} is found in this augmented space, using the configuration determined from the initial saddle point search as an initial guess. This process of augmentation of the set of flexible generalized coordinates and determination of a saddle point in the augmented set is repeated, until further inclusion of coordinates leaves the saddle point energy unchanged. The Cerjan–Miller algorithm described by Baker [102, 104,108] has been found to give satisfactory results. In Greenfield’s original work, the saddle point determination was conducted in generalized degrees of freedom, using a polymer model with constant bond lengths. Since then, a formulation in Cartesian coordinates appropriate for fully flexible models has been developed.

In the general case where the saddle point search is conducted in generalized coordinates, the system satisfies the following equations at the saddle point:

$$\nabla_{\mathbf{q}_f} \mathcal{V} = \mathbf{0} \quad (2.56)$$

and:

$$\mathbf{H}_{qq}^0 d\mathbf{q}_f = \lambda \mathbf{a}^0 d\mathbf{q}_f \quad (2.57)$$

with all eigenvalues λ positive, except one. In the above, \mathbf{H}_{qq}^0 is the Hessian matrix of second derivatives of the potential energy \mathcal{V} with respect to the flexible generalized coordinates \mathbf{q}_f , $\nabla_{\mathbf{q}_f} \mathcal{V}$ is the gradient vector of \mathcal{V} with respect to \mathbf{q}_f , $d\mathbf{q}_f$ denotes an eigenvector in the space of flexible generalized coordinates and \mathbf{a}^0 is the covariant metric tensor in the subset of flexible generalized coordinates [101,102,104], defined by:

$$a_{\alpha\beta}^0 = \sum_k \frac{\partial x^k}{\partial q_f^\alpha} \frac{\partial x^k}{\partial q_f^\beta} \quad (2.58)$$

where superscripts indicate elements of the vectors \mathbf{x} and \mathbf{q}_f .

Figure 2.14 shows results from application of this saddle point determination strategy, in Cartesian coordinates, to CO_2 within the glassy poly-(amide imide) whose repeat unit is shown in Figure 2.1(b). The center of mass of the CO_2 penetrant was initially placed at the geometric ‘neck’ depicted by the light sphere at the center of Figure 2.1(a). The initial orientation of the CO_2 molecule was assigned randomly, subject to the condition that it does not result in excessive overlap with the surrounding polymer atoms. The first saddle point determination was carried out in nine degrees of freedom (Cartesian coordinates of the atoms constituting the CO_2 molecule in the fully flexible representation employed). Degrees of freedom of the polymer were then added successively, as shown pictorially by the concentric spheres of increasing radius. Figure 2.14(b) displays the variation of the saddle point energy obtained through this progressive increase of the dimensionality of the saddle point calculation. In all cases, an asymptotic behavior is observed, wherein further increase of the number of degrees of freedom leaves the saddle point energy unaltered. The configuration and energy corresponding to this asymptotic value are taken as the converged saddle point for the particular transition examined.

In Figure 2.15, we see the initial guess configuration and the converged configuration for one saddle point determination in the CO_2 /poly(amide imide) system. The shaded surfaces provide a pictorial representation of the accessible volume dis-

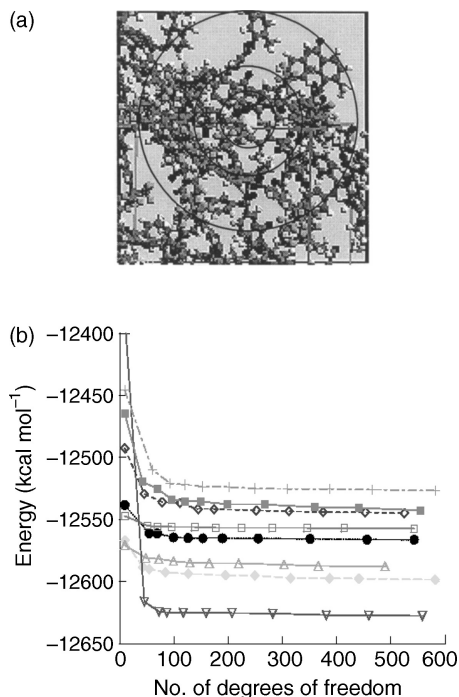


Figure 2.14 (a) Schematic of the process for a saddle point determination with respect to polymer + penetrant degrees of freedom in a CO_2 /poly(amide imide) system modeled with the COMPASS force field. The light sphere at the center marks the position of the ‘geometric neck’ that serves as an initial ‘guess’ for the penetrant center of mass at the saddle point. The concentric spheres show the progressive inclusion of more and more polymer degrees of freedom in the saddle point calculation. (b) Saddle point energy as a function of the number of ‘flexible’ degrees of freedom included in the calculation, for a number of saddle point determinations carried out in this way. The energy is very high at the end of the initial nine-dimensional saddle point determination with respect to the degrees of freedom of the penetrant in a static polymer matrix. It drops quickly upon including degrees of freedom of the matrix and assumes a practically asymptotic value. Including all polymer atoms within 8 \AA of the penetrant results in 500 to 600 flexible degrees of freedom

tribution in the poly(amide imide) configuration; they encompass the volume accessible to a spherical probe of radius 0.9 \AA . Although there is obvious similarity between the initial and converged saddle point configurations, there are subtle but important differences. In the converged configuration, we see that the polymer atoms around the CO_2 molecule have given way

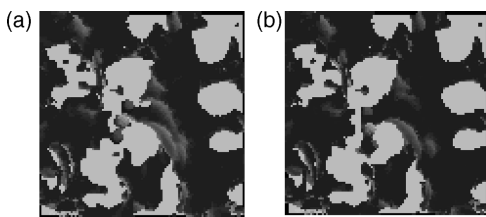


Figure 2.15 (a) Initial guess configuration (center of mass placed at the geometric neck, orientation assigned randomly) for a CO₂/poly(amide imide) saddle point. (b) Final configuration resulting from the converged multidimensional saddle point search. The CO₂ molecule has reoriented to align with the neck axis and surrounding polymer chains have retracted to create more accessible volume around the penetrant. The shaded surfaces outline the accessible volume of the matrix, as determined using a 0.9 Å radius sphere as a probe

somewhat; the passage through which the CO₂ has to go in order to accomplish the transition into the large cluster of accessible volume is now visible. The orientation of CO₂ has become more or less parallel to this passage, in order to minimize resistance to the transition.

Having determined a saddle point in multidimensional configuration space, we set out to compute the entire reaction path. As stated above [compare Equation (2.51)], we start off the reaction path on either side of the saddle point in the direction of the eigenvector $\mathbf{n}_{ij} = \mathbf{dx}/|\mathbf{dx}|$ corresponding to the negative eigenvalue of the Hessian \mathbf{H} with respect to mass-weighted Cartesian coordinates. The corresponding change in generalized coordinates is $d\mathbf{q} = \begin{pmatrix} dq_r \\ dq_s \end{pmatrix}$, with $d\mathbf{q}_r$ satisfying Equation (2.57) with negative λ at the saddle point and $d\mathbf{q}_s = \mathbf{0}$.

Once the first small step away from the saddle point has been taken, the entire reaction path down to the state i on one side, or to the state j on the other, is computed through a steepest descent construction in \mathbf{x} -space, following Fukui's intrinsic reaction coordinate (IRC) approach [109]. The IRC can be derived from the classical equations of motion of the system by imposing the condition of continuous dissipation of kinetic energy. It is readily constructed by taking small steps $d\mathbf{q}$ in the flexible generalized coordinates according to the equation:

$$\mathbf{a}^0 d\mathbf{q} = \nabla_{\mathbf{q}} \psi d\tau \quad (2.59)$$

with $d\tau$ being a quantity with dimensions of squared time, which measures how far we are along our way to the minimum.

The IRC construction need not be confined to the set of flexible (Cartesian or generalized) coordinates used for the initial identification of the multidimensional saddle point. It can be designed so as to encompass additional degrees of freedom associated with polymer atoms that start interacting with the penetrant as it shifts towards the minimum energy states and, conversely, to fade out degrees of freedom which are too far from the penetrant to play a role [101,102,104].

Figure 2.16 shows how the potential energy profile for a given transition changes as more and more degrees of freedom are incorporated in the IRC construction. For all three curves shown, the reaction coordinate is measured as a path length from the saddle point in the multidimensional configuration space of flexible Cartesian coordinates. On each side of the saddle point, path lengths have been normalized by the total path length between the saddle point and the corresponding minimum, so that the two states connected by the transition always appear at -1 and 1 , respectively. Clearly, the whole reaction path calculation becomes asymptotic as more and more polymer degrees of freedom are systematically included.

Having determined a reaction path leading from a state i to a state j through a saddle point ij in multidimensional configuration space, one can proceed to compute the rate constant $k_{i \rightarrow j}^{\text{TST}}$ based on Equation (2.45). This calculation could proceed via a free-energy perturbation scheme, wherein a set of closely spaced hyperplanes normal to the reaction path are considered, from state i up to the dividing hyperplane S_{ij} , and differences in free energy of the system confined in successive hyperplanes are estimated by MD [14]. Given the approximate nature of the overall calculation, Greenfield and Theodorou [102,104] invoked a simpler, harmonic approximation approach reminiscent of that originally proposed by Vineyard [105].

According to the harmonic approximation, the major contribution to the partition function of the system confined to the dividing surface (the numerator of Equation (2.45)) will come from the immediate vicinity of the saddle point \mathbf{x}_{ij} . In this region, $\psi(\mathbf{x})$ can be approximated by a Taylor expansion to second order in the subspace

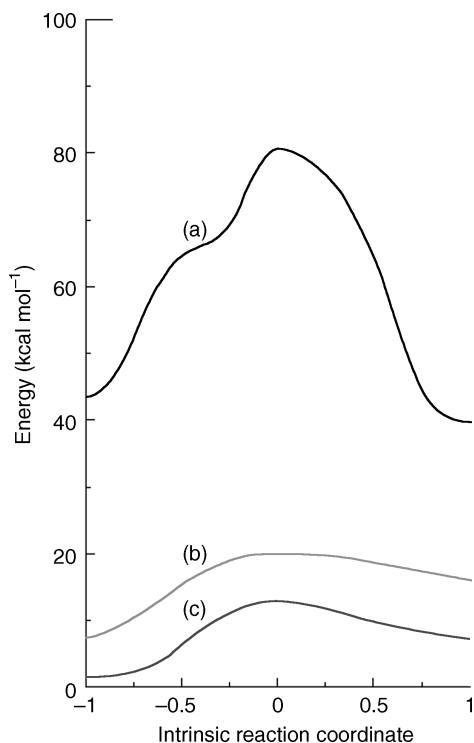


Figure 2.16 Energy profile along the reaction coordinate for a CO_2 molecule moving between two accessible volume clusters of poly(amide imide). Curve (a) shows the results of a nine-dimensional calculation with respect to the degrees of freedom of the penetrant only, while curve (b) has been obtained by including all polymer degrees of freedom within 4.5 \AA from the penetrant in the saddle point and intrinsic reaction coordinate calculations. In the calculations displayed by curve (c) all polymer degrees of freedom within 6 \AA of the penetrant have been included. The reaction coordinate (length along the reaction path in multidimensional space) has been scaled, so that -1 and 1 correspond to the origin and destination state, respectively. The similarity between the curves (b) and (c) indicates that the calculation is converging (curves have been displaced in the vertical direction, for clarity)

obtained by projecting the eigendirection \mathbf{n}_{ij} out of \mathbf{x} . Similarly, the major contribution to the partition function of i in the denominator of Equation (2.45) is assumed to come from the immediate vicinity of the state minimum \mathbf{x}_i , where $\mathcal{V}(\mathbf{x})$ can be approximated by a Taylor expansion to second order in \mathbf{x} -space. With this approximation, the integrals in Equation (2.54) become Gaussian and the partition functions Q_{ij} and Q_i reduce to

partition functions of independent harmonic oscillators. Using the quantum mechanical vibrational partition function for each harmonic oscillator, and assuming that zero point energies are incorporated in \mathcal{V} , the rate constant ultimately assumes the form:

$$k_{i \rightarrow j}^{\text{TST}} = \frac{k_B T}{h} \frac{\prod_{\alpha=1}^f [1 - \exp(-\beta h \nu_{\alpha}^{(i)})]}{\prod_{\alpha=2}^f [1 - \exp(-\beta h \nu_{\alpha}^{(j)})]} \times \exp \left[\frac{-\mathcal{V}(\mathbf{x}_{ij}) - \mathcal{V}(\mathbf{x}_i)}{k_B T} \right] \quad (2.60)$$

where $\nu_{\alpha}^{(ij)}$ are the frequencies obtained from the positive eigenvalues $\lambda_{\alpha}^{(ij)}$ of the Hessian \mathbf{H} at the saddle point \mathbf{x}_{ij} , determined through Equation (2.57), and $\nu_{\alpha}^{(i)}$ are the frequencies obtained from the eigenvalues of the Hessian at the minimum \mathbf{x}_i , obtained again through Equation (2.57). In Equation (2.60), f enumerates the generalized degrees of freedom which were flexible along any part of the reaction path. The frequencies at the saddle point are by one less than the frequencies at the minimum, since one eigenvalue is negative at the saddle point.

If all frequencies are much smaller than $k_B T/h$, Equation (2.60) reduces to its classical counterpart:

$$k_{i \rightarrow j}^{\text{TST}} = \frac{\prod_{\alpha=1}^f \nu_{\alpha}^{(i)}}{\prod_{\alpha=2}^f \nu_{\alpha}^{(j)}} \exp \left[\frac{-\mathcal{V}(\mathbf{x}_{ij}) - \mathcal{V}(\mathbf{x}_i)}{k_B T} \right] \quad (2.61)$$

Greenfield and Theodorou used the analysis outlined above for CH_4 in glassy atactic polypropylene [101,102]. They found it convenient to lump sorption states (energy minima) separated by low energy barriers in comparison to $k_B T$ into single ‘macrostates’, distinguishing between ‘intermacrostate’ and ‘intramacrostate’ (fast) transitions. This distinction can be based on the geometric analysis of accessible volume: states for which the penetrant positions lie in the same cluster of accessible volume belong to the same macrostate. Intermacrostate transitions are rate-limiting for diffusion. Reaction path constructions initiated at geometric necks between clusters of accessible

volume usually lead to the determination of intermacrostate transitions. In the system $\text{CH}_4/\text{glassy polypropylene}$, intermacrostate rate constants were found to be distributed extremely broadly, with most of them lying in the range 10^{-3} to $10^3 \mu\text{s}^{-1}$. On the contrary, the corresponding distribution of jump lengths (in three-dimensional space) between macrostates was rather narrow, with a maximum at around 0.5 nm. The multidimensional TST analysis permitted quantifying the extent of matrix motion required for effecting a jump as a function of distance from the penetrant and separating energetic from entropic contributions to the rate constants.

For the purpose of calculating the diffusivity, it is most efficient to coarse-grain the mathematical description of the Poisson process of successive penetrant jumps from the state to the macrostate level [102–104]. The KMC simulation of diffusion can be conducted in macrostate networks formed by periodic replication of the amorphous cells used to simulate the polymer. To avoid artifacts associated with such periodic networks, Greenfield and Theodorou [100,103] developed an alternative approach, which involves the generation of very large irregular networks of macrostates by reverse Monte Carlo (RMC) simulation. The objective of RMC is to find a configuration which matches a given set of distribution functions.

Greenfield and Theodorou's strategy uses two levels of RMC simulation. In the first level, the penetrant positions representative of the macrostates (nodes) are determined and the connections (bonds) are drawn, along which nonzero values of transition rate constants will be assigned. The distributions of intermacrostate jump distances, macrostate coordination numbers and angles between intermacrostate bonds are matched at this level. In a second level of RMC simulation, the macrostate equilibrium occupancy probabilities p_i^{eq} and intermacrostate fluxes $k_{IJ} = k_{I \rightarrow J} p_I^{\text{eq}}$ (compare Equation (2.38)) are assigned to all nodes and bonds of the network, respectively. Information used at this level includes the distributions of p_i^{eq} and k_{IJ} , as well as correlations between p_i^{eq} and the coordination number of I .

Diffusivities calculated from KMC simulations carried out on networks of macrostates representative of specific gas/glassy polymer systems through the Einstein equation (Equation (2.32))

are in favorable agreement with experiment [102].

2.5.7 Anomalous Diffusion: Its Origins and Implications

A remarkable finding from both MD and TST-based KMC simulations of diffusion in rubbery and glassy polymers is that, at short times, an 'anomalous regime' is observed, wherein the penetrant mean squared displacement scales with time as $\langle [\mathbf{r}_A(t) - \mathbf{r}_A(0)]^2 \rangle \propto t^\alpha$ with an exponent $\alpha < 1$. This behavior is quite general. It can be seen, for example, in Figure 2.13, plotted in log–log coordinates, despite the statistical noise present in that figure. While molecular motion in a simple liquid becomes diffusive ($\alpha = 1$) after a few picoseconds from the time origin of observation, penetrant motion in polymers requires much longer times to enter the linear, or 'Einstein', or 'Fickian' diffusion regime. For a simple oxygen/polyethylene model at room temperature, Chassapis *et al.* [110] found an anomalous diffusion regime extending out to $t \approx 150$ ps and $\langle [\mathbf{r}_A(t) - \mathbf{r}_A(0)]^2 \rangle^{1/2} \approx 1.5$ nm. For O_2 in the less mobile polyisobutylene, Müller-Plathe *et al.* report an extensive anomalous time scale of 6 ns [92]. In glassy matrices, the observed anomalous diffusion regime can easily extend to tenths of microseconds.

Anomalous diffusion is due to long-lived structural correlations in the polymer, which cause the diffusant to encounter a locally heterogeneous environment. In the case of a simple oxygen/polyethylene model [110], systematic analysis of MD trajectories revealed a weak but distinct tendency for penetrant motion to follow local chain orientation, in a manner reminiscent of the Pace–Datyner model. Orientational correlations between chain backbones persist over length scales of ca. 1.5 nm (commensurate with that over which anomalous diffusion is observed) and relax slowly in comparison to penetrant motion. Over short times, the penetrant tends to execute 'shuttling' motions along elongated cavities or strings of cavities directed more or less parallel to the chain backbones.

From a practical point of view, the existence of anomalous diffusion increases the computational cost of MD simulations required for the prediction of $D_{s,A}$, since such simulations must be long enough for the Einstein regime to be adequately

sampled. Extracting $D_{s,A}$ from the slope of the $\langle [\mathbf{r}_A(t) - \mathbf{r}_A(0)]^2 \rangle$ versus t curve at times shorter than the time at which crossover to normal diffusion occurs leads to significant overestimation of $D_{s,A}$.

In very slowly moving (primarily glassy) matrices, the crossover from anomalous to normal diffusion is often observed at root-mean-squared penetrant displacements roughly equal to the simulation box size. This is seen characteristically in the curves of Figure 2.13. The reader can confirm that, at the point where a slope of unity is attained in log-log coordinates, $\langle [\mathbf{r}_A(t) - \mathbf{r}_A(0)]^2 \rangle$ is roughly equal to the squared edge length of the simulation box, reported in the legend to the figure. This is a system size effect—at length scales larger than the simulation box size, the model matrix looks like a regular lattice to the penetrant; structural heterogeneities leading to anomalous diffusion are suppressed, precipitating a premature onset of the Einstein regime. The true duration of the anomalous regime can only be determined by conducting the KMC simulation on systems of progressively larger edge length, or by generating very large networks of sites governed by the structural correlations, site energy and rate constant distributions extracted from atomistic TST analysis, as proposed by Greenfield and Theodorou [103]. One wonders about the reliability of $D_{s,A}$ estimates extracted from such simulations that are subject to system size effects. There is strong indication from the work of Karayiannis *et al.* [111] that the news is good in this respect. Despite the premature onset of the Einstein regime, the estimate of $D_{s,A}$ extracted from the linear part of the mean-square displacement versus time curves is not significantly affected by system size, provided the model structures employed in the simulation are large enough and numerous enough.

Karayiannis *et al.* [111] conducted a systematic KMC study of diffusion in cubic lattices of sites, to the bonds of which were assigned jump rate constants according to prescribed distribution functions. Lattices of various sizes were considered, to ensure that results are free of system size effects. The form of the jump rate constant distributions was chosen to mimic that extracted from atomistic TST analyses [100–102]. The variance of the jump rate distributions was varied systematically from a very small value, representative of a homogeneous medium, to a very large

value, representative of a highly disordered, heterogeneous medium, such as a polymer glass. KMC results were compared against a time-dependent effective medium approximation (EMA) which uses the distribution of rate constants as input. In a first part of the study, rate constants from the distribution were assigned randomly to the bonds of the lattice. It was found that the variance of the rate constant distribution had a profound effect on the diffusion process, giving rise to an anomalous regime at short time scales. The higher the variance of the distribution, then the longer the duration of the anomalous regime and the smaller the diffusion coefficient in the long-time, Fickian regime. The crossover time from anomalous to Fickian diffusion was a strongly nonlinear function of the standard deviation of the distribution of rate constants; it increases dramatically beyond a certain standard deviation, in a manner reminiscent of percolation. EMA-based calculations of the mean-square displacement were in excellent quantitative agreement with the KMC simulations. In a second part of the study, simulations were performed on spatially correlated lattices, consisting of domains within each of which the rate constants assume similar values. Spatial correlations were found to prolong the duration of anomalous diffusion regime. At long time scales, however, the spatially correlated lattices were characterized by the same diffusivity as uncorrelated ones with the same rate constant distribution. In other words, the long-time self-diffusivity $D_{s,A}$ was a function of the distribution of rate constants and not of the manner in which these were spatially assigned. $D_{s,A}$ could be estimated very well by applying the static EMA. This gives one the hope that diffusivities in glassy polymers could be estimated directly from the rate constant distributions determined by atomistic TST without having to resort to KMC simulations. For this, static EMA would have to be extended to systems with variable coordination numbers, as are the networks of sites extracted from TST analysis of glassy polymer/penetrant systems.

2.6 Conclusions and Outlook

Interest in molecular simulations of polymer-penetrant systems has been steadily growing. We are now at a point where simulations are

providing critical understanding of fundamental processes of sorption and transport in polymers, and thus helping in the design of membrane materials with improved performance in separation applications.

The importance of having a good model for the polymer matrix cannot be overemphasized. Generating such models is a challenging problem, even if an accurate force field is available for the description of intra- and intermolecular interactions. We have discussed molecular mechanics, molecular dynamics and, in particular, Monte Carlo strategies that can equilibrate atomistic models of amorphous polymer melts. Coarse-graining to models with fewer degrees of freedom, equilibrating at the coarse-grained level, and reverse mapping to the atomistic level can accelerate equilibration calculations, especially in the case of polymers of complex chemical constitution. Model glassy configurations are best generated through molecular mechanics and molecular dynamics methods, starting from well-equilibrated melt configurations. The problem of generating glasses with a formation history that is both well-defined and consistent with common laboratory and industrial processing practices is still unsolved; nevertheless, model polymer glasses that are useful for sorption and diffusion calculations can be generated with existing methodology.

Before embarking on the calculation of permeability properties, it is important to validate the model polymer configurations against high-quality experimental data. We have discussed examples of validation against experimental volumetric measurements, static structure factors from X-ray and neutron diffraction, NMR relaxation and quasielastic neutron scattering measurements of segmental dynamics, and positron annihilation lifetime spectroscopy measurements of accessible volume.

The prediction of sorption isotherms can be based on either closed system ($N_1N_2N_3\dots N_c$ PT) or open system ($N_1f_2f_3\dots f_c$ PT) simulations. We have discussed ways of calculating entire sorption isotherms, Henry's constants and heats of sorption from such simulations, carried out using either molecular dynamics or Monte Carlo techniques. Widom insertion, with configurational bias for multisite molecules, is perhaps the most straightforward way for computing solubilities from closed-system simulations. When the

penetrant molecules of interest are bulky or exhibit complex interactions with the matrix, Widom insertion in closed-system simulations and insertion moves in open-system simulations become inefficient. We have discussed ways of overcoming this insertion problem and achieving reliable predictions of sorption thermodynamics.

We have presented a statistical mechanical formulation of diffusion in binary polymer-penetrant systems, pointing out how the self- and binary diffusivities can be computed through simulation. Straightforward molecular dynamics is a convenient method for predicting diffusivities of light gases in rubbery polymers. A reliable prediction of the diffusivity requires times of observation long enough for the system to have crossed over from the anomalous to the normal, Fickian or Einstein regime of diffusion.

In low-temperature rubbery and glassy matrices, the time scales governing diffusion are typically too long to be addressed reliably with 'brute-force' MD simulation. In these cases, the use of techniques for the analysis and simulation of infrequent jumps of the penetrant between accessible regions of the polymer matrix becomes imperative. We have discussed two hierarchical approaches based on such techniques.

The Gusev-Suter approach proceeds by the following steps: (a) a free energy field is computed for the penetrant as a function of its position within the polymer matrix, on the assumption that matrix atoms execute uncorrelated harmonic vibrations around their equilibrium positions in the minimum-energy configuration; (b) three-dimensional states and two-dimensional dividing surfaces are identified by partitioning the space of penetrant positions into small cubic voxels; (c) equilibrium state probabilities and interstate transition rate constants are determined by numerical computation of configurational integrals over the state domains and dividing surfaces; (d) diffusive progress of the penetrant is tracked as a succession of jumps in the periodically replicated polymer configuration.

In the approach of Greenfield and Theodorou, which we discussed in somewhat greater detail, coupling between penetrant and polymer degrees of freedom along the reaction path of a jump is taken into account explicitly. In this approach: (a) an initial picture of states and 'macrostates' (i.e. collections of states communicating over

barriers small relative to $k_B T$) is obtained through geometric analysis of accessible volume in each glassy polymer configuration; (b) saddle points of the potential energy of the penetrant + polymer system are computed using the ‘necks’ between accessible volume clusters as initial guesses and progressively augmenting the set of degrees of freedom with respect to which the saddle point is calculated; (c) starting from the saddle points, states and reaction paths are mapped out in the multidimensional space of penetrant and polymer degrees of freedom using Fukui’s intrinsic reaction coordinate approach in a subset of flexible Cartesian or generalized coordinates; (d) rate constants for the interstate transitions are computed by multidimensional transition-state theory, after invoking a harmonic approximation; (e) macrostate equilibrium probabilities and intermacrostate rate constants are computed from the corresponding state properties; (f) large, disordered networks representing macrostates and their connectivity are generated in three-dimensional space by reverse Monte Carlo methods, which conform to the atomistically determined spatial distribution of, connectivity of, occupancy probabilities of and transition fluxes between macrostates; (g) the diffusivity is calculated through kinetic Monte Carlo simulation of a long succession of jumps in this network.

Space limitations did not allow us to discuss mesoscopic techniques for predicting the morphology of multiphase, microphase-separated or self-assembled materials often used in industrial separations. Examples of recent work in this direction include mesoscopic simulations of phase-inversion membranes formed from polymer solutions [112], dissipative particle dynamics (DPD) [113] and dynamic Density Functional Theory (Mesodyn) [114] simulations of morphology development in block copolymers and other amphiphilic systems. Today, these mesoscopic techniques are being applied to an ever widening range of problems in the materials and biological sciences. In parallel, their fundamental underpinnings are being developed further with an eye towards establishing rigorous connections to more detailed molecular modeling approaches. The hierarchy of modeling and simulation methods developed through these efforts is already having an impact on membrane design and development.

Acknowledgements

Most of the examples of sorption and diffusion modeling presented in this chapter resulted from the painstaking work of my doctoral students and collaborators Mike Greenfield, Nikos Karayiannis, Niki Vergadou, Nikos Zacharopoulos, Vasilios Raptis, George Boulougouris, Costas Chassapis, Vanessa Zervopoulou, Vlasios Mavrantzas, Ioannis Economou, John Petrou and Vasilis Melissas. The examples of polymer modeling and validation were derived from the work of Manolis Doxastakis, Vagelis Harmandaris, Christina Samara, Stelios Antoniadis, Loukas Peristeras and Dora Spyriouni. I am grateful to all of these scientists for a very stimulating and fruitful collaboration. Dr John Petropoulos’s seminal contributions to the areas of sorption and diffusion in polymers have been a lasting inspiration, and the innumerable rigorous discussions I have had the privilege of holding with him have been immensely helpful. Dr Issam Dairanieh of BP-Amoco, Naperville, IL, USA, is deeply thanked for stimulating our group’s interest in permeability problems, securing financial support to pursue this interest and providing valuable guidance. Interactions with Dr Dieter Hofmann, Dr Matthias Heuchel and Mr Martin Siegert of GKSS, Teltow, Germany, are deeply appreciated. The group is indebted to the European Commission for financial support through the PERMOD project (Project Number G5RD-CT-2000-00200) and to all PERMOD partners for an excellent collaboration.

References

- [1] E. Cussler and G. D. Moggridge, *Chemical Product Design*, Cambridge University Press, Cambridge, UK (2001).
- [2] D. N. Theodorou, ‘Understanding and predicting structure–property relations in polymeric materials through molecular simulations’, *Mol. Phys.*, **102**, 147–166 (2004).
- [3] H. Sun, ‘An ab initio force-field optimized for condensed-phase applications—overview with details on alkane and benzene compounds’, *J. Phys. Chem. B*, **102**, 7338–7364 (1998).
- [4] G. D. Smith and W. Paul, ‘United atom force field for molecular dynamics simulations of 1,4-polybutadiene based on quantum chemistry calculations on model molecules’, *J. Phys. Chem. A*, **102**, 1200–1208 (1998).

- [5] G. D. Smith, D. Y. Yoon and R. L. Jaffe, 'A force field for simulations of 1,2-dimethoxyethane and polyoxyethylene based upon ab-initio electronic structure calculations on model molecules', *J. Phys. Chem.*, **97**, 12752–12759 (1993).
- [6] S. J. Antoniadis, C. T. Samara and D. N. Theodorou, 'Molecular dynamics of atactic polypropylene melts', *Macromolecules*, **31**, 7944–7952 (1998).
- [7] V. E. Raptis, I. G. Economou, D. N. Theodorou, J. Petrou and J. H. Petropoulos, 'Molecular dynamics simulation of structure and thermodynamic properties of polydimethylsilamethylene and hydrocarbon solubility therein: Toward the development of novel membrane materials for hydrocarbon separation', *Macromolecules*, **37**, 1102–1112 (2004).
- [8] J.-P. Ryckaert, G. Ariedi and S. Melchionna, 'Molecular dynamics of polymers with explicit but frozen hydrogens', *Mol. Phys.*, **99**, 155–165 (2001).
- [9] M. P. Allen and D. J. Tildesley, *Computer Simulation of Liquids*, Clarendon Press, Oxford, UK (1987).
- [10] M. G. Martin and J. L. Siepmann, 'Transferable potentials for phase equilibria: 1. United atom description of n-alkanes', *J. Phys. Chem. B*, **102**, 2569–2577 (1998).
- [11] S. K. Nath, F. A. Escobedo and J. J. de Pablo, 'On the simulation of vapor-liquid equilibria for alkanes', *J. Chem. Phys.*, **108**, 9905–9911 (1998).
- [12] N. Ch. Karayiannis, V. G. Mavrantzas and D. N. Theodorou, 'A novel Monte Carlo scheme for the rapid equilibration of atomistic model polymer systems of precisely defined molecular architecture', *Phys. Rev. Lett.*, **88**, 105503 (2002).
- [13] P. Ungerer, C. Beauvais, J. Delhomelle, A. Boutin, B. Rousseau and A. H. Fuchs, 'Optimization of the anisotropic united atoms intermolecular potential for n-alkanes', *J. Chem. Phys.*, **112**, 5499–5510 (2000).
- [14] D. N. Theodorou, 'Molecular simulation of sorption and diffusion in amorphous polymers', in *Diffusion in Polymers*, P. Neogi (Ed.), Marcel Dekker, New York, NY, USA, pp. 67–142 (1996).
- [15] S. J. Marrink and H. J. C. Berendsen, 'Permeation process of small molecules across lipid membranes studied by molecular dynamics simulations', *J. Phys. Chem.*, **100**, 16729–16738 (1996).
- [16] D. Hofmann, L. Fritz, J. Ulbrich, C. Schepers and M. Böhning, 'Detailed atomistic molecular modeling of small molecule diffusion and solution processes in polymeric membrane materials', *Macromol. Theor. Simul.*, **9**, 293–327 (2000).
- [17] D. N. Theodorou and U. W. Suter, 'Detailed molecular structure of a vinyl polymer glass', *Macromolecules*, **18**, 1467–1478 (1985).
- [18] P. J. Flory, *Statistical Mechanics of Chain Molecules*, John Wiley & Sons, Inc. New York, NY, USA (1969).
- [19] R. Auhl, R. Everaers, G. S. Grest, K. Kremer and S. J. Plimpton, 'Equilibration of long chain polymer melts in computer simulations', *J. Chem. Phys.*, **119**, 12718–12728 (2003).
- [20] D. Frenkel and B. Smit, *Understanding Molecular Simulations*, Academic Press, New York, NY, USA (1996).
- [21] D. C. Rapoport, *The Art of Molecular Dynamics Simulation*, Cambridge University Press, Cambridge, UK (2001).
- [22] M. Tuckerman, B. J. Berne and G. J. Martyna, 'Reversible multiple time scale molecular dynamics', *J. Chem. Phys.*, **97**, 1990–2001 (1992).
- [23] G. J. Martyna, M. E. Tuckerman, D. J. Tobias and M. L. Klein, 'Explicit reversible integrators for extended system dynamics', *Mol. Phys.*, **87**, 1117–1157 (1996).
- [24] V. Harmandaris, V. G. Mavrantzas, D. N. Theodorou, M. Kröger, J. Ramírez, H. C. Öttinger and D. Vlassopoulos, 'Crossover from the Rouse to the entangled polymer melt regime: Signals from long, detailed atomistic molecular dynamics simulations, supported by rheological experiments', *Macromolecules*, **36**, 1376–1387 (2003).
- [25] V. A. Harmandaris and V. G. Mavrantzas, 'Molecular dynamics simulations of polymers', in *Simulation Methods for Polymers*, M. Kotelyanskii and D. N. Theodorou (Eds), Marcel Dekker, New York, NY, USA, pp. 177–222 (2004).
- [26] <http://www.cs.sandia.gov/~sjplimp/lammps.html>.
- [27] M. Vacatello, G. Avitabile, P. Corradini and A. Tuzi, 'A computer model of molecular arrangement in an n-paraffinic liquid', *J. Chem. Phys.*, **72**, 543–552 (1980).
- [28] (a) J. I. Siepmann and D. Frenkel, 'Configurational bias Monte Carlo: A new sampling scheme for flexible chains', *Mol. Phys.*, **75**, 59–70 (1992); (b) J. J. de Pablo, M. Laso and U. W. Suter, 'Simulation of polyethylene above and below the melting point', *J. Chem. Phys.*, **96**, 2395–2403 (1992).
- [29] T. S. Jain and J. J. de Pablo, 'Configurational bias techniques for simulation of complex fluids', in *Simulation Methods for Polymers*, M. Kotelyanskii and D. N. Theodorou (Eds), Marcel Dekker, New York, NY, USA, pp. 223–258 (2004).
- [30] L. D. Dodd, T. D. Boone and D. N. Theodorou, 'A concerted rotation algorithm for atomistic Monte Carlo simulation of polymer melts and glasses', *Mol. Phys.*, **78**, 961–996 (1993).
- [31] D. N. Theodorou, 'Variable connectivity Monte Carlo algorithms for the atomistic simulation of long-chain polymer systems', in *Bridging Time Scales: Molecular Simulations for the Next*

- Decade*, P. Nielaba, M. Mareschal and G. Ciccotti (Eds), Springer-Verlag, Berlin, Germany, pp. 69–128 (2002).
- [32] P. V. K. Pant and D. N. Theodorou, 'Variable connectivity method for the atomistic Monte Carlo simulation of polydisperse polymer melts', *Macromolecules*, **28**, 7224–7234 (1995).
- [33] V. G. Mavrantzas, T. D. Boone, E. Zervopoulou and D. N. Theodorou, 'End-bridging Monte Carlo: A fast algorithm for atomistic simulation of condensed phases of long polymer chains', *Macromolecules*, **32**, 5072–5096 (1999).
- [34] N. Ch. Karayiannis, A. E. Giannousaki, V. G. Mavrantzas and D. N. Theodorou, 'Atomistic Monte Carlo of strictly monodisperse long polyethylene melts through a generalized chain bridging algorithm', *J. Chem. Phys.*, **117**, 5465–5479 (2002).
- [35] M. Doxastakis, V. G. Mavrantzas and D. N. Theodorou, 'Atomistic Monte Carlo simulation of *cis*-1,4 polyisoprene melts II. Parallel tempering end-bridging Monte Carlo simulations', *J. Chem. Phys.*, **115**, 11352–11361 (2001).
- [36] J. Baschnagel, K. Binder, W. Paul, M. Laso, U. W. Suter, J. Batoulis, W. Jilge and T. Bürger, 'On the construction of coarse-grained models for linear flexible polymer chains: Distribution functions for groups of consecutive monomers', *J. Chem. Phys.*, **95**, 6014–6025 (1991).
- [37] W. Paul, K. Binder, K. Kremer and D. W. Heermann, 'Structure–property correlation of polymers, a Monte Carlo approach', *Macromolecules*, **24**, 6332–6334 (1991).
- [38] R. F. Rapold and W. L. Mattice, 'Introduction of short and long range energies to simulate real chains on the 2nd lattice', *Macromolecules*, **29**, 2457–2466 (1996).
- [39] P. Doruker and W. L. Mattice, 'Reverse mapping of coarse-grained polyethylene chains from the second nearest neighbor diamond lattice to an atomistic model in continuous space', *Macromolecules*, **30**, 5520–5526 (1997).
- [40] J. T. Padding and W. J. Briels, 'Time and length scales of polymer melts studied by coarse-grained molecular dynamics simulations', *J. Chem. Phys.*, **117**, 925–943 (2002).
- [41] V. G. Mavrantzas and D. N. Theodorou, 'Atomistic simulation of polymer melt elasticity: calculation of the free energy of an oriented polymer melt', *Macromolecules*, **31**, 6310–6332 (1998).
- [42] M. Murat and K. Kremer, 'From many monomers to many polymers: Soft ellipsoid model for polymer melts and mixtures', *J. Chem. Phys.*, **108**, 4340–4348 (1998).
- [43] A. A. Louis, P. G. Bolhuis, J. P. Hansen and E. J. Meijer, 'Can polymer coils be modeled as soft colloids?', *Phys. Rev. Lett.*, **85**, 2522–2525 (2000).
- [44] K. Binder, W. Paul, S. Santos and U. W. Suter, 'Coarse-graining techniques', in *Simulation Methods for Polymers*, M. Kotelyanskii and D. N. Theodorou (Eds), Marcel Dekker, New York, NY, USA, pp. 491–510 (2004).
- [45] W. Tchöp, K. Kremer, J. Batoulis, T. Bürger and O. Hahn, 'Simulation of polymer melts I. Coarse-graining procedure for polycarbonates', *Acta Polym.*, **41**, 61–74 (1998).
- [46] W. Tchöp, K. Kremer, J. Batoulis, T. Bürger and O. Hahn, 'Simulation of polymer melts II. From coarse-grained models back to atomistic description', *Acta Polym.*, **41**, 75–79 (1998).
- [47] D. Reith, M. Pütz and F. Müller-Plathe, 'Deriving effective mesoscale potentials from atomistic simulations', *J. Comput. Chem.*, **24**, 1624–1636 (2003).
- [48] N. Zacharopoulos, N. Vergadou and D. N. Theodorou, 'Coarse-graining using pre-tabulated potentials: liquid benzene', *J. Chem. Phys.*, **122**, 244111 (2005).
- [49] D. Rigby and R.-J. Roe, 'Molecular dynamics simulation of polymer liquid and glass I. Glass transition', *J. Chem. Phys.*, **87**, 7285–7292 (1987).
- [50] D. W. van Krevelen and P. J. Hoftyzer, *Properties of Polymers: Their Estimation and Correlation with Chemical Structure*, Elsevier, Amsterdam, The Netherlands (1976).
- [51] S. J. Antoniadis, C. T. Samara and D. N. Theodorou, 'Effect of tacticity on the molecular dynamics of polypropylene melts', *Macromolecules*, **32**, 8635–8644 (1999).
- [52] J. Higgins and H. Benoit, *Polymers and Neutron Scattering*, Clarendon Press, Oxford, UK (1994).
- [53] P. Gestoso, E. Nicol, M. Doxastakis and D. N. Theodorou, 'Atomistic Monte Carlo simulation of polybutadiene isomers: *cis*-1,4-polybutadiene and 1,2-polybutadiene', *Macromolecules*, **36**, 6925–6938 (2003).
- [54] W. L. Mattice and U. W. Suter, *Conformational Theory of Large Molecules*, John Wiley & Sons, Inc., New York, NY, USA (1994).
- [55] J. D. Ferry, *Viscoelastic Properties of Polymers*, John Wiley & Sons, Inc., New York, NY, USA (1980).
- [56] M. D. Ediger, D. Y. Yoon and W. Paul, 'Polymer melt dynamics', in *Simulation Methods for Polymers*, M. Kotelyanskii and D. N. Theodorou (Eds), Marcel Dekker, New York, NY, USA, pp. 407–424 (2004).
- [57] M. Doxastakis, D. N. Theodorou, G. Fytas, F. Kremer, R. Faller, F. Müller-Plathe and N. Hadjichristidis, 'Chain and local dynamics of polyisoprene as probed by experiments and molecular dynamics simulations', *J. Chem. Phys.*, **119**, 6883–6894 (2003).

- [58] G. Strobl, *The Physics of Polymers: Concepts for Understanding their Structures and Behavior*, Springer Verlag, Berlin, Germany (1997).
- [59] M. Doxastakis, M. Kitsiou, G. Fytas, D. N. Theodorou, N. Hadjichristidis, G. Meier and B. Frick, 'Component segmental mobility in an athermal polymer blend: Quasielastic neutron scattering vs simulation', *J. Chem. Phys.*, **112**, 8687–8694 (2000).
- [60] J. L. Duda and J. M. Zielinski, 'Free volume theory', in *Diffusion in Polymers*, P. Neogi (Ed.), Marcel Dekker, New York, NY, USA, pp. 143–171 (1996).
- [61] L. R. Dodd and D. N. Theodorou, 'Analytical treatment of the volume and surface area of molecules formed by an arbitrary collection of unequal spheres intersected by planes', *Mol. Phys.*, **72**, 1313–1345 (1991).
- [62] D. Hofmann, M. Entrialgo-Castano, A. Lerbret, M. Heuchel and Y. Yampolskii, 'Molecular modeling investigation of free volume distributions in stiff chain polymers with conventional and ultrahigh free volume: Comparison between molecular modeling and positron lifetime studies', *Macromolecules*, **36**, 8528–8538 (2003).
- [63] M. L. Greenfield and D. N. Theodorou, 'Geometric analysis of diffusion pathways in glassy and melt atactic polypropylene', *Macromolecules*, **26**, 5461–5672 (1993).
- [64] G. C. Boulougouris, I. E. Economou and D. N. Theodorou, 'Calculation of the chemical potential of chain molecules using the staged particle deletion scheme', *J. Chem. Phys.*, **115**, 8231–8237 (2001).
- [65] S. Arizzi, P. H. Mott, and U. W. Suter, 'Space available to small diffusants in polymeric glasses – Analysis of unoccupied volume and its connectivity', *J. Polym. Sci., Part B: Polym. Phys. Ed.*, **30**, 415–426 (1992).
- [66] H. Takeuchi and K. Okazaki, 'Relation between amorphous structure of polymers and penetrant diffusion: A molecular dynamics simulation', *Makromol. Chem., Macromol. Symp.*, **65**, 81–88 (1993).
- [67] K. Nagai, B. D. Freeman and A. J. Hill, 'Effect of physical aging of poly(1-trimethylsilyl-1-propyne) films synthesized with TaCl₅ and NbCl₅ on gas permeability, fractional free volume and positron annihilation lifetime spectroscopy parameters', *J. Polym. Sci., Part B: Polym. Phys. Ed.*, **38**, 1222–1239 (2000).
- [68] S. J. Tao, 'Positronium annihilation in molecular substances', *J. Chem. Phys.*, **56**, 5499–5510 (1972).
- [69] M. Eldrup, D. Lightbody and J. N. Sherwood, 'The temperature-dependence of positron lifetimes in solid pivalic acid', *Chem. Phys.*, **63**, 51–58 (1981).
- [70] H. Schmitz and F. Müller-Plathe, 'Calculation of the lifetime of positronium in polymers via molecular dynamics simulations', *J. Chem. Phys.*, **112**, 1040–1045 (2000).
- [71] C. Nagel, E. Schmidke, K. Günther-Schade, D. Hofmann, D. Frisch, T. Strunskus and F. Faupel, 'Free volume distributions in glassy polymer membranes: Comparison between molecular modeling and experiments', *Macromolecules*, **33**, 2242–2248 (2000).
- [72] A. Z. Panagiotopoulos, 'Monte Carlo methods for phase equilibria of fluids', *J. Phys. Condensed Matter*, **12**, R25–R52 (2000).
- [73] T. Spyriouni, I. G. Economou and D. N. Theodorou, 'Thermodynamics of chain fluids from atomistic simulation: A test of the chain increment method for chemical potential', *Macromolecules*, **30**, 4744–4755 (1997).
- [74] J. H. Petropoulos, 'Mechanisms and theories for sorption and diffusion of gases in polymers', in *Polymeric Gas Separation Membranes*, D. R. Paul and Yu. P. Yampolskii (Eds), CRC Press, Boca Raton, FL, USA, pp. 17–82 (1994).
- [75] E. Zervopoulou, V. G. Mavrantzas and D. N. Theodorou, 'A new Monte Carlo simulation approach to the prediction of sorption equilibria of oligomers in polymer melts: Solubility of long alkanes in linear polyethylene', *J. Chem. Phys.*, **115**, 2860–2875 (2001).
- [76] N. F. A. van der Vegt, 'Molecular dynamics simulations of sorption and diffusion in rubbery and glassy polymers', *Ph.D. Thesis*, University of Twente, Enschede, The Netherlands (1998).
- [77] W. C. Swope and H. C. Andersen, 'A molecular-dynamics method for calculating the solubility of gases in liquids and the hydrophobic hydration of inert-gas atoms in aqueous solution', *J. Phys. Chem.*, **88**, 6548–6556 (1984).
- [78] (a) B. Knopp, U. W. Suter and A. A. Gusev, 'Atomistically modeling the chemical potential of small molecules in dense polymer microstructures 1. Theory', *Macromolecules*, **30**, 6107–6113 (1997); (b) B. Knopp and U. W. Suter, 'Atomistically modeling the chemical potential of small molecules in dense polymer microstructures 2. Water sorption by polyamides', *Macromolecules*, **30**, 6114–6119 (1997).
- [79] A. P. Lyubartsev, A. A. Martynovskii, S. V. Shavkunov and P. N. Vorontsov-Velyaminov, 'New approach to Monte-Carlo calculation of the free energy: Method of expanded ensembles', *J. Chem. Phys.*, **96**, 1776–1783 (1992).
- [80] J. J. de Pablo, Q. Yan and F. A. Escobedo, 'Simulation of phase transitions in fluids', *Annu. Rev. Phys. Chem.*, **50**, 377–411 (1999).

- [81] Q. L. Yan and J. J. de Pablo, 'Hyperparallel tempering Monte Carlo simulation of polymeric systems', *J. Chem. Phys.*, **113**, 1276–1282 (2000).
- [82] N. F. A. van der Vegt and W. J. Briels, 'Efficient sampling of solvent free energies in polymers', *J. Chem. Phys.*, **109**, 7578–7582 (1998).
- [83] G. C. Boulougouris, I. G. Economou and D. N. Theodorou, 'On the calculation of the chemical potential using the particle deletion scheme', *Mol. Phys.*, **96**, 905–913 (1999).
- [84] S. R. de Groot and P. Mazur, *Non-Equilibrium Thermodynamics*, Dover, New York, NY, USA (1984).
- [85] R. B. Bird, W. E. Stewart and E. N. Lightfoot, *Transport Phenomena*, John Wiley & Sons, Inc., New York, NY, USA (1960).
- [86] A. A. Gusev, F. Müller-Plathe, W. R. van Gunsteren and U. W. Suter, 'Dynamics of small molecules in bulk polymers', *Adv. Polym. Sci.*, **116**, 207–247 (1994).
- [87] V. A. Harmandaris, D. Angelopoulou, V. G. Mavrantzas and D. N. Theodorou, 'Atomistic molecular dynamics simulation of diffusion in binary liquid *n*-alkane mixtures', *J. Chem. Phys.*, **116**, 7656–7665 (2002).
- [88] E. von Meerwall, E. J. Feick, R. Ozisik and W. L. Mattice, 'Diffusion in binary *n*-alkane and alkane–polyethylene blends', *J. Chem. Phys.*, **111**, 750–757 (1999).
- [89] V. A. Harmandaris, M. Doxastakis, V. G. Mavrantzas and D. N. Theodorou, 'Detailed molecular dynamics simulation of the self-diffusion of *n*-alkane and *cis*-1,4-polyisoprene oligomer melts', *J. Chem. Phys.*, **116**, 436–446 (2002).
- [90] E. von Meerwall, S. Beckman, J. Jang and W. L. Mattice, 'Diffusion of liquid *n*-alkanes: Free-volume and density effects', *J. Chem. Phys.*, **108**, 4299–4304 (1999).
- [91] J. S. Vrentas and C. M. Vrentas, 'Energy effects for solvent self-diffusion in polymer–solvent systems', *Macromolecules*, **26**, 1277–1281 (1993).
- [92] F. Müller-Plathe, S. R. Rogers and W. F. van Gunsteren, 'Gas sorption and transport in polyisobutylene – Equilibrium and nonequilibrium molecular dynamics simulations', *J. Chem. Phys.*, **98**, 9895–9904 (1993).
- [93] N. F. A. van der Vegt, W. J. Briels, M. Wessling and H. Strathmann, 'A nonequilibrium simulation method for calculating tracer diffusion coefficients of small solutes in *n*-alkane liquids and polymers', *J. Chem. Phys.*, **108**, 9558–9565 (1998).
- [94] W. Feller, *An Introduction to Probability Theory and Its Applications*, Vol. II, John Wiley & Sons, Inc., New York, NY, USA (1957).
- [95] R. L. June, A. T. Bell and D. N. Theodorou, 'Transition state studies of xenon and SF₆ diffusion in silicalite', *J. Phys. Chem.*, **95**, 8866–8878 (1991).
- [96] A. A. Gusev, S. Arizzi, U. W. Suter and D. J. Moll, 'Dynamics of light gases in rigid matrices of dense polymers', *J. Chem. Phys.*, **99**, 2221–2227 (1993).
- [97] A. A. Gusev and U. W. Suter, 'Dynamics of small molecules in dense polymers subject to thermal motion', *J. Chem. Phys.*, **99**, 2228–2234 (1993).
- [98] N. Ch. Karayiannis, V. G. Mavrantzas and D. N. Theodorou, 'Detailed atomistic simulation of the segmental dynamics and barrier properties of amorphous poly(ethylene terephthalate) and poly(ethylene isophthalate)', *Macromolecules*, **37**, 2978–2995 (2004).
- [99] (a) H. Sun, S. J. Mumby, J. R. Maple and A. Hagler, 'An ab initio CFF93 all-atom force field for polycarbonates', *J. Am. Chem. Soc.*, **116**, 2978–2987 (1994); (b) H. Sun, 'Ab initio calculations and force-field development for computer simulation of polysilanes', *Macromolecules*, **28**, 701–712 (1995).
- [100] M. L. Greenfield, 'Molecular modeling of dilute penetrant gas diffusion in a glassy polymer using multidimensional transition-state theory', *Ph.D. Thesis*, University of California, Berkeley, CA, USA (1996).
- [101] M. L. Greenfield and D. N. Theodorou, 'Coupling of penetrant and polymer motions during small-molecule diffusion in a glassy polymer', *Mol. Simul.*, **19**, 329–361 (1997).
- [102] M. L. Greenfield and D. N. Theodorou, 'Molecular modeling of methane diffusion in glassy atactic polypropylene via multidimensional Transition State Theory', *Macromolecules*, **31**, 7068–7090 (1998).
- [103] M. L. Greenfield and D. N. Theodorou, 'Coarse-grained molecular simulation of penetrant diffusion in a glassy polymer using reverse and Kinetic Monte Carlo', *Macromolecules*, **34**, 8541–8553 (2001).
- [104] M. L. Greenfield, 'Sorption and diffusion of small molecules using Transition State Theory, in *Simulation Methods for Polymers*, M. Kotelyanskii and D. N. Theodorou (Eds), Marcel Dekker, New York, NY, USA, pp. 425–490 (2004).
- [105] G. H. Vineyard, 'Frequency factors and isotope effects in solid state rate processes', *J. Phys. Chem. Solids*, **3**, 121–127 (1957).
- [106] E. M. Sevick, A. T. Bell and D. N. Theodorou, 'A chain of states method for investigating infrequent event processes occurring in multistate, multidimensional systems', *J. Chem. Phys.*, **88**, 3196–3212 (1993).
- [107] D. N. Theodorou, 'Transition-state theory investigations of small molecule diffusion in glassy polymers', in *Classical and Quantum Dynamics in Condensed Phase Simulations*, B. J. Berne,

- G. Ciccotti and D. F. Coker (Eds), World Scientific, Singapore, pp. 211–249 (1998).
- [108] J. Baker, 'An algorithm for the location of transition-states', *J. Comput. Chem.*, **7**, 385–395 (1986).
- [109] K. Fukui, 'The path of chemical reactions – the IRC approach', *Acc. Chem. Res.*, **14**, 363–368 (1981).
- [110] C. S. Chassapis, J. K. Petrou, J. H. Petropoulos and D. N. Theodorou, 'Analysis of computed trajectories of penetrant micromolecules in a simulated polymeric material', *Macromolecules*, **29**, 3615–3624 (1996).
- [111] N. Ch. Karayiannis, V. G. Mavrantzas and D. N. Theodorou, 'Diffusion of small molecules in disordered media: study of the effect of kinetic and spatial heterogeneities', *Chem. Eng. Sci.*, **56**, 2789–2801 (2001).
- [112] Y. Termonia, 'Molecular modeling of phase-inversion membranes – Effect of additives in the coagulant', *J. Membrane Sci.*, **104**, 173–179 (1995).
- [113] P. J. Hoogerbrugge and J. M. V. A. Koelman, 'Simulating microscopic hydrodynamic phenomena with dissipative particle dynamics', *Europhys. Lett.*, **19**, 155–160 (1992).
- [114] J. G. E. M. Fraaije, 'Dynamic density-functional theory for microphase separation kinetics of block-copolymer melts', *J. Chem. Phys.*, **99**, 9202–9212 (1993).

Molecular Simulation of Gas and Vapor Transport in Highly Permeable Polymers

Joel R. Fried

Advances in computer technology, the continuing development of atomistic and coarse-grained simulation methods and increased availability and sophistication of commercial and public-domain software have provided an important opportunity for significant understanding of the mechanism of diffusion of small molecules in polymeric and other systems. In Sections 3.1 and 3.2 of this chapter, relevant aspects of membrane transport and the simulation methods used to study diffusion, sorption and free volume are briefly reviewed. A summary of simulation studies of moderately to highly permeable polymers is provided in Section 3.3.

3.1 Fundamentals of Membrane Transport

There have been many excellent reviews of the diffusion and sorption of gases and vapors in polymeric membranes [1–11]. In this section, only the most important fundamental relationships for molecular transport in polymeric membranes are reviewed as background to the discussion of the molecular simulation results discussed in Section 3.3.

3.1.1 Solubility

In the case of amorphous rubbery (i.e. $T > T_g$) polymers, sorption of gases and organic vapors

at low activities can be represented by a form of Henry's law [10], as follows:

$$C = Sp_1 \quad (3.1)$$

where C is the concentration of sorbed gas or vapor, S is the solubility coefficient and p_1 is the partial pressure. At higher concentrations, S is a function of concentration [6] and Equation (3.1) can be written as:

$$C = S(C)p \quad (3.2)$$

The sorption isotherm of a rubbery polymer is no longer linear but becomes convex to the pressure axis as the penetrant pressure increases. For example, deviation from Henry's law was observed at 35 °C for the CO₂–silicone rubber system at pressures above 300 psi [12]. In that case, the Flory–Huggins equation was used to relate the penetrant activity as:

$$\ln a_1 = \ln(1 - \phi_2) + \phi_2 + \chi\phi_2^2 \quad (3.3)$$

where ϕ_2 is the polymer volume fraction, χ is the (Flory) interaction energy parameter and the penetrant activity was obtained as:

$$a_1 = \frac{p_1}{p_1^0} \quad (3.4)$$

where p_1^0 is the penetrant vapor pressure.

3.1.1.1 Temperature Dependence

The temperature dependence of the solubility coefficient is given by the van Hoff equation in the following form [13]:

$$S = S_0 \exp\left(\frac{-\Delta H_S}{RT}\right) \quad (3.5)$$

where ΔH_S is the heat of solution.

3.1.1.2 Dual-Mode Model

In the case of amorphous glassy polymers (i.e. $T < T_g$), sorption is described by the dual-mode equation [14]:

$$C = k_D p + \frac{C_H' b p}{1 + b p} \quad (3.6)$$

where k_D (typical units of $\text{cm}^3(\text{STP})/\text{cm}^3 \text{cmHg}$) is the Henry's law coefficient, C_H' is the Langmuir or hole-filling capacity of the glass and b (typical units of $(\text{cmHg})^{-1}$) is the hole-affinity constant. Both b and k_D are exponential functions of the Lennard-Jones potential-well depth-parameter, ε/k . The Henry's law coefficient may be taken as a limiting value of the solubility coefficient at zero concentration:

$$k_D = \lim_{C \rightarrow 0} S(C) \quad (3.7)$$

The Langmuir capacity is equal to the maximum concentration of solute molecules in the unrelaxed (i.e. Langmuir) domains of a glassy polymer and can be considered to be a measure of the non-equilibrium or excess free volume, V_{ex} , of the polymer, as discussed in Section 3.1.4.

3.1.1.3 Correlations

The solubility coefficient can be correlated with several quantitative measures of the condensability of the gas, such as the critical temperature, normal boiling point or ε/k . A frequently used relationship links the solubility coefficient with ε/k , as given by the following equation [15,16]:

$$\log S = \log S^0 + m(\varepsilon/k) \quad (3.8)$$

where m has a value of approximately 0.01 K^{-1} . Values of S^0 range from 0.005 to about $0.02 \text{ cm}^3(\text{STP})/\text{cm}^3 \text{ atm}$ and depend upon the polymer. Values of ε/k and other physical properties for six common gases and methane are given in Table 3.1.

3.1.2 Diffusivity

3.1.2.1 Time-Lag Measurements

In the case that the diffusion coefficients, D , are independent of penetrant concentration, D can be determined by time-lag or by equilibrium sorption measurements [14]. In the case of time-lag measurements, flux through a membrane is measured as a function of time when pressure is applied to one side of the membrane and vacuum is pulled at the other. Extrapolation of the linear region of a plot of the steady-state flux versus time provides an intercept with the time axis called the time lag, θ , from which D is obtained as follows [13,17]:

$$D = \frac{\ell}{6\theta} \quad (3.9)$$

where ℓ is the membrane thickness.

Table 3.1 Properties of gases

Parameter	Gas						
	He	H ₂	CO ₂	O ₂	N ₂	CO	CH ₄
Kinetic diameter (\AA) ^a	2.6	2.89	3.3	3.46	3.64	3.76	3.80
Diffusant diameter (\AA) ^b	2.58	—	—	3.35	3.48	—	3.79
Effective diameter, d_{eff} (\AA) ^c	1.78	2.14	3.02	2.89	3.04	3.04	3.18
Lennard-Jones potential parameter, ε/k (K) ^c	9.5	62.2	213.4	112.7	83.0	102.3	154.7
Molar volume ($\text{cm}^3 \text{ mol}^{-1}$) ^d	—	—	55.0	33.0	32.4	—	52.0
Solubility parameter (J cm^{-3}) ^{1/2d}	—	—	12.3	8.2	5.3	—	11.6

^aBased on sorption in zeolites [168].

^bGentile *et al.* [115].

^cTeplyakov and Meares [16].

^dLaPack *et al.* [246].

3.1.2.2 Dual-Mode Model

Equation (3.9) applies strictly to diffusion in rubbery polymers. In the partial immobilization model of Paul and Koros [18], separate diffusion coefficients are assigned to the two sorption sites. These are the Henry's law (D_D) and Langmuir (D_H) diffusion coefficients. The Henry's law domains are perceived as having a quasi-liquid structure similar to those occurring in rubbery polymers. The Henry's law diffusion coefficient, D_D , can be obtained from the time lag as follows:

$$D_D = \frac{\ell^2}{6\theta} [1 + f(K, F, bp_2)] \quad (3.10)$$

where $F = D_H/D_D$, $K = C'_H b/k_D$, and therefore, $f(K, F, bp_2)$ is a function of both upstream pressure, bp_2 , and the dual-mode parameters (k_D , C'_H and b). In the limit where C'_H approaches zero (i.e. the limiting case of a rubbery polymer), $f(K, F, bp_2)$ reduces to zero and Equation (3.10) reduces to the limiting case of Fickian diffusion represented by Equation (3.9).

3.1.2.3 Diffusivity from Sorption Measurements

In the case of gas or vapor sorption by a membrane, D can be obtained from the ratio of the mass of sorbed gas at time t (M_t) to the equilibrium sorption mass (M_∞) by the following relationship [19]:

$$\frac{M_t}{M_\infty} = \frac{4}{\pi^{1/2}} \left(\frac{Dt}{\ell^2} \right)^{1/2} \quad (3.11)$$

where ℓ is the thickness of the membrane. The diffusion coefficient can be obtained from the initial gradient of a plot of M_t/M_∞ versus $(t/\ell^2)^{1/2}$.

3.1.2.4 Temperature-Dependence

The diffusion coefficient increases with increasing temperature, following the Arrhenius relationship in the form [13,20]:

$$D = D_0 \exp\left(-\frac{E_D}{RT}\right) \quad (3.12)$$

where E_D is the activation energy for diffusion. In the transition-state theory of Eyring [21],

the pre-exponential factor, D_0 , is given as follows:

$$D_0 = e\lambda^2 \frac{kT}{h} \exp\left(\frac{\Delta S^*}{R}\right) \quad (3.13)$$

where λ is the mean-free path of the diffusing species, k is the Boltzmann constant, h is the Planck constant and ΔS^* is the entropy of the activated state. Meares [20] has suggested that the activation energy for diffusion can be related to the energy required to create a hole of sufficient size to allow a diffusive jump, according to the relation:

$$E_d = \lambda\pi N_A \sigma^2 \text{CED}/4 \quad (3.14)$$

where CED is the cohesive energy density of the polymer, λ is the jump length and σ is the penetrant L-J parameter.

3.1.2.5 Displacements

Bueche [22] has suggested that the diffusion coefficient can be related to diffusive jump events as follows:

$$D = \frac{\phi\lambda^2}{6} \quad (3.15)$$

where ϕ is the frequency of diffusive jumps (related to segmental mobility rate) and λ is the jump length (characteristic of the polymer).

3.1.2.6 Correlations

Teplyakov and Meares [16] have proposed a simple correlation for D as a function of the effective molecular diameter of the diffusant as follows:

$$\log D = K_1 - K_2 d_{\text{eff}}^2 \quad (3.16)$$

where K_1 is nearly independent of the polymer, while K_2 increases with increasing CED.

3.1.3 Permeability

For rubbery polymers when the diffusion coefficient is independent of pressure, the permeability coefficient can be obtained as:

$$P = DS \quad (3.17)$$

Equation (3.17) can be used to define an effective solubility coefficient as:

$$S^{\text{eff}} = \frac{P}{D} \quad (3.18)$$

where D is often obtained from time-lag measurements.

3.1.3.1 Permselectivity

The permselectivity of a polymer to one gas compared to another is expressed as the ratio of the permeabilities as follows:

$$\alpha_{ij} = \frac{P_i}{P_j} = \left(\frac{D_i}{D_j}\right) \left(\frac{S_i}{S_j}\right) \quad (3.19)$$

Ideal permselectivity is specifically defined as the ratio of *pure* gas permeabilities and is typically the reported value. As shown by Equation (3.19), diffusive and solubility selectivity both contribute to overall permselectivity. In gas separations, diffusive selectivity is usually the controlling contribution to permselectivity.

As shown by Robeson and others [23–25], permselectivity is a decreasing function of permeability, as given by the following equation:

$$P_i = k\alpha_{ij}^n \quad (3.20)$$

where the parameters k and n define an upper boundary. For O_2/N_2 separation, these values are 389 224 barrer and -5.800 , respectively, while for CO_2/CH_4 they are 1 073 700 barrer and -2.6264 , respectively [23]. Robeson plots that show the upper boundaries and include experimental permeability data for many of the polymers included in this review are given in Figures 3.1 and 3.2.

3.1.3.2 Temperature-Dependence

The temperature-dependence of the permeability coefficient can be expressed by the Arrhenius relationship [13]:

$$P = P_0 \exp\left(-\frac{E_P}{RT}\right) \quad (3.21)$$

where E_P is the activation energy of permeation. For rubbery polymers, equating Equations (3.5),

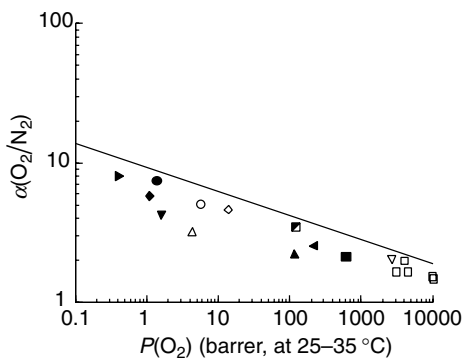


Figure 3.1 Plot of ideal permselectivity of oxygen over nitrogen against oxygen permeability at 25–35 °C. Experimental data: (■) polydimethylsiloxane; (□) poly[1-(trimethylsilyl)-1-propyne]; (◇) poly(2,6-dimethyl-1,4-phenylene oxide); (◆) bisphenol-A polysulfone; (○) tetramethylbisphenol-A polycarbonate; (●) tetrabromobisphenol-A polycarbonate; (▲) poly[bis(2,2,2-trifluoroethoxy)phosphazene] (PTFEP) [179]; (△) amorphous Teflon; (▼) bisphenol-A polycarbonate [6]; (▽) poly(4-methyl-2-pentyne) [249]; (◻) 6FDA-durene polyimide [71]; (▶) polyetherimide [250]; (◀) polytrifluoropropylmethylsiloxane [250]. Continuous line represents Robeson upper boundary [23]

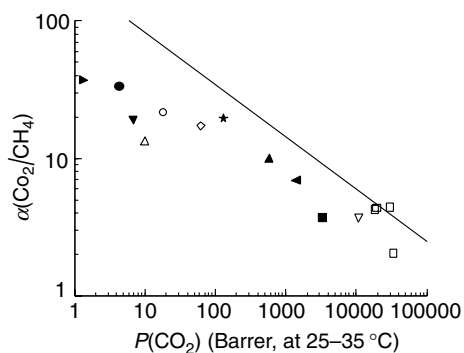


Figure 3.2 Plot of ideal permselectivity of carbon dioxide over methane against carbon dioxide permeability at 25–35 °C. Experimental data: (■) polydimethylsiloxane; (□) poly[1-(trimethylsilyl)-1-propyne]; (◇) poly(2,6-dimethyl-1,4-phenylene oxide); (◆) bisphenol-A polysulfone; (○) tetramethylbisphenol-A polycarbonate; (●) tetrabromobisphenol-A polycarbonate; (△) amorphous Teflon; (▲) poly[bis(2,2,2-trifluoroethoxy)phosphazene]; (▼) bisphenol-A polycarbonate [6]; (▽) poly(4-methyl-2-pentyne) [249]; (★) poly[*o*-(trifluoromethyl)phenylacetylene] [207]; (▶) polyetherimide [250]; (◀) poly(trifluoropropyl methyl siloxane) [250]. Continuous line represents Robeson upper boundary [23]

(3.12) and (3.21) yields the following relationship between activation energies:

$$E_P = \Delta H_S + E_D \quad (3.22)$$

3.1.3.3 Dual-Mode Model

The permeability coefficient, P , of a glassy polymer in the partial immobilization model [10] is related to D_D , D_H and the dual-mode parameters through the relationship:

$$P = k_{DP} \left(1 + \frac{FK}{1 + bp} \right) \quad (3.23)$$

3.1.4 Free Volume

3.1.4.1 Fractional Free Volume

Fractional free volume, taken as the ratio of the estimated specific free volume obtained by group-contribution methods and the polymer specific volume obtained from density measurements, is a good measure of the openness of a polymer matrix

[26,27]. Specifically, fractional free volume can be estimated from group-contribution methods as:

$$f = \frac{v - v_0}{v_0} \quad (3.24)$$

where v is the molar volume of the polymer and v_0 represents the occupied volume at 0 K per mole of repeat unit of the polymer. This occupied volume can be estimated from the van der Waals (vdw) volume, calculated as:

$$v_0 = 1.3 \times v_{vdw} \quad (3.25)$$

where v_{vdw} is the van der Waals volume calculated by the group-contribution method of Bondi [28] or the method of Sugden [29]. Representative fractional free volumes calculated by Equation (3.24) for most of the polymers cited in this review are given in Table 3.2. As shown, values range from about 0.11 for polyetherimide (PEI) to 0.34 for poly[1-(trimethylsilyl)-1-propyne] (PTMSP). Simulation studies of both PEI and PTMSP are reviewed in Sections 3.3.1 and 3.3.8, respectively. In the case of PTMSP, where both simulation results and experimental data for free volume and free volume distribution

Table 3.2 Experimental densities and free volumes of selected polymers

Polymer	ρ (g cm ⁻³)	f	V_{ex} (%)
Poly[1-(trimethylsilyl)-1-propyne] (PTMSP)	0.75 ^a	0.34 ^a	27.7
AF2400 – copolymer of 87 mol% 2,2-bis(trifluoromethyl)-4,5-difluoro-1,3-dioxole (BDD) and 13 mole% tetrafluoroethylene (TFE)	1.74 ^a	0.32 ^a	—
AF1600 – copolymer of 65 mole% 2,2-bis(trifluoromethyl)-4,5-difluoro-1,3-dioxole (BDD) and 35 mole% tetrafluoroethylene (TFE)	1.8 ^a	0.28 ^a	—
Polyvinyltrimethylsilane (PVTMS)	0.86 ^a	0.195 ^a	—
Poly(2,6-dimethyl-1,4-phenylene oxide)	1.066 ^b	0.202 ^c ; 0.206 ^b	7.4
Polyimide (6FDA–6FpDA PI)	—	0.190 ^d	—
Polyimide (6FDA–ODA PI)	1.432 ^b	0.165 ^b	—
Tetramethylbisphenol-A polycarbonate (TMPC)	1.083 ^e	0.160 ^c ; 0.168 ^e	—
Hexafluorodianhydride-3,3',4,4'-tetraaminodiphenyl oxide poly pyrrolone (6FDA–TADPO) ^f	1.405 ^f	0.196 ^f	8.8
Tetramethylhexafluoro polycarbonate (TMHFPC)	1.289 ^e	0.216 ^e	6.5
Bisphenol-A polycarbonate (PC)	1.164 ^g	0.144 ^c ; 0.158 ^g ; 0.164 ^e	3.2
Polysulfone (PSF)	1.198 ^g	0.132 ^c ; 0.138 ^g	—
Polyetherimide (PEI)	1.244 ^g	0.112 ^g	—

^aShantarovich *et al.* [195].

^bTanaka *et al.* [248].

^cHaraya and Hwang [50].

^dStern [6].

^eCostello and Koros [159].

^fWalker and Koros [54].

^gHu *et al.* [247].

are available, there is good agreement between correlation, simulation and experiment.

The temperature dependence of f is given as:

$$f = f_0 + \alpha_f(T - T_0) \quad (3.26)$$

where f_0 is the fractional free volume at the reference temperature (T_0) and α_f is the thermal expansion coefficient of the fractional free volume. Values of α_f for several polymers have been reported for the first time from positron annihilation lifetime measurements; these indicate that the range of α_f values is larger than that of the overall thermal expansion coefficients for specific volume, α [30].

3.1.4.2 Specific Free Volume

A related measure of free volume is the specific free volume (SFV) defined by Lee [31] as

$$\text{SFV} = \frac{v - v_0}{M} \quad (3.27)$$

where M is the molecular weight of the polymer repeat unit. Pilato *et al.* [32] and Lee [31] have shown reasonable correlation between SFV and permeation flux.

3.1.4.3 Packing Density

A third approach is the use of packing density, defined as follows [33]:

$$K = \frac{N_A \sum \Delta V_i}{M_0 v} \quad (3.28)$$

where N_A is the Avogadro number and ΔV_i represents atomic group-contributions to the vdv volume.

3.1.4.4 Excess Volume

An alternative parameter that is sometimes used to represent free or available volume in glassy polymers is the excess free volume, V_{ex} . The excess volume can be obtained from a dual-mode fit of a sorption isotherm (e.g. CO_2) as follows:

$$V_{\text{ex}} = \frac{C'_H V_{\text{CO}_2}}{22400} \quad (3.29)$$

where C'_H is the Langmuir capacity appearing in Equation (3.6) and V_{CO_2} is the molar volume of liquid-like CO_2 (ca. $55 \text{ cm}^3 \text{ mol}^{-1}$) [34]. Values of V_{ex} for selected polymers are included in Table 3.2 and are consistent with the ordering of f values in most cases. For example, the highest excess volume is that obtained for PTMSP (i.e. 27.7%) which also has the highest fractional free volume.

3.1.4.5 Measurements of Free Volume

Free volume can be experimentally determined by means of several methods, in particular Positron Annihilation Lifetime Spectroscopy (PALS) [35–37]. Other methods include inverse gas chromatography [38], ^{129}Xe NMR spectroscopy [39], wide-angle X-ray scattering (WAXS), photochromic and fluorescence techniques [40,41] and spin-probe measurements [42]. In the case of PALS, it has been shown that a good correlation exists between the lifetime of ortho-positronium (*o*-PS) atoms and the free volume for both simple liquids and polymers [43,44]. It is noted that there has been controversy as to whether PALS can meaningfully measure the distribution of free volume hole sizes [45–47]. Different probe methods for the estimation of free volume are considered in more length in Chapter 7 of this text.

3.1.4.6 Free Volume and Diffusion

In their classical paper, Cohen and Turnbull [48] proposed a model for self-diffusion based upon a statistical redistribution of the free volume in a liquid of hard-sphere molecules. Their relationship between the self-diffusion coefficient, D , and the average free volume per molecule, v_f , was given as:

$$D = A \exp\left(\frac{-\gamma v^*}{v_f}\right) \quad (3.30)$$

where A and γ are constants and v^* is the minimum required volume of the void. Fujita [49] applied the Cohen–Turnbull model to polymer–penetrant systems by using the fractional free volume, f , of the polymer in place of v_f , as follows:

$$D = A_d RT \exp\left(-\frac{B_d}{f}\right) \quad (3.31)$$

where values for the parameters A_d and B_d depend only on the type of the gas [50]. Simulation studies of diffusion and fractional free volume have shown that the diffusion coefficient does not follow the same correlation with total free volume over a wide range of polymers [51]. In addition to the overall static free volume, the distribution of free volume [52] and thermal fluctuations of the polymer matrix [53] are also believed to play an important role in the diffusion of small molecules.

3.1.5 *d*-Spacing

The intersegmental spacing, or *d*-spacing, can be obtained from wide-angle X-ray diffraction (WAXD) by means of the Bragg equation, in the form:

$$d = \frac{n\lambda}{2 \sin \theta} \quad (3.32)$$

where λ is the wavelength (1.54 Å for CuK α radiation) and θ is the scattering angle corresponding to the maximum of the principal peak in a plot of intensity versus the scattering angle, 2θ . Experimental *d*-spacing data has been reported for many different polymers including fluorinated polycarbonates [27] and polypyrrolone [54]. In general, *f* correlates well with values of *d*-spacing and diffusivity has been reported to increase with increasing *d*-spacing in a homologous series of polymers [55,56]. It is noted that *d*-spacing may not always provide good correlation with diffusivity (or free volume data), particularly when comparing aromatic chain polymers, with and without aromatic ring substitution [27]. In addition, there is evidence that some peak assignments may be influenced by *intramolecular* contributions [57].

3.1.6 Transport in Semicrystalline Polymers

Most polymers with high permeability are amorphous but several, such as poly(4-methyl-1-pentene) (P4M1P) [58], are semicrystalline. It has been widely accepted that crystallites act as impermeable barriers to gas diffusion in crystalline polymers, such as polyethylene. This may be attributed to the higher packing density of

most polymer crystallites. Following a two-phase model, the Henry's law solubility coefficient, k_D , of the semicrystalline polymer is proportional to the solubility coefficient of the amorphous phase (k_D^*) as:

$$k_D = \alpha k_D^* \quad (3.33)$$

where the proportional constant, α , represents the amorphous volume fraction of the polymer. On the other hand, the diffusion coefficient is influenced by restrictions of segmental mobility of the amorphous-phase chains near the amorphous-crystalline interface. A relationship between the diffusion coefficient of the semicrystalline polymer, D , and the diffusion coefficient of the totally amorphous phase, D^* , is given by:

$$D = \frac{D^*}{\tau\beta} \quad (3.34)$$

where τ is the tortuosity factor and β accounts for restricted segmental mobility near the interface. Horas and Rizzotto [59] have proposed a model for the effective diffusion coefficient of gases in partially crystalline polymers, such as polyethylene, that assumes that there is no diffusion through the crystallites and uses a Fujita-like free-volume theory for diffusion through the rubbery fraction.

3.2 Computational Methods

Computational approaches to obtain solubility and diffusion coefficients of small molecules in polymers have focused primarily upon equilibrium molecular dynamics (MD) and Monte Carlo (MC) methods. These have been thoroughly reviewed by several investigators [60–62]. For purposes of facilitating the discussion of the simulation studies reported in this chapter, some of the fundamental relationships are briefly discussed in this section as a basis of reference. A discussion of many of these aspects has been given in depth in the previous chapter by Theodorou.¹

An alternative to MD simulation to obtain diffusion coefficients is the *Transition-State Theory* (TST) of Gusev and Suter [63]. The TST is based

¹D. N. Theodorou, Chapter 2 – *Principles of Molecular Simulation of Gas Transport in Polymers*.

on the Eyring model of activated states [21]. It is particularly useful for the simulation of slow diffusion events ($D < 10^{-8} \text{ cm}^2 \text{ s}^{-1}$), such as occur in zeolites [64,65] and in several glassy polymers such as poly(vinyl chloride) [66,67], polyimides [68–71] and polycarbonate (PC) [63,72–76]. The TST approach also can be used in the determination of solubility in addition to the determination of free volume and free volume distribution. A detailed discussion of this method and a related multidimensional TST approach developed by Greenfield and Theodorou [77] has been described in detail in the previous chapter and will not be repeated here, except to briefly mention some of the relationships used to determine solubility and diffusion coefficients.

3.2.1 Solubility

The solubility of gases and vapors can be obtained by means of several computational approaches, principally the Widom particle insertion [78] and the Grand Canonical Monte Carlo (GCMC) [79] methods developed to simulate sorption isotherms for zeolites. Another approach of more limited applicability is the Polymer-Reference Interaction Site Model (PRISM) [80] which has been used to calculate the solubility of gases in amorphous polyethylene [81,82]. A fourth approach is an application of the TST method that shares a similarity with the Widom method, with the exception that probe (solute) molecules are placed at distinct grid points in the TST approach when compared to the random insertion employed by the Widom approach.

3.2.1.1 Particle Insertion Method

The solubility coefficient in the Widom particle insertion method [78] is calculated as:

$$S = \frac{22400 \text{ cm}^3(\text{STP})}{\text{mol}} \frac{1}{RT} \exp\left(-\frac{\mu^{\text{ex}}}{RT}\right) \quad (3.35)$$

where the excess chemical potential, μ^{ex} , is obtained from the simulation as:

$$\mu^{\text{ex}} = -kT \left\langle \exp\left(-\frac{E}{kT}\right) \right\rangle \quad (3.36)$$

In Equation (3.36) E is the interaction energy, k is the Boltzmann constant and the use of brackets indicates an ensemble average.

3.2.1.2 GCMC Simulation

Gas sorption isotherms can be obtained by a Grand Canonical Monte Carlo (GCMC) method [79]. This procedure employs a Metropolis algorithm [83] for sorbate insertion and deletion as well as accepting or rejecting configurational moves (i.e. orientation and position changes of sorbate molecules). The solubility coefficient is then calculated from the sorption data as:

$$S = \lim_{p \rightarrow 0} \left(\frac{C}{p} \right) \quad (3.37)$$

where C is the concentration of sorbate species in the units of $\text{cm}^3(\text{STP})/\text{cm}^3$ polymer and p is simulation pressure in atm.

3.2.1.3 TST Method

A Henry's constant H can be obtained from the TST method as [63]:

$$H = \frac{1}{VkT} \int_V \exp\left(-\frac{A(\mathbf{X})}{kT}\right) dV \quad (3.38)$$

where $A(\mathbf{X})$ is the Helmholtz energy of the dissolved gas and V is the volume of the system. As previously mentioned, the Widom and the Gusev–Suter methods are comparable in approach since both use an energy of interaction of a probe (solute) molecule with the host matrix to calculate solubilities. A difference is that insertion sites are randomly selected in the Widom method but are constrained to grid points of a regular cubic lattice in the Gusev–Suter TST model.

3.2.2 Diffusivity

The most common approach to obtain diffusion coefficients for gases and vapors is equilibrium molecular dynamics (MD). The diffusion coefficient that is obtained is a self-diffusion coefficient. Transport-related diffusion coefficients are less frequently studied by simulation but several approaches using non-equilibrium MD (NEMD) simulation have been used, as discussed briefly in this section.

3.2.2.1 MD Simulation

A self-diffusion coefficient, D_z , can be obtained from the mean-square displacement (MSD) of

one gas molecule by means of the Einstein equation in the form [84]:

$$D_z = \frac{1}{6N_z} \lim_{t \rightarrow \infty} \frac{d}{dt} \langle [\mathbf{r}_i(t) - \mathbf{r}_i(0)]^2 \rangle \quad (3.39)$$

where N_z is the number of gas molecules of type α (e.g. He, O₂, N₂, CH₄ and CO₂), $\mathbf{r}_i(0)$ and $\mathbf{r}_i(t)$ are the initial and final (at time t) positions of the center of mass of one gas molecule i over the time interval t , and $\langle [\mathbf{r}_i(t) - \mathbf{r}_i(0)]^2 \rangle$ is the mean-squared displacement (MSD) averaged over the ensemble. The Einstein relationship assumes a random walk for the diffusing species. For slow diffusing species, anomalous diffusion is sometimes observed and is characterized by:

$$\langle |\mathbf{r}_i(t) - \mathbf{r}_i(0)|^2 \rangle \propto t^n \quad (3.40)$$

where $n < 1$ ($n = 1$ for the Einstein diffusion regime) [61]. At very short times (e.g. $t < 1$ ps), the MSD may be quadratic in time (i.e. $n = 2$) which is characteristic of ‘free flight’ as may occur in a pore or solvent cage prior to collision with the pore or cage wall [61]. The result of anomalous diffusion, which may or may not occur in intermediate time scales, is to create a smaller slope at short times, resulting in a larger value for the diffusion coefficient. At sufficiently long times (i.e. the hydrodynamic limit), a transition from anomalous to Einstein diffusion ($n = 1$) may be observed.

An alternative approach to MSD analysis makes use of the center-of-mass velocity autocorrelation function (VACF) or Green–Kubo relation, given as follows [85]:

$$D = \frac{1}{3} \int \langle \mathbf{v}_i(t) \cdot \mathbf{v}_i(0) \rangle dt \quad (3.41)$$

where $\mathbf{v}_i(t)$ is the center-of-mass velocity of a single molecule. In the calculation of D from MD simulations, the Einstein relationship is usually preferred because the VACF approach tends to be ‘noisy’ at long times and often an analytical expression for the long-tail must be assumed [85]. Integration of the VACF introduces additional errors [86].

Mutual diffusion coefficients for the diffusion of a gas molecule in a polymer matrix can also be obtained from analysis of MD trajectories [87], although this is seldom pursued. A reason for this is that in most cases the penetrant

concentration in the simulation cell is extremely low and its diffusion coefficient is an order of magnitude larger than that of the polymeric segments. Under these circumstances, the self-diffusion and mutual diffusion coefficients of the penetrant are approximately equal, as related by the Darken equation [88] in the following form [89]:

$$D_{AB} = (D_A^{*x_B} + D_B^{*x_A}) \left(\frac{d \ln f_A}{d \ln c_A} \right) \quad (3.42)$$

where D_A^* is the self-diffusion coefficient, f_A is the fugacity and c_A is the concentration of diffusing A. In the limit of low concentration of diffusing A ($x_A \approx 0$), Equation (3.42) reduces to:

$$D_{AB} \equiv D_A^* \quad (3.43)$$

3.2.2.2 Diffusive Jump Events

A special opportunity afforded by molecular simulations is the ability to study the diffusion process. From plots of the MD displacement as a function of time, it has been shown that the diffusing species undergoes a ‘rattling’ motion within small cages or cavities, coupled with occasional jumps to a new cavity site in a time frame short when compared to the residence time in the cavity, as proposed by Barrer [13,90]. According to this model, the diffusion coefficient can be obtained as:

$$D = \frac{\lambda f}{6} \quad (3.44)$$

where λ is the jump distance and f is the jump frequency. At high temperatures, the jump size increases and jumps are more frequent and may become difficult to resolve in time [91,92]. The solid-like hopping mode takes place well above the glass transition temperature due to the short-time nature of the diffusive jumps for small diffusing species [92].

3.2.2.3 Non-equilibrium MD Simulation

Experimental diffusion coefficients, as obtained from time-lag measurements, report a transport diffusion coefficient which cannot be obtained from equilibrium MD simulation. Comparisons made in the simulation literature are typically

between time-lag diffusion coefficients (even calculated for glassy polymers without correction for dual-mode contributions, as discussed in Section 3.1.2) and self-diffusion coefficients. As discussed above, mutual diffusion coefficients can be obtained directly from equilibrium MD simulation but simulation of transport diffusion coefficients require the use of non-equilibrium MD (NEMD) methods [93] that are less commonly available and more computationally expensive. For these reasons, they have not been frequently used. One successful approach is to simulate a chemical potential gradient and combine MD with GCMC methods (GCMC–MD), as developed by Heffelfinger and coworkers [94,95] and MacElroy [96]. This approach has been used to simulate permeation of a variety of small molecules through nanoporous carbon membranes [97–100], carbon nanotubes [101], porous silica [102,103] and self-assembled monolayers [104]. A pseudo-non-equilibrium approach using a three-phase model and a traditional NPT–MD simulation approach has been used recently by Kikuchi *et al.* [105] to study the permeation of CO₂ in *cis*-polyisoprene. Coarse-grained methods have been combined with a NEMD method to study permeation of methane through siliceous zeolite [106]. Still another approach is to apply a directional force to the diffusing particle [107]. A diffusion coefficient then can be obtained from the relation:

$$D = \frac{kT}{F} \langle V \rangle \quad (3.45)$$

where F is an applied external force and $\langle V \rangle$ is the center-of-mass velocity component in the direction of the force averaged over time.

3.2.3 Free Volume

Free volume, as well as free volume distribution (see Section 3.1.4), can be obtained by geometric methods, including the tessellation of space within a periodic cell [108,109], by the Voorintholt method [110] which generates a van der Waals surface of the polymer chain, and by application of the TST method of Gusev and Suter, as described in the previous chapter by Theodorou. Recent alternative approaches, such as the phantom bubble method [111], have been proposed. Tessellation methods and the Voorintholt methods are described briefly below.

3.2.3.1 Tessellation of Space

Voronoi tessellation produces a distribution of polyhedra obtained through a procedure that bisects the vectors connecting one atom to all other atoms by a plane perpendicular to itself [108,109]. In an early study, Rigby and Roe [112] used Voronoi tessellations to study free volume in a hard-sphere model of *n*-alkanes. A related tessellation procedure, called the Delaunay tessellation, is obtained by joining all contiguous pairs of atoms (i.e. pairs of atoms whose polyhedra have a common face). Each set of four contiguous atoms describes a tetrahedron whose circumcenter constitutes the vertice of a Voronoi tessellation. A schematic representation of Voronoi and Delaunay tessellations in two dimensions is shown in Figure 3.3.

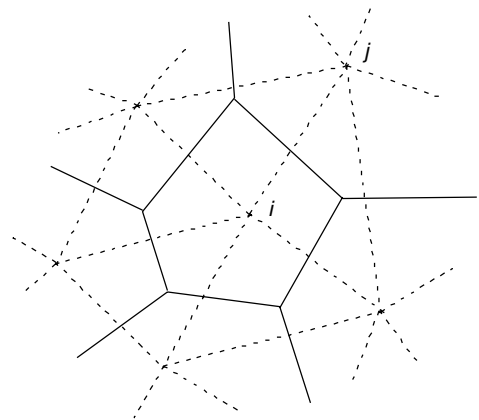


Figure 3.3 Two-dimensional representation of a Voronoi polygon around atom i . The network formed by the dashed lines is the result of the Delaunay tessellation. After Arizzi *et al.* [161]

3.2.3.2 Voorintholt Method

The Voorintholt method [110] generate a smooth van der Waals surface of a polymer chain by a grid mapping procedure. The fractional free volume is then obtained as the difference between the cell volume and the total polymer volume. The accessible free volume can be obtained by determining the surface volume of the polymer chain accessible to a probe molecule at a grid point located near around the nearest atom [113].

3.2.3.3 Accessible Free Volume

Accessible or available free volume (AFV) is the fractional free volume available to a probe molecule such as He. Shah *et al.* [114] have shown that the AFV can be determined by a MC insertion of spherical penetrant molecules of different sizes. Gentile *et al.* [115] have shown good correlation between $\log D$ and $1/\text{AFV}$. Accessible free volume also can be obtained by the TST method and in a related fashion by the Voorinhtolt method, as mentioned above.

3.2.4 d-Spacing

Simulated and experimental scattering profiles can be compared as a means of validation of the simulation methodology and the quality of the force field parameterization. From the simulation data, d -spacings can be obtained from the principal intermolecular peaks (Equation (3.32)) and used to compare with experimental values and to correlate diffusion data obtained from dynamics.

3.2.5 Pair Correlation Functions

The pair correlation function, $g_{\alpha\beta}(r)$, (or radial distribution function (RDF)) represents the probability that, given the presence of an atom at the origin of an arbitrary reference frame, there will be an atom with its center located in a spherical shell of infinitesimal thickness at a distance r from the reference atom. Pair correlations can be used to verify whether constructed periodic cells are amorphous or if some artificial ordering of chains or chain segments remain after equilibration. They can also be used to study associations of gas molecules and molecular groups or atoms along the polymer backbone or in side-chains.

3.2.6 Molecular Mobility

Information concerning main-chain and side-chain mobility from torsional [52,116] or vectorial autocorrelation function (VACF) analysis of dynamics trajectories. The autocorrelation function of torsional angle, $R_\phi(\tau)$, can be calculated as follows [116]:

$$R_\phi(\tau) = \frac{\langle \cos \phi(t - \tau) \cos \phi(t) \rangle - \langle \cos \phi(t) \rangle^2}{\langle \cos^2 \phi(t) \rangle - \langle \cos \phi(t) \rangle^2} \quad (3.46)$$

where ϕ is a time-dependent torsional angle.

In the VACF approach, a time-dependent vector, $\mathbf{u}(t)$, is assigned to a chain segment in the main chain or side chain. Orientational changes over time t can be expressed as:

$$m(t) = \langle \mathbf{u}(t_0) \cdot \mathbf{u}(t_0 + t) \rangle \quad (3.47)$$

A value of unity indicates total rigidity over the time period of the dynamics, while a value of zero indicates totally free rotation.

3.2.7 Guidelines for Molecular Simulations

3.2.7.1 Force Fields

Many different force fields have been used for MD simulation of diffusion, including early attempts to use United Atom (UA) and Anisotropic United Atom (AUA) models. The most frequently used force fields include several customized Class-I force fields – CHARMM (Chemistry at HARvard Macromolecular Mechanics) [117], DREIDING [118] and GROMOS, an early version of the current program GROMACS (*GRO*ningen *MA*chine for *C*hemical *S*imulation) [119]. One Class-II force field that is particularly successful for the simulation of polymeric systems is COMPASS (Condensed-phase Optimized Molecular Potentials for Atomistic Simulation Studies) that developed out of the ab initio-based Polymer-Consistent Force Field (pcff) [120] and its predecessor, the Consistent Valence Force Field (CVFF) [121]. COMPASS has been extensively parameterized for alkane and benzene compounds [122], phosphazenes and poly(organophosphazenes) [123], and fourteen inorganic molecules and gases, including He, Ne, Ar, Kr, Xe, H₂, O₂, N₂, NO, CO, CO₂, NO₂, CS₂ and SO₂ [124]. Force fields have been discussed in detail in the previous chapter by Theodorou. Potential energy terms for each of the major force fields used in the simulation studies discussed in Section 3.3 of this chapter are summarized in the appendices.

3.2.7.2 Cell Construction and Equilibration

To minimize the effect of chain-ends in the simulation of gas diffusion, a single polymeric chain is frequently used for building a periodic cell [60]. Careful consideration to the construction and equilibration procedures are necessary to insure a physically realistic cell. In the cases of polymers having heterocyclic or aromatic

side- or main-chain groups, such as polyimides, ring catenation and 'spearing' effects can be a problem during the building procedure. These effects can be minimized by the construction of multiple cells in order to eliminate cells with high energies or by a number of strategies such as density ramping during the building process or incorporation of small 'dummy' molecules such as methane that can be removed in subsequent equilibration steps after cell building [125]. Several recent approaches for selecting box length [126] and for equilibration [127] have been given.

3.2.7.3 Cell Size

The use of small periodic cells ($<20 \text{ \AA}$ on a side) may have an effect on the value of the diffusion coefficients and a significant effect on the value of the solubility coefficient obtained from simulation. Gusev *et al.* [60] have reported finding a 30 % difference in diffusion coefficients for He in bisphenol-A polycarbonate using simulation boxes with dimensions between 33 and 50 \AA in length. In contrast, Müller-Plathe *et al.* [128] report no significant differences in the case of O_2 diffusion in atactic polypropylene (aPP) (or O_2 in polyisobutylene) for dimensions between 20 and 30 \AA . Cuthbert *et al.* [129] looked at the effect of box size to the diffusion of three gas molecules (He and the UA equivalents of Ar and CO_2) in aPP. The largest cell was 2197 'mers' (54.5 \AA box length). There was little difference in the X-ray structure factors between the smallest (i.e. 125 'mers', 20.95 \AA) and the largest box, although the smallest box exhibited a much lower and broader distribution. They reported that a lower value of D for He was obtained when the box size was increased. Chitra and Yashonath [86] have suggested that for dimensions near 50 \AA and larger, there is little effect of cell size on the diffusion coefficient obtained from MD simulation. Recently, Neyertz and Brown [130] have extensively investigated the effect of the size of the simulation system on He diffusion in an ODPa-ODA polyimide (see Section 3.3.5) and noticed little effect of size on D when the number of atoms was varied between 4150 atoms (36.2 \AA cell length) and 56 025 atoms (86.1 \AA cell length).

Several studies have indicated that solubility may be more significantly affected by small cell size than diffusivity. For example, Cuthbert *et al.* [131] have investigated the effect of cell size on the solubility (i.e. excess chemical potential) of

gases (Ar, O_2 , N_2 , CH_4 and CO_2) in polystyrene using the Widom [78] method and a new excluded-volume map sampling technique. The five gases were represented as L-J spheres. Calculated excess chemical potentials were smaller than experimental values. A linear correlation was obtained for the largest structure (364 'mers', 39.39 \AA). They showed that CO_2 had a significantly higher excess chemical potential (i.e. lower solubility) in the smaller structures (i.e. 40, 52 and 171 'mers', or 30.63 \AA box length). These results were interpreted to indicate that there were a larger number of high-energy (overlapping) configurations when CO_2 is inserted into the polymer matrix due to a statistically smaller number of cavities of sufficient size for larger penetrants (e.g. CO_2 and CH_4 in the small boxes). It was noted that the diameter of the largest spherical cavity in the polymer structure increases from approximately 3.5 to 4.5 \AA as the simulation box length was doubled from approximately 20 to 40 \AA .

3.2.7.4 Choice of Ensembles

Molecular dynamics simulations are typically performed in the microcanonical (i.e. constant N, E, V) or in the canonical (constant N, V, T) ensembles. The former is the most straightforward approach, while choice of the frequently used NVT ensemble may cause perturbations from equilibrium as a result of energy fluctuations and consequently lead to differences in dynamic properties, such as the MSD and pair-correlation functions [132]. In the case of NVT dynamics, however, the method of temperature control can be important. For example, the use of the Nosé method was reported to reduce the discrepancy between NPT and NVE results when compared to the use of simple velocity scaling to maintain constant temperature [132]. In general, the difference between diffusion coefficients obtained using the NVT and NVE ensembles are typically insignificant [133].

3.3 Polymer Studies

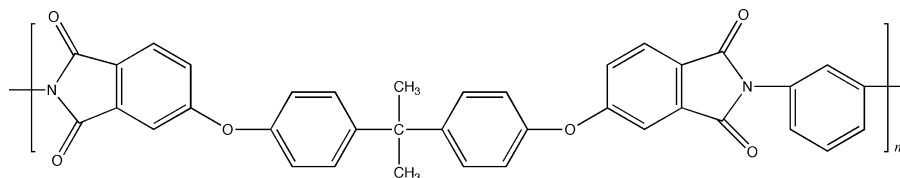
Early molecular simulations of gas solubility and diffusion focused upon the transport of small molecules such as Ar and O_2 in such polymers as polyethylene [52,84,134–139], polyisobutylene [128,140–142], atactic polypropylene [143,144],

polybutadiene [91] and polystyrene [92]. In these early studies, force fields were simple, often using united atom (UA) rather than atomistic approaches, and periods of dynamics were kept short due to the limitations of available computational facilities. For many of these reasons, results of these early simulations were less than satisfactory.

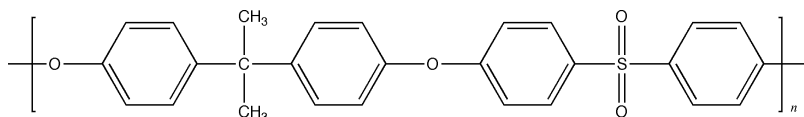
More recent simulation studies have focused on polymers with more attractive permeability and permselectivity for important gas separations, such as O_2 from N_2 and CO_2 from CH_4 . These polymers typically occupy positions near the boundaries of the Robeson plots for O_2/N_2 and CO_2/CH_4 , as shown in Figures 3.1 and 3.2, respectively. As discussed earlier, the most permeable polymer is poly[1-(trimethylsilyl)-1-propyne] (PTMSP). The latter is a high- T_g , low-density glassy polymer. The next important permeable polymer is polydimethylsiloxane (PDMS). Although less permeable, polyetherimide, polysulfones and polycarbonates have commercial importance for some membrane separation applications. Simulations studies of diffusivity, solubility and free volume for each of these polymers or polymer families, as represented in these Robeson plots – polyetherimide, polysulfones, polycarbonates, poly(2,6-dimethyl-1,4-phenylene oxide), polyimides, polyphosphazenes, polysiloxanes, poly[1-(trimethylsilyl)-1-propyne], and amorphous Teflon – as well as recent data for polysilanes and silalkylene polymers, are reviewed in the following sections.

3.3.1 Polyetherimide

Polyetherimide (PEI) (Structure 3.1) is a high-temperature ($T_g \sim 490$ K), glassy, amorphous



Structure 3.1

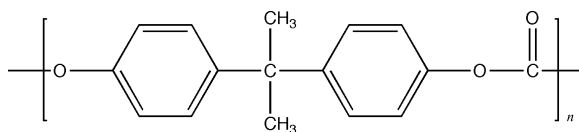


Structure 3.2

polymer which is characterized by high permselectivity for He relative to N_2 [4]. Polyetherimide has also been used as a membrane polymer for pervaporation [145]. Gas permeability and permselectivity to O_2/N_2 and CO_2/CH_4 , however, is low relative to other engineering thermoplastics, as shown by the Robeson plots of Figures 3.1 and 3.2. Recently, Lim *et al.* [146] have reported MD studies of the diffusion and solubility (Widom method [78]) of CH_4 and CO_2 in PEI using the polymer-consistent force field (pcff) approach [120]. Two chains, each built from 20 repeat units, were used to construct an amorphous cell, approximately 30 Å in length, using the self-avoiding walk method of Theodorou and Suter [147]. The density obtained from NPT dynamics was 1.18 g cm^{-3} ; this is approximately 7% lower than the experimental value of 1.27 g cm^{-3} and may signal a problem with the building or equilibration procedures. Self-diffusion coefficients obtained from simulation were significantly larger than experimental values. The high simulation values for the diffusion coefficients are consistent with the low density of the simulation cell; however, there was reasonable agreement between simulated and experimental sorption isotherms.

3.3.2 Polysulfones

Substantial permeability data has been reported for a wide variety of polysulfone structures [148–153]. The most commercially important of these is bisphenol-A polysulfone (PSF) (Structure 3.2) which is used in hollow-fiber form for commercial gas separations. The permeability properties of PSF have been widely



Structure 3.3

reported. Permeability and permselectivity of PSF for O_2/N_2 and CO_2/CH_4 are compared with other major polymers in the Robeson plots of Figures 3.1 and 3.2. Some substituted polysulfones, such as tetramethylbisphenol A polysulfone (TMPSF), exhibit permeabilities that are about four or five times higher than those for PSF.

Niemelä *et al.* [154] have used MD simulation (the pcff force field [120]) to study free volume and diffusion of He and O_2 in thirteen different polysulfones, including PSF and TMPSF. Fractional free volumes, obtained from Voronoi tessellation (Section 3.2.3) ranged from 0.149 to 0.178. Distributions of Voronoi polyhedra volumes were reported to be bimodal and even trimodal. Simulated d -spacings (Section 3.2.4) agree within about 10% of the experimental values for the wide range of polysulfones reported in this study.

3.3.3 Polycarbonates

Substantial experimental data exists for a variety of polycarbonate structures [27,148,149,155–159], especially the most important member of this family, bisphenol-A polycarbonate (PC) [160], whose structure is shown above (Structure 3.3). As illustrated in Figures 3.1 and 3.2, permeability and permselectivity for O_2/N_2 and CO_2/CH_4 for PC are roughly comparable to that of PSF. Substituted polycarbonates, especially tetramethylbisphenol-A polycarbonate (TMPC), are more permeable, as above in Figures 3.1 and 3.2. Simulation studies of PC and TMPC are reviewed below.

3.3.3.1 Simulation of Gas Transport

Experimental values of the diffusion coefficient of CO_2 in glassy PC are in the order of $10^{-8} \text{ cm}^2 \text{ s}^{-1}$. This is sufficiently low that the use of atomistic molecular dynamics to study gas diffusion in PC is computationally expensive

and most simulation studies have focused on the application of the transition-state theory (TST) of Suter and Gusev. For example, Gusev and Suter [63] have demonstrated an order-of-magnitude agreement between experimental and calculated diffusion coefficients for He, H_2 , Ar, O_2 , and N_2 at 300 K obtained by use of the TST method and a simple force field. In a subsequent study, Gusev *et al.* [73], using the pcff force field [120], showed good agreement for the activation energies of He permeation and diffusion in PC over at temperatures of 110, 175 and 300 K. Logarithmic plots of the MSD versus time, obtained by the TST method for He in PC at these three temperatures, are presented in Figure 3.4. As shown, use of the TST approach enables dynamics simulations up to the ms range which is unattainable by traditional MD methods.

López-González *et al.* [74] have reported a TST study of O_2 , N_2 and CO transport in a highly permeable copolymer of bisphenol-A polycarbonate, i.e. poly[bisphenol A carbonate-co-4,4'-(3,3,5-trimethylcyclohexylidene) diphenol carbo-

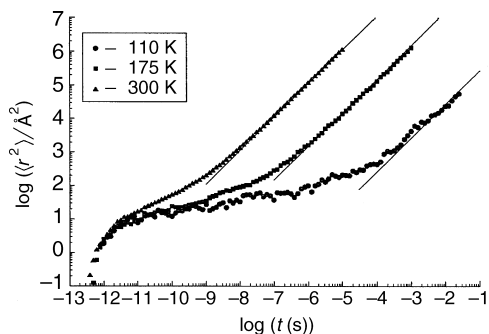
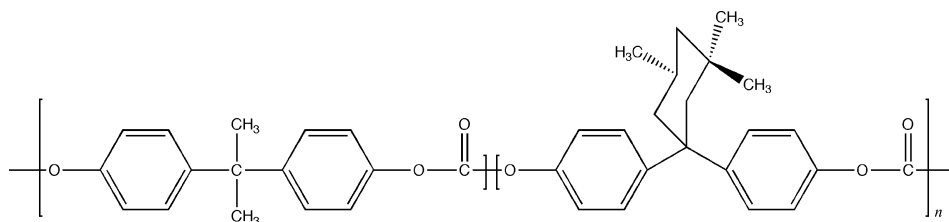


Figure 3.4 Dynamics of He molecules in bisphenol-A polycarbonate at 110, 175 and 300 K. Continuous lines represent fit of the Einstein region of the MSD data obtained from transition state method of Suter and Gusev. Reprinted with permission from A. A. Gusev, U. W. Suter and D. J. Moll, *Macromolecules*, **28**, 2582–2584 (1995). Copyright (1995) American Chemical Society



Structure 3.4

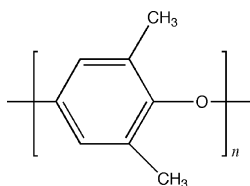
nate] (PC/PCZM) (Structure 3.4). Reasonable agreement was obtained for dynamics of these three diatomic molecules but agreement was less satisfactory for solubility and, consequently, permeability coefficients. Similar results were reported by López-González *et al.* in TST studies of the transport of Ar [75] and He [76] in PC/PCZM.

3.3.3.2 Free Volume

Hagiwara *et al.* [30] have reported free volume and the thermal expansion coefficients of volume and free volume of PC. Arizzi *et al.* [161] have reported results of Delaunay tessellation of PC. Gentile *et al.* [115] have shown that a plot of $\log D$ versus $1/\text{AFV}$ yields a straight line for both TMPC and TBPC where free volume was obtained by Delauney tessellation of space (Section 3.2.3). It was found that TMPC had a greater number of larger clusters, consistent with the higher diffusivity of this polymer. Following Equation (3.31), the inverse of the total available volumes varied linearly with $\log D$ for four gases (He, O₂, N₂ and CH₄).

3.3.4 Poly(2,6-dimethyl-1,4-phenylene oxide)

Poly(2,6-dimethyl-1,4-phenylene oxide) (PDMPO) (Structure 3.5) is a high- T_g (ca. 214 °C) engineering thermoplastic with high permeability [15,



Structure 3.5

162,163]. As shown by the Robeson plots of Figures 3.1 and 3.2, permeabilities and permselectivities lie near the middle of the group. As indicated in Table 3.2, the fractional free volume of PDMPO obtained from group contributions lies in a range between polycarbonate and PTMSP. Positron annihilation lifetime studies of PDMPO indicate that the free volume of PDMPO does not expand substantially with increasing temperature when compared to some other polymers.

3.3.4.1 Molecular Simulation Studies

Fried *et al.* [164] have reported simulation studies of the solubility and diffusivity of four gas molecules (O₂, N₂, CH₄ and CO₂) in PDMPO using the COMPASS force field [122]. Self-diffusion coefficients were obtained using 2 ns dynamics (NVT ensemble) following Equation (3.39). Solubility coefficients were obtained using the Widom particle insertion method [78]. The COMPASS force field was validated using experimental data and results from *ab initio* (e.g. HF/6-31G*) calculations of bond lengths and angles of a PDMPO dimer. As an additional validation, COMPASS results using different cutoffs for non-bonded interactions and a full Ewald summation [165] were compared to experimental unit cell data for a related polymer, poly(*p*-phenylene oxide). A 10.0 Å cutoff was found to be a reasonable tradeoff between prediction and computational efficiency. In this preliminary study, relatively small cells (single chain of 45 repeat units, 767 atoms, 20.3 Å on a side) were used and cross-terms in the COMPASS force field were excluded in the implementation of COMPASS. Simulated X-ray and glass transition data reasonably agreed with experimental values; however, the simulation density at 35 °C was significantly lower than the experimental value. This

may be attributed to a combination of simulation limitations, such as small cell size, the elimination of cross-terms as mentioned above, and perhaps incomplete equilibration. It was also noted that phenylene oxide torsion parameters were not available in the early version of COMPASS used in this study. Nevertheless, self-diffusion and solubility coefficients for O₂, N₂ and CH₄ obtained from NVT dynamics at 35 °C were in reasonable agreement with reported experimental values; however, the solubility coefficient for CO₂ was higher than that reported from experiment while the diffusion coefficient was lower. In the case of CO₂ diffusion, it was noted that traditional diffusive jumps were not evident in the displacement plots over 1 ns NVT dynamics. An argument was made that CO₂ may be trapped in a Langmuir-type hole consistent with the partial immobilization dual-mode theory of glassy polymers. The apparent diffusion coefficient calculated from the MSD data for CO₂ was comparable to that identified with D_H (see Section 3.1.2) obtained from dual-mode analysis of the experimental sorption isotherm. Results of this study suggest that simulation results should improve using longer equilibration times for this glassy polymer, longer (i.e. 5 to 10 ns) dynamics for diffusion trajectories, larger sampling statistics for solubility calculations, larger cell size (see discussion in Section 3.2.7) and a full imple-

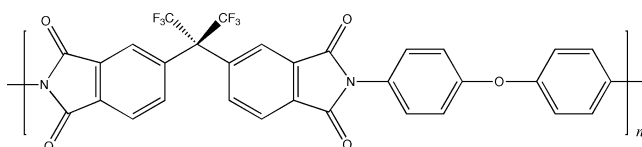
mentation of COMPASS using better defined potentials for phenylene torsion.

3.3.5 Polyimides

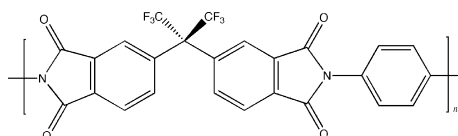
Polyimides have potential membrane applications for the separation of oxygen and nitrogen from air and for the purification of natural gas. The effect of different substituent groups on gas separation by polyimides has been reviewed by several groups [157,166–170]. The gas separation properties of fluorinated polyimides, particularly those with hexafluoroisopropylidene moieties, such as 6FDA-4,4-ODA² (Structure 3.6), have been widely studied due to their higher permeabilities and permselectivities attributed to a higher chain rigidity [27].

3.3.5.1 Molecular Simulation of Gas Transport

In an early attempt to study gas diffusion in a glassy polymer, Smit *et al.* [171] have used MD simulation to study the diffusion of CO₂ in the matrices of two polyimides – 6FDA-4,4-ODA (Structure 3.6) and 6FDA-4PDA (Structure 3.7). The GROMOS force field [119] (see Appendix 1 for details of the force field parameterization) was used for MD simulation. A soft-core potential method was used to construct small amorphous



Structure 3.6



Structure 3.7

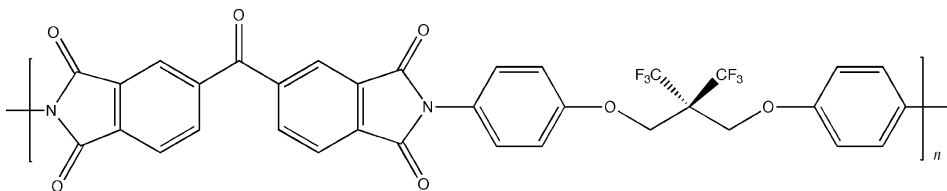
²6FDA is used to represent 2,2'-bis(3,4-dicarboxyphenyl) hexafluoropropane dianhydride.

cells containing five short polymer chains (11 repeat units each). Self-diffusion coefficients obtained at 298 K from MSD data by use of the Einstein equation (Equation (3.39)) are approximately three orders of magnitude *larger* than reported values. The authors suggest a number of reasons for this large discrepancy in diffusion results. These include the use of small polymer chains and short dynamics (maximum of 200 ps). While simulation densities were not directly compared with experimental data in this study, comparison with the experimental density reported by Heuchel and Hofmann [70] for 6FDA-4,4'-ODA reveals that the equilibration procedure used by Smit *et al.* lead to unrealistically low densities. It is probable that these equilibration issues and the very short dynamics used in this study are most likely responsible for the very high values obtained for diffusion coefficients. Of value in this study is the qualitative evidence for distinct diffusive jumps from the displacement plots.

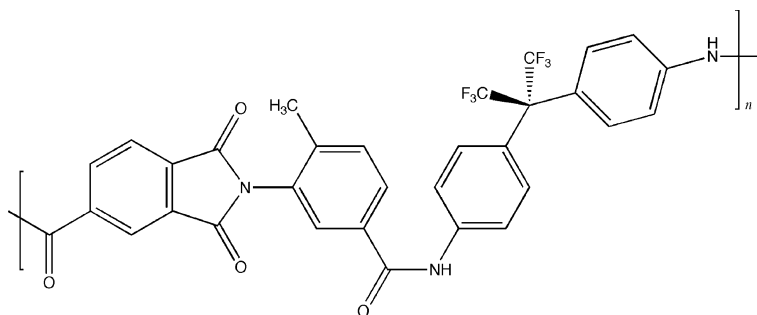
Zhang and Mattice [172] have used MD simulation (the DREIDING II force field [118]) to determine the self-diffusion coefficients of O₂ and N₂ in a high-temperature, semicrystalline PI from 3,3',4,4'-benzophenonetetracarboxylic dianhydride and 2,2-dimethyl-1,3-(4-aminophenoxy)propane (Structure 3.8) at 500 K, just below its

T_g at 503 K. Twenty-three repeat units were used for constructing an amorphous cell. To facilitate computation, a united-atom (UA) approach was used. Diffusion coefficients were obtained from the Einstein equation (Equation (3.39)) using a NVT ensemble, a time step of 3 fs, and dynamics runs up to 1.34 ns. Values for diffusion coefficients were $6.7 \times 10^{-6} \text{ cm}^2 \text{ s}^{-1}$ for O₂ and $1.7 \times 10^{-6} \text{ cm}^2 \text{ s}^{-1}$ for N₂. Although experimental diffusion data was not available for comparison, the ratio $D_{\text{O}_2}/D_{\text{N}_2} = 3.9$ was characterized as typical of other glassy polyimides. Results of the simulation indicated that for most of the time, an oxygen molecule is trapped in a void but occasionally goes into fast motion and translates rapidly to a neighboring void. During this time, there is no significant relaxation of the polymer chain, so indicating that such motions may not be important for the diffusion process. This is consistent with arguments made by Gusev and Suter in the development of the TST model. Pair correlation functions between O₂ and specific pairs of atom types were used to explore which atoms in the repeat unit experience the maximum exposure to O₂.

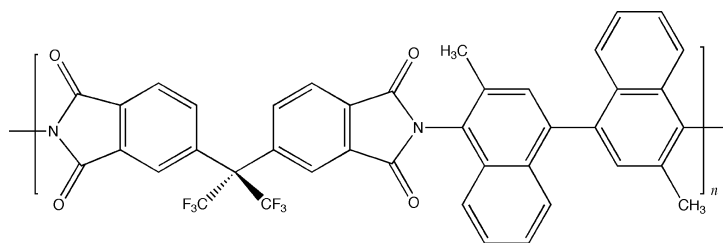
Hofmann *et al.* [173] have used MD simulation to determine the diffusion coefficients and solubilities of several gases in a 6F poly(amide imide) (PAI) (Structure 3.9) and two polyimides having



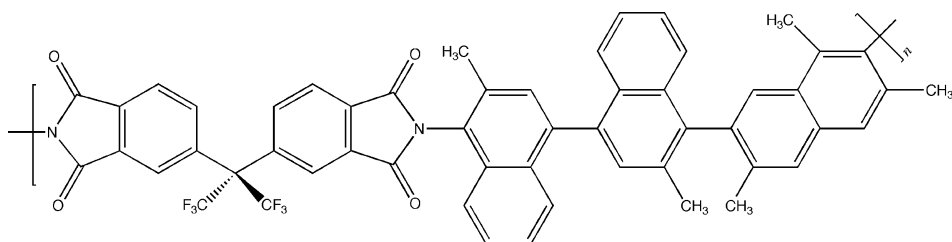
Structure 3.8



Structure 3.9



Structure 3.10



Structure 3.11

a hexafluoro group (i.e. 6FDA) functionality – PI1 (Structure 3.10) and PI2 (Structure 3.11). These polyimides were selected for their potential in O_2/N_2 and H_2/N_2 separations. PI1 has one of the highest permeabilities in the polyimide family, while PI2 is a polyimide structure that has not yet been synthesized in the laboratory. Simulation studies focused on diffusion of three to ten molecules of O_2 and N_2 in PI1 (37 repeat units) and in PI2 (30 repeat units). In the case of PAI, only H_2 diffusion was investigated in this study, due to the low gas permeability of PAI (i.e. two orders of magnitude lower than for PI1 and PI2). Two procedures for the construction of amorphous cells that involved the scaling of force field terms were investigated. For simulation of diffusion, the authors used the Insight/Discover program (Accelrys), the consistent valence force field (CVFF) [121,174], and up to 2.4 ns of NPT dynamics at 303 K. In the case of PAI, there was significant scatter of simulation values for the diffusion coefficient of H_2 but in general values were higher and sometimes significantly higher than reported values. Better agreement was achieved for simulated diffusion coefficients (in the range from 10^{-6} to 10^{-7} $cm^2 s^{-1}$) of O_2 and N_2 in PI1. Although experimental diffusion data are not available for PI2, the results were similar to PI1, hence suggesting that the addition of a

trimethylphenyl group in PI2 may have little effect on gas diffusion. Solubilities were estimated using the Widom method [78] (see Section 3.2.1). For these simulations, solubility coefficients were obtained for all three gases in PAI, PI1 and PI2. Calculated solubility coefficients were substantially higher, especially for O_2 and N_2 (up to three orders of magnitude), than the experimental values of the effective solubility coefficients (Equation (3.18)); better agreement was observed for H_2 . It was suggested that longer simulation runs (up to 100 ns), a larger number of gas molecules and a more extensive sampling of amorphous cells may provide better agreement between simulation results and the available experimental data.

In the previous study, Hofmann *et al.* [173] suggested the use of the TST method of Gusev and Suter to extend the effective simulation time to determine diffusivity and solubility. In fact, this approach was adopted in a subsequent study by Hofmann *et al.* [68] to determine the solubility and diffusion coefficients of H_2 , O_2 and N_2 in PAI and PI1. In this study, additional MD simulation data (1.2 ns at 300 K) were reported for the diffusion of H_2 in PI1 although experimental data were not available for comparison. Results for polydimethylsiloxane (PDMS), polyoctylmethylsiloxane (POMS) and

poly[1-(trimethylsilyl)-1-propyne] (PTMSP) were also included in this study. Simulation results for these three polymers are discussed in Sections 3.3.7.1 (polysiloxanes) and 3.3.8 (PTMSP). The PCFF force field [120] was used for the TST calculations. Agreement between experimental and simulation data for PAI and PII were substantially better due to the effectively longer simulation times sampled by the TST method.

In a later study, Heuchel and Hofmann [70] have used the TST method to obtain the diffusion and solubility coefficients for O₂, N₂ and CO₂ in seven different polyimides, primarily 6FDA polyimides and Kapton (PMDA-ODA) using the COMPASS force field [122]. In general, comparison between simulation and experimental values for solubility and diffusivity of O₂ and N₂ were reasonable. In the case of CO₂, solubility coefficients obtained from the TST calculations were substantially higher and diffusion coefficients were substantially lower than experimental data. This was attributed to limitations of the TST model to include structural relaxations of the polymer matrix resulting from CO₂ interaction with the PI structure.

In a recent study, Hofmann and coworkers [71] expanded their TST study (COMPASS force field [122]) to calculate solubility and diffusion coefficients of four gases (i.e. O₂, N₂, CH₄ and CO₂) in Kapton and nine 6FDA polyimides with permeabilities varying over two orders of magnitude. While there is reasonable agreement between TST simulation results and experimental data for diffusion and solubility coefficients of O₂ and N₂, the CH₄ and CO₂ solubility coefficients obtained by the TST model are too high and the diffusion coefficients are too low. As illustrated by a semilogarithmic plot of O₂/N₂ permselectivity versus O₂ permeability ($P = DS$) in Figure 3.5, there is a significant discrepancy between simulation and experimental results. Estimates of the distribution of available free volume elements available for O₂ molecules for the most perme-

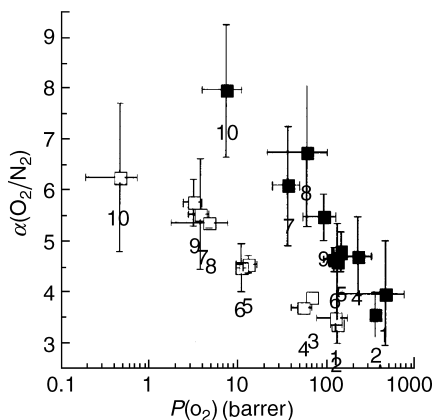
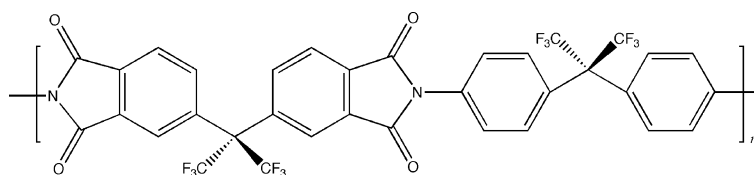


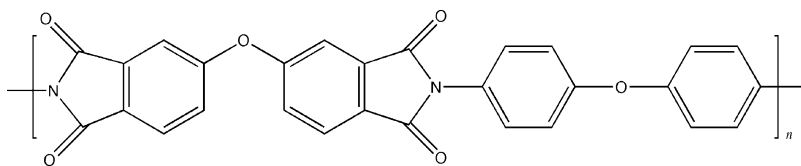
Figure 3.5 Robeson plot of experimental and simulation (TST method) values of ideal permselectivity P_{O_2}/P_{N_2} versus O₂ permeability (in units of barrer); (□) experimental data; (■) TST simulation results. Polyimide structures given in Heuchel *et al.* [71]: (1) 6FDA-durene; (2) 6FDA-3MPD; (3) 6FDA-6MTP; (4) 6FDA-TMB; (5) 6FDA-BAAF; (6) 6FDA-MDX; (7) 6FDA-ODA; (8) 6FDA-PDA; (9) 6FDA-DDS; (10) PMDA-ODA (Kapton). Reprinted with permission from M. Heuchel, D. Hofmann and P. Pullumbi, *Macromolecules*, **37**, 201–214 (2004). Copyright (2004) American Chemical Society

able polyimides, especially 6FDA-durene (O₂ permeability data compared with other polymers in Figure 3.1) demonstrate a binodal distribution that is observed for other highly permeable polymers, such as PTMSP.

One of the polymers investigated by Hoffmann and coworkers [71] in the previous study was a polyimide prepared from 6FDA and 2,2-bis(4-aminophenyl)hexafluoropropane (BAAF) (Structure 3.12). Shimazu *et al.* [57] have built a well-equilibrated amorphous cell of a single chain (30 repeat units) of 6FDA-BAAF. Simulation of wide-angle X-ray scattering (WAXS) using the DREIDING II [118] force field agreed well with experimental WAXS data. Comparison



Structure 3.12



Structure 3.13

with simulation results for a tetramer model of 6FDA–BAAF suggest that the peak corresponding to a d -spacing of 5.8 Å could not be totally attributed to intermolecular spacing but was affected by intramolecular distances containing F atoms.

Neyertz and Brown [130] have studied the effect of periodic cell size on He diffusion at 300 K in ODA–ODPA polyimide (Structure 3.13) using MD simulation. Structures containing 4150, 6225 and 56025 atoms were built using parameters from the TRIPOS 5.2 force field [175] and charges obtained from DFT (B3LYP/6-31G**) calculations [176]. Extensive structure generation and equilibration procedures resulted in simulation cells that gave excellent representation of physical properties, including densities that were within 0.7% of experimental values. The 56025-atom structure (27 uncorrelated chains) shown in Figure 3.6 is one of the largest

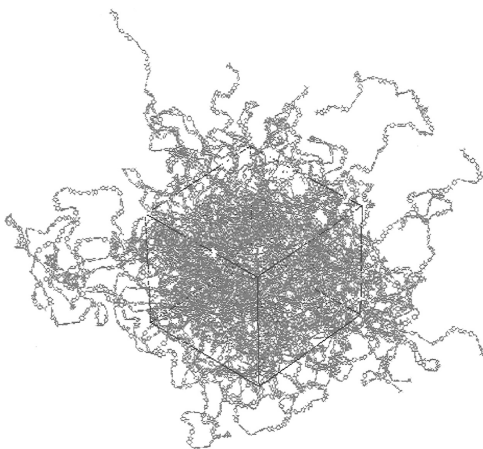
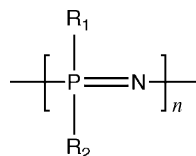


Figure 3.6 Periodic cell containing 27 chains (total of 56 025 atoms and 86.1 Å box length) of an ODA–ODPA polyimide and 225 molecules of helium. Wire-frame and space-filling models are used to represent the polyimide chains and helium molecules, respectively. Reprinted with permission from S. Neyertz and D. Brown, *Macromolecules*, **37**, 10 109–10 122 (2004). Copyright (2004) American Chemical Society

systems (86.1 Å cell length) ever used for the simulation of polymeric structures. Simulation times as long as 20 ns were employed. Crossover from anomalous to Fickian diffusion was observed by 1 ns within all cases. Results indicated that while diffusion coefficients (ca. 6.0 to $7.5 \times 10^{-6} \text{ cm}^2 \text{ s}^{-1}$) were independent of the number of atoms, they were approximately an order of magnitude larger than experimental values obtained from time-lag measurements. Reasons for this discrepancy, including force field factors, are being investigated.

3.3.6 Polyphosphazenes

A wide range of poly(organophosphazenes) have been synthesized, based upon the general structure shown in Structure 3.14, where R_1 and R_2 include a wide range of substituent groups such as alkoxy and aryloxy. The gas permeabilities of polyphosphazenes have been reported by several groups [177–181]. In terms of gas transport properties, the most extensively studied polymers of this group are polybutoxyphosphazene, where $R = \text{OC}_4\text{H}_9$, and poly[bis(2,2,2-trifluoroethoxy)-phosphazene] (PTFEP), where $R = \text{OCH}_2\text{CF}_3$.



Structure 3.14

3.3.6.1 Molecular Simulation of Gas Transport

Molecular simulation studies of polyphosphazenes have been reported by Fried and coworkers [182–184]. An early version of the COMPASS force field [122] was used in these studies. COMPASS has been fully parameterized and validated for phosphazenes [123] and has been used to

simulate the glass transition of four polyphosphazenes using NPT dynamics [185]. The first simulation study of gas transport in polyphosphazenes [182] focused on gas diffusion and solubility of He, Ne, O₂, N₂, CH₄ and CO₂ in two isomeric poly(butoxyphosphazenes) – poly[bis(*n*-butoxy)phosphazene] (PnBuP, $T_g = 165$ K) and poly[bis(*sec*-butoxy)phosphazene] (PsBuP, $T_g = 182$ K) – for which extensive gas transport properties have been reported by Hirose and Mizoguchi [178]. Self-diffusion coefficients (Equation (3.39)) were obtained from NVT dynamics using up to 3 ns simulation times. With the exception of He, good agreement was obtained between simulation and experimental (time-lag) diffusion coefficients, as correlated by the Teplyakov and Meares equation (Equation (3.16)) for both PnBuP and PsBuP. Diffusion coefficients obtained from simulation for He were significantly larger than experimental values for both polymers. This discrepancy may be attributed to force parameters for some gases. For example, force field parameters for He were obtained by fitting condensed-phase data for liquid He at 4 K [124]. The extension of this parameterization to represent diffusion of individual He molecules sorbed in a polymer at 298 K may be questionable.

Simulation values for solubility coefficients at 298 K were obtained from GCMC simulation of sorption isotherms. In the case of PnBuP, agreement between GCMC-derived solubility coefficients and effective solubility coefficients (Equation (3.18)) obtained from permeability measurements was good, with the exception that the solubility coefficient for He obtained from GCMC simulations was larger than that predicted by the Lennard–Jones correlation given by Equation (3.8). In the case of PsBuP, all GCMC-derived solubility coefficients were higher than the experimental values but followed the Lennard–Jones correlation. It was suggested that the higher solubilities obtained from GCMC simulation of an amorphous cell of PsBuP may indicate that the experimental sample used by Hirose and Mizoguchi [178] was not completely amorphous. Many polyphosphazenes exhibit two first-order transitions, $T(1)$ and T_m . In the case of alkoxy-substituted polyphosphazenes, the possibility for mesophase formation decreases as the length of the substituent group and, therefore, PnBuP would be more likely

amorphous than PsBuP, for example. Fractional free volumes of PnBuP, PsBuP and poly[bis(*iso*-butoxy)phosphazene] (PiBuP) calculated from group contributions (Equations (3.24) and (3.25)) were approximately equal, in the range between 0.084 and 0.097. The distribution of free volumes obtained from TST simulation of all three isomeric polybutoxyphosphazenes were each different and explains differences in the dependence of the diffusion coefficients on gas diameter (i.e. the slopes in the Teplyakov and Meares correlation).

Gas transport properties of PTFEP have been reported by Hirose and coworkers [177,186] and by Starannikova *et al.* [180]. The most notable feature is the high solubility of CO₂ in this polymer, as shown in the Lennard–Jones plot in Figure 3.6. For comparison are the solubility plots of two other fluorinated polymers – poly[5,5-difluoro-6,6-bis(trifluoromethyl)norbornene] (PFMNB) [187] and poly(trifluoropropyl methyl siloxane) (PTFPMS) [188] – which have been reported to show elevated CO₂ solubility. The latter has been attributed to interaction between CO₂ and the electron-withdrawing trifluoroethoxy group of PTFEP [180,186]. Interactions between CO₂ and three low-molecular-weight fluoroalkanes (CF₄, CH₃CF₃ and CH₃CH₂CF₃) were explored by high-level *ab initio* calculations (MP2/6-311++G**) [183]. Results indicated a weak interaction (up to -11.5 kJ mol⁻¹) between the quadrupole of CO₂ and the dipole of the fluoroalkyl group. Solubility coefficients obtained from GCMC simulation of sorption isotherms for He, N₂, O₂ and Xe in PTFEP followed a dependence on the Lennard–Jones potential well depth given by Equation (3.8) although values obtained from simulation using an amorphous cell were substantially larger than experimental values as previously observed for PsBuP. This can be attributed to the mesophasic structure of the experimental samples. In the case of CO₂, the solubility coefficient obtained from GCMC simulation fell above the correlation line as shown in Figure 3.7, in qualitative agreement with the experimental results (Figure 3.6). This is a strong demonstration of the ability of the COMPASS force field to represent even weak interactions due to extensive condensed-phase parameterization. As an additional validation of the utility of using COMPASS to reproduce gas–polymer interactions, results of pair-correlation

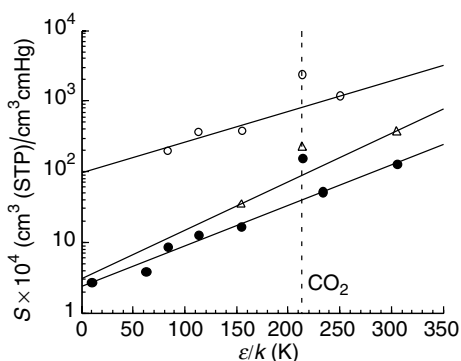


Figure 3.7 Semilogarithmic plots of gas solubility versus the Lennard–Jones potential well-depth parameters, ϵ/k . Experimental solubility data: (●) poly[bis(2,2,2-trifluoroethoxy)phosphazene], Hirose *et al.* [186]; (△) polytrifluoropropylmethylsiloxane, Stern *et al.* [188]; (○) poly[5,5-difluoro-6,6-bis(trifluoromethyl)-norbornene], Yampol’skii *et al.* [187]. Values of Lennard–Jones potential well-depth parameters were taken from Teplakov and Meares [16]. Lines are drawn by least-square fitting of the experimental data, with the exclusion of the CO₂ data point. Broken vertical line locates experimental solubility data for CO₂. Reprinted from *Polymer*, **44**, J. R. Fried and N. Hu, ‘The molecular basis of CO₂ interaction with polymers containing fluorinated groups: computational chemistry of model compounds and molecular simulation of poly[bis(2,2,2-trifluoroethoxy)-phosphazene]’, 4363–4372, Copyright (2003), with permission from Elsevier

analysis indicated a strong correlation of CO₂ with the trifluoromethyl group of PTFEP, as shown in Figure 3.8. These results agree well with the conclusions of the *ab initio* study of model compounds.

In a subsequent study, Hu and Fried [184] have reported results of the simulation of diffusion and solubility of seven gases (He, H₂, O₂, N₂, CH₄, CO₂ and Xe) in an amorphous cell and in an α -orthorhombic crystalline cell of PTFEP. Diffusion coefficients and displacements were similar in both amorphous and crystalline simulations and were comparable to experimental values. This indicates that gas diffusion is unrestricted in the crystalline state of PTFEP, as has been reported for poly(4-methyl-1-pentene) (PMP) [58,189]. In the case of PTFEP and PMP, the density of the crystalline phase is very close to that of the amorphous state due to loose packing of chains in the unit cell. In relation to solubility of the amorphous cell, it was shown that all solubility data, including that of CO₂,

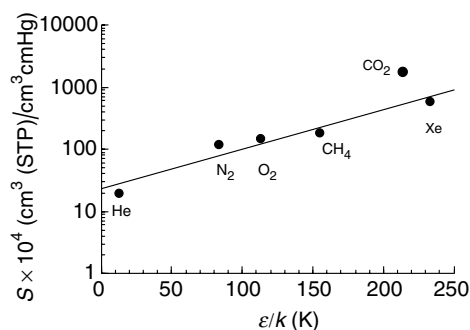


Figure 3.8 Semilogarithmic plot of gas solubility obtained at 298 K from GCMC simulation of a 150-repeat unit cell of poly[bis(2,2,2-trifluoroethoxy)phosphazene] (●) versus the Lennard–Jones potential well-depth parameters, ϵ/k , of He, N₂, O₂, CH₄, CO₂ and Xe. The Lennard–Jones potential well-depth parameters were taken from Teplakov and Meares [16]. The line represents the least-square fit ($R^2 = 0.9320$) of simulation data for the 150-repeat unit cell, with the exclusion of the CO₂ data point. Reprinted from *Polymer*, **44**, J. R. Fried and N. Hu, ‘The molecular basis of CO₂ interaction with polymers containing fluorinated groups: computational chemistry of model compounds and molecular simulation of poly[bis(2,2,2-trifluoroethoxy)-phosphazene]’, 4363–4372, Copyright (2003), with permission from Elsevier

could be correlated by the same line by incorporating a Flory interaction parameter, χ , in the form:

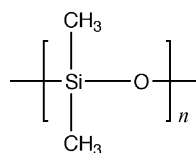
$$\log S = 0.026(\epsilon/k) - \chi - K \quad (3.48)$$

where K is a parameter that includes contribution from the partial molar volume of the sorbed gas.

3.3.7 Main-chain Silicon-containing Polymers

3.3.7.1 Polysiloxanes

Structure–permeability relationships for siloxane polymers have been reported by Stern *et al.* [188] and Lee *et al.* [26]. With the exception of the extremely high permeability of polydimethylsiloxane (PDMS) (Structure 3.15) to O₂ and CO₂



Structure 3.15

(second only to PTMSP, reviewed in Section 3.3.8), the permeability of other polysiloxanes, although moderately high, are otherwise unremarkable. Bulky substituents, such as phenyl groups, significantly reduce permeability and consequently decrease permselectivity. It has been suggested that the permeability and permselectivity of polytrifluoropropylmethylsiloxane (PMTFPS) to CO_2 is significantly enhanced due to an interaction with the trifluoropropyl group with CO_2 [188,190]; however, as shown in the Robeson plot in Figure 3.2, the position of PMTFPS in relation to the upper boundary is unremarkable. As discussed in the previous section, evidence for a weak dipole–quadrupole interaction between CO_2 and the trifluoroethoxy groups of poly[bis(2,2,2-trifluoroethoxy)phosphazene] (PTFEP) has been confirmed from both *ab initio* calculations of CO_2 and model compounds and by molecular dynamics simulation of CO_2 –PTFEP [183]. The reasons for the high permeability of PDMS are not definitely known; however, it has been suggested [191] that factors such as low intermolecular interactions, high methyl group mobility, the chain's irregular cross-section and low packing density due to the alternating dihedral angles of O–Si–O (109°) and Si–O–Si (ca. 140°) [192].

Several studies have reported results of the molecular simulation of solubility and diffusion of gases in PDMS [68,69,116,193,194]. In the earliest of these studies, Sok *et al.* [193] have reported simulation results for diffusion and solubility coefficients of He and CH_4 in PDMS at 300 K. They employed a simple force field with constrained bond lengths (SHAKE method) and simple functions for bond angle vibrations and dihedral rotations. A Lennard–Jones 6–12 potential function was used for steric interactions and a Coulombic potential was used for electrostatic interactions. In addition, a UA representation was used for CH_4 and for the CH_3 substituent groups. Diffusion coefficients were obtained using a NPT ensemble. A single penetrant molecule (He or CH_4) and five chains of 30 repeat units of PDMS were used for MD simulations. Dynamics runs for trajectory analysis were short by current standards (i.e. 150 ps for He and 250 ps for CH_4). Diffusion coefficients were obtained from MSD (Equation (3.39)). Solubility coefficients were obtained from the Widom method [78] (Equations (3.35) and (3.36)) using an acces-

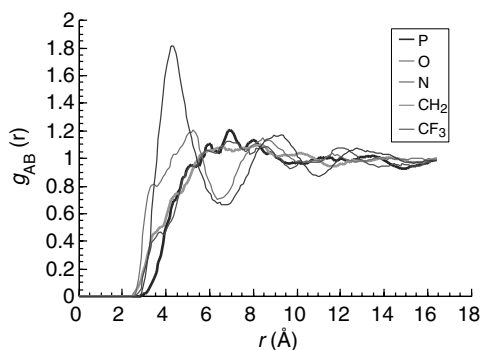


Figure 3.9 Plot of the pair correlation function, g_{AB} versus the separation distance, r , between CO_2 and the phosphorus and nitrogen atoms along the chain backbone and between CO_2 and the oxygen atoms, methylene groups and trifluoromethyl groups of the trifluoroethoxy side-chains of poly[bis(2,2,2-trifluoroethoxy)phosphazene]. Reprinted from *Polymer*, **44**, J. R. Fried and N. Hu, ‘The molecular basis of CO_2 interaction with polymers containing fluorinated groups: computational chemistry of model compounds and molecular simulation of poly[bis(2,2,2-trifluoroethoxy)phosphazene]’, 4363–4372, Copyright (2003), with permission from Elsevier

sible volume map and a probe radius that was 0.3 times the radius of the diffusant. Values for diffusion coefficients were claimed to be close to published data, as shown by comparison of simulation and experimental data in Figure 3.9 where diffusion coefficients are plotted against the square of the effective diameter of the gas molecules (Equation (3.16)) as given by Teplyakov and Meares [16]. Shantarovich *et al.* [195] have demonstrated a good correlation between $\log D$ and the square of the kinetic diameter (values given in Table 3.1) of the diffusing gases for both high- and low-free-volume glassy polymers including PTMSP, amorphous Teflon, PVTMS and PC. In contrast, solubility coefficients were significantly higher than experimental values. This discrepancy was tentatively attributed to inaccuracy of the interaction potentials and/or to an overestimation of chain flexibility. Unfortunately, subsequent simulation studies have not reported solubility results.

Trohalaki *et al.* [196] have estimated free volume fractions of PDMS and polymethylpropylsiloxane (PMPrS) using a RIS approximation to produce MC-generated conformations of short chain polysiloxanes ($DP = 10, 15, 20$ and

25) at 300 °C. Results indicated that the fractional free volume increased with increasing chain length and, at equivalent degrees of polymerization, the free volume fraction of PDMS was greater than that of PMPPrS. Fractional free volume fractions were 0.129 for PDMS and 0.109 for PMPPrS at $DP = 25$. The higher free volume fraction of PDMS (Equation (3.31)) suggests that its diffusion coefficients should exceed those of PMPPrS which is qualitatively consistent with experimental data.

Yang *et al.* [116] have used 2 ns NVT dynamics (pcff force field [120]) to compare the diffusion coefficients of He and Ne in PDMS and in poly[1-(trimethylsilyl)-1-propyne] (PTMSP) (see Section 3.3.8). An objective of this study was to explore the competition between free volume fraction and its redistribution in a low- T_g rubbery polymer and a high- T_g glass. In both cases, diffusion coefficients obtained from dynamics were in reasonable agreement with available experimental data, as shown for PDMS in Figure 3.10 where the simulation values reported from several studies are compared with experimental data. Autocorrelation function analysis of main-chain torsional angles (Equation

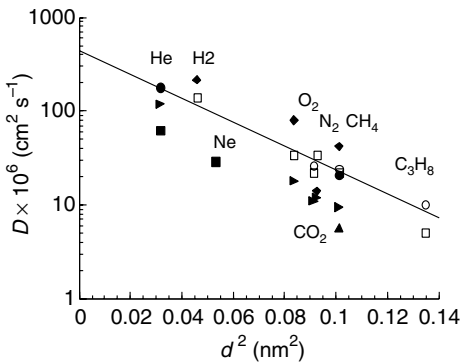


Figure 3.10 Semilogarithmic plot of self-diffusion coefficients of polydimethylsiloxane against the square of the effective gas diameter [16] of penetrant molecules (He, Ne, H₂, Ne, O₂, N₂, CO₂, CH₄ and C₃H₈): (●) MD simulation by Sok *et al.* [193]; (▲) MD simulation by Tamai *et al.* [251]; (►) MD simulation by Charati and Stern [194]; (■) MD simulation by Yang *et al.* [116]; (◆) TST simulation by Hoffman *et al.* [69,252]; (○) experimental data of Stern *et al.* [188]; (□) experimental data of Merkel *et al.* [253]. Solid line represents the least-squares fit of the combined experimental data of Stern *et al.* [188] and Merkel *et al.* [253]

(3.46)) indicated a significantly higher chain mobility of the PDMS backbone compared to PTMSP. The latter has a higher free volume due to its microporous structure resulting from its rigid chain conformation, as discussed in the following section.

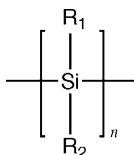
Hofmann *et al.* [69] reported the results of a TST calculation of H₂ and CH₄ diffusivity in PDMS and two other polysiloxanes (polyoctylmethylsiloxane and polymethylsilylsiloxane) using the TST approach of Gusev and Suter and the pcff [120] force field. Another study gave diffusion coefficients for O₂ and N₂ as well. As shown in Figure 3.10, diffusion coefficients obtained from TST for H₂, O₂, N₂ and CH₄ in PDMS agreed well with experimental data. Similar agreement was achieved for H₂ and CH₄ in the other two polysiloxanes. Diffusion and solubility were also determined from TST simulation for two 6F-polyimides and a PAI, as discussed in Section 3.3.5. In all cases, agreement with experiment was good. Procedures for constructing periodic cells of these rigid chain polymers were described. The most interesting part of this study was the ‘snapshots’ of 3.5 Å thick slices of the polysiloxanes, PAI and the polyimides. In the cases of both rubbery and glassy polymer simulations, channel formation was observed; however, channel formation and closure for the polysiloxanes was a rapid process (ca. 10 ps) compared to that observed for the polyimides (ca. occurring over a few ns).

Molecular simulation of transport across a membrane and under a concentration gradient, such as pervaporation, is a challenging area that has received attention only recently. In the case of pervaporation, relative solubility of the permeate(s) at the feed-membrane interface, rather than relative diffusivity, is the controlling factor affecting separation performance. Fritz and Hofmann [197] have employed molecular dynamics using a Class II force field to simulate the pervaporation of ethanol and water from aqueous solution through polydimethylsiloxane (PDMS). In this system, water exhibits a higher diffusion coefficient but a much lower solubility coefficient than ethanol in hydrophobic PDMS. Separate periodic boxes were used for modeling the bulk (i.e. membrane) phase (consisting of a single PDMS chain of 220 repeat units, three water molecules and three ethanol molecules) and the feed (ethanol and water molecules at different concentrations).

Very good agreement was found between experimental diffusion coefficients and those obtained from MD simulation for both water and ethanol in PDMS. In terms of the modeling the interfacial region, ethanol molecules preferentially moved to the PDMS–feed boundary when proper consideration of hydrogen bonding was made.

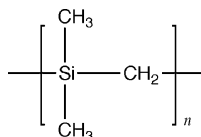
3.3.7.2 Polysilanes and Silalkylene Polymers

It has been suggested that polysilanes, with the general structure shown in Structure 3.16, have



Structure 3.16

lower permeabilities than polysiloxanes although no direct experimental studies have been reported [198]. Recently, Fried and Li [199] have reported results of a simulation study using MD, GCMC and TST methods and the COMPASS force field to investigate gas diffusion, solubility and free volume in four asymmetrically substituted polysilanes. The polysilanes included in this study were polyphenylmethylsilane (PPMSi), polycyclohexylmethylsilane (PcHMSi), poly(*n*-propylmethylsilane) (PPrMSDi) and polytrifluoropropylmethylsilane (PTFPrMSi). Comparison was made with simulation results for four different gases (O₂, N₂, CO₂ and CH₄) in two other silicon-containing polymers – PDMS (Structure 3.15) and polydimethylsilmethylene (PDMSM) (Structure 3.17). Self-diffusion coefficients obtained from NVT dynamics were intermediate between those for PDMS and PDMSM; however, gas solubility (GCMC



Structure 3.17

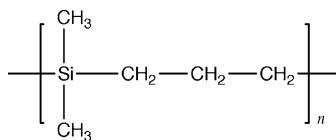
simulation) of the polysilanes was higher than any of the other silicone polymers. Fractional free volumes of the polysilanes obtained from application of TST ranged from 0.072 (PPrMSi) to 0.121 (PcHMSi). These values are intermediate between those obtained from use of TST for PDMS (0.157) and for PDMSM (0.055). Chain flexibility analysis using a vectorial autocorrelation function (VACF) (Equation (3.47)) indicates that the backbone of each of the polysilanes is very rigid compared to PDMSM and particularly PDMS. In comparison, methyl group rotation is rapid, as is the mobility of the other substituent groups. The polysilane with the highest side chain mobility is PPrMSi, which exhibits the highest diffusivity among the four polysilanes. As a consequence of high solubility, the polysilanes have high apparent permeability as estimated from the simulation results for self-diffusion and solubility coefficients (Equation (3.17)). Of the four polysilanes, PTFPrMSi may be the most interesting in terms of its high CO₂ permeability (ca. 3181 barrer³ at 298 K) and CO₂/CH₄ permselectivity (ca. 11) that would place it close to the Robeson boundary, as shown in Figure 3.2. Unfortunately, experimental permeability data are not available for comparison with the simulation results.

In another recent study, Raptis *et al.* [200] have reported results of the simulation of alkane solubility (methane to *n*-hexane) in polydimethylsilmethylene (PDMSM) which has interest as a membrane polymer for separating hydrocarbons. The simulation study used a United Atom (UA) force field parameterized from high-level (B3LYP/6-331G) DFT calculations of a dimer. Solubility coefficients at infinite dilution (S_0) were obtained at temperatures ranging from 300 to 400 K by means of the Widom particle insertion method described previously (Section 3.2.1). Heats of solution were obtained from Equation (3.5) as:

$$\Delta H_s = -R \frac{\partial(\ln S_0)}{\partial(1/T)} \quad (3.49)$$

In the cases where experimental values (IGC) for ΔH_s were available (i.e. for propane through *n*-hexane) [201], agreement was very good.

³1 barrer = 10⁻¹⁰ cm³(STP) cm/s cm² cmHg.

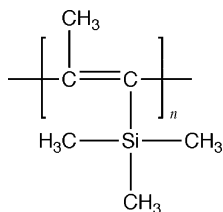


Structure 3.18

In a related study, Alentiev *et al.* [202] added experimental and simulation results for polydimethylsiltrimethylene (PDMSTM) (Structure 3.18) using the same UA force field and simulation approach employed in the previous study for PDMSM. Permeability was reported to be higher for PDMSM when compared to PDMSTM. The area of overlap between these studies and that by Fried and Li [199] was the simulation of methane permeability in PDMSM from separate determinations of CH_4 solubility and diffusivity coefficients. While individual values of CH_4 solubility and diffusivity obtained in these two research groups were higher or lower by a factor of 3 or 4, the simulated permeabilities (calculated as $P = DS$) were in good agreement (i.e. 141 barrer, obtained by Fried and Li [199] compared to 100 barrer obtained by Alentiev *et al.* [202] with the experimental value (130 barrer).

3.3.8 Poly[1-(trimethylsilyl)-1-propyne]

Several groups have reported gas permeability data for a number of disubstituted polyacetylenes [24,203–212]. As shown by the Robeson plot in Figure 3.1, permeability data for O_2 for several of the substituted polyacetylenes fall close to the upper boundary cited by Robeson [23]. A comprehensive plot of permeability data for substituted polyacetylenes has been published by Robeson *et al.* [24]. The most important and extensively studied member of this group is poly[1-(trimethylsilyl)-1-propyne] (PTMSP) (Structure 3.19) whose permeability is higher



Structure 3.19

than for PDMS and is the only one in this group whose free volume and transport properties has been studied by molecular simulation as reviewed in this section. PTMSP is a very high- T_g polymer ($T_g > 250^\circ\text{C}$) with extremely high gas permeability and free volume [213,214]. Estimates of FFV range from 0.20 to 0.36 [208,210,215]. The high end of this range lies at the low end of the range (0.37 to 0.64) typically cited for microporous carbon.

Poly[1-(trimethylsilyl)-1-propyne] also offers attractive performance for pervaporation of aqueous alcohol mixtures (e.g. ethanol–water) [216,217]. The reported O_2 permeability for PTMSP is $6 \times 10^{-7} \text{ cm}^3(\text{STP})/\text{cm}^2 \text{ s cmHg}$. This is the highest reported for any polymer [214], including PDMS, as shown in Figures 3.1 and 3.2. The permeability of PTMSP has been reported to decrease with aging [215,218] but can be stabilized by copolymerization with comonomers such as 1-phenyl-1-propyne [219]. Other than the extremely high permeability of this glassy polymer, there are several other aspects of the permeability behavior of PTMSP that are unusual. For example, the activation energy for gas permeability, E_p (Equation (3.21)), has been reported by Masuda *et al.* [207] and Nakagawa *et al.* [220] to be negative for all gases due to an extremely low activation energy for diffusion, E_D . Very recently, a study by Prabhakar *et al.* [221] has shown that the activation energy for permeation of perfluoropropane in PTMSP is positive due to its high activation energy for diffusion with respect to ΔH_s (see Equation (3.22)). In addition, large condensable vapors (e.g. C_{3+} and SF_6) show very high solubility and diffusivity in PTMSP [222,223]. In fact, PTMSP is more permeable to large, condensable organic vapors than to permanent gases such as O_2 and N_2 [224–226]. This behavior has been attributed to a competition between pore transport and surface diffusion and to pore blocking by the larger, more condensable diffusing species.

As shown by the values in Table 3.2, the fractional free volume, f , of PTMSP is the highest of any polymer, followed closely by amorphous Teflons (i.e. AF1600 and AF2400), discussed in Section 3.3.9. Results of positron annihilation studies indicate that PTMSP contains large microcavities (ca. 10 \AA) that do not change significantly in volume with time [227]. Consolati *et al.* [228] have shown from PALS that aging

reduces the number of large holes (but not their size) while the number of small holes does not change (but their size decreases). Estimates of excess volume (Equation (3.29)) range from 0.20 to 0.27 [34,229]. In a comprehensive PALS study of free volume and permeability of high- and low-free-volume glassy polymers, Shantarovich and coworkers [195,230] have reported that the size distribution of free volume elements in PTMSP and amorphous Teflons is typically bimodal; however, PTMSP has a higher concentration of large accessible free volume elements and, therefore, exhibits higher permeability than amorphous Teflons, as shown by the Robeson plots in Figures 3.1 and 3.2.

3.3.8.1 Conformational Studies

Early molecular mechanics simulations of polyacetylene and several substituted polyacetylenes, including PTMSP using the CHARMM force field [117], indicated a high torsional barrier for rotation of ca. 40 kcal mol⁻¹ around the backbone (24 repeat units) for PTMSP [231]. This value is in good agreement with more recent semiempirical (i.e. AM1 [232]) energy calculations of torsional rotations about the main chain, indicating a torsional barrier of 45 to 48 kcal mol⁻¹. These values indicate a very stiff backbone when compared to the highly flexible backbone of polydimethylsiloxane. By contrast, torsional barriers for methyl and trimethylsilyl groups of the dimer were low (i.e. 0.65 kcal mol⁻¹ and 4 to 5 kcal mol⁻¹, respectively).

3.3.8.2 Simulation of Gas Transport

Several studies have looked at the simulation of gas diffusion in PTMSP. The first simulation study of gas (He, O₂, N₂, CO₂ and CH₄) solubility and diffusivity in PTMSP was reported by Fried and Goyal [233]. The generic DREIDINGII force field [118] was used in this study; however, the parameterization of DREIDING is biased towards the first-row elements and carbon and gives high torsional energy barriers for silicon-containing molecules. For that reason, parameterization for bond lengths, bond angles and dihedral terms containing the Si atom in the trimethylsilyl group were obtained from semiempirical molecular orbital (AM1 [232]) calculations of a TMSP dimer. Charges (ESP) also were assigned from

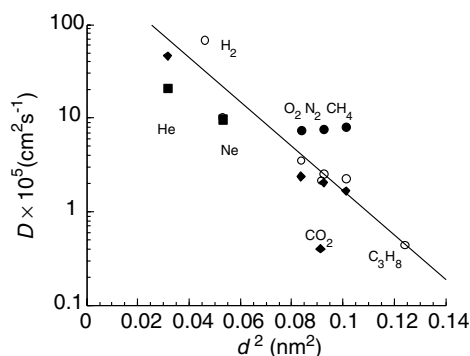


Figure 3.11 Semilogarithmic plot of self-diffusion coefficients of poly[1-(trimethylsilyl)-1-propyne] against the square of the effective gas diameter [16] of penetrant molecules (He, Ne, O₂, N₂, CO₂ and CH₄): (◆) MD data of Fried and Goyal [233]; (■) MD data of Yang *et al.* [116]; (●) TST data of Hofmann *et al.* [69,252]; (○) Experimental data of Nakagawa *et al.* [206]. Continuous line represents least-squares fit of the experimental data

MNDO (MOPAC 6.0) energy calculations of the dimer. Nonbonded terms were left unchained from the generic DREIDING values in this study. Diffusion coefficients were obtained from 0.5 ns NVT-dynamics using periodic cells about 23 Å on a side. Equilibrated cell densities of 100 cells averaged 0.821 g cm⁻³; this value agrees reasonably well with densities reported in the literature [24,205,234] in the range from 0.75 to 0.81 g cm⁻³. As shown in Figure 3.11, there is good agreement between self-diffusion coefficients obtained *in silico* and experimental (time-lag) data. One principal exception was of CO₂. Problems with the CO₂ simulation results for diffusion and solubility were attributed to issues with the force field parameterization for CO₂, as confirmed in a subsequent study [113]. A good correlation was obtained between gas diffusion coefficients for O₂ obtained from NVT dynamics and *d*-spacing obtained from simulation of the WAXD pattern for PTMSP and experimental diffusion and *d*-spacing data for PTMSP and other polymers, including polysulfone, polycarbonate, poly(2,6-dimethyl-1,4-phenylene oxide) and polydimethylsiloxane, and several polyimides. As shown in Figure 3.12, solubility coefficients obtained from GCMC and Widom particle insertion methods agreed reasonably well with experimental data and all correlated with the

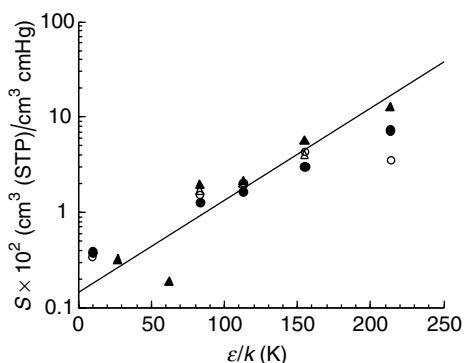


Figure 3.12 Semilogarithmic plot of solubility coefficients of gas molecules (He, Ne, O₂, N₂, CO₂ and CH₄) in poly[1-(trimethylsilyl)-1-propyne] against the square of the effective Lennard–Jones potential well-depth parameter, ϵ/k [16]: (○) Widom method, Fried and Goyal [233]; (●) GCMC method, Fried and Goyal [233]; (▲) TST method, Hofmann *et al.* [252]; (▲) Experimental data of Nakagawa *et al.* [206]. Continuous line represents least-squares fit of the experimental data

Lennard–Jones potential expression given by Equation (3.8).

In a subsequent study, Zheng and Fried [235] reported results of GCMC simulation (see Section 3.2.1) of sorption of four alkanes (methane, ethane, propane and *n*-butane) and several mixtures of alkanes or hydrogen and alkanes at 300 K and for pressures ranging from 2 to 50 kPa (0.02 to 0.5 atm). In this study, the DREIDINGII force field parameterized by Fried and Goyal [233] was used for simulation of both PTMSP and the alkanes. A single chain consisting of 160 repeat units was used to build amorphous cells (ca. 34.5 Å on a side); average density was 0.76 g cm⁻³ which compares well with the experimental values cited earlier. To facilitate computations, smaller cells (i.e. 80 repeat units; ca. 27 Å in length) were used to determine heats of solution at five additional temperatures (308, 320, 340, 360 and 400 K). Sorption isotherms obtained from the GCMC simulations were in good agreement with those reported by Merkel *et al.* [236] at low pressures (< 0.1 atm) but underestimated solubility at higher concentrations. The discrepancy noted in the high-pressure results can be attributed to the fixed volume constraint of the GCMC method that does not allow for swelling during sorption. Solubility coefficients obtained from the limiting

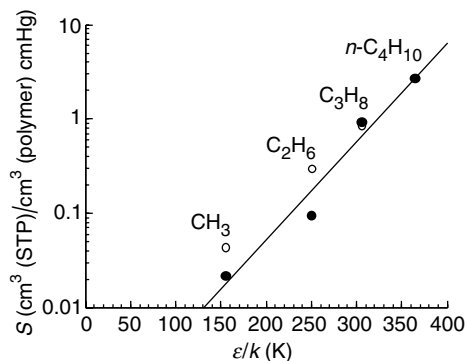


Figure 3.13 Semilogarithmic plot of solubility coefficients, S , as a function of the Lennard–Jones potential well-depth parameter, ϵ/k (values from Teplyakov and Meares [16]), for methane, ethane, propane and *n*-butane in poly[1-(trimethylsilyl)-1-propyne]. Solubility results include GCMC simulations (●) of Zheng and Fried [253] at 300 K (160-‘mer’ cell) and the gravimetric measurements (○) reported by Merkel *et al.* [236]. Continuous line represents the least-squares fit of simulation values. Copyright (2001) from ‘Monte Carlo simulation of the sorption of pure and mixed alkanes in poly[1-(trimethylsilyl)-1-propyne]’ by T. Zheng and J. R. Fried, *Sep. Sci. Technol.*, **36**(5–6) (2001). Reproduced by permission of Taylor & Francis Group, LLC., <http://www.taylorandfrancis.com>

slope of the GCMC sorption isotherms, however, were in excellent agreement with results of gravimetric measurements reported by Merkel *et al.* [236], as indicated by the Lennard–Jones potential-well plot (Equation (3.8)) shown in Figure 3.13. Heats of sorption were obtained from the van Hoff equation (Equation (3.5)) for all four alkanes; however, experimental values for comparison were available only for methane. In this case, the simulation value (−3.075 kcal mol⁻¹) agreed well with the experimental value (−3.3 kcal mol⁻¹) reported by Starannikova and Teplyakov [211]. GCMC simulation of sorption of 50/50 mol% mixtures of hydrogen/propane and hydrogen/*n*-butane confirmed the conclusions of several experimental studies [224–226] that there is a competition for sorption sites by more condensable organic vapors over permanent gases which results in this unusual permselectivity of PTMSP for larger molecular species. Free volume was explored in this study by application of the Voorintholt geometric method [110]. The fractional free volume of PTMSP was determined

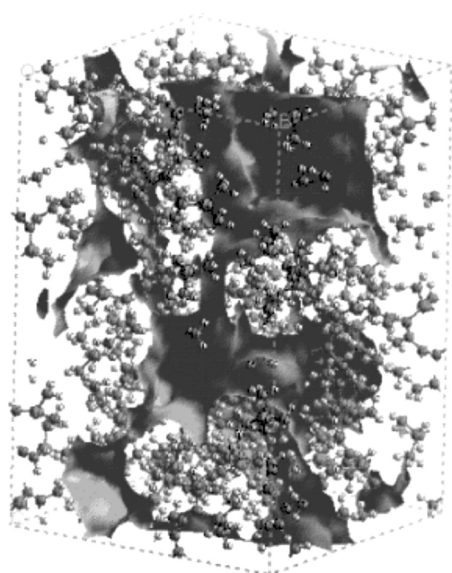


Figure 3.14 Methane-accessible free volume (black/grey) regions in a PTMSP amorphous cell (ball and stick representation), determined by application of the Voorintholt [110] method. Copyright (2001) from 'Monte Carlo simulation of the sorption of pure and mixed alkanes in poly[1-(trimethylsilyl)-1-propyne]' by T. Zheng and J. R. Fried, *Sep. Sci. Technol.*, **36**(5–6) (2001). Reproduced by permission of Taylor & Francis Group, LLC., <http://www.taylorandfrancis.com>

to be 0.35, which agrees well with Bondi group-contribution calculations (Table 3.2). In addition, accessible free volumes were determined by application of the Voorintholt method for methane. As shown in Figure 3.14, the available free volume sites have a broad distribution of small and large free volume elements. While the small free volume elements are dispersed throughout the polymer matrix, the large elements are interconnected to form continuous channels.

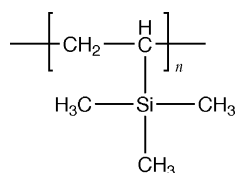
Madkour [237] has used the hard-probe method of Rigby and Roe [112] to determine the fractional free volume of PTMSP and the five other polymers related in structure. The MNDO-derived charges and the AM1-derived bonded parameterization for DREIDING obtained by Fried and Goyal [233] were used in the simulations. Interestingly, fractional free volume fell in the range of ca. 0.3 for all six polymers. Diffusivity obtained from analysis of the MD trajectories for Ar and N₂ also did not change significantly; however, MD time intervals were very short

(i.e. 50 ps) in this study. Madkour suggested that a combination of high free volume, high torsional barriers for rotation around the main chain and high specific electrostatic (i.e. Coulombic) interactions due to the high positive charge of Si all contribute to high diffusion coefficients.

Results of a comparative study of He and Ne diffusion in PTMSP and PDMS by Yang *et al.* [116] were discussed earlier in Section 3.3.7.1. MD simulation (2 ns NVT dynamics at 300 K) of He diffusion in PTMSP (50 repeat units) gave good agreement with experimental results. It was concluded in that study that the high fractional free volume of PTMSP was a more significant factor for the high diffusivity of light gases than free volume redistribution resulting from high segmental mobility as occurs in PDMS.

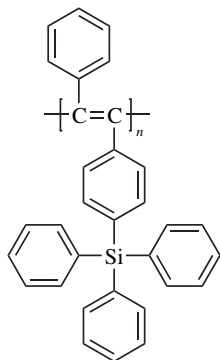
Hofmann *et al.* [238] have reported simulation studies for PTMSP and two moderate-free-volume Si-substituted polystyrenes using the COMPASS [123] force field. Free volume distributions were determined by the TST method of Suter and Gusev. Inspection of the free volume regions appearing in the simulation indicated a population of large, elongated microcavities in the amorphous cells of PTMSP (499 repeat units). Fractional free volumes obtained by the TST method were dependent upon probe size; values calculated by the method of Bondi ranged from 0.327 to 0.290. Free volume distribution obtained by the TST model indicated a broad, continuous distribution.

In a subsequent and more ambitious study, Hofmann *et al.* [125] expanded the study to include Teflon AF1600 and AF2400 (Section 3.3.9), polyvinyltrimethylsilane (PVTMS) (Structure 3.20) and two polyacetylenes with high aromatic substitution. These were poly{1-phenyl-2-[*p*-(triphenylsilyl)phenyl]acetylene} (PPhSiDPA) (Structure 3.21) and poly{1-phenyl-2-[*p*-(triisopropylsilyl)phenyl]acetylene} (PPrSiDPA) (Structure 3.22). Extensive equilibration procedures were used to build large amorphous cells (up to 49 Å in length

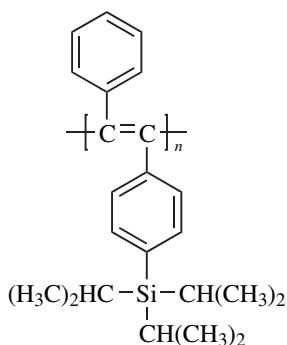


Structure 3.20

and containing as many as 9500 atoms). Solubility data (TST method) were used to evaluate the quality of the equilibrated structures. It was noted that the fractional free volumes obtained by the TST method were about 1.3 to 1.6 times larger than those calculated by the Bondi method (Section 3.1.4), suggesting that Equation (3.25) may not provide an adequate representation of packing density of glassy polymers. Fractional accessible free volumes (FAVs) obtained by the TST method using the COMPASS [123] force field were



Structure 3.21

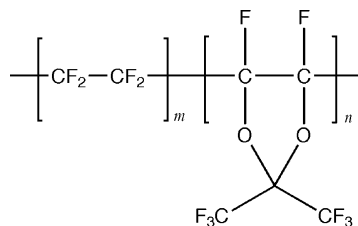


Structure 3.22

obtained by using a probe with the same radius (i.e. 1.1 Å) as an orthopositronium (o-PS) atom for comparison with PALS measurements. Fractional free volumes were also obtained by using an oxygen molecule as a probe (radius of 1.73 Å). There was reasonable correlation between $\log D(\text{O}_2)$ and $1/\text{FAV}$ (O_2 probe) for all polymers used in this study. As shown in Figure 3.15, the contribution of larger holes to free volume is greatest for PTMSP, followed by AF2400 and AF1600 in the order of decreasing permeability. The effect of physical aging on the free volume distribution of PTMSP was studied by simulation of a PTMSP cell built at a higher density (0.95 g cm^{-3}), as observed for actual aged samples. Two ways of evaluating FAV were used. The R_{max} method split holes of complex geometry into smaller ones of more compact shape. There was good agreement between the FFVs obtained from the o-PS probe data and PALS measurements. As shown in Figure 3.15 (PTMSP-095), this simulated annealing resulted in a loss of large free volume sites and a narrowing of the free volume distribution. The low permeabilities of PPrSiDPA, PPhSiDPA, PVTMS and PTMSS were consistent with their narrow free volume distribution at the low-free-volume end.

3.3.9 Amorphous Teflon

Teflon-AF is a statistical copolymer of tetrafluoroethylene (TFE) and a fluorinated cyclic ether (perfluorodioxole) such as 2,2-bis(trifluoromethyl)-4,5-difluoro-1,3-dioxole (BDD)⁴ that has very high permeability and excellent chemical resistance (Structure 3.23). The copolymerization serves to reduce crystallinity. Amorphous Teflons can be used to separate organic mixtures by pervaporation



Structure 3.23

⁴Poly[2,2-bis(trifluoromethyl)-4,5-difluoro-1,3-dioxole-co-tetrafluoroethylene].

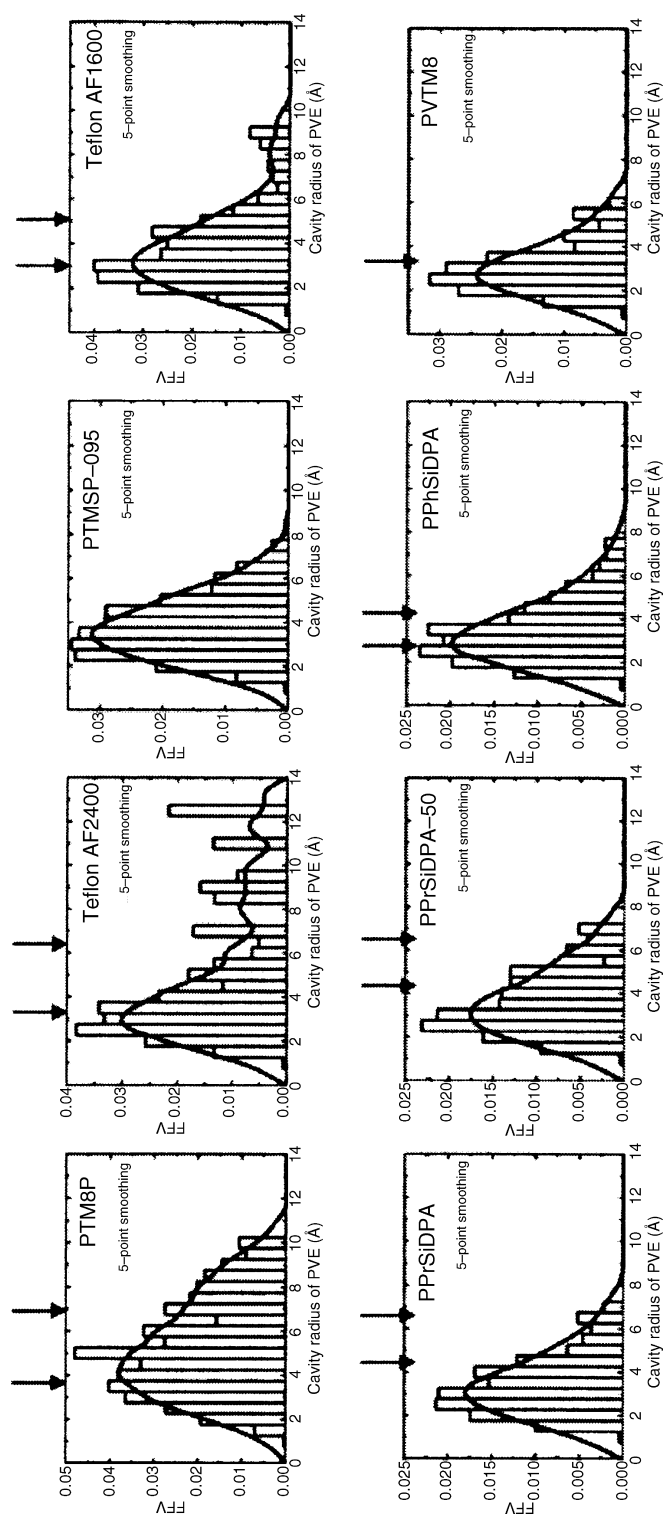


Figure 3.15 Free volume distributions (R_{max}) for a positronium probe molecule ($R = 1.1 \text{ \AA}$) obtained from molecular simulations for poly[1-(trimethylsilyl)-1-propyne] (PTMSP), amorphous Teflons (AF1600 and AF2400), polyvinyltrimethylsilane (PVTMS) and two highly substituted polyacetylenes (PPrSiDPA and PPhSiDPA). Arrows indicate average PALS peak positions. Reprinted with permission from D. Hofmann, M. Entriaigo-Castano, A. Lebret, M. Heuchel and Y. Yampol'skii, *Macromolecules*, **36**, 8528–8538 (2003). Copyright (2003) American Chemical Society

[239]. Commercial formulations include Teflon AF1600 ($m = 0.65$) and Teflon AF2400 ($m = 0.87$). As indicated by the values in Table 3.2, the FFVs of these TFE/BDD copolymers are comparable to PTMSP although the permeability of TFE/BDD is lower than that of PTMSP, as shown by Figures 3.1 and 3.2. This suggests that factors other than just FFV affect permeability. PALS of AF1600 indicate a bimodal free volume distribution with the larger free volume elements having a radius of approximately 5 Å [38]. ^{129}Xe NMR studies have indicated the presence of larger sorption sites in both amorphous Teflon and PTMSP [240]. Golemme *et al.* [39] have used ^{129}Xe NMR spectroscopy to characterize free volume in both AF1600 and AF2400. Results were consistent with other probe methods such as PALS. As in the case of P4M2P, the addition of nanoscale, nonporous fused silica to AF2400 suggests that FS addition increases the size of free volume elements and, therefore, increases the permeability [241].

Wang *et al.* [242] have reported a simulation study of the equivalent of AF2400 and PTMSP (see Section 3.3.8) using the COMPASS force field [122] to explore free volume and free-volume distributions. An experimental density of 1.74 g cm $^{-3}$ was used for AF2400. Application of a cavity size algorithm [243] indicated that the average cavity size of PTMSP was 11.2 Å (the largest was 16 Å) compared to 8.2 Å (the largest was 12 Å) for AF2400. In addition, the distribution of free volume for PTMSP was shifted towards larger cavity sizes.

3.4 Conclusions

As shown in this review, equilibrium molecular dynamics methods, especially using *ab initio*-based (Class II) force fields, can provide a realistic picture of gas solubility and diffusion in highly permeable polymers, including polysiloxanes, polysilanes and substituted polyacetylenes. Several approaches have been used to evaluate free volume and free volume distribution which have been shown to be consistent with the results from PALS measurements. Simulation methods such as pair correlation analysis has been used to identify the nature of interactions of some gases such as CO $_2$ with polymers such as fluorine-containing polyphosphazenes which exhibit unusually high CO $_2$ solubility. In cases of less permeable but

important membrane polymers, including polycarbonates and polyimides, the transition state theory (TST) method developed by Suter and Gusev and others has extended the temporal domain beyond limits of usual MD simulations to provide reasonable simulation of permeability for oxygen, nitrogen and other non-interacting gases. The current state of simulation methods provide a reliable approach for the molecular engineering of membrane polymers for specific gas separations.

Appendices: Primary Force Fields Used in the Simulation of Transport in Polymeric Systems

Appendix 1: DREIDING

DREIDING [118] is a generic force field applicable for organic, biological, and main-group inorganic molecules. The bonded terms include a harmonic or Morse function (DREIDING/M) for bond stretch and a harmonic for bond stretch and a harmonic cosine function for torsional and inversion. Nonbonded terms include a Lennard–Jones (LJ) 12–6 potential and exponential 6 (DREDING/x6) for van der Waals or dispersion, and a CHARMM-like potential function for hydrogen bonding. Parameterization is biased towards first-row elements and carbon):

$$\begin{aligned}
 E_{\text{total}} = & \sum \frac{1}{2} k_{\text{bond}} (r - R_0)^2 \\
 & + \sum \frac{1}{2} k_{\text{angle}} (\cos \theta - \cos \theta^0)^2 \\
 & + \sum \frac{1}{2} k_{\text{dihedral}} [1 - \cos n (\phi - \phi^0)] \\
 & + \sum \frac{1}{2} k_{\text{improper}} (\phi - \phi^0)^2 \\
 & + \sum [C_{12}(r_{1,2})^{-12} - \sum C_6(r_{1,2})^{-6}] \\
 & + \sum \frac{q_1 q_2}{4\pi\epsilon_0 r_{1,2}} + \sum D_{\text{hb}} [5(r_{\text{DH}}/r_{\text{DA}})^{12} \\
 & - 6(r_{\text{DH}}/r_{\text{DA}})^{10}] \cos^4 \theta_{\text{DHA}}
 \end{aligned} \tag{3.50}$$

Appendix 2: GROMOS

The GROMOS force field [119] utilizes simple harmonic functions for bond stretch and bending, torsional and improper torsional potential terms, a 6–12 Lennard–Jones potential for van der Waals interactions and a Coulombic expression for

electrostatic interactions. The k parameters in the potential terms are taken from CHARMM [117]:

$$\begin{aligned}
 E_{\text{total}} = & \sum \frac{1}{2} k_{\text{bond}} (r - R_0)^2 \\
 & + \sum \frac{1}{2} k_{\text{angle}} (\theta - \theta_0)^2 \\
 & + \sum \frac{1}{2} k_{\text{dihedral}} [1 + \cos(n\phi - \delta)] \\
 & + \sum \frac{1}{2} k_{\text{improper}} (\psi - \psi_0)^2 \\
 & + \sum [C_{12}(r_{1,2})^{-12} - \sum C_6(r_{1,2})^{-6}] \\
 & + \sum \frac{q_1 q_2}{4\pi\epsilon_0 r_{1,2}}
 \end{aligned} \tag{3.51}$$

Appendix 3: COMPASS

COMPASS (COndensed-phase optimized MOlecular Potentials for Atomistic Simulation Studies) is a Class II *ab initio* force field [122] which derives terms and some parameters from the Consistent Force Field (CFF) series of force fields (i.e., CFF93) [244,245] but uses condensed-phase data for final parameterization. COMPASS includes quartic bond stretch and angle-bend contributions, torsion, out-of-plane angle (χ) and cross-coupling term contributions to the bonded potential. Non-bonded terms include a Coulombic potential and a 6–9 L–J potential.

$$\begin{aligned}
 E_{\text{total}} = & \sum_b [k_2(b - b_0)^2 + k_3(b - b_0)^3 + k_4(b - b_0)^4] \\
 & + \sum_\theta [k_2(\theta - \theta_0)^2 + k_3(\theta - \theta_0)^3 + k_4(\theta - \theta_0)^4] \\
 & + \sum_\phi [k_1(1 - \cos\phi) + k_2(1 - \cos 2\phi) \\
 & + k_3(1 - \cos 3\phi)] \\
 & + \sum_\chi k_2 \chi^2 + \sum_{b,b'} k(b - b_0)(b' - b'_0) \\
 & + \sum_{b,\theta} k(b - b_0)(\theta - \theta_0) \\
 & + \sum_{b,\phi} k(b - b_0)[k_1 \cos\phi + k_2 \cos 2\phi + k_3 \cos 3\phi] \\
 & + \sum_{\theta,\phi} (\theta - \theta_0)[k_1 \cos\phi + k_2 \cos 2\phi + k_3 \cos 3\phi] \\
 & + \sum_{b,\theta} k(\theta' - \theta'_0)(\theta - \theta_0) \\
 & + \sum_{\theta,\theta,\phi} k(\theta - \theta_0)(\theta' - \theta'_0) \cos\phi \\
 & + \sum_{ij} \frac{q_1 q_2}{r_{ij}} + \sum_{ij} \epsilon_{ij} \left[2 \left(\frac{r_{ij}^0}{r_{ij}} \right)^9 - 3 \left(\frac{r_{ij}^0}{r_{ij}} \right)^6 \right]
 \end{aligned}$$

References

- [1] H. L. Frisch, 'Sorption and transport in glassy polymers – a review', *Polym. Eng. Sci.*, **20**, 2–13 (1980).
- [2] S. A. Stern and H. L. Frisch, 'The selective permeation of gases through polymers', *Annu. Rev. Mater. Sci.*, **11**, 523–550 (1981).
- [3] H. L. Frisch and S. A. Stern, 'Diffusion of small molecules in polymers', *Crit. Rev. Solid State Mater. Sci.*, **11**, 123–187 (1983).
- [4] S. A. Stern and S. Trohalaki, 'Fundamentals of gas diffusion in rubbery and glassy polymers', in *Barrier Polymers and Structures*, W. J. Koros (Ed.), American Chemical Society, Washington, DC, USA, pp. 22–59 (1990).
- [5] W. J. Koros, M. R. Coleman and D. R. B. Walker, 'Controlled permeability polymer membranes', *Annu. Rev. Mater. Sci.*, **22**, 47–89 (1992).
- [6] S. A. Stern, 'Polymers for gas separations: the next decade', *J. Membr. Sci.*, **94**, 1–65 (1994).
- [7] W. J. Koros and G. K. Fleming, 'Membrane-based gas separation', *J. Membr. Sci.*, **83**, 1–80 (1993).
- [8] J. H. Petropoulos, 'Mechanisms and theories for sorption and diffusion of gases in polymers', in *Polymeric Gas Separation Membranes*, D. R. Paul and Y. P. Yampol'skii (Eds), CRC Press, Boca Raton, FL, USA, pp. 17–81 (1994).
- [9] T. Aoki, 'Macromolecular design of permselective membranes', *Prog. Polym. Sci.*, **24**, 951–993 (1999).
- [10] D. R. Paul, 'Transport properties of polymers', in *Applied Polymer Science*, R. W. Tess and G. W. Poehlein (Eds), American Chemical Society, Washington, DC, USA, pp. 253–275 (1985).
- [11] H. B. Hopfenberg and V. Stannet, 'The diffusion and sorption of gases and vapours in glassy polymers', in *The Physics of Glassy Polymers*, R. N. Haward (Ed.), John Wiley & Sons, Inc., New York, NY, USA, pp. 504–547 (1973).
- [12] G. K. Fleming and W. J. Koros, 'Dilation of polymers by sorption of carbon dioxide at elevated pressures. 1. Silicone rubber and unconditioned polycarbonate', *Macromolecules*, **19**, 2285–2291 (1986).
- [13] R. M. Barrer, 'Permeation, diffusion and solution of gases in organic polymers', *Trans. Faraday Soc.*, **35**, 629–643 (1939).
- [14] W. R. Vieth, J. M. Howell and J. H. Hsieh, 'Dual sorption theory', *J. Membr. Sci.*, **1**, 177–220 (1976).
- [15] K. Toi, G. Morel and D. R. Paul, 'Gas sorption and transport in poly(phenylene oxide) and comparisons with other glassy polymers', *J. Appl. Polym. Sci.*, **27**, 1997–2005 (1982).
- [16] V. Tepliyakov and P. Meares, 'Correlation aspects of the selective gas permeabilities of polymeric materials and membranes', *Gas Sep. Purif.*, **4**, 66–74 (1990).

- [17] H. L. Frisch, 'The time lag in diffusion', *J. Phys. Chem.*, **61**, 93–95 (1957).
- [18] D. R. Paul and W. J. Koros, 'Effect of partially immobilizing sorption on permeability and the diffusion time lag', *J. Polym. Sci. Part B: Polym. Phys. Ed.*, **14**, 675–685 (1976).
- [19] J. Crank and G. S. Parks, *Diffusion in Polymers*, Academic Press, London, UK (1968).
- [20] P. Meares, 'The diffusion of gases through polyvinyl acetate', *J. Am. Chem. Soc.*, **76**, 3415–3422 (1954).
- [21] S. Glasstone, K. J. Laidler and H. Eyring, *The Theory of Rate Processes*, McGraw-Hill, New York, NY, USA (1941).
- [22] F. Bueche, *Physical Properties of Polymers*, John Wiley & Sons, Inc., New York, NY, USA (1962).
- [23] L. M. Robeson, 'Correlation of separation factor versus permeability for polymeric membranes', *J. Membr. Sci.*, **62**, 165–185 (1991).
- [24] L. M. Robeson, W. F. Burgoyne, M. Langsam, A. C. Savoca and C. F. Tien, 'High performance polymers for membrane separation', *Polymer*, **35**, 4970–4978 (1994).
- [25] B. D. Freeman, 'Basis of permeability/selectivity tradeoff relations in polymeric gas separation membranes', *Macromolecules*, **32**, 375–380 (1999).
- [26] C.-L. Lee, H. L. Chapman, M. E. Cifuentes, K. M. Lee, L. D. Merrill, K. L. Ulman and K. Venkataraman, 'Effects of polymer structure on the gas permeability of silicone membranes', *J. Membr. Sci.*, **38**, 55–70 (1988).
- [27] M. W. Hellums, W. J. Koros, G. R. Husk and D. R. Paul, 'Fluorinated polycarbonates for gas separation applications', *J. Membr. Sci.*, **46**, 93–112 (1989).
- [28] A. Bondi, 'van der Waals volumes and radii', *J. Phys. Chem.*, **68**, 441–451 (1964).
- [29] S. Sugden, 'Molecular volumes at absolute zero. Part. II. Zero volumes and chemical composition', *J. Chem. Soc.*, 1786–1798 (1927).
- [30] K. Hagiwara, T. Ougizawa, T. Inoue, K. Hirata and Y. Kobayashi, 'Studies on the free volume and the volume expansion behavior of amorphous polymers', *Rad. Phys. Chem.*, **58**, 525–530 (2000).
- [31] W. W. Lee, 'Selection of barrier materials from molecular structure', *Polym. Eng. Sci.*, **20**, 65–69 (1980).
- [32] L. A. Pilato, L. M. Litz, B. Hargitay, R. C. Osborne, A. G. Farnham, J. H. K. E. Fritze and J. E. McGrath, 'Polymers for permselective membrane gas separations', *Polym. Prepr.*, **16**, 41–46 (1975).
- [33] A. A. Askadskii, *Physical Properties of Polymers: Prediction and Control*, Gordon and Breach, Amsterdam, The Netherlands (1996).
- [34] I. Pinnau, C. G. Casillas, A. Morisato and B. D. Freeman, 'Long-term permeation properties of poly(1-trimethylsilyl-1-propyne) membranes in hydrocarbon-vapor environment', *J. Polym. Sci. Part B: Polym. Phys. Ed.*, **35**, 1483–1490 (1997).
- [35] Y. C. Jean, 'Characterizing free volumes and holes in polymers by positron annihilation spectroscopy', paper presented at the NATO Advanced Research Workshop, Varenna, Italy, July 16–17 (1993).
- [36] R. A. Pethrick, 'Positron annihilation – a probe for nanoscale voids and free volume', *Prog. Polym. Sci.*, **22**, 1–47 (1997).
- [37] G. Dlubek, D. Kilburn, V. Bondarenko, J. Pionteck, R. Krause-Rehberg and M. A. Alam, 'Positron annihilation: a unique method for studying polymers', *Macromol. Symp.*, **210**, 11–20 (2004).
- [38] A. Y. Alentiev, V. P. Shantarovich, T. C. Merkel, V. I. Bondar, B. D. Freeman and Y. P. Yampolskii, 'Gas and vapor sorption, permeation and diffusion in glassy amorphous Teflon AF1600', *Macromolecules*, **35**, 9513–9522 (2002).
- [39] G. Golemme, J. B. Nagy, A. Fonseca, C. Algieri and Y. Yampolskii, '¹²⁹Xe NMR study of free volume in amorphous perfluorinated polymers: comparison with other methods', *Polymer*, **44**, 5039–5045 (2003).
- [40] J. G. Victor and J. M. Torkelson, 'On measuring the distribution of local free volume in glassy polymers by photochromic and fluorescence techniques', *Macromolecules*, **20**, 2241–2250 (1987).
- [41] J. S. Royal and J. M. Torkelson, 'Photochromic and fluorescent probe studies in glassy polymer matrices. 5. Effects of physical aging on bisphenol-A polycarbonate and poly(vinyl acetate) as sensed by a size distribution of photochromic probes', *Macromolecules*, **25**, 4792–4796 (1992).
- [42] Y. P. Yampol'skii, M. V. Motyakin, A. M. Wasserman, T. Masuda, M. Teraguchi, V. S. Khotimskii and B. D. Freeman, 'Study of high permeability polymers by means of the spin probe technique', *Polymer*, **40**, 1745–1752 (1999).
- [43] Y. Kobayashi, K. Haraya, S. Hattori and T. Sasuga, 'Evaluation of polymer free volume by positron annihilation and gas diffusivity measurements', *Polymer*, **35**, 925–928 (1994).
- [44] Y. C. Jean, J.-P. Yuan, J. Liu, Q. Deng and H. Yang, 'Correlations between gas permeation and free-volume hole properties probed by positron annihilation spectroscopy', *J. Polym. Sci. Part B: Polym. Phys. Ed.*, **33**, 2365–2371 (1995).
- [45] Z. Yu, J. D. McGervey, A. M. Jamieson and R. Simha, 'Can positron annihilation lifetime spectroscopy measure the free-volume hole size distribution in amorphous polymers?', *Macromolecules*, **28**, 6268–6272 (1995).
- [46] Y. C. Jean, 'Comments on the paper "Can positron annihilation lifetime spectroscopy measure

- the free-volume hole size distribution in amorphous polymers?' *Macromolecules*, **26**, 5461–5757 (1996).
- [47] K. Suvegh, M. Kapper, A. Domjan and A. Vertes, 'Comparison of simulated and measured free volume distributions in polymers', *Rad. Phys. Chem.*, **58**, 539–543 (2000).
- [48] M. H. Cohen and D. Turnbull, 'Molecular transport in liquids and glasses', *J. Phys. Chem.*, **31**, 1164–1169 (1959).
- [49] H. Fujita, 'Diffusion in polymer–diluent systems', *Fortschr. Hochpolym.-Forsch.*, **3**, 1–47 (1961).
- [50] K. Haraya and S.-T. Hwang, 'Permeation of oxygen, argon and nitrogen through polymer membranes', *J. Membr. Sci.*, **71**, 13–27 (1992).
- [51] R. K. Bharadwaj and R. H. Boyd, 'Small molecule penetrant diffusion in aromatic polyesters: a molecular dynamics simulation study', *Polymer*, **40**, 4229–4236 (1999).
- [52] H. Takeuchi and K. Okazaki, 'Molecular dynamics simulation of diffusion of simple gas molecules in a short chain polymer', *J. Chem. Phys.*, **92**, 5643–5652 (1990).
- [53] C. Nagel, E. Schmidtke, K. Gunther-Schade, D. Hofmann, D. Fritsch, T. Strunskus and F. Faupel, 'Free volume distributions in glassy polymer membranes: comparison between molecular modeling and experiments', *Macromolecules*, **33**, 2242–2248 (2000).
- [54] D. R. B. Walker and W. J. Koros, 'Transport characterization of a polypyrrole for gas separations', *J. Membr. Sci.*, **55**, 99–117 (1991).
- [55] T.-H. Kim, W. J. Koros and G. R. Husk, 'Advanced separation membrane materials: rigid aromatic polyimides', *Sep. Sci. Technol.*, **23**, 1611–1626 (1988).
- [56] E. R. Hensema, M. H. V. Mulder and C. A. Smolders, 'On the mechanism of gas transport in rigid polymer membranes', *J. Appl. Polym. Sci.*, **49**, 2081–2090 (1993).
- [57] A. Shimazu, T. Miyazaki and K. Ikeda, 'Interpretation of *d*-spacing determined by wide-angle X-ray scattering in 6FDA-based polyimide by molecular modeling', *J. Membr. Sci.*, **166**, 113–118 (2000).
- [58] A. C. Puleo, D. R. Paul and P. K. Wong, 'Gas sorption and transport in semicrystalline poly(4-methyl-1-pentene)', *Polymer*, **30**, 1357–1366 (1989).
- [59] J. A. Horas and M. G. Rizzotto, 'On the diffusion of gases in partially crystalline polymers', *J. Polym. Sci. Part B: Polym. Phys. Ed.*, **27**, 175–187 (1989).
- [60] A. A. Gusev, F. Müller-Plathe, W. F. van Gunsteren and U. W. Suter, 'Dynamics of small molecules in bulk polymers', *Adv. Polym. Sci.*, **116**, 207–247 (1994).
- [61] F. Müller-Plathe, 'Permeation of polymers – a computational approach', *Acta Polym.*, **45**, 259–293 (1994).
- [62] D. N. Theodorou, 'Molecular simulations of sorption and diffusion in amorphous polymers', in *Diffusion in Polymers*, P. Neogi (Ed.), Marcel Dekker, New York, NY, USA, pp. 67–142 (1996).
- [63] A. A. Gusev and U. W. Suter, 'Dynamics of small molecules in dense polymers subject to thermal motion', *J. Chem. Phys.*, **99**, 2228–2234 (1993).
- [64] R. L. June, A. T. Bell and D. N. Theodorou, 'Transition-state studies of xenon and SF₆ diffusion in silicalite', *J. Phys. Chem.*, **95**, 8866–8878 (1991).
- [65] R. Q. Snurr, A. T. Bell and D. N. Theodorou, 'Investigation of the dynamics of benzene in silicalite using transition-state theory', *J. Phys. Chem.*, **98**, 11948–11962 (1994).
- [66] A. Gusev and U. W. Suter, 'A model for transport of diatomic molecules through elastic solids', *J. Comp.-Aided Mater. Des.*, **1**, 63–73 (1993).
- [67] A. A. Gray-Weale, R. H. Henchman, R. G. Gilbert, M. L. Greenfield and D. N. Theodorou, 'Transition-state theory model for the diffusion coefficients of small penetrants in glassy polymers', *Macromolecules*, **30**, 7296–7306 (1997).
- [68] D. Hofmann, L. Fritz, J. Ulbrich and D. Paul, 'Molecular modelling of amorphous membrane polymers', *Polymer*, **38**, 6145–6155 (1997).
- [69] D. Hofmann, L. Fritz, J. Ulbrich and D. Paul, 'Molecular simulation of small molecules diffusion and solution in dense amorphous polysiloxanes and polyimides', *Comp. Theor. Polym. Sci.*, **10**, 419–436 (2000).
- [70] M. Heuchel and D. Hofmann, 'Molecular modelling of polyimide membranes for gas separation', *Desalination*, **144**, 67–72 (2002).
- [71] M. Heuchel, D. Hofmann and P. Pullumbi, 'Molecular modeling of small-molecule permeation in polyimides and its correlation to free-volume distributions', *Macromolecules*, **37**, 201–214 (2004).
- [72] A. A. Gusev, S. Arizzi, U. W. Suter and D. J. Moll, 'Dynamics of light gases in rigid matrices of dense polymers', *J. Chem. Phys.*, **99**, 2221–2227 (1993).
- [73] A. A. Gusev, U. W. Suter and D. J. Moll, 'Relationship between helium transport and molecular motions in glassy polycarbonate', *Macromolecules*, **28**, 2582–2584 (1995).
- [74] M. Lopez-Gonzalez, E. Saiz, J. Guzman and E. Riande, 'Experimental and simulation studies on the transport of gaseous diatomic molecules in polycarbonate membranes', *J. Chem. Phys.*, **115**, 6728–6736 (2001).
- [75] M. Lopez-Gonzalez, E. Saiz, J. Guzman and E. Riande, 'Experimental and simulation studies on

- the transport of argon in polycarbonate membranes', *Macromolecules*, **34**, 4999–5004 (2001).
- [76] M. Lopez-Gonzalez, E. Saiz, E. Riande and J. Guzman, 'Transport of helium in polycarbonate membranes', *Polymer*, **43**, 409–413 (2002).
- [77] M. L. Greenfield and D. N. Theodorou, 'Molecular modeling of methane diffusion in glassy atactic polypropylene via multidimensional transition state theory', *Macromolecules*, **31**, 7068–7090 (1998).
- [78] B. Widom, 'Some topics in the theory of fluids', *J. Chem. Phys.*, **39**, 2808–2812 (1963).
- [79] D. M. Razmus and C. K. Hall, 'Prediction of gas adsorption in 5 Å zeolites using Monte Carlo simulation', *AIChE J.*, **37**, 769–779 (1991).
- [80] K. S. Schweizer and J. G. Curro, 'PRISM theory of the structure, thermodynamics and phase transitions of polymer liquids and alloys', in *Atomistic Modeling of Physical Properties*, L. Monnerie and U. W. Suter (Eds), Springer-Verlag, Berlin, Germany, pp. 319–377 (1994).
- [81] J. G. Curro, K. G. Honnell and J. D. McCoy, 'Theory for the solubility of gases in polymers: application to monatomic solutes', *Macromolecules*, **30**, 145–152 (1997).
- [82] J. L. Budzien, J. D. McCoy, D. H. Weinkauff, R. A. LaViolette and E. S. Peterson, 'Solubility of gases in amorphous polyethylene', *Macromolecules*, **31**, 3368–3371 (1998).
- [83] N. Metropolis, A. W. Rosenbluth, M. N. Rosenbluth, A. H. Teller and E. Teller, 'Equation of state calculations by fast computing machines', *J. Chem. Phys.*, **21**, 1087–1092 (1953).
- [84] S. Trohalaki, A. Kloczkowski, J. E. Mark, D. Rigby and R. J. Roe, 'Estimation of diffusion coefficients for small molecular penetrants in amorphous polyethylene', in *Computer Simulation of Polymers*, R. J. Roe (Ed.), Prentice Hall, Englewood Cliffs, NJ, USA, pp. 220–232 (1991).
- [85] M. P. Allen and D. J. Tildesley, *Computer Simulation of Liquids*, Oxford University Press, New York, NY, USA (1987).
- [86] R. Chitra and S. Yashonath, 'Estimation of error in the diffusion coefficient from molecular dynamics simulations', *J. Phys. Chem. B*, **101**, 5437–5445 (1997).
- [87] S. Trohalaki, A. Kloczkowski, J. E. Mark, R. J. Roe and D. Rigby, 'Molecular-dynamics simulations of small molecule diffusion in polyethylene', *Comp. Theor. Polym. Sci.*, **2**, 147–151 (1992).
- [88] L. S. Darken, 'Diffusion, mobility, and their interrelation through free energy in binary metallic systems', *Trans. AIMME*, **175**, 184–201 (1948).
- [89] S. Sunderrajan, C. K. Hall and B. D. Freeman, 'Estimation of mutual diffusion coefficients in polymer/penetrant systems using nonequilibrium molecular dynamics simulations', *J. Chem. Phys.*, **105**, 1621–1632 (1996).
- [90] R. M. Barrer, 'Nature of the diffusion process in rubber', *Nature*, **140**, 106–107 (1937).
- [91] R. H. Gee and R. H. Boyd, 'Small penetrant diffusion in polybutadiene: a molecular dynamics simulation study', *Polymer*, **36**, 1435–1440 (1995).
- [92] J. Han and R. H. Boyd, 'Molecular packing and small-penetrant diffusion in polystyrene: a molecular dynamics simulation study', *Polymer*, **38**, 1797–1804 (1996).
- [93] P. T. Cummings and D. J. Evans, 'Nonequilibrium molecular dynamics approaches to transport properties and non-Newtonian fluid rheology', *Ind. Eng. Chem. Res.*, **31**, 1237–1252 (1992).
- [94] G. S. Heffelfinger and F. van Swol, 'Diffusion in Lennard-Jones fluids using dual control volume grand canonical molecular dynamics simulation (DCV-GCMD)', *J. Chem. Phys.*, **100**, 7548–7552 (1994).
- [95] A. Thompson and G. S. Heffelfinger, 'Direct molecular simulation of gradient-driven diffusion of large molecules using constant pressure', *J. Chem. Phys.*, **110**, 10693–10705 (1999).
- [96] J. M. D. MacElroy, 'Nonequilibrium molecular dynamics simulation of diffusion and flow in thin microporous membranes', *J. Chem. Phys.*, **101**, 5274–5280 (1994).
- [97] S.-i. Furukawa, T. Shigeta and T. Nitta, 'Nonequilibrium molecular dynamics for simulating permeation of gas mixtures through nanoporous carbon membranes', *J. Chem. Eng. Jpn.*, **29**, 725–727 (1996).
- [98] S.-i. Furukawa and T. Nitta, 'Computer simulation studies on gas permeation through nanoporous carbon membranes by non-equilibrium molecular dynamics', *J. Chem. Eng. Jpn.*, **30**, 116–122 (1997).
- [99] L. Xu, M. G. Sedigh, M. Sahimi and T. T. Tsotsis, 'Nonequilibrium molecular dynamics simulation of transport of gas mixtures in nanopores', *Phys. Rev. Lett.*, **80**, 3511–3514 (1998).
- [100] S.-i. Furukawa and T. Nitta, 'Non-equilibrium molecular dynamics simulation studies on gas permeation across carbon membrane with different pore shape composed of micrographite crystallites', *J. Membr. Sci.*, **178**, 107–119 (2000).
- [101] T. Duren, F. J. Keil and N. A. Seaton, 'Composition dependent transport diffusion coefficients of CH₄/CF₄ mixtures in carbon nanotubes by non-equilibrium molecular dynamics simulations', *Chem. Eng. Sci.*, **57**, 1343–1354 (2002).
- [102] P. I. Pohl and G. S. Heffelfinger, 'Massively parallel molecular dynamics simulation of gas permeation across porous silica membranes', *J. Membr. Sci.*, **155**, 1–7 (1999).

- [103] M. G. Martin and A. P. Thompson, 'Effect of pressure, membrane thickness, and placement of control volumes on the flux of methane through thin silicalite membranes: a dual control volume grand canonical molecular dynamics study', *J. Chem. Phys.*, **114**, 7174–7181 (2001).
- [104] Q. Zhang, J. Zheng, A. Shevade, L. Zhang, S. H. Gehrke, G. S. Heffelfinger and S. Jiang, 'Transport diffusion of liquid water and methanol through membranes', *J. Chem. Phys.*, **117**, 808–818 (2002).
- [105] H. Kikuchi, S. Kuwajima and M. Fuluda, 'Permeability of gases in rubbery polymer membrane: application of pseudo-nonequilibrium simulation', *Chem. Phys. Lett.*, **358**, 466–472 (2002).
- [106] C. Tunca and D. F. Ford, 'Coarse-grained nonequilibrium approach to the molecular modeling of permeation through microporous membranes', *J. Chem. Phys.*, **120**, 10763–10767 (2004).
- [107] F. Müller-Plathe, 'Gas sorption and transport in polyisobutylene: equilibrium and nonequilibrium molecular dynamics simulations', *J. Chem. Phys.*, **98**, 9895–9904 (1993).
- [108] W. Brostow, J.-P. Dussault and B. L. Fox, 'Construction of Voronoi polyhedra', *J. Comp. Chem.*, **29**, 81–92 (1978).
- [109] M. Tanemura, T. Ogawa and N. Ogita, 'A new algorithm for three-dimensional Voronoi tessellation', *J. Comp. Phys.*, **51**, 191–207 (1983).
- [110] R. Voorintholt, M. T. Kusters, G. Vegter, G. Friend and W. G. J. Hol, 'A very fast program for visualizing proteins surfaces, channels and cavities', *J. Mol. Graphics*, **7**, 243–245 (1989).
- [111] S. Lee and W. L. Mattice, 'A "phantom bubble" model for the distribution of free volume in polymers', *Comp. Theor. Polym. Sci.*, **9**, 57–61 (1999).
- [112] D. Rigby and R. J. Roe, 'Molecular dynamics simulation of polymer liquid and glass. 4. Free-volume distribution', *Macromolecules*, **23**, 5312–5319 (1990).
- [113] T. Zheng, *Masters Thesis*, Department of Chemical Engineering, University of Cincinnati, OH, USA (2000).
- [114] V. M. Shah, S. A. Stern and P. J. Ludovice, 'Estimation of the free volume in polymers by means of a Monte Carlo technique', *Macromolecules*, **22**, 4660–4662 (1989).
- [115] F. T. Gentile, S. Arizzi, U. W. Suter and P. J. Ludovice, 'Structural characterization of polycarbonates for membrane applications by atomic level simulation', *Ind. Eng. Chem. Res.*, **34**, 4193–4201 (1995).
- [116] J. S. Yang, K. Choi and W. H. Jo, 'Comparison of gas diffusion in poly[1-(trimethylsilyl)-1-propyne] and polydimethylsiloxane by atomistic modeling', *Macromol. Theor. Simul.*, **9**, 287–291 (2000).
- [117] B. R. Brooks, R. E. Bruccoleri, B. D. Olafson, D. J. States, S. Swaminathan and M. Karplus, 'CHARMM: a program for macromolecular energy, minimization, and dynamics calculations', *J. Comp. Chem.*, **4**, 187–217 (1983).
- [118] S. L. Mayo, B. D. Olafson and W. A. Goddard, 'DREIDING: A generic force field for molecular simulation', *J. Phys. Chem.*, **94**, 8897–8909 (1990).
- [119] H. J. C. Berendsen, D. van de Spoel and R. van Drunen, 'GROMACS: A message-passing parallel molecular dynamics implementation', *Comp. Phys. Commun.*, **91**, 43–56 (1995).
- [120] H. Sun, S. J. Mumby, J. R. Maple and A. T. Hagler, 'An *ab initio* CFF93 all-atom force field for polycarbonates', *J. Am. Chem. Soc.*, **116**, 2978–2987 (1994).
- [121] A. T. Hagler, S. Lifson and P. Dauber, 'Consistent force field studies of intermolecular forces in hydrogen-bonded crystals. 2. A benchmark for the objective comparison of alternative force fields', *J. Am. Chem. Soc.*, **101**, 5122–5130 (1979).
- [122] H. Sun, 'COMPASS: An *ab initio* force-field optimized for condensed-phase applications – overview with details on alkane and benzene compounds', *J. Phys. Chem. B*, **102**, 7338–7364 (1998).
- [123] H. Sun, P. Ren and J. R. Fried, 'The COMPASS force field: parameterization and validation for phosphazenes', *Comp. Theor. Polym. Sci.*, **8**, 229–246 (1998).
- [124] J. Yang, Y. Ren, A.-m. Tian and H. Sun, 'COMPASS force field for 14 inorganic molecules, He, Ne, Ar, Kr, Xe, H₂, O₂, N₂, NO, CO, CO₂, NO₂, CS₂ and SO₂, in liquid phases', *J. Phys. Chem. B*, **104**, 4951–4957 (2000).
- [125] D. Hofmann, M. Entrialgo-Castano, A. Lerbret, M. Heuchel and Y. Yampolskii, 'Molecular modeling investigation of free volume distributions in stiff chain polymers with conventional and ultrahigh free volume: comparison between molecular modeling and positron lifetime studies', *Macromolecules*, **36**, 8528–8538 (2003).
- [126] A. J. Schultz, C. K. Hall and J. Genzer, 'Box search algorithm for molecular simulation of systems containing periodic structures', *J. Chem. Phys.*, **120**, 2049–2055 (2004).
- [127] R. Auhl, R. Everaers, G. S. Grest, K. Kremer and S. J. Plimpton, 'Equilibration of long chain polymer melts in computer simulations', *J. Chem. Phys.*, **119**, 12718–12728 (2003).
- [128] F. Müller-Plathe, S. C. Rogers and W. F. van Gunsteren, 'Diffusion coefficients of penetrant gases in polyisobutylene can be calculated correctly by molecular dynamics simulations', *Macromolecules*, **25**, 6722–6724 (1992).

- [129] T. R. Cuthbert, N. J. Wagner, M. E. Paulaitis, G. Murgia and B. D'Aguzzo, 'Molecular dynamics simulation of penetrant diffusion in amorphous polypropylene: diffusion mechanisms and simulation size effects', *Macromolecules*, **32**, 5017–5028 (1999).
- [130] S. Neyertz and D. Brown, 'Influence of system size in molecular dynamics simulation of gas permeation in glassy polymers', *Macromolecules*, **37**, 10109–10122 (2004).
- [131] T. R. Cuthbert, N. J. Wagner and M. E. Paulaitis, 'Molecular simulation of glassy polystyrene: size effects on gas solubilities', *Macromolecules*, **30**, 3058–3065 (1997).
- [132] M. Amini, M. Forsyth, S. Gruenhut, P. Meakin and D. R. MacFarlane, 'Equilibrium strategies in molecular dynamics', *Electrochim. Acta*, **43**, 1381–1386 (1998).
- [133] K. Choi and W. H. Jo, 'Effect of chain flexibility on selectivity in the gas separation process: molecular dynamics simulation', *Macromolecules*, **28**, 8598–8603 (1995).
- [134] F. Jagodic, B. Borstnik and A. Azman, 'Model calculation of the gas diffusion through polymer bulk', *Makromol. Chem.*, **173**, 221–231 (1973).
- [135] H. Takeuchi, 'A jump motion of small molecules in glassy polymers: a molecular dynamics simulation', *J. Chem. Phys.*, **93**, 2062–2067 (1990).
- [136] F. Müller-Plathe, 'Diffusion of penetrants in amorphous polymers: a molecular dynamics study', *J. Chem. Phys.*, **94**, 3192–3199 (1991).
- [137] P. V. K. Pant and R. H. Boyd, 'Simulation of diffusion of small-molecule penetrants in polymers', *Macromolecules*, **25**, 494–495 (1992).
- [138] S. Trohalaki, A. Kloczkowski, J. E. Mark, R. J. Roe and D. Rigby, 'Molecular dynamics simulations of small molecule diffusion in polyethylene', *Comp. Theor. Polym. Sci.*, **2**, 147–151 (1992).
- [139] P. V. K. Pant and R. H. Boyd, 'Molecular dynamics simulation of diffusion of small penetrants in polymers', *Macromolecules*, **26**, 679–686 (1993).
- [140] R. H. Boyd and P. V. K. Pant, 'Molecular packing and diffusion in polyisobutylene', *Macromolecules*, **24**, 6325–6331 (1991).
- [141] F. Müller-Plathe, S. C. Rogers and W. F. van Gunsteren, 'Computational evidence for anomalous diffusion of small molecules in amorphous polymers', *Chem. Phys. Lett.*, **199**, 237–243 (1992).
- [142] F. Müller-Plathe, L. Laaksonen and W. F. van Gunsteren, 'Cooperative effects in the transport of small molecules through an amorphous polymer matrix', *J. Mol. Graphics*, **11**, 118–126 (1993).
- [143] F. Müller-Plathe, 'Molecular dynamics simulation of gas transport in amorphous polypropylene', *J. Chem. Phys.*, **96**, 3200–3205 (1992).
- [144] J. Han and R. H. Boyd, 'Small-molecule penetrant diffusion in hydrocarbon polymers as studied by molecular dynamics simulation', *Macromolecules*, **27**, 5365–5370 (1994).
- [145] H. Qariouh, R. Schue, F. Schue and C. Bailly, 'Sorption, diffusion and pervaporation of water/ethanol mixtures in polyetherimide membranes', *Polym. Int.*, **48**, 171–180 (1999).
- [146] S. Y. Lim, T. T. Tsotsis and M. Sahimi, 'Molecular simulation of diffusion and sorption of gases in an amorphous polymer', *J. Chem. Phys.*, **119**, 496–504 (2003).
- [147] D. N. Theodorou and U. W. Suter, 'Detailed molecular structure of a vinyl polymer glass', *Macromolecules*, **18**, 2467–2478 (1985).
- [148] M. B. Moe, W. J. Koros and D. R. Paul, 'Effects of molecular structure and thermal annealing on gas transport in two tetramethyl bisphenol-A polymers', *J. Polym. Sci. Part B: Polym. Phys. Ed.*, **26**, 1931–1945 (1988).
- [149] M. Aguilar-Vega and D. R. Paul, 'Gas transport properties of polycarbonates and polysulfones with aromatic substituents on the bisphenol connect group', *J. Polym. Sci. Part B: Polym. Phys. Ed.*, **31**, 1599–1610 (1993).
- [150] C. L. Aitken, W. J. Koros and D. R. Paul, 'Gas transport properties of bisphenol polysulfones', *Macromolecules*, **25**, 3651–3658 (1992).
- [151] C. L. Aitken, W. J. Koros and D. R. Paul, 'Effects of structural symmetry on gas transport properties of polysulfones', *Macromolecules*, **25**, 3224–3434 (1992).
- [152] K. Ghosal, R. T. Chern, B. D. Freeman, W. H. Daly and I. I. Negulescu, 'Effect of basic substituents on gas sorption and permeation in polysulfone', *Macromolecules*, **29**, 4360–4369 (1996).
- [153] J. S. McHattie, W. J. Koros and D. R. Paul, 'Gas transport properties of polysulfones: 2. Effect of bisphenol connector groups', *Polymer*, **32**, 2618–2625 (1991).
- [154] S. Niemela, J. Lappanen and F. Sundholm, 'Structural effects on free volume distribution in glassy polysulfones: molecular modelling of gas permeability', *Polymer*, **37**, 4155–4165 (1996).
- [155] J. C. Schmidhauser and K. L. Longley, 'The effect of bisphenol-A monomer structure on the gas permeability of aromatic polycarbonates', *J. Appl. Polym. Sci.*, **39**, 2083–2096 (1990).
- [156] J. S. McHattie, W. J. Koros and D. R. Paul, 'Effect of isopropylidene replacement on gas transport properties of polycarbonates', *J. Polym. Sci. Part B: Polym. Phys. Ed.*, **29**, 731–746 (1991).
- [157] W. J. Koros and D. R. B. Walker, 'Gas separation membrane material selection criteria: weakly and

- strongly interacting feed component situations', *Polym. J.*, **23**, 481–490 (1991).
- [158] M.-B. Hagg, W. J. Koros and J. C. Schmidhauser, 'Gas sorption and transport properties of bisphenol-1-polycarbonate', *J. Polym. Sci. Part B: Polym. Phys. Ed.*, **32**, 1625–1633 (1994).
- [159] L. M. Costello and W. J. Koros, 'Effect of structure on the temperature dependence of gas transport and sorption in a series of polycarbonates', *J. Polym. Sci. Part B: Polym. Phys. Ed.*, **32**, 701–713 (1994).
- [160] W. J. Koros, A. H. Chan and D. R. Paul, 'Sorption and transport of various gases in polycarbonate', *J. Membr. Sci.*, **2**, 165–190 (1977).
- [161] S. Arizzi, P. H. Mott and U. W. Suter, 'Space available to small diffusants in polymeric glasses: analysis of unoccupied space and its connectivity', *J. Polym. Sci. Part B: Polym. Phys. Ed.*, **30**, 415–426 (1992).
- [162] M. Aguilar-Vega and D. R. Paul, 'Gas transport properties of polyphenylene ethers', *J. Polym. Sci. Part B: Polym. Phys. Ed.*, **31**, 1577–1589 (1993).
- [163] A. Alentiev, E. Drioli, M. Gokzhaev, G. Golemme, O. Ilinich, A. Lapkin, V. Volkov and Y. Yampolskii, 'Gas permeation properties of phenylene oxide polymers', *J. Membr. Sci.*, **138**, 99–107 (1998).
- [164] J. R. Fried, M. Sadat-Akhavi and J. E. Mark, 'Molecular simulation of gas permeability: poly(2,6-dimethyl-1,4-phenylene oxide)', *J. Membr. Sci.*, **149**, 115–126 (1998).
- [165] P. P. Ewald, 'Die Berechnung optischer und electrostatischer Gitterpotentiale', *Ann. Phys. (Leipzig)*, **64**, 253–287 (1921).
- [166] K. Toi, H. Tsuzumi and T. Ito, 'Substitution group effects in gas separation with polyimides', *Polym. Polym. Compos.*, **7**, 45–51 (1999).
- [167] D. Ayala, A. E. Lozano, J. d. Abajo, C. Garcia-Perez, J. G. d. l. Campa, K.-V. Peinemann, B. D. Freeman and R. Prabhakar, 'Gas separation properties of aromatic polyimides', *J. Membr. Sci.*, **215**, 61–73 (2003).
- [168] T. H. Kim, W. J. Koros, G. R. Husk and K. C. O'Brien, 'Relationship between gas separation properties and chemical structure in a series of aromatic polyimides', *J. Membr. Sci.*, **37**, 45–62 (1988).
- [169] S. A. Stern, Y. Mi, H. Yamamoto and A. K. S. Clair, 'Structure/permeability relationships of polyimide membranes. Applications to the separation of gas mixtures', *J. Polym. Sci. Part B: Polym. Phys. Ed.*, **27**, 1887–1909 (1989).
- [170] Y.-C. Wang, S.-H. Huang, C.-C. Hu, C.-L. Li, K.-R. Lee, D.-J. Liaw and J.-Y. Lai, 'Sorption and transport properties of gases in aromatic polyimide membranes', *J. Membr. Sci.*, **248**, 15–25 (2005).
- [171] E. Smit, M. H. V. Mulder, C. A. Smolders, H. Karrenbeld, J. van Eerden and D. Feil, 'Modelling of the diffusion of carbon dioxide in polyimide matrices by computer simulation', *J. Membr. Sci.*, **73**, 247–257 (1992).
- [172] R. Zhang and W. L. Mattice, 'Atomistic modeling of the diffusion of small penetrant molecules in the bulk amorphous polyimide of 3,3',4,4'-benzophenonetetracarboxylic dianhydride and 2,2-dimethyl-1,3-(4-aminophenoxy)propane', *J. Membr. Sci.*, **108**, 15–23 (1995).
- [173] D. Hofmann, J. Ulbrich, D. Fritsch and D. Paul, 'Molecular modelling simulation of gas transport in amorphous polyimide and poly(amide imide) membrane materials', *Polymer*, **37**, 4773–4785 (1996).
- [174] C. S. Ewig, T. S. Thacher and A. T. Hagler, 'Derivation of class II force fields. 7. Nonbonded force field parameters', *J. Phys. Chem. B*, **103**, 6889–7014 (1999).
- [175] M. Clark, R. D. Cramer and N. V. Opdenbosch, 'Validation of the general purpose Tripos 5.2 force field', *J. Comp. Chem.*, **10**, 982–1012 (1991).
- [176] E. Pinel, D. Brown, C. Bas, R. Mercier, N. D. Alberola and S. Neyertz, 'Chemical influence of the dianhydride and the diamine structure on a series of copolyimides studies by molecular dynamics simulations', *Macromolecules*, **35**, 10198–10209 (2002).
- [177] K. Mizoguchi, Y. Kamiya and T. Hirose, 'Gas transport in poly[bis(trifluoroethoxy)phosphazene] above the $T(1)$ transition', *J. Polym. Sci. Part B: Polym. Phys. Ed.*, **29**, 695–703 (1991).
- [178] T. Hirose and K. Mizoguchi, 'Gas transport in poly(alkoxyphosphazene)', *J. Appl. Polym. Sci.*, **43**, 891–900 (1991).
- [179] H. R. Allcock, C. J. Nelson, W. D. Coggio, I. Manners, W. J. Koros, D. R. B. Walker and L. A. Pessan, 'Gas permeation and selectivity of poly(organophosphazene) membranes', *Macromolecules*, **26**, 1493–1502 (1993).
- [180] L. E. Starannikova, D. R. Tur, V. V. Teplyakov and N. A. Platé, 'Gas separation properties of poly[bis(trifluoroethoxy)phosphazene]', *Polym. Sci.*, **36**, 1610–1615 (1994).
- [181] C. J. Orme, J. R. Klaehn and F. F. Stewart, 'Gas permeability and ideal selectivity of poly[bis-(4-*tert*-butylphenoxy)phosphazene]', *J. Membr. Sci.*, **238**, 47–55 (2004).
- [182] J. R. Fried and P. Ren, 'The atomistic simulation of the gas permeability of poly(organophosphazenes). Part I. Poly(dibutoxyphosphazenes)', *Comp. Theor. Polym. Sci.*, **10**, 447–463 (2000).
- [183] J. R. Fried and N. Hu, 'The molecular basis of CO₂ interaction with polymers containing fluorinated groups: computational chemistry of model compounds and molecular simulation of

- poly[bis(2,2,2-trifluoroethoxy)phosphazene]', *Polymer*, **44**, 4363–4372 (2003).
- [184] N. Hu and J. R. Fried, 'The atomistic simulation of the gas permeability of poly(organophosphazenes): 2. poly[bis(2,2,2-trifluoroethoxy)phosphazene]', *Polymer*, **46**, 4330–4343 (2005).
- [185] J. R. Fried and P. Ren, 'Molecular simulation of the glass transition of polyphosphazenes', *Comp. Theor. Polym. Sci.*, **9**, 111–116 (1999).
- [186] T. Hirose, Y. Kamiya and K. Mizoguchi, 'Gas transport in poly[bis(trifluoroethoxy)phosphazene]', *J. Appl. Polym. Sci.*, **38**, 809–820 (1989).
- [187] Y. P. Yampol'skii, N. B. Bespalova, E. S. Finkel'shtein, V. I. Bondar and A. V. Popov, 'Synthesis, gas permeability, and gas sorption properties of fluorine-containing norbornene polymers', *Macromolecules*, **27**, 2872–2878 (1994).
- [188] S. A. Stern, V. M. Shah and B. J. Hardy, 'Structure-permeability relationships in silicone polymers', *J. Polym. Sci. Part B: Polym. Phys. Ed.*, **25**, 1263–1298 (1987).
- [189] Y. Tsujita, 'Gas sorption, diffusion and permeation of ordered polymeric membranes', *Chin. J. Polym. Sci.*, **18**, 301–307 (2000).
- [190] V. M. Shah, B. J. Hardy and S. A. Stern, 'Solubility of carbon dioxide, methane and propane in silicone polymers. Effect of polymer backbone chains', *J. Polym. Sci. Part B: Polym. Phys. Ed.*, **31**, 313–317 (1993).
- [191] J. E. Mark, 'Overview of siloxane polymers', in *Silicones and Silicone-Modified Materials*, S. J. Clarson, J. J. Fitzgerald, M. J. Owen and S. D. Smith (Eds), American Chemical Society, Washington, DC, USA, pp. 1–10 (2000).
- [192] A. C. M. Kuo, 'Poly(dimethylsiloxane)', in *Polymer Data Handbook*, J. E. Mark (Ed.), Oxford University Press, New York, NY, USA, pp. 411–435 (1999).
- [193] R. M. Sok, H. J. C. Berendsen and W. F. V. Gunsteren, 'Molecular dynamics simulation of the transport of small molecules across a polymer membrane', *J. Chem. Phys.*, **96**, 4699–4704 (1992).
- [194] S. G. Charati and S. A. Stern, 'Diffusion of gases in silicone polymers: molecular dynamics simulations', *Macromolecules*, **31**, 5529–5535 (1998).
- [195] V. P. Shantarovich, I. B. Kevdina, Y. P. Yampol'skii and A. Y. Alentiev, 'Positron annihilation lifetime study of high and low free volume glassy polymers: effects of free volume sizes on the permeability and permselectivity', *Macromolecules*, **33**, 7453–7466 (2000).
- [196] S. Trohalaki, L. C. DeBolt, J. E. Mark and H. L. Frisch, 'Estimation of free volume for gaseous penetrants in elastomeric membranes by Monte Carlo simulations', *Macromolecules*, **23**, 813–816 (1990).
- [197] L. Fritz and D. Hofmann, 'Molecular dynamics simulations of the transport of water–ethanol mixtures through polydimethylsiloxane membranes', *Polymer*, **38**, 1035–1045 (1997).
- [198] J. E. Mark, 'Silicon-containing polymers', in *Silicon-Based Polymer Science: A Comprehensive Resource*, J. M. Ziegler and F. W. G. Fearon (Eds), American Chemical Society, Washington, DC, USA, pp. 48–68 (1990).
- [199] J. R. Fried and B. Li, 'Molecular simulation of gas sorption and diffusion in silicon-based polymers', in *Advanced Materials for Membrane Separations*, I. Pinnau and B. D. Freeman (Eds), American Chemical Society, Washington, DC, USA, pp. 24–38 (2004).
- [200] V. E. Raptis, I. G. Economou, D. N. Theodorou, J. Petrou and J. H. Petropoulos, 'Molecular dynamics simulation of structure and thermodynamic properties of poly(dimethylsilamethylene) and hydrocarbon solubility therein: toward the development of novel membrane materials for hydrocarbon separation', *Macromolecules*, **37**, 1102–1112 (2004).
- [201] S. A. Solov'ev, Y. P. Yampol'skii, I. G. Economou, N. V. Ushahov and E. S. Finkel'shtein, 'Thermodynamic parameters of hydrocarbon sorption by poly(silimethylenes)', *Polym. Sci. Ser. A*, **44**, 293–300 (2002).
- [202] A. Alentiev, I. G. Economou, E. Finkel'shtein, J. Petrou, V. E. Raptis, M. Sanopoulou, S. Soloviev, N. Ushakov and Y. Yampol'skii, 'Transport properties of silimethylene homo-polymers and random copolymers: experimental measurements and molecular simulation', *Polymer*, **45**, 6933–6944 (2004).
- [203] T. Higashimura, T. Masuda and M. Okada, 'Gas permeability of polyacetylenes with bulky substituents', *Polym. Bull.*, **10**, 114–117 (1983).
- [204] K. Takada, H. Matsuya, T. Masuda and T. Higashimura, 'Gas permeability of polyacetylenes carrying substituents', *J. Appl. Polym. Sci.*, **30**, 1605–1616 (1985).
- [205] Y. Ichiraku, S. A. Stern and T. Nakagawa, 'An investigation of the high gas permeability of poly(1-trimethylsilyl-1-propyne)', *J. Membr. Sci.*, **34**, 5–18 (1987).
- [206] T. Nakagawa, T. Saito, S. Asakawa and Y. Saito, 'Polyacetylene derivatives as membranes for gas separations', *Gas Sep. Purif.*, **2**, 3–8 (1988).
- [207] T. Masuda, Y. Iguchi, B.-Z. Tang and T. Higashimura, 'Diffusion and solution of gases in substituted polyacetylene membranes', *Polymer*, **29**, 2041–2049 (1988).
- [208] N. A. Platé, A. K. Bokarev, N. E. Kaliuzhnyi, E. G. Litvinova, V. S. Khotimskii, V. V. Volkov and Y. P. Yampol'skii, 'Gas and vapor permeation

- and sorption in poly(trimethylsilylpropyne)', *J. Membr. Sci.*, **60**, 13–24 (1991).
- [209] A. C. Savoca, A. D. Surnamer and C.-f. Tien, 'Gas transport in poly(silylpropynes): the chemical structure point of view', *Macromolecules*, **26**, 6211–6216 (1993).
- [210] A. Morisato, H. C. Shen, S. S. Sankar, B. D. Freeman, I. Pinnau and C. G. Casillas, 'Polymer characterization and gas permeability of poly(1-trimethylsilyl-1-propyne) [PTMSP], poly(1-phenyl-1-propyne) [PPP] and PTMSP/PPP blends', *J. Polym. Sci. Part B: Polym. Phys. Ed.*, **34**, 2209–2222 (1996).
- [211] L. E. Starannikova and V. V. Teplyakov, 'Gas permeability of poly[1-(trimethylsilyl)-1-propyne]: evaluation of experimental data and calculation methods', *Polym. Sci. Ser. A*, **39**, 1142–1147 (1997).
- [212] T. C. Merkel, V. Bondar, K. Nagai and B. D. Freeman, 'Hydrocarbon and perfluorocarbon gas sorption in poly(dimethylsiloxane), poly(1-trimethylsilyl-1-propyne) and copolymers of tetrafluoroethylene and 2,2-bis(trifluoromethyl)-4,5-difluoro-1,3-dioxole', *Macromolecules*, **32**, 370–374 (1999).
- [213] T. Masuda, E. Isobe and T. Higashimura, 'Poly[1-(trimethylsilyl)-1-propyne]: a new high polymer synthesized with transition-metal catalysts and characterized by extremely high gas permeability', *J. Am. Chem. Soc.*, **103**, 7473–7474 (1983).
- [214] K. Nagai, T. Masuda and T. Nakagawa, 'Poly[1-(trimethylsilyl)-1-propyne] and related polymers: synthesis, properties, and functions', *Prog. Polym. Sci.*, **26**, 721–798 (2001).
- [215] Y. P. Yampol'skii, S. M. Shishatskii, V. P. Shantorovich, E. M. Antipov, N. N. Kuzmin, S. V. Rykov, V. L. Khodjaeva and N. A. Platé, 'Transport characteristics and other physicochemical properties of aged poly(1-(trimethylsilyl)-1-propyne)', *J. Appl. Polym. Sci.*, **48**, 1935–1944 (1993).
- [216] K. Ishihara, Y. Nagasse and K. Matsui, 'Pervaporation of alcohol/water mixtures through poly[1-(trimethylsilyl)-1-propyne] mixtures', *Makromol. Chem., Rapid Commun.*, **7**, 43–46 (1986).
- [217] T. Masuda, B.-Z. Tang and T. Higashimura, 'Ethanol–water separation by pervaporation through substituted-polyacetylene membranes', *Polym. J.*, **18**, 565–567 (1986).
- [218] M. Langsam and L. M. Robeson, 'Substituted propyne polymers – Part II. Effects of aging on the gas permeability properties of poly[1-(trimethylsilyl)propyne] for gas separation membranes', *Polym. Eng. Sci.*, **29**, 44–54 (1989).
- [219] K. Nagai, M. Mori, T. Watanabe and T. Nakagawa, 'Gas permeation properties of blend and copolymer membranes composed of 1-trimethylsilyl-1-propyne and 1-phenyl-1-propyne structures', *J. Polym. Sci. Part B: Polym. Phys. Ed.*, **35**, 119–131 (1997).
- [220] T. Nakagawa, S. Fujisaki, H. Nakano and A. Higuchi, 'Physical modification of poly[1-(trimethylsilyl)-1-propyne] membranes for gas separation', *J. Membr. Sci.*, **94**, 183–193 (1994).
- [221] R. S. Prabhakar, T. C. Merkel, B. D. Freeman, T. Imizu and A. Higuchi, 'Sorption and transport properties of propane and perfluoropropane in poly(dimethylsiloxane) and poly(1-trimethylsilyl-1-propyne)', *Macromolecules*, **38**, 1899–1910 (2005).
- [222] L. C. Witchey-Lakshmanan, H. B. Hopfenberg and R. T. Chern, 'Sorption and transport of organic vapors in poly[1-(trimethylsilyl)-1-propyne]', *J. Membr. Sci.*, **48**, 321–331 (1990).
- [223] K. Nagai, A. Higuchi and T. Nakagawa, 'Bromination and gas permeability of poly(1-trimethylsilyl-1-propyne) membrane', *J. Appl. Polym. Sci.*, **54**, 1207–1217 (1994).
- [224] I. Pinnau and L. G. Toy, 'Transport of organic vapors through poly(1-trimethylsilyl-1-propyne)', *J. Membr. Sci.*, **116**, 199–209 (1996).
- [225] B. Freeman and I. Pinnau, 'Separation of gases using solubility-selective polymers', *TRIP*, **5**, 167–173 (1997).
- [226] V. V. Teplyakov, D. Roizard, E. Favre and V. S. Khotimsky, 'Investigations on the peculiar permeation properties of volatile organic compounds and permanent gases through PTMSP', *J. Membr. Sci.*, **220**, 165–175 (2003).
- [227] Y. P. Yampol'skii, V. P. Shantorovich, F. P. Chernyakovskii, A. I. Kornilov and N. A. Platé, 'Estimation of free volume of poly(trimethylsilyl propyne) by positron annihilation and electrochromism methods', *J. Appl. Polym. Sci.*, **47**, 85–92 (1993).
- [228] G. Consolati, I. Genco, M. Pegoraro and L. Zanderighi, 'Positron annihilation lifetime (PAL) in poly[1-(trimethylsilyl)propyne] (PTMSP): free volume determination and time dependence of permeability', *J. Polym. Sci. Part B: Polym. Phys. Ed.*, **34**, 357–367 (1996).
- [229] R. Srinivasan, S. R. Auvil and P. M. Burban, 'Elucidating the mechanism(s) of gas transport in poly[1-(trimethylsilyl)-1-propyne] (PTMSP) membranes', *J. Membr. Sci.*, **86**, 67–86 (1994).
- [230] Y. P. Yampol'skii and V. P. Shantarovich, 'Chemical structure, free volume of glassy polymers, and prediction of their membrane properties', *Polym. Sci., Ser. C*, **43**, 2329–2349 (2001).
- [231] S. B. Clough, X. F. Sun, S. K. Tripathy and G. L. Baker, 'Molecular dynamics simulation of substituted polyacetylene', *Macromolecules*, **24**, 4264–4269 (1991).

- [232] M. J. S. Dewar, E. G. Zoebisch, E. F. Healy and J. J. P. Stewart, 'AM1: a new general purpose quantum mechanical molecular model', *J. Am. Chem. Soc.*, **107**, 3902–3909 (1985).
- [233] J. R. Fried and D. K. Goyal, 'Molecular simulation of gas transport in poly[1-(trimethylsilyl)-1-propyne]', *J. Polym. Sci. Part B: Polym. Phys. Ed.*, **36**, 519–536 (1998).
- [234] S. V. Dixon-Garrett, K. Nagai and B. D. Freeman, 'Sorption, diffusion, and permeation of ethylbenzene in poly(1-trimethylsilyl-1-propyne)', *J. Polym. Sci. Part B: Polym. Phys. Ed.*, **38**, 1078–1089 (2000).
- [235] T. Zheng and J. R. Fried, 'Monte Carlo simulation of the sorption of pure and mixed alkanes in poly[1-(trimethylsilyl)-1-propyne]', *Sep. Sci. Technol.*, **36**, 959–973 (2001).
- [236] T. C. Merkel, V. Bondar, K. Nagai and B. D. Freeman, 'Sorption and transport of hydrocarbon and perfluorocarbon gases in poly(1-trimethylsilyl-1-propyne)', *J. Polym. Sci. Part B: Polym. Phys. Ed.*, **38**, 273–296 (2000).
- [237] T. M. Madkour, 'Development of the molecular design rules of ultra-permeable poly[1-(trimethylsilyl)-1-propyne]', *Polymer*, **41**, 7489–7497 (2000).
- [238] D. Hofmann, M. Heuchel, Y. Yampolskii, V. Khotimskii and V. Shantarovich, 'Free volume distributions in ultrahigh and lower free volume polymers: comparison between molecular modeling and positron lifetime studies', *Macromolecules*, **35**, 2129–2140 (2002).
- [239] A. M. Polyakov, L. E. Starannikova and Y. P. Yampolskii, 'Amorphous Teflons AF as organophilic pervaporation materials. Separation of mixtures of chloromethanes', *J. Membr. Sci.*, **238**, 21–32 (2004).
- [240] Y. Wang, P. T. Inglefield and A. A. Jones, 'NMR characterization of penetrants in high permeability polymers', *Polymer*, **43**, 1867–1872 (2002).
- [241] T. C. Merkel, Z. He, I. Pinnau, B. D. Freeman, P. Meakin and A. J. Hill, 'Sorption and transport in poly(2,2-bis(trifluoromethyl)-4,5-difluoro-1,3-dioxole-co-tetrafluoroethylene)', *Macromolecules*, **36**, 8406–8414 (2003).
- [242] X.-Y. Wang, K. M. Lee, Y. Lu, M. T. Stone, I. C. Sanchez and B. D. Freeman, 'Cavity size distributions in high free volume glass polymers by molecular simulation', *Polymer*, **45**, 3907–3912 (2004).
- [243] P. J. Veld, M. T. Stone, T. M. Trunskett and I. C. Sanchez, 'Liquid structure via cavity size distributions', *J. Phys. Chem. B*, **104**, 12028–12034 (2000).
- [244] M. J. Hwang, T. P. Stockfisch and A. T. Hagler, 'Derivation of class II force fields. 2. Derivation and characterization of a class II force field, CFF93, for the alkyl functional group and alkane molecules', *J. Am. Chem. Soc.*, **116**, 2515–2525 (1994).
- [245] J. A. Maple, M. J. Hwang, T. P. Stockfisch, U. Dinur, M. Waldman, C. S. Ewig and A. T. Hagler, 'Derivation of class II force fields. I. Methodology and quantum force field for the alkyl functional group and alkane molecules', *J. Comp. Chem.*, **15**, 162–182 (1994).
- [246] M. A. LaPack, J. C. Tou, V. L. McGuffin and C. G. Enke, 'The correlation of membrane permeability with Hildebrand solubility parameters', *J. Membr. Sci.*, **86**, 263–280 (1994).
- [247] C.-C. Hu, C.-S. Chang, R.-C. Ruaan and J.-Y. Lai, 'Effect of free volume and sorption on membrane gas transport', *J. Membr. Sci.*, **226**, 51–61 (2003).
- [248] K. Tanaka, T. Kawai, H. Kita, K.-i. Okamoto and Y. Ito, 'Correlation between gas diffusion coefficient and positron annihilation lifetime in polymers with rigid polymer chains', *Macromolecules*, **33**, 5513–5517 (2000).
- [249] A. Morisato and I. Pinnau, 'Synthesis and gas permeation properties of poly(4-methyl-2-pentyne)', *J. Membr. Sci.*, **121**, 243–250 (1996).
- [250] W. J. Koros, G. K. Fleming, S. M. Jordan, T. H. Kim and H. H. Hoehn, 'Polymeric membrane materials for solution-diffusion based permeation separations', *Prog. Polym. Sci.*, **13**, 339–401 (1988).
- [251] Y. Tamai, H. Tanaka and K. Nakanishi, 'Molecular simulation of permeation of small penetrants through membranes. 1. Diffusion coefficients', *Macromolecules*, **27**, 4498–4508 (1994).
- [252] D. Hofmann, L. Fritz, J. Ulbrich, C. Schepers and M. Bohning, 'Detailed-atomistic molecular modeling of small molecule diffusion and solution processes in polymeric membrane materials', *Macromol. Theory Simul.*, **9**, 293–327 (2000).
- [253] T. C. Merkel, V. I. Bondar, K. Nagai, B. D. Freeman and I. Pinnau, 'Gas sorption, diffusion and permeation in poly(dimethylsiloxane)', *J. Polym. Sci. Part B: Polym. Phys. Ed.*, **38**, 415–433 (2000).

Predicting Gas Solubility in Membranes through Non-Equilibrium Thermodynamics for Glassy Polymers

Ferruccio Doghieri, Massimiliano Quinzi, David G. Rethwisch and Giulio C. Sarti

The Non-Equilibrium Thermodynamic theory has already been applied to the Lattice Fluid (LF) model to describe the properties of glassy polymers; the resulting NELF model successfully represents the solubility of gases and vapors in amorphous organic glasses. The same general theory is extended here and applied to two interesting and widely used equations of state, that is (i) the Perturbed-Hard-Sphere-Chain (PHSC) theory and (ii) the Statistical-Associating-Fluid Theory (SAFT). As is also the case in the corresponding equilibrium equations, the material parameters used in the models are derived from volumetric data for the pure gas and polymer being considered and, when necessary, a temperature-independent binary interaction coefficient is used as the adjustable parameter. The use of the non-equilibrium thermodynamic approach to predict or correlate gas solubility in glassy polymers is presented here and discussed, including cases in which the dilation of the polymeric matrix is appreciable and plays an important role. Results from model calculations are compared with literature data for gas solubility in polycarbonate, polysulfone and poly(methyl methacrylate). Solubility coefficients were calculated for each model at different temperatures, by using the same fixed model parameters and applying the equilibrium expressions above T_g and the non-equilibrium approach below T_g . The very satisfactory comparison with experimental data strongly confirms the

reliability of the presented non-equilibrium approach to describe the thermodynamic properties of the glassy phases.

4.1 Introduction

The phase equilibria involving polymeric solutions in the liquid or rubbery state are commonly described by using well-established thermodynamic constitutive equations, either for the excess Gibbs free energy and activity coefficients [1–5] or for the equation of state of the mixtures [6–12]. Such models offer valuable correlations, or even reliable predictions, for the solubility of low-molecular-weight penetrants in rubbery polymers, which are useful to estimate the membrane performance in pervaporation, vapor permeation and gas separation.

On the contrary, gas and vapor solubility in amorphous glassy polymers are normally described and correlated by using empirical or semiempirical tools, the most popular of which is the Dual Mode Sorption (DMS) model [13]. Indeed, good correlations and useful insights into the polymer structure can be obtained from DMS, once the solubility data are available, but no predictive calculations can be made based on the physico-chemical properties of pure polymer and penetrant. It is well known that the solubility selectivity factor offers an important contribution to the selectivity of vapors and even of gases in

polymeric materials below the glass transition temperature (e.g. [14]), and thus models offering reliable estimates of gas and vapor solubility in glassy polymers are definitely needed and represent a relevant tool to develop and design gas separation membranes.

In the case of liquid-like or rubbery polymeric solutions, the thermodynamic model needs to describe properly the energy and entropy effects due to the different molecular interactions. For glassy polymers, the problem is without any doubt more complex in view of the non-equilibrium nature of the glassy state. Below the T_g , temperature, pressure and composition of the external environment are not enough to uniquely determine penetrant solubility, and samples of the same material can display quite different behaviors, according to the different pre-histories experienced. This is essentially associated to the hindered mobility of the polymer chains in the glassy state, which does not allow the system to access all possible microstates and ultimately prevents the structure from reaching the free volume that would minimize its Gibbs free energy (true equilibrium) at constant temperature and pressure. Only some of all possible microstates are accessible, and thus the system will finally reach a pseudo-equilibrium state, corresponding to the minimum free energy attainable from the initial state, with the constraint imposed by the hindered mobility. The departure from equilibrium inherently present in glassy phases does not allow the direct use of the well-known results of classical and statistical thermodynamics of mixtures and has inspired the development of several approaches [15–18] for the description of thermodynamic properties of glassy mixtures.

A detailed comparison of the different cited models is out of the scope of this present work; we simply remark that the Non-Equilibrium Lattice Fluid (NELF) model [17,19–21] is the most effective and has good predictive ability for the solubility of pure and mixed gases in pure polymers or polymer blends. From the theoretical point of view, the model represents a special application of the Non-Equilibrium Thermodynamics of Glassy Polymers (NET-GP) and offers the non-equilibrium description of glassy phases associated to the equilibrium Lattice Fluid (LF) theory. Nonetheless, the underlying NET-GP approach indicates the relationship existing in

general between the thermodynamic properties above and below the glass transition temperature and is not limited to any special equation of state model.

This present work presents the extension of the NET-GP approach to two relevant equations of state, both based on tangent-hard-spheres-chain theories, i.e. statistical-associating-fluid theory [9] and perturbed-hard-sphere-chain theory [10,11]. These appear of particular interest for two main reasons: on one side for the remarkable results obtained in describing phase equilibria above the glass transition temperature and, on the other side, because the pure component parameters are more directly related to molecular properties and thus could possibly be predicted based on structural considerations. Prediction and correlation examples for the solubility of light gas in different conventional glassy polymers, bisphenol-A polycarbonate (PC), a polysulfone (PSf) and poly(methyl methacrylate) (PMMA), are included. The model results are compared with experimental solubility data selected from the literature and the predictions offered by the different models are suitably discussed.

4.2 Background

The thermodynamic derivation of the basic results of the NELF model have been already presented in several publications [17,19–22], and for the sake of clarity the fundamental assumptions will be recalled hereafter, together with the general results relating the Helmholtz free energy of the glassy phase to the Helmholtz free energy of the corresponding equilibrium conditions.

The NET-GP analysis developed for the NELF model moves from the assumption that the glassy polymer–penetrant mixture is a homogeneous, isotropic and amorphous phase, whose properties not only depend on composition and externally imposed conditions such as temperature and pressure, but also on proper order parameters which describe the departure from equilibrium existing in the system.

The assumption is made that a proper quantitative description of the non-equilibrium conditions of the polymer–penetrant mixture is offered just by using the specific volume of the polymer network, or equivalently by the polymer density ρ_{pol} , as order parameter. According to this simplified

picture, all of the non-equilibrium pre-history effects are ‘lumped together’ into polymer density and two different polymeric samples, with the same composition, temperature and pressure, have the same thermodynamic properties as long as their polymer mass densities have the same value, irrespective of the details concerning their specific thermal, mechanical or sorption histories. In view of the hindered mobility of the polymer chains, a departure from true thermodynamic equilibrium is frozen into the glassy phase, which is measured by the difference between actual polymer density ρ_{pol} and its equilibrium value at the given temperature pressure and mixture composition, $\rho_{\text{pol}}^{\text{EQ}}$. The latter quantity can be expressed through the familiar condition of minimum Gibbs free energy for the system, namely:

$$\rho_{\text{pol}} = \rho_{\text{pol}}^{\text{EQ}}(T, p, \Omega_{\text{sol}}) \Leftrightarrow \left(\frac{\partial G}{\partial \rho_{\text{pol}}} \right)_{T, p, \Omega_{\text{sol}}} = 0 \quad (4.1)$$

where T, p and Ω_{sol} are temperature, pressure and solute-to-polymer mass ratio, respectively.

The second key assumption in the thermodynamic theory developed for the NELF model is related to the evolution in time of the order parameters ρ_{pol} , and states that its time rate of change depends only upon the state of the system, so that the following equation holds:

$$\frac{d\rho_{\text{pol}}}{dt} = f(T, p, \Omega_{\text{sol}}, \rho_{\text{pol}}) \quad (4.2)$$

where $f(\cdot)$ is an appropriate function which returns positive values for $\rho_{\text{pol}} < \rho_{\text{pol}}^{\text{EQ}}(T, p, \Omega_{\text{pol}})$ and negative values for $\rho_{\text{pol}} > \rho_{\text{pol}}^{\text{EQ}}(T, p, \Omega_{\text{pol}})$. True thermodynamic equilibrium is achieved when the rate function $f(\cdot)$ is exactly zero, while pseudo-equilibrium states associated to the hindered mobility of the glassy system correspond to negligibly small, though not exactly zero, values of the function $f(\cdot)$ in Equation (4.2), obtained at ρ_{pol} values different from $\rho_{\text{pol}}^{\text{EQ}}$. Accordingly, the order parameter ρ_{pol} plays the role of an internal state variable [23] for the system, and basic thermodynamic relations of the NELF model are directly derived by applying well-established thermodynamic results for systems endowed with internal-state variables.

The key consequence of the mentioned thermodynamic procedure [19], states that for the non-equilibrium conditions frozen into the glassy phase, the Helmholtz free energy density, a^{NE} , depends only on composition and polymer mass density, and its value is not affected by the pressure of the system:

$$\left(\frac{\partial a^{\text{NE}}}{\partial p} \right)_{T, \Omega_{\text{sol}}, \rho_{\text{pol}}} = 0 \quad (4.3)$$

An equally simple, but not trivial result is obtained for the penetrant chemical potential on a mass basis, $\mu_{\text{sol}}^{\text{NE}}$, under non-equilibrium conditions:

$$\mu_{\text{sol}}^{\text{NE}} = \left(\frac{\partial a^{\text{NE}}}{\partial \rho_{\text{sol}}} \right)_{T, p, \rho_{\text{pol}}} \quad (4.4)$$

It is worthwhile noticing that Equation (4.2) embodies the assumption that the specific volume of the polymer network evolves in time following a Voigt model for bulk rheology [19]. Consistently, specific information about rheological properties of the polymeric system could be used, within this approach, to recognize what values of polymer density correspond to pseudo-equilibrium conditions. In what follows, however, we will ignore any possible effort to predict pseudo-equilibrium values of the polymer density based on Equation (4.2) and rather rely on the availability of specific experimental information, or at least reasonable correlations, for the values of the order parameter ρ_{pol} in the pseudo-equilibrium states of interest.

Equations (4.3) and (4.4) embody the general key results of the NET-GP theory, insofar as they indicate how to obtain the univocal extension of the free energy (or penetrant chemical potential) function, from the subset of equilibrium states to the entire domain of non-equilibrium glassy states. Accordingly, once an expression for the equilibrium free energy a^{EQ} is found appropriate for the equilibrium polymer–penetrant mixture, the corresponding non-equilibrium equation is readily derived as function of temperature and species density:

$$a^{\text{NE}}(T, p, \Omega_{\text{sol}}, \rho_{\text{pol}}) = a^{\text{EQ}}(T, \Omega_{\text{sol}}, \rho_{\text{pol}}) \quad (4.5)$$

A corresponding relation can then be obtained for the non-equilibrium chemical potential $\mu_{\text{sol}}^{\text{NE}}$ in terms of the corresponding equilibrium function $\mu_{\text{sol}}^{\text{EQ}}$, based on the results given in Equations (4.4) and (4.5):

$$\mu_{\text{sol}}^{\text{NE}}(T, p, \Omega_{\text{sol}}, \rho_{\text{pol}}) = \mu_{\text{sol}}^{\text{EQ}}(T, \Omega_{\text{sol}}, \rho_{\text{pol}}) \quad (4.6)$$

It must be stated clearly that the above equations, although derived in the development of the NELF model, represent general non-equilibrium thermodynamic results, which can be applied to any equilibrium expression for the free energy function a^{EQ} , and are not restricted to a special equilibrium model. Non-equilibrium free energy functions can thus be obtained starting from the equations of states associated to the lattice fluid theories, as well as to the tangent-hard-sphere-chain theories, just to mention two relevant approaches which are of direct interest in this work. Of course, one would in general prefer models which satisfactorily describe the thermodynamic properties of polymeric phases under equilibrium conditions, although a word of caution is in order here. Indeed, an accurate representation of the equilibrium properties does not necessarily imply an equally accurate calculation of non-equilibrium properties, according to the above procedure. Different models may give different polymeric densities below the glass transition temperature, where the equilibrium models developed were not tested, thus also implying appreciable differences in the calculated departure from equilibrium; thus, it cannot be taken for granted that different models which are good in the representation of equilibrium properties remain equally appropriate when extended to non-equilibrium glassy phases. A later discussion will further clarify this point.

4.2.1 Pseudo-solubility Calculation

Calculation of the gas concentration reached in glassy polymers, under apparent equilibrium with an external pure gas, is now presented, at a given temperature T and pressure p .

The situation here considered is different from the case of true thermodynamic phase equilibrium, in which the minimum Gibbs free energy for the system is attained, so that the equilibrium

solute content, $\Omega_{\text{sol}}^{\text{EQ}}$, and polymer density, $\rho_{\text{pol}}^{\text{EQ}}$, are given by the following conditions:

$$\begin{cases} \mu_{\text{sol}}^{\text{EQ(s)}}(T, \Omega_{\text{sol}}^{\text{EQ}}, \rho_{\text{pol}}^{\text{EQ}}) = \mu_{\text{sol}}^{\text{EQ(g)}}(T, p) \\ \left(\frac{\partial G^{(s)}}{\partial \rho_{\text{pol}}} \right)_{T, p, \Omega_{\text{sol}}} = 0 \end{cases} \quad (4.7)$$

The symbol $G^{(s)}$ represents the Gibbs free energy of the polymeric mixture per unit polymer mass, $\Omega_{\text{sol}}^{\text{EQ}}$ is the penetrant-to-polymer mass ratio reached at phase equilibrium conditions, while $\mu_{\text{sol}}^{\text{EQ(s)}}$ and $\mu_{\text{sol}}^{\text{EQ(g)}}$ indicate equilibrium chemical potentials for the solute species in the solid and gaseous phases, respectively.

The pseudo-equilibrium condition reached with glassy polymeric phases is different insofar as the polymer density does not match its equilibrium value $\rho_{\text{pol}}^{\text{EQ}}$, but rather is finally immobilized to a value which depends on the history of the specific sample. Pseudo-equilibrium problems are then described through the condition of minimum Gibbs free energy for the system, under the constraint that polymer density is fixed in the condensed phase. This implies:

$$\mu_{\text{sol}}^{\text{NE(s)}}(T, p, \Omega_{\text{sol}}^{\text{PE}}, \rho_{\text{pol}}^{\text{PE}}) = \mu_{\text{sol}}^{\text{EQ(g)}}(T, p) \quad (4.8)$$

Once an appropriate equation of state is identified for the polymer-penetrant system, and the corresponding solute chemical potential in non equilibrium condition is obtained through Equation (4.4), Equation (4.8) can be used to obtain the pseudo-equilibrium penetrant content, $\Omega_{\text{sol}}^{\text{PE}}$, whenever the value of the pseudo-equilibrium polymer density $\rho_{\text{pol}}^{\text{PE}}$ is known. Clearly, the latter quantity represents a crucial input required by the non-equilibrium approach; its knowledge must be provided as a separate independent information, since $\rho_{\text{pol}}^{\text{PE}}$ cannot be calculated simply from temperature and pressure but depends on the thermomechanical history of the sample. Although in the general case such information may not be easily available, in several cases of practical interest the pseudo-equilibrium density of the polymer is unequivocal and easily determined. One of these cases is obtained at low gas pressures, under which conditions the polymeric mixture is at infinite dilution and the volume of the mixture is not affected by the

contributions of the partial molar volume of the solute. Pure glassy polymer density, ρ_{pol}^0 , then provides a very good estimate of the parameter $\rho_{\text{pol}}^{\text{PE}}$ at low gas pressures. The same is also true at moderate pressures, for the case of non-swelling agents, such as many permanent gases. Therefore, under these conditions we will consider the pseudo-equilibrium problem as described by the following low-pressure approximation [22]:

$$\mu_{\text{sol}}^{\text{NE(s)}}(T, p, \Omega_{\text{sol}}^{\text{PE}}, \rho_{\text{pol}}^0) = \mu_{\text{sol}}^{\text{EQ(g)}}(T, p) \quad (4.9)$$

For the gas solubility at higher pressures, it was generally observed [24–26] that polymer mass density during sorption changes linearly with gas pressure, so that the following condition may be assumed:

$$\rho_{\text{pol}}^{\text{PE}}(p) = \rho_{\text{pol}}^0(1 - k_{\text{sw}}p) \quad (4.10)$$

which represents the effect of gas pressure on pseudo-equilibrium polymer density in terms of the swelling coefficient k_{sw} . Several experimental data for volume dilation under sorption experiments confirm the validity of Equation (4.10) in a relatively large pressure range, at least for a temperature sufficiently below the glass transition of the pure polymer [24–26]. In addition, the swelling coefficient k_{sw} , as well as the pure polymer density ρ_{pol}^0 , is a non-equilibrium quantity, which thus depend on thermomechanical and sorption history of the specific polymer sample. In this work, we will assume that Equation (4.10) holds for pseudo-equilibrium polymer density for the case of high-pressure-gas sorption, so that the corresponding pseudo-equilibrium condition, Equation (4.8), now becomes:

$$\begin{aligned} \mu_{\text{sol}}^{\text{NE(s)}}(T, p, \Omega_{\text{sol}}^{\text{PE}}, \rho_{\text{pol}}^0(1 - k_{\text{sw}}p)) \\ = \mu_{\text{sol}}^{\text{EQ(g)}}(T, p) \end{aligned} \quad (4.11)$$

The pseudo-equilibrium conditions given in Equation (4.9) or Equation (4.11) hold in general for the cases of low-pressure and high-pressure-gas solubility, respectively, and are not limited to any specific thermodynamic model for the equilibrium properties of the polymer–solute mixture. From any chosen expression of the Helmholtz free energy in terms of temperature

and species densities, one obtains the corresponding expressions for the chemical potentials in the glassy phases and the phase pseudo-equilibrium problem is represented by Equation (4.8) or Equations (4.9) or (4.11), if applicable.

The fundamental objective of this work is to compare the results of the solubility calculations obtained from the pseudo-equilibrium formulation presented above, when use is made of different thermodynamic models for the thermodynamic equilibrium properties. In particular, equations of state based on lattice fluid or tangent-hard-sphere-chain theories will be considered, as SAFT and perturbed-hard-spheres-chain theory. A brief description is given hereafter of essential characteristics of the underlying equilibrium thermodynamic models whose extension to non-equilibrium states will then be considered.

4.2.2 Lattice Fluid Model (Sanchez and Lacombe)

Among all lattice fluid equations of state, we will consider in particular the model introduced by Sanchez and Lacombe [8,27–29], which considers a compressible lattice for the representation of microstates of either pure fluids or fluid mixtures. The resulting equation of state, hereafter indicated as the LF model, proved to be rather successful to describe phase equilibria conditions of both simple fluids and polymeric mixtures. The specific lattice considered by Sanchez and Lacombe is made of cells, whose volume depends on mixture composition, which can be empty or occupied by a molecular segment. In turn, molecules are pictured as linear chains of elementary segments. Only interactions between molecular segments which occupy adjacent cells are accounted for by the model. The pure component parameters in the LF model are molar mass (MM), cell volume (v^*) of the lattice, mass of molecular segment which can occupy a single cell (MM/r) and interaction energy between molecular segments (ϵ^*). The residual Helmholtz free energy density, a^{res} , defined as the free energy difference with respect to the corresponding ideal gas mixture at the same temperature and volume, is calculated as the sum of entropy and internal energy contributions, as follows:

$$a^{\text{res}} = u^{\text{res}} - T s^{\text{res}} \quad (4.12)$$

The residual entropy is calculated by assuming that all distributions of molecular segments in the lattice which obey the chain connectivity have the same probability. Use of simple mixing rules for relevant lattice fluid parameters leads to the representation of the thermodynamic properties of mixtures. As it is most often the case for mixtures, the mixing rules contain adjustable binary parameters, which are as many as the number of all possible different component pairs in the mixture. Each binary parameter, k_{ij} , enters the expression for the interaction energy ϵ_{ij}^* between molecular segments of species i and j occupying two adjacent cells, according to the following relationship:

$$\epsilon_{ij}^* = (1 - k_{ij}) \sqrt{\epsilon_{ii}^* \epsilon_{jj}^*} \quad (4.13)$$

The default value, $k_{ij}=0$, can be used to recover the usual first-order approximation for the characteristic interaction energy, represented by the geometrical mean rule.

4.2.3 Tangent-Hard-sphere-Chain Equation of State

For the tangent-hard-sphere-chain models, molecules are represented as chains of spherical segments with an assigned mass and a temperature-dependent volume. Adjacent segments are connected to each other in the chain, while they are able to interact with other segments according to a proper pair-interaction potential of spherical symmetry. We will consider in particular two relevant models of this type, i.e. the Self Associating Fluids Theory (SAFT) [9,30,31] and the Perturbed-Hard-Spheres Chain (PHSC) theory. [10,11,32].

Both models rely on suitable statistical thermodynamics arguments and take advantage of specific simplifying assumptions. In the SAFT model, the free energy contribution due to specific hydrogen-bond interactions between segments, if any, is treated separately through a specific contribution and requires a preliminary identification of the associating sites in each molecule. The PHSC model does not account separately for specific associating sites. In the calculations that follow, however, only non-associating species are considered and the difference between SAFT and

PHSC relative to specific hydrogen-bond interactions has no role in this present work. It is not the aim of this section to offer an exhaustive presentation of the characteristic features of the models, but rather to introduce the model parameters and to indicate the pure component and mixture properties that are needed for their retrieval. The reader is referred to the cited original papers for further details.

Several versions of the SAFT equation of state (EoS) have been proposed in the literature, after the initial works by Chapman *et al.* [30,31]. In the present work, we will use one of the earliest, described in details by Huang and Radosz [9]. In the SAFT model, the residual Helmholtz free energy of the system, a^{res} , results from the sum of different contributions due to *hard spheres*, *dispersion*, *chain* and *association*:

$$a^{\text{res}} = a^{\text{hs}} + a^{\text{disp}} + a^{\text{chain}} + a^{\text{assoc}} \quad (4.14)$$

The first two terms in Equation (4.14) refer to the segment-segment hard sphere and mean-field interactions, respectively. The chain term accounts for the free energy increment due to the permanent bonds between segments in the chain, while the last contribution refers to specific hydrogen bonding between associating sites, if any. The dispersion term is expressed by the power series expression developed by Chen and Kreglewski [33], after fitting accurate *PVT* data for argon. The SAFT free energy expression for a non-associating pure component, contains only three parameters besides the molar mass (MM), namely the sphere volume (v^{00}), the sphere mass (MM/m) and the characteristic energy of the interactions present in the dispersion contribution (u_{ii}^0).

The equilibrium free energy expression is extended to multicomponent solutions by using mixing rules, in which adjustable binary parameters appear. We will discuss here only the role of the binary interaction parameter k_{ij} , which enters the mixing rule for the characteristic interaction energy for pairs of unlike segments i and j :

$$u_{ij}^0 = (1 - k_{ij}) \sqrt{u_{ii}^0 u_{jj}^0} \quad (4.15)$$

As usual, the default value, $k_{ij}=0$, can be used to recover the typical first-order approximation for the characteristic interaction energy between

unlike segments, given by the geometrical mean rule.

Similarly, for the PHSC EoS several versions have been presented in the literature [10,11,32], which mainly differ in the expression used for the pair interaction potential between chain segments. In all PHSC models, the residual Helmholtz free energy is expressed as the sum of a *reference* term, accounting for chain connectivity and a hard sphere interaction and *perturbation* term, which represents the contributions of mean-field forces:

$$a^{\text{res}} = a^{\text{ref}} + a^{\text{pert}} \quad (4.16)$$

The first PHSC model considered here is the simplified perturbed-hard-sphere-chain theory by Song *et al.* [10] in which the reference term uses the modified Chiew equation of state, while the perturbation term is of the van der Waals type [10]. In what follows, this model is referred to as the PHSC(vdW) equation of state. The pure component parameters involved in the expression for the Helmholtz free energy are, in addition to the species molar mass, the sphere diameter σ , the mass per segment M/r and the characteristic energy for the pair interaction potential ε , following the notation of Song *et al.* [10].

When extended to mixtures, the free energy expressions are obtained through the introduction of mixing rules and the binary parameters contained therein. As in the case of the SAFT EoS, we will consider only the binary interaction parameters k_{ij} appearing, as usual, in the expression of the characteristic energy for the interaction between pairs of unlike segments:

$$\varepsilon_{ij} = (1 - k_{ij})\sqrt{\varepsilon_{ii}\varepsilon_{jj}} \quad (4.17)$$

A second version of the PHSC equation of state will also be used; this was introduced by Hino and Prausnitz [11] by replacing the simple van der Waals perturbation term with a second-order perturbation term for a square well potential of variable width, following Chang and Sandler [34]. This will be referred to as the 'square well version' of the perturbed-hard-sphere-chain theory, PHSC(SW). For pure fluids, a complete expression of the equilibrium residual free energy density as a function of temperature and specific

volume is obtained from PHSC(SW) by using four parameters, in addition to molar mass, that is, the sphere diameter σ , the sphere mass M/r , the characteristic energy ε and the reduced well width λ . For the sake of simplicity, in this work a fixed value of λ equal to 1.455 was used for all components analyzed. This value was chosen based on the reported work by Hino and Prausnitz [11].

4.2.4 Retrieving Parameters and Building Pseudo-Equilibrium Solubility Models

Use of any of the above equations of state for a polymer-penetrant mixture requires the pure component model parameters, both for the polymer and the low-molecular-weight species, and one binary parameter for the specific pair.

The pure component properties must be retrieved from convenient thermodynamic data for the pure species, under equilibrium conditions, that is above the glass transition temperature. Pure component phase equilibrium data, such as saturated vapor pressure and liquid density, are used in most cases to obtain EoS parameters for the low-molecular-weight species. For the case of polymeric components, use can be made of specific volume isotherms above the glass transition temperature.

Specific evaluation of the binary interaction parameter requires phase equilibrium data for the binary mixture; it is known that in order to obtain a good representation of binary vapor liquid equilibria (VLE) or liquid-liquid equilibria (LLE) data for usual mixtures, a temperature-dependence of the binary interaction parameters must often be taken into account. In this work, however, for the sake of simplicity, k_{ij} will be regarded as temperature-independent. Reasonable values for k_{ij} in Equations (4.13), (4.15) and (4.17) can sometimes be estimated, even in the absence of specific binary data, since k_{ij} is expected to be close to zero for a pair of chemically similar species, and small variations should result when one component of the mixture is substituted with another of the same family of components.

Once all of the necessary pure component and binary interaction parameters have been determined, for each model chosen an explicit predictive expression of the solute chemical potential in the glassy phase is obtained by using Equation (4.6), based on the corresponding equilibrium

expression. Although Equation (4.6) may lead one to consider that this step is easy and rather direct, the usual expressions for the equilibrium chemical potentials are currently available in terms of T , p and composition, while here we need to consider the dependence on temperature and species densities. As a consequence, significant algebraic work was involved in obtaining the expressions needed for each model. The corresponding equations are rather long and cumbersome and are omitted here for the sake of brevity. Direct calculation of the pseudo-equilibrium solubility is then straightforward, through the phase equilibrium condition given by Equation (4.8).

The non-equilibrium thermodynamic model for the calculation of pseudo-equilibrium solubility is given by Equation (4.8) in general, which may simplify into Equations (4.9) or (4.10) depending on the extent of swelling induced in the polymer matrix. For each thermodynamic model chosen, it is important to appreciate the number of material parameters which are required for the calculation of the solute chemical potential, both in the solid glass and in the external gaseous phase. For the models considered here, the parameters involved are summarized in Table 4.1.

For the case of low penetrant pressure or non-swelling solutes, the internal state variable is simply the density of the pure unpenetrated polymer ρ_{pol}^0 , while the swelling coefficient is also required in the presence of appreciable volume

dilation. In the list considered in Table 4.1, the molar mass of the solute has been explicitly indicated while for the polymer it was omitted, since its effect becomes negligible as the molecular weight increases, and all of the calculations reported in this study for NE-LF, NE-SAFT, NE-PHSC(vdW) or NE-PHSC(SW) were performed in the limit of an infinite value of MM_{pol} .

For all of the models considered in this work, explicit expressions for the solute non-equilibrium chemical potential have been obtained according to the NET-GP procedure indicated, in terms of the parameters listed in Table 4.1.

4.3 Solubility Calculation and Comparison with Experimental Data

4.3.1 Prediction of the Low-pressure Gas Solubility in Glassy Polymers

In this section, we consider the low-pressure solubility isotherms of methane in glassy polycarbonate (PC). The values are calculated using all of the pseudo-equilibrium solubility models presented above, and are then compared with the experimental data measured by Jordan and Koros [35].

The first step of the procedure requires retrieving pure component parameters for polycarbonate for all of the equilibrium models, i.e. LF, SAFT, PHSC(vdW) and PHSC(SW). Volumetric data for

Table 4.1 List of parameters needed for the different thermodynamic models considered in this work

Equilibrium model	LF	SAFT	PHSC(vdW) PHSC(SW)
Non-equilibrium model	NE-LF	NE-SAFT	NE-PHSC(vdW) NE-PHSC(SW)
	<i>Solute chemical potential in the glassy phase, $\mu_{\text{sol}}^{\text{NE(s)}}$</i>		
State variable	$T, p, \Omega_{\text{sol}}$	$T, p, \Omega_{\text{sol}}$	$T, p, \Omega_{\text{sol}}$
Internal-state variable	ρ_{pol}^0 or $\rho_{\text{pol}}^0, k_{\text{sw}}$	ρ_{pol}^0 or $\rho_{\text{pol}}^0, k_{\text{sw}}$	ρ_{pol}^0 or $\rho_{\text{pol}}^0, k_{\text{sw}}$
Pure solute parameter	$MM_{\text{sol}}, v_{\text{sol}}^*, (MM/r)_{\text{sol}}, \epsilon_{\text{sol}}^*$	$MM_{\text{sol}}, v_{\text{sol}}^{00}, (MM/m)_{\text{sol}}, u_{\text{sol}}^0$	$MM_{\text{sol}}, \sigma_{\text{sol}}, (M/r)_{\text{sol}}, \epsilon_{\text{sol}}$
Pure polymer parameter	$v_{\text{pol}}^*, (MM/r)_{\text{pol}}, \epsilon_{\text{pol}}^*$	$v_{\text{pol}}^{00}, (MM/m)_{\text{pol}}, u_{\text{pol}}^0$	$\sigma_{\text{pol}}, (M/r)_{\text{pol}}, \epsilon_{\text{pol}}$
Binary parameter	k_{ij}	k_{ij}	k_{ij}
	<i>Solute chemical potential in the external single gas phase, $\mu_{\text{sol}}^{\text{EQ(g)}}$</i>		
State variable	T, p	T, p	T, p
Pure solute parameter	$MM_{\text{sol}}, v_{\text{sol}}^*, (MM/r)_{\text{sol}}, \epsilon_{\text{sol}}^*$	$MM_{\text{sol}}, v_{\text{sol}}^{00}, (MM/m)_{\text{sol}}, u_{\text{sol}}^0$	$MM_{\text{sol}}, \sigma_{\text{sol}}, (M/r)_{\text{sol}}, \epsilon_{\text{sol}}$

pure polycarbonate in the rubbery state, reported by Zoller [36], were used to this aim. EoS parameters were determined for PC by obtaining the best-fit of the experimental volumetric data in the temperature range from 450 to 610 K and for pressures up to 180 MPa. The data were fitted only in the region above the glass transition temperature where the polymer exhibits true thermodynamic equilibrium behavior. The results of the data fitting procedure for LF and SAFT EoS are shown in Figure 4.1, while the corresponding pure component parameters thus obtained are indicated in Tables 4.2 and 4.3. In Figure 4.1, comparison between calculated specific volume and experimental measurements has been extended also below the glass transition temperature, in order to pinpoint the difference between the actual pure polymer density in the glassy phase and the corresponding equilibrium value predicted by each equation of state. The pure component parameters for methane for the LF and SAFT models, whose values were retrieved from the literature [9,19,37], are reported in Table 4.1. The pure component parameters of PC and CH₄ for PHSC(vdW) and PHSC(SW) were obtained from Song *et al.* [10] and Hino

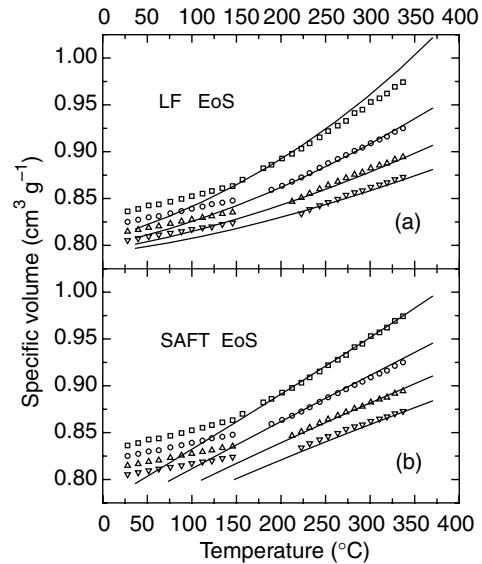


Figure 4.1 Results of the fitting procedure for *PVT* data for PC from Zoller [36] using the LF and SAFT equations of state. Experimental data: □, 0.1 MPa; ○, 59 MPa; △, 118 MPa; ▽, 177 MPa

Table 4.2 Pure component parameters for LF EoS

Component	MM (kg kmol ⁻¹)	v^* (L kmol ⁻¹)	MM/r (kg kmol ⁻¹)	ε^*/k (K)	Reference
PC	—	11.75	15.00	151.0	[17]
PSf	—	11.50	15.07	166.0	[22]
PMMA	—	10.32	13.10	139.0	[19]
CO ₂	44.01	3.96	6.00	60.0	[17]
C ₂ H ₄	28.05	7.11	4.83	59.0	[21]
N ₂ O	44.00	5.40	7.57	65.0	This work
CH ₄	16.04	7.15	3.58	43.0	[19]
N ₂	28.01	7.53	7.11	29.0	[19]
Ar	39.95	5.82	9.02	34.0	This work

Table 4.3 Pure component parameters for SAFT EoS

Component	MM (kg kmol ⁻¹)	v^{00} L kmol ⁻¹	MM/m (kg kmol ⁻¹)	u^0/k (K)	Reference
PC	—	12.00	25.00	371.0	This work
PSf	—	12.00	25.67	410.0	This work
PMMA	—	14.50	28.80	400.0	This work
CO ₂	44.01	13.58	31.06	216.1	[9]
C ₂ H ₄	28.05	18.16	19.16	212.1	[9]
N ₂ O	44.00	10.00	23.50	203.0	This work
CH ₄	16.04	21.58	16.04	190.3	[9]
N ₂	28.01	19.46	28.01	123.5	[9]
Ar	39.95	16.29	39.95	150.9	[9]

Table 4.4 Pure component parameters for PHSC(vdW) EoS

Component	MM (kg kmol ⁻¹)	σ (Å)	M/r (kg kmol ⁻¹)	ε/k (K)	Reference
PC	—	3.707	25.74	393.0	[10]
PSf	—	3.721	26.88	425.7	[10]
CO ₂	44.01	2.346	10.96	128.6	This work
C ₂ H ₄	28.05	3.839	17.43	196.8	[10]
CH ₄	16.04	4.126	16.04	182.1	This work
N ₂	28.01	3.990	28.01	122.0	This work
Ar	39.95	3.770	39.95	143.3	This work

Table 4.5 Pure component parameters for PHSC(SW) EoS

Component	MM (kg kmol ⁻¹)	σ (Å)	M/r (kg kmol ⁻¹)	ε/k (K)	Reference
PC	—	3.333	32.05	321.0	This work
PSf	—	3.400	35.00	350.0	This work
PMMA	—	3.400	33.20	320.0	This work
CO ₂	44.01	2.484	16.27	145.1	[11]
C ₂ H ₄	28.05	3.550	20.00	200.0	This work
N ₂ O	44.00	3.250	32.00	220.0	This work
CH ₄	16.04	3.672	16.01	164.9	[11]
N ₂	28.01	3.520	27.62	108.0	This work
Ar	39.95	3.340	39.95	129.0	This work

and Prausnitz [11], respectively. All values retrieved from the literature and used in this work are listed in Table 4.4 for PHSC(vdW) and in Table 4.5 for PHSC(SW). The specific PC volume calculated through PHSC models with the pure component parameters listed in Tables 4.4 and 4.5 are compared with the experimental values in Figure 4.2. It is quite evident that both models provide a satisfactory representation of polymer density above the glass transition temperature, and based on that there is no reason to prefer one model to the other. However, quite different values are obtained from PHSC(vdW) and PHSC(SW) for the equilibrium specific volume of PC below the glass transition temperature; consequently, the two models estimate different excess volumes of the glassy phase over the equilibrium state or equivalently different departures from equilibrium. In particular, the equilibrium polymer density calculated from PHSC(vdW) at low pressure and room temperature does not differ appreciably from the experimental value reported for the glassy material. This feature would be unimportant if use of the EoS was confined only to the equilibrium domains, i.e. to the rubbery state, as intended in the original formulation of the models; nonetheless, it is of great interest in this present work, in which the models

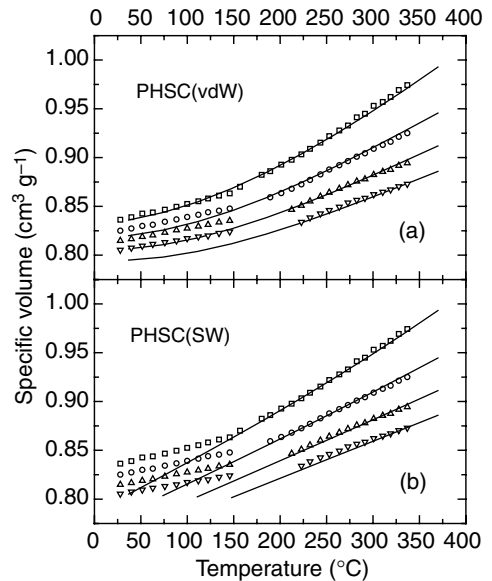


Figure 4.2 Results of the fitting procedure for PVT data for PC from Zoller [36] using the PHSC(vdW) and PHSC(SW) equations of state. Experimental data: □, 0.1 MPa; ○, 59 MPa; △, 118 MPa; ▽, 177 MPa

are extended to the non-equilibrium glassy state reached below T_g .

The list of parameters is then completed considering the dry polymer density, ρ_{pol}^0 , valid for the PC sample of interest; we can benefit here from the value reported by Jordan and Koros [35] who measured ρ_{pol}^0 to be equal to 1.200 kg L^{-1} for the PC samples used in their sorption experiments; this value is used in the following calculations.

Using the pure component parameters listed in Tables 4.2 and 4.3, the solubility isotherm for CH_4 in PC at 35°C was calculated from the NE-LF and NE-SAFT models, using the low pressure approximation (Equation (4.9)) since methane is definitely a non-swelling agent. The first-order approximation for the binary interaction parameters, $k_{ij} = 0$, was used in both cases. With this assumption the models do not contain any adjustable parameters and the solubility isotherms are then calculated in a predictive mode. Results of these calculations are shown in Figure 4.3 and compared with experimental data. The gas content predicted under pseudo-equilibrium conditions (continuous lines) offer a satisfactory representation of the solubility coefficient measured at low pressures, both for the case

of the NE-LF and NE-SAFT models. Calculated isotherms also exhibit a downward curvature towards the pressure axis, which follows the same trend of the experimental data, at least in the moderate-pressure range. This result is particularly interesting, being obtained through a purely predictive procedure, based only on the pure materials properties.

For the sake of comparison, the true equilibrium solubility isotherms are shown in Figure 4.3 (dashed lines); these were calculated using the corresponding equilibrium LF and SAFT EoS (see Equation (4.7)), and the same pure component and binary parameters listed in Tables 4.2 and 4.3. As evident from Figure 4.3, equilibrium LF and SAFT EoS calculations underestimate the low-pressure solubility coefficient of CH_4 in PC and fail to capture the downward curvature toward the pressure axis of the experimental isotherm. The phase equilibrium under true thermodynamic equilibrium conditions, calculated from Equation (4.7) and the corresponding pseudo-equilibrium problem, given by Equation (4.9), clearly differ in several respects. The major difference between the two problems arises from the departure of the glassy polymer density from the polymer density calculated at true thermodynamic equilibrium. In the present case, in which the low-pressure approximation is reasonable, ρ_{pol}^0 is used for the polymer glass density at all pressures (see Equation (4.9)). The remarkable difference between the pseudo-equilibrium solubility predicted by the NE-LF or NE-SAFT models and equilibrium solubility calculated from LF and SAFT EoS is essentially associated to the difference between the polymer density measured in the glassy state and the value calculated for the equilibrium phase at the same temperature and pressure.

The pseudo-equilibrium CH_4 solubility in PC at 35°C , calculated using the NE-PHSC(vdW) and NE-PHSC(SW) models with the binary parameter $k_{ij} = 0$, are shown in Figure 4.4. Methane solubilities calculated using the corresponding equilibrium EoS, PHSC(vdW) and PHSC(SW) are also included for comparison in the same figure. For PHSC(vdW) (Figure 4.4(a)), the calculated solubility in PC is an order of magnitude lower than the measured values. On the other side, there is no significant difference between the gas solubility predicted using NE-PHSC(vdW) and the true equilibrium solubility calculated

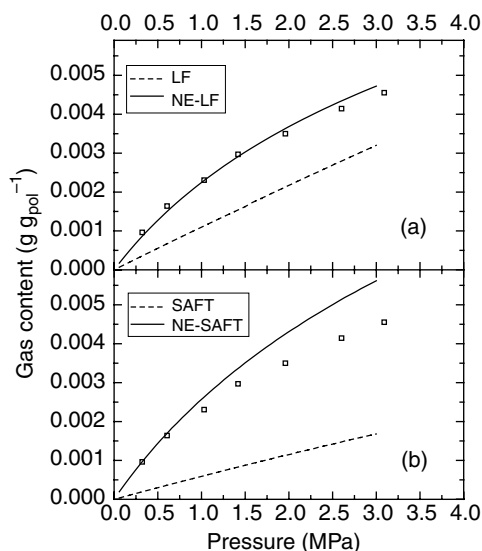


Figure 4.3 Comparison of experimental data for the CH_4 solubility isotherm in PC at 35°C from Jordan and Koros [35] (symbols) with predicted values from different equilibrium and pseudo-equilibrium models

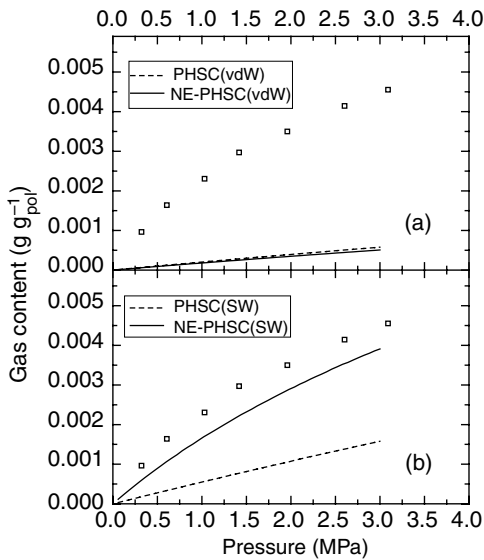


Figure 4.4 Comparison of experimental data for the CH_4 solubility isotherm in PC at 35°C from Jordan and Koros [35] (symbols) with predicted values from different equilibrium and pseudo-equilibrium models

from PHSC(vdW). It is interesting to observe that this result parallels the negligible ‘excess volume’ over the equilibrium state, estimated for glassy PC by the PHSC(vdW) EoS at atmospheric pressure (see Figure 4.2(a)).

On the contrary, the change in the form of the pair interaction potential used in PHSC(SW) originates a remarkable difference between the equilibrium specific volume calculated below T_g by the two equations of state, PHSC(SW) and PHSC(vdW). Indeed, when the specific volume of glassy PC is analyzed using equilibrium PHSC(SW) (Figure 4.2(b)), appreciable values for ‘excess volume’ are estimated. Consistently, the NE-PHSC(SW) model gives rise to solubility isotherms higher than the corresponding equilibrium model PHSC(SW) and are rather close to the experimental values reported for CH_4 in Figure 4.4(b).

4.3.2 Prediction of the Low-pressure Solubility Coefficient of Gases in Glassy Polymers

The analysis of gas solubility in PC has been extended to various solutes in the low-pressure range. For the sake of a compact representation,

the results are presented in terms of the infinite dilution solubility coefficient S_0 , for which the comparison with experimental data is more severe since it is the initial slope of the solubility isotherm:

$$S_0 = \lim_{p \rightarrow 0} \frac{C(p)}{p} \quad (4.18)$$

The quantity $C(p)$ indicates molar gas concentration in the polymeric mixture at pressure p .

In Figure 4.5(a), results for the infinite dilution solubility coefficients S_0 of N_2 , CH_4 , C_2H_4 and CO_2 in PC at 35°C , calculated using the NE-LF model, are reported as a function of gas critical temperature T_c , and compared with the experimental values reported by Jordan and Koros [35]. The corresponding LF pure component parameters used in these calculations are indicated in Table 4.2. In all cases, the binary interaction parameter $k_{ij} = 0$, and a dry polymer density of 1.200 kg L^{-1} were used. In the same figure, the solubility coefficients calculated

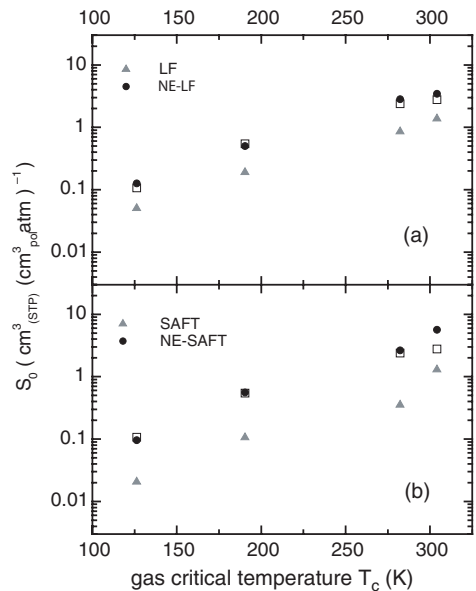


Figure 4.5 Comparison of experimental infinite dilution solubility coefficients for N_2 , CH_4 , C_2H_4 and CO_2 in polycarbonate at 35°C from Jordan and Koros [35] (open squares) with predicted values from different equilibrium and pseudo-equilibrium models

using equilibrium LF are also indicated. A large difference between equilibrium (LF) and pseudo-equilibrium (NE-LF) solubility is quite evident in all cases. Equilibrium LF underestimated the solubility coefficients by 50 % on the average. Pseudo-equilibrium solubility coefficients in PC calculated from the NE-LF model satisfactorily compare with experimental data for all of the gases considered, according to that already reported in previous studies [17,21,22].

The low-pressure gas solubility coefficients calculated from the NE-SAFT model for the same polymer–penetrant pairs are shown in Figure 4.5(b). The corresponding pure component parameters are reported in Table 4.3. The binary interaction parameters k_{ij} were set equal to zero, also in these cases, and the dry polymer density of 1.200 kg L^{-1} was used in the calculations. In the same figure, the solubility coefficients calculated from equilibrium SAFT are also reported for due comparison. The equilibrium EoS for this model would underestimate the solubility coefficient by an average value of 75 %. On the other hand, from NE-SAFT the pseudo-equilibrium solubility coefficients calculated for lighter gases compare well with the experimental data, while for CO_2 the model predictions using the first-order approximation of the binary parameter are overestimated by a factor of two.

Analogous comparison is given in Figure 4.6 for the case of PHSC models and their non-equilibrium versions. The results obtained for the NE-PHSC(vdW) model (Figure 4.6(a)) show only negligible differences with respect to equilibrium solubility coefficients calculated with the corresponding PHSC(vdW) EoS, and both results are more than one order of magnitude below the experimental data for N_2 , CH_4 and C_2H_4 in glassy PC, while good agreement is obtained for the case of CO_2 . The low-pressure gas solubility coefficients in PC, obtained from PHSC(SW) and NE-PHSC(SW) models, are finally presented in Figure 4.6(b). Unlike the case of PHSC(vdW), and similarly to that observed for the SAFT and LF models, also for this case there is a significant difference between the calculated equilibrium and pseudo-equilibrium solubility coefficients. The pseudo-equilibrium solubilities, calculated with the first-order approximation of the binary interaction parameters, compare reasonably with experimental data for N_2 , CH_4 , and C_2H_4 in glassy PC, although they are ‘underpredicted’

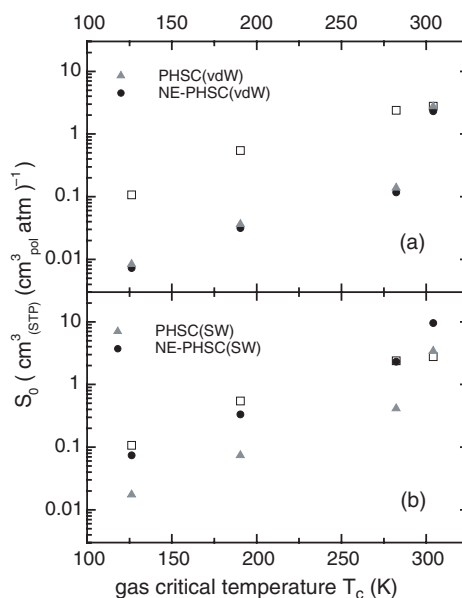


Figure 4.6 Comparison of experimental infinite dilution solubility coefficients for N_2 , CH_4 , C_2H_4 and CO_2 in polycarbonate at 35°C from Jordan and Koros [35] (open squares) with predicted values from different equilibrium and pseudo-equilibrium models

by ca. 20 %, while the calculated value for CO_2 is clearly overestimated.

The predictive ability of the pseudo-equilibrium solubility models presented here was also tested for the case of gas sorption in a polysulfone (PSf), by comparing the results with the experimental data from Erb and Paul [38]. The low-pressure solubility coefficients for argon, nitrogen, methane and carbon dioxide in PSf at 35°C have been calculated by using the NE-LF, NE-SAFT, NE-PHSC(vdW) and NE-PHSC(SW) models by employing a glassy polymer density equal to 1.235 kg L^{-1} . The latter value was obtained from a different collection of volumetric data for PSf [36], since no polymer density value was measured for the PSf samples used in Erb and Paul [38]. For all of the models considered, the values of the pure component parameters are reported in Tables 4.2–4.5, and the first-order approximation of the binary interaction parameters, $k_{ij} = 0$, was applied, for all polymer–gas pairs. The pseudo-equilibrium solubility coefficients obtained using NE-LF and NE-SAFT are compared with experimental data in Figure 4.7.

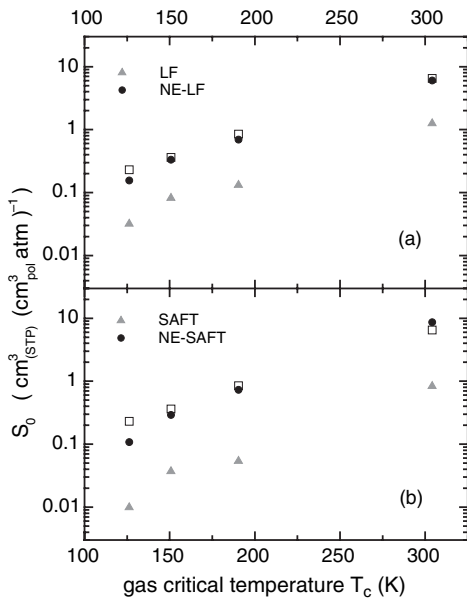


Figure 4.7 Comparison of experimental infinite dilution solubility coefficients for N_2 , Ar, CH_4 and CO_2 in polysulfone at $35^\circ C$ from Erb and Paul [38] (open squares) with predicted values from different equilibrium and pseudo-equilibrium models

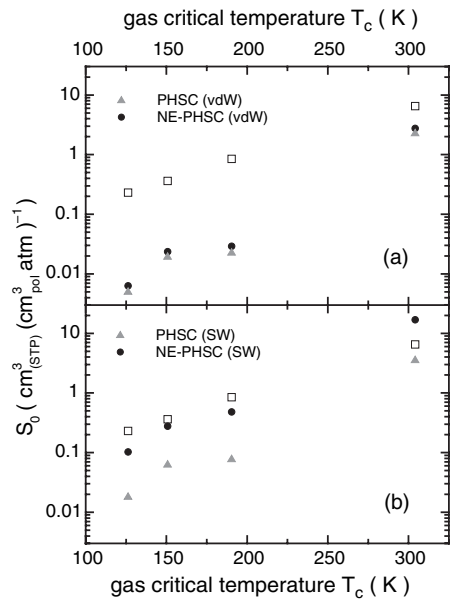


Figure 4.8 Comparison of experimental infinite dilution solubility coefficients for N_2 , Ar, CH_4 and CO_2 in polysulfone at $35^\circ C$ from Erb and Paul [38] (open squares) with predicted values from different equilibrium and pseudo-equilibrium models

The same is done for the cases of the NE-PHSC(vdW) and NE-PHSC(SW) models in Figure 4.8. For the sake of comparison, the solubility coefficients calculated under true thermodynamic equilibrium conditions, for each model, are also reported in the same figures. As is the case with gas solubility in glassy PC, for Psf unsatisfactory results are also obtained in most cases using NE-PHSC(vdW), and the predicted pseudo-equilibrium solubility coefficient S_0 is not significantly different from the equilibrium solubility coefficient calculated using equilibrium PHSC(vdW).

Better predictive results are obtained when using the NE-LF, NE-SAFT or NE-PHSC(SW) models, for which the calculated solubility is, in all cases, significantly larger than for the corresponding true equilibrium conditions estimated using LF, SAFT or PHSC(SW) respectively. The calculated pseudo-equilibrium solubility coefficients were underestimated for lighter gases, while the data for CO_2 solubility appear to be somewhat overestimated for both the NE-SAFT and NE-PHSC(SW) models. In comparing the

two PHSC models, only NE-PHSC(SW) appears adequate to represent the different behavior between glassy polymers and equilibrium phases, while for PHSC(vdW) such differences are indeed negligible, and the extension of this model to non-equilibrium glassy phases is unable to describe gas solubility.

It can be concluded that, for the case of NE-SAFT and NE-PHSC(SW), as well as for NE-LF, good predictions can be obtained for low-pressure pseudo-equilibrium solubilities in glassy polymers, based only on the pure component PVT data and the pure polymer glassy density. However, the completely predictive procedure described above relies on the assumption that the geometrical mean rule applies for the pair interaction characteristic energy ($k_{ij} = 0$). This assumption is typically reliable only for chemically similar polymer-penetrant pairs. It is thus expected that, in the more general case, a 'non-zero' value of the binary parameter k_{ij} in Equations (4.13), (4.15) and (4.17) is needed to obtain a good representation of experimental solubility data. In the following section, gas solubility

calculations in glassy polymers are performed using the non-equilibrium equation models, with a convenient value of the binary interaction parameter, different from its first-order approximation. In most cases, k_{ij} is a single parameter adjusted to the experimental solubility isotherm in the glassy phase; correspondingly, each model becomes a single-parameter correlation. In the cases in which solubility data were also available above the glass transition temperature, the k_{ij} values could be retrieved for the true equilibrium equations and used in the corresponding non-equilibrium models to predict the solubility in the glassy polymer.

In view of the results obtained in this section, the following analysis will not include the NE-PHSC(vdW) model which is unable to describe the departure from equilibrium existing in the glass, and only NE-PHSC(SW) will be considered as the non-equilibrium extension of the perturbed-hard-sphere-chain theory.

4.3.3 Correlation of Low-pressure Solubility Coefficients in Glassy Polymers

In this section, we examine the ability of the pseudo-equilibrium models to predict the effect of temperature changes on the infinite dilution gas solubility coefficient S_0 in glassy polymers. The proper values of the binary parameter k_{ij} will be retrieved from the solubility data at temperatures above the glass transition.

In Figure 4.9(a), the infinite dilution solubility coefficient of CO_2 in PC, obtained using equilibrium LF, are compared with the data by Wang and Kamiya [39], which span a relatively large temperature range. The values calculated using a purely predictive procedure, (i.e. by setting the binary parameter $k_{ij}=0$) are indicated by the dashed line in Figure 4.9(a). The predicted solubility S_0 for temperatures above the glass transition temperature ($T_g \cong 150^\circ\text{C}$), where the equilibrium LF model can be applied, allow for a satisfactory representation of the experimental data, although clear underestimation appears at higher temperatures. As expected, the equilibrium model results are unfit to represent the CO_2 solubility coefficient below the glass transition temperature.

To use NE-LF in the entire temperature range from 35 to 150°C , variations of the pure polymer PC glassy density, ρ_{pol}^0 , in the same temperature

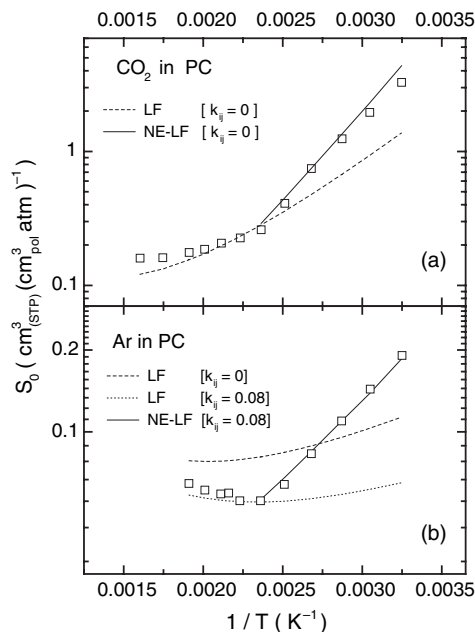


Figure 4.9 Comparison of experimental infinite dilution gas solubility coefficients in polycarbonate from Wang and Kamiya [39] (symbols) with predictions and correlations from equilibrium LF and non-equilibrium NE-LF models

range must be evaluated. As such data were not provided for the samples used by Wang and Kamiya, $\rho_{\text{pol}}^0(T)$ was estimated using for PC a mass density at T_g equal to 1.155 kg L^{-1} and a thermal volume dilation coefficient in the glassy state of $2.8 \times 10^{-4} \text{ K}^{-1}$ [36]. The corresponding predictions for the pseudo-equilibrium solubility coefficient, obtained from NE-LF by equally assuming $k_{ij}=0$, give quite accurate results over the entire temperature range explored (continuous line in Figure 4.9(a)).

Similar analysis was performed for the case of Ar solubility in PC, again considering the work by Wang and Kamiya [39] for the experimental data. The corresponding infinite dilution solubility coefficient calculated from the equilibrium LF model with a pure predictive procedure ($k_{ij}=0$) results in a significant overestimation with respect to the experimental value (dashed line in Figure 4.9(b)). Good representation of the experimental Ar solubility coefficient in PC above 150°C can be obtained through the LF model when a temperature-independent value for k_{ij} equal to 0.08 is assumed (dashed/dotted

line in Figure 4.9(b)). The pseudo-equilibrium solubility coefficient for Ar in PC below the glass transition temperature T_g is then performed through the NE-LF model, using the same binary interaction parameter $k_{ij} = 0.08$ evaluated from the best-fit of equilibrium data above T_g . The results of this calculation are plotted in Figure 4.9(b) (continuous line) and show a quite good agreement with the experimental data reported.

The infinite dilution solubility coefficient S_0 for CO_2 and Ar in PC were also calculated from the SAFT and NE-SAFT models. The equilibrium S_0 results calculated for CO_2 using a purely predictive procedure, $k_{ij} = 0$, are indicated by the dashed line in Figure 4.10(a) and are clearly overestimated with respect to the experimental values. This somehow parallels the overestimation of the pseudo-equilibrium CO_2 solubility coefficient in PC at 35°C , already obtained using NE-SAFT (Figure 4.5(b)). By adjusting the temperature-independent binary interaction parameter k_{ij} to the value of 0.06, one can represent the experimental solubility through the SAFT model to

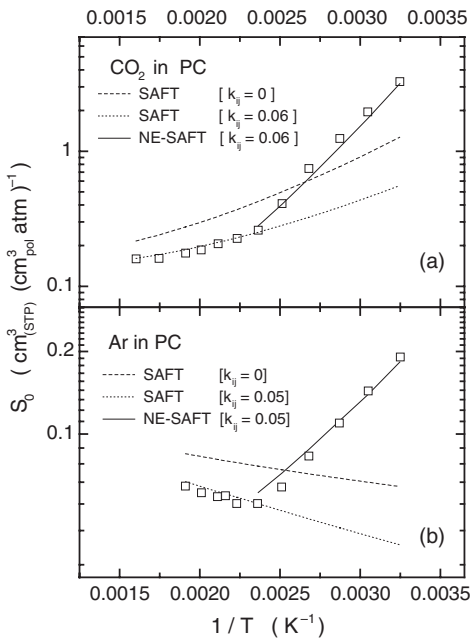


Figure 4.10 Comparison of experimental infinite dilution gas solubility coefficients in polycarbonate from Wang and Kamiya [39] (symbols) with predictions and correlations from equilibrium SAFT and non-equilibrium NE-SAFT models

within 2% deviation, for all of the temperatures above the glass transition (dashed/dotted line in Figure 4.10(a)). When the same CO_2 -PC binary interaction parameter is used in the pseudo-equilibrium NE-SAFT model, a quite good representation of the CO_2 solubility coefficient in glassy PC is obtained, over the entire temperature range inspected, as shown by the continuous line in Figure 4.10(a).

Similar results are obtained for the Ar solubility coefficient in PC, Figure 4.10(b), by using the SAFT and NE-SAFT models, above and below the glass transition temperatures, respectively. The same value for the binary parameter k_{ij} , equal to 0.05, allows us to obtain remarkably good correlations for the low-pressure solubility coefficient above T_g from SAFT EoS, and below T_g from the NE-SAFT model. The results are particularly impressive in this case, in which the low-pressure solubility coefficient is an increasing function of temperature in the rubbery phase, while it decreases with temperature below the glass transition.

Finally, the analysis of CO_2 and Ar solubility in PC was performed using the PHSC(SW) model and its non-equilibrium version NE-PHSC(SW) (Figure 4.11). A satisfactory correlation for CO_2 solubility in PC was obtained over the entire temperature range by considering $k_{ij} = 0.075$ in both the PHSC(SW) and NE-PHSC(SW) models, used above and below T_g , respectively. The equilibrium solubility calculated from PHSC(SW) with the binary parameter $k_{ij} = 0.075$ underestimates the experimental values observed for the glassy phase.

'Pure' predictions for the Ar solubility coefficient in PC from the PHSC(SW) EoS are shown by the dashed line in Figure 4.11(b). Although the results for solubility above the glass transition temperature predicted by $k_{ij} = 0$ appear already acceptable, the best-fit of experimental data close to the glass transition temperature was investigated by adjusting the binary interaction parameter, consistently with calculations done in the previous cases. The resulting best-fit gives $k_{ij} = 0.016$ and the solubility calculated correspondingly is plotted by the dashed/dotted line in the same figure. The pseudo-equilibrium solubility for Ar in PC below the glass transition temperature was finally calculated from the NE-PHSC(SW) model, by using the same k_{ij} value equal to 0.016 and the results of these predictive

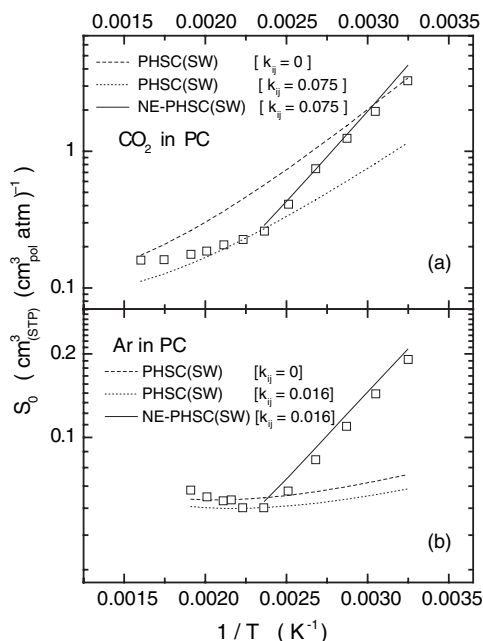


Figure 4.11 Comparison of experimental infinite dilution gas solubility coefficients in polycarbonate from Wang and Kamiya [39] (symbols) with predictions and correlations from equilibrium PHSC(SW) and non-equilibrium NE-PHSC(SW) models

calculations are plotted in Figure 4.11(b) by the continuous line. The pseudo-equilibrium solubility coefficients thus obtained compare satisfactorily with the experimental data available in the temperature range from 35 to 150 °C, although a slight, uniform overestimation could be appreciated. The results confirm, also in this case, the reliability of the NET-GP procedure, proposed in this work, to extend to the non-equilibrium glassy states the equilibrium thermodynamic models selected. A consistent representation of low-pressure gas solubility above and below the glass transition temperature can be obtained from a valid equilibrium EoS, through the non-equilibrium extension discussed here, using exactly the same values of the material model parameters, including the binary interaction coefficient.

4.3.4 Correlation of High-pressure Gas Solubility in Glassy Polymers

The general description of pseudo-equilibrium isotherms of gases in glassy polymers, up to the

high-pressure range, requires us to account for the volume dilation of the polymer matrix due to the sorption process. To that aim, we will rely on the simple assumption that volume dilation is proportional to gas pressure, so that polymer density can be expressed through Equation (4.10). The above assumption was suggested by several experimental observations [24–26] and was already successfully applied to calculate solubility isotherms in several cases examined in previous studies [21,40]. Correlation of high-pressure solubility data can be obtained through the use of the swelling coefficient k_{sw} as an adjustable parameter, according to the procedure illustrated by Giacinti Baschetti *et al.* [21]. The swelling coefficient k_{sw} is a non-equilibrium parameter, as it depends on the thermal and mechanical history of the sample, but it has a precise physical meaning and represents a variable which can be measured directly and independently of solubility. It has been shown [21] that the k_{sw} values obtained from best-fitting the solubility data with NE-LF correlation, are definitely consistent with the volume dilation coefficients measured experimentally. The correlation for high-pressure solubility isotherms, based on the use of the swelling coefficient, will now be extended to NE-SAFT and NE-PHSC(SW) models, including relevant comments on internal consistency and reliability of the results.

To this purpose, we will consider the sorption data in glassy PMMA for swelling penetrants, such as CO_2 , C_2H_4 and N_2O , reported by Sanders and Koros [41] at 35 °C. The pure component parameters used in calculations for PMMA and gaseous species are listed in Tables 4.2–4.5 for the different equations of state used.

The density value of pure PMMA samples used in the experiments was not specified by Sanders and Koros [41], and thus it has been estimated on the basis of the value reported for the glass transition temperature, $T_g = 120$ °C. From the polymer density of rubbery PMMA at 120 °C and the thermal dilation coefficient for glassy PMMA indicated by Zoller [36], the mass density of the polymeric samples of interest at 35 °C was estimated as equal to 1.176 kg L^{-1} . The relevant pure component parameters for each equation of state were retrieved from literature data [36,37] and, with the above estimation of ρ_{pol}^0 , every non-equilibrium model reduces to a correlation for the solubility data, containing only two adjustable

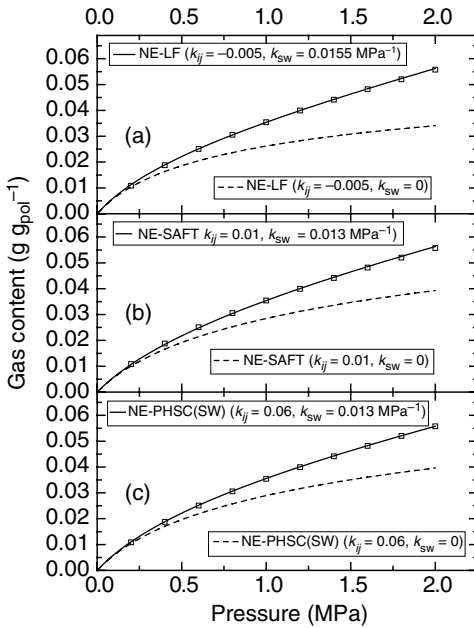


Figure 4.12 Comparison of experimental solubility values for CO_2 in PMMA at 35°C from Sanders and Koros [41] (open squares) with correlations from different pseudo-equilibrium models, with and without swelling

parameters, i.e. the binary interaction coefficient k_{ij} and the swelling coefficient k_{sw} .

The correlation results for CO_2 solubility in PMMA through the NE-LF model are shown in Figure 4.12(a). Best-fit results (continuous line) are compared with the calculation performed based on the low-pressure approximation, i.e. neglecting volume dilation (dashed line) and using the same binary interaction parameter value. From the comparison, one can clearly appreciate the excellent representation of the pseudo-solubility isotherm which is obtained by means of the two mentioned adjustable parameters, while in the low-pressure range satisfactory comparison with experimental data is obtained by assuming that the polymer density is constant and equal to ρ_{pol}^0 . Analogous fitting results for the solubility data of CO_2 in PMMA are presented in Figures 4.12(b) and 4.12(c) for the NE-SAFT and NE-PHSC(SW) models, respectively, including also the results derived from the low-pressure approximation. For these models as well it is evident that in the low-pressure range the solubility calculations for

constant polymer density deviate negligibly from the general results obtained when accounting for volume dilation. Indeed, data for the infinite dilution solubility coefficient can be used in the procedure to adjust the value for the binary interaction parameter, whatever is the choice considered for the volume dilation, while high-pressure solubility data are best used to retrieve the ‘proper’ dilation coefficient.

Of course, the binary interaction parameters associated with the different thermodynamic models are indeed different physical quantities and thus the values emerging from data-fitting are different from one thermodynamic model to another. It is significant to observe, on the contrary, that the swelling coefficients resulting from the best-fit procedure are very close for all models and range from 0.013 MPa^{-1} , for the case of NE-SAFT and NE-PHSC, to 0.0155 MPa^{-1} for the case of NE-LF; this is consistent with the fact that k_{sw} has the same physical meaning in all cases.

Similar considerations can be applied to the correlation results for C_2H_4 and N_2O solubility in PMMA, shown in Figures 4.13 and 4.14.

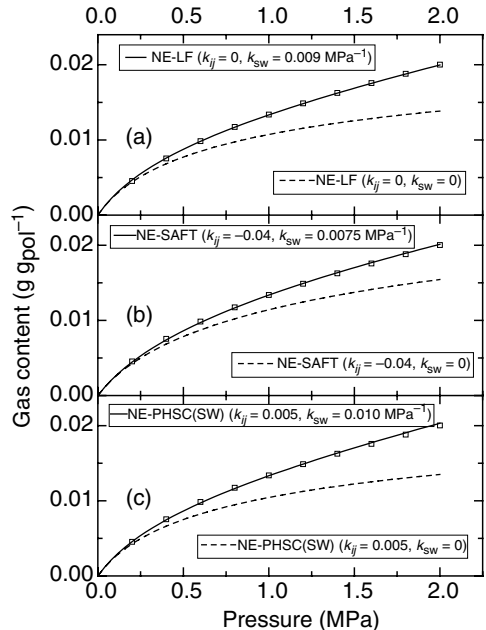


Figure 4.13 Comparison of experimental solubility values for C_2H_4 in PMMA at 35°C from Sanders and Koros [41] (open squares) with correlations from different pseudo-equilibrium models, with and without swelling

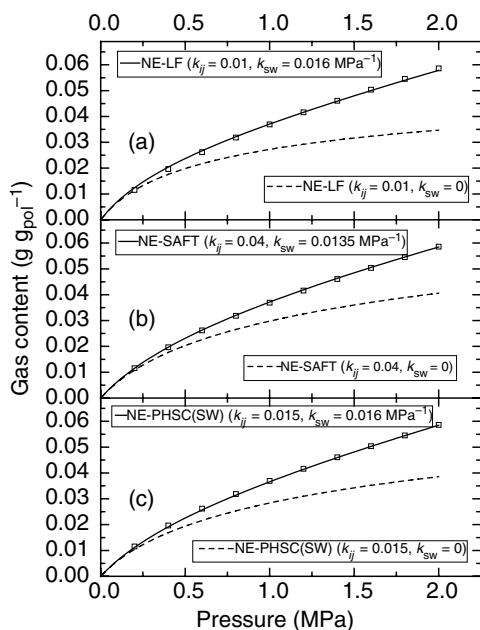


Figure 4.14 Comparison of experimental solubility values for N_2O in PMMA at 35°C from Sanders and Koros [41] (open squares) with correlations from different pseudo-equilibrium models, with and without swelling

Quite good data-fitting were obtained from the use of any of the non-equilibrium models considered here. The binary interaction parameter resulting from the fitting procedure can change substantially with the thermodynamic model used, but similar values are obtained for volume swelling coefficients for the same polymer–penetrant pair. The dilation coefficient calculated for ethylene sorption in PMMA changes from 0.0075 MPa^{-1} for NE-SAFT, up to 0.0100 MPa^{-1} for NE-PHSC(SW). For the case of N_2O sorption in PMMA, the swelling coefficient values emerging from the data analysis range from 0.0135 to 0.0160 MPa^{-1} , depending on the specific thermodynamic model used. The latter results further confirm that the approach used to extend the thermodynamic description to non-equilibrium glassy states is consistent and that the analysis of high-pressure solubility data can be confidently used to estimate the volume dilation coefficient of the polymeric matrix.

4.4 Discussion and Conclusions

The general procedure of Non-Equilibrium Thermodynamics for Glassy Polymers has been

presented, indicating how the thermodynamic equilibrium models which hold above T_g can be suitably applied to describe the behavior of glassy polymeric phases. The thermodynamic results obtained can be successfully used to calculate the pseudo-equilibrium gas solubility in glassy polymers, starting from any appropriate equilibrium equation of state. This procedure was originally followed to obtain the NELF model from the Lattice Fluid theory, and it has been extended here to important models derived from tangent-hard-spheres-chain theories.

The general assumptions of the NET-GP approach are as follows: (i) the mass density of the polymer network is the only order parameter needed to represent the departure from equilibrium immobilized in the matrix at any temperature, pressure and composition; (ii) the polymer density evolves in time following a Voigt viscoelastic model for bulk rheology. Based on these assumptions, it is straightforward to derive the general rule to extend free energy and solute chemical potential in a polymeric mixture from equilibrium conditions to the entire domain of non-equilibrium states.

The corresponding pseudo-equilibrium solubility models are then explicitly obtained, and can be used in a predictive mode whenever the non-equilibrium polymer density is known from separate information. This is the case, for example, of gas solubility in the low-pressure range, in which sorption-induced swelling of the glassy matrix can be neglected, and the pure glassy polymer density closely approximates pseudo-equilibrium values during sorption. At higher pressures, or for the case of swelling penetrants, the pseudo-equilibrium polymer density variations require further information, effectively ‘lumped into’ the swelling coefficient k_{sw} . The latter can be experimentally measured, but in most of the cases its value is not given by direct experimental evidence and must be treated as an adjustable parameter.

The pseudo-equilibrium solubility models associated with the LF, SAFT and PHSC equations have been explicitly derived and indicated with the acronyms NE-LF, NE-SAFT, NE-PHSC(vdW) and NE-PHSC(SW), respectively. The non-equilibrium models have been finally applied to calculate the solubilities of several gases in glassy PC, PSf and PMMA. The use of every equilibrium equation of state to describe the thermodynamic properties of binary gas–

polymer mixtures, requires the preliminary determination of the model pure components' parameters and one binary interaction coefficient, k_{ij} . In the applications considered, equilibrium *PVT* data are used for pure solute and pure polymer, while k_{ij} values are retrieved from phase equilibrium data above T_g ; its first order approximation is, in any case, $k_{ij} = 0$.

The pseudo-equilibrium solubility calculations analyzed are schematically grouped into the following different cases:

- (i) Calculation of zero-pressure solubility coefficients and solubility isotherms in the low-pressure range, by using the first-order approximation for the binary interaction parameter k_{ij} . In this case, all parameters entering the models are predetermined from the pure components' properties and no parameter remains to be adjusted, so that all models are used in an entirely predictive mode.
- (ii) Calculation of zero-pressure solubility coefficients, considering the value of the binary interaction coefficient which best-fits the data. In this case, all models become a single-parameter correlation, containing a temperature-independent adjustable parameter k_{ij} . In the cases examined, however, k_{ij} was retrieved from the experimental data available for phase equilibria above T_g , and the same value was used to calculate the solubility in the glassy phase. The pseudo-equilibrium calculations for the glassy phases are thus also performed with no adjustable parameter in this case.
- (iii) Calculation of the solubility isotherm up to high-pressure values in which volume dilation of the polymer matrix plays an important role. To this aim, the swelling coefficient k_{sw} was introduced as an adjustable parameter.

The relation between equilibrium and pseudo-equilibrium solubility calculations has been examined and the results obtained from the two procedures are compared in all the cases considered. The equilibrium models typically underestimate the gas solubility coefficients in glassy states, while the corresponding pseudo-equilibrium models are able to interpret the higher capacity of glassy samples, due to the difference between expected equilibrium polymer density and the actual polymer density below the glass transition temperature. In particular, low-pressure

gas solubility coefficients calculated using NE-LF, NE-SAFT and NE-PHSC(SW) for glassy PC, PSf and PMMA at 35 °C are significantly higher than the equilibrium values predicted by the corresponding equilibrium equations LF, SAFT and PHSC(SW), and compare well with the experimental values available.

The same difference is not encountered between NE-PHSC(vdW) and PHSC(vdW). Indeed, PHSC(vdW) [10] uses a simple pair interaction function of the van der Waals type, and does not provide appreciable excess volume over the equilibrium value, for glassy PC and PSf, so that PHSC(vdW) is unable to offer reasonable estimates for the gas solubility in the glassy states. On the contrary, PHSC(SW) [11], which uses a pair interaction function of square-well form, is able to fit the data considered (Figures 4.4(a) and 4.4(b)). Indeed for the case of PHSC(vdW), calculated solubilities are typically one order of magnitude lower than the measured values in glassy PC and PSf at 35 °C for all of the gases considered here, with the exception of CO₂ solubility in PC, for which matching appears to be fortuitous. Consistently with the NET-GP procedure, this result may be generalized to conclude that only the models which associate to the glassy state an excess polymer volume over the calculated equilibrium value can account for the higher solubility encountered in glassy phases. Remarkably, the increased solubility in glassy polymers is not merely a consequence of a higher storage capacity associated to the higher volume of the glassy state, but is rather calculated in all models as the result of the energy and entropy effects included in the thermodynamic equations.

The pseudo-solubility of methane in glassy PC and PSf are indeed well predicted by the NE-LF and NE-SAFT models, using $k_{ij} = 0$, and acceptable predictions are obtained from NE-PHSC(SW). Analogously, the zero-pressure solubility coefficients for nitrogen, methane and ethylene in PC are well predicted again by the NE-LF and NE-SAFT models and reasonably estimated by NE-PHSC(SW). The predictions for the low-pressure solubility coefficient of CO₂ in PC is very good for NE-LF, but barely acceptable for NE-SAFT and NE-PHSC(SW), while similar evaluations for PSf are very satisfactory for both NE-LF and NE-SAFT. The introduction of reasonable values for the binary interaction parameters enables all of the above models to calculate the correct values of the solubility coefficients for all of the

systems inspected. Interestingly, a single temperature-independent value of the binary interaction parameter, retrieved from the solubility data above T_g for each model, is sufficient to calculate the correct solubility coefficient over a broad temperature range, from well above T_g , using the equilibrium models (LF, SAFT and PHSC(SW)) all the way to well below T_g , using the corresponding pseudo-equilibrium models, namely NE-LF, NE-SAFT and NE-PHSC(SW).

The validity of the same value of k_{ij} to represent the solubility behavior, both above and below the glass transition temperature, was ascertained for all of the thermodynamic models considered, thus confirming that the NET-GP approach presented here is the ‘proper’ procedure to extend any equilibrium model to the pseudo-equilibrium conditions typical of glassy polymeric mixtures.

Finally, the solubility isotherms for swelling solutes in PMMA have been calculated up to pressures of 20 bar. For all of the gases inspected, i.e. CO₂, C₂H₄ and N₂O, the low-pressure approximation offers valid estimates only up to a few bars of external pressure. The complete isotherm is captured with the introduction of the swelling coefficient k_{sw} , representing the volume dilation of the matrix. This is sufficient to obtain, in all cases, an excellent representation of the entire sorption isotherms, for all of the models considered. In these cases, each model contains two adjustable parameters, namely, the binary interaction coefficient and the swelling coefficient. The former can be obtained by considering the best-fit procedure in the low-pressure range, while the latter is retrieved from the high-pressure portion of the isotherm. It is remarkable to notice that the swelling coefficients obtained for the different models for the same polymer–solute pairs not only are of the same order of magnitude of the swelling coefficients actually measured in other glassy systems, but have practically the same values for all of the different models, consistently with the physical meaning associated to k_{sw} . This result further confirms the solid robustness of the approach.

Acknowledgements

This research has been partially supported by the Italian Ministry for Education, University and Research (PRIN 2001).

References

- [1] P. J. Flory, *J. Chem Phys.*, **9**, 660 (1941).
- [2] M. L. Huggins, *J. Chem Phys.*, **9**, 440 (1941).
- [3] M. M. Abrams and J. M. Prausnitz, *AIChE J.*, **21**, 116 (1975).
- [4] T. Oishi, and J. M. Prausnitz, *Ind. Eng. Chem. Res.*, **17**, 333 (1978).
- [5] H. S. Elbro, A. Fredenslund and P. Rasmussen, *Macromolecules*, **23**, 4707 (1990).
- [6] D. Patterson, *Macromolecules*, **2**, 672 (1969).
- [7] P. J. Flory, *Discuss Faraday Soc.*, **49**, 7 (1970).
- [8] I. C. Sanchez and R. H. Lacombe, *Macromolecules*, **11**, 1145 (1978).
- [9] S. H. Huang, and M. Radosz, *Ind. Eng. Chem. Res.*, **29**, 2284 (1990).
- [10] Y. Song, T. Hino, S. M. Lambert, J. M. Prausnitz, *Fluid Phase Equilib.*, **117**, 69 (1996).
- [11] T. Hino and J. M. Prausnitz, *Fluid Phase Equilib.*, **138**, 105 (1997).
- [12] J. W. Kang, J. H. Lee, K. P. Yoo and C. S. Lee, *Fluid Phase Equilib.*, **194**, 77 (2002).
- [13] A. S. Michaels, W. R. Vieth and J. A. Barrie, *J. Appl. Phys.*, **34**, 1 (1963).
- [14] B. D. Freeman and I. Pinnau, ‘Polymeric Materials for Gas Separations’, in B. D. Freeman and I. Pinnau (Eds), *Polymer Membranes for Gas and Vapor Separations*, ACS Symposium Series 733, American Chemical Society, Washington, DC, USA, pp. 1–27 (1999).
- [15] R. G. Wissinger and M. E. Paulaitis, *J. Polym. Sci. Part B: Polym. Phys. Ed.*, **25**, 2497 (1987).
- [16] T. A. Barbari and R. M. Conforti, *J. Polym. Sci. Part B: Polym. Phys. Ed.*, **30**, 1261 (1992).
- [17] F. Doghieri, and G. C. Sarti, *Macromolecules, Part B*: **29**, 7885 (1996).
- [18] D. Boudouris and C. Panayiotou, *Macromolecules*, **31**, 7915 (1998).
- [19] G. C. Sarti and F. Doghieri, *Chem. Eng. Sci.*, **53**, 3435 (1998).
- [20] F. Doghieri, M. Canova and G. C. Sarti, ‘Solubility of Gaseous Mixtures in Glassy Polymers: NELF Predictions’, in B. D. Freeman and I. Pinnau (Eds), *Polymer Membranes for Gas and Vapor Separations*, ACS Symposium Series 733, American Chemical Society, Washington, DC, USA, pp. 179–193 (1999).
- [21] M. Giacinti Baschetti, F. Doghieri and G. C. Sarti, *Ind. Eng. Chem. Res.*, **40**, 3027 (2001).
- [22] F. Doghieri and G. C. Sarti, *J. Membr. Sci.*, **147**, 73 (1998).
- [23] B. D. Coleman and M. E. Gurtin, *J. Chem. Phys.*, **47**, 597 (1967).
- [24] W. J. Koros, D. R. Paul and A. A. Rocha, *J. Polym. Sci. Part B: Polym. Phys. Ed.*, **14**, 687 (1976).
- [25] W. J. Koros and D. R. Paul, *J. Polym. Sci. Part B: Polym. Phys. Ed.*, **16**, 1947 (1978).

- [26] G. K. Fleming and W. J. Koros, *Macromolecules*, **23**, 1353 (1990).
- [27] I. C. Sanchez and R. H. Lacombe, *J. Phys. Chem.*, **80**, 2352 (1976).
- [28] R. H. Lacombe, and I. C. Sanchez, *J. Phys. Chem.*, **80**, 2568 (1976).
- [29] I. C. Sanchez and R. H. Lacombe, *J. Polym. Sci., Polym. Lett. Ed.*, **15**, 71 (1977).
- [30] W. G. Chapman, K. E. Gubbins, G. Jackson and M. Radosz, *Fluid Phase Equilib.*, **52**, 31 (1989).
- [31] W. G. Chapman, K. E. Gubbins, G. Jackson and M. Radosz, *Ind. Eng. Chem. Res.*, **29**, 1709 (1990).
- [32] Y. Song, S. M. Lambert and J. M. Prausnitz, *Macromolecules*, **27**, 441 (1994).
- [33] S. S. Chen and A. Kreglewski, *Ber. Bunsen-Ges. Phys. Chem.*, **81**, 1048 (1977).
- [34] J. Chang and S. I. Sandler, *Mol. Phys.*, **81**, 735 (1994).
- [35] S. S. Jordan and W. J. Koros, *Macromolecules*, **28**, 2228 (1995).
- [36] P. Zoller, *J. Polym. Sci. Part B: Polym. Phys. Ed.*, **16**, 1261 (1978).
- [37] N. B. Vargaftik, *Handbook of Physical Properties of Liquids and Gases: Pure Substances and Mixtures*, 2nd Edn, Hemisphere Publishing, Washington, DC, USA (1975).
- [38] A. J. Erb and D. R. Paul, *J. Membr. Sci.*, **8**, 11 (1981).
- [39] J.-S. Wang and Y. Kamiya, *J. Polym. Sci. Part B: Polym. Phys. Ed.*, **38**, 883 (2000).
- [40] F. Grassia, M. Giacinti Baschetti, F. Doghieri and G. C. Sarti, 'Solubility of Gases and vapors in Glassy Polymer Blends', in B. D. Freeman and I. Pinnau (Eds), ACS Symposium Series 876, American Chemical Society, Washington, DC, USA, pp. 55–73 (2004).
- [41] E. S. Sanders and W. J. Koros, *J. Polym. Sci. Part B: Polym. Phys. Ed.*, **24**, 175 (1986).

The Solution–Diffusion Model: A Unified Approach to Membrane Permeation

Johannes G. (Hans) Wijmans and Richard W. Baker

5.1 Introduction

Over the last 40 years membrane technology has grown from a few analytical applications to a widely used industrial and medical process. Membrane sales are in the multibillion-dollar per year range. Our understanding of the underlying theory and science of membrane processes has also grown during these years. This paper covers the solution–diffusion model, the most widely used description of permeation through reverse osmosis, pervaporation and gas separation membranes. In the past, these different processes were often treated as completely separate entities. The solution–diffusion model allows these processes to be described in a single, unified way, as we will show.

Our approach is first to derive the base equations of the solution–diffusion model for a one-component fluid, and to illustrate the overall unity of the model. We then apply the model to multicomponent mixtures and explain the behavior of membranes when used to perform practical separations. At a number of points, rather than deriving the analytical solution to a specific problem, we simply present the basic equations and show the results of a computer calculation in graphical form. This approach avoids long, tedious derivations and reflects the reality of modern research. Even with the use of computers, this paper has more than 100 equations.

A subject like this requires a balance between rigor and clarity. Too much rigor produces a

paper only a handful of theoreticians will read. Too much clarity at the expense of rigor and the paper is clear but superficial. This paper is the collaboration of coworkers with different backgrounds. We have tried to present our combined thinking in a way that will be accessible to all, yet solid. ‘May the Force be with you’!

5.2 The Solution–Diffusion Model

The most easily understood description of a membrane is a porous structure containing a network of tiny pores that separate large from small molecules in a manner similar to a filter. This is a reasonably accurate description of a microfiltration membrane, with pores in the 1000 Å diameter range. Even ultrafiltration membranes, in which the pores are small enough to separate dissolved polymer molecules from water, are best described as ‘ultrafine’ filters. However, the pore model of membrane transport breaks down when the pore diameter falls to 5 Å or less. The pore diameter is then within the range of the thermal motion of the polymer chains from which the membrane is made. Permeation is no longer a pressure-driven flow through tiny pores but a diffusive process controlled by the motion of the polymer chains.

In the past, the transition point between pore flow and molecular diffusion, based on pore diameter, was an assumption. During the last

decade it has become possible to use computer simulations to calculate the motion of diffusing permeants at the molecular level. Computer simulation calculations have confirmed that the transition is at pore diameters (polymer chain spacings) in the 5 to 10 Å range. In computer simulation techniques, the position of every polymer atom in the membrane element is calculated at short enough intervals to represent the normal thermal motion of the polymer chains. When a permeant molecule is placed within one of the microcavities between the chains, its movement can be calculated. The results of a molecular dynamic simulation of the motion of carbon dioxide in a 6FDA-4PDA polyimide matrix are shown in Figure 5.1

[1]. During the first 100 ps, the carbon dioxide molecule ‘bounces’ around in the cavity where it has been placed, never moving more than 5 Å, the diameter of the microcavity. After 100 ps, however, a chance thermal motion moves a segment of the polymer chains sufficiently for the carbon dioxide molecule to jump approximately 10 Å to an adjacent cavity where it remains until another movement of the polymer chains allows it to jump to another cavity. By repeating these calculations many times and averaging the distance moved by the gas molecule, its diffusion coefficient can be calculated. Molecular dynamic simulations are not yet able to quantitatively predict permeant diffusion coefficients but the process

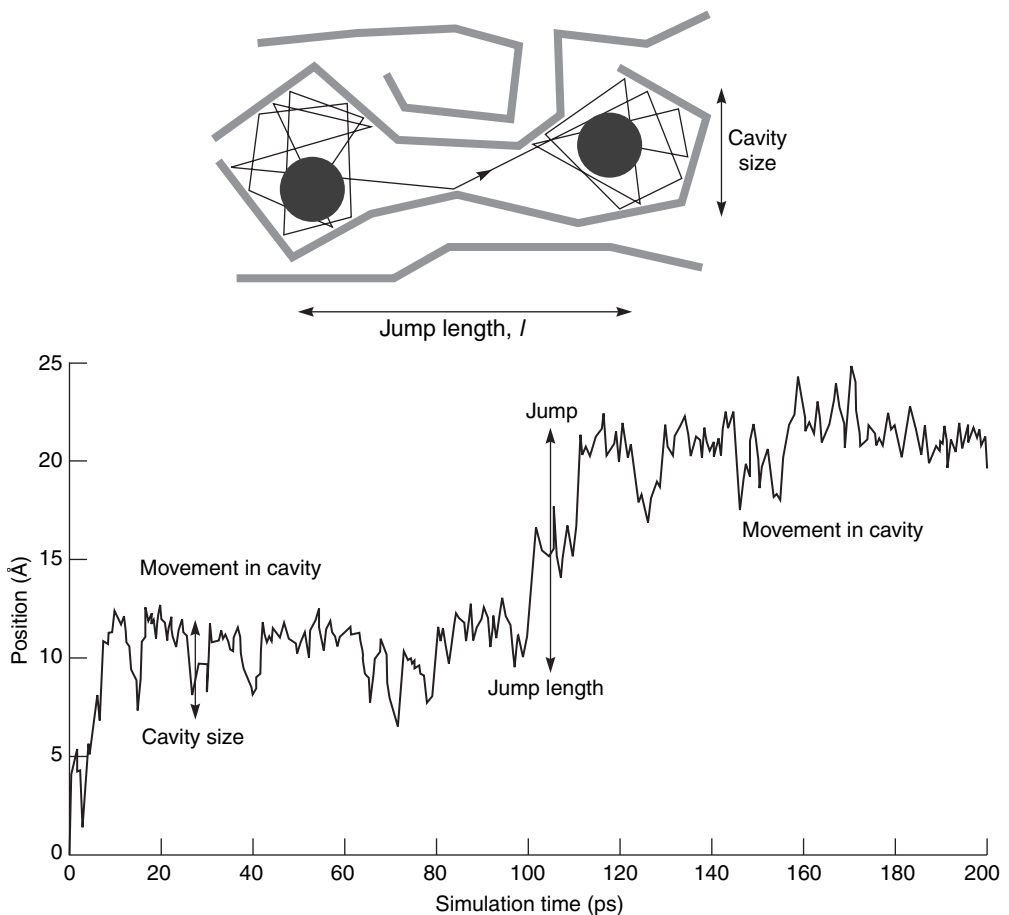


Figure 5.1 Motion of a carbon dioxide molecule in a 6FDA-4PDA polymer matrix [1]. Numerous examples of the results of computer modeling can be found in chapters 2 and 3. Reprinted from *Journal of Membrane Science*, **73**, E. Smit, M. H. V. Mulder, C. A. Smolders, H. Karrenbeld, J. van Eerden and D. Feil, ‘Modeling of the diffusion of carbon dioxide in polyimide matrices by computer simulation’, pp. 247–257, Copyright (1992), with permission from Elsevier

illustrated in Figure 5.1 is clearly diffusion rather than pore flow [2,3].

The starting point for the mathematical description of permeation in all membranes is the proposition, solidly based in thermodynamics, that the driving forces of pressure, temperature, concentration and electromotive force are interrelated and that the overall driving force producing movement of a permeant, i , is the gradient in its chemical potential, μ_i . Thus, the flux, $J_i(\text{g}/(\text{cm}^2\text{s}))$, is described by the simple equation:

$$J_i = c_i v_i = c_i U_i \frac{d\mu_i}{dx} \quad (5.1)$$

where $d\mu_i/dx$ is the gradient in chemical potential of component i and U_i is a coefficient of proportionality (not necessarily constant) linking the chemical potential driving force $d\mu_i/dx$ with the velocity of component i , v_i . When this velocity is multiplied by the concentration of component i molecules, c_i , the result is the flux of component i .

All the common driving forces, such as gradients of concentration, pressure, temperature and electromotive force, can be reduced to a chemical potential gradient, and their effect on flux expressed by this equation. This approach is extremely useful, because many processes involve more than one driving force, for example, pressure and concentration in reverse osmosis. Restricting ourselves to driving forces generated by concentration and pressure gradients, the chemical potential is written as:

$$d\mu_i = RT \ln(\gamma_i n_i) + v_i dp \quad (5.2)$$

where n_i is the mole fraction (mol/mol) of component i , γ_i is the activity coefficient linking concentration with activity, p is the pressure and v_i is the partial molar volume of component i .

In incompressible phases, such as a liquid or a solid membrane, volume does not change appreciably with pressure. Integrating Equation (5.2) with respect to concentration and pressure then gives:

$$\mu_i = \mu_i^o + RT \ln(\gamma_i n_i) + v_i(p - p_i^o) \quad (5.3)$$

where μ_i^o is the chemical potential of pure i at a reference pressure p_i^o .

In compressible gases, the molar volume changes with pressure; using the ideal gas laws

and integrating Equation (5.2) then gives:

$$\mu_i = \mu_i^o + RT \ln(\gamma_i n_i) + RT \ln\left(\frac{p}{p_i^o}\right) \quad (5.4)$$

To ensure that the reference chemical potential μ_i^o is identical in Equations (5.3) and (5.4), the reference pressure p_i^o is defined as the saturation vapor pressure of pure component i , $p_{i,\text{sat}}$. Equations (5.3) and (5.4) can then be rewritten for incompressible liquids and the membrane phase as:

$$\mu_i = \mu_i^o + RT \ln(\gamma_i n_i) + v_i(p - p_{i,\text{sat}}) \quad (5.5)$$

and for compressible gases as:

$$\mu_i = \mu_i^o + RT \ln(\gamma_i n_i) + RT \ln\left(\frac{p}{p_{i,\text{sat}}}\right) \quad (5.6)$$

A number of assumptions must be made to define any model of permeation. Usually, the first assumption is that the fluids on either side of the membrane are in equilibrium with the membrane material at the interface. This assumption means that there is a continuous gradient in chemical potential from one side of the membrane to the other. It is implicit in this assumption that the rates of absorption and desorption at the membrane interface are much higher than the rate of diffusion through the membrane. This appears to be the case in almost all membrane processes, but may fail, for example, in transport processes involving chemical reactions, such as facilitated transport, or in diffusion of gases through metals, where interfacial absorption can be slow.

The second assumption concerns the way this chemical potential across the membrane is expressed within the membrane. The solution–diffusion and pore–flow models differ in the way the chemical potential gradient is expressed [4–8]:

- The solution–diffusion model assumes that the pressure within a membrane is uniform and that the chemical potential gradient of a permeant across the membrane is represented only as a concentration gradient.
- The pore–flow model assumes that the permeant concentration within a membrane is uniform and that the chemical potential gradient across the membrane is represented only as a pressure gradient.

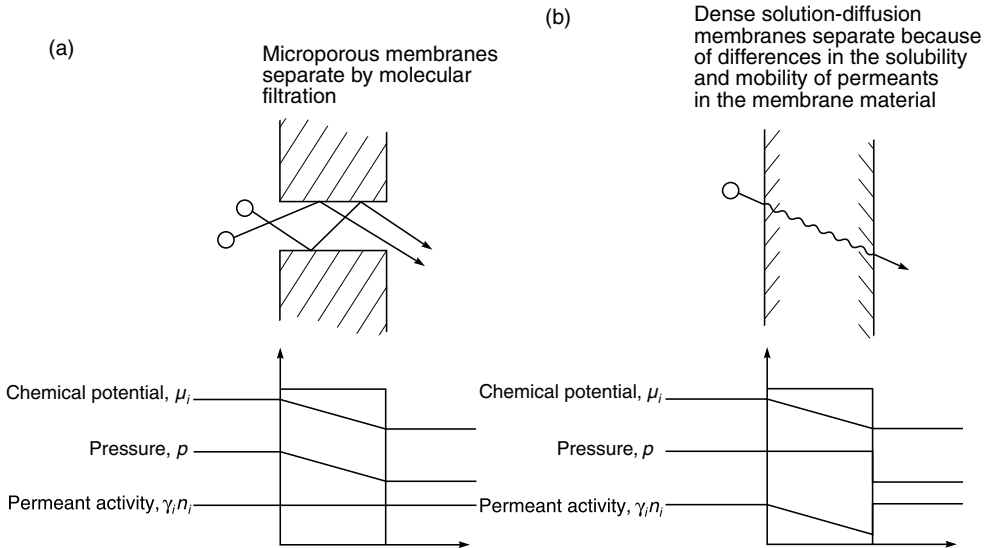


Figure 5.2 Comparison of the driving force gradients for permeation through a membrane according to (a) the pore-flow model and (b) the solution–diffusion model

The consequences of these two assumptions are illustrated in Figure 5.2, which compares pressure-driven permeation of a one-component solution by solution–diffusion and by pore-flow. In both models, the difference in pressure across the membrane ($p_o - p_\ell$) produces a gradient in chemical potential according to Equations (5.5) and (5.6). In the pore-flow model, the pressure difference produces a smooth gradient in pressure through the membrane, but the solvent concentration remains constant within the membrane. The solution–diffusion model on the other hand assumes that when a pressure is applied across a dense membrane, the pressure everywhere within the membrane is constant at the high-pressure value. This assumes, in effect, that solution–diffusion membranes transmit pressure in the same way as liquids. Consequently, the pressure difference across the membranes is represented as a concentration gradient within the membrane, with Equations (5.1) and (5.2) providing the mathematical link between pressure and concentration.

Consider the pore-flow model first. Combining Equations (5.1) and (5.2) in the absence of a concentration gradient in the membrane gives:

$$J_i = c_i U_i v_i \frac{dp}{dx} \quad (5.7)$$

This equation can be integrated across the membrane to give Darcy's law:

$$J_i = \frac{k(p_o - p_\ell)}{\ell} \quad (5.8)$$

where k is the Darcy's law coefficient, equal to $U_i v_i$, and ℓ is the membrane thickness.

In the solution–diffusion model, the pressure within the membrane is constant at the high-pressure value (p_o), and the gradient in chemical potential across the membrane is expressed as a smooth gradient in permeant activity ($\gamma_i n_i$). The flow that occurs down this gradient is again expressed by combining Equations (5.1) and (5.2), but, this time in the absence of a pressure gradient, to give:

$$J_i = \left(\frac{-RTc_i U_i}{\gamma_i n_i} \right) \left[\frac{d(\gamma_i n_i)}{dx} \right] \quad (5.9)$$

In Equation (5.9), the gradient of component i across the membrane is given as a gradient in mole fraction of component i . Equation (5.9) can be written in a more practical form using the term for concentration c_i (g/cm^3) defined as:

$$c_i = m_i \rho n_i \quad (5.10)$$

where m_i is the molecular weight of i (g/mol) and ρ is the molar density (total number of mol/cm³). Equation (5.9) then becomes:

$$J_i = \left(\frac{-RTU_i}{\gamma_i} \right) \cdot \left[\frac{d(\gamma_i c_i)}{dx} \right] \quad (5.11)$$

This has the same form as Fick’s law, where the term RTU_i is replaced by the diffusion coefficient D_i . Assuming the activity coefficient (γ_i) is constant, then:

$$J_i = - \frac{D_i dc_i}{dx} \quad (5.12)$$

Integrating Equation (5.12) over the thickness of the membrane gives:¹

$$J_i = \frac{D_i (c_{i_o(m)} - c_{i_\ell(m)})}{\ell} \quad (5.13)$$

In the derivations that follow, we will use Equation (5.13) repeatedly, making the implicit assumption that the ideal form of Fick’s law is valid; that is, the diffusion coefficient D_i is a constant, independent of concentration. This simplifying assumption is invalid where swelling and plasticization of the membrane by absorbed permeate occurs. These effects do not change the fundamental process involved, but concentration-dependent diffusion and sorption effects must then be used to accurately describe membrane transport.

5.3 One-component Transport in Hyperfiltration (Reverse Osmosis), Gas Separation and Pervaporation Membranes

In this section, the appropriate solution–diffusion model transport equations are derived for three membrane separation processes: hyperfiltration (reverse osmosis), gas permeation and pervaporation. The resulting equations linking the driving forces of pressure and concentration with flow are then shown to be consistent with experimental observations. To simplify this treatment, the equations will be derived for a single permeating species; that is, pure component i .

The general approach assumes that the chemical potentials at the fluid/membrane interface are equal on both sides of the interface. That is, the chemical potential μ_{i_o} of component i in the feed fluid adjacent to the membrane is the same as the chemical potential $\mu_{i_o(m)}$ of the component in the membrane at the feed surface. Likewise, the chemical potential μ_{i_ℓ} of component i in the permeate fluid adjacent to the membrane is the same as the chemical potential $\mu_{i_\ell(m)}$ of the component in the membrane at the permeate surface.

Using these equalities and the expressions for chemical potential given in Equations (5.5) and (5.6), the concentration of the component in the membrane at the membrane feed interface, $c_{i_o(m)}$, and the membrane permeate interface, $c_{i_\ell(m)}$, can be obtained in terms of the pressure and composition of the adjacent feed and permeate fluids. These values for $c_{i_o(m)}$ and $c_{i_\ell(m)}$ are substituted into the Fick’s law expression, Equation (5.13), to give the transport equation for the particular process.

5.3.1 Hyperfiltration (Reverse Osmosis)

Reverse osmosis was developed as a process for desalting water and the term is still used to describe liquid separations where the solvent is water. We use the term ‘hyperfiltration’ as a more general term to include permeation of all liquids, including organic liquids. In hyperfiltration, liquid flow occurs because of a pressure difference across the membrane. This pressure difference across the membrane can be written as:

$$p_{i_o} \geq p_{i_\ell} \geq p_{i_{sat}} \quad (5.14)$$

where p_{i_o} is the pressure of the liquid at the feed interface, p_{i_ℓ} is the pressure of liquid at the permeate interface and $p_{i_{sat}}$ is the saturation vapor pressure of component i . In such a process, equating the chemical potentials in the liquid and membrane phases at the feed side interface of the membrane gives:

$$\mu_{i_o} = \mu_{i_o(m)} \quad (5.15)$$

¹ In the equations that follow, the terms i and j represent components of a fluid and the terms o and ℓ represent the positions of the feed and permeate interfaces, respectively, of the membrane. Thus, the term c_{i_o} represent the concentration of component i in the fluid (gas or liquid) in contact with the membrane at the feed interface. The subscript m is used to represent the membrane phase. Thus, $c_{i_o(m)}$ represents the concentration of component i in the membrane at the interface (point o).

Substituting the expression for the chemical potential of incompressible fluids from Equation (5.5) into Equation (5.15) gives:²

$$\begin{aligned} \mu_{i_o} + RT \ln \left(\gamma_{i_o}^L n_{i_o} \right) + v_i (p_o - p_{i_{\text{sat}}}) \\ = \mu_{i_o} + RT \ln \left(\gamma_{i_o(m)} n_{i_o(m)} \right) \\ + v_{i_o(m)} (p_o - p_{i_{\text{sat}}}) \end{aligned} \quad (5.16)$$

which leads to:

$$\ln \left(\gamma_{i_o}^L n_{i_o} \right) = \ln \left(\gamma_{i_o(m)} n_{i_o(m)} \right) \quad (5.17)$$

and thus:

$$n_{i_o(m)} = \left(\frac{\gamma_{i_o}^L}{\gamma_{i_o(m)}} \right) n_{i_o} \quad (5.18)$$

Converting from mole fractions to concentration, using Equation (5.10), Equation (5.18) becomes:

$$c_{i_o(m)} = \left(\frac{\gamma_{i_o}^L \rho_m}{\gamma_{i_o(m)} \rho_o} \right) c_{i_o} \quad (5.19)$$

Hence, defining a sorption coefficient K_i^L as:

$$K_i^L = \frac{\gamma_{i_o}^L \rho_m}{\gamma_{i_o(m)} \rho_o} \quad (5.20)$$

allows Equation (5.19) to be written as:

$$c_{i_o(m)} = K_i^L c_{i_o} \quad (5.21)$$

At the permeate interface, a pressure difference exists from p_o , within the membrane, to p_ℓ in the permeate solution, as shown in Figure 5.2(b). Equating the chemical potentials in the liquid and membrane phases at this interface gives:

$$\mu_{i_\ell} = \mu_{i_\ell(m)} \quad (5.22)$$

Substituting the appropriate expression for the chemical potential of an incompressible fluid (Equation (5.5)) for the permeate liquid and the adjacent membrane phase yields:

$$\begin{aligned} \mu_{i_\ell}^o + RT \ln \left(\gamma_{i_\ell}^L n_{i_\ell} \right) + v_i (p_\ell - p_{i_{\text{sat}}}) \\ = \mu_{i_\ell}^o + RT \ln \left(\gamma_{i_\ell(m)} n_{i_\ell(m)} \right) + v_i (p_o - p_{i_{\text{sat}}}) \end{aligned} \quad (5.23)$$

which leads to:

$$\ln \left(\gamma_{i_\ell}^L n_{i_\ell} \right) = \ln \left(\gamma_{i_\ell(m)} n_{i_\ell(m)} \right) + \frac{v_i (p_o - p_\ell)}{RT} \quad (5.24)$$

Rearranging and substituting for the sorption coefficient, K_i^L and converting from mole fraction to concentration using Equation (5.10) gives the expression:

$$c_{i_\ell(m)} = K_i^L c_{i_\ell} \exp \left[\frac{-v_i (p_o - p_\ell)}{RT} \right] \quad (5.25)$$

The expressions for the concentration within the membrane at the interface in Equations (5.21) and (5.25) can now be substituted into the Fick's law expression, Equation (5.13), to yield:

$$J_i = \frac{D_i K_i^L}{\ell} \left\{ c_{i_o} - c_{i_\ell} \exp \left[\frac{-v_i (p_o - p_\ell)}{RT} \right] \right\} \quad (5.26)$$

The term $D_i K_i^L$ can be written as a permeability and so Equation (5.26) becomes:

$$J_i = \frac{P_i}{\ell} \left\{ c_{i_o} - c_{i_\ell} \exp \left[\frac{-v_i (p_o - p_\ell)}{RT} \right] \right\} \quad (5.27)$$

One result of Equation (5.25) and the solution-diffusion model described above is that the action of an applied pressure on the feed side of the membrane is to *decrease* the concentration of the permeant on the *low-pressure* side of the membrane. A number of workers have verified this prediction experimentally with a variety of membrane permeant combinations, ranging from diffusion of water in glassy cellulose acetate membranes to diffusion of organics in swollen rubbers [6,7,9]. Convincing examples include the results of Rosenbaum and Cotton shown in Figure 5.3 [6]. In these experiments, four thin cellulose acetate films were laminated together, placed in a high-pressure reverse osmosis cell and subjected to feed pressures of 68 or 136 atm. The permeate was maintained at atmospheric pressure. After the membrane laminate had reached a steady state, the membrane was quickly

² The superscripts G and L are used here and later to distinguish between gas and liquid-phase coefficients.

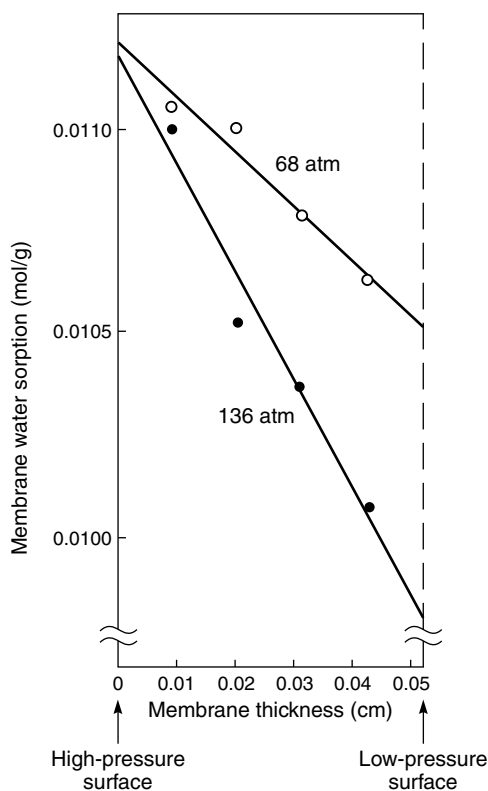


Figure 5.3 Measurements of Rosenbaum and Cotton [6] of the water concentration gradients in a laminated reverse osmosis cellulose acetate membrane under applied pressures of 68 and 136 atm. From 'Steady-state distribution of water in cellulose acetate membranes', S. Rosenbaum and O. Cotton, *J. Polym. Sci.*, 7, 101 Copyright © 1969, John Wiley & Sons, Inc. Reprinted with permission of John Wiley & Sons, Inc.

removed from the cell and the water concentration in each laminate measured. As predicted by the solution-diffusion model and shown in Figure 5.3, the applied pressure decreases the concentration of water on the permeate side of the membrane. In addition, the concentration difference across the membrane at 136 atm applied pressure is about twice that observed at 68 atm and the measured concentration on the permeate side is within 20% of the expected value calculated from Equation (5.25).

This result is completely consistent with the profiles for concentration gradients in a solution-diffusion membrane, as shown in Figure 5.2. The result is inconsistent with the pore-flow

model. Another consequence of Equation (5.25), shown experimentally in Figure 5.3, is that very large pressure differences across reverse osmosis membranes produce relatively small water concentration gradients. As Figure 5.3 shows, even at pressure differences of 68 to 136 atm, water sorption into the membrane, and hence water flux, is still in the linear part of the curve predicted by Equation (5.27) and shown in Figure 5.4. This result is because the molar volume (v_i) of water is small – 18 cm³/mol. Solvents of larger molar volume, for example, isooctane (molar volume 162 cm³/mol) have much larger concentration gradients at comparable pressures. Figure 5.4 shows the flux of isooctane as a function of applied pressure, calculated using Equation (5.27). At transmembrane pressure differences of 500 atm and above, the concentration on the permeate side of the membrane tends to zero and flux levels off to a limiting value $J_{i,max}$. This plateauing of flux with applied pressure is not seen in reverse osmosis but has been observed in hyperfiltration of organic liquids [9]. The above derivation of

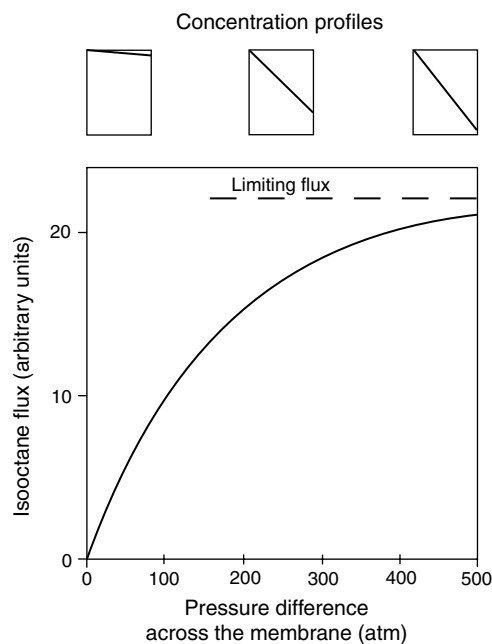


Figure 5.4 Calculated flux (arbitrary units) of liquid isooctane as a function of applied pressure on the feed side of a hyperfiltration membrane (Equation (5.27)). The change in concentration profile through the membrane as the pressure difference is increased is shown in the small boxes above the flux graph

Equation (5.27) relies on the simplifying assumption that the molar volumes of the permeant in the membrane phase and in the liquid phases in contact with the membrane are equal. This assumption is not always valid. Transport equations can be derived for the case when the molar volumes in the membrane phase and liquid phase are different [10]. The resulting equations differ by a term called the ‘molar volume correction factor.’ This correction factor is absent in the gas transport equation, and is insignificant for dialysis and pervaporation. For high-pressure hyperfiltration of mixtures containing relatively large molecules, the molar volume correction factor can be large enough to affect the dependence of flux on pressure.

5.3.2 Gas Separation

In gas separation, a gas mixture at a pressure p_o is applied to the feed side of the membrane, and the permeate gas at a lower pressure p_ℓ is removed from the downstream side of the membrane.

The concentration and pressure gradients through a gas separation membrane are shown graphically in Figure 5.5. As for hyperfiltration, the pressure within the membrane phase is the feed pressure and the chemical potential gradient is created by a gradient in concentration. This gradient in concentration can be changed by changing the feed or permeate pressure. As the pressure is increased on the feed side of the membrane, the concentration in the membrane at the feed interface ($c_{i_o(m)}$) increases, reaching a maxi-

imum value when the vapor pressure of component i , p_{i_o} , reaches the saturation vapor pressure, $p_{i_{sat}}$. Similarly, the concentration in the membrane at the permeate side interface decreases with decreasing permeate pressure, reaching zero when a hard vacuum is created on the permeate side of the membrane. In gas separation therefore, the expression of the pressures on either side of the membrane can be linked by the expression:

$$p_{i_{sat}} \geq p_{i_o} \geq p_{i_\ell} \tag{5.28}$$

As before, the starting point for the derivation of the gas separation transport equation is to equate the chemical potentials on either side of the gas/membrane interface. This time, however, the chemical potential for the gas phase is given by Equation (5.6) for a compressible fluid, and Equation (5.5), for an incompressible medium, is applied to the membrane phase. Equating the chemical potentials at the feed side interface, first:

$$\mu_{i_\ell} = \mu_{i_\ell(m)} \tag{5.29}$$

Substitution of Equations (5.5) and (5.6) into Equation (5.29) at the gas/membrane feed interface yields:

$$\begin{aligned} \mu_i^o + RT \ln \left(\gamma_{i_o}^G n_{i_o} \right) + RT \ln \left(\frac{p_o}{p_{i_{sat}}} \right) \\ = \mu_i^o + RT \ln \left(\gamma_{i_o(m)} n_{i_o(m)} \right) + v_i (p_o - p_{i_{sat}}) \end{aligned} \tag{5.30}$$

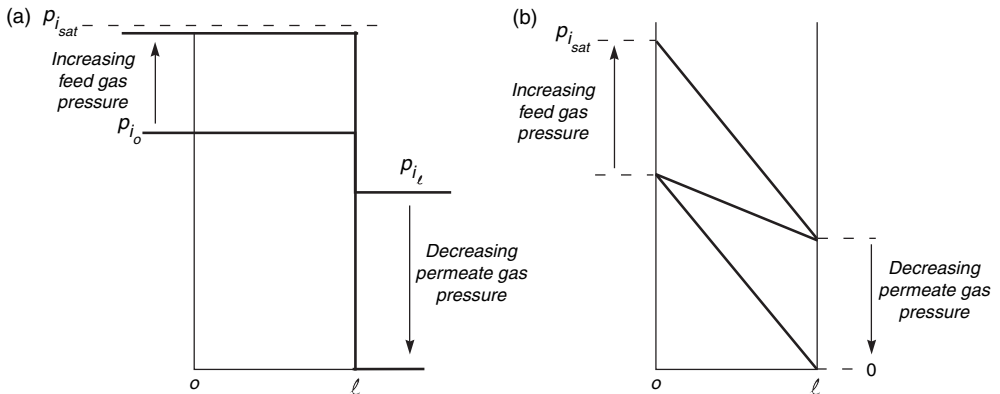


Figure 5.5 Changes in (a) the pressure and (b) the concentration profiles through a gas permeation membrane as the feed and permeate pressures change, according to the solution–diffusion model

which rearranges to:

$$n_{i_o(m)} = \left(\frac{\gamma_{i_o}^G}{\gamma_{i_o(m)}} \right) \left(\frac{p_o}{p_{i_{sat}}} \right) n_{i_o} \exp \left[\frac{-v_i(p_o - p_{i_{sat}})}{RT} \right] \quad (5.31)$$

The term $n_{i_o}p_o$ is the partial pressure of i in the feed gas, p_{i_o} , and so Equation (5.31) then simplifies to:

$$n_{i_o(m)} = \left(\frac{\gamma_{i_o}^G}{\gamma_{i_o(m)}} \right) \left(\frac{p_{i_o}}{p_{i_{sat}}} \right) \exp \left[\frac{-v_i(p_o - p_{i_{sat}})}{RT} \right] \quad (5.32)$$

To convert Equation (5.32) from mole fractions to concentrations using Equation (5.10), we define a gas phase sorption coefficient K_i^G as:

$$K_i^G = \frac{m_i \rho_m \gamma_{i_o}^G}{\gamma_{i_o(m)} p_{i_{sat}}} \quad (5.33)$$

The concentration of component i at the feed interface of the membrane can be converted from mole fraction to concentration and written as:

$$c_{i_o(m)} = K_i^G p_{i_o} \exp \left[\frac{-v_i(p_o - p_{i_{sat}})}{RT} \right] \quad (5.34)$$

In exactly the same way, the process represented by Equations (5.29)–(5.34) can be repeated at the membrane/permeate interface and the concentration of component i in the membrane at the membrane/permeate interface can be shown to be:

$$c_{i_t(m)} = K_i^G p_{i_t} \exp \left[\frac{-v_i(p_o - p_{i_{sat}})}{RT} \right] \quad (5.35)$$

Combining Equations (5.34) and (5.35) with the Fick's law expression, Equation (5.13), then gives:

$$J_i = \frac{D_i K_i^G (p_{i_o} - p_{i_t})}{\ell} \exp \left[\frac{-v_i(p_o - p_{i_{sat}})}{\ell} \right] \quad (5.36)$$

It should be noted that v_i in Equation (5.36) is not the molar volume of i in the gas phase, but the *partial* molar volume of i dissolved in the mem-

brane material, which is approximately equal to the molar volume of liquid i . As a result, the exponential term (known as the Poynting correction) usually is very close to one for permanent gases (but not for vapors with larger molar volumes), and Equation (5.36) reduces to:

$$J_i = \frac{D_i K_i^G (p_{i_o} - p_{i_t})}{\ell} \quad (5.37)$$

The product $D_i K_i^G$ is often abbreviated to a permeability coefficient P_i^G , leading to the familiar expression:

$$J_i = \frac{P_i^G (p_{i_o} - p_{i_t})}{\ell} \quad (5.38)$$

Equation (5.38) is widely used to rationalize and predict the properties of gas permeation membranes with very good accuracy.

5.3.3 Pervaporation

Pervaporation is a process intermediate between gas separation and hyperfiltration. The feed membrane interface is contacted with a feed fluid in the liquid phase at a pressure greater than the saturation vapor pressure; the permeate interface is in contact with a permeate fluid in the gas phase at a pressure below the saturation vapor pressure.

Pressure and concentration profiles across the membrane in pervaporation are shown in Figure 5.6. The pressure within the membrane is the same as the feed pressure. At the permeate side interface, the pressure then drops to a value below the saturation vapor pressure. The pressures on either side of the membrane can be linked by the expression:

$$p_{i_o} \geq p_{i_{sat}} \geq p_{i_t} \quad (5.39)$$

As before, the flux through the membrane can be determined by calculating the concentration in the membrane at the two interfaces. At the feed-side liquid solution/membrane interface, the chemical potential of the feed liquid is the same as the chemical potential in the membrane at the same pressure. Equation (5.5) then gives:

$$\begin{aligned} \mu_i^o + RT \ln \left(\gamma_{i_o}^L n_{i_o} \right) + v_i(p_o - p_{i_{sat}}) \\ = \mu_i^o + RT \ln \left(\gamma_{i_o(m)} n_{i_o(m)} \right) v_i(p_o - p_{i_{sat}}) \end{aligned} \quad (5.40)$$

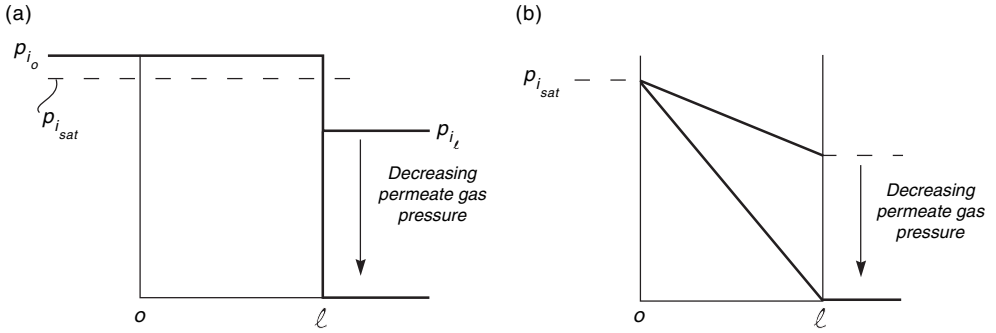


Figure 5.6 Changes in (a) the pressure and (b) the concentration profiles through a pervaporation membrane as the permeate pressure changes, according to the solution–diffusion model. In pervaporation, the feed is a liquid; therefore, the feed pressure p_{i_o} exceeds the saturated pressure $p_{i_{sat}}$

which in an analogous way to the derivation of Equation (5.21) leads to an expression for the concentration at the feed-side interface:

$$c_{i_{\ell(m)}} = K_i^L c_{i_o} \quad (5.41)$$

where K_i^L is the liquid-phase sorption coefficient defined by Equation (5.20) in Section 5.3.1 above. At the permeate gas/membrane interface, the pressure drops from p_o in the membrane to p_ℓ in the permeate vapor. The equivalent expression for the chemical potentials in each phase is then:

$$\begin{aligned} \mu_i^o + RT \ln(\gamma_{i_\ell}^G n_{i_\ell}) + RT \ln\left(\frac{p_\ell}{p_{i_{sat}}}\right) \\ = \mu_i^o + RT \ln(\gamma_{i_{\ell(m)}} n_{i_{\ell(m)}}) + v_i(p_o - p_{i_{sat}}) \end{aligned} \quad (5.42)$$

Rearranging Equation (5.42) gives:

$$n_{i_{\ell(m)}} = \left(\frac{\gamma_{i_\ell}^G}{\gamma_{i_{\ell(m)}}}\right) \left(\frac{p_\ell}{p_{i_{sat}}}\right) n_{i_\ell} \exp\left[\frac{-v_i(p_o - p_{i_{sat}})}{RT}\right] \quad (5.43)$$

As before, the exponential term is close to unity; thus, the concentration at the permeate side interface is:

$$n_{i_{\ell(m)}} = \left(\frac{\gamma_{i_\ell}^G}{\gamma_{i_{\ell(m)}}}\right) n_{i_\ell} \left(\frac{p_\ell}{p_{i_{sat}}}\right) \quad (5.44)$$

The product $n_{i_\ell} p_\ell$ can be replaced by the partial pressure term p_{i_ℓ} and thus:

$$n_{i_{\ell(m)}} = \left(\frac{\gamma_{i_\ell}^G}{\gamma_{i_{\ell(m)}}}\right) \left(\frac{p_{i_\ell}}{p_{i_{sat}}}\right) \quad (5.45)$$

and, substituting concentration for mole fraction from Equation (5.10) gives:

$$c_{i_{\ell(m)}} = m_i \rho_m \left(\frac{\gamma_{i_\ell}^G p_{i_\ell}}{\gamma_{i_{\ell(m)}} p_{i_{sat}}}\right) = K_i^G p_{i_\ell} \quad (5.46)$$

where K_i^G is the gas-phase sorption coefficient defined in Equation (5.33). The concentration terms in Equations (5.41) and (5.46) can then be substituted into Equation (5.13) (Fick's law) to obtain the expression for membrane flux:

$$J_i = \frac{D_i(K_i^L c_{i_o} - K_i^G p_{i_\ell})}{\ell} \quad (5.47)$$

Equation (5.47) contains two different sorption coefficients, deriving from Equations (5.41) and (5.46). The sorption coefficient in Equation (5.41) is a liquid-phase coefficient, whereas the sorption coefficient in Equation (5.46) is a gas-phase coefficient. The interconversion of these two coefficients can be handled by considering a hypothetical vapor in equilibrium with the feed solution. The vapor–liquid equilibrium can then be written as:

$$\begin{aligned} \mu_i^o + RT \ln(\gamma_i^L n_{i_o}^L) + v_i(p_o - p_{i_{sat}}) \\ = \mu_i^o + RT \ln(\gamma_{i_o}^G n_{i_o}^G) + RT \ln\left(\frac{p_o}{p_{i_{sat}}}\right) \end{aligned} \quad (5.48)$$

Following the same steps as were taken from Equations (5.42)–(5.46), Equation (5.48) becomes:

$$n_i^L = \frac{\gamma_i^G p_i}{\gamma_i^L p_{i,\text{sat}}} \quad (5.49)$$

Converting from mole fraction to concentration using Equation (5.10) gives:

$$c_i^L = m_i \rho \left(\frac{\gamma_i^G p_i}{\gamma_i^L p_{i,\text{sat}}} \right) \quad (5.50)$$

and so:

$$c_i^L = \left(\frac{K_i^G}{K_i^L} \right) p_i \quad (5.51)$$

This expression links the concentration of component i in the liquid phase, c_i^L , with p_i , the partial vapor pressure of i in equilibrium with the liquid. Substitution of Equation (5.51) into Equation (5.47) yields:

$$J_i = \frac{D_i K_i^G (p_{i_o} - p_{i_e})}{\ell} \quad (5.52)$$

where p_{i_o} and p_{i_e} are the partial vapor pressures of component i on either side of the membrane. Equation (5.52) can also be written as:

$$J_i = \left(\frac{P_i^G}{\ell} \right) (p_{i_o} - p_{i_e}) \quad (5.53)$$

where P_i^G is the gas permeation permeability coefficient. Equation (5.53) explicitly expresses the driving force in pervaporation as the vapor pressure difference across the membrane, a form of the pervaporation transport equation derived first by Kataoka *et al.* [11].

In the derivations given above, Equation (5.51) links the concentration of a sorbed vapor in the liquid phase (c_i^L) with the equilibrium partial pressure of the vapor. This relationship is more familiarly known as Henry’s law, written as:

$$H_i c_i^L = p_i \quad (5.54)$$

where H_i is the Henry’s law coefficient.

From Equations (5.51) and (5.54), it follows that H_i can be written as:

$$H_i = \frac{K_i^L}{K_i^G} = \frac{\gamma_i^L p_{i,\text{sat}}}{m_i \rho \gamma_i^G} \quad (5.55)$$

These expressions can be used to rewrite Equation (5.47) as:

$$J_i = \frac{P_i^G}{\ell} (c_{i_o} H_i - p_{i_e}) \quad (5.56)$$

or:

$$J_i = \frac{P_i^L}{\ell} (c_{i_o} - p_{i_e}/H_i) \quad (5.57)$$

where P_i^L is the liquid (hyperfiltration) permeability coefficient.

Equations (5.53) and (5.57) are alternative ways to describe the pervaporation flux. Equation (5.53) expresses the driving force in terms of vapor pressure; Equation (5.57) in terms of concentration difference. As a practical matter, the use of vapor pressure driving force leads to a more useful result. For example, in pervaporation with a hard vacuum on the permeate side ($p_{i_e} \sim 0$), Equation (5.57) shows the flux equals $P_i^L c_{i_o}/\ell$. Since flux usually increases exponentially with temperature, P_i^L must increase exponentially with temperature. On the other hand, in the alternative expression for flux expressed in Equation (5.53), when $p_{i_e} \sim 0$, flux equals $P_i^G p_{i_o}/\ell$. The exponential increase in flux with increasing temperature is taken into account by the vapor pressure term p_{i_o} , which also increases exponentially. As a result, the permeability term P_i^G is almost constant and independent of temperature.

The benefit of using the gas permeability constant P_i^G and Equation (5.53) to describe pervaporation has been amply demonstrated experimentally [11–13]. For example, Figure 5.7 shows data for water flux as a function of permeate pressure. As the permeate pressure (p_{i_e}) increases, the water flux falls in accordance with Equation (5.53), reaching zero flux when the permeate pressure is equal to the vapor pressure (p_{i_o}) of the feed liquid at the temperature of the experiment. The straight lines in Figure 5.7 indicate that the permeability coefficient of water in silicone rubber is constant. This can be expected in systems in which the membrane material is a rubbery polymer and the permeant swells the polymer only moderately.

Thompson and coworkers [13] have studied the effect of feed and permeate pressure on pervaporation flux in some detail. Some illustrative

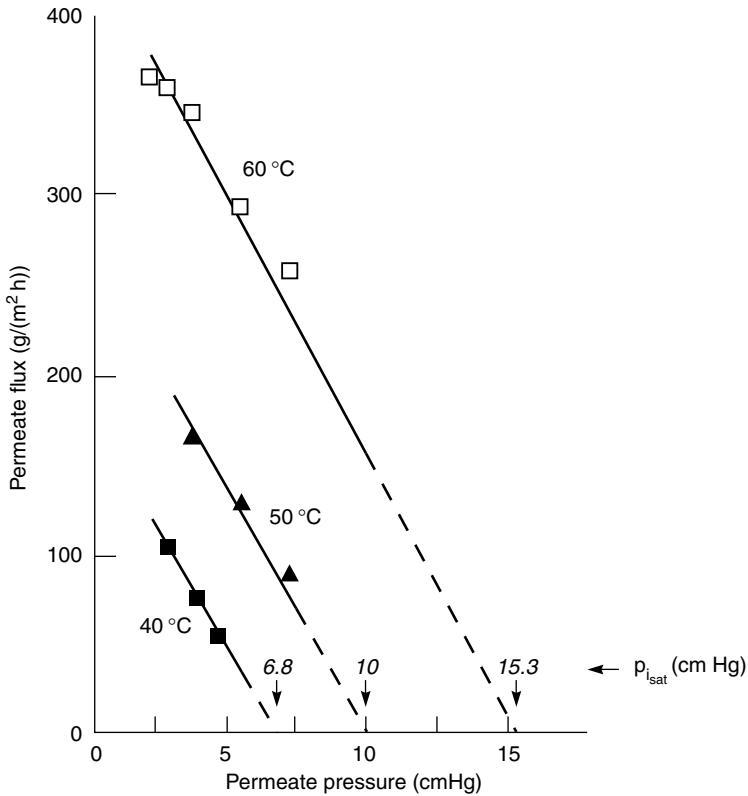


Figure 5.7 The effect of permeate pressure on the water flux through a silicone rubber membrane during pervaporation [12]. The arrows on the horizontal axis represent the saturation vapor pressures of the feed solution at the experimental temperatures. Reprinted from *Journal of Membrane Science*, **107**, J. G. Wijmans, and R. W. Baker, 'The solution–diffusion model: A Review', pp. 1–21, Copyright (1995), with permission from Elsevier

results are shown in Figure 5.8. As Figure 5.8(a) shows, the dependence of flux on permeate pressure is in accordance with Equation (5.53). At very low permeate pressures, p_{i_e} approaches zero ($p_{i_e} \rightarrow 0$) and the membrane flux has its maximum value $J_{i_{\max}}$ equal to $P_i^C p_{i_o} / \ell$. As the permeate pressure increases, the flux decreases, reaching a zero flux when the permeate pressure equals the saturation vapor pressure of the feed ($p_{i_e} = p_{i_o}$).

The line linking flux and permeate pressure in Figure 5.8(a) is curved. This curvature shows that the permeability coefficient decreases with decreasing permeate pressure, that is, P_{hexane} decreases with a decrease in hexane concentration in the membrane. This behavior is typical of membranes that are swollen significantly by the permeant. If on the other hand, as shown in

Figure 5.8(b), the permeate pressure is fixed at a low value, the hydrostatic pressure of the feed liquid can be increased to as much as 20 atm without any significant change in the flux. This is because the vapor pressure of a liquid (p_{i_o}) increases very little with increased hydrostatic pressure. Equation (5.53) shows that the feed vapor pressure is the true measure of the driving force for transport through the membrane. Thus, the properties of pervaporation membranes illustrated in Figures 5.7 and 5.8 are easily rationalized by the solution–diffusion model as given above but are much more difficult to explain by a pore-flow mechanism.

5.4 A Unified View

In the preceding section, the solution–diffusion model was used to calculate the concentration

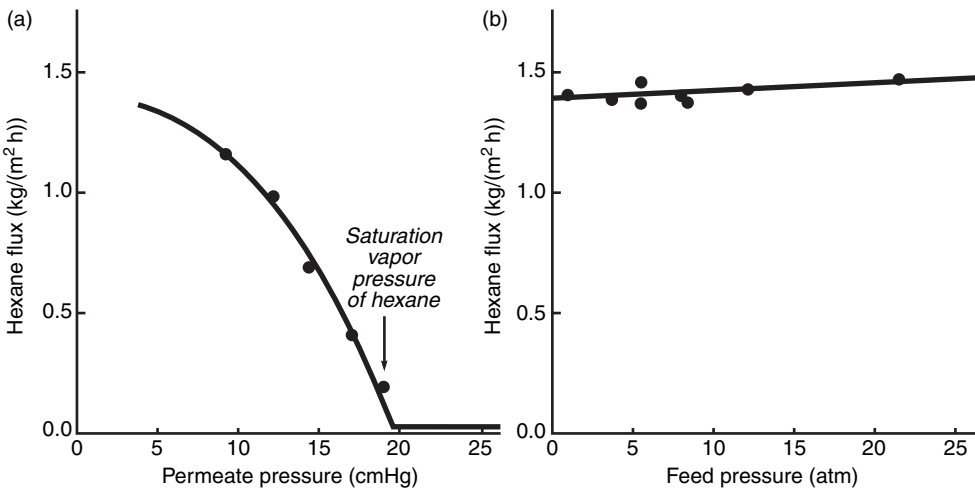


Figure 5.8 The effect of (a) permeate pressure and (b) feed pressure on the flux of hexane through a rubbery pervaporation membrane. The flux is essentially independent of feed pressures up to 20 atm, but is extremely sensitive to permeate pressure [13]. Equation (5.53) explains this behavior. Reprinted from *Journal of Membrane Science*, 2, F. W. Greenlaw, W. D. Prince, R. A. Sheldon and E. V. Thompson, ‘The effect of diffusive permeation rates by upstream and downstream pressures’, pp. 141–151, Copyright (1977), with permission from Elsevier

gradients formed through gas separation, pervaporation and hyperfiltration membranes. The equations describing the flux through the membranes contain the same coefficients D_i , K_i and P_i , irrespective of the actual process. This happens because the driving force affecting the permeating component is the same for each process – a concentration gradient within the membrane. The fluid on either side of the membrane can change from a gas to a pressurized liquid but the only effect of these changes on permeation within the membrane is to alter the concentration gradient driving force.

The pressure and concentration profiles within a solution–diffusion membrane for gas separation, pervaporation and hyperfiltration (reverse osmosis) are shown in Figure 5.9. Considering gas separation first, the feed and permeate sides of the membrane are both below the saturation vapor pressure and we can write:

$$P_{i_{sat}} > P_{i_o} > P_{i_t} \quad (\text{Gas separation})$$

The concentration in the membrane at the interfaces is proportional to the adjacent gas phase pressure, as described in Equations (5.34) and (5.35).

If the feed gas pressure, P_{i_o} , is raised until it exceeds the saturation vapor pressure, then the membrane enters the pervaporation region, liquid forms on the feed side of the membrane and:

$$P_{i_o} > P_{i_{sat}} > P_{i_t} \quad (\text{Pervaporation})$$

At this point, the concentrations in the membrane at the interfaces are described by Equations (5.41) and (5.46).

If the permeate side pressure, P_{i_t} , is then increased, so that the saturation vapor pressure is exceeded on both sides of the membrane, liquid forms at both membrane interfaces. The membrane then enters the hyperfiltration (reverse osmosis) region and:

$$P_{i_o} > P_{i_t} > P_{i_{sat}} \quad (\text{Hyperfiltration (reverse osmosis)})$$

At this point, the concentrations in the membrane at the interfaces are described by Equations (5.21) and (5.25).

The connection between the three permeation processes can be represented in graphical form, as shown in Figure 5.10. This figure shows the transition between the different operating regions

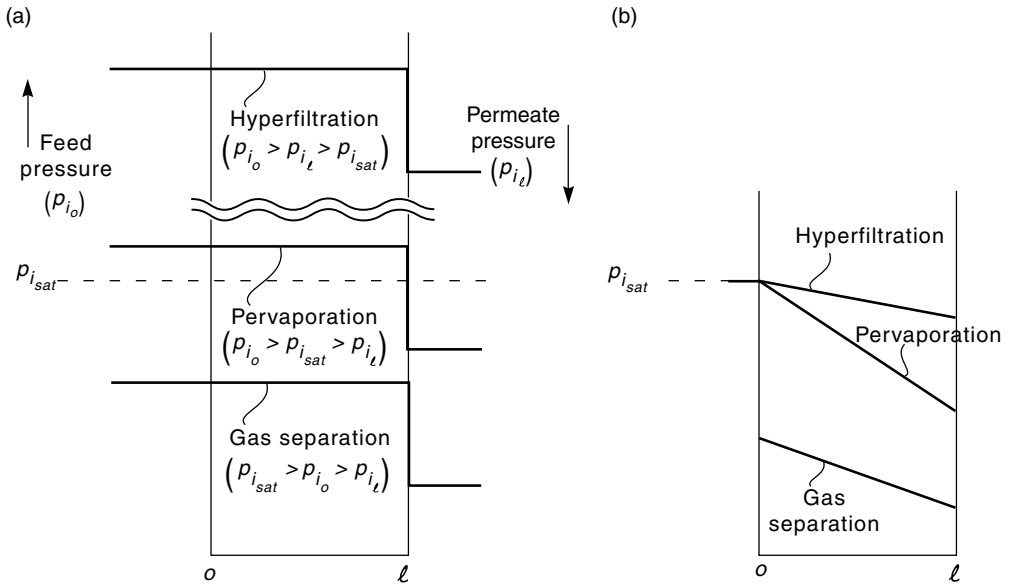


Figure 5.9 (a) Pressure profiles in gas separation, pervaporation and hyperfiltration membranes, relative to the saturation vapor pressure ($p_{i_{sat}}$). (b) Concentration profile created within the same membranes by the pressure profiles shown in (a)

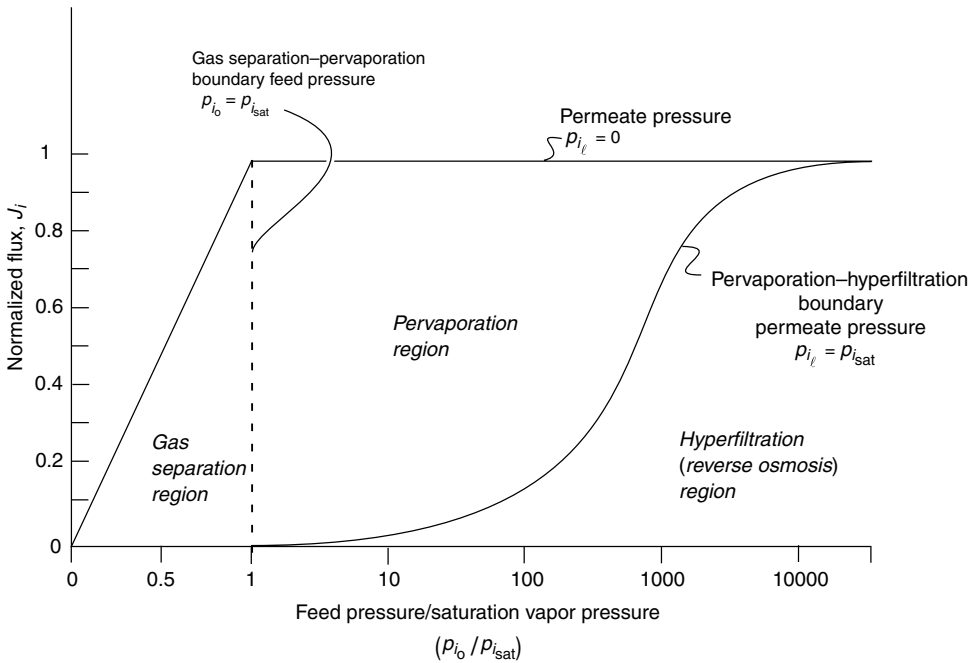


Figure 5.10 Permeation through a membrane, expressed as normalized flux, as a function of normalized feed pressure ($p_{i_o}/p_{i_{sat}}$). This figure shows the smooth transition from gas separation, to pervaporation, to hyperfiltration. The curves shown are calculated by using Equations (5.38), (5.27) and (5.53) in the gas separation, hyperfiltration and pervaporation regions, respectively

as the feed and permeate pressures change. The permeate flux through the membrane is plotted as a function of the normalized driving force, measured by the ratio of the feed pressure to saturation vapor pressure ($p_{i_o}/p_{i_{sat}}$). A linear scale is used for feed pressure below the saturation vapor pressure, corresponding to the linear dependence of gas flux on feed pressure shown in Equation (5.37). Above the saturation vapor pressure an exponential scale is used, because the hyperfiltration equation (Equation (5.27)) shows the membrane flux to be an exponential function of feed pressure. The flux axis of Figure 5.10 has also been normalized by setting $J_{i_{max}}$ to 1 according to the equation:

$$J_{i_{max}} = \frac{P_i^G p_{i_{sat}}}{\ell} = \frac{P_i^L c_{i_o}}{\ell} = 1 \quad (5.58)$$

Two lines are shown in Figure 5.10. The first line represents the normalized flux when the permeate pressure p_{i_e} is set to zero and the normalized feed pressure p_{i_o} increases from zero to ∞ . This line represents gas separation and pervaporation with a hard vacuum on the permeate side. In these cases, at low feed pressures, the membrane is in the gas separation region and as the normalized feed pressure ($p_{i_o}/p_{i_{sat}}$) increases, the gas flux also increases. The gas flux reaches its maximum value (arbitrarily set to 1) when the feed pressure reaches the saturation vapor pressure ($p_{i_o}/p_{i_{sat}} = 1$). The gas flux at this point is $P_i^G p_{i_{sat}}/\ell$. When the feed pressure is increased further, it exceeds the saturation vapor pressure and the feed gas liquefies. The process then enters the pervaporation region. At this point, further increases in feed pressure do not increase the flux. This is consistent with the pervaporation flux equation (Equation (5.53)), in which p_{i_o} is set at the saturation vapor pressure $p_{i_{sat}}$ and p_{i_e} is set to zero. That is:

$$J_i = \frac{P_i^G}{\ell} (p_{i_o} - p_{i_e}) = \frac{P_i^G}{\ell} (p_{i_{sat}} - 0) = \frac{P_i^G p_{i_{sat}}}{\ell} \quad (5.59)$$

The second line shown in Figure 5.10 represents the membrane flux at a permeate pressure just above the saturation vapor pressure. Under these conditions, liquid forms on both sides of the membrane and Equation (5.27) for hyperfiltration, repeated below as Equation (5.60), can be

used to calculate the membrane flux:

$$J_i = \frac{P_i^L}{\ell} \left\{ c_{i_o} - c_{i_e} \exp \left[\frac{-v_i (p_o - p_e)}{RT} \right] \right\} \quad (5.60)$$

Initially, the flux increases linearly with increasing feed pressure, but then asymptotically approaches a maximum value $J_{i_{max}}$ of $P_i^L c_{i_o}/\ell$ at very high feed pressures. This is consistent with Equation (5.60), because as $(p_o - p_e) \rightarrow \infty$, then:

$$J_i \rightarrow \left(\frac{P_i^L}{\ell} \right) c_{i_o} \quad (5.61)$$

and following Equation (5.58) the maximum value of J_i is arbitrarily normalized to 1. Figure 5.10 is thus divided into three regions; gas separation, pervaporation and hyperfiltration (reverse osmosis), depending on the feed and permeate pressures. The ability of the solution–diffusion model to show the connection between these diverse processes is its great strength. The performance of a membrane at any feed and permeate pressures can be represented as a point within this figure.

The effect of other permeate pressures on membrane flux is illustrated in Figure 5.11. This figure has the same form as Figure 5.10 but shows additional lines calculated for intermediate permeate pressures from permeate pressures of 0 to $1000 p_{i_{sat}}$. The simple equations required to create these lines were derived earlier and are referred to in the figure.

5.5 Multi-component Transport in Hyperfiltration (Reverse Osmosis), Gas Separation and Pervaporation Membranes

5.5.1 Hyperfiltration (Reverse Osmosis)

Pressure-driven liquid permeation through membranes has historically been called reverse osmosis after the principal application, desalination of water. Recently, pressure-driven liquid permeation has also begun to be used to separate organic mixtures. A milestone in this development was the installation by Mobil Oil of a large lube oil/solvent membrane separation plant in 1998 [14,15]. To recognize this increasing scope of liquid separation, we prefer to use the more generic term ‘hyperfiltration’. We start our treatment by considering a model liquid – a 50/50 mixture

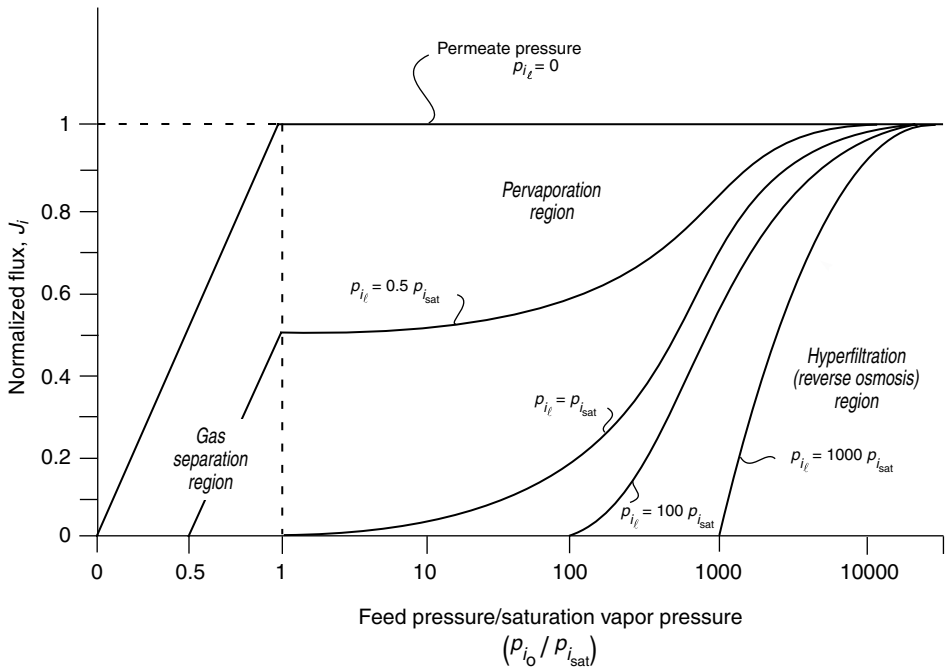


Figure 5.11 Permeation through a membrane, expressed as normalized flux, as a function of normalized feed pressure ($p_{i_o}/p_{i_{sat}}$). This figure shows the smooth transition from gas separation, to pervaporation, to hyperfiltration. The curves shown are calculated by using Equations (5.38), (5.27) and (5.53) in the gas separation, hyperfiltration and pervaporation regions, respectively

of *n*-octane and isooctane (trimethylpentane). We then describe reverse osmosis (the separation of salt from water) as a special case of the general hyperfiltration process.

The permeation rates of components *i* and *j* in a two-component mixture are described by the permeation equations given earlier. That is:

$$J_i = \frac{P_i^L}{\ell} \left\{ c_{i_o} - c_{i_i} \exp \left[-v_i \frac{(p_o - p_\ell)}{RT} \right] \right\} \quad (5.62)$$

and:

$$J_j = \frac{P_j^L}{\ell} \left\{ c_{j_o} - c_{j_i} \exp \left[-v_j \frac{(p_o - p_\ell)}{RT} \right] \right\} \quad (5.63)$$

Substituting a range of the membrane permeance for the two components, curves based on Equations (5.62) and (5.63) can be calculated. Sample curves are shown in Figure 5.12 for a 50/50

n-octane/isooctane mixture. The *n*-octane permeance (P_i^L/ℓ) is assumed to be 1 kg/(m² h psi) while the isooctane permeance is assumed to be one hundred-fold less at 0.01 kg/(m² h psi). At low feed pressures, the total flux is small because the osmotic pressure of the retained isooctane is high, at approximately 100 bar (The osmotic pressure ($\Delta\pi$) for an ideal membrane can be calculated from Equation (5.62) by assuming that at osmotic equilibrium, $J_i = 0$ when $p_i - p_\ell = \Delta\pi$). As the feed pressure increases above 100 bar, the flux of *n*-octane increases roughly linearly with pressure up to a pressure of 300 to 400 bar, at which point the flux begins to increase less rapidly with increased pressure and asymptotically tends to its limiting value. At these high pressures, the exponential term in Equation (5.62) is small and the *n*-octane flux approaches a limiting value expressed by:

$$J_{i_{max}} = \left(\frac{P_i^L}{\ell} \right) c_{i_o} \quad (5.64)$$

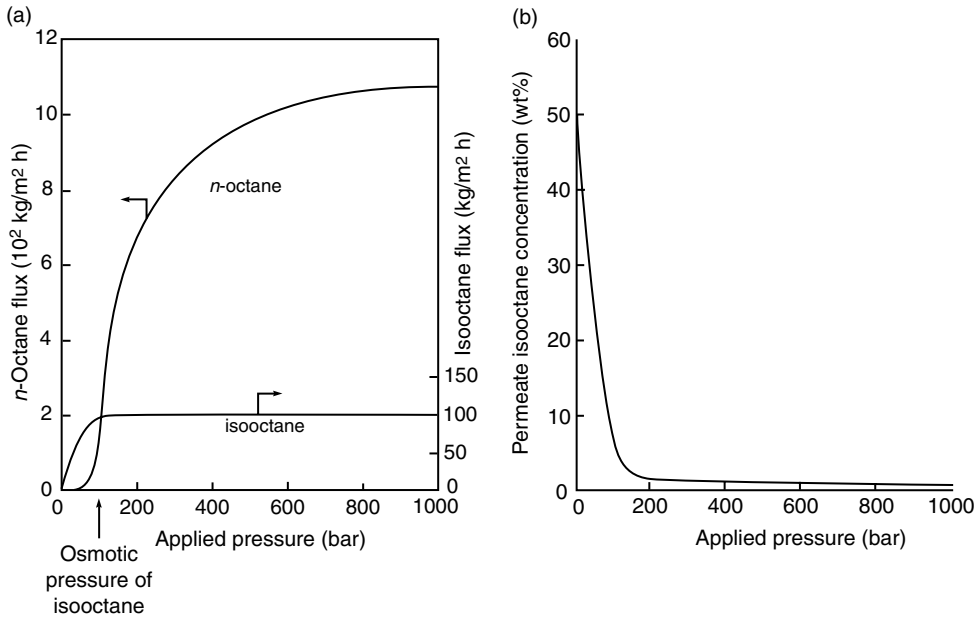


Figure 5.12 Calculated (a) permeate flux and (b) isooctane permeate concentration curves for a 50/50 *n*-octane/isooctane feed solution, with assumed membrane permeances of 1 kg/(m² h psi) and 0.01 kg/(m² h psi) for *n*-octane and isooctane, respectively

The flux of isooctane follows the same pattern but reaches its limiting value:

$$J_{j_{\max}} = \left(\frac{P_j^L}{\ell} \right) c_{j_o} \quad (5.65)$$

at lower pressures.

Because the pressure-dependence of the flux of the two components is different, the isooctane concentration in the permeate decreases with increasing pressure. At very low pressures, the permeate isooctane concentration is equal to the feed concentration and no separation is produced. As the applied pressure increases, the permeate isooctane concentration falls rapidly. When the osmotic pressure of the feed isooctane reaches 100 bar, the permeate isooctane concentration is 10 wt%; at 200 bar, the permeate isooctane concentration is 2 wt%. At pressures above 200 bar, the isooctane permeate concentration approaches its limiting value of 1 wt%. An analytical solution for Equations (5.62) and (5.63) deriving the molar permeate concentration as a function of applied permeate pressure has been detailed elsewhere [10].

The results shown in Figure 5.12 illustrate one of the key problems inhibiting application of hyperfiltration to the separation of concentrated organic mixtures: with selective membranes, very high pressures are required to achieve a good separation. Additional calculations in support of this conclusion are shown in Figure 5.13. This figure shows the effect of membrane selectivity on flux and permeate concentration for the same 50/50 *n*-octane/isooctane feed solution. The selectivity (permeability ratio) is varied from 1/1, no selectivity, to 1/0.01, an extremely selective membrane. In all cases, the *n*-octane permeance is set at 1 kg/(m² h psi) and selectivity is increased by reducing the permeance of isooctane. For membranes of high selectivity (selectivity = 100), pressures in excess of 120 bar are required to obtain useful fluxes. On the other hand, the less selective membranes (selectivity = 10) yield good fluxes at pressures as low as 50 bar, but the separations obtained are poor. The optimum membrane achieves a balance between applied pressure requirements and achieved separation. By inspection, it appears that the optimum membranes have selectivities of 10 to

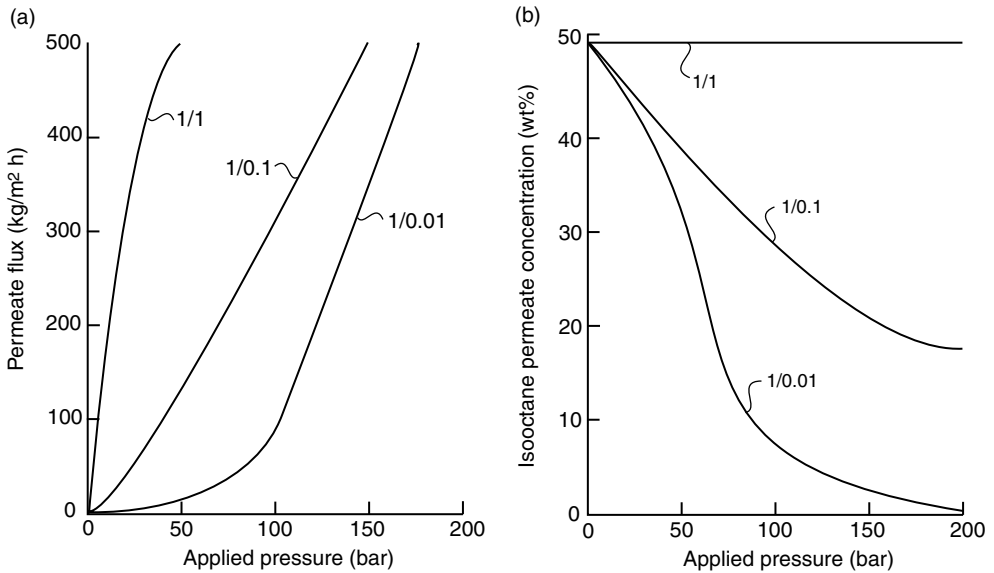


Figure 5.13 Calculated (a) permeate flux and (b) isooctane permeate concentration curves for a 50/50 *n*-octane/isooctane feed solution, with assumed membrane permeances of 1 kg/(m² h psi) and 0.01–1.0 kg/(m² h psi) for *n*-octane and isooctane, respectively

30. In this range, a good separation is produced and useful fluxes are obtained at pressures of 100 bar. Operating pressures of this magnitude are high but within normal experience for membrane producers and plant operators. For example, an ExxonMobil (formerly Mobil) lube/oil solvent dewaxing plant operates at a feed pressure of about 70 bar [14].

5.5.1.1 Reverse Osmosis

Reverse osmosis, the most common pressure-driven liquid membrane separation process, is a special case of hyperfiltration, and the same general equations apply. However, a number of simplifications can be made because the membranes used are very selective ($P_i^l/P_j^l > 100$), the concentration of the less permeable component (salt) is generally less than 5 wt% and because the molar volume of the solvent (water) is small.

For example, the flux of water across the membrane is zero at the point at which the applied hydrostatic pressure balances the water activity gradient (the point of osmotic equilibrium). At this point, if water is component *i*, Equation

(5.62) becomes:

$$J_i = 0 = \frac{P_i}{\ell} \left\{ c_{i_o} - c_{i_l} \exp \left[\frac{-v_i(\Delta\pi)}{RT} \right] \right\} \tag{5.66}$$

where $\Delta\pi$, the hydrostatic pressure difference ($p_o - p_l$) required to stop water flow, is the osmotic pressure of the salt solution.

On rearranging:

$$c_{i_l} = c_{i_o} \exp \frac{v_i(\Delta\pi)}{RT} \tag{5.67}$$

This is a form of the van't Hoff equation.

This expression for c_{i_l} can then be substituted into Equation (5.62) to yield:

$$J_i = \frac{P_i c_{i_o}}{\ell} \left(1 - \exp \left\{ \frac{-v_i[(p_o - p_l) - \Delta\pi]}{RT} \right\} \right) \tag{5.68}$$

which is equivalent to:

$$J_i = \frac{P_i c_{i_o}}{\ell} \left\{ 1 - \exp \left[\frac{-v_i(\Delta p - \Delta\pi)}{RT} \right] \right\} \tag{5.69}$$

where Δp is the difference in hydrostatic pressure across the membrane, $p_o - p_\ell$.

Under the normal conditions of reverse osmosis, a trial calculation shows that the term $-v_i(\Delta p - \Delta \pi)/(RT)$ is small. For example, when $\Delta p = 100$ atm, $\Delta \pi = 10$ atm, and $v_i = 18$ cm³/mol, the term $v_i(\Delta p - \Delta \pi)/(RT)$ is about 0.06. Under these conditions, the simplification $1 - \exp x \rightarrow x$ as $x \rightarrow 0$ can be used and Equation (5.69) can be written to a very good approximation as:

$$J_i = \frac{P_i c_i v_i (\Delta p - \Delta \pi)}{\ell RT} \quad (5.70)$$

This equation is usually further simplified to:

$$J_i = A(\Delta p - \Delta \pi) \quad (5.71)$$

where A is a constant equal to the term $P_i c_i v_i / (\ell RT)$. In the reverse osmosis literature, the constant A is usually called the *water permeability constant*. This equation is reliable for highly selective reverse osmosis membranes at pressures above the osmotic pressure $\Delta \pi$. At pressures below the osmotic pressure, the water flux is so small that it becomes comparable to the salt flux. The membrane then loses its selectivity and the term $\Delta \pi$ in Equation (5.71) is no longer constant and becomes smaller.

A similar simplified expression for the salt flux J_j through the membrane can be derived, starting with Equation (5.63):

$$J_j = \frac{P_j}{\ell} \left\{ c_{j_o} - c_{j_\ell} \exp \left[\frac{-v_j(p_o - p_\ell)}{RT} \right] \right\} \quad (5.72)$$

Because the term $-v_j(p_o - p_\ell)/RT$ is small, the exponential term in Equation (5.72) is close to 1, and so this equation can then be written as:

$$J_j = \frac{P_j}{\ell} (c_{j_o} - c_{j_\ell}) \quad (5.73)$$

or:

$$J_j = B(c_{j_o} - c_{j_\ell}) \quad (5.74)$$

where B is usually called the *salt permeability constant* and has the value:

$$B = \frac{P_j}{\ell} \quad (5.75)$$

Predictions of salt and water transport can be made from this application of the solution–diffusion model to reverse osmosis (first derived by Merten

and coworkers) [16,17]. According to Equation (5.71), the water flux through a reverse osmosis membrane remains small up to the osmotic pressure of the salt solution and then increases with applied pressure, whereas according to Equation (5.74), the salt flux is essentially independent of pressure. Some experimental results in good agreement with the model are shown in Figure 5.14. Also shown in this figure is a term

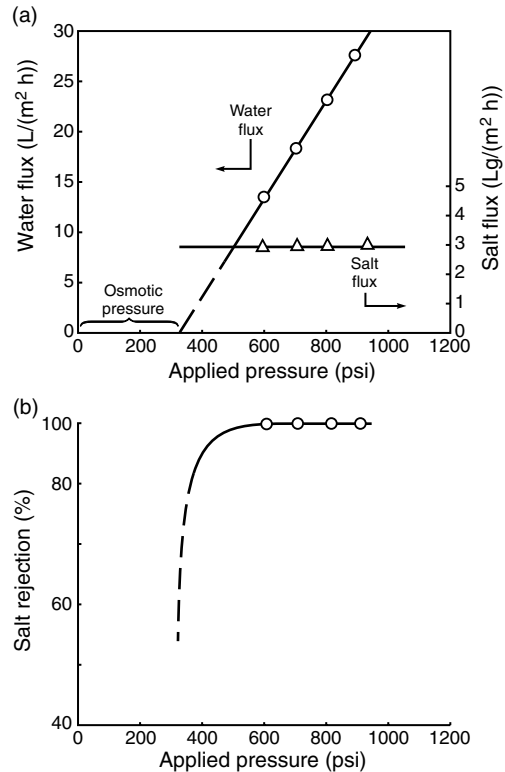


Figure 5.14 (a) Flux and (b) rejection data for a model seawater solution (3.5 % sodium chloride) in a ‘good-quality’ reverse osmosis membrane (FilmTec Corporation, FT30 membrane) as a function of pressure [12]. The water flux, in accordance with Equation (5.71), increases with pressure and, at zero flux, meets the pressure axis at the osmotic pressure of seawater (at ca. 350 psi). The salt flux, in accordance with Equation (5.74), is essentially constant and independent of pressure [18]. Reprinted from *Journal of Membrane Science*, **107**, J. G. Wijmans, and R. W. Baker, ‘The solution–diffusion model: A Review’, pp. 1–21, Copyright (1995), with permission from Elsevier. J.G Wijmans and R.W. Baker, ‘The Solution-Diffusion Model: A Review,’ *J. Memb. Sci.* **107**, 1–21 (1995)

called the rejection coefficient \mathfrak{R} , which is defined as:

$$\mathfrak{R} = \left(1 - \frac{c_{j_i}}{c_{j_o}}\right) \times 100\% \quad (5.76)$$

The rejection coefficient is a measure of the ability of the membrane to separate salt from the feed solution. For a perfectly selective membrane, the permeate salt concentration $c_{j_i} = 0$ and $\mathfrak{R} = 100\%$. For a completely unselective membrane, the permeate salt concentration is the same as the feed salt concentration $c_{j_i} = c_{j_o}$ and $\mathfrak{R} = 0$. The rejection coefficient increases with applied pressure, as shown in Figure 5.14, because the water flux increases with pressure, but the salt flux does not.

5.5.2 Gas Separation

5.5.2.1 Membrane Selectivity

The flux of components i and j through dense polymer membranes is governed by the expression derived earlier (Equation (5.37)):

$$J_i = \frac{D_i K_i^G (p_{i_o} - p_{i_i})}{\ell} \quad (5.77)$$

where J_i is the flux of component i ($\text{g}/(\text{cm}^2 \text{s})$), p_{i_o} and p_{i_i} are the partial pressures of component i on either side of the membrane, ℓ is the membrane thickness, D_i is the permeate diffusion coefficient and K_i^G is the Henry's law sorption coefficient ($\text{g}/(\text{cm}^3 \text{ cmHg})$). An analogous equation to Equation (5.77) can be written for component j . In gas permeation, it is much easier to measure the volume flux through the membrane than the mass flux. The molar flux j_i can be linked to the volume flux J_i by the expression:

$$j_i = J_i \frac{v_i^G}{m_i} \quad (5.78)$$

where v_i^G is the molar volume of gas i ($\text{cm}^3(\text{STP})/\text{mol}$). Similarly, the mass permeability unit P_i^G , defined in Equation (5.38), can be linked to the molar gas permeability \mathcal{P}_i^G , usually in the units ($\text{cm}^3(\text{STP})\text{cm}/(\text{cm}^2 \text{ s cmHg})$), as:

$$\mathcal{P}_i^G = \frac{P_i^G v_i^G}{m_i} \quad (5.79)$$

Equation (5.77) can then be written as:

$$j_i = \frac{\mathcal{P}_i^G (p_{i_o} - p_{i_i})}{\ell} \quad (5.80)$$

Likewise, for component j :

$$j_j = \frac{\mathcal{P}_j^G (p_{j_o} - p_{j_i})}{\ell} \quad (5.81)$$

where j_i is the volume (molar) flux expressed as ($\text{cm}^3(\text{STP})$ of component i)/($\text{cm}^2 \text{ s}$).

The measure of the ability of a membrane to separate two gases i and j is the ratio of their permeabilities, called the membrane selectivity $\alpha_{i/j}$

$$\alpha_{i/j} = \frac{\mathcal{P}_i^G}{\mathcal{P}_j^G} \quad (5.82)$$

The permeability, \mathcal{P}_i^G , can be expressed as the product of two terms. One, the diffusion coefficient, D_i , reflects the mobility of the individual molecules in the membrane material; the other, the gas sorption coefficient, K_i^G , reflects the number of molecules dissolved in the membrane material. Thus, Equation (5.82) can also be written as:

$$\alpha_{i/j} = \left(\frac{D_i}{D_j}\right) \left(\frac{K_i^G}{K_j^G}\right) \quad (5.83)$$

The ratio D_i/D_j is the ratio of the diffusion coefficients of the two gases and can be viewed as the mobility selectivity, reflecting the different sizes of the two molecules. The ratio K_i^G/K_j^G is the ratio of the sorption coefficients of the two gases and can be viewed as the sorption or solubility selectivity, reflecting the relative condensabilities of the two gases. In all polymer materials, the diffusion coefficient decreases with increasing molecular size, because large molecules interact with more segments of the polymer chain than do small molecules. Hence, the mobility selectivity always favors the passage of small molecules over large ones. On the other hand, the sorption of permeants in a polymer increases with increasing condensability. Since condensability usually increases with molecular size, this means that the sorption selectivity generally favors the passage of large molecules over small ones.

The balance between mobility selectivity and sorption selectivity in Equation (5.83) depends on the nature of the polymer. In general, the selectivity of polymers at temperatures below their glass transition temperature is dominated by the mobility selectivity term. Polymers at temperatures above the glass transition temperature are more affected by the sorption selectivity term. This type of structure/property relationship is discussed in Chapter 1 and in other literature sources [18–20].

The selectivity of membrane materials for a gas pair is often reported as the ratio of the permeabilities of the individual pure gases. This practice usually predicts higher selectivity than observed with gas mixtures, especially when one permeant is sufficiently sorbed by the membrane material to plasticize the membrane. The gas mixture selectivity may then be a fraction of the selectivity calculated from pure gas measurements. Pure gas selectivities are more commonly reported than gas mixture data because they are easier to measure. However, neglecting the difference between pure gas and mixed gas values has led a number of workers to seriously overestimate the ability of a membrane to separate a target gas mixture.

5.5.2.2 Importance of Pressure Ratio Limits in Gas Separations

In the section on separation of liquid mixtures by hyperfiltration (Section 5.5.1), the separation achieved was shown to be a function of the intrinsic selectivity of the membrane and the pressure difference across the membrane. These same two factors affect the separation of gas mixtures. In gas separations, the effect of pressure is usually characterized by the pressure ratio across the membrane, that is, the ratio of feed to permeate pressure, p_o/p_ℓ . The importance of the pressure ratio can be illustrated by considering the separation of a gas mixture with component mole fractions (mol/mol), n_{i_o} and n_{j_o} , at a feed pressure p_o . A component flow across the membrane can only occur if the partial pressure of component i on the feed side of the membrane, $n_{i_o}p_o$, is greater than the partial pressure of component i on the permeate side of the membrane, $n_{i_\ell}p_\ell$. That is:

$$n_{i_o} p_o > n_{i_\ell} p_\ell \tag{5.84}$$

It follows that the maximum enrichment achieved by the membrane can be expressed as:

$$\frac{n_{i_\ell}}{n_{i_o}} \leq \frac{p_o}{p_\ell} \tag{5.85}$$

This means that the separation achieved can never exceed the pressure ratio p_o/p_ℓ (usually called ϕ), no matter how selective the membrane. An analytical solution linking the membrane selectivity, $\alpha_{i/j}$, and pressure ratio, ϕ , can be derived for a two-component gas mixture starting from the molar flux equations (Equations (5.84) and (5.85)). This derivation is described elsewhere [21] and has the form:

$$n_{i_\ell} = \frac{\phi}{2} \left[n_{i_o} + \frac{1}{\phi} + \frac{1}{\alpha_{i/j} - 1} - \sqrt{\left(n_{i_o} + \frac{1}{\phi} + \frac{1}{\alpha_{i/j} - 1} \right)^2 - \frac{4 \alpha_{i/j} n_{i_o}}{(\alpha_{i/j} - 1) \phi}} \right] \tag{5.86}$$

This long expression breaks down to two limiting cases depending on the relative magnitudes of ϕ and $\alpha_{i/j}$. First, if the membrane selectivity is very much larger than the pressure ratio, that is:

$$\alpha_{i/j} \gg \phi \tag{5.87}$$

then Equation (5.86) becomes:

$$n_{i_\ell} = n_{i_o} \phi \tag{5.88}$$

This is called the *pressure-ratio-limited region*, in which performance is determined only by the pressure ratio across the membrane and is independent of the membrane selectivity. If the membrane selectivity α is very much smaller than the pressure ratio ϕ , that is:

$$\alpha_{i/j} \ll \phi \tag{5.89}$$

then Equation (5.86) becomes:

$$n_{i_\ell} = \frac{\alpha_{i/j} n_{i_o}}{1 - n_{i_o} (1 - \alpha_{i/j})} \tag{5.90}$$

This is called the *membrane-selectivity-controlled region*, in which the membrane performance is determined only by the membrane selectivity and is independent of the pressure ratio. In the intermediate region between these limiting

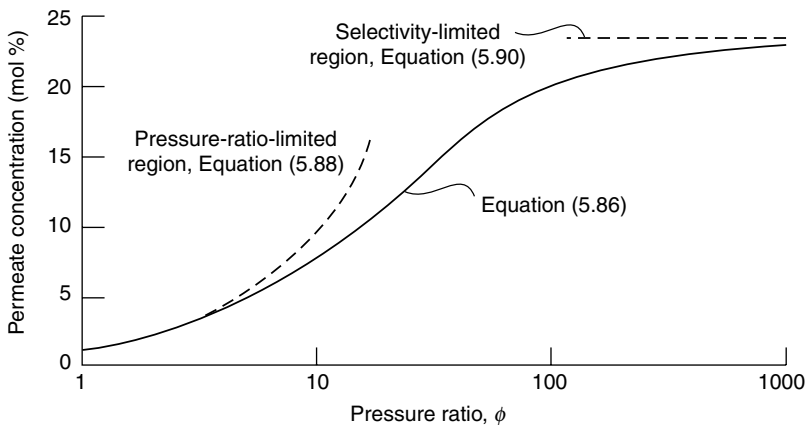


Figure 5.15 Calculated permeate concentrations of the ‘more permeable’ components, i , as a function of pressure ratio (membrane selectivity, $\alpha_{ij} = 30$). The concentration of i in the feed is 1%. Below pressure ratios of ca. 10, separation is limited by the pressure ratio across the membrane, while at pressure ratios above ca. 100, separation is limited by the membrane selectivity

cases, both the pressure ratio and the membrane selectivity affect the membrane system performance. The three regions are illustrated in Figure 5.15 for a sample separation. The calculated permeate concentration (n_i) is plotted against pressure ratio (ϕ) for a membrane with a selectivity of 30. At a pressure ratio of one, that is, feed pressure equals permeate pressure, no separation is achieved by the membrane. As the difference between the feed and permeate pressure increases, the concentration of the more permeable component in the permeate gas begins to increase, first according to Equation (5.88) and then, when the pressure ratio and membrane selectivity are comparable, according to Equation (5.86). When the pressure ratio is four to five times higher than the membrane selectivity, the concentration enters the membrane-selectivity-controlled region. In this region the permeate concentration reaches the limiting value given by Equation (5.90).

The relationship between pressure ratio and selectivity is important because there is usually a practical upper limit on the pressure ratio. Compressing the feed gases to very high pressure or drawing a very hard vacuum on the permeate side can achieve large pressure ratios and optimum separation, but requires large amounts of energy and expensive pumps. Consequently, pressure ratios in industrial applications are in the range of 5 to 20.

Because attainable pressure ratios are limited, the benefit of very highly selective membranes is often less than might be expected. For example, as shown in Figure 5.16, if the pressure ratio is 20, increasing the membrane selectivity from 10 to 20 significantly improves system performance. However, increasing the selectivity from 20 to 40 produces a much smaller incremental improvement. Increases in selectivity above 100 produce negligible improvements. A selectivity of 100 is five times the pressure ratio of 20, and the system is in the pressure-ratio-limited region.

The significance of pressure ratio when choosing the best membrane for a particular separation should not be ignored. For example, given the choice between two hydrogen-selective membranes with equal hydrogen permeances, one with a hydrogen/methane selectivity of 100 and the other with a selectivity of 20, many researchers would automatically choose the more selective membrane for any hydrogen/methane separation application. The process modeling results given in Figure 5.17 show that this is not always the correct choice.

Figure 5.17 shows three membrane units arranged in series to remove hydrogen from a 70% hydrogen/30% methane feed gas. Two types of membrane are used: (a) a high-selectivity membrane with a selectivity $\alpha_{\text{H}_2/\text{CH}_4}$ of 100, and (b) a low-selectivity membrane with $\alpha_{\text{H}_2/\text{CH}_4}$ of 20. The feed gas is at 50 bar, the permeate gas

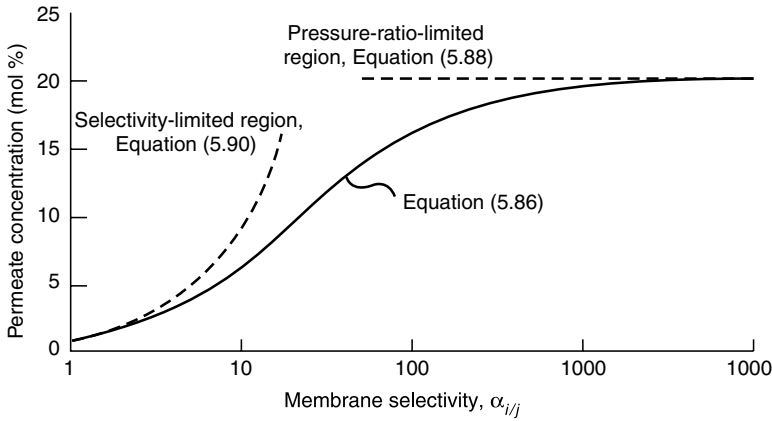


Figure 5.16 Calculated permeate concentration as a function of selectivity, α_{ij} . The feed concentration of component i is 1 %, while the pressure ratio is fixed at 20. Below a selectivity of ca. 10, separation is limited by the low membrane selectivity, while at selectivities above ca. 100, separation is limited by the low-pressure ratio across the membrane

at 10 bar and so the pressure ratio is 5. The hydrogen permeance for both membranes is $100 \times 10^{-6} \text{ cm}^3(\text{STP})/(\text{cm}^2 \text{ s cmHg})$ (100 gpu). The three membrane units are sized to produce the same separation. The first membrane unit

reduces the hydrogen concentration from 70 to 30 %, the second from 30 to 10 %, and the third from 10 to 1 %. The membrane area needed in each step has been calculated by using a differential element computer simulation.

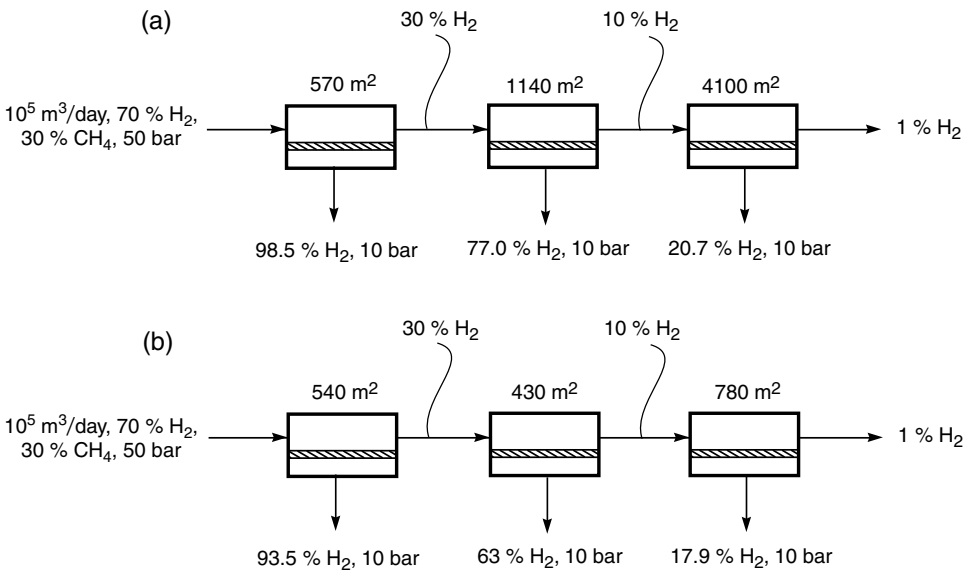


Figure 5.17 The effect of membrane selectivity on separation performance in pressure-ratio-limited separations for (a) high-selectivity (100 gpu H_2 ; 1 gpu CH_4 ; $\alpha_{\text{H}_2/\text{CH}_4} = 100$) and (b) low-selectivity (100 gpu H_2 ; 5 gpu CH_4 ; $\alpha_{\text{H}_2/\text{CH}_4} = 20$) membranes, where both membranes have equal permeances for the more permeable gas (hydrogen). At high-feed-gas concentrations (first step), the highly selective membrane is preferred, while at low-feed-gas concentrations the less selective membrane is preferred (almost equivalent separation and a membrane area of 1/5). This 'odd' result is due to the low feed-to-permeate pressure ratio

In the first membrane step, the membrane area required to lower the concentration of hydrogen in the feed from 70 to 30 % is almost the same for both the high- and low-selectivity membranes. However, the more selective membrane produces a significantly better quality permeate gas containing only 1.5 % methane (compared to 6.5 % methane for the less selective membrane) and so would be preferred. This separation step is governed by the hydrogen/methane selectivity and hydrogen permeance of the membrane. Although the pressure ratio is only five, the feed gas hydrogen concentration (n_{i_o}) is sufficiently high that even if the permeate hydrogen concentration (n_{i_ℓ}) were to reach its maximum value of 100 % hydrogen, the separation would not be pressure-ratio-controlled. That is:

$$\frac{n_{i_\ell}}{n_{i_o}} < \frac{p_o}{p_\ell} \quad (5.91)$$

and so this separation step is controlled by the membrane selectivity, and not the pressure ratio.

In the second membrane unit, the feed gas hydrogen concentration is reduced from 30 to 10 %. At the residue end of the unit, the membrane is operating in the pressure-ratio-limited region. No matter how selective the membrane, the permeate gas hydrogen concentration is controlled by Equation (5.88) and cannot exceed 50 % hydrogen at the residue end of the second membrane unit. Put another way, at this end of the second module at least half of the gas permeating the module must be methane. Because the methane permeance is much lower than the hydrogen permeance, it is methane permeation that determines the membrane area required to perform the separation at this end of the module. For this intermediate separation, the more selective, lower methane permeance, membrane still produces a better quality permeate but requires more than twice the membrane area to achieve the same hydrogen level in the residue stream.

The final membrane unit reduces the hydrogen concentration of the feed gas from 10 to 1 %. Since the pressure ratio is only 5, this membrane unit is well into the pressure-ratio-limited region and Equation (5.88) applies. Consequently, the hydrogen concentrations in the permeate gases are almost equal at 20 % hydrogen for both the high- and low-selectivity membranes. However, this also means 80 % of the permeate gas must be methane. Since methane has a much lower per-

meance than hydrogen, the membrane area required to perform the separation is determined by the membrane's methane permeance and not its hydrogen permeance. The less selective membrane has a five-fold higher methane permeance, and so requires only one-fifth of the membrane area. For this type of separation, the low selectivity high methane permeance membrane is preferred.

5.5.3 Pervaporation

Pervaporation of a two-component mixture is best described by the permeation equations:

$$J_i = \frac{P_i^G(p_{i_o} - p_{i_\ell})}{\ell} \quad (5.92)$$

and:

$$J_j = \frac{P_j^G(p_{j_o} - p_{j_\ell})}{\ell} \quad (5.93)$$

In these equations, the fluxes J_i and J_j are weight fluxes ($\text{g}/(\text{cm}^2 \text{ s})$); similarly, the permeability coefficient P_i^G and P_j^G are weight-based ($(\text{g cm}/(\text{cm}^2 \text{ s cmHg}))$). To allow easy comparison to gas permeation, Equations (5.92) and (5.93) are more conveniently written in molar terms, in which case they can be combined to give:

$$\frac{j_i}{j_j} = \frac{\mathcal{P}_i^G(p_{i_o} - p_{i_\ell})}{\mathcal{P}_j^G(p_{j_o} - p_{j_\ell})} \quad (5.94)$$

where j_i and j_j are molar fluxes with units of $\text{mol}/(\text{cm}^2 \text{ s})$ or $(\text{cm}^3(\text{STP})/(\text{cm}^2 \text{ s}))$ and \mathcal{P}_i^G and \mathcal{P}_j^G are molar permeabilities with units of $(\text{mol cm})/(\text{cm}^2 \text{ s unit pressure})$, or more conventionally, $(\text{cm}^3(\text{STP cm})/(\text{cm}^2 \text{ s cmHg}))$. The ratio of the molar permeability coefficients $\mathcal{P}_i^G/\mathcal{P}_j^G$ is then the conventional gas membrane selectivity, $\alpha_{i/j}$ (cf. Equation (5.82)).

Expressing pervaporation fluxes in terms of permeabilities and selectivities using Equations (5.92)–(5.94) is by far the best method of reporting pervaporation data because these quantities are independent of operating conditions [22]. However, to report data in this way requires a knowledge of the partial vapor pressures of components i and j at the conditions of the feed liquid. In the past, this was troublesome because vapor pressures had to be extrapolated from tabulated values or laboriously calculated using an equation of state. Nowadays, these numbers can be obtained with good reliability from commercial computer process simulation packages (ChemCAD, HySys and the like).

Having said this, the bulk of the pervaporation literature continues to report membrane performance in terms of the total flux through the membrane and a separation factor. The separation factor, β_{pervap} is defined, for a two-component fluid, as the ratio of the two components on the permeate side of the membrane divided by the ratio of the two components on the feed side of the membrane. The term β_{pervap} can be written in several ways:

$$\beta_{\text{pervap}} = \frac{c_{i_e}/c_{j_e}}{c_{i_o}/c_{j_o}} = \frac{n_{i_e}/n_{j_e}}{n_{i_o}/n_{j_o}} = \frac{p_{i_e}/p_{j_e}}{n_{i_o}/n_{j_o}} \quad (5.95)$$

where c_i and c_j are the concentrations, n_i and n_j are mole fractions and p_i and p_j are vapor pressures of the two components i and j .

The separation factor can be linked to membrane selectivity, $\alpha_{i/j}$, by rewriting Equation (5.94) in the form:

$$\frac{j_i}{j_j} = \alpha_{i/j} \frac{(p_{i_o} - p_{i_e})}{(p_{j_o} - p_{j_e})} \quad (5.96)$$

In the permeate, the molar proportions of i and j determine the partial pressures of i and j .

That is:

$$\frac{j_i}{j_j} = \frac{p_{i_e}}{p_{j_e}} \quad (5.97)$$

Substituting the partial pressure ratio of Equation (5.97) into Equation (5.96) and combining the result with the partial pressure expression of β_{pervap} from Equation (5.95):

$$\beta_{\text{pervap}} = \frac{p_{i_e}/p_{j_e}}{n_{i_o}/n_{j_o}} \quad (5.98)$$

then yields:

$$\beta_{\text{pervap}} = \frac{\alpha_{i/j}(p_{i_o} - p_{i_e})}{(p_{j_o} - p_{j_e})} \left(\frac{n_{j_o}}{n_{i_o}} \right) \quad (5.99)$$

In Equation (5.99), $\alpha_{i/j}$ is the contribution of the membrane to the separation factor while the other terms are the contributions of the membranes' operating conditions. By reporting pervaporation data in terms of selectivities and membrane permeances rather than separation factors, these operating condition terms are eliminated.

The advantage of reporting permeation data in terms of the intrinsic properties of the membrane is illustrated by the results shown in Table 5.1.

Table 5.1 Selected pervaporation data for dehydration of ethanol. The original data were all reported as fluxes and separation factors. Results have been translated to permeabilities and selectivities by using Equations (5.92) and (5.93).

Membrane	Thickness (μm)	Feed water Concentration (wt%)	Flux ($\text{g}/(\text{m}^2 \text{ h})$)	Separation factor (β_{pervap})	Water permeability, $P_{\text{H}_2\text{O}}$ (10^3 barrer) ^a	Selectivity, $\alpha_{\text{H}_2\text{O}/\text{EtOH}}$
<i>Chitosan</i>	10	10	18	102	5.2	120
<i>Cyanoethyl</i>	10	10	16	166	4.6	210
<i>(CECS)</i> ^b	30	10	30	301	27.2	400
	10	10	121	110	34.5	130
<i>Nafion C_a⁺</i> ^c	90	22	180	10.4	194	17
<i>Nafion K⁺</i> ^c	90	22	264	8.4	266	14
<i>SO₄²⁻ anion</i> ^d	140	3	80	70	102	69
<i>OH⁻ anion</i> ^d	140	7	380	53	277	53
<i>SCN⁻ anion</i> ^d	140	15	470	38	227	51
<i>Cl⁻ anion</i> ^d	140	20	830	27	350	41
<i>Cellulose triacetate</i> ^d	140	13	920	14	107	18
<i>Perfluoro</i>	30	20	800	69	51	105
<i>grafts</i> ^e	52	20	2800	56	303	83
	80	20	2000	250	351	380

^a1 barrer = $1 \times 10^{-10} \text{ cm}^3 \text{ (STP) cm}/(\text{cm}^2 \text{ s cmHg})$.

^bLee *et al.* [23], 25 °C.

^cCabasso and Lin [24], 29 °C.

^dWenzlaff *et al.* [25], 60 °C.

^eNiemöller *et al.* [26], 70 °C.

This table shows four different sets of pervaporation data for the separation of water from ethanol [23–26]. The data were obtained with different feed solutions at very different temperatures; as a consequence, membrane fluxes and separation factors vary over a wide range. When converted to permeabilities, however, the data are much more tightly grouped, and it is much easier to compare the properties of one membrane to another.

The expression for the pervaporation separation factor β_{pervap} (Equation (5.95)) is often divided into two terms, β_{evap} and β_{mem} . These terms are illustrated in Figure 5.18, in which the pervaporation process is divided into two steps. The first step is evaporation of the feed liquid to form a saturated

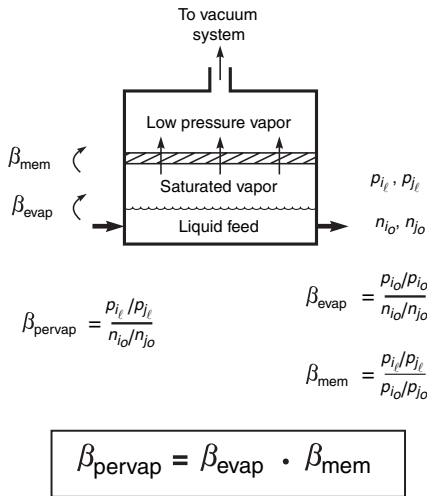


Figure 5.18 Pervaporation represented as a hypothetical two-step process of evaporation, followed by vapor permeation [12]. Reprinted from *Journal of Membrane Science*, 79, J. G. Wijmans and R. W. Baker, 'A simple predictive treatment of the permeation processes in pervaporation', pp. 101–113, Copyright (1993), with permission from Elsevier

vapor in contact with the membrane; the second step is diffusion of this vapor through the membrane to the low-pressure permeate side, as in gas permeation. This two-step description is only a conceptual representation; in pervaporation no vapor phase actually contacts the membrane surface. Nonetheless the representation of Figure 5.18 is thermodynamically completely equivalent to the actual pervaporation process.

The first step is evaporation from the feed liquid to form a saturated vapor phase in equilibrium with the liquid. This step produces a separation because of the different volatilities of the components of the feed liquid. The separation can be defined as β_{evap} , the ratio of the component concentrations in the feed vapor to their concentrations in the feed liquid:

$$\beta_{\text{evap}} = \frac{p_{i0}/p_{j0}}{n_{i0}/n_{j0}} \quad (5.100)$$

The second step is permeation of the vapors i and j through the membrane; this step is equivalent to conventional gas separation. The driving force for permeation is the difference in the vapor pressures of the components in the feed and permeate vapors. The separation achieved in this step, denoted by β_{mem} , can be defined as the ratio of the components in the permeate vapor to the ratio of the components in the feed vapor:

$$\beta_{\text{mem}} = \frac{p_{i\ell}/p_{j\ell}}{p_{i0}/p_{j0}} \quad (5.101)$$

It follows that the separation achieved in pervaporation is equal to the product of the separation achieved by evaporation of the liquid and the separation achieved by selective permeation through the membrane.³

$$\beta_{\text{pervap}} = \beta_{\text{evap}} \beta_{\text{mem}} \quad (5.102)$$

or by substituting Equation (5.100) into Equation (5.99):

$$\beta_{\text{pervap}} = \frac{\beta_{\text{evap}} \alpha_{i/j} (p_{i0} - p_{i\ell})}{(p_{j0} - p_{j\ell}) (p_{i0}/p_{j0})} \quad (5.103)$$

³Figure 5.18 illustrates the concept of permeation from a saturated vapor phase in equilibrium with the feed liquid as a tool to obtain Equation (5.102). A number of workers have compared vapor permeation and pervaporation separations experimentally and have generally shown that permeation from the liquid is faster and less selective than permeation from the equilibrium vapor. This is an experimental artifact. In vapor permeation experiments, the vapor in contact with the membrane is never completely saturated. This means that the activities of the feed components in vapor permeation experiments are less than their activities in pervaporation experiments. Because sorption by the membrane in this range is extremely sensitive to activity, the vapor permeation fluxes are lower than pervaporation fluxes.

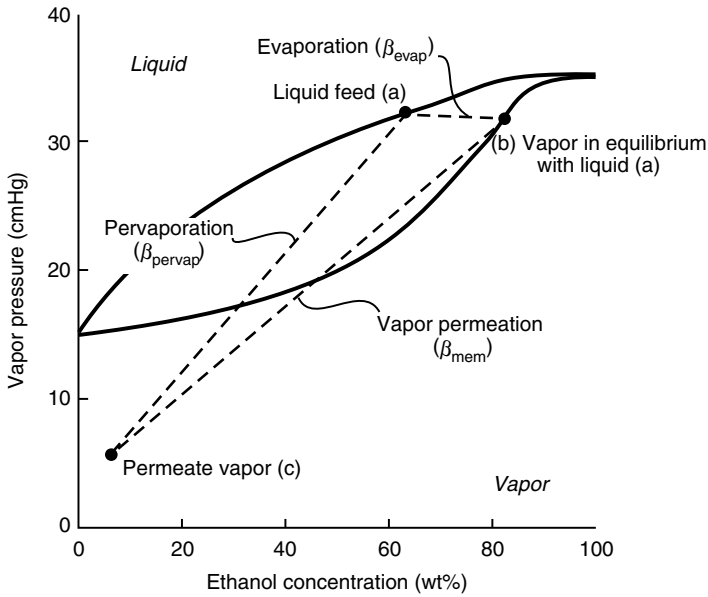


Figure 5.19 Graphical representation of the pervaporation process as direct pervaporation (liquid (a) to vapor (c)) or as a combination of evaporation (liquid (a) to equilibrium vapor (b)) followed by membrane permeation (high-pressure vapor (b) to low-pressure vapor (c)). Representation is based on separation of water from an ethanol/water mixture

and therefore:

$$\beta_{\text{mem}} = \frac{\alpha_{i/j}(p_{i_o} - p_{i_i})}{(p_{j_o} - p_{j_i})(p_{i_o}/p_{j_o})} \quad (5.104)$$

The process shown in Figure 5.18 and described in Equation (5.102) is illustrated graphically in Figure 5.19 for separation of water from an ethanol/water mixture, using a membrane that selectively permeates water. This is the largest industrial application of pervaporation. The pervaporation process can be represented as the change from liquid (a) (60 wt% ethanol) to permeate vapor (c) (~5 wt% ethanol at 5 cmHg). This separation is represented by Equations (5.102) and (5.103). The alternative representation is evaporation of liquid (a) to vapor (b) at the same vapor pressure (represented by Equation (5.100)), followed by permeation of the vapor mixture (b) (at 30 cmHg) to produce permeate vapor (c) (at 5 cmHg), represented by Equations (5.101) and (5.104).

Equation (5.103) has a similar form to Equation (5.86), describing permeation of a two-component mixture through a gas separation

membrane. As with the gas separation expression, Equation (5.103) contains terms proportional to the membrane selectivity and the pressure ratio across the membrane. In addition, as with the gas separation equation, there are two limiting cases in which one of the two factors dominates the separation achieved. The first limiting case is when the membrane selectivity is very large when compared to the vapor pressure ratio between the feed liquid and the permeate vapor:

$$\alpha_{\text{mem}} \gg \frac{p_o}{p_l} \quad (5.105)$$

This means that because the membrane is much more permeable to component *i* than component *j*, the vapor pressure of component *i* in the permeate will equal the vapor pressure of *i* in the feed. That is:

$$p_{i_l} \rightarrow p_{i_o}, \quad \text{if } p_l \leq p_{i_o} \quad (5.106)$$

Equation (5.106), combined with Equation (5.101), then gives:

$$\beta_{\text{mem}} = \frac{p_{j_o}}{p_{j_i}} \quad (5.107)$$

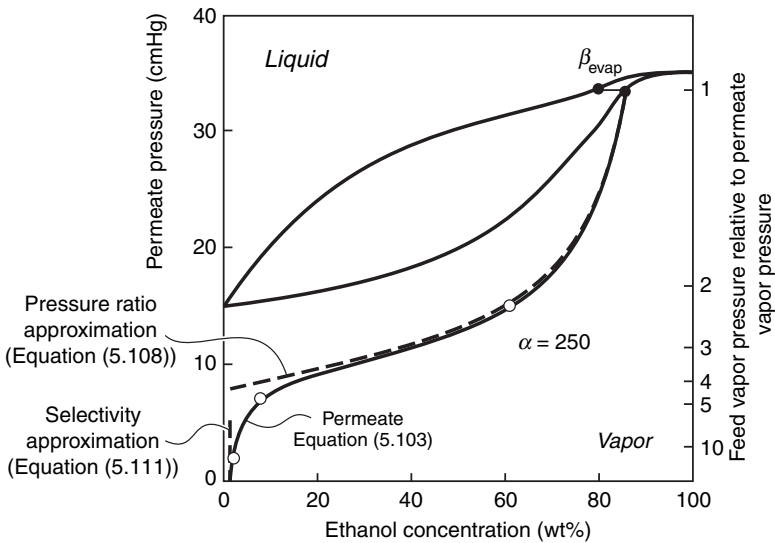


Figure 5.20 The effect of permeate pressure on the separation of ethanol/water mixtures with a poly(vinyl alcohol) membrane. The feed solution contains 20 wt% water and 80 wt% ethanol. The continuous line drawn through the experimental data points is calculated from Equation (5.103)

which, combined with Equation (5.103), leads to the limiting case:

$$\beta_{\text{pervap}} = \beta_{\text{evap}} \frac{p_{j_o}}{p_{j_i}}, \quad \text{when } \alpha_{\text{mem}} \gg \frac{p_o}{p_\ell} \quad (5.108)$$

Similarly, in the case of a very large membrane selectivity in favor of component *j*:

$$\beta_{\text{pervap}} = \beta_{\text{evap}} \left(\frac{p_{i_o}}{p_{i_i}} \right) \quad (5.109)$$

For the special case in which component *i* is the minor component in the feed liquid, p_{j_o} approaches p_o , p_{j_i} approaches p_ℓ and Equation (5.108) reverts to:

$$\beta_{\text{pervap}} = \beta_{\text{evap}} \frac{p_o}{p_\ell} \quad (5.110)$$

where p_o/p_ℓ is the feed-to-permeate ratio of the total vapor pressures.

The second limiting case occurs when the vapor pressure ratio is very large when compared to the membrane selectivity. This means that the permeate partial pressure is smaller than the feed

partial vapor pressures, and p_{i_ℓ} and $p_{j_\ell} \rightarrow 0$. Equation (5.103) then becomes:

$$\beta_{\text{pervap}} = \beta_{\text{evap}} \alpha_{\text{mem}}, \quad \text{when } \alpha_{\text{mem}} \ll \left(\frac{p_o}{p_\ell} \right) \quad (5.111)$$

The relationship between the three separation factors, β_{pervap} , β_{evap} and β_{mem} , is illustrated in Figure 5.20. This type of plot was introduced by Thompson and coworkers [13,27] to illustrate the effect of permeate pressure on pervaporation separation and is a convenient method to represent the pervaporation process graphically. When the permeate pressure, p_ℓ ($p_{i_\ell} + p_{j_\ell}$), approaches the feed vapor pressure, p_o ($p_{i_o} + p_{j_o}$), the vapor pressure ratio across the membrane shown on the right-hand axis of the figure approaches unity. The composition of the permeate vapor then approaches the composition obtained by simple evaporation of the feed liquid, shown by the point at which β_{pervap} equals β_{evap} . As the permeate pressure is decreased to below the feed vapor pressure, the vapor pressure ratio increases. The overall separation obtained, β_{pervap} , is then the product of the separation due to evaporation of the feed liquid, β_{evap} , and the separation due to permeation through the membrane, β_{mem} . The line labeled “permeate” in

Figure 5.20 can be calculated from Equation (5.103). Two limiting cases are also shown in this figure. The first limiting case, when the membrane selectivity α_{mem} is much larger than the pressure ratio p_o/p_t , is calculated from Equation (5.108). The second limiting case, for the region in which the membrane selectivity is much smaller than the pressure ratio, is calculated from Equation (5.110). Figure 5.20 is the pervaporation equivalent of Figures 5.15 and 5.16 for gas separation, discussed earlier.

The example shown in Figure 5.20 includes experimental data from GFT, now owned by Sulzer, which show the effect of permeate pressure on the pervaporation separation of an 80 wt% aqueous ethanol solution using a highly selective poly(vinyl alcohol) membrane. The line obtained from Equation (5.103) passes through all the data points when the water/ethanol membrane selectivity (α) is assumed to be 250. Although this membrane is very selective, a good separation between the feed solution and the permeate vapor is only achieved at low permeate pressures, when a high vapor pressure ratio exists across the membrane and the high intrinsic selectivity of the GFT membrane is utilized. In practical applications of this membrane, the feed solution is heated to about 120 °C (raising the feed vapor pressure to 2 to 4 atmospheres), and the permeate vapor is condensed at –10 to –20 °C (lowering the vapor permeate pressure to about 1 cmHg). This combination achieves the vapor pressure ratio of more than 200 required for a good separation.

5.6 Conclusions and Future Directions

The solution–diffusion model as described above has been the basis for the theory of permeation in dense membranes for more than 30 years. The model is popular because the same model and set of assumptions can be used to describe permeation in a variety of seemingly different processes. This unity was illustrated in Figures 5.10 and 5.11 and the equations used to draw these graphs. The basis of the model is straightforward and mathematically simple to apply. The resulting transport equations are easy to use because the contributions of diffusion and sorption are conveniently combined into one permeability coefficient and the permeant concentrations in the membrane are not explicitly included in the equations (although they are implicitly included via the

sorption coefficient). This inherent simplicity derives from our use of Fick’s Law for diffusion, Equation (5.13). However, Fick’s Law in the strictest sense is only valid for a two-component system comprised of a membrane and one diffusing component. In addition, in highly permeant swollen membranes, a ‘frame-of-reference correction’ is needed because the difference in velocity between the stationary membrane material and the permeating components is not accounted for. Fortunately for all of us, the deviations from Fick’s Law are minor when the permeant concentrations in the membrane are small and the equations presented in this paper are applicable to the majority of membrane applications without major error.

The application of Fick’s Law to the diffusion part of the solution–diffusion model has to be re-examined, however, when the membrane is highly swollen by the permeants. The frame-of-reference correction to Fick’s Law, described in papers by Paul [28,29] and Kamaruddin and Koros [30], can be applied, but this does not extend the description to more than two components and a membrane separation problem has a minimum of three components: the membrane material and at least two permeants which are being separated. An alternative approach is to replace Fick’s Law in the solution–diffusion model by the Maxwell–Stefan diffusive transport equation. This equation is based on the relative velocities of the components of the system to one another. The frame-of-reference problem is then ‘sidestepped’. A very readable introduction to the Maxwell–Stefan equation and its application to membrane processes is given in the book by Wessling and Krishna [31]. A recent paper by Paul [32] discusses the use of the Maxwell–Stefan equation for organic hyperfiltration processes.

One drawback of the Maxwell–Stefan equation is that the concentrations of all permeants in the membrane material are required to calculate the permeant fluxes. This significantly reduces the practical value of the transport equations. Most readers are also likely to find the Maxwell–Stefan approach very heavy going. It is doubtful if the advantage of Maxwell–Stefan formalism will ever persuade the average membrane researcher to switch from the relative simplicity of Fick’s Law. Nonetheless, the Maxwell–Stefan approach has its supporters, particularly for use in fundamental investigations of membrane transport behavior. In conclu-

sion, we believe the simple solution–diffusion model is likely to continue to be the main description of membrane permeation for the foreseeable future. In the longer term, improvements in molecular dynamic simulation techniques may one day produce an alternative method of describing membrane permeation. Fick's law will then finally be abandoned for direct calculation of the movement of individual permeating molecules.

References

- [1] E. Smit, M. H. V. Mulder, C. A. Smolders, H. Karrenbeld, J. van Eerden and D. Feil, 'Modeling of the diffusion of carbon dioxide in polyimide matrices by computer simulation', *J. Membr. Sci.*, **73**, 247 (1992).
- [2] J. R. Fried, M. Sadat, A. Khavi and J. E. Mark, 'Molecular simulation of gas permeability of poly (2,6-dimethyl-1,4-phenylene oxide)', *J. Membr. Sci.*, **149**, 115 (1998).
- [3] J. M. Haile, *Molecular Dynamics Simulation*, John Wiley & Sons, Inc., New York NY, USA (1992).
- [4] D. R. Paul, 'Diffusive transport in swollen polymer membranes', in H. B. Hopfenberg (Ed.), *Permeability of Plastic Films and Coatings*, Pergamon, New York, NY, USA, pp. 35–48 (1974).
- [5] D. R. Paul, 'The solution–diffusion model for swollen membranes', *Separation and Purification Meth.*, **5**(1), 33–50 (1976).
- [6] S. Rosenbaum and O. Cotton, 'Steady-state distribution of water in cellulose acetate membranes', *J. Polym. Sci.*, **7**, 101 (1969).
- [7] S. N. Kim and K. Kammermeyer, 'Actual concentration profiles in membrane permeation', *Seprn Sci.*, **5**, 679 (1970).
- [8] A. Mauro, 'Some properties of ionic and non-ionic semipermeable membranes', *Circulation*, **21**, 845 (1960).
- [9] D. R. Paul and J. D. Paciotti, 'Driving force for hydraulic and pervaporation transport in homogeneous membranes', *J. Polym. Sci. Part B: Polym. Phys. Ed.*, **13**, 1201 (1975).
- [10] J. G. Wijmans, 'The role of permeant molar volume in the solution–diffusion model transport equations', *J. Membr. Sci.*, **237**, 39 (2004).
- [11] T. Kataoka, T. Tsuru, S.-I. Nakao and S. Kimura, 'Permeation equations developed for prediction of membrane performance in pervaporation, vapor permeation and reverse osmosis based on the solution–diffusion model', *J. Chem. Eng. Jpn.*, **24**, 326 (1991).
- [12] J. G. Wijmans and R. W. Baker, 'A simple predictive treatment of the permeation processes in pervaporation', *J. Membr. Sci.*, **79**, 101 (1993).
- [13] F. W. Greenlaw, W. D. Prince, R. A. Shelden and E. V. Thompson, 'The effect of diffusive permeation rates by upstream and downstream pressures', *J. Membr. Sci.*, **2**, 141 (1977).
- [14] N. Bhole, R. M. Gould, S. M. Jacob, P. O. Staffield, D. McNally, P. H. Smiley and C. R. Wildemuth, 'New membrane process debottle-necks solvent dewaxing unit', *Oil Gas J.*, **97**, 67 (1999).
- [15] L. S. White and A. R. Nitsch, 'Solvent recovery from lube oil filtrates with polyimide membranes', *J. Membr. Sci.*, **179**, 267 (2000).
- [16] H. K. Lonsdale, U. Merten and R. L. Riley, 'Transport properties of cellulose acetate osmotic membranes', *J. Appl. Polym. Sci.*, **9**, 1341 (1965).
- [17] U. Merten, 'Transport Properties of Osmotic Membranes', in U. Merten (Ed.), *Desalination by Reverse Osmosis*, MIT Press, Cambridge, MA, USA, pp. 15–54 (1966).
- [18] S. A. Stern, 'Polymers for gas separation: the next decade', *J. Membr. Sci.*, **94**, (1994).
- [19] D. R. Paul and Y. P. Yampolski (Eds), *Polymeric Gas Separation Membranes*, CRC Press, Boca Raton, FL, USA (1994).
- [20] B. D. Freeman and I. Pinnau, 'Polymeric Materials for Gas Separations', in B. D. Freeman and I. Pinnau (Eds.), *Polymer Membranes for Gas and Vapor Separation*, ACS Symposium Series 733, American Chemical Society, Washington, DC, USA pp. 1–27 (1999).
- [21] K. V. Pienemann, J. M. Mohr and R. W. Baker, 'The separation of organic vapors from air', in N. N. Li (Ed.), *Recent Advances in Separations III*, AIChE Symposium Series 250, Vol. 82, AIChE Press, New York, NY, USA, pp. 19–26.
- [22] J. G. Wijmans, 'Letter to the Editor', *J. Membr. Sci.*, **220**, 1 (2003).
- [23] Y. M. Lee, E. M. Shin and S. T. Noh, 'Pervaporation separation of ethanol–water through modified chitosan', *Macromol. Chem.*, **192**, 169 (1991).
- [24] I. Cabasso and Z.-Z. Lin, 'The permselectivity of ion-exchanging membranes for non-electrolyte liquid mixtures', *J. Membr. Sci.*, **24**, 101 (1985).
- [25] A. Wenzlaff, K. W. Boddeker and K. Hattenbach, 'Pervaporation of water–ethanol through ion exchange membranes', *J. Membr. Sci.*, **22**, 333 (1985).
- [26] A. Niemöller, H. Scholz, B. Gotz and G. Ellinghorst, 'Radiation-grafted membranes for pervaporation of ethanol/water mixtures', *J. Membr. Sci.*, **36**, 385 (1988).
- [27] R. A. Shelden and E. V. Thompson, 'Dependence of diffusive permeation rates on upstream and downstream pressures', *J. Membr. Sci.*, **4**, 115 (1978).
- [28] D. R. Paul, 'Relation between hydraulic permeation and diffusion in homogenous swollen membranes', *J. Polym. Sci. Part B: Polym. Phys. Ed.*, **11**, 289 (1973).

- [29] D. R. Paul, 'Further comments on the relation between hydraulic permeation and diffusion', *J. Polym. Sci. Part B: Polym. Phys. Ed.*, **12**, 1221 (1974).
- [30] H. D. Kamaruddin and W. J. Koros, 'Some observations about the application of fick's first law for membrane separation of multicomponent mixtures', *J. Membr. Sci.*, **135**, 147 (1997).
- [31] J. A. Wesselingh and R. Krishna, *Mass Transfer in Multi-Component Mixtures*, Delft University Press, Delft, The Netherlands (2000) (<http://www.library.tudelft.nl/dnp>).
- [32] D. R. Paul, 'Reformulation of the solution–diffusion theory of reverse osmosis', *J. Membr. Sci.*, **241**, 371 (2004).

Positron Annihilation Lifetime Spectroscopy and Other Methods for Free Volume Evaluation in Polymers*

Yuri Yampolskii and Victor Shantarovich

The softest things in the world overcome the hardest things in the world. Non-being penetrates that in which there is no space.

Lao-tsu (604-531 BC)

There is plenty of room at the bottom.

Richard Feynman

6.1 Introduction

Free volume is an extremely important characteristic of polymer materials which influences their numerous properties, such as viscosity, diffusivity and permeability and, to some extent, the parameters of sorption thermodynamics and mechanical behavior. However, in contrast to other properties of polymers, free volume can be regarded as a complex physical object within polymers that can be characterized by size and size distribution of microcavities or free volume element (FVEs)¹ that form it, by topology and architecture of its nanostructure. Initially, free volume was merely regarded as a theoretical concept that could explain many aspects of polymer behavior but could not be determined directly. Later, much attention was drawn to the problem of experimental evaluation of free volume in polymers. Attempts to characterize free

volume resulted in development of various methods that are often united by the term 'probe methods'. A common feature of these methods is that probes of different nature and size (atoms or molecules) are introduced into a polymer and observation of their behavior, which is sensitive to free volume, makes it possible to deduce some information on nano-structure of free volume.

Table 6.1 gives a survey of various probe methods. The probes differ by their size and shape, whereas the methods are based on different principles of observation of behavior of the probes in polymers. The smallest probe is used in the positron annihilation lifetime spectroscopy (PALS): in this method, information on free volume is provided by the lifetimes of o-positronium (o-Ps) atoms, that is, hydrogen-like electron-positron pairs (e^-e^+) having the size of about 1 Å. Much larger probe molecules are used in the methods of electrochromic, photochromic and spin probes and in inverse gas chromatography: their size can be as large as 10–20 Å. In these methods, the relative dimensions of the probes and microcavities where they reside determine the behavior of the probes in polymer materials. Thus, different parameters which characterize the probes dissolved in polymers can shed light on free volumes

*See Appendix for the acronyms used to define the various polymers identified in this chapter

¹In the literature, several synonyms are accepted to describe elementary free volumes, e.g. microcavities, holes, voids, FVEs, etc.

Table 6.1 Methods used for probing free volumes in polymers

Method	Probe	Size	Information
Positron annihilation lifetime spectroscopy	o-Ps	1.06 Å	Size, size distribution, concentration of the FVE and dependence of the size of the FVE on temperature and pressure
Inverse gas chromatography	Organic vapors	> 5 Å (> C ₃)	Temperature-averaged mean size of the FVE
¹²⁹ Xe NMR	¹²⁹ Xe	ca. 4 Å	Size of the FVE and its temperature-dependence
Spin probe method	2,2,6,6-tetra-methylpyperidine-1-oxyl (TEMPO) and other stable nitroxyl radicals	> 100 Å ³	Information on the part of the size distribution of the free volume which corresponds to larger holes; temperature-dependence of larger hole sizes
Photochromic probe method	Stilbene and azobenzene derivatives	120–600 Å ³	
Electrochromic probe method	Azo-dyes	> 800 Å ³	

in such polymers. For example, in inverse gas chromatography, vapor retention characteristics and thermodynamic parameters deduced from them depend on the relative size of solute molecules and microcavities. A peculiarity of the PALS and ¹²⁹Xe NMR methods is small (atomic) probes having a certain size are used. These are capable of sampling holes of different sizes in polymers. All other probe methods employ series of probes with varying sizes: by observing the behavior of smaller and larger probes, conclusions on the hole size of a polymer can be made.

In this chapter, we will focus on information regarding free volume that can be obtained via probe methods. The most detailed information has been accumulated by the PALS method and so this will be considered in the most systematic way. On the other hand, the significance of the results of other probe methods should not be underestimated. Application of various methods, based on different principles and using probes with different sizes, gives one assurance that their combined applications provide a physically meaningful representation of free volume in polymers.

6.2 Free Volume: Definitions and Effects on the Transport Parameters

Originally, the concept of free volume was introduced in relation to the liquid state [1,2] and then transferred to polymers [3,4]. According to Frenkel, the thermal movement of molecules in the liquid

phase is impossible without random fluctuation of the local density. Molecules in liquids perform irregular oscillations around their equilibrium positions. The average “local” lifetime, τ , of a molecule coincides with the mean fluctuation time of the potential field in its closest neighborhood: with the frequency, $1/\tau$, molecules are shifted to the distance close to molecular size. In liquids with low viscosities (e.g. liquid Ar), this lifetime (or duration of the existence of the FVE in liquids) has the order of 10^{-11} s. The lifetime τ increases with the viscosity of the liquid. The same concept holds for rubbery polymers; however, here kinetic segments play the role of individual molecules in low-molecular-mass liquid compounds. As the size of the kinetic segments is relatively large, the lifetimes τ in rubbers should be much longer. In glassy polymers, where all of the segmental mobility is frozen, the lifetimes τ become infinitely long, and so FVEs should be viewed as areas with reduced local density imbedded in the frozen matrix.

The simplest assumption that can be made regarding free volume is based on its representation as the difference between the total or specific volumes of polymers (V_{sp}), which can be defined as the reciprocal density and occupied volume:

$$V_f = V_{sp} - V_{occ} \quad (6.1)$$

For application of this equation, there should be ways to calculate V_{occ} . An approach to find the occupied volume of polymers was proposed by

Bondi [5], who suggested calculation of the van der Waals volume (V_w) of repeat units of polymers by using the tabulated increments in V_w for smaller groups and postulated that $V_{occ} = 1.3V_w$. This method is very simple and so became popular for finding the 'Bondi' free volume or fractional free volume (FFV) = V_f/V_{sp} and for drawing various correlations between the transport parameters (D and P values) with V_f and FFV. By using the found values of FFVs, polymers can be arranged in series, in accordance with their gas permeabilities.

For several reasons, such an approach seems to be unsatisfactory and can serve only for very rough estimates:

- (1) The assumption of a unified packing density factor of 1.3 for all polymers appears to be quite unrealistic. Note that this was postulated by Bondi on the basis of the packing densities of molecular crystals (low-molecular-mass organic compounds) at 0 K and, strictly speaking, its applicability to polymer systems has never been proven.
- (2) Common values the FFV are 10–20 %; for some polymers, they can be as large as 30 %, or even more. All of these values are in stark contradiction with the results of other, more sophisticated methods of study of free volume, including computer modeling. On the other hand, there are examples when V_f , estimated as the difference (Equation (6.1)), has negative, meaningless values.
- (3) The additive scheme of computing V_w of repeat units ignores peculiarities of the conformations of polymers.
- (4) For various groups of polymers, one can find either rather good correlations of the P and D parameters with the FFV, or extremely poor ones with no obvious explanation. As a possible reason for such behavior, one can note that the free volume defined in such a manner is a property of a polymer, while the permeation rates of different gases in polymers should be sensitive to different parts of the free-volume size distribution.

All of this justifies a development of other methods for estimation of free volume. It should be noted that in glassy polymers physically different components of the free volume can be separated: static and dynamic free volume, with the

latter enabling vibrations of small structural elements of the polymer; free volume, accessible and inaccessible to probes of different sizes. This problem is considered in more details in Chapters 2 and 3 of this volume.

6.3 Positron Annihilation Lifetime Spectroscopy

The PALS method provides information on the size and size distribution of free volume elements, their concentrations and the effects on free volume of such factors as temperature, pressure, mechanical deformation and polymer phase composition [6,7]. It is sensitive to free volume changes during polymer aging and those due to swelling, crosslinking and gas sorption. The parameters of PAL spectra related to free volume strongly depend on the chemical structure of polymers and are fairly well reproducible for different samples of the same polymer and between the data measured by various laboratories [8].

The PALS method is based on the measurement of positron lifetimes in a material. Having entered a polymer, positrons can exist as free positrons, e^+ , and as the form of a bound state – hydrogen-like positronium atoms (Ps or e^-e^+ pairs). Its singlet state, p-Ps, having anti-parallel spins, is short-lived (lifetime, 0.125 ns), whereas the triplet state (o-Ps) has a lifetime of 142 ns in vacuum. It is assumed that the o-Ps is trapped in regions with reduced electron densities or in the FVE [9–11]. As a result of overlapping of the wave functions of o-Ps and electrons from 'the walls' of the microcavities, the lifetimes of trapped positronium atoms become much shorter and are usually in the range 1.5–4.0 ns. These lifetimes depend on the size of these holes – the larger the hole, then the longer are the lifetimes. It is also assumed that the intensity of the positronium component of the lifetime spectrum is related to the hole number density (concentration).

Various e^+ -active isotopes can be used as positron sources; however, the most convenient is the application of ^{22}Na which has a half-life of 2.6 years. In the experimental setups, the source of e^+ is sandwiched by two layers of polymers (a plate, a stack of films or even powder) which have a thickness sufficient for total annihilation of the positrons within the sample (usually about 1 mm). Lifetimes are measured by an electronic coincidence circuit as the

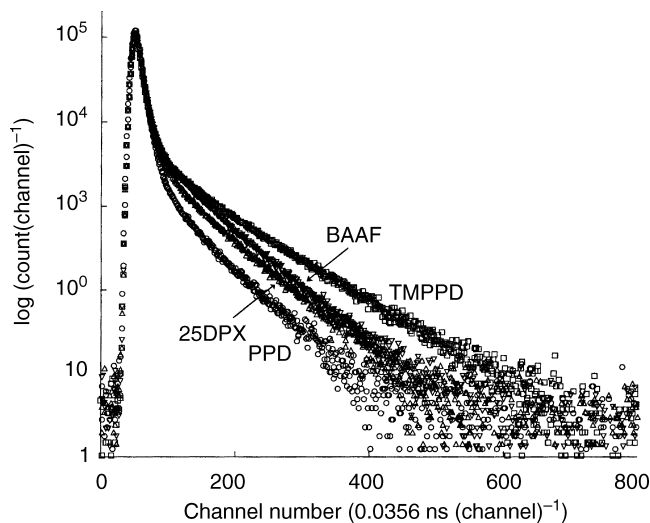


Figure 6.1 Typical experimental positron annihilation lifetime spectrum (according to Shimazu *et al.* [12]). From 'Permeability, permselectivity and penetrant-induced plasticization of fluorinated polyimides studied by positron lifetime measurements', A. Shimazu, T. Miyazaki, S. Katayama and Y. Ito, *J. Polym. Sci. Part B: Polym. Phys. Ed.*, **41**, 308–318, Copyright © 2003, John Wiley & Sons, Inc. Reprinted with permission of John Wiley & Sons, Inc.

difference in time span between the two events, registered by emitted γ -quanta: creation of positrons by radioactive decay of ^{22}Na and their annihilation within the material. After the circuit has registered 10^5 – 10^7 of such events, the experimental distribution curve is obtained, which shows the number of events with the lifetime within a certain range (Figure 6.1).

The primary experimental curves, $y(t)$, can be interpreted within the framework of finite-term or continuous analysis. In the former case, the $y(t)$ curve is described by the sum of several exponential terms, $I_i \lambda_i \exp(-\lambda_i t)$, including the annihilation rate $\lambda_i (= 1/\tau_i \text{ (ns}^{-1}\text{)})$ and intensities I_i (%), with the number of terms n being defined independently. Traditionally it was assumed that $n=3$, although, as we will see later, in many cases $n > 3$. The shortest lifetime τ_1 (about 0.2 ns) is due to the annihilation of p-Ps and e^+ , the intermediate lifetime τ_2 (about 0.3–0.5 ns) is due mainly to free positrons and finally, the long-lived lifetime(s) τ_i ($i=3$ or 4) are due to o-Ps localized in holes. The primary data in the finite-term approximation are processed by using different computer programs, e.g. PATFIT [13]. In the continuous analysis, the CONTIN program [14,15], based on the inverse Laplace transformation, is used. Another method of con-

tinuous analysis of the PAL spectra, i.e. the maximum entropy lifetime method (MELT) [16], has attracted recently much attention. The advantages of these programs is that they give continuous lifetime (and hole size) distribution curves and, in addition, the number of components of the lifetime spectrum is established automatically. The lifetimes τ_i , ($i=3$ or 4) depend on the size of the FVE and thus can be used to characterize the free volume.

A semi-empirical equation was proposed [10,11] to relate the ortho-positronium lifetimes τ_3 to the average radius R_i of the spherical FVE:

$$\tau_3 = 1/2[1 - (R_i/R_o) + (1/2\pi)\sin(2\pi R_i/R_o)]^{-1} \quad (6.2)$$

where τ_3 is the positronium lifetime (a similar equation is used in the case of several o-Ps lifetimes) and, $R_o = R + \Delta R$ (the adjustable parameter $\Delta R = 1.66 \text{ \AA}$). Assuming that all the microcavities have a spherical geometry and knowing R_i , it is possible to determine the average volume of a single microcavity (in the finite-term analysis), $v_f = (4\pi/3)R_i^3$ or to obtain the size distribution of these microcavities in a polymer by continuous analysis. Note that assumption of the spherical symmetry of free

Table 6.2 Sizes of free volume elements in glassy polymers

Polymer	P(O ₂) (barrer)	R_{3s} (Å)	v_{f3s} (Å) ³	R_4 (Å)	v_{f4} (Å) ³	Reference
'Vectra' copolyester	0.0005	2.1	39	—	—	20
PMMA	0.09	2.6	74	—	—	21
PS	2.9	2.9	102	—	—	23
PC	1.6	2.94	106	—	—	22
<i>Polyimides</i>						
6FDA-ODA	2.4	3.19	136	—	—	24
6FDA-BAHF	14.2	3.62	198	—	—	
PVTMS	44	3.21	138	4.35	345	25
PTMSS	56	2.71	83	3.74	219	25
PPrSiDPA	230	3.83	235	6.38	1088	25
AF2400	1140	2.68	81	5.95	882	25
PTMSP	7700	3.41	166	6.81	1323	25

volume elements, which seems to be plausible in liquids, is doubtful in polymers. It can be supposed that they have cylindrical, ellipsoidal or other geometries. Different geometries of microcavities can be realized in different polymers, as computer modeling studies have indicated [17]. Recently, novel equations have been proposed to calculate the radii and lengths of cylindrical microcavities [18,19] However, most results obtained by the PALS technique for polymers are interpreted from an approximation of spherical geometry of the FVE.

Table 6.2 shows the variation in the hole volume in glassy polymers, sequenced in order of increasing gas permeability. In barrier polymers (Vectra copolyester is an example), the size of the FVE is the smallest. For polymers with larger permeabilities, the o-Ps lifetimes and the hole volumes increase. It has been conclusively shown (see Jean *et al.* [22]) that in conventional glassy polymers the size distribution of the FVE is monomodal (one o-Ps component in the PAL spectra) and can be represented by Gaussian peaks in the CONTIN analysis. However, starting from a certain level of gas permeability better fits in treating the PAL spectra are obtained [25] for two o-Ps lifetimes and, hence a bimodal size distribution of the FVE (Figure 6.2). Thus, for PVTMS the long-lived component is partly unresolved, whereas for polymers with larger permeabilities two o-Ps lifetimes are evident (Figure 6.2). It can also be noted that the maxima of the peaks in the CONTIN lifetime distribution agree well with the results of the PATFIT treatment. Bimodal (or even multimodal) size distributions have been also reported in other studies

of high-permeability polymers and porous polymeric materials [26–32]. It is interesting that the size distribution of the FVE found in the PALS experiments agree well with the results obtained from inverse gas chromatography (see Figure 6.3, which will be discussed in detail in Section 6.5). Extremely wide size distributions were also revealed by atomic modeling of the free volume in some glassy polymers [17].

Thus, the PALS method can give a microscopic description of the free volume in terms of the radii R_i and hole volumes v_f . In order to relate this to the macroscopic behavior of polymers, one has to know the hole number density N (cm⁻³), as the fractional free volume FFV is the product $v_f N$. Several approaches have been proposed for solving this problem.

According to the simplest and earliest assumption [23,33,34], I_3 (%) was assumed to be proportional to N . Then, if the scaling parameter A is known from independent volumetric properties of the polymers, N can be found as $N = AI_3$, (A is about 0.001–0.002 Å in several polymers) and, hence $FFV = AI_3 v_f$. However, more accurate analysis indicates that I_3 depends as well on the probability of formation of an o-Ps and on the rate of trapping of the o-Ps by microcavities and quenching by polar groups (e.g. polar C=O groups in polyimides) [35]. Because of this, several, more sophisticated methods were proposed for determination of N and, via the latter, the FFV in polymers:

- (1) The temperature dependence of τ_3 and the elementary free volume v_f is very similar to common dilatometric curves which characterize the

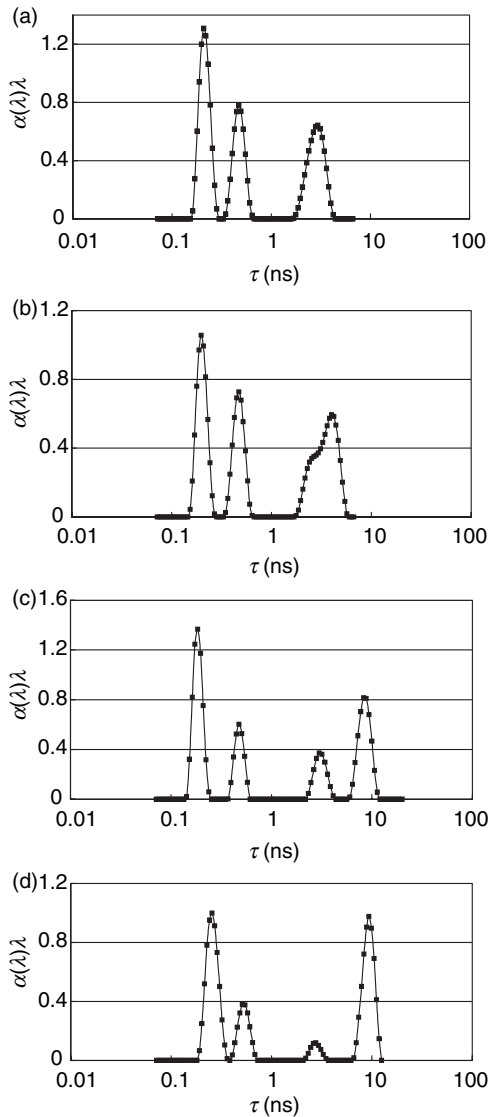


Figure 6.2 CONTIN PAL spectra of various glassy polymers with increasing free volume: (a) PFPDMSS; (b) PVTMS; (c) PPrSIDPA; (d) PTMSP [25]. Reprinted from V. Shantarovich, I. Kevdina, Yu. Yampolskii and A. Alentiev, *Macromolecules*, **33**, 7453–7466 (2000). Copyright (2000) American Chemical Society

expansion of the bulk volume in polymers. However, these dependences have significantly different slopes: the thermal expansion coefficients of the specific volume below and above the T_g (α_g , α_r) have the order of 10^{-4} K^{-1} , whereas the thermal expansion coefficients of holes (α_{h1} , α_{h2}) are

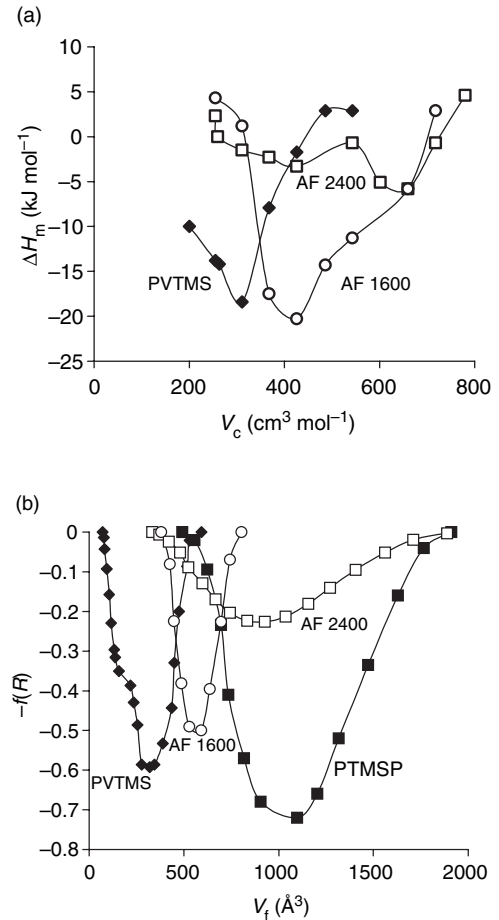


Figure 6.3 Estimation of the size of free volume elements in glassy polymers: (a) partial molar enthalpy of mixing ΔH_m , as a function of critical volume of solvent, V_c , according to IGC; (b) probability density function, $f(R)$, in polymers with different sizes of free volume elements, according to PALS [77]. Reprinted from A. Yu. Alentiev, V. P. Shantarovich, T. C. Mertel, V. I. Bondar, B. D. Freeman and Yu. P. Yampolskii, *Macromolecules*, **35**, 9513–9522 (2002). Copyright (2002) American Chemical Society

one order larger. A natural explanation of this is related to the fact that the former mirrors the thermal expansion of both holes sampled by PALS and more densely packed polymer chains in ‘the walls’ of microcavities. By comparing the temperature dependences of V_{sp} and τ_3 , it is possible to obtain N [36–38]. This approach was extensively used in determination of the hole number density N in various polymers [39–43].

It was shown that the N values reveal a very weak dependence of the chemical structure and in most polymers the concentration of FVE is in the range $2\text{--}7 \times 10^{20} \text{ cm}^{-3}$ at the T_g and should not strongly depend on the temperature.

(2) Another method for the estimation of N is based on measuring the changes in the PAL spectra caused by gas sorption in polymers. When gas is sorbed in glassy polymers, the lifetime τ_3 noticeably decreases and this can be interpreted as an indication that in the presence of a hole-filling gas only smaller holes are accessible by an o-Ps. Assuming different forms of the V_f size distribution (Gaussian, triangular and rectangular), Kirchheim and coworkers [44] found N values that fit the equations which describe these distributions, accounting for the observed pressure dependences, $\tau_3(p)$ and $I_3(p)$. However, N values equal to $2\text{--}4 \times 10^{21} \text{ cm}^{-3}$ found in PC and tetramethyl polycarbonate seem to be too large. Indeed, the fractional free volumes calculated by using them is in the range 30–100 % in these polymers. On the other hand, the volume of the bulk polymer per single hole amounts only to 200 \AA^3 , which corresponds to a cube with edges of 6 \AA , that is, the holes should nearly touch each other at such concentrations. Interestingly, another attempt to calculate the hole number densities N by using sorption data gave more realistic values of about $4 \times 10^{20} \text{ cm}^{-3}$ for three polycarbonates [45].

(3) The third approach for estimation of N is based on a detailed analysis of the kinetics of formation and annihilation of ortho-positrons in polymers. It is assumed that the o-Ps is formed in the polymer matrix from positrons and so-called spur electrons (electrons formed by ionization of molecules in the vicinity of ‘slowing-down’ positrons). The o-Ps atoms can diffuse until they reach the FVE. If the o-Ps succeeds in finding the latter before annihilation, its presence in the polymer is manifested as long-lived components (τ_3, I_3 and τ_4, I_4). In this approximation, only a fraction of positrons, which forms o-Ps, is observed as the long-lived component of the PAL spectrum. Hence I_3 and I_4 should depend not only on the hole number density N but also on the probability of trapping of the o-Ps. The behavior of e^+ and o-Ps can be described [46,47] by a system of kinetic equations, where the relation between the positronium trapping

rate v_i^+ by the i th-type hole and the annihilation rate of the non-localized positronium λ_f^{Ps} (which is likely to be the same as the free positron annihilation rate λ_f^+ , i.e. $\lambda_f^{\text{Ps}} = \lambda_f^+ \equiv \lambda_f$) determines the choice of the precursor for a localized o-Ps:

$$\begin{cases} dP_f^+/dt = -(\lambda_f^+ + v_{\text{form}})P_f^+, & P_f^+(0) = 1 \\ dP_f^{\text{Ps}}/dt = (3/4)v_{\text{form}}P_f^+ - (\lambda_f + \sum_i v_i^+)P_f^{\text{Ps}}, & P_f^{\text{Ps}}(0) = 0 \\ dP_{t,i}^{\text{Ps}} = v_i^+P_f^{\text{Ps}} - \gamma_i P_{t,i}^{\text{Ps}}, & P_{t,i}^{\text{Ps}}(0) = 0 \end{cases} \quad (6.3)$$

with summing up over the numbers of the long-lived components or over the types of holes ($i = 3, 4$, etc.) and also with $P_f^+, P_f^{\text{Ps}}, P_{t,i}^{\text{Ps}}$ standing for the probabilities of finding free positrons, non-localized or trapped positronium atoms, respectively; $\gamma_i = 1/\tau_i$ is the rate of annihilation in the i th-hole (elementary free volume, EFV). For convenience of discussion, we assign the same label i for the lifetime component and for the type of hole in a sample. In the simplest case of three-component analysis of the PAL spectrum, when only the third component is related to o-Ps, $i = 3$, transitions between the EFVs of different types are neglected. The factor $3/4$ in Equation (6.3) appears because we consider the behavior of the long-lived triplet positronium. The intensity of the long-lived component(s) is given by the following:

$$I_i = (3/4)Q \left[v_i^+ / \left(\lambda_f - \gamma_i + \sum_i v_i^+ \right) \right] \quad (6.4)$$

where $Q = v_{\text{form}}/(\lambda_f - \gamma_i + v_{\text{form}}) \approx v_{\text{form}}/(\lambda_f + v_{\text{form}})$ and is a fraction of the positrons forming positronium atoms in a system. In addition, the trapping rate is given by:

$$v_i^+ = 4\pi D^{\text{Ps}} R_i N_i \quad (i = 3, 4, \text{ etc.}) \quad (6.5)$$

where D^{Ps} represents the diffusion coefficient of nonlocalized Ps atoms, R_i is a radius for interaction, which we suppose to be equal to the EFV effective radius, and N_i is the number of trapping centers of a given type.

In order to find N_i , one has to know D^{Ps} independently. Different estimations of this value in polymers are within the range $0.5\text{--}15 \times 10^{-5} \text{ cm}^2 \text{ s}^{-1}$

[21]. The value $D^{\text{Ps}} = 1.3 \times 10^{-5} \text{ cm}^2\text{s}^{-1}$ obtained for polyimides [35] can be considered as the most reliable, because the number density found via this was consistent with the N value determined from the temperature-dependence of τ_i below and above the T_g . It is important to know to what extent the D^{Ps} values vary in different polymers. The size-dependences, $D(d^2)$, of gases (d in the range 2.5–4 Å) indicate that extrapolation to the size of an o-Ps (1 Å) gives the diffusivities of different polymers over a rather narrow range of one order (see Figure 6.5).

Fortunately, rather narrow restrictions can be imposed on the PALS results to obtain 'correct' values of N in glassy polymers. On the one hand, the fractional free volume, $\text{FFV} = v_f N$, should be within one order. The lower limit of this value is given by the iso-free volume concept of Simha and Boyer, according to which the FFV in glassy polymers should be 2.5 % or somewhat larger. This approach is based on the analysis of the viscosity properties of polymers and hence this estimate characterizes only the largest part of the free volume size distribution. An application of Bondi's method for calculation of the FFV accounts for the whole free volume ($V_{\text{sp}} - V_{\text{occ}}$) and therefore it gives the upper limit of the FFV. Calculations using the increments of the van der Waals volume give the FFVs of conventional glassy polymers as being 10–20 % and reach the value of about 30 % only in the case of extra-high-permeability polymers. If we assume that $v_f = 100\text{--}1000 \text{ \AA}$ and $\text{FFV} = 3\text{--}30 \%$, the N values should be in the range from 1×10^{20} to $1 \times 10^{21} \text{ cm}^{-3}$.

Another estimate is possible because the average size of the bulk volume per one FVE (v) should be significantly larger than the mean diameter of the FVE. Assuming that the specific volume is about $1 \text{ cm}^3 \text{ g}^{-1}$ and N is about 10^{20} g^{-1} , we obtain v as $10^4\text{--}10^3 \text{ \AA}$. This corresponds to the edge of a cube of 20–10 Å. Bearing in mind the mean diameter of these holes is 5–13 Å, one concludes that the mean distance between the adjacent holes should be $k = 5\text{--}10 \text{ \AA}$. If this is smaller, the regularities of gas transport in polymers will be similar to that in a medium with open pores, and this is, as a rule, not the case. The value $N > 10^{21} \text{ cm}^{-3}$ seems to be unlikely, because it can result in negative values of k . Note that the found k values are consistent with the diffusion jump lengths in polymers found by using Meares equation for the activation energy

of gas diffusion [48]. So, the most plausible N values should be in the range $10^{20}\text{--}10^{21} \text{ cm}^{-3}$.

Thus, the PALS method enables one to make two fundamental conclusions regarding the free volume in glassy polymers:

- (i) the chemical structure of polymers strongly affects the sizes of the FVEs and the character of their size distributions;
- (ii) the hole number densities of various polymers only weakly depend on their chemical structures and are limited to a rather narrow range of values in different polymers.

In early studies using the PALS method [49], it was already observed that more permeable polymers exhibit longer lifetimes τ_3 , and so attempts were made to correlate the diffusivity of polymers with primary parameters of the PAL spectra, such as $\tau_3, \tau_3^2, \tau_3 I_3$, etc. [7,47,48]. Since according to the Tao–Eldrup model [8,9] positronium lifetimes can be related to the size of the FVE, these results open a possibility to check the free volume models and to apply directly the results of the PALS method for the description of gas transport processes in polymers.

Indeed, correlations of the diffusion coefficients in polymers with the volumes of the microcavities (v_f) have been reported for polyimides [50–52], polycarbonates [22], terephthalate copolymers [53], rubbery polymers [54,55]. An example of such a correlation [51] is shown in Figure 6.4. Similar correlations are observed for permeability coefficients [25,53,56]. At first sight, it seems unexpected that the D and P values in different polymers are determined by only the sizes of the FVEs and, seemingly, do not depend on their concentrations, N . The explanation of this result is, as has been noted earlier, that the N values in different polymers do not differ significantly and therefore $\text{FFV} = v_f N$ is determined predominantly by the volume of the microcavity, v_f . In fact, accounting for the concentrations N that were found by using some of the described methods did not result in significant improvements of the correlations with the transport parameters [22,25,53]. On the other hand, this suggests that other factors should be taken into account, namely the processes that occur in the 'walls' of the FVE [48,51].

Thus, the results obtained so far show that there exists a strong correlation between the PAL distri-

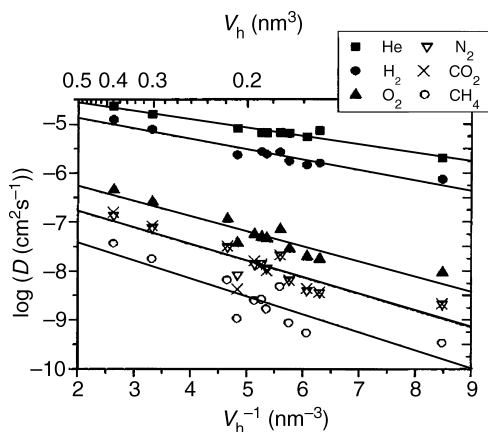


Figure 6.4 Diffusion coefficients of various gases versus reciprocal average hole volume, obtained from positron annihilation measurements [51]. Reprinted from C. Nagel, K. Guenther-Schade, D. Fritsch, T. Strunskus and F. Faupel, *Macromolecules*, **35**, 2071–2077 (2002). Copyright (2002) American Chemical Society

butions and free volumes in glassy polymers and their gas permeabilities and diffusivities. However, another property is of even more importance for membrane materials, i.e. their permselectivities or ideal separation factors, $\alpha_{ij} = P_i/P_j$, where P_i and P_j are the permeability coefficients of gases, M_i and M_j . As the permeability coefficient is the product of the diffusion and solubility coefficients, $P = DS$, the selectivity of solubility, $\alpha_{ij}^S = S_i/S_j$, and the diffusivity, $\alpha_{ij}^D = D_i/D_j$, can be defined. It is known that the permselectivity for light gases in conventional glassy polymers is determined mainly by their diffusion selectivity.

Figure 6.5 illustrates the dependence of the diffusion coefficients in several polymers on the square of the kinetic diameter, d^2 , of the diffusing molecules. It can be seen that the larger the diffusion coefficient in a polymer for a certain gas, then the smaller is the slope of the dependency of D on d^2 . The slopes of these lines determine the diffusion selectivity of a polymer. Thus, the diffusion selectivity of large-free-volume polymers, such as PTMSP and AF2400, is markedly lower than that of conventional glassy polymers such as polycarbonates.

It is interesting to examine this regularity in a more quantitative manner. This is shown in Figure 6.6 for high free volume polymers, as well as some conventional glassy polymers

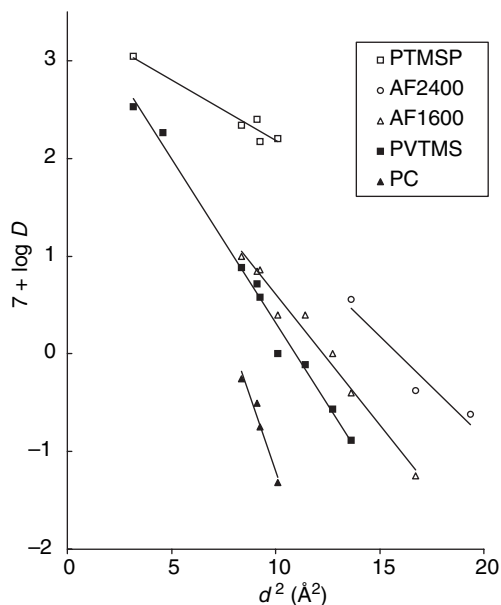


Figure 6.5 Dependence of diffusion coefficients of various gases in polymers as a function of gas kinetic cross-section [25]. Reprinted from V. Shantarovich, I. Kevdina, Yu. Yampolskii and A. Alentiev, *Macromolecules*, **33**, 7453–7466 (2000). Copyright (2000) American Chemical Society

(e.g. polycarbonate and PVTMS) [25]. The parameter a , which is used as a measure of diffusion selectivity, was found by least-squares treatment of the equation $\log D_i = a(d_i)^2 + b$, which describes the dependences shown in Figure 6.5. It is seen that when the size (in \AA^3) of the FVE of glassy polymers increases, the diffusion selectivity monotonically decreases. This dependence is characteristic only for glassy polymers since rubbers, which exhibit relatively small τ_3 values and hence smaller sizes of the FVE, are characterized by much lower diffusion selectivity as the data point for polydimethylsiloxane, which is also shown as an example in Figure 6.6, indicates. Doubtless, this is related to different mechanisms of gas permeation in glassy and rubbery polymers. On the other hand, this result enables an application of PAL spectroscopy for fast assessment of the selectivity of prospective glassy membrane materials, because obtaining the dependencies shown in Figure 6.5 is often a time- and effort-consuming procedure.

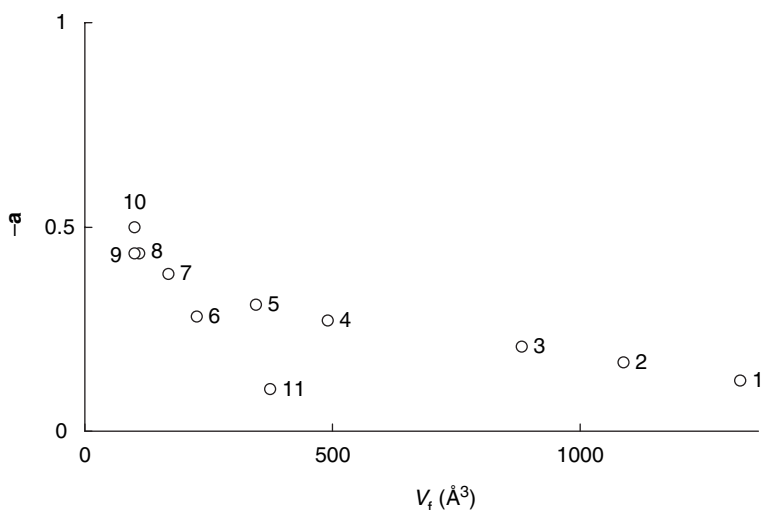


Figure 6.6 Gas diffusion selectivity, α , in various polymers versus size of FVE: (1) PTMSP; (2) PPrSiDPA; (3) AF2400; (4) AF1600; (5) PVTMS; (6) PPhSiDPA; (7) PVPDMS; (8) PS; (9) PC; (10) PSF; (11) PDMS [25]. Reprinted from V. Shantarovich, I. Kevdina, Yu. Yampolskii and A. Alentiev, *Macromolecules*, **33**, 7453–7466 (2000). Copyright (2000) American Chemical Society

6.4 ^{129}Xe NMR Study

The chemical shift of ^{129}Xe nuclei is very sensitive to the local environment of the material, where Xe gas is sorbed. Thus, the size of the FVE associated with gas sorption can be probed. Qualitatively, the larger the FVE, the smaller the chemical shift of ^{129}Xe relative to the gas phase is observed. A Xe atom in an FVE in a polymer is in a low refractive index environment and produces a smaller chemical shift [57].

According to Fraissard and Ito [58], the NMR chemical shift of ^{129}Xe atoms sorbed in a nanoporous medium in the absence of paramagnetic particles or particles that form local electrostatic fields (e.g. cations) can be presented as a sum:

$$\delta_{\Sigma} = \delta_o + \delta_s + \delta_{\text{Xe}/\text{Xe}} \times \rho \quad (6.6)$$

where δ_o is the reference value, δ_s is the value related to the collisions with the wall, $\delta_{\text{Xe}/\text{Xe}}$ is the chemical shift related to collisions of Xe molecules in the gas phase and ρ is the density of the gas phase. Therefore, if the δ_{Σ} value is extrapolated to the zero pressure of Xe gas, the difference $\delta = (\delta_{\Sigma} - \delta_o)$ characterizes only the collision with the walls of the microcavity. An

empirical relationship was proposed [58] based on the data for various zeolites:

$$\delta = 499.1 / (2.054 + \lambda) \quad (6.7)$$

where λ (\AA) is the mean free path of a Xe atom in a microcavity. Depending on the geometry of the microcavity, the λ value can be related to the diameter of a spherical hole (D_{sp}) or a cylindrical hole (D_c) with the length much larger than the diameter:

$$\lambda = (D_{\text{sp}}/2) - 2.2 \quad (6.8)$$

$$\lambda = D_c - 4.4 \quad (6.9)$$

The parameter 2.054 in the denominator of Equation (6.7) is the radius of a Xe atom.

As the chemical shifts of ^{129}Xe have been reported in many polymers, it is possible to calculate the sizes of the FVEs according to this method and compare them with the results of other probe methods (Table 6.3). Both assumptions regarding the geometry of the FVE were considered. Several conclusions can be made from this table.

First, the ^{129}Xe chemical shifts can be regarded as reliable characteristics of a polymer, because independent studies of different samples of the

Table 6.3 Free volume sizes (radii R (Å)) in polymers based on ^{129}Xe NMR and other probe methods

Polymer	δ (ppm)	λ (Å)	^{129}Xe NMR		PALS		IGC
			R_{sp}	R_{c}	R_{sp}	R_{c}	
AF2400	63.3 [59]	5.83	8.04	5.12	5.95 [25]	6.33	6.4 [65]
AF1600	76.7 [59]	4.46	6.66	4.43	4.89 [25]	5.43	5.8 [66]
AD 80X	83.6 [59]	3.92	6.12	4.16	—	—	—
AD 60X	85.3 [59]	3.80	6.00	4.10	—	—	—
PTFE	90 [18]	3.49	5.69	3.94	4.2 [18]	4.9	—
PPO	180 [18]	0.72	2.92	2.56	3.4 [18]	4.2	3.4 [67]
	185 [60]	0.64	2.84	2.52	—	—	—
LDPE	203 [18]	0.40	2.60	2.40	3.3 [18]	4.1	—
	200 [61]	0.44	2.64	2.42	—	—	—
	200 [62]	0.44	2.64	2.42	—	—	—
PC	214 [18]	0.28	2.48	2.34	2.9 [18]	3.8	—
	212 [61]	0.30	2.50	2.35	—	—	—
PS	210 [63]	0.32	2.52	2.36	2.88 [23]	3.76	—
PEMA	203 [62]	0.40	2.60	2.40	3.0 [64]	3.9	—

same polymers resulted in close values of δ . It is also seen that according to the ^{129}Xe NMR method the radii of spherical microcavities in polymers are in the range 2.5–8.0 Å (or 2.3–5.0 Å with the assumption of cylindrical symmetry). For comparison, the ranges of radii determined by means of the PALS method are 2.9–6.0 and 3.8–6.3 Å, respectively. Thus, the results of the two methods are in reasonable agreement. One can also observe correlations of the ^{129}Xe NMR data with other properties of polymers. The AF Teflons, having the highest gas permeabilities and large FFVs reveal the smallest δ values and the largest radii, R_{sp} and R_{c} , according to the ^{129}Xe NMR method.

The accuracy of determination of the hole radii should not be overestimated. On the one hand, an assumption that the FVEs have the shapes of spheres and cylinders with a single diameter is rather ‘rough’, especially for high-free-volume polymers. Thus, it has been shown [17] that the free volume in PTMSP can be represented as a system of interpenetrating pores with widely varying diameters.

Another problem that can affect the accuracy of estimation of free volume size when using the ^{129}Xe NMR method is related to the uncertainty of the van der Waals size of the Xe atom (3.2–4.9 Å, according to different scales). Therefore, depending on the choice of the size of the Xe atom, the radii of the FVE, as determined by the ^{129}Xe NMR method, would be 7.2–8.1 or

4.4–5.3 Å for spherical and cylindrical geometries of the hole, respectively. The recent results from experiments on the incorporation of ^{129}Xe atoms inside the cavity of fullerene C_{60} [68] are in favor of a smaller size for the Xe atom.

Figure 6.7 indicates that the diameter of a spherical microcavity, D_{sp} , as determined by the ^{129}Xe NMR method correlates reasonably well with the permeability coefficients of gases in different polymers. A similar correlation holds for the D_{c} values. A fulfillment of such correlations is consistent with the observation that the concentration of free volume elements is approximately the same in various polymers [25].

It is tempting to obtain the size distributions of free volumes based on chemical shifts in ^{129}Xe NMR measurements. At first sight, this can be carried out for glassy polymers by ascribing certain contributions in the observed δ_{Σ} values responsible for the ‘Langmuir’ and ‘Henry’ sites within a glassy polymer by using the parameters of sorption isotherms [69]. However, such an assessment should take into account the pressure dependent term, $\delta_{\text{Xe}/\text{Xe}}$, in Equation (6.6), which must be determined independently by measuring chemical shifts for gaseous Xe at different pressures.

6.5 Inverse Gas Chromatography

Inverse gas chromatography (IGC) is a method used for investigation of sorption thermodynamics in

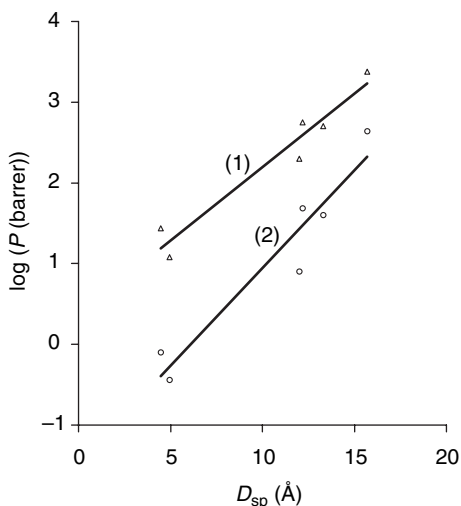


Figure 6.7 Permeability coefficients of (1) hydrogen and (2) methane versus the diameters of microcavities in various polymers (perfluorinated polymers, PS and PC), estimated by using the ^{129}Xe NMR method [59]. Reprinted from *Polymer*, **44**, G. Golemmé, J. B. Nagy, A. Fonseca, C. Algieri and Yu. Yampolskii, ^{129}Xe NMR study of free volume in amorphous perfluorinated polymers: comparison with other methods', pp. 5039–5045, Copyright (2003), with permission from Elsevier

polymers and for determination of their physical parameters [70]. In this method, a polymer is coated on the surface of a porous solid carrier and a solute (in a form of a vapor of a low-molecular-mass organic compound) is injected into the gas-carrier stream. Under fulfillment of certain conditions, the measured retention times enable estimation of numerous physico-chemical parameters of the polymer.

If the retention times, t_r , of a solute is known, it can be related to the net retention volume, V_N , as follows:

$$V_N = (t_r - t_a)J_n^m F_c \left(\frac{273}{T} \right) \quad (6.10)$$

where t_a is the retention time of a 'non-sorbing' component (e.g. air), F_c is the flow rate of the gas carrier, J_n^m is a correction factor for the pressure drop in the column and T is the column temperature (K).

Interpretation of the results of the IGC method depends on the prevailing mechanism of sorption (retention) in the column. Depending on the

diffusion coefficients D of the sorbed molecules in the polymer film, the retention times and volumes can be determined by surface adsorption (small D) or bulk sorption (absorption) when D is large. Intermediate cases are also possible when the absorption equilibrium is not attained in the full volume of the polymer film. For determination of the bulk sorption parameters, the intrinsic times of the diffusion of solutes into the polymer film, $\langle \tau_D \rangle = l^2/D$, where l is the film thickness, must be much larger than $\langle 1/v_s \rangle$, where v_s is the rate of the movement of the injected solute layer in the column. Only provided this condition is fulfilled, the sorption equilibrium is established in the whole volume of the polymer phase. The process of bulk sorption is characterized by the specific retention volume, V_g , defined as:

$$V_g = \frac{V_N}{\omega_L} \quad (6.11)$$

where ω_L is the mass of the polymer in the column. The fulfillment of the aforementioned condition can be proven by the independence of V_g on the flow rate of the gas carrier. In addition, the specific retention volume should be independent of the mass of the polymer in the column, ω_L . Equilibrium is attained more easily the higher the temperature, the smaller the solute molecule and the thinner the polymer film are. On the other hand, at elevated temperatures and with very thin films, the retention times decrease, and so for every solute there is an optimal range of conditions, where the chromatographic experiment is feasible.

The solubility coefficients in the infinite dilution limit, S , are given [71] by:

$$S = V_g \frac{\rho}{p_0} \exp \left[(2B_{11} - V_1) J_n^m \left(\frac{p_0}{RT} \right) \right] \quad (6.12)$$

where p_0 is the standard pressure (1 atm), ρ is the density of the polymer at temperature T and the exponential term accounts for non-ideal gas behavior (B_{11} is the second virial coefficient and V_1 is the solute molar volume). From the temperature-dependence of S , the enthalpy of sorption can be estimated as follows:

$$S = S_o \exp \left(- \frac{\Delta H_s}{RT} \right) \quad (6.13)$$

Vapor dissolution in a polymer may be viewed as a sequence of two steps – penetrant condensa-

tion to a pure liquid state and mixing of the pure liquid with the polymer. Hence, the enthalpy of sorption can be represented as:

$$\Delta H_s = \Delta H_c + \Delta H_m \quad (6.14)$$

where ΔH_c and ΔH_m are the enthalpies of condensation and the partial molar enthalpy of mixing, respectively. The former quantity is a characteristic of the phase transition of a pure solute, while only the latter characterizes the polymer – solute interactions (or polymer structure). ΔH_m can be found as the difference, $\Delta H_s - \Delta H_c$, or from the temperature-dependence of the activity coefficients calculated via specific retention volumes [70].

It has been shown [72–74] that the dependences of the ΔH_m values on the size of the solute are entirely different for sorption in rubbers and in glassy polymers. In rubbers, the enthalpies of mixing are slightly positive or close to zero and hardly change when the size of the solutes is varied, as studies of, e.g. siloxanes [72], silmethylenes [73] and polystyrene above its T_g [74] have shown. On the other hand, in all of the glassy polymers studied by using the IGC method, without a single exception (polysulfone [75], polyvinyltrimethyl silane) [76], poly(phenylene oxide) [67] and amorphous Teflons AF [65,77], the ΔH_m values are strong functions of the solute size. Up until a certain size of the solute molecule, different for different polymers, the ΔH_m values decrease with increasing size of the molecule and assume strongly negative values. After some critical size of the solute is reached, the ΔH_m values pass through a minimum and then start to increase. Upon further growth of the size of the solutes, they reach the values typical for sorption in rubbers, that is, athermal or slightly endothermal mixing is observed. It has been supposed that this critical size corresponds to the mean size of the free volume element, where the prevailing hole-filling mechanism of sorption takes place [78]. Later, it was shown that these minimal values of ΔH_m correlate with the gas permeability and diffusivity of glassy polymers. It was hypothesized that such behavior resulted from the ability of the free volume elements to accommodate most efficiently solute molecules smaller than the intrinsic size of the free volume elements. Minimum intermolecular forces would be overcome to accom-

modate such solutes, and so negative ΔH_m values would be observed. The more similar the size of a sorbed molecule is to that of the FVE, the more restrictions are imposed on the internal degrees of freedom of the molecule sorbed within the FVE. As the ΔH_m values correlate with the partial molar entropies of mixing, ΔS_m [78], this explains the strongly negative values of ΔS_m observed in the vicinity of this minimum. Thus, the IGC method provides information on the sizes of the FVEs and, hence, can be compared with the results from other probe methods.

Figure 6.3(a) shows the effect of critical volume on the excess enthalpy of mixing, ΔH_m , in three polymers, i.e. AF1600, AF2400 and PVTMS. The critical volume was selected as a convenient parameter to characterize the size of the solutes (*n*-alkanes). It can be noted that ΔH_m passes through a minimum for each polymer and the positions of the minima, $V_{c,\min}$, are qualitatively consistent with the gas permeabilities and diffusivities of the polymers being considered. That is, the polymer with the highest $V_{c,\min}$ has the highest diffusivity and permeability and vice versa.

Figure 6.3(b) presents schematically the size distribution of the larger-free-volume elements obtained from CONTIN lifetime distributions. For a more convenient comparison, the ordinate of this figure shows the values $-f(R)$, where $f(R)$ is the probability density function found using CONTIN lifetime distribution. Based on lifetime distributions such as the one shown in Figure 6.2, the corresponding radii and free volume distributions were calculated for approximation of the spherical geometry of the free volume elements, v_f (\AA^3). In order to have a scaling parameter similar to V_c , the volume distribution was plotted versus $v_f = v_f N_A$ ($\text{cm}^3 \text{mol}^{-1}$), where N_A is the Avogadro constant. A comparison of Figures 6.3(a) and 6.3(b) shows a thorough analogy between the results of both methods, as follows:

- (1) The relative positions of the curves in both plots are very similar. According to the two methods, the minimum size of the free volume elements is characteristic for PVTMS and a maximum for AF2400. For AF1600 and PVTMS, the curves $\Delta H_m(V_c)$ pass through maxima for C_6 – C_7 alkanes, whereas the

- maximum for AF2400 occurs at much larger solutes (ca. C₁₀–C₁₁).
- (2) Based on the PALS results in Figure 6.3(b), AF1600 exhibits a much narrower size distribution of the free volume element sizes than AF2400. Presumably the narrower the distribution, then the more drastic will be the segregation of sorbed molecules based on size. In fact, this notion is supported by the IGC-based estimates of ΔH_m : as shown in Figure 6.3(a), the minimum in ΔH_m is much wider in AF2400 than in AF1600.

It should be noted that Figure 6.3(a), strictly speaking, gives only a correlation. The task of the quantitative determination of the free volume size by using the IGC method must depend on a choice of molecular volume of *n*-alkanes, the solutes used by us as probes in free volume determination. Different scales can be employed as measures of the molecular volumes: the van der Waals volume, V_w , the molecular volume in the liquid phase, V_b (at the corresponding boiling point, T_b), and the critical volume, V_c . These are compared in Table 6.4 for the *n*-alkanes in the regions where the dependences, ΔH_m versus V_c , pass through minima for the various polymers being studied. The van der Waals volumes, V_w , were found by using the group contributions tabulated by Van Krevelen [79], while the molecular volumes, V_b , were computed using the Benson formula [80]:

$$V_c/V_b = 0.422 \log p_c + 1.981 \quad (6.15)$$

where p_c is the critical pressure. This equation had been checked for experimental mole densities at T_b for hydrocarbon gases [81]. Finally, the V_c values were taken from the text by Read and Sherwood [82]. As is clear from this table,

these quantities vary significantly and differ from each other; however, the general trends are the same. A comparison with other probe methods (PALS, ¹²⁹Xe NMR) and with the results of computer modeling of the free volume [83] shows that somewhat better agreement is reached when V_b or even V_c are selected as measures of the molecular volume. Indeed, when a molecule of the linear probe (*n*-alkane) accommodates the free volume elements with a postulated spherical geometry, it must take the form of a coiled conformation, and so much excluded volume should be added to the probe's molecular volume. On the other hand, an assumption that the free volume elements in polymers have spherical geometries is rather unlikely, as has been mentioned previously.

When estimating the benefits of the IGC method for investigation free volumes in polymers, it should be noted that it gives only temperature-averaged dimensions of the free volume elements. Indeed, ΔH_m is defined as the slope of the temperature-dependence of the activity coefficients and therefore it characterizes the mean value of the microcavity size over the whole temperature range and is not sensitive to possible temperature-dependences of the free volume sizes. However, temperature-dependent variations of the free volume size according to PALS are well within other uncertainties of free volume determination characteristic of different methods.

Another problem can be related to the aforementioned diffusion limitations in IGC experiments with glassy polymers. So far, the results have been obtained mainly for those polymers with relatively large free volumes and gas permeabilities (e.g. $P(O_2) > 20$ barrer at room temperature). However, less permeable polymers can be studied at elevated temperatures, where these limitations are absent.

Table 6.4 Molecular volumes (\AA^3 per Molecule) and corresponding radii (\AA) of spherical free volume elements; the polymers in the first column indicate the sizes of the probe which correspond to the minimum ΔH_m Values

Alkane	V_w/R	V_b/R	V_c/R
C ₆ (PVTMS)	113/3.0	235/3.8	611/5.3
C ₇ (AF1600)	130/3.1	269/4.0	708/5.5
C ₈	147	316	807
C ₉	164	349	902
C ₁₀	181	394	1000
C ₁₁ (AF2400)	198/3.6	435/4.7	1096/6.4

6.6 Other Probe Methods

In polymers, many processes involving low-molecular-mass compounds are limited by their small-scale movements. The rates of these movements strongly depend on the relationship between the molecular sizes of these compounds (probes) and the free volume elements in the polymers. Hence, observation of these movements for probes of different sizes and in various polymers gives some insight into the sizes and size distributions of the free volumes. A general problem of the methods that will be briefly considered in this section is that the dimensions of the probes used are large relative to the mean sizes of the FVEs in polymers and therefore it is likely that they 'sample' mainly the parts of the size distribution of the free volume which correspond to a small fraction of the larger holes.

6.6.1 Photochromic Probes

This method is based on adopting a hypothesis [84] that monomolecular chemical reactions (and particularly photoisomerization) in the glassy state requires a minimum, critical size of the local free volume in the vicinity of the dissolved probe molecule. In this method, the amount of the probe *cis-trans* photoisomerization in a glassy polymer relative to that in dilute solution in a non-viscous model solvent, where the free volume is not a constraint to isomerization, is measured as a function of the volume required for photoisomerization of the probe. Victor and Torkelson [85] studied the free volume in glassy polystyrene (PS) using various stilbene and azobenzene derivatives as the probes, with van der Waals volumes in the range 127–571 Å³. Photoisomerization requires an additional volume, which is 'swept' by the van der Waals area of a probe molecule during excited-state rearrangement. This volume can be found by using a simple geometrical consideration.

The ratio of the extent of *cis-trans*-photoisomerization of the probes in polystyrene films to that in toluene is shown as a function of the extra volume needed by the probes to photoisomerize in Figure 6.8. The curve shown is the cumulative distribution of local free volumes by an amount equal to the extra volume contributed by the isomerizing half of each probe molecule. It can be seen that more than 90 % of the local free

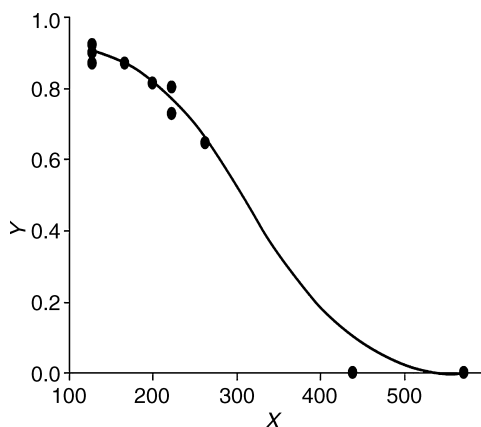


Figure 6.8 Cumulative distribution of local free volume in polystyrene at 25 °C, measured by the photochromic probes & method (X is the probe size in Å³, while the continuous line was drawn by fitting the data from Victor and Torkelson [85]). Reprinted from J. G. Victor and J. M. Torkelson, *Macromolecules*, **20**, 2241–2250 (1987). Copyright (1987) American Chemical Society

volume in PS is larger than 120–130 Å³, none of it is larger than about 400 Å³, and the maximum of the distribution that corresponds to the steepest part of the curve gives a free volume of ca. 270 Å³. An assumption of the spherical symmetry of the free volume elements leads to the radius of about 4 Å, which is somewhat larger than the results of estimation of this value when using other methods but does not differ dramatically from the values of 2.4–3.8 Å presented in Table 6.3. This method also gave interesting information on the changes in free volume in glassy polymers during their physicals aging. It was shown that in the aging of poly(methyl methacrylate) and polystyrene, the larger free volume elements disappear first [86]. On the other hand, in polycarbonates having broader size distributions, both smaller and larger free volume elements disappear due to aging [87].

6.6.2 Electrochromic Probes

The phenomenon of electrochromism involves the effects of an electric field on the absorption spectra of organic molecules. Orientation of light-absorbing molecules in the electric field results in changes in their extinction coefficients.

This effect can be used to monitor the molecular mobility or free volume in polymers [88]. For this purpose, light-absorbing molecules that play the role as probes are sorbed in polymers, and the changes in their absorption spectra induced, first, by the electric field and, secondly, by reorientation after the field was switched off, are monitored. For strong variations of extinction coefficients, molecules with large dipole moments are needed. It was suggested that nitrogen-containing dyes, mainly azo-dyes with van der Waals volumes in the range 770–2900 Å³ could be used as probes [89]. Analysis of the kinetic curves of the changes in optical density allows one to estimate the mean size of the free volume elements where the rotation of the probes takes place, provided that the kinetic curves are obtained for several probes with different sizes. In this treatment, the formalism based on the Cohen–Turnbull model [3] was used.

The method of electrochromic probes has been applied to several glassy polymers – PS, PVTMS and PTMSP [90,91]. This gave the plausible sequence of variation of free volume in these polymers, which correlates with their diffusivities. The estimation of the local free volume size, v_f , in PS was in good agreement with the results obtained from the method of photochromic probes [85]. However the found values of v_f seem to be overstated. Thus, for PTMSP it gave $v_f = 3290 \text{ \AA}^3$, which corresponds to the radius of a spherical microcavity, R , of 9 Å. This is significantly higher than the results from more-refined estimations of these values when using the PALS method and molecular modeling [17]. This leads one to return to the arguments that have been often advanced in analysis of the probe methods using larger probes. Apparently, the local chain packing in the vicinity of such probes is substantially perturbed, and the probe's mobility can only qualitatively characterize the free volume that exists in the polymer before the introduction of the probe molecules.² Nevertheless, these methods have played a particular role in obtaining more insight into and understanding the nature of the free volume in glassy polymers and in finding relationships between

the free volumes and chemical structures of membrane materials.

6.7 Conclusions

Thus, the combined application of different probe methods gives a consistent and comprehensive picture of the free volume in glassy polymers. However, there are a number of problems which cannot be answered by the existing methods. These refer to the topology and architecture of the free volume in polymers, to the typical geometry of the FVE. Presumably, the final word will be made here by using atomistic modeling of polymer nanostructures. On the background of the impressive success of the probe methods achieved during the last decade, it is obvious that we strongly lack experimental approaches for investigation of the nanostructure of the chemical environment in the vicinity of the FVE, that is, the processes that take place in the 'walls' of the microcavities in polymers. One can assume that in these studies computer modeling will also be very useful.

Appendix: List of Polymers

AF2400: random copolymer of 87 mol% 2,2-bis(trifluoromethyl)-4,5-difluoro-1,3-dioxole and 13 mol% tetrafluoroethylene

AF1600: random copolymer of 65 mol% 2,2-bis(trifluoromethyl)-4,5-difluoro-1,3-dioxole and 35 mol% tetrafluoroethylene

6FDA-ODA: dianhydride, 1,1,1,3,3,3-hexafluoro-2,2-bis(3,4-dicarboxy)propane-oxydianiline

6FDA-BAHF: dianhydride, 1,1,1,3,3,3-hexafluoro-2,2-bis(3,4-dicarboxy)propane-1,1,1,3,3,3-hexafluoro-bis(aminophenyl)propane

Hyflon AD80X: random copolymer of 80 mol% 2,2,4-trifluoro-5-trifluoromethoxy-1,3-dioxole and 20 mol% tetrafluoroethylene

Hyflon AD60X: random copolymer of 60 mol% 2,2,4-trifluoro-5-trifluoromethoxy-1,3-dioxole and 40 mol% tetrafluoroethylene

LDPE: low-density polyethylene

PC: bisphenol A polycarbonate

²This also refers to the method of spin probes in which the mobility of stable free nitroxile radicals (the smallest one, TEMPO, has a van der Waals volume of 300–500 Å³) is estimated by variations in their ESR spectra [92,93].

PDMS: polydimethylsiloxane
PEMA: poly(ethyl methacrylate)
PFPMSS: poly(γ -trifluoropropyl dimethylsilyl-styrene)
PMMA: poly(methyl methacrylate)
PTMSS: poly(*p*-trimethylsilyl styrene)
PPO: poly(1,3-dimethyl-2,6-phenylene oxide)
PPhSiDPA: poly[1-phenyl-2-[*p*-(triphenylsilyl)-phenyl]acetylene
PPrSiDPA: poly[1-phenyl-2-[*p*-(triisopropylsilyl)-phenyl]acetylene
PS: polystyrene
PSF: polysulfone
PTFE: polytetrafluoroethylene
PTMSP: poly(trimethylsilyl propyne)
PVPDMS: poly(vinylphenyldimethyl silane)
PVTMS: poly(vinyltrimethyl silane)
Vectra copolyesters: copolymers of *p*-oxybenzoic and 2-oxy-6-naphthoic acids

References

- [1] Ya. I. Frenkel, *Kinetic Theory of Liquids*, Izdatelstvo Acad. Nauk SSSR, Moscow–Leningrad, USSR (1945).
- [2] J. O. Hirschfelder, C. F. Curtiss and R. B. Bird, *Molecular Theory of Gases and Liquids*, J. Wiley, New York (1954).
- [3] M. H. Cohen and D. Turnbull, ‘Molecular transport in liquids and glasses’, *J. Chem. Phys.*, **31**, 1164–1969 (1959).
- [4] J. L. Duda and J. M. Zielinski, ‘Free Volume Theory, in Diffusion in Polymers’, Ed. by P. Neogi, *Marcel Dekker*, New York, 1996, p. 143–171.
- [5] A. Bondi, *Physical Properties of Molecular Crystals, Liquids and Gases*, John Wiley & Sons, Inc., New York, NY, USA (1968).
- [6] D. M. Shrader and Y. C. Jean (Eds), *Positron and Positronium Chemistry*, Elsevier, Amsterdam, The Netherlands (1988).
- [7] A. Hill, ‘Positron annihilation lifetime spectroscopy to probe free-volume effects in high temperature polymers and composites’, in *High Temperature Properties and Applications of Polymeric Materials*, M. R. Tant, J. W. Connell and H. L. N. McManus (Eds), ACS Symposium Series 603, American Chemical Society, Washington, DC, USA, pp. 63–80 (1995).
- [8] C. Westlund, M. Eldrup and F. H. J. Maurer, ‘Interlaboratory comparison of positron and positronium lifetimes in polymers’, *Nucl. Instrum. Methods Phys. Res., B*, **143**, 575–583 (1998).
- [9] W. Brandt and J. Spirn, ‘Positron lifetime spectra in molecular substances’, *Phys. Rev.*, **142**, 231–237 (1966).
- [10] J. Tao, ‘Positron annihilation in molecular substances’, *J. Chem. Phys.*, **56**, 5499–5510 (1972).
- [11] M. Eldrup, D. Lightbody and J. N. Sherwood, ‘The temperature dependence of positron lifetimes in solid pivalic acid’, *Chem. Phys.*, **63**, 51–58 (1981).
- [12] A. Shimazu, T. Miyazaki, S. Katayama and Y. Ito, ‘Permeability, permselectivity and penetrant-induced plasticization of fluorinated polyimides studied by positron lifetime measurements’, *J. Polym. Sci. Part B: Polym. Phys. Ed.*, **41**, 308–318 (2003).
- [13] P. Kirkegaard, N. J. Pederson and M. Eldrup, *PATFIT-88: A Data Processing System for Positron Annihilation Spectra on Mainframe and Personal Computers*, Risoe-M-2740, Risoe National Laboratory, DK-4000, Roskilde, Denmark, February (1989).
- [14] S. W. Provencher, ‘CONTIN: A general purpose constrained regularization program for inverting noisy linear algebraic and integral equations’, *Comput. Phys. Commun.*, **27**, 229–242 (1982).
- [15] R. B. Gregory, ‘Free-volume and pore-size distributions determined by PALS’, *J. Appl. Phys.*, **70**, 4665–4670 (1991).
- [16] C.-L. Wang and F. H. J. Maurer, ‘New approach to determine o-Ps lifetime distribution in polymers: a comparison between maximum entropy and the numerical Laplace inversion method’, *Macromolecules*, **29**, 8249–8253 (1996).
- [17] D. Hoffman, M. Heuchel, Yu. Yampolskii, V. Khotimskii and V. Shantarovich, ‘Free volume distribution in ultrahigh and lower free volume polymers: comparison between molecular modeling and positron lifetime studies’, *Macromolecules*, **35**, 2129–2140 (2002).
- [18] B. Nagasaka, T. Eguchi, H. Nakayama, N. Nakamura and Y. Ito, ‘Positron annihilation and ^{129}Xe NMR studies of free volume in polymers’, *Radiat. Phys. Chem.*, **58**, 581–585 (2000).
- [19] B. G. Olson, T. Prodpran, A. M. Jamieson and S. Nazarenko, ‘Positron annihilation in syndiotactic polystyrene containing α and β crystalline forms’, *Polymer*, **43**, 6775–6784 (2002).
- [20] T. Hsieh, C. Tiu and G. P. Simon, ‘Correlation between molecular structure, free volume and physical properties of thermotropic LC polymers’, *J. Appl. Polym. Sci.*, **82**, 2252–2267 (2001).
- [21] V. Shantarovich, Yu. Yampolskii, Yu. Sivergin, O. Salamatina, V. Gustov and D. Hofmann, ‘On possibilities of investigation of nano-structure of free volume in polymers by positron annihilation method’, *Khim. Fizika*, **22**, 87–101 (2003).
- [22] Y. C. Jean, J.-P. Yuan, J. Liu, Q. Deng and H. Yang, ‘Correlation between gas permeation and free-volume hole properties probed by positron

- annihilation spectroscopy', *J. Polym. Sci. Part B: Polym. Phys. Ed.*, **33**, 2365–2371 (1995).
- [23] J. Liu, Q. Deng and Y. C. Jean, 'Free volume distribution of polystyrene probed by positron annihilation: comparing with free volume theories', *Macromolecules*, **26**, 7149–7155 (1993).
- [24] K. Tanaka, K. Okamoto, H. Kita and Y. Ito, 'Correlation between positron annihilation and sorption of CO₂ in glassy polymers', *Polym. J.*, **25**, 577–584 (1993).
- [25] V. Shantarovich, I. Kevdina, Yu. Yampolskii and A. Alentiev, 'Positron annihilation lifetime study of high and low free volume glassy polymers: effects of free volume sizes on the permeability and permselectivity', *Macromolecules*, **33**, 7453–7466 (2000).
- [26] K. Okamoto, K. Tanaka, M. Ito, H. Kita and Y. Ito, 'Positron annihilation lifetime studies of free volume in poly[1-(trimethylsilyl)-1-propyne] films', *Mater. Sci. Forum*, **175–178**, 743–746 (1995).
- [27] V. Shantarovich, Z. Azamatova, Yu. Novikov and Yu. Yampolskii, 'Free volume distribution of high permeability membrane materials probed by positron annihilation', *Macromolecules*, **31**, 3963–3966 (1998).
- [28] G. Consolati, I. Genco, M. Pegoraro and L. Zanderighi, 'Positron annihilation lifetime in poly[1-(trimethylsilyl)-1-propyne]: free volume determination and time dependence of permeability', *J. Polym. Sci. Part B: Polym. Phys. Ed.*, **34**, 357–367 (1996).
- [29] W. J. Davies and R. A. Pethrick, 'Positron annihilation lifetime and Doppler broadening studies of amorphous Teflon AF', *Eur. Polym. J.*, **30**, 1289–1293 (1994).
- [30] A. Yu. Alentiev, Yu. P. Yampolskii, V. P. Shantarovich, S. M. Nemsler and N. A. Plate, 'High transport parameters and free volume of perfluorodioxole copolymers', *J. Membr. Sci.*, **126**, 123–132 (1997).
- [31] G. Consolati, R. Rurali and M. Stefanetti, 'An experimental test on the distribution of positronium lifetimes in polymers', *Chem. Phys.*, **237**, 493–499 (1998).
- [32] V. P. Shantarovich, T. Suzuki, C. He, V. A. Davankov, A. V. Pastukhov, M. P. Tsyurupa, K. Kondo and Y. Ito, 'Positron annihilation study of hyper-cross-linked polystyrene networks', *Macromolecules*, **35**, 9723–9729 (2002).
- [33] Y. Kobayashi, W. Zheng, E. F. Meyer, J. D. McGervey, A. M. Jamieson and R. Simha, 'Free volume and physical aging of poly(vinyl acetate) studied by positron annihilation', *Macromolecules*, **22**, 2302–2306 (1989).
- [34] Y. Y. Wang, H. Nakanishi, Y. C. Jean and T. C. Sandreczki, 'Positron annihilation in amine-cured epoxy polymers – pressure dependence', *J. Polym. Sci. Part B: Polym. Phys. Eds.*, **28**, 1431–1441 (1990).
- [35] V. Shantarovich, T. Suzuki, C. He, Y. Ito, Yu. Yampolskii and A. Alentiev, 'Positron annihilation in polyimides', *Rad. Phys. Chem.*, **73**, 45–53 (2005).
- [36] J. Kristiak, J. Bartos, K. Kristiakova, O. Sausa and P. Bandzuch, 'Free-volume microstructure of amorphous polycarbonate at low temperatures determined by positron annihilation-lifetime spectroscopy', *Phys. Rev. B*, **49**, 6601–6607 (1994).
- [37] H. A. Christov, B. Bolan, A. F. Yee, L. Xie and D. W. Gidley, 'Measurement of hole volume in amorphous polymers using positron spectroscopy', *Macromolecules*, **29**, 8507–8516 (1996).
- [38] R. Srihawatpong, Z. L. Peng, B. G. Olson, A. M. Jamieson, R. Simha, J. D. McGervey, T. R. Meier, A. F. Halasa and H. Ishida, 'Positron annihilation lifetime studies of changes in free volume on cross-linking *cis*-polypropylene, high-vinyl polybutadiene and their miscible blends', *J. Polym. Sci. Part B: Polym. Phys. Ed.*, **37**, 2754–2770 (1999).
- [39] G. Dlubek, K. Saarinen K and H. M. Fretwell, 'The temperature dependence of the local free volume in PE and PTFE: a positron lifetime study', *J. Polym. Sci. Part B: Polym. Phys. Ed.*, **36**, 1513–1528 (1998).
- [40] G. Dlubek, J. Stejny and M. A. Alam, 'Effect of cross-linking on the free-volume properties of diethylene glycol bis(allyl carbonate) polymer networks: a positron annihilation lifetime study', *Macromolecules*, **31**, 4574–4580 (1998).
- [41] G. Dlubek, Th. Lupke, J. Stejny, M. A. Alam and M. Arnold, 'Local free volume in ethylene–vinyl acetate copolymers: a positron lifetime study', *Macromolecules*, **33**, 990–996 (2000).
- [42] G. Dlubek, J. Stejny, Th. Lupke, D. Bamford, K. Peters, Ch. Hubner, M. A. Alam and M. J. Hill, 'Free volume variation in polyethylene of different crystallinities: positron lifetime, density and X-ray studies', *J. Polym. Sci. Part B: Polym. Phys. Ed.*, **40**, 65–81 (2002).
- [43] G. Dlubek, V. Bondarenko, J. Pionteck, M. Supej, A. Wutzler and R. Krause-Rehberg, 'Free volume in two different plastized poly(vinyl chlorides): a positron lifetimes and PVT study', *Polymer*, **44**, 1921–1926 (2003).
- [44] J. Bohlen, J. Wolff and R. Kirchheim, 'Determination of free-volume and hole number density in polycarbonates by positron lifetime spectroscopy', *Macromolecules*, **32**, 3766–3773 (1999).
- [45] S. S. Jordan and W. J. Koros, 'A free volume distribution model of gas sorption and dilation in glassy polymers', *Macromolecules*, **28**, 2228–2235 (1995).

- [46] V. P. Shantarovich, 'On the role of free volume in pick-off annihilation and positron chemical reactions', *J. Radioanal. Nucl. Chem.*, **210**, 357–369 (1996).
- [47] V. P. Shantarovich and V. I. Goldanskii, 'Positron annihilation in free volume elements of polymer structure', *Hyperfine Interactions*, **116**, 67–81 (1998).
- [48] A. Alentiev and Yu. Yampolskii, 'Meares equation and the role of cohesion energy density in diffusion in polymers', *J. Membr. Sci.*, **206**, 291–306 (2002).
- [49] V. Volkov, A. Goldansky, S. Durgaryan, V. Onishuk, V. Shantarovich and Yu. Yampolskii, 'Positron annihilation study of microstructure of polymers and its effects on their diffusion properties', *Vysokomol. Soed., A*, **29**, 192–197 (1987).
- [50] K. Tanaka, M. Katsube, K. Okamoto, H. Kita, O. Sueoka and Y. Ito, 'Correlation between positronium annihilation and gas diffusion properties of a series of polyimides', *Bull. Chem. Soc. Jpn.*, **65**, 1891–1897 (1992).
- [51] C. Nagel, K. Guenther-Schade, D. Fritsch, T. Strunskus and F. Faupel, 'Free volume and transport properties in highly selective polymer membranes', *Macromolecules*, **35**, 2071–2077 (2002).
- [52] K. Tanaka, T. Kawai, H. Kita, K. Okamoto and Y. Ito, 'Correlation between gas diffusion coefficients and positron annihilation lifetime in polymers with rigid polymer chains', *Macromolecules*, **33**, 5513–5517 (2000).
- [53] A. J. Hill, S. Weinhold, G. M. Stack and M. R. Tant, 'Effect of copolymer composition on free volume and gas permeability in poly(ethylene terephthalate)–poly(1,4-cyclohexylnedimethyleneterephthalate copolyesters)', *Eur. Polym. J.*, **32**, 843–849 (1996).
- [54] K. Okamoto, K. Tanaka, M. Katsube, H. Kita, O. Sueoka and Y. Ito, 'Correlation between positron annihilation and gas diffusion properties of various rubbery polymers', *Polym. J.*, **25**, 275–284 (1993).
- [55] Y. Kobayashi, K. Haraya, S. Hattori and T. Sasuga, 'Evaluation of polymer free volume by positron annihilation and gas diffusivity measurements', *Polymer*, **35**, 925–928 (1994).
- [56] G. C. Eastmond, J. H. Daly, A. S. McKinnon and R. A. Pethrick, 'Poly(ether imides): correlation of positron annihilation lifetime studies with polymer structure and gas permeability', *Polymer*, **40**, 3605–3610 (1999).
- [57] Y. Wang, P. T. Inglefield and A. J. Jones, 'NMR characterization of penetrants in high permeability polymers', *Polymer*, **43**, 1867–1872 (2002).
- [58] J. Fraissard and T. Ito, ' ^{129}Xe NMR study of adsorbed Xenon: a new method for studying zeolites and metal-zeolites', *Zeolites*, **8**, 350–361 (1988).
- [59] G. Golemme, J. B. Nagy, A. Fonseca, C. Algieri and Yu. Yampolskii, ' ^{129}Xe -NMR study of free volume in amorphous perfluorinated polymers: comparison with other methods', *Polymer*, **44**, 5039–5045 (2003).
- [60] G. Golemme, J. B. Nagy, A. Fonseca and C. Algieri, ' ^{129}Xe NMR study of free volume in glassy polymers', in *Proceedings of Euromembrane*, Jerusalem, Israel, September 24–27, pp. 312–313 (2000).
- [61] A. P. M. Kentgens, H. A. van Boxtel, R. J. Verweel and W. S. Veeman, 'Line-broadening effects for ^{129}Xe absorbed in the amorphous state of solid polymers', *Macromolecules*, **24**, 3712–3714 (1991).
- [62] T. R. Stengle and K. L. Williamson, 'NMR of xenon absorbed in solid polymers: a probe of the amorphous state', *Macromolecules*, **20**, 1428–1430 (1987).
- [63] J. H. Simpson, W. Wen, A. A. Jones and J. T. Bandler, 'Diffusion coefficients of xenon in polystyrene determined by Xe-129 NMR spectroscopy', *Macromolecules*, **29**, 2138–2142 (1996).
- [64] B. D. Malhotra and R. A. Pethrick, 'Positron annihilation studies of glass–rubber transitions in poly(alkyl methacrylate)s', *Macromolecules*, **16**, 1175–1179 (1983).
- [65] V. I. Bondar, B. D. Freeman and Yu. P. Yampolskii, 'Sorption of gases and vapors in an amorphous glassy perfluorodioxole copolymer', *Macromolecules*, **32**, 6163–6171 (1999).
- [66] Yu. P. Yampolskii, V. G. Berezkin, T. P. Popova, A. P. Korikov, B. D. Freeman, V. I. Bondar and T. C. Merkel, 'Thermodynamics of gas and vapor sorption by amorphous glassy Teflons AF', *Polym. Sci., A*, **42**, 679–688 (2000).
- [67] M. B. Davydova and Yu. P. Yampolskii, 'Study of sorption in poly(phenylene oxide) using inverse gas chromatography method', *Vysokomol. Soed., A*, **33**, 574–578 (1991).
- [68] M. S. Syamala, R. J. Cross and M. Saunders, ' ^{129}Xe NMR spectrum of xenon inside C_{60} ', *J. Am. Chem. Soc.*, **124**, 6216–6219 (2002).
- [69] T. Suzuki, H. Yoshimizu and Y. Tsujita, 'Analysis of gas transport properties of PPO/PS blends by ^{129}Xe NMR spectroscopy', *Polymer*, **44**, 2975–2982 (2003).
- [70] J. M. Braun and J. E. Guillet, 'Study of polymers by inverse gas chromatography', *Adv. Polym. Sci.*, **21**, 107–145 (1976).
- [71] M. Kawakami and S. Kagawa, 'Measurement of solubility coefficients of gases and vapors in natural rubber by the gas chromatography technique', *Bull. Chem. Soc. Jpn.*, **51**, 75–78 (1978).
- [72] M. Galin, 'GC investigation of the thermodynamic interactions of PDMS and PDES with some

- solvents between 60 and 180 °C', *Macromolecules*, **10**, 1239–1244 (1977).
- [73] S. Soloviev, Yu. Yampolskii, I. Economou, N. Ushakov and E. Finkelshtein, 'Parameters of sorption thermodynamics of hydrocarbons in polysilimethylenes as studied by inverse gas chromatography', *Polym. Sci., A*, **44**, 293–300 (2002).
- [74] R. D. Newman and J. M. Prausnitz, 'Polymer – solvent interactions from gas–liquid partition chromatography', *J. Phys. Chem.*, **76**, 1492–1496 (1972).
- [75] K. C. B. Dangayach and D. C. Bonner, 'Solvent interactions with polysulfone', *Polym. Eng. Sci.*, **20**, 59–64 (1980).
- [76] Yu. P. Yampolskii, N. E. Kaliuzhnyi and S. G. Durgaryan, 'Thermodynamics of sorption in glassy poly(vinyltrimethyl silane)', *Macromolecules*, **19**, 846–850 (1986).
- [77] A. Yu. Alentiev, V. P. Shantarovich, T. C. Merkel, V. I. Bondar, B. D. Freeman and Yu. P. Yampolskii, 'Gas and vapor sorption, permeation and diffusion in glassy amorphous Teflon AF1600', *Macromolecules*, **35**, 9513–9522 (2002).
- [78] Yu. Yampolskii and S. Durgaryan, 'Sorption thermodynamics in glassy polymers', in *Chromatography and Thermodynamics: Determination of Physicochemical Parameters*, R. Stryek, Yu. Yampolskii (Eds), Institute of Physical Chemistry, PAN, Warsaw, Poland, pp. 185–241 (1986).
- [79] D. W. Van Krevelen, *Properties of Polymers*, Elsevier, Amsterdam, The Netherlands, pp. 74 (1990).
- [80] S. W. Benson, 'Critical densities and related properties of liquids', *J. Phys. Colloid Chem.*, **52**, 1060–1074 (1948).
- [81] English translation by N. Marshall, *Gas Encyclopaedia*, Single Volume, Elsevier, Amsterdam, The Netherlands, pp. 1–1149 (1976).
- [82] R. C. Reid and T. K. Sherwood, *The Properties of Gases and Liquids*, McGraw-Hill, New York, NY, USA (1966).
- [83] D. Hofmann, M. Entrialgo-Castano, A. Lerbret, M. Heuchel and Y. Yampolskii, 'Molecular modeling investigation of free volume distributions in stiff chain polymers with conventional and ultrahigh free volume: comparison between molecular modeling and positron lifetime studies', *Macromolecules*, **36**, 8528–8538 (2003).
- [84] C. S. Paik and H. Morawetz, 'Photochemical and thermal isomerization of azoaromatic residues in the side chains and backbone of polymers in bulk', *Macromolecules*, **5**, 171–176 (1972).
- [85] J. G. Victor and J. M. Torkelson, 'On measuring the distribution of local free volume in glassy polymers by photochromic and fluorescence techniques', *Macromolecules*, **20**, 2241–2250 (1987).
- [86] J. S. Royal, J. G. Victor and J. M. Torkelson, 'Photochromic and fluorescent probe studies in glassy polymers matrices. 4. Effects of physical aging on poly(methyl methacrylate) as sensed by a size distribution of photochromic probes', *Macromolecules*, **25**, 729–734 (1992).
- [87] J. S. Royal and J. M. Torkelson, 'Photochromic and fluorescent probe studies in glassy polymers matrices. 5. Effects of physical aging on bisphenol-A polycarbonate and poly(vinyl acetate) as sensed by a size distribution of photochromic probes', *Macromolecules*, **25**, 4792–4796 (1992).
- [88] F. P. Chernyakovskii, 'Electrochromism as method for study of slow movements in macromolecules', *Usp. Khim.*, **47**, 563–582 (1979).
- [89] A. I. Kornilov, A. N. Shchapov, E. F. Oleinik, N. L. Muravieva and F. P. Chernyakovskii, 'Application of the free volume model for investigation of molecular mobility in polymers by the electrochromism method', *Dokl. AN SSSR*, **260**, 124–129 (1981).
- [90] N. L. Muravieva, F. P. Chernyakovskii, Yu. P. Yampolskii and S. G. Durgaryan, 'Free volume in glassy polymers measured using the electrochromism method and the gas diffusion coefficients', *J. Phys. Chem. (Russ.)*, **61**, 1894–1898 (1987).
- [91] Yu. P. Yampolskii, V. P. Shantarovich, F. P. Chernyakovskii, A. I. Kornilov and N. A. Plate, 'Estimation of free volume in poly(trimethylsilyl propyne) by positron annihilation and electrochromism methods', *J. Appl. Polym. Sci.*, **47**, 85–92 (1993).
- [92] A. M. Wasserman and A. L. Kovarskii, *Spin Probes and Labels in Physical Chemistry of Polymers*, Nauka, Moscow, USSR (1986) (in Russian).
- [93] Yu. P. Yampolskii, M. V. Motyakin, A. M. Wasserman, T. Masuda, M. Teraguchi, V. S. Khotimskii and B. D. Freeman, 'Study of high permeability polymers by means of the spin probe method', *Polymer*, **40**, 1745–1752 (1999).

Prediction of Gas Permeation Parameters of Polymers

Alexander Alentiev and Yuri Yampolskii

Let's hear it, said Humpty Dumpty. I can explain all the poems that ever were invented – and a good many that haven't been invented just yet.

Lewis Carroll

7.1 Introduction

Among many striking results made in the very early studies of membrane properties of polymers was the observation of strong effects of the chemical structure of polymers on their gas permeation parameters. It has been found that the permeabilities of different polymers vary over several orders and there exist certain correlations between the chemical structures of main and side chains and permeability. Thus, the most permeable polymer among those studied until the 1980s was polydimethylsiloxane rubber whose great permeability (600 barrer for O₂) was attributed to the large mobility of the Si–O bonds in main chains. This mobility is manifested, in particular, in an extremely low glass transition temperature (150 K) [1]. In amorphous polyethylene, which also has rather flexible chains, the glass transition temperature is somewhat higher (about 200 K) and the permeability is lower by 1–2 orders [2]. However, a replacement of one hydrogen atom by the CN group in polyacrylonitrile results in a further dramatic decrease in the permeability (down to 0.001–0.01 barrer) [3]. These phenomena can be and have been explained by the mobility of

polymer chains, interchain interactions, efficiency of packing of macromolecules in membranes, etc.; however, the physical factors governing the transport behavior of polymers were not completely comprehensive. In addition, it was hardly possible to take them into account in a quantitative manner. On the other hand, all of these properties in the first place seem to be sensitive to the chemical structures of polymers. So, there was a natural temptation to avoid analyzing actual physical models that determine the permeability of a material and focus on a direct *quantitative* relationship between the chemical structures of polymer repeat units and the observed gas permeation parameters.

Detailed studies have been carried out on the effects of polymer chemical structures on permeability and diffusivity. The main results have been summarized in numerous reviews (e.g. [4–6]). More systematic data have been accumulated on the effects of the following elements of the repeat units design:

- structures of connector groups [–O–, –CH₂–, –C(CH₃)₂–, –C(CF₃)₂–] in polymers with aromatic backbones
- alkylation of phenylene rings
- *meta/para* substitution of aromatic groups of backbones
- *cis/trans* configuration of double bonds in aliphatic polymers
- *iso/syndio* configuration of polyolefins
- effects of bulky groups as side chains in various polymers

Table 7.1 Effects of the Si(CH₃)₃ group on the permeabilities of polymers

Polymer	$P(O_2)$ (barrer)	$\alpha(O_2/N_2)$	$P(CO_2)$ (barrer)	$\alpha(CO_2/CH_4)$
Polyethylene [9]	2.9	3.0	12.6	4.4
Polyvinyltrimethylsilane [10]	44	4	190	10.5
Polystyrene [11]	2.9	5.5	12	15.7
Polytrimethylsilylstyrene [12]	56	3.5	227	6.7
Poly(methyl methacrylate) [13]	0.091	7.8	0.361	65.6
Poly(trimethylsilyl methyl methacrylate) [14]	35	3.9	140	7
Polynorbomene [15]	2.8	1.9	15	6.2
Polytrimethylsilylnorbomene [15]	30	4.2	89	5.2
Poly(bis-trimethylsilylnorbomene) [16]	95	3.8	445	9.9
Poly(phenylene oxide) [17]	15	4.6	82	12.8
Silylated poly(phenylene oxide) [17]	41	3.9	144	9.9
Polysulfone [18]	—	—	4.6	21.9
Silylated polysulfone [18]	—	—	15	16

The most drastic variation of the gas permeation parameters was observed due to introduction of bulky, trimethylsilyl groups in various main chains. First, this effect was observed for the vinyl polymer – poly(vinyltrimethyl silane) [7,8], an amorphous glassy material that showed much higher gas permeability and selectivity than polyethylene, which can be considered as its structural prototype. Later, the same Si(CH₃)₃ group was introduced into various main chains, as illustrated by Table 7.1.

Further progress was made in the 1980s when Masuda *et al.* [19] prepared and tested poly(trimethylsilyl propyne) – the most permeable polymer known (both at that time and still now). Subsequently, numerous other polyacetylenes with different bulky groups containing Si, Ge and F were synthesized, and, as a rule, these exhibit large gas permeabilities (see Chapter 8).

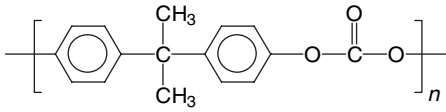
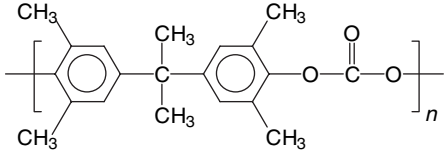
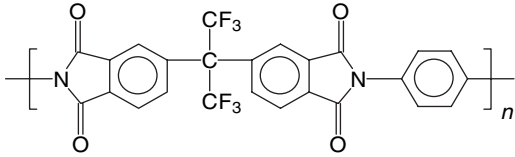
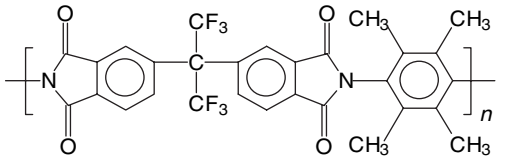
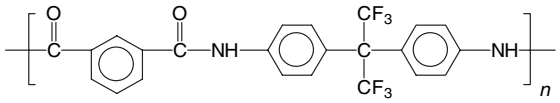
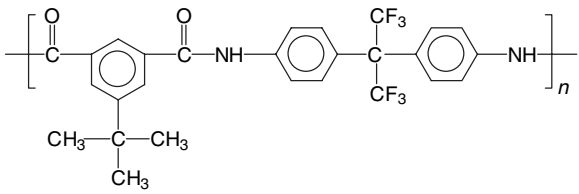
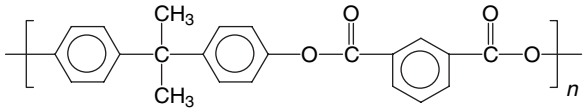
If one considers certain chemical transformations (e.g. alkylation, introduction of polar groups, etc.) within the repeat units of polymers that belong to different classes, one can conclude that similar variations of permeability caused by those changes can be observed. This can be substantiated by the data presented in Tables 7.1 and 7.2. Note that similar variations are revealed in other physical properties of polymers such as glass transition temperatures and densities. This implies that, for certain structural elements, some increments can be ascribed that would account for the observed variation of permeability and diffusivity. So, finding these increments (or indices) and equations (empiric or semi-empiric) for the calculation of properties of polymers using them

would make it possible to predict gas permeation parameters before their experimental determination. The results of the different approaches for such predictions are the subject of this chapter.

Today, there is a wealth of data available on the gas permeation parameters of polymers (gas permeability and diffusion coefficients, separation factors, activation energies of diffusion and permeation). This information was accumulated in the process of empirical searching for improved materials for gas separating membranes. Another aim of this work, which was often present but not always explicitly stated, was the development of rules for prediction of the permeation parameters of polymers that had not yet been investigated or even prepared. Such rules, had they been formulated, would simplify or facilitate significantly the task of directed synthesis of novel membrane materials with improved properties. Now this is an ambitious but realistic goal. The gas transport parameters now available for polymers having diverse chemical structures and properties provide an opportunity for quantitative interpretation and examination of various hypotheses.

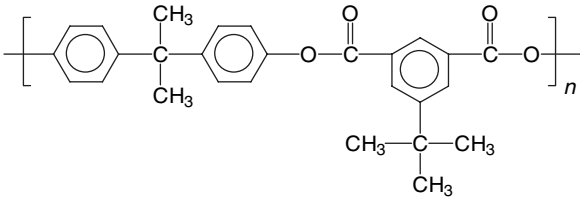
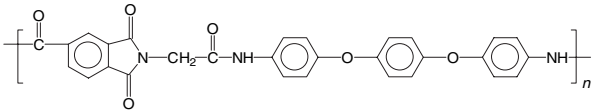
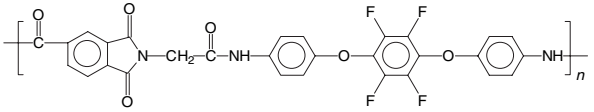
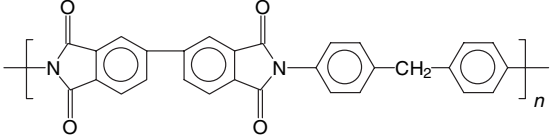
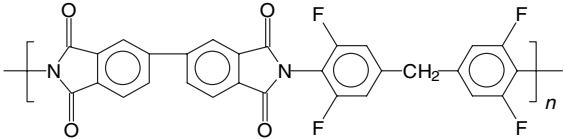
Permeability, diffusion and solubility coefficients are the properties of ‘gas – polymer’ systems under certain conditions (temperature, pressure, gas composition). So first, one should consider briefly the possibilities of correlative predictions of these parameters using the physical properties of components – gases and polymers. Gases are much simpler and better defined species than polymers, and so rather successful correlations with gas properties have been reported.

Table 7.2 Structural effects on the permeability coefficients and permselectivities

Polymer	$P(\text{O}_2)$ (barrer)	$\alpha(\text{O}_2/\text{N}_2)$	Reference
<i>Introduction of Me</i>			
	1.6	4.8	20
	5.6	5.1	20
	4.2	5.3	21
	122	3.4	21
<i>Introduction of t-Bu</i>			
	2.4	5.7	22
	11.5	4.6	22
	1.3	5.5	23

(Continued)

Table 7.2 (Continued)

Polymer	$P(\text{O}_2)$ (barrer)	$\alpha(\text{O}_2/\text{N}_2)$	Reference
	5.9	5.0	23
<i>Fluorination</i>			
	0.18	9.3	24
	0.28	4.0	24
	0.21	6.9	25
	1.5	5.5	26

Thus, the diffusion coefficients correlate with the sizes of diffusant molecules, expressed as molecular diameter d , cross-section d^2 or even molecular volume (critical volume of gases), as has been demonstrated in numerous papers [9,27–29]. Solubility coefficients equally well correlate with boiling point T_b , critical temperature T_c or Lennard–Jones energy parameters ε/k , since these three parameters are interrelated. Apparently, the increased van der Waals interactions of larger molecules having higher values of T_b , T_c and ε/k with polymer matrices are responsible for this behavior, as has been confirmed by good correlations of the solubility coefficients and solute–solvent interaction energies with gas mole-

cular surface areas [30,31]. However, the utility of the predictions based on those correlations is not so valuable, because they allow one to find only the permeability and diffusion coefficients for various gases in a polymer after they have been determined for certain gases in the same material.

A problem of the prediction of transport properties for novel polymers is much more difficult because of the complexity of polymers: there is no single property or a simple combination of several ones that would permit a reliable and accurate prediction of permeabilities for different polymers. Correlations have been proposed where permeability or diffusion coefficients are related to such properties of polymers as free volume

[32–34], van der Waals volume of the polymer repeat unit [35], polymer density [36], d -spacing in wide-angle X-ray diffraction [37], cohesion energy density [38], glass transition temperatures [39,40], permittivity [41] and mechanical modulus [25]. However, a unified scheme for such a prediction has not been found so far. Correlations valid for one group of polymers sometimes fail to exist for another one (e.g. [25] and [33]).

In this chapter, we will consider the three existing approaches (the group contribution method, use of the graph theory and artificial neural networks) for predicting gas transport parameters such as permeability coefficients, diffusivity, separation factors and some others on the basis of polymer chemical structure. A brief historic background and perspective, main premises, limitations and predictive possibilities of each method will be discussed in the corresponding sections. To avoid coincidences in the notations, we have used in some formulae different symbols to those in the original works.

7.2 Group Contribution Methods

The method of group contributions is based on the validity of several assumptions:

- (1) The structure of complex molecules and, in particular, of polymers can be represented as a sum of several groups or fragments, which are common for the whole set of structures (atoms, mono- or multivalent radicals). Each fragment can be characterized by a certain increment into the property in question (e. g. gas permeability (P) and diffusion (D) coefficients). A way of ‘splitting’ repeat units into fragments is an extremely subtle issue, which can strongly affect the success of eventual predictions: these fragments can be as small as individual atoms or can consist of much larger parts of repeat units.
- (2) The increments are constant for the whole set of complex structures, i. e. they do not depend on a mutual arrangement of the groups or their possible interactions.
- (3) The properties of complex molecules can be represented as sums of the corresponding increments after accounting for weight factors.

In this formulation, no fundamental laws or semi-empirical rules are used relating the proper-

ties and chemical structure of polymers. Let us consider some property Y of a polymer as the sum:

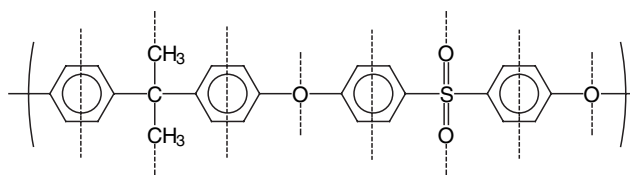
$$\log Y = \frac{1}{k} \sum_i q_i X_i \quad (7.1)$$

where k is a normalizing coefficient, X_i is the increment characteristic of a group of the i th type in the repeat unit and q_i is the number of these groups in the repeat unit.

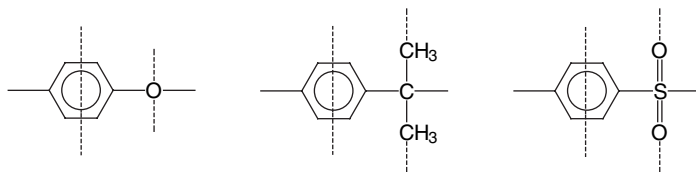
The task of the prediction of polymer gas permeation properties is based on a search for the best values of increments or group contributions X_i using the experimentally known Y_j (e.g. P_j , D_j) values obtained for a set of N polymers. The prerequisite for this is $N \gg n$, where n is the number of different groups that are used to draw the structures of repeat units of all N polymers. In other words, one has an ‘overdetermined’ system of equations, the solution of which by means of the least squares method gives averaged values of the group contributions X_i .

The group contribution methods are well developed in relation to the thermodynamic and kinetic properties of low-molecular-mass compounds [42]. They are widely used for polymers due to the classical book by Van Krevelen for the calculation of numerous properties of polymers such as glass transition temperatures, melting points, cohesion energies, heat capacities and many others [39]. There is a basic difference in application of the group contribution method for polymers and low-molecular-mass compounds. In the former case, the repeat unit is not a ‘real’ structure of a macromolecule. Hence, introduction of certain normalizing factors is necessary, and this poses another question. Different normalization parameters can be used (molecular mass of the group, van der Waals volume or molecular volume, etc.).

Pioneer works in using the group contribution method for prediction of permeability were made by Salame and coworkers [43–45] who proposed the new parameter, ‘Permachor’ (π), for prediction of gas permeabilities of polymers. It can be noted that originally a similar scheme of predictions had been proposed for liquid permeation [46]. The repeat units were split into fragments of different sizes: in some cases into individual atoms (Si, quaternary C, ether —O—), while in



Structure 7.1



Structure 7.2

other cases much larger groups were selected (phenylene, ester group $-\text{C}(\text{O})-\text{O}-$, etc.). By using a very limited set of data available at that time, he proposed a simple formula for the calculation of permeability coefficients of three gases:

$$P = A \exp(-s\pi) \quad (7.2)$$

Its parameters (A , barrer, s , dimensionless) have the following values for different gases, respectively: $\text{O}_2 - 53, 0.112$; $\text{N}_2 - 18, 0.121$; $\text{CO}_2 - 330, 0.122$. A problem of the Permachor model is that it yields a single value of permselectivity, $\alpha(\text{O}_2/\text{N}_2)$, for all polymers having the same permeability of oxygen, which is, of course, not the case. Today, the Permachor model can hardly be used because it includes a limited set of fragments and neglects basic differences in the media it attempts to characterize (amorphous, semicrystalline, rubbery, glassy), let alone its other shortcomings. However, it demonstrated the general possibilities of the group contribution approach for predictions and promoted further progress in the field.

A much more systematic attempt was made by Robeson *et al.* [47] who considered a rather large set of structurally related polymers. This set included 65 amorphous polymers with aromatic backbones and was based primarily on the experimental results obtained in a single group from the University of Texas at Austin. In subdividing the repeat units, the structural units were chosen around each chemical bond, as illustrated for

polysulfone (Structure 7.1), which can be represented by three sub-units (Structure 7.2).

Molecular volumes were taken as normalizing parameters. These were computed by using the Molecular Simulation, Inc. 'Quanta' package and are tabulated in Jia and Xu [38] for 24 fragments. This model allows rather accurate predictions, not only of permeability coefficients (Figure 7.1) but also of separation factors

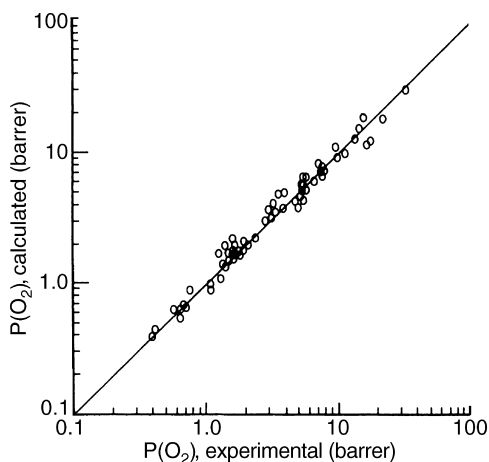


Figure 7.1 Comparison of predicted versus experimental values of O_2 permeability coefficients of polymers [47]. Reprinted from *Journal of Membrane Science*, **132**, L. M. Robeson, C. D. Smith and M. Langsam, 'A group contribution approach to predict permeability and permselectivity of aromatic polymers', pp. 33–54, Copyright (1997), with permission from Elsevier

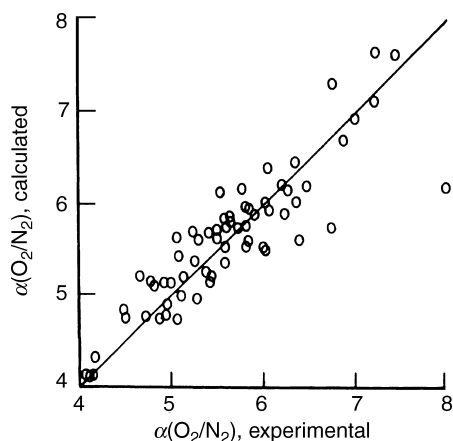


Figure 7.2 Comparison of predicted versus experimental values of separation factors $\alpha(\text{O}_2/\text{N}_2)$ [47]. Reprinted from *Journal of Membrane Science*, **132**, L. M. Robeson, C. D. Smith and M. Langsam, 'A group contribution approach to predict permeability and permselectivity of aromatic polymers', pp. 33–54, Copyright (1997), with permission from Elsevier

(Figure 7.2). Later, the database was extended [48] to 87 polymers, and so a larger number of the subunits (from 24 to 35) could be considered with seemingly better fits of the experimental and predicted values.

An opposite possibility, that is, subdividing the repeat units into the smallest fragment was analyzed by ourselves [49], where atomic increments were sought for when dealing with a large group of glassy polymers (nearly 300) which belonged to various chemical classes. First, the following basic set of the atomic groups was chosen: H, C(sp³), C(sp²), C(ar–sp²), O=, –O–, Si, Cl, Br, F, N≡ (in nitriles), –N<, =S=, –S–. On the other hand, as the permeation parameters with respect to the most popular set of gases (He, H₂, N₂, O₂, CO₂, CH₄) have been reported for several hundred polymer structures, i. e. for a sufficiently large N , there is a possibility to increase the number n or discriminate between different positions of the same group within a repeat unit. Both opportunities were considered [49] for calculations of the diffusion and permeability coefficients of different glassy polymers.

An examination of the effects of the ratio N/n showed that the increase in N from 60 to about 200 does not improve the fit of the correlations, P_{pred} versus P_{exp} , although in both cases about 93 % of the P_{pred} values were within one order

of magnitude from the P_{exp} values. In order to improve the fit, different reasons for this discrepancy were considered. Two factors were assumed to be mainly responsible, namely:

- differences in temperatures of the reported P and D values
- too small a set of the basic fragments

Note that we could not consider the pressure effects on permeability, which might be important, especially in the case of carbon dioxide. To avoid the complications related to this factor, experimental permeability coefficients were taken at the lowest pressure reported.

Numerous P and D values have been reported at 35 °C. On the other hand, many P and D values have been measured at ambient temperature (20–25 °C) but reported data on activation energies are rather scarce. In order to overcome this difficulty, several semi-empirical methods for prediction of the activation energies of diffusion, E_D , and permeation, E_P , were considered [50]. It was concluded that the most reliable correlation for the E_D and E_P values can be obtained on the basis of a compensation effect between E_D , E_P and the pre-exponential factors, D_0 and P_0 , respectively, as defined by the Arrhenius equations: $D = D_0 \exp(-E_D/RT)$ and $P = P_0 \exp(-E_P/RT)$. Thus, it became possible to recalculate all the data to the standard temperature (35 °C) and to avoid 'noise' caused by the non-isothermal character of the basis set of P and D values. The scheme of calculation of the basic isothermal set of transport parameters is shown in Figure 7.3.

A second step for improving the fit was to expand the number of the basic groups. It was decided to ascribe different increments for the side groups attached to aliphatic and aromatic carbons of the main chains. This possibility was examined by using the polyimide class as an example: abundant gas permeation parameters have been reported for polyimides, and so the inequality $N \gg n$ is easily fulfilled for these polymers. The number of types of atoms in the polyimide structure was increased to 20 (8 types in the main chains and 12 in the side groups). In addition, different methods of normalization were tested: normalization by number atoms and molecular mass of the repeat units. Some of the results are shown in Figure 7.4 and 7.5.

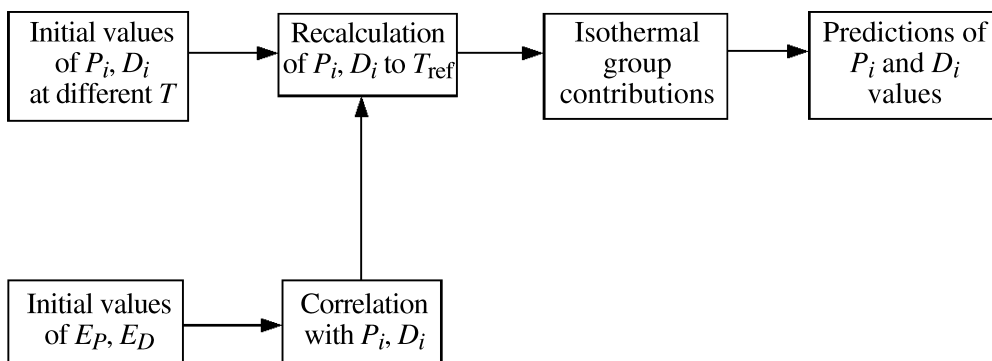


Figure 7.3 The scheme of recalculating all the P and D values to the reference temperature [49]. Reprinted from *Journal of Membrane Science*, **149**, Yu. Yampolskii, S. Shishatskii, A. Alentiev and K. Loza, 'Group contribution method for transport property prediction of glassy polymers: focus on polyimides and polynorbomenes', pp. 203–220, Copyright (1988), with permission from Elsevier

Figure 7.4 presents a correlation between the CO_2 permeability coefficients, $\log P_{\text{pred}}$ and $\log P_{\text{exp}}$, in various polyimides with normalization by molecular mass. This shows that the described method of atomic group contributions gives, in the case of polyimides, satisfactory results. Different approaches to subdividing and normalization are compared in Figure 7.5. This indicates that the deviations are notably less for the modified scheme, which discriminates between atoms attached to aliphatic and aromatic carbons in the polymer structure. It was also shown that the dispersion:

$$\sigma = \sqrt{\frac{\sum_1^n (\log P_{\text{pred}} - \log P_{\text{exp}})^2}{n - 1}} \quad (7.3)$$

is minimum for this way of normalization and corresponds to about a twofold deviation between experimental and predicted permeability.

Polyimides provide an opportunity to test another tactic in predicting the gas permeation parameters. Homopolymers which belong to the polyimide class can be considered as alternating copolymers of certain dianhydrides and diamines. The basic set of about 120 'homopolyimides' structures included

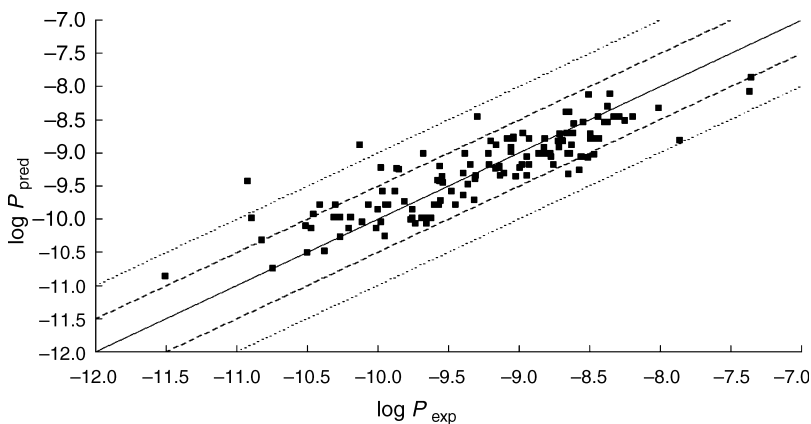


Figure 7.4 Correlation of predicted and experimental permeability coefficients of glassy polymers in respect of CO_2 : distinction between substitution on aliphatic and aromatic groups, normalizing on molecular mass of repeat unit [49]. Reprinted from *Journal of Membrane Science*, **149**, Yu. Yampolskii, S. Shishatskii, A. Alentiev and K. Loza, 'Group contribution method for transport property prediction of glassy polymers: focus on polyimides and polynorbomenes', pp. 203–220, Copyright (1998), with permission from Elsevier

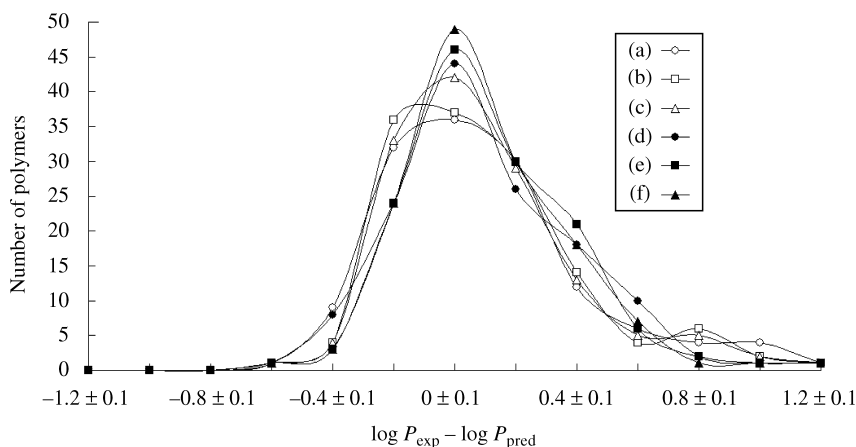


Figure 7.5 Distributions of the deviations of predicted from experimental P values according to different schemes of the predictions: no distinction for positions of atomic groups, (a) no normalization; (b) normalizing on number of atoms; (c) normalizing on molecular mass of repeat unit; distinction between substitution in aliphatic and aromatic side chains, (d) no normalization; (e) normalizing on number of atoms; (f) normalizing on molecular mass of repeat unit [49]. Reprinted from *Journal of Membrane Science*, **149**, Yu. Yampolskii, S. Shishatskii, A. Alentiev and K. Loza, 'Group contribution method for transport property prediction of glassy polymers: focus on polyimides and polynorbornenes', pp. 203–220, Copyright (1998). with permission from Elsevier

the products of polycondensation of 9 dianhydrides with about 70 diamines having different structures. Not all of the possible combinations of dianhydrides and diamines were represented in this basic set of data. For example, the dianhydride of the hexafluoroisopropylidene series was used in the preparation of about 50 various polyimides, whereas some other dianhydrides were combined with only a few diamines. So, if the additive scheme holds, one would be able to estimate the transport parameters of 630 different polyimides, provided that the corresponding increments are known for all of the dianhydrides and diamines.

In this case, the task of the prediction of polymer transport properties (permeability and diffusion coefficients) is based on a search for the best values of the increments or group contributions, x_j and y_k , using experimentally known A_{0i} (P_i , D_i) values obtained for a set of polyimides. Here, x_j and y_k are the increments characteristic for certain dianhydrides and diamines residues, respectively, included in the structures of polyimides. Therefore, we obtain the overestimated system of linear equations:

$$x_1 + y_1 = \log A_{01} \quad (7.4a)$$

$$x_1 + y_2 = \log A_{02} \quad (7.4a)$$

$$x_2 + y_1 = \log A_{0n} \quad (7.4b)$$

$$x_j + y_k = \log A_{0z} \quad (7.4c)$$

where j is the number of a dianhydride and k is the number of a diamine. Obviously, every 'line' corresponds to a certain polyimide. If several equally reliable A_i values have been reported by several authors for the same polyimide, they were included as independent equations in the system (Equations (7.4a–7.4c)). The system was solved with respect to x_1 , x_2, \dots, x_j and y_1, y_2, \dots, y_k using the method of multiple linear regression by means of "Application for statistical calculations (SPSS for Windows)". Calculation of the permeability coefficients was performed for the following gases: He, H₂, O₂, N₂, CO₂ and CH₄. The data for diffusion coefficients were less abundant, and so the calculations could be carried out only for N₂, CO₂ and CH₄.

Figure 7.6 shows correlation of the experimental and predicted permeability coefficients of different polyimides with respect to O₂ [51]. It can be seen that, in most cases, a difference between the predicted P_{pred} and experimental P_{exp} values corresponds to a factor of 2 or less, whereas the experimental P values of polyimides vary over the range 4–5 orders. In fact, the observed scatter is close to deviations of the results of different determination of permeability of the same polymer from analysis of the database [52]. These deviations can be caused by the effects of molecular mass, residual solvent, film casting protocol, etc.

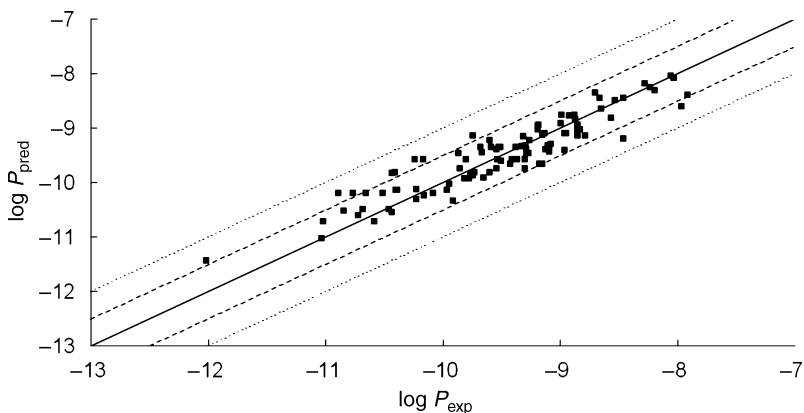


Figure 7.6 Correlation of the predicted and experimental permeability coefficients of polyimides with respect to O_2 : polyimides are treated as alternating copolymers [51]. Reprinted from *Journal of Membrane Science*, **167**, A. Alentiev, K. Loza and Yu. Yampolskii, 'Development of the methods for prediction of gas permeation parameters of glassy polymers: polyimides as alternating copolymers', pp. 91–106, Copyright (2000), with permission from Elsevier

An enhanced accuracy of the predictions allows an approach to a more difficult problem – a prediction of the separation factors of the polyimides. Figure 7.7 compares experimental and predicted separation factors, $\alpha(O_2/N_2)$, found as the ratio of the predicted values, $P(O_2)/P(N_2)$. It is evident that such a scheme of the search for the group contributions gives satisfactory results in prediction of the permselectivity of polyimides as well.

A convenient form of analysis of the transport parameters of polymers is the permeability/

permselectivity diagrams that have been discussed in detail by Robeson [53]. Such diagrams were constructed for the transport of different gas pairs in polyimides [51]. Bearing in mind the good correlations between predicted and experimental permeabilities, they are similar to the original Robeson diagrams. Some of the data points lie above the upper bound lines of Robeson. Interestingly, for different gas pairs, the different polyimide structures determine improved the predicted gas permeation parameters. For example,

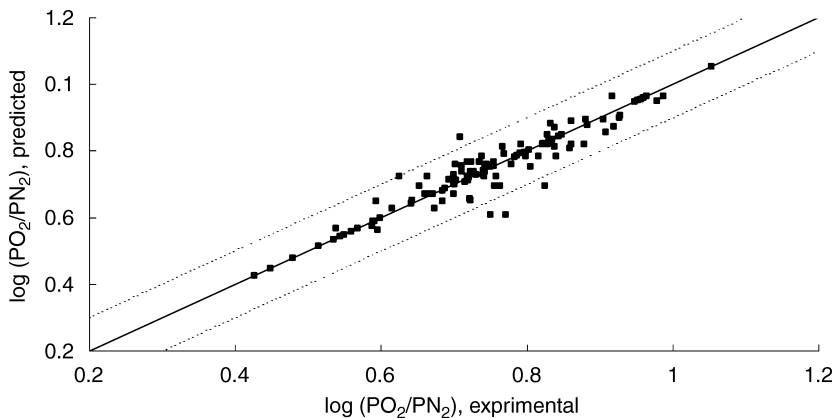


Figure 7.7 Correlation of the predicted and experimental separation factors $\alpha(O_2/N_2)$ [51]. Reprinted from *Journal of Membrane Science*, **167**, A. Alentiev, K. Loza and Yu. Yampolskii, 'Development of the methods for prediction of gas permeation parameters of glassy polymers: polyimides as alternating copolymers', pp. 91–106 Copyright (2000), with permission from Elsevier

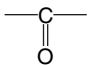
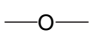

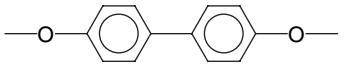
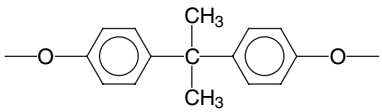
polyimides obtained from *m*-(5-carboxy)phenylenediamine showed an 'above-upper-bound' behavior for the O₂/N₂ pair, while for the He/N₂ pair all of the data points above the upper bound belong to the polyimides that are derivatives of *m*-phenylenediamine. Hence, such predictions may help to reduce synthetic experimental efforts in directed searches for better membrane materials.

Figures 7.3, 7.4 and 7.6 characterize a general agreement between the predicted and experimental transport parameters for the whole data set. It will be more interesting to compare the predicted permeability coefficients for a particular group of polymers, whose transport parameters have not been included in the basic set used in computation of the group contributions. This can be illustrated by Table 7.3, where the permeability

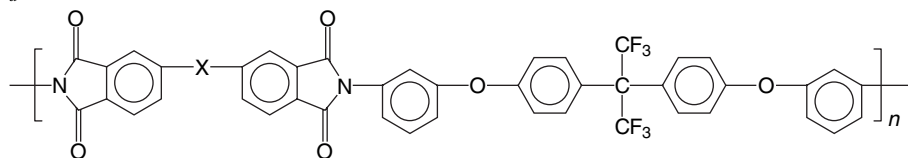
coefficients are presented for a group of poly(ether imide)s. It is seen that the largest deviations between P_{pred} and P_{exp} amount to a factor 2–2.5, while most of the predicted parameters agree much better with the experimental data.

It is possible also to consider group contributions, not in the target transport parameters such as P and D , but in some physical properties of the polymers which correlate with them. In this regard, it is worthwhile to mention the work by Park and Paul [34], who suggested group contributions in the occupied volume, V_{oc} , of polymers and calculated the free volume using the found V_{oc} values. The main idea of such an approach is that different gases 'sample' different fractions of the total free volume. In other words, the occupied volumes in polymers 'sampled' by hydrogen are systematically smaller than those 'sensed' by larger molecules like

Table 7.3 Experimental and predicted permeability coefficients, $P_{\text{exp}}/P_{\text{pred}}$, at 35 °C for a group of poly(ether imide)s^a [54]. Reproduced from Polymer Science, MAIK Nauka, Interperiodica

X	P , (barrer)		
	H ₂	O ₂	N ₂
—	12.2/14.5	0.90/1.17	0.26/0.18
	10.8/13.9	1.06/0.92	0.30/0.13
	12.3/15.2	0.90/1.37	0.19/0.22
	6.90/12.1	0.42/1.10	0.2/0.17
	5.40/9.60	0.43/0.81	0.10/.11
	13.1/23.3	1.15/1.25	0.15/0.18

^a



methane. It was shown that this method can also be used for prediction of permeability coefficients in polymers with aromatic backbones using correlations with free volume found in this manner.

7.3 Graph Theoretical Approach

Graph theory has been successfully used to predict important properties of organic compounds. Accordingly, it has been applied to predict the gas permeabilities of polymers [55,56] using the formalism developed by Kier and Hall [57]. Graph theory is a topological approach that assigns a set of indices to various items, e.g. molecules, which can uniquely characterize their structure and properties that are structure-dependent. The so-called connectivity or Randic indices [58] are particularly suitable for this task.

The basic assumptions of molecular connectivity theory is that the molecular structures of repeat units can be represented by certain graphs and described by the indices ${}^m\chi_t$, which are calculated for different sub-graphs that form this structure. Here, m refers to the number of edges (bonds connecting two vertices or atoms) in the graph (repeat unit) and t refers to the type of sub-graph. Chemical structures are drawn for simplicity in the 'hydrogen-depleted form' and can be constructed as a sum of the following sub-graphs:

- p , single continuous path connecting two or more atoms
- c , cluster type where one atom is connected to three or more atoms (branching)
- ch , chain type, which describes cyclic sub-graphs
- pc , combination of linear (p) and branched (c) sub-graphs

In order to calculate ${}^m\chi_t$, special parameters δ are assigned to each atom included in the repeat units. To the first approximation, this parameter can be considered as the valence of the i th atom minus the number of hydrogen atoms it is connected to (e.g. 1 for methyl, 2 for methylene, etc). Some semi-empirical rules for computing δ for elements with d electrons were suggested in Kier and Hall [57]. Then, one has to calculate the sub-graph indices mS_j :

$${}^mS_j = \prod_{i=1}^d (\delta_i)^{-0.5} \quad (7.5)$$

Collecting the total sub-graphs of m edges yields:

$${}^m\chi_t = \sum_{j=1}^{n_m} {}^mS_j \quad (7.6)$$

In these equations, i is the atom number, j is the sub-graph number, n_m is the number of the sub-graph of m edges and t is the χ descriptor (p , c , pc or ch type); while computing the number m of edges (bonds), single and double bonds are all considered as one edge, d is the total number in the graph theory representation of the repeat unit. The property of interest, that is, the permeability coefficient in logarithmic form, $\log P(\chi)$, can be expressed as a power series function of ${}^m\chi_t$:

$$\log P(\chi) = \sum C_i ({}^m\chi_t)^z i + b_0 \quad (7.7)$$

where the parameters A_i and b_0 can be found by regression for certain arbitrary fixed values of z_i (e.g. $z = 0.5, 1, 2$).

A set of only 19 different polymers (glassy and rubbery, amorphous and semicrystalline) was selected by Surgi *et al.* [55] for testing this approach. The polymers included the following sorts of atoms: C(sp³), C(sp²), C(sp² aromatic), F, Cl, O and Si. It was shown that statistically significant correlations were displayed for the ${}^4\chi_p$ and ${}^3\chi_p$ connectivity indices. The best fit for calculation of oxygen permeability was accomplished by using the equation:

$$\log P = 1.75({}^4\chi_p) - 2.70({}^3\chi_p) - 7.19 \quad (7.8)$$

where P is expressed in cm³(STP) cm/(cm² s (cmHg)). The equation relating the calculated and experimental P values has a rather high correlation coefficient, $R = 0.95$ which corresponds to the mean uncertainty, $d = 0.22$: the value d was defined as the ratio $|P_{\text{pred}} - P_{\text{exp}}|/P_{\text{exp}}$. However, the graph theory model systematically overestimates P for low-permeable polymers and underestimates it for highly permeable polymers. It should be noted that this high correlation coefficient could be obtained only with adjustable δ parameters having no physical significance. Thus, the largest value was ascribed to the Si atom ($\delta(\text{Si}) = 3000$), while the smallest one

corresponded to Cl ($\delta(\text{Cl}) = 0.05$). No doubt, this is related to the high permeability of PDMS, the only silicon-containing polymer in the set, and the low permeabilities of poly(vinyl chloride) and poly(vinylidene chloride).

Another version of application of graph theory for prediction gas permeabilities was described by Bicerano [56]. In this case, the semi-empirical model, including cohesion energy density (CED) and free volume terms, was used, and so only corrections based on graph theory are employed to improve the fit. The δ parameters were calculated according to the scheme of Kier and Hall [58]. For a basic set which included 60 polymers (again, rubbery, glassy, amorphous and semi-crystalline), an equation for computing the oxygen permeability was proposed as follows:

$$P = A^* \exp(-B^* v) \quad (7.9)$$

In this formula, $A^* > 0$ and $B^* > 0$ are constants ($A^* = 0.047 \text{ cm}^3(\text{STP}) \text{ cm}/(\text{cm}^2 \text{ s} (\text{cmHg}))$; $B^* = 0.017622$) and the novel parameter ('newchor') v is defined by the empirical equation:

$$v = \text{CED} - 196(1/\text{FFV}) + 110(N_{\text{rot}}/N) - 57(N_{\text{per}}/N) \quad (7.10)$$

Here, CED is the cohesion energy density, FFV is the fractional free volume, or ratio of free volume and specific volume, and N_{rot} , N and N_{per} are adjustable parameters having no physical significance and included to improve fits of the calculations based on connectivity indices. These corrections account for the presence of certain groups in the repeat units (e.g. C=C, CN, ester groups, hydrogen-bonded groups, etc.). Thus, group contributions are introduced in a 'hidden form' in Bicerano's model as well. An attempt to avoid this practice to use adjustable parameters was made recently [59]. It was proposed to use correlations incorporating higher-order connectivity indices. However, the accuracy of such a prediction is approximately the same as that indicated by Bicerano [56].

7.4 Artificial Neural Networks

Another, recently emerging approach for predictions can be provided by Artificial Neural Net-

work (ANN) methodology. An ANN is a special mathematical tool or so-called 'parallel distributed processor', capable of correlating different input and output information and for storing 'experience-based' knowledge and make it available for use. The term for this approach was coined, because it resembles nerve or brain actions in two respects: (1) knowledge is acquired by the network through learning process; (2) interneuron connection strengths, known as 'synaptic weights', are used to store information. The ability of an ANN to identify mathematical models which closely fit collected data, without any need to make assumptions on the mechanism of the processes being considered, is especially valuable for the analysis of transport parameters in glassy polymers because of all of the uncertainties related to material and mass transfer models. If properly implemented, the resulting mathematical formulations distinguish signals from 'noise'. An important feature of the ANN technique is the ability to increase its predictive accuracy as more data is made available ('learning from experience'). A wide application of ANNs in chemistry [60] offers ample justification for the use of this method in membrane science and technology.

While searching for relationships between polymer structures and their transport parameters when using the ANN technique, one has to assume certain input parameters, which would characterize the structure in a unique way. As such 'fingerprint' parameters, one can 'imagine' NMR spectra, IR spectra and even topological connectivity indices. Gas permeability coefficients are the output parameters. It is not implied that the input parameters are related, in any mechanistic way, to the output parameters. IR spectra are maybe one of the most convenient type of input parameters: the complex character of IR spectra guarantees that every structure is characterized by its own spectrum, and they are available for numerous polymers or can be easily measured for novel polymers. An application of IR spectra as input parameters was described by Wessling [61]; we will describe the ANN method by using this work.

An ANN consists of network-processing elements, so-called 'Neurons', which are organized in layers, as illustrated in Figure 7.8. Every neuron calculates outputs o_i out of all incoming inputs x_j . All inputs x_j are weighted by a factor

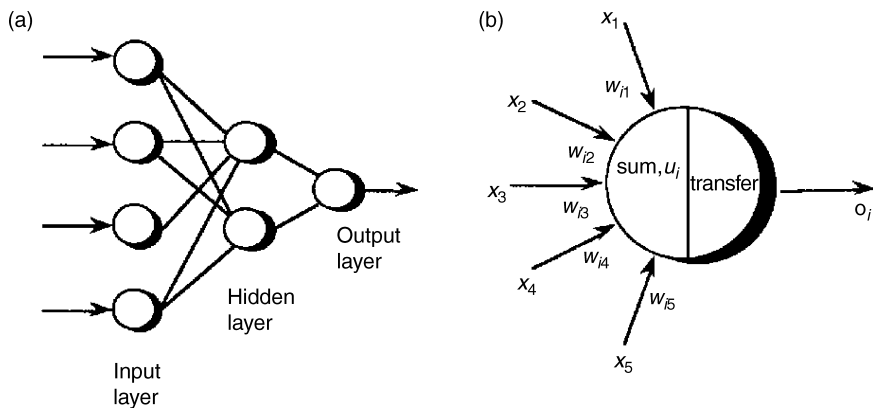


Figure 7.8 Schematic representation of (a) a neural network topology (b) a processing element (neuron) [61]. Reproduced by permission of Matthias Wessling from *Relaxation Phenomena in Dense Gas Separation Membranes*, PhD Thesis, Twente University, Twente, The Netherlands (1993)

w_{ij} , which can be found by iterations, giving the final input u_i :

$$u_i = \sum w_{ij}x_j \quad (7.11)$$

Different mathematical functions can be used to transfer the inputs, u_i , into the output, o_i . The correct input–output relations of the network as a whole are ‘learnt’ from examples by adapting the weights iteratively.

First, an adequate number of neurons in the input layer is chosen. Secondly, a certain set of digitized IR spectra, together with permeabilities, is presented to the network. In a third step, the network is ‘trained’ by changing the weights in such a way that a minimum deviation is obtained between the predicted and measured permeabilities. In this process, one polymer is left out of the set of n polymers and, after ‘training’ with $(n - 1)$ polymers is over, the permeability of this polymer is predicted on the basis of its IR spectrum. Then, the same procedure is repeated for all other polymers. Legendre polynomials were used to give adequate quantitative descriptions of the IR spectra: it was shown that about 48 polynomials were sufficient to represent the main bands in the IR spectra of aromatic backbone polymers. A set of 33 amorphous glassy polymers of different classes, with permeability coefficients in the range 0.4–60 barrer, was used. The quality of fit was characterized by the so-called performance factor, C :

$$C = \frac{\sum |P_{\text{pred}} - P_{\text{exp}}|}{\sum |P_{\text{av}} - P_{\text{exp}}|} \quad (7.12)$$

where P_{av} is the average permeability coefficients over the whole set. The best results were obtained for an ANN with 24 input neurons and 16 neurons in a single hidden layer (see Figure 7.8). ‘Training’ required 3000 iterations for each polymer.

Figure 7.9 shows a correlation of the predicted and experimental permeabilities. The performance factor of this correlation is 0.77, while for the ‘perfect fit’ it would correspond to unity. Seemingly, the quality of this correlation is not very good; however, one has to bear in mind that enlargement of the basic sets of polymers should provide significant improvements of the prediction quality. The importance of this work was mainly in demonstration of the capability of this contemporary approach.

7.5 Computer Simulations

Computer modeling of the nanostructures of membrane materials and calculation on this basis of the solubility (S) and diffusion (D) coefficients (and, hence, permeability coefficients) for small molecules of penetrants in different polymers, is another method for prediction of the transport parameters that emerged 10–15 years ago and has made recently amazing progress. This approach is the subject of Chapters 2 and 3 of this book, and so here only brief illustrations of the predictive ability of this approach will be given.

It should be noted that, so far, the methods based on molecular dynamics, molecular mechanics, Monte Carlo methods and transition state

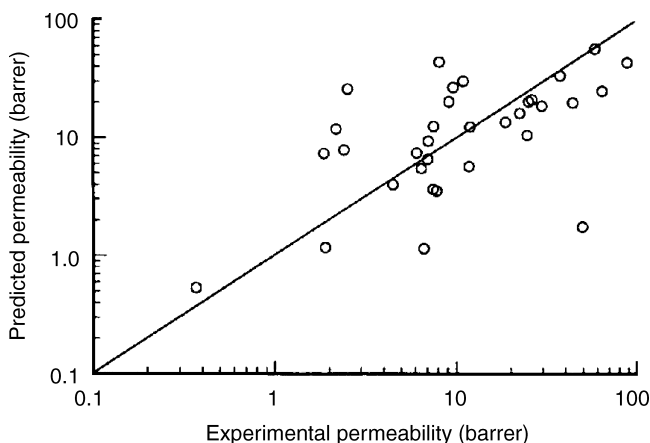


Figure 7.9 Comparison of the permeabilities of different polymers for CO₂, predicted (neural network approach) and experimental [61]. Reproduced by permission of Matthias Wessling from *Relaxation Phenomena in Dense Gas Separation Membranes*, PhD Thesis, Twente University, Twente, The Netherlands (1993)

theory are, as a rule, less accurate than, for example, predictions using the group contribution methods. However, rapid improvements in force fields which characterize polymer matrices and the software used in calculations lead one to expect that during the next decade they will successfully compete with other methods for predictions considered in this present chapter.

Since rubbery membrane materials are in thermodynamic equilibrium, many uncertainties of atomistic modeling are eliminated and even the current predictions of the transport parameters are impressively accurate. Table 7.4 shows, as an example, a comparison of the predicted and experimental permeability, solubility and diffusion coefficients of gaseous hydrocarbons in

polydimethylsilimethylene, a rubber with a T_g of -92°C [62]. A good agreement between the predicted and experimental parameters seems to be a consequence of the very efficient united-atom force field used in molecular dynamics simulation of this polymer.

In contrast to rubbery materials, up until now there exist only relatively few successful modeling results concerning the structure and gas transport parameters of glassy polymers. One of the major problems here is equilibration of the systems, which requires very long computation times. There are additional difficulties in comparisons with experimentally measured permeabilities because of inherent features of glassy polymer films related to the effects of film-casting

Table 7.4 Permeability coefficients P (barrer), solubility coefficients S ($\text{cm}^3(\text{STP})/(\text{cm}^3 \text{atm})$) and diffusion coefficients D (cm^2/s) of hydrocarbons in polydimethylsilimethylene [62]. Reprinted from *Polymer*, **45**, A. Alentiev, I. G. Economou, E. Finkelshtein, J. Petrou, V. E. Raptis, M. Sanopoulou, S. Soloviev, N. Ushakov and Yu. Yampolskii, 'Transport properties of silimethylene homopolymers and random copolymers: experimental measurements and molecular simulation', pp. 6933–6944, Copyright (2004), with permission from Elsevier

Parameter	CH ₄	C ₂ H ₆	C ₃ H ₈	<i>n</i> -C ₄ H ₁₀
P_{exp}	130	345	434	1360
P_{pred}	100	262	555	1240
S_{exp}	0.33	1.73	6.2	22.1
S_{pred}	0.33	1.4	3.7	10
$D_{\text{exp}} \times 10^7$	30	15	5.3	4.7
$D_{\text{pred}} \times 10^7$	23	14.2	11.4	9.4

Table 7.5 Permeability coefficients P (barrer), solubility coefficients S ($\text{cm}^3(\text{STP})/(\text{cm}^3 \text{ atm})$) and diffusion coefficients D (cm^2/s) of light gases in polytrimethylsilylpropyne (PTMSP) and 6FDA-durene polyimide (PI): predicted [63,64] and experimental [65,66] values

Parameter	O ₂	N ₂	CH ₄
<i>PTMSP</i> [64,65]			
P_{exp}	7700	5000	13 000
P_{pred}	13 800	11 600	30 000
S_{exp}	1.26	1.08	3.74
S_{pred}	1.4	1.16	2.8
$D_{\text{exp}} \cdot 10^{-5}$	4.7	3.5	2.6
$D_{\text{pred}} \cdot 10^{-5}$	7.5	7.6	8.2
<i>PI</i> [63,66]			
P_{exp}	122	36	28
P_{pred}	500	160	160
S_{exp}	1.4	1.1	2.2
S_{pred}	3.6 ± 0.3	2.5 ± 0.2	11 ± 1
$D_{\text{exp}} \times 10^{-7}$	6.6	2.3	0.96
$D_{\text{pred}} \times 10^{-7}$	10.6 ± 7.9	4.9 ± 4.5	1.1 ± 0.1

protocols, the presence of residual solvents and some peculiarities of the non-equilibrium states of polymers below the T_g . Table 7.5 gives two recent examples of computer simulation of the transport and sorption parameters of light gases in glassy polymers [63,64]. In both cases, the modeling resulted in determination of the solubility and diffusion coefficients, while the permeability coefficient P was found as the product (DS).

The two considered polymers illustrate different trends that can be encountered in computer simulations of glassy polymers. For PTMSP, the predicted solubility coefficients agree with the experimental ones much better than the corresponding diffusion coefficients, and so the total deviations between P_{exp} and P_{pred} are caused mainly by the differences in diffusivity. An opposite situation is observed for the 6FDA-durene polyimide. For example, D_{exp} and D_{pred} of methane in this polymer nearly coincide and all the differences in the P values are induced by uncertainty in S_{pred} . It is rather difficult to find specific reasons for such deviations in particular cases. Even relatively small errors of the particle insertion energies employed in modeling, which are determined by the quality of the model, may lead to fairly high errors for D_{pred} and S_{pred} . At present, it is generally accepted to consider a coincidence between the measured and simulated diffusivity

and solubility values within a factor of 3–5 as being reasonable [63].

7.6 Conclusions

We have considered various contemporary methods for the prediction of gas permeation parameters. The most refined one at present is the group contribution (or additivity) method. The accuracy of prediction when using this for a sufficiently large and adequate basic set of polymers approaches today the level of ‘noise’ of the reported values of the permeability coefficients. Therefore, further improvements in the scheme of prediction within the framework of this approach will hardly lead to significant progress and does not seem to be reasonable. On the other hand, these methods are incapable of explaining large deviations from the mean values of P_i which are often encountered; meanwhile, such deviations are probably the most interesting for development of membrane materials for the ‘next generation’. In addition, predictions can be made only for polymers assembled from the same “building blocks” as the polymers from the basic set used in computation of the group contributions. In other words, predictions cannot be made for polymers with an “innovative” design of repeat units. Thus, although development of the methods for prediction of the transport parameters helps to diminish or even replace much

of the synthetic and physico-chemical efforts required to optimize gas-separation membranes, it does not cancel out any random search or chemical intuition in the strategy of directed synthesis or search for improved materials.

References

- [1] W. L. Robb, 'Silicon membranes; their permeability and applications', *Ann. NY Acad. Sci.*, **146**, 119–137 (1968).
- [2] S. A. Reutlinger, *Permeability of Polymeric Materials*, Khimiya, Moscow, USSR (1974) (in Russian).
- [3] S. M. Allen, M. Fujii, V. Stannett, H. B. Hopfenberg and J. A. Willims, The Barrier properties of polyacrylonitrile, *J. Membr. Sci.*, **2**, 153–163 (1977).
- [4] W. J. Koros and G. K. Fleming, 'Membrane based gas separation', *J. Membr. Sci.*, **82**, 1–80 (1993).
- [5] S. A. Stern, 'Polymers for gas separation', *J. Membr. Sci.*, **94**, 1–65 (1994).
- [6] D. R. Paul and Yu. P. Yampolskii (Eds), *Polymeric Gas Separation Membranes*, CRC Press, Boca Raton, FL, USA (1994).
- [7] A. V. Topchiev, N. S. Nametkin, S. Tsu, S. G. Durgaryan and N. A. Kuzmina, 'Polymerization of monovinylalkyl(phenyl) derivatives of silicon in the presence of ethyl lithium', *Izv. Acad. Sci. USSR*, 1497–1498 (1962).
- [8] V. F. Gustov, L. N. Chekalov, O. G. Talakin, D. A. Ivashchenko, S. G. Durgaryan and E. G. Novitskii, 'Study of gas permeability of polymeric membranes', 1st All-Union Conference, *Membrane Methods for Mixture Separation*, Moscow, USSR, Abstracts, pp. 175–177 (1973).
- [9] A. S. Michaels and H. J. Bixler, 'Flow of gases through polyethylene', *J. Polym. Sci.*, **50**, 413–439 (1961).
- [10] N. A. Plate, S. G. Durgaryan, V. S. Khotimskii, V. V. Teplyakov and Yu. P. Yampolskii, 'Novel poly(siliconolefins) for gas separation', *J. Membr. Sci.*, **52**, 289–304 (1990).
- [11] A. C. Puleo, N. Miruganandam and D. R. Paul, 'Gas sorption and transport in substituted polystyrenes', *J. Polym. Sci. Part B: Polym. Phys. Ed.*, **27**, 2385–2406 (1989).
- [12] V. S. Khotimskii, V. G. Fillipova, I. S. Bryantseva, V. I. Bondar, V. P. Shantarovich and Yu. P. Yampolskii, 'Synthesis, transport and sorption properties and free volume of polystyrene derivatives containing Si and F', *J. Appl. Polym. Sci.*, **78**, 1612–1620 (2000).
- [13] K. E. Min and D. R. Paul, 'Effect of tacticity on permeation properties of poly(methyl methacrylate)', *J. Polym. Sci. Part B: Polym. Phys. Ed.*, **26**, 1021–1033 (1988).
- [14] J. Li, K. Tashihara, K. Nagai and T. Nakagawa, 'Selective permeation of sour gases through polymeric membranes modified by sulfonates. I. Study of selective permeation of CO₂ through modified polymeric membranes determined on different systems', *J. Appl. Polym. Sci.*, **60**, 1645–1654 (1996).
- [15] V. I. Bondar, Yu. M. Kukharskii, Yu. P. Yampolskii, E. Sh. Finkelshtein and K. L. Makovetskii, 'Permeation and sorption of polynorbomenes with organosilicon substituents', *J. Polym. Sci. Part B: Polym. Phys. Ed.*, **31**, 1273–1283 (1993).
- [16] E. Sh. Finkelshtein, M. L. Gringolts, N. V. Ushakov, V. G. Lakhtin, S. A. Soloviev and Yu. P. Yampol'skii., 'Synthesis and gas permeation properties of new ROMP polymers from silicon substituted norbornadienes and norbornenes', *Polymer*, **44**, 2843–2851 (2003).
- [17] G. Perego, A. Roggero, R. Sisto and C. Valentini, 'Membranes for gas separation based on silylated polyphenylene oxide', *J. Membr. Sci.*, **55**, 325–331 (1991).
- [18] H.-J. Kim and S.-I. Hong, 'The transport properties of CO₂ and CH₄ for chemically modified polysulfones', *J. Appl. Polym. Sci.*, **76**, 391–400 (2000).
- [19] T. Masuda, E. Isobe, T. Higashimura and K. Takada, 'Poly[1-trimethylsilyl]-1-propyne]: a new high polymer synthesized with transition-metal catalysts and characterized by extremely high gas permeability', *J. Am. Chem. Soc.*, **105**, 7473–7474 (1983).
- [20] M. R. Pixton and D. R. Paul, Relationship between structure and transport properties for polymers with aromatic backbones, in D. R. Paul and Yu. P. Yampolskii (Eds.), *Polymeric Gas Separation Membranes*, CRC Press, Boca Raton, FL, USA, pp. 83–153 (1994).
- [21] K. Tanaka, M. Okano, H. Toshino, H. Kita and K. Okamoto, 'Effect of methyl substituents on permeability and permselectivity of gases in polyimides prepared from methyl-substituted phenylenediamines', *J. Polym. Sci. Part B: Polym. Phys. Ed.*, **30**, 907–914 (1992).
- [22] K. Ghosal, A. Morisato, B. D. Freeman, R. T. Chern, J. C. Alvarez, J. G. de la Campa and J. de Abajo, 'Synthesis and gas separation properties of a family of new aromatic polyamides for petrochemical application', *Polym. Prepr., Am. Chem. Soc., Div. Polym. Chem.*, **35**, 731 (1994).
- [23] M. R. Pixton and D. R. Paul, 'Gas transport properties of polyarylates: substituent size and symmetry effects', *Macromolecules*, **28**, 8277–8286 (1995).
- [24] I. Kresse, A. Usenko, J. Springer and V. Privalko, 'Gas transport properties of soluble poly(amide imide)s', *J. Polym. Sci. Part B: Polym. Phys. Ed.*, **37**, 2183–2193 (1999).

- [25] Y. Hirayama, T. Yoshinaga, Y. Kusuki, K. Ninomiya, T. Sakakibara and T. Tamari, 'Relation of gas permeability with structure of aromatic polyimides I', *J. Membr. Sci.*, **111**, 169–192 (1996).
- [26] Y. Hirayama, T. Yoshinaga, S. Nakanishi and Y. Kusuki, 'Relation between gas permeabilities and structure of polyimides', in B. D. Freeman and I. Pinnau (Eds), *Polymer Membranes for Gas and Vapor Separation*, ACS Symposium Series 733, American Chemical Society, Washington, DC, USA, pp. 194–214 (1999).
- [27] G. J. Van Amerongen, 'Diffusion in elastomers', *Rubber Chem. Technol.*, **37**, 1065–1152 (1964).
- [28] A. R. Berens and H. B. Hopfenberg, 'Diffusion of organic vapors at low concentration in glassy polyvinylchloride, polystyrene and polymethylmethacrylate', *J. Membr. Sci.*, **10**, 283–303 (1982).
- [29] V. V. Teplyakov and P. Meares, 'Correlation aspects of the selective gas permeabilities of polymeric materials and membranes', *Gas Sepn Purif.*, **4**, 66–73 (1990).
- [30] Y. Yampolskii, D. Wiley and C. Maher, 'Novel correlation for solubility of gases in polymers: effect of molecular surface area of gases', *J. Appl. Polym. Sci.*, **76**, 552–560 (2000).
- [31] N. F. A. van der Vegt, 'A molecular dynamics simulation study of solvation thermodynamic quantities of gases in polymeric solvents', *J. Membr. Sci.*, **205**, 125–139 (2002).
- [32] W. M. Lee, 'Selection of barrier materials from molecular structure', *Polym. Eng. Sci.*, **20**, 65–69 (1980).
- [33] Y. Maeda and D. R. Paul, 'Effect of antiplasticization on gas sorption and transport. III. Free volume interpretation', *J. Polym. Sci. Part B: Polym. Phys. Ed.*, **25**, 1005–1016 (1987).
- [34] J. Y. Park and D. R. Paul, 'Correlation and prediction of gas permeability in glassy polymer membrane materials via a modified free volume based group contribution method', *J. Membr. Sci.*, **125**, 23–39 (1997).
- [35] Yu. P. Yampolskii and S. M. Shishatskii, 'On some regularities of diffusivity and permeability of glassy polymers', *Dokl. Akad. Nauk SSSR*, **318**, 653–656 (1991).
- [36] L. A. Pilato, L. M. Lutz, B. Hargitay, A. G. Farnham, J. H. Kawakami, P. E. Frotze and J. E. McGrath, 'Polymers for permselective membrane gas separation', *Polym. Prepr., Am. Chem. Soc., Div. Polym. Chem.*, **16** (2), 41–53 (1975).
- [37] S. G. Charati, A. Y. Houde, S. S. Kulkarni and M. G. Kulkarni, 'Transport of gases in aromatic polyesters: correlation with WAXD studies', *J. Polym. Sci. Part B: Polym. Phys. Ed.*, **29**, 921–31 (1991).
- [38] L. Jia and J. Xu, 'A simple method for prediction of gas permeability of polymers from their molecular structure', *Polym. J.*, **23**, 417–421 (1991).
- [39] D. W. Van Krevelen, *Properties of Polymers*, Elsevier, Amsterdam, The Netherlands, 1st Ed. (1972); 3rd Ed. (1990).
- [40] Yu. P. Yampolskii, S. G. Durgaryan and N. S. Nametkin, 'Translational and rotational mobility of low molecular weight compounds in polymers with different glass transition temperatures', *Vysokomol. Soed., A*, **24**, 536–541 (1982).
- [41] K. Matsumoto, P. Xu and T. Nishikami, 'Gas permeation of aromatic polyimides. I. Relationship between gas permeabilities and dielectric constants', *J. Membr. Sci.*, **81**, 15–22 (1993).
- [42] S. W. Benson, *Thermochemical Kinetics*, John Wiley & Sons, Inc., New York, NY, USA (1968).
- [43] M. Salame, *Polym. Prepr., Am. Chem. Soc., Div. Polym. Chem.*, **8**, 137–144 (1967).
- [44] M. Salame and S. Steingiser, 'Barrier polymers', *Polym. Plast. Technol. Eng.*, **8**, 155 (1977).
- [45] M. Salame, 'Prediction of gas barrier properties of high polymers', *Polym. Eng. Sci.*, **26**, 1543–1546 (1986).
- [46] M. Salame, 'The prediction of liquid permeation in polyethylene and related polymers', *SPE Trans.*, (October 1961), 153–163.
- [47] L. M. Robeson, C. D. Smith and M. Langsam, 'A group contribution approach to predict permeability and permselectivity of aromatic polymers', *J. Membr. Sci.*, **132**, 33–54 (1997).
- [48] D. V. Laciak, L. M. Robeson and C. D. Smith, 'Group contribution modeling of gas transport in polymeric membranes', in B. D. Freeman and I. Pinnau (Eds), *Polymer Membranes for Gas and Vapor Separation*, ACS Symposium Series 733, American Chemical Society, Washington, DC, USA, pp. 151–177 (1999).
- [49] Yu. Yampolskii, S. Shishatskii, A. Alentiev and K. Loza, 'Group contribution method for transport property prediction of glassy polymers: focus on polyimides and polynorbornenes', *J. Membr. Sci.*, **149**, 203–220 (1998).
- [50] Yu. Yampolskii, S. Shishatskii, A. Alentiev and K. Loza, 'Correlation with and prediction of activation energies of gas permeation and diffusion in glassy polymers', *J. Membr. Sci.*, **148**, 59–69 (1998).
- [51] A. Alentiev, K. Loza and Yu. Yampolskii, 'Development of the methods for prediction of gas permeation parameters of glassy polymers: polyimides as alternating copolymers', *J. Membr. Sci.*, **167**, 91–106 (2000).
- [52] 'Gas Permeation Parameters of Glassy Polymers', Database, No. 3585, Informregistr RF, Moscow (1998).

- [53] L. M. Robeson, 'Correlation of separation factor versus permeability for polymeric membranes', *J. Membr. Sci.*, **62**, 165–185 (1991).
- [54] A. Yu. Alentiev, Yu. P. Yampolskii, A. L. Rusanov, D. Yu. Likhachev, G. V. Kazakova, L. G. Komarova and M. P. Prigozhina, 'Transport properties of polyetherimides', *Polym. Sci. A*, **45**, 933–939 (2003).
- [55] M. R. Surgi, A. J. Polak and R. C. Sundhal, 'Description of oxygen permeability in various high polymers using a graph theoretical approach', *J. Polym. Sci. Part A: Polym. Chem. Ed.*, **27**, 2761–2776 (1989).
- [56] J. Bicerano, *Prediction of Polymer Properties*, Marcel Dekker, New York, NY, USA (1996).
- [57] L. B. Kier and L. H. Hall, *Molecular Connectivity in Chemistry and Drug Research*, Academic Press, New York, NY, USA (1976).
- [58] M. Randic, 'On characterization of molecular branching', *J. Am. Chem. Soc.*, **97**, 6609–6615 (1975).
- [59] C. Zhong and C. Yang, 'Approach for the calculation of high order connectivity indices of polymers and its application', *J. Polym. Sci. Part B: Polym. Phys. Ed.*, **40**, 401–407 (2002).
- [60] J. Zupan and J. Gasteiger, *Neural Network for Chemists*, VCH, Weinheim, Germany (1996).
- [61] M. Wessling, *Relaxation Phenomena in Dense Gas Separation Membranes*, PhD Thesis, Twente University, Twente, The Netherlands (1993).
- [62] A. Alentiev, I. G. Economou, E. Finkelshtein, J. Petrou, V. E. Raptis, M. Sanopoulou, S. Soloviev, N. Ushakov and Yu. Yampolskii, 'Transport properties of silmethylene homopolymers and random copolymers: experimental measurements and molecular simulation', *Polymer*, **45**, 6933–6944 (2004).
- [63] M. Heuchel, D. Hofmann and P. Pullumbi, 'Molecular modeling of small-molecule permeation and its correlation to free-volume distributions', *Macromolecules*, **37**, 201–214 (2004).
- [64] D. Hofmann, M. Heuchel, Yu. Yampolskii, V. Khotimskii and V. Shantarovich, 'Free volume distribution in ultrahigh and lower free volume polymers: comparison between molecular modeling and positron lifetime studies', *Macromolecules*, **35**, 2129–2140 (2002).
- [65] Y. Ichiraku, S. A. Stern and T. Nakagawa, 'An investigation of the high gas permeability of poly(1-trimethylsilyl-1-propyne)', *J. Membr. Sci.*, **34**, 5–18 (1987).
- [66] K. Tanaka, M. Okano, H. Toshino, H. Kita and K. Okamoto, 'Effect of methyl substituents on permeability and permselectivity of gases in polyimides prepared from methyl-substituted phenylenediamines', *J. Polym. Sci. Part B: Polym. Phys. Ed.*, **30**, 907–914 (1992).

Synthesis and Permeation Properties of Substituted Polyacetylenes for Gas Separation and Pervaporation

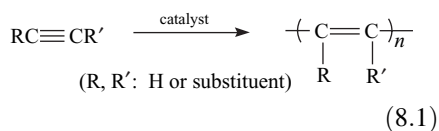
Toshio Masuda and Kazukiyo Nagai

8.1 Introduction

A variety of polymers have been investigated as membrane materials for gas separation and pervaporation. At present, many data are available regarding the gas permeability, gas permeation mechanism and pervaporation behavior of many conventional polymers. From the practical viewpoint, some highly permeable polymers, such as polydimethylsiloxane and highly permselective polymers, such as polyimides, have already been used in industry. There is a large possibility that the discovery of new polymeric materials that feature high permeability or permselectivity will lead to the development of new separation membrane science and technology.

Since 1974, when the synthesis of a high-molecular-weight polymer from phenylacetylene, a substituted acetylene, was achieved with WCl_6 , various substituted acetylenes have been polymerized by so-called metathesis catalysts (W, Mo, Ta and Nb) into high-molecular-weight polymers (Equation (8.1)) [1]. Free-standing membranes for the separation of gases and liquids have been successfully prepared from more than 70 substituted polyacetylenes so far [2]. Among these substituted polyacetylenes, poly[1-(trimethylsilyl)-1-propyne] (poly(TMSP)) is the most permeable polyacetylene known to date. More importantly, poly(TMSP) exhibits the highest gas

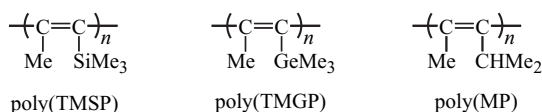
permeability of all known synthetic polymers. Its oxygen permeability coefficient (P_{O_2}) is ca. 6000 barrer (1 barrer = 1×10^{-10} cm³(STP) cm/(cm² s cmHg)) at 25 °C [3]. The extremely high gas permeability of poly(TMSP) prompted many researchers to investigate its possible use as a separation membrane material. An in-depth review of journal articles and important patents on poly(TMSP) is available [2].



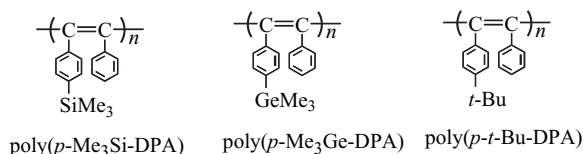
Since the discovery of poly(TMSP) in 1983 [3], the unique properties of this polymer have motivated the synthesis and characterization of other, highly gas-permeable substituted polyacetylenes. Table 8.1 shows representative gas-permeable substituted polyacetylenes. All of these substituted polyacetylenes are more 'gas-permeable' than or similar to polydimethylsiloxane, the most permeable commercial membrane material. Two polyacetylenes, poly[1-(trimethylgermyl)-1-propyne] (poly(TMGP)) [4,5a,5b] and poly(4-methyl-2-pentyne) (poly(MP)) [6a,6b], also have very high oxygen permeability values,

Table 8.1 Representative gas-permeable substituted polyacetylenes

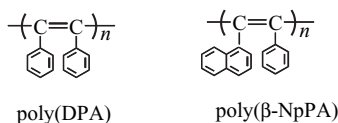
(a) Poly(TMSP) and its analogues



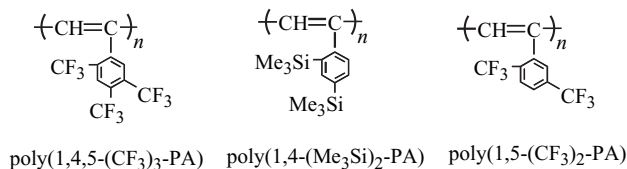
(b) Ring-substituted polydiphenylacetylenes



(c) Polydiarylacetylenes



(d) Ring-substituted polyphenylacetylenes



i.e. 1800 and 2700 barrer, respectively. Furthermore, the concept that a stiff main chain and bulky side-groups are both essential for a polymer to have high gas permeability stimulated the synthesis of poly[1-phenyl-2-(*p*-trimethylsilylphenyl)acetylene] (poly(*p*-Me₃Si-DPA)) [7,8] and its trimethylgermyl and *tert*-butyl homologues, (poly(*m*-Me₃Ge-DPA)) [9] (poly(*p*-*t*-Bu-DPA)) [10], both of which exhibit high and similar oxygen permeabilities up to around 1500 barrer. This has revealed that membranes of polydiphenylacetylene (poly(DPA)) and poly(1- β -naphthyl-2-phenylacetylene) (poly(β -NpPhA)), which are obtained by the desilylation of *p*-trimethylsilyl derivatives, are very permeable to oxygen (P_{O_2} = 4000 – 6000 barrer) [11,12].

Among polymers from monosubstituted acetylenes, poly[2,4,5-tris-(trifluoromethyl)-phenylacetylene] (poly(2,4,5-(CF₃)₃-PA)) [13] (P_{O_2} = 780 barrer) and other ring-substituted polyphenylacetylenes, such as poly(2,4-(Me₃Si)₂-PA) and poly(2,5-(CF₃)₂-PA), are known to be very permeable to oxygen [13,14].

Interestingly some of these highly permeable substituted polyacetylenes show permeation properties ‘opposite’ to other glassy polymers [2]. In general, the gas permeabilities of common glassy polymers decrease with increasing penetrant size, based on a strong ‘size-sieving’ effect. The selectivity of a small molecule to a large molecule is then always greater than 1. Most of the substituted polyacetylenes obey this behavior; however,

some of them show the opposite behavior. The gas permeability increases with increasing penetrant size. Substituted polyacetylenes are able to be designed to have both 'small-molecule-selective' membranes and 'large-molecule-selective' membranes by choosing their substituents. The same trend is found for separation of liquids by pervaporation. For instance, in the case of separation of ethanol–water mixtures, substituted polyacetylenes show either 'ethanol-selective' or 'water-selective' behavior. The substituted polyacetylenes are a rare family of polymers having both selectivities within the family. Other interesting permeation properties, such as a decline in gas permeability, have been summarized for poly(TMSP) in a recent review article [2] (see also Chapter 11).

This chapter deals with the synthesis and separation properties of polyacetylene membranes having substituents (substituted polyacetylenes) as potential materials bearing such a capability. The sources of feed components for separation focused on herein are gas–gas mixtures, gas–vapor mixtures and vapor–vapor mixtures for gas separation and alcohol–water mixtures, organic liquid–water mixtures and organic liquid–organic liquid mixtures for liquid separation by pervaporation.

8.2 Polymer Synthesis

8.2.1 General Features of the Polymerization

Readers are encouraged to access other reviews and monographs on the synthesis of substituted polyacetylenes [1,2,15–20]. Table 8.2 shows

typical acetylenic monomers that provide high-molecular-weight polymers. The unsubstituted acetylene can be polymerized in the presence of $\text{Ti}(\text{O}-n\text{-Bu})_4\text{-Et}_3\text{Al}$ by the Shirakawa method.

Various monosubstituted acetylenes, not only hydrocarbons but also heteroatom-containing materials, and furthermore, not only sterically unhindered monomers but very 'crowded' ones as well, polymerize when suitable catalysts are chosen. For instance, sterically 'uncrowded' acetylenes, such as *n*-alkylacetylenes, polymerize well with Ziegler–Natta type-catalysts, whereas 'crowded' monomers, such as *tert*-butylacetylene and *ortho*-substituted phenylacetylenes, give polymers in the presence of Mo and W catalysts. Phenylacetylene and alkyl propiolates polymerize with Rh catalysts to yield stereoregular polymers.

A variety of disubstituted acetylenes are also polymerizable. The catalysts effective for them, however, are virtually restricted to Groups 5 and 6 transition-metal catalysts. Disubstituted monomers with less steric hindrance (e.g. *n*-dialkylacetylenes and 1-chloro-1-alkynes) tend to polymerize with Mo and W catalysts, while their sterically 'crowded' counterparts (e.g. 1-(trimethylsilyl)-1-propyne and diphenylacetylenes) polymerize only with Nb and Ta catalysts. The details will be discussed below.

Table 8.3 lists typical transition-metal catalysts used for the polymerization of acetylenes. The monomer types polymerizable with a particular catalyst are rather restricted; hence, it is important to recognize the characteristics of each catalyst. The catalysts for substituted acetylenes are roughly divided into two kinds: Groups 5 and 6

Table 8.2 Acetylenes which form high-molecular-weight polymers

Type	Unsubstituted	Monosubstituted	Disubstituted
Hydrocarbon	$\text{HC}\equiv\text{CH}$	$\text{HC}\equiv\text{C}-n\text{-Bu}$	$\text{MeC}\equiv\text{C}-n\text{-C}_3\text{H}_{11}$
		$\text{HC}\equiv\text{C}-t\text{-Bu}$	$\text{MeC}\equiv\text{C}-\text{C}_6\text{H}_5$
		$\text{HC}\equiv\text{C}-\text{C}_6\text{H}_4$	$\text{C}_6\text{H}_5-\text{C}\equiv\text{C}-\text{C}_6\text{H}_4-t\text{-Bu}$
Heteroatom-containing	—	$\text{HC}\equiv\text{C CO}_2-n\text{-Bu}$	$\text{ClC}\equiv\text{C}-n\text{-C}_6\text{H}_{13}$
		$\text{HC}\equiv\text{C}-\text{C}_6\text{H}_4-\text{SiMe}_3$	$\text{ClC}\equiv\text{C}-\text{C}_6\text{H}_5$
		$\text{HC}\equiv\text{C}-\text{C}_6\text{H}_4-\text{CF}_3$	$\text{MeC}\equiv\text{CSiMe}_3$
		$\text{C}_6\text{H}_5-\text{C}\equiv\text{C}-\text{C}_6\text{H}_4-\text{SiMe}_3$	

Table 8.3 Typical catalysts for the polymerization of acetylenes

Group	4	5	6	8–10
Catalyst (monomer ^a) (HC≡CH)	Ti(O- <i>n</i> -Bu) ₄ -Et ₃ Al	NbCl ₅ , TaCl ₅ (RC≡CR')	MoCl ₅ - <i>n</i> -Bu ₄ Sn, WCl ₆ -Ph ₄ Sn (HC≡CR, RC≡CR')	Fe(acac) ₃ -Et ₃ Al (HC≡CR)
		TaCl ₅ - <i>n</i> -Bu ₄ Sn (PhC≡CC ₆ H ₄ - <i>p</i> -X)	M(CO) ₆ -CCl ₄ - <i>hν</i> (M = Mo, W) (HC≡CR, ClC≡CR)	[(<i>nbd</i>)RhCl] ₂ (HC≡CPh, HC≡CCO ₂ R)

^aHC≡CR and RC≡CR' denote mono- and disubstituted acetylenes, respectively.

transition-metal (metathesis) catalysts and Groups 8 to 10 transition-metal catalysts.

Polymerization of substituted acetylenes when using Groups 5 and 6 transition-metal catalysts proceeds by the metathesis mechanism in which the propagating species is the metal carbene. Groups 5 and 6 transition-metal catalysts can be classified into several types: (i) metal-chloride-based catalysts, (ii) metal-carbonyl-based catalysts and (iii) metal carbene catalysts. Among these, metal-chloride-based catalysts are the most convenient and active. MoCl₅ and WCl₆ are useful for polymerizing various monosubstituted acetylenes, especially those with bulky substituents (e.g. HC≡C-*t*-Bu and HC≡CC₆H₄-*o*-SiMe₃). When these catalysts are combined with suitable organometallic cocatalysts (e.g. *n*-Bu₄Sn, Ph₄Sn and Et₃SiH), they polymerize not only monosubstituted but also disubstituted monomers. In contrast, NbCl₅ and TaCl₅ are effective catalysts for polymerizing disubstituted acetylenes. Only binary catalyst systems composed of TaCl₅ and a cocatalyst polymerize di-

phenylacetylenes, which are sterically very 'crowded'.

Groups 8 to 10 transition-metal catalysts include Fe(acac)₃-Et₃Al (acac, acetylacetonate) and (*nbd*-RhCl)₂ (*nbd*, 2,5-norbornadiene). Fe(acac)₃-Et₃Al is an inhomogeneous catalyst which polymerizes *n*-alkyl-, *sec*-alkyl- and phenylacetylenes. Rh catalysts polymerize phenylacetylene and alkyl propiolates in various solvents, including alcohols and amines, to give *cis-trans* polymers.

8.2.2 Poly[1-(trimethylsilyl)-1-propyne] and its Analogues

Table 8.4 shows effective catalysts for the polymerization of TMSP [21]. Halides of Ta(v) and Nb(v), specifically TaCl₅, TaBr₅, NbF₅, NbCl₅ and NbBr₅, provide poly(TMSP) in high yields. The poly(TMSP) product obtained with TaCl₅, TaBr₅ and NbCl₅ is completely soluble in toluene and has a *M_w* value (for TaCl₅-synthesized polymers) as high as several hundred thousand, which is confirmed by high intrinsic viscosity values.

Table 8.4 Polymerization of 1-(trimethylsilyl)-1-propyne (TMSP) by halides of niobium and tantalum^a

Number	Catalyst	Polymer			
		Yield (%)	<i>M_n</i> /10 ⁴ ^b	<i>M_w</i> /10 ⁴ ^b	[η] (dL/g) ^c
1	TaF ₅	0	—	—	—
2	TaCl ₅	100	13	73	5.43
3	TaBr ₅	95	11	41	3.80
4	TaI ₅	0	—	—	—
5	NbF ₅	94 ^d	—	—	—
6	NbCl ₅	100	21	31	0.71
7	NbBr ₅	100 ^e	11	28	0.63
8	NbI ₅	0	—	—	—

^aPolymerized in toluene at 80 °C for 24 h; [M]₀ = 1.0 M, [Cat.] = 20 mM.

^bDetermined by gel permeation chromatograph (GPC).

^cMeasured in toluene at 30 °C.

^dCompletely insoluble in toluene.

^ePartly insoluble (~ 20 %) in toluene.

Table 8.5 Solvent effect on the polymerization of TMSP by TaCl₅ and NbCl₅^a

Solvent	Yield (%)	Polymer	
		$M_n/10^{4b}$	$M_w/10^{4b}$
<i>TaCl₅ catalyst</i>			
Toluene	100	13	73
Cyclohexane	100	21	95
Heptane	62	17	78
CCl ₄	31	1.1	3.8
(CH ₂ Cl) ₂	100	3.2	25
PhCl	62	14	39
<i>NbCl₅ catalyst</i>			
Toluene	100	21	31
Cyclohexane	86	6.2	7.8
Heptane	59	20	30
CCl ₄	96	7.5	13
(CH ₂ Cl) ₂	100 ^c	—	—
PhCl	59	22	35

^aPolymerized at 80 °C for 24 h: [M]₀ = 1.0 M; [Cat.] = 20 mM.

^bDetermined by GPC.

^cCompletely insoluble in toluene.

TaF₅, TaI₅ and NbI₅ exhibit no catalytic activity because no monomer is consumed in the presence of these metal halides.

The effect of solvent type on the polymerization of TMSP is shown in Table 8.5. In general, hydrocarbon and halogenated hydrocarbon solvents achieve good polymer yields. Aromatic hydrocarbons, such as toluene, are especially favorable because they dissolve both catalyst and polymer well and keep the propagating species sufficiently active due to their low coordinating ability and low reactivity toward the propagating species. The M_w of the polymer is the highest when TMSP is polymerized with TaCl₅ in hydrocarbon solvents. In most solvents, TaCl₅ gives polymer with higher molecular weights than NbCl₅.

Regarding the effect of temperature on the polymerization of TMSP, the polymer can be obtained with nearly 100 % yield over the temperature range 30–100 °C with TaCl₅ or NbCl₅. Its M_w exhibits a maximum of ca. 7×10^5 at 80 °C when TaCl₅ is used but does not change very much with temperature when NbCl₅ is used.

Polymerization of TMSP by TaCl₅ in toluene at 80 °C approaches 100 % yield in approximately 1 h. The intrinsic viscosity is essentially constant

at 5.0–5.5 dL/g during the entire polymerization time, indicating the formation of high-molecular-weight polymer and no polymer degradation. Polymerization of TMSP by NbCl₅ also reaches a polymer yield of 100 % in 1 h. In this case, the intrinsic viscosity of the polymer is appreciably smaller (ca. 0.7 dL/g) and, except during the initial stage, hardly changes over the course of the polymerization.

Based on the results described above, standard conditions for the preparation of poly(TMSP) are as follows: TaCl₅, in toluene, 80 °C, 24 h, [TMSP]₀ = 1.0 M, [TaCl₅]₀ = 20 mM. Under these polymerization conditions, a quantitative yield of poly(TMSP) having $M_w = 73 \times 10^4$ and $M_n = 13 \times 10^4$ can be obtained. Further details of the polymerization procedure are available in the literature [21,22]. Polymer samples prepared by this procedure have been used most frequently for studies of poly(TMSP).

In the course of a study on cocatalyst effects on polymerization, it was found that the TaCl₅–Ph₃Bi catalyst system produces poly(TMSP) with extremely high M_w (up to 4×10^6) [23]. Addition of the cocatalyst Ph₃Bi appreciably accelerates the polymerization reaction, allowing 100 % yield to be achieved within 30 min under the standard conditions. Addition of this cocatalyst increases the M_w of the polymer five-fold, indicating that a more active propagating species forms in smaller quantity in this system than in the system with TaCl₅ alone. When the cocatalyst Ph₃Bi is used with NbCl₅, an insoluble poly(TMSP) is formed. The polymer formed using TaCl₅–Ph₃Bi has $M_w = 4 \times 10^6$, $M_n = 1.8 \times 10^6$ and intrinsic viscosity $[\eta] = 13.2$ dL/g (in toluene, 30 °C). These data are higher than those of other substituted polyacetylenes. Thus, by using a suitable catalyst system, poly(TMSP) with a M_w of several hundred thousand to several million can be easily obtained.

In a study of the influence of solvent on the polymerization of TMSP, it was found that a catalyst/solvent combination of NbCl₅ and cyclohexane produces a polymer with a rather narrow molecular weight distribution (MWD) [24]. Under these polymerization conditions, M_n increases in direct proportion to monomer conversion, while the MWD of the polymer remains narrow (M_w/M_n , ca. 1.2) irrespective of conversion. By changing the monomer-to-catalyst ratio, poly(TMSP) having a narrow MWD and M_n

Table 8.6 Polymerization of TMSP analogues, $\text{CH}_3\text{C}\equiv\text{CXR}_1\text{R}_2\text{R}_3^a$

X/R ₁ /R ₂ /R ₃	Catalyst	Yield (%)	$M_w \times 10^{-3}^b$
Si/Et/Et/Et	TaCl ₅ -Ph ₄ Sn	25	510
Si/Me/Me/ <i>n</i> -C ₆ H ₁₃	TaCl ₅ -Ph ₃ Bi	75	1400
Si/Me/Me/Ph	TaCl ₅ -Ph ₄ Sn	15	460
Si/Me/Me/ -CH ₂ Si(CH ₃) ₃	TaCl ₅	100	1500
Si/Me/Me/ -CH ₂ CH ₂ Si(CH ₃) ₃	TaCl ₅ -Ph ₄ Sn	58	400
Ge/Me/Me/Me	TaCl ₅	82	1400
C/H/Me/Me	TaCl ₅	70	—

^aPolymerizations were performed in toluene at 80 °C for 24 h: [M]₀ = 1.0 M; [TaCl₅] = [cocatalyst] = 20 mM.

^bThe values of M_w were measured by GPC.

values ranging from 1×10^4 to 20×10^4 can be obtained. This finding indicates the presence of a long-lived propagating species and provides a useful method for preparing poly(TMSP) with a narrow MWD.

Polymerization of various analogues of TMSP has been examined (Table 8.6). $\text{MeC}\equiv\text{CSiMe}_2(\textit{n}\text{-C}_6\text{H}_{13})$ polymerizes with 1:1 mixtures of TaCl₅ and organometallic cocatalysts such as Ph₃Bi and Ph₄Sn. The polymers are obtained in good yields and have M_w values exceeding 1×10^6 [25]. $\text{MeC}\equiv\text{CSiMe}_2\text{Ph}$ and $\text{MeC}\equiv\text{CSiEt}_3$ form polymers with an M_w of ca. 5×10^5 in moderate yields in the presence of TaCl₅-based catalysts [25]. A monomer having two Si atoms, $\text{MeC}\equiv\text{CSiMe}_2(\text{CH}_2\text{SiMe}_3)$, polymerizes quantitatively with TaCl₅ alone to form a polymer having an M_w of over 1×10^6 [26]. A slightly different monomer, $\text{MeC}\equiv\text{CSiMe}_2(\text{CH}_2\text{CH}_2\text{SiMe}_3)$, gives a polymer of M_w ca. 4×10^5 with TaCl₅-cocatalyst systems [26]. Nb catalysts are less active toward these monomers than the corresponding Ta catalysts.

The Ge-containing analogue of TMSP, 1-(trimethylgermyl)-1-propyne (TMGP), can also be polymerized by TaCl₅ under the same conditions as those used for TMSP, according to a patent [27]. This monomer shows much higher reactivity in polymerization, and its polymerization is completed almost instantaneously. In contrast, the polymerization of TMSP is completed in about 1 h under standard conditions. No detailed information is available about the polymer molecular weight, but, because this polymer is film-forming,

it can be deduced that the molecular weight is high. Interestingly, this polymer has been reported to be soluble in carbon disulfide, but insoluble in other organic solvents, such as toluene and chloroform [27]. However, according to a more recently published paper, poly(TMGP) is soluble in common solvents such as toluene, and its M_w has been determined to be higher than 1×10^6 [4].

4,4-Dimethyl-2-pentyne ($\text{MeC}\equiv\text{C}\textit{-t}\text{-Bu}$), which possesses the same skeletal structure as TMSP, except that the silicon atom is replaced by a carbon atom, does not polymerize at all under the conditions suited for TMSP [28]. 4-Methyl-2-pentyne ($\text{MeC}\equiv\text{C}\textit{-i}\text{-Pr}$; MP), which is sterically less 'crowded', can be polymerized by NbCl₅ and TaCl₅ alone or in conjunction with suitable cocatalysts to provide the corresponding polymer, which has a molecular weight of several hundred thousand [6a,29]. Poly(MP) is soluble only in carbon tetrachloride, cyclohexane and methylcyclohexane but appreciably swells in other organic liquids (e.g. it absorbs about 160 wt% toluene).

8.2.3 Polydiarylacetylenes and their Derivatives

In the presence of TaCl₅-based catalysts, diphenylacetylene (DPA) forms a polymer which is thermally very stable but insoluble in any solvent [30]. Generally, polyacetylenes having two identical alkyl groups in the repeat unit are insoluble, while polyacetylenes having a methyl group and a long alkyl group are soluble in organic solvents. This tendency is explained in terms of the difference in surface area between these two types of macromolecules. Along these lines, polymerization of DPAs with bulky ring substituents has been examined, since, if a bulky substituent is incorporated into one of the phenyl groups of DPA, the polymer may become soluble. Eventually, the synthesis of many novel, soluble high-molecular-weight polymers from DPAs has been achieved. The polymers prepared are poly(-DPAs) having Me₃Si, *i*-butyl, *n*-butyl, phenoxy and carbazolyl groups and so forth at the *para* or *meta* positions [8].

Table 8.7 shows the results for the polymerization of various DPAs by TaCl₅-*n*-Bu₄Sn. Poly-[1-phenyl-2-*p*-(trimethylsilyl)phenylacetylene] (*p*-Me₃Si-DPA) polymerizes in high yield (up to 85 %) [31]. As expected, this polymer is completely soluble in many common solvents, such as

Table 8.7 Polymerization of diphenylacetylenes with substituents ($C_6H_5C\equiv CC_6H_4$ -*p* or *m*-R) catalyzed by $TaCl_5$ -*n*- Bu_4Sn (1:2)^a

R	Monomer conversion (%)	Yield (%)	Polymer (MeOH-insoluble product)		
			$M_w/10^3$		$M_n/10^3$ GPC
			GPC	LS ^b	
<i>p</i> -Me ₃ Si	95	85	2200	—	750
<i>m</i> -Me ₃ Si	100	87	1400	—	250
<i>m</i> -Me ₃ Ge	91	60	1800	—	730
<i>p</i> - <i>t</i> -Bu	100	84	3600	1600	1400
<i>p</i> - <i>n</i> -Bu	100	82	1300	940	460
<i>p</i> -PhCH ₂	100	74	870	430	350
<i>p</i> -PhO	100	69	1700	1200	400
<i>p</i> - <i>N</i> -carbazolyl	100	67 ^c	490	—	190

^aIn toluene, 80 °C, 3–24 h: $[M]_0$, 0.1–0.5 M; $[TaCl_5]$, 20 mM.

^bLight scattering.

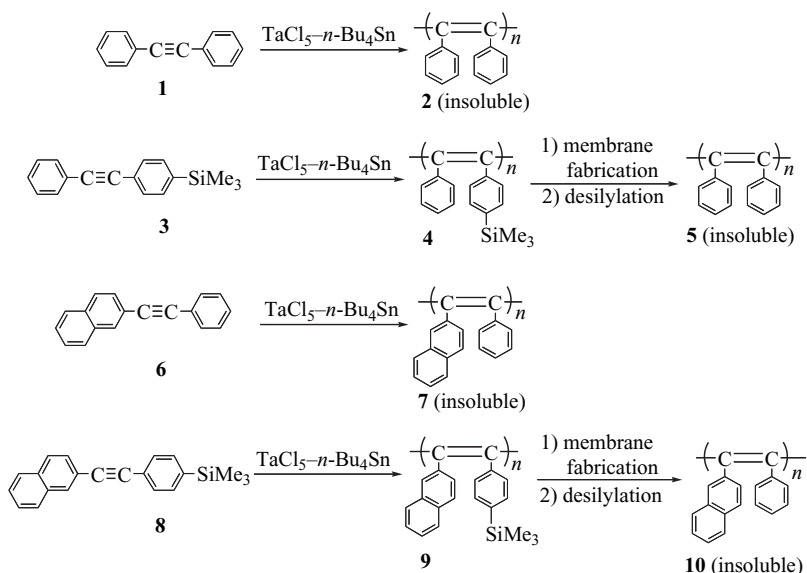
^cPartly insoluble in $CHCl_3$.

toluene and chloroform. Quite interestingly, the molecular weight of this polymer reaches about two million. The *m*-Me₃Si derivative also yields a soluble polymer with a molecular weight exceeding one million. Although Nb and Ta belong to the same group in the Periodic Table, the analogous Nb catalyst does not polymerize these DPA monomers. Both *p*- and *m*-Me₃Ge derivatives polymerize in a similar way to the Me₃Si-substituted counterparts. Whereas the polymer from the *p*-Me₃Ge monomer is not totally soluble in any solvents, the *m*-Me₃Ge polymer is completely soluble in toluene and chloroform [9]. Among alkyl-containing DPAs, the *t*-Bu derivative forms a polymer with a yield of 84 % (cf. Table 8.7) [10]. This polymer is totally soluble in toluene and chloroform, and its weight-average molecular weight reaches 3.6 million, as determined by gel permeation chromatography (GPC). Interestingly, the absolute M_w value determined by light scattering is smaller, by about a factor of two, than the value obtained by GPC. The *n*-Bu-containing polymer is also completely soluble in toluene and chloroform, and its M_w value is about one million. Additionally, the phenoxy derivative achieves a high polymer yield (around 70 %), despite the presence of an ether linkage [32]. The molecular weight of this phenoxy polymer is higher than one million, which is as high as for other derivatives. The carbazolyl-containing monomer gives a mostly soluble polymer with a molecular weight of about 5×10^5 [33].

In the UV–visible spectra of ring-substituted poly(DPAs) in THF, every polymer shows two absorption maxima at about 370 and 430 nm. Their molar absorptivities range from 4000 to 6000 $M^{-1} cm^{-1}$. The band edges are about 500 nm, irrespective of the ring-substituents. The spectra correspond to the yellow color of the polymers. In thermogravimetric analysis (TGA) in air, polyphenylacetylene begins to lose weight at temperatures as low as 200 °C. Poly(DPA), in contrast, maintains its weight up to 500 °C and is more stable than any other substituted polyacetylene. The onset of weight loss for poly(DPA)s having substituents is usually between 400 and 500 °C, indicating very high thermal stability.

Poly(DPAs) having bulky, nonpolar, more or less spherical ring substituents, such as Me₃Si and *t*-Bu groups, are very permeable to gases (see Section 8.2.4). These polymers have oxygen permeability coefficients, P_{O_2} , of about 1000 barrer, nearly twice that of polydimethylsiloxane. Apparently, the shape of ring substituents in poly(DPA) plays an important role in gas permeability. Thus, poly(DPA) derivatives form a new class of polyacetylenes which exhibit interesting properties, and further development of their unique functions is expected [8].

As described above, poly(DPA) (Scheme 8.1, 2) is insoluble in any solvent, whereas its derivatives with bulky ring-substituents, such as poly[1-phenyl-2-*p*-(trimethylsilyl)phenylacetylene] (4), are usually soluble in common solvents such as



Scheme 8.1 Polymerization of diphenylacetylene and its derivatives with bulky ring-substituents

toluene and chloroform and give membranes by solution casting. If the desilylation reaction of a membrane of **4** is possible, one will be able to obtain a membrane of **2** which cannot be obtained by polymerization and the subsequent solution casting, i.e. by the conventional method. In fact, a poly(DPA) membrane, **5**, has been prepared by the desilylation of a membrane of **4** catalyzed by trifluoroacetic acid in a hexane/trifluoroacetic acid mixture (volume ratio 1:1) [11]. The completion of the reaction is confirmed by IR spectroscopy. The prepared polymer membrane (**5**) shows high thermal stability, insolubility in any solvent and very high gas permeability (e.g. an oxygen permeability of 6000 barrer at 25 °C), which is comparable to that of poly(TMSP). The high gas permeability of **5** seems to be due to the generation of molecular-scale voids. Poly(1- β -naphthyl-2-phenylacetylene) (**7**) is insoluble in any solvent like poly(DPA) (**2**), whereas poly[1- β -naphthyl-2-(*p*-(trimethylsilyl)phenyl)acetylene] (**9**) is obtained with TaCl₅-*n*-Bu₄Sn in cyclohexane, has a high molecular weight ($M_w = 3.4 \times 10^6$), and is soluble in common solvents. Thus, in a similar way to the case of polymer **4**, the desilylation of a membrane of polymer **9** was performed to yield a membrane of poly(1- β -naphthyl-2-phenylacetylene) (**10**) which is insoluble and thermally very stable [12]. Both of the starting and desilylated polymers **9** and

10 show large P_{O_2} values up to ca. 4000 barrer at 25 °C.

8.2.4 Ring-substituted Polyphenylacetylenes

Phenylacetylene polymerizes with both W and Rh catalysts in almost quantitative yields under suitable conditions. The polymer molecular weight of phenylacetylene and its *para*- or *meta*-substituted derivatives, which are not sterically very 'crowded', reaches several hundred thousand or even higher with Rh catalysts [34,35], but is only several tens of thousands with W catalysts [36]. Thus, Rh catalysts are preferred for obtaining high-molecular-weight, film-forming polymers from, for instance, phenylacetylene and (*p*-adamantyl)phenylacetylene [37]. On the other hand, in the polymerization of monosubstituted acetylenes by W and Mo catalysts, it has been observed, thus far, that sterically 'uncrowded' acetylenes, such as 1-hexyne, do not produce high-molecular-weight polymers. However, monomers with bulky groups, such as *tert*-butylacetylene, do provide high-molecular-weight polymers. The molecular weight of polyphenylacetylene is 'intermediate'. From this viewpoint, the polymerizations of *ortho*-substituted phenylacetylenes are interesting, and high-molecular-weight polymers have been obtained from them, as discussed below (see Table 8.8).

Table 8.8 Polymerization of phenylacetylene and its ring-substituted derivatives

Monomer	Catalyst	$M_w/10^3, M_n/10^3$ or [η] (dL/g)
HC \equiv CPh	WCl ₆ -Ph ₄ Sn	15 (M_n)
HC \equiv CPh	(nbd-RhCl) ₂	350 (M_w)
HC \equiv CC ₆ H ₅ - <i>p</i> -Adm	(nbd-RhCl) ₂	>1000 (M_w)
HC \equiv CC ₆ H ₂ - <i>o</i> , <i>o</i> -Me ₂ - <i>p</i> - <i>t</i> -Bu	W(CO) ₆ -CCl ₄ - <i>hv</i>	2600 (M_w)
HC \equiv CC ₆ H ₄ - <i>o</i> -SiMe ₃	W(CO) ₆ -CCl ₄ - <i>hv</i>	3400 (M_w)
HC \equiv CC ₆ H ₄ - <i>o</i> -GeMe ₃	WCl ₆	690 (M_w)
HC \equiv CC ₆ H ₄ - <i>o</i> -CF ₃	W(CO) ₆ -CCl ₄ - <i>hv</i>	1600 (M_w)
HC \equiv CC ₆ H ₃ -2,5-(CF ₃) ₂	W(CO) ₆ -CCl ₄ - <i>hv</i>	0.35 ([η])
HC \equiv CC ₆ F ₅	WCl ₆ -Ph ₄ Sn	0.61 ([η])
HC \equiv CC ₆ F ₄ - <i>p</i> - <i>n</i> -Bu	WCl ₆ -Ph ₄ Sn	110 (M_w)

Under suitable conditions, *o*-(methylphenyl)acetylene, one of the simplest *ortho*-substituted phenylacetylenes, polymerizes in nearly 100 % yield with W catalysts [38]. Using W(CO)₆-CCl₄-*hv* as the catalyst gives the highest M_w of poly[*o*-(methylphenyl)acetylene] (ca. 8×10^5). Quite interestingly, (*p*-*tert*-butyl-*o*,*o*-dimethylphenyl)acetylene, an *ortho*-dimethyl-substituted phenylacetylene, polymerizes in the presence of W(CO)₆-CCl₄-*hv* to provide a totally soluble, high-molecular-weight polymer ($M_w > 2 \times 10^6$) in high yield [39]. Both trimethylsilyl and trimethylgermyl groups are sterically very 'crowded' and electron-donating. The two phenylacetylenes having these bulky groups at the *ortho* position polymerize in high yield with both W and Mo catalysts [40,41]. The M_w of the resulting polymers exceeds one million. *o*-(Trifluoromethyl)phenylacetylene, which has a bulky and electron-withdrawing *ortho*-substituent, also polymerizes in a similar way with W and Mo catalysts to yield high-molecular-weight polymer [42]. Thus, the steric effect of the *ortho*-substituents greatly affects both the polymerizability and the molecular weight of the phenylacetylenes. The electronic effect, though, has little influence on these properties. Polymers have also been prepared from other F-containing monomers (e.g. HC \equiv C-C₆F₅ [43], HC \equiv C-C₆F₄-*p*-*n*-Bu [43] and HC \equiv C-C₆H₃-2,5-(CF₃)₂ [13,44]). Furthermore, in an attempt to achieve high gas permeability, polyphenylacetylenes with several trifluoromethyl and trimethylsilyl groups, such as poly[2,4,5-tris(trifluoromethyl)phenylacetylene] [13] and poly[2,4-bis(trimethylsilyl)phenylacetylene] [14], have been synthesized.

8.3 Gas and Vapor Separation

8.3.1 Gas/Gas Separation

The separation of a gas mixture is an example of successfully developed membrane processes that found real application in industry. Major applications of membrane separation processes in industry are, for instance, H₂/N₂ separation in an ammonia synthesis and purge recycle system and O₂/N₂ separation for N₂ enrichment. The gas transport through a polymer membrane is thought to obey a solution-diffusion mechanism. Because gases are generally noncondensable under operating conditions at membrane separation systems, the gas diffusion is a dominant factor relative to the gas solution. Therefore, a small gas molecule permeates faster through a polymer membrane than a large gas molecule based on a 'size-sieving' effect.

More than 70 substituted polyacetylenes have been synthesized so far. All of them are glassy at ambient conditions. Changing substituents in polyacetylenes provides a wide variety of permeabilities of gases and liquids. For example, the oxygen permeability of substituted polyacetylenes at 25 °C varies from ca. 1 to 6000 barrer [2]. This permeability range is wider than that of other glassy polymers, such as families of polysulfones and polycarbonates. In addition, several substituted polyacetylenes are more permeable to oxygen than commercially available polymer membrane materials for oxygen enrichment, such as polydimethylsiloxane ($P_{O_2} = 600$ barrer, $P_{O_2}/P_{N_2} = 2.0$), poly(4-methyl-1-pentene) ($P_{O_2} = 32$ barrer) and poly(oxy-2,6-dimethylphenylene) ($P_{O_2} = 15$ barrer) [45-47].

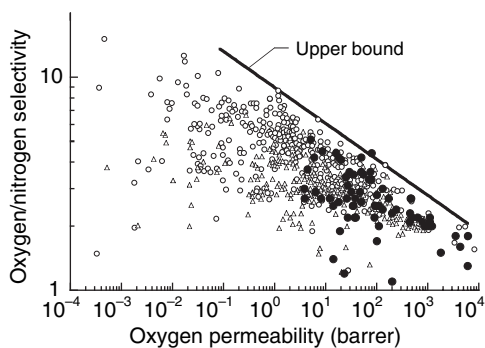


Figure 8.1 Relationship between oxygen permeability and oxygen/nitrogen selectivity for substituted polyacetylenes (data in Table 8.9 and from the literature [2]) (●) and common glassy (○) and rubbery polymers (Δ) [48]; 1 barrer = 1×10^{-10} cm³(STP) cm/(cm²s cmHg). Reprinted from *Journal of Membrane Science*, **62**, L. M. Robeson, 'Correlation of separation factor versus permeability for polymeric membranes', pp. 165–185, Copyright (1991), with permission from Elsevier

Approximately 10 substituted polyacetylenes are more permeable than polydimethylsiloxane, which is the most permeable polymer used commercially in industrial-scale membrane plants.

In general, highly permeable polymers have low selectivities and vice versa. The upper bound of this tradeoff relationship was proposed by Robeson for several gas pairs [48]. As can be seen from Figure 8.1, the data points between the oxygen permeability and the oxygen/nitrogen selectivity for the substituted polyacetylenes are scattered under the upper bound drawn by Robeson. Even though polymers have virtually the same permeability, their selectivities are often different from each other, hence suggesting differences in free volume elements and their distribution. Among these substituted polyacetylenes, highly permeable substituted polyacetylenes tend to contain spherical substituents, such as *t*-Bu, Me₃Si and Me₃Ge groups [14,49–53]. On the other hand, many of the less-permeable polyacetylenes possess long *n*-alkyl groups, such as the *n*-C₆H₁₃ group [2]. Furthermore, when one of the substituents is a phenyl group without any additional spherical ring substituent onto its phenyl group, their gas permeability is usually considerably low among the substituted polyacetylenes.

For those substituted polyacetylenes with oxygen permeabilities greater than 100 barrer, these

polymers are classified into four categories and their oxygen permeability and oxygen/nitrogen selectivity values are summarized in Table 8.9. The unusually high oxygen permeabilities of these polyacetylenes is attributed to the high free volume and 'untypical' free volume distribution, which presumably derives from a combination of their low cohesive energy structure, stiff main chain and spherical substituents.

High-molecular-weight ring-substituted polydiphenylacetylenes are thermally very stable (softening temperature, $T_0 > 400^\circ\text{C}$) among substituted polyacetylenes and possess film-forming ability by solvent-casting. Polydiphenylacetylenes tend to show higher permeabilities than polyphenylacetylenes do. In particular, polydiphenylacetylenes with spherical ring substituents such as *t*-Bu, Me₃Si and Me₃Ge groups, exhibit very large oxygen permeabilities of around 1100–1500 barrer [7,10,31]. When one of these spherical ring substituents is replaced by other substituents, such as *n*-butyl and phenoxy groups, the permeability decreases by about 10-fold.

Unlike these ring-substituted polydiphenylacetylenes, polydiphenylacetylene without any ring substituents is insoluble in any solvent. Thus, a polydiphenylacetylene membrane has been prepared by the desilylation of a poly[1-phenyl-2-*p*-(trimethylsilyl)phenylacetylene] membrane catalyzed by trifluoroacetic acid [11]. The desilylated membrane is free-standing and has high thermal stability, insolubility in any solvents and very high gas permeability (e.g. $P_{\text{O}_2} = 6000$ barrer at 25°C), which is comparable to that of poly(TMSP). The oxygen permeability increases by about four times after the desilylation. The high gas permeability of polydiphenylacetylene probably results from the generation of molecular-scale voids after removal of the Me₃Si group, which is much larger than the gas molecules, from the membrane. In a similar way, a poly(1- β -naphthyl-2-phenylacetylene) membrane can be obtained by desilylation of a poly[1- β -naphthyl-2-(*p*-(trimethylsilyl)phenyl)acetylene] membrane [12]. The desilylated membrane has an oxygen permeability coefficient of 4300 barrer at 25°C . The permeability is about 20% enhanced by the desilylation. The effect of the desilylation on the gas permeability is much larger for polydiphenylacetylene than for poly(1- β -naphthyl-2-phenylacetylene).

Table 8.9 Oxygen permeability coefficients (P_{O_2}) and P_{O_2}/P_{N_2} of highly permeable substituted polyacetylenes ($P_{O_2} \geq 100$ barrer)

$\begin{array}{c} \text{-(C=C)-} \\ \quad \\ \text{R}^1 \quad \text{R}^2 \end{array}$		P_{O_2} (barrer) ^a	P_{O_2}/P_{N_2}	Reference
<i>Poly(TMSP) and its analogues</i>				
Me	SiMe ₃	4×10^3 – 9×10^3	1.8	2
Me	SiEt ₃	860	2.0	25,50
Me	SiMe ₂ Et	500	2.2	49,50,53
Me	SiMeEt ₂	440	2.1	50
Me	SiMe ₂ - <i>i</i> -Pr	460	2.7	50,53
Me	SiMe ₂ - <i>n</i> -C ₃ H ₇	100	2.8	49
Me	GeMe ₃	7800	—	4,27
Me	<i>i</i> -Pr	2700	2.0	6a
Me	(CH ₂) ₃ SiMe ₃	130	2.4	50
Me	C ₆ H ₄ - <i>p</i> -SiMe ₃	240	2.4	50,53
<i>Ring-substituted polydiphenylacetylenes</i>				
Ph	C ₆ H ₄ - <i>p</i> -SiMe ₃	1100–1550	2.1	7,31
Ph	C ₆ H ₄ - <i>m</i> -SiMe ₃	1200	2.0	7,31
Ph	C ₆ H ₄ - <i>p</i> -SiMe ₂ - <i>i</i> -Pr	200	2.3	51
Ph	C ₆ H ₄ - <i>m</i> -SiMe ₂ - <i>t</i> -Bu	110	2.5	51
Ph	C ₆ H ₄ - <i>m</i> -GeMe ₃	1100	2.0	9
Ph	C ₆ H ₄ - <i>p</i> - <i>t</i> -Bu	1100	2.2	10
Ph	C ₆ H ₄ - <i>p</i> - <i>n</i> -Bu	100	1.7	10
β -naphthyl	C ₆ H ₄ - <i>p</i> -SiMe ₃	3500	1.8	12
<i>Polydiarylacetylenes</i>				
Ph	Ph	6000	1.3	11
Ph	β -naphthyl	4300	1.6	12
<i>Ring-substituted polyphenylacetylenes and tert-butylacetylene</i>				
H	C ₆ H ₂ -2,4,5-(CF ₃) ₃	780	2.1	13
H	C ₆ H ₃ -2,5-(CF ₃) ₃	450	2.3	13
H	C ₆ H ₃ - <i>o,p</i> -(SiMe ₃) ₂	470	2.7	14
H	C ₆ H ₄ - <i>p</i> -SiMe ₃	170	2.7	14
H	C ₆ H ₄ - <i>o</i> -GeMe ₃	110	2.0	41
H	<i>t</i> -Bu	130	3.0	52

^a1 barrer = 1×10^{-10} cm³(STP) cm/(cm²s cmHg).

As evidenced from Table 8.9, the oxygen/nitrogen selectivities of the highly permeable substituted polyacetylenes are around 2. For poly(TMSP), fluorination of its polymer membrane is the most effective to the increase of selectivity among various modifications [2]. The surface fluorination of the poly(TMSP) membrane using F₂ gas in nitrogen (ca. 0.1 % F₂) enhances the oxygen/nitrogen selectivity of poly(TMSP) from 1.5 to 5.1 [54]. Another approach is that hexafluorobutyl methacrylate was incorporated in to poly(TMSP) films and then irradiated with UV light [55]. The oxygen/nitrogen selectivity of the treated poly(TMSP) increases up to 5.4 at 20 °C. The maximum

oxygen/nitrogen selectivity may be around 5 for poly(TMSP)-based membranes.

8.3.2 Vapor/Gas Separation

A membrane separation process of a vapor/gas mixture was commercially established in late 1980s. Applications already developed are, for example, C₃₊ hydrocarbons/CH₄ separation in natural gas and volatile organic vapor (VOC) removal from air. Vapor is usually required to be removed selectively from a vapor–gas mixture, that is, vapor (i.e. a large molecule in the mixture) needs to permeate faster through a polymer membrane than gas (i.e. a small molecule in the

mixture). Because glassy polymers have strong 'size-sieving' abilities, they are not suitable as membrane materials for these applications. Hence, rubbery polymers, such as polydimethylsiloxane, are used in industry.

Interestingly, some of the highly permeable substituted polyacetylenes presented in Table 8.9 show permeation properties opposite to common glassy polymers. A relationship between the gas permeability and the penetrant size is presented in Figure 8.2 for poly(TMSP) [56], a highly permeable substituted polyacetylene, poly(1-phenyl-1-propyne) (poly(PP)) [57], a less permeable substituted polyacetylene and a polysulfone [58], a conventional glassy polymer. In general, the gas permeabilities of conventional glassy polymers, such as polysulfones and polycarbonates, decrease with increasing penetrant size, based on a strong 'size-sieving' effect. The selectivity of a small molecule over a large molecule is then always greater than 1. Most of the

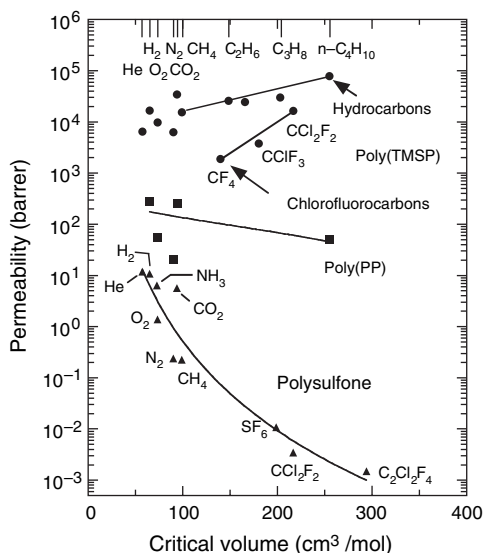


Figure 8.2 Permeability coefficients of various gases at 23 °C in poly(1-trimethylsilyl-1-propyne) (poly(TMSP)) (●) [56], poly(1-phenyl-1-propyne) (poly(PP)) (■) [57] and a polysulfone (▲) [58] as a function of the critical volume of various gases; 1 barrer = 1×10^{-10} cm³(STP)cm/(cm²s cmHg). Reprinted from *Journal of Membrane Science*, **116**, I. Pinnau and L. G. Toy, 'Transport of organic vapors through poly(1-trimethylsilyl-1-propyne)', pp. 199–209, Copyright (1996), with permission from Elsevier

substituted polyacetylenes such as poly(PP) obey this behavior. However, some of the highly permeable substituted polyacetylenes, such as poly(TMSP), show the opposite behavior. Their gas permeabilities increase with increasing penetrant size [5a,6a,56,59,60]. This behavior results in weak 'size-sieving' ability of these highly permeable substituted polyacetylenes, based on their large free volumes and unusual free volume distributions relative to those of less permeable substituted polyacetylenes and conventional glassy polymers. Substituted polyacetylenes can be designed to have both 'small-molecule-selective' (e.g. poly(PP)) and 'large-molecule-selective' (e.g. poly(TMSP)) properties by choosing their substituents.

The selectivity of a vapor–gas mixture in polymers is usually equal or lower than the ratio of each permeability of the pure components in the mixture. Interestingly, the opposite behavior was discovered for some 'large-molecule-selective' substituted polyacetylenes. The vapor/gas selectivity of a vapor–gas mixture for these polymers is much higher than that obtained from *pure-gas* measurements [56]. This behavior results from the fact that the gas permeability is dramatically reduced by the presence of the vapor in a vapor–gas mixture. Table 8.10 summarizes the *n*-C₄H₁₀/CH₄ separation results for poly(TMSP) and poly(MP) in comparison with those of a common glassy polymer, a polysulfone, and a rubbery polymer, polydimethylsiloxane [56,61]. The polydimethylsiloxane and polysulfone have the same permeability of each component for both mixed-gas and pure-gas measurements. In contrast, for poly(TMSP), the *n*-C₄H₁₀ permeability in an *n*-C₄H₁₀/CH₄ mixture is about 30 % lower than the pure *n*-C₄H₁₀ permeability, while the CH₄ permeability in the mixture is about 90 % lower than the pure CH₄ permeability. The *n*-C₄H₁₀/CH₄ selectivity in the mixture is then 6 times larger than the permeability ratio of pure *n*-C₄H₁₀ over pure CH₄. As a result, poly(TMSP) provides a mixed-gas *n*-C₄H₁₀/CH₄ selectivity of 30, the highest value ever observed for any known polymer for this binary mixture, with much higher permeabilities compared to any other polymer. Other vapor–gas mixtures where such blocking effects are observed for poly(TMSP) are SF₆–He and SF₆–N₂ mixtures [62], C₃+–CH₄ mixtures [56,63,64] and chlorofluorocarbon–N₂ mixtures [56].

Table 8.10 Mixed-gas permeation properties of highly permeable substituted polyacetylenes and conventional polymers^a

Polymer	Temperature (°C)	Permeability (barrer) ^b		Selectivity, <i>n</i> -C ₄ H ₁₀ /CH ₄	Permeability ratio, CH ₄ (mixed-gas)/ CH ₄ (pure-gas)	Reference
		<i>n</i> -C ₄ H ₁₀	CH ₄			
Poly(TMSP)	23	53500	1800	30	0.1	56
Poly(MP)	25	7500	530	14	0.2	61
Poly(MP)/silica (45 wt%) nanocomposite	25	25000	1100	23	—	65
Polysulfone	23	0.13	0.21	0.6	1	56
Polydimethylsiloxane	23	7200	1200	6	1	56

^aGas mixture: 2 mol% *n*-butane/98 mol% methane (relative *n*-butane pressure (p/p_{sat}) = 0.16). Mixture feed pressure: 250 psig (18 atm) for poly(TMSP), polysulfone and polydimethylsiloxane; 150 psig (10 atm) for poly(MP). 165 psig (11.2 atm) for poly(MP)/silica (45 wt%) nanocomposite. Permeate pressure for all polymers: 0 psig (1 atm).

^b1 barrer = 1×10^{-10} cm³(STP) cm/(cm²s cmHg).

This blocking effect in the presence of condensable co-components results from the extremely large free volumes in these substituted polyacetylenes, such as poly(TMSP) and poly(MP). Filling-fumed silica in poly(MP) provides an increase in free volume elements and, in turn,

an increase in both the mixed-gas *n*-C₄H₁₀/CH₄ selectivity and the *n*-C₄H₁₀ permeability as the silica content in poly(MP) increases, as shown in Figure 8.3 [65].

For the separation of CO₂ in CO₂-*iso*-C₄H₁₀ mixtures (i.e. mixtures of more condensable-gas and vapor) in aged poly(TMSP) at 30 °C, the permeability is 300 barrer for CO₂ at a partial pressure of 60 cmHg and 80 barrer for *iso*-C₄H₁₀ at a partial pressure of 16 cmHg in a CO₂-*iso*-C₄H₁₀ mixture [66]. The CO₂-*iso*-C₄H₁₀ selectivity is then 3.8. Unlike the *n*-C₄H₁₀/CH₄ separation, in the separation of CO₂-*iso*-C₄H₁₀ mixtures in poly(TMSP), however, no blocking effect is observed. The co-permeation of *iso*-C₄H₁₀ has no effect on the carbon dioxide permeation. In another case of CO₂-acetone mixtures, the CO₂ permeability slightly increases with increasing acetone partial pressure, while the acetone permeability does not depend on the carbon dioxide partial pressure. For *iso*-C₄H₁₀-acetone mixtures, the *mixed*-gas permeability of each component is higher than the respective pure-component values at the corresponding pressure. Based on these researches, the decline in the gas permeability in the presence of vapor in highly permeable substituted polyacetylenes is a rare case observed only for the separation of mixtures of vapor and less polar, less condensable gas.

Publisher's Note:

Permission to reproduce this image online was not granted by the copyright holder. Readers are kindly requested to refer to the printed version of this chapter.

Figure 8.3 The effect of fumed silica content on *n*-butane permeability and *n*-butane/methane selectivity of poly(4-methyl-2-pentyne) (poly(MP)) at 25 °C in mixtures composed of 98 mol % methane and 2 mol % *n*-butane at a feed pressure of 11.2 atm and a permeate pressure of 1 atm [65]. Reprinted with permission from T. C. Merkel, B. D. Freeman, R. J. Spontak, Z. He, I. Pinnau, P. Meakin and A. J. Hill, 'Ultrapervaporation, reverse-selective nanocomposite membranes', *Science*, **296**, 519–522 (2002). Copyright (2002) American Association for the Advancement of Science

8.3.3 Vapor/Vapor Separation

The separation of mixtures of condensable molecules using membranes is developing in

Table 8.11 Separation factors ($\alpha_{\text{H}_2\text{O}}^{\text{EtOH}}$) and permeation rates (R) of substituted polyacetylenes in ethanol–water pervaporation (EtOH feed concentration; 10 wt%) at 30 °C

$-(\text{CR}=\text{CR}')_{\text{n}}$		Downstream pressure (mmHg)	Thickness (μm)	$\alpha_{\text{H}_2\text{O}}^{\text{EtOH}}$	$R \times 10^3$ ($\text{gm}/(\text{m}^2 \text{ h})$)	Reference
R	R'					
<i>'EtOH-selective'</i>						
Me	SiMe ₃	1.0	ca. 20	12	4.5	71
Ph	C ₆ H ₄ - <i>p</i> -SiMe ₃	2.0	53	6.9	4.2	72
Ph	Ph	2.0	46	6.0	5.9	72
β -naphthyl	C ₆ H ₄ - <i>p</i> -SiMe ₃	2.0	32	5.3	6.9	72
Ph	β -naphthyl	2.0	45	3.4	14	72
Cl	<i>n</i> -C ₆ H ₁₃	1.0	ca. 20	1.1	0.41	71
<i>'Water-selective'</i>						
Me	<i>n</i> -C ₅ H ₁₁	1.0	ca. 20	0.72	0.57	71
H	<i>t</i> -Bu	1.0	ca. 20	0.58	0.65	71
H	CH(<i>n</i> -C ₅ H ₁₁)SiMe ₃	1.0	ca. 20	0.52	0.40	71
Me	Ph	1.0	ca. 20	0.28	0.24	71
Cl	Ph	1.0	ca. 20	0.21	0.23	71

applications such as separation of each component from either VOC mixtures or C₃₊ hydrocarbon isomers. The separation properties of vapor mixtures have rarely been studied so far. Substituted polyacetylenes have high permeabilities but very low selectivities for mixtures of vapors. Poly(TMSP) has a C₃H₆/C₃H₈ selectivity of 1.7 [67]. Bromination of poly(TMSP) enhances its selectivity up to 2.3 at a bromine content of 13 wt % in brominated poly(TMSP) [67]. Unlike the C₃H₆/C₃H₈ separation, this polymer is more permeable to paraffin than to olefin in C₂ mixtures. The C₂H₄/C₂H₆ selectivity of poly(TMSP) is 0.88.

For mixtures of C₄ hydrocarbons, poly(TMSP) has an *iso*-C₄H₈/*iso*-C₄H₁₀ selectivity of 3.0 [68,69]. This selectivity is enhanced by the addition of AgClO₄ into poly(TMSP) to become 5.6 at an AgClO₄ content of 32.7 wt % in a poly(TMSP)/AgClO₄ composite film [68]. Substituted polyacetylenes themselves have no attractive separation properties in vapor/vapor separation applications and require new strategies for improvement of the selectivity.

8.4 Pervaporation

8.4.1 Alcohol/Water Separation

The first commercial-scale membrane system of liquid separation was established for the separation of an ethanol–water mixture by pervaporation in 1982 [70]. The pervaporation process

has the advantage of avoiding the azeotropic distillation problem of liquid mixtures. In general, a family of polymers have either 'water-selective' or 'alcohol-selective' behaviors. In the case of separation of ethanol–water mixtures, a family of substituted polyacetylenes shows both 'ethanol-selective' and 'water-selective' behaviors. Substituted polyacetylenes represent a rare family of polymers having the opposite selectivity within the same family.

Table 8.11 summarizes the total flux and ethanol/water selectivity measured for various substituted polyacetylenes used in the pervaporation of alcohols/water mixtures [71a,71b,71c,72]. Highly permeable substituted polyacetylenes are 'ethanol-selective' (i.e. ethanol/water selectivity > 1), whereas less permeable substituted polyacetylenes are 'water-selective' (i.e. ethanol/water selectivity < 1). Poly(TMSP) with a membrane thickness of about 20 μm has a total flux of $4.5 \times 10^{-3} \text{ gm}/(\text{m}^2 \text{ h})$ with an ethanol/water selectivity of 12, whereas poly(1-phenyl-2-chloroacetylene) has a total flux of $0.23 \times 10^{-3} \text{ gm}/(\text{m}^2 \text{ h})$ with an ethanol/water selectivity of 0.21. For example, poly(TMSP), one of the 'alcohol selective' substituted polyacetylenes, sorbs ethanol and butanol [71a,71b] preferentially but diffuses water faster than ethanol. Because the solubility selectivity dominates the overall permeability selectivity in this case, poly(TMSP) permeates ethanol preferentially. In contrast, the diffusivity is a dominant factor for the transport in the 'water-selective' substituted polyacetylenes.

The flux and alcohol/water selectivity of an alcohol/water mixture by pervaporation of 'alcohol-selective' poly(TMSP) decrease (e.g. methanol > ethanol > 1-propanol) with increasing size of alcohol (e.g. methanol < ethanol < 1-propanol) [73]. The pervaporation properties of poly(TMSP) depend on solubility, based on the polarity of alcohols. The less polar poly(TMSP) sorbs less polar alcohols preferentially. The selectivity of 2-propanol/water is higher than that of 1-propanol/water, due, presumably, to the higher affinity of 2-propanol to poly(TMSP) than 1-propanol.

The most effective modification of the ethanol/water separation in poly(TMSP), summarized in a recent review [2], is the graft of polydimethylsiloxane onto the α -methyl carbon of poly(TMSP) [74]. In the separation of a 7 wt% ethanol–water solution at 30 °C, poly(TMSP) has a flux of 1.2×10^{-3} gm/(m²h) and an ethanol/water selectivity of 11. When polydimethylsiloxane is grafted onto poly(TMSP) at a 12 mol% polydimethylsiloxane content in the graft copolymer, the flux increases to 2.5×10^{-3} gm/(m²h) and the ethanol/water selectivity is also enhanced up to 28.

8.4.2 Organic Liquid/Water Separation

A process for the removal of organic liquid from contaminated water by pervaporation is commercially available. In pervaporation of mixtures of water and various organic liquids (e.g. toluene and trichloroethylene), rubbery polymers (e.g. polydimethylsiloxane and ethylene–propylene terpolymers) are always organic 'liquid-selective', regardless of the polymer structures [75]. In contrast, substituted polyacetylenes are either organic 'liquid-selective' or 'water-selective', depending on their substituents. Poly(TMSP) is one of the organic 'liquid-selective' substituted polyacetylenes, as presented in Figure 8.4. This polymer increases the acetonitrile content of an acetonitrile/water mixture from 7 to 88 wt% at 30 °C with a total flux of 7×10^{-2} gm/(m²h) [76]. The acetonitrile/water selectivity is then 101. As the concentration of organic liquids in the feed increases, the total flux of the mixtures increases, whereas the organic 'liquid/water selectivity' decreases, except for acetic acid. The selectivity of acetic acid increases up to the 25 wt% acetic acid concentration in feed mixtures, and then

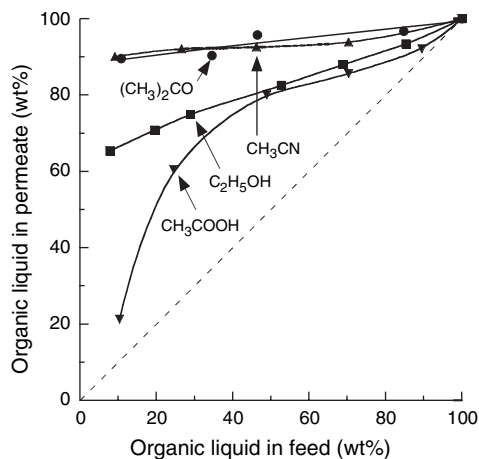


Figure 8.4 Permeate composition curves for a poly(TMSP) membrane used for organic liquid–H₂O pervaporation at 30 °C [76]. Organic liquids: (CH₃)₂CO (●), CH₃CN (▲), C₂H₅OH (■) and CH₃COOH (▼). Reprinted from *Journal of Membrane Science*, 49, T. Masuda, M. Takatsuka, B. Z. Tang and T. Higashimura, 'Pervaporation of organic liquid–water mixtures through substituted polyacetylene membranes', pp. 69–83, Copyright (1990), with permission from Elsevier

decreases further with increasing concentration. When the trimethylsilyl group is introduced on a 10 mol% of the α -methyl carbon of poly(TMSP), both the flux and acetonitrile/water selectivity is two-fold enhanced at 50 °C [77]. This trimethylsilyl-group-modified poly(TMSP) also shows higher fluxes and higher organic liquid/water selectivities than poly(TMSP) for various solvents such as acetone and dioxane.

Poly(TMSP) membranes irradiated with γ -rays in the presence of fluoroalkyl methacrylate monomers, show increases in both flux and chloroform/water selectivity for a 0.5 wt% chloroform/water feed mixture at 25 °C [78]. The chloroform/water selectivity is 860 for poly(TMSP) and 1500 for a 9 wt% fluorine-containing poly(TMSP). Blends of poly(TMSP) with 62 wt% poly(1H, 1H, 9H-hexadecafluorononyl methacrylate) have an ethyl butanoate/water selectivity of about 600 for 0.02 wt% ethyl butanoate feed mixtures at 25 °C [79]. The diffusivity of ethyl butanoate is much lower than that of water, whereas the solubility of ethyl butanoate is much higher than that

of water. Because the solubility factor is dominant for the transport, ethyl butanoate permeates faster through this modified polymer than water.

In the separation of benzene/water mixtures (benzene concentration: 600 ppm in the feed) by pervaporation at 25 °C, the selectivity of benzene over water is 1600 for poly(TMSP) and 400 for poly(PP) [80]. As the poly(PP) content increases in these blends, the water flux decreases gradually, while the benzene flux stays almost constant up to 25 wt% of poly(PP) content in the blends. As a result, interestingly, poly(TMSP)/poly(PP) blends have benzene/water selectivities higher than those of each polymer (see Figure 8.5). For example, poly(TMSP)/poly(PP) (75/25) blends have a benzene/water selectivity of 2900.

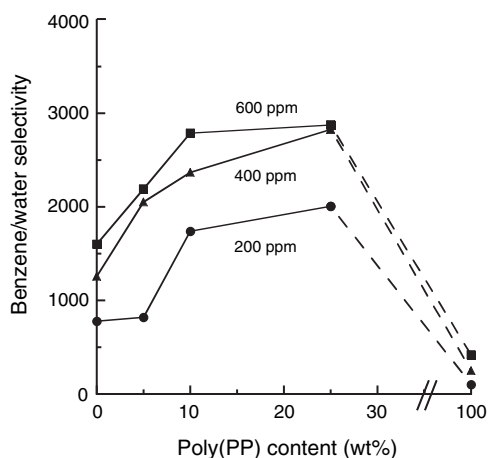


Figure 8.5 The effect of poly(1-phenyl-1-propyne) (poly(PP)) content on the benzene/water selectivity in poly(1-trimethylsilyl-1-propyne) (poly(TMSP))/poly(PP) blends at 25 °C in the pervaporation of aqueous solutions containing 200 (●), 400 (▲) and 600 (■) ppm benzene [80]. Reproduced by permission of The Society of Polymer Science, Japan from S. Takahashi, Y. Yoshida, T. Kamada and T. Nakagawa, *Kobunshi Ronbunshu*, **58**, 213–220 (2001).

8.4.3 Organic Liquid/Organic Liquid Separation

The pervaporation technology of the separation of mixtures of organic liquids is still developing in industry. In fact, the separation properties of organic liquid mixtures by pervaporation have rarely been investigated so far. In the separation

of benzene–cyclohexane mixtures by pervaporation, phenyl-group-containing substituted polyacetylenes show benzene permselectivities like other common polymers [72]. When the feed solution contains about 50 wt% benzene, the benzene/cyclohexane selectivity of poly(DPA) is 1.6 at 30 °C. This is about 10 times lower than that of cellulose acetate. However, poly(DPA) with a membrane thickness of 46 μm has a total flux of 191 gm/(m²h), which is 560 times faster than that of cellulose acetate. When the benzene content is 10 wt% in the feed, the selectivity is slightly higher when compared to the value at 50 wt% benzene concentration in the feed, but the flux is about a half of the value at 50 wt% benzene concentration. The β-naphthyl group in poly(β-NpPA) enhances the selectivity relative to the value of poly(DPA). The flux is, however, reduced by replacement of the phenyl group by the β-naphthyl group. The substituted polyacetylenes seem to have little potential for the separation of organic liquids.

8.5 Concluding Remarks

A variety of substituted polyacetylenes can be synthesized by using metathesis catalysts and show various interesting properties for separation of gases and liquids, as described in this chapter. Based on the results performed by various researchers, some of the highly permeable substituted polyacetylenes, such as poly(TMSP), have great potential as membrane materials, as described in the following three applications.

The first application is the oxygen enrichment of air. This application does not require an extremely high oxygen/nitrogen selectivity. Highly permeable substituted polyacetylenes have oxygen/nitrogen selectivities of around 2, although the selectivity can be enhanced up to around 5 by modifications of the polymers. The second is the removal of vapor as a minor component from vapor–gas mixtures for applications such as natural gas treatment and volatile organic compound (VOC) removal from air. It is possible to design ‘vapor-selective’ substituted polyacetylenes. In fact, one of the ‘vapor-selective’ substituted polyacetylenes, poly(TMSP), provides a mixed-gas *n*-C₄H₁₀/CH₄ selectivity of 30, the highest value ever observed for any polymer known so far for this binary mixture, with much higher permeabilities than any other polymer. The

final expected field is the removal of organic liquids, such as VOCs (e.g. halogenated hydrocarbons), from water. The organic liquid is a minor component in aqueous solutions and should be selectively removed. Several substituted polyacetylenes show organic 'liquid-selective' behavior with high flux. These polymers do not swell very much with such dilute aqueous solutions and maintain their mechanical stabilities during permeation.

These separation properties of substituted polyacetylenes are attributed to the combination of large free volume elements and their unusual distributions. There are still great possibilities for designing 'optimum-substituted' polyacetylenes by controlling their substituents for these applications and therefore the discovery of more new attractive applications.

References

- [1] T. Masuda and T. Higashimura, 'Polyacetylenes with substituents: their synthesis and properties', *Adv. Polym. Sci.*, **81**, 121–165 (1987).
- [2] K. Nagai, T. Masuda, T. Nakagawa, B. D. Freeman and I. Pinnau, 'Poly[1-(trimethylsilyl-1-propyne)] and related polymers: synthesis, properties and functions', *Prog. Polym. Sci.*, **26**, 721–798 (2001).
- [3] T. Masuda, E. Isobe, T. Higashimura and K. Takada, 'Poly[1-(trimethylsilyl)-1-propyne]: a new high polymer synthesized with transition-metal catalysts and characterized by extremely high gas permeability', *J. Am. Chem. Soc.*, **105**, 7473–7474 (1983).
- [4] G. S. Kwak and T. Masuda, 'Synthesis, structure and properties of poly[1-(trimethylgermyl)-1-propyne]', *J. Polym. Sci. Part A: Polym. Chem. Ed.*, **38**, 2964–2969 (2000).
- [5a] K. Nagai, L. G. Toy, B. D. Freeman, M. Teraguchi, G. Kwak, T. Masuda and I. Pinnau, 'Gas permeability and *n*-butane solubility of poly(1-trimethylgermyl-1-propyne)', *J. Polym. Sci. Part B: Polym. Phys. Ed.*, **40**, 2228–2236 (2002).
- [5b] V. S. Khotimsky, M. V. Tchirkova, E. G. Litvinova, A. I. Rebrov, G. N. Bondarenko, Poly[1-(trimethylgermyl)-1-propyne] and poly[1-(trimethylsilyl)-1-propyne] with various geometries: their synthesis and properties, *J. Polym. Sci. Part A, Polym. Chem.*, **41**, 2133–2155 (2003).
- [6a] A. Morisato and I. Pinnau, 'Synthesis and gas permeation properties of poly(4-methyl-2-pentyne)', *J. Membr. Sci.*, **121**, 243–250 (1996).
- [6b] V. S. Khotimsky, S. M. Matson, E. G. Litvinova, G. N. Bondarenko, A. I. Rebrov, Synthesis of poly(4-methyl-2-pentyne) with various configurations of micromolecular chains, *Polymer Science, A*, **45**, 740–746 (2003).
- [7] K. Tsuchihara, T. Masuda and T. Higashimura, 'Tractable silicon-containing polydiphenylacetylenes: their synthesis and high gas permeability', *J. Am. Chem. Soc.*, **113**, 8548–8549 (1991).
- [8] T. Masuda, M. Teraguchi and R. Nomura, 'Synthesis and gas permeability of polydiphenylacetylenes with substituents', in *Polymer Membranes for Gas and Vapor Separation, Chemistry and Materials Science*, ACS Symposium Series 733, B. D. Freeman and I. Pinnau (Eds), American Chemical Society, Washington, DC, USA, pp. 28–37 (1999).
- [9] H. Ito, T. Masuda and T. Higashimura, 'Synthesis and properties of germanium-containing polydiphenylacetylenes', *J. Polym. Sci. Part A: Polym. Chem. Ed.*, **34**, 2925–2929 (1996).
- [10] H. Kouzai, T. Masuda and T. Higashimura, 'Synthesis and properties of polydiphenylacetylenes having aliphatic *para*-substituents', *J. Polym. Sci. Part A: Polym. Chem. Ed.*, **32**, 2523–2530 (1994).
- [11] M. Teraguchi and T. Masuda, 'Polydiphenylacetylene membranes with high gas permeability and remarkable chiral memory', *Macromolecules*, **35**, 1149–1151 (2002).
- [12] T. Sakaguchi, G. Kwak and T. Masuda, 'Synthesis of poly(1-*beta*-naphthyl-2-phenylacetylene) membranes through desilylation and their properties', *Polymer*, **43**, 3937–3942 (2002).
- [13] Y. Hayakawa, M. Nishida, T. Aoki and H. Muramatsu, 'Synthesis of polyphenylacetylenes containing trifluoromethyl groups for gas permeable membrane', *J. Polym. Sci. Part A: Polym. Chem. Ed.*, **30**, 873–877 (1992).
- [14] T. Aoki, H. Nakahara, Y. Hayakawa, M. Kokai and E. Oikawa, 'Trimethylsilyl-group containing polyphenylacetylenes for oxygen and ethanol permselective membranes', *J. Polym. Sci. Part A: Polym. Chem. Ed.*, **32**, 849–858 (1994).
- [15] G. Costa, 'Polymerization of mono- and disubstituted acetylenes', in *Comprehensive Polymer Science. The Synthesis, Characterization, Reactions and Applications of Polymers*, Vol. 4, Chain Polymerization II, G. Allen and J. C. Bevington (Eds), Pergamon Press, Oxford, UK, pp. 155–161 (1989).
- [16] H. Shirakawa, T. Masuda and K. Takeda, 'Synthesis and properties of acetylenic polymers', in *The Chemistry of Triple-Bonded Functional Groups*, Supplement C2, Vol. 2, S. Patai (Ed.), John Wiley & Sons, Ltd, Chichester, UK, pp. 945–1016 (1994).
- [17] T. Masuda, 'Acetylenic polymers', in *Polymeric Material Encyclopedia*, Vol. 1, J. C. Salamone

- (Ed.), CRC Press, Boca Raton, FL, USA, pp. 32–40 (1996).
- [18] T. Masuda, 'Acetylene polymerization', in *Catalysis in Precision Polymerization*, S. Kobayashi (Ed.), John Wiley & Sons, Ltd, Chichester, UK, pp. 67–97 (1997).
- [19] M. Tabata, T. Sone and Y. Sadahiro, 'Precise synthesis of monosubstituted polyacetylenes using Rh complex catalysts. Control of solid structure and pi-conjugation length', *Macromol. Chem. Phys.*, **200**, 265–282 (1999).
- [20] R. Nomura and T. Masuda, *Encyclopedia of Polymer Science and Technology*, 3rd Edn, Vol IA, J. I. Kroshwitz (Ed.), Wiley, Hoboken, NJ, p. 1 (2003).
- [21] T. Masuda, E. Isobe and T. Higashimura, 'Polymerization of 1-(trimethylsilyl)-1-propyne by halides of niobium (v) and tantalum (v) and polymer properties', *Macromolecules*, **18**, 841–845 (1985).
- [22] T. Masuda, 'Poly[1-(trimethylsilyl)-1-propyne]', in *Macromolecular Synthesis*, Vol. 11, D. A. Tirrell (Ed.), MRG Polymer Press, Hattiesburg, MS, USA, pp. 45–47 (1992).
- [23] T. Masuda, E. Isobe, T. Hamano and T. Higashimura, 'Synthesis of poly[1-(trimethylsilyl)-1-propyne] with extremely high molecular weight by using TaCl₅-Ph₃Bi (1:1) catalyst', *Macromolecules*, **19**, 2448–2450 (1986).
- [24] J. Fujimori, T. Masuda and T. Higashimura, 'Synthesis of poly[1-(trimethylsilyl)-1-propyne] with a narrow molecular weight distribution by using NbCl₅ catalyst in cyclohexane', *Polym. Bull.*, **20**, 1–6 (1988).
- [25] T. Masuda, E. Isobe, T. Hamano and T. Higashimura, 'Polymerization of silicon-containing acetylenes. 5. Polymerization of 1-silyl-1-propynes by TaCl₅-based catalysts', *J. Polym. Sci. Part A: Polym. Chem. Ed.*, **25**, 1353–1362 (1987).
- [26] E. Isobe, T. Masuda, T. Higashimura and A. Yamamoto, 'Polymerization of 1-(trimethylsilyl)-1-propyne homologs containing two silicon atoms by tantalum- and niobium-based catalysts', *J. Polym. Sci. Part A: Polym. Chem. Ed.*, **24**, 1839–1848 (1986).
- [27] M. Langsam and A. C. L. Savoca, 'Trialkylgermylpropyne polymers and gas separation membranes therefrom', Air Products and Chemicals, Inc., *US Patent 4 759 776*, *Eur. Patent Application*, EP 270 985 (1988).
- [28] T. Masuda and S. Kunita, unpublished data.
- [29] T. Masuda, M. Kawasaki, Y. Okano and T. Higashimura, 'Polymerization of methylpentynes by transition metal catalysts: monomer structure, reactivity, and polymer properties', *Polym. J.*, **14**, 371–377 (1982).
- [30] A. Niki, T. Masuda and T. Higashimura, 'Effects of organometallic cocatalysts on the polymerization of disubstituted acetylenes by TaCl₅ and NbCl₅', *J. Polym. Sci. Part A: Polym. Chem. Ed.*, **25**, 1553–1562 (1987).
- [31] K. Tsuchihara, T. Masuda and T. Higashimura, 'Polymerization of silicon-containing diphenylacetylenes and high gas permeability of the product polymers', *Macromolecules*, **25**, 5816–5820 (1992).
- [32] H. Tachimori, T. Masuda, H. Kouzai and T. Higashimura, 'Synthesis and properties of polydiphenylacetylenes having ether linkages', *Polym. Bull.*, **32**, 133–140 (1994).
- [33] H. Tachimori and T. Masuda, 'Synthesis and properties of a polydiphenylacetylene containing carbazolyl groups', *J. Polym. Sci. Part A: Polym. Chem. Ed.*, **33**, 2079–2085 (1995).
- [34] W. Yang, M. Tabata, S. Kobayashi, K. Yokota and A. Shimizu, 'Synthesis of ultrahigh-molecular-weight aromatic polyacetylenes with [Rh(norbornadiene)Cl]₂-triethylamine and solvent-induced crystallization of the obtained amorphous polyacetylenes', *Polym. J.*, **23**, 1135–1138 (1991).
- [35] M. Tabata, W. Yang and K. Yokota, '¹H-NMR and UV studies of Rh complexes as stereoregular polymerization catalysts for phenylacetylenes: effects of ligands and solvents on their catalyst activities', *J. Polym. Sci. Part A: Polym. Chem. Ed.*, **32**, 1113–1120 (1994).
- [36] T. Masuda, K. Q. Thieu, N. Sasaki and T. Higashimura, 'Polymerization of phenylacetylenes. 4. Effects of tetraphenyltin and initiation mechanism in WCl₆-catalyzed polymerization', *Macromolecules*, **9**, 661–664 (1976).
- [37] Y. Fujita, Y. Misumi, M. Tabata and T. Masuda, 'Synthesis, geometric structure and properties of polyphenylacetylenes with bulky *para*-substituents', *J. Polym. Sci. Part A: Polym. Chem. Ed.*, **36**, 3157–3163 (1998).
- [38] Y. Abe, T. Masuda and T. Higashimura, 'Polymerization of (*o*-methylphenyl)acetylene and polymer characterization', *J. Polym. Sci. Part A: Polym. Chem. Ed.*, **27**, 4267–4279 (1989).
- [39] T. Yoshida, Y. Abe, T. Masuda and T. Higashimura, 'Polymerization and polymer properties of (*p*-*tert*-butyl-*o*,*o*-dimethylphenyl)acetylene', *J. Polym. Sci. Part A: Polym. Chem. Ed.*, **34**, 2229–2236 (1996).
- [40] T. Masuda, T. Hamano, K. Tsuchihara and T. Higashimura, 'Synthesis and characterization of poly[[*o*-(trimethylsilyl)phenyl]acetylene]', *Macromolecules*, **23**, 1374–1380 (1990).
- [41] T. Mizumoto, T. Masuda and T. Higashimura, 'Polymerization of [*o*-(trimethylgermyl)phenyl]acetylene and polymer characterization', *J. Polym. Sci. Part A: Polym. Chem. Ed.*, **31**, 2555–2561 (1993).
- [42] T. Masuda, T. Hamano, T. Higashimura, T. Ueda and H. Muramatsu, 'Synthesis and characteriz-

- ation of poly[*o*-(trifluoromethyl)phenyl]acetylene', *Macromolecules*, **21**, 281–286 (1988).
- [43] T. Yoshimura, T. Masuda, T. Higashimura, K. Okuhara and T. Ueda, 'Polymerization of (pentafluorophenyl)acetylene and (*p*-butyl-*o,o,m*-tetrafluorophenyl)acetylene and polymer properties', *Macromolecules*, **24**, 6053–6058 (1991).
- [44] K. Tsuchihara, T. Masuda, T. Higashimura, M. Nishida and H. Muramatsu, 'Polymerization of [2,5-bis(trifluoromethyl)phenyl]acetylene and polymer properties', *Polym. Bull.*, **23**, 505–511 (1990).
- [45] S. A. Stern, 'Polymers for gas separations: the next decade', *J. Membr. Sci.*, **94**, 1–65 (1994).
- [46] R. E. Kesting and A. K. Fritzsche, *Polymeric Gas Separation Membranes*, John Wiley & Sons, Inc., New York, NY, USA (1993).
- [47] S. 'Pauly, 'Permeability and diffusion data', in *Polymer Handbook*, 4th Edn, J. Brandrup, E. H. Immergut and E. A. Grulke (Eds), John Wiley & Sons, Inc., New York, NY, USA, pp. VI/543–VI/569 (1999).
- [48] L. M. Robeson, 'Correlation of separation factor versus permeability for polymeric membranes', *J. Membr. Sci.*, **62**, 165–185 (1991).
- [49] K. Takada, H. Matsuya, T. Masuda and T. Higashimura, 'Gas permeability of polyacetylenes carrying substituents', *J. Appl. Polym. Sci.*, **30**, 1605–1616 (1985).
- [50] L. M. Robeson, W. F. Burgoyne, M. Langsam, A. C. Savoca and C. F. Tien, 'High performance polymers for membrane separation', *Polymer*, **35**, 4970–4978 (1994).
- [51] K. Tsuchihara, T. Masuda and T. Higashimura, 'Polymerization of Si-containing acetylenes. XIV. Polymerization of diphenylacetylenes with bulky silyl groups and polymer properties', *J. Polym. Sci. Part A: Polym. Chem. Ed.*, **31**, 547–552 (1993).
- [52] T. Masuda, Y. Iguchi, B.Z. Tang and T. Higashimura, 'Diffusion and solution of gases in substituted polyacetylene membranes', *Polymer*, **29**, 2041–2049 (1988).
- [53] A. C. Savoca, A. D. Surnamer and C. F. Tien, 'Gas transport in poly(silylpropynes): the chemical structure point of view', *Macromolecules*, **26**, 6211–6216 (1993).
- [54] M. Langsam, M. Anand and E. J. Karwacki, 'Substituted propyne polymers I. Chemical surface modification of poly[1-(trimethylsilyl)propyne] for gas separation membranes', *Gas Sepn. Pur.*, **2**, 162–170 (1988).
- [55] G. Chen, H. J. Griesser and A. W. H. Mau, 'Gas permeability of poly[1-(trimethylsilyl)-1-propyne] membranes modified by hexafluorobutyl methacrylate', *J. Membr. Sci.*, **82**, 99–115 (1993).
- [56] I. Pinnau and L. G. Toy, 'Transport of organic vapors through poly(1-trimethylsilyl-1-propyne)', *J. Membr. Sci.*, **116**, 199–209 (1996).
- [57] A. Morisato, H. C. Shen, S. S. Sankar, B. D. Freeman, I. Pinnau and C. G. Casillas, 'Polymer characterization and gas permeability of poly(1-trimethylsilyl-1-propyne) [PTMSP], poly(1-phenyl-1-propyne) [PPP] and PTMSP/PPP blends', *J. Polym. Sci. Part B: Polym. Phys. Ed.*, **34**, 2209–2222 (1996).
- [58] *Permeability and Other Film Properties*, Plastics Design Library, (1995).
- [59] L. G. Toy, K. Nagai, B. D. Freeman, I. Pinnau, Z. He, T. Masuda, M. Teraguchi and Y. P. Yampolskii, 'Pure-gas and vapor permeation and sorption properties of poly[1-phenyl-2-[*p*-(trimethylsilyl)phenyl]acetylene] (PTMSDPA)', *Macromolecules*, **33**, 2516–2524 (2000).
- [60] K. Nagai, L. G. Toy, B. D. Freeman, M. Teraguchi, T. Masuda and I. Pinnau, 'Gas permeability and hydrocarbon solubility of poly[1-phenyl-2-[*p*-(triisopropylsilyl)phenyl]acetylene]', *J. Polym. Sci. Part B: Polym. Phys. Ed.*, **38**, 1474–1484 (2000).
- [61] A. Morisato, Z. He and I. Pinnau, 'Mixed-gas permeation properties and physical aging of poly(4-methyl-2-pentyne)', in *Polymer Membranes for Gas and Vapor Separation, Chemistry and Materials Science*, ACS Symposium Series 733, B. D. Freeman and I. Pinnau (Eds), American Chemical Society, Washington, DC, USA, pp. 56–67 (1999).
- [62] R. Srinivasan, S. R. Auvil and P. M. Burban, 'Elucidating the mechanism(s) of gas transport in poly[1-(trimethylsilyl)-1-propyne] (PTMSP) membranes', *J. Membr. Sci.*, **86**, 67–86 (1994).
- [63] M. Anand, M. Langsam, M. B. Rao and S. Sircar, 'Multicomponent gas separation by selective surface flow (SSF) and poly-trimethylsilylpropyne (PTMSP) membranes', *J. Membr. Sci.*, **123**, 17–25 (1997).
- [64] J. Schultz and K. V. Peinemann, 'Membranes for separation of higher hydrocarbons from methane', *J. Membr. Sci.*, **110**, 37–45 (1996).
- [65] T. C. Merkel, B. D. Freeman, R. J. Spontak, Z. He, I. Pinnau, P. Meakin and A. J. Hill, 'Ultrapermselective, reverse-selective nanocomposite membranes', *Science*, **296**, 519–522 (2002).
- [66] H. Shimomura, T. Uyeda, K. Nakanishi, H. Odani and M. Kurata, 'Studies of permeation of gases through polymer membranes in the temperature region encompassing the glass transition permeation of gas/vapor mixtures through disubstituted polyacetylene and poly (vinyl acetate) mem-

- branes', *Rep. Asahi Glass Foundation Ind. Technol.*, **53**, 293–301 (1988).
- [67] K. Nagai, A. Higuchi and T. Nakagawa, 'Bromination and gas permeability of a poly(1-trimethylsilyl-1-propyne) membrane', *J. Appl. Polym. Sci.*, **54**, 1207–1217 (1994).
- [68] J. S. Yang and G. H. Hsiue, 'Novel dry poly-[(1-trimethylsilyl)-1-propyne]-AgClO₄ complex membranes for olefin/paraffin separations', *J. Membr. Sci.*, **120**, 69–76 (1996).
- [69] J. S. Yang and G. H. Hsiue, 'Swollen polymeric complex membranes for olefin/paraffin separation', *J. Membr. Sci.*, **138**, 203–211 (1998).
- [70] R. W. Baker, *Membrane Technology and Applications*, McGraw-Hill, New York, NY, USA (2000).
- [71a] T. Masuda, B. Z. Tang and T. Higashimura, 'Ethanol–water separation by pervaporation through substituted polyacetylene membranes', *Polym. J.*, **18**, 565–657 (1986).
- [71b] A. G. Fadeev, Ya. A. Selinskaya, S. S. Kelly, M. M. Meagher, E. G. Litvinova, V. S. Khotimsky, V. V. Volkov, Extraction of butanol from aqueous solutions by pervaporation through poly(1-trimethylsilyl-1-propyne), *J. Membr. Sci.*, **186**, 205–217 (2001).
- [71c] V. V. Volkov, A. G. Fadeev, V. S. Khotimsky, E. G. Litvinova, Y. A. Selinskaya, J. D. McMillan, S. S. Kelly, Effects of synthesis conditions on the pervaporation properties of poly-[1-(trimethylsilyl)-1-propyne] useful for membrane bioreaction, *J. Appl. Polym. Sci.*, **91**, 2271–2277 (2004).
- [72] T. Sakaguchi, K. Yumoto, G. Kwak, M. Yoshikawa and T. Masuda, 'Pervaporation of ethanol/water and benzene/cyclohexane mixtures using novel substituted polyacetylene membranes', *Polym. Bull.*, **48**, 271–276 (2002).
- [73] K. Ishihara, Y. Nagase and K. Matsui, 'Pervaporation of alcohol/water mixtures through a poly[1-(trimethylsilyl)-1-propyne] membrane', *Makromol. Chem., Rapid Commun.*, **7**, 43–46 (1986).
- [74] Y. Nagase, K. Ishihara and K. Matsui, 'Chemical modification of a poly(substituted-acetylene): II. Pervaporation of an ethanol/water mixture through a poly(1-trimethylsilyl-1-propyne)/polydimethylsiloxane graft copolymer membrane', *J. Polym. Sci. Part B: Polym. Phys. Ed.*, **28**, 377–386 (1990).
- [75] H. H. Nijhuis, M. H. V. Mulder and C. A. Smolders, 'Selection of elastomeric membranes for the removal of volatile organics from water', *J. Appl. Polym. Sci.*, **47**, 2227–2243 (1993).
- [76] T. Masuda, M. Takatsuka, B. Z. Tang and T. Higashimura, 'Pervaporation of organic liquid–water mixtures through substituted polyacetylene membranes', *J. Membr. Sci.*, **49**, 69–83 (1990).
- [77] Y. Nagase, Y. Takamura and K. Matsui, 'Chemical modification of a poly(substituted-acetylene). V. Alkylsilylation of poly(1-trimethylsilyl-1-propyne) and improved liquid separating properties at pervaporation', *J. Appl. Polym. Sci.*, **42**, 185–190 (1991).
- [78] T. Nakagawa, T. Arai, Y. Ookawara and K. Nagai, 'Modification of poly(1-trimethylsilyl-1-propyne) membranes containing fluorinated monomers by gamma-ray irradiation and their halogenated hydrocarbon separation properties for pervaporation', *Sen'i Gakkaishi*, **53**, 423–430 (1997).
- [79] S. Mishima and T. Nakagawa, 'Pervaporation of volatile organic compounds/water mixtures through poly(1*H*, 1*H*, 9*H*-hexadecafluoronyl methacrylate)-filled poly(1-trimethylsilyl-1-propyne) membranes', *J. Appl. Polym. Sci.*, **83**, 1054–1060 (2002).
- [80] S. Takahashi, Y. Yoshida, T. Kamada and T. Nakagawa, 'Separation of benzene using poly[1-(trimethylsilyl)-1-propyne] blend membranes', *Kobunshi Ronbunshu*, **58**, 213–220 (2001).

Gas and Vapor Transport Properties of Perfluoropolymers

Tim C. Merkel, Ingo Pinnau, Rajeev Prabhakar and Benny D. Freeman

9.1 Introduction

The discovery of polytetrafluoroethylene (PTFE) in 1938 by Roy Plunkett [1] at DuPont spurred the development of a wide variety of rubbery and glassy fluoropolymers. Early researchers recognized that fluorinated polymers possessed many unique and useful properties. Chief among these is the extraordinary thermal and chemical resistance of fluoropolymers. These attributes stem from their strong covalent carbon-carbon (360 kJ/mol) [2] and carbon-fluorine (485 kJ/mol) [2] bonds and the protective sheath of fluorine atoms around the carbon backbone. As a result, fluoropolymers are unaffected by most chemicals, including acids, bases, organic solvents, oils and strong oxidizers. Consequently, they are often the material of choice for use in hostile chemical environments. Fluoropolymers also possess exceptional optical, electrical and surface properties [2,3]. Such qualities have resulted in the commercial use of fluoropolymers in numerous areas, including the automotive, electronic, aerospace, chemical, specialty packaging and medical industries [2–5].

Prior to the mid-1980s, there were relatively few studies of gas or vapor transport through dense fluoropolymer membranes. This was due in part to the low permeability of the existing semicrystalline fluoropolymers, but perhaps primarily due to processing difficulties that limited their potential use as gas separation membranes [6]. For example, PTFE is insoluble in all

common solvents and not melt-processable by conventional means because of its high melting point (325 °C) [2]. This makes it difficult to use PTFE or related fluoropolymers as selective materials in commercial asymmetric hollow fibers or composite membranes where solution-casting fabrication techniques are generally used. Nevertheless, a number of early studies on gas transport in nonporous fluoropolymer membranes were conducted and are briefly reviewed here for an historical perspective.

The first systematic report on transport in dense fluorocarbon-based polymer films was an examination of gas diffusion in PTFE, tetrafluoroethylene-hexafluoropropylene copolymer (FEP) and polychlorotrifluoroethylene (PCTFE) by Brandt and Anysas [7]. These authors found anomalously low activation energies of diffusion in the fluoropolymers compared to results in hydrocarbon polymers. They suggested this unexpected behavior might be related to pre-existing holes or microchannels frozen into the fluoropolymer films during fabrication. Pasternak *et al.* reported permeability, diffusion and solubility data for several gases and vapors in PTFE [8] and FEP [9]. These authors found that activation energies of diffusion were lower in PTFE than in polyethylene (PE), consistent with the results of Brandt and Anysas. Pasternak *et al.* also reported that light-gas solubilities were higher in FEP than in PE, whereas the reverse was true for hydrocarbon

gases and vapors. The authors recognized that compared to PE the fluoropolymers were more permeable to light gases, but much less permeable to higher-boiling hydrocarbons [9]. These results were consistent with a growing body of patent data, which indicated that fluoropolymers were excellent permeation barriers to hydrocarbon liquids and vapors and thus useful as gas tank and flexible hose liners [10–15].

In the early 1980s, Koros and coworkers [16,17] examined hydrocarbon gas and vapor transport in PTFE and FEP. The results were similar to those of Pasternak *et al.*, but also included mixed-gas experiments and the effects of polymer annealing. These authors found that annealing the fluoropolymers reduced both gas solubility and diffusivity, presumably due to polymer recrystallization at the annealing temperature. El-Hibri and Paul [18] reported on the effects of drawing and processing temperature on gas transport in poly(vinylidene fluoride) (PVDF). They found that uniaxial drawing reduced gas permeability and diffusivity, whereas annealing increased these transport parameters. It was suggested that such transport effects were caused by changes to both the amorphous and crystalline regions of PVDF resulting from the drawing conditions. Paul's research group also investigated gas transport in a dry perfluorosulfonic acid polymer (Nafion) and found unusually high He/H₂ and N₂/CH₄ separation factors [19]. Finally, around this same time frame, Fitz [4] reported a large amount of gas permeation data in commercial fluoropolymers. Much of this early fluoropolymer transport data is available in tabular form in the *Polymer Handbook* [20].

Since the mid-1980s, a significant amount of research has been conducted on polymer gas separation membranes containing fluorinated functional groups. Some of the materials investigated have included fluorinated polysulfones [21], polycarbonates [22] and polyimides [23,24]. In general, bulky fluorine-containing groups were added to these 'size-sieving', glassy polymers to inhibit chain packing and increase polymer permeability [25]. In this chapter, however, we will not discuss these fluorine-containing polymers, instead focusing on transport in completely fluorinated or perfluoropolymers. It is in perfluoropolymers that the unique nature of the carbon–fluorine bond has its greatest impact on transport properties.

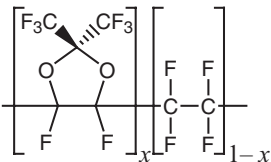
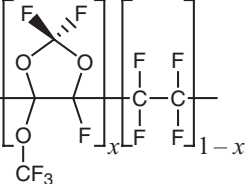
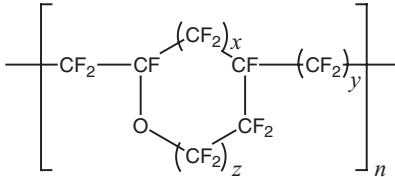
The discovery in the past 20 years of amorphous, solvent-processable perfluoropolymers, such as Teflon[®] AF, Cytop[™] and Hyflon[®] AD, has created new opportunities for perfluorinated materials in membrane separations. These amorphous perfluoropolymers can be fabricated into thin, high-flux, composite membranes while retaining the excellent chemical stability typical of fluorinated materials. As will be discussed in the remainder of this chapter, the unique chemical properties of perfluoropolymers endow them with performance advantages over hydrocarbon-based polymers in some important membrane applications.

9.2 Amorphous Perfluoropolymers as Membrane Materials

A major breakthrough in the use of perfluoropolymers for gas separation membranes was the development of Teflon[®] AF by DuPont in the 1980s [26,27]. This family of glassy polymers, based on copolymers of tetrafluoroethylene and 2,2-bis(trifluoromethyl)-4,5-difluoro-1,3-dioxole, can be readily dissolved in and cast from perfluorinated solvents. The large, bulky dioxole monomer hinders efficient polymer chain packing, thereby preventing crystal formation and yielding a completely amorphous polymer that exhibits high gas permeability^[6,28,29]. This attribute, combined with the usual perfluoropolymer chemical and thermal stability, makes Teflon[®] AF and related polymers intriguing membrane materials for gas and vapor separations.

In addition to Teflon[®] AF, two other glassy, amorphous perfluoropolymers have been developed in the past 20 years: Cytop[™] by Asahi Glass [30] and Hyflon[®] AD by Ausimont (now Solvay Solexis) [31]. The chemical structures and selected properties for these polymers are shown in Table 9.1. For comparison, semicrystalline polytetrafluoroethylene is included in this table as well. Relative to PTFE, Teflon AF is significantly less dense due to the large, rigid dioxole monomer, which 'frustrates' efficient chain packing. The resultant 'open' polymer structure causes Teflon AF2400 to be more than two orders of magnitude more permeable to nitrogen than PTFE. Similarly, the other amorphous perfluoropolymers are also substantially more permeable than PTFE. In addition, and perhaps most important from an applications standpoint, all three

Table 9.1 Structures and properties of selected perfluoropolymers

Polymer	Chemical structure	Density (g/cm ³)	Glass transition temperature (°C)	Nitrogen permeability (barrer) ^a
PTFE	$\left[\text{CF}_2 - \text{CF}_2 \right]_n$	2.1	30	1.3 [20]
Teflon [®] AF ^b		1.74	240	480 [36]
Hyflon [®] AD ^c		1.92	134	24 [93]
Cytop		2.03	108	5.0 [93]

^a1 Barrer = 10⁻¹⁰ cm³(STP) cm/(cm² s cmHg).

^bThe listed properties are for Teflon AF2400, where $x = 0.87$. The other frequently studied commercial grade offered by DuPont is Teflon AF1600, where $x = 0.65$.

^cThe listed properties are for Hyflon AD80 where $x = 0.80$. Another commercial grade offered by Solvay Solexis, whose gas transport properties have been examined, is Hyflon AD60, where $x = 0.60$.

amorphous perfluoropolymer types are soluble in selected perfluorinated solvents, which renders them amenable to composite membrane fabrication via solution casting. The combination of high permeability, chemical stability and casting solubility has led to a considerable and growing body of literature describing gas and vapor transport in these polymers [3,28,29,32–44].

Tables 9.2 and 9.3 present gas permeabilities and selectivities for five different amorphous, glassy perfluoropolymers. These materials cover a broad permeability range from Teflon AF2400, one of the most permeable polymers known, to Cytop, the least permeable of the perfluorinated amorphous glasses (although it is still about ten times more permeable than conven-

Table 9.2 Pure-gas permeabilities of selected amorphous perfluorinated glassy polymers at 35 °C^H

Permeability (barrer)	Teflon AF2400 (FFV = 0.33) [36]	Teflon AF1600 (FFV = 0.31) [39]	Hyflon AD80 (FFV = 0.23) [93]	HyflonAD60 (FFV = 0.23) [93]	Cytop (FFV = 0.21) [93]
He	—	—	430	390	170
H ₂	2090	550	210	180	59
CO ₂	2200	520	150	130	35
O ₂	960	270	67	57	16
N ₂	480	110	24	20	5.0
CH ₄	390	80	12	10	2.0

^HThe copolymer compositions of the Teflon AF and Hyflon AD grades described in this table are given in the Table 9.1 footnotes.

Table 9.3 Pure-gas selectivities of selected amorphous perfluorinated glassy polymers at 35 °C

Selectivity	Teflon AF2400 [36]	Teflon AF1600 [39]	Hyflon AD80 [93]	Hyflon AD60 [93]	Cytop [93]
He/H ₂	—	—	2.0	2.1	2.8
He/CH ₄	—	—	35	39	84
H ₂ /CH ₄	5.3	6.9	18	18	30
CO ₂ /CH ₄	5.7	6.5	13	13	18
O ₂ /N ₂	2.0	2.4	2.8	2.9	3.2
N ₂ /CH ₄	1.2	1.4	2.0	2.0	2.5

tional glassy polymers, such as polycarbonates). The relative permeability of the perfluoropolymers is well-described by their fractional free volume (FFV), a common measure of the free space in a polymer matrix available for molecular transport. For instance, both gas permeability and FFV exhibit the following order:

Teflon AF2400 > Teflon AF1600 > Hyflon AD80 ≈ Hyflon AD60 > Cytop.

Typically, for polymer membranes, the logarithm of gas permeability decreases linearly with increasing inverse FFV. A correlation of this type is presented in Figure 9.1 for nitrogen permeability in the amorphous perfluoropolymers. A conventional glassy polymer, a polycarbonate, is

included in this figure to highlight the relatively high permeability of the perfluoropolymers.

Ideally, when selecting polymers for membrane applications, it is desirable to find materials that are both highly permeable and highly selective. High permeability reduces the amount of membrane area required to perform a separation, and thereby reduces system cost. High selectivity increases product purity and reduces operating costs. For most light-gas pairs of interest to the membrane industry, the permeability and selectivity combinations of the amorphous perfluoropolymers are not extraordinary. For example, the most permeable perfluoropolymer, Teflon AF2400, has an O₂/N₂ selectivity of 2.0, about the same as polydimethylsiloxane, a rubbery polymer with comparable permeability. At the other end of the perfluoropolymer permeability scale, Cytop has an O₂/N₂ selectivity of only 3.2, significantly less than some polyimides of similar permeability. Nevertheless, despite their unspectacular O₂/N₂ selectivities, perfluoropolymer membranes have been considered for oxygen-enrichment applications because of their high permeability combined with chemical and thermal stability [45].

On the other hand, there are some examples of light-gas pairs where perfluoropolymers have exceptional transport properties. One example is shown in Figure 9.2, a selectivity–permeability trade-off plot for helium and hydrogen. This type of plot, first popularized by Robeson [46], can be used to define an ‘upper bound’ on the combination of permeability and selectivity beyond which no polymer materials are known. Such plots have been created for numerous important gas pairs and a theoretical description of the upper bound has been presented [47]. The data in Figure 9.2 indicate that perfluoropolymers have a unique combination of helium/hydrogen selectivity and helium permeability

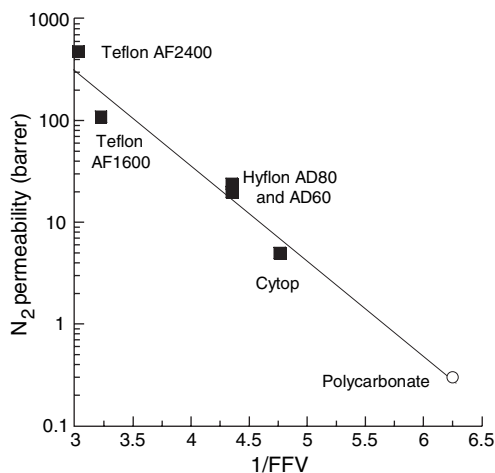


Figure 9.1 Nitrogen permeability in Teflon AF2400 [36], Teflon AF1600 [39], Hyflon AD80 [32], Hyflon AD60 [93], Cytop [93] and polycarbonate [20] as a function of polymer inverse fractional free volume at 35 °C

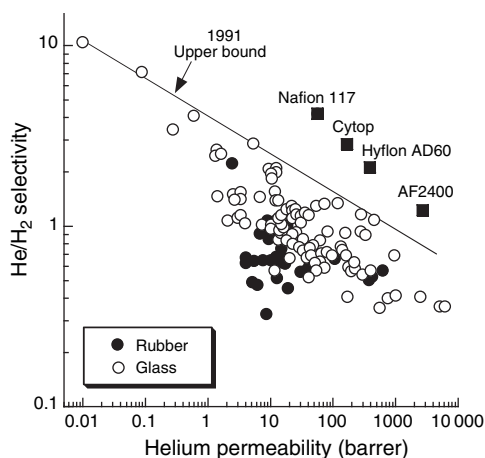


Figure 9.2 Helium/hydrogen selectivity–permeability trade-off relationship for a wide variety of rubbery and glassy polymers. The upper bound curve and non-perfluorinated polymer data are taken from Robeson [46], while the perfluoropolymer data are from Membrane Technology and Research [93], with the exception of Nafion 117 data of Chiou and Paul [19]

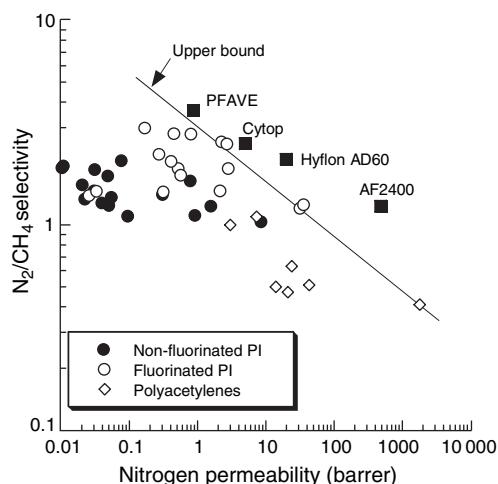


Figure 9.3 Nitrogen/methane selectivity–permeability trade-off relationships for a variety of glassy polymers. Polyimide (PI) data are taken from Tanaka *et al.* [23], Polyacetylene data are those of Odani and Masuda [96], while the perfluoropolymer data are from Membrane Technology and Research [93] (PFAVE is poly perfluoroallyl vinyl ether)

that allows them to exceed the upper bound for this gas pair. While helium/hydrogen separation is not a large industrial application, there is a need to separate these gases in, for example, the space industry [48]. If this is to be carried out with membranes, perfluoropolymers would be the obvious choice based on their excellent separation properties.

A more important industrial gas pair where perfluoropolymers also exhibit unique behavior is nitrogen/methane. A recent study reports that nearly 20 % of known USA natural gas reserves are ‘sub-quality’ due to high nitrogen content [49]. Much of this nitrogen-rich natural gas (10–30 % N_2) exists in small fields where distillation treatment is not economical. An ideal membrane to upgrade the natural gas would preferentially permeate nitrogen and leave methane as a high-pressure product. Unfortunately, separation of nitrogen from methane is very difficult for polymer membranes. This point is highlighted in Figure 9.3, a selectivity–permeability trade-off plot for this gas pair. Most polymers have nearly equal permeation rates for nitrogen and methane, while some rubbery polymers are even slightly ‘methane-selective’. The polymers with the highest com-

ination of N_2/CH_4 selectivity and nitrogen permeability are perfluoropolymers, which once again exceed the upper bound line.

The reason nitrogen/methane is such a difficult membrane separation is related to the molecular properties of the gases and the nature of the permeation process. Gas permeation through a dense polymer membrane follows a solution–diffusion mechanism, that is, the permeability, P , is equal to the product of gas solubility in the polymer, S , and the gas diffusion through the membrane, D :

$$P = S \times D \quad (9.1)$$

Gas solubility in a polymer typically scales with measures of gas condensability, such as normal boiling point (T_b) or critical temperature; in the absence of specific interactions, the more condensable a species, then the higher its solubility. Gas diffusion coefficients in a polymer scale with measures of molecular size, such as kinetic diameter or critical volume (V_c); the larger the molecule, then the lower the diffusion coefficient. In light of Equation (9.1), the selectivity of a

membrane for component A over component B, $\alpha_{A/B}$, can be expressed as the product of solubility selectivity and diffusivity selectivity:

$$\alpha_{A/B} = \frac{P_A}{P_B} = \frac{S_A}{S_B} \times \frac{D_A}{D_B} \quad (9.2)$$

Nitrogen molecules ($V_c = 93 \text{ cm}^3/\text{mol}$) are slightly smaller than those of methane ($99.3 \text{ cm}^3/\text{mol}$), and thus diffusion favors nitrogen. However, methane ($T_b = 112 \text{ K}$) is more condensable than nitrogen (77 K), and so solubility favors methane. Because the molecular property differences are rather small, the differences in solubility and diffusivity are small, and work in opposite directions. Consequently, nitrogen/methane selectivities tend to be low in polymer membranes.

An examination of the individual effects of solubility and diffusivity on nitrogen/methane selectivity provides insight on how the perfluoropolymers differ from other polymer membranes. Figure 9.4 presents N_2/CH_4 diffusivity selectivity versus N_2 diffusivity for several high-performance polyimides, two conventional glassy polymers (a polycarbonate and a polysulfone) and two perfluoropolymers. The polyimides, which are on the upper bound line in Figure 9.3, have relatively high N_2/CH_4 diffusivity selectivity. The diffusion coefficient of the smaller nitrogen is 4–5 times higher than that of methane in these rigid, ‘size-

sieving’ polymers. In contrast, the perfluoropolymers have significantly lower N_2/CH_4 diffusivity selectivities, combined with diffusion coefficients more than one order of magnitude higher than those in the polyimides. The relatively low diffusion selectivities of the perfluoropolymers are initially surprising, considering their position above the upper bound in Figure 9.3. As it turns out, what the perfluoropolymers lack in N_2/CH_4 diffusion selectivity is more than compensated for by their unique solubility properties.

Figure 9.5 presents N_2/CH_4 solubility selectivity versus nitrogen solubility for the same polyimides and perfluoropolymers described in Figures 9.3 and 9.4. Because methane is more condensable than nitrogen, methane is more soluble in all of the polymers examined. Consequently, the N_2/CH_4 solubility selectivity is less than one, and acts to reduce the overall N_2/CH_4 selectivity of all polymers. For the polyimides, methane is considerably more soluble than nitrogen ($S_{\text{N}_2}/S_{\text{CH}_4} < 0.4$). This detracts significantly from their relatively high diffusion selectivity. In contrast, for the perfluoropolymers, nitrogen is nearly as soluble as methane ($S_{\text{N}_2}/S_{\text{CH}_4} \rightarrow 1$). Because of this unusual N_2/CH_4 solubility selectivity, the perfluoropolymers have higher overall N_2/CH_4 selectivities even though they are not as effective at ‘size-sieving’ as polyimides. The solubility behavior of the amorphous perfluoropolymers is consistent with the early reports of Pasternak *et al.*,

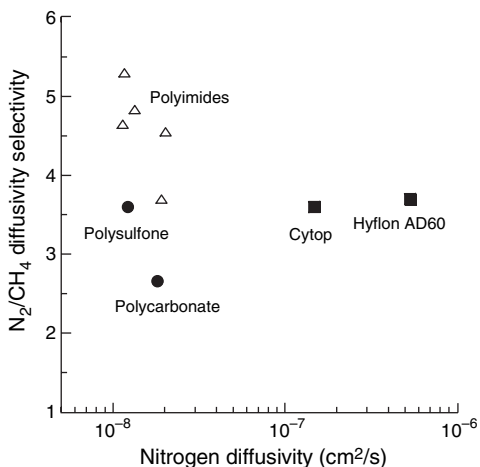


Figure 9.4 Nitrogen/methane diffusivity selectivity as a function of the nitrogen diffusion coefficient (diffusivity) for selected polyimides [23], a polycarbonate [20], a polysulfone [20] and two perfluoropolymers [93]

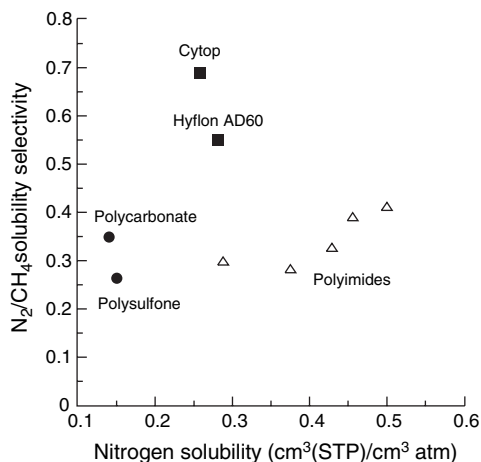


Figure 9.5 Nitrogen/methane solubility selectivity as a function of the nitrogen solubility coefficient (diffusivity) for selected polyimides [23], polycarbonate [20], polysulfone [20] and two perfluoropolymers [93]

who found relatively high light-gas solubility (e.g. N_2) but low hydrocarbon solubility (e.g. CH_4) in FEP [9]. While the impact of this unusual sorption behavior on methane/nitrogen selectivity is rather subtle, these atypical solubility properties provide the amorphous perfluoropolymers with other useful membrane characteristics.

At this point, it is informative to examine and compare, in some detail, gas and vapor solubility in perfluoropolymers and hydrocarbon-based polymers. As mentioned previously, in the absence of specific interactions between a polymer and penetrant molecule, solubility in a polymer typically scales with gas condensability. Over the years, researchers have proposed a number of correlations of gas solubility in liquids and polymers with gas critical temperature, normal boiling temperature or Lennard–Jones force constant.^{50–52} Figure 9.6 shows a correlation of this type between penetrant solubility in

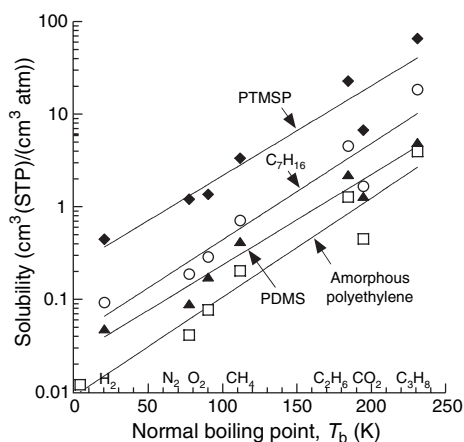


Figure 9.6 Gas solubility in *n*-heptane [97], poly(1-trimethylsilyl-1-propyne) (PTMSP) [55], polydimethylsiloxane (PDMS) [54] and amorphous polyethylene [53] as a function of penetrant normal boiling point

n-heptane, polydimethylsiloxane (PDMS) poly(1-trimethylsilyl-1-propyne) (PTMSP) and amorphous polyethylene with penetrant normal boiling point. For both hydrocarbon liquids and hydrocarbon-based polymers, the logarithm of penetrant solubility increases linearly with T_b . The correlation shown in Figure 9.6 can be expressed mathematically as:

$$\log S = M + N(T_b) \quad (9.3)$$

where the slope, N , characterizes the effect of condensability on solubility in a given media and is a measure of solubility selectivity. The intercept, M , is a measure of the relative sorption level in a material. The values of these parameters for various media are summarized in Table 9.4. The slope, N , is nearly identical for the hydrocarbon liquid and polymers, indicating that the sorption selectivity of these media is roughly equivalent. More broadly speaking, these results suggest that there is little variation in solubility selectivity among hydrocarbon-based media for non-polar light gases and hydrocarbon vapors.

Figure 9.7 presents penetrant solubility in four different fluorinated media as a function of T_b . Similar to results for the hydrocarbon media, the logarithm of solubility increases linearly with penetrant boiling point in the fluorinated polymers and liquid. Moreover, trend lines through the solubility data are approximately parallel to one another in the four fluorinated materials, analogous to the behavior in the hydrocarbon media. However, the slopes of these trend lines are different for the fluorocarbon and hydrocarbon materials. This point is quantified by the Equation (9.3) correlation parameter N , recorded in Table 9.4. The values of N are 30–40% lower in fluorinated media compared to those in hydrocarbon polymers or liquids. This result indicates that fluoropolymers have different solu-

Table 9.4 Solubility correlation parameters for hydrocarbon and fluorocarbon media

Polymer or liquid	Chemical nature	M (intercept)	$N \times 10^4$ (slope)
<i>n</i> -Heptane	Hydrocarbon	-1.39	104
Amorphous polyethylene		-2.04	107
Polydimethylsiloxane		-1.61	98
Poly(1-trimethylsilyl-1-propyne)		-0.69	108
Perfluoroheptane	Fluorocarbon	-1.01	73
Teflon AF2400		-0.75	68
Hyflon AD80		-1.07	65
Cytop		-1.38	73

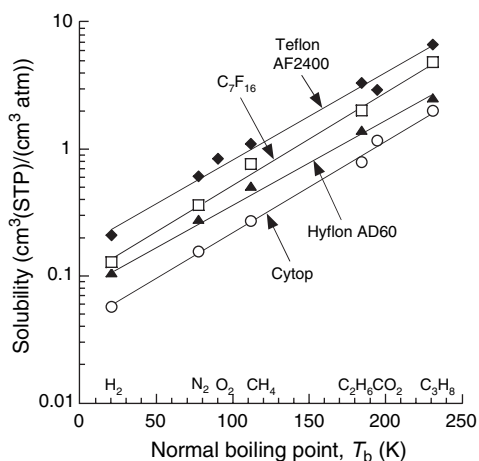


Figure 9.7 Gas solubility in perfluoroheptane [97], Teflon AF2400 [36], Hyflon AD60 [93] and Cytop [93] as a function of penetrant normal boiling point

bility selectivities than hydrocarbon-based polymers for light gases and hydrocarbon vapors.

The reason for the difference in slopes shown in Table 9.4 is primarily related to low hydrocarbon gas and vapor solubility in perfluorinated materials compared to the solubility of these same species in hydrocarbon-based media. A number of recent studies have described this surprisingly low hydrocarbon solubility in perfluoropolymers and vice versa (i.e. low fluorocarbon solubility in hydrocarbon-based polymers) [36,37,53–56]. These gas–polymer sorption results parallel findings from studies of hydrocarbon–fluorocarbon liquid solubilities conducted more than 50 years ago [57]. While the solubility behavior of these non-polar species follows an intuitive ‘like dissolves like’ guideline, it is not easily explained by classical or modern solubility

theories. The nature of this anomalous hydrocarbon–fluorocarbon solubility behavior will be examined in more detail later in this chapter. For now, we will focus on how low hydrocarbon solubility in perfluoropolymers impacts membrane separations.

There are two clear membrane-related implications of the unusual hydrocarbon sorption behavior in perfluoropolymers. First, perfluoropolymers have significantly lower hydrocarbon-vapor/light-gas solubility selectivities compared to hydrocarbon-based polymers. This is advantageous in ‘size-sieving’ membrane applications involving these species because the solubility selectivity (which favors the larger hydrocarbon vapor) works against overall selectivity. In this sense, fluorination represents a means to ‘tune’ membrane separation properties through solubility selectivity changes rather than the usual approach, which is to make changes to polymer structure to alter diffusion selectivity. Secondly, and perhaps more importantly, low hydrocarbon vapor solubility in perfluoropolymers renders them more resistant to sorption-induced plasticization than hydrocarbon-based polymers. Plasticization of glassy, ‘size-sieving’ membranes is an undesirable phenomenon caused by sorption of large, condensable species and the resulting swelling of the polymer matrix. This swelling can dramatically reduce the diffusion selectivity of a polymer, limiting and even preventing the use of membranes in some cases [58]. Applications where perfluoropolymers may have the most promise as gas separation membrane materials will exploit their low hydrocarbon solubility and resistance to plasticization.

Table 9.5 compares various hydrocarbon/light-gas solubility selectivities in hydrocarbon and fluorocarbon polymers and liquids. All of the

Table 9.5 Solubility selectivity of various gas pairs in perfluorinated- and hydrocarbon-base polymers and liquids

Gas pair	Polymer or liquid solubility selectivity				
	Fluorocarbon		Hydrocarbon		
	Hyflon AD 60	Cytop	C ₇ F ₁₆	Polyethylene	C ₇ H ₁₆
CO ₂ /CH ₄	3.6	4.3	2.6	2.7	2.4
CH ₄ /N ₂	1.8	1.7	2.1	4.9	3.8
CH ₄ /H ₂	6.5	4.8	5.9	8.1	7.7
C ₂ H ₆ /H ₂	19	14	16	54	49
C ₃ H ₈ /H ₂	36	35	38	165	200

hydrocarbon/light-gas solubility selectivities are lower in the fluorinated material (polymer or liquid) as compared to the hydrocarbon media. For example, the propane/hydrogen solubility selectivity is 35 in perfluorinated Cytop, while it is 165 and 200 in polyethylene and *n*-heptane, respectively. This result suggests that for polymers of equal diffusion selectivity, a perfluoropolymer would have roughly five times higher hydrogen/propane selectivity than a hydrocarbon-based membrane.

An example of low hydrocarbon solubility in perfluoropolymers is illustrated in Figure 9.8, which presents a propane sorption isotherm in Cytop. For comparison, propane sorption in a polyimide with similar fractional free volume is also shown in this figure. Often, in the absence of specific interactions, the solubility of any given penetrant in polymers will scale with the FFV of the materials. For the three perfluorinated polymers described in Figure 9.7, for instance, penetrant solubility increases with polymer FFV. That is, polymer FFV and penetrant solubility exhibit the following order:

Teflon AF2400 > Hyflon AD80 > Cytop.

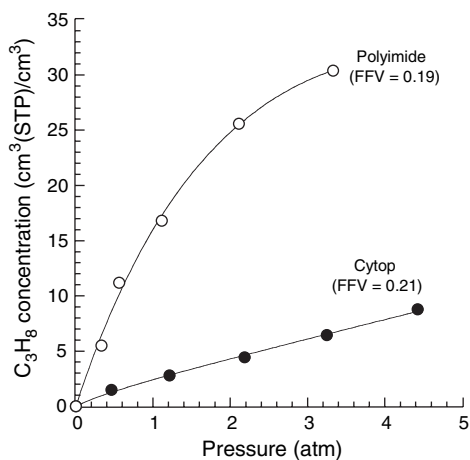


Figure 9.8 Propane sorption isotherms in Cytop [93] and 4,4'-(hexafluoroisopropylidene) diphthalic anhydride-4,4'-(hexafluoroisopropylidene) dianiline (6FDA-6FpPA) polyimide at 35 °C [60]. While this polyimide contains fluorinated pendant groups, the chain backbone is 'aromatic hydrocarbon-based' and its solubility properties reflect this fact

This result is reasonable in the sense that a higher FFV material such as Teflon AF2400 has more spacing between polymer chains to accommodate penetrant molecules than lower-FFV materials such as Cytop. In a similar manner, two polymers with equivalent FFVs would be expected to have nearly equal penetrant sorption levels in the absence of specific interactions. As demonstrated in Figure 9.8, this is not the case for propane sorption in perfluorinated Cytop (FFV = 0.21) and a hydrocarbon-backbone polyimide (FFV = 0.19). Propane solubility in Cytop is much lower than that in the polyimide. For example, at 3.3 atm, propane sorption levels in Cytop and in the polyimide are 6.4 and 30 cm³(STP)/(cm³ polymer), respectively. This roughly five-fold difference in propane sorption is consistent with the difference in solubility selectivity between fluorinated and hydrocarbon media reported in Table 9.5.

An important consequence of the solubility behavior shown in Figure 9.8 is its impact on polymer plasticization. It is well-known that high penetrant sorption levels tend to favor polymer plasticization. As the amount of sorbed penetrant increases, the polymer chains are forced apart to accommodate penetrant molecules. At the same time, the penetrant molecules can act to 'lubricate' the polymer matrix, hence facilitating chain motion. Both of these mechanisms act to reduce the size-sieving ability of a polymer membrane [58].

An excellent example of the detrimental effects of plasticization on membrane performance is the use of polyimides for propylene/propane separation. Many polyimides have very high propylene/propane pure-gas selectivity [59,60]. The high pure-gas selectivity results from the large difference in diffusion coefficient between smaller propylene molecules and larger propane. While very promising when tested under ideal conditions, the selectivities of these polyimides are greatly reduced when operated with industrial gas mixtures at high, near saturation, pressures [59]. This reduction in performance is due to sorption-induced plasticization [59]. Figure 9.9 shows an example of this behavior for polyimide and Cytop composite membranes. At low pressure, the polyimide has a mixed-gas propylene/propane selectivity of 8 (the pure-gas value is near 50). As the pressure is increased, the selectivity drops dramatically, eventually approaching 1.

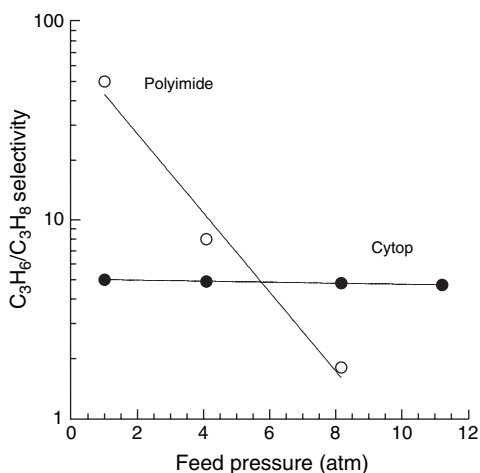


Figure 9.9 Mixed-gas propylene/propane selectivity as a function of feed pressure for a perfluorinated Cytop membrane and a hydrocarbon-based polyimide membrane [93]. The representative polyimide data shown is for 3,3',4,4'-biphenyltetracarboxylic dianhydride–2,4,6-trimethyl-1,3-phenylenediamine (BPDA–TmPD). The feed gas in these experiments was a 50/50 (mol/mol) C₃ mixture, except for the lowest pressure (1 atm) BPDA–TmPD data point, which was measured with pure gases. All measurements were conducted at room temperature

In contrast, Cytop has a much lower mixed-gas selectivity (4–5); however, its selectivity is completely stable with pressure. In fact, the last data point at 1 atm is for a liquid hydrocarbon feed. This result suggests that perfluoropolymers can be used in applications where highly selective hydrocarbon polymers fail due to hydrocarbon-vapor-induced plasticization.

Another membrane application where plasticization resistance is beneficial is in the removal of carbon dioxide from natural gas. Typical polymer membranes used for this separation are made from cellulose acetate (CA) or polyimides (PIs) [61,62]. These polymers have very high ideal (low pressure, pure-gas) carbon dioxide/methane selectivities ($\alpha_{\text{CO}_2/\text{CH}_4}^{\text{ideal}} > 30$); however, they are subject to plasticization by high-pressure carbon dioxide or trace heavy hydrocarbon components [63]. The typical industrial strategy employed to minimize plasticization is to use expensive pre-treatment schemes to limit membrane exposure to swelling species [61]. At the research level, considerable effort has been directed toward

cross-linking the selective polymer layer to limit membrane swelling [62,64,65]. This effort has had some success, although it typically results in lower permeabilities for membranes that are already 'plagued' by low fluxes.

The use of plasticization-resistant perfluorinated membranes represents an alternate strategy for membrane-based natural gas treatment. A recent review has suggested that under industrial operating conditions, membranes using perfluorinated Cytop as a selective layer have carbon dioxide/methane selectivities equivalent to those of CA or PI membranes ($\alpha_{\text{CO}_2/\text{CH}_4} = 10\text{--}15$) [61], despite the fact that Cytop membranes have lower ideal pure-gas selectivities ($\alpha_{\text{CO}_2/\text{CH}_4}^{\text{ideal}} = 20$). Moreover, the perfluorinated membranes have considerably higher carbon dioxide fluxes. These results suggest that perfluorinated membranes could prove particularly useful in natural gas treatment of 'rich' feed gas mixtures containing high levels of plasticizing components.

9.3 The Nature of Fluorocarbon/Hydrocarbon Interactions

The interesting transport properties of perfluoropolymers, described in the previous section, are rooted primarily in the atypical hydrocarbon solubility properties of these polymers. Anomalously low hydrocarbon solubility gives perfluoropolymer membranes their unique selectivities and plasticization resistance. As was shown in Figures 9.6 and 9.7, this solubility behavior is common to fluorocarbon liquids and polymers. In this section, we will examine hydrocarbon–fluorocarbon solubility and the nature of interactions between these species.

The unusual hydrocarbon solubility properties of fluorocarbons have been extensively researched, but, so far, no theory has fully explained the underlying molecular phenomena responsible for these properties. The behavior of fluorocarbon–hydrocarbon mixtures is often at odds with the predictions of regular solution theory, even though fluorocarbon–fluorocarbon mixtures and hydrocarbon–hydrocarbon mixtures obey the theory to a reasonable extent in most cases [66,67]. For example, the systems C₇H₁₆–C₇F₁₆, C₃H₁₂–C₅F₁₂ and C₄H₁₀–C₄F₁₀ show sizeable two-phase liquid–liquid regions, while theoretical predictions indicate that they should be miscible [67]. In addition, many hydrocarbon–

fluorocarbon solutions exhibit abnormally large enthalpies of mixing and volume expansions on mixing; these properties are mutually consistent, but at variance with their predicted values from regular solution theory [68].

The anomalous behavior of hydrocarbon–fluorocarbon solutions attracted significant scientific interest in the 1940s and 1950s [69–76]. Extensive experimental data were reported on fluorocarbon-containing solutions, and several theories were proposed to account for the observed deviations from regular solution theory. In a critical review of these theories, Scott suggested that the failure of the geometric mean approximation, which is used to describe interactions between unlike molecules (hydrocarbons and fluorocarbons, in this case), was the most likely reason for the inability of regular solution theory to describe hydrocarbon–fluorocarbon solution behavior [67].

Regular solution theory predicts the behavior of mixtures based upon (a) properties of the pure components and (b) mixing rules that describe unlike molecular interactions [77]. For example, the Lennard–Jones 6–12 potential function is often used to describe the intermolecular potential energy, Γ_{ii} , for a pair of spherically symmetric, neutral molecules of type i [78]:

$$\Gamma_{ii} = 4\epsilon_{ii} \left[\left(\frac{\sigma_{ii}}{r} \right)^{12} - \left(\frac{\sigma_{ii}}{r} \right)^6 \right] \quad (9.4)$$

where σ_{ii} is the intermolecular separation at zero potential energy, ϵ_{ii} is the minimum interaction energy, which corresponds to equilibrium separation, and r is the center-to-center distance between the two molecules. The interaction potential between two unlike molecules i and j , Γ_{ij} , is assumed to have the same functional form, with σ_{ij} being the arithmetic mean (the ‘Lorentz’ rule of Equation (9.5)) and ϵ_{ij} being the geometric mean (the ‘Berthelot’ rule of Equation (9.6)) of the pure substance parameter values [79]:

$$\sigma_{ij} = \frac{(\sigma_{ii} + \sigma_{jj})}{2} \quad (9.5)$$

and:

$$\epsilon_{ij} = \sqrt{\epsilon_{ii}\epsilon_{jj}} \quad (9.6)$$

Scott observed that the geometric mean approximation for the minimum interaction energy (Equation (9.6)) systematically overestimates

the interaction energy between hydrocarbon and fluorocarbon molecules [67]. He suggested that two factors arising from differences in molecular properties – the difference in ionization potentials between fluorocarbons and hydrocarbons, and the importance of non-central force fields in intermolecular interactions – were primarily responsible for the failure of the geometric mean approximation to predict hydrocarbon–fluorocarbon mixture behavior. These key factors violate assumptions inherent in the geometric mean approximation, and the extent to which each factor contributes to deviations from the geometric mean approximation is discussed below [67].

9.3.1 Differences in Ionization Potentials between Fluorocarbons and Hydrocarbons

In 1930, the intermolecular forces acting between non-polar molecules were first described by London using quantum mechanics [80]. The London equation for the attractive energy due to dispersion forces between two spherically symmetric, non-polar molecules i and j , Γ_{ij}^D , is [81,82]:

$$\Gamma_{ij}^D = -\frac{3\alpha_i\alpha_j}{2r^6} \left(\frac{I_i I_j}{I_i + I_j} \right) \quad (9.7)$$

where α_i and α_j are the polarizability of molecules i and j , and I_i and I_j are their respective ionization potentials. If the ionization potentials of the molecules are equal, then the London dispersion force potential between unlike molecules is given by the geometric mean rule. This can be seen by considering the product of the interaction energies for pairs of like molecules. From Equation (9.7):

$$\Gamma_{ii}^D \Gamma_{jj}^D = \left[-\frac{3\alpha_i\alpha_i}{2r^6} \left(\frac{I_i I_i}{I_i + I_i} \right) \right] \left[-\frac{3\alpha_j\alpha_j}{2r^6} \left(\frac{I_j I_j}{I_j + I_j} \right) \right] \quad (9.8)$$

Therefore:

$$\sqrt{\Gamma_{ii}^D \Gamma_{jj}^D} = \left[-\frac{3\alpha_i\alpha_j}{2r^6} \left(\frac{\sqrt{I_i I_j}}{2} \right) \right] \quad (9.9)$$

where the negative root is chosen on the right-hand side of the equation since the interaction potential is attractive in nature. If the ionization potential I_j is equal to I_i , then from Equation (9.7), the attractive energy can be expressed as:

$$\Gamma_{ij}^D = \left[-\frac{3\alpha_i\alpha_j}{2r^6} \left(\frac{I_i^2}{I_i + I_i} \right) \right] = \left[-\frac{3\alpha_i\alpha_j}{2r^6} \left(\frac{I_i}{2} \right) \right] \quad (9.10)$$

Comparing Equations (9.9) and (9.10) yields:

$$\Gamma_{ij}^D = \sqrt{\frac{D_{ij}^D}{I_i I_j}} \quad (9.11)$$

if the ionization potential I_j is equal to I_i in Equation (9.9).

Normally, the polarizabilities of two substances differ by much more than their ionization potentials, and so the assumption of equal ionization potentials introduces little error. Table 9.6 presents polarizabilities and ionization potentials of saturated linear hydrocarbon and fluorocarbon penetrants. With increasing carbon number in the hydrocarbon series or in the fluorocarbon series, the polarizability values vary to a much larger extent than the ionization potentials. For example, the difference between the ionization potentials of CH_4 and $n\text{-C}_4\text{H}_{10}$ is about 25 %, while the polarizability of $n\text{-C}_4\text{H}_{10}$ is more than three times that of CH_4 . However, the ionization potentials of the fluorocarbons (15–18 eV) are significantly higher than those of the hydrocarbons (10–13 eV). As a result, differences in ionization potentials between hydrocarbons and their fluorocarbon analogs are comparable to differences in their polarizabilities. Table 9.6 shows that the ionization potential of $n\text{-C}_4\text{F}_{10}$ is about 70 % higher than that of $n\text{-C}_4\text{H}_{10}$, while the polarizability of this fluorocarbon is only 50 % higher than that of its hydrocarbon analog.

Such large differences in ionization potentials can lead to significant deviations in calculated thermodynamic properties from those obtained using the geometric mean approximation. For example, from regular solution theory, the enthalpy of mixing two non-polar, non-electrolytes, i and j , is related to the cohesive energy density of the

pure substances, c_{ii} and c_{jj} , and of the mixture, c_{ij} , by the term K [67]:

$$K = c_{ii} + c_{jj} - 2c_{ij} \quad (9.12)$$

If the geometric mean approximation ($c_{ij} = \sqrt{c_{ii}c_{jj}}$) is applied, then:

$$K = (\sqrt{c_{ii}} - \sqrt{c_{jj}})^2 = (\delta_i - \delta_j)^2 \quad (9.13)$$

where δ is the solubility parameter, which is defined as the square root of the cohesive energy density ($\delta_i \equiv \sqrt{c_{ii}}$). [77]. Equation (9.13) is a result of the geometric mean approximation and, therefore, assumes the equality of ionization potentials. If, however, the difference in ionization potentials is taken into account in the intermolecular potential function by using, for example, the Lennard–Jones potential combined with the attractive component described by the London equation, then K is modified as follows [67]:

$$K = (\delta_i - \delta_j)^2 \left[1 + (1 - f_i f_j) \frac{2\delta_i \delta_j}{(\delta_i - \delta_j)^2} \right] \quad (9.14)$$

where:

$$f_i = \frac{2\sqrt{I_i I_j}}{I_i + I_j} \quad (9.15)$$

and:

$$f_\sigma = \left[\frac{2\sqrt{\sigma_{ii}\sigma_{jj}}}{(\sigma_{ii} + \sigma_{jj})} \right]^3 \quad (9.16)$$

Using a semi-empirical method to estimate the ionization potentials of fluorocarbons and hydrocarbons, Reed calculated f_i and f_σ values for $n\text{-C}_4\text{F}_{10}/n\text{-C}_4\text{H}_{10}$ mixtures. From this calculation,

Table 9.6 Polarizabilities and ionization potentials of selected compounds

Penetrant	Polarizability ($\times 10^{-24} \text{ cm}^3$)	Ionization potential (eV)
CH_4	2.6 [94]	13.1 [67]
$n\text{-C}_4\text{H}_{10}$	8.3 [94]	10.3 [83]
$n\text{-C}_5\text{H}_{12}$	10.0 [94]	10.6 [94]
CF_4	3.9 [95]	16–18 [67]
$n\text{-C}_4\text{F}_{10}$	12.7 [95]	17.4 [83]
$n\text{-C}_5\text{F}_{12}$	18.3 [95]	15.8 [88]
C_6H_6	—	9.2 [67]
I_2	—	9.7 [67]
CCl_4	—	11.0 [67]

f_I and f_σ are 0.9666 and 0.9944, respectively [83]. Using these values, the term in square brackets in Equation (9.14) has a value of about 3.5 (solubility parameters for *n*-butane and its perfluorinated analog are 7.4 and 6.2 (cal/cm³)^{0.5}, respectively, at 259.95 K [84]). As a result, the modified expression for K in equation (9.14) has a value of 5 cal/cm³, compared to 1.44 cal/cm³ from the original expression Equation (9.13). The value of K calculated from free energy of mixing values obtained from vapor–liquid equilibrium measurements is 7.7 cal/cm³ and thus the modified expression Equation (9.14) explains a large part of the discrepancy between the experimental observations and predictions based on the geometric mean approximation [67,84].

Interestingly, a seemingly small correction due to ionization potential differences (i.e. $(1 - f_I f_\sigma) \approx 0.04$) explains a large portion of the observed discrepancy. This correction becomes even more important in predicting observed properties such as solubility, because solubility varies exponentially with enthalpy [85]. Thus, accounting for the significant differences in ionization potentials of hydrocarbons and fluorocarbons can provide better agreement between observed results and regular solution theory predictions, at least for the case of *n*-C₄F₁₀/*n*-C₄H₁₀ mixtures.

There are mixtures, however, having large differences in ionization potentials that obey regular solution theory without taking these differences into account. As shown in Table 9.6, the differences in ionization potentials of fluorocarbons and compounds like benzene, carbon tetrachloride and iodine are as large as, or even larger, than those between fluorocarbons and aliphatic hydrocarbons. However, solutions of these compounds with fluorocarbons obey regular solution theory, which implies that differences in ionization potentials between molecules in a mixture cannot consistently account for observed differences in solution thermodynamic properties

[67]. This suggests that, in addition to ionization potential differences, there must be other factors behind the breakdown of regular solution theory for hydrocarbon–fluorocarbon mixtures. One possibility implicated by Scott is non-central force fields.

9.3.2 Non-central Force Fields

A recognized oversimplification in the treatment of intermolecular forces is the assumption of a spherically symmetric force potential located on the central atom in a molecule [67]. This assumption is strictly valid only for monatomic substances (e.g. He, Ne, etc.), and can, at best, be extended to substances like methane where the electronic distribution is nearly spherically symmetric around the carbon nucleus [67]. For larger, more complex molecules, Hamann *et al.* showed that the assumption of central force fields is often not valid, even if the molecules are nearly spherical [86]. They calculated interactions between a monatomic gas, A, and a hypothetical tetrahedral molecule, AA₄, by modeling the tetrahedral molecule as consisting of point forces centered at the position of each atom. To the extent that the weak forces between hydrogen atoms can be ignored, this model can be considered to be a reasonable description of interactions in methane–neopentane mixtures. Each atom, A, was modeled using a Lennard–Jones 6–12 potential, and interactions of a molecule with other molecules (A or AA₄) were calculated by summing over all pairs of interactions, averaged over all orientations of the molecules. The mixture interaction results were then fitted to the Lennard–Jones potential, and the results are shown in Table 9.7.

Table 9.7 is organized so that:

- The first two rows of the table present the arithmetic mean (σ) and geometric mean (ϵ) values for interactions between like molecules, A–A

Table 9.7 Calculations of interactions between hypothetical monatomic and polyatomic substances [86]

Interaction	<i>i</i>	<i>j</i>	Arithmetic mean interaction energy $\sigma_{ij}/\sigma_{AA}^a$	Geometric mean interaction energy $\epsilon_{ij}/\epsilon_{AA}^a$
A–A	A	A	1.00	1.00
AA ₄ –AA ₄	AA ₄	AA ₄	1.74	2.64
A–AA ₄ (mixing rules)	A	AA ₄	1.37	1.62
A–AA ₄ (model)	A	AA ₄	1.375	1.53

^aThe column values are normalized by A–A interaction energies.

and AA₄-AA₄. These values are normalized by the σ and ε values for A-A interactions.

- The third row presents σ and ε values for interactions between A and AA₄, calculated using the arithmetic and geometric mean mixing rules, respectively (cf. Equations (9.5) and (9.6)).
- The final row presents results from the calculations of Hamann *et al.* [86], according to the procedure described above.

Based on the table data, $\sigma_{A-AA_4}(\text{model})$ is quite close to the arithmetic mean of the pure component σ values, but $\varepsilon_{A-AA_4}(\text{model})$ is appreciably less than the geometric mean of the pure component ε values [86]. Thus, description of the potential field of the mixture by summing over individual atomic interactions does not match that obtained from the geometric mean approximation for ε . This discrepancy exposes another shortcoming of the geometric mean approximation when applied to certain mixtures. However, the non-central force field explanation is not specific to fluorocarbon-hydrocarbon mixtures. In addition, similar to ionization potential differences, non-central force field corrections fail to predict the qualitative behavior of all hydrocarbon-fluorocarbon mixtures [67]. Consequently, Scott concluded that, although they were the leading candidates at the time, neither of these theories satisfactorily described the anomalous hydrocarbon-fluorocarbon solubility behavior.

The inadequacy of the geometric mean approximation to describe unlike molecular interactions in some cases has led to empirical modifications of this mixing rule for modeling the thermodynamic properties of mixtures. Hildebrand used Equation (9.14) with an arbitrary adjustable constant, l_{12} , in place of the term $(1 - f_i f_j / \sigma)$ to model the excess Gibbs free energy, ΔG^E , of methane-tetrafluoromethane mixtures at 110.5 K [77]:

$$\Delta G^E = (x_1 v_1 + x_2 v_2) \phi_1 \phi_2 (\delta_1 - \delta_2)^2 \times \left[1 + l_{12} \frac{2\delta_1 \delta_2}{(\delta_1 - \delta_2)^2} \right] \quad (9.17)$$

where x_i , v_i and ϕ_i are the mole fraction, molar volume and volume fraction of component i , respectively, in the mixture. Figure 9.10 presents experimental data for excess Gibbs free energy for methane-tetrafluoromethane mixtures as

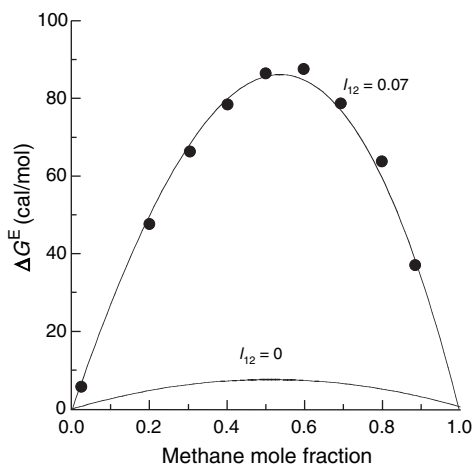


Figure 9.10 Excess Gibbs free energy for the methane-tetrafluoromethane system at 110.5 K [77]

well as model predictions with $l_{12} = 0$ (i.e. using the geometric mean approximation) and $l_{12} = 0.07$. The experimental excess Gibbs free energy can be modeled well with $l_{12} = 0.07$, while the theoretical prediction using the geometric mean approximation deviates substantially from the experimental data. Thus, a small change in the value of l_{12} provides a large improvement in predicting solution behavior. This is especially true for mixtures where the solubility parameters of the solution components are quite close to each other. For the above example, the solubility parameters of methane and tetrafluoromethane at 110.5 K are 7.2 and 8.0 (cal/cm³)^{0.5}, as determined from enthalpy of vaporization and liquid molar volume values at that temperature [87]. Using these solubility parameter values, the term in the square brackets in Equation (9.17) has a value of about 13.6 (when $l_{12} = 0.07$). Thus, even very low l_{12} values can be significant and result in large differences in thermodynamic property predictions, as shown in Figure 9.10.

Another empirical modification of the geometric mean approximation is shown below:

$$\varepsilon_{12} = (1 - k_{12}) \sqrt{\varepsilon_{11} \varepsilon_{22}} \quad (9.18)$$

where k_{12} is an empirical coefficient [77]. Dantzer-Siebert and Knobler used this modified mixing rule in the Kihara potential to model small molecule hydrocarbon-fluorocarbon mixture behavior [88]. They observed that interac-

tions between hydrocarbons and fluorocarbons were 10 % weaker than those predicted by the geometric mean (i.e. $k_{12} = 0.10$) [88].

Empirical corrections of the geometric mean approximation have also been shown to improve the description of fluorocarbon gas solubility in hydrocarbon-based polymers and vice versa. Based on the modeling of polymer-penetrant interactions using equations of state, De Angelis *et al.* showed that a reduction in the unlike molecular interaction (or geometric mean assumption) of about 10 % was required to accurately model solubility in hydrocarbon-fluorocarbon gas-polymer systems [89,90].

Figure 9.11(a) shows experimental C_2F_6 sorption data in polydimethylsiloxane (PDMS) that illustrate this point. In the Sanchez-Lacombe lattice fluid equation of state, the characteristic pressure of a binary mixture, P_{12}^* , which is closely related to the energy of interaction between species 1 and 2, is calculated as [89]:

$$P_{12}^* = \psi \sqrt{P_1^* P_2^*} \quad (9.19)$$

where P_i^* is the characteristic pressure of component i , and ψ is an empirical mixing parameter that corrects for deviations of P_{12}^* from the geometric mean approximation value. When ψ is unity, P_{12}^* is given by the geometric mean of the pure component values. Using this equation Equation (9.19) with $\psi = 1$, the C_2F_6 solubility in PDMS is over-predicted by a factor of about 9 [89]. A ψ value of 0.863 was required to fit the experimental sorption data to the Sanchez-Lacombe model [89]. In contrast, the C_2H_6 solubility in PDMS could be predicted with a ψ value of 0.963 (cf. Figure 9.11(b)) [89].

In other related work using the high free volume, glassy perfluoropolymers Teflon AF1600 and AF2400, ψ had to be reduced to about 0.9 in the non-equilibrium lattice fluid (NELF) model, which is based on the Sanchez-Lacombe model, to describe C_2H_6 (hydrocarbon) sorption in these fluoropolymers satisfactorily (cf. Figure 9.12(a)) [90]. However, as shown in Figure 9.12(b), with ψ equal to unity, a reasonable fit of the model to experimental C_2F_6 (fluorocarbon) sorption data in these two fluoropolymers was obtained [90]. Similar results were obtained in a recent study of the same systems using the non-equilibrium statistical associating fluid (NE-SAFT) and non-equilibrium

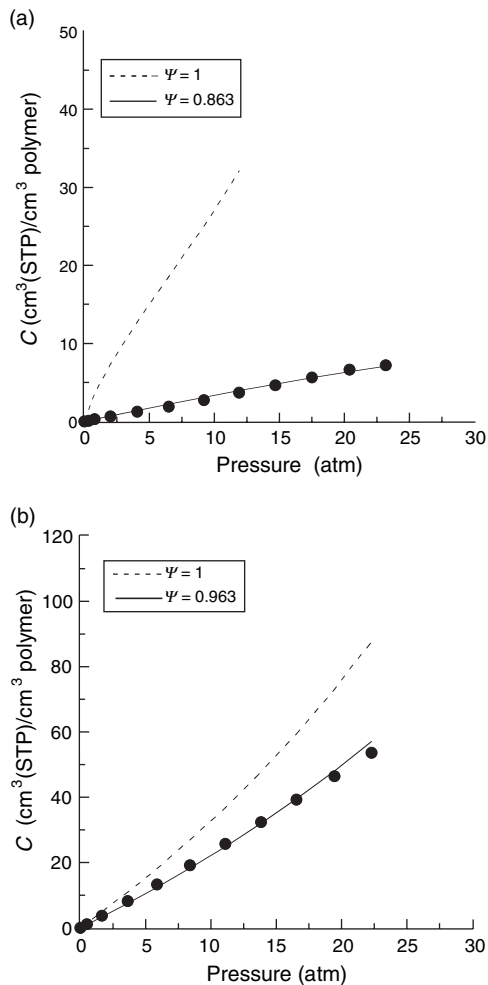


Figure 9.11 Comparison of experimental and predicted sorption isotherms of (a) C_2F_6 and (b) C_2H_6 in PDMS at 35°C using the Sanchez-Lacombe with $\psi = 1$ (dashed line) and ψ adjusted (continuous line) [89]

perturbed hard-sphere chain (NE-PHSC) theories [91].

Thus, in each of these studies, the fluorocarbon gas solubility in fluoropolymers and hydrocarbon gas solubility in hydrocarbon-based polymers could be described with little or no deviation from the geometric mean approximation. However, the fluorocarbon gas solubility in hydrocarbon-based polymers or hydrocarbon gas solubility in fluoropolymers required a significant (approximately 10 %) correction to the geometric mean estimates of the interaction

energies. Interestingly, the 10% reduction in interaction energy relative to that suggested by the geometric mean rule observed in these gas-polymer systems is strikingly similar to that reported by Hildebrand [77] and Dantzler-Siebert and Knobler [88] in small-molecule systems, suggesting that the molecular phenomena at work here are rather general in nature.

The *empirical* modifications described above do not provide a molecular *explanation* for the weaker-than-expected interactions between hydrocarbon and fluorocarbons. In a recent attempt to address this issue, Song *et al.* used state-of-the-art computer simulation to calculate thermodynamic properties (e.g. second virial coefficients) of methane/perfluoromethane mixtures from first principles [92]. They employed the recently developed all-atom-optimized potentials for liquid simulations (OPLS-AA) potential energy model and used the geometric mean approximation to model interactions between alkanes and perfluoroalkanes. The objective was to determine whether the subtleties of molecular geometry and molecular charge distribution incorporated in the OPLS-AA potential would account for the apparent departure from the geometric mean approximation in calculating interaction energies between fluorocarbon and hydrocarbon molecules. Surprisingly, these refined models of molecular structure and electron distribution could not describe experimental second virial coefficients of mixing for methane and perfluoromethane, even though the models provided accurate predictions of the thermodynamic properties of the pure components. The model calculations and experimental data could only be brought into concordance if the interaction energy between a methane molecule and a perfluoromethane molecule was reduced to a value 10% lower than that suggested by the geometric mean approximation [92]. Because the thermodynamic properties of mixtures, such as solubility, depend exponentially on these interaction energies, small deviations in interaction energies yield large effects in observed properties (cf. Figure 12(a)). After exploring many combinations of mixing rules and examining in detail the various contributions to the potential model, Song *et al.* concluded 'At this point, it must be admitted that the origins of the weaker-than-expected interactions between perfluoroalkanes and alkanes remain a mystery' [92].

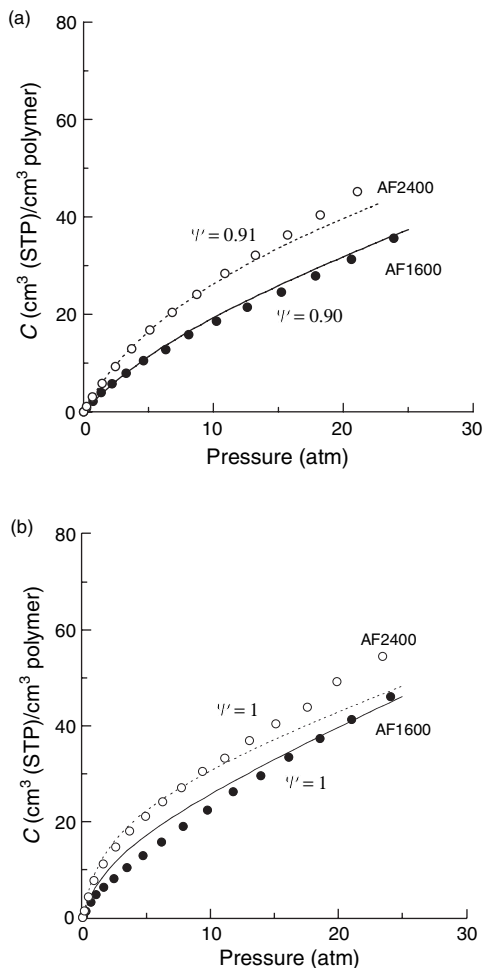


Figure 9.12 Comparison of experimental and predicted sorption isotherms of (a) C_2H_6 and (b) C_2F_6 in Tefflon AF1600 and Tefflon AF2400 at $35^\circ C$ using the non-equilibrium lattice fluid (NELF) model [90]. The continuous and dashed lines represent NELF model fits to the experimental data for penetrant sorption in Tefflon AF1600 and Tefflon AF2400, respectively

9.4 Conclusions

The discovery of amorphous, glassy perfluoropolymers that can be readily solvent-cast has allowed these materials to be considered for use in high-performance gas separation membrane applications. Studies of gas and vapor transport properties in perfluoropolymers have revealed that these materials exhibit unusual solubility behavior. Perfluoropolymers demonstrate low

hydrocarbon-vapor solubility. These results are similar to the behavior observed in small molecule mixtures of hydrocarbons and fluorocarbons. This behavior is not predicted by regular solution theory or modern computer simulations of molecular interactions, although it does follow an intuitive 'like dissolves like' guideline. The anomalously low solubility of hydrocarbons (gas or liquid) in fluorocarbons (polymer or liquid) and vice versa can be traced to unlike molecule interactions that are roughly 10% weaker than those predicted by the geometric mean approximation. The reason for this deviation from the geometric mean is not known.

The unusual solubility of gases and vapors in perfluoropolymers has several implications relevant to membrane separations. Perfluoropolymers have solubility selectivities that are significantly different from those of hydrocarbon-based polymers. As a result, perfluoropolymers have permeability-selectivity combinations that exceed the upper bound for some gas pairs. More broadly speaking, the substantial difference in hydrocarbon-vapor/light-gas solubility selectivities for perfluoropolymers compared to hydrocarbon-based polymers is a useful materials development guideline. In this sense, fluorination can be viewed as a means of 'tuning' membrane selectivities for non-polar species via solubility selectivity changes. This guideline complements the usual efforts to alter membrane selectivities through polymer structural modifications geared at influencing diffusivity selectivity.

From an applications standpoint, perhaps the most important consequence of low hydrocarbon sorption in perfluoropolymers is the degree of plasticization resistance inherent in membranes containing these polymers. Because perfluoropolymers sorb a relatively small amount of hydrocarbon species, the driving force for polymer swelling and the associated membrane plasticization is minimized. Such swelling resistance can be useful in challenging membrane separations, such as olefin/paraffin or natural gas applications, where size-selective polymers that can tolerate high levels of plasticizing species are desired. For these cases, the unique nature of the carbon-fluorine bond can be harnessed to yield high-performance membranes with properties unlike those of conventional polymeric membrane materials.

References

- [1] R. J. Plunkett, 'Tetrafluoroethylene polymers', *US Patent 2 230 654* (1941).
- [2] J. G. Drobny, *Technology of Fluoropolymers*, CRC Press, Boca Raton, FL, USA, pp. 172 (2001).
- [3] V. Arcella, A. Ghielmi and G. Tommasi, 'High performance perfluoropolymer films and membranes', *Ann. NY Acad. Sci.*, **984**, 226–244 (2003).
- [4] H. Fitz, 'Folien aus Fluorkunststoffen', *Kunststoffe*, 1980, **70**, 27–33 (1980).
- [5] H. Schroeder, Fluorocarbon elastomers, in *Rubber Technology*, M. Morton (Ed.), Van Nostrand Reinhold, New York, NY, USA, pp. 631 (1987).
- [6] P. R. Resnick and W. H. Buck, Teflon AF amorphous fluoropolymers, in *Modern Fluoropolymers: High Performance Polymers for Diverse Applications*, J. Scheirs, (Ed.), John Wiley & Sons, Ltd, Chichester, UK, pp. 397–419 (1997).
- [7] W. W. Brandt and G. A. Anysas, Diffusion of gases in fluorocarbon polymers, *J. Appl. Polym. Sci.*, **7**, 1919–1931 (1963).
- [8] R. A. Pasternak, M. V. Christensen and J. Heller, Diffusion and Permeation of oxygen, nitrogen, carbon dioxide, and nitrogen dioxide through Polytetrafluoroethylene, *Macromolecules*, **3**, 366–371 (1970).
- [9] R. A. Pasternak, G. L. Burns and J. Heller, Diffusion and solubility of simple gases through a copolymer of hexafluoropropylene and tetrafluoroethylene, *Macromolecules*, **4**, 470–475 (1971).
- [10] D. R. Rexford, 'Copolymer Elastomer of vinylidene-fluoride and hexafluoropropene', *US Patent 3 051 677* (1962).
- [11] S. Satoh and T. Suzuki, 'Rubber hose for automotive fuel line', *US Patent 4 330 017* (1982).
- [12] D. Stivers, 'Fluoroelastomer/polypichlorohydrin elastomer articles', *US Patent 4 343 861* (1982).
- [13] J. R. Pailthorp and H. E. Schroeder, 'elastomeric terpolymers', *US Patent 2 968 649* (1961).
- [14] A. Nersasian, 'Effect of "sour" gasoline on fuel hose rubber materials', Paper No. 790659 at *SAE Passenger Car Meeting*, Detroit, MI, USA (1979).
- [15] J. D. MacLachlan, 'Automotive fuel permeation resistance – A comparison of elastomeric materials', Paper No. 790657 at *SAE Passenger Car Meeting*, Detroit, MI, USA (1979).
- [16] N. Yi-Yan, R. M. Felder and W. J. Koros, 'Selective permeation of hydrocarbon gases in poly tetrafluoroethylene and poly(fluoroethylene-propylene) copolymer', *J. Appl. Polym. Sci.*, **25**, 1755–1774 (1980).
- [17] T. Duncan, W. J. Koros and R. M. Felder, 'Permeation of methyl chloride and benzene through FEP Teflon', *J. Appl. Polym. Sci.*, **28**, 209–218 (1983).

- [18] M. J. El-Hibri and D. R. Paul, 'Gas transport in poly(vinylidene fluoride): effects of uniaxial drawing and processing temperature', *J. Appl. Polym. Sci.*, **31**, 2533–2560 (1986).
- [19] J. S. Chiou and D. R. Paul, 'Gas permeation in a dry Nafion membrane', *Ind. Eng. Chem. Res.*, **27**, 2161–2164 (1988).
- [20] S. Pauly, 'Permeability and diffusion data', in *Polymer Handbook*, J. Brandrup and E. H. Immergut (Eds.), John Wiley & Sons, Inc., New York, NY, USA, (1989).
- [21] J. S. McHattie, W. J. Koros and D. R. Paul, 'Gas transport properties of polysulphones: 2. Effect of bisphenol connector groups', *Polymer*, **32**, 2618–2625 (1991).
- [22] M. W. Hellums, W. J. Koros, G. R. Husk and D. R. Paul, 'Fluorinated polycarbonates for gas separation applications', *J. Membr. Sci.*, **46**, 93–112 (1989).
- [23] K. Tanaka, H. Kita, M. Okano and K. Okamoto, 'Permeability and permselectivity of gases in fluorinated and non-fluorinated polyimides', *Polymer*, **33**, 585–592 (1992).
- [24] T. H. Kim, W. J. Koros and G. R. Husk, 'Relationship between gas separation properties and chemical structure in a series of aromatic polyimides', *J. Membr. Sci.*, **37**, 45–62 (1988).
- [25] S. A. Stern, 'Polymers for gas separations: the next decade', *J. Membr. Sci.*, **94**, 1–65 (1994).
- [26] E. N. Squire, 'Amorphous copolymers of perfluoro-2,2-dimethyl-1,3-dioxole', *US Patent 4 754 009* (1988).
- [27] E. N. Squire, 'Optical fibers comprising cores clad with amorphous copolymers of perfluoro-2,2-dimethyl-1,3-dioxole', *US Patent 4 530 569* (1985).
- [28] S. M. Nemser and I. A. Roman, 'Perfluorodioxole Membranes', *US Patent 5 051 114* (1991).
- [29] I. Pinnau and L. G. Toy, 'Gas and vapor transport properties of amorphous perfluorinated copolymer membranes based on 2,2-bistrifluoromethyl-4,5-difluoro-1,3-dioxole/tetrafluoroethylene', *J. Membr. Sci.*, **109**, 125–133 (1996).
- [30] M. Nakamura, I. Kaneko, K. Oharu, G. Kojima, M. Matsuo, S. Samejima and M. Kamba, 'Cyclic polymerization', *US Patent 4 910 276* (1990).
- [31] P. Colaianna, G. Brinati and V. Arcella, 'Amorphous perfluoropolymers', *US Patent 5 883 177* (1999).
- [32] R. S. Prabhakar, B. D. Freeman and I. Roman, 'Gas and vapor sorption and permeation in poly((2,2,4-trifluoro-5-trifluoromethoxy-1,3-dioxole-co-tetrafluoroethylene)', *Macromolecules*, **37**, 7688–7697 (2004).
- [33] R. S. Prabhakar, T. C. Merkel, B. D. Freeman, T. Imizu and A. Higuchi, 'Sorption and transport properties of propane and perfluoropropane in polydimethylsiloxane and poly(1-trimethylsilyl-1-propyne)', *Macromolecules*, **38**, 1899–1910 (2005).
- [34] I. Pinnau, Z. He, A. R. DaCosta, K. D. Amo and R. Daniels, 'Gas separation using organic-vapor-resistant membranes', *US Patent 6 361 583* (2002).
- [35] I. Pinnau, Z. He, A. R. DaCosta, K. D. Amo and R. Daniels, 'Gas separation using C3+ hydrocarbon-resistant membranes', *US Patent 6 361 582* (2002).
- [36] T. C. Merkel, V. I. Bondar, K. Nagai, B. D. Freeman and Y. Yampolskii, 'Gas sorption, diffusion and permeation in poly(2,2-bistrifluoromethyl-4,5-difluoro-1,3-dioxole-co-tetrafluoroethylene)', *Macromolecules*, **32**, 8427–8440 (1999).
- [37] T. C. Merkel, V. Bondar, K. Nagai and B. D. Freeman, 'Hydrocarbon and perfluorocarbon gas sorption in polydimethylsiloxane, poly(1-trimethylsilyl-1-propyne) and copolymers of tetrafluoroethylene and 2,2-bis(trifluoromethyl)-4,5-difluoro-1,3-dioxole', *Macromolecules*, **32**, 370–374 (1999).
- [38] A. Y. Alentiev, Y. P. Yampolskii, V. P. Shantarovich, S. M. Nemser and N. A. Plate, 'High transport parameters and free volume of perfluorodioxole copolymers', *J. Membr. Sci.*, **126**, 123–132 (1997).
- [39] A. Y. Alentiev, V. P. Shantarovich, T. C. Merkel, V. I. Bondar, B. D. Freeman and Y. P. Yampolskii, 'Gas and vapor sorption, permeation and diffusion in glassy amorphous Teflon AF1600', *Macromolecules*, **35**, 9513–9522 (2002).
- [40] V. Arcella, P. Colaianna, P. Maccone, A. Sanguineti, A. Gordanò, G. Clarizia and E. Drioli, 'A study on a perfluoropolymer purification and its application to membrane formation', *J. Membr. Sci.*, **163**, 203–209 (1999).
- [41] V. I. Bondar, B. D. Freeman and Y. Yampolskii, 'Sorption of gases and vapors in an amorphous glassy perfluorodioxole copolymer', *Macromolecules*, **32**, 6163–6171 (1999).
- [42] V. Bondar, A. Singh and B. D. Freeman, 'Gas sorption and transport properties of poly(tetrafluoroethylene-co-2,2-bistrifluoromethyl-4,5-difluoro-1,3-dioxole)', *AIChE Topical Conference on Separation Science and Technologies*, **2**, 831–837 (1997).
- [43] A. Singh, V. Bondar, S. Dixon, B. D. Freeman and A. J. Hill, 'Gas sorption, transport properties and PALS analysis of poly(tetrafluoroethylene [TFE]-co-2,2-bistrifluoromethyl-4,5-difluoro-1,3-dioxole [PDD])', *Proc. Am. Chem. Soc. Div. Polym. Mater. Sci. Eng.*, **77**, 316–317 (1997).
- [44] T. Merkel, V. Bondar, K. Nagai, M. G. DeAngelis, B. Freeman and F. Doghieri, 'Hydrocarbon and perfluorocarbon vapor sorption in rubbery and

- glassy hydrocarbon-based polymers and fluoropolymers', *Polym. Prepr. Am. Chem. Soc. Div. Polym. Chem.*, **39**(2), 916–917 (1998).
- [45] S. M. Nemser, K. P. Callaghan and T. C. Reppert, 'Combustion engine air supply system', *US Patent 5 960 777* (1999).
- [46] L. M. Robeson, 'Correlation of separation factor versus permeability for polymeric membranes', *J. Membr. Sci.*, **62**, 165–185 (1991).
- [47] B. D. Freeman, 'Basis of permeability/selectivity tradeoff relations in polymeric gas separation membranes', *Macromolecules*, **32**, 375–380 (1999).
- [48] D. Slattery and M. Hampton, *Metal Hydrides for Hydrogen Separation, Recovery and Purification*, University of Central Florida, FL, USA (2005).
- [49] C. Tannehill, *Nitrogen Removal Requirements for Natural Gas*, Topical Report, Gas Research Institute, (1999).
- [50] G. Gee, 'Some thermodynamic properties of high polymers and their molecular interpretation', *Q. Rev.*, **1**, 265–298 (1947).
- [51] A. S. Michaels and H. J. Bixler, 'Solubility of gases in polyethylene', *J. Polym. Sci.*, **L**, 393–412 (1961).
- [52] M. S. Suwandi and S. A. Stern, 'Transport of heavy organic vapors through silicone rubber', *J. Polym. Sci.*, **11**, 663 (1973).
- [53] Y. Kamiya, Y. Naito, K. Terada, K. Mizoguchi and A. Tsuboi, 'Volumetric properties and interaction parameters of dissolved gases in polydimethylsiloxane and polyethylene', *Macromolecules*, **33**, 3111–3119 (2000).
- [54] T. C. Merkel, V. Bondar, K. Nagai and B. D. Freeman, 'Gas sorption and transport of perfluorocarbons in polydimethylsiloxane', *J. Polym. Sci. Part B: Polym. Phys. Ed.*, **38**, 415–434 (2000).
- [55] T. C. Merkel, V. Bondar, K. Nagai and B. D. Freeman, 'Sorption and transport of hydrocarbon and perfluorocarbon gases in poly(1-trimethylsilyl-1-propyne)', *J. of Polym. Sci. Part B: Polym. Phys. Ed.*, **38**, 273–296 (2000).
- [56] R. S. Prabhakar, M. G. DeAngelis, G. C. Sarti, B. D. Freeman and M. C. Coughlin, 'Gas and vapor sorption, permeation and diffusion in poly(tetrafluoroethylene-co-perfluoromethyl vinyl ether)', *Macromolecules*, (2000).
- [57] J. H. Hildebrand and R. L. Scott, *The Solubility of Nonelectrolytes*, 3rd Ed., Dover Publications, Inc., New York, NY, USA (1964).
- [58] W. J. Koros and M. W. Hellums, 'Transport Properties', in *Encyclopedia of Polymer Science and Technology*, J. I. Kroschwitz (Ed.), pp. 1211 (1990).
- [59] K. Tanaka, A. Taguchi, J. Hao, H. Kita and K. Okamoto, 'Permeation and separation properties of polyimide membranes to olefins and paraffins', *J. Membr. Sci.*, **121**, 197–207 (1996).
- [60] C. Staudt-Bickel, W. J. Koros, 'Olefin/paraffin gas separations with 6FDA-based polyimide membranes', *J. Membr. Sci.*, **170**, 205 (2000).
- [61] R. W. Baker, *Membrane Technology and Applications*, 2nd Ed., John Wiley & Sons, Inc., New York, NY, USA, pp. 544 (2004).
- [62] J. D. Wind, D. R. Paul and W. J. Koros, 'Natural gas permeation in polyimide membranes', *J. Membr. Sci.*, **228**, 227–236 (2004).
- [63] L. S. White, T. A. Blinks, H. A. Kloczewski and I. Wang, 'Properties of a polyimide gas separation membrane in natural gas streams', *J. Membr. Sci.*, **103**, 73–82 (1995).
- [64] C. Staudt-Bickel and W. J. Koros, 'Improvement of CO₂/CH₄ separation characteristics of polyimides by chemical crosslinking', *J. Membr. Sci.*, **155**, 145–154 (1999).
- [65] J. D. Wind, C. Staudt-Bickel, D. R. Paul and W. J. Koros, 'Solid-state covalent cross-linking of polyimide membranes for carbon dioxide plasticization reduction', *Macromolecules*, **36**, 1882–1888 (2003).
- [66] R. L. Scott, 'Solutions of non-electrolytes', *Ann. Rev. Phys. Chem.*, **7**, 43–66 (1956).
- [67] R. L. Scott, 'The Anomalous Behavior of Fluorocarbon Solutions', *J. Phys. Chem.*, **62**, 136–145 (1958).
- [68] R. L. Scott, 'Some unsolved problems of liquids and solutions', *J. Chem. Edu.*, **30**, 542–549 (1953).
- [69] J. H. Hildebrand, 'The entropy of solution of molecules of different size', *J. Chem. Phys.*, **15**, 225–228 (1947).
- [70] R. L. Scott, 'The solubility of fluorocarbons', *J. Am. Chem. Soc.*, **70**, 4090 (1948).
- [71] J. H. Simons and R. D. Dunlap, 'The properties of *n*-pentforane and its mixtures with *n*-pentane', *J. Chem. Phys.*, **18**, 335 (1950).
- [72] J. H. Hildebrand, B. B. Fisher and H. A. Benesi, 'Solubility of perfluoro-*n*-heptane with benzene, carbon tetrachloride, chloroform, *n*-heptane and 2,2,4-trimethylpentane', *J. Am. Chem. Soc.*, **72**, 4348 (1950).
- [73] J. H. Simons and J. W. Mausteller, 'The properties of *n*-butforane and its mixtures with *n*-butane', *J. Chem. Phys.*, **20**, 1516 (1952).
- [74] D. N. Campell and J. B. Hickman, 'Solubility characteristics of some binary liquid mixtures', *J. Am. Chem. Soc.*, **75**, 2879–2881 (1953).
- [75] N. Thorp and R. L. Scott, 'Fluorocarbon solutions at low temperatures. I. The liquid mixtures' CF₄-CHF₃, CF₄-CH₄, CF₄-Kr, CH₄-Kr', *J. Phys. Chem.*, **60**, 670–673 (1956).
- [76] N. Thorp and R. L. Scott, 'Fluorocarbon solutions at low temperatures. II. The liquid mixtures C₂H₆-C₂F₆, C₂F₆-CHF₃, CH₂F₂-CHF₃, C₂H₆-CHF₃, and Xe-CHF₃ *J. Phys. Chem.*, **60**, 1441–1443 (1956).

- [77] J. H. Hildebrand, J. M. Prausnitz and R. L. Scott, *Regular and Related Solutions*, Van Nostrand Reinhold, New York, NY, USA (1970).
- [78] J. M. Smith, H. C. Van Ness and M. M. Abbott, *Introduction to Chemical Engineering Thermodynamics*, 6th Ed., McGraw Hill, New York, NY, USA (2001).
- [79] A. J. Stone, *The Theory of Intermolecular Forces*, Clarendon Press, Oxford, UK (1996).
- [80] F. London, 'Über einige Eigenschaften und Anwendungen der Molekularkräfte', *Z. Phys. Chem., B*, **11**, 222–251 (1930).
- [81] J. H. Hildebrand and R. L. Scott, *The Solubility of Nonelectrolytes*, Reinhold Publishing Corporation, New York, NY, USA (1950).
- [82] F. London, 'On centers of van der waals attractions', *J. Phys. Chem.*, **46**, 305–316 (1942).
- [83] T. M. Reed III, 'The theoretical energies of mixing for fluorocarbon-hydrocarbon mixtures', *J. Phys. Chem.*, **59**, 425–428 (1955).
- [84] J. H. Simons and J. W. Mausteller, 'The properties of *n*-butforane and its mixtures with *n*-butane', *J. Chem. Phys.*, **20**, 1516–1519 (1952).
- [85] K. Ghosal and B. D. Freeman, 'Gas separation using polymer membranes: an overview', *Polym. Adv. Technol.*, **5**, 673–697 (1993).
- [86] S. D. Hamann, J. A. Lambert and R. B. Thomas, 'The second virial coefficients of some gas mixtures', *Aust. J. Chem.*, **8**, 149–157 (1955).
- [87] *DIPPR Chemical Database*, Thermophysical Properties Laboratory, Brigham Young University, Provo, UT, USA [<http://dippr.byu.edu/public/chemsearch.asp>].
- [88] E. M. Dantzer-Siebert and C. M. Knobler, 'Interaction virial coefficients in hydrocarbon-fluorocarbon mixtures', *J. Phys. Chem.*, **75**, 3863–3870 (1971).
- [89] M.-G. De Angelis, T. C. Merkel, V. I. Bondar, B. D. Freeman, F. Doghieri and G. C. Sarti, 'hydrocarbon and fluorocarbon solubility and dilation in polydimethylsiloxane: comparison of experimental data with predictions of the Sanchez–Lacombe equation of state', *J. Polym. Sci. Part B: Polym. Phys. Ed.*, **37**, 3011–3026 (1999).
- [90] M.-G. De Angelis, T. C. Merkel, V. I. Bondar, B. D. Freeman, F. Doghieri and G. C. Sarti, 'Gas sorption and dilation in poly(2,2-bis(trifluoromethyl)-4,5-difluoro-1,3-dioxole-co-tetrafluoroethylene): comparison of experimental data with predictions of the nonequilibrium lattice fluid model', *Macromolecules*, **35**, 1276–1288 (2002).
- [91] M. G. DeAngelis, F. Doghieri, G. C. Sarti and B. D. Freeman, 'Modeling gas sorption in amorphous Teflon through the non equilibrium thermodynamics for glassy polymers (NET-GP) approach', *Desalination*, (2000).
- [92] W. Song, P. J. Rossky and M. Maroncelli, 'Modeling alkane + perfluoroalkane interactions using all-atom potentials: failure of the usual combining rules', *J. Chem. Phys.*, **119**, 9145–9162 (2003).
- [93] Membrane Technology and Research, Mento Park, CA, USA, unpublished data.
- [94] T. M. Reed III, 'The ionization potential and the polarizability of molecules', *J. Phys. Chem.*, **59**, 428–432 (1955).
- [95] J. A. Beran and L. Kevan, 'Semiempirical calculation of molecular polarizabilities and diamagnetic susceptibilities of fluorocarbons, substituted fluorocarbons, ethers, esters, ketones and aldehydes', *J. Phys. Chem.*, **73**, 3860–3866 (1969).
- [96] H. Odani and T. Masuda, 'Design of membranes for gas separation', in *Polymers for Gas Separation*, N. Toshima (Ed.), VCH Publishers, New York, NY, USA, (1992).
- [97] P. G. T. Fogg and W. Gerrard, *Solubility of Gases in Liquids*, John Wiley & Sons, Inc. New York, NY, USA (1991).

Structure and Transport Properties of Polyimides as Materials for Gas and Vapor Membrane Separation

Kazuhiro Tanaka and Ken-Ichi Okamoto

10.1 Introduction

Polyimides have become increasingly popular polymers with researchers investigating membrane materials for gas and vapor separation over the past two decades. Polyimides have excellent thermal, chemical and mechanical properties, as well as excellent film-forming properties. These are desirable for membrane materials. Polyimides have been found to exhibit higher membrane gas separation performance than more common glassy polymers such as polysulfones and polycarbonates. Another excellent feature of polyimides is the relative ease in preparing a series of polyimides with systematically different chemical structures, because a variety of acid dianhydrides and diamines are commercially available or have been developed in laboratories. Polyimides are generally made by the polycondensation of aromatic acid dianhydrides and aromatic diamines [1]. Homopolyimides can be basically prepared from as many as the number of combinations of acid dianhydrides and diamines. Copolyimides are also prepared by using two or more acid dianhydrides and/or diamines. Most polyimides have molecular weights high enough to be fabricated into tough films that can withstand gas permeation measurements. Therefore, polyimides are suitable for systematic investigations on the relationships between chemical structures and transport properties to design

the chemical structure suitable for a given separation system.

The first publication on structure–property relationships of a series of polyimides was a patent of Hoehn at DuPont, filed in 1972 [2]. Hoehn derived criteria for the chemical structures of polyimides, polyesters and polyamides being useful as gas separation membranes.

- (1) The repeating unit of the main polymer chain has at least one rigid divalent subunit, the two main chain single bonds extending from which are not collinear.
- (2) The polymer chain is sterically unable to rotate 360° around at least one of the bonds noted in (a).
- (3) The structure has 50 % or more of the atoms in the main chain of the polymer repeating unit as members of aromatic rings.

Many scientific papers on the structure–property relationships have been published since the middle of the 1980s[3–48]. Some papers included some of the examples described in that patent [2]. In these papers, the permeation properties for various polyimides with different chemical structures have been compared in order to deduce the effect of chemical structure.

The gas permeation properties have been often explained in terms of free volume and

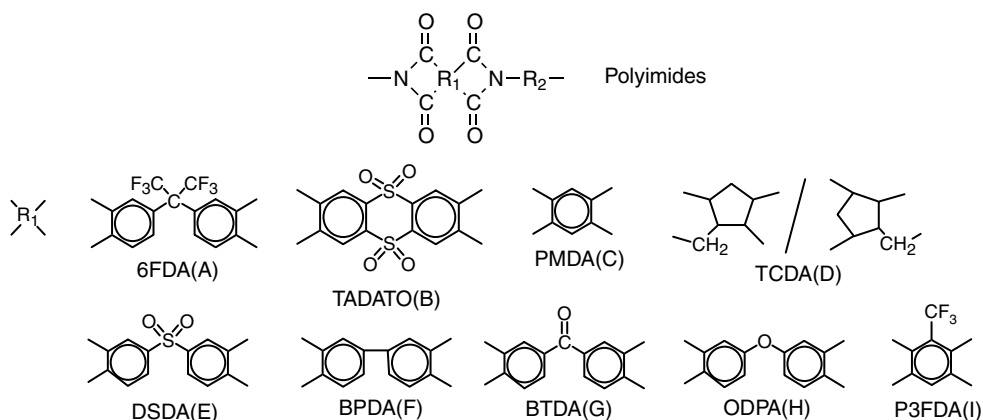


Figure 10.1 Chemical structures of acid dianhydrides

also sometimes in terms of cohesive energy, dielectric constant or a group contribution method. The analyses have promoted our understanding of factors controlling gas permeation and separation and of the relationship between the factors and the chemical structures of polyimides.

The vapor permeation properties of polyimides are also important. Polyimides have been applied to the removal of vapors from gases, or the separation of vapor mixtures such as dehumidifi-

cation of air or organic vapors, removal of air pollutants and separation of water from ethanol [49]. However, the effect of chemical structure on vapor permeability and permselectivity in polyimides has not been investigated extensively. There are a few papers reporting water permeability and water-ethanol permselectivity [50,51].

In this chapter we intend to summarize our knowledge about the relationship between gas and vapor permeation properties of polyimides and their chemical structures. Figures 10.1 and 10.2

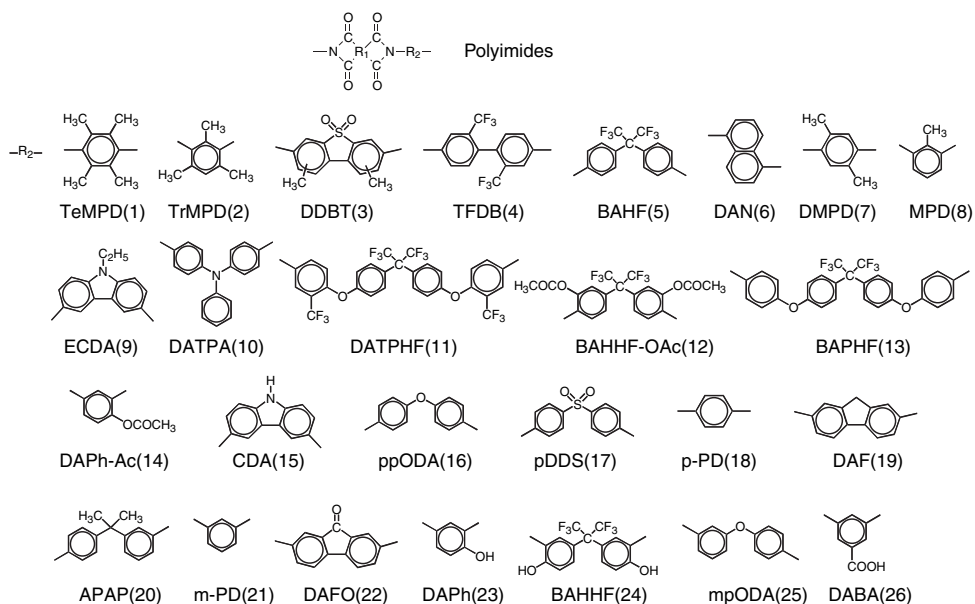


Figure 10.2 Chemical structures of diamines

show the chemical structures of acid dianhydrides and diamines, respectively, mentioned in this chapter. The polyimides are denoted by a combination of letters of the alphabet, in parenthesis, for each acid dianhydride and the number in parenthesis for each diamine in this chapter, mainly in figures. For example, the polyimide prepared from 6FDA and ppODA is denoted by the abbreviation 'A16'.

10.2 Fundamentals

10.2.1 Packing Density of Polyimides

An important property of polymeric membranes for gas separation is the packing density of polymer chains because this strongly affects diffusivity and diffusivity selectivity, and partly affects solubility. The packing density is often evaluated by the fractional free volume, V_F , calculated from the following equation for discussion about the diffusion of gases in polymers:

$$V_F = (V_T - V_0)/V_T \quad (10.1)$$

where V_T is the molar volume at temperature T and V_0 is the volume occupied by the molecules at 0 K per mole of repeat unit of the polymer; V_T can be calculated from the density, while V_0 is estimated to be 1.3 times [52] the van der Waals volume calculated by the group contribution method of Bondi [53]. The V_F corresponds to the volume fraction of the 'expansion volume' [54], which is composed of a spectrum of microcavities among polymer chains caused by thermal motion of polymer chains.

The V_F is sometimes referred to as fractional 'free space' in order to emphasize that it is different from the William-Landel-Ferry (WLF) fractional free volume, f_{WLF} , derived from the viscosity theory, in which the fractional free volume at T_g is taken as 0.025 [55]. The f_{WLF} is often used to interpret the diffusion coefficient of a penetrant in a rubbery polymer [56]. In the rubbery state, the segmental motion frequently generates and dissipates free volume holes among polymer chains, allowing a penetrant molecule to have frequent chances of diffusion jumps. In the glassy state, segmental motion is frozen and the f_{WLF} cannot be applied. However, local motions of polymer chains and side groups are not frozen and they are considered to frequently

generate and dissipate small free volume holes, some of which are large enough for a penetrant molecule to pass through. Recently, the V_F is now commonly referred to as fractional free volume. In this chapter, we refer to the V_F as 'fractional free volume' and to the microcavities as 'free volume holes'.

Packing density depends on chain stiffness, strength of polymer chain-chain interactions and chain bulkiness. Stiffer polymer chains have a lower degree of conformational freedom, making chain packing less efficient [11,20]. The glass transition temperature, T_g , is a rough measure of chain stiffness. Aromatic polyimides have T_g s higher than 200 °C and their polymer chains are stiff.

The strong chain-chain interaction makes the chain packing efficient if any steric hindrances do not exist [29]. Polyimides have four polar carbonyl groups in a repeat unit. In addition to the van der Waals interaction and the polar interaction, charge transfer (CT) interactions between the acid dianhydride moieties and the diamine moieties play an important role in the polymer chain-chain interactions in aromatic polyimides. The CT interaction is an electronic interaction between an aromatic dianhydride moiety as an electron acceptor and an aromatic diamine moiety as an electron donor, as shown in Figure 10.3. The magnitude of CT interaction depends on the electron affinity of the acid dianhydride moiety and the ionization potential of the diamine moiety [57]. The colors of aromatic polyimide films are attributed to the CT absorption [57]. For example, the P3FDA-TFDB, PMDA-TFDB and 6FDA-TFDB polyimide films are yellow, pale yellow and colorless, respectively [29]. This indicates that the magnitude of CT interaction is in the order P3FDA-TFDB > PMDA-TFDB > 6FDA-TFDB. The introduction of an electron-withdrawing substituent, such as CF_3 , on the benzene ring in the acid dianhydride moiety increases its electron affinity and therefore enhances CT interaction. On the other hand, the $-C(CF_3)_2-$ linkage interrupts the π -conjugation of the acid dianhydride moiety, resulting in reduced electron affinity of the moiety and therefore significant reduction in the CT interaction. The V_{Fs} of P3FDA-TFDB, PMDA-TFDB and 6FDA-TFDB polyimide films are 0.142, 0.160 and 0.190, respectively [29]. This indicates that stronger CT interaction makes chain packing efficient.

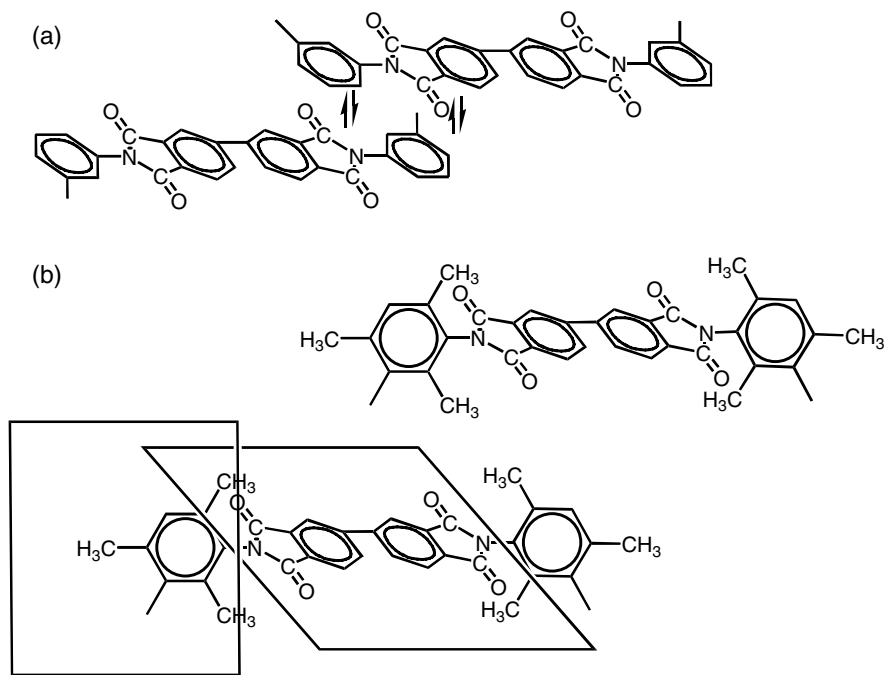


Figure 10.3 Schematic illustration of charge transfer (CT) interactions between acid dianhydride and diamine moieties. (a) CT interactions can be operative in the BPDA–mPD polyimide, while (b) cannot be operative in the BPDA–TrMPD polyimide

However, bulky structure or kink units inhibit chain packing, resulting in significantly reduced CT interactions. For example, the BPDA–TrMPD polyimide has the largest V_F ($= 0.155$) among the BPDA-based polyimides [21]. Its film is colorless. The methyl groups in TeMPD(1) and TrMPD(2) diamines are connected on both *ortho* positions to each imide ring and sterically inhibit internal rotation around the bond between the diamine moiety ring and the imide ring, resulting in the imide and aromatic diamine rings being perpendicular to each other, as shown in Figure 10.3. The steric hindrance caused by both the nonplanar structure and the bulky methyl groups inhibit dense packing of the rigid polymer chains. Since an electronic interaction is sensitive to the distance between a donor and an acceptor, the inhibition of dense packing of polymer chains significantly reduces CT interaction, hence resulting in a colorless film.

The V_F values for polyimides cited in this chapter range from 0.10 to 0.19. The V_F is larger than

0.15 for most of the fluorinated polyimides and tends to increase with increasing fluorine content [20]. Because of the high electronegativity of fluorine atoms, the C–F bond has a very small polarizability and thus very weak van der Waals interactions. The CT interaction in 6FDA-based polyimides is very weak, as mentioned above. The CF_3 groups in the linkage are also bulky and cause steric hindrance to polymer chain packing.

10.2.2 Transport Properties

The steady state permeation flux, J_s , is normally proportional to the difference in partial pressures at the feed and permeate sides, p_h and p_l , respectively, and inversely proportional to the membrane thickness, L . The gas permeability of a membrane is evaluated in terms of the permeability coefficient, P , defined by the following equation.

$$P = J_s L / (p_h - p_l) \quad (10.2)$$

When one compares the permeabilities of asymmetric or composite membranes whose thicknesses are unknown, the term 'Permeance' is often used. Permeance is defined as follows:

$$R = P/L \quad (10.3)$$

The permselectivity of a membrane to a binary gas mixture including component A over component B is evaluated in terms of the separation factor, α , defined by the following equation:

$$\alpha_{A/B} = (y_A/y_B)/(x_A/x_B) \quad (10.4)$$

where x_A and y_A are the mole fractions of component A at the permeate and feed sides, respectively. The ratio of the permeability coefficient of component A, P_A , to that of component B, P_B , measured by single-gas permeation experiments, is conveniently used as a measure of permselectivity, referred as to the ideal separation factor:

$$\alpha_{\text{ideal}} = P_A/P_B = R_A/R_B \quad (10.5)$$

The ideal separation factor provides a good measure of the $\alpha_{A/B}$ of a membrane for the separation system where each penetrant in the membrane hardly affects the permeation of another penetrant, for example, H_2/CH_4 and O_2/N_2 separations. However, it should be noted that the difference between the actual and ideal separation factors is often significant for systems where interaction of one component with another component in the membrane is rather large, for example, olefin/paraffin or vapor separations.

Gas permeation through dense polymeric membranes is a solution-diffusion process. The permeability coefficient can be expressed in terms of the concentration-averaged diffusion coefficient D and the solubility coefficient S :

$$P = DS \quad (10.6)$$

The ideal separation factor can be, therefore, separated into two selectivities, the diffusivity selectivity and solubility selectivity:

$$\alpha_{\text{ideal}} = P_A/P_B = (D_A/D_B)(S_A/S_B) \quad (10.7)$$

P and S are determined by permeation and sorption measurements using pure gases, and then D can be calculated from $D = P/S$.

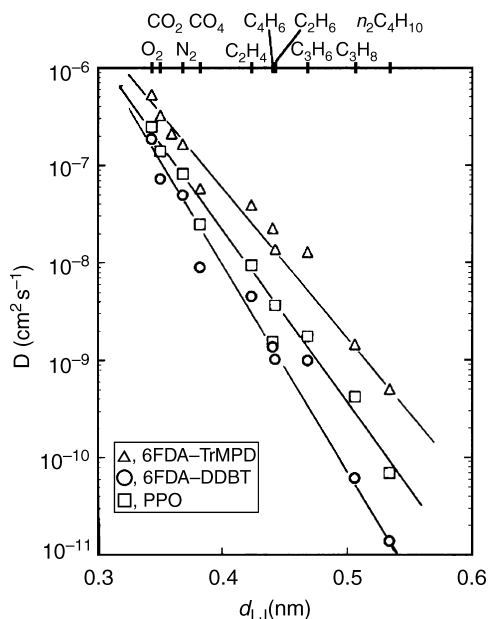


Figure 10.4 Plots of $\log D$ versus effective diameter d_{LJ} of gases for 6FDA-TrMPD(A2), 6FDA-DDBT(A3) and poly(2,6-dimethyl-1,4-phenyleneoxide) (PPO) membranes at 50 °C and 2 atm (1 atm for 1,3-butadiene (C_4H_6) and n -butane (C_4H_{10})). The d_{LJ} values used are 0.35 nm for CO_2 , 0.44 nm for C_4H_6 and the collision diameters of Lennard-Jones potentials for the other gases [42]. Reprinted from *Journal of Membrane Science*, **134**, K. Okamoto, K. Noborio, J. Hao, K. Tanaka and H. Kita, 'Permeation and separation properties of polyimide membranes to 1,3-butadiene and n -butane', 171–179, Copyright (1997), with permission from Elsevier

10.2.3 Diffusion and Solubility Coefficients of Gases

In general, diffusion coefficients of penetrants in a polymer decrease with increasing molecular size of the penetrant [58]. Figure 10.4 shows plots of $\log D$ versus collision diameter of the Lennard-Jones potential, d_{LJ} , of gases, except for CO_2 and 1,3-butadiene (C_3H_6) for two polyimides and poly(2,6-dimethyl-1,4-phenyleneoxide) (PPO) [42]. There is a good linear correlation between $\log D$ and d_{LJ} for inorganic gases and C_1 to C_3 hydrocarbons and n -butane (C_4H_{10}) for each polymer. The effective diameter for the diffusion of C_3H_6 can be regarded as 0.44 nm, based on these good correlations. Although the d_{LJ} of C_3H_6 is not available, it may be estimated to be around 0.51 nm from the fact that the

d_{LJ} values of C_1 – C_4 hydrocarbons are close to the corresponding values of the logarithmic means of the longest and shortest dimensions of the molecules. The effective diameter is much smaller than the estimated d_{LJ} and rather close to the diameter of a circle with the same area as the minimum cross-section of the molecule. Similarly, the effective diameter of CO_2 for diffusion in polyimides can be regarded as 0.35 nm [17], which is much smaller than the d_{LJ} (0.40 nm) and rather close to the kinetic diameter (0.33 nm) [59]. This is probably because these penetrant molecules are rigid rod-like or planar rather than spherical in shape.

Sorption of gases in polymers can be thermodynamically divided into two processes, that is, condensation of gas into liquid and mixing of the liquid with polymer. This means that the solubility coefficients depend on the condensability of gases and interactions of the gases

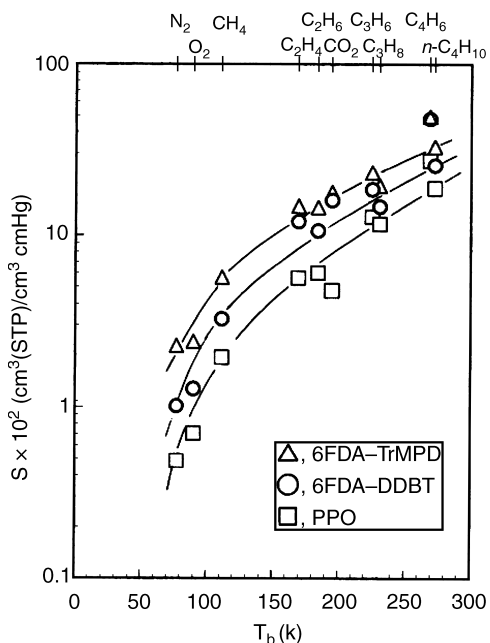


Figure 10.5 Plots of $\log S$ versus normal boiling point T_b of gases for 6FDA–TrMPD(A2), 6FDA–DDBT(A3) and PPO membranes at 50 °C and 2 atm (1 atm for 1,3-butadiene (C_4H_6) and n -butane (C_4H_{10})). Reprinted from *Journal of Membrane Science*, **134**, K. Okamoto, K. Noborio, J. Hao, K. Tanaka and H. Kita, Permeation and separation properties of polyimide membranes to 1,3-butadiene and n -butane, 171–179, Copyright (1997), with permission from Elsevier

with polymers. Condensability can be measured by the normal boiling point, T_b , critical temperature or Lennard–Jones force constant ϵ/k , of gases. Figure 10.5 shows plots of $\log S$ versus normal boiling point T_b of gases for particular polymers [42]. There is a tendency that S in each polyimide is larger for more condensable gases. The tendencies are similar to each other. This similarity indicates that specific interactions of gases with polyimides are not present.

10.3 Effect of Morphology

For the BPDA–ODA polyimide, the films annealed above or around the T_g have some degree of ordering due to aggregation of molecular chain segments, although the as-cast film is totally amorphous, as shown in Figure 10.6

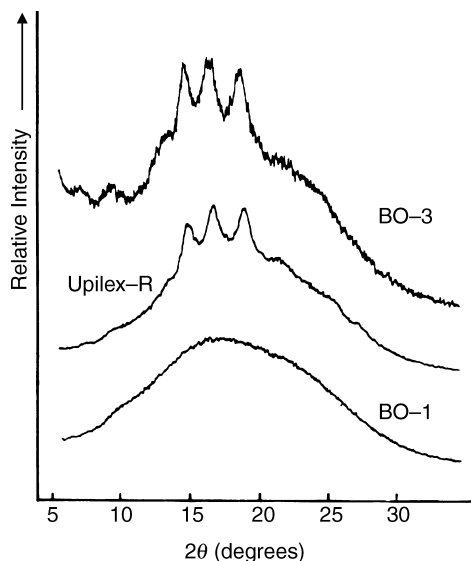


Figure 10.6 Wide-angle X-ray diffraction curves for BPDA–ODA films annealed at different temperatures: BO-1 is a film dried at 170 °C for 20 h and its density is 1.366 g/cm³; BO-3 is a film annealed at 300 °C for 2 h in N_2 , and its density is 1.409 g/cm³; Upilex-R is a commercial film produced by Ube Industries Ltd and is chemically identical to the BPDA–ODA polyimide (its density is 1.398 g/cm³) [60]. Reproduced by permission of John Wiley & Sons, Inc. from ‘The effect of morphology on sorption and transport of carbon dioxide in a polyimide from 3,3′,4,4′-biphenyltetracarboxylic dianhydride and 4,4′-oxydianiline’, K. Okamoto, K. Tanaka, H. Kita, A. Nakamura and Y. Kusuki, *J. Polym. Sci. Part B: Polym. Phys. Ed.*, **27**, 1221–1233 (1989)

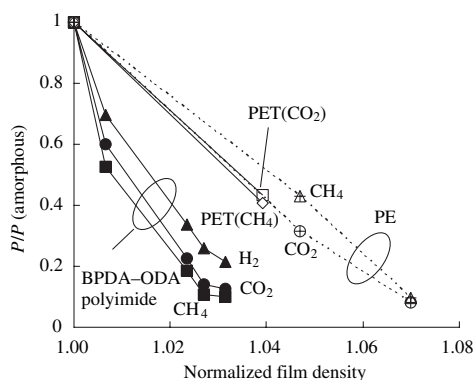


Figure 10.7 Plots of P versus normalized film density (film density divided by amorphous film density) for a BPDA-ODA polyimide at 50 °C and 10 atm [65], poly(ethylene terephthalate) (PET) [66] at 35 °C and polyethylene (PE) at 25 °C and 1 atm [67]

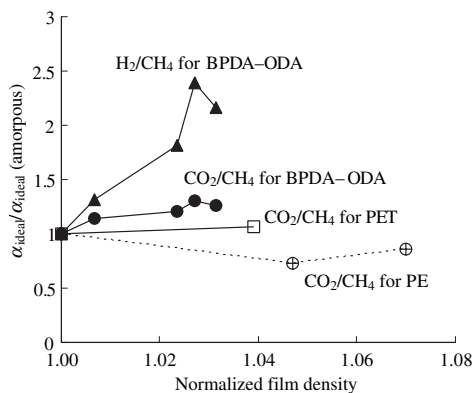


Figure 10.8 Plots of ideal separation factors versus normalized density (film density divided by amorphous film density) for a BPDA-ODA polyimide at 50 °C and 10 atm [65], poly(ethylene terephthalate) (PET) [66] at 35 °C and polyethylene (PE) at 25 °C and 1 atm [67]

[60]. For the PMDA-ODA polyimide, similar molecular aggregation is observed in the films thermally imidized at temperature higher than 280 °C [61,62]. The effect of morphology on gas transport properties in BPDA-ODA and PMDA-ODA polyimides has been investigated [63–65]. Figure 10.7 shows gas permeability for the BPDA-ODA polyimide, poly(ethylene terephthalate) (PET) and polyethylene (PE) films with different densities as a function of film density [65–67]. Permeability coefficients decrease with increasing film density. A decrease in gas permeability is larger for the BPDA-ODA polyimide than for PET and PE. Figure 10.8 shows permselectivity to H_2/CH_4 or CO_2/CH_4 systems for these polymers as a function of film density [65–67]. Permselectivity for the BPDA-ODA polyimide increases with increasing film density. On the other hand, the permselectivities for PET and PE hardly change. The large decrease in permeability and the increase in permselectivity for the BPDA-ODA polyimide are attributed to a decrease in chain segmental mobility in the amorphous phase caused by the ordered phase according to the two-phase model [66,67], which is commonly used to explain the gas permeation through typical crystalline polymers such as PET and PE. Some researchers have proposed another model, that is, a ‘more-diffuse’ model, for the morphology of PMDA-ODA polyimide films [61,62]. They have investigated this

by using small-angle X-ray scattering. Isoda *et al.* [61] have found that the density difference between the two phases is only a few percent. This is much smaller than those (10 to 20 %) [52] for most typical crystalline polymers. From gas sorption results, the density difference of the BPDA-ODA polyimide was estimated to be 7 % [65], which is also significantly smaller than those for typical crystalline polymers.

The morphology of the BPDA-DDS polyimide film does not change on annealing above its T_g and remains amorphous [10]. To our knowledge, the polyimides showing the unique morphology mentioned above are only the BPDA-ODA and PMDA-ODA polyimides, although there are some crystalline polyimides [68]. Although gas permselectivities for the H_2/CH_4 and CO_2/CH_4 systems increase with increasing film density for these two polyimides, the decreases in gas permeability are relatively large. Therefore, it can be concluded that totally amorphous polyimides are suitable for gas separation film materials. All of the polyimides we will mention below in this chapter are amorphous.

10.4 Factors Controlling Transport Properties

10.4.1 Factors Controlling Diffusion Coefficient

The main factors controlling the gas diffusion coefficient and diffusivity selectivity for glassy

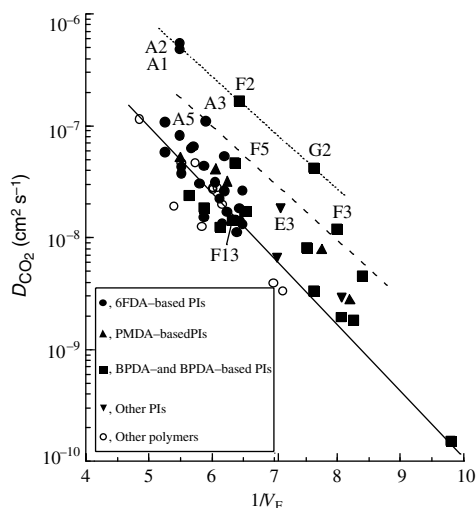


Figure 10.9 Plots of $\log D_{\text{CO}_2}$ at 35 °C and 10 atm versus $1/V_F$ for polyimides containing different acid dianhydride moieties [12,17,20,21,29,35]. The data for other glassy polymers are summarized in Table 4 in Okamoto *et al.* [10]

polymers are considered to be packing density and local mobility of polymer chains [7,8,11, 20]. The packing density of polymer chains determines the fractional free volume and size distribution of free volume holes. Figure 10.9 shows plots of $\log D_{\text{CO}_2}$ versus $1/V_F$ for polyimides containing different acid dianhydride moieties together with the data for other glassy polymers [12,17,20,21,29,35]. There is a rough linear correlation between $\log D$ and $1/V_F$, as shown by the continuous line in Figure 10.9, for most polyimides and glassy polymers. This correlation indicates that D strongly depends on the V_F . However, some polyimides display significantly different D values compared to polyimides with a similar V_F , for example, the group of polyimides A1, A2 and A5 and the group of polyimides F2, F5 and F13. The polyimides derived from diamines TeMPD and TrMPD (A1, A2, F2 and G2), shown by the dotted line, displayed 7–10 times larger D values than expected from the continuous line. The difference in D between polyimides with similar V_F values is attributed to the difference in size distribution of free volume holes. This has been demonstrated by positron annihilation (PA) lifetime spectroscopy [18,69].

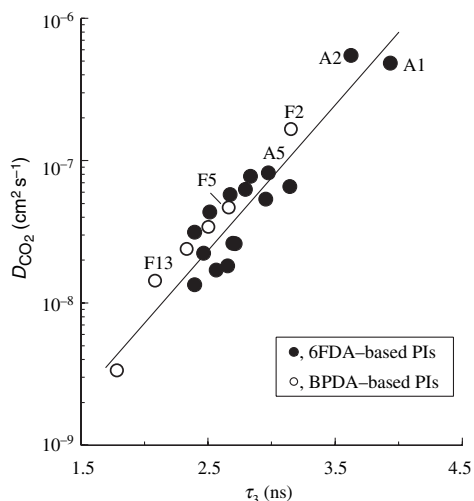


Figure 10.10 Plots of $\log D_{\text{CO}_2}$ at 35 °C and 10 atm versus τ_3 for 6FDA-based polyimides [18], and BPDA-based polyimides

The PA lifetime spectra of polymers have a long-lived component which is attributed to ortho-positronium (o-Ps) formed and annihilated in a microvacancy in the amorphous region. The larger the microvacancy, the longer the lifetime of the component τ_3 is. Because of the size distribution of free volume holes, the τ_3 is a measure of its average size. Figure 10.10 shows plots of $\log D_{\text{CO}_2}$ versus τ_3 for the 6FDA-polyimides [18] and BPDA-based polyimides. There is a linear correlation between $\log D$ and τ_3 . The plots for the polyimides with similar V_F values, but displaying significantly different D , lie on the same correlation line, indicating that the size of free volume holes is another factor controlling diffusion coefficients. Figure 10.11 shows a speculative schematic representation that is consistent with these results. Polymer 1, with a larger average size of free volume holes, contains more free volume holes large enough for a penetrant molecule to pass through and thus displays a higher D value for the gas, compared with polymer 2 with a smaller average size, even if their V_F values are the same. The PA technique is a powerful method to obtain information on the size of free volume holes. However, care must be taken when it is applied to some polyimides such as those based on PMDA and BTDA because the formation of o-Ps and τ_3 depend on electron acceptability of their acid dianhydride moieties [70,71].

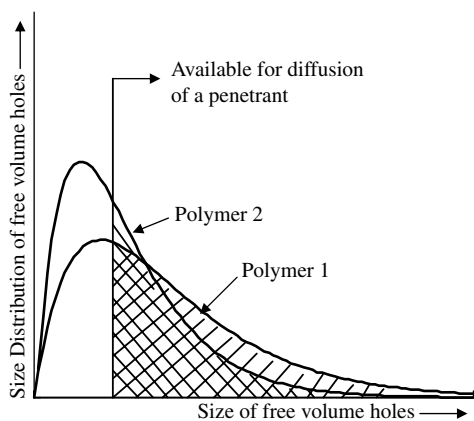


Figure 10.11 Speculative schematic representation of different size distributions of free volume holes

Figure 10.12 shows plots of D_{CO_2}/D_{CH_4} versus $1/V_F$ for several series of polyimides [12,17,20, 21,29,35]. The D ratio decreases with $1/V_F$ for the polyimides prepared from each acid dianhydride. This is because the effect of fractional free volume on the diffusion coefficient is significantly larger for a gas with a larger molecular size. The polyimides prepared from diamines TrMPD and TePMD, A1, A2, F2 and G2, shown by the dotted line, displayed much lower selectivity than the other polyimides. This suggests that the size distribution of free volume holes also affects the diffusion coefficient more for a gas with a larger molecular size. The diffusivity

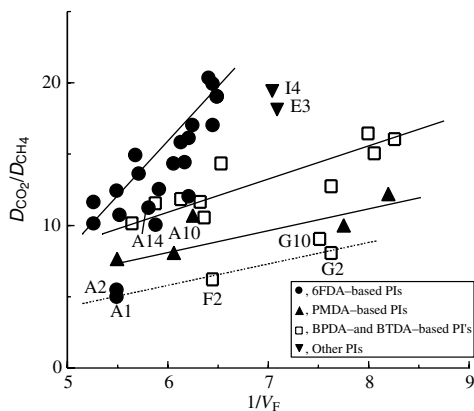


Figure 10.12 Plots of D ratios for the CO_2/CH_4 system at 35 °C and 10 atm versus $1/V_F$ [12,17,20,21,29,35]

selectivity also significantly depends on the kind of acid dianhydride; this is in the order 6FDA > BPDA, BTDA > PMDA. This suggests that local mobility of polymer chains affects the diffusion coefficient and as a result diffusivity selectivity [20]. The local motion of polymer chains and side groups plays an important role in generation and dissipation of small free volume holes or change in the size of free volume holes in the glassy state. Restricted local chain motion reduces more chances of diffusional jumps of larger penetrant molecules, resulting in an increase in the diffusivity selectivity. The bulky CF_3 groups in 6FDA-based polyimides restrict the torsional motion of neighboring phenyl rings, whereas the single bonds or carbonyl linkages in BPDA- and BTDA-based polyimides do not restrict the motion. The restriction of intra-segmental mobility in 6FDA-based polyimides leads to higher selectivity than the BPDA- and BTDA-based polyimides. On the other hand, the polyimides A14, A10 and G10, which have side groups with enhanced local mobility, displayed much lower diffusivity selectivity.

Correlations between the diffusion coefficients of gases with other physical properties of polyimides have been reported. Hirayama *et al.* reported that there was a correlation between the logarithms of apparent diffusion coefficients of CO_2 and cohesive energy densities (CED) for polyimides and other glassy polymers [40,41]. They concluded that CED was an effective and significant factor to estimate the gas diffusivity, because CED was considered as a factor including an energy needed to expand intersegment space. Matsumoto and coworkers reported that a correlation between dielectric constant and gas permeability was observed for polyimides [26,27]. They considered that polymer structure could be better characterized by using the dielectric constant than by using the fractional free volume because the dielectric constant is a function of the free volume factor and the polarity factor. Although the CED and dielectric constant have the advantage of being calculated by a group contribution method from the chemical structures for prediction of diffusivity, the correlation between each physical property and diffusion coefficients does not seem so good. These factors affect the diffusion coefficients indirectly. Consequently, a better understanding of the relationship between diffusivities and structures can

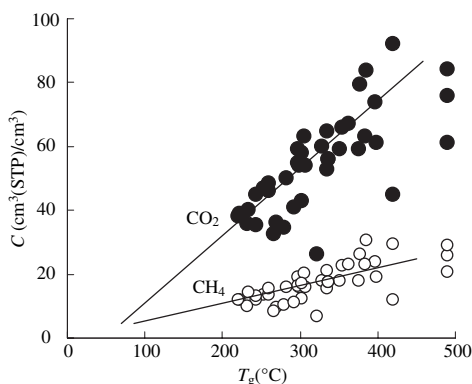


Figure 10.13 Plots of equilibrium sorption amounts C of CO_2 and CH_4 for polyimides at 35°C and 10 atm versus their glass transition temperatures, T_g [10,23,44]. The plots of three polyimides for which T_g 's were not observed up to 490°C by DSC are plotted at 490°C

be gained by analyzing the experimental results in terms of fractional free volume, size distribution of free volume holes and local mobility of polymer chains, as discussed above, because of the direct affecting factors and the good correlation.

10.4.2 Factors Controlling Solubility Coefficient

Figure 10.13 shows plots of equilibrium sorption amount, C , of CO_2 and CH_4 for polyimides versus their T_g 's [10,23,44]. There is a rough correlation between C and T_g for each gas. On the other hand, there was not a clear correlation between C of CO_2 and the concentration of functional groups [FG] to CO_2 , i.e. carbonyl and sulfonyl groups, for the polyimides. Sorption of CO_2 in polyimides with different chemical structures and other glassy polymers have been investigated by using the dual sorption model [10,23]. According to the model, the C of a penetrant in the polymer is a sum of Henry's law and Langmuir sorption amounts, that is, the following equation:

$$C = k_D p + C'_H b p / (1 + b p) \quad (10.8)$$

where k_D is the Henry's law solubility coefficient, b the Langmuir affinity constant, C'_H the Langmuir capacity constant and p the equilibrium gas pressure. The three parameters k_D , b and C'_H have been correlated with physical properties and chemical structures [10,23]. The b clearly increases with an increase in [FG] for polyimides

and other glassy polymers. This is reasonable because the carbonyl and sulfonyl groups have an affinity to CO_2 . Although there is a trend that k_D increases with [FG], the correlation is rather poor. There is a better correlation between k_D and a composite parameter reflecting both [FG] and V_F [10]. This is because the solution in Henry's law mode includes a process to make the interchain space large enough to accommodate CO_2 and it is easier to make such a space in a less-efficiently packed polymer matrix, that is, larger V_F . There is a good correlation between C'_H versus T_g . This is probably because C'_H is proportional to the amount of microvoids, which is proportional to the difference between the glass transition temperature T_g and the measuring temperature. The fraction of the Langmuir sorption amount in the total sorption amount is $2/3$ or higher at pressures lower than 10 atm. As a result, C of CO_2 at 10 atm is well correlated to T_g , not to [FG]. The correlation for CH_4 is considered to be due to the major contribution of Langmuir sorption amount and no affinity to carbonyl and sulfonyl groups.

Figure 10.14 shows plots of $S_{\text{CO}_2}/S_{\text{CH}_4}$ versus [FG] for PPO and polyimides [12,17,20,21,29,35]. Although the S ratio tends to increase with increasing [FG], the variation, including PPO, is 60% at best. Introduction of carbonyl and sulfonyl groups into polyimides is not so effective for enhancement of the solubility selectivity of CO_2/CH_4 . This is reasonable because the total amounts of sorption for both gases are dependent on T_g , not on [FG], as mentioned above. The solubility

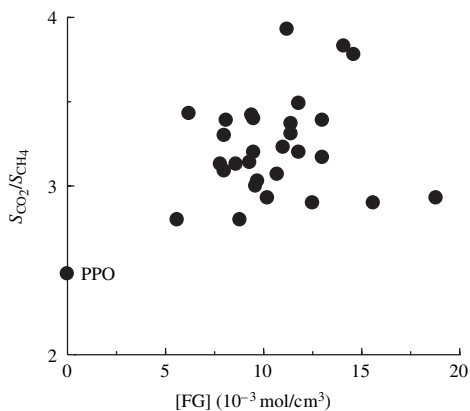


Figure 10.14 Plots of S ratios for the CO_2/CH_4 system at 35°C and 10 atm versus [FG] [12,17,20,21,29,35]

selectivity of O_2/N_2 hardly changes among these polyimides [20]. This is also because there are no specific interactions of gases with most of polyimides investigated so far, as indicated by Figure 10.5.

10.5 Structure–Property Relationship

10.5.1 Effect of Structures of Acid Dianhydrides

We mainly use P_{CO_2} and P_{CO_2}/P_{CH_4} as a representative gas pair in the discussion of gas permeability and permselectivity. The features for particular separation systems will be described later.

Figure 10.15 shows the variation in permeability coefficients of CO_2 in a series of polyimides prepared from four diamines by changing the acid dianhydrides in order to investigate the effect of chemical structure of acid dianhydrides on gas permeability for polyimides [12,17,20,29,35,44]. The acid dianhydrides from A to I are arranged in order of increasing permeability of polyimides, that is, 6FDA(A) > TADATO(B) > PMDA(C) > TCDA(D) > DSDA(E) > BPDA(F) > BTDA(G) > ODPA(H) > P3FDA(I). The 6FDA-based polyimides display higher gas permeability than the polyimides based on other acid anhydrides. The $-C(CF_3)_2-$ linkage is bulky and reduces CT interaction, and the C–F bond has a very weak van der Waals interaction, resulting in high V_F , as mentioned above. Interestingly, the P3FDA–TFDB polyimide (I) is less permeable to gases in spite of being a fluorinated

polyimide. This is due to relatively low V_F caused by enhancement of CT interaction, as mentioned above. The TADATO- and PMDA-based polyimides display relatively high gas permeabilities. This may be due to their fairly stiff polymer chains, in spite of relatively strong CT interactions indicated by their film colors. On the other hand, BTDA- and ODPA-based polyimides display low gas permeabilities because mobile linkages in their acid dianhydride moieties, carbonyl and ether linkages make the packing of polymer chains more efficient, due to a high degree of conformational freedom. The BPDA-based polyimides have a somewhat rigid acid dianhydride moiety. However, the torsional motion around the single bond linkage permits conformation of the polymer chain to change, leading to more efficient packing of polymer chain compared to the PMDA-based polyimides. Such a conformational freedom is also related to the solubility of polymers in solvents. Most BPDA-based polyimides are soluble in specific solvents, whereas the PMDA-based polyimides are not. The sulfonyl linkage is also mobile. However, the sulfonyl group is bulky and this is considered to be the reason that the DSDA-based polyimides have relatively high gas permeabilities. The TCDA-based polyimide seems to have a gas permeability as high as the DSDA-based polyimides. The aliphatic acid dianhydride interrupts the CT interaction and the moiety is also bulky because of isomeric mixtures.

Figure 10.16 shows the ideal separation factor for CO_2/CH_4 system in a series of polyimides with systematically different acid dianhydrides in the same order as the Figure 10.15. [12,17,20,29,35,44]. The acid dianhydride leading to higher gas permeability does not always lead to lower permselectivity. The 6FDA-based polyimides have relatively high permselectivities in spite of high gas permeabilities because of lower local mobility of polymer chains, as shown in Figure 10.12. The TADATO- and TCDA-based polyimides also have high permselectivities compared to other polyimides having similar gas permeabilities. The PMDA-based polyimides display lower permselectivity in spite of restricted intrasegmental mobility of their acid dianhydride moieties. The reason is not clear but it may be related to an undesirable distribution of fractional free volume.

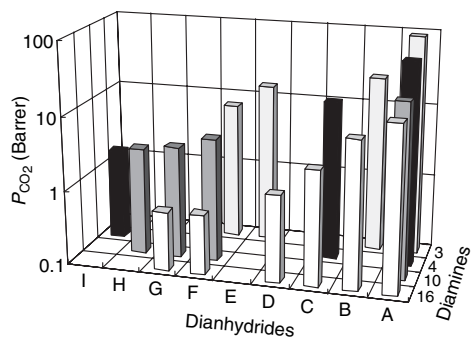


Figure 10.15 Permeability coefficients of CO_2 in a series of polyimides having systematically different acid dianhydrides at 35 °C and 10 atm [12,17,20,29,35]. The data for the TADATO(B)-based polyimides are at 2 atm [44]

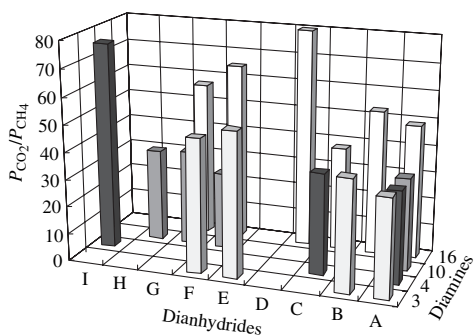


Figure 10.16 Ideal separation factors for CO_2/CH_4 systems in a series of polyimides having systematic variation of dianhydrides at 35°C and 10 atm. It should be noted that the axis of the diamines is inverse to the corresponding axis of Figure 10.15 in order to make low bars visible [12,17,20,29,35]. The data for the TADA-TO(B)-based polyimides are at 2 atm. [44]

10.5.2 Effect of Structures of Diamines

In order to compare the effect of diamines on the gas permeability of polyimides, the variation in P_{CO_2} and $P_{\text{CO}_2}/P_{\text{CH}_4}$ in a series of polyimides prepared from 6FDA with various diamines is shown in Figure 10.17 [12,17,20,21,29,35,72]. The polyimides having high gas permeability tend to display low permselectivity. However, there are some polyimides displaying significantly lower $P_{\text{CO}_2}/P_{\text{CH}_4}$ compared to other polyimides with a similar P_{CO_2} . These polyimides are divided into two groups. The first group are

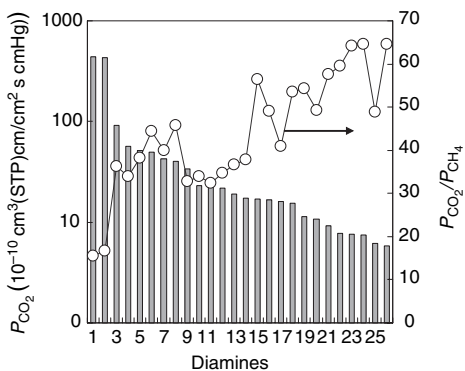


Figure 10.17 P_{CO_2} and $P_{\text{CO}_2}/P_{\text{CH}_4}$ in a series of polyimides having systematic variation of diamines at 35°C . The data for A17 are at 1 atm [12,17,20,21,29,35,72]

those polyimides prepared from the diamines ECDA(9), DATPA(10), BAHHF-OAc(12) and DAPh-OAc(14), which have side groups with high local mobility. The second group consists of polyimides prepared from the diamines BATPHF(11) and BTPHF(13), which have two ether linkages in their repeat units. The ether linkage is mobile and enhances local segmental mobility. The higher local segmental mobility results in a slightly higher gas permeability but much lower diffusivity selectivity for gas pairs with a large difference in their molecular size. The polyimides prepared from TeMPD(1) and TrMPD(2) also display low $P_{\text{CO}_2}/P_{\text{CH}_4}$ but extremely high P_{CO_2} . These properties of the polyimides are caused by the methyl groups of the diamine moiety connected on both *ortho* positions to each imide ring. The methyl groups inhibit internal rotation around the bond between the diamine moiety ring and the imide ring and both aromatic rings are perpendicular to each other. The very rigid, bulky, nonplanar molecular structure makes chain packing much ‘looser’ and results in larger free volume holes [21]. The polyimides prepared from DDBT(3) have one methyl group on the *ortho* position but a large and rigid diamine moiety, resulting in lower D values than the TeMPD- and TePMD-based polyimides but slightly higher D values than expected from the continuous line, as shown in Figure 10.9 [35]. The methyl groups of diamines DMPD(7) and MPD(8) are also on one side of the *ortho* positions to the imide ring, resulting in moderately large V_F and low local segmental mobility and relatively high gas permeability and permselectivity. The diamines pPD(18) and mPD(21), which have no methyl group, lead to relatively low gas permeability. The TFDB(4) polyimide has a similar gas permeability to the BAHF(5) polyimide. The two CF_3 groups on the *ortho* positions to the single bond of biphenyl in the TFDB moiety restrict the internal rotation of biphenyl by steric hindrance and reduce local segmental mobility. This situation is similar to that for the $-\text{C}(\text{CF}_3)_2-$ linkage mentioned above. A similar effect appears in 2,2',4,4'-tetramethyldiaminobenzidine(TMBZ), where four methyl groups on the *ortho* positions to the single bond of biphenyl restrict the internal rotation [19,29].

The polyimides prepared from diamines having a *meta*-linked phenylene, such as m-PD(21), display lower gas permeability and higher perms-

electivity than those from the corresponding diamines having a *para*-linked phenylene such as p-PD(18). A *meta*-linked polymer has a lower V_F than the corresponding *para*-linked polymer because of a higher degree of conformational freedom of the polymer chains. The lower T_g for a *meta*-linked polymer is due to the same reason. In addition to the lower V_F , the local mobility of the *meta*-linked phenylene ring is restricted because the phenylene ring connected at a *meta*-position cannot rotate without cooperative motion of the neighboring moieties, which results in lower gas diffusivity and higher diffusivity selectivity. The naphthyl moieties, DAN(6), act as kinks in the polymer chains. These kinks inhibit local mobility of polymer chains because of the same reason as the *meta*-linked phenylene diamines. However, the kinks simultaneously inhibit packing of the polymer chain and lead to a large V_F . Because of these two effects of the kinks, the polyimide prepared from DAN(6) has both high permeability and permselectivity.

The introduction of polar groups such as hydroxyl or carboxyl groups (DAPh(23), BAHHF(24), and DABA(26)) decreases gas permeability and increases permselectivity. This is because the enhanced interchain interaction reduces V_F . The polyimides with large aromatic diamines such as CDA(15), DAF(19) and DAFO(22) have a small enhanced CT interaction and a smaller V_F , resulting in a relatively lower gas permeability.

10.5.3 Separation Performance for Particular Systems

Figure 10.18 shows plots of ideal separation factor of CO₂/CH₄ versus P_{CO_2} for the polyimides mentioned above [12,17,20,21,29,35,44,72]. There is a clear tendency that the separation factor decreases with increasing gas permeability, the so-called trade-off relationship. The CO₂ and CH₄ molecules have similar collision diameters but different effective molecular sizes, due to the rod-like shape of the CO₂ molecule

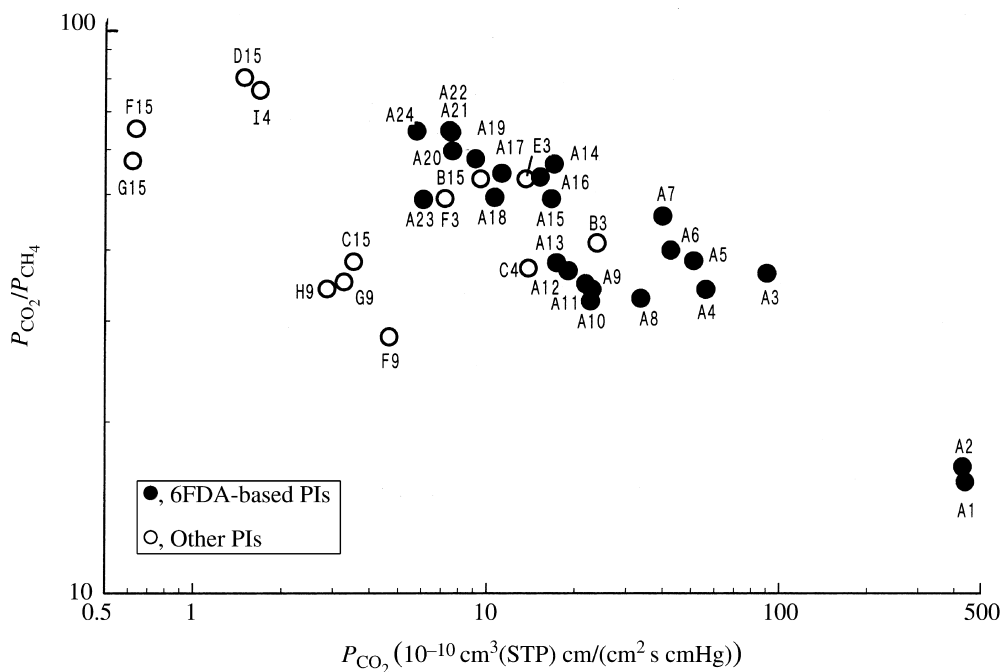


Figure 10.18 Plots of P_{CO_2}/P_{CH_4} versus P_{CO_2} at 35 °C and 10 atm for polyimides, except for the data for A17 which are at 1 atm [12,17,20,21,29,35,72]

(0.35 nm for CO₂ and 0.38 nm for CH₄) and the diffusivity selectivity is rather sensitive to the fractional free volume, the size distribution of free volume holes and the local segmental mobility, as mentioned above. As a result, the plots for the polyimides with 'loose' polymer chain packing and simultaneously low local segmental mobility lie on the so-called Robeson upper bound line [73]. The polyimides with high V_F and hindered local segmental mobility, such as 6FDA-DDBT(A3) and 6FDA-DAN(A6), are favorable for CO₂/CH₄ separation.

In the case of the H₂/CH₄ system with a much smaller molecular size of the more permeable penetrant (H₂, 0.29 nm) and a much larger size difference of the gas pair, the diffusivity selectivity is more sensitive to the three factors controlling diffusivity, whereas the diffusivity of H₂ is less sensitive to them, namely, P_{H_2} is reasonably high even for polyimides with moderately dense polymer chain packing. Therefore, as shown in Figure 10.19, the permselectivity of H₂/CH₄ increases more significantly with decreasing P_{H_2} for the polyimides designed to increase the diffusivity selectivity [12,17,20,21,29,35,72]. The polyimides with moderately low V_F and low local segmental mobility, such as 6FDA-DABA(A26), are favorable for H₂/CH₄ separation

In the case of the O₂/N₂ system with very similar molecular size and shape of the gas pair (0.343 for O₂ and 0.368 nm for N₂), the factors controlling diffusivity very similarly affect the diffusiv-

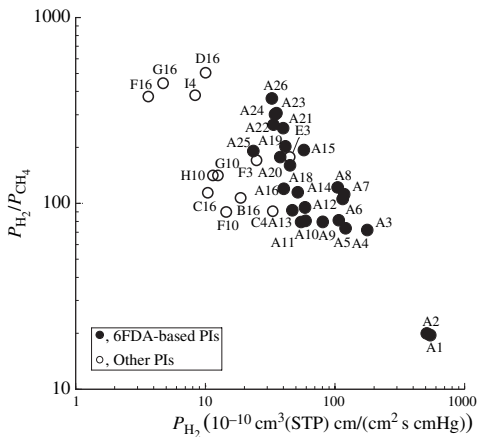


Figure 10.19 Plots of P_{H_2}/P_{CH_4} versus P_{H_2} at 35 °C and 10 atm for polyimides [12,17,20,21,29,35,72]

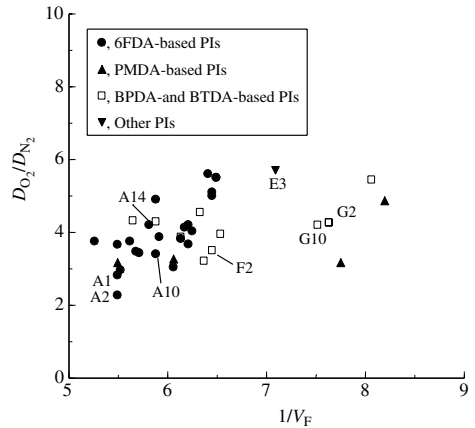


Figure 10.20 Plots of D ratios for the O₂/N₂ system at 35 °C and 2 atm versus $1/V_F$ for polyimides [17,20,21,29,35]

ity of O₂ and N₂. As a result, the diffusivity selectivity of O₂/N₂ is much less sensitive to the chemical structures of polyimides, as shown in Figure 10.20 [17,20,21,29,35]. This is quite different from the case of CO₂/CH₄ shown in Figure 10.12. The D_{O_2}/D_{N_2} increases slightly with a decrease in V_F , but is hardly dependent on both the size distribution of free volume holes and the local segmental mobility. As shown in Figure 10.21, plots of P_{O_2}/P_{N_2} versus P_{O_2} of all polyimides fall on almost the same trade-off line [17,20,21,29,35,72]. It is very

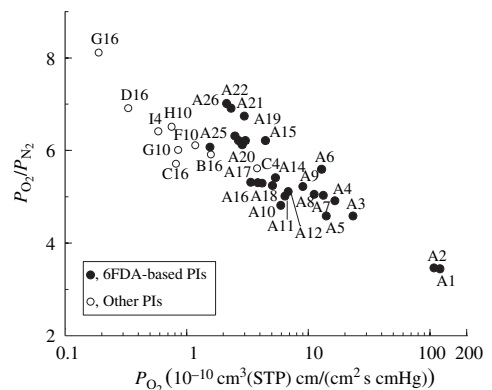


Figure 10.21 Plots of P_{O_2}/P_{N_2} versus P_{O_2} at 35 °C and 2 atm for polyimides, except for the data for A17 which is at 1 atm [17,20,21,29,35,72]

difficult to shift the trade-off line upward by designing the chemical structure to enhance the diffusivity selectivity.

The situation is quite similar for CO_2/N_2 separation because of their similar molecular sizes. The diffusivity selectivity of CO_2/N_2 for most polyimides ranges from 2 to 4. The ideal separation factor ranges from 15 to 30, being hardly sensitive to their chemical structures. It is important and effective to enhance the solubility selectivity by designing the membrane matrix with a specific affinity to CO_2 . This will be described later.

Membrane separation of olefins/paraffins has great potential because the separations currently performed are 'energy-intensive'. There are several papers reporting on the $\text{C}_3\text{H}_6/\text{C}_3\text{H}_8$ separation properties of polyimides [38,48,74,75]. Burns and Koros have conducted a comprehensive review by evaluating all of the available literature data to define the upper bound relationship for the separation, as shown in Figure 10.22 [48]. The polymers currently defining the upper bound include 6FDA-DDBT(A3) and 6FDA-TrMPD(A2), which have high V_F , larger average size of free volume holes and rigid polymer chains. The experimentally observed upper bound is consistent with the prediction presented by using an extension of the analysis by Freeman [76]. The molecular size of the more permeable gas C_3H_6 is much larger than the sizes of inorganic gases and polyimides with high V_F are essential for reasonably high C_3H_6 permeability.

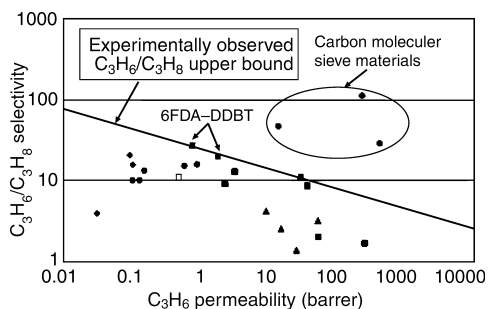


Figure 10.22 Plots of $P_{\text{C}_3\text{H}_6}/P_{\text{C}_3\text{H}_8}$ versus $P_{\text{C}_3\text{H}_6}$ for 1–4 atm and the upper bound: (□), 100 °C; (■), 50 °C; (●), 35 °C; (▲), 30 °C; (◆) 26 °C [48]. Reprinted from *Journal of Membrane Science*, **211**, R. L. Burns and W. J. Koros, 'Defining the challenges for $\text{C}_3\text{H}_6/\text{C}_3\text{H}_8$ separation using polymeric membranes', 299–309, Copyright (2003), with permission from Elsevier

However, the separation factors for mixed $\text{C}_3\text{H}_6/\text{C}_3\text{H}_8$ gases are lower by about 40 % of the ideal separation factors due to an increase in $P_{\text{C}_3\text{H}_8}$ caused by the coexisting C_3H_6 . It is not easy to achieve both high permeability and permselectivity by the molecular design mentioned above.

10.5.4 A Group Contribution Method for Polyimides

Alentiev *et al.* have developed a group contribution method to predict gas permeability coefficients for polyimides. They used acid dianhydride and diamine residues as building blocks for calculation [43]. The group contribution was deduced from a database including about 120 polyimides prepared from 9 acid anhydrides and about 70 diamines. This method may predict gas permeability and diffusion coefficients for 400–500 amorphous polyimides. This is a comprehensive analysis of structure–property relationships. The group contribution method can predict the permeability and permselectivity for a wide variety of polyimides prepared from any acid dianhydrides and diamines ever tested. Robeson *et al.* [77] and Park and Paul [78] had developed group contribution methods to predict gas permeability coefficients for a wide variety of glassy polymers, such as polysulfones and polycarbonates. Alentiev *et al.* have developed it for one class of polymers, polyimides, to achieve more accurate prediction [43]. It may be possible to design polyimides displaying a slightly better performance than the upper bound performance by using this method.

The polyimides collected in the database of the group contribution method do not have appreciable specific interactions with gas molecules. It was expected that the performance beyond the upper bound line would be achieved when the solubility selectivity is significantly enhanced. This idea has already been demonstrated by the poly(ethylene oxide imide)-segmented copolymers (PEO-PI)_s [22,36] and amine-modified polyimides [39] for CO_2/N_2 separation, as described below.

10.5.5 Enhancement of Solubility Selectivity for CO_2/N_2 Separation

Figure 10.23 shows plots of ideal separation factor versus P_{CO_2} for the CO_2/N_2 system for the PEO-PIs, together with the data for other

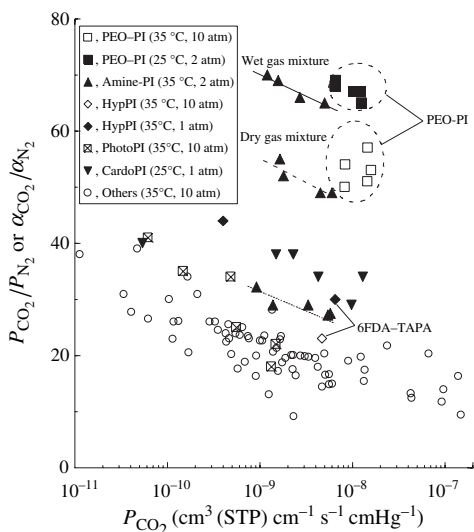


Figure 10.23 Comparison of membrane performance for CO_2/N_2 separation. It should be noted that the performance depends on conditions such as temperature, pressure and single-gas or mixed-gas permeation; the data are obtained for single-gas permeations unless otherwise stated. The binary-gas mixture is composed of 18% CO_2 and 82% N_2 ; PEO-PI, poly(ethylene oxide imide)-segmented copolymers [36]; Amine-PI, amine-modified polyimides [39]; HypPI, hyperbranched polyimides [45]; PhotoPI, photocrosslinked polyimides [30]; Cardo-PI, bis(phenyl)fluorene-based cardo polyimides [46]

polymers and separation performance to a CO_2/N_2 gas mixture for amine-modified polyimides [30,36,39,45,46]. It should be noted that the CO_2/N_2 separation performance significantly depends on temperature; it is better at lower temperature, because the permselectivity decreases sharply with increasing temperature, whereas the permeability of CO_2 increases moderately or only slightly. For example, with a decrease in temperature from 40 to 25 °C, the permselectivity increased from 22 to 36 for a polysulfone asymmetric hollow fiber membrane [79]. The performance also depends on pressure; it is better at lower pressure, because the permeability for CO_2 decreases with increasing pressure more than the permeability for N_2 does. For example, with a decrease from 10 to 1 atm, the permselectivity increased from 23 to 30 for a hyperbranched polyimide (6FDA-TAPA, denoted by HypPI in Figure 10.23) [45].

The PEO-PIs display excellent CO_2/N_2 separation properties compared to other polyimides. The PEO-PIs have microphase-separated structures consisting of microdomains of hydrophilic and rubbery polyether segments and of hydrophobic and glassy polyimide segments [36]. The diffusion and permeation occur through the PEO segment microdomains. The solubility coefficient for CO_2 for a PEO-PI is about three times larger than that predicted from the correlation between $\log S$ versus ε/k . This is probably due to an affinity of the polar PEO segments to CO_2 , which has a high polarizability and a high quadrupole moment when compared with other gases. The PEO-PIs display excellent membrane performances for CO_2/N_2 separation; for example, $P_{\text{CO}_2} = 140$ barrer and $P_{\text{CO}_2}/P_{\text{N}_2} = 70$ at 25 °C. The transport properties for PEO-PIs are independent of feed pressure, at least up to 10 atm.

Figure 10.23 also shows the data for amine-modified polyimides prepared by immersing methyl-brominated polyimide membranes into aqueous amine solutions [39]. There is no special effect of the amine moieties for pure gas permeation. However, the performances for dry mixed gases are higher when compared with pure gas permeation. It should be noted that the α for unmodified polyimides under the same conditions was 1.5 times higher than the P ratio for pure gas permeation. They display a higher performance for CO_2/N_2 separation in the presence of water vapor. The sorbed water may enhance the interaction between the amine moieties and CO_2 molecules and/or polarity of the membrane matrix to enhance the solubility selectivity of CO_2 over N_2 [39]. The enhancement effect of the coexisting water vapor on α is high, even at low humidity. This is advantageous in practical applications for flue gases.

For practical applications, these membrane materials should be fabricated into a thin skin-layer membrane such as an asymmetric membrane and a membrane with a large area such as a hollow fiber membrane. The PEO-PIs have good film-forming properties and good mechanical strength, and have been successfully fabricated into composite hollow fiber membranes by a dry-jet wet spinning process using a double layer spinneret [80]. These membranes were composed of a thin and a dense outer layer of PEO-PI and a sponge-like inner layer of non-PEO-PI (BPDA-ODA/DABA polyimide). The

outer layer was responsible for the separation and was fabricated as thin as 1 μm . The permeance of CO_2 , R_{CO_2} and the CO_2/N_2 selectivity for the PEO-PI composite hollow fiber membranes in a desiccator decreased by 40 % and 10 ± 20 %, respectively, for one month after membrane preparation. These values did not decrease with time, at least up to five months later. The steady-state performance was still high; for example, the R_{CO_2} was $69 \times 10^{-6} \text{ cm}^3(\text{STP})/(\text{cm}^2 \text{ s cmHg})$ and the CO_2/N_2 selectivity was 33 at 50°C . The decline of permeance may be due to densification of the inner layer at the interface to the outer layer. A similar densification of the skin layer has been observed for an asymmetric hollow fiber membrane [75]. It should be noted that the transport properties determined on thick films of glassy polymers differed significantly from the properties of thin, gas permeation membranes [81]. Asymmetric amine-modified membranes have been also prepared. Typical performance values for wet condition were $R_{\text{CO}_2} = 16 \times 10^{-6} \text{ cm}^3(\text{STP})/(\text{cm}^2 \text{ s cmHg})$ and $\alpha = 64$.

10.5.6 Enhancement of Diffusivity Selectivity for H_2/CH_4 Separation

Photocrosslinking of polyimide membranes successfully enhances diffusivity selectivity for H_2/CH_4 separation [30]. When the polyimides containing the benzophenone moiety and methyl groups on the phenylene rings are irradiated by an ultraviolet lamp, crosslinking reactions take place between the benzophenone and methyl groups. UV irradiation increases the permselectivity markedly and decreases the gas permeability to some extent. Figure 10.24 shows plots of $P_{\text{H}_2}/P_{\text{CH}_4}$ versus P_{H_2} for the crosslinked polyimides, together with the data for other polyimides [30]. The UV irradiated polyimides display much higher permselectivity of H_2/CH_4 compared to the polyimides with the same gas permeability. This increase in permselectivity is due to enhancement of the diffusivity selectivity. Consequently, the treatment is very effective for the H_2/CH_4 system with a larger difference in molecular size and is effective for the CO_2/CH_4 system to some extent. It is, however, not effective for CO_2/N_2 separation with a small difference in molecular size, as shown in Figure 10.23 (denoted by PhotoPI).

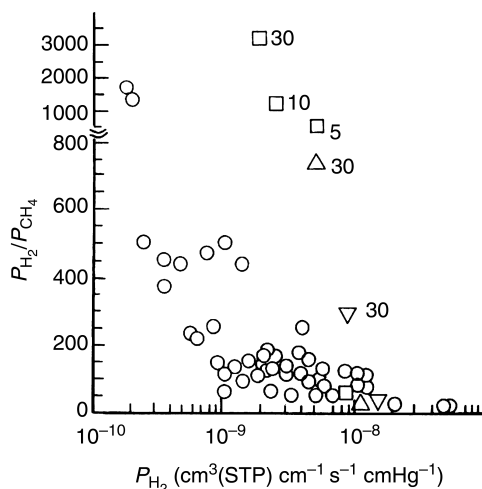


Figure 10.24 Comparison of various polyimides with regard to the separation of H_2/CH_4 at 35°C and 10 atm: (\square), BTDA-TrMPD; (\triangle), BTDA/6FDA-TrMPD (1:1); (∇), BTDA/6FDA-TrMPD (1:3); (\bullet), polyimides. The times indicated are UV irradiation times. (in min) [30] Reprinted from *Journal of Membrane Science*, 87, H. Kita, T. Inada, K. Tanaka and K. Okamoto, 'Effect of photocrosslinking on permeability and permselectivity of gases through a benzophenone-containing polyimide', 139-147, Copyright (1994), with permission from Elsevier

10.5.7 Water Vapor Permeation

Water is generally the most permeable species to polymeric membranes. The $P_{\text{H}_2\text{O}}$ for a BPDA-based polyimide is about 10 times higher than P_{H_2} , and about 500 times higher than P for air at room temperature [82,83]. This polyimide has been commercialized for dehumidification of air.

The effect of chemical structure on the vapor permeation properties of water and ethanol has been investigated for a series of polyimides [50]. Figure 10.25 shows plots of separation factors of $\text{H}_2\text{O}/\text{EtOH}$ versus permeability coefficient to H_2O for the polyimides. Changing (partly) the diamine from ODA to DABA in BPDA-ODA polyimides results in a small increase in water permeability, while high permselectivity is maintained. Introduction of polar carboxyl groups increases the water vapor solubility considerably but simultaneously significantly reduces the diffusivity, probably because of enhanced molecular interactions of polymer chains. The two opposite effects explain the results. The BPDA-DDBT(F3) and BPDA-DDS(F17) polyimides have fairly

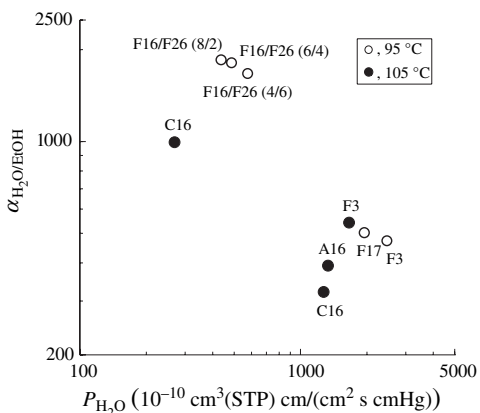


Figure 10.25 Plots of separation factors for H₂O–EtOH versus permeability coefficients for H₂O for various polyimides [50]

high selectivity with high permeability to H₂O. Although having fairly ‘loose’ polymer chain packing, BPDA–DDBT retains the high diffusivity selectivity of H₂O over EtOH because of a large difference in their molecular sizes. 6FDA–ODA(A15) is inferior to BPDA–DDBT, because of the lower solubility for water caused by the hydrophobic CF₃ groups. A reasonable hydrophilicity of the matrix is important for separation of H₂O from organic solvents.

In general, polyimides are unstable at high temperatures and high humidities, or in boiling water, due to hydrolysis of the imide rings. However, most of the polyimides can be used for dehumidification of air or dehydration of alcohols because of the moderate conditions employed.

10.6 Conclusions

The effects of chemical and physical structures on gas permeability and permselectivity were discussed, mainly using the data for a series of polyimides prepared in our laboratory. The packing densities and local mobilities of the polymer chains are the important factors controlling gas permeability and permselectivity for polyimides without appreciable specific interactions with a gas molecule. The packing density depends on chain stiffness, strength of polymer chain–chain interactions and chain bulkiness. It should be noted that the CT interaction is an important factor strongly affecting packing density for polyimides. Since the effect of each structural and

functional group on them is basically additive, group contribution methods are useful tools to predict gas permeability for a wide variety of polyimides.

The performance beyond the upper bound line for a given separation system is expected to be achieved by adding structures having appreciable specific interactions with a certain gas molecule. The poly(ethylene oxide imide)-segmented copolymers (PEO–PIs) and amine-modified polyimides for CO₂/N₂ separation mentioned here are good examples. Polyimides can easily be designed by combining acid anhydrides and diamines. New monomers are still being developed. Polyimides hold the possibility of developing new materials displaying performance beyond the upper bound line.

References

- [1] F. W. Harris, ‘Synthesis of aromatic polyimides from dianhydrides and diamines’, in *Polyimides*, D. Wilson, H. D. Stenzenberger and P. M. Hergenrother (Eds), Chapman & Hall, New York, NY, USA, pp. 1–37 (1990).
- [2] H. H. Hoehn, Heat treatment of membranes of selected polyimides, polyesters and polyamides. *US Patent 3 822 202* (1972).
- [3] H. H. Hoehn, ‘Aromatic polyamide membranes’, in *Material Science of Synthetic Membranes*, D. R. Lloyd, (Ed.), ACS Symposium Series 269, American Chemical Society, Washington, DC, USA, pp. 81–98 (1985).
- [4] G. F. Sykes and A. K. St. Clair, ‘The effect of molecular structure on the gas transmission rates of aromatic polyimides’, *J. Appl. Polym. Sci.*, **32**, 3725–3735 (1986).
- [5] T. H. Kim, W. J. Koros and G. R. Husk, ‘Advanced gas separation membrane materials: Rigid aromatic polyimides’, *Sepr. Sci. Technol.*, **23**, 1611–1626 (1988).
- [6] W. J. Koros, G. K. Fleming, S. M. Jordan, T. H. Kim and H. H. Hoehn, ‘Polymeric membrane materials for solution–diffusion based permeation separations’, *Prog. Polym. Sci.*, **13**, 339–401 (1988).
- [7] T. H. Kim, W. J. Koros, G. R. Husk and K. C. O’Brien, ‘Relationship between gas separation properties and chemical structure in a series of aromatic polyimides’, *J. Membr. Sci.*, **37**, 45–62 (1988).
- [8] S. A. Stern, Y. Mi, H. Yamamoto and A. K. St. Clair, ‘Structure/permeability relationships of polyimide membranes. Applications of the separation of gas mixtures’, *J. Polym. Sci. Part B: Polym. Phys. Ed.*, **27**, 1887–1909 (1989).

- [9] K. Tanaka, H. Kita, K. Okamoto, A. Nakamura and Y. Kusuki, 'Gas permeability and permselectivity in polyimides based on 3,3',4,4'-biphenyltetracarboxylic dianhydride', *J. Membr. Sci.*, **47**, 203–215 (1989).
- [10] K. Okamoto, K. Tanaka, H. Kita, A. Nakamura and Y. Kusuki, 'Sorption and transport of carbon dioxide in a polyimide from 3,3',4,4'-biphenyltetracarboxylic dianhydride and 4,4'-diaminodiphenyl sulfone', *J. Polym. Sci. Part B: Polym. Phys. Ed.*, **27**, 2621–2635 (1989).
- [11] K. Tanaka, H. Kita, K. Okamoto, A. Nakamura and Y. Kusuki, 'Gas permeability and permselectivity in homo- and copolyimides from 3,3',4,4'-biphenyltetracarboxylic dianhydride and 3,3'- and 4,4'-diaminodiphenylsulfones', *Polym. J.*, **22**, 381–385 (1990).
- [12] K. Tanaka, H. Kita and K. Okamoto, 'Gas permeability and permselectivity in polyimide films', *Kobunshi Ronbunshu*, **47**, 945–951 (1990).
- [13] M. R. Coleman and W. J. Koros, 'Isomeric polyimides based on fluorinated dianhydrides and diamines for gas separation applications', *J. Membr. Sci.*, **50**, 285–297 (1990).
- [14] H. Yamamoto, Y. Mi, S. A. Stern and A. K. St. Clair, 'Structure/permeability relationships of polyimide membranes. II', *J. Polym. Sci. Part B: Polym. Phys. Ed.*, **28**, 2291–2304 (1990).
- [15] S. A. Stern, R. Vaidyanathan and J. R. Pratt, 'Structure/permeability relationships of silicon-containing polyimides', *J. Membr. Sci.*, **49**, 1–14 (1990).
- [16] T. Hirose, Y. Mi, S. A. Stern and A. K. St. Clair, 'The solubility of carbon dioxide and methane in polyimides at elevated pressures', *J. Polym. Sci. Part B: Polym. Phys. Ed.*, **29**, 341–347 (1991).
- [17] K. Okamoto, Tanaka, H. Kita, M. Ishida, M. Kakimoto and Y. Imai, 'Gas permeability and permselectivity of polyimides prepared from 4,4'-diaminotriphenylamine', *Polym. J.*, **24**, 451–457 (1992).
- [18] K. Tanaka, M. Katsube, K. Okamoto, H. Kita, O. Sueoka and Y. Ito, 'Correlation between position annihilation and gas diffusion properties of a series of polyimides', *Bull. Chem. Soc. Jpn*, **65**, 1891–1897 (1992).
- [19] T. Kasai, Y. Sakata, H. Takeuchi and Y. Kobayashi, 'Development of high performance polyimide gas separation membranes', *Mitsubishi Kasei R & D Rev.*, **6**, 77–84 (1992).
- [20] K. Tanaka, H. Kita, M. Okano and K. Okamoto, 'Permeability and permselectivity of gases in fluorinated and non-fluorinated polyimides', *Polymer*, **33**, 585–592 (1992).
- [21] K. Tanaka, M. Okano, H. Toshino, H. Kita and K. Okamoto, 'Effect of methyl substituents on permeability and permselectivity of gases in polyimides prepared from methyl-substituted phenylenediamines', *J. Polym. Sci. Part B: Polym. Phys. Ed.*, **30**, 907–914 (1992).
- [22] K. Okamoto, N. Umeo, S. Okamoto, K. Tanaka and H. Kita, 'Selective permeation of carbon dioxide over nitrogen through poly(ethylene oxide)-containing polyimide membranes', *Chem. Lett.*, 225–228 (1993).
- [23] K. Tanaka, H. Kita and K. Okamoto, 'Sorption of carbon dioxide in fluorinated polyimides', *J. Polym. Sci. Part B: Polym. Phys. Ed.*, **31**, 1127–1133 (1993).
- [24] Y. P. Yampol'skii, 'New polymeric materials for gas-separation membranes', *Vysokomol. Soedin.*, **35**, 51–62 (1993).
- [25] S. A. Stern, Y. Liu and W. A. Feld, 'Structure/permeability relationships of polyimides with branched or extended diamine moieties', *J. Polym. Sci. Part B: Polym. Phys. Ed.*, **31**, 939–951 (1993).
- [26] K. Matsumoto, P. Xu and T. Nishikimi, 'Gas permeation of aromatic polyimides. I. Relationship between gas permeabilities and dielectric constants', *J. Membr. Sci.*, **81**, 15–22 (1993).
- [27] K. Matsumoto and P. Xu, 'Gas permeation of aromatic polyimides. II. Influence of chemical structure', *J. Membr. Sci.*, **81**, 23–30 (1993).
- [28] M. Langsam and W. F. Burgoyne, 'Effects of diamine monomer structure on the gas permeability of polyimides. I. Bridged diamines', *J. Polym. Sci. Part A: Polym. Chem. Ed.*, **31**, 909–921 (1993).
- [29] K. Tanaka, M. Okano, H. Kita, K. Okamoto and S. Nishi, 'Effects of trifluoromethyl side groups on gas permeability and permselectivity in polyimides', *Polym. J.*, **26**, 1186–1189 (1994).
- [30] H. Kita, T. Inada, K. Tanaka and K. Okamoto, 'Effect of photocrosslinking on permeability and permselectivity of gases through a benzophenone-containing polyimide', *J. Membr. Sci.*, **87**, 139–147 (1994).
- [31] M. R. Pixton and D. R. Paul, 'Relationships between structure and transport properties for polymers with aromatic backbones', in *Polymeric Gas Separation Membranes*, D. R. Paul and Y. P. Yampol'skii (Eds), CRC Press, Boca Raton, FL, USA, pp. 83–153 (1994).
- [32] S. A. Stern, 'Polymers for gas separations: the next decade', *J. Membr. Sci.*, **94**, 1–65 (1994).
- [33] M. R. Coleman and W. J. Koros, 'The transport properties of polyimide isomers containing hexafluoroisopropylidene in the diamine residue', *J. Polym. Sci. Part B: Polym. Phys. Ed.*, **32**, 1915–1926 (1994).
- [34] G. Zoia, S. A. Stern, A. K. St. Clair and J. R. Pratt, 'Permeability relationships of polyimide copolymers', *J. Polym. Sci. Part B: Polym. Phys. Ed.*, **32**, 53–58 (1994).

- [35] K. Tanaka, O. Osada, H. Kita and K. Okamoto, 'Gas permeability and permselectivity of polyimides with large aromatic rings', *J. Polym. Sci. Part B: Polym. Phys. Ed.*, **33**, 1907–1915 (1995).
- [36] K. Okamoto, M. Fujii, S. Okamoto, H. Suzuki, K. Tanaka and H. Kita, 'Gas permeation properties of poly(ether imide) segmented copolymers', *Macromolecules*, **28**, 6950–6956 (1995).
- [37] C. Byong-wa, 'Packing density and gas permeability of copolyimides containing a bicyclo [2,2,2]oct-7-ene-2,3,5,6-tetracarboxylic dianhydride constituent', *J. Polym. Sci. Part B: Polym. Phys. Ed.*, **33**, 731–737 (1995).
- [38] K. Tanaka, A. Taguchi, J. Hao, H. Kita and K. Okamoto, 'Permeation and separation properties of polyimide membranes to olefins and paraffins', *J. Membr. Sci.*, **121**, 197–207 (1996).
- [39] K. Okamoto, N. Yasugi, T. Kawabata, K. Tanaka and H. Kita, 'Selective permeation of carbon dioxide through amine-modified polyimide membranes', *Chem. Lett.*, 613–614 (1996).
- [40] Y. Hirayama, T. Yoshinaga, Y. Kusuki, K. Ninomiya, T. Sakakibara and T. Tamari, 'Relation of gas permeability with structure of aromatic polyimides I', *J. Membr. Sci.*, **111**, 169–182 (1996).
- [41] Y. Hirayama, T. Yoshinaga, Y. Kusuki, K. Ninomiya, T. Sakakibara and T. Tamari, 'Relation of gas permeability with structure of aromatic polyimides II', *J. Membr. Sci.*, **111**, 183–192 (1996).
- [42] K. Okamoto, K. Noborio, J. Hao, K. Tanaka and H. Kita, 'Permeation and separation properties of polyimide membranes to 1,3-butadiene and *n*-butane', *J. Membr. Sci.*, **134**, 171–179 (1997).
- [43] A. Y. Alentiev, K. A. Loza and Y. P. Yampolskii, 'Development of the methods for prediction of gas permeation parameters of glassy polymers: polyimides as alternating copolymers', *J. Membr. Sci.*, **167**, 91–106 (2000).
- [44] L. Yang, J. Fang, N. Meichin, K. Tanaka, H. Kita and K. Okamoto, 'Gas permeation properties of thianthrene-5,5,10,10-tetraoxide-containing polyimides', *Polymer*, **42**, 2021–2029 (2001).
- [45] J. Fang, H. Kita and K. Okamoto, 'Gas permeation properties of hyperbranched polyimide membranes', *J. Membr. Sci.*, **182**, 245–256 (2001).
- [46] S. Kazama, T. Teramoto and K. Haraya, 'Carbon dioxide and nitrogen transport properties of bis(phenyl)fluorene-based cardo polymer membranes', *J. Membr. Sci.*, **207**, 91–104 (2002).
- [47] F. Piroux, E. Espuche, R. Mercier, M. Pineri and G. Gebel, 'Gas transport mechanism in sulfonated polyimides: Consequences on gas selectivity', *J. Membr. Sci.*, **209**, 241–253 (2002).
- [48] R. L. Burns and W. J. Koros, 'Defining the challenges for C₃H₆/C₃H₈ separation using polymeric membranes', *J. Membr. Sci.*, **211**, 299–309 (2003).
- [49] Y. Cen and R. N. Lichtenthaler, 'Vapor permeation', in *Membrane Separations Technology. Principles and Applications*, R. D. Noble and S. A. Stern (Eds), Elsevier, Amsterdam, The Netherlands, pp. 85–112 (1995).
- [50] K. Okamoto, N. Tanihara, H. Watanabe, K. Tanaka, H. Kita, A. Nakamura, Y. Kusuki and K. Nakagawa, 'Vapor permeation and pervaporation separation of water-ethanol mixtures through polyimide membranes', *J. Membr. Sci.*, **68**, 53–63 (1992).
- [51] K. Okamoto, 'Sorption and diffusion of water vapor in polyimides films', in *Polyimides. Fundamentals and Applications*, M. K. Ghosh and K. L. Mittal (Eds), Marcel Dekker, New York, NY, USA, pp. 265–278 (1992).
- [52] D. W. van Krevelen, *Properties of Polymers*, Elsevier, Amsterdam, The Netherlands (1976).
- [53] (a) A. Bondi, 'van der Waals volumes and radii', *J. Phys. Chem.*, **68**, 441–451 (1964); (b) A. Bondi, in *Physical Properties of Molecular Crystals, Liquids, and Glasses*, John Wiley & Sons, Inc., New York, NY, USA, pp. 450–471 (1968).
- [54] R. N. Haward, 'Occupied volume of liquids and polymers', *J. Macromol. Sci., Rev. Macromol. Chem.*, **C4**, 191–242 (1970).
- [55] M. I. Williams, R. F. Landel, and J. D. Ferry, 'The temperature dependence of relaxation mechanisms in amorphous polymers and other glass-forming liquids', *J. Am. Chem. Soc.*, **77**, 3701–3707 (1955).
- [56] H. Fujita, 'Diffusion in polymer-diluent systems', *Fortschr. Hochpolym. Forsch.*, **3**, 1–47 (1961).
- [57] T. L. St. Clair, 'Structure-property relationships in linear aromatic polyimides', in *Polyimides*, D. Wilson, H. D. Stenzenberger and P. M. Hergenrother (Eds), Chapman & Hall, New York, NY, USA, pp. 58–78 (1990).
- [58] A. R. Berens and H. B. Hopfenberg, 'Diffusion of organic vapors at low concentrations in glassy PVC, polystyrene and PMMA', *J. Membr. Sci.*, **10**, 283–303 (1982).
- [59] D. W. Breck, *Zeolite Molecular Sieves*, Robert R. Krieger Publishing Company, Malabar, FL, USA, pp. 632–641 (1984).
- [60] K. Okamoto, K. Tanaka, H. Kita, A. Nakamura and Y. Kusuki, 'The effect of morphology on sorption and transport of carbon dioxide in a polyimide from 3,3',4,4'-biphenyltetracarboxylic dianhydride and 4,4'-oxydianiline', *J. Polym. Sci. Part B: Polym. Phys. Ed.*, **27**, 1221–1233 (1989).
- [61] S. Isoda, H. Shimada, M. Kochi and H. Kambe, 'Molecular aggregation of solid aromatic polymers. 1. Small-angle X-ray scattering from aromatic polyimide films', *J. Polym. Sci. Part B: Polym. Phys. Ed.*, **19**, 1293–1312 (1981).
- [62] T. P. Russell, 'A small-angle X-ray scattering study of an aromatic polyimide', *J. Polym. Sci. Part B: Polym. Phys. Ed.*, **22**, 1105–1117 (1984).

- [63] K. C. O'Brien, W. J. Koros and G. R. Husk, 'Influence of casting and curing conditions on gas sorption and transport in polyimide films', *Polym. Eng. Sci.*, **27**, 211–217 (1987).
- [64] K. Okamoto, K. Tanaka, O. Yokoshi and H. Kita, 'The effect of morphology on sorption and transport of carbon dioxide in poly(4,4'-oxydiphenylene pyromellitimide)', *J. Polym. Sci. Part B: Polym. Phys. Ed.*, **27**, 643–654 (1989).
- [65] K. Tanaka, H. Kita, K. Okamoto, A. Nakamura and Y. Kusuki, 'The effect of morphology on gas permeability and permselectivity in polyimide, based on 3,3',4,4'-biphenyltetracarboxylic dianhydride and 4,4'-oxydianiline', *Polym. J.*, **21**, 127–135 (1989).
- [66] A. S. Michaels, W. R. Vieth and J. A. Barrie, 'Diffusion of gases in poly(ethylene terephthalate)', *J. Appl. Phys.*, **34**, 13–20 (1963).
- [67] A. S. Michaels and H. J. Bixler, 'Flow of gases through polyethylene', *J. Polym. Sci.*, **50**, 413–439 (1961).
- [68] P. M. Hergenrother, N. T. Wakelyn and S. J. Havens, 'Polyimides containing carbonyl and ether connecting groups', *J. Polym. Sci. Part A: Polym. Chem. Ed.*, **25**, 1093–1103 (1987).
- [69] K. Tanaka, T. Kawai, H. Kita, K. Okamoto and Y. Ito, 'Correlation between gas diffusion coefficient and positron annihilation lifetime in polymers with rigid polymer chains', *Macromolecules*, **33**, 5513–5517 (2000).
- [70] K. Okamoto, K. Tanaka, M. Katsube, O. Sueoka and Y. Ito, 'Positronium formation in various polyimides', *Radiat. Phys. Chem.*, **41**, 497–502 (1993).
- [71] K. Tanaka, M. Katsube, N. Tanihara, H. Kita, K. Okamoto and Y. Ito, 'Anomalous temperature dependence of lifetime of ortho-positronium in polyimides', *Radiat. Phys. Chem.*, **55**, 417–422 (1999).
- [72] H. Kawakami, K. Nakajima and S. Nagaoka, 'Gas separation characteristics of an isomeric polyimide membrane prepared under shear stress', *J. Membr. Sci.*, **211**, 291–298 (2003).
- [73] L. M. Robeson, 'Correlation of separation factor versus permeability for polymeric membranes', *J. Membr. Sci.*, **62**, 165–185 (1991).
- [74] A. Shimazu, T. Miyazaki, M. Maeda and K. Ikeda, 'Relationships between the chemical structures and the solubility diffusivity and permselectivity of propylene and propane in 6FDA-based polyimides', *J. Polym. Sci. Part B: Polym. Phys. Ed.*, **38**, 2525–2536 (2000).
- [75] M. Yoshino, S. Nakamura, H. Kita, K. Okamoto, N. Tanihara and Y. Kusuki, 'Olefin/paraffin separation performance of asymmetric hollow fiber membrane of 6FDA/BPDA-DDBT copolyimide', *J. Membr. Sci.*, **212**, 13–27 (2003).
- [76] B. D. Freeman, 'Basis of permeability/selectivity trade-off relations in polymeric gas separation', *Macromolecules*, **32**, 375–380 (1999).
- [77] L. M. Robeson, C. D. Smith and M. Langsam, 'A group contribution approach to predict permeability and permselectivity of aromatic polymers', *J. Membr. Sci.*, **132**, 33–54 (1997).
- [78] J. Y. Park and D. R. Paul, 'Correlation and prediction of gas permeability in glassy polymer membrane materials via a modified free volume based group contribution method', *J. Membr. Sci.*, **125**, 23–39 (1997).
- [79] A. Saji, H. Noda, M. Ichikawa, N. Kuroda and M. Sakai, 'Technology for recovery treatment and recycling of CO₂, Kagaku Sochi', **37**, 79–82 (1995) (Japanese).
- [80] H. Suzuki, K. Tanaka, H. Kita, K. Okamoto, H. Hoshino, T. Yoshinaga and Y. Kusuki, 'Preparation of composite hollow fiber membranes of a poly(ethylene oxide)-containing polyimide and their CO₂/N₂ separation properties', *J. Membr. Sci.*, **146**, 31–37 (1998).
- [81] M. E. Rezac, P. H. Pfromm, L. M. Costello and W. J. Koros, 'Aging of thin polyimide-ceramic and polycarbonate-ceramic composite membranes', *Ind. Eng. Chem. Res.*, **32**, 1921–1926 (1993).
- [82] A. Nakamura and H. Makino, 'Application of aromatic polyimide membranes. I. Drying by vapor phase permeation process', *Maku*, **12**, 289–292 (1987) (in Japanese).
- [83] M. Kikuchi, A. Asano and K. Ninomiya, 'Dehumidification by polyimide membranes', *Kagaku Kougaku*, **53**, 51–53 (1989) (in Japanese).

The Impact of Physical Aging of Amorphous Glassy Polymers on Gas Separation Membranes

Peter H. Pfromm

11.1 Introduction

Amorphous glassy polymers are the basic materials for the separation of gases by membrane permeation [1]. Membrane gas separation capitalizes on differences in solubility and diffusivity of gases in the membrane material. The solubility and diffusivity of gases in polymeric glasses can be 'tuned' somewhat independently by changes in the molecular architecture and polymer chain arrangement [2,3]. This avenue of optimization has given rise to prolific research. The gas transport properties of an enormous number of glassy polymers have been investigated, and the literature in this regard continues to expand. The versatility of amorphous glassy polymers is shown by the fact that they encompass both very low gas permeabilities and the highest gas permeabilities currently known for all organic polymers [4,5]. However, the low range of permeation rates is far more typical for amorphous glassy polymers.

Due to the generally low gas permeability of glassy polymers, any attempt to use them as practical membranes for gas separations involves the production of very thin films. The thickness of the selective layer is often of the order of less than one micrometer. For mechanical strength, the selective layer can be an integral part of an asymmetric polymer structure, or it can be applied to porous or highly permeable substrates. To achieve

an economically viable process, relatively large areas on the order of square meters, and often up to hundreds or thousands of square meters of these membranes must be produced substantially without defects on the size scale of the gas molecules to be separated.

Physical aging (or structural relaxation) is a fundamental phenomenon of glassy polymers related to their non-equilibrium state and affecting many properties of glassy materials. The literature on aging of glassy polymers is vast, and no attempt is made here to summarize this field. The fundamentals of this process are described, e.g. in the monograph by Struik [6] (see also Tant and Hill [7] and Hodge [8]). We will here limit our interest mainly to physical aging of amorphous glassy polymers in form of the thin films generally desirable in gas separations using membranes. The main emphasis will be made on the properties pertaining to membrane gas separation, such as permeability, diffusivity and solubility, as well as density and free volume. As it has been recognized that the rate of the aging process strongly depends on film thickness, we will consider briefly the differences in properties of the polymer 'bulk' state (often referred to in membrane science as dense or thick films) and thin films, which can exist in confined form, as free standing films or, most important for membrane applications, thin selective layers on a solid support and contacting a gas phase on the

opposite side. Since a significant body of experimental evidence has been accumulated indicating that polymer properties in thin films and in the bulk are quite different, those who are interested in the aging of thin polymer films must pay attention to the dependence of various physical properties of polymer films on their thickness, a subject now well documented in the literature. No summary of general principles of gas permeation behavior will be given here, because this subject is dealt with in other chapters of this volume.

11.2 Scope

Amorphous glassy organic polymers deep in the temperature range of these glassy state, that is, much lower than their glass transition temperature T_g are the subject of our interest. The thermodynamic system of interest here is the polymer. Physical aging of glassy polymers will be defined here as the change of a chosen property with time in the absence of chemical changes of the polymer, and in the absence of highly sorbing materials, e.g. carbon dioxide or hydrocarbons. Helium or nitrogen are examples, on the other hand, of weakly sorbing gases. Hence, we are interested here in time changes of 'pure' polymer properties and not phenomena like removal of solvents, plasticizers etc. from the polymer, or its surface fouling, which may occur in practical membrane gas separation processes. Penetrant-induced effects such as, for example, lingering property changes of a membrane after a brief exposure to a highly sorbing penetrant are briefly discussed below in regard to thin polymer films compared to thick samples.

The thickness of a glassy polymer layer that is responsible for the gas separation characteristics of a membrane is the issue here. We will define, maybe tentatively, 'thin films' as those having a thickness below one micrometer (1 μm), and preferably in the range of a fraction of a micrometer. In some cases, properties of films as thin as 300 \AA have been studied and will be discussed later. Free standing films are at the center of our interest, since interactions with a support may convolute the aging behavior of the polymer. Samples with a minimum thickness of several micrometers and above will be termed a 'thick film' or 'bulk material'. Given the range of interest for the thickness defined above, it becomes immediately

clear that it is a challenge to determine property changes of thin films with time.

11.3 Observations on Integral-Asymmetric Membranes

Evidence for the possibility of thickness-dependent aging of amorphous glassy polymers in gas separation membranes was found by observing the gas selectivities of integral-asymmetric membranes made from glassy polymers [9]. It could be assumed intuitively, and had been confirmed in numerous studies of gas separation membranes, that very selective thin separating layers of integral-asymmetric membranes would be expected to possibly always have defects or pinholes, thus allowing non-selective gas transport and thereby showing *lower* selectivities than thick films. The ideal gas selectivities, taken as the ratio of the normalized single-gas fluxes of membranes with very thin active separating layers between several hundred and thousand \AA , in some cases were shown to exceed the selectivities of bulk (thick) films with many micrometers thickness made from the same polymer [9,10,11]. Activation energies of gas permeation were found to be larger for thin-skinned integral-asymmetric membranes than for bulk films from the same polymer. Some decrease of the gas permeability of the integral-asymmetric membranes with time was also found [12], while the highly sorbing gas CO_2 showed increased permeability with time [9].

Results comparing aging of thin-skinned integral-asymmetric hollow fibers and thick films made from a polyimide copolymer were reported recently [13]. For thick dense films, the authors report significant permeability reductions and selectivity increases for gases such as hydrogen and nitrogen over 9 months and 2.5 years. Thick films were cast from solution in *n*-methyl pyrrolidone (NMP), dried at 523 K for 24 h and under vacuum at 543 K for 3 h. Slow removal of some residual solvent due to the relatively high boiling point of NMP may have been responsible for an initial drop in permeability. The authors conclude that diffusivity changes are mainly responsible for the drop in gas permeability. Integral-asymmetric hollow fibers from the same polymer with 1000–1500 \AA skin thickness, as measured by SEM, showed H_2/N_2 selectivities that exceeded those of all thick films, aged or not.

This confirms the observations discussed above [9] that thin-skinned membranes from glassy polymers can clearly exceed the ideal gas selectivities of thick isotropic films from the same material.

Arguments can be made that data from integral-asymmetric membranes may be convoluted by changes in the membrane substructure. This issue does not exist with porous ceramic membranes supporting a selective glassy polymer layer. However, accelerated aging of thin films is still observed [14]. Aging in glassy polymer layers on porous ceramic substrates does persist; however, most of the gas flux decline and selectivity increase seems to take place in the first few weeks [15].

These types of observations are not easily explained since the likelihood of defects is much larger in thin membranes than in thick isotropic films. However, it is quite challenging to investigate the properties of just the skin layers of supported membranes. Therefore, a motivation for comparative studies of unsupported thin and thick films of glassy polymers under well-controlled conditions was given. The results and conclusions of these studies require in-depth consideration of aging phenomena of glassy polymers and are discussed below.

The following discussion can be summarized, i.e., physical aging deep in the glassy state of polymers proceeds very rapidly in thin films compared to thick films. Some assumptions are made regarding the molecular mechanism of aging; however, the situation is not completely clear at present. However, film thickness effects on the glass transition temperature and other physical properties of polymers are currently being investigated [16–22]. Since physical aging is related to polymer chain mobility, some interesting views of aging deep in the glassy state might emerge from the current interest in thickness dependent near- T_g events.

11.4 Physical Aging of Glassy Polymers

11.4.1 The Experimental Challenge Posed by Glassy Polymers

A significant complication to any kind of experimental and theoretical work is introduced with glassy materials, since their properties are generally history-dependent. It is not sufficient to sim-

ply state how a sample to be tested was made. One needs to know when this was done (relative to testing) and how the sample was treated from manufacture until measurement. If this information is not taken in account, then reproducibility may be elusive. Although many methods of characterization could be used to try to determine if polymer samples with unknown histories are identical, there will always be lingering doubt if there was not a small or undetected difference. It seems best to keep track of the sample history rather than attempting to characterize a sample of undefined history with absolute certainty.

Another experimental challenge is the presence of residual solvents and other penetrants. The use of mechanical vacuum pumps only allows removal of solvents from polymer films to a finite vapor pressure. Using a purge gas is superior because the partial pressure of the solvent to be removed can be lowered to zero, resulting in most complete removal of small molecules that could convolute observations of physical aging in the film.

In summary, samples should be as well characterized as possible, and their histories must be known. Solvent removal above T_g using a purge gas should be done if at all possible. The time when the polymer sample passes through T_g is a convenient reference time for aging studies.

11.4.2 The Glassy State in Amorphous Polymers

If a polymer is cooled at a finite rate from the rubbery state, a virtual step change is observed in its specific heat capacity [23], and its coefficient of thermal expansion [24]. Both properties are second derivatives of the free energy. The temperature of the step change is the glass transition temperature T_g .

Often a schematic plot of the specific volume as a function of the temperature for a glass-forming polymer is used. This plot shows a change in slope. The intersection of the two slopes of the volume/temperature relationship is often defined as T_g [25]. A non-crystalline material at a temperature below this transition is said to be in the glassy state. The T_g is assigned to the intersection of the two slopes, although there is not a sharp transition point but rather a temperature interval [26].

The energy and volume changes of a glass with temperature are more similar to a crystalline

solid, while its lack of long-range order on a molecular scale seems more related to the liquid state [26].

At T_g , the time scale for molecular rearrangement approaches the time scale of the experiment (for example, the cooling rate). The mobility of the macromolecules decreases to a point where they are not able to reach their equilibrium conformations in the time frame of cooling [25]. Increased cooling speeds therefore lead to increased T_g s.

It is often said that long-range chain motions involving several tens of backbone carbon atoms are 'effectively frozen' below T_g . The well-documented change of properties of glassy polymers by aging shows, however, that molecular rearrangement is still possible. Thermal and thermomechanical methods have been used to investigate aging of bulk polymer samples deep in the glassy state [27].

Theories for the glass transition fall into two broad categories: thermodynamic [28] and kinetic or free volume theories [29,30]. It is clear, independent of the theoretical explanation of the glass transition, that glassy materials are not in equilibrium [31], since many of their properties change with time [6].

Below the T_g of a glassy polymer, other more subtle transitions are often observed [32,33]. However, the molecular reasons for specific sub- T_g transitions are often not entirely clear [33].

11.4.3 Aging Mechanisms and Models

Physical aging of a glassy polymer is the gradual approach to thermodynamic equilibrium. It is accompanied by a change of many properties with time. For example, physical aging at a constant temperature leads to increased stiffness, brittleness and volume contraction with time. An excellent review of physical aging and its influence on polymer properties is available. All of these phenomena are considered in detail in the treatise by Struik [6].

Aging is a basic feature of the glassy state and is generally found in all low-molecular-mass and polymeric glasses, whether organic or inorganic in nature. Purely thermodynamic treatments of the glassy state have not been successful in describing aging [25]. Most often, some form of a free volume theory is used. The basic idea is that the mobility of the polymer chains is related

to the packing of the chains, e.g., [30,34,35]. Some of the theories attempting quantitative descriptions of polymer aging are reviewed below.

The volume change of glassy polymer samples with time has been studied in a classic paper by Kovacs [24]. Subsequently, a model was developed based on the deviation of the actual specific volume v from its equilibrium value v_∞ (see a review in Greiner and Schwarzl [36]). A parameter that measures the deviation of the fractional free volume from its equilibrium value is introduced:

$$\delta = (v - v_\infty)/v_\infty \quad (11.1)$$

and δ is then related to a fixed number of N ordering parameters n_i and to N retardation times τ_i by N differential equations. The retardation times τ_i are the characteristic times for molecular rearrangement. The differential equations for each change of the system can then be written as:

$$-d\delta_i/dt = \Delta\alpha_i(dT/dt) + \delta_i/\tau_i, \quad i = 1 \dots N \quad (11.2)$$

with $\Delta\alpha_i$ being the contribution of the i th ordering parameter to the difference of the coefficients of thermal expansion in the rubbery and glassy state, (dT/dt) the experimental heating rate and the total deviation from equilibrium defined by:

$$\delta = \sum \delta_i \quad (11.3)$$

No direct physical meaning is attached to the ordering parameters or the retardation times. An influence of the thickness of a sample is not included. The theory of Kovacs has recently been critically evaluated in the light of new experimental evidence for the customary thick samples. It was found [37] that volume recovery seems to be more severe when a higher excess free volume is initially trapped in the polymer. The authors conclude that there is an influence of the δ_{i-1} on the δ_i . This demonstrates that the complete picture of the glassy state is still evolving.

Hirai and Eyring [38] considered an equilibrium between holes (defects) in the polymer and phonons (elastic waves) that can convert into each other similar to the kinetics of a chemical

reaction. Such a theory fails to reproduce some experimental observations. Sample geometry is not included in this theory.

An apparently more successful phenomenological model is the diffusion model for the volume recovery of glasses [39]. A single diffusion coefficient for holes that depends on the amount of free volume available according to the Doolittle equation [40] is introduced. A single ordering parameter and a single relaxation mechanism are assumed. It is concluded by the authors that if the macroscopic dimension of the sample were the length scale for hole diffusion, unrealistically large hole diffusion coefficients would result. For a 1 cm thick sample, a diffusion coefficient of 10^{-4} cm²/s would result from this assumption whereas if the length scale is 10^{-5} cm, a diffusion coefficient should be much smaller, 10^{-14} cm²/s. The thickness of interest for gas separation membranes is namely of the latter order and so the theory by Curro *et al.* [39] implies that the hole elimination would indeed be influenced by the external dimensions of the sample. For thin samples, the internal and external length scales apparently overlap. A quite important concept that later was used by other researchers is that both a network contraction (a bulk effect) and local diffusion of free volume to the sample surface contribute to aging.

Other models using the assumption of diffusion of free volume packets have been presented [41]. A dependence of free volume elimination on the size and shape of the sample is stated, but there is no experimental evidence given.

Hence, a clear and unambiguous picture of aging phenomena in glassy polymers has not yet emerged. This may be partly due to the protracted and tedious experiments necessary to investigate aging. Many aspects are involved in aging phenomena. The interactions between polymer chains, the free volume and geometrical constraints on the motion of polymer molecules in a solid are only some of them.

11.5 The Thickness-dependence of Aging in Glassy Polymers

11.5.1 Influence of the Thickness on T_g , Density, and Free Volume

The main focus here is the physical aging of glassy polymer films far below T_g . However, a

common feature of thin film physical aging deep in the glassy state and unusual phenomena near T_g in thin films is the mobility of the polymer chains. Therefore, the influence of film thickness on T_g will be discussed here.

Properties of thin films differ drastically from those of a bulk material. It is also essential in what form films exist. In the vicinity of a solid support, e.g. the porous support of composite membranes, chain mobility in thin polymer films is on average reduced. This can be revealed in an increase of the T_g s. Opposite effects can take place near a 'free' film surface that contacts a gas phase or vacuum, or a solid that has little affinity to the polymer chains. An interplay between these two competing effects can determine the prevailing properties observed experimentally.

A substantial decrease in T_g can affect strongly the aging phenomena in films with different thicknesses. Indeed, if the T_g of a thin glassy film is reduced substantially, then aging of this film at ambient temperature can be thermodynamically very similar to (and kinetically as fast as) sub- T_g annealing of the bulk phase of this polymer. So, local properties of thin films like chain mobility, T_g , density and free volume should affect strongly the aging behavior of membranes.

Keddie *et al.* [16] showed that the thin polystyrene (PS) films coated over the (111) surface of a silicon crystal revealed decreasing T_g when film thickness decreased in the range 1000–100 Å. The maximum reduction of T_g was as much as 30 K for the thinnest film. To explain these observations, it was suggested that at the surface of the glassy film there exists a liquid-like layer with enhanced chain mobility. A much larger reduction of T_g , however, was observed [17] for *free standing* PS films: for a thickness of about 300 Å, T_g was as low as 250 K (a reduction by 100 K)! This indicates that these thin PS films are virtually in the equilibrium state at room temperature. All this points towards fast aging of thinner polymeric films.

Another factor that can influence the rate of aging is the density and the related free volume. Enhanced mobility of polymer chains in the vicinity of a 'free' polymer surface should promote formation of more equilibrated, that is, more densely packed layers. Hence, in the vicinity of a free surface, free volume and diffusivity should be

reduced. The effects of the thickness on density have been experimentally observed for many polymers. First, Rozenberg *et al.* [42] reported a significant increase in the density of supported films of various, mainly barrier materials (poly (methyl methacrylate), epoxy resins, etc.), when the film thickness decreased in the range of 100–200 μm . Later, the same effect was confirmed for free standing films of polymers with much higher permeability – poly(vinyltrimethyl silane) and poly(trimethylsilyl norbornene) [43]. It was also shown that as the film thickness and fractional free volume calculated using the measured density decrease, the diffusion coefficients of various gases are reduced significantly.

11.5.2 A Phenomenological Model for Thickness-Dependent Aging

A phenomenological model of aging of thin glassy polymer films has been presented [44]. The basis of the model is the classical description of aging in glassy polymers by Kovacs [45]. Through introduction of a thickness-dependent T_g (see Forrest *et al.* [17]), it was found that after solving the resulting differential equations a qualitative match was obtained with experimental thin and thick film aging data. Particularly, the reduction of gas permeability with time that is experimentally observed in thin films, but not in thick films, was reproduced by the model. It is rewarding to see that a classical model of glassy polymer aging can be adapted using new experimental evidence to reproduce a physical behavior that was not well-known when the basic model was developed.

11.5.3 Influence of the Thickness on Time-dependent Properties of Thin Polymer Films far below the T_g

It has been pointed out above that some observations on the gas selectivity and activation energy of permeation for thin-skinned integral-asymmetric gas separation membranes were found to be counter-intuitive since selectivities in thin membranes were higher than in thick films. To decouple the suspected aging phenomena in the thin skin from possible changes in the substructure of integral-asymmetric membranes and from traces of solvents, a study was undertaken on thin free glassy polymer films pro-

duced and then heat-treated without a substrate [12,46]. Samples were carefully heat-treated to remove solvents and obtain a defined starting point for aging by passing into the glassy state at a known time. Subsequent work on properties of thin films far below T_g with relevance to gas separation using membranes is also reviewed below.

It is important to show thickness-dependent aging of glassy polymer films not only by monitoring gas transport properties. Independent confirmation by other methods is a powerful argument that the observed accelerated aging of thin free polymer films is an actual physical phenomenon. Therefore, densities and *x*-ray crystallography results are also reported.

The thin, intermediate and thick films under investigation were generally about 0.5, 2.5 and 25 μm thick, respectively.

11.5.3.1 Gas Permeability and Selectivity

The differences in aging behavior, as tracked by He, N₂, and O₂ permeability, for a polyimide (6FDA–IPDA) and polysulfone films with standardized history were found to be striking [12,46]. The films were solvent-cast and all solvent was removed by heating above T_g in a purge gas stream. For example, the ideal He/N₂ selectivities of thin polyimide films (5000 Å) increased to almost 70 in the first 4000 h of aging at 35 °C, while thick films remained at about 45. For polysulfone, the thick film selectivity was just below 50, while thin films during aging reached about 77 in 1400 h. Permeability measurements with gas pressure as the parameter showed a much decreased dependence of the permeability on gas pressure for thin films. This supports the argument of accelerated densification by aging of thin films since non-equilibrium free volume is mainly responsible for decreasing N₂ permeability with increasing pressure. Aging removes non-equilibrium free volume and if thin films age more rapidly, then the pressure dependence of permeation should decrease. This was experimentally confirmed [46].

McCaig and Paul [47] later compared aging for thick and thin (2.5–3.3 μm) films made from a polyacrylate based on bisphenol-A-benzophenone dicarboxylic acid. In careful experiments including reversing aging by heating above T_g , they concluded that two distinct aging

mechanisms seemed to be at work: one mechanism that is thickness-dependent and one that is not. The thickness-dependent mechanism was assumed to be free volume diffusion to the surface where the free volume is eliminated. Another mechanism implies uniform densification that proceeds equally in the bulk and in the vicinity of the surface. Hence, this component is thickness-independent. It can be noted that the concept of this work is similar to the ideas advanced by Curro *et al.* [39] and Rozenberg *et al.* [42]. However, the work by McCaig and Paul [47] gave a conclusive corroboration of these concepts.

Recently, similar ideas on chain mobility mechanisms that are significant in thin films at T_g but that are not observed in thick films were put forward by de Gennes [18].

11.5.3.2 Macroscopic Density

Figure 11.1 shows the density of standard thick and thin polyimide samples of different ages as a function of residence time in a density gradient column. The thick samples settle quickly. The two thin samples were brought to their initial positions by submersing the samples in the column. The 9 day 'old' sample was in this way moved to a density that was higher than the apparent sample density, and the sample therefore retreated to a lower density. The 220 day 'old' thin sample appeared steady at its location in the column. These results suggest a time-dependent

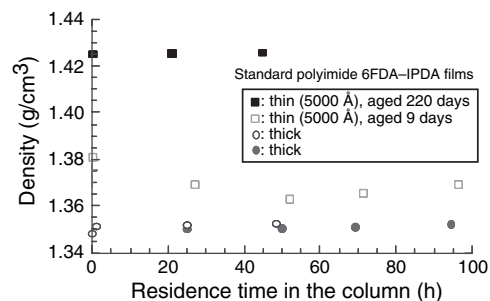


Figure 11.1 Settling of thick- and intermediate-thickness polyimide films in the density gradient column (26°C) [46]. Reproduced by permission of P. H. Pfromm from 'Gas transport properties and aging of thin and thick films made from amorphous glassy polymers', *PhD Dissertation*, The University of Texas at Austin, Austin, TX, USA (1994)

density of the thin polyimide films, although the absolute values may be skewed by effects of the density gradient on samples with large specific surface area.

The results obtained in a gradient column were confirmed by tests of flotation in a series of solutions of known densities [46]. Hence, in agreement with the results by Rozenberg *et al.* [42] and Shishatskii *et al.* [43] thin films have systematically higher densities than thick films of the same polymer. Aging tends to increase the density more rapidly in thin films.

Pressure-Volume-Temperature (PVT) data for polysulfone are available [48]. A hypothetical rubber (equilibrium) density of 1.2936 g/cm³ can be calculated for polysulfone by using the PVT data. This can be used to check results that were obtained for the time-dependent density of thin polysulfone films by submersion in a series of aqueous calcium nitrate solutions, checking if the samples sunk or floated [46]. This avoids density gradient effects. The density of a thin polysulfone film aged for 236 days was between 1.268 and 1.252 g/cm³, while the density of bulk polysulfone was 1.240 g/cm³. It can be seen that the thin film density is increasing towards the equilibrium value predicted by PVT data.

Thus, density determinations showed that accelerated aging and densification does take place in the thin films, and that densities larger than those in thick films, but below the hypothetical equilibrium density, are reached. This is consistent with the results from permeation experiments.

11.5.3.3 Wide-Angle X-Ray Diffraction (WAXD) Patterns

To obtain a sufficient amount of material exposed to the X-ray beam, the intermediate thickness films and the thin films were sandwiched before scanning. The total thickness of these sandwiched samples was at least 2.5 μm for the thin films and 5 μm for the intermediate films. Thick films were about 25.4 μm thick.

Figure 11.2 shows scans for thick, intermediate and thin polysulfone films [46]. Two aging times for each film are shown. The magnitude of the number of counts (y-axis) was 1000 for the thick films and 400–500 for the thin and intermediate thickness films.

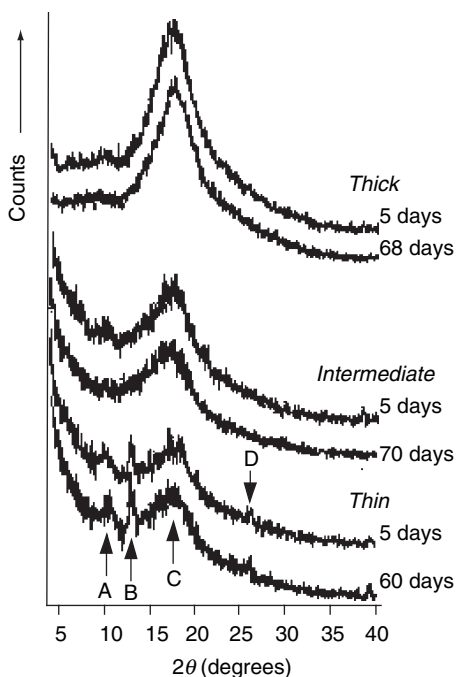


Figure 11.2 Wide-angle X-ray scans for thick ($\sim 25.4 \mu\text{m}$), intermediate ($2.54 \mu\text{m}$) and thin ($0.5 \mu\text{m}$) standard polysulfone films. Reproduced by permission of P. H. Pfromm from 'Gas transport properties and aging of thin and thick films made from amorphous glassy polymers', *PhD Dissertation*, The University of Texas at Austin, Austin, TX, USA (1994)

The magnitude of the signal for thin and intermediate films is lower than for the thick films, likely due to the lower amount of scattering material present in the beam. It can be seen that the thick and the intermediate films do not change significantly with age. The thin films show distinctly different features from the thick and intermediate films.

The main peak (C) is located approximately where the main peak of intermediate and thick films can be seen. There is, however, a rather pronounced peak (B) located at about $12.8\text{--}12.9^\circ$ (2θ) for the thin films. This peak appears to be virtually absent in thick and intermediate films.

A second peak (A) is located at about $9.9\text{--}10.6^\circ$ (2θ). This peak is less pronounced in the intermediate thickness film and even less visible in the thick films. A third small peak (D) is found at 25.9° (2θ). This peak is absent in the intermediate and thick films. An apparent feature at $39\text{--}40^\circ$ (2θ) is most likely an artifact caused by the material of the supporting frame entering

the beam. A time-dependence of the features in these spectra is detectable only in the thin films. The peak B narrows and increases with aging; the peak A behaves similarly. The additional peaks (A, B and D) found for the thin films point towards additional ordering of the polymer chains in these films. The time-dependence appears to be unique to the thin films. Accelerated aging and elimination of excess free volume from the thin films would possibly necessitate increased ordering on a local scale giving rise to features in WAXD spectra. Only the thin films appear to be aging in a way that is detectable by WAXD.

11.5.3.4 Activation Energy of Permeation

The activation energies of permeation (E_p) for N_2 , O_2 and He were determined for thick, intermediate and thin films of the polyimide 6FDA-IPDA [46]. Figure 11.3 shows that the two thin films have similar activation energies. The air-dried film was 'older' than the standard dried thin film, yet it did not exceed the E_p values for the standard dried film.

The intermediate thickness film and both the standard dried and slow quenched thick films show similar activation energies. Different aging times or thickness differences of a factor of about 10, down to $2.54 \mu\text{m}$, apparently do not change the activation energy of permeation significantly. These results agree with the similar gas selectivities and permeabilities determined for thick and intermediate films.

The comparison between the thin films, on the one hand, and the intermediate and thick films, on the other hand, shows clearly increased E_p values for the thin films. This result agrees with the increased gas selectivities and decreased gas permeabilities that were found for the thin films. An accelerated densification of the polymeric matrix of the thin films by physical aging appears to be a possible explanation. The thick and intermediate thickness films do not reach this level of densification, nor do they show the strongly time-dependent permeation behavior of the thin films.

Using the maximum difference in E_p (for N_2) between aged thin and thick films, the increase in the cohesive energy density (CED) can be estimated, that would be needed to cause this increase in E_p . This estimation is based on Meares' work [49]. The assumption that the increase in E_p is mainly due to an

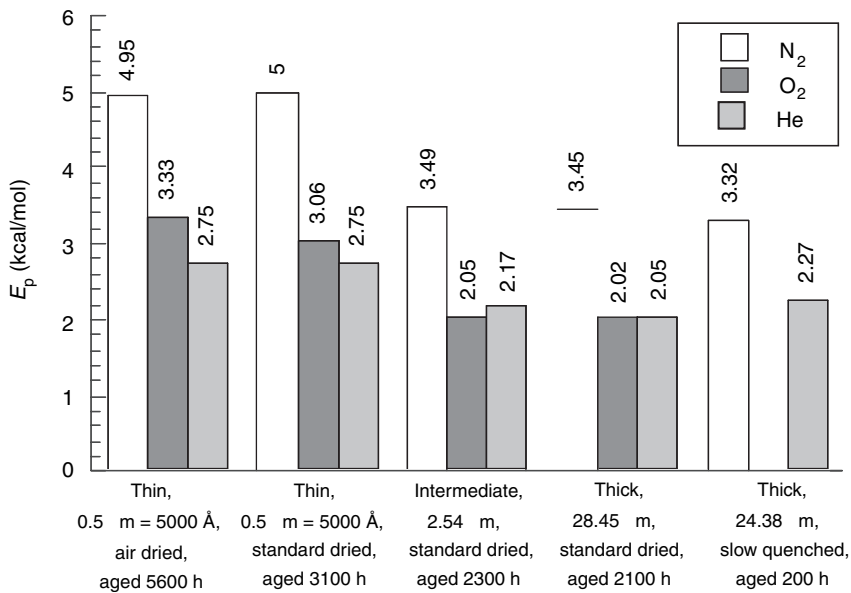


Figure 11.3 Activation energies of permeation for two thin, one intermediate and two thick films from the 6FDA-IPDA polyimide (150 psi, 20–50 °C). Reproduced by permission of P. H. Pfromm from ‘Gas transport properties and aging of thin and thick films made from amorphous glassy polymers’, *PhD Dissertation*, The University of Texas at Austin, Austin, TX, USA (1994)

crease in the activation energy of diffusion, E_D , is made and the result shall only be used as a plausibility check of the E_p data. This estimation yields:

$$\Delta CED_{\text{thin/thick}} \approx E_{p,\text{thin}} - E_{p,\text{thick}} = 1.68 \text{ kcal/mol} \quad (11.4)$$

Using a bulk density for the 6FDA-IPDA polyimide of 1.352 g/cm³ and a molecular weight per repeat unit of 634 g/mol, a value of 14.99 J/cm³ is found for $\Delta CED_{\text{thin/thick}}$. Values for the CEDs of polymers are in the range of several hundred J/cm³ [50]. Such a change in CED by densification does not seem unreasonable. The results for the activation energies of permeation of polysulfone give a similar picture as for the polyimide.

11.5.3.5 Exposure of Thin and Thick Films to a Highly Sorbing Penetrant

The dual-mode behavior of glassy polymers generally causes the permeability to decrease with increasing pressure. Pressure-dependent N₂ permeability data for polyimide films is shown in

Figure 11.4 [46]. The characteristic decrease of the permeability with pressure is less apparent for the thin polyimide film. This is evidence that the thin film may have progressed further towards the densified equilibrium state of the polymer than the thick film, and that Langmuir sites may have been eliminated from the thin film.

Figure 11.5 shows the pressure-dependent CO₂ permeabilities for thick, intermediate and thin polyimide films. The pressure-dependence of the thin film is strongly reduced. The thick film aged more than twice as long as the thin film, yet it still shows a clear decrease of CO₂ permeability with time, indicating the non-equilibrium nature of a glassy polymer due to significant presence of Langmuir sites. The curve shape and absolute values of the intermediate thickness film are very close to the thick film. The thin film shows evidence of its much faster approach to the densified equilibrium state of the polymer.

Figure 11.6 shows the time-dependent CO₂ permeability at 200 psi, which is a continuation of the experiment in Figure 11.5. The permeability increase for the thin film exceeds that for the thick and intermediate films. This may be somewhat unexpected. If it is accepted that the thin

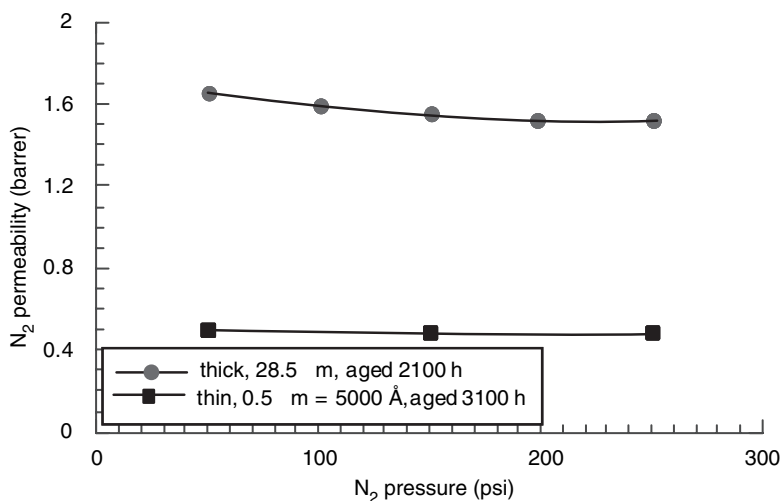


Figure 11.4 N₂ permeability as a function of pressure for a thin and a thick standard dried 6FDA-IPDA polyimide film (35 °C). Reproduced by permission of P. H. Pfromm from 'Gas transport properties and aging of thin and thick films made from amorphous glassy polymers', *PhD Dissertation*, The University of Texas at Austin, Austin, TX, USA (1994)

film is more densified and that free volume has been eliminated, it might be expected that the response to the CO₂ exposure should be less severe for the thin film, due to a potentially increased cohesive energy density. However, the increase in CO₂ permeability with time for the thin film, shown in Figure 11.6, necessitates some change in the polymer chain arrangement to increase either the solubility, diffusivity, or both, for CO₂

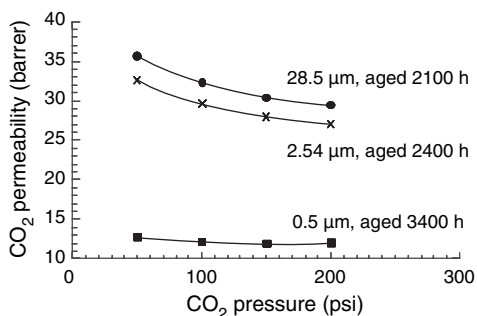


Figure 11.5 CO₂ permeability as a function of pressure for thick, intermediate and thin polyimide films (35 °C, 15 min 'wait time' at each pressure). Reproduced by permission of P. H. Pfromm from 'Gas transport properties and aging of thin and thick films made from amorphous glassy polymers', *PhD Dissertation*, The University of Texas at Austin, Austin, TX, USA (1994)

in the polymer. Such a rearrangement may be facilitated in a film where a large fraction of the polymer chains is directly exposed to the film surface and can therefore rearrange more freely.

Figure 11.7 shows the residual effect of the exposure to a CO₂ pressure of 13.8 atm on the permeability of N₂ at 13.8 atm. Initially, increased permeabilities are observed for all films. The permeabilities decline quickly, and only little time-dependence over the time scale of this experiment is observed after the first 20 h. The N₂ permeabilities return to the values that were measured before exposure to CO₂. No lasting changes by the CO₂ exposure at 13.8 atm are observed.

11.5.4 Special Case: Aging of Poly(trimethylsilyl propyne)

Poly(trimethylsilyl propyne) (PTMSP) is distinguished by many properties, which make this glassy polymer an interesting exception: extremely high gas permeability and diffusivity, very large free volume and unusually low density. They are discussed in more length in Chapter 8 of this volume.

A property, which in fact precluded practical applications of PTMSP as a membrane material, is its very fast aging. The rate of reduction of

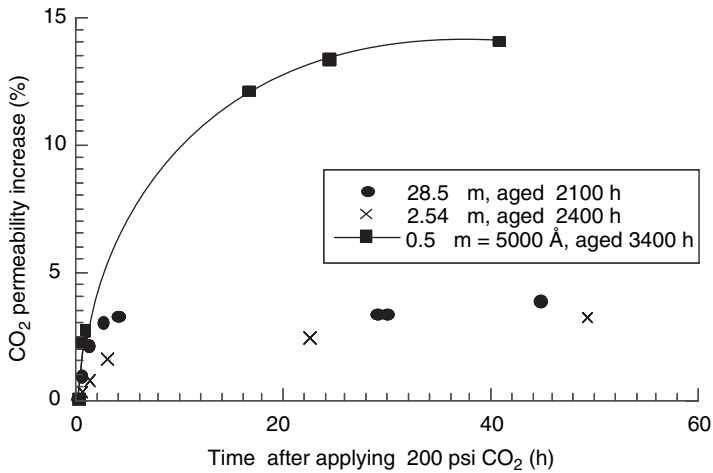


Figure 11.6 CO₂ permeability increase as a function of time for thick, intermediate and thin polyimide films (35 °C, 200 psi CO₂ (continued from Figure 11.5)): 0% = permeability after 15 min of 200 psi CO₂ applied. Reproduced by permission of P. H. Pfromm from 'Gas transport properties and aging of thin and thick films made from amorphous glassy polymers', *PhD Dissertation*, The University of Texas at Austin, Austin, TX, USA (1994)

permeability of this polymer, which is deeply in its glassy state ($T_g > 560$ K) at room temperature, are several orders of magnitude higher than those typical rates of aging of conventional glassy polymers. Thus, it was shown that the permeation rate of isobutane through PTMSP films decreases twofold during 10–20 days [51]. Even faster rates of aging were observed by Asakawa *et al.* [52].

The aging process is strongly accelerated by heating [53]. A storage of PTMSP samples for several years resulted in a decrease in permeability by two orders of magnitude, accompanied by some increases in permselectivity [54]. Aging in contact with individual light gases (H₂) proceeds faster than in conditions when a mixture of light (H₂) and condensable (C₄H₁₀) gases permeates through the film [55]. The

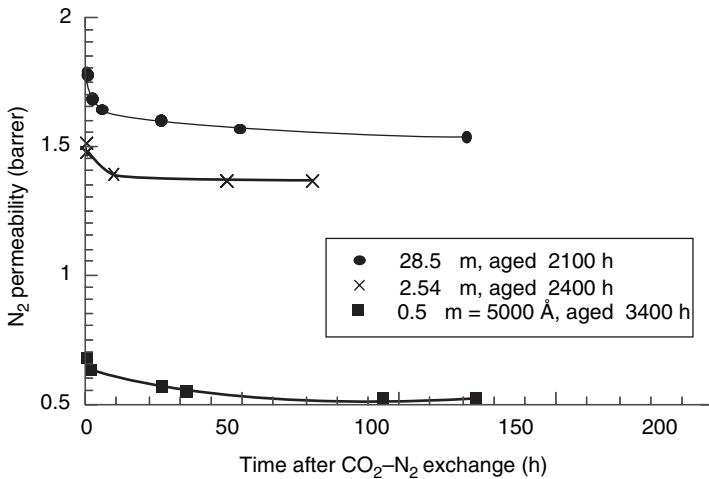


Figure 11.7 N₂ permeability as a function of time after exchange of CO₂ for N₂ for thick, intermediate and thin polyimide films (35 °C, 200 psi). Reproduced by permission of P. H. Pfromm from 'Gas transport properties and aging of thin and thick films made from amorphous glassy polymers', *PhD Dissertation*, The University of Texas at Austin, Austin, TX, USA (1994)

rate of aging is much faster for thin films (1 and 3 μm) than for thick films (85 μm) [44].

A decline in gas permeability of PTMSP is accompanied by changes of many physical properties of the polymer. The density shows spectacular increases while aging from 0.70–0.75 g/cm^3 , characteristic for freshly cast films, to 0.95–1.05 g/cm^3 for aged material [53,54,56]. A reduction of free volume as measured by positron annihilation lifetime spectroscopy was also reported [54,56,57]. Aging leads also to more restricted chain movements as measured by spin-lattice relaxation times (NMR) [58] and to decrease in interchain spacing (WAXD data) [54].

Although all of these observations do not contradict to interpreting aging of PTMSP as a simple structural relaxation process, there is much evidence that in this case the process is complicated by other phenomena: absorption of impurities that can block free volume and thus reduce the permeation rate and chemical (oxidative) degradation of PTMSP [54,56,57,59]. Apparently, these three mechanisms of aging (relaxation, absorption of impurities and oxidative degradation) operative in the PTMSP films can explain the unusually fast reduction of permeability of this polymer.

11.6 Implications of Thickness-dependent Aging for Practical Membrane Gas Separations

The discussions above indicate that the performance of practical gas separation membranes with selective layers that are made from glassy polymers is time-dependent. It should not be surprising that a gas separation module loses a significant amount of productivity while gaining some selectivity during the first months of operation. This can be expected, even in complete absence of membrane fouling or presence of contaminants in the feed, simply by physical aging.

The response to process excursions such as exposure to sorbing penetrants is expected to be different for gas separation membranes compared to thick films from the same material. The thin films used in membrane gas separation with glassy polymers are more prone to quick increases in permeability compared to thick films when exposed to CO_2 , for example. However, these effects do subside quickly when the CO_2 is removed.

The sample history should always be taken in account when thin films and high-performance

membranes are the subject of research and development. Re-testing after some time has elapsed will likely show different results for thin films, while thick samples may remain unchanged. When comparing thick and thin films, it is of great importance to make the thermal history as comparable as possible by tracking the history after passing through T_g . Careful removal of solvents and other contaminants is essential.

System design for gas separation processes should rely on data obtained with membranes that have aged sufficiently (order of weeks) if glassy membrane materials are used. The same is true for determination of the effects of process excursions.

11.7 Concluding Remarks

Although experimentation with thin glassy polymer films is challenging, it cannot be replaced by testing bulk polymer properties. At this time, we have no a priori method to extrapolate from the gas transport behavior of a thick glassy polymer film to the behavior of a thin film or thin-skinned membrane. The differences in gas selectivities and permeabilities can be quite significant and the time-dependent behavior can be surprising.

The behavior of thin glassy polymer films is not only interesting for gas separation membranes but for many other areas of technology, such as microelectronics, optics and coatings. It seems likely that near T_g , phenomena in thin glassy films will spark more discussion and that the rationalization of thin film aging deep in the glassy state may benefit from this interest.

References

- [1] R. W. Baker, 'Future directions of membrane gas separation technology', *Industrial & Engineering Chemistry Research*, **41**, 1393–1411 (2002).
- [2] R. T. Chern, W. J. Koros, H. B. Hopfenberg and V. T. Stannett, *Material Selection for Membrane-Based Gas Separations*, ACS Symposium Series 269, American Chemical Society, Washington, DC, USA (1985).
- [3] Yu. P. Yampol'skii and V. P. Shantarovich, 'Chemical structure and free volume of polymers in prediction of their membrane properties', *Vysokomolekulyarnye Soedineniya, Seriya A i Seriya B*, **43**, 2329–2349 (2001).
- [4] T. Masuda, E. Isobe, T. Higashimura and K. Takada, 'Poly[1-(trimethylsilyl)-1-propyne]: a new high

- polymer synthesized with transition-metal catalysts and characterized by extremely high gas permeability', *Journal of the American Chemical Society*, **105**, 7473–7474 (1983).
- [5] H. J. Bixler and O. J. Sweeting, 'Barrier properties of polymer films', in *The Science and Technology of Polymer Films*, Vol. 2, O. J. Sweeting (Ed.), John Wiley and Sons, Inc. New York, NY, USA, pp. 1–130 (1971).
- [6] L. C. E. Struik, *Physical Aging in Amorphous Polymers and Other Materials*, Elsevier, New York, NY, USA (1978).
- [7] M. R. Tant and A. J. Hill, *Structure and Properties of Glassy Polymers*, ACS Symposium Series 710, American Chemical Society, Washington, DC, USA (1998).
- [8] I. M. Hodge, 'Physical aging in polymer glasses', *Science*, **67**, 1945–1947 (1955).
- [9] P. H. Pfromm, I. Pinnau and W. J. Koros, 'Gas transport through integral–asymmetric membranes: a comparison to isotropic film properties', *Journal of Applied Polymer Science*, **48**, 2161–2171 (1993).
- [10] Yu. P. Yampolskii, 'Permeation and sorption of hydrocarbons in poly(vinyltrimethyl silane)', in *Synthetic Polymeric Membranes*, B. Sedlacek and J. Kahovec (Eds), W. De Gruyter, Berlin, Germany, pp. 327 (1987).
- [11] M. Niwa, H. Kawakami, S. Nagaoka, T. Kanamori and T. Shinbo, 'Fabrication of an asymmetric polyimide hollow fiber with a defect-free surface skin layer', *Journal of Membrane Science*, **171**, 253–261 (2000).
- [12] P. H. Pfromm and W. J. Koros, 'Accelerated aging of thin glassy polymer films', *Polymer*, **36**, 2379–2387 (1995).
- [13] M. Yoshino, S. Nakamura, H. Kita, K. Okamoto, N. Tanihara and Y. Kusuki, 'Olefin/paraffin separation performance of asymmetric hollow fibre membrane of 6FDA/BPDA–DDBT copolyimide', *Journal of Membrane Science*, **212**, 13–27 (2003).
- [14] M. E. Rezac, P. H. Pfromm, L. M. Costello and W. J. Koros, 'Aging of thin polyimide–ceramic and polycarbonate–ceramic composite membranes', *Industrial & Engineering Chemistry Research*, **32**, 1921–1926 (1994).
- [15] M. E. Rezac, 'Update on the aging of a thin polycarbonate–ceramic composite membrane', *Industrial & Engineering Chemistry Research*, **34**, 3170–3172 (1995).
- [16] J. L. Keddie, R. A. L. Jones and R. A. Cory, 'Size-dependent depression of the glass transition temperature in polymer films', *Europhysics Letters*, **27**, 59–64 (1994).
- [17] J. A. Forrest, K. Dalnoki-Veress, J. R. Stevens and J. R. Dutcher, 'Effect of free surfaces on the glass transition temperature of thin polymer films', *Physics Review Letters*, **77**, 2002–2005 (1996).
- [18] P. G. de Gennes, 'Glass transitions in thin polymer films', *European Physical Journal E*, **2**, 201–205 (2000).
- [19] G. Reiter and P. G. de Gennes, 'Spin-cast, thin, glassy polymer films: highly metastable forms of matter', *European Physical Journal E*, **6**, 25–28 (2001).
- [20] G. Reiter, 'Dewetting as a probe of polymer mobility in thin films', *Macromolecules*, **27**, 3046–3052 (1994).
- [21] H.-C. Liou, P. S. Ho and R. Stierman, 'Thickness dependence of the anisotropy in thermal expansion of PMDA–ODA and BPDA–PDA thin films', *Thin Solid Films*, **339**, 68–73 (1999).
- [22] D. B. Hall and J. M. Torkelson, 'Small molecule probe diffusion in thin and ultrathin supported polymer films', *Macromolecules*, **31**, 8817–8825 (1998).
- [23] S. E. B. Petric, 'The effect of excess thermodynamic properties versus structure formation on the physical properties of glassy polymers', *Journal of Macromolecular Science Physics*, **B12**, 225–247 (1976).
- [24] A. J. Kovacs, 'La contraction isotherme du volume des polymères amorphes', *Journal of Polymer Science*, **30**, 131–147 (1958).
- [25] M. R. Tant and G. L. Wilkes, 'An overview of the nonequilibrium behavior of polymer glasses', *Polymer Engineering and Science*, **21**, 874–895 (1981).
- [26] W. Kauzmann, 'The nature of the glassy state and the behavior of liquids at low temperatures', *Chemical Reviews*, **43**, 219–256 (1948).
- [27] E. Muzeau, G. Vigier and R. Vassoille, 'Physical aging phenomena in an amorphous polymer at temperatures far below the glass transition', *Journal of Non-Crystalline Solids*, **172–174**, 575–579 (1994).
- [28] J. H. Gibbs and E. A. DiMarzio, 'Nature of the glass transition and the glassy state', *Journal of Chemical Physics*, **28**, 373–383 (1958).
- [29] T. Alfrey, G. Goldfinger and H. Mark, 'The apparent second-order transition point of polystyrene', *Journal of Applied Physics*, **14**, 700–705 (1943).
- [30] D. Turnbull and M. H. Cohen, 'Free-volume model of the amorphous phase: glass transition', *Journal of Chemical Physics*, **34**, 120–125 (1961).
- [31] F. Simon, 'Über den Zustand der unterkühlten Flüssigkeiten und Gläser', *Zeitschrift für Anorganische und Allgemeine Chemie*, **203**, 219–227 (1931).
- [32] R. F. Boyer, 'Dependence of mechanical properties on molecular motion in polymers', *Polymer Engineering and Science*, **8**, 161–185 (1968).
- [33] J. M. O'Reilly and F. E. Karasz, 'Specific heat studies of transition and relaxation behavior in polymers', *Journal of Polymer Science Part C*, **14**, 49–68 (1966).

- [34] C. Bailey, *Lucretius on the Nature of Things*, Clarendon Press, Oxford, UK (1921).
- [35] J. Frenkel, *Kinetic Theory of Liquids*, Clarendon Press, Oxford, UK (1946).
- [36] R. Greiner and F. R. Schwarzl, 'Volume relaxation and physical aging of amorphous polymers. I. Theory of volume relaxation after single temperature jumps', *Colloid and Polymer Science*, **267**, 39–47 (1989).
- [37] H. H. D. Lee and F. J. McGarry, 'Some previously unexpected phenomena of volume recovery', *Journal of Macromolecular Science Physics*, **30**, 185–200 (1991).
- [38] N. Hirai and H. Eyring, 'Bulk viscosity of polymeric systems', *Journal of Applied Physics*, **37**, 51–70 (1959).
- [39] J. G. Curro, R. R. Lagasse and R. Simha, 'Diffusion model for volume recovery in glasses', *Macromolecules*, **15**, 1621–1626 (1982).
- [40] A. K. Doolittle, 'Newtonian flow. II. The dependence of the viscosity of liquids on free space', *Journal of Applied Physics*, **22**, 1471–1475 (1951).
- [41] M. L. Mansfield, 'Volume relaxation in glasses', *Journal of Chemical Physics*, **94**, 7521–7525 (1991).
- [42] B. A. Rozenberg, V. I. Irzhak and L. M. Bogdanova, 'The role of diffusion of free volume at volume relaxation of amorphous polymers', *Progress in Colloid and Polymer Science*, **80**, 187–197 (1989).
- [43] S. M. Shishatskii, Yu. P. Yampolskii and K.-V. Peinemann, 'Effects of film thickness on density and gas permeation parameters of glassy polymers', *Journal of Membrane Science*, **112**, 275–285 (1996).
- [44] K. D. Dorkenoo and P. H. Pfromm, 'Experimental evidence and theoretical analysis of physical aging in thin and thick amorphous glassy polymer films', *Journal of Polymer Science, Part B: Polymer Physics*, **37**, 2239–2251 (1999).
- [45] A. J. Kovacs, 'Transition vitreuse dans les polymères amorphes. Etude phénoménologique', *Fortschritte der Hochpolymeren-Forschung*, **3**, 394–507 (1963).
- [46] P. H. Pfromm, *Gas Transport Properties and Aging of Thin and Thick Films made from Amorphous Glassy Polymers*, PhD Dissertation, The University of Texas at Austin, Austin, TX, USA (1994).
- [47] M. S. McCaig and D. R. Paul, 'Effect of film thickness on the changes in gas permeability of a glassy polyarylate due to physical aging, Part I. Experimental observations', *Polymer*, **41**, 629–637 (2000).
- [48] T. A. Callaghan, *Molecular Structural Design of Polymer Blends*, PhD Dissertation, The University of Texas at Austin, Austin, TX, USA (1992).
- [49] P. Meares, 'The diffusion of gases through polyvinyl acetate', *Journal of the American Chemical Society*, **76**, 3415–3422 (1954).
- [50] D. W. van Krevelen (Ed.), *Properties of Polymers: Their Correlation with Chemical Structure; Their Numerical Estimation and Prediction from Additive Group Contributions*, 3rd (Completely Revised) Ed., Elsevier, Amsterdam, The Netherlands (1997).
- [51] H. Shimomura, K. Nakanishi, H. Odani, and M. Kurata, 'Effects of physical aging on permeation of gases in a disubstituted polyacetylene', *Reports on Progress in Polymer Physics in Japan*, **30**, 233–236 (1987).
- [52] S. Asakawa, Y. Saito, K. Waragai and T. Nakagawa, 'Composite membrane of poly[1-(trimethylsilyl)-propyne] as a potential oxygen separating membranes', *Gas Separation Purification*, **3**, 117–122 (1989).
- [53] S. Tasaka, N. Inagaki and M. Igawa, 'Effect of annealing on structure and permeability of poly[1-(trimethylsilyl)-1-propyne]', *Journal of Polymer Science, Part B: Polymer Physics*, **29**, 691–694 (1991).
- [54] Yu. P. Yampolskii, S. M. Shishatskii, V. P. Shantarovich, E. M. Antipov, N. N. Kuzmin, S. V. Rykov, V. L. Khodjaeva and N. A. Plate, 'Transport characteristics and other physicochemical properties of aged poly[1-(trimethylsilyl)-1-propyne]', *Journal of Applied Polymer Science*, **48**, 1935–1944 (1993).
- [55] I. Pinnau, C. G. Casillas, A. Morisato and B. D. Freeman, 'Long-term permeation properties of poly[1-(trimethylsilyl)-1-propyne] membranes in hydrocarbon-vapor environment', *Journal of Polymer Science, Part B: Polymer Physics*, **35**, 1483–1490 (1997).
- [56] G. Consolati, I. Genco, M. Pegoraro and L. Zanderighi, 'Positron annihilation lifetime (PAL) in poly[1-(trimethylsilyl)-1-propyne] (PTMSP): free volume determination and time dependence of permeability', *Journal of Polymer Science Part B: Polymer Physics*, **34**, 357–367 (1996).
- [57] K. Nagai, B. D. Freeman and A. J. Hill, *Journal of Polymer Science Part B: Polymer Physics*, **38**, 1222–1239 (2000).
- [58] K. Nagai, T. Watanabe and T. Nakagawa, 'Effects of aging on molecular motion of poly(1-trimethylsilyl-1-propyne) membranes synthesized using various catalysts', *Polymer Journal*, **28**, 933–935 (1996).
- [59] K. Nagai and T. Nakagawa, 'Oxidation of poly(1-trimethylsilyl-1-propyne)', *Journal of Applied Polymer Science*, **54**, 1651–1658 (1994).

Zeolite Membranes for Gas and Liquid Separations

George R. Gavalas

This review of zeolite membranes includes sections on preparation, characterization, permeation properties and separation of gas and liquid mixtures, and a short section on modeling of transport through the membranes. After a brief introduction, preparation of zeolites MFI, A and Y is presented in some detail. Emphasis is placed on the role of precursor mixture composition, physical structure of the support, seeding and calcination. Membrane characterization is discussed with emphasis on the origin and detection of membrane defects. Permeation measurement techniques and survey of permeation measurements for single compounds and mixtures are treated in some detail. Most of the discussion is devoted to hydrocarbon separations but the separation of alcohol–water mixtures by pervaporation is also reviewed. In each of the separations it is attempted to assess the relative importance of the adsorption and mobility factors. A few comments are made as to which separations have potential for industrial use. The final section is a brief introduction to modeling of zeolite membrane transport. Two important approaches are singled out of the voluminous literature and a brief introduction to each is provided.

12.1 Introduction

Considered as one of the frontier areas in separation technology, inorganic membranes have captured the imagination of academic researchers. Zeolite membranes are particularly popular,

with over fifty laboratories worldwide conducting research on this subject. The annual number of publications on zeolite membranes (limited to those in the web of science database) increased from 14 in 1991 to over 70 in 2001. Recent reviews on the subject include those of Caro *et. al.* [1] and Lin *et. al.* [2], covering preparation as well as permeation properties, and providing extensive references.

Along with other inorganic membranes, zeolite membranes are of interest on account of their thermal and chemical stability, and their high selectivity in certain important separations. A key feature of zeolite membranes shared by sol–gel silica and alumina membranes is that they are made in supported form. The cost of support elements and the lengthy steps involved in film growth make zeolite membranes much more expensive than the well-established polymeric membranes, so that industrial applications can be considered only for separations where they offer some unique advantages in terms of selectivity, or thermal and chemical stability. One process that has already been commercialized is the separation of ethanol–water and other organic–water mixtures by pervaporation using zeolite A membranes. Table 12.1 lists a few potential applications to separations of gas and liquid mixtures. The first two entries in the table refer to separation of liquid mixtures by pervaporation. Based primarily on adsorption differences, this type of separation is relatively tolerant of membrane defects. Separations based primarily on mobility

Table 12.1 Examples of potential applications for zeolite membranes^a

Separation	Zeolite membrane	Advantages and limitations
Organic–water mixtures by pervaporation	MFI, zeolite A (zeolite A membranes already commercialized)	Highly selective separation with water (zeolite A) or the organic (MFI) as the selective penetrant
Separation of miscellaneous organic compounds that have close boiling points or are heat-sensitive	MFI, zeolite A, others	Potentially useful for specialty chemicals and natural products
CO ₂ –CH ₄ (natural gas upgrading)	Na–Y	Resistance to plasticization and fouling by higher hydrocarbons ^b
CH ₄ –higher hydrocarbons (natural gas processing)	MFI	Higher alkanes are the selective penetrants; has to be compared with separation by liquefaction
Normal alkanes from branched alkanes; aromatics or cycloalkanes from alkanes; separation of xylenes (petroleum refining and petrochemicals)	MFI	Very high selectivity unattainable with polymeric membranes; separation by distillation difficult

^aSee also Chapter 15.

^bHollow fiber glass membranes have much higher CO₂:CH₄ separation factors (as high as 500) but their mechanical properties are uncertain.

differences are more demanding in terms of membrane quality. For example, the currently available zeolite A membranes have excellent separation properties for ethanol–water and other organic–water mixtures but do not have useful selectivity for separation of gaseous mixtures such as O₂–N₂, CH₄–CO₂, etc. Table 12.2 lists typical permeances and separation factors or ideal selectivities that have been achieved using zeolite membranes.

What are the structural differences among various zeolites that result in different separation properties? Obviously, a key difference relates

to the pore geometry and the connectivity of the pore network. A second difference is the atom and ion arrangement on the pore surface conferring the adsorptive properties. The key features from the point of view of adsorption are the cations (balancing the charge at anionic sites associated with aluminum atoms) and the hydroxyl groups (silanols) associated with broken siloxane bonds. In addition to the size of the channels or the openings between cages, the entire geometry of the pore system (for example, the size of cages for zeolites like A or Y) influ-

Table 12.2 Survey of productivities and selectivities of zeolite membranes

Membrane	Separation ^a	Temperature (K)	Permeance (GPU) or (flux (kg/(m ² h)) ^b	Separation factor or (ideal selectivity)	Reference
NaA	Water–ethanol PV	348	(2.15)	16 000 ^c	[3]
MFI	<i>n</i> -Hexane–dimethylbutane VP	350	(0.15) ^d	1200	[4]
MFI	<i>n</i> -Hexane–dimethylbutane PV	350	(0.15)	50	[4]
MFI	Benzene–cyclohexane VP	373	(0.056) ^d	55	[5]
MFI	<i>p</i> -Toluene– <i>o</i> -toluene VP	450	(0.016)	400	[31]
NaY	CO ₂ –CH ₄ GP	303	295	20	[6]
MFI ^e	H ₂ –N ₂ GP	423	354	(109)	[7]

^aGP, gas permeation; VP, vapor permeation; PV, pervaporation.

^bFlux or permeance given for the selective penetrant listed first in the separation column; fluxes measured at low feed pressures: 1 GPU = 10⁻⁶ cm³/(cm² s cmHg).

^c5 wt% water.

^d50:50 mixture in He (organic ~ 10 vol %).

^ePrepared from template-free mixtures.

Table 12.3 Elemental composition and pore structure of zeolites that have been made in membrane form

Zeolite structure	Si:Al atom ratio	Channel diameter or pore opening, nm	Pore network dimensionality
A	1	4.1 ^a	3
Y	2.25	0.74	3
MFI (Silicalite, ZSM-5)	25-∞	0.51 × 0.55	3
Ferrierite	5.55	0.34 × 0.48	1

^a4.1 for the Na form (NaA), ~ 3 for the potassium form, ~ 5 for the Ca form.

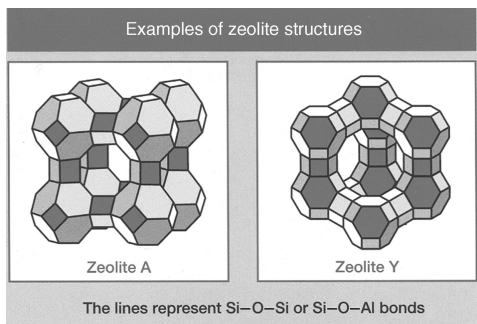
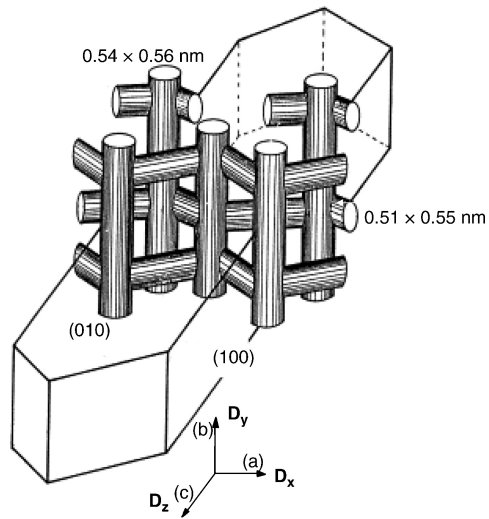
ences the adsorption, as well as the mobility of the guest molecules.

Table 12.3 lists the pore opening size and the dimensionality of the pore network for a few zeolites that have been made in membrane form. Figure 12.1 is a schematic of the structure of zeolites A and Y, the pore structure of which consists of cages connected through windows, referred to as 'pore openings' in this chapter. Figure 12.2 is a schematic of the three-dimensional pore network of MFI that consists of two intersecting channel systems [1]. The channel diameter in this case is referred to as the 'pore diameter'. However, the channel intersections are somewhat wider, offering adsorption sites distinct from those of the channels.

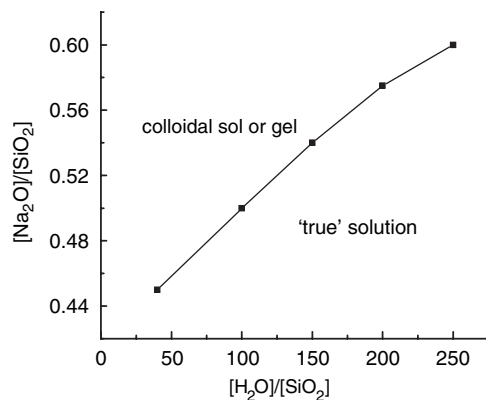
12.2 Membrane Preparation

12.2.1 General Issues

Silicate solutions or gels containing the components SiO₂, Na₂O (or another alkali metal

**Figure 12.1** Cage-window zeolite pores structures**Figure 12.2** MFI channels and crystal faces [1]. Reprinted from *Microporous and Mesoporous Materials*, 38, J. Caro, M. Noack, P. Kolsch and R. Schafer, 'Zeolite membranes – state of their development and perspective', 3–24, Copyright (2000), with permission from Elsevier Science

oxide) and H₂O have been studied extensively over the years and the older literature is reviewed in the comprehensive treaty of Iler [8]. Figure 12.3 shows the regions of true solution and colloidal sol or gel in this ternary system. For compositions above the stability line, the mixture is a true solution of silicate anions (with one to six Si atoms) and sodium cations. Compositions below the stability line are colloidal sols or gels with particle

**Figure 12.3** Regions of 'true' and colloidal solutions for the SiO₂-N₂O-H₂O system

size distributions determined by the preparation history of the mixture. It is interesting to note that the solution stability depends strongly on the $\text{Na}_2\text{O}:\text{SiO}_2$ ratio and less strongly on dilution. When a fourth component, Al_2O_3 , is added to the mixture, the situation becomes much more complicated. The region of instability (colloidal sol or gel) expands due to the higher strength of the Si—O—Al bonds (to dissociation by OH⁻ attack) compared to that of the Si—O—Si bonds. Aluminate ions also act as ‘cement’ between colloidal particles, causing gel formation.

When heated, mixtures of SiO_2 , Al_2O_3 , Na_2O and H_2O can crystallize various zeolites. Crystallization is controlled by kinetic factors so that most zeolites are not in true thermodynamic equilibrium with their synthesis mixture. Nevertheless, ranges of initial composition that favor crystallization of particular zeolites (‘crystallization field’) have been experimentally determined [9,10].

Zeolite crystal growth must be preceded by nucleation, but nucleation does not take place immediately after the mixture is brought to the right temperature. It is preceded by an induction period during which the mixture undergoes chemical rearrangements to form the building blocks that nucleate the zeolite, the precise chemical structure of which are not known. Once nucleation gets started, it continues until supersaturation falls below a certain level by consumption from the growing crystals. Crystal growth can continue further, as long as the mixture maintains some supersaturation. A mixture with low initial supersaturation cannot generate new nuclei but can support growth of crystals added to the mixture. These ‘seed’ crystals can be prepared by diminution of larger crystals or they can be grown from mixtures of suitable composition. Seeded crystallization is a very useful tool in membrane synthesis, as will be discussed below.

How does growth of supported films vary from bulk growth? When a piece of alumina or some other support material is immersed in a synthesis mixture, crystals will generally grow on the solid, as well as in the bulk. Whether nucleation takes place more readily on the solid than in the bulk depends on the particular system, but coating the solid with a seed layer and using a relatively dilute solution can be used to reduce bulk crystallization and favor formation of a surface crystal layer.

12.2.2 MFI Membrane Preparation

MFI membranes have attracted the majority of research on preparation and characterization, both because of historical reasons and because these membranes are selective for hydrocarbon separations of interest to the petroleum and natural gas industries. Most of this review will consequently be devoted to MFI membranes but some of the material will also apply to other zeolite membranes. Significant differences with respect to preparation will be noted in the sections on membranes A and Y.

The designation MFI that we are using here includes ZSM-5, defined conventionally having Si:Al ratios between 25 and 300, and silicalite having Si:Al ratios above 300. The presence of Al (as negatively charged sites balanced by Na^+ or other cations) imparts acidity and hydrophilicity to the zeolite. Silicalite is hydrophobic and has negligible acidity. When there is no concern about these properties, both subtypes will be designated as MFI.

Preparation is deceptively simple. It involves immersing the support in the synthesis mixture, and maintaining it at some elevated temperature for the required length of time. As practiced so far it is a batch process. Figure 12.4 shows a general flow sheet of MFI membrane preparation that is also applicable to membranes A and Y discussed in subsequent sections. The various blocks in this preparation are described separately below.

12.2.2.1 Synthesis Mixture

The term ‘synthesis mixture’ denotes the clear sol or gel used to crystallize the zeolite in the bulk or on the surface of the support. ZSM-5 powder can be crystallized from a gel containing the four components SiO_2 , Al_2O_3 , Na_2O and H_2O in a narrow range of composition. MFI powders and membranes are usually grown from mixtures containing the tetrapropylammonium cation (C_3H_7)₄N⁺ (or TPA⁺), either as a salt, e.g. TPABr, or as the free base, i.e. TPAOH. A few other organic compounds like triethylamine also facilitate MFI crystallization, but not as effectively as TPA⁺.

The role of TPA⁺ in MFI crystallization has been the subject of several studies, e.g. [11–16]. According to these studies, silicate ions displace water molecules surrounding the TPA⁺ ions to form silicate-TPA⁺ clusters of 1–3 nm size.

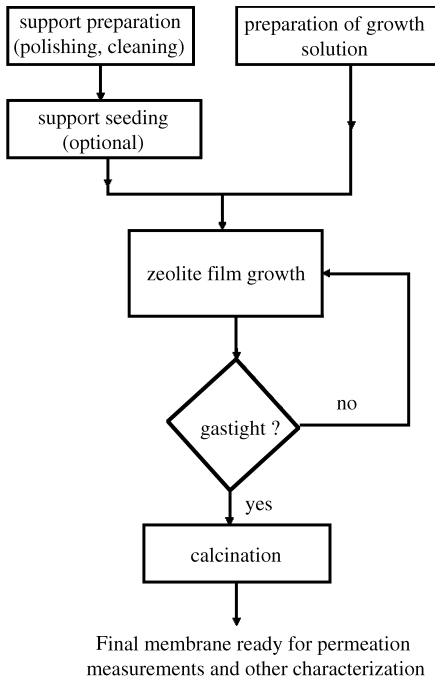


Figure 12.4 Protocol for MFI membrane preparation

Some authors consider these clusters as the building blocks that nucleate the zeolite (homogeneous mechanism) [11–13,15]. Other authors believe that nucleation takes place within larger particles produced by aggregation of the primary clusters (heterogeneous mechanism) [14]. It is possible that aggregation and nucleation take place in either order or concurrently.

Using TPA^+ greatly expands the composition range conducive to MFI crystallization. In particular, mixtures containing TPA^+ need not

contain Al which is known to retard crystal nucleation and crystal growth. Moreover, Na^+ ions are not essential in the presence of TPA^+ . The essential ingredients are SiO_2 , OH^- , TPA^+ and H_2O . Silica is naturally the main component of the zeolite (the elemental composition of silicalite is essentially SiO_2), while water and OH^- are needed to solubilize these components. OH^- , which in the zeolite literature is referred to as the mineralizing agent, attacks the siloxane bonds (Si-O-Si) to form SiO^- and SiOH (reversibly), permitting reorganization of the solution components to form the precursor clusters mentioned earlier.

The simplest synthesis mixture, therefore, contains only the components SiO_2 , TPAOH and H_2O . In this three-component mixture, OH^- and TPA are fixed to a 1:1 ratio. Table 12.4 lists compositions that have been used successfully to make MFI membranes. The first four entries in this table refer to preparations using three-component mixtures and illustrate the wide range of feasible compositions. All of the preparations listed in this table are suitable in conjunction with good quality supports and provided certain precautions are taken, such as careful cleaning of the support before membrane growth and careful calcination of the membrane.

Sodium ions are frequently added to the mixture for two reasons. One is to enhance the rate of crystal growth, within a certain range of compositions. By adding NaOH , one may vary the $\text{TPA}^+:\text{OH}^-$ ratio as well as the OH^- and use the less expensive TPABr instead of TPAOH . With the addition of Na^+ , the mixture contains one or two additional components: TPABr and NaOH . It is also possible to add NaCl or some

Table 12.4 Examples of synthesis compositions for MFI membranes

Seeding?	OH^-/SiO_2	$\text{TPA}^+/\text{SiO}_2^a$	Na^+/SiO_2	Al/Si	$\text{H}_2\text{O}/\text{SiO}_2$	Reference
Yes	5.9	5.9	0	0	706	[19]
No	0.5	0.5	0	0	28	[20]
Yes	0.12	0.12	0	0	60 ^b	[21,22]
Yes	0.04	0.05	0.04 ^c	0	25	[18]
No	0.406	0.3	0.106	0	14.2	[22]
No	0.2	0.048	0.153	0.01	47	[23]
Yes	0.535	0	0.535	0.025	46	[7]
Yes	0.28	0.2	0.08	0	60 ^b	[24]

^aWhen $[\text{TPA}^+] > [\text{OH}^-] - [\text{Na}^+]$, the difference $[\text{TPA}^+] + [\text{Na}^+] - [\text{OH}^-]$ equals $[\text{Br}^-]$, i.e. the mixture contains TPABr .

^bIndicates that TEOS was the silica source with the corresponding ethanol included in the mixture ($\text{EtOH}/\text{SiO}_2 = 4$).

^cKOH used instead of NaOH.

other sodium salt in order to increase Na^+ without increasing OH^- , but this addition has not been used in membrane preparations.

Finally, a small quantity of Al (e.g. Al:Si = 60–1000) is sometimes added as an additional control for modifying membrane structure. Aluminum slows down the rates of nucleation and growth but enhances crystal intergrowth. It is essential in TPA-free membrane preparation. Aluminum can be substituted by other elements such as Fe, B or Ge, allowing further flexibility and modulation of permeation properties [25,26].

The silica and alumina components which have so far been denoted as SiO_2 and Al_2O_3 , are introduced in various forms. Silica is introduced in the form of $\text{Si}(\text{OC}_2\text{H}_5)_4$ or TEOS, as colloidal solution (e.g. Ludox, containing SiO_2 and a small amount of Na_2O), as fumed silica (fine powder of SiO_2 made by high-temperature gas phase reactions) and, less commonly, as sodium silicate (Na_2SiO_3) or waterglass. Aluminum sources include aluminum sulfate, aluminum hydroxide, sodium aluminate and, less commonly, aluminum foil. Since zeolite crystallization is kinetically controlled, the sequence of addition of the silica or alumina components, and other details of mixture preparation, influence nucleation and crystal growth. TEOS, for example, will quickly hydrolyze and result in a fast rise of monomer silicate and rapid nucleation. Silicic acid and Ludox dissolve more slowly. When using TEOS as the silica source, the synthesis mixture contains the corresponding amount of ethanol unless special care is exercised to remove it by vaporization. Ethanol does not seem to have any adverse effects; in fact, under some conditions (e.g. in TPA-free preparations) it has a beneficial effect [17]; therefore, it is almost always left in the mixture. Here are two examples of mixture preparation:

- Example 1 (from Pilar-Bernal *et al.* [18]): KOH pellets, TPABr powder and a colloidal silica solution (Ludox) were added to deionized water and stirred for 2–3 h until a clear solution was obtained.
- Example 2 (from Lai and Gavalas [7]): $\text{Al}_2(\text{SO}_4)_3 \cdot 18\text{H}_2\text{O}$ powder was dissolved in NaOH solution. Colloidal silica sol (Ludox) was added to the solution dropwise under stirring and the resulting hydrogel was left at room temperature for one day.

After the components are mixed in the proper sequence, the mixture is frequently allowed to stand for a few hours before introducing the support. During this ‘aging’, the silicate and TPA ions undergo rearrangements that may be useful to the subsequent crystallization.

Zeolite film growth is often observed to proceed by transformation of a gel layer formed on the external surface and in the pores of the solid. This gel derives from small colloidal particles attracted to the solid by dispersion forces. Nucleation takes place inside the gel which is gradually consumed by the subsequent crystal growth [27–29].

12.2.2.2 Support Effects

Almost all MFI membrane preparations to date have been carried out using porous alumina or stainless steel supports in the form of tubes or disks. Tubes are better suited to eventual applications, but disks are more easily made in the laboratory, yield more easily low-defect membranes and are better suited for characterization. A more important consideration is the pore size distribution of the support. To appreciate the importance of the support physical structure, it is necessary to first examine the geometry of the zeolite layer in relation to the support. Zeolite can nucleate and grow at any point on the support pore surface. After growth begins, the balance between consumption and diffusion of growth components will obviously favor growth at or near the external surface. The concentration profile of the growth components will depend on the growth rate and on the diffusion coefficients of the zeolite precursors. These diffusion coefficients (based on total cross-sectional area) are proportional to the void fraction. The reaction rate coefficient(s), on the other hand, are higher for smaller pores (larger reaction area per unit volume). As reaction progresses and the void fraction is reduced, the diffusion-reaction balance shifts such that growth becomes further localized near the external surface. The separating layer of the final membrane can be located outside of the pores (external membrane), or inside the pores (internal membrane), as shown schematically in Figure 12.5. In this stylized example, the location of the membrane varies because of the different seed penetration (see also Section 12.2.2.4, on ‘seeding’). Deposition of crystalline or amorphous

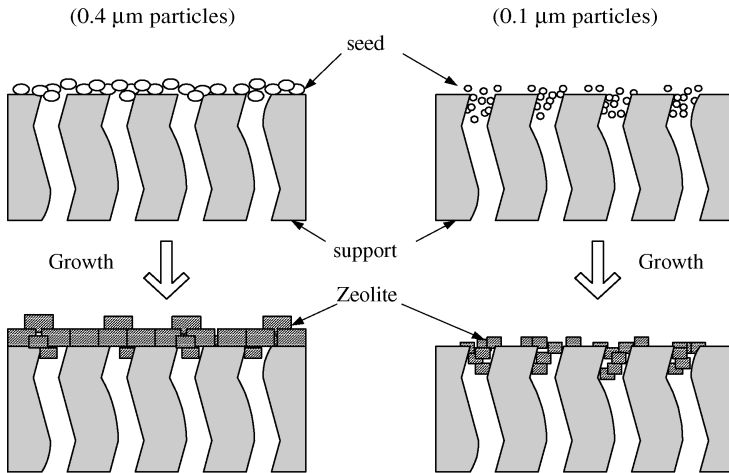


Figure 12.5 Internal and external membranes resulting from different seed sizes

material sometimes partially blocks the pores several tens of micrometers below the selective layer and adversely affects permeance and selectivity. Efforts have been made to limit the unwanted internal growth by introducing a barrier substance before membrane growth and removing it after growth. Carbon has been tried as a barrier substance with little success [30]. Wax has been recently used as a barrier substance, making it possible to obtain very high flux membranes [21].

A complication, encountered when using alumina as the support is the slow dissolution of the solid in the high-pH mixture. Even very low concentrations of aluminum buildup in the immediate vicinity of the support and inside the pores can have a profound influence on membrane growth in view of the aforementioned role of aluminum in gel formation, nucleation and crystal growth [29]. With the concentration of dissolved aluminum varying with the mixing pattern and the placement of the support in the reaction vessel, it is more difficult to obtain reproducible membrane properties. Among alumina supports, γ - Al_2O_3 dissolves more easily at high pH and is generally avoided as a membrane support, with some notable exceptions [23].

To promote good adhesion of the membrane layer, the supports are subjected to various cleaning treatments (such as washing with water, acetone, acids, bases and even oxidizing mixtures) to remove loose particles, adsorbed salts, hydrocarbons or other organic compounds. Subsequent to

cleaning, the supports can be stored in water to prevent adsorption of organic compounds from the laboratory environment.

In the case of internal membranes, the pore size has a different significance. For an internal (intrapore) selective layer to be formed, the crystallites must grow to fill their surrounding pores. The larger pores, in the tail of the pore size distribution, will take longer to fill, perhaps requiring repeated growth periods (using fresh mixtures each time). In the section on 'membrane defects' (Section 12.3.2) the issue of pore size will be examined further.

While small pore size is favorable from the standpoint of defect formation, it increases the resistance to permeation. This difficulty is overcome by using composite (asymmetric) supports consisting of two or more layers of decreasing thickness and pore size, the last of which is in direct contact with the zeolite membrane. Frequently used asymmetric supports include α - Al_2O_3 tubes of about 0.7 cm ID and 1 cm OD, of about 3 μm pore size throughout, except in a 10 μm -thick inner layer of 0.1–0.2 μm pore size.

In a recent study [31], the macroporous alumina support was coated with a layer of mesoporous silica (2 nm pore size) prior to seeding and hydrothermal treatment. This intermediate layer provides a suitable substrate for seeding and seems to suppress the leaching of alumina and reduce defect formation during calcination.

12.2.2.3 Calcination

After template-assisted growth of a membrane it is necessary to remove the template by calcination at temperatures above 400 °C to free the pores for transport. Heating to such high temperatures and subsequent cooling generates stresses because of the larger thermal expansion coefficient of alumina (or stainless steel) compared to zeolite. Stresses also develop because the crystal lattice parameters change upon removal of the occluded TPA [32–34]. These stresses often cause cracks of different sizes to form and damage membrane selectivity. To limit crack formation, it is necessary to conduct heating and cooling very slowly. In most preparations reported in the literature, heating was conducted at less than one degree per minute. Crack generation also depends on crystal orientation, support pore size and surface roughness. In the case of external membranes, smaller pore size and a smooth surface are generally beneficial from the standpoint of crack formation, and so the support is often polished to reduce surface roughness.

12.2.2.4 Seeding

As mentioned earlier, seeding provides a means of bypassing nucleation and going directly to crystal growth. Bypassing nucleation eliminates a serious source of irreproducibility deriving from adsorbed impurities, aluminum leaching, etc. It also expands the range of synthesis compositions and, in particular, permits the use of more dilute solutions. On account of these advantages, most of the researchers are now incorporating seeding in their preparation protocols.

Seeding involves two steps: growth and purification of seeds, and coating the support with seeds. Growing the seeds is straightforward and several protocols have been published for this purpose [35,36]. The seed size is usually in the range 0.05 to 2 μm and can be controlled by varying the reaction time. The often used protocol of reference [35] involves adding TPAOH and NaOH solutions to TEOS under vigorous stirring to reach the composition SiO₂: 0.36 TPAOH, 0.08 NaOH: 19.2 H₂O (and 4 EtOH). After 12 h of stirring at room temperature, the mixture is kept at 98 °C for 24 h. The resulting colloidal particles have a narrow size distribution with 0.95 μm mean diameter. Purification of the seeds can be

carried out by repeated centrifugation and decanting and addition of fresh water, or more simply by filtering the mixture and washing the filter cake to remove unreacted components [24]. After drying, the seeds can be resuspended with the help of ultrasonication.

Coating the support with the seeds is a critical task. One technique involves immersing the support for a specified period (a few minutes) in the suspension at an appropriate pH and, after withdrawal, gently washing to remove all seed particles except those in a surface monolayer held by strong dispersion and/or electrostatic forces [37]. Another technique of achieving a seed monolayer is to first coat the surface with a cationic polymer and then immerse it in a suspension of pH imparting a negative charge on the particles. Washing is again applied to remove excess particles [21]. The polymer-assisted coating can be repeated to increase the particle loading. In another technique, the support is immersed in a suspension of a particular pH, and withdrawn at constant speed (dip-coating) [36]. Yet another seeding technique [38] involves functionalizing the support surface and the seeds so that the latter become covalently attached during drying or heat treatment. Achieving a strongly attached uniform seed layer, free of unseeded patches, is essential to the growth of high quality membranes, because unseeded patches result in pinhole defects [39].

After seeding, the support is heated to bond the particles on the surface by condensation of hydroxyl groups. A temperature of 200 °C is sufficient for that purpose, but if seeding is carried out with the help of a cationic polymer or grafted organic groups, calcination to at least 400 °C is needed to decompose and ‘burn out’ the organic. This calcination treatment will also remove the TPA templates from the seed particles.

In the discussion so far, the seed particles were assumed large enough in relation to the pore size so that seeding results in a thin filter cake on the external support surface. Smaller seeds will penetrate and become deposited deeper in the support by processes characteristic of depth filtration (deep-bed filtration). Internal seeding and relatively low temperatures (about 95 °C) cause the membrane to grow internally, as shown schematically in Figure 12.5 and discussed in reference [24]. Preparation of internal membranes is less demanding with respect to the quality of the

support. The pore size can be larger (e.g. 1 μm) and the external surface need not be smooth. On the other hand, in internal growth the larger pores, at the tail of the distribution, may fail to be blocked by the slowly growing crystals, resulting in relatively large defects.

12.2.2.5 Temperature, Time and other Conditions of Membrane Growth

The temperature range for MFI membrane preparation is 95–200 °C, with most preparations being carried out between 150 and 180 °C. The reaction time is often in the range 16–24 h, although in some cases it was extended to as long as 72 h. In preparations that are carried out above 100 °C, the reaction is conducted under autogenous pressure using Teflon-coated steel autoclaves. Flat supports (disks) are mounted horizontally or vertically in the autoclave with the active surface often facing downward to prevent settling of crystals grown in the bulk of the mixture on the membrane layer. One side of the disk can be masked to prevent film growth on both sides. Tubular supports are placed vertically and some times only the ID or OD is in contact with the synthesis mixture.

Mass transfer can have a significant effect on membrane growth. At temperatures below 100 °C, membrane growth can be carried out in a plastic reaction vessel with water reflux. Stirring is easily provided if desired. For reaction above 100 °C, autoclaves were used, in most cases without stirring, although in some cases mixing was achieved by tumbling the partially filled autoclave. In the absence of forced mixing, severe concentration gradients can develop so that only a fraction of the synthesis solution will be available for membrane growth. The possible contribution of natural convection to mass transfer has not been analyzed but the geometry of the autoclave and the location of the support are obviously relevant in this respect. Similarly relevant is the ratio of mixture volume to support surface area. Few publications report all of these experimental details.

Crystal growth on the support and in the bulk will eventually bring the solution below supersaturation. If at that point the membrane is not fully developed, growth must be repeated using fresh solution. To determine whether additional growth periods are needed, the membrane is washed,

dried to at about 200 °C and tested by permeation of N_2 . With the zeolitic channels blocked by the TPA ions, permeation takes place only through the membrane defects so that if the permeance exceeds some chosen value (such as 0.1 MPU, where 1 MPU = 10^{-8} mol/m² s Pa) growth must be repeated. Two or three growth periods have been used in many membrane preparations.

12.2.3 Zeolite A Membrane Preparation

Zeolite A has a Si:Al ratio of 1, with the unit cell containing 12 SiO_4 tetrahedra and 12 AlO_4 tetrahedra. Each AlO_4 tetrahedron carries a unit negative charge that is balanced by Na^+ (or other cations) that render the material strongly hydrophilic and cause strong adsorption of polar molecules. When saturated with water, the zeolite contains 27 H_2O molecules per unit cell. The pore structure is a cubic array of cages (Figure 12.1) connected with windows, the size of which varies with the charge-balancing cation. In the common NaA (zeolite A with Na cation), the windows are 0.41 nm wide, which in principle is useful for separation of small molecules such as O_2 – N_2 . So far, however, it has not been possible to prepare zeolite A membranes selective for gas separations. This failure is probably due to the relatively large contribution to transport of grain boundaries, given the low permeability of the zeolitic pores. While unable to separate gases, zeolite A membranes have shown excellent selectivity for separation by pervaporation of EtOH– H_2O and other organic–water mixtures.

12.2.3.1 Synthesis Mixture

A four-component synthesis mixture is used: SiO_2 – Al_2O_3 – Na_2O – H_2O . Table 12.5 lists a few compositions reported in the literature and as in

Table 12.5 Solution compositions for zeolite A membranes

Al:Si	$\text{Na}_2\text{O}:\text{SiO}_2$	$\text{H}_2\text{O}:\text{SiO}_2$	State	Reference
0.4	1	60	Gel	[41]
0.22	8.9	556	Clear solution	[42]
0.5	1.5	100	Gel	[43]
0.4	10	200	Clear solution	[44]
1	1	240	Gel	[55]

the case of MFI there is a wide variation. In the 2nd and 4th entries of this table, the mixture was a clear solution on account of the very high $\text{Na}_2\text{O}:\text{SiO}_2$ ratio and low Al:Si ratio. The other mixtures were gels. Clear solutions were used for the purpose of suppressing homogeneous nucleation to limit growth to the seeded surface. A clear solution also provides better spatial uniformity of composition, especially under stirring. Growing membranes in such a wide range of compositions (well outside the conventional crystallization field for the zeolite [9,10]) is only possible using seeded supports.

12.2.3.2 Seeding

Zeolites A, X and Y and sodalite have crystallization fields close to each other; therefore, seeding is essential to direct the synthesis to the desired zeolite, despite the change of composition taking place during the batch reaction. Seeding can be accomplished simply by rubbing the support with the zeolite powder [40,43,44], or by especially immersing the support in a suspension of crystals [41,42].

12.2.3.3 Other Preparation Conditions

There are significant differences in the preparation of MFI and zeolite A membranes. Zeolite A membranes are commonly grown at temperatures of 80–100 °C, hence eliminating the need of a pressurized vessel. Using an open vessel permits ready replacement of the solution or midway addition of depleted reaction components. Reaction times between 3 and 24 h are common but excessive reaction times can lead to dissolution of zeolite A and growth of another zeolite like sodalite. The latter has no useful separation properties. Since zeolite A membranes are grown without the aid of an organic template, no calcination treatment is needed, but before permeation testing, the membrane may need to be heated to 200–300 °C to remove adsorbed water.

Microwave heating has been used with some success to accelerate membrane growth [2,45]. Under microwave heating, alumina supports reach higher temperatures than the liquid, thus making it possible to accelerate surface growth while limiting bulk growth. Some investigators believe that in addition to providing rapid heat-

ing and changing the temperature distribution, microwave power accelerates crystallization by a direct chemical effect.

12.2.4 Zeolite Y Membrane Preparation

Zeolites X and Y have the 'Faujasite structure' but the Al:Si ratio varies according to the preparation conditions [9]: X has ratios of 0.670–1 and is strongly hydrophilic, while Y has ratios of 0.33–0.67 and is less hydrophilic, but both zeolites have pore openings of 0.74 nm.

12.2.4.1 Synthesis Conditions

Table 12.6 lists compositions that have been used for zeolite Y membranes. All preparations were carried out on seeded supports using reaction temperatures and times similar to those used for zeolite A membranes (80–110 °C and 12–24 h). Kumakiri *et al.* [40] report preparation of A and Y membranes using the same clear solution but different seeds.

Table 12.6 Synthesis mixtures for zeolite Y membranes

Al:Si	Na ₂ O:SiO ₂	H ₂ O:SiO ₂	State ^a	Reference
0.080	0.88	45	Gel	[45]
0.156	1.33	76	NA	[46]
0.222	8.9	556	CS	[39]
0.078	0.66	38	Gel	[47,48]

^aNA, not applicable; CS, clear solution.

12.3 Characterization

12.3.1 General on Techniques and Results

X-Ray analysis of zeolite films grown on nonporous or porous supports is used to verify the crystal structure, while analysis of peak intensities provides information about crystal orientation. Orientation has a marked effect on the transport properties of the membrane [39] and affects the formation of defects during calcination [33]. Figure 12.6 shows the diffraction patterns of MFI powder and two MFI films grown on quartz after 6 and 19 h reactions. Comparison of the patterns of the two films with those of the powder reveals prominence of the (101) peak at long reaction times (thicker film) showing an increasing fraction of crystalline material oriented with the *c*-axis at an angle of 35 ° from the normal

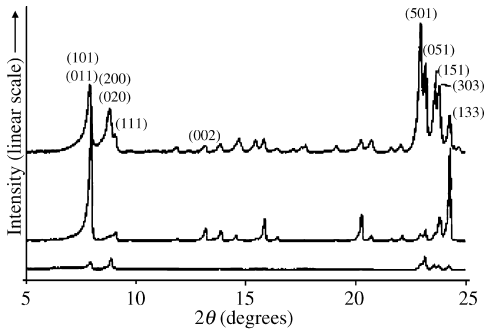


Figure 12.6 XRD micrographs of a powder sample (top) and films grown on quartz after 6 h (bottom) and after 19 h (middle) hydrothermal reactions [50]. From S. Mintova, J. Hedlund, V. Valtchev, B. J. Schoeman and B. J. Sterte, *J. Mater. Chem.*, **8**, 2217–2221 (1998). Reproduced by permission of The Royal Society of Chemistry

to the surface [50]. Figure 12.7 shows diffraction patterns of two membranes grown on porous alumina disks under different conditions [51]. The intense (002) peak of the membrane at the left shows the preferred orientation with the c -axis perpendicular to the surface, as shown schematically in the inset. At the right, the dominant (101) peak reveals preferred orientation with the c -axis tilted by about 34° from the vertical. Pole figure analysis has been employed for a more quantitative determination of crystallite orientation [50,51].

Orientation turns out to be a very important factor on membrane transport properties; b -oriented MFI membranes (crystal b -axis normal to the membrane) had higher permeance and selectivity compared to c -oriented or a - b -oriented membranes in the separation of xylenes [31]. Control of crystal orientation was achieved by using different organic-structure-directing agents. While the commonly used TPA⁺ produced c -oriented crystals, the trimer TPA resulted in b -axis orientation.

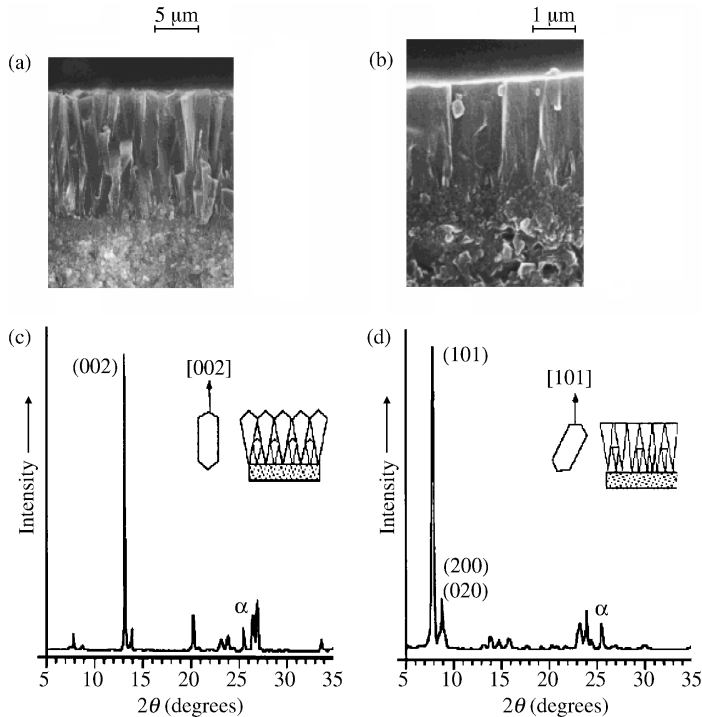


Figure 12.7 SEM cross-sections and XRD patterns of two MFI membranes grown on porous α - Al_2O_3 disks. The thick membrane on the left (a,c) was grown at 175°C for 24 h, while the thin membrane on the right (b,d) was grown at 90°C for 120 h [51]. Reprinted with permission from G. Xomeritakis, Z. Lai and M. Tsapatsis, *I&EC Res.*, **40**, 544–552 (2001). Copyright (2001) American Chemical Society

Scanning electron microscopy with a resolution of about $0.5\ \mu\text{m}$ is used as a standard technique to examine membrane morphology. A top-view scanning electron micrograph shows the size and shape of the crystals and the possible presence of large gaps or cracks, while a cross-sectional view shows the thickness of the film extending outside of the support pores, as shown in Figure 12.8 [54]. The top view of this figure reveals crystals preferentially oriented with the c -axis normal to the surface and about $1.7\ \mu\text{m}$ width along the a -axis. The cross-sectional view indicates an external film about

$3\ \mu\text{m}$ thick. The EDX (energy dispersive X-ray) trace indicates high silicon concentration over a width of $3\ \mu\text{m}$ and some invasion of the alumina pore structure, consistent with the micrograph of the cross-section. In Figure 12.9, the zeolite layer and two $\alpha\text{-Al}_2\text{O}_3$ layers of an asymmetric tube are clearly distinguishable [7]. Figure 12.10 shows scanning electron micrographs of top and cross-sections of membranes grown on $\alpha\text{-Al}_2\text{O}_3$ and stainless steel tubular supports [18]. The top film appears quite continuous at the magnification employed. The bottom micrographs suggest the possible presence of larger defects that can be

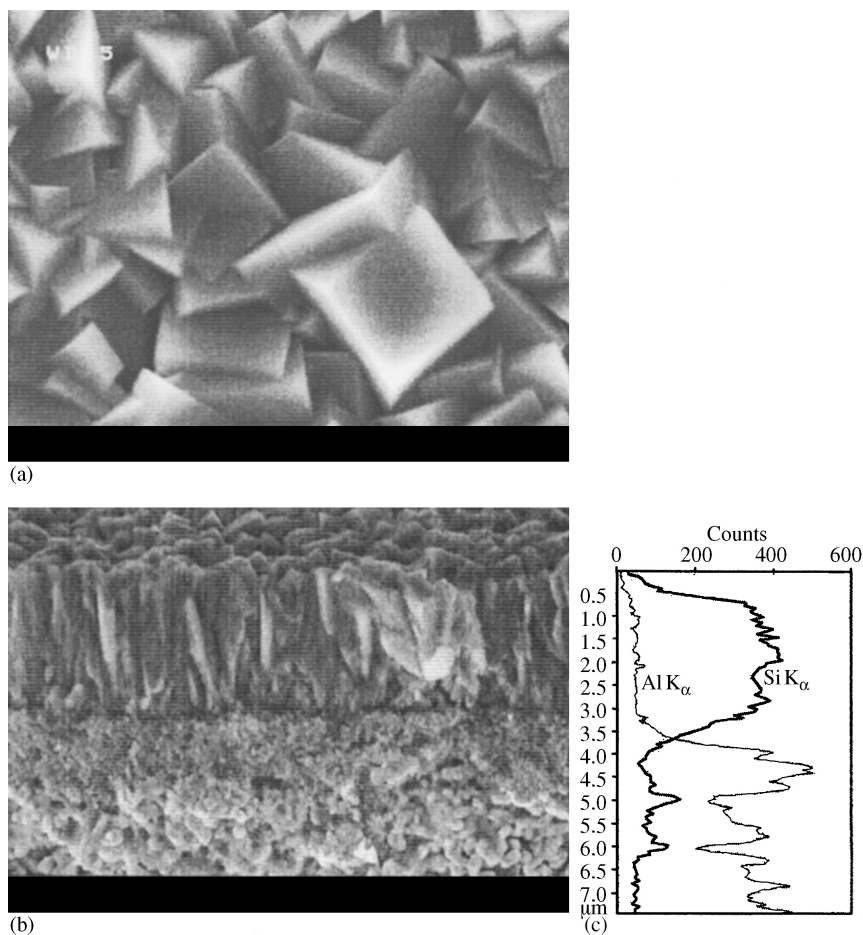


Figure 12.8 Scanning electron micrographs of the top (a) and cross-section (b) of an MFI membrane; (c) on the right, shows an EDX trace of Si and Al over the cross-section [54]. Reprinted from *Microporous and Mesoporous Materials*, 35–36, M. Noack, P. Kolsch, J. Caro, M. Schneider, P. Toussaint and I. Sieber, ‘MFI membranes of different Si/Al ratios for pervaporation and steam permeation’, 253–265, Copyright (2000), with permission from Elsevier Science

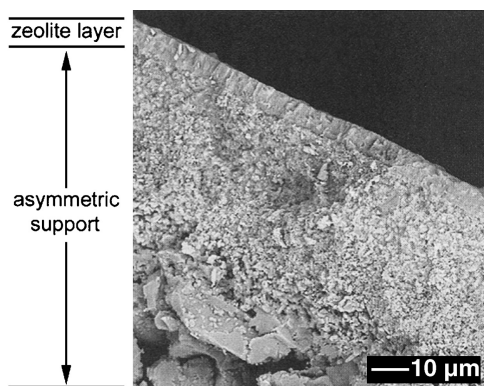


Figure 12.9 Scanning electron micrograph of a membrane cross-section, showing the membrane layer and the two support layers [7]. Reprinted from *Microporous and Mesoporous Materials*, **38**, R. Lai and G. R. Gavalas, 'ZSM-5 membrane synthesis with organic-free mixtures', 239–245, Copyright (2000), with permission from Elsevier Science

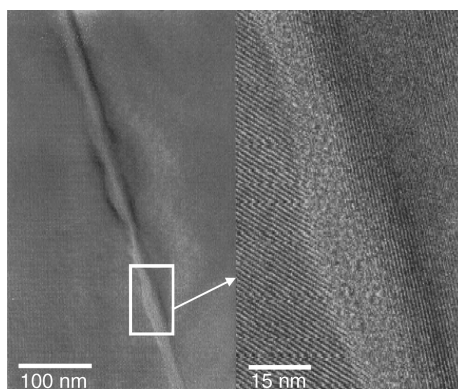


Figure 12.11 Transmission electron micrographs of the interface between two grains in an external MFI layer supported on porous alumina [55]. Reprinted from *Microporous and Mesoporous Materials*, **40**, Y. Sasaki, W. Shimizu, Y. Ando and H. Saka, 'Microstructure analysis with TEM for a zeolite layer formed in the pores of porous alumina substrate', 63–71, Copyright (2000), with permission from Elsevier Science

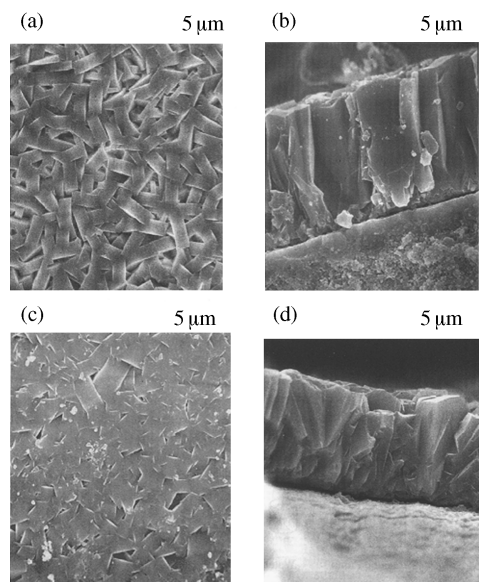


Figure 12.10 Scanning electron micrographs of the tops and cross-sections of MFI membranes grown on α -alumina (a,b) and stainless steel (c,d) supports [18]. Reprinted from *Catalysis Today*, **67**, M. Pilar-Bernal, G. Xomeritakis and M. Tsapatsis, 'Tubular MFI zeolite membranes by secondary (seeded) growth', 101–107, Copyright (2001), with permission from Elsevier Science

explained by the larger mean pore size ($0.5\ \mu\text{m}$ vs. $0.2\ \mu\text{m}$) and the wider pore size distribution of the stainless steel support.

Transmission electron microscopy has been used less widely but has provided some unique information about the nanoscale structure of membranes. Figure 12.11 shows the structure of the grain boundary in the external layer of an alumina-supported MFI membrane. There is an amorphous region of over 10 nm between the two grains (crystallites) [55]. The widespread presence of grain boundaries and larger inter-crystalline defects has also been examined by fluorescence confocal microscopy [56].

Measurement of gas adsorption isotherms has been used to characterize the microporous structures of MFI membranes [37]. When measured by the static method using a sensitive instrument, the part of the isotherm at relative pressures below 0.001 provides a semi-quantitative measure of crystallinity, by calibration with MFI powder and given the total product mass. Figure 12.12 shows that much of adsorption in the zeolite takes place below a relative pressure of 10^{-5} [37]. At this low pressure range, there is no adsorption before calcination.

As will be discussed further below, the transport properties of MFI membranes, especially

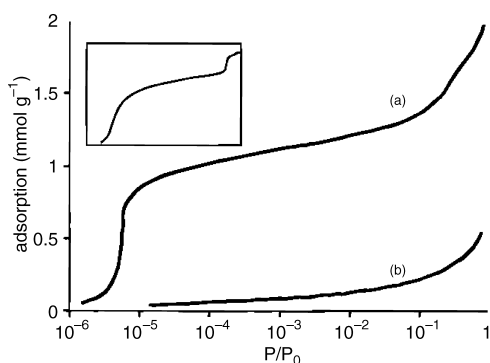


Figure 12.12 Nitrogen adsorption isotherms of an MFI membrane before (b) and after (a) calcination; the inset shows the nitrogen adsorption isotherm of silicalite powder [37]. Reprinted with permission from R. Lai and G. R. Gavalas, *I&EC Res.*, **37**, 4275–4283 (1998). Copyright (1998) American Chemical Society

the membrane selectivity, are sensitive to the defect size distribution which varies widely with the details of preparation. Good quality membranes have a low incidence of defects so that the traditional methods of mercury intrusion and nitrogen adsorption are not applicable because of insufficient material in the thin membrane film. Even if the pore size distribution could be estimated, it would not be very informative because the contributing pores are located throughout the membrane and are not necessarily connected to the separating layer (feed side) responsible for the selectivity. In particular, pores in the membrane interior that are accessible through the permeate side, but not through the feed side, are not membrane defects. The method of choice for characterization of membrane defects is ‘permporometry’ [57]. This simple method involves measurement of the transmembrane flux of a permanent gas like He, containing a condensable gas like cyclohexane. The relative pressure of the condensable gas is initially near unity so that all pores are blocked by capillary condensation and there is no He flow. As the relative pressure is lowered, the condensable gas desorbs and frees the largest defects so that the He flow starts increasing. The curve of He flux vs. relative pressure can be interpreted with the aid of a pore model to estimate the defect size distribution.

12.3.2 Membrane Defects

This section provides a brief discussion of membrane defects as background for the section on permeation measurements. Table 12.7 provides an attempt to classify defects according to size and to relate their origin to specific processes, keeping in mind that the size limits are only indicative and have no absolute significance. Insufficient time or reactant depletion is an obvious source of defects. This can be eliminated by using a longer reaction period or repeated growth periods. The minimum time needed for this purpose depends on many factors, including the rate of crystal growth, and the competition with growth in the bulk and the volume of solution per unit membrane area. It also depends on seed size and surface roughness, both of which influence the detailed seed geometry.

As discussed in the ‘preparation’ section, calcination is a very common cause of large cracks in MFI and other membranes made by using organic templates. Incomplete seeding has also been identified as a source of large, pinhole-shaped defects [39]. Unreactive gel accumulating in the space between the crystals may be another factor contributing to defect formation, especially for internally grown MFI membranes where the level of leached aluminum is high. Gel accumulating around the internally grown crystals would become unreactive when its aluminum content becomes excessive. Membrane testing before calcination would indicate a ‘gas-tight’ membrane but gel shrinkage and TPA removal during calcination would open up non-zeolitic porosity within the gel-occupied region.

The finite size of the growth molecules or clusters is probably one source of the defects known as ‘grain boundaries’. The earlier-cited publications on the growth of colloidal MFI particles [14–16] identify TPA-containing particles 1–4 nm in diameter as the building blocks of MFI.

Table 12.7 Origin and size of membrane defects

Origin	Size (nm)		
	0.5–4	40–50	> 50
Insufficient time or reactant depletion	—	×	×
Calcination	—	×	×
Defective seeding	—	×	×
Gel interference	—	×	×
Finite size of precursor	×	—	—

Intercrystalline gaps below that size would be inaccessible to these growth particles, especially if the gaps contain adsorbed TPA. Similar limitations arising from the size of the growth component must apply to zeolites A and Y made without using templates.

In addition to the intercrystalline defects listed above, membranes may carry intracrystalline defects, such as —OH groups from broken Si—O—Si bonds on the internal pore surface or at the pore mouths on the external surface. Alternatively, the crystals may contain occluded material like NaOH [58].

12.4 Permeation Measurements

12.4.1 Measurement Techniques

Techniques for measuring the key membrane properties of permeance and selectivity are addressed to single components or mixtures. Although the mixture properties are relevant to applications, single gas properties are also useful for membrane characterization. In order to be able to discuss measurement techniques, we first consider some basic physical ideas and modeling concepts for single-component transport. Modeling of multicomponent transport will be taken up in Section 12.5.

Single gas measurements are reported in terms of the permeance:

$$P_i^* = N_i / (p_1 - p_2) \quad (12.1)$$

and the ideal selectivity (single component selectivity) between components i and j :

$$S_{ij} = P_i^* / P_j^* \quad (12.2)$$

where N_i is the molar flux of i and p_1, p_2 are the pressures at the feed side and permeate side. In the case of mixtures the permeance is defined by:

$$P_i^* = N_i / (p_{i1} - p_{i2}) \quad (12.3)$$

and the mixture selectivity or separation factor:

$$\alpha_{ij} = (y_{i2}/y_{j2}) / (y_{i1}/y_{j1}) \quad (12.4)$$

where the subscripts '1' and '2' refer to the feed side and permeate side, respectively, and the pressures are partial pressures. In view of the varying composition along the membrane, the separation factors depend on the feed and sweep flowrates. In the zeolite membrane literature the separation factor is alternatively defined by the ratio of the permeances measured for each component in the mixture:

$$\alpha_{ij} = P_i^* / P_j^* \quad (12.5)$$

which also depends on the flowrates but is simpler to interpret. In general, calculation of the permeances should take into account the variation of composition along the membrane, both at the feed side and permeate side.

Measurements of permeation fluxes for single components and mixtures are quite sensitive to the technique used, so that comparison of membrane performance based on measurements by different techniques can be misleading. The measurements are particularly influenced by the use of a sweep gas (not a component of the feed) and by whether or not the permeate side is kept under vacuum. Figure 12.13 is a schematic diagram of various measurement techniques.

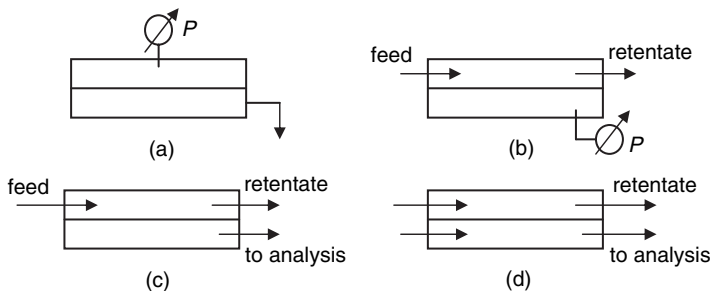


Figure 12.13 Four measurement techniques for single components and mixtures: (a) batch measuring pressure decline at feed side; (b) batch measuring pressure rise at permeate side; (c) steady, 'dead end' at permeate side; (d) steady, using sweep gas (W-K technique)

The batch techniques (a) and (b) are used for single component measurements. In (a), the feed side is brought to some initial pressure and then the supply is shut off. The transmembrane flux is then determined from the measurement of the transient pressure decline at feed side pressure during application of vacuum at the permeate side, provided that the feed side volume (including the line to the pressure gauge) has been appropriately calibrated. It is also possible (not shown here) to collect the permeate gas at atmospheric pressure and measure the flowrate using a bubble flowmeter. In (b), continuous flow is applied at the feed side, while the permeate side is isolated after being evacuated. Measurement of the rising pressure at the permeate side provides the permeation flux through the membrane, this time provided that the permeate side volume (including the volume of the line to the pressure gauge) has been calibrated. Measurements are commonly conducted with the membrane module held at fixed temperature, at or above ambient.

Arrangements (c) and (d) involve constant flows at both feed and permeate sides. In (c), the feed side is maintained at higher pressure than the 'dead-end' permeate side which is usually under atmospheric pressure. The technique can be applied to a single component or to a mixture by conducting the permeate stream to a bubble flow meter or a gas chromatograph, respectively. Finally, in technique (d) the permeate side is usually at atmospheric pressure while the feed side is maintained at atmospheric or higher pressure. The permeate gas mixed with the sweep gas is conducted to a gas chromatograph or some other analytical instrument for measurement of composition.

To understand the differences among the measurement techniques, we consider some simple concepts regarding the permeation of a single gas. At sufficiently low pressures, there is low occupancy and adsorption in the membrane follows Henry's law, namely:

$$q = \rho K p \quad (12.6)$$

where ρ is the membrane density, q is the number of moles adsorbed per unit mass of the solid, p is the pressure and K is an adsorption equilibrium constant. The constant K is analogous to the solubility involved in the case of polymeric mem-

branes. The molar flux N of the gas through the membrane can then be expressed in the usual way:

$$N = -D_0 dq/dz = -D_0 K \rho dp/dz \quad (12.7)$$

where the diffusion coefficient D_0 is appropriate to the Henry's law case. The product $\rho K D_0$ is proportional to the membrane permeability P , that is usually defined in terms of volume (at standard conditions) rather than number of moles: $P = (RT/p) K \rho D_0$. In the Henry's law regime, the diffusion coefficient D_0 is independent of concentration so that Equation (12.2) yields the simple expression:

$$N = D_0 K \rho (p_1 - p_2)/L \quad (12.8)$$

where L is the membrane thickness. The permeance is then given by:

$$P^* = D_0 K \rho / L \quad (12.9)$$

which in the low pressure limit is independent of the feed side or permeate side pressures.

In the case where the feed and possibly the permeate pressures are in the range of nonlinearity of the adsorption isotherm:

$$q = q_0 f(p) \quad (12.10)$$

where q_0 is the maximum possible adsorbed concentration and $f(p)$ is dimensionless ($f(\infty) = 1$), Equation (12.7) is replaced by:

$$N = -D dq/dz \quad (12.11)$$

where the Fick's diffusion coefficient D is a function of the adsorbed concentration q . Separating variables and integrating yields:

$$N = (1/L) \int D(q) dq = (1/L) \int D(f(p)) f'(p) dp \quad (12.12)$$

the limits being between p_1 and p_2 . The permeance is now given by:

$$P^* = (1/L) \left[\int D(f(p)) f'(p) dp / (p_1 - p_2) \right] \quad (12.13)$$

The two factors are now intertwined because of the isotherm nonlinearity and the dependence of D on concentration.

The diffusion coefficient D can increase, decrease or remain approximately constant with increasing concentration. Assuming for the moment constant D , we find:

$$P^* = (D/L)(f(p_1) - f(p_2))/(p_1 - p_2) \quad (12.14)$$

Because of the convex shape of the isotherm, the permeance decreases with increasing p_2 , keeping the pressure difference $p_1 - p_2$ constant. It follows that the permeance is maximum when the permeate side is evacuated. Techniques (a) and (b), therefore, yield larger permeance than technique (c). Techniques (a) and (b) are fundamentally identical but (a) takes a longer time to record a measurable decline of pressure at the feed side, while technique (b) is faster because a low pressure buildup at the evacuated permeate side can be measured accurately by using a sensitive capacitance pressure gauge.

The last technique (d) is useful mainly for mixtures when the flux is low so that (c) is not practical. However, technique (d) introduces an extraneous agent, the sweep gas, which by moving through the membrane in the opposite direction (counterdiffusion) lowers the fluxes of the feed components and changes the separation factor. The total pressure is usually maintained equal at both sides of the membrane when the measurement technique is referred to as the Wicke-Kallenbach (W-K) technique in recognition of an early paper by these authors dealing with measurement of diffusion coefficients in porous catalysts.

To maintain constant partial pressure at the feed side when using technique (d), it is necessary to apply a sufficiently high flowrate, otherwise it will be necessary to measure and take into account the retentate composition changes in the calculation of permeances and separation factors. Likewise, the sweep gas flowrate must be sufficiently high to allow neglecting the buildup of partial pressures along the membrane at the permeate side.

A comparison of techniques (c) and (d) is instructive for the case of a binary mixture with the pressure of the permeate side set at one atmosphere in both measurements. In the case of technique (c), the mole fraction of the two components at the permeate side will be proportional to the respective fluxes; hence, the selective component will have higher partial pressure. If

that pressure lies in the nonlinear part of the isotherm, the flux will be relatively low, being proportional to $q_1 - q_2 = f(p_1) - f(p_2)$. The same effect will apply to the less selective compound, but because its partial pressure at the permeate side will be lower, due to its lower flux, the nonlinear effect on the flux will be less pronounced. The net result is that technique (d) will give a higher separation factor than technique (c), provided that the sweep gas flowrate is sufficiently high. Detailed interpretation of such measurements requires using multicomponent diffusion models, an introduction to which is provided in Section 12.5. A comparison of experimental data obtained with different methods is given in Van de Graaf et al. [59].

12.4.2 Survey of Permeation Results

It must be emphasized at the outset that permeation properties vary widely from membrane to membrane because of differences in the distribution of defects and other structural features such as thickness and crystal orientation. These differences result from different supports and preparation protocols. Even when using nominally the same type of support, differences between batches or even from sample to sample within the same batch can cause wide variation of selectivity.

12.4.2.1 Small Molecules

This survey begins by considering the separation of small molecules like H_2 , CO_2 , O_2 , N_2 , CO and CH_4 , having kinetic diameters of 0.289, 0.33, 0.346, 0.364, 0.376 and 0.38 nm, respectively. Separation can be by adsorption, mobility or both. In the case of MFI, all the kinetic diameters listed above are substantially below the ~ 0.55 nm MFI channel diameter; therefore, there can be no strong mobility difference or molecular sieving. Likewise, the adsorption differences are not dramatic. As a result, MFI does not provide high separation selectivity for these gases.

Permeation of small molecules through 'good quality' MFI membranes proceeds relatively rapidly through zeolitic pores so that contribution of the limited defects is relatively small. Selectivity is controlled by the zeolitic pores. Figure 12.14 [60] shows single gas permeances through a Na-ZSM-5 membrane with Si:Al = 25. At low temperatures, CO_2 is the fastest permeating gas

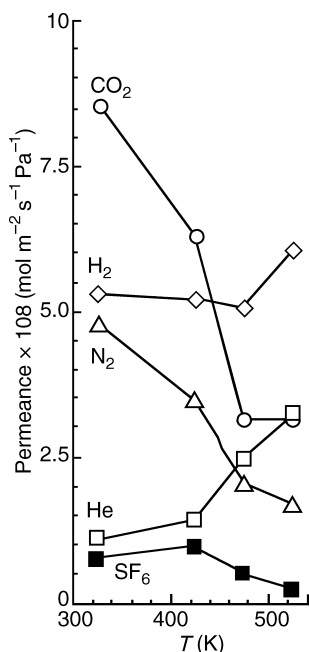


Figure 12.14 Single gas permeances through an MFI membrane as a function of temperature [60]. Reprinted from *Microporous and Mesoporous Materials*, **39**, K. Aoki, V. A. Tuan, J. L. Falconer and R. D. Noble, 'Gas permeation properties of ion-exchanged ZSM-5 zeolite membranes', 485–492, Copyright (2000), with permission from Elsevier Science

because of its stronger adsorption. Its permeance declines with temperature over the whole temperature range. With somewhat weaker adsorption, N₂ has a similar behavior. Having much weaker adsorption, H₂ and He rise with temperature over the range examined.

Other membranes gave different responses. An example is given in Figure 12.15 [23] where the hydrogen permeance has a shallow minimum at 370 K but substantially exceeds the permeance of CO₂ over the same temperature range. An exceptional case is encountered with membranes prepared using template-free mixtures [7]. These membranes yielded single-component ideal selectivities: H₂:N₂ = 109; H₂:CO₂ = 15; H₂:CH₄ = 230; H₂:isobutane = 10 000 at 423 K. Occluded species or other defects could have narrowed the zeolitic channels, resulting in stronger molecular sieving behavior.

What about the capability of the other two zeolite membranes, A and Y, for separation of small

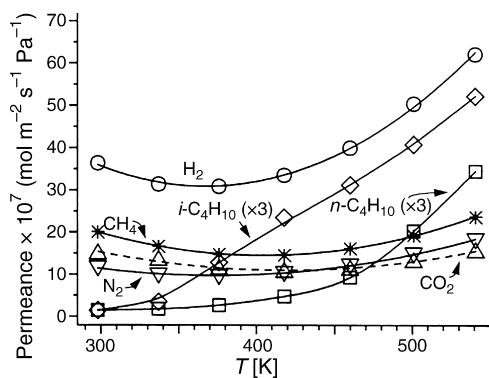


Figure 12.15 Single gas permeances through an MFI membrane as a function of temperature [23]. From J. Coronas, J. L. Falconer and R.D. Noble, 'Characterization and permeation properties of ZSM-5 tubular membranes', *AIChE J.*, **43**, 1797–1812 (1997). Reproduced with permission of the American Institute of Engineers. Copyright © 1997. All rights reserved

molecules? In principle, zeolite A with its smaller pore opening (~ 0.4 nm) would be ideal for separation by molecular sieving. In practice, the membrane defects (grain boundaries and others) 'kill' that separation because of the low permeance of the zeolite. Zeolite Y, on the other hand, has large pores (~ 0.74 nm) so that separation by mobility alone is out of the question. However, the larger concentration of charge balancing cations opens the possibility of preferential adsorption and selective permeation of acidic gases like CO₂. Figure 12.16, from Kusakabe *et al.* [6], compares CO₂ and N₂ single component and mixture permeation. The permeance of CO₂ is about the same for the single component and the mixture but the permeance of N₂ is substantially lower in the mixture. Being the more strongly adsorbed component, CO₂ 'crowds out' and suppresses the flux of N₂, resulting in respectable separation factors. This 'crowding-out' effect will be encountered in hydrocarbon separations, discussed later on. Figure 12.16 shows a steeper increase for the N₂ flux with increasing temperature, with consequent decline of the separation factor. This is an example of the general principle that selectivity based on adsorption declines with increasing temperature. The CO₂–CH₄ separation follows the same general trend except that the separation factor is somewhat lower (Table 12.3). At the

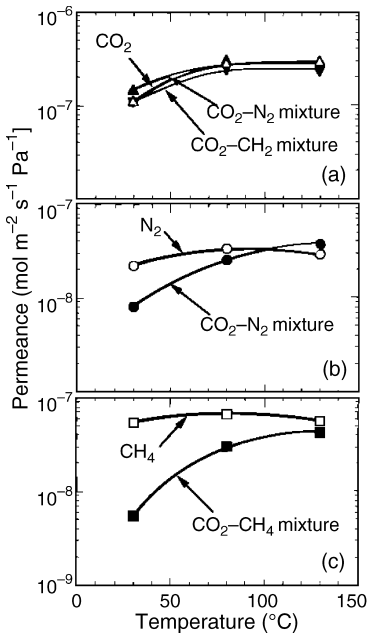


Figure 12.16 Single gas and mixture permeances of CO₂(a), N₂(b) and CH₄(c) through a zeolite NaY membrane as a function of temperature [6]. Reprinted with permission from K. Kusakabe, T. Kuroda, A. Murata and S. Morooka, *I&EC Res.*, **36**, 649–655 (1997). Copyright (1997) American Chemical Society

pressures and temperatures of interest, the adsorption isotherm of methane is intermediate between those of nitrogen and carbon dioxide. Mobility difference plays a lesser role in this case.

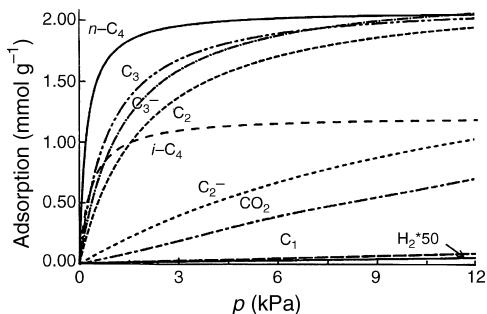


Figure 12.17 Adsorption isotherms of several gases on MFI powder at 275 K [61]. Reprinted from *Journal of Membrane Science*, **117**, W. J. W. Bakker, F. Kapteijn, J. Poppe and J. A. Moulijn, 'Permeation characteristics of a metal-supported silicalite-1 zeolite membrane', 57–78, Copyright (1996), with permission from Elsevier Science

12.4.2.2 Hydrocarbon Gases

Perhaps the most promising application of MFI membranes is in hydrocarbon separations. The first separation that comes to mind is that of C₂–C₄ hydrocarbons from natural gas. Figure 12.17, from Bakker *et al.* [61], shows single-component adsorption of C₁–C₄ hydrocarbons. Adsorption increases with the carbon number for the straight-chain components and isobutane is much below *n*-butane. Figure 12.18, also from Bakker *et al.* [61], shows single-component permeance versus temperature for the C₁–C₄ hydrocarbons. At low temperatures, the permeance decreases with the carbon number but at higher temperatures there is some crossover due to the different temperature variation of the adsorption and mobility factors. Figure 12.19 shows permeance data for CH₄ and C₂H₆ in a 50–50 mixture at 295 K as a function of total pressure [61]. The 'tables have now been turned' and C₂H₆ becomes the selective penetrant with separation factor 5–6. Figure 12.20 [62] shows the separation factors of several hydrocarbon pairs in a natural gas mixture. The heavier gas is the selective penetrant in all pairs on account of the 'crowding-out' factor discussed earlier. The effect is more pronounced for the C₁–C₄ pair. These separation results may be of interest for extracting C₂–C₅ hydrocarbons from natural gas where the heavier compounds (especially C₄) would be obtained at atmospheric pressure but the majority component,

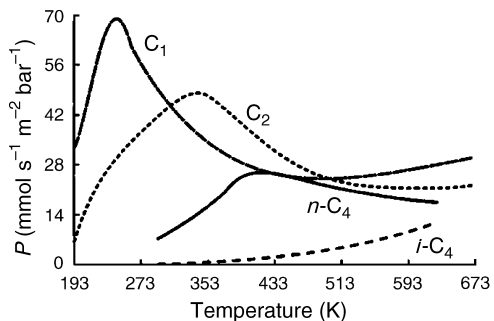


Figure 12.18 Temperature-dependence of the permeances of methane, ethane, *n*-butane and isobutane as single gases through an MFI membrane [61]. Reprinted from *Journal of Membrane Science*, **117**, W. J. W. Bakker, F. Kapteijn, J. Poppe and J. A. Moulijn, 'Permeation characteristics of a metal-supported silicalite-1 zeolite membrane', 57–78, Copyright (1996), with permission from Elsevier Science

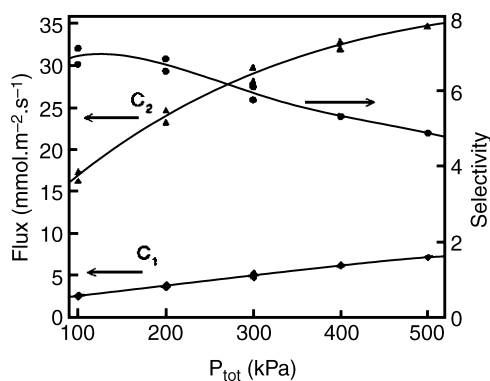


Figure 12.19 Permeance and separation factor data as a function of feed-side pressure for a 50:50 methane-ethane mixture, measured by using the W-K technique; the permeate side was maintained at 100 kPa under an He sweep flow [61]. Reprinted from *Journal of Membrane Science*, **117**, W. J. W. Bakker, F. Kapteijn, J. Poppe and J. A. Moulijn, 'Permeation characteristics of a metal-supported silicalite-1 zeolite membrane', 57-78, Copyright (1996), with permission from Elsevier Science

methane, would remain at the high pressure of the feed. Another separation of interest is that of hydrogen from lower hydrocarbons in refinery hydrotreating product streams. The 'crowding-out' factor is again at play. Figure 12.21 [63] shows the single gas transient permeation of hydrogen and *n*-butane with ideal selectivity over 20 in favor of hydrogen. In mixture permeation on

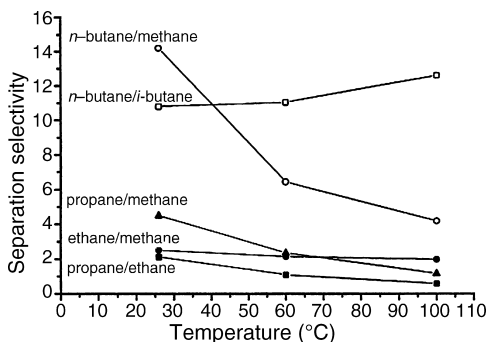


Figure 12.20 Separation factors of several gas pairs as a function of temperature in a natural gas feed to an MFI membrane [62]. Reprinted from *Separation and Purification Technology*, **25**, M. Arreubo, J. Coronas, M. Menendez and J. Santamaria, 'Separation of hydrocarbon from natural gas using silicalite membranes', 275-286, Copyright (2001), with permission from Elsevier Science

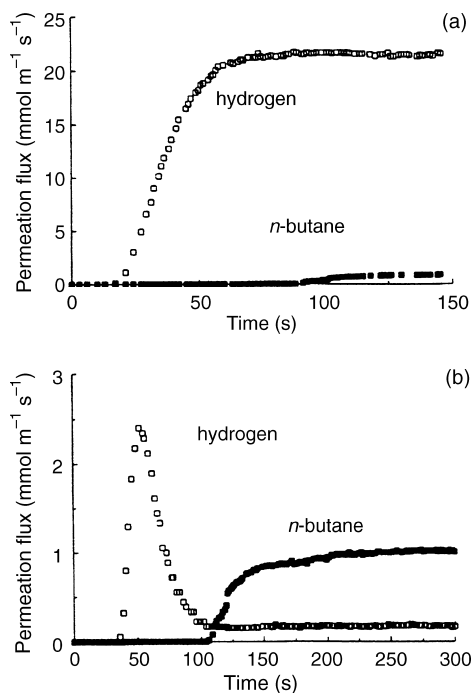


Figure 12.21 Transient permeate fluxes of hydrogen and *n*-butane as single gases and as a mixture through an MFI membrane: (a) feed, hydrogen at 95 kPa, *n*-butane at 5 kPa; 300 K; (b) feed, hydrogen (95 kPa)-*n*-butane (5 kPa) mixture; 300 K [63]. Reprinted from *Catalysis Today*, **25**, F. Kapteijn, W. J. W. Bakker, J. van der Graff, G. Zheng, J. Poppe and J. A. Moulijn, 'Permeation and separation behavior of a silicalite-1 membrane', 213-218, Copyright (1995), with permission from Elsevier Science

the other hand, *n*-butane becomes the selective gas with a separation factor around 20. The separation of hydrogen from an eight-component mixture with C1-C4 hydrocarbons was reported by Dong *et al.* [64]. The hydrocarbons are the selective penetrants at temperatures below 100 °C, with the hydrocarbon-to-hydrogen separation factor rising with carbon number and feed pressure. At 3.7 bar and 75 °C, the separation factors were about 2, 9, 25, 23, 66 and 31 for methane, ethane, ethene, propane, propene and *n*-butane, respectively. In the separation of 50-50 H₂-*n*-butane mixtures through a B-ZSM-5 membrane at 1.4 bar and room temperature, separation factors as high as 110 in favor of *n*-butane were obtained [25].

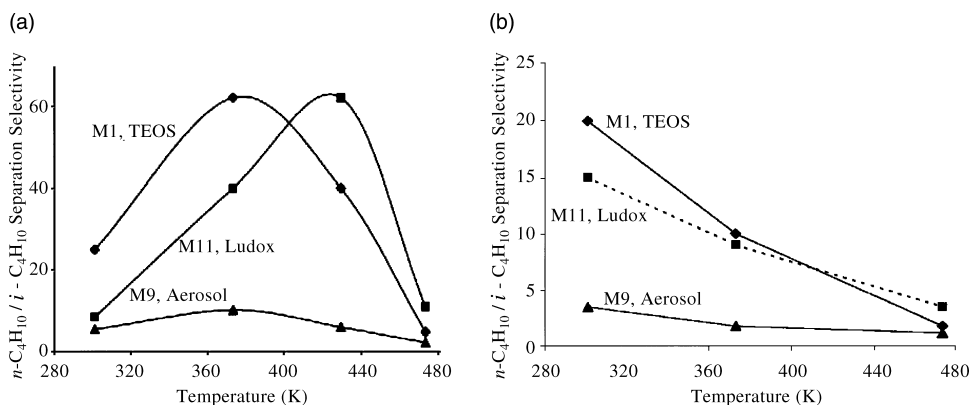


Figure 12.22 Separation selectivities (a) and ideal selectivities (b) for *n*-butane/isobutane as a function of temperature for three membranes prepared by using different silica precursors [66]. Reprinted with permission from V. A. Tuan, J. L. Falconer and R. D. Noble, *I&EC Res.*, **38**, 3635–3646 (1999). Copyright (1999) American Chemical Society

A separation that has received a lot of attention in the MFI membrane literature is that between *n*-butane and isobutane (kinetic diameters are 0.43 and 0.50 nm, respectively). This separation has little practical importance but is useful as a ‘litmus’ of membrane quality. The relative adsorption of the two butanes is shown in Figure 12.17, and the diffusion coefficients were estimated to be 4×10^{-12} and 10^{-12} m²/s, respectively [65]. Both factors are in favor of *n*-butane and, in fact, depending on the measurement technique employed, selectivities or separation factors as high as 200 have been reported, although values of 10–50 are more common. Figure 12.22 [66] shows ideal selectivities and separation factors of three membranes as a function of temperature. The membranes were prepared using the same protocol, except that the silica source varied. The ideal selectivities decline monotonically with temperature as one would expect from the higher activation energy for the diffusion coefficient of isobutane but the mixture selectivity goes through a maximum. The selectivity between the two butanes is not always larger than unity. MFI membranes have been reported where isobutane is the selective penetrant in single component permeation, e.g. Coronas *et al.* [23]. One possible explanation for this very puzzling piece of data is the presence of large defects admitting viscous flow where the lower viscosity of isobutane is the decisive factor.

Another separation that has been used as a means of membrane characterization is that between N₂ and SF₆, either as single gases or as

a mixture. The kinetic diameter of SF₆ is 0.55 nm [6], very close to the MFI pore diameter: therefore, its diffusion coefficient is expected to be much lower than that of N₂. Although the adsorption of SF₆ is probably stronger than that of nitrogen, the diffusion factor should be dominant. In the case of low flux through the zeolitic pores, the total flux of SF₆ should provide a measure of the contribution of defects. Membranes with N₂:SF₆ ideal selectivities in the range of several hundred have been reported in several studies, signifying very low incidence of defects. Membranes have also been reported with selectivities below 10. Unfortunately, in only in a few studies were both the *n*C₄:iC₄ and the N₂:SF₆ selectivities measured for the same membranes. For these few cases, there is no correlation between the two selectivities.

12.4.2.3 Liquid Hydrocarbon Separations

The hydrocarbons of interest in this section are C₅–C₈ parafins (or olefins) and aromatics such as benzene, toluene and xylenes. ‘Vapor permeation’ is the term which refers to a feed which is liquid at ambient conditions but at the elevated temperatures and/or low partial pressure (dilution in a carrier gas) of the measurements the feed and permeate sides are both in the gaseous state. In ‘pervaporation’, on the other hand, the feed is in the liquid state, while the permeate is under vacuum. The driving force in the second case is based on the solution fugacity at the feed side. Otherwise, there is no difference in the mechanism

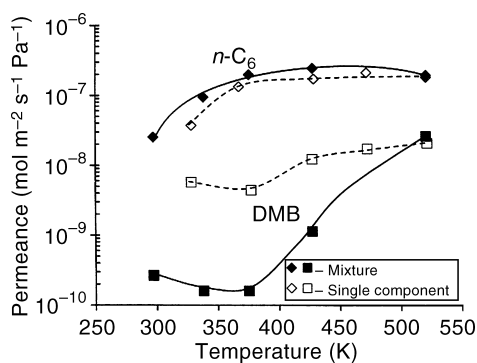


Figure 12.23 Permeance of *n*-hexane and 2,2-dimethylbutane as pure or as a 50:50 mixture through an MFI membrane as a function of temperature [4]. Reprinted from *Journal of Membrane Science*, **176**, C. L. Flanders, V. A. Tuan, R. D. Noble and J. L. Falconer, 'Separation of C-6 isomers by vapor permeation and pervaporation through ZSM-5 membranes', 43–53, Copyright (2000), with permission from Elsevier Science

of permeation. Adsorption differences, 'crowding out', and mobility differences can all be at play. A highly selective separation with MFI membranes is that of straight-chain and branched alkanes [4,5,21,67–69]. The mixture that has served as a model for this type of separation is *n*-hexane–2,2 dimethylbutane. Figure 12.23, from Flanders *et al.* [4], shows the ideal and mixture permeance for the two components versus temperature. The permeance of *n*-hexane attains a maximum of 10 MPU at about 400 K, while the separation factor peaks at 375 K at a value close to 1000. Beyond 400 K, both the permeance and the separation factor decline. The permeance of the branched hydrocarbon is much lower in the mixture than in the single-component measurement, while there is little difference for the straight-chain hydrocarbon permeance, providing separation factors higher than the ideal selectivity. The general mechanism of this separation is 'transparent'. The straight-chain hydrocarbon fits well in the zeolitic channels while the branched hydrocarbon has lower adsorption and much lower mobility because of its larger cross-section, resulting in a strong 'crowding-out' effect. The very high separation factors also suggest that small defects like grain boundaries are also selective in this separation, mainly on account of adsorption differences. The strong temperature-dependence of the branched hydrocarbon permeance is discussed

in Flanders *et al.* [4]. Higher *n*-hexane permeance (50 MPU) but lower separation factors were reported in Hedlund *et al.* [21]. The separation factor in the latter study increased with temperature up to at least 660 K.

More complex mixtures have also been examined and unusual results were obtained for mixtures of *n*-hexane, *n*-octane, and 2,2,4-trimethylpentane [70]. The separation factor for a binary mixture of the two octanes was relatively modest, below 10, but when *n*-hexane was added to the mixture, the permeance of *n*-octane increased, while that of isooctane decreased, resulting in a separation factor as high as 40. For these ternary mixtures, *n*-octane was always the selective penetrant and depressed the permeance of the other two components, signifying again a 'crowding-out' effect. Other ternary mixture separations were reported by Funke *et al.* [71,72].

Most of the hydrocarbon separation experiments considered in this section were carried out using diluted feed mixtures, about 10% hydrocarbon, with the balance being He. In view of the prominent role of adsorption in these separations, there is a strong effect of total hydrocarbon pressure as well as composition. Increasing the partial pressure of the selective penetrant generally results in lower permeance but higher separation factors, as exemplified by Figure 12.24, from Gump *et al.* [68].

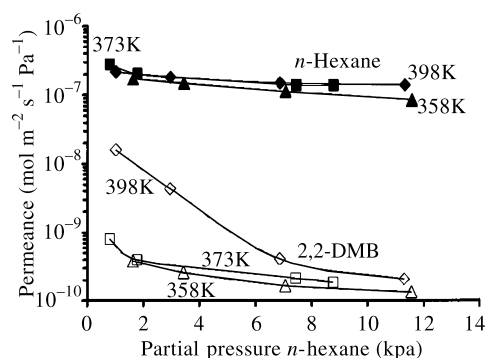


Figure 12.24 Permeance of *n*-hexane and 2,2-dimethylbutane in a 50:50 mixture through an MFI membrane as a function of feed *n*-hexane partial pressure; feed and permeate He carrier and are at atmospheric pressure on each side [68]. Reprinted with permission from C. J. Gump, R. D. Noble and J. L. Falconer, *I&EC Res.*, **38**, 2775–2781 (1999). Copyright (1999) American Chemical Society

Permeation measurements for straight-chain alkanes, branched alkanes and aromatic hydrocarbons through MFI membranes were reported by Funke *et al.* [72]. For the *n*-hexane–benzene pair, the ideal selectivity was close to unity but the mixture selectivity was as high as 219 at 363 K, again due to the ‘crowding-out’ effect. Increasing the temperature further predictably caused a decline in the separation factor. Sufficiently high fluxes were recorded to make some of these separations of practical interest.

Zeolite NaY membranes were also tested in the separation of C6–C8 hydrocarbons [5,73]. Nair *et al.* [5] reported separation factors as high as 150 for a 50:50 mixture of benzene and *n*-hexane, and as high as 50 for a 50:50 mixture of toluene and *n*-heptane with the aromatic component always being the selective penetrant. The separation factors for these two mixtures had opposite temperature-dependences, the first decreasing while the second increasing with temperature suggesting that separation in the first mixture was controlled mainly by adsorption, in the second mixture mainly by mobility. In both cases, however, the fluxes were rather low. Permeation measurements of single component and binary mixtures of the hydrocarbons *n*-hexane, 3-methylpentane, and 2,2-dimethylbutane were reported by Jeong *et al.* [73]. There was little difference in the adsorption isotherms of the three C6 components and the separation factor of binary mixtures was near unity. However, in benzene–alkane mixtures separation factors of 5–10 were obtained in favor of the more strongly adsorbed benzene.

Of considerable practical importance is the separation of the three xylene isomers, because only the *para*-isomer is useful as a feedstock for the important monomer phthalic anhydride. After considerable effort, MFI membranes with selectivity as high as 400 for the *para* isomer were prepared [5,31,51,69]. These high selectivities were achieved by eliminating the larger defects using ‘postsynthetic’ sealing with a silica sol, or by achieving crystal *b*-orientation and reducing defects as discussed earlier [31]. Otherwise, the fluxes through such defects would ‘overwhelm’ the low zeolitic fluxes. It should be mentioned that xylene feed pressures below 1 kPa were used in these experiments, giving high permeance but low flux. At higher feed

pressures, saturation may limit the attainable fluxes.

12.4.2.4 Separation by Pervaporation

This separation is based on the hydrophobic/hydrophilic property of the zeolite channels and the external crystal surfaces. Pervaporation is an attractive alternative to distillation, especially for separation of heat-sensitive, closely boiling or azeotropic mixtures. It has the additional advantages of lower energy consumption and simple, scaleable equipment. Zeolite membranes were found to have higher separation factors, as well as better chemical stability than polymeric membranes that have been tested in the same separations, but as mentioned in the introduction have considerably higher fabrication cost.

The majority of pervaporation studies using zeolite membranes were performed for water–organic mixtures such as alcohol–water and ketone–water. Two distinct types of separation are of interest. The first is to remove the organic (in the permeate stream) from relatively dilute aqueous mixtures, for the purpose of concentrating organics or purifying water. The second separation is to remove water (in the permeate stream) in order again to concentrate or purify the organic, as e.g. for azeotropic ethanol–water mixtures. The first separation can be carried out using MFI or some other hydrophobic membrane, while the second requires a hydrophilic membrane, typically zeolite A, X or Y.

Separation of dilute alcohol–water mixtures was the earliest pervaporation study using MFI membranes [74–76] and will serve to illustrate the key effects. The main point of interest is the dependence of flux and separation factor on feed temperature and composition. Figure 12.25 [74] shows fluxes and separation factors versus temperature for several dilute (1 mol%) alcohol–water mixtures. The separation is obviously controlled by preferential adsorption of the alcohols on the hydrophobic membrane. The dominant role of adsorption is also reflected in the separation factor increasing with the carbon number of the alcohol. The exception is isopropanol which has weaker adsorption because of its nonlinear molecular geometry. Both alcohol and water fluxes increase with temperature but the flux of the alcohol increases more slowly because of declining adsorption resulting in the separation

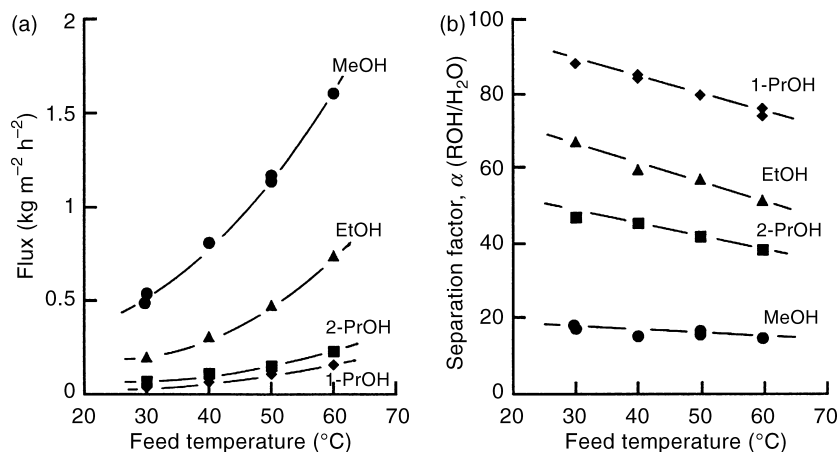


Figure 12.25 Separation of alcohol–water mixtures (1 mol% alcohol) by pervaporation using a zeolite NaA membrane: alcohol fluxes (a) and alcohol: water separation factors (b) as a function of temperature [74]. Reproduced by permission of the authors from T. Sano, Y. Kawakami, Y. Kiyozumi, D. Kitamoto and F. Mizukami, ‘Potentials of silicalite membranes for the separation of alcohol/water mixtures’, *Studies in Surface Science and Catalysis*, **84**, 1175–1182 (1994)

factor declining with the temperature. The dependence of flux and separation factor on feed composition is shown in Figure 12.26 [74]. The trend is opposite to that observed for several adsorption-controlled gas mixtures such as methane–butane. The separation factor passes through a

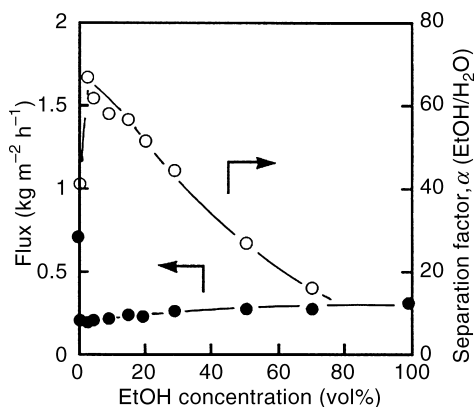


Figure 12.26 Separation of ethanol–water mixtures by pervaporation through a zeolite NaA membrane at 30 °C: ethanol flux and ethanol:water separation factor as a function of feed ethanol concentration [74]. Reproduced by permission of the authors from T. Sano, Y. Kawakami, Y. Kiyozumi, D. Kitamoto and F. Mizukami, ‘Potentials of silicalite membranes for the separation of alcohol/water mixtures’, *Studies in Surface Science and Catalysis*, **84**, 1175–1182 (1994)

maximum at an ethanol concentration of about 3% and subsequently declines with increasing ethanol mole fraction. To explain this unusual trend, it is recalled that the fluxes depend on fugacity differences rather than on concentration differences. Ethanol adsorption is near saturation so that there is only a modest increase of the fugacity gradient with increasing ethanol mole fraction in the feed. The water fugacity gradient on the other hand increases with increasing ethanol mole fraction due to the azeotropic geometry of the phase diagram. Attractive separation factors were measured for the alcohol–water mixtures, of about 20, 50 and 90 for methanol, ethanol and propanol, respectively, and, as expected, the alcohol fluxes declined with the carbon number. The fluxes were modest, in the range 0.1–1.5 kg/(m² h). Water–organic separations were also studied by using B- and Ge-substituted ZSM-5 membranes and compared to silicalite membranes. The B-ZSM-5 membrane yielded the highest methanol–water separation factor while the Ge-ZSM-5 membrane yielded the highest factors for ethanol–water and 2-propanol–water [26]. The fluxes were in the range of 0.1–0.3 kg/(m² h).

Other mixtures that have shown similar trends with respect to temperature and composition are acetone–water and methyl ethyl ketone–water [26,76,77]. High selectivities, about 200, were

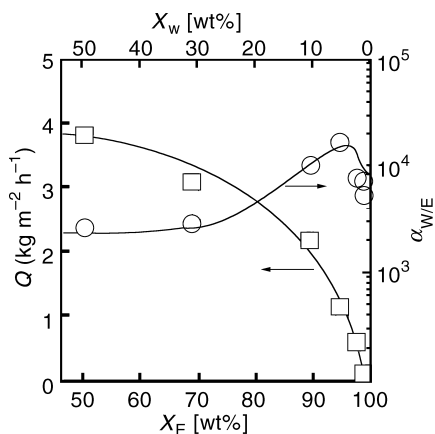


Figure 12.27 Separation of ethanol–water mixtures by pervaporation through a zeolite NaA membrane at 75 °C: ethanol flux and ethanol:water separation factor as a function of feed composition [81]. Reprinted with permission from K. Okamoto, H. Kita, K. Horii, K. Tanaka and M. Kondo, *I&EC Res.*, **40**, 163–175 (2001). Copyright (2001) American Chemical Society

obtained, but the organic fluxes were in most cases below $1 \text{ kg}/(\text{m}^2 \text{ h})$. Separation of aqueous mixtures of propane diol, glycerol and glucose has been studied with several types of membranes [79].

The second type of separation is also exemplified by alcohol–water mixtures, but this time water is to be removed in the permeate and the membrane of choice is the strongly hydrophilic zeolite NaA. A few years ago, good fluxes and extremely high separation factors were demonstrated for the separation of mixtures with $\sim 5\%$ water and after improvements in membrane preparation recent publications report excellent results in alcohol–water (alcohol: methanol, ethanol, *n*-propanol and *i*-propanol), acetone, dioxane, THF and dimethylformamide, the water always being the selective penetrant [80–82]. Figure 12.27 [81] shows the dependence of water flux and separation factor on feed composition. Similar to the trend of Figure 12.26, the separation factor is maximum at about 95% ethanol. As the water mole fraction increases beyond that point the separation factor declines, again based on the shape of the phase diagram. NaA membranes have been commercialized and at present are the only zeolite membranes that have been put into practical application.

A previous section dealt with the separation of C6 hydrocarbons by vapor permeation. The same separations can be carried out by pervaporation [4,82]. Comparison between the two operations should not be based on equal feed mole fractions but on the basis of fugacities. Maintaining equal fugacities, however, would require different temperatures so that direct comparison of experimental data is not meaningful.

12.5 Theory and Modeling of Transport in Zeolite Membranes

Transport in zeolites is a vast subject so that this section will only serve as a guide to relevant literature. Some introductory concepts of single component transport were presented in Section 12.4 without dealing with the temperature- and composition-dependence of the diffusion coefficients. These dependencies can be approached at several levels. Diffusion coefficients can be measured at different temperatures and occupancies (adsorbed concentration) and the results can be somehow correlated. Molecular simulation can be carried out using Monte Carlo techniques on lattice models or, more fundamentally but at great computational cost, using molecular dynamics on the actual crystal structure. Experiments and simulations provide valuable insight on the temperature- and occupancy-dependence of the diffusion coefficients, but cannot be extended over a wide range of conditions, even for the single component range. Extension of these approaches to multicomponent transport would be extremely laborious experimentally and computationally. An approximate but physically meaningful theory for single component transport has been lucidly presented in a number of references [83–86]. Tsikoyannis and Wei [83] formulated lattice models of single component and multicomponent transport by means of the Masters equation and developed Monte Carlo and approximate analytical solutions including a few adjustable parameters. The solutions provide useful insight on the dependence on occupancy. Experimental results and comparisons with theory are given in Tsikoyannis and Wei [84].

An approximate theory treating explicitly the zeolite structure, the molecular size and the zeolite–guest molecule interaction is presented in Xiao and Wei [85]. This reference is a must for any student or researcher of transport in zeolites.

Two types of sites were distinguished: channels (e.g. in MFI) and cages (e.g. in A) or channel intersections in MFI. These are modeled as cylindrical and spherical cavities, respectively, and their dimensions are assigned from known structural data. For nonpolar molecules, depending on the ratio of molecular diameter to channel diameter λ , diffusion is classified as Knudsen ($\lambda < 0.7$) or configurational ($\lambda > 0.9$) with some transition between the two. Unlike Knudsen diffusion, configurational diffusion is activated with activation energies that vary widely from system to system. The coefficient of configurational diffusion is further expressed as the product of an Arrhenius factor and a frequency factor. The activation energy is estimated from structural data using the value of the previously defined ratio λ . The frequency factor is estimated without introducing adjustable parameters by making a further distinction between the type of adsorption site, leading to the ‘gas translation model’ and the ‘solid vibration model’. These general results are applicable at the limit of low occupancy. Extension to higher occupancy involving consideration of attractive or repulsive interactions between adsorbed molecules was made by utilizing the approach of Tsikoyannis and Wei [83]. The estimated diffusion coefficients, along with experimental adsorption isotherms, were used to calculate uptake of several hydrocarbons in MFI powder at different temperatures and pressures and gave good agreement with thermogravimetric uptake measurements [86].

The theoretical approach becomes difficult to extend to multicomponent mixtures and polar molecules. A phenomenological theory based on momentum transfer considerations was developed over several years by research groups at the University of Amsterdam and at the Delft University of Technology [87–92]. Multicomponent transport was described by these researchers using ‘Generalized Maxwell–Stefan’ (GMS) equations [87]:

$$-\rho \frac{\theta_i}{RT} \nabla \mu_i = \sum_{\substack{j \neq i \\ j=1}}^n \frac{q_j N_i - q_i N_j}{q_i^{\text{sat}} q_j^{\text{sat}} D_{ij}} + \frac{N_i}{q_i^{\text{sat}} D_i}, \quad i = 1, 2, \dots, n \quad (12.15)$$

where θ_i is the fraction of sites occupied by component i , ρ is the density of the solid, q_i is the adsorbed amount of component i in moles per

unit mass of zeolite and q_i^{sat} is the maximum possible adsorbed amount of i (at saturation). Furthermore, μ_i is the chemical potential of i , and D_i and D_{ij} are the GMS or ‘corrected’ diffusion coefficients. Of these, D_i is the diffusion coefficient for single component i and differs from the Fick diffusion coefficient introduced in Equation (12.7). D_{ij} is a binary diffusion coefficient (also known as the interchange coefficient) describing the interaction between adsorbed species i and j . Finally, N_i are the molar fluxes. The gradient of μ_i can be written as:

$$\frac{\theta_i}{RT} \nabla \mu_i = \sum_{j=1}^n \Gamma_{ij} \nabla \theta_j, \quad \Gamma_{ij} \equiv \frac{\theta_i}{p_i} \frac{\partial p_i}{\partial \theta_j}, \quad i, j = 1, n \quad (12.16)$$

where now the coefficients Γ_{ij} are thermodynamic parameters that can be calculated from the multicomponent adsorption isotherms. The objective is to solve Equations (12.15) and (12.16) for the fluxes N_i in terms of the occupancies θ_j . The information needed for this purpose is single and multicomponent adsorption isotherms, and the GMS diffusion coefficients. The isotherms employed in van den Broeke *et al.* [91] assume two distinct adsorption sites (e.g. channels and channel intersections) with different single-component saturation amounts. Multicomponent isotherms are based on single-component isotherms using suitable models [91,92]. The GMS diffusion coefficients are treated as adjustable parameters, where D_i must be estimated from experimental data, while the D_{ij} values are obtained by empirical correlations in terms of D_i and D_j . The GMS model was successfully applied to interpret measurements of membrane transport for hydrocarbons and other gases, single and binary [89–92]. For many membranes, it is necessary to consider the defects as well as the zeolitic pathways for modeling transport. Some first steps in this direction were reported by Nelson *et al.* [93].

12.6 Concluding Remarks

Preparation of zeolite membranes of satisfactory permeance and selectivity requires careful attention to several details such as preparation of the support surface, uniform seeding and slow calcination. In several reported studies, reproducibility has been poor and several reaction periods were

required to achieve sufficient selectivity. Scale-up for industrial applications would require some standardization of conditions and additional attention to fluid flow and mass transfer during membrane growth. Recently, technology for extruding alumina hollow fibers was reported, promising future availability of relatively inexpensive supports and high packing density of membrane modules [94].

Within each type of zeolite membranes there is considerable variation in permeation properties due to differences in crystal orientation, defect size distribution, type of charge-balancing ion and other structural details. These differences are frustrating to the researcher but expand the range of possible applications.

At this present time, the only commercialized membrane is zeolite A for water–organics separation by pervaporation. Liquids separation in general appears a promising area of application. Certain hydrocarbon separations like that between normal and branched alkanes and aromatics versus aliphatics also offer some possibilities. Separation of C1–C4 hydrocarbons from hydrogen in hydrotreating mixtures is also promising. A whole class of applications that has not been considered in this review is that of membrane reactors where the zeolite can serve only as a membrane or as a membrane and a catalyst simultaneously.

Acknowledgements

Preparation of this paper was supported by a grant from the National Science Foundation.

References

- [1] J. Caro, M. Noack, P. Kolsch and R. Schafer, 'Zeolite membranes – state of their development and perspective', *Micropor. Mesopor. Mater.*, **38**, 3–24 (2000).
- [2] Y. S. Lin, I. Kumakiri, B. N. Nair and H. Alsayouri, 'Microporous inorganic membranes', *Sepr. Purif. Methods*, **31**, 229–379 (2002).
- [3] K. Okamoto, H. Kita, K. Horii, K. Tanaka and M. Kondo, 'Zeolite NaA membrane: preparation, single-gas permeation and pervaporation and vapor permeation of water/organic liquid mixtures', *I&EC Res.*, **40**, 163–175 (2001).
- [4] C. L. Flanders, V. A. Tuan, R. D. Noble and J. L. Falconer, 'Separation of C-6 isomers by vapor permeation and pervaporation through ZSM-5 membranes', *J. Membr. Sci.*, **176**, 43–53 (2000).
- [5] S. Nair, Z. Lai, V. Nicolakis, G. Xomeritakis, G. Bonilla and M. Tsapatsis, 'Separation of close-boiling hydrocarbon mixtures by MFI and FAU membranes made by secondary growth', *Micropor. Mesopor. Mater.*, **48**, 219–228 (2001).
- [6] K. Kusakabe, T. Kuroda, A. Murata and S. Morooka, 'Formation of a Y-type zeolite membrane on a porous alpha-alumina tube for gas separation', *I&EC Res.*, **36**, 649–655 (1997).
- [7] R. Lai and G. R. Gavalas, 'ZSM-5 membrane synthesis with organic-free mixtures', *Micropor. Mesopor. Mater.*, **38**, 239–245 (2000).
- [8] R. K. Iler, *The Chemistry of Silica*, John Wiley & Sons, Inc., New York, NY, USA (1979).
- [9] D. W. Breck, *Zeolite Molecular Sieves*, Krieger, Malabar, India (1974).
- [10] R. Szostak, *Molecular Sieves, Principles of Synthesis and Identification*, Van Nostrand Reinhold, New York, NY, USA (1989).
- [11] S. L. Burkett and M. E. Davis, 'Mechanism of structure direction in the synthesis of Si-ZSM-5: an investigation by intermolecular ^1H - ^{29}Si CP MAS NMR', *J. Phys. Chem.*, **98**, 4647–4653 (1994).
- [12] S. L. Burkett and M. E. Davis, 'Mechanism of structure direction in the synthesis of pure silica zeolites 1. Synthesis of TPA/Si-ZSM-5', *Chem. Mater.*, **7**, 920–928 (1995).
- [13] S. L. Burkett and M. E. Davis, 'Mechanism of structure direction in the synthesis of pure-silica zeolites 2. Hydrophobic hydration and structural specificity', *Chem. Mater.*, **7**, 1453–1463 (1995).
- [14] W. H. Dokter, H. F. van Garderen, T. P. M. Beelen, R. A. van Santen and W. Bras, 'Homogeneous versus heterogeneous zeolite nucleation', *Angew. Chem. Int. Ed. Engl.*, **34**, 73–75 (1995).
- [15] Q. Li, D. Creaser and J. Sterte, 'The nucleation period for TPA-silicalite-1 crystallization determined by a two-stage varying-temperature synthesis', *Micropor. Mesopor. Mater.*, **31**, 141–150 (1999).
- [16] C. E. A. Kirschock, R. Ravishankar, L. Van Looveren, P. A. Jacobs and J. A. J. Martens, 'Mechanism of transformation of precursors into nanoslabs in the early stages of MFI and MEL zeolite formation from TPAOH–TEOS–H₂O mixtures', *J. Phys. Chem. B*, **103**, 4972–4978 (1999).
- [17] M. A. Uguina, A. de Lucas, F. Ruiz and D. P. Serrano, 'Synthesis of ZSM-5 from ethanol-containing systems. Influence of the gel composition', *I&EC Res.*, **34**, 451–456 (1995).
- [18] M. Pilar-Bernal, G. Xomeritakis and M. Tsapatsis, 'Tubular MFI zeolite membranes by secondary (seeded) growth', *Catal. Today*, **67**, 101–107 (2001).
- [19] X. Lin, H. Kita and K. Okamoto, 'Silicalite membrane preparation, characterization and separation performance', *I&EC Res.*, **40**, 4069–4078 (2001).

- [20] A. Giroir-fendler, Julbe, J. D. F. Ramsay and J. A. Dalmon, 'Porous inorganic materials and structures, especially membranes, and their manufacture', *French Patent FR 2 719 238-A1* (1994).
- [21] J. Hedlund, J. Sterte, M. Anthonis, A.-J. Bons, B. Carstensen, N. Corcoran, D. Cox, H. Deckman, W. De Gijnst, P.-P. de Moor, F. Lai, J. McHenry, W. Mortier, J. Reinoso and J. Peters, 'High-flux MFI membranes', *Micropor. Mesopor. Mater.*, **52**, 179–189 (2002).
- [22] Z. A. E. P. Vroon, K. Keizer, A. J. Burggraaf and H. J. Verweij, 'Preparation and characterization of thin zeolite MFI membranes on porous supports', *J. Membr. Sci.*, **144**, 65–76 (1998).
- [23] J. Coronas, J. L. Falconer and R. D. Noble, 'Characterization and permeation properties of ZSM-5 tubular membranes', *AIChE. J.*, **43**, 1797–1812 (1997).
- [24] B.-S. Kang and G. R. Gavalas, 'Intrapore synthesis of silicalite membranes at temperatures below 100 °C', *I&EC Res.*, **41**, 3145–3150 (2001).
- [25] V. A. Tuan, J. L. Falconer and R. D. Noble, 'Isomorphous substitution of Al, Fe, B and Ge into MFI-zeolite membranes', *Micropor. Mesopor. Mater.*, **41**, 269–280 (2000).
- [26] V. A. Tuan, S. Li, J. L. Falconer and R. D. Noble, 'Separating organics from water by pervaporation with isomorphously substituted MFI zeolite membranes', *J. Membr. Sci.*, **196**, 111–123 (2002).
- [27] J. C. Jansen, W. Nugroho H. van Bekkum, 'Controlled growth of thin films of molecular sieves on various supports', in *Proceedings of the Ninth International Zeolite Conference*, Butterworth-Heinemann, Oxford, UK, pp. 247–254 (1993).
- [28] J. H. Koegler, H. van Bekkum and J. C. Jansen, 'Growth model of oriented crystals of zeolite Si-ZSM-5', *Zeolites*, **19**, 262–269 (1997).
- [29] R. Lai, Y. Yan and G. R. Gavalas, 'Growth of ZSM-5 films on alumina and other surfaces', *Micropor. Mesopor. Mater.*, **37**, 9–19 (2000).
- [30] Y. Yan, M. E. Davis and G. R. Gavalas, 'Preparation of highly selective zeolite ZSM-5 membranes by a post-synthetic coking treatment', *J. Membr. Sci.*, **123**, 95–103 (1997).
- [31] Z. Lai, G. Bonilla, I. Diaz, G. Nery, K. Sujaoti, M. A. Amat, E. Kokkoli, O. Terasaki, R. W. Thompson, M. Tsapatsis and D. G. Vlachos, 'Microstructural optimization of a zeolite membrane for organic vapor separation', *Science*, **300**, 456–460 (2003).
- [32] E. R. Geus and H. van Bekkum, 'Calcination of large MFI-type single crystals, Part 2', *Zeolites*, **15**, 333–341 (1994).
- [33] M. J. den Exter, H. van Bekkum, C. J. M. Rijn, F. Kapteijn, J. A. Moulijn, H. Schellevis and C. I. N. Beenaker, 'Stability of oriented silicalite-1 films in view of zeolite membrane preparation', *Zeolites*, **19**, 13–20 (1997).
- [34] J. Dong, Y. S. Lin, M. Z.-C. Hu, R. A. Peascoe and E. A. Payzant, 'Template-removal-associated microstructural development of porous-ceramic-supported MFI zeolite membranes', *Micropor. Mesopor. Mater.*, **34**, 241–253 (2000).
- [35] A. E. Persson, B. J. Schoeman, J. Sterte and J.-E. Otterstedt, 'The synthesis of discrete colloidal particles of TPA-silicalite-1', *Zeolites*, **14**, 557–567 (1994).
- [36] M. C. Lovallo and M. Tsapatsis, 'Preferentially oriented submicron silicalite membranes', *AIChE J.*, **42**, 3020–3029 (1996).
- [37] R. Lai and G. R. Gavalas, 'Surface seeding in ZSM-5 membrane preparation', *I&EC Res.*, **37**, 4275–4283 (1998).
- [38] K. Ha, Y.-J. Lee, H. J. Lee and K. B. Yoon, 'Facile assembly of zeolite monolayers on glass, silica, alumina and other zeolites using 3-halopropylsilyl reagents as covalent linkers', *Adv. Mater.*, **12**, 1114–1117 (2000).
- [39] G. Xomeritakis, A. Gouzinis, S. Nair, T. Okubo, M. He, R. Overney and M. Tsapatsis, 'Growth, microstructure and permeation properties of supported zeolite (MFI) films and membranes prepared by secondary growth', *Chem. Eng. Sci.*, **54**, 3521–3531 (1999).
- [40] I. Kumakiri, T. Yamaguchi and S. Nakao, 'Preparation of zeolite A and Faujasite membranes from a clear solution', *I&EC Res.*, **38**, 4682–4688 (1999).
- [41] X. Xu, W. Yang, J. Liu, X. Chen, L. Lin, N. Stroh and H. Brunner, 'Synthesis and gas permeation properties of an NaA zeolite membrane', *J. Chem. Soc. Chem. Commun.*, 603–604 (2000).
- [42] X. Xu, W. Yang, J. Liu and L. Lin, 'Synthesis of NaA zeolite membranes from clear solution', *Micropor. Mesopor. Mater.*, **43**, 299–311 (2001).
- [43] K. Aoki, K. Kusakabe and S. Morooka, 'Separation of gases with an A-type zeolite membrane', *I&EC Res.*, **39**, 2245–2251 (2000).
- [44] K. Aoki, K. Kusakabe and S. Morooka, 'Preparation of oriented A-type zeolite membranes', *AIChE J.*, **46**, 221–224 (2000).
- [45] X. Xu, W. Yang, J. Liu, X. Chen and L. Lin, 'Synthesis of NaA zeolite membrane by microwave heating', *Sepr Purif. Technol.*, **25**, 241–249 (2001).
- [46] H. Kita, K. Fuchida, T. Horita, H. Asamura and K. Okamoto, 'Preparation of Faujasite membranes and their permeation properties', *Sepr Purif. Technol.*, **25**, 261–268 (2001).
- [47] K. Kusakabe, T. Kuroda and S. Morooka, 'Separation of carbon dioxide from nitrogen using ion-exchanged Faujasite-type zeolite membranes

- formed on porous support tubes', *J. Membr. Sci.*, **148**, 13–23 (1998).
- [48] I. Kumakiri, T. Yamaguchi and S. Nakao, 'Preparation of zeolite A and Faujasite membranes from a clear solution', *I&EC Res.*, **38**, 4682–4688 (1999).
- [49] G. Guan, K. Kusakabe and S. Morooka, 'Separation of N₂ from O₂ and other gases using FAU-type zeolite membranes', *J. Chem. Eng. Jpn.*, **34**, 990–997 (2001).
- [50] S. Mintova, J. Hedlund, V. Valtchev, B. J. Schoeman and B. J. Sterte, 'ZSM-5 films prepared from template-free precursors', *J. Mater. Chem.*, **8**, 2217–2221 (1998).
- [51] G. Xomeritakis, Z. Lai and M. Tsapatsis, 'Separation of xylene isomer vapors with oriented MFI membranes made by seeded growth', *I&EC Res.*, **40**, 544–552 (2001).
- [52] M. C. Lovallo, A. Gouzinis and M. Tsapatsis, 'Synthesis and characterization of oriented MFI membranes prepared by secondary growth', *AIChE J.*, **44**, 1903–1913 (1998).
- [53] A. Gouzinis and M. Tsapatsis, 'On the preferred orientation and microstructural manipulation of molecular sieve films prepared by secondary growth', *Chem. Mater.*, **10**, 2497–2504 (1998).
- [54] M. Noack, P. Kolsch, J. Caro, M. Schneider, P. Toussaint and I. Sieber, 'MFI membranes of different Si/Al ratios for pervaporation and steam permeation', *Micropor. Mesopor. Mater.*, **35–36**, 253–265 (2000).
- [55] Y. Sasaki, W. Shimizu, Y. Ando and H. Saka, 'Microstructure analysis with TEM for zeolite layer formed in pore of porous alumina substrate', *Micropor. Mesopor. Mater.*, **40**, 63–71 (2000).
- [56] G. Bonilla, M. Tsapatsis, D. G. Vlachos and G. Xomeritakis, 'Fluorescence confocal optical microscopy imaging of the grain boundary structure of zeolite MFI membranes made by secondary (seeded) growth', *J. Membr. Sci.* **182**, 103–109 (2001).
- [57] A. Julbe and J. D. F. Ramsay, 'Methods for the characterization of porous structure in membrane materials', in A. J. Burggraaf and L. Cot (Eds), *Fundamentals of Inorganic Membrane Science and Technology*, Elsevier, Amsterdam, The Netherlands, pp. 67–117 (1996).
- [58] S. G. Fegan and B. M. Lowe, 'Effect of alkalinity on the crystallization of silicalite-1 precursors', *J. Chem. Soc., Faraday Trans. 1*, **82**, 785–799 (1986).
- [59] J. M. van de Graaf, F. Kapteijn and J. A. Moulijn, 'Methodological and operational aspects of permeation measurements on silicalite-1 membranes', *J. Membr. Sci.*, **144**, 87–104 (1998).
- [60] K. Aoki, V. A. Tuan, J. L. Falconer and R. D. Noble, 'Gas permeation properties of ion-exchanged ZSM-5 zeolite membranes', *Microp. Mesopor. Mater.*, **39**, 485–492 (2000).
- [61] W. J. W. Bakker, F. Kapteijn, J. Poppe and J. A. Moulijn, 'Permeation characteristics of a metal-supported silicalite-1 zeolite membrane', *J. Membr. Sci.*, **117**, 57–78 (1996).
- [62] M. Arruebo, J. Coronas, M. Menendez and J. Santamaria, 'Separation of hydrocarbons from natural gas using silicalite membranes', *Sept. Purif. Technol.*, **25**, 275–286 (2001).
- [63] F. Kapteijn, W. J. W. Bakker, J. van der Graaf, G. Zheng, J. Poppe and J. A. Moulijn, 'Permeation and separation behavior of a silicalite-1 membrane', *Catal. Today*, **25**, 213–218 (1995).
- [64] J. Dong, Y. S. Lin and W. Lin, 'Multicomponent hydrogen/hydrocarbon separation by MFI-type zeolite membrane', *AIChE J.*, **46**, 1957–1966 (2000).
- [65] Z. A. E. P. Vroon, K. Keizer, M. J. Gilde, H. Verweij and A. J. Burggraaf, 'Transport properties of alkanes through ceramic thin zeolite MFI membranes', *J. Membr. Sci.*, **113**, 293–300 (1996).
- [66] V. A. Tuan, J. L. Falconer and R. D. Noble, 'Alkali-free ZSM-5 membranes: Preparation conditions and separation performance', *I&EC Res.*, **38**, 3635–3646 (1999).
- [67] J. Coronas, R. D. Noble and J. L. Falconer, 'Separations of C₄ and C₆ isomers in ZSM-5 tubular membranes', *I&EC Res.*, **37**, 166–176 (1998).
- [68] C. J. Gump, R. D. Noble and J. L. Falconer, 'Separation of hexane isomers through nonzeolite pores in ZSM-5 zeolite membranes', *I&EC Res.*, **38**, 2775–2781 (1999).
- [69] G. Xomeritakis, S. Nair and M. Tsapatsis, 'Transport properties of alumina-supported MFI membranes made by secondary (seeded) growth', *Micropor. Mesopor. Mater.*, **38**, 61–73 (2000).
- [70] H. H. Funke, M. G. Kovalchick, J. L. Falconer and R. D. Noble, 'Separation of hydrocarbon isomer vapors with silicalite zeolite membranes', *I&EC Res.*, **35**, 1575–1582 (1996).
- [71] H. H. Funke, A. M. Argo, C. D. Baertsch, J. L. Falconer and R. D. Noble, 'Separation of close-boiling hydrocarbons with silicalite zeolite membranes', *J. Chem. Soc., Faraday Trans.*, **92**, 2499–2502 (1996).
- [72] H. H. Funke, A. M. Argo, J. L. Falconer and R. D. Noble, 'Separations of cyclic, branched and linear hydrocarbon mixtures through silicalite membranes', *I&EC Res.*, **36**, 137–143 (1997).
- [73] B. H. Jeong, Y. Hasegawa, K. I. Sotowa, K. Kusakabe and S. Morooka, 'Vapor permeation properties of an NaY-type zeolite membrane for normal and branched hexanes', *I&EC Res.*, **41**, 1768–1773 (2002).

- [74] T. Sano, Y. Kawakami, Y. Kiyozumi, H. Yanagishita, D. Kitamoto and F. Mizukami, 'Potentials of silicalite membranes for the separation of alcohol/water mixtures', *Studies Surface Sci. Catal.*, **84**, 1175–1182 (1994).
- [75] T. Sano, H. Yanagishita, Y. Kiyozumi, F. Mizukami and K. Haraya, 'Separation of ethanol/water mixture by silicalite membrane on pervaporation', *J. Membr. Sci.*, **95**, 221–228 (1994).
- [76] Q. Liu, R. D. Noble, J. L. Falconer and H. H. Funke, 'Organics/water separation by pervaporation with a zeolite membrane', *J. Membr. Sci.*, **117**, 163–174 (1996).
- [77] J. F. Smetana, J. L. Falconer and R. D. Noble, 'Separation of methyl ethyl ketone from water by pervaporation using a silicalite membrane', *J. Membr. Sci.*, **114**, 127–130 (1996).
- [78] X. Lin, H. Kita and K. Okamoto, 'Silicalite membrane preparation, characterization and separation performance', *I&EC Res.*, **40**, 4069–4078 (2001).
- [79] S. Li, V. A. Tuan, J. L. Falconer and R. D. Noble, 'Effects of zeolite membrane structure on the separation of 1,3-propanediol from glycerol and glucose by pervaporation', *Chem. Mater.*, **13**, 1865–1873 (2001).
- [80] M. Kondo, M. Komori, H. Kita and K. Okamoto, 'Tubular-type-pervaporation module with zeolite NaA membrane', *J. membr. Sci.*, **133**, 133–141 (1997).
- [81] K. Okamoto, H. Kita, K. Horii, K. Tanaka and M. Kondo, 'Zeolite NaA membrane: preparation, single-gas permeation, and pervaporation and vapor permeation of water/organic liquid mixtures', *I&EC Res.*, **40**, 163–175 (2001).
- [82] H. Kita, K. Fuchida, T. Horita, H. Asamura and K. Okamoto, 'Preparation of Faujasite membranes and their permeation properties', *Seppn Purif. Technol.*, **25**, 261–268 (2001).
- [83] J. G. Tsikoyannis and J. Wei, 'Diffusion and reaction in high-occupancy zeolite catalysts – I. A stochastic theory', *Chem. Eng. Sci.*, **46**, 233–253 (1991).
- [84] J. G. Tsikoyannis and J. Wei, 'Diffusion and reaction in high-occupancy zeolite catalysts – II. Experimental results', *Chem. Eng. Sci.*, **46**, 255–264 (1991).
- [85] J. Xiao and J. Wei, 'Diffusion mechanism of hydrocarbons in zeolites–I. Theory', *Chem. Eng. Sci.*, **47**, 1123–1142 (1992).
- [86] J. Xiao and J. Wei, 'Diffusion mechanism of hydrocarbons in zeolites – II. Analysis of experimental observations', *Chem. Eng. Sci.*, **47**, 1143–1159 (1992).
- [87] R. Krishna, 'Multicomponent surface diffusion of adsorbed species: a description based on the generalized Maxwell–Stefan equations', *Chem. Eng. Sci.*, **45**, 1779–1791 (1990).
- [88] L. J. P. van den Broeke, 'Simulation of diffusion in zeolitic structures', *AIChE. J.*, **41**, 2399–2414 (1995).
- [89] F. Kapteijn, J. A. Moulijn and R. Krishna, 'The generalized Maxwell–Stefan model for diffusion in zeolites: sorbate molecules with different saturation loadings', *Chem. Eng. Sci.*, **55**, 2923–2930 (2000).
- [90] R. Krishna, 'Diffusion of binary mixtures across zeolite membranes: entropy effects on permeation selectivity', *Int. Commun. Heat Mass Transfer*, **28**, 337–346 (2001).
- [91] L. J. P. van den Broeke, W. J. W. Bakker, F. Kapteijn and J. A. Moulijn, 'Binary permeation through a silicalite-1 membrane', *AIChE. J.*, **45**, 976–985 (1999).
- [92] R. Krishna and D. Paschek, 'Permeation of hexane isomers across ZSM-5 zeolite membranes', *I&EC Res.*, **39**, 2618–2622 (2000).
- [93] P. H. Nelson, M. Tsapatsis and S. M. Auerbach, 'Modeling permeation through anisotropic zeolite membranes with nanoscopic defects', *J. Membr. Sci.*, **184**, 245–255 (2001).
- [94] *Seventh International Conference on Inorganic Membranes*, June 24–27, Dalian, China (2002).

Gas and Vapor Separation Membranes Based on Carbon Membranes

Hidetoshi Kita

13.1 Introduction

The development of membrane processes for the separation of gas mixtures has made remarkable progress during the last two decades and there is growing interest in using a molecular sieving membrane to separate gas and/or vapor mixtures with very similar molecular dimensions. Figure 13.1 illustrates the separation mechanism through microporous membranes. Four types of mechanisms can be utilized to effect separation of gas or vapor molecules through porous membranes [1–3]. In some cases, gas molecules can permeate through the membrane by more than one mechanism. If the pore size of the membrane is smaller than 0.1 μm , the pore diameter is the same as or smaller than the mean free path of the gas molecules. Then, separation through this membrane is governed by the Knudsen diffusion regime, where the permeation rate of a gas molecule is inversely proportional to the square root of its molecular weight. Thus, the selectivity due to Knudsen diffusion is given by $\alpha_{ij} = (M_j/M_i)^{1/2}$ and an economical separation cannot be obtained because the molecular weight difference between various gas mixture is usually small. If gas molecules can adsorb on the pore wall of the membrane and migrate along the surface of the pore, surface diffusion can occur in combination with Knudsen diffusion. Surface diffusion becomes important when the pore diameter drops in 1–2 nm, where the surface area of the pore wall increases and significant amounts of gas mole-

cules adsorb onto the pore wall. There are many examples of surface diffusion through porous membranes [4]. If the gas molecules are condensable, the pores can completely fill with these molecules, resulting in capillary condensation or micropore filling into the membrane pores. In this case, extremely high selectivity in favor of the more condensable component is possible due to blocking the permeation of the non-condensable gases. When the pore size of the microporous membrane are of gas molecular size (~ 0.5 nm), gases are separated by a molecular sieving effect. There are several materials that exhibit molecular sieving properties, such as zeolite, sol-gel derived silica or alumina, microporous glass, carbon, etc. Among these, carbon molecular sieves produced from the pyrolysis of polymeric materials have been studied extensively in adsorption application. The carbon membranes were first studied by Barrer and coworkers [5,6] from the early 1960s by compressing high surface-area microporous carbon powders at very high pressures. More recently, various types of carbon membranes have been prepared by pyrolyzing polymeric materials since these membranes have been proved to have high selectivity for gas separation by Koresh and Soffer [7,8]. The polymeric precursors of carbon membranes that have been reported to date mainly include polyacrylonitrile, poly(furfuryl alcohol), polyimides, poly(vinylidene chloride) copolymers, phenolic resin, cellulose derivatives, etc. The gas separation performance of carbon membranes largely

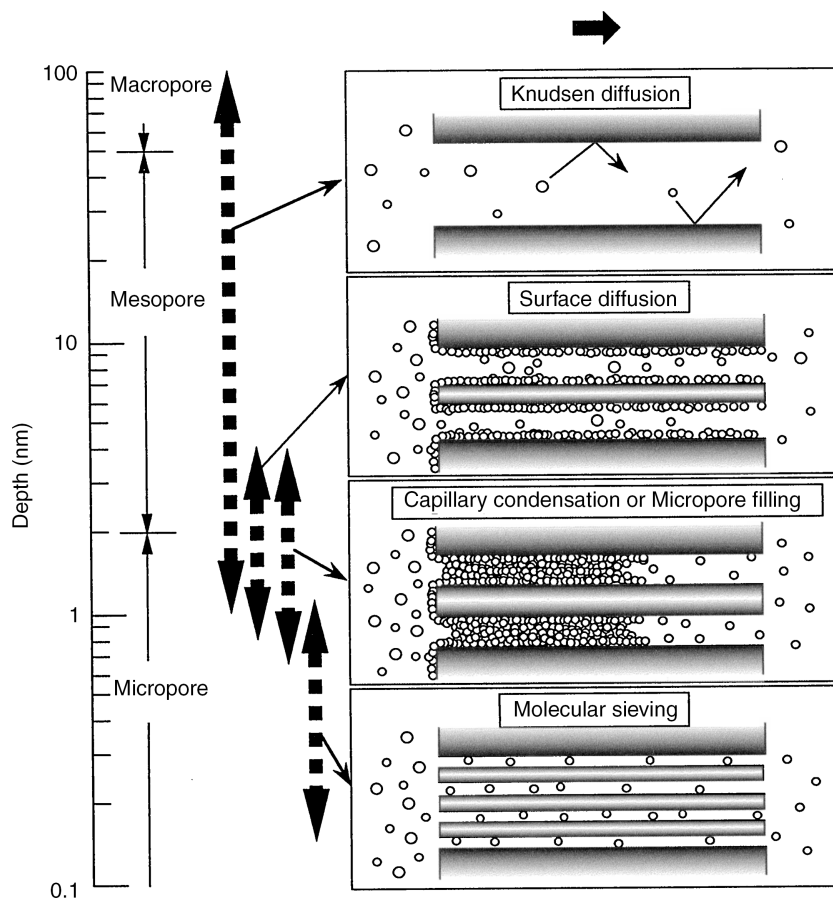


Figure 13.1 Separation mechanisms in porous membranes

depends on the polymeric precursor, membrane formation method (composite or hollow fiber), pyrolysis variable (heating and cooling rate, pyrolysis atmosphere, flow rate of purge gas, pyrolysis temperature and pyrolysis holding time) and post-treatment method. This chapter describes the preparation of high-performance carbon membranes and their permeation characteristics.

13.2 Preparation and Characterization of Carbon Membranes

13.2.1 Self-supported Carbon Membranes

13.2.1.1 Flat Sheet Membranes

Carbon membranes are attractive candidates in the field of gas separation, in terms of both high separation performance and high chemical stabi-

lity. Figure 13.2 shows plots of the permeability ratio of CO_2/CH_4 versus CO_2 permeability for self-supported flat sheet carbon membranes derived from polyimides and polypyrrolone of about $50\ \mu\text{m}$ thickness by heating at $700\ ^\circ\text{C}$ for 1 h. The polymer membranes are converted to carbon by pyrolysis at high temperature and become more permeable than the precursor polymers. The understanding of the thermal decomposition and gas-evolving properties of precursors is instructive to determine the appropriate pyrolysis conditions. Thermogravimetry–mass spectrometry (TG–MS) has been carried out for several polyimides and polypyrrolone precursors derived from 3,3',4,4'-diphenylhexafluoroisopropylidene tetracarboxylic dianhydride (6FDA), 3,3',4,4'-biphenyltetracarboxylic dianhydride (BPDA), 3,3',4,4'-benzophenone tetracarboxylic dianhy-

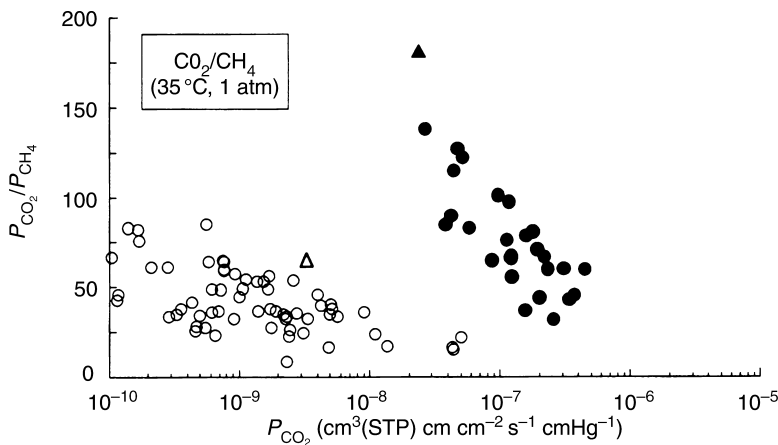


Figure 13.2 Membrane performance for CO_2/CH_4 separation: \circ , polyimides; Δ , polypyrrolones; \bullet , \blacktriangle , carbonized polyimides and polypyrrolones at 700°C for 1 h

dride (BTDA) or pyromellitic dianhydride (PMDA) with several aromatic diamines [9–11].

Figure 13.3 shows thermograms of 6FDA, BPDA, BTDA and PMDA–polypyrrolone membranes heated at a heating rate of $5^\circ\text{C}/\text{min}$. Under a nitrogen atmosphere, polyimides and polypyrrolones exhibited excellent stability up to 500°C without weight loss of the membrane, and the weight of BPDA, BTDA and PMDA

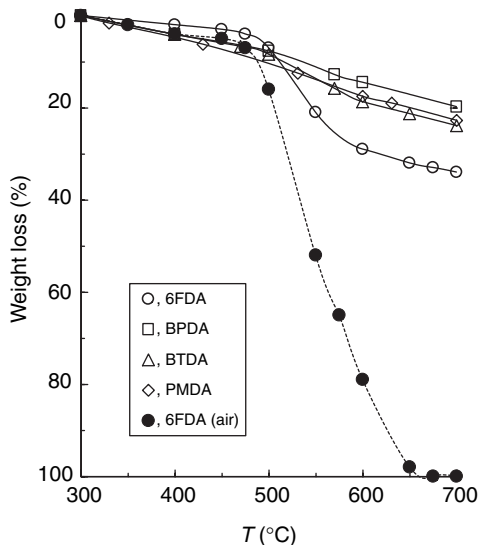


Figure 13.3 Thermograms of 6FDA, BPDA, BTDA and PMDA polyimide membranes in N_2

membranes decreased by approximately 20 % in the range $500\text{--}700^\circ\text{C}$, while the weight loss of the 6FDA membrane was larger than the others. On the other hand, all of the membranes rapidly degrade at about 650°C when heated in air. The gaseous products evolved from the 6FDA membrane in the range $500\text{--}700^\circ\text{C}$ included carbon monoxide, carbon dioxide, hydrogen fluoride and carbon tetrafluoride, with traces of ammonia and hydrogen cyanide. Elemental analysis data of the heat-treated 6FDA membrane showed that the oxygen and fluorine contents decrease and the carbon content increases significantly at $500\text{--}600^\circ\text{C}$, and the nitrogen content is almost constant, as shown in Table 13.1. Decreasing oxygen and fluorine contents of the 6FDA membrane at $500\text{--}600^\circ\text{C}$ can be explained by cleavage of the hexafluoroisopropylidene group and cyclic imide group. Cleavage of the hexafluoroisopropylidene group leads to evolution of HF and CF_4 . The cleavage of the cyclic imide group leads to evolution of CO and formation of cyclic imidazole, while cleavage of cyclic imidazole leads to evolution of CO and formation of nitrile groups. The presence of nitrile groups in the membranes pyrolyzed at $500\text{--}600^\circ\text{C}$ was confirmed from IR spectra [12].

The microstructure of the pyrolyzed membranes develops by the small gaseous molecules channeling their way out of the membrane matrix by the pyrolysis process. The adsorption and desorption isotherms of N_2 for the carbonized

Table 13.1 Characterization of the precursor and carbonized membranes of polyimide (6FDA-mPD) and polypyrrolone (6FDA-DABZ)

Membrane ^a	Density (g/cm ³)	Micropore volume (cm ³ /g)	Atom content (wt%)			
			C	H	N	O, F
<i>6FDA-mPD</i>						
Precursor	1.475	—	58	2	5	35
Pyrolyzed at 500 °C	1.41	0.21	70	3	6	21
Pyrolyzed at 700 °C	1.53	0.22	78	3	5	14
<i>6FDA-DABZ</i>						
Precursor	1.412	—	62	2	10	26
Pyrolyzed at 500 °C	1.40	0.22	68	2	10	20
Pyrolyzed at 700 °C	1.58	0.24	80	1	9	10

^am-PD, *m*-phenylenediamine; DABZ, 3,3'-diaminobenzidine.

polyimide and polypyrrolone membranes belonged to a Type 1 sorption isotherm without hysteresis in the desorption isotherms, indicated by no capillary condensation [11]. The adsorption amounts were larger for the membranes pyrolyzed at a higher temperature. The micropore volumes determined from CO₂ adsorption by using the Dubinin–Radushkevich equation [13] increased slightly with increasing pyrolysis temperature, as shown in Table 13.1.

Carbon membranes derived from polyimides have been extensively studied by several research groups [14–39]. Among the factors determining the separation performance of carbon membranes, one of the most important of these is the polymeric precursor. Figure 13.4 shows the chemical structures of precursor polyimides used in order to investigate the effect of precursor structure on the carbon membranes performance, although these self-supported flat sheet membranes lack mechanical strength for practical applications. The membranes became more permeable by the pyrolysis process, as shown in Figures 13.5 and 13.6. There was a rough trade-off relationship between permeability and selectivity. With increasing pyrolysis temperature, the permeability decreased but the selectivity increased. Carbon membranes derived from these polyimide precursors may be classified into two groups based on the magnitude of the permeability and the selectivity of the membranes. The more permeable and less-selective membranes were prepared from 6FDA polyimides and BPDA-TrMPD (group 1). TPDA-ODA, PMDA-ODA, BPDA-ODA and BPDA-pPD polyimides (group 2) tended to give the less permeable carbonized membranes with

higher selectivity. Polyimide precursors of group 1 have lower T_{gs} than group 2 polyimides. Their polymer chains are more loosely packed when they started to be pyrolyzed. Polyimide precursors of group 2 have some degree of ordering due to the molecular aggregation of polymer chains. PMDA-ODA, BPDA-ODA and BPDA-pPD polyimides have been reported to have some degree of ordering due to molecular aggregation of the polymer chains [40,41] so that their polymer chains should be densely packed even at the starting temperature of pyrolysis. The TPDA-ODA polyimide heated above 300 °C is also considered to have some degree of ordering due to the molecular aggregation of polymer chains, judging from wide-angle X-ray diffraction (WAXD) measurements where its WAXD curve had sharp reflections superimposed on a broad diffuse one. Thus, it should be concluded that the more permeable and less-selective carbonized polyimide membranes are prepared from precursors whose polymer chains are packed more loosely at the starting temperature of pyrolysis.

The effect of pyrolysis variables, such as pyrolysis temperature and pyrolysis atmosphere, on carbon membranes derived from polyimide precursors has been studied by the research group of Koros. Steel and Koros [39] investigated the effect of the pyrolysis temperature on the separation performance of carbon films and reported the hypothetical ultramicropore size distribution as a tool to interpret a combination of parameter effects and trends of separation properties. Park and Lee [42] also investigated the structure relationship between the precursor poly(imide siloxane)s and the pyrolytic carbon membranes. From gas permeation results, they found that carbon

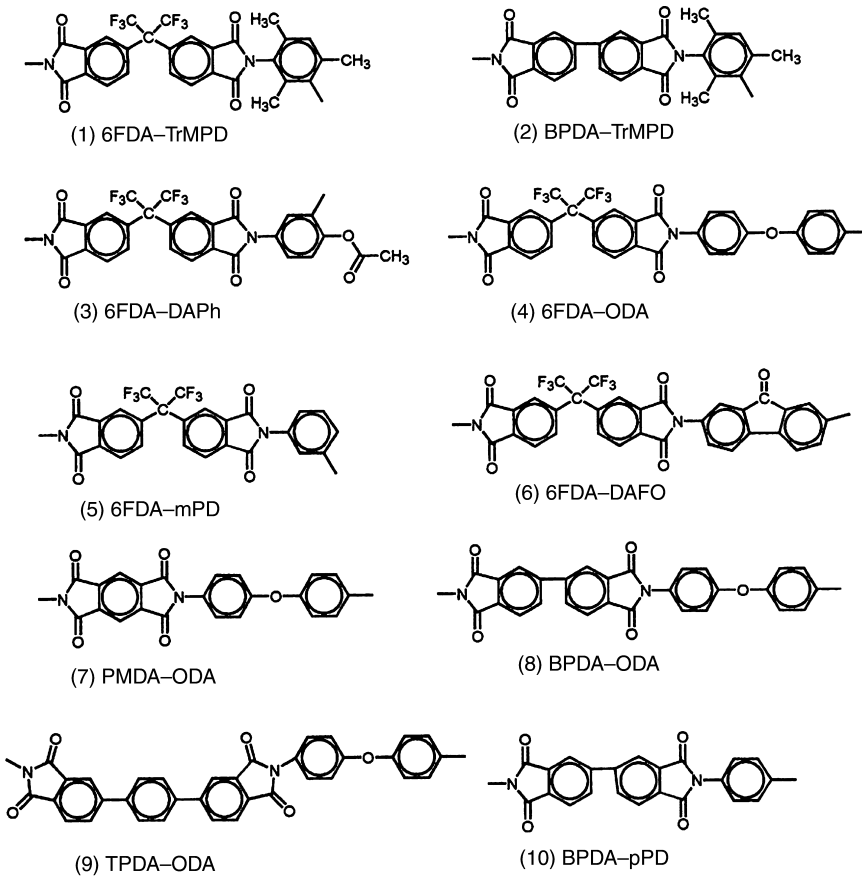


Figure 13.4 Chemical structures of the polyimide precursors used in Figures 13.5 and 13.6

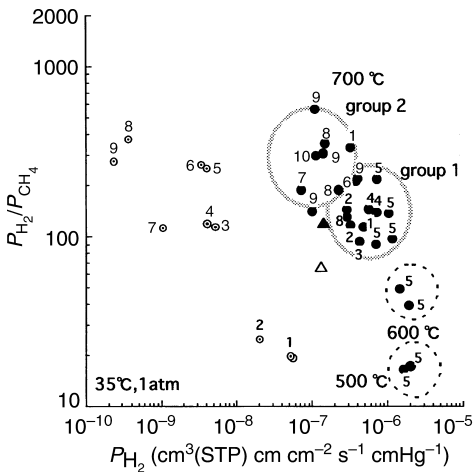


Figure 13.5 Plots of H₂ permeability versus H₂/CH₄ selectivity for carbon membranes derived from polyimide precursors

membranes exhibited excellent gas separation properties and the control of initial morphology of the polymeric precursor may be a significant factor in the preparation of such membranes.

Flexible pyrolytic membranes were obtained by pyrolysis of dense and flat membranes of sulfonated polyimides (Figure 13.7) of about 20 μm in thickness [43]. In order to prepare flexible pyrolytic membranes, it is important to select a proper pyrolysis temperature, at which most of the sulfonic acid groups decompose but substantial cleavage of polyimide backbone has not yet occurred. Such a temperature could be readily determined by analysis of the thermal decomposition behavior of sulfonated polyimides. Figure 13.8 shows the weight loss and simultaneous mass spectra of evolved gases of a sulfonated polyimide during pyrolysis. Two decomposition stages can be observed in this figure. In the first

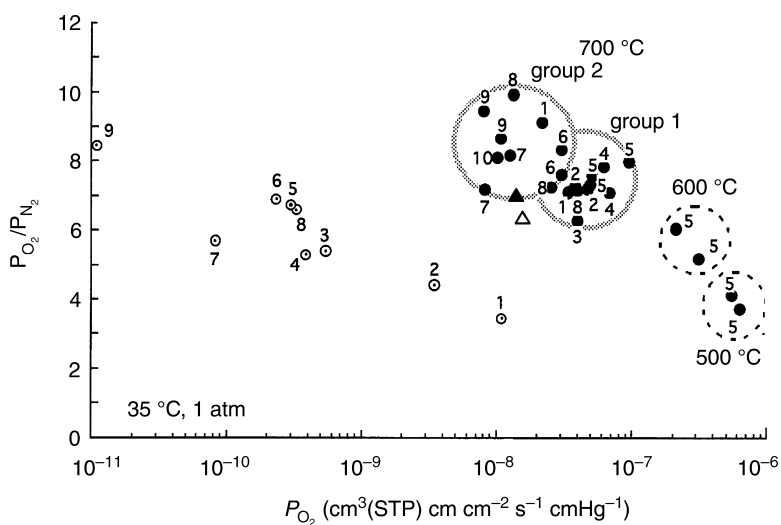


Figure 13.6 Plots of O_2 permeability versus O_2/N_2 selectivity for carbon membranes derived from polyimide precursors

stage, the 15 % weight loss occurring in the range 110 to 450 °C was mainly attributed to H_2O and SO_2 . Then, a short plateau in the weight loss curve was observed at around 450 °C. This temperature corresponds to 'valleys' in the mass

spectra of H_2O and SO_2 . On the other hand, rather small amounts of CO_2 and CO was observed below 450 °C, implying that cleavage of the polyimide backbone hardly occurred below 450 °C. CO_2 and CO increasingly evolved above 450 °C

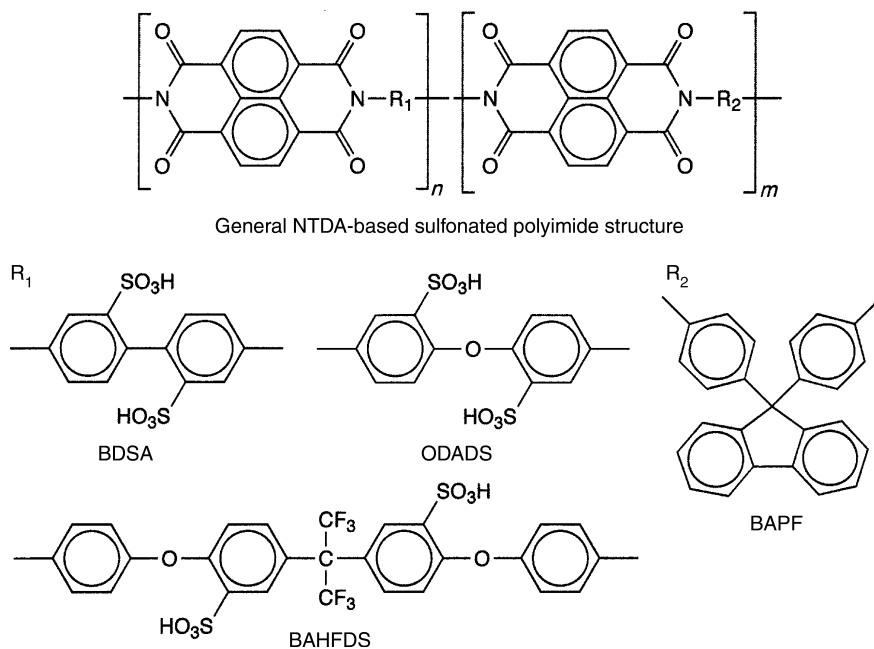


Figure 13.7 Chemical structures of NTDA-based sulfonated polyimides

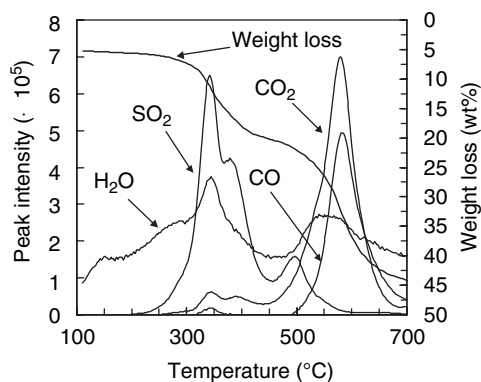


Figure 13.8 TG-MS spectra of evolved gases during pyrolysis of NTDA-BDSA/BAPF (8/2)

and reached their maximums at around 580 °C, indicating that substantial decomposition of the polyimide ring developed at around 580 °C. The IR spectrum shows that the peaks at 1099 and 1031 cm^{-1} (assigned to S=O stretching), which are observed for a NTDA-BDSA polyimide film, disappeared in the spectrum of the film pyrolyzed at 450 °C, indicating the decomposition of sulfonic acid groups. Most of the other peaks assigned to various bonds hardly changed, hence suggesting that the skeleton of the polyimide matrix still remained after pyrolysis at 450 °C. Table 13.2 lists the single gas permeation properties and ideal separation performance of CO_2/N_2 and $\text{C}_3\text{H}_6/\text{C}_3\text{H}_8$ gas pairs for the membranes pyrolyzed at 450 °C for 1.5 h. Dense and flexible flat membranes produced by the pyrolysis at relatively low temperature display high separation performance.

13.2.1.2 Hollow Fiber Membranes

Koresh and Soffer first reported high-quality carbon membranes with a hollow fiber geometry by the pyrolysis of a thermosetting polymer composed of cellulosic or phenolic resin as well as polyacrylonitrile [7,8]. These membranes are brittle and difficult to produce on a large scale, but have exceptional separation properties for H_2/CH_4 , CO_2/CH_4 and $\text{C}_3\text{H}_6/\text{C}_3\text{H}_8$, with permeances of 370 GPU (1 GPU = $10^{-6} \text{cm}^3(\text{STP})/(\text{cm}^2 \text{s cmHg})$) (H_2), 90 GPU (CO_2) and 180 GPU (C_3H_6) and selectivities of 500, 50 and 12–15, respectively.

Hollow fiber carbon membranes derived from a copolyimide (BPDA/6FDA-TrMPD) were extensively studied by Jones and Koros [15,16]. The membranes were optimized for air separation and exhibited a high performance of O_2/N_2 separation, that is, an O_2 permeance of 15–40 GPU and a selectivity of 11–14. The membranes were also effective for the separation of H_2/CH_4 , CO_2/CH_4 and CO_2/N_2 , with selectivities of 400–520, 140–190 and 55, respectively. The O_2/N_2 separation performance deteriorated by the presence of H_2O in the feed air. It was found, however, that the negative effect of moisture in feed air could be reduced by coating the carbon membrane with a thin layer of a hydrophobic polymer such as Teflon. It was also found that the performance of the carbon membrane was severely reduced by the presence of trace hydrocarbon contamination such as vacuum pump oil in the feed air. However, the properties of the membrane could be largely restored by flushing them with gaseous propylene. Geiszler and Koros investigated effects of the pyrolysis atmosphere on the membrane performance and reported that inert

Table 13.2 Gas separation performance of sulfonated polyimides and their pyrolyzed membranes at 35 °C and 1 atm [43]

Membrane (Pyrolysis temperature (°C))	Permeability ^a				Selectivity			
	CO_2	O_2	C_2H_4	C_3H_6	$P_{\text{O}_2}/P_{\text{N}_2}$	$P_{\text{CO}_2}/P_{\text{N}_2}$	$P_{\text{C}_2\text{H}_4}/P_{\text{C}_2\text{H}_6}$	$P_{\text{C}_3\text{H}_6}/P_{\text{C}_3\text{H}_8}$
NTDA-BDSA/BAPF (8/2) precursor	2	0.42	0.059	—	10.5	50	—	—
NTDA-BDSA/BAPF (8/2) (450)	424	64	32.1	18.1	4.4	29	4.4	26
NTDA-BAHFDS precursor	5.77	1.28	0.146	—	4.4	20	1	—
NTDA-BAHFDS (450)	720	119	51.9	29.1	3.7	23	4.3	29
NTDA-BDSA (450)	171	23	10.1	—	4.8	36	5.6	—

^aIn barrer; 1 barrer = $10^{-10} \text{cm}^3(\text{STP}) \text{cm cm}^{-2} \text{s}^{-1} \text{cmHg}^{-1}$.

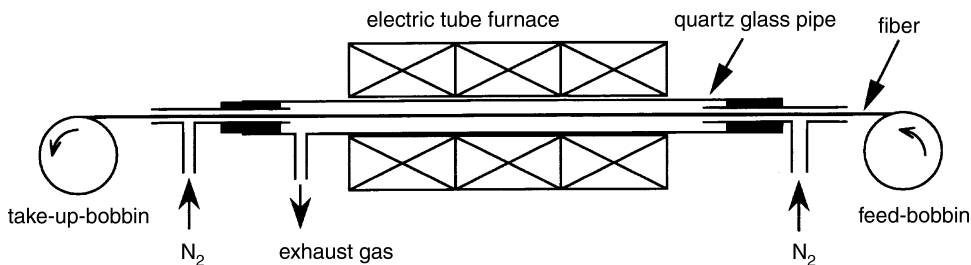


Figure 13.9 Schematic diagram of the continuous preparation of hollow fiber carbon membranes

purge pyrolysis produced carbon membranes with higher permeances and lower selectivities compared with vacuum pyrolysis [17]. The presence of a purge gas or increasing purge gas rate enhances the removal of the volatile byproducts from the polymer precursor during pyrolysis, resulting in a more open microstructure of the carbon membrane.

Haraya and coworkers reported a preparation of asymmetric capillary carbon membranes from Kapton polyimide. They described that the structure of the membrane was formed in the gelation step of the polyamic acid and was maintained in the imidization and shrank about 30 % during pyrolysis [19–23]. Kusuki and coworkers [29,30,44] developed a manufacturing method to continuously prepare asymmetric hollow fiber carbon membranes with a high performance of H_2/CH_4 separation. Figure 13.9 shows a schematic diagram of the continuous carbonization of an asymmetric hollow fiber carbon membrane [45]. The dried precursor hollow fiber had 0.40 mm OD and 0.12 mm ID. It was heat-treated in air at 400 °C for 30 min and then pyrolyzed at 600–1000 °C for 3.6 min. They also reported that the presence of trace amounts of toluene (7500 ppm) in the feed gas did not affect the membrane performance over a long test period.

Hollow fiber carbon membranes derived from a BPDA-based copolyimide showed fairly high performances for olefin/paraffin separation [33]: for example, an C_3H_6 permeance of 50 GPU and a selectivity of 13 for C_3H_6/C_3H_8 mixed gas (50/50 mol%) at 100 °C and 1 atm through a membrane pyrolyzed at 600 °C, although the precursor membrane showed rather low performance of the C_3H_6 permeance of 1.8 GPU and a selectivity of 3.7. Introduction of the 6FDA moiety into the precursor structure tends to display smaller C_3H_6 permeance and higher $C_3H_6/$

C_3H_8 selectivities than those from the BPDA-based polymers mentioned above [34]. The smaller permeances might be due to the densification of the membrane by pyrolysis. The pyrolyzed hollow fiber had a nodular morphology, significantly different from that of the precursor fiber; namely, significant densification occurred in the support layer just below the skin layer, as shown in Figure 13.10. This carbon membrane

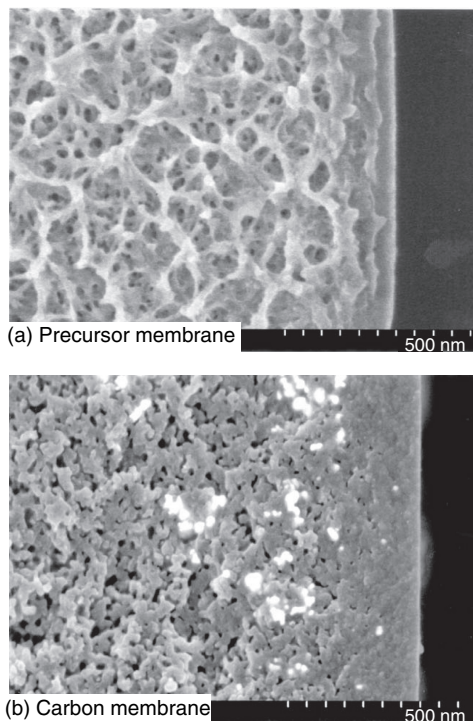


Figure 13.10 Scanning electron micrographs of the cross-sections of a hollow fiber of the 6FDA/BPDA–DBBT polyimide ($\times 10^4$): (a) precursor; (b) pyrolyzed at 600 °C

pyrolyzed at 540 °C for 1 h showed the high performance of the C_3H_6 permeance of 26 GPU and a selectivity of 22 for C_3H_6/C_3H_8 . Separation of olefins and paraffins is of great significance to petrochemical industries and is currently performed by energy-intensive low-temperature distillation. The membrane separation of olefins from paraffins has a high potential impact as a new separation process with less energy consumption. Polymeric membranes have been studied for olefin/paraffin separations [35]. However, their permeabilities to olefins are not high enough and their selectivities are significantly reduced in mixed-gas systems due to the plasticization effects of the olefins. Carbon membranes have attractive potential for olefin/paraffin separations.

13.2.2 Supported Carbon Membranes

Carbon membranes are typically formed on a support because of the inherent fragility of the membranes. They are prepared by converting thin polymer precursor films supported on a porous substrate. Therefore, it is important to choose a membrane formation method that can form thinner permselective layers on an appropriate porous support. Usually, a coating method, which includes dipping, spinning, spraying and ultrasonic deposition, is adopted to prepare supported membranes.

Rao and Sircar have developed a new class of nanoporous carbon membranes [46]. A disk of macroporous graphite or an alumina tube was coated with a thin uniform layer of a poly(vinylidene chloride)-acrylate terpolymer latex containing 0.1–0.14 μm polymer beads in an aqueous solution. The coated support was dried and pyro-

lyzed under a dry nitrogen purge. The resulting carbon membrane was 2–3 μm thick, containing a very narrow distribution of 0.5–0.6 nm pores. The membrane obtained exhibited surface selective diffusion properties and was capable of separating hydrocarbons from hydrogen. This transport mechanism differs from the molecular sieving mechanism; therefore, these membranes were named as selective surface flow (SSFTM) membranes. SSF membranes have been used on a pilot-plant scale for the production of hydrogen from refinery waste gas. However, this development now appears to have been terminated due to problems caused by higher-molecular-weight impurities. The permeance of the desired hydrocarbons declined much further in the presence of strongly adsorbing components.

Centeno and Fuertes reported that a small quantity of phenolic resin (Novalak type) could be spread on the finely polished surface of a porous carbon support by means of the spin-coating technique [47]. The pyrolyzed membrane exhibited an O_2/N_2 permselectivity of 10 and an O_2 permeance of around 3 GPU at 25 °C. Phenolic resin is one of the popular polymer precursors for preparation of carbon membranes because of its high carbon yield, thermosetting properties without deforming the precursor polymer layer on a substrate during heating and pyrolysis and, last but not least, low cost. Figure 13.11 shows an example of the schematic structure for a phenolic resin [48]. The dip-coating method was employed for preparation of supported carbon membranes, where a porous ceramic support was dipped into the solution of the phenolic resin and then pulled out at a rate of 1 to 10 cm/min. After drying, the coated precursor supported membrane was heated at a specific temperature

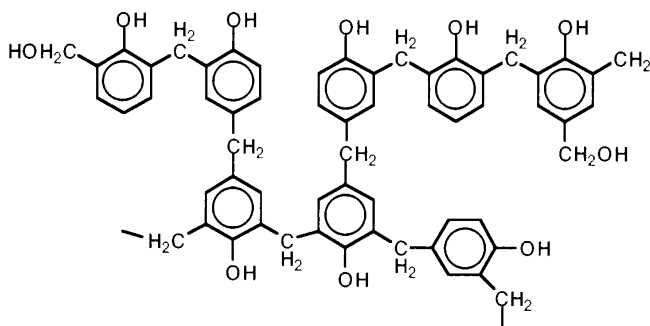


Figure 13.11 Schematic structure of the phenolic resin used as a precursor for carbon membranes

under an inert atmosphere. The coating–pyrolysis cycle was repeated several times.

Pyrolyzed membranes prepared from a novel sulfonated phenolic resin showed higher O₂ permeances than those of membranes from other precursor materials [49]. When being introduced into thermostable polymer chains, sulfonic acid groups might act as ‘bonded templates’ during the pyrolysis and have attractive potential in manipulating carbon membranes. Sulfonic acid groups bonded to polymer chains are supposed to decompose at relatively low temperatures and evolve small molecules or fragments, such as SO₂ and H₂O, during pyrolysis. When combined with thermosetting phenolic resins, sulfonic acid groups will evolve small molecular gases or fragments and leave spaces in the thermoset matrix during pyrolysis. Decomposition of sulfonic acid groups takes place before substantial carbonization occurs. These carbon membranes prepared under optimized conditions displayed a high performance of the O₂/N₂ permselectivity of 12 and an O₂ permeance of 30 GPU at 35 °C and 1 atm [50].

Acharya and Foley employed spray coating of porous stainless steel disks with a solution of poly(furfuryl alcohol) (PFA) to produce nanoporous carbon membranes in a reproducible manner [51]. In addition, Shiflett and Foley developed an ultrasonic deposition method to create a thin film of PFA on a tubular, macroporous, stainless steel support [52]. A membrane after three coating–pyrolysis cycles showed an O₂/N₂ permselectivity of 30 and an O₂ permeance of around 0.17 GPU. Wang *et al.* used vapor deposition polymerization to prepare supported carbon membranes from furfuryl alcohol [53]. The selectivity for CO₂/CH₄ separation was 82, with a CO₂ permeance of 8 GPU.

Hayashi *et al.* [24,25] have produced carbon membranes by the dip-coating of BPDA-based polyamic acid solution on an α -alumina porous tube, followed by pyrolysis at 500–900 °C in an inert atmosphere. In particular, the membrane carbonized at 800–900 °C exhibited a selectivity of more than 100 for the CO₂/CH₄ separation. For further improvement of permselectivity, Hayashi *et al.* modified the carbon membrane via chemical vapor deposition (CVD) of propylene at 650 °C and investigated the effect of the CVD period on the O₂/N₂ and CO₂/N₂ permselectivities [27]. Both permselectivities are increased

upon CVD for 2 min; however, a longer CVD period significantly reduced the permeance of each gas. In further studies, Marooka and coworkers oxidized the carbon membrane with O₂ at 300 °C for 3 h [26,28]. The oxidation treatment increased each permeance with no observable change in permselectivity. This suggests that the micropore volume was increased by the oxidation while the pore size distribution remained almost unchanged.

It is important to produce functional materials from renewable resources in order to sustain the production of materials for human life under a sound ecological system. Among renewable resources, forests provide excellent raw materials, carbohydrates (cellulose and hemicellulose) and polyphenol (lignin) in both quantity and quality. Although carbohydrates have been incorporated into human life for a long time, for example, cellulose acetate is one of the important membrane materials, lignin is nature’s most abundant polymeric material. However, lignin derivatives have several structural characteristics, such as being highly stable and highly phenolics, as shown in Figure 13.12. Such lignin derivatives (lignophenol or lignocresol), synthesized and isolated from ‘wood meals’ by phase-separation treatment [54], offer greater versatility and are particularly suitable as novel membrane materials for supported carbon membranes on the basis of high carbon yield and thermosetting properties [55]. Figure 13.13 shows a comparison of the gaseous products evolved from lignocresol and a commercially available phenolic resin (Bellpearl S-895, supplied from Kanebo Ltd) in the range 350–450 °C. The gaseous products evolved from the phenolic resin were mainly due to phenol and methylphenol, whereas those from lignocresol included a number of fragments with higher molecular weights. Therefore, a total weight loss of lignocresol up to 800 °C was 1.5 times larger than that of the phenolic resin. These evolved pyrolysis fragments seem to contribute effectively to the micropore formation of carbonized lignocresol. Scanning electron microscopy (SEM) observations of the membrane indicated that there were no cracks but pinholes at the surface of a single-coated layer. However, ‘multiple-coated’ samples had a smooth surface and the thickness of the ‘four-times’ coating membrane is about 1 μ m, as shown in Figure 13.14. Phenolic resin is one of the popular polymeric precursors

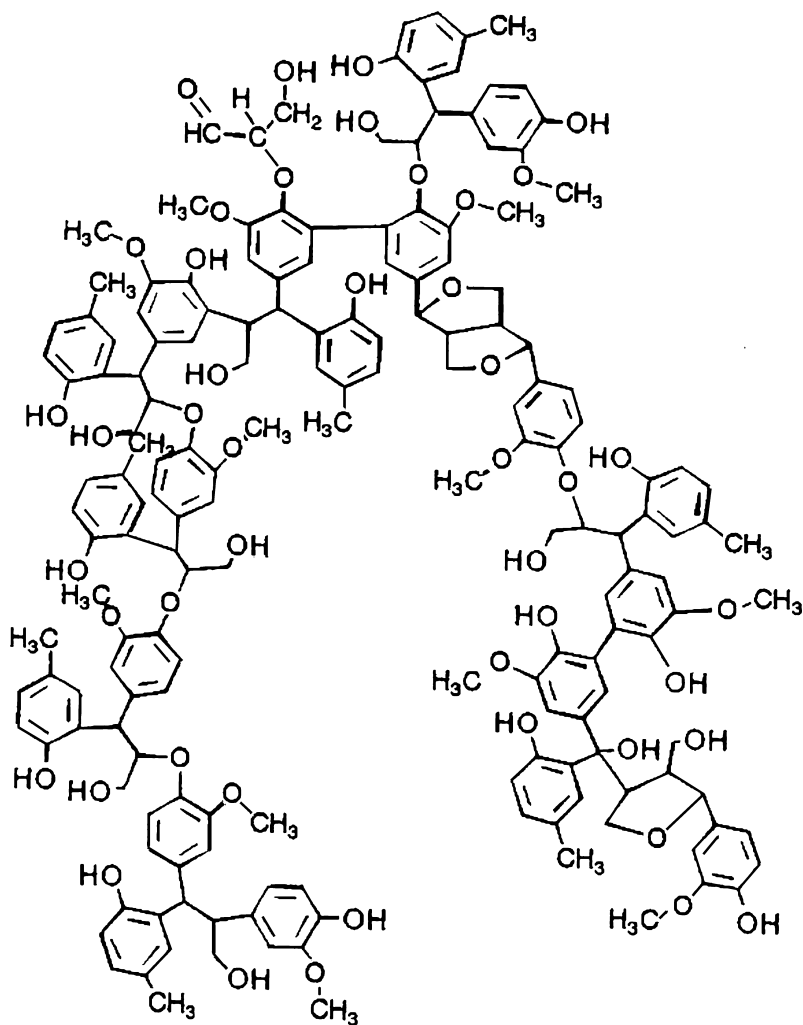


Figure 13.12 Schematic structure of lignocresol

for the preparation of carbon membranes. It has been observed that the permeation rates of carbon membranes derived from phenolic resins were increased with increasing pyrolysis temperature over the range 500–700 °C and a microporous structure appeared at about 500 °C [48]. In the case of carbon membranes derived from lignocresol, large increases in permeation rates occurred up to 400 °C, which were due to formation of a microporous structure as a result of decomposition of lignocresol. In the range 400–600 °C, the gas permeation rates and separation factors increased further, which is due to further development of the microporous structure. When the pyr-

olysis temperature was raised from 600 to 700 °C, the permeation rates of relatively large gas molecules, such as O₂, N₂ and CH₄, increased still further due to the pore size enlargement, whereas the separation factors decreased drastically. Heating to a higher temperature, such as 800 °C, caused the pores to shrink and the resulting carbon membranes were less permeable. Thus, a pyrolysis temperature of 600 °C gave the best membrane performance. The gas selectivities of the membrane prepared on a porous α -alumina tube at 600 °C were 50, 8, 290 and 87 for CO₂/N₂, O₂/N₂, H₂/CH₄ and CO₂/CH₄ at 35 °C, respectively. Furthermore, it should be noted

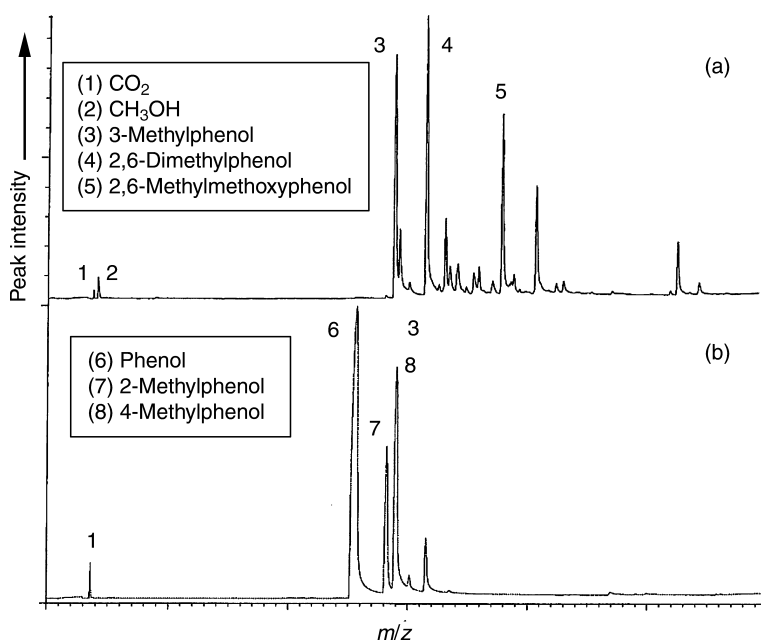


Figure 13.13 Comparison of evolved gases during pyrolysis of lignocresol (a) and phenolic resin (b) in the range 350–450 °C

that the permeation rate of CO_2 is of the same order as that of H_2 . The faster permeation of CO_2 seems to be caused by the adsorption and surface flow of CO_2 . The activation energy for the gas permeation through these membranes

increased with increasing molecular diameter of the gases, except for CO_2 . The activation energy of CO_2 permeation (3.6–6.4 kJ/mol) was smaller than those of He (5.0–12 kJ/mol) and H_2 (4.5–14 kJ/mol), which is consistent with the surface flow

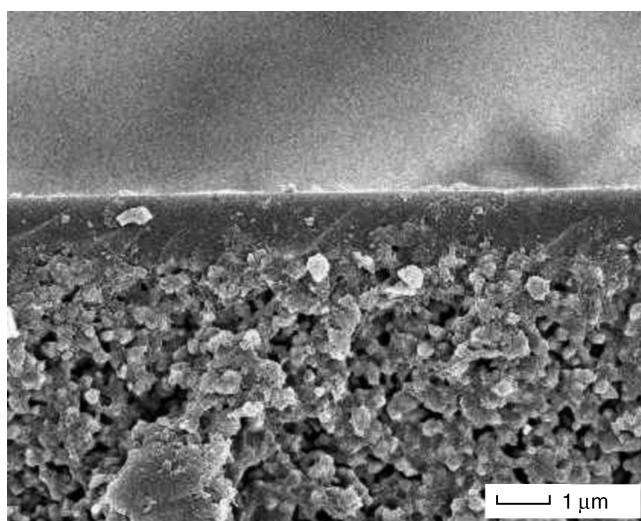


Figure 13.14 Scanning electron micrograph of a carbonized lignophenol membrane formed on a porous α -alumina support

studies of CO₂. Lignin-based materials provide one of the most promising candidates for the precursor materials of carbon membranes.

13.3 Gas Transport and Separation

Among the pyrolysis conditions, the pyrolysis temperature has the greatest effect on the gas permeation properties of the membranes. Figure 13.15 shows an example of the influence of pyrolysis temperature on the gas permeation properties through carbon membranes derived from hollow fiber copolyimide membranes [34]. These membranes were pyrolyzed under a nitrogen stream without any 'holding time'. The gas permeance increased with increasing the pyrolysis temperature up to 550 °C. The degree of the

increase was larger for the larger gas. For example, pyrolysis at 550 °C increased the gas permeances four and nine times for H₂ and C₃H₆, respectively, compared with the precursor membrane. As a result, the selectivity decreased for the gas pair with a largely different molecular size, such as H₂/CH₄, but hardly changed for the other gas pairs in the range of the lower pyrolysis temperatures. With further increasing the pyrolysis temperature up to 650 °C, the gas permeances decreased, except for the gases with small molecules: the permeances to He and H₂ hardly changed. The degree of the decrease in permeance was larger for the other gases. As a result, the selectivity increased more for the gas pair with the more different molecular size, such as H₂/CH₄ and CO₂/CH₄, whereas the increase in the selectivity was rather small for the gas pair with a similar molecular size, such as CO₂/N₂ and O₂/N₂. The membranes pyrolyzed at 700 °C displayed much lower gas permeances than even the precursor membrane. Heating to higher temperatures causes the pores to shrink and the resulting carbon membranes were less permeable. The membranes pyrolyzed in the range 550–600 °C displayed the highest gas permeances, whereas the membranes pyrolyzed at 650 °C displayed the highest selectivities for every gas pairs.

Table 13.3 shows a comparison of the gas separation performances among various carbon membranes. As mentioned earlier, the vacuum-pyrolyzed membranes of a 6FDA/BPDA–TrMPD copolyimide hollow fiber displayed a very sharp size-dependence of gas permeance in the kinetic diameter range 0.33–0.38 nm, resulting in a very high O₂/N₂ selectivity of 14 and a high O₂ permeance of 16 GPU [15]. The similar high level of O₂/N₂ separation performance was also achieved for pyrolyzed membranes from composite disk-type membranes of poly(furfuryl alcohol) (PFA) [52] and composite tubular membranes of phenolic resin with pendant sulfonic acid groups (S-PF/PF) [50]. These three membranes form the highest level of trade-off line between O₂ permeance and O₂/N₂ selectivity [57].

Table 13.4 shows the performances for propylene/propane separation of the carbon membranes. The membrane derived from the phenolic resin displayed a fairly high performance for single-gas permeation, but in mixed-gas permeation experiments, the propylene

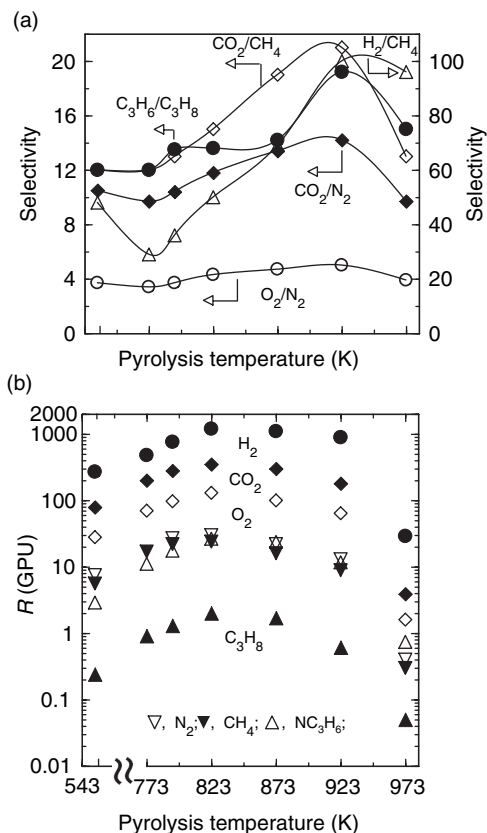


Figure 13.15 Effects of pyrolysis temperature on separation factor (a) and permeance (b) at 100 °C and 1 atm for 6FDA/BPDA–DDBT copolyimide hollow fiber membranes

Table 13.3 Comparison of gas separation performance among various carbon membranes

Membrane	Type ^a	Pyrolysis		Permeance (GPU) ^b			Ideal selectivity			Reference
		Temperature (°C)	T(°C)	H ₂	CO ₂	O ₂	H ₂ /CH ₄	CO ₂ /CH ₄	O ₂ /N ₂	
Resol PF	ST	500, 1 h	35	380	83	19	370	82	7.9	[10,48]
	ST	700, 1 h	35	110	20	4.2	690	140	8.9	[10,48]
S-PF/PF	ST	500, 1.5 h	35	167	31	6.8	930	170	11	[50]
	ST	500, 1.5 h	35	400	120	30	180	54	12	[50]
Novalac PF	SF	700	25	—	6.0	3.3	—	70	10	[47]
Lignocresol	ST	600, 2 h	35	210	35	8.9	680	110	10	[55]
PFA	SF	450	23	1.81	—	0.17	—	—	30	[52]
PFA	ST	600	25	18.0	8.0	2.52	55	82	13	[53]
PVDC-PVC	SF	700	25	—	—	1.4	—	—	14	[56]
BPDA/6FDA-TrMPD	HF	550	20	171	73	14–15	450	190	11–14	[15] ^c
BPDA-DDBT/BADA	HF	600	35	—	400	100	—	—	6	[33]
6FDA-DABZ	FM	700, 1 h	35	34	5.0	1.4	1200	180	11	[9,10]
6FDA-mPD	FM	700, 1 h	35	220	92	19	140	60	8	[10]
Kapton	FM	800, 2 h	35	13.4	2.6	0.7	—	—	12	[19,20]
	FM	950, 1 h	35	1.06	0.07	0.018	—	—	22	[19,20]
BPDA-ODA	ST	700, 0 h	65	—	79	22	—	57	7.5	[24]
BPDA-based PI	HF	700	50	420	—	—	540	—	—	[30] ^c
	HF	850	120	310	—	—	680	—	—	[29]

^aSF, supported flat membrane; ST, supported tubular membrane; FM, non-supported flat membrane; HF, hollow fiber membrane.

^b1 GPU = 10⁻⁶ cm³(STP)/(cm² s cmHg).

Table 13.4 Performances of carbon membranes for propylene/propane (50/50 mol%) separation at 1 atm^a

Membrane	Type ^b	Pyrolysis temperature (°C)	T (°C)	Permeance, R _{C₃H₆}	Selectivity, α _{C₃H₆/C₃H₈}	Reference
Resol PF	ST	500, 1 h	35	0.19 (7.7)	27 (30)	[10]
			90	2.0	18	[10]
6FDA-mPD	FM	500, 1 h	90	11 (19)	11 (54)	[10]
			35	19 (28)	13 (25)	[10]
6FDA-DABZ	FM	500, 1 h	35	1.7 (3.1)	44 (78)	[10]
BPDA/6FDA-DDBT precursor	FM		100	2.9	12	[34]
BPDA/6FDA-DDBT	FM	600, 0 h	100	34	11	[34]
BPDA/6FDA-DDBT	HF	540, 1 h	100	26	22	[34]
			580, 0.25 h	35	2.1	27
BPDA-DDBT/DABA	HF	650, 0 h	100	8.3	23	[34]
			100	11	20	[34]
			35	26 (20)	11 (14)	[33]
BPDA-ODA	ST	700, 0 h	100	43 (32)	11 (12)	[33]
			100	32 (34)	15 (17)	[33]
			35	2.4 (2.6)	46 (54)	[25]
NTDA-BDSA/BAPF(8/2)	FM	450, 1.5 h	100	8.7 (9.3)	33 (29)	[25]
			35	12 (14)	14 (27)	[58]

^aData in parentheses were obtained for a single-component system.

^bST, supported tubular membrane; FM, non-supported flat membrane; HF, hollow fiber membrane.

permeance decreased significantly and the propylene/propane selectivity decreased [10,48]. A similar behavior was observed for carbonized 6FDA-based polyimide and polypyrrolone membranes [10]. 6FDA-based polyimide membranes carbonized at 700 °C displayed a significant reduction in gas permeability after exposure to propane, probably because of micropore clogging due to irreversible adsorption. Only a slight recovery of the permeability was observed by desorption treatment at 150 °C in vacuum. After exposure to propane, the membrane reached a newly organized state and, thereafter, gave a reproducible performance for propylene/propane separation. On the other hand, carbon membranes derived from an asymmetric polyimide hollow fiber membrane displayed similar performances between the single-component and the mixed-components systems [33,34]. The differences in the permeation and separation behavior between these carbon membranes might originate from the difference in the morphological structure of the membranes. Among the present pyrolyzed membranes, the highest performance of the propylene permeance of 26 GPU and a selectivity of 22 for propylene/propane separation was achieved, as shown in Table 13.4. Thus, carbon membranes are promising candidates for the

separation of light alkenes/alkanes, especially propylene/propane separations. This technique is expected to be superior to other methods, such as distillation, adsorption and absorption based on energy consumption.

13.4 Vapor Permeation and Pervaporation

Application of vapor permeation and pervaporation to separate organic liquid mixtures, such as aromatic/aliphatic hydrocarbons, is still very limited because of low selectivity due to swelling of the polymer membrane. In the design of organic liquid permselective membranes, it is important to suppress the membrane swelling. Microporous materials with excellent thermal and chemical stabilities are of particular interest for preparing membranes used for the separation of organic liquid mixtures. Table 13.5 shows pervaporation and vapor permeation performances of carbon membranes derived from phenolic resins [59]. The carbon membrane preferentially permeated water from water/ethanol mixtures and methanol from methanol/benzene mixtures. Carbon membranes also show a high benzene selectivity in benzene/cyclohexane and benzene/*n*-hexane separation, as well as microporous FAU

Table 13.5 Pervaporation (50 °C and 75 °C) and vapor permeation (100 °C and 150 °C) performances of carbon membranes from phenolic resins

Pyrolysis condition		Feed solution, A/B (wt% of A)	T(°C)	Flux (g/(m ² h))	Separation factor, A/B ^a
T(°C)	Coating time (h)				
500	3	Water/ethanol (50)	75	94	100
		Methanol/benzene (50)	50	45	51
		Benzene/cyclohexane (50)	75	7	28
500	4	Methanol/benzene (50)	50	80	46
			100	370	280
		Benzene/cyclohexane (50)	75	7	65
			100	41	210
			150	160	140
		Benzene/ <i>n</i> -hexane (50)	75	< 5	—
	100	15	12		
	150	110	11		
700	3	Water/ethanol (50)	75	110	570
		Methanol/benzene (50)	50	20	7
		Benzene/cyclohexane (50)	75	9	6
700	4	Methanol/benzene (50)	50	13	22
		Benzene/cyclohexane (50)	75	< 5	—

^aSeparation factor was determined as $(Y_A/Y_B)/(X_A/X_B)$ where X_A , X_B , Y_A and Y_B denote the weight fractions of components A and B in the feed and the permeate, respectively, and A is the species which is preferentially permeated.

zeolite membranes. Both the separation factor and the flux of the membrane carbonized at 500 °C were larger than those of the membrane carbonized at 700 °C, probably due to the less permeable structure of the 700 °C-carbonized membrane.

In these systems, the sorption process presumably determined the permeation performance, as previously reported for Y-type zeolite membranes [60,61] Benzene sorption into these membranes increases with increasing benzene feed concentration and the increasing sorption causes a decrease in the flux of cyclohexane or *n*-hexane. The pore size of the Y-type zeolite membrane (0.74 nm) is larger than benzene, cyclohexane and *n*-hexane and also the size of the graphitic slit pore of the carbon membrane is presumably larger than the benzene and *n*-hexane molecules. Thus, in the case of a single component such molecules can pass through these membranes. In a binary system, however, selective sorption of benzene determines the separation performance. Adsorbed benzene molecules obstruct the transport of cyclohexane or *n*-hexane molecules. The performance of the microporous membranes is far superior to any other membrane previously reported in terms of both pervaporation and vapor permeation. Separation of these systems is difficult by a conventional distillation process

because these components form close-boiling-point mixtures. Although azeotropic distillation and extractive distillation are used at the present time, these processes suffer from complexity and high energy consumption. It may, therefore, be concluded that carbon membranes provide one of the most promising candidates for the separation of organic liquid mixtures.

13.5 Conclusions

Carbon membranes provide potentially higher selectivity and thermal and chemical stabilities, when compared to conventional polymeric membranes. Gas mixtures can be separated by their molecular sizes, as well as by adsorptive interactions and differences in the diffusion coefficients. These membranes can exceed upper bound curves in the trade-off relationship between the permeability and the selectivity. Furthermore, practical industrial applications have been proposed recently by Carbon Membrane, Ltd of Israel and Blue Membranes, GmbH of Germany. The former company produced hollow fiber carbon membranes while the latter prepared supported flat carbon membranes. Despite these technical successes, much research and development effort is still needed in order to reduce ultimate membrane and module costs. The first commercial applica-

tions for a microporous membrane (zeolite A in pervaporation) are now appearing and there is a pilot-scale application for silica membranes. These applications will advance the acceptance of microporous membranes. Since carbon membranes are intrinsically brittle, they are difficult to produce on a large scale with high reproducibility. However, carbon membranes have great potential to replace other membranes in the large market of gas separations and exciting opportunities exist, not only in gas separations, but also in membrane microreactors.

References

- [1] J. L. Falconer, R. D. Noble, D. P. Sperry, in R. D. Noble and S. A. Stern (Eds), *Membrane Separations Technology, Principles and Applications*, Elsevier, Amsterdam, The Netherlands, pp. 684 (1995).
- [2] H. P. Hsieh, *Inorganic Membranes for Separation and Reaction*, Elsevier, Amsterdam, The Netherlands, pp. 124 (1996).
- [3] R. W. Baker, *Membrane Technology and Application*, McGraw Hill, New York, NY, USA, pp. 77 (2000).
- [4] A. J. Burggraaf, in A. J. Burggraaf and L. Cot (Eds), *Fundamentals of Inorganic Membrane Science and Technology*, Elsevier, Amsterdam, The Netherlands, pp. 345 (1996).
- [5] R. Ash, R. M. Barrer and C. G. Pope, *Proc. R. Soc., A*, **271**, 19 (1963).
- [6] R. Ash, R. M. Barrer and T. Foley, *J. Membr. Sci.*, **1**, 355 (1976).
- [7] J. E. Koresh and A. Soffer, *J. Chem. Soc., Faraday Trans.*, **26**, 2457 (1980).
- [8] J. E. Koresh and A. Soffer, *Sepr. Sci. Technol.*, **18**, 723 (1983).
- [9] H. Kita, M. Yoshino, K. Tanaka and K. Okamoto, *J. Chem. Soc., Chem. Commun.*, 1051 (1997).
- [10] K. Okamoto, M. Yoshino, K. Noborio, H. Maeda, K. Tanaka and H. Kita, *ACS Symp. Ser.*, **744**, 314 (2000).
- [11] M. Yoshino, *PhD Dissertation*, Yamaguchi University, Yamaguchi, Japan (2002).
- [12] H. Kita, T. Yamada, K. Tanaka and K. Okamoto, in *Proceedings of the 5th International Conference on Inorganic Membranes*, Nagoya, Japan, pp. 556 (1998).
- [13] Y. H. Ma, in A. J. Burggraaf and L. Cot (Eds), *Fundamentals of Inorganic Membrane Science and Technology*, Elsevier, Amsterdam, The Netherlands, pp. 43 (1996).
- [14] H. Hatori, Y. Yamada, M. Shiraiishi, H. Nakata, S. Yoshitomi, I. Carbon, **30**, 305 (1992).
- [15] C. W. Jones and W. J. Koros, *Carbon*, **32**, 1419 (1994).
- [16] C. W. Jones and W. J. Koros, *Ind. Eng. Chem. Res.*, **34**, 158 (1995).
- [17] V. C. Geiszler and W. J. Koros, *Ind. Eng. Chem. Res.*, **35**, 2999 (1996).
- [18] A. Singh-Ghosal and W. J. Koros, *J. Membr. Sci.*, **174**, 177 (2000).
- [19] H. Suda and K. Haraya, *J. Chem. Soc., Chem. Commun.*, 1179 (1995).
- [20] H. Suda and K. Haraya, *J. Phys. Chem. B*, **101**, 3988 (1997).
- [21] J. Petersen, M. Matsuda and K. Haraya, *J. Membr. Sci.*, **131**, 85 (1997).
- [22] H. Suda and K. Haraya, *J. Chem. Soc., Chem. Commun.*, 93 (1997).
- [23] H. Suda and K. Haraya, *ACS Symp. Ser.*, **744**, 295 (2000).
- [24] J. Hayashi, M. Yamamoto, K. Kusakabe and S. Morooka, *Ind. Eng. Chem. Res.*, **34**, 4364 (1995).
- [25] J. Hayashi, H. Mizuta, M. Yamamoto, K. Kusakabe and S. Morooka, *Ind. Eng. Chem. Res.*, **35**, 4176 (1996).
- [26] J. Hayashi, M. Yamamoto, K. Kusakabe and S. Morooka, *Ind. Eng. Chem. Res.*, **36**, 2134 (1997).
- [27] J. Hayashi, H. Mizuta, M. Yamamoto, K. Kusakabe and S. Morooka, *J. Membr. Sci.*, **124**, 243 (1997).
- [28] K. Kusakabe, M. Yamamoto and S. Morooka, *J. Membr. Sci.*, **149**, 59 (1998).
- [29] Y. Kusuki, H. Shimazaki, T. Tanihara, S. Nakanishi and T. Yoshinaga, *J. Membr. Sci.*, **134**, 245 (1997).
- [30] N. Tanihara, H. Shimazaki, Y. Hirayama, S. Nakanishi, T. Yoshinaga and Y. Kusuki, *J. Membr. Sci.*, **160**, 179 (1999).
- [31] A. B. Fuertes and T. A. Centeno, *Micropor. Mesopor. Mater.*, **26**, 23 (1998).
- [32] A. B. Fuertes, D. M. Nevskaja and T. A. Centeno, *Micropor. Mesopor. Mater.*, **33**, 115 (1999).
- [33] K. Okamoto, S. Kawamura, M. Yoshino, H. Kita, Y. Hirayama, N. Tanihara and Y. Kusuki, *Ind. Eng. Chem. Res.*, **38**, 4424 (1999).
- [34] M. Yoshino, S. Nakamura, H. Kita, K. Okamoto, N. Tanihara and Y. Kusuki, *J. Membr. Sci.*, **215**, 169 (2003).
- [35] M. Ogawa and Y. Nakano, *J. Membr. Sci.*, **162**, 189 (1999).
- [36] M. Ogawa and Y. Nakano, *J. Membr. Sci.*, **173**, 123 (2000).
- [37] M. G. Sedigh, L. Xu, T. T. Tsotsis and M. Sahimi, *Ind. Eng. Chem. Res.*, **38**, 3367 (1999).
- [38] J. N. Barsema, J. Balster, V. Jordan, N. F. A. van der Vegt and M. Wessling, *J. Membr. Sci.*, **219**, 47 (2003).
- [39] K. M. Steel and W. J. Koros, *Carbon*, **41**, 253 (2003).

- [40] K. Okamoto, K. Tanaka, O. Yokoshi and H. Kita, *J. Polym. Sci., Polym. Phys. Ed.*, **27**, 643 (1989).
- [41] K. Okamoto, K. Tanaka, H. Kita, A. Nakamura and Y. Kusuki, *J. Polym. Sci., Polym. Phys. Ed.*, **27**, 1221 (1989).
- [42] H. B. Park and Y. M. Lee, *J. Membr. Sci.*, **213**, 263 (2003).
- [43] W. Zhou, T. Watari, H. Kita and K. Okamoto, *Chem. Lett.*, 534 (2002).
- [44] T. Yoshinaga, H. Shimazaki, Y. Kusuki and Y. Sumiyama, *Eur. Patent* 0459623B1 (1991).
- [45] Y. Kusuki, *PhD Dissertation*, Yamaguchi University, Yamaguchi, Japan (1998).
- [46] M. B. Rao and S. Sircar, *J. Membr. Sci.*, **110**, 109 (1996).
- [47] T. A. Centeno and A. B. Fuertes, *J. Membr. Sci.*, **160**, 201 (1999).
- [48] H. Kita, H. Maeda, K. Tanaka and K. Okamoto, *Chem. Lett.*, 179 (1997).
- [49] W. Zhou, M. Yoshino, H. Kita and K. Okamoto, *Ind. Eng. Chem. Res.*, **40**, 4801 (2001).
- [50] W. Zhou, M. Yoshino, H. Kita and K. Okamoto, *J. Membr. Sci.*, **217**, 55 (2003).
- [51] M. Acharya and H. C. Foley, *J. Membr. Sci.*, **161**, 1 (1999).
- [52] M. B. Shiflett and H. C. Foley, *Science*, **285**, 1902 (1999).
- [53] H. Wang, L. Zhang and G. R. Gavalas, *J. Membr. Sci.*, **177**, 25 (2000).
- [54] M. Funaoka and S. Fukatsu, *Holzforschung*, **50**, 245 (1996).
- [55] H. Kita, K. Nanbu, T. Hamano, M. Yoshino, K. Okamoto and M. Funaoka, *J. Polym. Environ.*, **10**, 69 (2002).
- [56] T. A. Centeno and A. B. Fuertes, *Carbon*, **38**, 1067 (2000).
- [57] M. Robeson, *J. Membr. Sci.*, **62**, 165 (1991).
- [58] W. Zhou, *PhD Dissertation*, Yamaguchi University, Yamaguchi, Japan (2002).
- [59] H. Kita, K. Nanbu, H. Maeda and K. Okamoto, *ACS Symp. Ser.*, **876**, 203 (2004).
- [60] H. Kita, H. Asamura, K. Tanaka and K. Okamoto, *ACS Symp. Ser.*, **744**, 330 (2000).
- [61] H. Kita, K. Fuchida, T. Horita, H. Asamura and K. Okamoto, *Sepn Purif. Technol.*, **25**, 261 (2001).

Polymer Membranes for Separation of Organic Liquid Mixtures

Tadashi Uragami

14.1 Introduction

Dialysis, ion-exchange, reverse osmosis and ultrafiltration membranes have widely been used for the separation of materials in the medical and industrial fields, such as in blood dialysis, electrolytic cells in chlor-alkali plants, desalination and food-processing. In particular, ultrafiltration, reverse osmosis and ion-exchange membranes have contributed significantly to the generation of ultrapure water, which is indispensable to the production of microelectronic products. In all of these processes, the membranes are primarily used to separate aqueous solutions.

Because of their efficiency, membrane separation technologies have been examined as a way to conserve resources, energy and the environment. In particular, the concentration of alcohol in biofermentation, concentration and recovery of organic solvents in the chemical process industry, and removal of organic vapors from air have been extensively studied. In the separation of organic liquid mixtures, the design of the membrane structure that can selectively interact with a specific component in the feed mixture determines if a membrane-based separation process is technically and economically feasible [1].

In this chapter, the principles of membrane separation techniques that can be applied to the concentration and separation of organic liquid mixtures, the structural design of highly selective polymer membranes and several applications for these membranes are discussed.

14.2 Structural Design of Polymer Membranes

The chemical design and physical construction of polymer membranes are very important considerations in balancing the functions of the membranes. The structural design of a high-performance membrane depends on the development of advanced membrane materials, membrane surface modification and the membrane preparation method [2].

14.2.1 Chemical Design of Membrane Materials

Novel materials for separation membranes are selected based on: (i) development of systematic structure/property relationships in polymers to provide membranes with enhanced permeability and selectivity, (ii) the ease of membrane preparation, and (iii) their stability under permeation conditions, such as pH, temperature and pressure. Furthermore, synthesis of new membrane materials and modification of existing membrane materials are often employed to develop membranes with higher permeability and/or higher selectivity. For polymeric membranes, modification and synthesis of membrane materials are accomplished by polymer blending, cross-linking, formation of internal hydrogen bonding, copolymerization and graft and block copolymerization [2]. In addition, polymer membranes may also be significantly altered by surface modification techniques. There are two

general types of polymer membrane surface modifications techniques: chemical or physical modifications. In the case of a chemical treatment, the membrane is contacted with a chemical agent, solvent, coupling agent, vapor, surface active agent, surface grafting or other additives. Physical membrane treatment techniques include ultraviolet irradiation, plasma irradiation and sputtering.

14.2.2 Physical Construction of Polymer Membranes

For the development of high-performance membranes, it is important to construct the membranes by choosing an optimum polymer material based on its physical and chemical properties. This is reflected in improved permeability, selectivity and durability of the resultant membrane. The physical structure of polymer membranes is strongly dependent on the membrane preparation method and the conditions of membrane formation.

In a membrane permeation process, the chemical composition and the physical structure of the membrane can both be important factors. For example, when molecules are permeated and separated by a dense, non-porous polymer membrane that has small transient free volume elements generated by thermal vibrations of the polymer chains, the chemical composition of the polymer governs the solubility of permeants in the membrane. On the other hand, permeant diffusion in the polymer membrane depends largely on the physical structure of a membrane. Such non-porous membranes can be applied to the separation of gases, vapors and liquids. Their selectivity is significantly influenced by both the difference in the solubility of the permeants in the membrane (solution process) and the diffusivity of the permeants in the membrane (diffusion process) [3,4].

In contrast, for polymer membranes with pores larger than the molecular size of the permeants, the interaction between the permeant and the membrane is negligible and the contribution of the chemical membrane composition to permeation is low. In such porous membranes, typically used in ultrafiltration and microfiltration applications, the physical structure mainly governs the permeation and separation characteristics.

Porous and non-porous membranes can be easily prepared by various methods. Because

there are many factors involved in the fabrication of a polymer membrane, it is very important to control the preparation conditions precisely. The physical structure of a polymer membrane, which governs its permeability and separation characteristics, depends largely on the membrane preparation conditions. If chemical reactions occur during the membrane preparation process, the chemical and physical structures are formed simultaneously, and thus, control of reaction conditions strongly influences the permeation and separation characteristics of the polymer membrane.

14.3 Separation Mechanism

14.3.1 Pervaporation

Figure 14.1 illustrates the principles of pervaporation. In this separation process, when a liquid mixture is fed to the upstream side of a polymer membrane and the downstream side is evacuated, a component in the feed mixture can preferentially permeate through the membrane. In a pervaporation process, differences between the solubility and diffusivity of the mixture components in the polymer membrane and the relative volatility of the permeants determine the permeability and selectivity [5–7]. In general, pervaporation exhibits the following characteristics [1,2]:

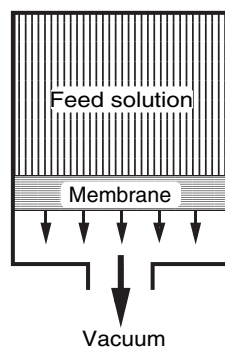


Figure 14.1 Schematic representation of the pervaporation process [7]. Copyright © 1998 from 'Structures and properties of membranes from polysaccharide derivatives' by T. Uragami in *Polysaccharides – Structural Diversity and Functional Versatility* (S. Dumitriu (Ed.)). Reproduced by permission of Routledge/Taylor & Francis Group, LLC

- (1) Selective transport across the non-porous membrane is achieved by a three-step process of solution, diffusion and evaporation.
- (2) Because the driving force for permeation is the vapor pressure for each component rather than the total system pressure, this method is effective for separation of organic liquid mixtures with high osmotic pressures.
- (3) Pervaporation can be applied to the separation and concentration of mixtures that are difficult to separate by distillation. For example, it is useful for the separations of azeotropic mixtures close-boiling-point mixtures and structural isomers.
- (4) Pervaporation can be used for the removal of certain components in equilibrium reactions.
- (5) Polymer membrane compaction, a frequent problem in high-pressure gas separations, is not encountered in pervaporation because the feed pressure is typically low.

14.3.1.1 Fundamental Equations for Permeation

The permeation rate, Q_i , of component i is expressed by Fick's first law as follows:

$$Q_i = -D(C_i)dC_i/dx \quad (14.1)$$

where $D(C_i)$ is the diffusion coefficient, C_i is the concentration of component i in the membrane and x is the distance from the membrane/feed-solution interface.

Fick's second law of diffusion is:

$$\begin{aligned} dC_i/dt &= D(C_i)d/dx(dC_i/dx) \\ &= D(C_i)(d^2C_i/dx^2) \end{aligned} \quad (14.2)$$

where $D(C_i)$ is given by the following equation:

$$D(C_i) = D_0 \exp(\gamma C_i) \quad (14.3)$$

Here, D_0 is the infinite dilution diffusion coefficient and γ is a measure of membrane plasticization which is dependent on temperature.

At steady-state permeation, the boundary conditions are $dC_i/dt, C_i = C_1$ at $x = 0$, and $C_i = C_2$ at $x = l$. When Equation (14.3) is inserted

into Equation (14.2) and integrated, Equation (14.4) is obtained:

$$Q_i = (D_0/\gamma l)(\exp \gamma C_1 - \exp \gamma C_2) \quad (14.4)$$

The concentration distribution is expressed as follows:

$$C_i = (1/\gamma) \ln [\exp \gamma C_1 - x/l(\exp \gamma C_1 - \exp \gamma C_2)] \quad (14.5)$$

If the concentration at the boundary of the feed solution and the membrane is equilibrated thermodynamically, the following equations hold:

$$C_1 = C^*(p^0) \quad (14.6)$$

$$C_2 = C^*(p_2) \quad (14.7)$$

where C^* is a pressure-dependant function, p^0 is the saturated vapor pressure, and p_2 is the vapor pressure on the down-stream side of the membrane.

Using these expressions, Equations (14.4) and (14.5) may be rewritten with p^0 and p_2 . At the same time, the permeability, P_i , is derived as follows:

$$P_i = Q_i l / \Delta p = (D_0/\gamma \Delta p)(\exp \gamma C_1 - \exp \gamma C_2) \quad (14.8)$$

where $\Delta p = p^0 - p_2$. When Equations (14.6) and (14.7) obey Henry's law, $C^*(p) = Sp$, and Equations (14.4), (14.5) and (14.8) are easily expressed as a function of p^0 and p_2 :

$$Q_i = (D_0/\gamma l)(\exp \gamma Sp^0 - \exp \gamma Sp_2) \quad (14.9)$$

$$C_i = (1/\gamma) \ln [\exp \gamma Sp^0 - x/l(\exp \gamma Sp^0 - \exp \gamma Sp_2)] \quad (14.10)$$

$$P_i = (D_0/\gamma \Delta p) \times (\exp \gamma Sp^0 - \exp \gamma Sp_2) \quad (14.11)$$

14.3.1.2 Solution-Diffusion Model

When a similar treatment is applied to gas or vapor permeation, the following equations are obtained:

$$Q_i l = \int_{C_1}^{C_2} D(C_i) dC_i \quad (14.12)$$

$$Q_i = P_i(p_1 - p_2)/l \quad (14.13)$$

where p_1 and p_2 are the vapor pressures on the high-concentration side and low-concentration side of the membrane, respectively.

Combining Equations (14.12) and (14.13) yields the following:

$$P_i = \left[\int_{C_1}^{C_2} D(C_i) dC_i \right] (p_1 - p_2) \quad (14.14)$$

Rearrangement gives:

$$Q_i l = R = P_i (p_1 - p_2) = \int_{C_1}^{C_2} D(C_i) dC_i \quad (14.15)$$

where R is the normalized permeation rate. When the concentration-averaged diffusion coefficient, \bar{D}_i , is defined as in Equation (14.16), P_i and R are expressed as in Equations (14.17) and (14.18), respectively.

$$\bar{D}_i = \int_{C_1}^{C_2} D(C_i) dC_i / (C_1 - C_2) \quad (14.16)$$

$$P_i = \bar{D}_i (C_1 - C_2) / (p_1 - p_2) \quad (14.17)$$

$$R = \bar{D}_i (C_1 - C_2) \quad (14.18)$$

If the diffusion coefficient is not dependent on permeant concentration, then D_i equals D . In pervaporation, the downstream pressure is much lower than the upstream pressure ($p_1 \gg p_2$). Hence, Equations (14.16)–(14.18) can be represented as follows:

$$\bar{D}_i = \int_{C_1}^{C_2} D(C_i) dC_i / C_1 \quad (14.19)$$

$$P_i = \bar{D}_i (C_1 / p_1) \quad (14.20)$$

$$R = \bar{D}_i C_1 \quad (14.21)$$

where $C_1 / p_1 = S_1$, which is the ‘pseudo-solubility’ coefficient. Under these conditions, P_i may be expressed by:

$$P_i = \bar{D}_i S_1 \quad (14.22)$$

In pervaporation, the separation factor, $\alpha_{B/A}$, a relative measure for the degree of separation,

can be represented by the component mole fractions in the feed and permeate as follows:

$$\alpha_{B/A} = (Y_B / Y_A) / (X_B / X_A) \quad (14.23)$$

where X_A and X_B are the weight fractions or mole fractions of the A and B components in the upstream-side, respectively, while Y_A and Y_B are the weight fractions or mole fractions of the A and B components in the downstream-side, respectively.

14.3.2 Evapomeation

Pervaporation is an efficient method for the separation of organic liquid mixtures and many studies have been performed using this process. Because the polymer membranes used in pervaporation are in direct contact with the liquid feed mixtures, however, carefully designed membrane characteristics are often impaired by swelling or shrinking of the membrane due to sorption of the feed components. This swelling or shrinking is not advantageous for membrane performance with respect to the separation of mixtures. Another membrane separation technique, known as ‘evapomeation’, makes use of the advantages of pervaporation while simultaneously eliminating the disadvantages of pervaporation [7–9]. Figure 14.2 shows the principles of evapomeation. In this technique, liquid feed

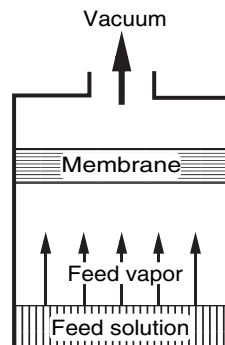


Figure 14.2 Schematic representation of the evapomeation process [7,8]. Copyright © 1998 from ‘Structures and properties of membranes from polysaccharide derivatives’ by T. Uragami in *Polysaccharides – Structural Diversity and Functional Versatility* (S. Dumitriu (Ed.)). Reproduced by permission of Routledge/Taylor & Francis Group, LLC

solution is fed to the membrane without directly contacting the polymer membrane. This is accomplished by vaporizing the liquid feed so that only vapor is supplied to the polymer membrane. Therefore, swelling or shrinking of the polymer membranes due to contact with the feed solutions is minimized. The advantages of evaporation compared to pervaporation are as follows [1,2]:

- (1) In the evaporation process, membranes are not in direct contact with liquid feed mixtures as only vapors are supplied to the membranes. Accordingly, any swelling or shrinking of the membrane due to the feed mixtures is minimized and consequently an improvement in membrane performance may be expected.
- (2) Because the organic liquid mixtures are vaporized, interactions between component molecules are significantly weakened and consequently the separation performance is remarkably improved.
- (3) In evaporation, contaminants in a liquid feed mixture, such as macromolecular solutes, can lead to fouling of the membrane; this problem is avoided in evaporation.
- (4) During evaporation, the temperature of the feed solution and the membrane surroundings can both be controlled; hence, an improvement in the permeation and separation characteristics of the membrane can be achieved.

14.3.3 Temperature-difference Controlled Evaporation

As mentioned above, a new evaporation method for membrane separation that improves upon the shortcomings of pervaporation, while still keeping the advantages of this technique, was developed [7–9]. In evaporation, the temperatures of the feed solution (a) and the membrane surroundings (b) are controlled, and consequently a differential between these temperatures can be established, as shown in Figure 14.3. Such an evaporation method, in which this temperature difference is controlled, is called ‘temperature–difference controlled evaporation’ (TDEV) [7,10–12]. In TDEV, the permeant, having a lower freezing point in a binary liquid mixture, is selectively permeated, as shown in Figure 14.4. In addition, when the membrane has a stronger affinity to the preferentially per-

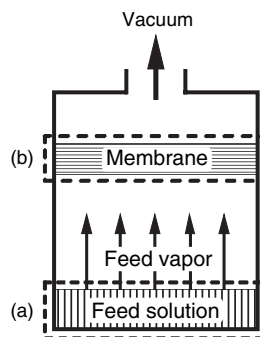


Figure 14.3 Control of temperature difference in evaporation (TDEV) [7,10,11,40]. Copyright © 1998 from ‘Structures and properties of membranes from polysaccharide derivatives’ by T. Uragami in *Polysaccharides – Structural Diversity and Functional Versatility* (S. Dumitriu (Ed.)), Reproduced by permission of Routledge/Taylor & Francis Group, LLC

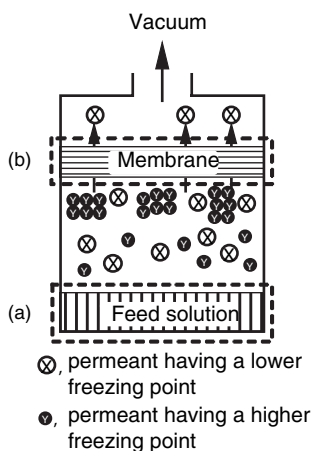


Figure 14.4 Separation mechanism in TDEV

meating mixture component, an increase in selectivity can result.

14.4 Separation of Organic Liquid Mixtures

14.4.1 Alcohol/Water Separation

Aqueous ethanol solutions obtained from the fermentation of biomass such as cellulose and starch contain about 5–10 wt% ethanol. To obtain ethanol by concentrating these aqueous ethanol

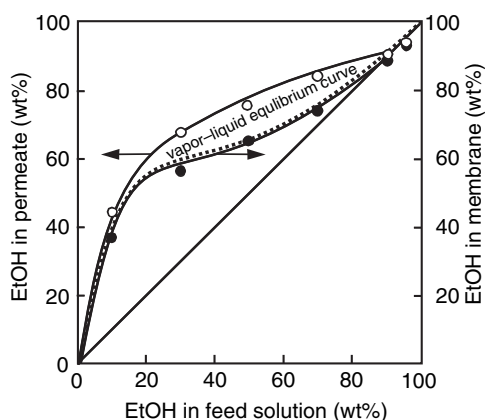


Figure 14.5 Permeation and separation characteristics of aqueous ethanol solutions through a PDMS membrane during pervaporation

solutions, ethanol-selective membranes are effective, which can result in significant energy savings compared to other separation techniques, such as distillation. For water/ethanol membranes, the higher permeation rate of water over organics is due to both a higher solubility and diffusivity for water as compared to the other organic feed components. In alcohol-selective membranes, diffusivity also favors water because it is the smaller molecule. Therefore, it is presumed that an alcohol/water selectivity can be attributed to the difference in solubility of the permeants. Figure 14.5 shows the ethanol concentration in the permeate stream of a polydimethylsiloxane (PDMS) membrane during (i) pervaporation and (ii) the ethanol concentration sorbed into the PDMS membrane [13]. These results support the hypothesis that the difference in the solubility of the permeants is the determining factor for the ethanol/water selectivity of a membrane. PDMS membranes show high ethanol/water selectivity, but their mechanical strength is weak and it is difficult to prepare thin membranes from PDMS. In order to obtain both high ethanol/water selectivity and mechanical strength, graft copolymers composed of the PDMS macromonomer and vinyl monomers were synthesized [14–16].

Graft copolymer membranes, which were either ethanol- or water-selective, were prepared by copolymerization of an oligodimethylsiloxane (DMS) monomer with methyl methacrylate (MMA) [13,14]. Two glass transition tempera-

tures (T_g) were observed at about 120 °C and –127 °C in the graft copolymer membranes. Transmission electron micrographs demonstrated that the MMA-g-DMS membranes showed microphase-separated structures. When an aqueous solution of 10 wt% ethanol was permeated through the MMA-g-DMS membranes by pervaporation, the ethanol concentration in the permeate and the permeation rate increased drastically with the DMS content in the copolymer. In particular, at a DMS content of less than about 40 mol%, water permeates preferentially from an aqueous solution of 10 wt% ethanol, whereas membranes with more than about 40 mol% of DMS are ethanol-selective, as shown in Figure 14.6. The change in the selectivity of the MMA-g-DMS membranes can be explained by a microphase-separated polymer structure using Maxwell's model and a combined model consisting of both parallel and series expressions. Furthermore, image processing of the transmission electron micrographs allowed determination of the percolation transition of the DMS phase at a DMS content of about 40 mol%. These results

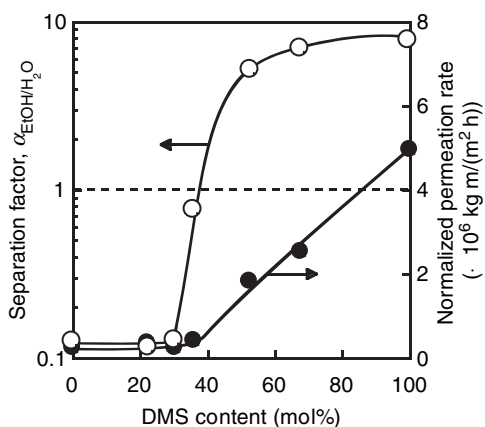


Figure 14.6 Effects of the DMS content on the separation factor (○) and normalized permeation rate (●) through the PMMA-g-PDMS membrane during pervaporation: feed, aqueous solution of 10 wt% ethanol; the dashed line represents the feed composition [15]. Reprinted with permission from T. Miyata, T. Tanaka and T. Urugami, 'Microphase separation in graft copolymer membranes with pendent oligodimethylsiloxanes and their permselectivity for aqueous ethanol solutions', *Macromolecules*, **29**, 7787–7794 (1996). Copyright (1996) American Chemical Society

suggest that the continuity of the DMS phases in the microphase-separated MMA-g-DMS membranes directly affects their selectivity for aqueous ethanol solutions [14,15].

The selectivity of block copolymer membranes consisting of ethanol-selective PDMS and water-selective PMMA was compared to the selectivity of graft copolymer membranes for the separation of an aqueous ethanol solution. With increasing DMS content, the block copolymer membranes changed from water- to ethanol-selective at a DMS content of 55 mol%. The graft copolymer membranes showed a dramatic change in their selectivity at a DMS content of 40 mol%. Transmission electron micrographs demonstrated that both membranes had a distinct microphase-separated structure consisting of PDMS and PMMA phases, and that the morphology was quite different between the block and graft copolymer membranes. The morphological changes in these membranes were investigated by image processing of micrographs and analysis using a combined model consisting of both parallel and series models. These investigations revealed that the percolation transition of the PDMS phase in the block and graft copolymer membranes takes place at a DMS content of about 55 and 40 mol%, respectively. This suggests that the continuity of the PDMS phase in these microphase-separated membranes strongly influences their ethanol selectivity [16].

The effects of annealing on selectivity during pervaporation was also investigated for these block and graft copolymer membranes. The ethanol selectivity of the block copolymer membranes was strongly influenced by annealing, but that of the graft copolymer membranes was essentially not affected. The original block copolymer membranes changed from being water- to ethanol-selective at a DMS content of 55 mol%, but the annealed block copolymer membranes changed at a DMS content of 37 mol%. Transmission electron micrographs demonstrated that the annealing of block copolymer membranes with a DMS content between 37 and 55 mol% resulted in dramatic changes in their morphology. However, annealing of the graft copolymer membranes had very little effect on their microphase-separated morphology, which was quite different from the morphology of the block copolymer membranes. Again, an analysis using a combined model consisting of parallel and series models revealed that a continuous

PDMS phase in the direction of the membrane thickness was readily formed by annealing of the block copolymer membranes. As a result, the continuity of the PDMS phase in the microphase-separated structure governed the ethanol selectivity of these membranes for an aqueous ethanol feed solution [17].

It is well known that poly[1-(trimethylsilyl)-1-propyne] (PTMSP) membranes show high ethanol/water selectivity [18,19]. In order to enhance the ethanol/water selectivity of PTMSP membranes, surface-modified PTMSP membranes were prepared by adding a small amount of a polymer additive, a graft copolymer (PFA-g-PDMS) consisting of polyfluoroacrylate (PFA) and PDMS, in the casting solution of PTMSP. Modified PTMSP membranes were cast on glass plates and the contact angles of water on the membrane surfaces exposed to the air side and the glass side, respectively, were measured [20,21]. The contact angle for water on surface-modified PTMSP membranes was significantly different on the air side versus that on the glass side; the contact angles on the air side were more hydrophobic. Furthermore, the contact angle for water increased in hydrophobicity with additional amounts of PFA-g-PDMS. The high hydrophobicity of the membrane surface on the air side and the increase in hydrophobicity with additional amounts of polymer additive were also confirmed by X-ray photoelectron spectroscopy. The permeation rate for an aqueous solution of 10 wt% ethanol in pervaporation experiments using surface-modified PTMSP membranes decreased slightly. However, the ethanol/water selectivity increased considerably with increasing amounts of PFA-g-PDMS [20,21].

The permeation and separation characteristics for aqueous alcohol solutions, such as methanol/water, ethanol/water and 1-propanol/water, were studied using a PDMS membrane in pervaporation and evapomeation modes. The PDMS membrane preferentially permeated methanol, ethanol and 1-propanol from aqueous solutions in both methods. The concentration of alcohol in the permeate by evapomeation was higher than that obtained by pervaporation. However, the permeation rate in evapomeation was lower. In evapomeation with a temperature difference between the feed solution and the membrane surroundings (TDEV), when the temperature of the membrane surroundings was

kept constant and the temperature of the feed solution was raised, both the permeation rate and the ethanol/water selectivity increased with increasing temperature of the feed solution. On the other hand, as the temperature of the feed solution was kept constant and the temperature of the membrane surroundings was changed, the permeation rate decreased. However, the selectivity for ethanol increased remarkably upon decreasing the temperature of the membrane surroundings, as shown in Figure 14.7. Under TDEV permeation conditions of a feed solution at 40 °C and a membrane surrounding temperature of -30 °C, an aqueous solution of 10 wt% ethanol in the feed was concentrated to about 90 wt% in the permeate. The selectivity for aliphatic alcohols in PDMS membranes follows the order of methanol < ethanol < 1-propanol [10,11].

In Table 14.1, the performances of the ethanol/water selective polymer membranes are compared. As can be seen in this table, the addition of PFA-*g*-PDMS to the PTMSP membrane was very effective and the application of TDEV method to the membrane separation technique was also very interesting for enhancement of the ethanol-selectivity for the ethanol/water mixtures.

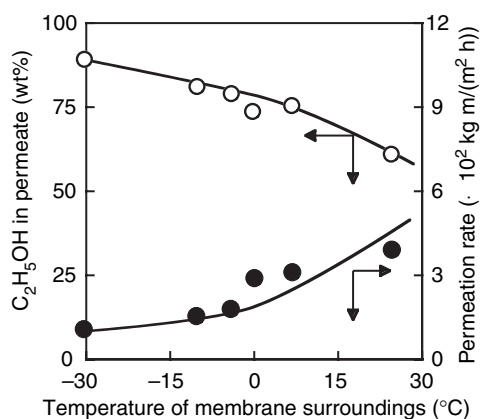


Figure 14.7 Effects of the temperature of the membrane surroundings on the permeation rate (●) and ethanol concentration in the permeate (○) for an aqueous solution of 10 wt% ethanol through a PDMS membrane: temperature of feed solution, 40 °C [10,11]. From T. Uragami and T. Morikawa, *J. Appl. Polym. Sci.*, **44**, 2009–2018. Copyright 1992. © John Wiley & Sons, Inc. Reproduced with permission

14.4.2 Hydrocarbon/Water Separation

The removal and enrichment of chlorinated hydrocarbons, such as 1,1,2-trichloroethane (TCE), trichloroethylene (TCET) and tetrachlor-

Table 14.1 Performance of ethanol/water-selective polymer membranes

Membrane	Feed (wt%)	Method	Applied temperature (°C)	$\alpha_{\text{EtOH}/\text{H}_2\text{O}}$	NPR ^a	Reference
PDMS	7	PV	25	11.8	2.1	[22]
PTMSP	7	PV	25	11.2	1.1	[18]
PTMSP	10	PV	30	12.0	4.5	[19]
PFA- <i>g</i> -PDMS/PTMSP ^b	10	PV	40	20.0	24.1	[21]
PPP- <i>g</i> -PDMS	7.28	PV	30	22.5	5.5	[23]
PSt- <i>g</i> -PhdFDA (87.6/12.4)	8	PV	30	45.9	0.6	[24]
TFE/ <i>i</i> -OcVE/C ₁₈ VE terpolymer (50/25/25)	15	PV	50	7.13	5.0	[25]
Modified silicone	10	PV	40	3.65	11.0	[12]
Modified silicone	10	TDEV	-30/40	19.3	16.6	[12]
PDMS	10	PV	40	7.44	6.4	[10,11]
PDMS	10	TDEV	-30/40	85.7	0.9	[10,11]
PMMA- <i>g</i> -PDMS (34/66)	10	PV	40	7.1	4.8	[15]
PMMA- <i>b</i> -PDMS (27/73)	10	PV	40	8.0	5.1	[16]
PMMA- <i>b</i> -PDMS (38/62) ^c	10	PV	40	6.8	3.5	[17]

^aNormalized permeation rate (units of kg $\mu\text{m}/(\text{m}^2 \text{ h})$).

^b0.2 wt% PFA-*g*-PDMS.

^cAnnealing at 120 °C for 2 h.

oethylene (TECET) from dilute aqueous solutions by pervaporation was investigated by Nakagawa and Kanemura [26]. Novel polymers with high selectivity for these solvents were synthesized by radical polymerization, i.e. glassy copolymers composed of (trimethylsilyl) methyl methacrylate (TMSMMA) and rubbery *n*-butyl acrylate (*n*-BA). The effect of the molar ratio of TMSMMA/*n*-BA on the permeation rate of TCE and the separation factor, $\alpha_{\text{TCE}/\text{H}_2\text{O}}$, was examined. The glass transition temperatures of the copolymers decreased with an increase in *n*-BA content, which resulted in high segmental mobility and thus high diffusivity. The copolymer membrane containing about 70 mol% of *n*-BA showed the highest separation factor, in the range 600–1000, for TCE. The high selectivity of these copolymer membranes for chlorinated hydrocarbons was mainly attributed to high partition coefficients for chlorinated hydrocarbons [26].

The removal of volatile organic compounds (VOCs), such as benzene and chloroform, from aqueous benzene and chloroform solutions using poly(methyl methacrylate)-PDMS (PMMA-*g*-PDMS), poly(ethyl methacrylate)-PDMS (PEMA-*g*-PDMS) and poly(*n*-butyl methacrylate)-PDMS (PBMA-*g*-PDMS) graft copolymer membranes was investigated by pervaporation. When aqueous solutions of dilute VOCs were permeated through the PMMA-*g*-PDMS and PEMA-*g*-PDMS membranes, these membranes were benzene/water- and chloroform/water-selective. The permeation and separation characteristics of the PMMA-*g*-PDMS and PEMA-*g*-PDMS membranes changed drastically at a DMS content of about 40 and 70 mol%, respectively, as shown in Figure 14.8. The permeation rate and VOC/water selectivity of the PBMA-*g*-PDMS membranes, however, increased gradually with increasing DMS content, unlike those of PMMA-*g*-PDMS and PEMA-*g*-PDMS membranes. Furthermore, transmission electron microscopy (TEM) observations revealed that the PMMA-*g*-PDMS and PEMA-*g*-PDMS membranes had microphase-separated structures, consisting of a PDMS phase and a poly(alkyl methacrylate) phase. On the other hand, the PBMA-*g*-PDMS membrane was homogeneous. The permeability and selectivity of these graft copolymer membranes for treatment of aqueous VOC solutions by pervaporation have been discussed in detail with respect to their membrane structure and solution-diffusion theory [27,28].

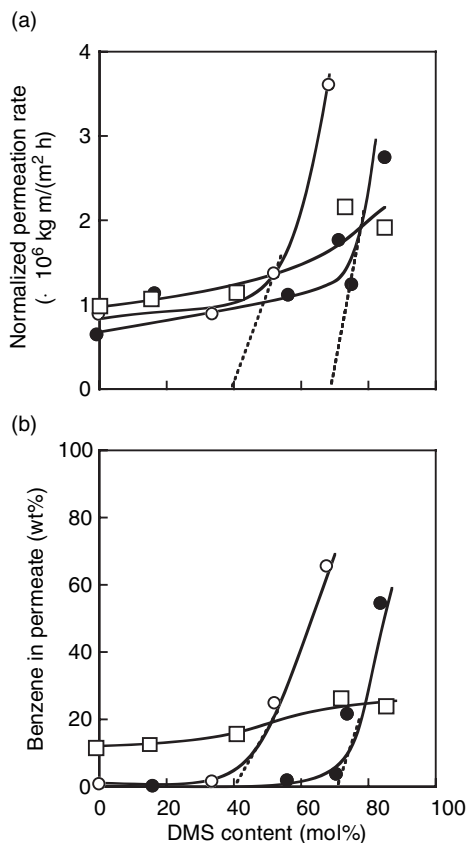


Figure 14.8 Effects of the DMS content on (a) the normalized permeation rate and (b) the benzene concentration in the permeate for an aqueous solution of 10 wt% ethanol through (○) PMMA-*g*-PDMS, (●) PEMA-*g*-PDMS and (□) PBMA-*g*-PDMS membranes during pervaporation [28]. Reprinted from *Journal of Membrane Science*, **187**, T. Uragami, H. Yamada and T. Miyata, 'Removal of dilute volatile organic compounds in water through graft copolymer membranes consisting of poly(alkyl methacrylate)s and polydimethylsiloxane by pervaporation and their membrane morphology', 255–269, Copyright (2001), with permission from Elsevier

Hydrophobically surface-modified membranes were prepared by adding a fluorine-containing graft copolymer to a microphase-separated membrane consisting of PDMS and PMMA. Contact angle measurements and X-ray photoelectron spectroscopy revealed that the addition of a fluorine-containing copolymer produced a hydrophobic surface at the air side of the membrane due to surface localization of the fluorinated copolymer. It was apparent from TEM that adding a

fluorine-containing copolymer of less than 1.2 wt% did not affect the morphology of the microphase-separated membrane. However, adding a fluorine-containing copolymer over 1.2 wt% resulted in a morphological change, from a continuous PDMS phase to a discontinuous PDMS phase. The addition of a small amount of fluorine-containing copolymer to the microphase-separated membranes enhanced both their permeability and selectivity for a dilute aqueous solution of benzene during pervaporation because of their hydrophobic surfaces and microphase-separated structures. Specifically, the microphase-separated membrane with 1.2 wt% of fluorine-containing copolymer concentrated an aqueous solution from 0.05 to 70 wt% benzene, and, therefore, removed the benzene from water very effectively [29].

PMMA-*g*-PDMS and PMMA-*b*-PDMS membranes containing *tert*-butylcalix[4]arene (CA) (CA/PMMA-*g*-PDMS and CA/PMMA-*b*-PDMS) were applied to the removal of benzene from a dilute aqueous solution of benzene by pervaporation [30]. When an aqueous solution of 0.05 wt% benzene was permeated through CA/PMMA-*g*-PDMS and CA/PMMA-*b*-PDMS membranes, these membranes showed high benzene/water selectivity. Both the permeability and benzene/water selectivity of the CA/PMMA-*g*-PDMS and CA/PMMA-*b*-PDMS membranes were enhanced by increasing the CA content, due to the affinity of CA for benzene. The permeability and benzene/water selectivity of CA/PMMA-*b*-PDMS membranes were much greater than those of CA/PMMA-*g*-PDMS membranes. TEM observations revealed that both the CA/PMMA-*g*-PDMS and CA/PMMA-*b*-PDMS membranes had microphase-separated structures, consisting of a PMMA phase and a PDMS phase-containing CA. The microphase-separated structure of the latter membranes was much clearer than that of the former and was lamellar. The distribution of CA in the microphase-separated structure of the CA/PMMA-*g*-PDMS and CA/PMMA-*b*-PDMS membranes was analyzed by differential scanning calorimetry [30,31].

14.4.3 Organic/Organic Separation

PVA membranes containing cyclodextrin (CD-PVA membrane) were prepared and the permeation and separation characteristics for propanol (PrOH) isomers through the CD-PVA membranes were investigated by pervaporation and evapomea-

tion [32]. Evapomeation was more effective for the separation of PrOH isomers through the CD-PVA membrane than pervaporation. The CD-PVA membrane preferentially permeated 1-PrOH rather than 2-PrOH from their mixtures. In particular, a mixture of 10 wt% 1-PrOH concentration was concentrated to about 45 wt% through the CD-PVA membrane. These CD-PVA membranes were also used to separate xylene isomers in pervaporation and evapomeation mode. The CD-PVA membranes showed *p*-xylene selectivity for *p*-xylene/*o*-xylene mixtures during evapomeation [33].

Park *et al.* reported on membranes made from a polymer blend of PAA and PVA [34]. These blend membranes were evaluated for the separation of methanol (MeOH) from methyl *tert*-butyl ether (MTBE) by pervaporation. Methanol permeated preferentially through all blend membranes tested, and the selectivity increased with increasing PVA content in the blends. However, a decrease in the permeation rate was observed with increasing PVA content. Upon increasing the feed temperature, the permeation rate increased and the selectivity remained constant. In addition, the influence of cross-linking on the selectivity was investigated. The pervaporation permeation rate decreased with increasing cross-linking density; however, this was coupled with an increase in MeOH/MTBE selectivity. This was due to a more rapid decrease in the partial permeation rate of MTBE compared to that of methanol [34].

Chen and Martin prepared thin-film composite membranes by coating a thin film of polystyrene-sulfonate (PSS) onto the surface of a microporous alumina (Al₂O₃) support [35]. The PSS composite membrane was applied to the separation of MTBE/MeOH mixtures in pervaporation mode and exhibited excellent performance. The PSS/Al₂O₃ composite membranes showed high MeOH selectivity, relative to MTBE. The MeOH concentration in the permeate was always greater than 99.5 wt% for all membranes tested and for all feed solution compositions studied. Membranes of the Mg²⁺-counterion form (PSS-Mg) showed higher separation factors than membranes having Na⁺ as the counterion (PSS-Na). Extremely high separation factors (25 000 to 35 000) were observed for the PSS-Mg/Al₂O₃ composite membrane containing 27.5 mol% sulfonate [35].

The pervaporation properties of a poly(urethane imide) block copolymer membrane for separation

of ethyl *tert*-butyl ether (ETBE)–ethanol (EtOH) mixtures have been investigated by Jonquieres *et al.* over the entire composition range [36]. The pervaporation selectivity towards ethanol was higher than the simple sorption selectivity of EtOH over ETBE. The features of sorption were examined in relation to the corresponding pervaporation properties and were analyzed in terms of the activity of each penetrant to take into account the ‘non-ideality’ of the system. Sorption isotherms could be expressed in terms of a single linear relationship for ETBE but required two linear relationships in the case of EtOH. The discontinuity in the EtOH isotherm corresponds to the composition of a critical feed mixture and was ascribed to the complete ‘mono-solvation’ of the polymer’s most basic site, i.e. urethane groups, by the protic penetrant [36].

Okuno *et al.* evaluated the preferential sorption and pervaporation selectivities of a poly(vinyl chloride) (PVC) membrane for various binary liquid mixtures [37]. Methanol/1-propanol, benzene/*n*-hexane and ethanol/water mixtures were selected as model mixtures in this study. For the methanol/1-propanol mixture, methanol preferentially sorbed in the PVC membrane, resulting in selective methanol permeation. For the benzene/*n*-hexane mixture, benzene exhibited higher sorption uptake and permeated preferentially. In the ethanol/water mixture, ethanol preferentially sorbed in the PVC membrane but water was the preferentially permeating component. This result suggested that the overall selectivity in the membrane was determined by a high water/ethanol diffusivity selectivity. The sorption data were analyzed according to Mulder’s model derived from Flory-Huggins thermodynamics. The pervaporation selectivity in these systems was analyzed using a sorption and diffusion selectivity model [37].

Composite membranes of polystyrene (PS) and a hydrophilic polymer were prepared by Ruckenstein and Sun via the concentrated emulsion polymerization method [38]. In the concentrated emulsion precursor, styrene-containing styrene-butadiene–styrene (SBS) block copolymers constituted the dispersed phase and a solution of a hydrophilic monomer in water was the continuous phase. The polymerized systems were transformed into membranes by hot pressing at 150 °C. The mechanical properties of the membranes were affected by the amount of SBS in the dispersed phase and by the nature of the hydrophilic monomers improved the mechanical properties of the

membrane significantly. The membranes were then subjected to sorption and pervaporation of benzene–ethanol mixtures. They exhibited preferential sorption of benzene over the entire benzene concentration range. The swelling ratio increased with increasing benzene concentration and the sorption selectivity decreased. These membranes had permeation rates as high as 1040 g/(m² h) and separation factors as high as 25 for benzene–ethanol mixtures [38].

Zhou *et al.* developed composite membranes based on a selective polypyrrole layer for the separation of ethanol and cyclohexane [39]. Polypyrrole films were deposited on stainless steel meshes by anodic electropolymerization of pyrrole dissolved in acetonitrile. Electrochemical and morphological studies on the growth of the polypyrrole films, both oxidized with PF₆⁻ as the counterion and with neutral polypyrrole membranes, were conducted. The performance of these membranes for ethanol/cyclohexane separation by pervaporation was investigated. The results indicated preferential permeation of ethanol and clearly demonstrated the feasibility of exploiting conducting polymers in the pervaporation process [39].

Johnson and Thomas investigated the pervaporation characteristics for acetone/chlorinated hydrocarbon mixtures using blend membranes of natural rubber (NR) with epoxidized NR (ENR) [40]. The permeation rate and selectivity of these membranes were determined both as a function of the blend composition and of the feed mixture composition. The results showed that the membrane performance could be optimized by adjusting the blend composition. NR/ENR (70/30) and NR/ENR (30/70) compositions showed a decrease in flux and chlorinated hydrocarbon/acetone selectivity, whereas the 50/50 composition showed an increased permeation rate and increased selectivity. Chlorinated hydrocarbons permeated preferentially through all of the tested membranes. The feed mixture composition also strongly influenced the pervaporation characteristics of the blend membranes. The chlorinated hydrocarbon/acetone selectivity was found to depend on the molecular size of the penetrants [40].

14.4.4 Benzene/Cyclohexane Separation

The separation of cyclohexane and benzene by distillation is a very energy-intensive process,

because the boiling points of the components are very similar. Pervaporation may be an alternative, more energy-efficient process for the separation of benzene/cyclohexane mixtures. Therefore, many studies have investigated the pervaporation properties of polymeric membranes for benzene/cyclohexane separations.

For example, Inui *et al.* investigated poly(methyl methacrylate) (PMMA) and poly(ethyl methacrylate) (PEMA) membranes, both of which have a strong affinity for benzene [41]. The pervaporation permeation and separation characteristics for benzene/cyclohexane mixtures in these poly(alkyl methacrylate) membranes cross-linked with ethylene glycol dimethacrylate (EGDM) were studied [41]. The cross-linked poly(alkyl methacrylate) membranes exhibited benzene selectivity for benzene/cyclohexane mixtures and the permeation rate increased with increasing benzene concentrations in the feed solution. The benzene/cyclohexane selectivity of these membranes was strongly governed by the diffusion selectivity and depended on the difference in molecular size between the benzene molecule and the cyclohexane molecule. With an increase in the cross-linker content in the membrane, swelling of the membranes was reduced, enhancing the benzene/cyclohexane selectivity. This result was attributed to an increase in the sorption selectivity caused by reduced swelling of the membrane. Cross-linked tertiary copolymer (PMMA-PEMA-EGDM) membranes also showed excellent benzene/cyclohexane selectivity. These results suggested that both the increase in the affinity of the membrane for benzene and the reduction in the swelling of the membrane are very important variables in the separation of benzene/cyclohexane mixtures [41].

Poly(dimethyl acrylamide)-random-poly(methyl methacrylate) (DMAA-*r*-MMA) and poly(dimethyl acrylamide)-graft-poly(methyl methacrylate) (DMAA-*g*-MMA) membranes were also examined for benzene/cyclohexane separation by pervaporation. The benzene selectivity of the DMAA-*r*-MMA membrane changed from diffusion-selectivity-controlled to solubility-selectivity-controlled with increasing DMAA content. In contrast, DMAA-*g*-MMA membranes with higher DMAA contents had higher apparent diffusivity selectivity than the apparent solubility selectivity. Furthermore, the apparent benzene/cyclohexane

solubility selectivity for the DMAA-*r*-MMA membrane and the DMAA-*g*-MMA membrane with a higher DMAA content was remarkably different. These results were attributed to the difference in structure between the copolymers [42].

A side-chain liquid-crystalline polymer (LCP) was synthesized by the addition of a mesogenic monomer to polymethylsiloxane with a Pt catalyst. When benzene/cyclohexane mixtures were permeated through the LCP membranes by pervaporation at various temperatures, the permeation rate increased with increasing benzene concentration in the feed solution and permeation temperature. Although the LCP membranes exhibited benzene/cyclohexane selectivity, the mechanism responsible for the permeation and separation of the benzene/cyclohexane mixtures was different in the glassy, liquid-crystalline state versus the isotropic state of the LCP membranes. These results suggest that the selectivity was moderately influenced by the change in LCP membrane structure (i.e. a state transformation). The balance between the orientation of the mesogenic groups and the flexibility of the siloxane chain is very important with respect to permeability and selectivity [43,44]. When benzene/cyclohexane, toluene/cyclohexane and *o*-xylene/cyclohexane mixtures are subjected to pervaporation through a LCP membrane in the liquid-crystalline state, the permeation rate increases with increasing temperature and the LCP membrane exhibits selectivity for the aromatic hydrocarbons. The permeation rate and selectivity of the LCP membrane for each mixture decreased with increasing molecular size of the aromatic hydrocarbon in the binary feed mixture [45]. When benzene/cyclohexane mixtures were permeated through nematic and smectic side-chain liquid-crystalline polymers (*n*- and *s*-LCPs) membranes under various conditions during pervaporation, the *n*- and *s*-LCP membranes exhibited benzene/cyclohexane selectivity. The selectivity of the *n*-LCP membrane changed from sorption selectivity to diffusion selectivity upon the state transformation of the membrane, induced by an increase in the permeation temperature. In contrast, the selectivity of the *s*-LCP membrane was governed by diffusion selectivity, regardless of the state of this membrane. At low permeation temperatures, the *n*-LCP membrane in the liquid-crystalline state exhibited lower permeability but higher selectivity than the *s*-LCP membrane. However,

at high permeation temperatures, the relationship between the permeability and selectivity of the *n*-LCP and *s*-LCP membranes in the liquid-crystalline state was reversed. These results are caused by differences in the chemical and physical structure of the *n*-LCP and *s*-LCP membranes [46].

Chitosan and its derivatives have been used as membrane materials for a wide variety of pervaporation applications, including dehydration of ethanol/water mixtures. Uragami *et al.* [47] synthesized benzoylchitosan (BzChitos) with different degrees of benzylation as a durable membrane material for the separation of benzene/cyclohexane mixtures. The characteristics of BzChito membranes, such as contact angle, crystallinity and the degree of swelling, were significantly influenced by the degree of benzylation. The BzChitos membranes showed high benzene/cyclohexane selectivity for a mixture containing 50 wt% benzene during pervaporation. The difference in benzene/cyclohexane selectivity of the BzChitos membranes with different degrees of benzylation corresponded to differences in the physical structure of the membranes. When a benzene/cyclohexane mixture of 50 wt% benzene was permeated through the BzChitos membranes, the permeation rate increased and the benzene/cyclohexane selectivity decreased slightly with an increasing degree of benzylation [47,48].

Uragami *et al.* also investigated the use of modified cellulose-based membranes for benzene/cyclohexane separation [49,50]. Various types of benzoylcellulose (BzCell) were synthesized and the effect of the degree of benzylation on the pervaporation properties of the membranes was investigated [49]. A BzCell membrane with a benzylation degree of 2 showed high benzene/cyclohexane selectivity for benzene/cyclohexane mixtures during pervaporation. The permeation rate of the BzCell membrane increased but the benzene/cyclohexane selectivity decreased with increasing benzene concentration in the feed mixture. This increase in the permeation rate was due to an increase in the swelling of the membrane, whereas the benzene selectivity decrease was attributed to a decrease in the sorption selectivity. With increasing benzylation of the BzCells, the permeation rate increased significantly, but the benzene selectivity decreased slightly.

These results cannot be explained by the degree of swelling, the density or the contact angle of the BzCell membranes [49].

Tosylcellulose (TosCell) compounds, with different degrees of tosylation were synthesized as membrane materials for the separation of benzene/cyclohexane mixtures. TosCell membranes showed high benzene/cyclohexane selectivity when tested in pervaporation mode. An increase in the benzene concentration of the feed mixtures increased the permeation rate but decreased the benzene/cyclohexane selectivity of the TosCell membranes. This increase in the permeation rate was attributed to an increase in the degree of swelling of the TosCell membranes due to sorption of the feed mixture. The decrease in benzene/cyclohexane selectivity was mainly caused by a decrease in sorption selectivity. With low benzene concentrations in the mixtures, the permeation rate of a TosCell membrane with a higher degree of tosylation was greater than that with a lower degree of tosylation; however, the reverse was observed for high benzene concentrations. The benzene/cyclohexane selectivity of the former TosCell membrane was higher than that of the latter membrane. Differences in the permeation rate and benzene/cyclohexane selectivity with changes in the benzene concentration of the feed mixture and the degree of tosylation of the TosCell membrane were significantly influenced by the degree of swelling of the TosCell membrane, which is related to the benzene concentration sorbed into the membrane. The mechanism responsible for the separation of benzene/cyclohexane mixtures through the TosCell membranes was analyzed and discussed by using the solution-diffusion model [50].

Methyl methacrylate-methacrylic acid (MMA-M4MA) copolymer membranes, ionically cross-linked with Fe^{3+} and Co^{2+} ions (MMA-M4MA- Fe^{3+} and - Co^{2+}), were prepared, and their permeation and separation characteristics for a benzene/cyclohexane mixture containing 50 wt% benzene by pervaporation were studied. Although the introduction of the metal ions into the MMA-M4MA membrane enhanced both benzene/cyclohexane selectivity and permeability for a benzene/cyclohexane mixture, the pervaporation characteristics of the MMA-M4MA- Fe^{3+} and - Co^{2+} membranes were significantly different. The difference in performance between these membranes was strongly governed by

differences in their membrane structures, as indicated by their glass transition temperature, contact angle to methylene iodide, degree of swelling and mixture composition sorbed into the membrane [51].

Ren *et al.* investigated the pervaporation properties of a series of cross-linked 4,4'-hexafluoro-isopropylidene dianhydride (6FDA)-based copolyimide membranes for the separation of benzene/cyclohexane mixtures [52]. The glassy, highly rigid copolyimides were obtained by polycondensation of 6FDA with various diamines. To obtain high permeability as well as high selectivity, a combination of the diamines 2,3,5,6-tetramethyl-1,4-phenylene diamine (4MPD), 4,4'-hexafluoro-isopropylidene dianiline (6FpDA) and 3,5-diaminobenzoic acid (DABA) as monomers with a cross-linkable group were used. Cross-linking is necessary to prevent undesirable swelling effects, which generally occur with non-cross-linked polyimides, especially if high benzene concentrations are reached during pervaporation. The degree of cross-linking was kept constant at 20%, whereas the ratio of the diamine monomers 6FpDA and 4MPD was varied. The pervaporation experiments were performed at 60 °C, using benzene/cyclohexane mixtures with benzene concentrations covering the entire concentration range. All of the cross-linked polymers had excellent chemical and thermal stability in the pervaporation experiments. In all cases, conditioning of the membrane samples with pure benzene was a suitable pretreatment to enhance the permeation rate without decreasing the selectivity significantly. For the most promising membrane material, 6FDA-4MPD/DABA (4:1) cross-linked with ethylene glycol, the pervaporation experiments were performed with a 50:50 wt% benzene/cyclohexane feed mixture over a temperature range between 60 and 110 °C to determine the effect of temperature on the separation characteristics [52].

The sorption and pervaporation properties of PVC membranes in benzene/cyclohexane mixtures were studied by Yildirim *et al.* [53]. The effects of the Bz/Chx mixture composition and the temperature on the sorption and pervaporation characteristics were determined at 30, 40, and 50 °C, respectively, for membranes containing 8 wt% PVC. The total sorption increased with increasing concentrations of

benzene. Increasing the concentration of benzene resulted in an increase in permeation rate and a decrease in the selectivity. The permeation rates increased and the selectivity decreased with increasing temperature. The selectivity was not affected significantly by varying the concentration of polymer in the casting solution, but, as expected for a non-porous membrane, the permeation rate decreased with increasing concentration of the polymer in the casting solution due to an increase in membrane thickness [53].

In Table 14.2, the pervaporation performance of various polymer membranes for the separation of benzene/cyclohexane mixtures are listed [54]. When the pervaporation performance is estimated by the pervaporation separation index (PSI) [62], which is the product of the permeation rate and the separation factor, PSI can be used as a measure of membrane performance during pervaporation. It is found that polystyrene/poly(acrylic acid) (PS/PAA), benzoylchitosan (BzChitos) and benzoylcellulose (BzCell) membranes showed higher performance for the separation of benzene/cyclohexane mixtures during pervaporation.

14.5 Conclusions

Water-selective membranes designed for the separation of organic liquid mixtures by pervaporation have already been put into practical use and future expansion is expected. These membranes have found applications in the chemical and electronics industries. Specifically, water-selective membranes, such as poly(vinyl alcohol), are currently used for dehydration of alcohols. On the other hand, organic-selective membranes are still being developed with improvements in selectivity, permeability and the durability necessary for their practical use. The membrane materials, membrane preparation techniques and separation process parameters for organic-selective membranes are still being refined. It will be important to develop novel membrane separation methods based on the solution-diffusion mechanism. We expect that superior membranes for organic liquid mixtures can be developed in the near future.

Table 14.2 Pervaporation performance of various polymer membranes for the separation of benzene/cyclohexane mixtures

Membrane ^a	Benzene in feed (wt%)	Temperature (°C)	NPR ^b	$\alpha_{\text{Bz/Chx}}$	PSI ^c	Reference
PVA/PAAm	50	25	2.3	11.9	27.4	[55]
BP-3MPD/PD	50	70	2.7	14	37.8	[56]
BP-PEO	60	25–70	2.1	9.1	19.1	[57]
DSDA-DDBT	60	78	0.93	32	29.8	[58]
DSDA-DDBT	60	78	2.4	20	48	[58]
PU-TEOS	50	50	0.65	19	12.4	[59]
PGMA grafted	60	40–70	8.7	22	191.4	[60]
PS/PAA	50	20	48.4	9.6	464.6	[61]
PEMA-EGDM	10	40	8.7	6.7	58.3	[41]
PEMA-EGDM	10	40	55.1	3.9	214.9	[41]
<i>n</i> -LPC	50	10	13.1	2.0	26.2	[43]
<i>s</i> -LPC	50	10	7.5	1.9	14.3	[46]
BzChitos	10	40	6.4	65	416.0	[47]
BzChitos	50	40	1.5	13	19.5	[47]
BzCell	10	40	0.6	2.3	13.8	[49]
BzCell	50	40	33.6	9.1	305.7	[49]
TosCell	40	40	0.06	28.9	1.7	[50]

^a3MPD, 2,4,6-trimethyl-1,3-phenylenediamine; BzChitos, benzoyl chitosan; BzCell, benzoyl cellulose; BP, 3,3',4,4'-biphenyltetracarboxylic dianhydride; DDBT, dimethyl-3,7-diaminibenzothiophene-5,5'-dioxide; DSDA, 3,3',4,4'-diphenylsulphone tetracarboxylic dianhydride; EGDM, ethylene glycol dimethacrylate; *n*-LPC: nematic liquid-crystalline polymer; PAA, poly(acrylic acid); PAAm, poly(allyl amine); PAS, polyacrylonitrile-*co*-styrene; PD, 1,3-phenylenediamine; PEMA, poly(ethyl methacrylate); PEO, poly(ethylene oxide); PGMA, poly(glycidyl methacrylate); PMMA, poly(methyl methacrylate); PS, polystyrene; PU, polyurethane; TEOS, tetraethylorthosilicate; *s*-LPC: smectic liquid-crystalline polymer; TosCell, tosyl cellulose.

^bNormalized permeation rate (units of kg $\mu\text{m}/(\text{m}^2 \text{h})$).

^cPervaporation separation index.

References

- [1] (a) T. Uragami, 'Functions of membrane separation and membrane structure', *Hyomen*, **21**, 482 (1983); (b) Separation membranes of organic liquid mixtures - Their characteristics and applications, *Hyomen*, **30**, 52 (1992).
- [2] T. Uragami, 'Separation membranes', in *Advanced High Functional Materials*, A. Yoshikawa, H. Miyairi, E. Iizuka, T. Takeshita, M. Matsushima and T. Moroya (Eds), NGT, Tokyo, Japan, pp. 182–196 (2001).
- [3] R. C. Binding, R. J. Lee, J. F. Jennings and E. C. Mertin, 'Separation of liquid mixtures by permeation', *Ind. Eng. Chem.*, **53**, 47 (1961).
- [4] P. Aptel, J. Cuny, J. Jozefonvice, G. Morel and J. Neel, 'Liquid transport through membranes prepared by grafting of polar monomers onto poly(tetrafluoroethylene) films. II. Some factors determining pervaporation rate and selectivity', *J. Appl. Polym. Sci.*, **18**, 365 (1974).
- [5] C. Y. Choo, 'Membrane permeation', in *Membrane Permeation in Advances in Petroleum Chemistry and Refining*, T. Meketta (Ed.), John Wiley & Sons, Inc., New York, NY, USA, pp. 72–117 (1962).
- [6] S. Yamada, 'Estimation of performance of liquid-liquid permeation membranes', in *Estimation of Performance of Artificial Membranes*, Membrane Society of Japan (Ed.), Membrane Society of Japan, Tokyo, Japan, pp. 30–41 (1981).
- [7] T. Uragami, 'Structures and properties of membranes from polysaccharide derivatives', in *Polysaccharides - Structural Diversity and Functional Versatility*, S. Dumitriu (Ed.), Marcel Dekker, New York, NY, USA, pp. 887–924 (1998).
- [8] T. Uragami, M. Saito and K. Takigawa, 'Comparison of permeation and separation characteristics for aqueous alcoholic solutions by pervaporation and new evaporation methods through chitosan membranes', *Makromol. Chem., Rapid Commun.*, **9**, 361 (1988).
- [9] T. Uragami, M. Saito and M. Sugihara, 'Analysis of permeation and separation characteristics: a new technique for separation of aqueous alcoholic solution through alginate acid membranes', *Seppn Sci. Technol.*, **24**, 541 (1989).

- [10] T. Uragami and T. Morikawa, 'Permeation of ethanol through polydimethyl siloxane membranes using temperature difference in membrane permeation process of the evaporation method', *Makromol. Chem., Rapid Commun.*, **10**, 287 (1987).
- [11] T. Uragami and T. Morikawa, 'Permeation and separation characteristics of alcohol-water mixtures through dimethylsiloxane membrane by pervaporation and evaporation', *J. Appl. Polym. Sci.*, **44**, 2009 (1992).
- [12] T. Uragami and H. Shinomiya, 'Concentration of aqueous alcoholic solutions through a modified silicone rubber membrane by pervaporation and evaporation', *Makromol. Chem. Phys.*, **192**, 2293 (1991).
- [13] S. Kimura and T. Nomura, 'Pervaporation of an alcohol-water mixture with a silicon rubber membrane', *Membrane*, **7**, 353 (1982).
- [14] T. Miyata, T. Takagi, T. Kadota and T. Uragami, 'Characteristics of permeation and separation for aqueous ethanol solutions through methyl methacrylate-dimethylsiloxane graft copolymer membranes', *Macromol. Chem. Phys.*, **196**, 1211 (1995).
- [15] T. Miyata, T. Takagi and T. Uragami, 'Microphase separation in graft copolymer membranes with pendant oligodimethylsiloxanes and their permselectivity for aqueous ethanol solutions', *Macromolecules*, **29**, 7787 (1996).
- [16] T. Miyata, S. Obata and T. Uragami, 'Morphological effects of microphase separation on the permselectivity for aqueous ethanol solutions of block and graft copolymer membranes containing polydimethylsiloxane', *Macromolecules*, **32**, 3712 (1999).
- [17] T. Miyata, S. Obata and T. Uragami, 'Annealing effect of microphase-separated membranes containing polydimethylsiloxane on their permselectivity for aqueous ethanol solutions', *Macromolecules*, **32**, 8465 (1999).
- [18] K. Ishihara, Y. Nagase and K. Matsui, 'Pervaporation of alcohol/water mixtures through poly[1-(trimethylsilyl)-1-propyne] membrane', *Makromol. Chem., Rapid. Commun.*, **7**, 43 (1986).
- [19] T. Masuda, B.-Z. Tang and T. Higashimura, 'Ethanol-water separation by pervaporation through substituted polyacetylene membranes', *Polym. J.*, **18**, 565 (1986).
- [20] T. Uragami, T. Doi and T. Miyata, 'Control of permselectivity with surface modifications of poly[1-(trimethylsilyl)-1-propyne] membranes', *Int. J. Adhes Adhes.*, **19**, 405 (1999).
- [21] T. Uragami, T. Doi and T. Miyata, 'Pervaporation properties of surface-modified poly[1-(trimethylsilyl)-1-propyne] membranes', in *Membrane Formation and Modification*, I. Pinnau and B. D. Freeman (Eds), American Chemical Society, Washington, DC, USA, pp. 263-279 (2000).
- [22] H. Eustache and G. Histi, 'Separation of aqueous organic mixtures by pervaporation and analysis by mass spectrometry or a coupled gas chromatograph-mass spectrometer', *J. Membr. Sci.*, **8**, 105 (1981).
- [23] Y. Nagase, S. Mori and K. Matsui, 'Chemical modification of poly(substituted-acetylene). 4. Pervaporation of an organic liquid-water mixture through a poly(1-phenyl-1-propylene)-polydimethylsiloxane graft copolymer membrane', *J. Appl. Polym. Sci.*, **37**, 1259 (1989).
- [24] K. Ishihara and K. Matsui, 'Ethanol permselective polymer membranes 3. Pervaporation of an ethanol-water mixture through composite membranes composed of styrene-fluoroalkylacrylate graft copolymers and cross-linked polydimethylsiloxane membranes', *J. Appl. Polym. Sci.*, **34**, 437 (1987).
- [25] T. Kashiwagi, K. Okabe and K. Okita, 'Separation of ethanol from ethanol/water mixtures by plasma-polymerized membranes from silicone compounds', *J. Membr. Sci.*, **36**, 353 (1988).
- [26] T. Nakagawa and A. Kanemura, 'Synthesis and permeability of novel polymeric membranes with high permselectivity for chlorinated hydrocarbons', *SENI GAKAISHI*, **51**, 123 (1995).
- [27] T. Uragami, H. Yamada and T. Miyata, 'Removal of volatile organic compounds from dilute aqueous solutions by pervaporation', *Trans. Mater. Res. Soc. Jpn.*, **24**, 165 (1999).
- [28] T. Uragami, H. Yamada and T. Miyata, 'Removal of dilute volatile organic compounds in water through graft copolymer membranes consisting of poly(alkyl methacrylate)s and polydimethylsiloxane by pervaporation and their membrane morphology', *J. Membr. Sci.*, **187**, 255 (2001).
- [29] T. Miyata, H. Yamada and T. Uragami, 'Surface modification of microphase-separated membranes by fluorine-containing polymer additives and removal of dilute benzene in water through these membranes', *Macromolecules*, **34**, 8026 (2001).
- [30] T. Uragami, T. Meotoiwa and T. Miyata, 'Effects of addition of calixarene to microphase-separated membranes for the removal of volatile organic compounds from dilute aqueous solutions', *Macromolecules*, **34**, 6806 (2001).
- [31] T. Uragami, T. Meotoiwa and T. Miyata, 'Effects of morphology of multicomponent polymer membranes containing calixarene on permselective removal of benzene from a dilute aqueous solution of benzene', *Macromolecules*, **36**, 2041 (2003).
- [32] T. Miyata, T. Iwamoto and T. Uragami, 'Characteristics of permeation and separation for pro-

- panol isomers through poly(vinyl alcohol) membranes containing cyclodextrin', *J. Appl. Polym. Sci.*, **51**, 2007 (1994).
- [33] T. Miyata, T. Iwamoto and T. Urugami, 'Characteristics of permeation and separation of xylene isomers through poly(vinyl alcohol) membranes containing cyclodextrin', *Macromol. Chem. Phys.*, **197**, 2909 (1996).
- [34] H. C. Park, N. E. Ramaker, M. H. V. Mulder and C. A. Smolders, 'Separation of MTBE-methanol mixtures by pervaporation', *Sepr Sci. Technol.*, **30**, 419 (1995).
- [35] W.-J. Chen and C. R. Martin, 'Highly methanol-selective membranes for the pervaporation separation of methyl *t*-butyl ether/methanol mixtures', *J. Membr. Sci.*, **104**, 101 (1995).
- [36] A. Jonquieres, D. Roizard and P. Lochon, 'Contribution of sorption to global mass transfer during pervaporation of ethyl *tert*-butyl ether-ethanol mixtures through a polyurethaneimide film', *J. Chem. Soc., Faraday Trans., Part 1*, **91**, 1247 (1995).
- [37] H. Okuno, T. Nishida and T. Urugami, 'Preferential sorption and permeation of binary liquid mixtures in a poly(vinyl chloride) membrane by pervaporation', *J. Polym. Sci., Part B: Polym. Phys. Ed.*, **33**, 299 (1995).
- [38] E. Ruckenstein and F. Sun, 'Hydrophobic-hydrophilic composite membranes for the pervaporation of benzene-ethanol mixtures', *J. Membr. Sci.*, **103**, 271 (1995).
- [39] M. Zhou, M. Persin, W. Kujawski and J. Sarrazin, 'Electrochemical preparation of polypyrrole membranes and their application in ethanol-cyclohexane separation by pervaporation', *J. Membr. Sci.*, **108**, 89 (1995).
- [40] T. Johnson and S. Thomas, 'Pervaporation of acetone-chlorinated hydrocarbon mixtures through polymer blend membranes of natural rubber and epoxidized natural rubber', *J. Appl. Polym. Sci.*, **71**, 2365 (1999).
- [41] K. Inui, H. Okumura, T. Miyata and T. Urugami, 'Permeation and separation of benzene/cyclohexane mixtures through cross-linked poly(alkyl methacrylate) membranes', *J. Membr. Sci.*, **132**, 193 (1997).
- [42] K. Inui, H. Okumura, T. Miyata and T. Urugami, 'Characteristics of permeation and separation of dimethyl acrylamide-methyl methacrylate random and graft copolymer membranes for a benzene/cyclohexane mixture', *Polym. Bull.*, **39**, 733 (1997).
- [43] K. Inui, T. Miyata and T. Urugami, 'Permeation and separation of benzene/cyclohexane mixtures through liquid-crystalline polymer membranes', *J. Polym. Sci., Part B: Polym. Phys. Ed.*, **35**, 699 (1997).
- [44] K. Inui, T. Miyata and T. Urugami, 'Effect of permeation temperature on permeation and separation of a benzene/cyclohexane mixture through liquid-crystalline polymer membranes', *J. Polym. Sci., Part B: Polym. Phys. Ed.*, **36**, 281 (1998).
- [45] K. Inui, T. Miyata and T. Urugami, 'Permeation and separation of binary organic mixtures through a liquid-crystalline polymer membrane', *Macromol. Chem. Phys.*, **199**, 589 (1998).
- [46] K. Inui, K. Okazaki, T. Miyata and T. Urugami, 'Effect of mesogenic groups on characteristics of permeation and separation for benzene/cyclohexane mixtures of side-chain liquid-crystalline polymer membranes', *J. Membr. Sci.*, **143**, 93 (1998).
- [47] T. Urugami, K. Tsukamoto, K. Inui and T. Miyata, 'Pervaporation characteristics of a benzoylchitosan membrane for benzene-cyclohexane mixtures', *Macromol. Chem. Phys.*, **199**, 49 (1998).
- [48] K. Inui, K. Tsukamoto, T. Miyata and T. Urugami, 'Permeation and separation of a benzene/cyclohexane mixture through benzoylchitosan membranes', *J. Membr. Sci.*, **138**, 67 (1998).
- [49] T. Urugami, K. Tsukamoto, T. Miyata and T. Heinze, 'Pervaporation characteristics for benzene/cyclohexane mixtures through benzoylcellulose membranes', *Macromol. Chem. Phys.*, **200**, 1985 (1999).
- [50] T. Urugami, K. Tsukamoto, T. Miyata and T. Heinze, 'Permeation and separation characteristics for benzene/cyclohexane mixtures through toscylcellulose membranes in pervaporation', *Cellulose*, **6**, 221 (1999).
- [51] K. Inui, T. Noguchi, T. Miyata and T. Urugami, 'Pervaporation characteristics of methyl methacrylate-methacrylic acid copolymer membranes ionically cross-linked with metal ions for a benzene/cyclohexane mixture', *J. Appl. Polym. Sci.*, **71**, 233 (1999).
- [52] J. Ren, C. Standt-Bickel and R. Lichtenthaler, 'Separation of aromatics/aliphatics with cross-linked 6FDA-based copolyimides', *Sepr Purif. Technol.*, **22-23**, 31 (2001).
- [53] A. Yildirim, N. Hilmioglu and S. Tulbentci, 'Pervaporation separation of benzene/cyclohexane mixtures by poly(vinyl chloride) membranes', *Chem. Eng. Technol.*, **24**, 275 (2001).
- [54] J. P. Garcia Villalengua and A. Tabe-Mohammadi, 'A review on the separation of benzene/cyclohexane mixtures by pervaporation processes', *J. Membr. Sci.*, **169**, 159 (2000).
- [55] C. K. Park, B. K. Oh, M. J. Choi and Y. M. Lee, 'Separation of benzene/cyclohexane by pervaporation through chelate poly(vinyl alcohol)/poly(allyl amine) blend membranes', *Polym. Bull.*, **33**, 591 (1994).

- [56] N. Tanihara, K. Tanaka, H. Kita and K. Okamoto, 'Pervaporation of organic liquid mixtures through membranes of polyimides containing methyl-substituted phenylenediamine moieties', *J. Membr. Sci.*, **95**, 161 (1994).
- [57] N. Tanihara, N. Umeo, T. Kawabata, K. Tanaka, H. Kita and K. Okamoto, 'Pervaporation of organic liquid mixtures through poly(ether imide) segmented copolymer membranes', *J. Membr. Sci.*, **104**, 181 (1995).
- [58] J. Hao, K. Tanaka, H. Kita and K. Okamoto, 'The pervaporation properties of sulfonyl-containing polyimide membranes to aromatic/aliphatic hydrocarbon mixtures', *J. Membr. Sci.*, **132**, 97 (1997).
- [59] K. Kusakabe, S. Yoneshige and S. Morooka, 'Separation of benzene/cyclohexane mixtures using polyurethane-silica hybrid membranes', *J. Membr. Sci.*, **149**, 29 (1998).
- [60] H. Wang, X. Lin, K. Tanaka, H. Kita and K. Okamoto, 'Preparation of plasma-grafted polymer membranes and their morphology and pervaporation properties toward benzene/cyclohexane mixtures', *J. Polym. Sci., Part A: Polym. Chem. Ed.*, **36**, 2247 (1998).
- [61] F. Sum and E. Ruckenstein, 'Sorption and pervaporation of benzene/cyclohexane mixtures through composite membranes prepared via concentrated emulsion polymerization', *J. Membr. Sci.*, **99**, 273 (1995).
- [62] R. Y. M. Huang and J. W. Rhim, 'Separations characteristics of pervaporation membrane separation processes', in *Pervaporation Membrane Separation Processes*, R. Y. M. Huang (Ed.), Elsevier, Amsterdam, The Netherlands, pp. 111-180 (1991).

Zeolite Membranes for Pervaporation and Vapor Permeation

Hidetoshi Kita

15.1 Introduction

Separation processes play critical roles in manufacturing and their proper application can significantly reduce costs and increase profits. Alternative energy-saving and high efficiency separation process are strongly expected to be applied to many industries. Membrane separation appears to be a promising candidate because of low energy consumption, compact units, simple operation and low environmental impact. Therefore, strong interest exists in the synthesis of membranes that exhibit both higher permeabilities and higher selectivities than presently available polymers. Membranes made from inorganic materials are generally superior to organo-polymeric materials in thermal and mechanical stability and chemical resistance. The introduction of microporous properties in inorganic membranes appears to have strong potential application with respect to high-temperature gas separation, pervaporation and vapor permeation for liquid mixtures and catalysis. In the past decade, there has been a rapid growth in the number of publication dealing with synthesis and characterization of microporous inorganic membranes, especially zeolite membranes. Among these preparative studies of zeolite membranes, the most promising method is preparation of composite membranes, where a thin zeolite top layer is crystallized hydrothermally on the top support or inside the pores of the support. During the last five years, some excellent reviews on zeolite membranes have appeared [1–5].

This present chapter is, therefore, focused on pervaporation and vapor permeation membranes made from several zeolites, as shown in Figure 15.1. Small-pore membranes of A-type (LTA) zeolites can separate mixtures of water and alcohol by hydrophilic interaction and molecular sieving. Large-pore membranes of the X- and Y-type (FAU) zeolites, with a pore size of 0.74 nm, can be applicable to separate mixtures of methanol/methyl-*tert*-butyl ether or benzene/cyclohexane.

Pervaporation has gained some acceptance in the chemical industry as an effective process for the separation of azeotropic mixtures [6,7]. The pervaporation process involves a sequence of three steps: (1) selective sorption in the membrane on the feed side, (2) selective diffusion through the membrane and (3) desorption into a vapor phase on the permeate side. The separation principle in pervaporation is based on differences in solubility and diffusivity. Thus, the permeability (P) of the membrane can be written as a product of two terms, i.e. the solubility S and the diffusibility D , as shown in following:

$$P = SD \quad (15.1)$$

Under ideal conditions, with a zero downstream pressure of the membrane, the ideal separation factor of the membrane for components A and B is expressed as the ratio of the permeabilities of the two penetrants:

$$\alpha_{A/B} = P_A/P_B = [S_A/S_B][D_A/D_B] \quad (15.2)$$

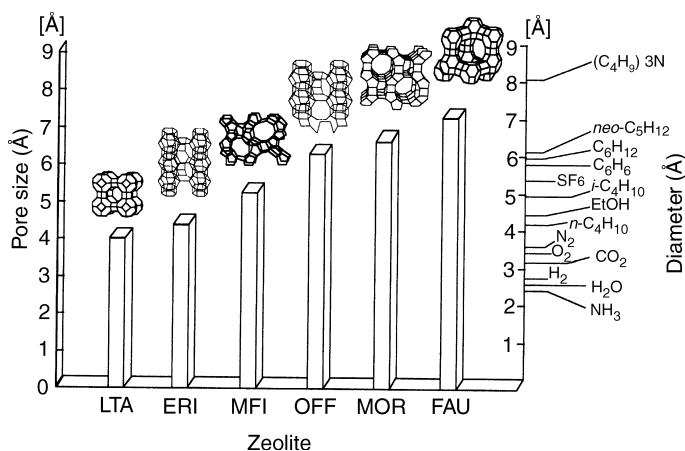


Figure 15.1 Correlation between the pore sizes of the zeolites used for pervaporation and vapor permeation and the diameters of various molecules

This factor provides a good measure of the ability of a given membrane material. The separation factor is experimentally determined as:

$$\alpha_{A/B} = [Y_A/Y_B]/[X_A/X_B] \quad (15.3)$$

where A is the preferentially permeating component and X_A , X_B , Y_A and Y_B denote the fractions of components A and B in the feed and the permeate, respectively. The economical advantages of pervaporation plants can amount up to 30% in the investment and up to 50% in the operating cost in comparison to rectification plants [8]. However, pervaporation has not found widespread distribution in the industry, mainly because of swelling and the limited thermal stabilities of the polymeric membranes being used. The performance of zeolite membranes is the most favorable one yet for pervaporation membranes which have been reported so far and is high enough to allow such membranes to be put into practical use (see also Chapter 12).

15.2 Zeolite Membranes for Water/Organic Liquid Separation

15.2.1 Hydrophilic Membranes

15.2.1.1 LTA Zeolite Membranes

Removal of water from liquid organic mixtures has now become the largest segment of industrial pervaporation applications. Among these, dehydration of fermentation products (ethanol dehydration) is a classic example of pervaporation and there are many membrane researches regarding water/ethanol separation. Table 15.1 shows the pervaporation performance of representative membranes for the water/ethanol system. Pervaporation experiments are carried out with either a batchwise system [7] or a flow cell system [9]. The membrane performance is evaluated by a permeation flux in ($\text{kg m}^{-2} \text{h}^{-1}$) and a separation factor (α). The separation factor is determined as $\alpha_{A/B} = (Y_A/Y_B)/(X_A/X_B)$, where X_A , X_B , Y_A and Y_B denote the weight fractions of components A and B in

Table 15.1 Pervaporation performances of representative membranes for water/ethanol systems

Membrane	$T(^{\circ}\text{C})$	Feed (wt% water)	$Q(\text{Kg}/(\text{m}^2 \text{h}))$	α	Reference
A-type zeolite	75	5	1.10	> 10 000	[9,10]
	75	10	2.15	> 10 000	[9,10]
	105	10 (vapor)	4.53	> 10 000	[9,10]
Silica/acrylamide	50	10	0.3	3 200	[11]
GFT	80	5	0.24	9 500	[12]
PAA/polyion complex	60	5	1.63	3 500	[13]
Chitosan	60	10	0.1	6 000	[14]

the feed and the permeate, respectively, and A is the species which preferentially permeates.

Hydrophillic membranes of poly(vinyl alcohol) (PVA) [12], poly(acrylic acid) (PAA) [13] or Chitosan [14] are the most widely studied for dehydration membranes. The commercial membrane GFT is made from cross-linked PVA. Aromatic polyimides with excellent thermal, chemical and mechanical stability are also used for making dehydration membranes [15]. Although previous research has focused on water/organic liquid separation, membranes which have both high selectivity and high flux are not commonly available. The A-type zeolite membranes shows the most promising performance of all pervaporation membranes studied to date.

A-type zeolite membranes, composed of a continuous intergrowth of LTA crystals, have been synthesized hydrothermally on various substrates [1,4]. Figure 15.2 shows the synthetic procedure used to produce the A-type zeolite membranes identified in Table 15.1. An aluminate solution is prepared by dissolving sodium hydroxide and aluminum hydroxide in distilled water, while a silicate solution is prepared by dissolving sodium silicate in distilled water. The aluminate solution is then added to the silicate solution and the resulting mixture is stirred vigorously, producing a homogeneous gel or clear solution. The solution is transferred to a glass or stainless steel vessel fitted with a condenser and a heater. Then, the porous inorganic support (alumina or mullite tubes: 1.0 or 1.2 cm outer diameter, 10–20 cm length and 1–2 μm average pore size), coated by the seed crystals of the A-type zeolite, is placed in

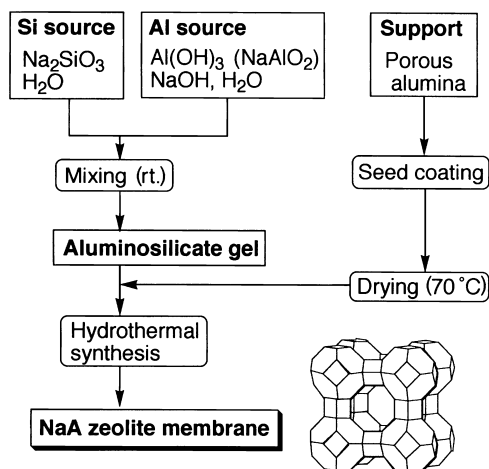


Figure 15.2 Schematic illustration of the synthetic procedure used to prepare A-type zeolite membranes

the solution. After hydrothermal treatment, the support is taken out, washed by water and dried. An example of the synthesis conditions employed for preparation of an A-type zeolite membrane is shown in Table 15.2. The compositions of this membrane is almost the same as that reported for the A-type zeolite crystal [16]. Without any coating of the seed crystals, however, it is necessary to carry out the procedure more than several times in order to obtain a membrane which is fully covered by a continuous polycrystalline A-type zeolite on the porous support. The synthesis of T-, X- and Y-type zeolite membranes on porous

Table 15.2 Synthesis conditions for A-type zeolite membranes

Al ^a	Molar ratio			T (°C)	t (h)	Seed	Membrane formation
	Na ₂ O/SiO ₂	SiO ₂ /Al ₂ O ₃	H ₂ O/Na ₂ O				
A	1.2	2.0	30–60	100	3, 16	–	Partial
A	1.2	2.0	130	100	16	–	No crystals
A	1.6	1.8	50	100	3, 16	–	Partial
A	0.6	7.2	130	100	3, 16	–	Partial
B	1.2	2.0	60–250	80	3, 10, 12, 16	–	Partial
B	1.1	2.3	260	80	3, 12, 16	–	Partial
B	1.0	2.0	60	100	3, 12, 16	–	Partial
B	2.0	2.1	50–470	80–90	12	–	No crystals
B	0.4	4.3	300	90	30	–	No crystals
B	1.2	4.2	170–330	90–95	12	–	No crystals
B	1.0–1.2	2.0	40–200	80–100	3–6	+	Full

^aAl source: A, sodium aluminate; B, aluminium hydroxide.

supports has been achieved with the *in situ* hydrothermal synthesis similar to that mentioned above for the A-type zeolite.

The variation in the morphology of the membrane with crystallization time is shown in Figure 15.3. These photomicrographs show that

a gel layer is formed on the surface of the alumina support after heating for 30 min. In the sample synthesized for 2 h, crystals with the well-known cubic LTA shape appeared. These are formed via nucleation in the gel near the surface of the support. Seeded crystals are used to enhance the

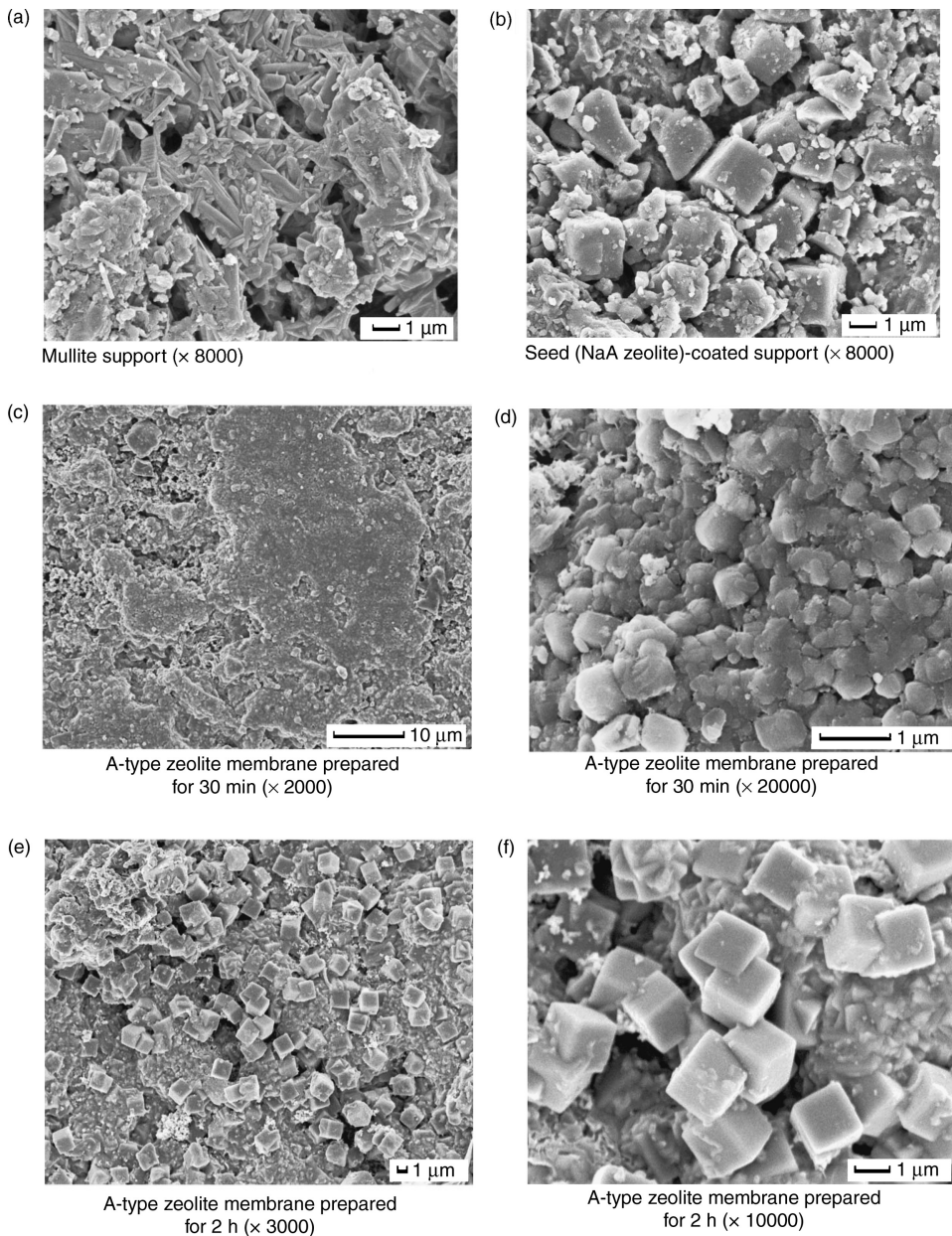


Figure 15.3 Scanning electron micrographs of (a) the surface of the mullite support, (b) the seeded support and A-type zeolite membranes prepared for (c,d) 0.5 and (e,f) 2 h

Table 15.3 The effect of synthesis time for A-type zeolite membranes^a prepared at 100 °C with coatings of seed crystals on the pervaporation performance for water (10 wt%)/ethanol (90 wt%) mixtures at 75 °C

Synthesis time(h)	Flux (kg/(m ² h))	Separation factor
0.5	Very large	1
1	Very large	1
2	2.46	1 400
3	2.15	10 000
6	1.89	2 700

^aStarting gel composition, Al₂O₃:SiO₂:Na₂O:H₂O = 1:2:2:120.

nucleation. The zeolite layer, however, is loosely packed and contains voids between the crystals.

The permeation and separation properties for A-type zeolite membranes depend on the method of preparation. It is noted that the membrane prepared by hydrothermal synthesis at 100 °C for 3–4 h at a molar composition of SiO₂/Al₂O₃ = 2.0, Na₂O/SiO₂ = 1.0 and H₂O/Na₂O = 60–75 with the aid of seed crystals, is highly selective for permeating water preferentially with a high permeation flux. Table 15.3 shows an example of the effect of the synthesis time of A-type zeolite membranes on the pervaporation performance for water/ethanol mixtures at 75 °C. With an increase in the synthesis time, the separation factor increases and reaches a maximum value after 3 h. On the other hand, the flux decreases slightly with time, but remains at a high value for the membrane prepared for 3 h. The growth of a P-type zeolite with a prolonged crys-

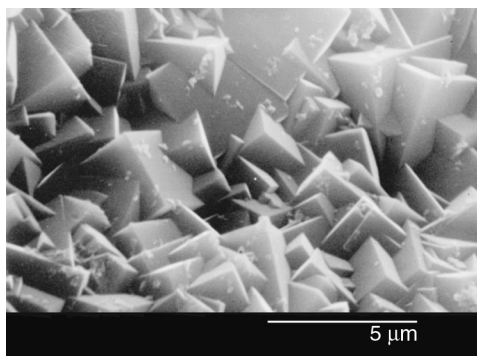


Figure 15.4 Scanning electron micrograph of the surface of an A-type zeolite membrane prepared at 100 °C for 3 h

tallization, however, results in a large decrease in both the flux and the selectivity of the membrane. The membrane prepared for 3 h appears, from scanning electron microscopy (SEM) examination, to have a continuous layer of A-type cubic zeolite crystals on the surface of the porous support, as shown in Figure 15.4. The thickness of the membrane is about 30 μm judging from the cross-sectional view of the photomicrograph and electron probe microanalysis (EPMA) [17]. In contrast, other membranes which were prepared under different synthesis conditions, as shown in Table 15.2, show a low selectivity and/or a low flux for water/ethanol mixtures, indicating the presence of ‘pinholes’ and low crystallinity.

Table 15.4 shows the permeation flux and the separation factor of pervaporation at 30–75 °C and vapor permeation at 105 °C for water/

Table 15.4 Pervaporation (30–75 °C) and vapor permeation (105 °C) performances of A-type zeolite membranes for water/organic liquid mixtures

Feed solution, A/B (wt% of A)	T(°C)	Flux (kg/(m ² h))	Separation factor, A/B	Reference
Water/methanol (10)	50	0.57	2 100	[9,10]
	105	3.50	5 700	[9,10]
Water/ethanol (5)	75	1.10	10 000	[9,10]
	Water/ethanol (10)	75	2.15	10 000
Water/2-propanol (10)		105	4.53	30 000
	30	0.75	10 000	[4]
	75	1.76	10 000	[9,10]
Water/acetone (10)	70	0.79	4 000	[18]
	50	0.91	5 600	[9,10]
Water/DMF (10)	60	0.95	8 700	[9,10]
Water/dioxane (10)	60	1.87	9 300	[9,10]
	105	7.80	8 900	[9,10]

organic liquid mixtures through A-type zeolite membranes. These membranes are highly selective for permeating water preferentially, with a high permeation flux, because of the micropore filling of water in the zeolite pores or in the intercrystalline pores between the zeolite crystals to afford water-selective permeation through the membranes. The permeation flux of these membranes increases linearly with an increase in the water concentration of the feed mixture until saturation is reached. The separation factor also increases linearly, reaches a maximum at around a water concentration of 5–10 wt% and then decreases to a constant value. Even in water/methanol mixtures, a high separation factor is observed. Furthermore, quite a large flux and a high separation factor are also observed for the dehydration of acetone or dioxane, where most of the polymeric membranes become very swollen, hence resulting in a reduction of the selectivity. With increasing temperature, the water flux increases significantly, whereas the alcohol flux hardly changes, and as a result, the separation factor increases. Thus, the performance of these membranes is higher for vapor permeation at 105 °C than for pervaporation at 50–75 °C.

15.2.1.2 T-Type Zeolite Membranes

Although the A-type zeolite membranes are highly selective for permeating water preferentially with a high permeation flux, application of these membranes is limited, mainly because of their insufficient acid resistance. It is well-known that Si-rich zeolite structures exhibit a much higher stability against acids than Al-rich structures [5]. A-type zeolite membranes with a Si/Al ratio of 1 are ‘damaged’ after a few hours from the presence of traces of acid. T-type (ERI and OFF) zeolite membranes, with a Si/Al ratio of 3.6, are stable up to pH 3–4. After immersion in an acetic acid solution at pH 3 for 7 days, the pervaporation flux and the separation factor for water (10 wt%)/ethanol mixtures at 75 °C were $1.19 \text{ kg m}^{-2} \text{ h}^{-1}$ and 1300, respectively [19].

T-type zeolite membranes are grown hydrothermally on the surface of a porous cylindrical support. The aluminosilicate gel used in the synthesis of the zeolite membranes is prepared by mixing a colloidal silica solution and an alkaline aluminate solution. The molar compositions of the starting

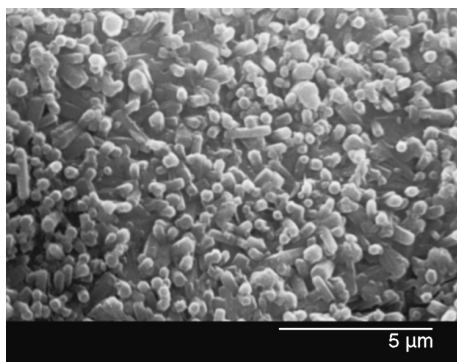


Figure 15.5 Scanning electron micrograph of the surface of a T-type zeolite membrane prepared at 100 °C for 24 h

gel are $\text{SiO}_2/\text{Al}_2\text{O}_3 = 20\text{--}112$, $(\text{Na}+\text{K})/\text{SiO}_2 = 0.70\text{--}0.77$, $\text{Na}/(\text{Na}+\text{K}) = 0.76$ and $\text{H}_2\text{O}/(\text{Na}+\text{K}) = 20.75$. The outer surface of the membrane prepared at 100 °C for 24 h is completely covered with ‘intergrown’ T-type zeolite crystals, as shown in Figure 15.5. The thickness of the membrane was about 20–30 μm, judging from the cross-sectional SEM image.

As shown in Figure 15.6, the adsorption amounts of water on an A-type zeolite is two

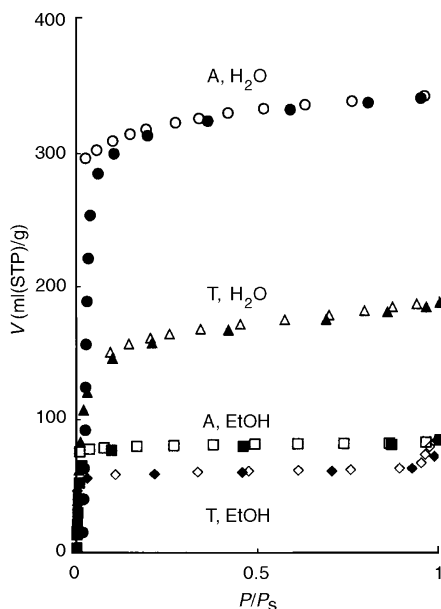


Figure 15.6 Adsorption isotherms of water and ethanol for A-type and T-type zeolite at 25 °C: the open and closed symbols refer to the adsorption and desorption runs, respectively

Table 15.5 Pervaporation (50 and 75 °C) and vapor permeation (105 °C) performances of zeolite membranes for water/organic liquid mixtures

Feed solution, A/B (wt% of A)	Zeolite	T (°C)	Flux (kg/(m ² h))	Separation factor, A/B
Water/ethanol (10)	A	75	2.15	10 000
	A	105	4.53	30 000
	X	75	1.91	170
	Y	75	1.59	130
	T	75	1.25	2 200
	T	105	2.48	3 900
	MOR	75	0.11	10 000
Water/methanol (10)	ZSM-5 ^a	75	1.6	63
	N	50	0.57	2 100
	N	105	3.50	5 700
	T	50	0.37	27
	T	105	1.74	45
Water/2-propanol (10)	A	75	1.76	10 000
	T	75	1.77	10 000
	MOR	75	0.13	10 000
Water/acetic acid (50) ^b	T	75	1.82	37
Water/acetic acid (50)	MOR	75	0.15	200
Water/tetrahydrofuran (10)	T	75	1.8	10 000
	T	100	2.5	10 000
Water/tetrahydrofuran (6.7) ^c	X	60	2.4	290

^aStarting gel composition: SiO₂:Al₂O₃:NaF:H₂O = 1:0.05:0.6:30; 165 °C; 72 h.

^bAfter immersion for a month.

^cLi *et al.* [20].

times larger than that of water on a T-type zeolite, whereas the adsorption amount of ethanol on A-type and T-type zeolites is almost the same. Table 15.5 shows the flux and the separation factor of pervaporation for dehydration of liquid mixtures through several zeolite membranes. The T-type membranes also preferentially permeated water from water/alcohol mixtures. However, both the separation factor and the flux of the zeolite membranes are smaller than those of the A-type zeolite membrane, probably due to the less hydrophilic properties of this zeolite.

15.2.1.3 Other Hydrophilic Zeolite Membranes

Hydrophilic zeolite membrane, like Faujasite (FAU) and Mordenite (MOR) zeolites, preferentially permeated water from water/alcohol mixtures. Due to the large pore diameter of these zeolites (see Figure 15.1), the selectivity of these membranes are based on hydrophilic interactions and *not* on molecular sieving. For FAU membranes [21,22], the X-type membranes exhibit higher water/ethanol selectivity than the

Y-type membranes. The X-type has a lower Si/Al ratio (1.3) and is more hydrophilic than the Y-type (Si/Al ratio = 2.1). The hydrophilicity of the zeolite pores plays an important role and by variation of the Si/Al ratio the membrane performance can be changed, without changing the crystallographic structure. Figure 15.7 shows SEM images of the surface of these zeolite membranes prepared under optimized conditions. The surface of the porous support is completely covered with randomly oriented, 'intergrown' zeolite crystals. The thickness of the membrane is about 10–30 μm, judging from cross-sectional SEM observations. X-type zeolite membranes have also been reported to separate 1,3-propanediol from glycerol in aqueous mixtures by pervaporation, where the flux was 2.7 kg m⁻² h⁻¹ and the selectivity was 41 at 35 °C [23,24].

15.2.2 Organophilic Membranes

15.2.2.1 MFI Zeolite Membranes

The majority of the zeolite membranes reported so far are highly silicious MFI-type zeolites. Caro *et al.* [2] have suggested that the main

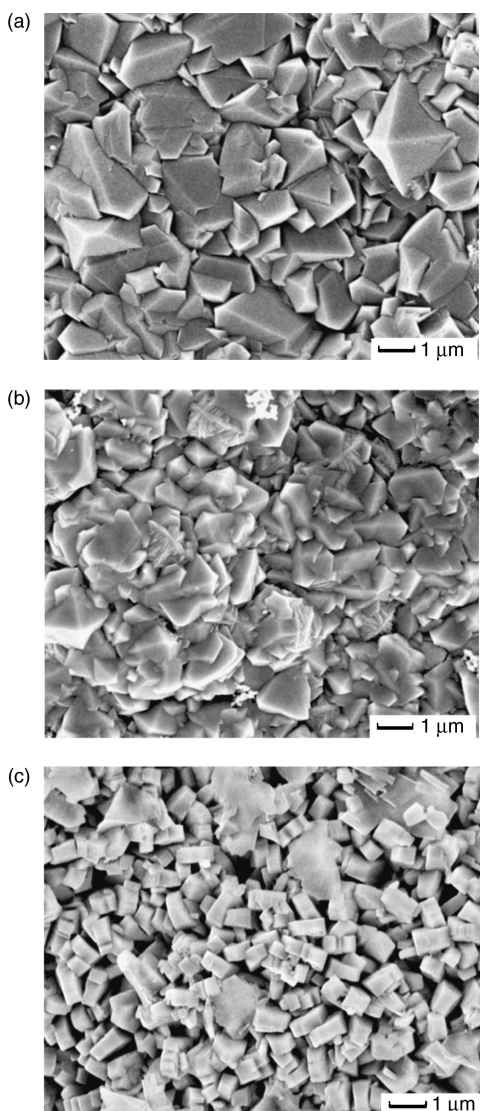


Figure 15.7 Scanning electron micrographs ($\times 10^4$) of the surfaces of (a) an X-type zeolite membrane prepared at 100 °C for 24 h, (b) a Y-type membrane prepared at 100 °C for 6 h and (c) a mordenite membrane prepared at 165 °C for 72 h

reasons for this are the accumulated knowledge in the synthesis of the MFI structure, the suitable pore diameter of 0.55 nm which is interesting for industrial applications, the relative ease of preparation, the possible modifications in the chemical compositions including cation-exchange and last, but not least, a relatively high thermal and chemical stability due to the high Si/Al

ratio. MFI zeolites (ZSM-5 and silicalite) are usually synthesized hydrothermally in an autoclave at 438 to 473 K under an autogenous pressure, using organic-structure-directing agents (SDAs), such as tetrapropyl ammonium salts. After hydrothermal synthesis, these SDAs have to be removed by calcination at 673 to 823 K, where crack formation must be avoided by slow heating rates of less than 0.3 °C/min.

There are two typical methods used to synthesize MFI membranes: (1) *in situ* crystallization – crystal growth on an untreated support from a synthesis gel or solution; (2) seeding method – formation of a crystal layer on a seeded support where seeds not only enhance crystallization but also promote the formation of a uniform amorphous gel layer on the support, which results in a ‘well-intergrown’ crystal layer. Especially in the second case, Xomeritakis *et al.* [25] have reported that ‘nanoscale-seeds’ grew directly to form oriented silicalite membranes with columnar microstructures. Figure 15.8 shows the typical

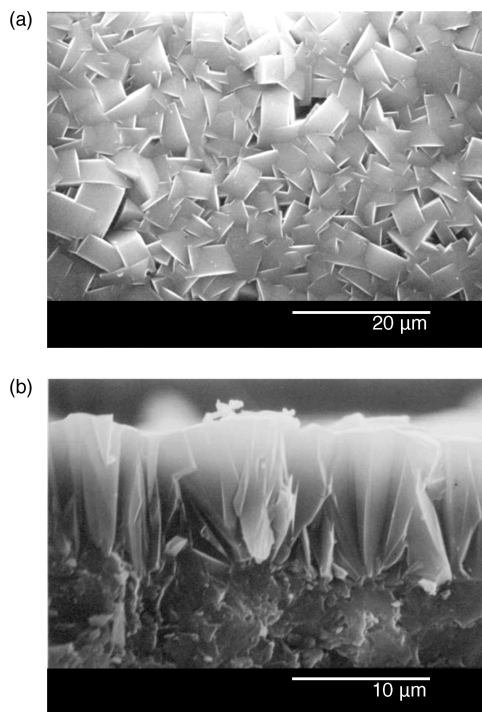


Figure 15.8 Scanning electron micrographs of (a) the surface and (b) the cross-section of a silicalite membrane prepared on a silicalite-seeded mullite support at 175 °C for 16 h with colloidal silica

Table 15.6 Pervaporation performances of MFI (silicalite and ZSM-5) and MEL (ZSM-11) membranes for organic/water mixtures

Zeolite	Support	Feed solution, A/B (wt% of A)	T ($^{\circ}\text{C}$)	Flux ($\text{kg}/(\text{m}^2 \text{h})$)	Separation factor, A/B	Reference
Silicalite	SS disk	Methanol/water (1.8)	60	1.6	17	[26]
	γ - Al_2O_3 tube	Methanol/water (3.5)	32	0.75	7.5	[27]
B-ZSM-5	SS tube	Methanol/water (5)	60	0.44	78	[28]
B-ZSM-11	SS tube	Methanol/water (5)	60	1.7	18	[29]
Silicalite	SS disk	Ethanol/water (4)	60	0.76	58	[26]
	SS disk	Ethanol/water (4)	30	0.29	120	[30]
			60	0.97	84	[30]
	γ - Al_2O_3 tube	Ethanol/water (9.7)	24	0.1	12	[27]
	SS disk	Ethanol/water (4.7)	30	0.50	64	[31]
	Mullite tube	Ethanol/water (5)	60	1.42	72	[32]
	Mullite tube	Ethanol/water (5)	60	0.93	106	[33]
B-ZSM-5	SS tube	Ethanol/water (5)	60	0.09	9.4	[28]
B-ZSM-11	SS tube	Ethanol/water (5)	60	0.93	42	[29]
Silicalite	SS disk	<i>n</i> -Propanol/water (3.3)	60	0.16	76	[26]
B-ZSM-11	SS tube	<i>n</i> -Propanol/water (5)	60	0.25	25	[29]
Silicalite	SS disk	2-Propanol/water (3.3)	60	0.22	36	[26]
B-ZSM-11	SS tube	2-Propanol/water (5)	60	0.31	16	[29]
Silicalite	SS disk	Acetone/water (5)	30	1.06	106	[26]
	SS tube	Acetone/water (0.8)	32	0.2	250	[27]
	Mullite tube	Acetone/water (5)	60	1.43	460	[34]
	SS disk	MEK/water (5)	30	0.41	266	[26]
	SS tube	MEK/water (5)	30	0.25	146	[35]
	Mullite tube	MEK/water (5)	60	0.36	1000	[34]

morphology of the columnar microstructure for well-oriented silicalite membranes prepared on a silicalite-seeded mullite support.

Although a hydrophilic ZSM-5 membrane with a low Si/Al ratio (~ 30) preferentially permeates water from a water/organic liquid mixture, as shown in Table 15.5, a hydrophobic silicalite membrane (Si/Al = 500 – ∞) exhibits preferential organic compound permeation from water, such as in ethanol/water mixtures, because the silicalite has not only strong hydrophobic properties but also preferentially adsorbs organic compounds. Table 15.6 summarizes the pervaporation performance of hydrophobic zeolite membranes. Randomly oriented membranes, with dense intermediate layers, have higher separation selectivities than the oriented membranes due to fewer defects, while the main advantage of seeding seems to shorten the synthesis time [33]. Recently, Noble and coworkers have investigated the effects of isomorphous substitution of the MFI and MEL framework. The separation selectivity of the boron-substituted ZSM-11 membrane for alcohol/water solutions is controlled by both the

preferential adsorption and diffusion rate [29]. Furthermore, a Ge-substituted ZSM-5 membrane exhibits higher acetic acid fluxes and lower pure water fluxes than a silicalite membrane because it is more hydrophobic than the silicalite material. For a 5 wt% acetic acid feed, the membrane shows a flux of $0.43 \text{ kg m}^{-2} \text{ h}^{-1}$ and a separation factor of 14 at 90°C [36].

Compared to the membrane performance of hydrophilic zeolite membranes, hydrophobic zeolite membranes exhibit much lower selectivities with relatively low fluxes. A qualitative improvement of the membrane synthesis and an increase in the permeation temperature can be expected in the near future.

15.3 Zeolite Membranes for Organic/Organic Separation

15.3.1 Alcohol/Ether Separation

FAU membranes show a high alcohol-selectivity for several feed mixtures with methanol or ethanol, as shown in Table 15.7. Pervaporation through a Y-type zeolite membrane can break

Table 15.7 Pervaporation (PV) and vapor permeation (VP) performances of zeolite membranes for organic liquid mixtures

Feed solution, A/B (wt% of A)	Zeolite	Method	T ($^{\circ}\text{C}$)	Flux ($\text{kg}/(\text{m}^2 \text{h})$)	Separation factor, A/B
Methanol/benzene (10)	ZSM-5	PV	50	0.06	5
	T	PV	50	0.02	930
	Y	PV	50	1.02	7 000
Methanol/benzene (50)	Y	VP	100	2.42	10 000
Methanol/DMC (50)	Y	PV	50	1.53	480
	X	PV	50	0.92	1 000
Methanol/MTBE (10)	ZSM-5	PV	50	0.02	3
	T	PV	50	0.02	1 900
	Y	PV	50	2.13	10 000
	Y	VP	105	2.13	6 400
	Y	VP	150	2.59	600
	X	PV	50	1.37	10 000
	X	VP	150	2.51	300
Ethanol/benzene (10)	Y	PV	60	0.22	930
Ethanol/cyclohexane (10)	Y	PV	60	0.27	1 000
Ethanol/ETBE (10)	Y	PV	50	0.43	4 500
	X	PV	50	0.15	300
Benzene/ <i>n</i> -Hexane (50)	Y	PV	65	0.007	46
	Y	VP	100	0.03	260
	Y	VP	120	0.20	98
	Y	VP	150	0.50	44
Benzene/cyclohexane (50)	ZSM-5	PV	75	0.03	1
	Y	PV	75	0.014	22
	Y	VP	100	0.023	28
	Y	VP	120	0.075	180
	Y	VP	150	0.30	190
	X	VP	150	0.54	94

up the vapor–liquid azeotrope of methanol and methyl *tert*-butyl ether (MTBE) and the PV process is more selective than distillation [21]. High separation factors through Y-type zeolite membranes are obtained over a wide range of feed compositions. The flux increased from $0.83 \text{ kg m}^{-2} \text{ h}^{-1}$ at 2.7 wt% methanol in MTBE to $1.27 \text{ kg m}^{-2} \text{ h}^{-1}$ at 20 wt% methanol and is almost constant over the range from 20 to 50 wt% methanol. It has been reported that the polycrystalline silicalite membrane also permeates methanol preferentially [37]. The flux and the methanol selectivity of the Y-type membrane is considerably higher than those of the silicalite membrane. Pervaporation using the silicalite membrane may not be feasible because the flux is very low, due to its highly hydrophobic properties, so resulting in strong adsorption of organic molecules. Although methanol/MTBE mixtures can be separated by pervaporation using polymer or inorganic membranes, a membrane that has

both a high selectivity and a high flux is not available. The performance of the Y-type zeolite membrane may be good enough to be economically feasible in commercial pervaporation systems.

It is well-known that the overall selectivity of a pervaporation process is determined by diffusivity selectivity and sorption selectivity. In the case of alcohol/ether mixtures, the sorption process presumably determines the pervaporation performance. Methanol sorption into the membrane increases with increasing methanol feed concentration while an increasing sorption causes an increase in the pervaporation flux. When the sorption of methanol approaches saturation, the flux becomes constant. A sharp increase in alcohol flux is observed in the low-concentration region. Above 40 wt% feed, the flux becomes constant. On the other hand, the MTBE or ethyl *tert*-butyl ether (ETBE) flux is almost constant over a wide range of feed compositions and is much smaller than the alcohol flux. In order to clarify the hypothesis that

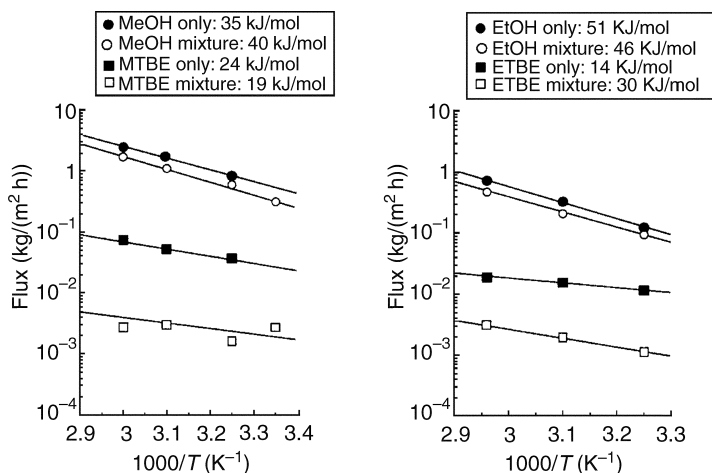


Figure 15.9 Arrhenius plots of the pure-component pervaporation fluxes and mixed-pervaporation fluxes of (a) MeOH/MTBE and (b) EtOH/ETBE mixtures (feed concentrations, 10 wt% alcohol)

the high selectivity of the Y-type membrane can be attributed to the selective sorption of alcohol into the membrane, the fluxes of the individual components are compared in Figure 15.9. In this figure, the temperature-dependence of the pure-alcohol flux and that of a mixture (10% alcohol/90% ether) are compared. The pure-alcohol flux and the alcohol flux obtained in this mixture are almost the same. On the other hand, the mixture-ether flux decreases remarkably, compared with that of the pure-ether flux. Thus, permeation of MTBE or ETBE is hindered by the presence of alcohol. From these results, it can be concluded that the alcohol molecules adsorbed in the zeolite pores obstruct the permeation of ether and that the high selectivity of the Y-type zeolite membrane can be attributed to the selective sorption of alcohol into the membrane.

15.3.2 Aromatic/Non-Aromatic Separation

The Y-type and X-type zeolite membranes also show a high benzene selectivity in benzene/*n*-hexane and benzene/cyclohexane separation, as shown in Table 15.7. Separation of these systems is difficult by a conventional distillation process because these components form close-boiling mixtures. Although azeotropic distillation and extractive distillation are used at the present time, these processes suffer from complexity and high energy consumption [38]. Application of

pervaporation to separate mixtures of aliphatic-aromatic hydrocarbons is still very limited, because of swelling of the polymer membranes. Pervaporation through Y- and X-type zeolite membranes indeed affords an alternative to industrial separation of organic liquid mixtures. Figure 15.10 shows the membrane performance for benzene-cyclohexane separation. The performance of the Y-type zeolite membrane is far

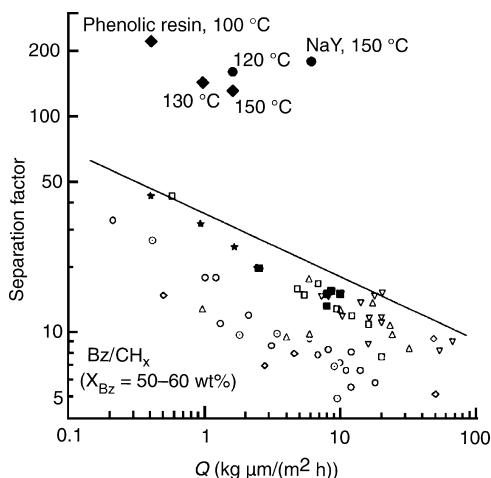


Figure 15.10 Comparison of membrane performances of a Y-type carbon membrane derived from phenolic resin and polymer membranes for the pervaporation of benzene/cyclohexane mixtures

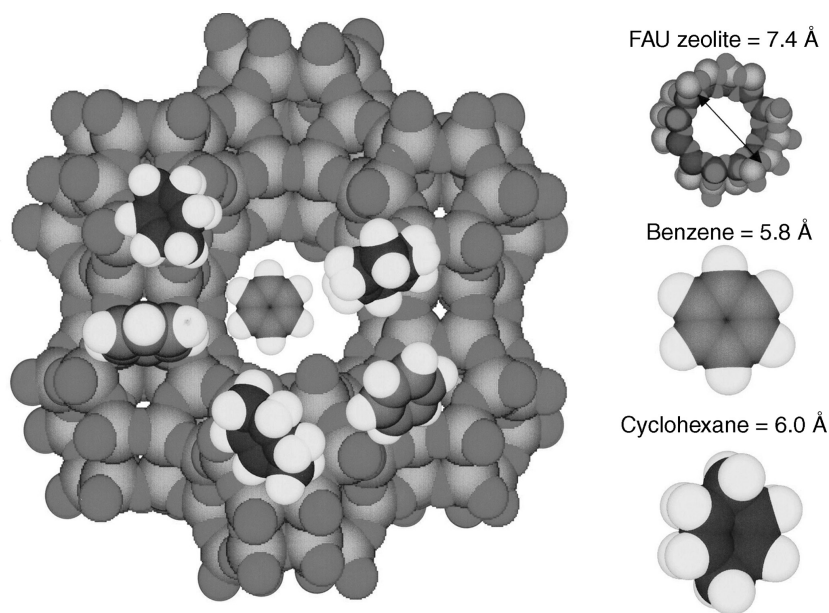


Figure 15.11 Comparison of the channel opening of an FAU zeolite and the molecular sizes of benzene and cyclohexane

superior to any other membrane previously reported in terms of both pervaporation and vapor permeation [39]. High permselectivity of the zeolite membrane can be attributed to selective sorption into the membrane [22,40,41]. Benzene, cyclohexane and *n*-hexane molecules can permeate through the pores of an FAU zeolite, as shown in Figure 15.11. On the other hand, the adsorption amount of benzene is four times larger than those of *n*-hexane and cyclohexane. The permeation flux of benzene rapidly increases with increasing benzene feed concentration and at above 20 wt% benzene feed the benzene flux becomes constant, while the *n*-hexane or cyclohexane fluxes linearly decrease with increasing benzene feed concentration and is much smaller than the benzene flux. In these systems, the sorption process determines the permeation performance. Although the pure-benzene flux and the benzene flux of the mixture are almost the same in benzene (50 wt%)/*n*-hexane (50 wt%) or benzene (50 wt%)/cyclohexane (50 wt%) mixtures, the *n*-hexane or cyclohexane fluxes decrease remarkably when compared with the pure fluxes of *n*-hexane or cyclohexane. Permeation of *n*-hexane and cyclohexane is, therefore, hindered by the presence of benzene.

15.3.3 Xylene Isomer Separation

Production of *p*-xylene, which is the raw material used for production of polyesters and poly-(ethylene terephthalate), represents a significant proportion of the chemical industry's output. Development of membranes that can separate *p*-xylene more efficiently than by conventional methods could result in substantial energy savings. The separation of xylene isomers on MFI membranes has been studied by several groups, since the use of MFI zeolites seems to be promising because of the diffusion coefficient of *p*-xylene in MFI crystals is $10\text{--}10^3$ larger than those of *m*- and *o*-xylenes [42]. Sakai *et al.* [43] have reported that MFI membranes can separate *p*-xylene selectively from ternary mixtures of xylene isomers above 473 K. The permeation flux of *p*-xylene showed a maximum at 473 K at a *p*-xylene partial pressure of 0.3 kPa and this could be explained by the competitive effects between the amount of equilibrium adsorption and the diffusivity. As the permeations of *m*- and *o*-xylene have small values and almost constant between 473 and 673 K, the separation factors of *p*- to *m*-xylenes and *p*- to *o*-xylenes show maximum values of 250 at 473 K. Lai *et al.* [44]

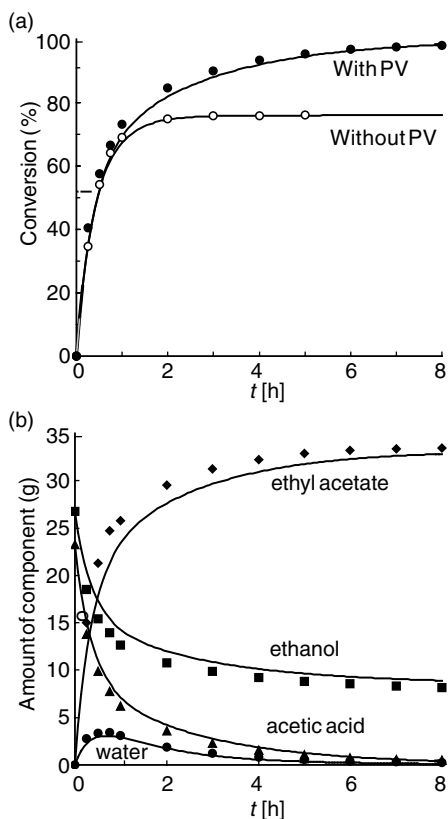


Figure 15.12 Variation in (a) the conversion and (b) the amount of each component in the esterification mixture with reaction time for an initial molar ratio of ethanol to acetic acid of 1.5 at 70 °C

have also reported that xylene separation can be achieved by appropriate channel orientation throughout thin films (1 μm) synthesized by seeded growth of oriented particle monolayers.

15.4 Integrated Systems Involving Pervaporation or Vapor Permeation by Zeolite Membranes

Pervaporation (PV) is often applied in combination with another technology as a 'hybrid process'. The pervaporation–distillation hybrid process is already finding industrial applications [45]. The combination of pervaporation with chemical reaction is also increasingly attracting much attention [46]. Pervaporation membrane reactors using water-permeable membrane are applicable to liquid-phase reversible reactions such as esterifications of

carboxylic acid with alcohol [47,48]. For example [49], conversion of the reaction of acetic acid with ethanol exceeds the equilibrium limit and reaches almost 100% over a short time, as shown in Figure 15.12. Water content in the reaction mixture increases in the early stage of less than 1 h and then decreases gradually. The water content is less than 7 wt% during the reaction. The total permeated amount of ethanol, which is the major organic component in the permeate, is 0.4 wt% of the initial amount of ethanol. The selective removal of water by pervaporation shifts the equilibrium in favor of ester formation. Furthermore, vapor permeation also improves the esterification, where a batch reactor containing the reacting mixture of alcohol with acid, together with a catalyst, combines with a tubular hydrophilic membrane, as shown in Figure 15.13. The alcohol and water vapors escaping from the reactor pass through the membrane, which removes water selectively, and then condenses and recycles them back to the reactor. The conversion for the vapor-permeation-aided reaction exceeds the thermodynamic equilibrium, as shown in Figure 15.14. An almost complete conversion of 100% is reached within 8 h in the esterification of lactic acid with ethanol using vapor permeation with a T-type membrane [50]. Lactate esters are versatile solvents which are biodegradable, nontoxic

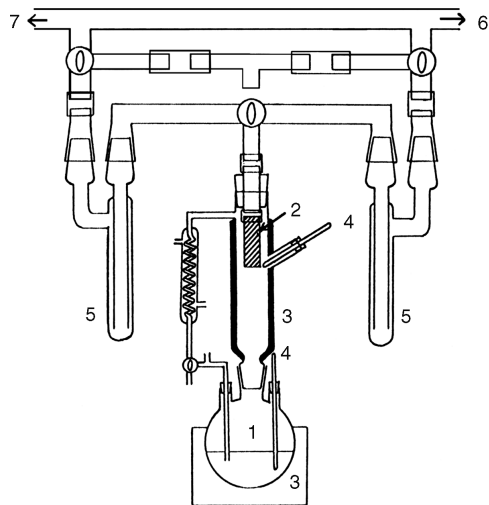


Figure 15.13 Schematic diagram of the vapor-permeation-aided esterification apparatus: 1, reaction cell; 2, membrane; 3, heater; 4, thermometer; 5, cold trap; 6, vacuum pump; 7, Pirani gauge

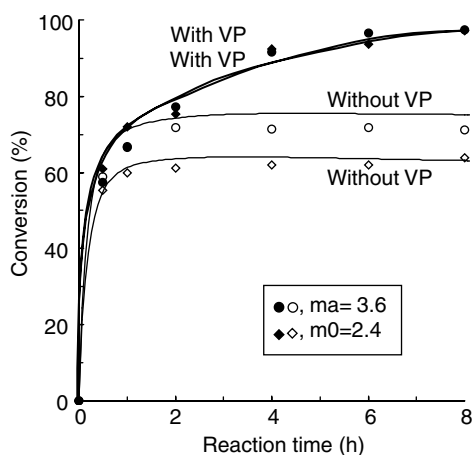


Figure 15.14 Variation in the conversion with reaction time for the vapor-permeation (VP)-aided esterification of lactic acid with ethanol for an initial molar ratio of ethanol to lactic acid (m_0) of 2.4 and 3.6 at boiling temperature

and applicable to a wide range of industrial and consumer uses. Vapor-permeation-aided esterification is energy-efficient and cost-effective.

15.5 Manufacture of Zeolite Membranes for Pervaporation and Vapor Separation

The first large-scale pervaporation plant [51] using an A-type membrane, with a 3.7 m² mem-

brane area in 'tube-type' geometry, for the removal of water from organic solvents is now in operation in Japan. 600 L of a solvent containing 10 wt% water can be dried per hour to a final water content of less than 0.2%. This plant is equipped with 16 modules, each of which consists of 125 of (80 cm) tubes. The module configuration and layout are shown in Figure 15.15. This pervaporation plant was planned for multi-purpose dehydration of various alcohols, such as ethanol, isopropanol and methanol. Membranes, sealed at one end of a support tube are inserted, alternatively, at the designated pitches from both of the tube sheets and then fixed at these tube sheets [22]. The module is equipped with 'dividers' for the purpose of accelerating the flow rate. The feed is on the 'shell side' of the tubes and the permeate is removed from the 'tube side' of the membrane by a vacuum system, via a cooling/condensation unit. The efficiency of the module on the flux increases in proportion to the feed flow rate and exhibits 100% at a Reynolds number (defined by the geometric mean of the mass velocities in the cross-flow and window region, respectively, membrane outside diameter and viscosity of the shell-side fluid) of more than 80. However, the separation factor changed little, regardless of the feed flow rate. This is a remarkable improvement upon the plate-and-frame module with polymeric membranes, previously in use. In order to decrease the cost of

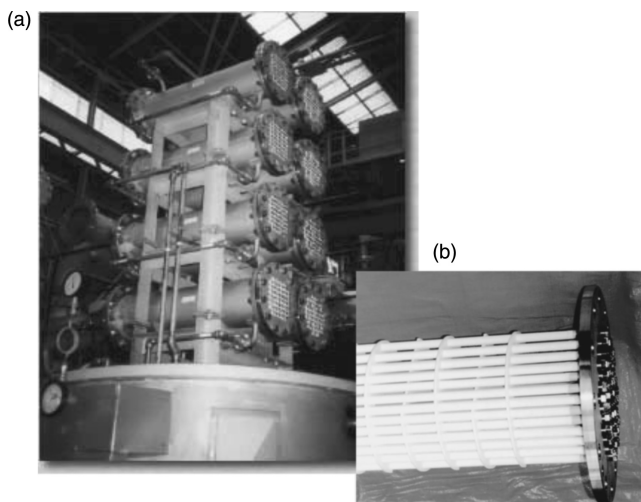


Figure 15.15 (a) Pervaporation and vapor permeation plant using A-type zeolite membranes and (b) the module configuration

the zeolite membrane, zeolite layers have been prepared on the outer surfaces of a porous mullite support, which is much cheaper than alumina supports [17]. The preparation of zeolite layers inside the support is a cost-intensive and multi-step preparation technique [5].

In Japan, the industrialization of pervaporation technology was started in 1986 when the Mitsui Engineering & Shipbuilding Company (MES) introduced commercial dehydration membranes of GFT (Germany) into the Japanese market. These zeolite membranes for dehydration of alcohol are taking the place of the commercialized pervaporation modules using polyimide hollow fibers because of high membrane performance and high temperature and chemical stability. The number of pervaporation and vapor permeation plants using tubular modules with A-type zeolite membranes is more than 60.¹ Figure 15.16 shows the tubular type module which uses an A-type zeolite for isopropanol (IPA) purification. Presently, IPA is drawing attention as a cleaning agent in industries such a



Figure 15.16 IPA purification plant using vapor permeation with A-type zeolite membranes

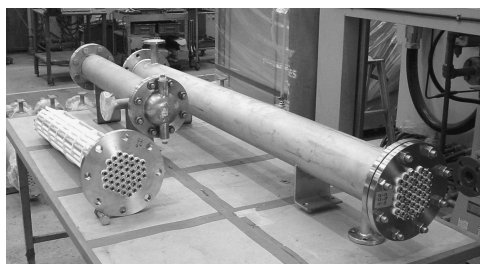


Figure 15.17 Tubular-type modules with 160 cm and 80 cm membranes for the dehydration of biomass ethanol

precision machinery and electronics. These industries require IPA of high purity, under 0.05 % of water content. The state-of-the-art technology for the dehydration of IPA is extractive-distillation with ethylene glycol as the 'entrainer'. The main disadvantages of the conventional process are product impurities due to the auxiliary and high investment and energy costs because of the operation of three distillation columns with high reflux ratios and recirculation streams. The highest potential of pervaporation and vapor permeation can be realized in combination with distillation. Using A-type membranes, water concentration in IPA could be reduced from 12 wt% to less than 500 ppm. A hybrid system composed of simple distillation and vapor permeation is effective and 'compact' enough for purposes of IPA purification and re-use from industrial electronic-component-cleaning processes.

Recently, a tubular module using A-type membranes (1.6 m length) (Figure 15.17) has been investigated in order to develop more energy-efficient concentration of the biomass ethanol. A 'semi-commercial' tubular type module, composed of 7 silicalite membranes (50 cm length), has also been developed by MES [52]. Thus, pervaporation and vapor permeation using zeolite membranes may provide an opportunity for making significant contributions to more energy-efficient production of ethanol from biomass.

15.6 Conclusions

During the past decade, significant progress has been made in the synthesis of microporous inorganic membranes. Although there are no commercial gas-separation ceramic membranes at the present time, A-type zeolite and silica

¹As at 1998.

membranes have just started to be commercialized in water-removal pervaporation and vapor permeation processes. The disadvantages of inorganic membranes in comparison with polymer membranes are the presently higher production costs of these membranes and modules. The A-type zeolite membranes, however, provide potentially higher selectivity, when compared to silica membranes and conventional polymer membranes. Thus, pervaporation processes using zeolite membranes should create possibilities for the separation of liquid mixtures for which polymer membranes are not applicable and will certainly advance the acceptance of such microporous ceramic membranes.

References

- [1] A. Tavoraro and E. Drioli, *Adv. Mater.*, **11**, 975 (1999).
- [2] J. Caro, M. Noack, P. Koelsch and R. Schaefer, *Micropor. Mesopor. Mater.*, **38**, 3 (2000).
- [3] N. K. Kanellopoulos (Ed.), *Recent Advances in Gas Separation by Microporous Ceramic Membranes*, Elsevier, Amsterdam, The Netherlands (2000).
- [4] Y. S. Lin, I. Kumakiri, B. N. Nair and H. Alsayouri, *Sepr. Purif. Methods*, **31**, 229 (2002).
- [5] M. Noack, P. Koelsch, R. Schaefer P. Toussaint and J. Caro, *Chem. Eng. Technol.*, **25**, 221 (2002).
- [6] H. L. Fleming, *Chem. Eng. Prog.*, **46** (July 1992).
- [7] J. Neel, in R. Y. M. Huang (Ed.), *Pervaporation Membrane Separation Processes*, Elsevier, Amsterdam, The Netherlands, pp. 1 (1991).
- [8] F. Lipnitzki, R. W. Field and P-K. Ten, *J. Membr. Sci.*, **153**, 182 (1999).
- [9] H. Kita, K. Horii, Y. Ohtoshi, K. Tanaka and K. Okamoto, *J. Mater. Sci., Lett.*, **14**, 206 (1995).
- [10] H. Kita, K. Horii, K. Tanaka, K. Okamoto, N. Miyake and M. Kondo, in *Proceedings of the 7th International Conference on Pervaporation Processes in the Chemical Industry*, R. Bakish (Ed.), Bakish Materials, Englewood Cliffs, NJ, USA, pp. 364 (1995).
- [11] S. Sakohara, F. Muramoto, T. Sakata and M. Asaeda, *J. Chem. Eng. Jpn.*, **23**, 40 (1990).
- [12] H. E. A. Bruschke and G. F. Tusel, *ACS Symp. Ser.*, **281**, 467 (1985).
- [13] Y. Maeda, M. Tsuyumoto, H. Karagane and H. Tsugaya, *Polym. J.*, **23**, 501 (1991).
- [14] A. Mochizuki, Y. Sato, H. Ogawara and S. Yamashita, *J. Appl. Polym. Sci.*, **37**, 3375 (1989).
- [15] K. Nakagawa, Y. Kusuki and R. Ninomiya, in *Proceedings of the 4th International Conference on Pervaporation Processes in the Chemical Industry*, R. Bakish (Ed.), Bakish Materials, Englewood Cliffs, NJ, USA, pp. 250 (1989).
- [16] D. W. Breck (Ed.), *Zeolite Molecular Sieves*, John Wiley & Sons, Inc., New York, NY, USA (1974).
- [17] M. Kondo, M. Komori, H. Kita, K. Tanaka and K. Okamoto, *J. Memb. Sci.*, **133**, 133 (1997).
- [18] L. J. Jafar and P. M. Budd, *Micropor. Mesopor. Mater.*, **12**, 305 (1997).
- [19] H. Kita, H. Minaki, S. Takaki, K. Tanaka and K. Okamoto, in *Proceedings of the 1999 International Congress on Membranes and Membrane Processes*, pp., 248 (1999).
- [20] S. Li, V. A. Tuan, R. D. Noble and J. L. Falconer, *Ind. Eng. Chem. Res.*, **40**, 4577 (2001).
- [21] H. Kita, H. Asamura, K. Tanaka and K. Okamoto, *ACS Symp. Ser.*, **744**, 330 (2000).
- [22] H. Kita, K. Fuchida, T. Horita, H. Asamura and K. Okamoto, *Sepr. Purif. Technol.*, **25**, 261 (2001).
- [23] S. Li, V. A. Tuan, J. L. Falconer and R. D. Noble, *Ind. Eng. Chem. Res.*, **40**, 1952 (2001).
- [24] S. Li, V. A. Tuan, J. L. Falconer and R. D. Noble, *Micropor. Mesopor. Mater.*, **53**, 59 (2002).
- [25] G. Xomeritakis, S. Nair and M. Tsapatsis, *Micropor. Mesopor. Mater.*, **38**, 61 (2000).
- [26] T. Sano, M. Hasegawa, Y. Kawakami, Y. Kiyozumi, H. Yanagishita, D. Kitamoto and F. Mizukami, *Studies Surf. Sci. Catal.*, **84**, 1175 (1994).
- [27] Q. Liu, R. D. Noble, J. L. Falconer and H. H. Funke, *J. Membr. Sci.*, **117**, 163 (1996).
- [28] V. A. Tuan, S. Li, J. L. Falconer and R. D. Noble, *J. Membr. Sci.*, **196**, 111 (2002).
- [29] S. Li, V. A. Tuan, R. D. Noble and J. L. Falconer, *AIChE J.*, **48**, 269 (2002).
- [30] H. Matsuda, H. Yanagishita, D. Kitamoto, T. Nakane, K. Haraya, N. Koura and T. Sano, *Maku (Membrane)*, **23**, 259 (1998).
- [31] M. Nomura, T. Yamaguchi and S. Nakao, *J. Membr. Sci.*, **144**, 161 (1998).
- [32] X. Lin, H. Kita and K. Okamoto, *Ind. Eng. Chem. Res.*, **40**, 4069 (2001).
- [33] X. Lin, H. Kita and K. Okamoto, *AIChE J.*, **49**, 245 (2003).
- [34] H. Kita, X. Chen, X. Lin, K. Okamoto, T. Yamamura and J. Abe, *ACS Fuel Chem. Div. Prepr.*, **47**, 230 (2003).
- [35] J. F. Smetana, J. L. Falconer and R. D. Noble, *J. Membr. Sci.*, **114**, 127 (1996).
- [36] S. Li, V. A. Tuan, R. D. Noble and J. L. Falconer, *Ind. Eng. Chem. Res.*, **40**, 6165 (2001).
- [37] T. Sano, M. Hasegawa, Y. Kawakami and H. Yanagishita, *J. Membr. Sci.*, **107**, 193 (1995).
- [38] J. P. Garcia, A. Villaluenga and A. Tabe-Mohammadi, *J. Membr. Sci.*, **169**, 159 (2000).

- [39] J. Hao, K. Tanaka, H. Kita and K. Okamoto, *J. Membr. Sci.*, **132**, 97 (1997).
- [40] V. Nikolakis, G. Xomeritakis, A. Abibi, M. Dickson, M. Tsapatsis and D. G. Vlachos, *J. Membr. Sci.*, **184**, 209 (2001).
- [41] B. Jeong, Y. Hasegawa, K. Sotowa, K. Kusakabe and S. Morooka, *J. Membr. Sci.*, **213**, 115 (2003).
- [42] J. Kaerger and D. M. Ruthven, *Diffusion in Zeolites*, John Wiley & Sons, Inc., New York, NY, USA, pp. 467 (1992).
- [43] H. Sakai, T. Tomita and T. Takahashi, *Seprn Purif. Technol.*, **25**, 297 (2001).
- [44] Z. Lai, G. Bonilla, I. Diaz, J. G. Nery, K. Sujaoti, M. A. Amat, E. Kokkoli, O. Terasaki, R. W. Thompson, M. Tsapatsis and D. Vlachos, *Science*, **300**, 456 (2003).
- [45] U. H. F. Sander, R. Y. M. Huang (Ed.), in *Pervaporation Membrane Separation Processes*, Elsevier, Amsterdam, The Netherlands, pp. 519 (1991).
- [46] J. G. S. Marcano and T. T. Tsotsis, *Catalytic Membranes and Membrane Reactors*, Wiley-VCH, Weinheim, Germany (2002).
- [47] H. Kita, K. Tanaka, K. Okamoto and M. Yamamoto, *Chem. Lett.*, 2053 (1987).
- [48] H. Kita, K. Tanaka, K. Okamoto and M. Yamamoto, *Chem. Lett.*, 2025 (1988).
- [49] K. Tanaka, R. Yoshikawa, C. Ying, H. Kita and K. Okamoto, *Catal. Today*, **67**, 121 (2001).
- [50] K. Tanaka, R. Yoshikawa, C. Ying, H. Kita and K. Okamoto, *Chem. Eng. Sci.*, **57**, 1577 (2002).
- [51] Y. Morigami, M. Kondo, J. Abe, H. Kita and K. Okamoto, *Seprn Purif. Technol.*, **25**, 251 (2001).
- [52] H. Kita, K. Okamoto, T. Yamamura and J. Abe, *ACS Fuel Chem. Div. Prepr.*, **47**, 206 (2003).

Solid-State Facilitated Transport Membranes for Separation of Olefins/Paraffins and Oxygen/Nitrogen

Yong Soo Kang, Jong Hak Kim, Jongok Won and Hoon Sik Kim

16.1 Introduction

Solid-state facilitated transport membranes comprising carriers dissolved in a polymer matrix have been demonstrated to be very effective in simultaneously improving gas permeability and selectivity, which are normally in conflict for common polymeric materials. Thus, facilitated transport membranes are considered to be an alternative approach to overcome the permeability/selectivity trade-off behavior. For example, the separation performance of facilitated transport membranes consisting of polymer–silver salts complexes [1–3] for propylene/propane mixtures is improved by several orders of magnitude compared to that of conventional polymeric membranes [4], such as polyimides, polysulfones, poly(phenylene oxide), ethyl cellulose, polydimethylsiloxane, etc., as shown in Figure 16.1. The propylene permeance reaches more than $4.5 \times 10^{-5} \text{ cm}^3(\text{STP})/(\text{cm}^2 \text{ s cmHg})$ and the ideal separation factor of propylene over propane is extremely high at several thousands, although the mixed gas selectivity drops to around 50. The oxygen/nitrogen separation performance is also improved markedly through facilitated oxygen transport membranes containing metalloporphyrins, as shown in Figure 16.2 [5–9].

Facilitated transport phenomena are often observed in a living body and their application for gas separation started with liquid membranes, where a liquid solvent was necessary to carry carrier–solute complexes. Liquid-state facilitated transport membranes are described in detail in another chapter in this text.

A basic understanding of facilitated transport phenomena in the solid state is that carrier-mediated transport occurs because of the reversible reaction of a fixed carrier with a specific solute in addition to normal Fickian transport. Thus, the total solute transport is represented by summation of the Fickian transport and the carrier-mediated transport. Therefore, the thermodynamics and kinetics of the reversible interaction of the solute with the carrier in facilitated transport membranes are critically important in determining transport properties.

The main objective of this chapter is to provide readers with a general overview of the present knowledge of solid-state facilitated transport membranes with reference to (i) carrier properties, (ii) transport mechanism, (iii) mathematical models, (iv) separation performances and (v) membrane stability. The discussion is focused only on olefins/paraffins and oxygen/nitrogen separations.

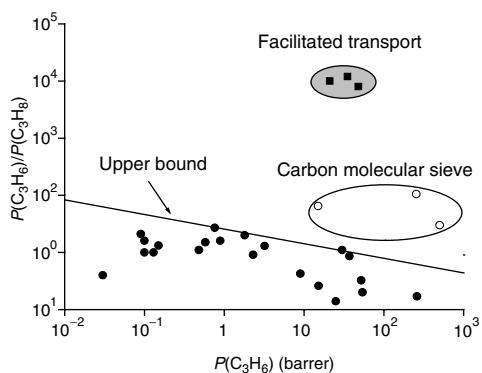


Figure 16.1 Relationship between propylene permeability and its ideal separation factor over propane. The data for the facilitated transport membranes are taken from Hong *et al.* [1], Pinnau *et al.* [2] and Kim *et al.* [3], while the data for conventional polymers and carbon molecular sieve membranes are taken from Burns and Koros [4]. Permeabilities of the facilitated transport membranes were calculated from the permeances by the fact that the effective membrane thickness is 1 μm , obtained from SEM cross-section images

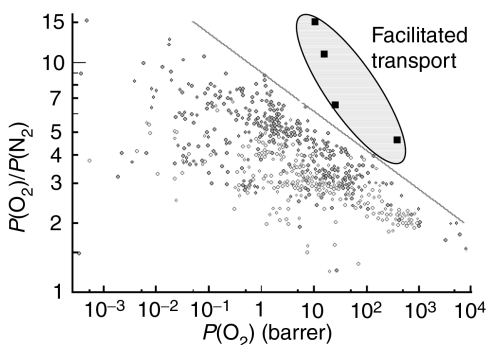


Figure 16.2 Relationship between oxygen permeability and its ideal separation factor over nitrogen. The data for the facilitated transport membranes are taken from Nishide *et al.* [5], Tsuchida *et al.* [6], Nishide *et al.* [7] and Nishide *et al.* [8], while those for conventional polymers are taken from Robeson [9]

16.2 Carrier Properties and Transport Mechanism

Facilitated transport membranes in the solid state comprise a carrier incorporated into a dry polymeric matrix. The carrier can be any chemical, normally a metal ion, which reversibly reacts

with a specific solute. Thus, its interaction with the solute is essential in determining transport properties. In the case of olefins/paraffins separation, transition-metal ions, such as Ag^+ or Cu^+ dissolved in a polymeric matrix have been used as an olefin carrier [1,10–24]. It is also known that oxygen interacts reversibly with Co^{++} or Fe^{++} ions coordinated by nitrogens and/or oxygens of porphyrins or Schiff's bases [5–8,25–32]. In this section, carrier properties, as well as possible facilitated transport mechanisms of olefins, are reviewed briefly.

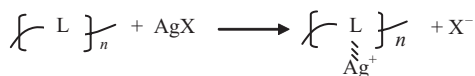
16.2.1 Carrier Properties

16.2.1.1 Olefin Carrier

When silver ions are dissolved in a polymer–solvent to form polymer silver salt complexes or silver–polymer electrolytes, they can be successfully used as an olefin carrier because they react reversibly with olefins. Thus, the formation and structure of silver–polymer electrolytes, and their olefin sorption and reversibility, are important to understand facilitated transport phenomena.

Formation and Structures of Silver Polymer Electrolytes

In order to dissolve silver salts in a polymer solvent, the polymer should have appropriate ligands (L) for coordinative interaction with silver ions, as follows:



where X^- is a counter anion. It is found that silver salts are readily dissolved to form silver–polymer electrolytes when their lattice energies are small, with large anions such as BF_4^- , CF_3SO_3^- , ClO_4^- and SbF_6^- [33,34]. On the other hand, when the anion is small, such as F^- , Cl^- and NO_3^- , its interaction with a silver ion is very strong so that silver salts are much less soluble in a polymer solvent.

The coordinative interaction between Ag^+ and L induces the dissolution of silver salts in a polar polymer solvent containing oxygen or nitrogen atoms, such as poly(ethylene oxide) (PEO) [2,10, 11], nylon-12/tetramethylene oxide block copolymer (PA12–PTMO)

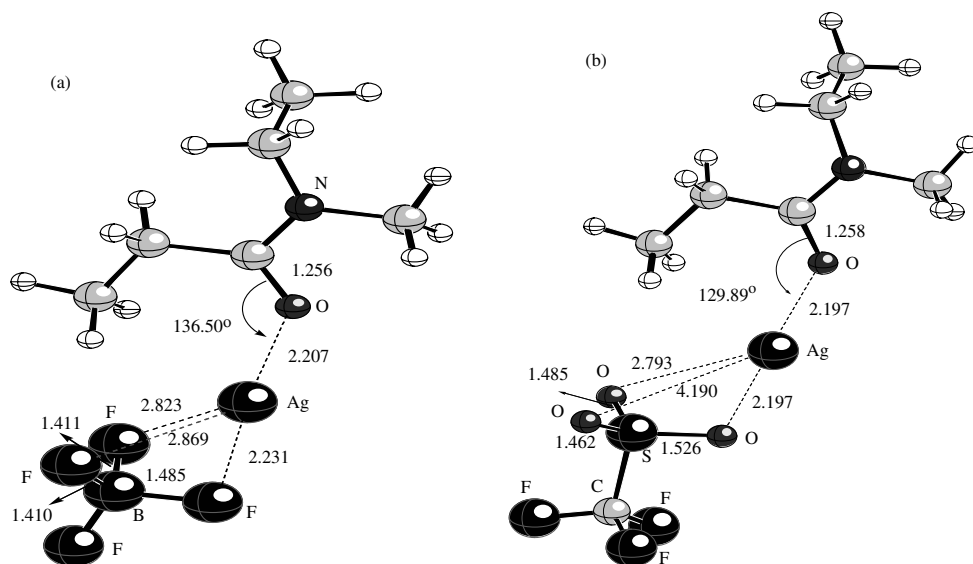


Figure 16.3 Molecular structures of POZ complexes with (a) AgBF_4 and (b) AgCF_3SO_3 , where *N*-methyl-*N*-ethylpropionamide is used as a model compound of POZ [16]

[14,18], poly(2-ethyl-2-oxazoline) (POZ) [1,3, 13,16], poly(*N*-vinyl pyrrolidone) (PVP) [1,12, 19], poly(vinyl methyl ketone) (PVMK) [20], polymethacrylates (PMAs) [21], cellulose acetate (CA) [22] and polyether-block-amide copolymer (Pebax) [23]. The coordinative interaction of Ag^+ with the carbonyl oxygen of POZ was confirmed by both theoretical structure calculations based on the density functional theory [16] and IR spectra in which the carbonyl band shifted from 1641 to 1595 cm^{-1} upon incorporation of silver salts [34], as shown in Figures 16.3 and 16.4, respectively.

Figure 16.3 shows that Ag^+ is coordinated by one carbonyl oxygen and three fluorine atoms of AgBF_4 , whereas it is coordinated by one carbonyl oxygen and two sulfonate oxygens of AgCF_3SO_3 . Both the bond length between Ag^+ and the carbonyl oxygen and that between Ag^+ and the closest anion atom are longer in AgBF_4 than in AgCF_3SO_3 . The longer lengths in both bonds lead to weaker interactions of the silver ion with carbonyl oxygen and with the anion, and thus silver ions in AgBF_4 will be more active in coordinating with olefins than those in AgCF_3SO_3 .

The coordinative interaction between Ag^+ and L strongly influences the structural changes. For instance, when the Ag^+ ion is coordinated by

more than one carbonyl oxygen of POZ or PVP, it acts as a transient cross-linker to make the polymer chains more rigid. Therefore, physical properties, such as the glass transition temperature (T_g), intersegmental distance and propane permeability are changed [3,35].

The T_g s of POZ/silver salt complexes were measured using differential scanning calorimetry (DSC) and are shown in Figure 16.5 [16]. Each data set for a given silver salt exhibits the same general feature of an increasing T_g with increasing salt content, reaches a broad maximum, followed

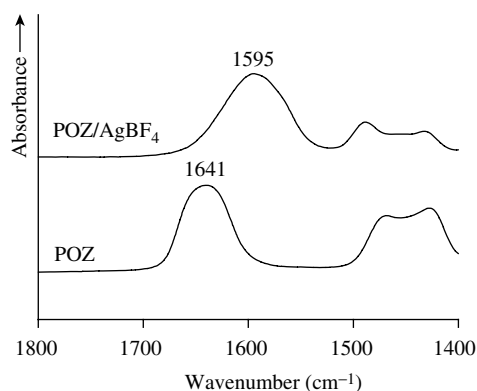


Figure 16.4 Carbonyl peak shift upon dissolution of silver salts in POZ [1]

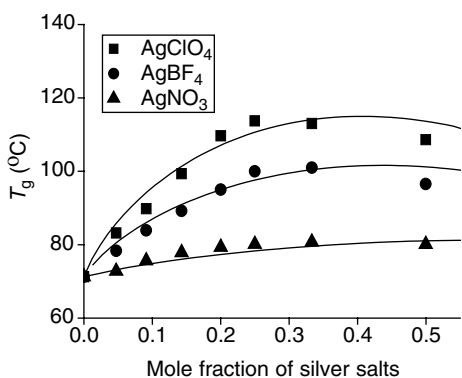


Figure 16.5 Variation of the glass transition temperature for POZ/silver salts complexes as a function of the silver salt concentration. The continuous lines are based on the configurational entropy theory [35] using Equation (16.1) with $\gamma_{12} = 1.07, 0.95$ and 0.80 for AgClO_4 , AgBF_4 and AgNO_3 , respectively

by a slight decrease. The experimental T_g s are in a good agreement with theoretical predictions from the configurational entropy theory [35]:

$$\ln\left(\frac{T_{g12}}{T_{g1}}\right) = \beta_1 \left[\left(\frac{\phi_1}{r_1} \ln \phi_1 + \frac{\phi_2}{r_2} \ln \phi_2 \right) \times \left(1 - \gamma_{12} \ln \left(\frac{z-1}{e} \right) \right) \right] \quad (16.1)$$

where T_{g12} and T_{g1} are the T_g s for the polymer (1)/metal salt (2) complex and pure polymer, respectively; ϕ_i is the volume fraction of component i , r_i is the degree of polymerization of component i and $r_2 = 1$ here for the metal salt. In addition, $\beta_1 = zR/M_u \Delta C_{pp}$, where z is the Flory lattice coordination number, M_u is the molecular weight of the repeating unit and ΔC_{pp} is the difference in the specific heat capacity of the polymer between the supercooled liquid and the glassy state; γ_{12} represents the extent of the interaction between the polymer and the metal salt. The continuous lines in Figure 16.5 were obtained from Equation (16.1) with interaction parameters γ_{12} , of 1.07, 0.95 and 0.80 for AgClO_4 , AgBF_4 and AgNO_3 complexes with POZ, respectively. The increase in T_g upon addition of metal salts is primarily attributed to both the transient cross-links of polymer segments by silver ions and the ‘dangling’ of silver ions on the

chain and is more pronounced in AgClO_4 than other salts, owing to the larger γ_{12} value [16].

Olefin Sorption in Silver Polymer Electrolytes

Extremely large amounts of olefins can be dissolved in polymer electrolytes containing silver salts. For example, the propylene solubility is $245 \text{ cm}^3 \text{ (STP)/cm}^3$ in 1:1 [C=O]:[Ag] POZ/ AgBF_4 , whereas it is as low as 3 in pure POZ at 224 kPa [1]. On the other hand, the paraffin solubility significantly decreases upon incorporation of the silver salt into a polymer matrix. The ethane solubility in PA12-PTMO is $5.0 \text{ cm}^3 \text{ (STP)/cm}^3$, whereas that in PA12-PTMO/ AgBF_4 (70 wt% AgBF_4) is 0.25 at 506.5 kPa [14].

The olefin solubility also strongly depends on the anion type. It is almost two-fold higher in POZ or PVP electrolytes containing AgBF_4 than those containing AgCF_3SO_3 , as shown in Figure 16.6 [13]. In the case of PEO/silver salt membranes, 1:1 [EO:Ag] PEO/ AgBF_4 and 1:1 PEO/ AgCF_3SO_3 sorb 8.46 and 1.76 g of propylene per 100 g of polymer electrolyte, respectively, at 30 °C and 70 cmHg pressure. In contrast, 1:1 PEO/ AgNO_3 only sorbs 0.52 g of propylene per 100 g of polymer electrolyte [10].

The propylene solubilities in silver-polymer electrolytes are analyzed by the dual sorption model of Equation (16.2) and its parameters are listed in Table 16.1:

$$C = k_D p + \frac{C'_c K p}{1 + K p} \quad (16.2)$$

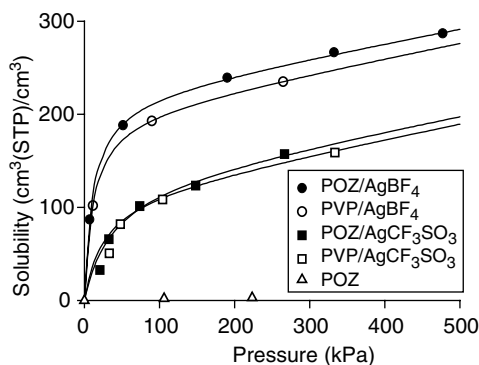


Figure 16.6 Solubility of propylene in solid polymer electrolyte films at 25 °C. The continuous lines were calculated from the dual-sorption model [36] using Equation (16.2)

Table 16.1 Dual-mode sorption parameters of propylene for silver–polymer electrolytes (25 °C, [C=O]:[Ag] = 1:1)

Electrolyte	$k_D(\text{cm}^3(\text{STP})/(\text{cm}^3 \text{ cmHg}))$	$K (1/\text{cmHg})$	$C'_c(\text{cm}^3(\text{STP})/\text{cm}^3)$
POZ/AgBF ₄	0.20	0.12	222.14
PVP/AgBF ₄	0.21	0.12	201.59
POZ/AgCF ₃ SO ₃	0.20	0.04	131.41
PVP/AgCF ₃ SO ₃	0.21	0.05	115.93

where k_D is the Henry's law solubility coefficient, p is the applied pressure, K is the equilibrium binding constant and C'_c is the saturated amount of the gas reversibly bound to the carrier. The first term of Equation (16.2) represents 'ordinary' dissolution by Henry's law while the second represents complexation according to the Langmuir sorption isotherm [36]. The 'Langmuirian term' in silver–polymer electrolytes is much larger in comparison with conventional glassy polymers. For example, 1:1 POZ/AgBF₄ shows 0.12 1/cmHg of K and 222 cm³(STP)/cm³ of C'_c , whereas the polyimide prepared from 4,4'-(hexafluoroisopropylidene)diphthalic anhydride (6FDA) and 2,4,6-trimethyl-1,3-phenylenediamine (TrMPD) exhibits 0.038 of K and 26 of C'_H [37]. This suggests that the total solubilities of olefins in silver–polymer electrolytes depend mostly on the complexation of propylene with silver ions.

Reversible Interaction of Silver Ions with Olefins

The reversible olefin coordination to silver ions in solid polymer electrolytes was investigated spectroscopically [20,22]. When a 1:3 CA/AgBF₄ complex was exposed to 207 kPa of propylene and then purged with N₂ for a short time (~1 s), a new peak appeared in the IR spectra at 1586 cm⁻¹ for the C=C stretching vibration of the coordinated propylene (Figure 16.7(a)). It is interesting to note that the peak at 1586 cm⁻¹ remains even after degassing at 10⁻⁵ torr for 4 h at room temperature. However, exposure of the propylene-coordinated complex to 207 kPa of 1,3-butadiene and subsequent treatment with N₂ gave a new peak at 1551 cm⁻¹ with the concomitant disappearance of the peak at 1586 cm⁻¹. The peak at 1551 cm⁻¹ can be assigned to the C=C stretching frequency of the coordinated 1,3-butadiene

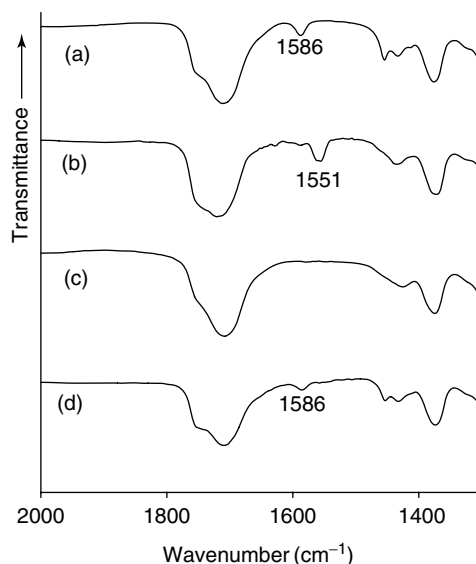


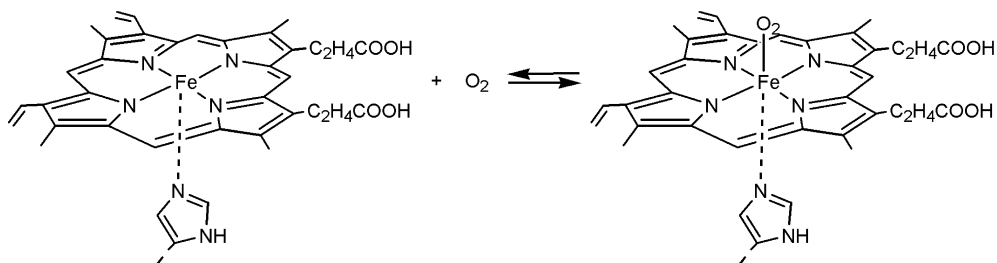
Figure 16.7 IR spectra for reversible olefin interactions of 1:3 CA/AgBF₄ membranes: (a) propylene-coordinated virgin membrane; (b) 1,3-butadiene-coordinated membrane; (c) ethylene-coordinated membrane; (d) propylene-coordinated membrane [22]

(Figure 16.7(b)). This peak at 1551 cm⁻¹ disappeared again when ethylene was introduced into the complex. The peak at 1586 cm⁻¹ reappeared when ethylene was replaced by propylene. These results indicate that the coordinated propylene is labile to be easily exchanged by other olefins, but strong enough not to be readily removed by application of a vacuum. The same reversible olefin coordination behavior was also observed by UV spectroscopy [20,22].

16.2.1.2 Oxygen Carriers

Metalloporphyrin or Schiff's Base Complex

Co⁺⁺ and Fe⁺⁺ ions coordinated by porphyrin or a Schiff's base react reversibly with oxygen and, therefore, can act as an oxygen carrier. When Co⁺⁺ or Fe⁺⁺ ion coordinates with four nitrogens from a planar porphyrin, two of its coordination sites are still unfilled, because both ions have a coordination number of six. For instance, when the fifth coordination site is coordinated by a histidyl residue, the sixth site is left open and is able to bind oxygen reversibly, as presented in Scheme 16.1.



Scheme 16.1 Reversible oxygen coordination to iron(II) porphyrin

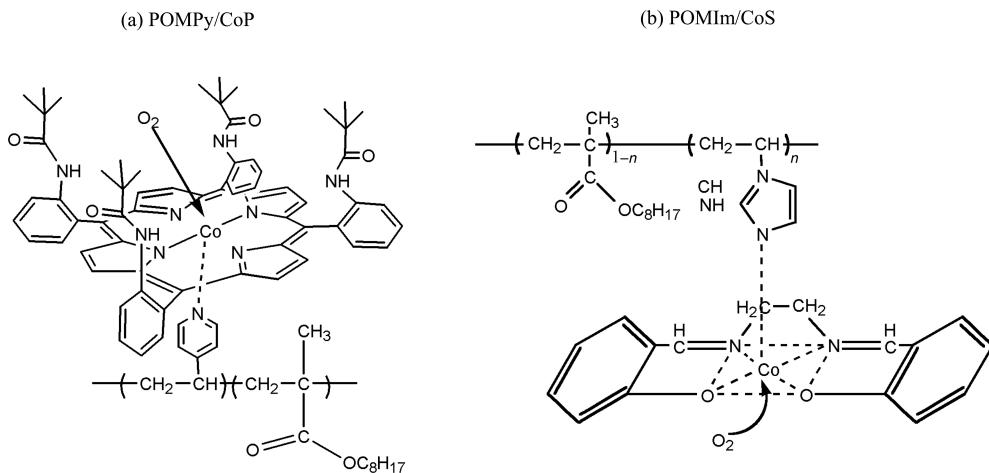
Although the oxygen binding reaction with Co^{++} and Fe^{++} ions is known to be reversible, they can be irreversibly oxidized to Co^{+++} and Fe^{+++} ions, respectively, and consequently lose their oxygen-binding capability. Thus, oxidation should be prevented to maintain the oxygen carrier activity. This has been achieved mostly by introducing 'picket-fence' porphyrins into the hydrophobic polymer matrix to provide steric hindrance as well as to exclude water molecules for suppressing proton-driven oxidation. Typical examples of a 'picket-fence' cobalt porphyrin and a Schiff's base are shown in Scheme 16.2 [6,36,38,39].

Oxygen Solubility and Reversibility

When oxygen is in contact with a membrane containing cobalt porphyrins, it forms oxygen-cobalt adducts. Thus, its solubility is enhanced markedly

compared to that of the pure polymer matrix. For example, the oxygen solubility for a poly[(octyl methacrylate)-*co*-(4-vinylpyridine)] (POMPy) membrane containing 37 wt% [$\alpha,\alpha',\alpha'',\alpha'''$ -*meso*-tetrakis(*o*-pivalamidophenyl)porphinato] cobalt(II) (CoP) complex was ca. $6.2 \text{ cm}^3(\text{STP})/\text{cm}^3$ polymer, which is more than six times greater than the oxygen solubility of the pure polymer (ca. $1 \text{ cm}^3(\text{STP})/\text{cm}^3$ polymer), as shown in Figure 16.8 [36]. The oxygen sorption isotherm follows the dual-sorption model and its parameter values of k_D , K and C'_c are listed in Table 16.2.

The reversible oxygen binding to the poly(*n*-butyl methacrylate) (PBMA)/CoP with 1-methylimidazole (CoPIIm) complex was confirmed by the visible absorption spectroscopy and is shown in Figure 16.9 [40]. The λ_{max} at 528 nm of the deoxy-CoPIIm was changed to 545 nm for the oxy-CoPIIm ($[\text{O}_2]:[\text{Co}] = 1:1$ adduct), immediately after exposure of the membrane to



Scheme 16.2 Typical examples of (a) a 'picket-fence' cobalt porphyrin and (b) a Schiff's base [6,36,38,39]

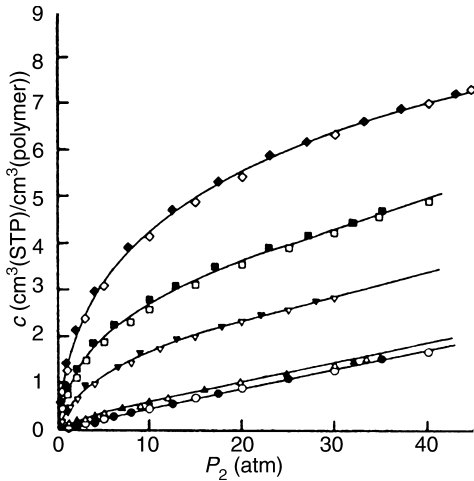


Figure 16.8 Oxygen sorption isotherms for POMPy/CoP membranes at 45 °C where the open and filled symbols represent the sorption and desorption runs, respectively: ○, CoP = 0 wt%; △, 1.8 wt%; ▽, 15 wt%; □, 25 wt%; ◇, 37 wt% [36]. Reprinted with permission from H. Nishide, H. Kawakami, S. Toda, E. Tsuchida and Y. Kamiya, *Macromolecules*, **24**, 5852 (1991). Copyright (1991) American Chemical Society

oxygen. The oxy-deoxy spectral change was reversible in response to a partial pressure of oxygen with isosbestic points at 480, 538 and 667 nm. The reversible oxygen binding ability in the POMPy complex membrane containing (*N,N'*-disalicylideneethylenediamine) cobalt (CoS) was also confirmed by ESR spectroscopy [6].

Reversible Binding Kinetics

The rates of the reversible oxygen binding to the PBMA/CoPIIm membrane were measured by pulse and laser flash spectroscopy [40]. The oxygen binding (k_1) and dissociation (k_2) rate constants

Table 16.2 Dual-mode sorption parameters of oxygen for POMPy/CoP membranes at 45 °C [36]

CoP (wt %)	$k_D \times 10^4$ (cm ³ (STP)/cm ³ cmHg)	$K \times 10^3$ (1/cmHg)	C'_c (cm ³ (STP)/cm ³)
0	4.6	—	—
1.8	5.5	5.0	0.1
15	7.1	5.5	1.4
25	7.7	5.2	2.7
37	8.6	4.7	4.8

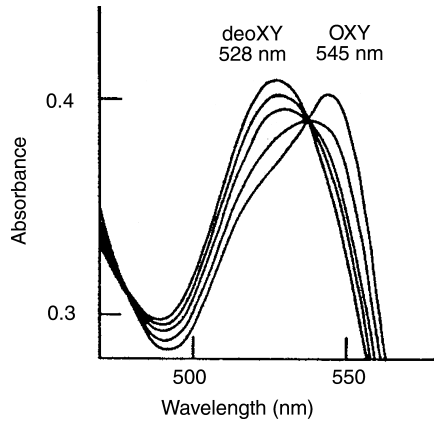


Figure 16.9 Visible absorption spectrum changes for the reversible oxygen binding to the PBMA/CoPIIm membrane at 25 °C; [CoPIIm] = 2.5 wt% [40]. Reprinted with permission from H. Nishide, M. Ohyanagi, O. Okada and E. Tsuchida, *Macromolecules*, **20**, 417 (1987). Copyright (1987) American Chemical Society

in Equation (16.3) were estimated by assuming ‘pseudo-first-order kinetics’ (Figure 16.10) [40].



The k_1 and k_2 values of the CoPIIm complex membrane are very high, at 5.2×10^5 l/(mol s)

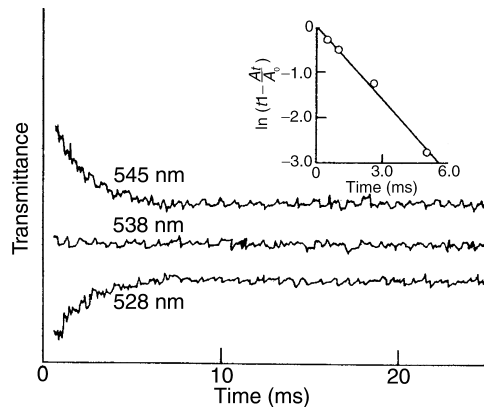


Figure 16.10 Flash photolysis of the PBMA/CoPIIm membrane upon exposure to air and approximation to pseudo-first-order kinetics for the membrane at 25 °C; [CoPIIm] = 2.5 wt% [40]. Reprinted with permission from H. Nishide, M. Ohyanagi, O. Okada and E. Tsuchida, *Macromolecules*, **20**, 417 (1987). Copyright (1987) American Chemical Society

and 2.8×10^4 l/(mol s), respectively, and $K = 18.6$ l/mol, indicating that the CoPIIm complex is active for oxygen binding in the solid membrane and acts as an effective carrier of oxygen.

16.2.2 Transport Mechanism

16.2.2.1 Two-Step Reaction Mechanism of Silver Ions with Olefins

The reaction mechanism between silver ions and olefins can be elucidated by calculating the theoretical structure of a silver-polymer complex in the gas phase and the electronic energies of its reaction step with the olefin. The theoretical structure (a) of AgBF_4 dissolved in ethylene glycol dimethyl ether, used as a model compound of Poly(ethylene oxide) (PEO), was calculated by the density functional theory and is presented in Figure 16.11 [41]. When one ethylene molecule is introduced into the complex (a), a new complex (b) is formed by substituting one of the sites of the anion ligand with an ethylene molecule. This step is a diffusion-controlled type without activation, as expressed by the 1st step of Scheme 16.3.

When another ethylene molecule approaches the complex (b), the ethylene molecule already bonded to the silver ion is substituted with a new ethylene molecule by an activated process through a transition state (c) of a normal 'push-pull' $\text{S}_{\text{N}}2$ type as shown by the 2nd step of Scheme 16.3. The transition state has a typical trigonal bipyramid 5-coordinate structure, as is well-known in common $\text{S}_{\text{N}}2$ reactions. Thus, the reversible reaction mechanism of olefins with silver cations in polymer electrolyte membranes is expressed by the two steps of Scheme 16.3 [41].

The first complexation step is apparently not completely reversible and is slow to form silver-olefin complexes as an intermediate, while the second exchange step is rapid and reversible, which appears to be the key step in determining facilitated olefin transport. Note that the second step is only observed when a concentration gradient is present.

16.2.2.2 Threshold Concentration and the Most Favorable Coordination Number

In facilitated olefin transport through silver-polymer electrolytes, the threshold concentration was observed at a silver mole fraction of approxi-

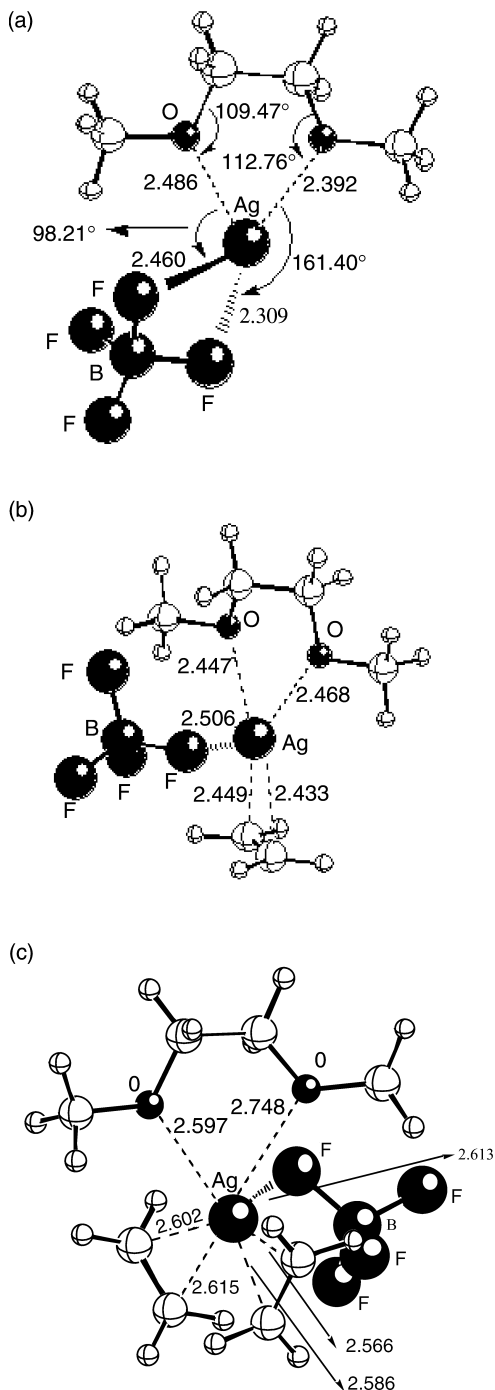
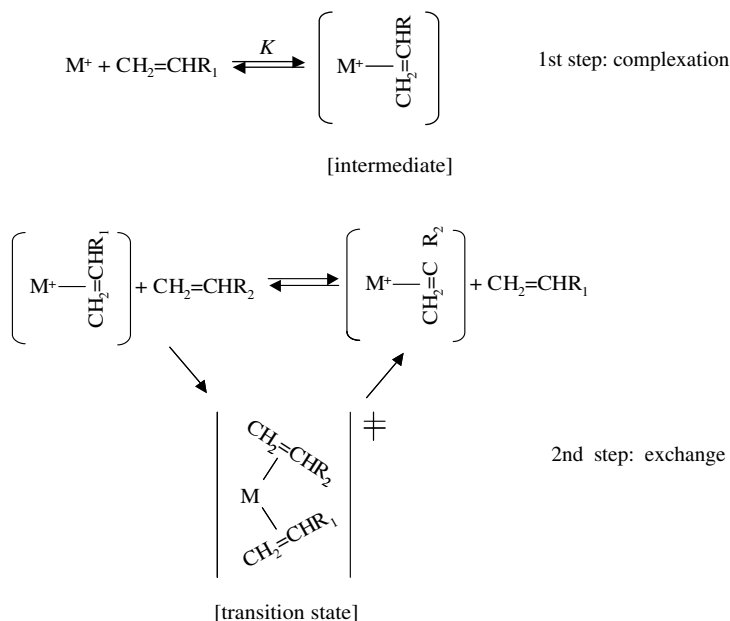


Figure 16.11 Optimized structures of (a) the PEO/ AgBF_4 complex (b) the PEO/ AgBF_4 complex coordinated by one ethylene and (c) the PEO/ AgBF_4 complex coordinated by two ethylenes (transition state) [41]



Scheme 16.3 Two-step reaction mechanism of a silver ion with an olefin in polymer electrolyte membranes: R_1 and R_2 represent either a hydrogen atom or an alkyl group [41]

mately 0.25 for $AgBF_4$ or $AgCF_3SO_3$ dissolved in POZ or PVP, below which facilitated transport was not observed [12]. However, the propylene permeance increased nearly linearly with the silver concentration at silver concentrations above the threshold concentration, as shown in Figure 16.12.

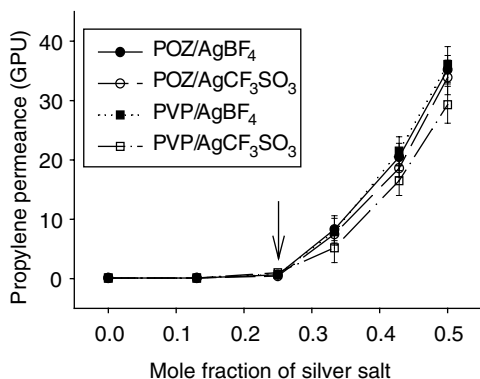


Figure 16.12 Propylene permeance for polymer electrolyte membranes as a function of the silver concentration at 23 °C; $\Delta p = 413.5$ kPa (1 GPU = 1×10^{-6} cm³(STP)/(cm² s cmHg)) [12]

The threshold concentration is found to be strongly associated with the coordination behavior of the silver ion by both carbonyl oxygens and olefin molecules [3].

The coordination number of the silver ion, m , by carbonyl oxygens (C=O) can be obtained simply by the concentration ratio of the complexed carbonyl oxygen to the silver ion from IR and Raman spectra [34]. The coordination number of the silver ion, n , by olefin molecules is obtained from the concentration ratio of propylene molecules coordinated to silver ions (C'_i) to the silver ion concentration [3]. The coordination numbers of silver ions in POZ/ $AgCF_3SO_3$ are plotted against the mole fraction of silver salt, as shown in Figure 16.13 [3]. It is clear from this figure that m decreases exponentially with the silver concentration whereas n increases slightly. Surprisingly, the total coordination number, $(m + n)$, becomes nearly invariant and is around 3. This result strongly suggests that the most favorable coordination number of the silver ion dissolved in a polymer matrix under propylene environment is ~ 3 . However, the actual coordination number is slightly smaller than 3, seemingly owing to the limited accessibility of

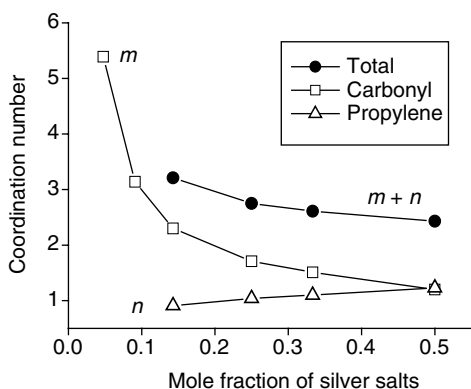
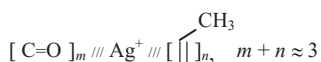


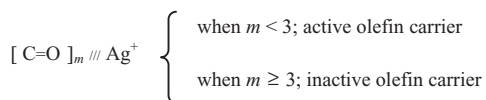
Figure 16.13 Coordination number of the silver ion by carbonyl oxygen and propylene in POZ/AgCF₃SO₃ as a function of the silver salt concentration [3]

propylene molecules by rather rigid polymeric chains:



It was also found from IR spectra [19] and theoretical calculations [3] that the interactions of silver ions with the carbonyl oxygens of POZ are slightly stronger than that with olefin molecules. Therefore, the relationship between the threshold concentration and the most probable coordination number of the silver ions can be deduced from the favorable coordination number and difference in the interactions.

When $m \geq 3$, silver ions may not be able to interact with the surrounding olefin molecules, implying that the silver ion does not act as an olefin carrier. However, when $m < 3$, the coordination sites of the silver ions are not completely occupied by carbonyl oxygens and thus vacant sites are available for olefin coordination. Therefore, it is concluded that silver ions can act as olefin carriers only when $m < 3$; in other words, the threshold concentration of the mole fraction of the silver salts is 0.25 ($= 1/(1+3)$), which is consistent with the data presented in Figure 16.12:



This is the first report on the importance of the coordination behavior of metal ions in determining the activity of silver ions as olefin carriers, and the presence of the threshold concentration for facilitated transport membranes in the solid state. However, it should be noted that the threshold concentration depends on the polymer matrix type, as well as the silver salt type [11].

16.3 Mathematical Models

Mathematical models for facilitated transport phenomena in solid-state membranes, such as dual-sorption, effective diffusion coefficient, limited mobility of 'chained' carriers and concentration fluctuation models are described in brief and are compared with each other in the following.

16.3.1 Dual-sorption Model

The dual-sorption model, originally developed to interpret the sorption behavior of gases or vapors in glassy polymers, has been commonly employed to explain facilitated transport properties because it is conceptually analogous to the mass transport in a facilitated transport membrane in the solid state. The permeability, P , through facilitated transport membranes is given [42] as follows:

$$P = k_D D_D + D_C C'_C \frac{K}{1 + Kp} \quad (16.4)$$

where D_D is the Fickian diffusion coefficient and D_C is the effective diffusion coefficient between carriers. A fairly linear relationship between P and $(1 + Kp)^{-1}$ was obtained from the experimental oxygen permeabilities of PBMA/CoPIIm membranes demonstrating the validity of the dual-sorption model [42].

The simple dual-sorption model was developed by assuming that only two independent diffusional pathways of the ordinary diffusion and the direct diffusion between carriers were present. However, it may not be valid in a real system. Thus, this assumption was relaxed to adopt four diffusional pathways with four different diffusion coefficients: (1) diffusion between dissolved modes, (2) diffusion from dissolved to carrier modes, (3) diffusion from carrier to dissolved modes, and (4) diffusion between fixed carriers [38].

The dual-sorption model predicts the dependency of permeability on upstream pressure qualitatively. However, it does not predict facilitated transport without direct diffusion between carriers. Furthermore, it neglects the importance of the reversible complexation kinetics between solute and carrier on facilitated transport, which is found to be very important in determining facilitated transport.

16.3.2 Effective Diffusion Coefficient Model

A more rigorous analysis of facilitated transport in the solid state was presented by introducing the concept of 'the effective diffusion coefficient' between fixed site carriers [43]. If the excess carrier is assumed, the concentration of the unreacted carrier is constant, which leads to:

$$\frac{J}{J_0} = \frac{1 + \left(\frac{D_{AB}}{D_A}\right) \left(\frac{K[B]_0}{1 + Kp}\right)}{1 + \left(\frac{D_{AB}}{D_A}\right) \left(\frac{K[B]_0}{1 + Kp}\right) \left(\frac{\tanh \phi}{\phi}\right)} \quad (16.5)$$

where J_0 and J are solute fluxes for Fickian transport and for facilitated transport with carriers, respectively, and $[B]_0$ is the carrier concentration. D_A is the Fickian diffusion coefficient, $D_{AB} = h^2[(k_j^+ + k_{j+1}^-)/2]$ is the effective diffusion coefficient where k_j^+ is the mobility at the j th location, h is the unit cell thickness, + and - indicate direction and $\phi = \sqrt{[(k_2 L^2)/D_{AB}]\{1 + [(D_{AB}/D_A)K[B]_0 + Kp]/(1 + k_p)\}}/2$.

Equation (16.5) is identical to that of facilitated transport in liquid membranes developed by Smith and Quinn [44]. If the reaction rate is assumed to be much faster than the diffusion rate, $\tanh \phi/\phi \approx 0$ and then the model is reduced to the dual-sorption transport model:

$$\frac{J}{J_0} = 1 + \left(\frac{D_{AB}}{D_A}\right) \frac{K[B]_0}{1 + Kp} \quad (16.6)$$

The validity of the model was examined against the experimental data for PBMA/CoPIIm, as shown in Figure 16.14, where $E = J/J_0 - 1$. At low pressure, Equation (16.6) fits them well, but starts to deviate gradually as the oxygen pressure increases. This is because the excess carrier assumption is violated at high oxygen pressures.

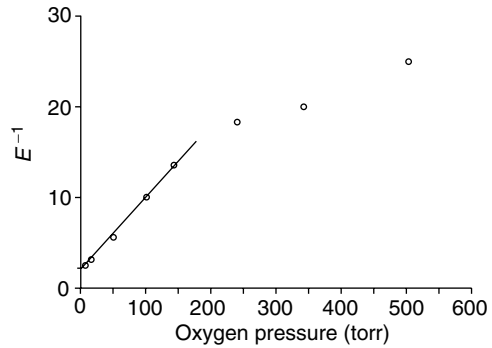


Figure 16.14 Plot of E^{-1} for a PBMA/CoPIIm membrane as a function of oxygen pressure at 25 °C ([CoPIIm] = 2.5 wt%), where $E = J/J_0 - 1$ [43]. Reprinted from *Journal of Membrane Science*, **50**, R. D. Noble, 'Analysis of facilitated transport with fixed site carrier membranes', 207–214, Copyright (1990), with permission from Elsevier

16.3.3 Limited Mobility of Chained Carriers Model

Cussler *et al.* [45] analyzed fixed site facilitated transport with the concept of 'limited mobility of chained carriers'. It was assumed that no uncomplexed solute can exist in the membrane, and the reaction between a carrier and solute occurs only at the surface of the membrane and is fast.

The mobility of a chained carrier, commonly pending on a side-chain, can allow the carrier-solute complex to encounter a second, uncomplexed carrier, resulting in facilitated transport, as follows:

$$J = \frac{D_{AB}[B]_0}{L} \left(\frac{Kp}{1 + Kp}\right) \left(\frac{2\lambda/\lambda_0}{3 - \lambda_0/\lambda}\right) \quad (16.7)$$

where λ is the distance between carriers and λ_0 represents the distance for limited chain mobility. In this case, carrier-mediated transport is only allowed over a limited distance due to the limited mobility of the chained carriers, which, in turn, leads to a percolation threshold at $\lambda = \lambda_0$. However, the existence of the percolation threshold is unlikely because facilitated transport has been experimentally observed at low concentrations of CoPIIm in PBMA, as low as 0.6 wt% [6]. The details are described below.

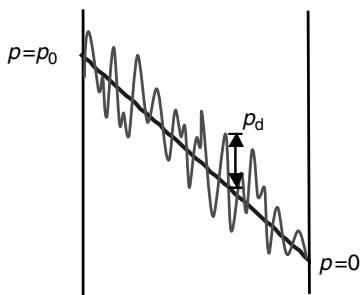


Figure 16.15 Fluctuated concentration profile in a solid-state facilitated transport membrane under solid-state conditions [47]

16.3.4 Concentration Fluctuation Model

In facilitated transport membranes, a reversible chemical reaction occurs between a carrier and a solute continuously. At a certain moment, the local solute concentration may fluctuate slightly and instantaneously owing to the reversible reaction. However, the time-average concentration profile still remains linear, as shown in Figure 16.15. When a solute reacts with a carrier to form carrier-solute complexes, the local solute concentration at that specific site will decrease instantaneously from its average value. On the other hand, it will increase when the complex releases the solute into the matrix. The concentration fluctuation induces the increase in the chemical potential of the solute according to Cahn's theory [46]. The increased chemical potential will result in a higher driving force for mass transfer and lead to facilitated transport. Based on the above concepts and the analogy between electron transfer in a series of parallel resistor-capacitor circuits and mass transport in a fixed site carrier membrane, Kang and coworkers [47,48] proposed a concentration fluctuation model to explain facilitated transport behavior in the solid state:

$$\frac{P}{P_0} = 1 + \left(\frac{p_d}{p} \right) \times \sqrt{n^2 + \left[\frac{2\pi k_2 L^2 [B]_0 \ln(1 + Kp)}{P_0 p} \right]^2} \quad (16.8)$$

where P_0 is the permeability of the membrane matrix without a carrier, p_d is the pressure fluctuation due to the reversible reaction, $n = N[B]_0(\pi r^2 L)$ (where N is the Avogadro constant), L is the membrane thickness and r is the permeant radius; k_2 and K are the backward reaction rate constant and the equilibrium constant of the carrier-solute reaction, respectively.

According to this model, P increases linearly with $[B]_0$, demonstrating the importance of the carrier concentration, and with decreasing p , as observed experimentally [1,42]. In most experimental data analysis, it has been accepted that facilitated transport occurs primarily due to the increased solubility (K) without considering the kinetic effect. However, the concentration fluctuation model suggests that P increases linearly with the reverse reaction rate (k_2) and logarithmically with the equilibrium constant (K), thus demonstrating the importance of the kinetics. Therefore, it is claimed that both the kinetic (k_2) and thermodynamic (K) terms play an important role in improving the permeation properties, but the former is much more effective than the latter, according to the sensitivity analysis [48].

The concentration fluctuation model was examined against the experimental data on facilitated oxygen transport through PBMA containing cobalt porphyrins, as shown in Figure 16.16 [42].

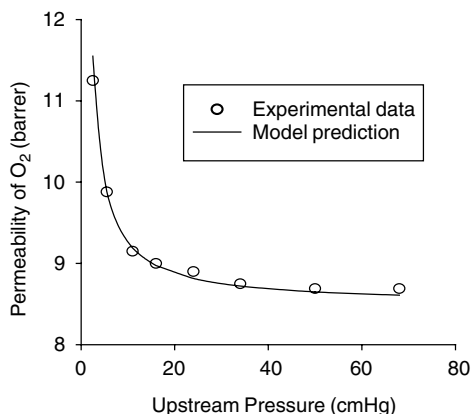


Figure 16.16 Comparison between the concentration fluctuation model predictions and experimental data [42] for a PBMA membrane containing cobalt porphyrin: $P_0 = 8.4$ barrer; $L = 65$ m; $k_2 = 2.8 \times 10^4$ s; $K = 18.6$ l/mol ($= 7.97 \times 10^{-4}$ /(cmHg)); $k_D = 9.6 \times 10^{-4}$ cm³(STP)/(cm³ cmHg); $[B]_0 = 2.5$ wt % ($= 2.23 \times 10^{-5}$ mol/cm³); $p_d = 2.55 \times 10^{-7}$ cmHg

All parameter values were independently measured by Nishide and coworkers [42], except the pressure fluctuation p_d . This model predicts the experimental results exceptionally well, even at the high pressure range where the ‘effective diffusion coefficient’ model fails to predict. This suggests the validity of the concentration fluctuation model.

16.3.5 Hopping Model versus Concentration Fluctuation Model

In the case of the simple dual-sorption and the effective diffusion coefficient models, facilitated transport is not predicted when the effective diffusion coefficient becomes zero. In other words, without direct diffusion between carriers, facilitated transport does not occur. The limited mobility of the chained carrier model does not predict facilitated transport without direct mass transport between carriers either. Thus, these three models are under the category of a ‘hopping’ model. In this section, the validity of the hopping model is examined.

In order to allow a solute to directly hop between two carriers, the distance, λ , between two carriers should be shorter than the diffusional jump distance, δ . According to the hopping model, facilitated transport occurs only when $\lambda < \delta$ and the threshold concentration will be present at $\lambda = \delta$.

The distance, λ , between two carriers is simply expressed by:

$$\lambda = (1/N[B]_0)^{1/3} \quad (16.9)$$

where $[B]_0$ is the molar concentration of the carrier in the matrix. The λ values for 0.6, 4.5 and 30 wt% of CoPIIm in PBMA are approximately 68, 35 and 18 Å, respectively, and experimental facilitated oxygen transport was observed even when the CoPIIm concentration was as low as 0.6 wt% [6].

The average diffusional jump distance, δ , is obtained from the diffusional activation energy via the following relationship [49]:

$$E_D = \delta \left(\frac{\pi r^2}{4} \right) (CED)N \quad (16.10)$$

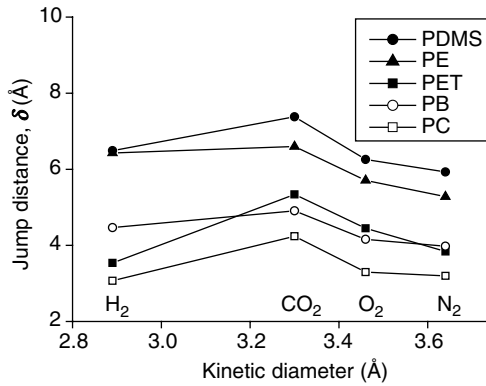


Figure 16.17 The average diffusional jump distance, δ , of various gases for calculated from polymers equation (16.10) where E_D and CED are taken from Crank and Park [49] and van Krevelen [50], respectively

where E_D is the diffusion activation energy and CED is the cohesive energy density of the polymer [50]. The δ values of common polymers are plotted as a function of the kinetic diameter of various gases, as shown in Figure 16.17.

The value of δ for oxygen is in the range 3.0–7.0 Å for common polymers and 6.3 Å for polydimethyl siloxane which is known as a high-permeable rubbery polymer to gas. Thus, $\lambda > \delta$ for the polymer membranes containing 0.6 to 30 wt% of CoPIIm in PBMA. If the hopping mechanism is valid, the CoPIIm membranes should not show facilitated transport behavior over the experimental range, although this does occur [6]. Therefore, the hopping mechanism may not be valid for interpreting facilitated transport phenomena.

Among the four mathematical models described above, only the concentration fluctuation model is not categorized to the hopping model, but predicts facilitated transport even without direct hopping between two carriers. Furthermore, it counts for the importance of the reversible reaction rate, in particular, the reverse rate constant, k_2 , and agrees with experimental results very well.

16.4 Separation Performance of Olefins and Oxygen

Separation of olefin/paraffin gas mixtures is one of the most energy-intensive processes in the

petrochemical industries because it is performed mainly by cryogenic distillations. Solid polymer electrolyte membranes have offered a promise for highly efficient membranes to separate olefin/paraffin mixtures [1–3,10–24]. For example, a 99% pure propylene concentration can be obtained by a single pass of silver–polymer electrolyte membranes when the feed stream concentration is 50% propylene [1,2]. Facilitated oxygen transport membranes containing cobalt porphyrins are also interesting for potential applications in removing oxygen from gas mixtures containing small amount of oxygen because the oxygen permeability and its selectivity over nitrogen are remarkably high at low oxygen partial pressure. In this section, the separation performances of olefin/paraffin and oxygen/nitrogen mixtures through polymer–metal complex membranes are described.

16.4.1 Olefins/Paraffins Separation

The pure gas permeance through composite membranes consisting of PEO and AgBF_4 are presented in Table 16.3 [2,11]. The ethylene/ethane and propylene/propane selectivities of a pure PEO membrane are only 1.2 and 2.5, respectively. However, when the silver salt concentration reaches $[\text{EO}]:[\text{Ag}] = 1:1$ (~ 80 wt% of silver salt), the pure ethylene and propylene permeances are 55 and 48 GPU (1 GPU = 1.0×10^{-6} $\text{cm}^3(\text{STP})/(\text{cm}^2 \text{ s cmHg})$), respectively, 50–100 times higher than those of the pure PEO membrane, while the ideal separation factor is more than several thousands.

The propylene permeances through POZ– and PVP–silver salt membranes are plotted as a func-

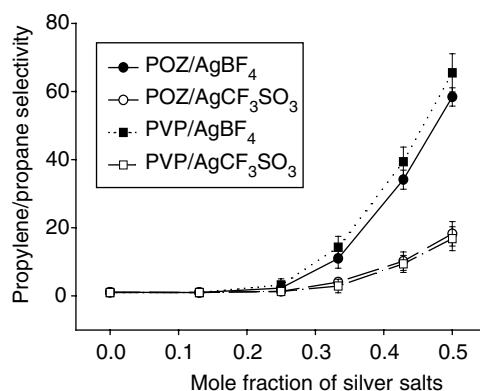


Figure 16.18 Mixed-gas propylene/propane selectivity for silver polymer electrolyte membranes with increasing carrier concentration at 23 °C ($\Delta p = 276$ kPa) [12]

tion of the concentration of silver salt at 413.5 kPa, as already shown in Figure 16.12 [12]. There is no significant improvement of the propylene permeance until the mole ratio of silver to carbonyl reaches approximately 0.25. However, the propylene permeance increases up to almost 40 GPU with increasing silver ion content, while the propane permeance is reduced to as low as 0.003 GPU [3]. Thus, the ideal separation factor of propylene over propane is approximately 10 000. The maximum actual selectivity for gaseous mixtures, defined by the ratio of the mole fractions of the gas components in the permeate and feed streams, is higher than 60, as shown in Figure 16.18. The polymer electrolyte membranes containing AgBF_4 showed better separation performance than those containing

Table 16.3 Effect of silver concentration on olefin/paraffin separation in PEO/ AgBF_4 membranes at 690 kPa feed pressure and 23 °C [2,11]

[EO]:[Ag]	Pure gas permeance (GPU) ^a				Pure gas selectivity	
	C_2H_4	C_2H_6	C_3H_6	C_3H_8	$\text{C}_2\text{H}_4/\text{C}_2\text{H}_6$	$\text{C}_3\text{H}_6/\text{C}_3\text{H}_8$
No Ag	0.55	0.46	0.89	0.36	1.2	2.5
8:1	0.18	0.10	0.22	0.11	1.8	2.0
4:1	1.6	< 0.01 ^b	2.6	< 0.01 ^b	> 160	> 260
2:1	10	< 0.01 ^b	10	< 0.01 ^b	> 1000	> 1000
1:1	55	< 0.01 ^b	48	< 0.01 ^b	> 5500	> 4800

^a1 GPU = 1×10^{-6} $\text{cm}^3(\text{STP})/(\text{cm}^2 \text{ s cmHg})$.

^bGas flux is too low to be accurately measured using the constant pressure method.

Table 16.4 Summary of olefin permeabilities (or permeances) and selectivities over the corresponding paraffins in solid-state facilitated transport membranes^a

Year	Carrier	Polymer	Selectivity, $P_{\text{olefin}}/P_{\text{paraffin}}$	Permeability(barrer) or permeance (GPU)	Reference
1996	AgClO ₄	Poly(1-trimethylsilyl-1-propyne)	C4: 5.6	C4: 3110 barrer	[51]
1997	AgNO ₃	Nafion + polypyrrole	C2: 8–15	C2: 0.2–1 barrer	[52]
1997	AgBF ₄	Poly(ethylene oxide)	C2: > 5500 (120) C3: > 4000	C2: 55 GPU C3: 48 GPU	[2,11]
1998	AgNO ₃	Poly(phenylene oxide)	C3: 5.7	C3: 4–8 barrer	[53]
2000	AgNO ₃	Ethyl cellulose	C3: 10 C4: 4.5	C3: 57 barrer C4: 10 barrer	[54]
2000	AgBF ₄ , AgCF ₃ SO ₃	Poly(2-ethyl-2-oxazoline), poly(<i>N</i> -vinyl pyrrolidone)	C3: 15 000 (55)	C3: 45 GPU	[1,3]
2000	AgBF ₄	Poly(vinyl methyl ketone)	C2: (250) C3: (100)	— —	[20]
2001	AgClO ₄	Poly(2-ethyl-2-oxazoline)	C2: (103.4)	C2: 0.3 GPU	[16]
2001	AgBF ₄	Polyacrylamide	C3: > 104 (170)	C3: 10.4 GPU	[15]
2001	AgBF ₄	Cellulose acetate	C2: (270)	—	[22]
2001	Cu(1,3-butadiene) OTF	Cellulose acetate	C2: (11) C3: (13)	— —	[24]
2001	AgBF ₄	Poly(<i>N</i> -vinyl pyrrolidone) + phthalates	C3: (150)	C3: (10) GPU	[55,56]
2002	AgSbF ₆	Crosslinked poly(vinyl alcohol)	C3: (125)	C3: (4.2) GPU	[17]
2002	AgCF ₃ SO ₃	Poly(<i>n</i> -butyl methacrylate)	C3: 140	C3: 9.0 barrer	[21]
2002	AgBF ₄	Nylon-12/tetramethylene oxide block copolymer	C3: (30)	C2: (20) GPU	[14]

^aData given in parentheses represent mixed-gas systems.

AgCF₃SO₃. Other experimental data for facilitated olefin transport through membranes containing different carriers are summarized in Table 16.4.

The improved separation permeance may arise predominantly from the high concentration of the silver ion, and the fast reversible complexation reaction between the silver ion and the olefin molecule.

16.4.2 Oxygen/Nitrogen Separation

A representative example of facilitated oxygen transport through the PBMA/CoPIIm membrane is provided in Figure 16.19 [5]. The oxygen permeability is significantly larger than the nitrogen permeability and steeply increases with decreasing oxygen pressure. On the other hand, the nitrogen permeability is very small and independent of the upstream pressure. The membrane without CoPIIm exhibits small oxygen permeability, inde-

pendent of oxygen pressure. The oxygen permeability is ca. 8.7 barrer and its ideal separation factor over nitrogen is ca. 4.3 at 70 mmHg. The temperature effect on transport properties was investigated through the POMIm membrane containing CoS, depending on the upstream gas pressure, as shown in Figure 16.20 [6]. The permeability improved markedly with temperature and maintained its general trend, except at 25 °C. The dependency of oxygen permeability on upstream pressure is rather enhanced at higher temperatures. Other experimental data for facilitated oxygen transport through solid-state membranes containing different oxygen carriers are summarized in Table 16.5.

16.5 Membrane Stability

Despite the high separation performance of facilitated transport membranes in the solid state, a pending question for industrial applications is the

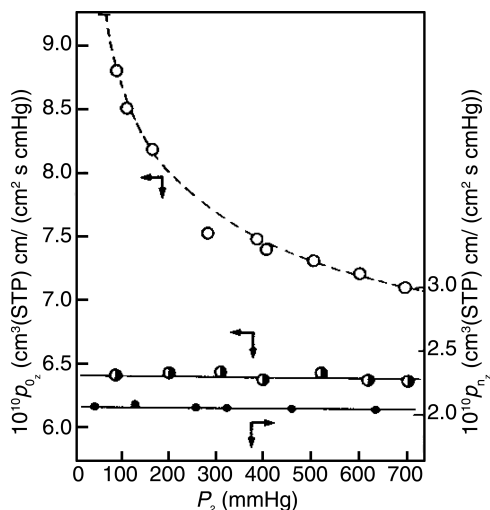


Figure 16.19 Effect of upstream pressure on oxygen (○) and nitrogen (●) permeabilities in the PBMA membrane containing 2.5 wt% CoPIIm and oxygen permeability (○) in the membrane without CoPIIm [5]. Reprinted with permission from H. Nishide, M. Ohyanagi, O. Okada and E. Tsuchida, *Macromolecules*, **19**, 494 (1986). Copyright (1986) American Chemical Society

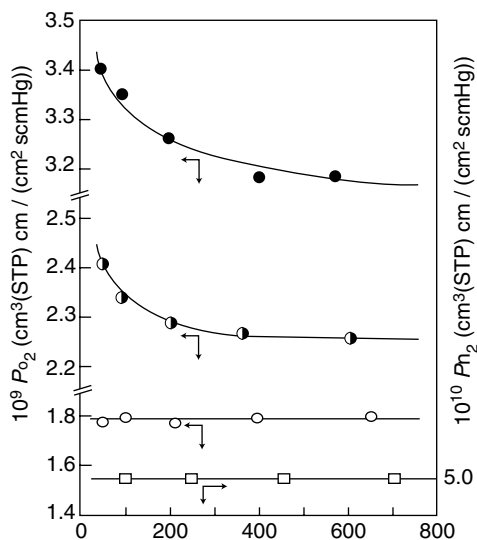


Figure 16.20 Effect of temperature on permeability for the POMIm/CoS membrane, with oxygen at: (○) 25 °C; (●) 35 °C; (●) 45 °C; (□) nitrogen at 25 °C: [CoS] = 0.6 wt % [6]. Reprinted with permission from E. Tsuchida, H. Nishide, M. Ohyanagi and H. Kawakami, *Macromolecules*, **20**, 1907 (1987). Copyright (1987) American Chemical Society

stabilization of the metal ion carrier. They frequently suffer from a lack of long-term stability because the metal ion is either reduced to form metallic nanoparticles or oxidized to lose its carrier activity. For example, the reduction of silver ions to silver metallic nanoparticles and the irreversible formation of oxygen-bridged metal dimers are believed to be responsible for the carrier deactivation in facilitated olefin and oxygen transport membranes, respectively.

Solid polymer electrolyte membranes, consisting of a propylene oxide/allylglycidylether copolymer and $AgBF_4$, were subjected to a 40-day permeation test with a dry mixture of 70/30 ethylene/ethane at a feed pressure of 50 psig and a permeate pressure of 0 psig [2]. The normalized gas permeances of ethylene and ethane are shown in Figure 16.21. The separation performance remained excellent although the permeance and selectivity marginally decreased continuously with time.

Similarly, polymer electrolyte membranes consisting of $AgBF_4$ dissolved in POZ or PVP con-

taining amide groups also show a continuous decrease in separation performance [55,56]. This is possibly due to the reduction of silver ions to silver metal nanoparticles during the separation process, because PEO, POZ or PVP, used as polymer solvents in the solid polymer electrolytes, also play roles as reducing agents for the silver salts [62,63]. However it has been reported that such reduction was mostly prevented by introducing phthalates, as shown in Figure 16.22 [55,56]. The stability enhancement seems to be attributed to the fact that the silver ions are more strongly coordinated by the two ester groups of phthalates by forming chelating bonds, and consequently the reduction reaction is effectively hindered.

Studies on the lifetimes of facilitated oxygen transport membranes has also been carried out [7,29]. The absorbance ratios, A_t/A_0 , representing the oxygen binding capability of CoP were measured for POFIm/CoP and POMIm/CoP membranes within the first 21 days after preparation. They decreased with time, possibly due to the irreversible oxidation of CoP [29].

Table 16.5 Summary of oxygen permeability and its selectivity over nitrogen in solid-state facilitated transport membranes

Year	Carrier ^a	Polymer	Selectivity, P_{O_2}/P_{N_2}	Permeability, P_{O_2} (barrer)	Reference
1986	CoMP	Poly(butyl methacrylate) (PBMA)	3.2–12	6–14	[5,40]
1987	CoS	Poly[octyl methacrylate- <i>co</i> - (4-vinylpyridine)] (POMPy) Poly[octyl methacrylate- <i>co</i> - (1-vinylimidazole)] (POMIm)	3.5–15	13.7–29.5 16–34	[6]
1987	CoPIIm	Poly(butyl methacrylate) (PBMA)	5.7–12	12–23	[6]
1988	CoP	Polydimethyl siloxane (PDMS) Poly(butyl methacrylate) (PBMA) Poly(methyl methacrylate) (PMMA)	5–12	730–800 8.7–11.3 0.6–0.92	[42]
1990	CoTPP	Poly[octyl methacrylate- <i>co</i> - (1-vinylimidazole)] (POMIm)	6.1–12	15–40	[8,39]
1990	CoS	Styrene–butadiene–styrene	3.4	23.4	[57]
1991	CoMPP	Poly [butyl methacrylate- <i>co</i> - (1-vinylimidazole)] (PBMIm) Poly [octyl methacrylate- <i>co</i> - (1-vinylimidazole)] (POMIm) Poly [lauryl methacrylate- <i>co</i> - (1-vinylimidazole)] (PLMIm)	2.9–5.9 2.8–4.5 2.3–3.0	10.5–18.5 18–25 51–63	[38]
1991	Co3	Styrene–butadiene–styrene	2.94	62	[58]
1992	CoP	Poly[(alkyl methacrylate)- <i>co</i> - (1-vinylimidazole)]/ poly(1-trimethylsilyl-1-propyne) blend	2.9–4.5	782–1450	[59]
1995	Co(acetate) ₂	Poly(vinyl alcohol)/poly (<i>N</i> -salicylidene allyl amine) blend	2.19–8.50	215–228	[60]
1997	Co(SalPr)	Polycarbonate	5–7	1–2	[61]
1998	CoS, CoST	Polydimethylsiloxane (PDMS) Ethyl cellulose (EC)	2.1–2.3 3.4–4.1	580–605 10–14.5	[32]
2000	CoTPP	Ethyl cellulose (EC)	4.0–4.4	10.7–12.4	[30]

^aCoP, [$\alpha, \alpha', \alpha'', \alpha'''$ -*meso*-tetrakis(*o*-pivalamidophenyl)porphinato]cobalt; CoPIIm, [$\alpha, \alpha', \alpha'', \alpha'''$ -*meso*-tetrakis(*o*-pivalamidophenyl)porphinato]cobalt 1-methylimidazole; CoMP, [$\alpha, \alpha', \alpha'', \alpha'''$ -*meso*-tetrakis(*o*-methacrylamidophenyl porphinato)]cobalt; CoMPP, [α -mono(*o*-methacrylamidophenyl)- α, α, α -tris(*o*-pivalamidophenyl) porphinato]cobalt; CoTPP, [*meso*-tetrakis(substituted phenyl) porphyrin]cobalt; CoS, [*N,N'*-disalicylideneethylenediamine]cobalt; CoST, [di-(3-methoxysalicyl) *tert*-butylamine]cobalt; Co(SalPr), [*N,N'*-bis(salicylideneimino)di-*n*-propylamine]cobalt; Co3, [*N,N'*-ethylene-bis(3-methyl-7-phenylsalicylidendiminato)]cobalt.

16.6 Conclusions

In this chapter, recent researches and developments on solid-state facilitated transport membranes of polymer–metal complexes are described. Polymer–metal complex membranes have been demonstrated to be promising candidates for separation of both olefin/paraffin and oxygen/nitrogen mixtures. We hope that this review will be of some help in providing insight into facilitated transport phenomena in the solid state, the molecular structures of polymer–metal

complexes and reducing the current limitations of membrane technology for practical applications.

Despite the high separation performance of facilitated transport membranes in the solid state, a pending question for industrial applications is stabilization of the metal ion carrier. They frequently suffer from a lack of long-term stability because the metal ion is either reduced to form nanometal particles in polymer electrolyte membranes [55,56] or are irreversibly oxidized by the formation of oxygen-bridged

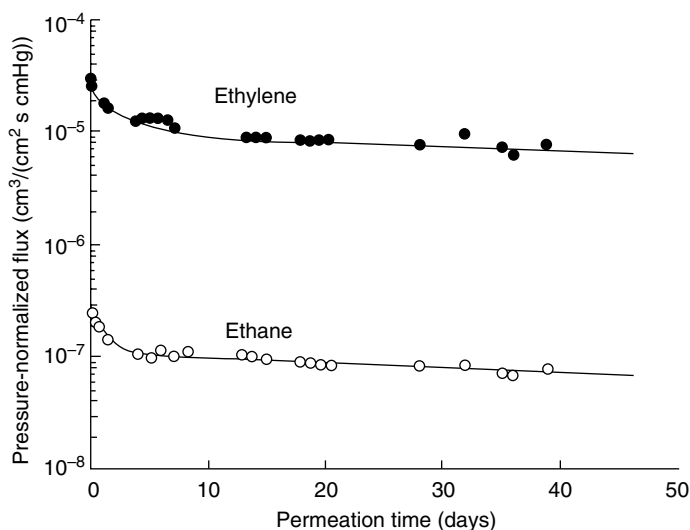


Figure 16.21 Gas permeance data for a propylene oxide/allyl glycidyl ether copolymer electrolyte membrane containing AgBF_4 with a 70/30 ethylene/ethane mixture [2]

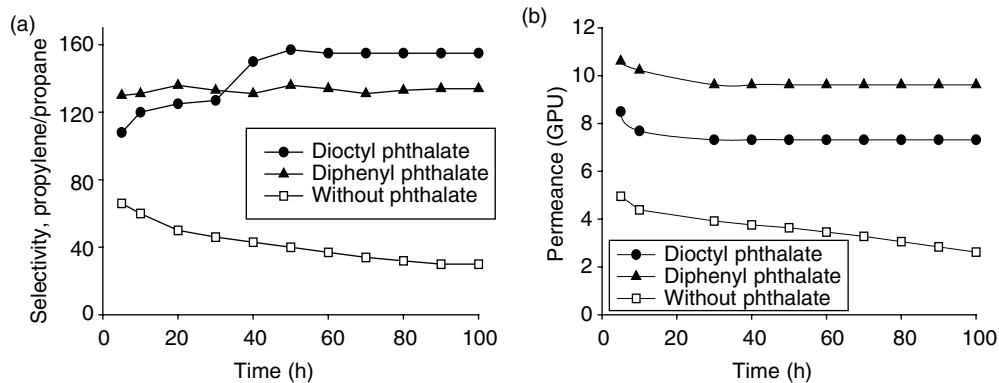


Figure 16.22 Mixed gas selectivity (a) and permeance (b) of PVP/ AgBF_4 membranes, with and without phthalate, as a function of time [55,56]

metal dimers [29]. Deterioration of the carrier activity may also seriously occur in the presence of sulfur compounds and acetylene, which should be, thus, properly treated for practical applications.

References

- [1] S. U. Hong, J. H. Jin, J. Won and Y. S. Kang, *Adv. Mater.*, **12**, 968 (2000).
- [2] I. Pinnau, L. G. Toy and C. Casillas, *US Patent 5 670 051* (1997).
- [3] J. H. Kim, B. R. Min, C. K. Kim, J. Won and Y. S. Kang, *Macromolecules*, **35**, 5250 (2002).
- [4] R. L. Burns and W. J. Koros, *J. Membr. Sci.*, **211**, 299 (2003).
- [5] H. Nishide, M. Ohyanagi, O. Okada and E. Tsuchida, *Macromolecules*, **19**, 494 (1986).
- [6] E. Tsuchida, H. Nishide, M. Ohyanagi and H. Kawakami, *Macromolecules*, **20**, 1907 (1987).

- [7] H. Nishide, H. Kawakami, Y. Sasame, K. Ishiwata and E. Tsuchida, *J. Polym. Sci., Part A: Polym. Chem. Ed.*, **30**, 77 (1992).
- [8] H. Nishide, T. Suzuki, H. Kawakami and E. Tsuchida, *J. Phys. Chem.*, **98**, 5084 (1994).
- [9] L. M. Robeson, *J. Membr. Sci.*, **62**, 165 (1991).
- [10] S. Sunderrajan, B. D. Freeman, C. K. Hall and I. Pinnau, *J. Membr. Sci.*, **182**, 1 (2001).
- [11] I. Pinnau and L. G. Toy, *J. Membr. Sci.*, **184**, 39 (2001).
- [12] Y. Yoon, J. Won and Y. S. Kang, *Macromolecules*, **33**, 3185 (2000).
- [13] S. U. Hong, C. K. Kim and Y. S. Kang, *Macromolecules*, **33**, 7918 (2000).
- [14] A. Morisato, Z. He, I. Pinnau and T. C. Merkel, *Desalination*, **347**, 351 (2002).
- [15] Y. S. Park, J. Won and Y. S. Kang, *J. Membr. Sci.*, **183**, 163 (2001).
- [16] J. H. Kim, B. R. Min, C. J. Kim, J. Won and Y. S. Kang, *Macromolecules*, **34**, 6502 (2001).
- [17] J. H. Kim, B. R. Min, K. B. Lee, J. Won and Y. S. Kang, *J. Chem. Soc., Chem. Commun.*, 2732 (2002).
- [18] T. C. Merkel, Z. He, A. Morisato and I. Pinnau, *J. Chem. Soc., Chem. Commun.*, 1596 (2003).
- [19] J. H. Kim, B. R. Min, J. Won and Y. S. Kang, *Chem. Eur. J.*, **8**, 650 (2002).
- [20] H. S. Kim, J. H. Ryu, H. Kim, B. S. Ahn and Y. S. Kang, *J. Chem. Soc., Chem. Commun.*, 1261 (2000).
- [21] K. J. Lee, J. Y. Jho, J. Won and Y. S. Kang, *Macromol., Rapid Commun.*, **23**, 839 (2002).
- [22] J. H. Ryu, H. Lee, Y. J. Kim, Y. S. Kang and H. S. Kim, *Chem. Eur. J.*, **7**, 1525 (2001).
- [23] J. Müller, K.-V. Peinemann and J. Müller, *Desalination*, **145**, 339 (2002).
- [24] H. S. Kim, Y. J. Kim, J. J. Kim, S. D. Lee, Y. S. Kang and C. S. Chin, *Chem. Mater.*, **13**, 1720 (2001).
- [25] H. Nishide, T. Suzuki, R. Nakagawa and E. Tsuchida, *J. Am. Chem. Soc.*, **116**, 4503 (1994).
- [26] T. Suzuki, H. Yasuda, H. Nishide, X. Chen and E. Tsuchida, *J. Membr. Sci.*, **112**, 155 (1996).
- [27] H. Nishide, Y. Tsukahara and E. Tsuchida, *J. Phys. Chem., B*, **102**, 8766 (1998).
- [28] Y. Suzuki, H. Nishide and E. Tsuchida, *Macromolecules*, **33**, 2530 (2000).
- [29] S. Rössli, E. Pretsch, W. E. Morf, E. Tsuchida and H. Nishide, *Anal. Chim. Acta*, **338**, 119 (1997).
- [30] J. Yang and P. Huang, *Chem. Mater.*, **12**, 2693 (2000).
- [31] J. Yang and P. Huang, *J. Appl. Polym. Sci.*, **77**, 484 (2000).
- [32] Y. He, J. Yang, H. Li and P. Huang, *Polymer*, **39**, 3393 (1998).
- [33] C. K. Kim, J. Won, H. S. Kim, Y. S. Kang, H. G. Li and C. K. Kim, *J. Comput. Chem.*, **22**, 827 (2001).
- [34] J. H. Jin, S. U. Hong, J. Won and Y. S. Kang, *Macromolecules*, **33**, 4932 (2000).
- [35] J. Y. Kim, S. U. Hong, J. Won and Y. S. Kang, *Macromolecules*, **33**, 3161 (2000).
- [36] H. Nishide, H. Kawakami, S. Toda, E. Tsuchida and Y. Kamiya, *Macromolecules*, **24**, 5851 (1991).
- [37] K. Tanaka, A. Taguchi, J. Hao, H. Kita and K. Okamoto, *J. Membr. Sci.*, **121**, 197 (1996).
- [38] H. Nishide, H. Kawakami, T. Suzuki, Y. Azechi, Y. Soejima and E. Tsuchida, *Macromolecules*, **24**, 6306 (1991).
- [39] H. Nishide, H. Kawakami, T. Suzuki, Y. Azechi and E. Tsuchida, *Macromolecules*, **23**, 3714 (1990).
- [40] H. Nishide, M. Ohyanagi, O. Okada and E. Tsuchida, *Macromolecules*, **20**, 417 (1987).
- [41] C. K. Kim, H. S. Kim, J. Won, Y. S. Kang, C. K. Kim and C. K. Kim, *J. Phys. Chem. A*, **105**, 9024 (2001).
- [42] M. Ohyangai, H. Nishide, K. Suenaga and E. Tsuchida, *Macromolecules*, **21**, 1590 (1988).
- [43] R. D. Noble, *J. Membr. Sci.*, **50**, 207 (1990).
- [44] D. R. Smith and J. A. Quinn, *AIChE J.*, **25**, 197 (1979).
- [45] E. L. Cussler, R. Aris and A. Bhowan, *J. Membr. Sci.*, **43**, 149 (1989).
- [46] J. W. Cahn, *J. Chem. Phys.*, **42**, 93 (1965).
- [47] Y. S. Kang, J. M. Hong, U. Y. Kim, J. Jang, *J. Membr. Sci.*, **109**, 149 (1996).
- [48] S. U. Hong, J. Won, H. C. Park and Y. S. Kang, *J. Membr. Sci.*, **163**, 103 (1999).
- [49] J. Crank and G. S. Park, *Diffusion in Polymers*, Academic Press, p. 46 (1968).
- [50] D. W. van Krevelen, *Properties of Polymers*, Elsevier, Amsterdam, The Netherlands (1990).
- [51] J. S. Yang and G. H. Hsue, *J. Membr. Sci.*, **120**, 69 (1996).
- [52] A. Sungpet, J. D. Way, P. M. Thoen and J. R. Dorgan, *J. Membr. Sci.*, **136**, 111 (1997).
- [53] S. Bai, S. Sridhar and A. A. Khan, *J. Membr. Sci.*, **147**, 131 (1998).
- [54] S. Bai, S. Sridhar and A. A. Khan, *J. Membr. Sci.*, **174**, 67 (2000).
- [55] B. Jose, J. H. Ryu, B. G. Lee, H. Lee, Y. S. Kang and H. S. Kim, *J. Chem. Soc., Chem. Commun.*, 2046 (2001).
- [56] B. Jose, J. H. Ryu, Y. J. Kim, H. Kim, Y. S. Kang, S. D. Lee and H. S. Kim, *Chem. Mater.*, **14**, 2134 (2002).
- [57] J. M. Yang and G. H. Hsue, *J. Appl. Polym. Sci.*, **41**, 1141 (1990).

- [58] G. H. Hsiue and J. M. Yang, *Macromolecules*, **24**, 4010 (1991).
- [59] H. Nishide, H. Kawakami, Y. Sasame, K. Ishiwata and E. Tsuchida, *J. Polym. Sci., Part A: Polym. Chem. Ed.*, **30**, 77 (1992).
- [60] C. K. Park, M. J. Choi and Y. M. Lee, *J. Appl. Polym. Sci.*, **66**, 483 (1997).
- [61] R. C. Ruaan, S. H. Chen and J. Y. Lai, *J. Memb. Sci.*, **135**, 9 (1997).
- [62] P. Y. Silvert, R. Herrera-Urbina and K. Tekaia-Elhsissen, *J. Mater. Chem.*, **6**, 573 (1996).
- [63] H. H. Huang, X. P. Ni, G. L. Loy, C. H. Chew, K. L. Tan, F. C. Loh, J. F. Deng and G. Q. Xu, *Langmuir* **12**, 909 (1996).

Review of Facilitated Transport Membranes

Richard D. Noble and Carl A. Koval

17.1 Introduction

There have been previous review articles and book chapters on the topic of facilitated transport (FT) membranes [1–3]. The reader should refer to the previous reviews to gain a longer term perspective, if needed.

A good starting point for a discussion of facilitated transport is a general description of this process and its relationship to other types of membranes. Solution–diffusion is the typical solute transport mechanism in a dense, non-porous polymer or liquid membrane. The solute partitions into the membrane from the feed phase and diffuses across the membrane due to a concentration gradient. Facilitated transport membranes operate based on solute partitioning (solubility) and diffusion but also include a reversible complexation reaction as a component of the membrane separation.

The complexation reaction in the membrane creates an additional transport mechanism that is synergistic with the solution–diffusion mechanism. Facilitated transport is analogous to a chemical absorption process on the feed (high-partial-pressure) side and a stripping process on the product, or permeate, side of the membrane. After the solute dissolves in the membrane, it can diffuse or react with the complexing agent. Solute diffusion across the facilitated transport membrane can take place by two mechanisms: (a) diffusion of the uncomplexed species or (b) diffusion of the carrier–solute complex. The

selectivity and reversibility of the complexation reaction is critical for the separation performance of facilitated transport membranes. To be selective, the reactive transport mechanism should not interact with other solutes in the feed phase.

The total solute flux is the sum of the flux of the carrier–solute complex and the uncomplexed solute (see Figure 17.1(a)). In this figure, the flux value associated with line ‘a’ is the contribution from solution–diffusion. The vertical distance between lines ‘a’ and ‘b’ for a given driving force (ΔP) represents the contribution due to facilitation. In the limit of fast reaction to diffusion time, the diffusion rate controls the mass transfer, while the reaction rate is controlling when the complexation reaction is slow compared to diffusion. In between these two limiting regimes, the contributions of both reaction and diffusion are important. A method to calculate which regime is controlling will be presented later.

The carrier–solute reaction mechanism is the reason that the flux of facilitated transport membranes is not always linearly proportional to the concentration driving force across the membrane (Figures 17.1). At very high driving forces, all of the carrier species are bound to solute molecules and an increase in driving force does not result in an increased flux from the reactive pathway. Under these conditions (carrier saturation), the carrier cannot provide any additional facilitation effect. The flux is linearly proportional to the

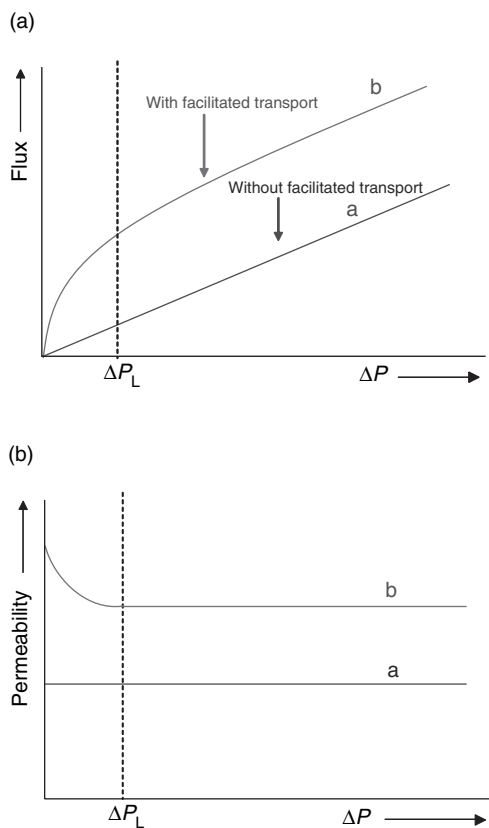


Figure 17.1 (a) Resulting flux versus driving force plot and (b) resulting permeability

driving force since the primary contribution to the flux is transport of unbound solute by diffusion. At very low driving force conditions, the flux due to the solution–diffusion pathway is very small, and the majority of the transport is due to diffusion of the carrier–solute complex. As the driving force decreases further, the flux of the uncomplexed solute molecules decreases much faster than the carrier-based transport. Therefore, the flux is not linearly proportional to the driving force under these conditions. ΔP_L represents the approximate upper limit on the driving force where one would observe a facilitation effect.

The bond energy for the solute and carrier interaction for the reversible reaction must fall within a certain range to be effective [4]. If the binding energy is too weak, very little solute is transported by this reactive pathway; if the binding is too strong, the solute cannot be removed

effectively at the downstream side of the membrane. In either extreme, the use of the reactive pathway for increased flux and selectivity is inefficient [5].

Facilitated transport membranes have several general characteristics:

- (1) They can be highly selective, especially at low driving forces where other separation methods are not.
- (2) Very high permeabilities compared to conventional membranes can be obtained for the solute of interest at very low concentration driving forces (Figure 17.1(b)).
- (3) A minimum permeability is reached at high concentration driving forces due to saturation of the reactive transport pathway (Figure 17.1(b)).
- (4) The amount of solvent used is very small in comparison with conventional solvent extraction separation approaches for liquid membranes.
- (5) The quantity of complexing agent used is also very small in comparison with other techniques. This allows the use of a wide range of complexation chemistry that would not be feasible to implement otherwise.
- (6) Membrane technology allows for continuous separation. However, it can be used ‘on demand’ since it is very simple to implement.
- (7) Membrane technology is easily scaled for various applications. In particular, it is very cost-effective for small-scale applications.
- (8) The use of a chemical reaction provides enhanced solute flux as well as selectivity. This translates to less surface area required for a given application in comparison to conventional membrane systems.
- (9) They are often unstable in the conventional immobilized liquid membrane configuration due to evaporation and/or solvent displacement.

17.2 Experimental Methods

The typical approach is to perform diffusion ‘time lag’ experiments using a diaphragm cell consisting of two (top and bottom) compartments separated by the membrane (Figure 17.2).

The top compartment is initially evacuated, but the lower one is filled with the feed components.

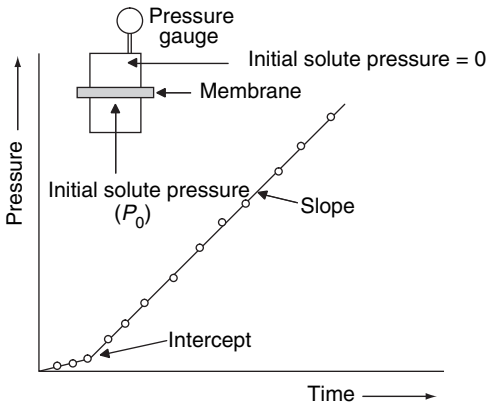


Figure 17.2 Schematic of a diaphragm cell for gas-diffusion 'time-lag' experiments

The pressure in the upper compartment is measured as a function of time. The pressure in the lower compartment is p_0 . Initially, the pressure in the upper compartment varies in a complex way, but it will eventually approach that in the lower compartment. At moderate times, the pressure in the upper compartment is linearly proportional to time, with a known slope and a definite intercept (time lag). The analysis of this data for simple permeation through a homogeneous film is [6]:

$$p = (ARTp_0/Vl)[Hdt - (Hl^2/6)] \quad (17.1)$$

where V and p are the volume and pressure of the upper compartment, respectively, and l and A are, respectively, the thickness and cross-sectional area of the membrane; H is the Henry's law coefficient and D is the diffusion coefficient. The first quantity on the right-hand side of Equation 17.1 in brackets is known experimentally. The intercept (time lag), t_L , on the time axis is then determined by setting the terms in the second bracketed group equal to each other:

$$t_L = l^2/6D \quad (17.2)$$

The slope of the linear portion of the pressure vs. time curve is related to the effective permeability HD ; D is known from the intercept. The slope

then gives values of the Henry's law coefficient H , that is, it is related to the solubility of the feed component in the membrane.

For facilitated transport experiments, these measurements are used to obtain the flux across the membrane. The measurements for each membrane and gas feed are used to obtain the steady-state flux as a function of the feed pressure. These experiments are done for each component individually and for mixtures. The results can then be analyzed as described below.

17.3 Modeling

The performance of a facilitated transport membrane process is dependent upon a number of system properties which determine the solute mass transfer rates to and through the membrane. The important variables are listed below for the simplest case of 1:1 binding for solute and carrier:

- k = mass transfer coefficient based on concentration driving force
- D_A = solute diffusion coefficient
- D_{AB} = diffusion coefficient of solute + carrier complex
- k_f, k_r = forward and reverse rate coefficients, respectively, of a 1:1 complexation reaction
- C_{A0} = concentration of gas in the liquid membrane at feed interface
- C_T = total concentration of carrier
- l = effective membrane thickness (includes tortuosity)

These physical properties can be combined into a number of dimensionless groups. These dimensionless variables have physical significance and are presented below. The various terms in these dimensionless variables can be independently measured or estimated. The use of dimensionless variables provides a basis for determining some relationships between system properties and performance:

- F = facilitation factor = (solute flux with carrier present)/(solute diffusion flux)
- ε = inverse Damköhler number ($D_{AB}/k_r l^2$), ratio of characteristic reverse reaction to diffusion times
- K = dimensionless reaction equilibrium constant ($k_f C_{A0}/k_r$)

- α = mobility ratio, ratio of carrier to solute mobility ($D_{AB}C_T/D_A C_{A0}$)
- Sh = Sherwood number for solute mass transfer (kl/D_A)

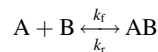
The facilitation factor, F , is the ratio of the total solute flux with the carrier present to the solute diffusional flux. In Figure 17.1(a), this is the ratio of the value on line 'b' to the value on line 'a' for a given ΔP . This can be viewed as a measure of increased solute productivity and selectivity for multi-component feed mixtures. In addition, multiplying the solute diffusion coefficient by F gives an effective 'overall' diffusion coefficient. A mobility ratio, α , can be defined for the reactive versus the diffusive pathway. K is a dimensionless equilibrium constant, while ε is the inverse of a Damköhler number and is a measure of the characteristic reverse reaction time to the characteristic diffusion time; this serves the same function as a Thiele modulus in catalysis. The Sherwood number, Sh , includes the effect of external mass transfer resistance which is a measure of external boundary layer resistance to the diffusional resistance of the membrane.

As noted above, an 'overall' diffusion coefficient can be obtained by multiplying the solute diffusion coefficient by the facilitation factor, F . In this way, standard design equations for membrane systems can be used with this correction [7]. It is important to note that F will vary with the solute feed concentration. So, if the feed concentration is changing along the membrane/feed interface (in hollow fiber modules, for example), the value of F needs to be adjusted accordingly [8,9]. Metayer *et al.* [10] reported a theoretical description of facilitated transport inside an ion-exchange membrane and in a tubular membrane system. A two-dimensional convective-diffusion model in coaxial systems is developed. Experimental data on the transport through Nafion 120 and Nafion 811X membranes facilitated by alanine (Ala) and phenylalanine (Phe) amino acids are examined with the help of the model developed. Li [11] formulated a model predicting the gas separation performance of a hollow-fiber module with facilitated transport membrane. The influence of feed rate, operation pressure and permeant-feed flow pattern on the module performance are analyzed and the effect of the non-uniform distribution of the reaction equilibrium constant is examined. The calculated

results show that a non-uniform active distribution may cause an improved module performance.

The symbol α is used here to represent two different quantities. When this symbol is used, it will refer to the mobility ratio described above. When the symbol α_{ij} is used, it will refer to the separation factor or selectivity of a membrane and is defined as the ratio of the permeability of species i divided by the permeability of species j . For example, the symbol $\alpha_{O_2-N_2}$ is the separation factor of oxygen over nitrogen.

Most modeling and analysis of facilitated transport systems has used the following one-step reaction mechanism:



where A is the solute being transported, B is the carrier and AB is the solute-carrier complex.

Analytical solutions for the facilitation factor under diffusion-limited (small ε) and reaction-limited (large ε) regimes have been derived [12]. Normally, it is best to operate in the diffusion-limited regime where the carrier pathway is fully utilized. The solution for the diffusion-limited regime, when the permeate solute concentration is negligible and the diffusion coefficients of species B and AB are assumed to be equal, is:

$$F = 1 + \frac{\alpha K}{1 + K} \quad (17.3)$$

The range of the analytical solution can be extended by assuming a large excess of carrier ($C_T \approx C_B$ throughout the membrane) [13] The differential equations for solute transport across the membrane can then be linearized and the result is:

$$F = \frac{1 + \left(\frac{\alpha K}{1 + K}\right)}{1 + \left(\frac{\alpha K}{1 + K}\right) \left(\frac{\tanh \lambda}{\lambda}\right)} \quad (17.4)$$

where:

$$\lambda = \frac{1}{2} \sqrt{\frac{1 + (\alpha + 1)K}{\varepsilon(1 + K)}} \quad (17.5)$$

The solution has the proper behavior in both the diffusion-limited and reaction-limited regimes. Of course, by assuming an excess of carrier, this solution does not display the leveling of performance as the carrier is saturated (see Figure 17.1).

Recently, Al-Marzouqi *et al.* developed an analytical solution that allows for arbitrary diffusion coefficients of all species and non-zero permeate solute concentration [14]. They showed that their model has the proper behavior to predict the facilitation factor over the entire range of K where the Smith and Quinn model does not match well for large values of K . The maximum facilitation factor occurs at higher values of K as the ratio of the permeate-complex over carrier diffusivity (D_{AB}/D_B) is reduced, whereas the maximum facilitation factor occurs at the same value of K for all values of D_A/D_B (ratio of the permeate over carrier diffusivity). A similar behavior is seen for the flux of A as a function of K . The facilitation factor remains constant with changes in the film thickness, whereas the flux of A reduces with an increase in the thickness of the film. A linear increase of the facilitation factor and flux of A are seen with increasing C_T .

Teramoto [15] developed an improved approximate solution of the facilitation factors for the above case of 1:1 complexation. It was confirmed that the facilitation factors calculated by the approximate method agreed with the results which had been obtained previously by numerical integration of the governing differential equations over the entire range from the diffusion to reaction-limited cases, as well as both equal and unequal carrier and complex diffusivities and also for the case of non-zero downstream permeate concentration. Furthermore, the behavior of the concentration profiles in the membrane could be explained by this analysis.

Teremoto [16] extended his approximate analytical solution for the facilitation factor by using the facilitated transport of CO_2 transport through a liquid membrane containing a primary or secondary amine as examples. The solution was developed for the case where a reversible reaction ($\text{A} (\text{CO}_2) + 2\text{B} (\text{amine}) \rightleftharpoons \text{E} (\text{carbamate}) + \text{F} (\text{protonated amine})$) occurs in the membrane, and the reaction rate is expressed by $k_f(C_A C_B - (C_E C_F / K_{\text{eq}} C_B)) / (1 + (K' / C_B))$. In this approximate method, separate constant

concentrations of the carrier B and the protonated amine F are assumed at the two boundaries of the membrane for evaluating the influx and outflux of the permeant species, and these concentrations are determined so that these fluxes agree with each other at the steady state. The facilitation factors calculated by this method agree with the results obtained previously by numerical integration of the governing differential equations. Calculated results for the system-parameter dependence of the facilitation factor are also presented.

Equation (17.4) can be further extended to incorporate external mass transfer effects by including a Sherwood number (Sh) [17]:

$$F = \frac{\left[1 + \left(\frac{\alpha K}{1+K}\right)\right] \left(1 + \frac{2}{Sh}\right)}{\left[1 + \left(\frac{\alpha K}{1+K}\right) \frac{\tanh \lambda}{\lambda}\right] + \left[1 + \left(\frac{\alpha K}{1+K}\right)\right] \left(\frac{2}{Sh}\right)} \quad (17.6)$$

As the external mass transfer resistance decreases, Sh becomes larger. In the limit $Sh \rightarrow \infty$, Equation (17.6) reduces to Equation (17.4). Juang *et al.* considered aqueous film diffusion, interfacial chemical reaction and membrane diffusion in a model [18]. The transport rates of lactic and citric acids from binary solutions across supported liquid membranes containing tri-*n*-octylamine were measured and compared to the model. They proposed a rationale for the differences between the experimental and modeling results.

The above results can be used in the following ways [7]. By comparing Equations (17.3) and (17.4), the value of $(\tanh \lambda)/\lambda$ is a measure of the facilitation in the absence of external mass transfer resistance ($Sh \rightarrow \infty$). A simple and quick calculation of this one term can provide an estimate of the facilitation effect:

$$\begin{array}{ll} \frac{\tanh \lambda}{\lambda} \rightarrow 0 & \text{maximum facilitation} \\ \frac{\tanh \lambda}{\lambda} \rightarrow 1 & \text{minimum facilitation} \end{array}$$

A rearrangement of Equation (17.6) can be used to analyze the results of transport experiments and estimate some system properties [7].

Assuming reaction equilibrium ($(\tanh \lambda)/\lambda \rightarrow 0$), Equation (17.6) can be rearranged as:

$$(F - 1)^{-1} = E^{-1} = \left(1 + \frac{2}{Sh}\right)\alpha^{-1} + \left[\left(\frac{2}{Sh}\right)\left(1 + \frac{1}{\alpha K}\right) + \frac{1}{\alpha K}\right] \quad (17.7)$$

where α^{-1} is directly proportional to the solute feed concentration (C_{AO}). A plot of E^{-1} versus C_{AO} can be constructed for the experimental results. The experimental results shown in Figure 17.1(a) can be used to generate this plot if the permeate solute pressure (i.e. permeate solute concentration) is negligible. As C_{AO} is reduced, the plot should be linear and Equation (17.7) is valid. For the straight line portion of the curve, the slope and intercept can be used to estimate two unknown quantities if all other properties have been independently measured or estimated. Typically, the two unknown quantities are Sh and D_{AB} .

Equation (17.6) can be used to quickly and easily estimate F . Properties such as membrane thickness l or carrier concentration C_T can be varied to predict their effect on performance.

The governing differential equations for facilitated transport, based on the one-step reaction, have been solved numerically [5]. The optimal values of K and F for a given ε and α were determined. The results showed that the optimal value of K ranged from 1 to 10 for orders of magnitude changes in ε and α . Al-Marzouqi *et al.* [14] showed a very similar result using their more general model. This result has several useful features and allows one to determine an optimal property set. Thus, the set of physical and chemical properties which will result in the maximum facilitation effect can be determined. This result forms the basis for the uses discussed below.

The above results are very useful for screening potential carriers. The narrow range of optimal values for K provides a rapid method of selecting good carriers. A single measurement (equilibrium constant) combined with the solute feed concentration yields K . Therefore, using literature values and/or measurements, a number of candidate carriers can be quickly evaluated. Those carriers for which K falls in or near the optimal range can be used for facilitated transport systems. The other

carriers can be eliminated before any transport experiments are started.

The range for optimal K can be used as the basis for modifying carriers. If K is too large or too small, this indicates the direction needed to modify the rate constants for the reversible reaction. This can be useful information to the synthetic chemist. Carrier modifications can be chosen to attempt to move toward the optimal range for K .

The optimal range of solute feed concentration can be estimated for a given carrier (equilibrium constant). The optimal values of K can be divided by the equilibrium constant to obtain the optimal range of feed concentrations in the membrane.

This analysis has been extended to multiple-step complexation reactions [19]. The results show that this same range of $1 < K < 10$ holds for each step in multiple step reactions where one complexing agent can bind more than one solute molecule.

One valuable use of the above factor is in comparison of actual to optimal performance. This comparison can be used to estimate if large improvements are possible in system performance. For a given set of experimental results, the actual values of the dimensionless numbers can be calculated and compared to the optimal values.

17.4 Membrane Configurations

There are three general configurations for facilitated transport membranes: an immobilized liquid film, a solvent-swollen polymer and a solid polymer film containing reactive functional groups (a fixed-site carrier membrane). Emulsion liquid membranes and hollow-fiber-contained liquid membranes have been discussed as separate topics in a previous review [20] and will not be further discussed here.

The stability of facilitated transport membranes is a very important issue that will ultimately determine whether this technology is used for large-scale gas separations [21]. Instability can result from the complexation chemistry, the support configuration or both. For example, the solvent can be lost from the membrane, destroying the membrane integrity. To alleviate this, the solvent concentration in the feed and permeate gas streams could be perfectly controlled and the liquid membrane itself would be stable, but if

the carrier is lost or deactivated, the selectivity is also lost. Three methods to address the stability problems with facilitated transport membranes are the use of fixed-site carrier membranes, hollow-fiber-contained liquid membranes and the use of molten salts with negligible vapor pressure as solvents.

An immobilized liquid membrane (ILM) is usually prepared by impregnating the pore structure of a very thin, microporous support with a solution of the carrier in a solvent or even a pure carrier if it is a liquid. Typical thicknesses range from 5 to 25 μm , which is one to two orders of magnitude thicker than the dense skin layer of an asymmetric polymer membrane. However, liquid phase diffusivities are of the order of 10^{-6} to 10^{-5} cm^2/s , much larger than diffusivities in glassy polymers (10^{-8} cm^2/s). Therefore, fluxes for ILMs and polymer membranes are often comparable. The carrier solution is held in place by capillary forces and the solvent concentration of the feed and/or permeate gases must be carefully controlled to avoid drying out the membrane or condensing solvent on the membrane surface [22]. The ILM is generally considered to be the least stable configuration due to solvent evaporation and/or displacement due to pressure differences across the membrane.

A facilitated transport membrane structure that is intermediate between the liquid and solid phases can be made by swelling a polymer film in a solvent and introducing the carrier species by diffusion, or by ion-exchange in the case of ionomer membranes [23,24]. If the solvent used to swell the polymer film is a good physical solvent for the gas of interest, solvent swollen polymer films can be used as gas separation membranes without a carrier species present [25]. Ion-exchange membranes have several unique advantages as supports for facilitated transport membranes. Once the charged carrier species is exchanged into the membrane, the carrier cannot be removed from the membrane unless it is replaced by another ion. This is quite unlikely in a gas separation application. Secondly, the carrier loading in an ion-exchange membrane is determined by the ion-exchange site density, not the solubility of the carrier in the solvent. Consequently, the local carrier concentration obtained in heterogeneous materials such as perfluorosulfonic acid ionomers can be very high. Way *et al.* [24] reported that local carrier concentrations of up to

8 M were obtained when using perfluorosulfonic acid ionomer membranes as supports for ethylenediamine cations. Solvent-swollen polymer membranes are intermediate in stability between ILMs and fixed carrier membranes. If solvent is lost, the membrane typically becomes a barrier to transport and there is not any 'short-circuiting'. The carrier remains in place due to electrostatic forces. The membrane can be resolvated and the initial performance can be recovered.

In order to improve the stability of facilitated transport membranes, complexation agents have been attached to polymer chains and membranes have been made from these reactive polymer materials. This configuration, known as *fixed-site carrier* or *chained-carrier* membranes, have the potential to be highly selective and stable. Solid facilitated transport membranes containing reactive sites selective for acid gases, oxygen and nitrogen have been reported [26–29]. These studies provide some evidence that facilitated diffusion can occur in the solid state.

A theory for fixed site carrier membranes has been developed [30–32]. Solute molecules can migrate between complexing agent molecules by moving along the polymer chain. The result is an expression that is analogous to Equation (17.4). In the limit as $(\tanh \lambda)/\lambda$ approaches zero, Equation (17.4) approaches Equation (17.3). The latter equation is analogous to the dual-mode sorption model that has been used to describe gas transport in glassy polymers. Using the analysis based on Equation (17.7), the effective diffusion coefficient D_{AB} (effective mobility of this pathway) can be determined. Literature data for O_2 transport in fixed carrier membranes was used to support the theory.

Cussler *et al.* [33] proposed a theory for fixed site carrier membranes based on the chained-carrier or 'Tarzan swing' mechanism. Two complexing agents must be close enough to each other to 'pass off' a solute molecule. The distance between the carrier molecules increases as the carrier concentration decreases. At some concentration, a percolation threshold is reached. The distance becomes too large for the 'pass off' and the solute flux precipitously decreases. The existence of a percolation threshold is an important component of this model. Equations for the diffusion- and reaction-limited cases were derived and shown to have the same form as normal facilitated transport.

A model for facilitated mass transport with a fixed site carrier membrane was recently derived by assuming an instantaneous, microscopic concentration (activity) fluctuation in the membrane [34]. The concentration fluctuation, developed due to the reversible chemical reaction between carrier and solute, could cause the higher chemical potential gradient and facilitated transport. The fluctuating concentration profile was assumed to be sinusoidal, which is analogous to an alternating voltage in an electrical circuit. An analogy was employed between mass transfer for facilitated transport with a fixed site carrier membrane and the electron transfer in a single parallel resistor–capacitor (RC) circuit. The model showed that the facilitation factor, F , increased linearly with the extent of the pressure fluctuation, $\alpha_p (= P_d/P_o)$, the ratio of the time scales of diffusion to chemical reaction, $\Psi (= k_r t^2/D)$, and the ratio of the total carrier concentration to the solute solubility in the membrane, $\gamma (= C_T/C_{AO})$. F also increased logarithmically with one plus the combined driving force for facilitation, $(\Delta (= KP_o))$, i.e. $(1 + \Delta)$. The model was examined against experimental data on oxygen transport in dimethylsiloxane, poly(butyl methacrylate) and poly(methyl methacrylate) with a metallo-porphyrin carrier and the agreement was very good compared to the dual sorption model. In an extension of this model [35], a series of parallel RC circuits was employed instead of the single RC circuit to account for the four diffusion pathways, including solute transfer between the membrane and carrier. This extension showed a better agreement than the single circuit model but the difference was minor (see also Chapter 16).

17.5 Hybrid Processes

Modeling of synergistic facilitated transport membrane–distillation separation processes has been conducted. Moganti *et al.* [36] developed two design methods to minimize the number of trays in a distillation column that contains a membrane unit: the minimum area method and the Smoker's equation method. The Smoker's equation method is used to study the effect of different membrane variables on the tray number. The optimal position of the membrane on the distillation column is close to the feed to the column. An analytical expression is given for a special case by

using the minimum area method. Simulations showed that each method was equally valid. The minimum area method was expanded by Stephan *et al.* [37] to provide some guidelines and general rules which can be applied to distillation/membrane hybrid processes. Both new column design and augmentation of an existing distillation column by a membrane module are discussed. Pettersen *et al.* [38] used propene/propane separation as a representative case to evaluate three cases: the membrane at the top of the column, bottom or along the column. If the membrane is placed parallel to the column, the optimal position for the membrane is close to the feed tray, which represents a potential 'pinch-point' in the column. The optimal membrane 'cut rate' for this configuration is generally close to the mole fraction of propene in the membrane feed stream. Comparison of system performance indicated that placing the membrane in parallel or at the bottom of the column gives the best performance, both in terms of compressor duty and installed membrane area.

Hybrid processes have also been used for non-facilitated separation and recovery of gases. Agrawal *et al.* [39] showed that one could use a hybrid process for hydrogen purification. The cold box from a fluidized catalytic cracker process is operated at a much higher temperature and the non-condensate is passed through a membrane to produce permeate hydrogen as a product and non-permeate is recycled to the cold box. Argon separation from oxygen [40] in a cryogenic distillation system is enhanced with the use of an oxygen-selective membrane. The distillate from the column is sent to the membrane. The retentate from the membrane is the final argon product and the permeate is recycled to the column. Nitrogen can also be recovered in cryogenic distillation systems through the use of a hybrid process [41].

17.6 Additional Driving Forces

The application of an external force field can provide an additional driving force for the separation. When the force field also provides a means for concentration of the solute, this is called *active transport*. This latter has two important components: (1) a complexing agent (binding site) in the membrane that can selectively bind and release the solute of interest and (2) an energy

source (gradient) that interacts with the complexing agent. This gradient provides the driving force to transport the solute across the membrane and, in some cases, to ‘pump’ the solute uphill against the concentration gradient. Thus, the result is a separation as well as concentration of the desired solute.

17.7 Methods for Implementation of Active Transport

Figure 17.3 illustrates the various energy sources and reaction mechanisms that can be used to implement active transport. For metal ion separation and concentration, Figure 17.3(a) illustrates a reversible interfacial reaction that is used in conjunction with a pH gradient to generate the counter transport of the metal ion (M^{n+}) and protons (H^+); C is an ion-exchange complexing agent. At the feed interface, the metal ions are partitioned into the membrane due to the interfacial reaction and protons are released into the feed phase at high pH. The complex diffuses to the receiving (permeate) side where the reverse reaction takes place at low pH. The large pH gradient provides the energy to separate and concentrate the metal ions in the receiving phase. The absolute values of the pH needed on each side of the membrane are a function of the ion-exchange complexing agent used [42].

This same approach of competitive transport can be used with a concentration gradient. The

complexing agent can react with both solutes. The counter transport of one solute provides the gradient to ‘pump’ the second solute uphill against its concentration gradient [43,44]. Figure 17.3(b) shows how a homogeneous reaction within the membrane is combined with redox reactions at each electrode to separate and concentrate an electrically neutral (i.e. gases and vapors) molecule (A) from a feed phase. At the feed/membrane interface, the electrode reaction converts the oxidation state of the complexing agent (B) from a low affinity binding state (B_L) to a high binding affinity state (B_H) [45,46]. Component A partitions into the membrane and forms the complex AB_H due to the high binding affinity of the complexing agent. This complex diffuses across the membrane where the reverse redox reaction occurs. The complexing agent is converted to the low-binding affinity state. This results in the release of A and its concentration in the receiving phase.

An electric field can also be used to induce convection in the membrane, eliminating any diffusional resistance to transport [47–49].

The use of a photon field is shown in Figure 17.3(c). The ‘switch’ of the complexing agent from a high- to low-binding-affinity state is accomplished in two possible manners. A photon of the appropriate energy level can excite electrons participating in the binding of A to B [50]. This provides the energy to break the bond and release A. Alternatively, some complexing

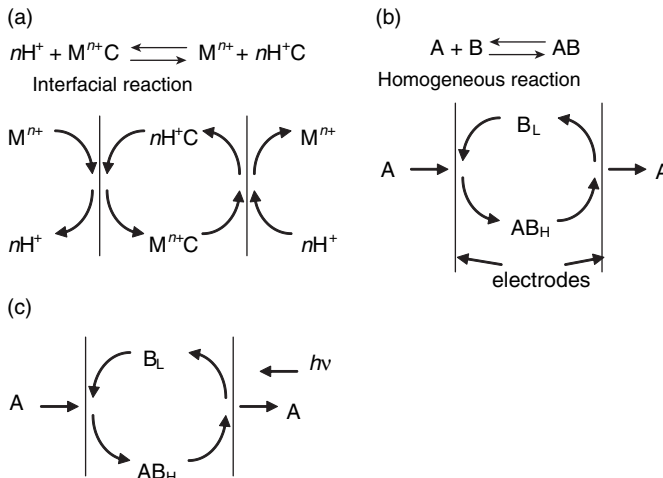


Figure 17.3 Active transport mechanisms: (a) pH gradient; (b) electric field; (c) photon field

agents undergo a conformational change in response to light. The change opens or closes access to the binding site [51].

Xu *et al.* [52] investigated alkali metal ion extraction from an aqueous solution to an organic phase and the ion transport across a liquid membrane facilitated by anthracene end-labeled oligoxyethylenes and their photodimers. The ion-extraction equilibrium constants for the photodimers are 10–100 times greater than those for the monomeric form. The non-cyclic monomers are also able to act as carriers to facilitate transport of alkali metal ions across an organic liquid membrane with moderate efficiency. Alternate irradiation of the membrane in contact with the source phase with light ($\lambda > 300\text{ nm}$) and that in contact with the receiving phase with light ($\lambda < 300\text{ nm}$) resulted in an increase of ion transport selectivity and 6–10 times enhancement of the transport rate. These observations are interpreted in terms of the photoinduced interconversion between the dimeric and monomeric forms which are responsible for ion complexation and ion release in the overall transport process, respectively. These authors reported that the stable complex, which may rapidly extract an ion into the membrane phase, cannot release the ion efficiently from the complex. The electric and photon fields can be applied as needed to provide a membrane ‘switch’ with on–off capability.

Modeling has been extended to account for active transport. Noble [53] determined the optimal equilibrium constants for maximizing the active transport for interfacial reactions.

Cussler [54] used a simplified analysis which describes this effect for the competitive transport of two solutes. Using the assumptions of equal diffusion coefficients for all components and a reaction equilibrium within the membrane, he developed an analytical solution for the solute flux. The solution contains three terms: solute diffusion, facilitated solute transport and a term to account for the effect of the second solute on the transport of the first solute. It is this last term that supplies the energy to ‘pump’ the first solute uphill. The magnitude of the last term to the other terms provides a measure of the competitive effect.

Niiya and Noble [43] studied the competitive effect for both transient and steady-state conditions. They demonstrated that a solute could be ‘pumped uphill’. In addition, they pointed out

that solute ‘1’ would have a competitive advantage over solute ‘2’ if the binding and release rate of solute ‘1’ were greater than that of solute ‘2’. Some comparison with the literature data gave very good results. Way and Noble [44] have published experimental data on the competitive transport of CO_2 and H_2S through ion-exchange membranes with ethylenediamine as the carrier. They used a numerical model based on Niiya and Noble and found very good agreement between model predictions and experimental results. Dindi *et al.* [55] developed an analytical solution for competitive transport with no adjustable parameters.

Recently, a model for ‘photofacilitation’ and ‘photopumping’ in liquid membranes, which is general yet conceptually and mathematically simple, has been reported [56–58]. This model incorporates a thorough treatment of the interaction of light with the carrier and carrier–solute complex. This model is a significant improvement over previous mathematical treatments of this topic in several respects. The photochemistry is described by a change of the complexing agent from a strong to a weak binding form (or vice versa). Each form of the complexing agent can then reversibly bind with the solute of interest. The kinetics and equilibrium constant for each form would be different. Previous models only included a light-dependent kinetic term in the complexation reaction. In addition, this model uses a Beer’s law relationship to describe the variation of light intensity across the membrane, while previous models used a step change in light intensity (on–off) at a given position in the membrane. Under the proper conditions, ‘photofacilitated’ liquid membranes should maintain solute transport against a solute concentration gradient greater than a factor of five; this ‘photopumping’ is very sensitive to light intensity.

Goyette *et al.* [59] used a photoactive crown ether carrier to ‘photofacilitate’ the transport of sodium ions across a liquid membrane. They showed that the sodium flux was five to seven times larger under illumination when compared to the dark condition. Their results were in qualitative agreement with the Longin model.

Athayde and Ivory [60] developed a model on the use of a DC or alternating electric field for active transport of an ionic carrier within a membrane. Their results showed that one could ‘pump’ uphill under the proper set of conditions.

A previous experimental and modeling study on this topic [46] used membrane contactors and this configuration was modeled.

Heat transfer can also affect facilitated transport. Kemp and Noble [61] demonstrated that a temperature gradient across the membrane can cause a significant increase or decrease in the facilitation effect. In extreme cases, the flux direction can be reversed. Rockman *et al.* [62] formulated a model that depicts thermally enhanced facilitated transport (TEFT) under the combined framework of liquid–liquid extraction (LLX) and facilitated transport (FT). Assuming negligible mutual miscibility between the solute and the solvent, an analytical solution is presented with simulations of TEFT of citric acid by a tertiary amine. Simulations are compared with experimental data. These simulations confirm the existence of an optimal operating temperature that coincides with that obtained experimentally, without the need of any parameter fitting. Selegny *et al.* [63,64] also developed models to account for thermal effects in facilitated transport. The non-isothermal facilitated transport of CO₂ through a cross-linked sulfonated polystyrene grafted onto a polyethylene membrane cation exchanger (Permion 5010) containing ethylenediamine was studied experimentally and tested with a theoretical model based on the Nernst–Planck flux equation, with good agreement. Discussions also took into account measurements at different temperatures of isothermal passive and facilitated transports, membrane condition and corresponding Arrhenius plots, the stability constant of the permeant–carrier complex determined with a new technique and of heat of reaction (ΔH) obtained from Van't Hoff plots. Steady-state fluxes of carbon dioxide were measured at different temperature gradients (ΔT) and partial pressures in mixtures with N₂. A permeability of 7.4×10^{-7} mmol (cm s atm) was obtained for a ΔT of 8 K around 295 K at a steady state flux of 4×10^{-7} mmol (cm s) for 1% CO₂ in the mixture. Facilitation factors, as well as thermal gradient amplification factors, are presented. It is concluded that the effect of the thermal gradient on the flux is mediated by the modification of the concentration gradient inside the membrane. Stimulation or hindering is dependent on the sign of ΔH and of the orientation of ΔT relative to the gradient of partial pressure.

17.8 Novel Liquid Phases – Ionic Liquids

Recent research has focused on room-temperature ionic liquids (ILs) as novel, benign solvent replacements for volatile organic compounds traditionally used in organic synthesis [65,66] and liquid/liquid separations [67–72], including liquid membranes [73]. The cations of many ionic liquids contain a ring structure with one or more alkyl groups, which can be modified to adjust the solution properties. The anion structure is also available for modification. ILs combine into one solvent system a number of unique properties. ILs have high thermal stability, high ionic conductivity, negligible vapor pressure and are non-flammable. Unlike traditional organic media, the properties of ILs may be adjusted via chemical alteration of the cation or anion to produce ‘application-specific’ compounds. The potential exists for complexing agents to be one of the ions giving a maximum loading of a complexing agent in the solvent, much greater than the loadings typical in standard solvent systems. Complexing agents can also be added or ‘doped’ into the IL.

Large, asymmetric, organic cations and various anions make up the ILs (Figure 17.4), thereby creating non-volatile, non-flammable liquids, capable of solubilizing a variety of solutes. These ionic solvents consist entirely of ions, strongly resembling ionic melts obtained by heating metallic salts such as NaCl to high temperatures, but are liquid at much lower temperatures. Many ILs are liquids over a wide temperature range, with some known melting points as low as -96°C and some liquid ranges in excess of 300°C . High coulombic forces constrain the IL constituents and thus, the ILs exert practically no vapor pressure above the liquid surface. These features have led to current investigations of ILs as alternative media for a variety of applications which use organic solvents.

Initial studies on ILs have indicated that the combination of subtle (e.g. changing cation substitution patterns) and gross (e.g. changing anion type) modifications can permit very precise tuning of the IL solvent properties. Changes in density, viscosity, melting point and solvation properties are possible in this way, thus enabling the rational design of ‘application-specific’ ILs. In addition to ‘fine-tuning’ solvent properties, virtually unexplored is the potential for preparing ILs with structural or functional features that

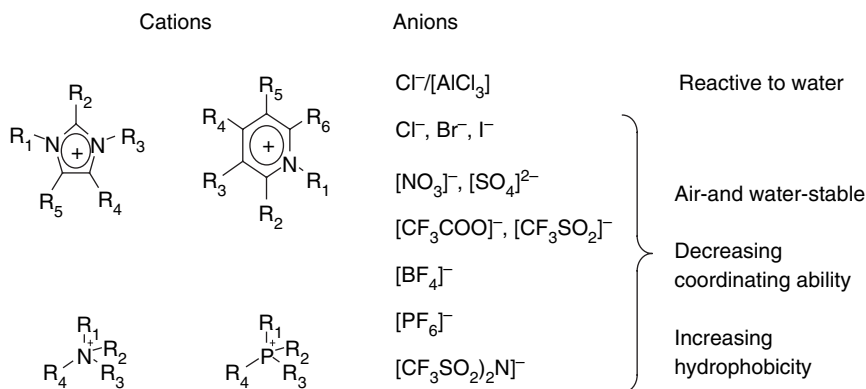


Figure 17.4 Typical ionic liquid cations and anions

might provide the resulting IL with ‘task-specific’ properties. The concept of ‘task-specific’ ILs (TSILs) has been demonstrated with the reported synthesis of an amine containing ILs for acid gas scrubbing and the preparation/utilization of ILs with good capacities to extract heavy metals from water in biphasic IL/water systems [70,74].

In addition to all of the above properties, a large subset of ILs exhibit liquid crystallinity [75–77]. The liquid crystalline phases can be either neat (thermotropic) or in solution (lyotropic). In these phases, they are oriented in supramolecular arrays, with remarkable mesophase stability.

Camper *et al.* [78] recently demonstrated that ‘Regular Solution Theory’ could be used to predict the solubility of gases in ionic liquids. Extensions to account for temperature and pressure effects were also provided.

17.9 Novel Liquid Phases – Electrohydrodynamic Fluids

Nematic liquid crystals (NLCs) are liquids characterized by long-range ordering of the long axes of their rod-shaped molecules. NLCs, by virtue of their fluidity and intrinsic anisotropy, exhibit dramatic electrohydrodynamic effects at low applied electric fields. *N*-(4-methoxybenzylidene)-4-butylaniline (MBBA) is a typical liquid crystal having negative dielectric anisotropy. In the absence of an applied field, it is ‘at rest’ and gas transport across this membrane material is limited by molecular diffusion. When an electric

field is applied, charge accumulates at the walls (defects) that are perpendicular to the electrodes. Forces due to the interaction of the electric field with the space charge at the wall tend to shear the sample. When the direction of the electric field is alternating, the walls are always charged in the alternating direction of the LC director. An AC field of approximately 100 V/mm produces fully developed turbulent flow. This chaotic flow disorders the NLC, generating ‘disinclinations’ in the molecular orientation field which strongly scatter light, producing the so-called ‘dynamic scattering’ LC electro-optic effect. The disinclination lines generated by electrohydrodynamic flow can be observed optically. The lines form parallel to the flow velocity, indicating the flow of the NLC perpendicular to the electrodes and back and forth between them. In this application, electrohydrodynamic flow mixes the LC layer, convecting dissolved species across the LC layer and forming an eddy-diffusion process, thereby enhancing its apparent permeability. Ambient temperature is used since this is just in the range of the nematic phase. The ability to increase the gas permeability by a factor of 50 for the liquid crystal phase has been demonstrated [47,48]. The permeability of the barrier film on the electrode limited the permeation rate.

As an alternative to the use of NLC solvents, polar solvents, such as 2-ethyl-hexanol (2EH), diethyl phthalate (DEP), *N*-methyl-2-pyrrolidone (NMP) and propylene carbonate, are electroconvective liquid membrane candidates. They are much cheaper than MBBA, more stable

chemically in air and could replace the liquid crystal. The price of the liquid crystal is about two orders of magnitude higher than that of ordinary solvents. MBBA has a very polar C=N bond between the two phenyl rings forming its core. 'Free charges' can cause dissociation at the phenyl-phenyl linkage. In addition, if water is present, some of these molecules are always dissociated into H_3O^+ and OH^- which can hydrogen-bond with this polar core and cause the molecule to break. Consequently, moisture in the feed gas stream can cause degradation.

An electrohydrodynamic solvent essentially must be an electrically insulating liquid. The conductivity of polar solvents is primarily due to electrolytic impurities. A deionization procedure has been developed to decrease the conductivity of the polar solvents below $10^{-10} \text{ ohm}^{-1} \text{ cm}^{-1}$ so they would exhibit convective motion in this approach. The observed threshold voltages for electrohydrodynamic motion were compared to threshold voltages using electrohydrodynamic instability criteria. The observed threshold voltages were two orders of magnitude lower than the predicted values [49].

The requirements for this electrohydrodynamic and chemically stable liquid phase are: (1) it must be electroconvective—the conductivity and dielectric constant must be reduced to the proper range, (2) it must be stable in air – the selectivity for separation should be as high as possible – measurement of the partition of various feed components can determine this factor, and (3) it must be compatible with the barrier film between the fluid and the electrodes and/or the electrode material itself.

There are also requirements for the electrodes themselves. Porous metals that are coated with a barrier film to prevent the loss of the fluid phase through the electrodes work well for initial screening tests [47,48]. An important materials development for this configuration, as well as others, using an electric field is a dense flexible film that is conductive. Recently, flexible polymer electrolyte films that have the mechanical properties of solids and processibility of liquids have been fabricated [79]. These materials are based on low-molecular-weight poly(ethylene oxide) (PEO), lithium salts and fumed silica. The silica and the electrolyte form separate phases, effectively decoupling the mechanical and conductive properties of the film.

17.10 Incorporation of the Complexing Agent into the Membrane

There are two basic approaches to incorporate complexation chemistry into the membrane. The first is to add the complexing agent as a dopant to the membrane matrix, while the second is to covalently bind the complexing agent to the membrane matrix. This second approach has two embodiments. Attached to the mobile membrane material, such as the solvent phase, the agent can move by diffusivity. Otherwise, attached to the immobile membrane materials, such as a cross-linked structure, the complexing agent will act as a fixed site carrier membrane.

17.11 Unsaturated Hydrocarbons

17.11.1 Scope of Research

During the 1980s and early 1990s, several groups reported selective olefin/paraffin separations based on membranes containing Ag(I) in a variety of forms. During the past ten years, this has remained a very active area of FT membrane research. Some sense of the scope of this research can be obtained by listing the range of hydrocarbon solutes (Table 17.1) and membrane materials (Table 17.2) that have been examined.

Many of the publications listed in these tables report permeabilities or permeability coefficients and separation factors for olefin/paraffin separations; a few representative examples are included below. For ethene/ethane separations, Teramoto *et al.* [84] reported a permeability of $4 \times 10^{-5} \text{ mol m}^{-2} \text{ s}^{-1} \text{ kPa}^{-1}$ with a selectivity of 1100 using a bulk-flow aqueous silver nitrate membrane. Pinnau and Toy [82] obtained a permeability of $8 \times 10^{-6} \text{ cm}^3 \text{ cm}^{-2} \text{ s}^{-1} \text{ cmHg}^{-1}$

Table 17.1 Range of hydrocarbon solutes that have been examined

Solutes examined	Representative publication(s)
Ethene/ethane	[80–84]
Propene/propane	[82,83,85–87]
Butene(s)/butane	[88–90]
Pentene(s)/pentane	[91]
Hexene(s)/hexane	[92,93]
Stryene/ethylbenzene	[94]
Benzene/cyclohexane	[94,95]
Olefin isomers	[96]

Table 17.2 Range of membrane materials that have been examined

Membrane material	Representative publication(s)
Poly(vinyl alcohol)	[88,95,97,98]
Poly [(1-trimethylsilyl)-1-propyne]-g-poly(acrylic acid)	[89]
Polyethylene-g-poly(acrylic acid)	[99]
Poly(acrylamide)	[86]
Poly(butyl methacrylate)	[87]
Polypyrrole	[80,92,100]
Poly(2-acrylamido-2-methyl-1-proprionic sulfonic acid)	[94]
Perfluorinated ionomer (Nafion)	[101]
Sulfonated divinylbenzene–styrene	[93,102,103]
Cellulose acetate	[83]
Polysulfone and poly(ether ether ketone)	[91]
Polymer electrolytes	[82,85,104]
Cation-exchange gels	[81]
Glycerol	[90]
Amino acids (polymer matrix)	[105]
Water	[84]

and a selectivity of 240 for ethene/ethane using a solid polymer electrolyte membrane. Park *et al.* [86] used a polyacrylamide/AgBF₄ composite-membrane for propene/propane separation and obtained a selectivity > 100 with a propene permeance of $10^{-5} \times \text{cm}^3 \text{cm}^{-2} \text{s}^{-1} \text{cmHg}^{-1}$. For butene/butane separation, Kovvali *et al.* [90] used a glycerol-based immobilized liquid membrane and achieved selectivities as high as 842 with a 1-butene permeance of $7 \times 10^{-7} \text{cm}^3 \text{cm}^{-2} \text{s}^{-1} \text{cmHg}^{-1}$.

17.11.2 Mechanistic Studies

While FT is nearly always invoked to explain at least a portion of the performance, a number of studies have attempted to address a variety of mechanistic aspects. By analyzing fluxes measured for Nafion films of varying thicknesses, Rabago *et al.* were able to show that the unusually high selectivities observed for 1,5-hexadiene vs. 1-hexene were due to parallel transport pathways [101]. One pathway showed the usual inverse relationship to membrane thickness, while the other pathway was thickness-independent. In addition, for Ag(i)-containing perfluorinated ionomer membranes, Kohls *et al.* measured fluxes and relative selectivities for a wide varieties of C-6 mono- and dienes [96]. The presence of terminal double bonds and larger distances between the double bonds led to higher fluxes.

17.11.3 Membrane Morphology

A number of attempts have been made to correlate some aspect of membrane morphology with separation performance. Manley *et al.* performed small-angle X-ray scattering (SAXS) studies on Nafion materials with equivalent weights ranging from 1100 to 1500 g/mol sites [106]. The data indicated that the ionic cluster sizes in the materials were similar in size even though the higher equivalent-weight materials absorb substantially less water and exhibit lower olefin fluxes. However, the amount of olefin absorbed per Ag(i) ion is nearly the same for all of the materials, as are the observed selectivities. Goering *et al.* performed SAXS analysis on Ag(i) Neosepta membranes (sulfonated divinylbenzene–styrene polymer) and found that, like Nafion, there were ca. 10 nm hydrophilic regions [102]. They also compared the ability of Nafion and Neosepta membranes for 1,5-hexadiene/1-hexene separations.

17.11.4 Olefin–Ag(i) Complexation

Several different types of spectroscopy have been used to investigate both the incorporation of Ag(i) into the membrane materials and the complexation of olefins to Ag(i). Yang and Hsiue used IR and NMR spectroscopy to examine the reaction of Ag(i) with the carboxylic acid groups in poly (acrylic acid) membranes [107]. They determined

that the coordination numbers for Ag(i) with olefins were always one, and they also studied the kinetics of olefin binding. For several membrane types, selective transport of diolefins with respect to monoolefins has been observed, causing speculation that Ag(i)-diolefin-Ag(i) complexes are formed. However, comparison of absorption of 1,5-hexadiene and 1-hexene into silver nitrate solutions indicated that both olefins only form 1:1 complexes with Ag(i) [93].

In several types of membranes, vibrational spectroscopy has been used to investigate the role of donor atoms that interact with Ag(i) and their effect on subsequent olefin complexation: poly(butyl methacrylate) membranes [87], poly(2-ethyl-2-oxazoline), poly(*N*-vinylpyrrolidone) membranes [104] and cellulose acetate membranes [83].

17.11.5 Effect of Water on Performance

One of the major problems with Ag(i)-containing membrane materials is the requirement for the membranes to remain hydrated in order to achieve high fluxes and selectivities. Several types of materials have been investigated, with the goal of reducing or eliminated this dependency.

One approach developed by Way's group involves preparing materials that are blends of ionically conductive polymers (e.g. Nafion) with electronically conductive polymers, such as polypyrrole [80,92,100]. When the composite membranes are in the Na(i)-form, they exhibit olefin permeabilities that are much lower than the analogous Nafion membranes. However, in the Ag(i)-form the membranes exhibited facilitation factors for olefin transport of 3.62, 12.4 and 18.1 for cyclohexene, 1,5-hexadiene and 1-hexene, respectively. The fluxes were stable for periods of days, even though the feed phases contained no water. Based on molecular orbital calculations, these authors postulated that simultaneous complexation of olefin, Ag(i) and polypyrrole allowed for FT in the absence of water.

A very promising approach to developing water-free Ag(i) based FT membranes has been through the incorporation of Ag(i) salts into membranes composed of polymer electrolytes. The membranes are prepared by dissolving Ag(i) salts into materials, such as poly(2-ethyl-2-oxazo-

line) (POZ), poly(vinyl pyrrolidone) (PVP) and poly(ethylene oxide) (PEO), and casting thin (ca. 1 μm) films onto asymmetric microporous substrates [82,85,108]. A rubbery nylon-12/tetramethylene oxide block copolymer has also been used [109]. The main advantages of these materials is that very high Ag(i) concentrations can be obtained and that facilitated transport occurs in the absence of hydration [110]. Very high selectivities have been observed for a variety of olefin-paraffin separations.

A number of studies have been directed to understanding the factors that influence the performance of silver ion-polymer electrolyte membranes:

- (1) The polymer microstructure does not appear to have a major effect on the FT of propylene in that POZ and PVP behave similarly with equal amounts of a silver salt. The main function of the polymer electrolyte is the interactions between the carbonyl oxygen atoms and the silver salt [111,112].
- (2) The performance of silver ion-polymer electrolyte membranes deteriorates at temperatures above 70 °C due to, or in the presence of UV light, on account of the reduction of Ag(i) to silver metal [113].
- (3) The specific type of carbonyl oxygen (e.g. amide, ketone or ester) contained in the polymeric material has a significant effect on the threshold concentration of Ag(i) required for facilitated oxygen transport [114].
- (4) The nature of the anion comprising the silver salt has a dramatic effect on the observed FT effects. Large relatively hydrophobic anions, such as BF_4^- , ClO_4^- and CF_3SO_3^- , allow a greater degree of olefin complexation than smaller more hydrophilic anions, such as NO_3^- [108,115].
- (5) The interaction of Ag(i) with the polymer and with their anions can be manipulated favorably through the addition other components such as amino acids [105,114].
- (6) The amount of silver salt dissolved in the polymer electrolyte effects the coordination number of the Ag(i) ions. Higher amounts of silver salts results in more vacant coordination sites which enhances olefin complexation [115]. FT is mostly associated with Ag(i) ions that are weakly coordinated to carbonyl oxygen atoms and olefins.

- (7) In certain materials, high selectivity is due, at least in part, to diminished paraffin solubility which results at high silver salt concentrations [116].

17.11.6 Other Complexing Agents

Cu(II) trifluoromethanesulfonate (CuOTf) has been shown to reversibly coordinate with unsaturated hydrocarbons under certain conditions. Suzuki *et al.* [117] showed that CuOTf formed a series of water-soluble complexes with vinyl sulfonate anions. These complexes also coordinated olefins such as ethylene, 1-butene and 1,3-butadiene [117]. Kim *et al.* incorporated the Cu(1,3-butadiene)-OTf complex into cellulose acetate membranes and demonstrated subsequent FT of propylene and ethylene [118].

17.12 Gas Separations

For some gas separations, the solution-diffusion mechanism that normally dictates performance of dense polymer membranes does not provide adequate selectivity. In these cases, FT membranes are an attractive alternative. The literature in this area is dominated by attempts to develop selective membranes for oxygen/nitrogen separations and for the separation of carbon dioxide from nitrogen, methane and hydrogen.

17.12.1 Oxygen/Nitrogen Separations

Research in this area was reviewed (62 references) by Mulder's group in Twente in 2001 [119]. The review explains why neither polymer nor FT membranes have been used commercially to produce oxygen in excess of 50–60 vol% from air. For polymer membranes, it has not been possible to exceed the 'upper bound' determined by the trade-off between selectivity and permeability. 'Table 4' of this review [119] contains a summary of oxygen permeability and O₂/N₂ selectivity values for FT membranes. The permeabilities range from 1–1000 barrer, while the selectivities range from 2.3 to 50. However, FT membranes, especially those involving mobile carriers, exhibit poor stability, usually due to irreversible oxidation of the carrier. A large portion of this review describes attempt to overcome these drawbacks through the fabrication of micro-encapsulated membranes. Suitable oxygen car-

riers are encapsulated in a solvent and capsules are dispersed in a polymer matrix to produce a membrane. Calculations indicated that high O₂/N₂ selectivities could be achieved for capsules in polymers such as PEO.

Since the 'Mulder review', there have been several reports on oxygen FT membranes. Bernal *et al.* reported selectivities of 2.44 for O₂/CH₄ and 2.75 for O₂/N₂ using an alumina-zeolyte composite membrane containing the organometallic carrier IrCl(CO)(PPh₃)₂ [120]. Using a 'soap-free' polymerization technique, Wang *et al.* immobilized Co(II) in rubbery copolymers and achieved oxygen/nitrogen permeabilities/selectivities that were above the upper bound in a Robeson plot [121]. Co(II) complexes were generated *in situ* in a silicone rubber polymer by Zhang *et al.*; the membranes exhibited a permeability for O₂ of 800 barrer and a selectivity of 3.34 [122]. A series of five Co porphyrins were immobilized in ethylcellulose membranes and the transport properties were correlated with the effects of porphyrin substituents and axial ligands on oxygen binding [123].

Chen *et al.* prepared a liquid membrane containing bovine Hb as an oxygen carrier and oxygen permeation through the membrane was measured by electrochemical reduction of the permeated oxygen [124]. The oxygen permeation was facilitated, as analyzed by a dual-mode model, to give permeation parameters of the membranes such as the diffusion coefficient (D_{Hb}) of the mobile carrier Hb and the solution-diffusion coefficient of oxygen (D_{O_2}). The facilitated permeation was the product of the Hb concentration, $[Hb]_0$ and D_{Hb} in the membrane solution. D_{Hb} decreased with $[Hb]_0$ or the solution viscosity; the maximum oxygen permeability ($6.2 \times 10^{-8} \text{ cm}^3(\text{STP}) \text{ cm}^{-2} \text{ s}^{-1} \text{ cm Hg}^{-1}$, at a feed stream oxygen pressure of 0.54 cmHg) was observed at $[Hb]_0 = 12.8 \text{ g dl}^{-1}$, where the facilitation factor and the oxygen/nitrogen permselectivity were approximately 10 and 18, respectively.

The most successful and well-studied strategy to date for producing stable O₂/N₂ FT membranes is the fixed-site carrier approach, which has been studied extensively by Nishide and coworkers [125–134]. In many of these studies, the so-called 'picket fence' porphyrins are utilized because that are far less susceptible to irreversible oxidation. The effectiveness of oxygen-facilitated transport

is determined by permeation and absorption measurements and by analysis using a dual-mode transport model. Several other groups have also reported on fixed site carrier systems that produce FT of oxygen [135–139] (see also Chapter 6).

17.12.2 Carbon Dioxide Separations

Most of the research in this area involves the use of amines or anionic bases as complexing agents. While there is still interest in membranes comprised of amine solutions and ion-exchange membranes containing charged (usually protonated) amines [140], membranes that incorporated amine functionality in less conventional ways have also been reported. Plasma graft polymerization was used to incorporate various amines in microporous polyethylene and polytetrafluoroethylene membranes; selectivities greater than 4000 for CO₂/N₂ were achieved with a CO₂ permeation rate of $1 \times 10^{-4} \text{ cm}^3 \text{ cm}^{-2} \text{ s}^{-1} \text{ cmHg}^{-1}$ [141]. Polyethyleneimine/PVA blend membranes exhibited selectivities over 200 for CO₂/N₂ separations at low CO₂ feed pressures [142]. Kovvali and coworkers reported on the use of poly-amidoamine dendrimers, in pure form and blended with glycerol, used as immobilized liquid membranes (flat films and hollow fibers) [143,144]. Very high permeabilities and selectivities for CO₂/N₂ separations were reported. Composite membranes containing both amine and carboxylate groups as fixed-site carriers were prepared by hydrolyzing the top layer of poly(vinyl pyrrolidone) and examined for CO₂/CH₄ separation [145]. For pure gases, an ideal CO₂/CH₄ selectivity of 212 was calculated and a CO₂ permeance of $7.9 \times 10^{-4} \text{ cm}^3 \text{ cm}^{-2} \text{ s}^{-1} \text{ cmHg}^{-1}$.

Recently, Teramoto's group has used aqueous amine solutions in an interesting configuration in which a feed solution containing absorbed CO₂ is forced through a filtration membrane. After the CO₂ is released on the sweep side, the carrier solution is recirculated. The process has been applied in a capillary membrane module for CO₂/N₂ separation [146] and in a 'dead-end' filtration cell for CO₂/CH₄ separation [84]. These systems displayed high permeance and stability. For the CO₂/N₂ separation, the CO₂ permeance was as high as $2.7 \times 10^{-2} \text{ mol m}^{-2} \text{ s}^{-1} \text{ kPa}^{-1}$ and the selectivity ranged from 430 to 1790.

In the early portion of this review period, there were a number of papers focused on modeling

CO₂ facilitation in amine-based systems. Examples include the following: a model that includes the effect of the state of protonation of the amine carrier on the complexation constant for CO₂ [147]; a comparison of FT in ion-exchanged versus covalently bound amine membranes [148]; a theory describing CO₂ transport in amine-supported liquid membranes [16]; a model that explicitly treats the effects of charge for carriers and complexes in ion-exchange membranes [149]; a model for competitive transport of CO₂ and H₂S in ion-exchange/amine membranes [150]; the effect of rate and equilibrium constants on CO₂ permeability for a variety of amines in supported liquid membranes [151].

After amines, solutions or molten salts containing carbonate, bicarbonate, fluoride or acetate ions are most commonly used for the FT of CO₂. For example, Quinn *et al.* used supported liquid membranes containing tetraalkylammonium fluoride and acetate hydrates to achieve high selectivities for CO₂/CH₄ and CO₂/H₂ separations under certain feed conditions [152]. Higuchi *et al.* studied CO₂ permeation through CsHCO₃ liquid membranes [153] while Park *et al.* studied transport through immobilized K₂CO₃ solutions containing various additives [154].

17.13 Organic Substances

Facilitated transport of carbohydrates, catecholamines and amino acids through bulk liquid membranes, supported liquid membranes and plasticized cellulose membranes was reviewed by Smith *et al.* in 1998 (20 references) [155]. The typical carriers for these types of separations are boronic acids, quaternary ammonium salts and crown ethers. Normal diffusional FT is observed in many of these systems, but in certain cases the observation of a percolation threshold is used to infer a fixed-site hopping mechanism. Further attempts to understand mechanistic issues related to these FT membrane separations has also been reported recently by Di Luccio *et al.* [156]. Research on these types of separations, including the use of some novel complexing agents, has continued to the present time. Some examples are shown in Table 17.3.

While the Ag(i) ion is most often used in the FT of unsaturated hydrocarbons (see above), it has also been used to enhance the transport of

Table 17.3 Examples of some novel complexing agents used in FT separations

Solute	Complexing agent	Membrane type	Reference
Sugar	Resorcinarene	Supported liquid	[157,158]
Amino acids	Macrocyclic receptors	Polysiloxane	[159,160]
Sodium phenolate	Tricaprylmethylammonium chloride and crown ether(s)	Supported liquid	[161]
Amino acids	Metal ions	Poly(vinyl alcohol)-supported liquid	[162,163] [164]
Aromatic hydrocarbons	Water-soluble cyclophanes	Supported liquid	[165]

long-chain fatty acid esters, such as ethyl eicosapentaenoate acid and and ethyl docosahexaenoate. Bulk liquid membranes containing AgNO_3 [166] and Ag(I) -exchanged Nafion membranes have been used [167,168].

17.14 Biological Complexing Agents

In principle, biological carriers incorporated into FT membranes are capable of achieving very selective separations due to the specificity of the complexation reaction. A few examples have appeared in the last decade. Lakshmi and Martin entrapped solutions containing apo-enzymes in microporous supports using polypyrrole plugs to cap the pores [169]. The membranes exhibited a 5-fold difference in transport rates for D- and L-amino acids. Cyclodextrins incorporated into poly(acrylic acid) membranes have been used to achieve selective separations for xylene isomers [170].

An interesting approach to a biologically based FT separation was reported recently by Miyako *et al* [171]. (S)-Ibuprofen is selectively esterified in the feed phase and selectively diffuses across a membrane composed of a hydrophobic ionic liquid immobilized on a polypropylene support. The esterification process is reversed enzymatically in the receiving phase.

17.15 Concluding Remarks

As shown in this review, research on facilitated transport membranes has progressed in a number of areas. Mathematical models, which describe transport for a variety of conditions, have been developed and tested. A major research thrust has been new materials, structures and methods for incorporating complexing agents that result in greater membrane stability. Examples include

fixed site carrier membranes, membranes composed of ionic liquids or electrohydrodynamic fluids, solid polymer electrolyte membranes and microencapsulated membranes. The use of external fields (electrical, thermal, photochemical, pH) have been used successfully to increase the driving force for separation/concentration. Numerous examples of facilitated transport of specific chemical compounds, ranging from simple gases to hydrocarbons, as well as complex organic molecules, have been reported. Progress to take this technology from the laboratory to commercialization is clearly an important step. Once facilitated transport is shown to be commercially viable, many opportunities will evolve.

References

- [1] J. D. Way and R. D. Noble, 'Facilitated transport', in *Membrane Handbook*, K. K. Sirkar and W. S. Ho (Eds), Van Nostrand Publishing Company, New York, NY, USA (1992).
- [2] E. L. Cussler, 'Facilitated and active transport', in *Polymeric Gas Separation Membranes*, D. R. Paul and Y. P. Yampol'skii (Ed), CRC Press, Boca Raton, FL, USA, pp. 273–300 (1994).
- [3] J. D. Way, *et al.*, 'Liquid membrane transport: a survey', *Journal of Membrane Science*, **12**, 239–259 (1982).
- [4] C. J. King, 'Separation processes based on reversible chemical complexation', in *Handbook of Separation Processes*, R. W. Rousseau (Ed), John Wiley & Sons, Inc., New York, NY, USA, pp. 760–774 (1988).
- [5] L. L. Kemena, R. D. Noble and N. J. Kemp, 'Optimal regimes of facilitated transport', *Journal of Membrane Science*, **15**, 259–274 (1983).
- [6] E. L. Cussler, *Diffusion: Mass Transfer in Fluid Systems*, Cambridge University Press, New York, NY, USA (1984).
- [7] R. D. Noble, 'Relationship of system properties to performance in facilitated transport systems',

- Gas Separation and Purification*, **2**, 16–19 (1988).
- [8] R. D. Noble, 'Two-dimensional permeate transport with facilitated transport membranes', *Separation Science and Technology*, **19**, 469–478 (1984).
- [9] J.-I. Kim and P. Stroeve, 'Mass transfer in separation devices with reactive hollow fibers', *Chemical Engineering Science*, **43**, 247–257 (1988).
- [10] M. Metayer, *et al.*, 'Facilitated transport of non-electrolytes through ion-exchange membranes: concentration polarization and rate-determining stage in a tubular membrane system', *Russian Journal of Electrochemistry* (translation of *Elektrokhimiya*), **38**, 873–883 (2002).
- [11] L. Li, 'Improvement of the performance of facilitated transport membrane process through non-uniformity', *Journal of Membrane Science*, **110**, 83–90 (1996).
- [12] W. J. Ward, 'Analytical and experimental studies of facilitated transport', *AIChE Journal*, **16**, 405–410 (1970).
- [13] D. R. Smith and J. A. Quinn, 'The prediction of facilitation factors for reaction augmented membrane transport', *AIChE Journal*, **21**, 197–200 (1979).
- [14] M. H. Al-Marzouqi, K. J. A. Hogendoorn and G. F. Versteeg, 'Analytical solution for facilitated transport across a membrane', *Chemical Engineering Science*, **57**, 4817–4829 (2002).
- [15] M. Teramoto, 'Approximate solution of facilitation factors in facilitated transport', *Industrial and Engineering Chemistry Research*, **33**, 2161–2167 (1994).
- [16] M. Teramoto, 'Approximate solution of facilitation factors for the transport of CO₂ through a liquid membrane of amine solution', *Industrial and Engineering Chemistry Research*, **34**, 1267–1272 (1995).
- [17] R. D. Noble, J. D. Way and L. A. Powers, 'Effect of external mass transfer resistance on facilitated transport', *Industrial and Engineering Chemistry Fundamentals*, **25**, 450–452 (1986).
- [18] R.-S. Juang, S.-H. Lee and R.-H. Huang, 'Modeling of amine-facilitated liquid membrane transport of binary organic acids', *Separation Science and Technology*, **33**, 2379–2395 (1998).
- [19] A. Kirkkopru-Dindi and R. D. Noble, 'Optimal regimes of facilitated transport for multiple site carriers', *Journal of Membrane Science*, **42**, 13–25 (1989).
- [20] W. S. Ho and K. K. Sirkar (Eds), *Membrane Handbook* Chapman & Hall, London, UK (1992).
- [21] R. W. Baker, 'Future directions of membrane gas separation technology', *Industrial and Engineering Chemistry Research*, **41**, 1393–1411 (2002).
- [22] D. W. Deetz and M. M. Kreevoy, 'Stabilized liquid films', *US Patent 4 710 205* (1987).
- [23] O. H. LeBlanc, *et al.*, 'Facilitated transport in ion exchange membranes', *Journal of Membrane Science*, **6**, 339–343 (1980).
- [24] J. D. Way, *et al.*, 'Facilitated transport of CO₂ in ion exchange membranes', *AIChE Journal*, **33**, 480–487 (1987).
- [25] S. L. Matson, *et al.*, 'Acid gas scrubbing by composite solvent-swollen membranes', *US Patent 4 737 166* (1988).
- [26] M. Yoshikawa, *et al.*, 'Synthetic polymer membranes with pyridine moiety for gas separation', *Kobunshi Ronbunshu*, **43**, 729–732. (1986).
- [27] H. Nishide, *et al.*, 'Oxygen binding and transport in the membrane of poly[[tetrakis(methacrylamidophenyl)porphinato]cobalt-co-hexyl methacrylate]', *Macromolecules*, **21**, 2910–2913 (1988).
- [28] H. Nishide, H. Kawakami and E. Tsuchida, 'Facilitated transport of nitrogen and acetylene in poly(vinylcyclopentadienylmanganese) membrane', *Polymeric Materials Science and Engineering*, **61**, 492–496 (1989).
- [29] K. Sugie, 'Highly selective oxygen separating membrane containing Schiff-base chelate bound to polymeric ligand', *Polymeric Materials Science and Engineering*, **59**, 139–143 (1988).
- [30] R. D. Noble, 'Analysis of facilitated transport with fixed site carrier membranes', *Journal of Membrane Science*, **50**, 207–214 (1990).
- [31] R. D. Noble, 'Facilitated transport mechanism in fixed site carrier membranes', *Journal of Membrane Science*, **60**, 297–306 (1991).
- [32] R. D. Noble, 'Generalized microscopic mechanism of facilitated transport in fixed site carrier membranes', *Journal of Membrane Science*, **75**, 121–129 (1992).
- [33] E. L. Cussler, R. Aris and A. Bhowan, 'On the limits of facilitated diffusion', *Journal of Membrane Science*, **43**, 149–164 (1989).
- [34] Y. S. Kang, *et al.*, 'Analysis of facilitated transport in fixed site carrier membranes: I. Single RC Model', *Journal of Membrane Science*, **109**, 149–157 (1996).
- [35] J.-M. Hong, *et al.*, 'Analysis of facilitated transport in polymeric membrane with fixed site carrier 2. Series RC circuit model', *Journal of Membrane Science*, **109**, 159–163 (1996).
- [36] S. Moganti, R. D. Noble and C. A. Koval, 'Analysis of a membrane/distillation column hybrid process', *Journal of Membrane Science*, **93**, 31–44 (1994).
- [37] W. Stephan, R. D. Noble and C. A. Koval, 'Design Methodology for a membrane/distillation column hybrid process', *Journal of Membrane Science*, **99**, 259–272 (1995).

- [38] T. Pettersen, *et al.*, 'Design of combined membrane and distillation processes', *Separations Technology*, **6**, 175–187 (1996).
- [39] R. Agrawal, *et al.*, 'Membrane/cryogenic hybrid processes for hydrogen purification', *Gas Separation and Purification*, **2**, 9 (March 1988).
- [40] R. Agrawal, *et al.*, 'Membrane/cryogenic hybrid scheme for argon production from air', *Gas Separation and Purification*, **4**, 75 (June 1990).
- [41] R. Agrawal and R. M. Thorogood, 'Production of medium pressure nitrogen by cryogenic air separation', *Gas Separation and Purification*, **5**, 203 (December 1991).
- [42] M. F. Jin, F. C. J. Michel and R. D. Noble, 'Kinetics of copper extraction using (anti)-2-hydroxy-5-nonylbenzophenone', *Industrial and Engineering Chemistry Research*, **28**, 193–198 (1989).
- [43] K. Y. Niiya and R. D. Noble, 'Competitive facilitated transport through liquid membranes', *Journal of Membrane Science*, **23**, 183–198 (1985).
- [44] J. D. Way and R. D. Noble, 'Competitive facilitated transport of acid gases in perfluorosulfonic acid membranes', *Journal of Membrane Science*, **46**, 309–324 (1989).
- [45] C. A. Koval, *et al.*, 'Concentration and removal of nitrogen and sulfur compounds from hydrocarbon phases using electrochemically reversed chemical complexation', *Separations Science and Technology*, **23**, 1389–1399 (1988).
- [46] P. A. Terry, *et al.*, 'Electrochemically modulated complexation process for gas removal and concentration', *AIChE Journal*, **41**, 2556–2564 (1995).
- [47] C. Wan, R. D. Noble and N. A. Clark, 'Control of gas permeation via electrohydrodynamic convection in a liquid crystal membrane', *Journal of Membrane Science*, **74**, 223–231 (1992).
- [48] C. Wan, R. D. Noble and N. A. Clark, 'Use of polar solvents in an electroconvective liquid membrane for gas separation', *Journal of Membrane Science*, **84**, 191–196 (1993).
- [49] J. P. Collins, *et al.*, 'Continued studies of an electroconvective liquid membrane for gas separation', *Journal of Membrane Science*, **99**, 249–257 (1995).
- [50] C. A. Koval, *et al.*, 'Selective transport of gaseous CO through liquid membranes using an Iron(II) macrocyclic complex', *Inorganic Chemistry*, **24**, 1147–1152 (1985).
- [51] S. Shinkai, K. Miyazaki and O. Manabe, 'Photoresponsive crown ethers. Part 18. Photochemically "switched-on" crown ethers containing an intra-annular azo substituent and their application to membrane transport', *Journal Of The Chemical Society, Perkin Transactions 1*, 449 (1987).
- [52] M. Xu, *et al.*, 'Photocontrollable ion transport across a liquid membrane by anthracene end-labeled oligo-oxyethylenes', *Physical Chemistry, Chemical Physics*, **4**, 4030–4035 (2002).
- [53] R. D. Noble, 'Optimal equilibrium constants for interfacial reactions used in liquid membrane transport', *Separations Science and Technology*, **24**, 1329–1336 (1989).
- [54] E. L. Cussler, 'Membranes which pump', *AIChE Journal*, **17**, 1300–1303 (1971).
- [55] A. Dindi, R. D. Noble and C. A. Koval, 'An analytical solution for competitive facilitated membrane transport', *Journal of Membrane Science*, **65**, 39–45 (1992).
- [56] T. L. Longin, C. A. Koval and R. D. Noble, 'Photomodulation and photopumping in membranes containing carriers optimized for facilitated transport in the dark', *Journal of Physical Chemistry*, **101**, 7172–7179 (1997).
- [57] T. L. Longin, C. A. Koval and R. D. Noble, 'Photomodulation of transport rates in liquid membranes containing photoactive carriers', *Journal of Physical Chemistry*, **101**, 1036–1052 (1998).
- [58] T. L. Longin, C. A. Koval and R. D. Noble, 'Photopumping in liquid membranes containing photoactive carriers', *Journal of Physical Chemistry*, **102**, 2064–2075 (1998).
- [59] M. L. Goyette, *et al.*, 'Selective photofacilitated transport of sodium ions through liquid membranes: key factors in experimental design, transport results and comparison with a mathematical model', *Journal of Membrane Science*, **212**, 225–235 (2003).
- [60] A. L. Athayde and C. F. Ivory, 'Electrical pumping on carrier-mediated membrane transport', *Journal of Membrane Science*, **24**, 309–323 (1985).
- [61] N. J. Kemp and R. D. Noble, 'Heat transfer effects in facilitated transport liquid membranes', *Separation Science and Technology*, **18**, 1147–1165 (1983).
- [62] J. T. Rockman, E. Kehat and R. Lavie, 'Mathematical model for thermally enhanced facilitated transport', *Industrial and Engineering Chemistry Research*, **34**, 2455–2463 (1995).
- [63] E. Selegny, *et al.*, 'Carrier-mediated, thermal energy-coupled, nonisothermal membrane transport. II. A gaseous system', *Journal of Membrane Science*, **108**, 161–169 (1995).
- [64] E. Selegny, *et al.*, 'Non-isothermal facilitated transport. III. Determination and prediction of simplified phenomenological direct and cross coefficients. Heat and/or mass driven transports', *Journal of Membrane Science*, **123**, 47–59 (1997).

- [65] T. Welton, 'Room-temperature ionic liquids. solvents for synthesis and catalysis', *Chemical Reviews*, **99**, 2071 (1999).
- [66] W. Keim and P. Wassercheid, 'Ionic liquids – new solutions for transition metal catalysis', *Angewandte Chemie International Edition*, **39**, 3772–3789 (2000).
- [67] A. E. Visser, R. P. Swatloski and R. D. Rogers, 'pH-dependent partitioning in room temperature ionic liquids provides a link to traditional solvent extraction behavior', *Green Chemistry*, **2**, 1 (2000).
- [68] A. E. Visser, *et al.*, 'Traditional extractants in nontraditional solvents: groups 1 and 2 Extraction by crown ethers in room-temperature ionic liquids', *Industrial and Engineering Chemistry Research*, **39**, 3596–3604 (2000).
- [69] A. E. Visser, *et al.*, 'Calixarenes as ligands in environmentally-benign liquid/liquid extraction media, aqueous biphasic systems and room temperature ionic liquids, in *Calixarenes for Separations*, G. J. Lumetta, R. D. Rogers and A. S. Gopalan, (Eds.) pp. 223–236 (2000).
- [70] A. E. Visser, *et al.*, 'Task-specific ionic liquids for the extraction of metal ions from aqueous solutions', *Chemical Society, Journal of the Chemical Communications*, 135 (2001).
- [71] A. E. Visser, *et al.*, 'Liquid/liquid extraction of metal ions in room temperature ionic liquids', *Separations Science and Technology*, **36**, 785 (2001).
- [72] A. E. Visser, *et al.*, 'Characterization of hydrophilic and hydrophobic ionic liquids: alternatives to volatile organic compounds for liquid–liquid separations, in *Ionic Liquids; Industrial Applications to Green Chemistry*, R. D. Rogers and K. R. Seddon (Eds), (2002).
- [73] P. Scovazzo, *et al.* 'Supported ionic liquid membranes (SILMs) and facilitated ionic liquid membranes (FILMs)', in *Ionic Liquids: Industrial Applications to Green Chemistry*, American Chemical Society Symposium Series 818, American Chemical Society, Washington, DC, USA, (2002).
- [74] A. E. Visser, *et al.*, 'Naphthol- and resorcinol-based azo dyes as metal ion complexants in aqueous biphasic systems', *Journal of Chromatography B: Biomedical Sciences and Applications*, **743**, 107 (2000).
- [75] C. M. Gordon, *et al.*, 'Ionic liquid crystals: hexafluorophosphate salts', *Journal Of Materials Chemistry*, **8**, 2627 (1998).
- [76] C. Hardacre, *et al.*, 'Crystal and liquid crystalline polymorphism in 1-alkyl-3-methylimidazolium tetrachloropalladate(II) salts', *Journal Of Materials Chemistry*, **11**, 346 (2001).
- [77] A. J. Carmichael, *et al.*, 'Molecular layering and local order in thin films of 1-alkyl-3-methylimidazolium ionic liquids using X-ray reflectivity', *Molecular Physics*, **99**, 795 (2001).
- [78] D. Camper, *et al.*, 'Gas solubilities in room temperature ionic liquids', *Ind. Eng. Chem. Res.*, 2004: p. in press. Industrial and Engineering Chemistry Research.
- [79] H. J. Walls, *et al.*, 'Fumed silica-based composite polymer electrolytes: synthesis, rheology, and electrochemistry', *Journal of Power Sources*, **89**, 156 (2000).
- [80] A. Sungpet, *et al.*, 'Reactive polymer membranes for ethylene/ethane separation', *Journal of Membrane Science*, **136**, 111–120 (1997).
- [81] P. Klausener and D. Woermann, 'Structure and transport properties of cation exchange gel membranes. Facilitated transport of ethene with silver ions as carriers', *Journal of Membrane Science*, **168**, 17–27 (2000).
- [82] I. Pinnau and L. G. Toy, 'Solid polymer electrolyte composite membranes for olefin/paraffin separation', *Journal of Membrane Science*, **184**, 39–48 (2001).
- [83] J. H. Ryu, *et al.*, 'Facilitated olefin transport by reversible olefin coordination to silver ions in a dry cellulose acetate membrane', *Chemistry – A European Journal*, **7**, 1525–1529 (2001).
- [84] M. Teramoto, *et al.*, 'Ethylene/ethane separation by facilitated transport membrane accompanied by permeation of aqueous silver nitrate solution', *Separation and Purification Technology*, **28**, 117–124 (2002).
- [85] Y. Yoon, J. Won and Y. S. Kang, 'Polymer electrolyte membranes containing silver ion for facilitated olefin transport', *Macromolecules*, **33**, 3185–3186 (2000).
- [86] Y. S. Park, J. Won and Y. S. Kang, 'Facilitated transport of olefin through solid PAAm and PAAm-graft composite membranes with silver ions', *Journal of Membrane Science*, **183**, 163–170 (2001).
- [87] K. J. Lee, *et al.*, 'Complexation of silver ions with poly(butyl methacrylate) and propylene toward facilitated propylene transport', *Macromolecular Rapid Communications*, **23**, 839–843 (2002).
- [88] W. S. Ho and D. C. Dalrymple, 'Facilitated transport of olefins in Ag⁺-containing polymer membranes', *Journal of Membrane Science*, **91**, 13–25 (1994).
- [89] J.-S. Yang and G.-H. Hsiue, 'C4 olefin/paraffin separation by poly[(1-trimethylsilyl)-1-propyne]-graft-poly(acrylic acid)–Ag⁺ complex membranes', *Journal of Membrane Science*, **111**, 27–38 (1996).
- [90] A. S. Kovvali, H. Chen and K. K. Sirkar, 'Glycerol-based immobilized liquid membranes for

- olefin-paraffin separation', *Industrial and Engineering Chemistry Research*, **41**, 347–356 (2002).
- [91] A. J. van Zyl, *et al.*, 'Application of new sulfonated ionomer membranes in the separation of pentene and pentane by facilitated transport', *Journal of Membrane Science*, **137**, 173–185 (1997).
- [92] A. Sungpet, *et al.*, 'Silver doped Nafion-poly (pyrrole) membranes for facilitated permeation of liquid-phase olefins', *Journal of Membrane Science*, **189**, 271–279 (2001).
- [93] R. M. Goering, *et al.*, 'Complexation structure and transport mechanism of 1,5-hexadiene and 1-hexene through silver facilitated transport membranes', *Journal of Membrane Science*, **172**, 49–57 (2000).
- [94] C. A. Koval, L. Kaljevic and R. D. Noble, 'Membrane materials as ligands for Ag(I) ions: design and use for hydrocarbon separations', *Macromolecular Symposia*, **156**, 27–44 (2000).
- [95] D. L. Bryant, R. D. Noble and C. A. Koval, 'Facilitated transport separation of benzene and cyclohexane with poly(vinyl alcohol)-AgNO₃ membranes', *Journal of Membrane Science*, **127**, 161–170 (1997).
- [96] S. L. Kohls, R. D. Noble and C. A. Koval, 'Effects of molecular structure and equivalent weight on facilitated transport of alkenes in Ag(I)-PFSI membranes', *Journal of Membrane Science*, **125**, 61–73 (1997).
- [97] J. H. Kim, *et al.*, 'Structure and coordination properties of facilitated olefin transport membranes consisting of crosslinked poly(vinyl alcohol) and silver hexafluoroantimonate', *Journal of Polymer Science, Part B: Polymer Physics*, **42**, 621–628 (2004).
- [98] C. A. Koval, D. L. Bryant and R. D. Noble, 'Poly(vinyl alcohol)-silver nitrate facilitated transport membranes for benzene/cyclohexane separations', *Polymeric Materials Science and Engineering*, **77**, 263–264 (1997).
- [99] J.-S. Yang and G.-H. Hsiue, 'Selective olefin permeation through Ag(I) contained silicone rubber-graft-poly(acrylic acid) membrane', *Journal of Membrane Science*, **126**, 139–149 (1997).
- [100] A. Sungpet, *et al.*, 'Facilitated transport of unsaturated hydrocarbons through water-swollen Nafion 112 incorporated with poly(pyrrole)', *Journal of Membrane Science*, **213**, 221–224 (2003).
- [101] R. Rabago, *et al.*, 'Evidence for parallel pathways in the facilitated transport of alkenes through Ag⁺-exchanged Nafion films', *Industrial and Engineering Chemistry Research*, **35**, 1090–1096 (1996).
- [102] R. M. Goering, *et al.*, 'Role of ion-exchange membrane morphology and sorption properties in facilitated transport di-olefin/mono-olefin separations', *Journal of Membrane Science*, **144**, 133–143 (1998).
- [103] M. Teramoto, T. Maeda and Q. F. Huang, 'Preparation of microporous ion exchange membranes and their application to facilitated transport of carbon dioxide and olefin', *Polymeric Materials Science and Engineering*, **77**, 258–259 (1997).
- [104] J. H. Jin, *et al.*, 'Spectroscopic studies for molecular structure and complexation of silver polymer electrolytes', *Macromolecules*, **33**, 4932–4935 (2000).
- [105] S. W. Kang, *et al.*, 'Enhancement of facilitated olefin transport by amino acid in silver-polymer complex membranes', *Journal of The Chemical Society, Chemical Communications*, 768–769 (2003).
- [106] D. S. Manley, *et al.*, 'Morphological changes and facilitated transport characteristics for Nafion membranes of various equivalent weights', *Chemistry of Materials*, **8**, 2595–2600 (1996).
- [107] J.-S. Yang and G.-H. Hsiue, 'Kinetics of Ag⁺ contained polymeric complex membranes for facilitated olefin transport', *Journal of Polymer Science, Part B: Polymer Physics*, **35**, 909–917 (1997).
- [108] S. Sunderrajan, *et al.*, 'Propane and propylene sorption in solid polymer electrolytes based on poly(ethylene oxide) and silver salts', *Journal of Membrane Science*, **182**, 1–12 (2001).
- [109] A. Morisato, *et al.*, 'Transport properties of PA12-PTMO/AgBF₄ solid polymer electrolyte membranes for olefin/paraffin separation', *Desalination*, **145**, 347–351 (2002).
- [110] S. U. Hong, J. Y. Kim and Y. S. Kang, 'Effect of water on the facilitated transport of olefins through solid polymer electrolyte membranes', *Journal of Membrane Science*, **181**, 289–293 (2001).
- [111] J. H. Kim, *et al.*, 'Structural changes of silver polymer electrolytes: Comparison between poly(2-ethyl-2-oxazoline) and poly(*N*-vinyl pyrrolidone) complexes with silver salt', *Journal of Polymer Science, Part B: Polymer Physics*, **42**, 232–237 (2004).
- [112] S. Choi, J. H. Kim and Y. S. Kang, 'Wide-angle X-ray scattering studies on the structural properties of polymer electrolytes containing silver ions', *Macromolecules*, **34**, 9087–9092 (2001).
- [113] J. H. Kim, *et al.*, 'Facilitated transport of ethylene across polymer membranes containing silver salt: effect of HBF₄ on the photoreduction of silver ions', *Journal of Membrane Science*, **212**, 283–288 (2003).
- [114] J. H. Kim, *et al.*, 'Role of polymer matrix in polymer/silver complexes for structure, interactions

- and facilitated olefin transport', *Macromolecules*, **36**, 6183–6188 (2003).
- [115] J. H. Kim, *et al.*, 'Spectroscopic interpretation of silver ion complexation with propylene in silver polymer electrolytes', *Journal of Physical Chemistry B*, **106**, 2786–2790 (2002).
- [116] T. C. Merkel, *et al.*, 'Olefin/paraffin solubility in a solid polymer electrolyte membrane', *Journal of The Chemical Society, Chemical communications*, **13**, 1596–1597 (2003).
- [117] T. Suzuki, R. D. Noble and C. A. Koval', 'Electrochemistry, stability and alkene complexation chemistry for copper(i) triflate in aqueous solution', *Inorganic Chemistry*, **36**, 136–140 (1997).
- [118] H. S. Kim, *et al.*, 'Spectroscopic characterization of cellulose acetate polymer membranes containing Cu(1,3-butadiene)OTf as a facilitated olefin transport carrier', *Chemistry of Materials*, **13**, 1720–1725 (2001).
- [119] A. Figoli, W. F. C. Sager and M. H. V. Mulder, 'Facilitated oxygen transport in liquid membranes: review and new concepts', *Journal of Membrane Science*, **181**, 97–110 (2001).
- [120] M. P. Bernal, *et al.*, 'Facilitated transport of O₂ through alumina–zeolite composite membranes containing a solution with a reducible metal complex', *Journal of Membrane Science*, **203**, 209–213 (2002).
- [121] C.-C. Wang, *et al.*, 'Facilitated transport of molecular oxygen in cobalt-chelated copolymer membranes prepared by soap-free emulsion polymerization', *Journal of Membrane Science*, **208**, 133–145 (2002).
- [122] Z.-Y. Zhang, 'Facilitated oxygen transport in a novel silicone polymer membrane containing carboxylic cobalt groups', *Journal of Applied Polymer Science*, **90**, 1038–1044 (2003).
- [123] J. Yang and P. Huang, 'A study of cobalt(ii) porphyrins on their oxygen-binding behaviors and oxygen-facilitated transport properties in polymeric membranes', *Chemistry of Materials*, **12**, 2693–2697 (2000).
- [124] X.-S. Chen, H. Nishide and E. Tsuchida, 'Analysis of facilitated oxygen transport in a liquid membrane of hemoglobin', *Bulletin of the Chemical Society of Japan*, **69**, 255–259 (1996).
- [125] H. Nishide, *et al.*, 'Cobalt porphyrin-mediated oxygen transport in a polymer membrane: effect of the cobalt porphyrin structure on the oxygen-binding reaction, oxygen-diffusion Constants and oxygen-transport efficiency', *Journal of Physical Chemistry*, **98**, 5084–5088 (1994).
- [126] H. Nishide, X. S. Chen and E. Tsuchida, 'Facilitated oxygen transport with modified and encapsulated hemoglobins across non-flowing solution membrane', *Artificial Cells, Blood Substitutes and Immobilization Biotechnology*, **25**, 335–346 (1997).
- [127] H. Nishide and E. Tsuchida, 'Facilitated transport of oxygen through the membrane of layered cobaltporphyrins', *Journal of Inorganic Biochemistry*, **67**, 122 (1997).
- [128] H. Nishide, Y. Tsukahara and E. Tsuchida, 'Highly selective oxygen permeation through a poly(vinylidene dichloride)–cobalt porphyrin membrane: hopping transport of oxygen via the fixed cobalt porphyrin carrier', *Journal of Physical Chemistry B*, **102**, 8766–8770 (1998).
- [129] T. Suzuki, *et al.*, 'Effect of carrier concentration on the facilitated oxygen transport in a polymer membrane', *Polymers for Advanced Technologies*, **5**, 253–256 (1994).
- [130] T. Suzuki, *et al.*, 'Effect of an oxygen-binding reaction at the cobalt porphyrin site fixed in a polymer membrane on facilitated oxygen transport', *Bulletin of the Chemical Society of Japan*, **68**, 1036–1041 (1995).
- [131] T. Suzuki, *et al.*, 'Electrochemical measurement of facilitated oxygen transport through a polymer membrane containing cobalt porphyrin as a fixed carrier', *Journal of Membrane Science*, **112**, 155–160 (1996).
- [132] T. Suzuki and H. Nishide, 'Effect of the reactivity of cobalt porphyrin carrier on the facilitated oxygen transport in polymer membrane', *Polymeric Materials Science and Engineering*, **77**, 275–276 (1997).
- [133] X.-S. Chen, H. Nishide and E. Tsuchida, 'Analysis of facilitated oxygen transport in a liquid membrane of hemoglobin', *Bulletin of the Chemical Society of Japan*, **69**, 255–259 (1996).
- [134] B. Shentu and H. Nishide, 'Facilitated oxygen transport membranes of picket-fence cobalt-porphyrin complexed with various polymer matrixes', *Industrial and Engineering Chemistry Research*, **42**, 5954–5958 (2003).
- [135] J. M. Yang and G. H. Hsiue, 'Modified styrene–butadiene–styrene block copolymer membranes complexed with (N,N'-disalicylideneethylenediamine)cobalt(ii) for oxygen permeation: polymeric axial ligand effect', *Journal of Membrane Science*, **87**, 233–244 (1994).
- [136] Z. Zhang and S. Lin, 'Facilitated oxygen transport in an ionomer membrane containing cobaltous ions', *Macromolecular Rapid Communications*, **16**, 927–933 (1995).
- [137] G.-H. Hsiue and J.-S. Yang, 'Polymeric complex membranes based on styrene–diene–styrene tri-block copolymers for oxygen enrichment', *Polymers for Advanced Technologies*, **7**, 686–692 (1996).

- [138] J.-M. Hong and S. W. Lee, Facilitated transport of oxygen in poly(dimethylsiloxane-co-styrene-co-4-vinyl pyridine) terpolymer membrane containing cobalt Schiff base carrier', *Journal of Industrial and Engineering Chemistry (Seoul)*, **3**, 165–170 (1997).
- [139] M. J. Choi, C. K. Park and Y. M. Lee, 'Chelate membrane from poly(vinyl alcohol)/poly(*N*-saliicylidene allyl amine blend, II. Effect of Co(II) content on oxygen/nitrogen separation', *Journal of Applied Polymer Science*, **58**, 2373–2379 (1995).
- [140] H. Matsuyama, *et al.*, 'Preparation of poly(acrylic acid)/poly(vinyl alcohol) membrane for the facilitated transport of CO₂', *Journal of Applied Polymer Science*, **81**, 936–942 (2001).
- [141] H. Matsuyama, *et al.*, 'Facilitated transport of CO₂ through various ion exchange membranes prepared by plasma graft polymerization', *Journal of Membrane Science*, **117**, 251–260 (1996).
- [142] H. Matsuyama, *et al.*, 'Facilitated transport of CO₂ through polyethylenimine/poly(vinyl alcohol) blend membrane', *Journal of Membrane Science*, **163**, 221–227 (1999).
- [143] A. S. Kovvali, H. Chen and K. K. Sirkar, 'Dendrimer membranes: a CO₂-selective molecular gate', *Journal of the American Chemical Society*, **122**, 7594–7595 (2000).
- [144] A. S. Kovvali and K. K. Sirkar, 'Dendrimer liquid membranes: CO₂ separation from gas mixtures', *Industrial and Engineering Chemistry Research*, **40**, 2502–2511 (2001).
- [145] Y. Zhang, Z. Wang and S. Wang, 'Novel fixed-carrier membranes for CO₂ separation', *Journal of Applied Polymer Science*, **86**, 2222–2226 (2002).
- [146] M. Teramoto, *et al.*, 'Separation and enrichment of carbon dioxide by capillary membrane module with permeation of carrier solution', *Separation and Purification Technology*, **30**, 215–227 (2003).
- [147] C. Ahmed, *et al.*, 'Reaction in ion-exchangers: characterization of the ethylenediamine protonation equilibrium in a sulfonic membrane devoted to carbon dioxide facilitated transport', *Reactive Polymers*, **24**, 213–218 (1995).
- [148] T. Yamaguchi, *et al.*, 'Transport properties of carbon dioxide through amine functionalized carrier membranes', *Industrial and Engineering Chemistry Research*, **34**, 4071–4077 (1995).
- [149] T. Yamaguchi, *et al.*, 'Transport mechanism of carbon dioxide through perfluorosulfonate ionomer membranes containing an amine carrier', *Chemical Engineering Science*, **51**, 4781–4789 (1996).
- [150] Z. Zeng, W. Xue and Y. Shi, 'Competitive facilitated transport of acid gases in modified carrier membranes', *Chinese Journal of Chemical Engineering*, **4**, 349–354 (1996).
- [151] M. Teramoto, *et al.*, 'Facilitated transport of CO₂ through supported liquid membranes of various amine solutions – effects of rate and equilibrium of reaction between CO₂ and amine', *Journal of Chemical Engineering of Japan*, **30**, 328–335 (1997).
- [152] R. Quinn, J. B. Appleby and G. P. Pez, 'New facilitated transport membranes for the separation of carbon dioxide from hydrogen and methane', *Journal of Membrane Science*, **104**, 139–146 (1995).
- [153] A. Higuchi, J. Komiyama and T. Lijima, 'Facilitated transport of CO₂ in liquid membrane of CsHCO₃ aqueous solution', *Sen'i Gakkaishi*, **56**, 282–289 (2000).
- [154] S.-W. Park, *et al.*, 'Facilitated transport of carbon dioxide through an immobilized liquid membrane of aqueous carbonate solution with additives', *Separation Science and Technology*, **35**, 2497–2512 (2000).
- [155] B. D. Smith, *et al.*, 'Facilitated transport of carbohydrates, catecholamines and amino acids through liquid and plasticized organic membranes', *Journal of Inclusion Phenomena and Molecular Recognition in Chemistry*, **32**, 121–131 (1998).
- [156] M. Di Luccio, *et al.*, 'Separation of fructose from a mixture of sugars using supported liquid membranes', *Journal of Membrane Science*, **174**, 217–224 (2000).
- [157] J.-F. Verchere, 'Facilitated transport of saccharides through a supported liquid membrane containing a neutral lipophilic resorcinarene carrier', *Macromolecular Symposi*, **188**, 105–116 (2002).
- [158] T. Rhlalou, *et al.*, 'Facilitated transport of sugars by a resorcinarene through a supported liquid membrane', *Journal of Membrane Science*, **168**, 63–73 (2000).
- [159] M. Barboiu, *et al.*, 'A new alternative to amino acids transport: facilitated transport of L-phenylalanine by hybrid siloxane membranes containing a fixed site macrocyclic complexant', *Journal of Membrane Science*, **161**, 193–206 (1999).
- [160] M. Barboiu, *et al.*, 'Facilitated transport of organics of biological interest II. Selective transport of organic acids by macrocyclic fixed site complexant membranes', *Journal of Membrane Science*, **174**, 277–286 (2000).
- [161] S.-W. Park, *et al.*, 'Facilitated transport of sodium phenolate through supported liquid membrane', *Separation and Purification Technology*, **19**, 43–45 (2000).
- [162] M. Nutt, D. Crookston and R. Beitle, 'Supported poly(vinyl alcohol) hydrogels for facilitated

- transport of histidine', *Separation Science and Technology*, **35**, 785–794 (2000).
- [163] C. Oxford, *et al.*, 'Effect of chelated metal on amino acid transport in facilitated transport membranes incorporating metal affinity', *Polymeric Materials Science and Engineering*, **77**, 273–274 (1997).
- [164] C. V. Uglea and M. Croitoru, 'Transport of amino acids through liquid membranes. III. The alkaline ion role', *Journal of Membrane Science*, **133**, 127–131 (1997).
- [165] T. Shinbo, Y. Shimabukuro and T. Yamaguchi, 'Facilitated transport of naphthalene derivatives through a supported liquid membrane containing a water-soluble cyclophane', *Separation Science and Technology*, **35**, 439–445 (2000).
- [166] M. Teramoto, *et al.*, 'Facilitated uphill transport of eicosapentaenoic acid ethyl ester through bulk liquid membrane and supported liquid membranes containing silver nitrate as a carrier: a new type of uphill transport', *Journal of Membrane Science*, **91**, 209–213 (1994).
- [167] H. Matsuyama, *et al.*, 'Facilitated transport of ethyl docosahexaenoate through solution-cast perfluorosulfonated ionomer membranes', *Journal of Applied Polymer Science*, **73**, 961–968 (1999).
- [168] H. Matsuyama, *et al.*, 'Influence of solvents on facilitated transport of ethyl ester of docosahexaenoic acid', *Journal of Membrane Science*, **159**, 1–10 (1999).
- [169] B. B. Lakshmi and C. R. Martin, 'Enantioseparation using apoenzymes immobilized in a porous polymeric membrane', *Nature*, **388**, 758–760 (1997).
- [170] S. P. Kusumocahyo, *et al.*, 'Pervaporation of xylene isomer mixture through cyclodextrins containing polyacrylic acid membranes', *Journal of Membrane Science*, **231**, 127–132 (2004).
- [171] E. Miyako, *et al.*, 'Enzyme-facilitated enantioselective transport of (S)-ibuprofen through a supported liquid membrane based on ionic liquids', *Journal of the Chemical Society, Chemical Communications*, 2926–2927 (2003).

Index

- acid dianhydride
 - effects in polyimides 281–2
 - structures 272
 - aging of membranes
 - activation energy of permeation 300–1
 - defined 294
 - density changes 299
 - gas permeability and selectivity 298–9
 - glass transition temperature 295–8
 - highly sorbing penetrant effects 301–2
 - implications for practical separations 304
 - mechanisms and models 296–7
 - overview 293–4
 - poly[1-(trimethylsilyl)-1-propyne] 302–3
 - thickness-dependency 294–5, 297–9
 - wide-angle X-ray diffraction 299–300
 - alcohol/water pervaporation 185–7
 - carbon membranes 351–2
 - polyacetylenes 233, 244–5
 - polyimides 287
 - polymer membranes 359–62, 374
 - zeolite membranes 329–30, 331, 374
 - Arrhenius–vant’ Hoff equations 30
 - artificial neural network
 - predictions 223–4
 - azeotropic mixtures *see under* pervaporation
 - barrer defined 3
 - bisphenol-A polycarbonate 108
 - carbon membranes
 - flat sheet, self-supported 338
 - carbon dioxide/methane separation 339
 - flexible from sulfonated polyimides 341–3
 - precursors and membranes characterized 340–1
 - thermogravimetry-mass spectrometry of precursors 338–9
 - hollow fiber, self-supported
 - cellulosic or phenolic precursors 343
 - continuous carbonization process 344
 - copolyimide precursors 343–4
 - membrane processes and overview 337–8
 - pervaporation and vapor permeation 351–2
 - propylene/propane separation 349, 351
 - pyrolysis temperature effects 349, 350
 - supported membranes and precursors 345
 - lignophenol and lignocresol 346–9
 - nanoporous SSSTM 345
 - phenolic 345–6
 - polyamic acid 346
 - poly(furfural alcohol) 346
- CHARMM force field 105, 121
- chlorinated hydrocarbons 362–3
- Chung diameter 6, 8, 10
- collision diameter 7–8, 10
- COMPASS force field 50–1, 105, 127
 - and fractional accessible free volume 124
 - poly[1-(trimethylsilyl)-1-propyne] 123
 - poly(2,6-dimethyl-1,4-phenylene oxide) 109–10
 - polyimide 113
 - polyphosphazene 114–15, 115–16
 - polysilane 119
 - potential energy equation 50–1
- conformational studies 121
- CONTIN program 194, 195, 196, 203
- critical temperature 10–11, 12
- critical volume 10, 13–14, 203–4
- Cytop[®] *see under* perfluoropolymers
- d*-spacing and free volume 101
 - computation 105
- Darcy’s law 162
- Darken equation 103
- dehumidification 288
- density of polymers
 - experimental 99
 - and membrane aging 297–8, 299
- polyimides 273–4, 276–7

- diamine structures 272
- diffusion and diffusion coefficient
- activation energy 30, 31, 97
 - computational methods 102–5
 - critical volume correlations 13
 - and *d*-spacing 101
 - dependency on concentration 22, 23
 - diffusive jump events 31, 75–7, 97, 103, 160
 - and free volume 12–13, 16, 100–1
 - as function of effective molecular diameter 97
 - glass transition temperature, influence of 14–15, 31–5
 - Knudsen diffusion 337, 338
 - microcavity volumes, correlations with 198–9
 - penetrant size
 - choice of parameter for correlation 9–10
 - and critical volume 13
 - dependence on 8, 12–14
 - polyimides 275–6
 - polymer connector groups 35–6, 211
 - predictive methods 211–15
 - artificial neural networks 223–4
 - computer simulations 224–6
 - graph theoretical approach 222–3
 - group contribution methods 215–22
 - semi-crystalline polymers 101
 - Solution-Diffusion model 163
 - from sorption measurements 97
 - temperature dependence 31, 97
 - time-lag measurements 96–7
 - see also under* molecular simulation
- DREIDING force field 105, 126
- poly[1-(trimethylsilyl)-1-propyne] simulation 121–2, 123
- polyimide simulation 111, 113
- Dual-Mode model 96, 97, 99, 137
- Einstein equation 103
- electrochromic probes 205–6
- enthalpies
 - condensation 11, 12, 203
 - mixing 203
 - sorption 11, 12
 - vaporization 11
- ethanol *see* alcohol
- evaporation 358–9
- excess volume 100
- facilitated transport membranes
 - reviewed
 - active transport
 - electric field 419
 - modeling 400–4, 413–16
 - pH gradient 419
 - photon field 419–20
 - temperature effects 421
 - carbon dioxide separations 427
 - characteristics of membranes 412
 - complexing agents
 - Ag(I) 424–5
 - biological 428
 - Cu(I) trifluoro-methanesulfonate 426
 - incorporating into film 423
 - configurations for
 - membranes 416
 - fixed-site (chained-carrier) membranes 417–18
 - immobilized liquid membrane 417
 - solvent swollen polymer film 417
 - electrodynamic fluids
 - electrode requirements 423
 - nematic liquid crystals 422
 - polar solvents 422–3
 - experimental (time-lag) methods 412–13
 - hybrid processes 418
 - ionic liquids 421–2
 - modeling 400–4, 413–16
 - active transport 418–19
 - facilitation factor 414–16
 - fixed site-carrier membrane 401, 418
 - hybrid processes 418
 - screening for potential carriers 416
 - olefin/paraffin separation 404–5, 423–4
 - Ag(I) complexation 392–4, 424
 - Cu(I) trifluoro-methanesulfonate 426
 - effect of water on membrane performance 425
 - mechanistic studies 424
 - membrane morphology 424
 - organic compound separations 428–9
 - overview 391–2, 411–12
 - oxygen/nitrogen separation 405, 426–7
 - silver ion-polymer electrolyte membranes 425–6
 - stability 412, 416
 - effect of water 425
 - fixed-site carrier membranes 417
 - see also* solid-state facilitated transport membranes
- Fick's law 1, 72, 163, 187–8
- Flory-Huggins equation 18, 22
- fluoropolymers *see* perfluoropolymers
- force fields 50–2, 105
- free volume 99–102
 - accessible 61–4, 105, 123, 124
 - aging of membranes 297–8
 - blocking effects in polyacetylenes 242–3
 - computation methods 104–5
 - definitions defined and discussed 191, 192–3
 - and diffusion 16–17, 100–1
 - excess 100
 - fractional 16, 99–100, 193
 - and packing density 273
 - perfluoropolymer permeability 254, 259
 - polyacetylenes simulation 123–4
 - table of for selected polymers 99
 - temperature dependence 31, 100

- free volume elements
 (microcavities)
 defined 192
 and diffusion coefficient
 198–200
 sizes in polymers 195, 196,
 201
- glass transition temperature
 14
- hole number density 195–8
- measurement of 100
- electrochromic probes
 205–6
- inverse gas
 chromatography 196,
 201–4
- photochromic probes 205
- positron lifetime
 annihilation
 spectroscopy 191–9
- ^{129}Xe NMR methods 192,
 200–1
- molecular positronium probe
 simulation 124–5
- and permeability/selectivity
 6, 7
- polycarbonate simulation 109
- polymer/penetrant interaction
 energy 11
- size-sieving 12–14, 242–3
- specific 16, 100
- Gas Permeation Units (GPU) 3
- gas separation
 and aging of membranes 304
- carbon dioxide/methane 260,
 263–4, 281–4
- carbon dioxide/nitrogen
 285–7
- helium/hydrogen 254–5
- hydrocarbons using zeolite
 membranes 325–7
- hydrogen/methane 284, 287
- mechanism 337, 338
- multi-component transport
 membrane selectivity
 178–9
- pressure ratio limits and
 membrane choice
 179–82
- nitrogen/methane difficulties
 discussed 255–7
- olefins/paraffins 285, 392,
 404–5, 423–6
- one-component transport
 166–7
- transport equation 167
- oxygen/nitrogen 254, 284–5
- facilitated transport 405,
 426–7
- vapor/gas and polyacetylenes
 241–3
- vapor/vapor and
 polyacetylenes 243–4
- see also* selectivity
- gas and vapor properties
 effect on diffusivity 7–10
- effect on solubility 10–14
- properties tabulated 6, 11, 12
- glass transition temperature
 aging of membranes 295–8
- connector groups 35–6
- effects on permeability and
 diffusivity 14–15,
 31–5
- side-chains 36–7
- and penetrant size 12
- and solid-state facilitated
 transport membranes
 393–4
- variation of Langmuir
 capacity 21
- graph theory predictions 222–3
- GROMOS force field 105,
 126–7
- polyimide simulation 110–11
- group contribution methods
 assumptions 215
- atomic group units 217
- calculation of isothermal
 parameters 211, 218
- normalizing factors 215–18
- Permachor 215–16
- polyimides 218–25, 285
- Henry's law 20, 66–7, 96, 97,
 102
- hole number density 195–8
- hydrocarbons 6–7
- benzene/cyclohexane 365–8
- octane/trimethylpentane
 174–6
- olefin/paraffin separation
 392, 404–5, 423–6
- organic liquid/water 362–5
- Hyflon[®] *see under*
 perfluoropolymers
- hyperfiltration (reverse
 osmosis)
- multi-component transport
 173
- octane isomers 174–6
- salt solutions (seawater)
 176–8
- one-component transport
 163–6
- concentration-pressure
 relationships 164–6
- molar volume correction
 factor 166
- Solution-Diffusion
 equations 164
- inorganic membranes 307
- see also* zeolite membranes
- intersegmental spacing 101
- inverse gas chromatography
 201–2
- critical volume 203–4
- interpretation of results 196,
 202–4
- partial molar enthalpy of
 mixing 203
- ionization potentials 261–3
- jump events 31, 75–7, 97, 103,
 160
- kinetic diameter 5, 7–9
- propane *versus* butane 9–10
- related to diffusion
 coefficients 8
- tabulated 6
- Knudsen diffusion 337, 338
- Langmuir affinity parameter 18
- Langmuir capacity 18, 20–2,
 96, 100
- Langmuir diffusion coefficient
 97
- Lattice Fluid model *see* Non-
 equilibrium
 Thermodynamics
 Lattice Fluid model
- Leonard-Jones collision
 diameter 7–9
- tabulated 6
- Leonard-Jones energy
 parameter 10
- liquid/liquid separation *see*
 alcohol/water;
 organic liquids
- MELT program 194
- methane
 low-pressure solubility
 isotherms 144–8
- methane/butane separation
 242–3
- methane/hydrogen separation
 180–2

- microcavities
 defined 191
 and diffusion coefficient 198–200
 sizes in polymers 195, 196, 201, 202
- molecular diameter, effective 97, 214
- molecular dynamics *see under* molecular simulation
- molecular mobility 105
- molecular shape and size
 penetrants 7–10, 12–14, 21, 30–1
 effective molecular diameter 97, 214
 polymers 15–18, 30–40
 and shape anisotropy 9
 and zeolite pore size 373, 374, 384
 see also structure of polymers and transport
- molecular simulation
 approaches summarized 88–9, 101–6
 carbon dioxide in polyimide matrix 160
 cell construction and equilibration 105–6
 cell size 106
 choice of ensembles 106
 diffusivity
 anomalous diffusion 86–7
 diffusive jump events 31, 75–7, 97, 103, 160
 Greenfield–Theodoros multidimensional TST approach 80–6
 diffusivity calculation and macrostate networks 86
 geometric analysis of accessible volume 82
 rate constants for interstate transitions 84–5
 saddle points 82–4
 Gusev–Suter transition state method 77–80
 low-temperature matrices and infrequent jump events 75–7, 103
 molecular dynamics simulation and self-diffusivity 73, 102–3
- non-equilibrium molecular dynamics simulation 74–5, 103–4
- statistical mechanics of diffusion 72–3
- force fields 50–2, 105
- free volume 61–4, 82, 104
- d*-spacing 105
- molecular mobility 105
- pair correction functions 105
- and positron annihilation lifetime spectroscopy 62–4
- tesselation of space 104
- Voorintholt method 104
- model configurations
 coarse-graining strategies 54–5, 56
 force fields 50–2, 105
 generating glasses from melts 55–7
 molecular dynamics 52–3
 molecular mechanics 52
 Monte Carlo strategies 53–4
- model validation 57
- accessible volume 61–2
- molecular packing 58
- neutron diffraction 58–9
- X-ray diffraction 58
- positron annihilation lifetime spectroscopy 62–4
- segmental dynamics 59
- NMR measurements 59–60
- quasielastic neutron scattering 60–1
- thermodynamic properties
 cohesive energy 57–8
- mass density 57
- overview 87–9, 224–6
- permeability 97–9
- polymer studies 106–7
- poly[1-(trimethylsilyl)-1-propyne] 120–4
- poly(2,6-dimethyl-1,4-phenylene oxide) 109–10
- polycarbonates 108–9
- polyetherimide 107
- polyimides 110–14
- polyphosphazenes 114–16
- polysilalkylenes 119–20
- polysilanes 119–20
- polysiloxanes 116–19
- polysulfones 107–8
- Teflon[®] 123–4, 126
- self-diffusion coefficient 102–3
- solubility
 and cell size 106
 Henry's constant 66–7, 102
 Monte Carlo and TST simulations 102
- sorption equilibria
 predictions 64
 heat of sorption 67
 Henry's law constant 66–7
 high pressure sorption 68–70
 low pressure sorption 67–8
 sorption isotherms 65–7
 Widom insertion 66, 67, 68, 102
 resolving problems 70–2
- zeolite membranes 331–2
- see also* Non-equilibrium Thermodynamic LF model
- molecular size *see* molecular shape
- molecular volume 203–4, 216
- Monte Carlo method 101, 102
- poly[1-(trimethylsilyl)-1-propyne] 122–3
- polyphosphazene 115, 116
- polysilane simulation 119
- solubility coefficient
 calculation 66–7, 102
- strategies in molecular simulation 53–4
- natural gas 6
- enrichment 255
- Non-equilibrium Thermodynamic Lattice Fluid model
 assumptions, key 138–40
 calculations and comparisons for glassy polymers
 correlation of high-pressure solubility 153–5
 correlation of solubility coefficients 151–3
 predicting low pressure-gas solubility 144–8
 predicting low-pressure solubility coefficients 148–51
- discussion and conclusions 155–7
- overview 137–8

- parameters and data
 requirements 143–4,
 145, 146
 and perfluoropolymers 265
 pseudo-solubility calculation
 140–1
 olefin/paraffin separation 392,
 404–5, 423–6
 organic liquid mixtures 355
 acetone/chlorinated
 hydrocarbon
 separation 365
 alcohol/alcohol and alcohol/
 ether separations
 polymer membranes 381–3
 zeolite membranes
 329–30, 381–3
 alcohol/water separation
 185–7
 carbon membranes 351–2
 polyacetylenes 233, 244–5
 polymer membranes 287,
 359–62
 zeolite membranes
 329–30, 331, 374,
 377, 386–7
 benzene/cyclohexane/hexane
 separation
 polymeric membranes
 365–7
 zeolite membranes 329,
 382, 383–4
 ethanol/cyclohexane
 separation 365
 evaporation 358
 temperature-difference
 control 359
 liquid aliphatic hydrocarbons
 327–8
 olefin/paraffin separation
 404–5, 423–6
 organic liquid/water
 polymeric membranes
 362–4
 zeolite membranes 377,
 379, 381
 permeation equations 357–8,
 373–4
 pervaporation principles and
 characteristics 356–7,
 373–4
 Solution-Diffusion model
 357–8
 xylene isomer separation
 329, 384–5
 oxygen/nitrogen separation 254,
 284–5
 facilitated transport 392, 405,
 426–7
 packing density 273–4
 pair correlation functions 105
 PATIT program 194, 195
 penetrant diameter (size) 7–10
 correlation with diffusion
 coefficient 9–10
 and critical volume 13
 dependence of diffusion on 8,
 12–14, 30–1
 and glass transition
 temperature 12
 perfluoropolymers
 characteristics and discovery
 overview 251–2,
 266–7
 Cytop[®] 252
 gas solubility correlations
 257, 258–9
 plasticization 259–60
 pure gas permeabilities/
 selectivities 253, 254
 structure and properties
 253
 fluorocarbon/hydrocarbon
 interactions 260–1
 ionization potentials 261–3
 non-central force fields
 263–6
 solution theory 261
 helium/hydrogen selectivity
 254–5
 Hyflon[®] 252
 gas solubility correlations
 257, 258
 pure gas permeabilities/
 selectivities 253, 254
 structure and properties 253
 nitrogen/methane selectivity
 255–7
 nitrogen/oxygen selectivity
 254
 plasticization 257–9
 solubility correlations,
 atypical 257–9,
 260–1
 Teflon[®] 252
 gas solubility correlations
 257, 258
 molecular simulation
 123–4, 126
 pure gas permeabilities
 253, 254
 pure gas selectivities
 254
 structure and properties
 253
 permeability and permeability
 coefficient 99
 aging of membranes 298–9,
 301–2
 bulky trimethylsilyl groups
 32–3, 211–12, 232
 coefficient defined and
 described 1–3, 97,
 167
 computer simulations 224–6
 dual-mode model 99
 effect of glass transition
 temperature 14–15,
 31–5
 and effective solubility
 coefficient 2, 98
 and microcavities 202
 penetrant critical volume
 correlation 13
 perfluoropolymers 253
 polymer density and chain
 packing 15–16,
 32–5
 pressure dependency 22, 24
 structure-based prediction
 211–15
 artificial neural networks
 223–4
 graph theoretical approach
 222–3
 group contribution method
 215–22
 temperature dependence
 98–9
 units 3
see also selectivity
 permeability/selectivity
 trade-off 4–7
 facilitated transport
 membranes 391
 free volume effects 6,
 12–14
 and kinetic diameter 5–6
 perfluoropolymers 254–5
 polyimides 283–4
 size-sieving 12–14
 upper bound lines 4–6
 permance 3
 permeation
 activation energy 30,
 300–1
 measurements in zeolite
 membranes 321–3
 rate (flux) 1, 161, 274–5
 permselectivity *see* selectivity

- Perturbed-Hard-Sphere-Chain theory 137, 138, 141, 142–3
solubility calculations and data comparisons 144–56
- pervaporation
carbon membranes 351–2
evaporation 358–9, 385–6
fundamental equations 357
large scale manufacturing plants 386–7
multi-component transport
alcohol/water mix described 185–7
choice of permeation equations 182–4
pervaporation separation factors 184–5
one-component transport 167–70
flux and pressure 169–70, 171
pressure and concentration profiles 167–8
transport equations 169
principles and characteristics 356–7, 373–4
Solution-Diffusion model 357–8
see also alcohol/water; organic liquid mixtures; zeolite membranes
- photochromic probes 205
physical aging *see* aging
plasticization 259–60
poly[1-(trimethylsilyl)-1-propyne] 231, 232
aging of membrane 302–3
conformational studies 121
ethanol/water selectivity 361, 362
free volume representation 123, 201
molecular simulation 107, 120–4
pervaporation
alcohol/water 244–5
organic liquid/water 245–6
polymerization 234–6
prediction of transport properties 211, 212
selectivity
carbon dioxide/*iso*-propane 243
methane/butane 242–3
oxygen/nitrogen 241
vapor/vapor separations 243–4
size-sieving and reverse selectivity 14, 27, 242
solubility coefficients and temperature 10–11, 257
- poly(2,6-dimethyl-1,4-phenylene oxide) simulation 109–10
- polyacetylenes
desilylation of membranes 238, 240
gas/gas separation 239–41
oxygen/nitrogen selectivity 240–1
permeability and structure overview 231–3
poly[1-(trimethylgermyl)-1-propyne] and analogues 231–2, 236
polydiarylacetylenes 232, 240
polydiphenylacetylenes 232, 240
- pervaporation
alcohol/water 244–5
organic liquid/organic liquid 246
organic liquid/water 245–6
- polymerization 233
catalysts, typical 234–5
cocatalysts 235, 236
mono- and disubstituted acetylenes 233–4
poly[1-(trimethylsilyl)-1-propyne] and analogues 234–6
polydiarylacetylenes and derivatives 236–8
ring-substituted polyphenylacetylenes 238–9
solvent effects 235
temperature effects 235
size-sieving and reverse-selectivity 232–3, 242–3
vapor/gas separation 241
vapor/vapor separation 243–4
see also poly[1-(trimethylsilyl)-1-propyne]
- polycarbonates 108
free volume simulation 109
gas transfer simulations 108–9
low-pressure solubility isotherms of methane 144–8
side-group effects 33–5
- polydimethylsiloxane 107, 231
ethanol/water selectivity 361, 362
molecular simulation 116–19
size-sieving 14
solubility coefficients and temperature 10–11, 257
- polyetherimide simulation 107
- polyimides
acid dianhydride structures 272
effects of 281–2
aging of membrane 298–9
connector group effects 35–6
diamine structures 272
effects of 282–3
diffusion coefficients 275–6
controlling factors 277–80
gas separation performance 283
carbon dioxide/methane 281–4
carbon dioxide/nitrogen 285–7
hydrogen/methane 284, 287–8
olefins/paraffins 285
oxygen/nitrogen 284–5
water vapor permeation 287–8
- group contribution predictive method 218–25, 285
molecular simulation 110–14, 160
morphology effects 276–7
overview of structure and properties 271–3
packing density 273
charge-transfer interactions 273–4
- photocrosslinking 287
precursors for carbon membranes 337–43
selectivity 275, 277, 281–7
solubility coefficients 277–80
controlling factors 280–1
structure-property relationships 272
- polymer structure *see* structure of polymers

- Polymer-Reference Interaction Site Model (PRISM) 102
- polynorbornenes 36, 37
- polyphosphazenes simulation 114–16
- polysilalkylenes simulation 119–20
- polysilanes simulation 119–20
- polysiloxanes
permeability and glass transition temperature 31–2
simulation 116–19
- polysulfones
aging of membrane 298–9
molecular simulation 107–8
side-group effects 33–5
wide-angle X-ray diffraction 299–300
- polytetrafluoroethylene 252–3
see also perfluoropolymers
- polytrifluoropropyl-methylsiloxane 117
- poly(vinylidene fluoride) 252
- pore transport model 159–60
- positron annihilation lifetime spectroscopy (PALS) 191–2
- CONTIN program 194, 195, 196
- diffusion coefficient
correlated with hole size 198–9
- diffusion selectivity 198–200
- fractional free volume 193
- free volume definitions
defined and discussed 192–3
- free volume probing methods
tabulated 192
- hole number density
estimation 195–8
- MELT program 194
- molecular model validation 62–4
- PALS method outlined 193–4
- PATFIT program 194, 195
- positronium atoms and sources 193–4
- simulation of molecular positronium probe 124–5
- sizes of free volume in glassy polymers 195, 196
- spectral data and initial analysis 194–5, 196
- positronium atoms 191, 193–4
- pressure effects
diffusion 22, 23
permeability 22–30
sorption 18–22
transport parameters 18–30
- PRISM *see* Polymer-Reference Interaction Site Model
- radial distribution function 105
- rejection coefficient 177, 178
- reverse osmosis *see* hyperfiltration
- reverse-selectivity *see* selectivity
- seawater and reverse osmosis 176–8
- selectivity 3–7, 98
and aging of membrane 298–9
diffusion selectivity *versus* microcavity size 199–200
diffusion-solution model 175–6, 178–9, 255–6, 275
ethanol/water-selective polymers 362
mixed-gas *versus* pure-gas effects 24–30
nitrogen/methane separation difficulties discussed 255–7
perfluoropolymers
helium/hydrogen 254–5
nitrogen/methane 255–7
oxygen/nitrogen 254
- polyacetylenes
methane/butane 242–3
oxygen/nitrogen 240–1
vapor/vapor separation 243–4
- polyimides 275, 277, 281–5
- pressure effects 22–30, 175–6
- pressure ratio limits and membrane choice 179–82
- reverse selectivity 5, 6–7, 25–9, 232–3
- separation factor 3–4, 275
- size-sieving and reverse selectivity 5, 6–7, 12–14, 25–9, 232–3, 242
- structural effects predicted 212, 213–14
- zeolite membranes and hydrocarbons 325–9
- see also* gas separation
- selectivity/permeability trade-off *see* permeability/selectivity
- self-diffusion coefficient in MD simulation 73, 102–3
- semi-crystalline polymers 101
- separation factor 3, 216–17, 220
- separation mechanisms 337–8
- side-chains *see under* structure of polymers
- simulation *see* molecular simulation
- size-sieving polymers 5, 6–7, 12–14
perfluoropolymers 258
polyacetylenes 232–3, 242–3
- solid-state facilitated transport membranes 391–2
- mathematical models
concentration fluctuation 402–3
dual-sorption model 400–1
effective diffusion coefficient 401
hopping model *versus* concentration fluctuation model 403
limited mobility of chained carrier 401
- membrane stability 405–6, 407, 408
- olefin carrier properties 392
formation and structure of silver polymer electrolytes 392–4
olefin sorption in silver polymer electrolytes 394–5
reversible interaction of silver ions 395
- olefin/paraffin separation 392, 403–5
permeabilities and selectivities 405
- oxygen carrier properties 395
metalloporphyrin or Schiff's base complex 395–6
oxygen solubility and reversibility 396–7
reversible binding kinetics 397–8
- oxygen/nitrogen separation 392, 405

- solid-state (*Continued*)
 permeability and
 selectivity 407
 transport mechanisms
 threshold concentration
 and coordination
 number 398–400
 two-step of silver ions with
 olefins 398, 399
- solubility and solubility
 coefficient
 computational methods and
 simulation 66–7,
 101–2, 106
 defined 2
 Dual-Mode model and
 Henry's law
 coefficient 96, 97
 effect of gas properties
 10–14, 94
 effective 98
 and fractional free volume
 16–17
 gas and vapor in
 perfluoropolymers
 257–9
 penetrant critical volume
 correlations 13
 perfluoropolymers, atypical
 behavior of 257–9,
 260–1
 polyimides 275–6
 semi-crystalline polymers
 101
 solution theory 261
 Statistical-Associating-Fluid
 Theory 144–6
 temperature dependence
 10–11, 96, 214
see also Non-Equilibrium
 Thermodynamics
 Lattice Fluid model
- Solution-Diffusion model 1,
 159, 187–8
 carbon dioxide/polyimide
 MA simulation 160–1
 diffusion coefficient 2, 163
 driving force gradients
 illustrated 162
 Fick's law 1, 163, 187–8
 gas separation 166–7,
 178–9
 hyperfiltration (reverse
 osmosis) 163–6,
 173–8
 mathematical development
 161–3
- multi-component transport
 alcohol/water mix
 described 185–7
 choice of permeation
 equations 182–4
 octane isomers 174–6
 pervaporation separation
 factors 184–5
 pressure ratio limits and
 membrane choice
 179–82
 salt solutions (seawater)
 176–8
- one-component transport
 concentration-pressure
 relationships 164–6
 molar volume correction
 factor 166
 pervaporation flux and
 pressure 169–70,
 171
 pressure and concentration
 profiles 166, 167–8
 transport equations 164,
 167, 169
 pervaporation 167–71,
 184–7, 357–8
 pore flow model 159–60,
 161–2
 unified view of separation
 processes 171–3, 174
- sorption
 and condensability 276
 diffusion coefficient from 97
 Dual-Mode model 96
 enthalpy of 11, 12
 isotherms 18–22
 Langmuir capacity 18, 20–2,
 96, 100
 molecular simulation 64–70
 olefin in silver polymer
 electrolytes 394–5
 thermodynamics 64–72
- Statistical-Associating-Fluid
 Theory 137, 141, 142
- solubility calculations and
 comparison with data
 144–56
- structural relaxation *see*
 physical aging
- structure of polymers and
 transport
 bulky trimethylsilyl groups
 32–3, 211–12, 232,
 237–8
- chemical and structural
 design 355–6
- cis* and *trans* configurations
 37–8, 211
 connector groups 35–6, 211
 fluorination 36–7, 214
 glass transition temperature
 30–5
isotactic configurations 211
 methyl and *t*-butyl groups
 213–14, 232, 237
 packing density 273–4
para and *meta* linkages 37,
 211, 282–3
 polar groups 33, 214
 polar and hydrogen bonding
 side-chains 36, 37, 38
 polycarbonates, substituted
 33–5
 polyimides 272, 281–3
 polysulfones 33–5
 predictive methods 211–15
 artificial neural networks
 223–4
 computer simulations
 224–6
 graph theoretical approach
 222–3
 group contribution
 methods 215–22
- Tangent-Hard-Sphere-Chain
 model 138, 142–3
- Teflon[®] *see under*
 perfluoropolymers
- temperature
 effects on transport
 parameters 30–1
 and solubility coefficients
 10–11
- thermodynamic model *see* Non-
 equilibrium
 Thermodynamic
 Lattice Fluid model
- time-lag measurements and
 diffusion coefficients
 96–7
- Transition-State Theory 101–2
 and fractional accessible free
 volume 124
- Greenfield–Theodorou
 multidimensional
 approach 80–6
- Gusev–Suter method 77–80
- Henry's constant
 determination 102
 polyimide simulation 112–13
 polysilane simulation 119
 polysiloxane simulation 118

- trimethylsilyl groups 32–3,
 211–12, 232,
 237–8
 TRIPOS force field 114
 United Atom model 51, 105
 van de Waals volume 10
 vapor/gas separation 241–4
 vapor/vapor separation 243–4
 vectorial autocorrelation
 function 103, 105
 Voorintholt method 104
 Voronoi tessellation 104
 water vapor permeation 287–8
 Widom particle insertion
 overcoming problems 70–2
 sorption equilibria 66, 67, 68,
 102
¹²⁹Xe NMR methods 192,
 200–1
 zeolite membranes
 A-type membrane
 morphology 376–7
 permeation and
 pervaporation
 performance 374,
 377–8
 preparation and conditions
 315–16, 375–6
 effects on performance
 377–8
 seeding 316, 376
 water/organic liquid
 separation 374,
 377–8
 characterization of zeolite
 films 316
 electron micrographs
 318–19, 376, 377,
 378, 380
 gas adsorption isotherms
 319–20
 orientation 317
 X-ray analysis 316–17
 Faujasite 379
 hydrophilic membranes
 374–8
 membrane defects 320–1
 MFI membrane preparation
 309–10, 379–81
 calcination and crack
 formation 314,
 380
 crystal growth and nucleation
 310, 314, 380
 factors affecting membrane
 growth 315
 seeding 314–15, 380
 support materials,
 preparation and
 effects 312–13
 synthesis mixture 310–12
 true and colloidal solutions
 309–10
 Mordenite 379
 morphology
 A-type 376–7
 MFI 380
 T-type 378
 organophilic membranes 379–
 81
 overview 307–9, 332–3, 373–4,
 387–8
 selectivities, permeances
 and separation factors
 308
 permeation
 hydrocarbon gases 325–7
 measurement techniques
 321–3
 small molecules 323–5
 pervaporation
 alcohol-water mixtures
 329–30, 331,
 386–7
 alcohol/ether separation
 381–3
 aromatic/non-aromatic
 separation 383–4
 integrated systems and
 esterification
 385–6
 ketone-water mixtures
 329–31
 large scale manufacturing
 plants 386–7
 liquid hydrocarbon
 separations
 327–9
 membrane performance
 compared 374, 377,
 379, 381, 382
 pore geometry and elemental
 composition 308–9
 pore size and molecular
 diameters 373, 374,
 384
 potential applications 308,
 373
 T-type membranes 375–6,
 378–9
 tetrapropylammonium ion
 310–11, 380
 theory and modeling of
 transport in
 membranes
 331–2
 X-type membranes 379
 preparation 375–6
 xylene isomer separation
 384–5
 Y-type membranes 316,
 375–6
 ZSM-5 membranes 380–1

With thanks to W. F. Farrington for creation of this index.